JAERI-Tech
2003-005

JP0350070

IFMIF-KEP
INTERNATIONAL FUSION MATERIALS IRRADIATION FACILITY
KEY ELEMENT TECHNOLOGY PHASE REPORT

March 2003

IFMIF International Team

日本原子力研究所
Japan Atomic Energy Research Institute

本レポートは，日本原子力研究所が不定期に公刊している研究報告書です。
入手の問合わせは，日本原子力研究所研究情報部研究情報課（〒319-1195　茨城県那珂郡東海村）あて，お申し越しください。なお，このほかに財団法人原子力弘済会資料センター（〒319-1195　茨城県那珂郡東海村日本原子力研究所内）で複写による実費頒布をおこなっております。

This report is issued irregularly.
Inquiries about availability of the reports should be addressed to Research Information Division, Department of Intellectual Resources, Japan Atomic Energy Research Institute, Tokai-mura, Naka-gun, Ibaraki-ken, 319-1195, Japan.

© Japan Atomic Energy Research Institute, 2003

編集兼発行　　日本原子力研究所

JAERI-Tech 2003-005

IFMIF - KEP
International Fusion Materials Irradiation Facility
Key Element Technology Phase
Report

IFMIF International Team

Department of Fusion Engineering Research
(Tokai Site)
Naka Fusion Research Establishment
Japan Atomic Energy Research Institute
Tokai-mura, Naka-gun, Ibaraki-ken

(Received January 23, 2003)

The International Fusion Materials Irradiation Facility (IFMIF) is an accelerator-based D-Li neutron source designed to produce an intense neutron field that will simulate the neutron environment of a D-T fusion reactor. IFMIF will provide a neutron flux equivalent to 2 MW/m^2, 20 dpa/y in Fe, in a volume of 500 cm^3 and will be used in the development and qualification of materials for fusion systems. The design activities of IFMIF are performed under an IEA collaboration which began in 1995. In 2000, a three-year Key Element Technology Phase (KEP) of IFMIF was undertaken to reduce the key technology risk factors. This KEP report describes the results of the three-year KEP activities in the major project areas of accelerator, target, test facilities and design integration.

Keywords: IFMIF, Fusion Materials, Neutron Source, Irradiation Facility, Task Report, Key Element Technology Phase

---

Edited by H.Nakamura, M.Ida, M.Sugimoto, M.Takeda, T.Yutani, and H.Takeuchi;
members of the JAERI Office of Fusion Materials Research Promotion.

国際核融合材料照射施設(IFMIF)要素技術確証フェーズ報告書

日本原子力研究所那珂研究所核融合工学部
IFMIF国際チーム

(2003年1月23日受理)

国際核融合材料照射施設(IFMIF)活動は1995年からIEA協力で国際的に実施されている。IFMIFは加速器を用いた重陽子-リチウム(Li)中性子源であり、核融合の候補材料の試験のため、強力な中性子場(2MW/m^2、鉄に対して20dpa/年)を発生する。IFMIFの重要要素の技術リスク低減のため、3年間の要素技術確証フェーズ(KEP)が2000年に開始された。KEPでは、電流250mAでエネルギー40MeVの高出力重陽子(D^+)加速器、体積9m^3の液体Liを循環するLiループ、温度制御された照射試験施設、照射後試験(PIE)施設およびその他の施設を運転するのに必要なIFMIF建屋およびユーティリティのシステム設計も実施された。本報告書では、3年間に実施した加速器、ターゲット、テストセル、設計統合の活動結果について記載した。

本報告書は、核融合炉材料開発推進室の以下のメンバーにより、編集された。
中村博雄、井田瑞穂、杉本昌義、竹田将夫、湯谷順明、竹内　浩
那珂研究所(東海駐在):〒319-1195　茨城県那珂郡東海村白方白根2-4

Contents

Preface 4
Executive Summary 5
1. Introduction 17
2. Outline of KEP Report 21
3. Results of KEP Activities 25
3.1 Accelerator Facilities 25
3.1.1 Accelerator Facilities 25
3.1.2 AC11A-EU : Very Long Test of the ECR Ion Source 30
3.1.3 AC11B-EU : Long-run Test of the Multi-cusp Ion Source 35
3.1.4 AC11C-JA : Test of ECR and Multi-cusp Type Ion Sources 39
3.1.5 AC12A/13A/14-EU : ECR Source Analyses 47
3.1.6 AC12B-EU : Ion Source Analysis 54
3.1.7 AC13B-EU : Low Energy Beam Transport 58
3.1.8 AC13C-JA : Test of Low Energy Beam Transport 65
3.1.9 AC34B-JA : Examination of Beam Matching to RFQ 69
3.1.10 AC20-US : Equipartitioned RFQ Beam Dynamics Design 72
3.1.11 AC34A-EU : RFQ Tuning Method, Electric Field Optimization on Cold Model 79
3.1.12 AC36-EU : Drift Tube Linac R&D Studies 83
3.1.13 AC37-US : Engineering Evaluation of the Drift Tube at 5 MeV 88
3.1.14 AC32-JA : Examination of the Drift Tube Cooling Scheme 97
3.1.15 AC33B-EU : Choice of RFQ Structure, Development of the 4-rod RFQ 101
3.1.16 AC35-EU : Choice of DTL Structure, and Investigation of CH-DTL 106
3.1.17 AC21C-US : Analysis of the Revised IFMIF High Energy Beam Transport System 114
3.1.18 AC33A/38-EU : End-to-end Beam Dynamics 118
3.1.19 AC21A-EU : Radio Frequency System 123
3.1.20 AC21B-JA : RF Power Tube Durability Test 126
3.1.21 AC22A-JA : Test of the RF Window 131
3.1.22 AC41A-EU : Diagnostics for High Power Beams 135
3.1.23 AC41B-EU : Diagnostics for High Power Beams 140
3.1.24 AC39-JA : Activation of Accelerator System Components 145
3.1.25 AC31-JA : Estimation of Beam Loss at Various Operating Conditions 150
3.1.26 AC22B-US : Cost Evaluation of Changes in the System Including the Revised HEBT and the Diacrode Based RF System 155
3.1.27 AC23-US : Examination of the Cost of a Fully Operational IFMIF Prototype 162

3.2 Target Facilities 169
3.2.1 TG11A-EU : Water Experiment at the Joint of the Replaceable Back-plate 169
3.2.2 TG11B-JA : Examination of the Lithium Target Free Surface Behavior under Low Pressure 177
3.2.3 TG12A-EU : Jet Flow Stability Analysis 182
3.2.4 TG12B-JA : Design of the Lithium Test Loop 188
3.2.5 TG12C-RF : Status and Plans for Water and Lithium Experiments 192
3.2.6 TG13-JA : Modification and Verification of an Existing Lithium Loop 198
3.2.7 **TG15-EU : Support of Japanese Tests for Cavitation Conditions at EMP and at the Joint of the Replaceable Backplate** 206
3.2.8 TG16-JA : Cavitation Verification in a Small Li Loop 212
3.2.9 TG21-JA : Measurement of Stainless Steel Erosion/Corrosion in a Li Loop 218
3.2.10 TG22/31A-EU : Lithium Corrosion and Chemistry 223
3.2.11 TG31B-JA : Control of Nitrogen Impurity in Lithium by Hot Trapping 230
3.2.12 TG33-JA : Diagnostic System for Target Temperature 237
3.2.13 TG35-JA : Design and Test of a Jet Thickness Monitor 245
3.2.14 TG37-JA : Design of a Target Distortion Monitor 248
3.2.15 TG51/52-JA : Collection of Li Reaction Data, and Characteristics and Suppression of Lithium Fires 252
3.2.16 TG61A/71-EU : Lithium Target Safety Analysis and Thermal Transient Analysis of Target Lithium Loop 258
3.2.17 TG61B-JA : Transient Behavior of the Lithium Loop 269
3.2.18 TG81-JA : Design of a Remote Handling Device for Target Back Wall Replacement 273
3.2.19 TG82-EU : Detailed Design, Fabrication and Remote Handling Test of the Removable Back-plate 279
3.3 Test Facilities 285
3.3.1 TF11/12-EU : He-cooled High Flux Test Module - Design Improvement, Fabrication of Sub-assembly and Thermal Hydraulics Testing 285
3.3.2 TF21-JA : Neutron Spectrum and ^{7}Be Production in Li(d,n) Reactions at 25 and 40 MeV 295
3.3.3 TF22-JA : Analysis of Asymmetry in the Neutron Irradiation Field 300
3.3.4 TF23/24-EU : Performance Improvement of the Medium Flux Test Module by Neutronics Calculations and Revised Design 307
3.3.5 TF31-JA : Vertical Test Assembles 315
3.3.6 TF33-EU : Development of Micro-tomography System 321
3.3.7 TF34-JA : Tritium Laboratory and Tritium Processing 327
3.3.8 TF35-JA : Arrangement of the Test Cell System 333
3.3.9 TF36-JA : Transfer of Heavy Equipment – Examination of Universal Robot System 339
3.3.10 TF38-JA : Operation Methods for Off/Normal Conditions of IFMIF 344

3.3.11 TF39-JA : Feasibility Study of the Gas Cooled High Flux Test Module 348
3.3.12 TF41-JA : Optimization of Staged Construction 359
3.3.13 TF42-JA : PIE Facility 366
3.3.14 TF51-EU : D-Li Reaction Source Term - Data Evaluation and Code Development 370
3.3.15 TF52-EU : D-Li Reaction Source Term - Experimental Verification of Neutron Yield 375
3.3.16 TF53-JA : Reliability Study of the Activation Cross Section Library 383
3.3.17 TF54-EU : Evaluation of Neutron Cross-section Data in the 20-50 MeV Range - Intermediate Energy Activation File 389
3.3.18 TF55-EU : Neutron Data above 20 MeV - Neutron Transport Benchmark Tests 395
3.3.19 TF56-EU : Nuclear Safety and Shielding 401
3.3.20 TF57/58-EU : Sub-miniature Fission Chambers - Development, Construction and Experimental Tests 408
3.3.21 TF61-EU : Re-calculation of Nuclear Response for Different Beam Footprints 419
3.3.22 TF62-JA : Review of the Concept for Materials Testing in IFMIF 428
3.3.23 TF63-JA : Small Specimen Test Technology - Development of Fracture Toughness Testing with Miniaturized Specimens 433
3.3.24 TF64-EU : SSTT - Fracture Toughness Specimen Development 443
3.4 Design Integration 449
3.4.1 DI11-JA : Diagnostics for the Spatial Distribution of Neutrons 449
3.4.2 DI21-JA : Selection of Elements Having Large Cross Section for Activation 453
3.4.3 DI41-JA : Design of Buildings 459
3.4.4 DI43-JA : Design of Utilities 467
3.4.5 DI51-JA : Examination of Central Control and Common Instruments 477
3.4.6 DI61-JA : Check of Consistency and Analysis of Operations Flow in IFMIF 481
3.4.7 DI71-JA : Verification of the Design of Radiation Shielding 486
3.4.8 DI81-JA : RAM Analysis for the Rationalized IFMIF Design 493
3.4.9 DI83A-EU : Safety Analysis and Assessment 500
3.4.10 DI83B-JA : Safety Assessment for Two-stage IFMIF 508
3.4.11 DI85-EU : Safety Analysis and Assessment - Occupational Radiation Exposure 512
3.4.12 DI91-JA : Examination of Licensing and Regulations 523
3.4.13 DI93-JA : Analysis of the Schedule and Future Plans of the IFMIF Project .. 533
3.4.14 DI95-JA : Cost Estimation 540

4. Summary 549
Acknowledgements 551
Appendix-A. Detailed list of development in KEP 552
Appendix-B. Acronyms 558

目 次

前書き…… 4
全体概要…… 5
1. 序論…… 17
2. KEP 報告書の概要…… 21
3. KEP 活動の結果…… 25
3.1 加速器系…… 25
3.1.1 加速器系…… 25
3.1.2 AC11A-EU : ECR イオン源の長期間試験…… 30
3.1.3 AC11B-EU : マルチカスプイオン源の長時間運転試験…… 35
3.1.4 AC11C-JA : ECR とマルチカスプ型イオン源の試験…… 39
3.1.5 AC12A/13A/14-EU : ECR イオン源の解析…… 47
3.1.6 AC12B-EU : イオン源の解析…… 54
3.1.7 AC13B-EU : 低エネルギービーム輸送…… 58
3.1.8 AC13C-JA : 低エネルギービーム輸送の試験…… 65
3.1.9 AC34B-JA : RFQ へのビームマッチングの検討…… 69
3.1.10 AC20-US : エネルギー等分配則に基づく RFQ のビームダイナミックス設計…… 72
3.1.11 AC34A-EU : RFQ コールドモデルの電場特性の最適化…… 79
3.1.12 AC36-EU : ドリフトチューブリニアックの研究開発…… 83
3.1.13 AC35-US : 5 MeV ドリフトチューブの工学技術評価…… 88
3.1.14 AC32-JA : ドリフトチューブ冷却方式の検討…… 97
3.1.15 AC33B-EU : RFQ 構造の選択、4 ロッド RFQ の開発…… 101
3.1.16 AC35-EU : DTL 構造の選択、 CH-DTL の研究…… 106
3.1.17 AC21C-US : 改訂された IFMIF 高エネルギービーム輸送系の解析…… 114
3.1.18 AC33A/38-EU : 連結ビームダイナミックス…… 118
3.1.19 AC21A-EU : 高周波システム…… 123
3.1.20 AC21B-JA : 高周波出力管耐久試験…… 126
3.1.21 AC22A-JA : 高周波窓試験…… 131
3.1.22 AC41A-EU : 大出力ビームの診断…… 135
3.1.23 AC41B-EU : 大出力ビームの診断…… 140
3.1.24 AC39-JA : 加速器系要素の放射化…… 145
3.1.25 AC31-JA : 各種運転条件でのビームロス評価…… 150
3.1.26 AC22B-US : 改訂された高エネルギービーム輸送系とダイアクロードを用いた高周波システムを取り入れたコスト評価…… 155
3.1.27 AC23-US : IFMIF プロトタイプ定格運転のコスト検討…… 162

3.2 ターゲット系 169
3.2.1 TG11A-EU：交換可能型背面壁の締結部模擬の水実験 169
3.2.2 TG11B-JA：減圧条件における液体リチウム自由表面挙動の評価 177
3.2.3 TG12A-EU：リチウムジェットの安定性解析 182
3.2.4 TG12B-JA：工学実証用の液体リチウム試験ループの設計 188
3.2.5 TG12C-RF：水およびリチウム実験の現状と計画 192
3.2.6 TG13-JA：既存リチウムループの改造と試験 198
3.2.7 TG15-EU：電磁ポンプと背面壁結合部のキャビテーション評価のための日本の試験への参加 206
3.2.8 TG16-JA：リチウムループにおけるキャビテーション評価 212
3.2.9 TG21-JA：リチウムループのステンレス鋼の腐食損耗の測定 218
3.2.10 TG22/31A-EU：リチウムによる腐食と化学 223
3.2.11 TG31B-JA：ホットトラップによるリチウム中窒素不純物の制御 230
3.2.12 TG33-JA：ターゲット温度の計測 237
3.2.13 TG35-JA：リチウムジェット厚さ計の設計と試験 245
3.2.14 TG37-JA：ターゲットの変位計の設計 248
3.2.15 TG51/52-JA：リチウム反応データの収集とリチウム火災の特性・消火 252
3.2.16 TG61A/71-EU：リチウムターゲットの安全解析とリチウムループの過渡解析 258
3.2.17 TG61B-JA：リチウムループの過渡解析 269
3.2.18 TG81-JA：ターゲット背面壁交換のための遠隔操作装置の設計 273
3.2.19 TG82-EU：交換可能型背面壁の設計、製作と遠隔操作試験 279
3.3 テストセル系 285
3.3.1 TF11/12-EU：He 冷却型高中性子束テストモジュール － 改良設計、サブアセンブリの製作および熱流動試験 285
3.3.2 TF21-JA：25 および 40 MeV における Li(d,n) 反応の中性子スペクトルと 7Be 生成 295
3.3.3 TF22-JA：中性子照射場の非対称性の解析 300
3.3.4 TF23/24-EU：核計算による中間中性子束テストモジュールの性能向上と改良設計 307
3.3.5 TF31-JA：垂直型テストアセンブリ 315
3.3.6 TF33-EU：マイクロトモグラフ・システムの開発 321
3.3.7 TF34-JA：トリチウム実験室とトリチウム処理 327
3.3.8 TF35-JA：テストセル・システムの配置 333
3.3.9 TF36-JA：重量機器の移送－ユニバーサルロボット・システムの調査 339
3.3.10 TF38-JA：IFMIF の定常時/非定常時の運転方法 344
3.3.11 TF39-JA：ガス冷却型高中性子束テストモジュールの温度制御に関する研究 348

3.3.12 TF41-JA：段階的建設の最適化 ····· 359
3.3.13 TF42-JA：照射後試験施設 ····· 366
3.3.14 TF51-EU：D-Li 反応ソースターム－データ評価とコード開発 ····· 370
3.3.15 TF52-EU：D-Li 反応ソースターム－ 中性子収率の実験的検証 ····· 375
3.3.16 TF53-JA：放射化断面積ライブラリーの信頼性研究 ····· 383
3.3.17 TF54-EU：20～50 MeV 領域の中性子反応断面積データの評価－中間エネルギー放射化断面積ファイル ····· 389
3.3.18 TF55-EU：20 MeV 以上の中性子データ－中性子輸送ベンチマーク試験 ····· 395
3.3.19 TF56-EU：核安全性と遮蔽 ····· 401
3.3.20 TF57/58-EU：小型核分裂電離箱－開発、製作および実験 ····· 408
3.3.21 TF61-EU：種々のフットプリントの核レスポンスの再計算 ····· 419
3.3.22 TF62-JA：IFMIF における材料試験概念のレビュー ····· 428
3.3.23 TF63-JA：微小試験片技術－微小試験片による破壊靱性試験法の開発 ····· 433
3.3.24 TF64-EU：微小試験片技術－破壊靱性試験片の開発 ····· 443
3.4 設計統合 ····· 449
3.4.1 DI11-JA：中性子空間分布の計測 ····· 449
3.4.2 DI21-JA：大きな放射化断面積を有する核種の選定 ····· 453
3.4.3 DI41-JA：建家の設計 ····· 459
3.4.4 DI43-JA：共通設備の設計 ····· 467
3.4.5 DI51-JA：中央制御設備の検討 ····· 477
3.4.6 DI61-JA：IFMIF 全システムの運転フローの一貫性検査と解析 ····· 481
3.4.7 DI71-JA：放射線遮蔽設計の実証 ····· 486
3.4.8 DI81-JA：合理化設計 IFMIF の RAM 解析 ····· 493
3.4.9 DI83A-EU：安全解析と評価 ····· 500
3.4.10 DI83B-JA：２段階 IFMIF の安全性評価 ····· 508
3.4.11 DI85-EU：安全解析と評価-作業者被曝 ····· 512
3.4.12 DI91-JA：許認可と規制法令の検討 ····· 523
3.4.13 DI93-JA：IFMIF 計画のスケジュールと将来計画の分析 ····· 533
3.4.14 DI95-JA：コスト評価 ····· 540
4. まとめ ····· 549
謝辞 ····· 551
付録-A. 要素技術確証タスクリスト ····· 552
付録-B. 略語集 ····· 558

This is a blank page.

IFMIF - KEP

International Fusion Materials Irradiation Facility

Key Element Technology Phase

Report

IFMIF International Team

An activity of:
The International Energy Agency (IEA)
Implementing Agreement for a Programme of Research and Development on Fusion Materials

IFMIF International Team

Design Leader
Shannon T.E.(University of Tennessee, US)

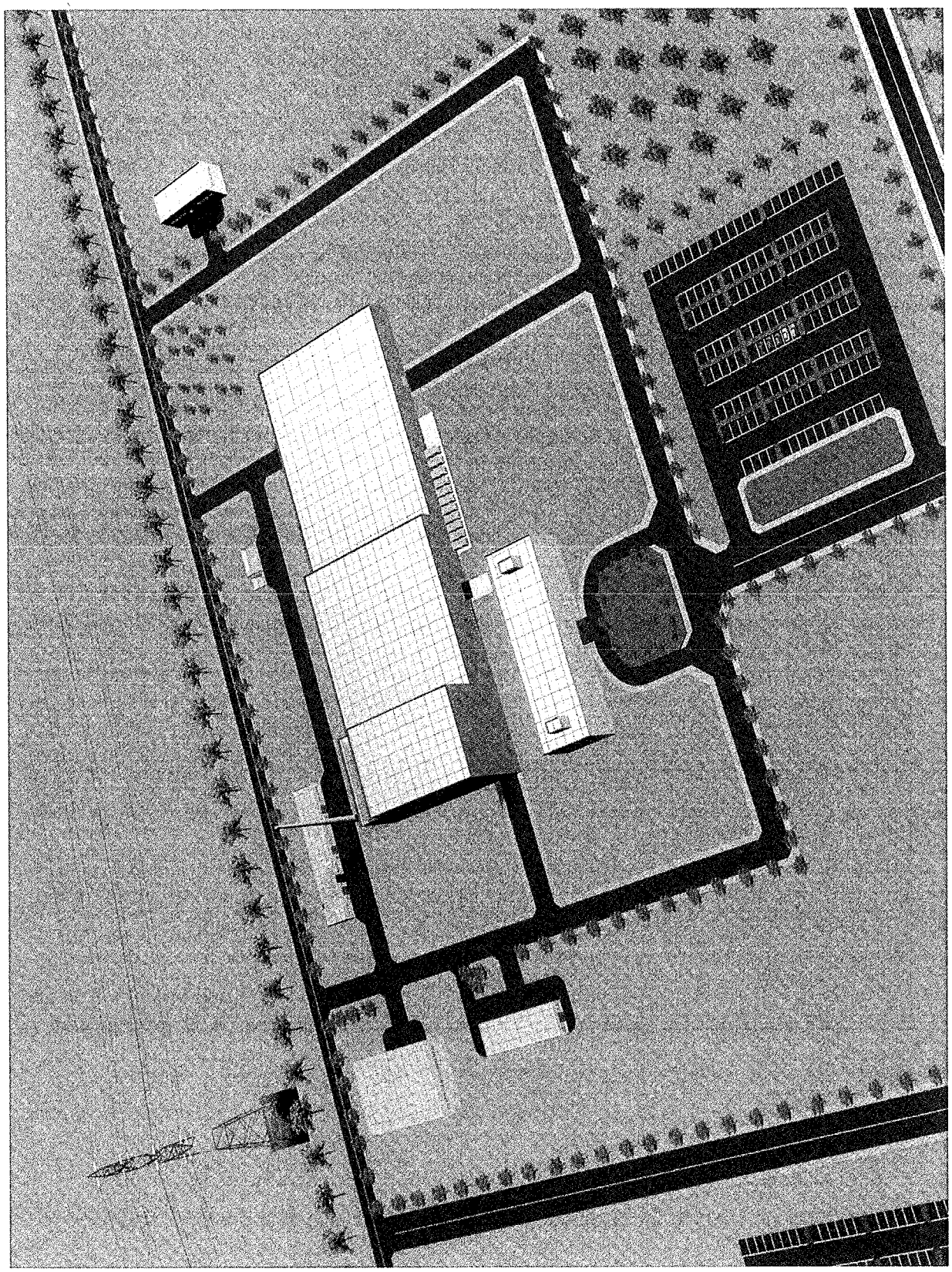
Design Integration Group
Takeuchi H.* (JAERI, JA), Burgazzi L.(ENEA, EU), Ida M.(JAERI, JA), Natalizio A. (ENSAC, EU), Pinna T. (ENEA, EU), Riccardi B.(ENEA, EU), Sugimoto M. (JAERI, JA), Takeda M.(JAERI,JA), Yutani T. (JAERI, JA)

Test Facility Group
Möslang A. *(FZK, EU), Angelone M. (ENEA, EU), Baba M. (Tohoku Univ., JA), Bém P. (NPI-Rez, EU), Blandin C. (CEA-Cadarache, EU), Bonade R. (CRPP, EU), Burjan V. (NPI-Rez, EU), Cambi G. (Bologna Univ., EU), Cepraga D.G. (ENEA, EU), Ebara S. (Kyushu Univ., JA), Esposito B. (ENEA, EU), Fischer U. (FZK, EU), Frisoni M. (Athena s.a.s., EU), Gordeev S. (FZK, EU), Götz M. (NPI, EU), Hagiwara M. (Tohoku Univ., JA), Heinzel V. (FZK, EU), Hudelot J.P. (CEA-Cadarache, EU), Jitsukawa S. (JAERI, JA), Kasada R. (Kyoto Univ., JA), Kato Y. (Kyoto Univ., JA), Kimura A. (Kyoto Univ., JA), Kohno Y. (Muroran Inst. Tech. JA), Konobeyev A. Yu. (INPE, RF), Korovin Yu. A. (INPE, RF), Kroha V. (NPI-Rez, EU), Kubo H. (Kyoto Univ., JA), Kurishita H. (Tohoku Univ., JA), Matsui H. (Tohoku Univ., JA) Möllendorff U. v. (FZK, EU), Morishita K. (Kyoto Univ., JA), Muroga T. (NIFS, JA), Nagasaka T. (NIFS, JA), Nakamura H. (JAERI, JA), Narui M. (Tohoku Univ., JA), Nishimura A. (NIFS, JA), Novák J. (NPI-Rez, EU), Pensa A. (ENEA, EU), Pereslavtsev P. E. (INPE/FZK, RF), Serizawa H. (Osaka Univ., JA), Shiba K. (JAERI, JA), Shimizu A. (Kyushu Univ., JA), Simakov S.P. (FZK, EU), Simecková E. (NPI-Rez, EU), Spätig P. (CRPP, EU), Stursa J. (NPI-Rez, EU), Sugimoto M. (JAERI, JA), Tiseanu I. (NILPRP, EU), Vesely F. (NPI-Rez, EU), Vincour J. (NPI, EU), Vladimirov P. (FZK, EU), Watanabe Y. (Kyushu Univ, JA), Wilson P. P. H. (UW/FZK, EU), Yamamoto T. (Tohoku Univ. JA), Yokomine T. (Kyushu Univ., JA), Yonemoto Y. (Kyushu Univ., JA), Yutani T. (JAERI, JA)

Accelerator Group
Jameson R.A.*(LANL, US), Ausset P.(CEA-Saclay, EU), Bechthold A.(IAP, EU), Beller P.(IAP, EU), Bernaudin P-E.(CEA-Saclay, EU), Deitinghoff H.(IAP, EU), Duperrier R.(CEA-Saclay, EU), Ferdinand R. (CEA-Saclay, EU), France A.(CEA-Saclay, EU), Fujii T.(JAERI, JA), Gobin R.(CEA-Saclay, EU), Hollinger R.(IAP, EU), Iga T.(JAERI, JA), Imai T.(JAERI, JA), Jakob A.(IAP, EU), Klein H.(IAP, EU), Liebermann H.(IAP, EU), Maaser A.(IAP, EU), Maebara S.(JAERI, JA), Margoto E.(THALES Electron devices, EU), Meusel O.(IAP, EU), Morishita T.(JAERI, JA), Moriyama S.(JAERI, JA), Myers T.(AES, US), Podlech H.(IAP, EU), Pozimski J.(IAP, EU), Rathke J.(AES, US), Ratzinger U.(IAP, EU), Saigusa M.(Ibaraki Univ. , JA), Sauer, A.(IAP, EU), Sazawa S.(Ibaraki Univ. , JA), Schempp A.(IAP, EU), Schultheiss T.(AES, US), Simoens F.(CEA-Saclay, EU), Sredniawski J.(AES, US), Sugimoto M.(JAERI, JA), Tiede R.(IAP, EU), Todd A.(AES, US), Uriot D.(CEA-Saclay, EU), Volk K.(IAP, EU), Watanabe K.(JAERI, JA), Weber M.(IAP, EU)

Target Group
Nakamura Hiroo*(JAERI, JA), Aksyonov J.(IPPE, RF), Ara K.(JNC, JA), Arnol'dov M. (IPPE, RF), Bailey A.(ENEA/University of Nottingham, EU), Berensky L.(IPPE, RF), Burgazzi L. (ENEA, EU), Cevolani S.(ENEA, EU), Chernov V.(IPPE, RF), Dell' Orco G. (ENEA, EU), Ezato K.(JAERI, JA), Fazio C. (ENEA, EU), Fedotovsky V.(IPPE, RF), Giusti D.(ENEA, EU), Hirabayashi M.(JNC,JA), Horiike H.(Osaka Univ. , JA), Ida M.(JAERI, JA), Iida T.(Osaka Univ. , JA), Inoue S. (Osaka Univ. , JA), Ise H.(KHI, JA), Kakui H.(IHI Co., Ltd. , JA), Kurosaki K.(Osaka Univ. , JA), Loginov N.(IPPE, RF), Matsui H. (Tohoku Univ., JA), Matsushita I.(Shinryoh High Tech. Ltd. , JA), Miccichè G.(ENEA), Mikheyev A.(IPPE, RF), Miyamoto S.(Osaka Univ. , JA), Miyazaki K. (Osaka Univ. , JA), Morozov V.(IPPE, RF), Muroga T.(NIFS, JA), Nakamura Hideo(JAERI, JA), Nakamura Hiroshi(JST, JA), Riccardi B.(ENEA, EU), Scaddozzo G.(ENEA/Politecnico di Torino, EU), Shimizu K.(MHI, JA), Shishulin V.(IPPE, RF), Suzuki A.(NIFS, JA), Tanaka S.(Univ. Tokyo, JA), Terai T.(Univ. Tokyo, JA), Tinti R.(ENEA, EU), Uda N.(Osaka Univ. , JA), Yamamura T.(IHI Co., Ltd. , JA), Yamaoka N. (Osaka Univ. , JA), Yoneoka T.(Univ. Tokyo, JA)

***Group Leader**



Artist's view of IFMIF site

Preface

The start of government-level international negotiations for construction of ITER, the International Thermonuclear Experimental Reactor, indicates that the world's fusion programs have entered a new era. The emphasis now is on fusion power development rather than on fundamental research on plasma physics. It is also recognized that low activation materials for fusion reactors have to be developed in parallel with plasma confinement technology. While the plasma technologies can be pursued mainly in ITER, fusion materials development requires higher neutron fluences than will be achieved during the ITER lifetime. For fusion materials testing in the absence of a fusion reactor, IFMIF, the International Fusion Materials Irradiation Facility, has been identified as the most appropriate machine to provide a fusion relevant neutron environment. The IFMIF conceptual design has been developed as a joint international program under the auspices of the IEA Implementing Agreement on Fusion Materials. The European Union, Japan, the Russian Federation, and the United States are currently participating in this activity on a voluntary basis. Very substantial accomplishments have been made through coordinated task sharing among the participating parties.

IFMIF would fill several roles in fusion power development. These include: a) Contributing to the engineering database on fusion materials required for the design and licensing of a fusion DEMO, the Demonstration Fusion Reactor, b) Providing data on the irradiation effects in high performance materials required for advanced fusion power reactors that will be competitive with other power sources, such as advanced fission reactors, fossil energy sources, etc., c) Obtaining data for fundamental understanding of fusion neutron irradiation effects, necessary to establish fission-fusion correlation that will allow utilization of the existing huge material database. In addition to these structural material-related missions, IFMIF would d) facilitate blanket related tasks, such as testing the performance of blanket component elements beyond the range of ITER operating parameters.

This report documents the activities of the KEP, the Key Element Technology Phase, conducted during the period 2000 to 2002. The future tentative plan for IFMIF is as follows: after a one-year transition phase, a six-year Engineering Validation/ Engineering Design Activity phase, EVEDA, is planned before the possible start of construction. Construction would take seven years before the first neutrons become available, by operation of the first accelerator with a deuteron beam current of 125 mA. This is half of the full-power specification for IFMIF. Another three years would allow completing the construction with two beam lines delivering in total a 250 mA current of deuterons on the lithium target. This full-power operation of IFMIF would allow irradiation of materials at greater than 20 dpa/year damage rate in a volume of 0.5 liter.

It is the strong desire of the IFMIF team members that the IFMIF activity makes a decisive step into the EVEDA phase, and eventually, into the construction phase. In this context, this document marks a major milestone along the path to IFMIF operation.

Hideki Matsui, Chairman
IFMIF Executive Subcommittee

December 2002

Executive Summary

1. IFMIF Mission

The development of fusion power plants requires materials that will provide safe, reliable long-life service at elevated temperatures in an intense neutron field. The structures must withstand a wall loading of 14 MeV neutrons at about 2 MW/m^2 for a fluence up to 10-15 MWy/m^2. The International Fusion Materials Irradiation Facility (IFMIF) has been proposed as an essential, near-term option for the development of these materials. The Conceptual Design of IFMIF was developed in 1995-96 in a joint effort of the European Union, Japan, and the United States, with the Russian Federation as an associated member, conducted under the auspice of the International Energy Agency (IEA), Implementing Agreement on Fusion Materials. The mission of IFMIF is to provide an accelerator-based, deuterium-lithium (D-Li) neutron source to produce high-energy neutrons at sufficient intensity and irradiation volume to irradiate samples of candidate materials up to about a full lifetime of anticipated use in fusion power production systems.

2. KEP Activity

The initial conceptual design was the basis for the "Conceptual Design Evaluation" phase (1997-98) and a subsequent design reconsideration (1999) that focused on cost reduction and preliminary facility deployment strategies. The "Key Element Technology Phase" (KEP) was initiated in 2000 with the objective of reducing some key technology risk factors. The risks were identified as those needed to achieve a continuous wave (CW) deuterium beam with the desired current in the accelerators, to verify relevant component designs on a laboratory scale both in the lithium target system and test cell system, and to validate design codes. Over the past three years, the EU, Japan, USA, and Russia have carried out 83 KEP tasks. This report summarizes the KEP achievements in the major areas of test facilities, target system, accelerator system, and design integration.

3. User Requirements

The design concept for IFMIF is based on input from the fusion materials community on neutron flux, irradiation parameters, specimen types and numbers, and the estimated test volume required to obtain useful irradiation data in reasonable operating times. Detailed design studies of the required test assemblies indicate that a test volume of about 0.5 L is required in a region producing a flux equivalent to 2 MW/m^2 (0.9 x 10^{18} n/m^2-s, uncollided flux) or greater. A fraction of this volume, about 0.1 L, is available at a flux equivalent to 5 MW/m^2 for accelerated testing. The design also provides greater volumes at lower flux levels, for the use in evaluation of materials other that the structural materials, for example, the tritium breeding system components.

Neutronics calculations indicate that 40 MeV deuterons on a lithium target provide a neutron spectrum that gives a reasonable simulation of the deuterium-tritium (D-T) fusion neutron atom displacement production rate and gaseous and solid transmutation rates in most candidate structural materials.

An estimate of the test volumes and the corresponding displacement rates for 250 mA of 40 MeV deuterons on a 100 cm^2 lithium target in a test assembly with iron-based specimens, per year of facility operation, is as follows:

0.1 L > 50 dpa/fpy (dpa: displacements per atom, fpy: full power year)
0.5 L > 20 dpa/fpy
6.0 L > 1 dpa/fpy

Assuming a total facility availability of 70%, these displacement numbers have to be multiplied by a factor of 0.7 to get damage rates per calendar year.

Quasi-continuous operation of a neutron irradiation facility is mandatory. Annealing times of point defects shorter than the repetition time of pulses and rate effects in the case of low duty-cycle sources would introduce unacceptable uncertainties in the observed radiation effects. It is planned

that IFMIF will operate with two accelerators providing identical, overlapping beam footprints on either one of two lithium targets. This configuration minimizes flux perturbations caused by a beam-off transient in one of the accelerators (i.e., the maximum likely temporal variation in the flux would be a factor of 2).

4. Facility Layout

IFMIF is driven by two 40 MeV deuteron continuous-wave (CW) linear accelerators each with 125 mA beam current delivered to a single thick, flowing lithium target under a 20 degree impinging angle. Neutrons are produced in the stripping reaction with a broad energy maximum peaked at 14-16 MeV. As the neutrons produced within the common beam footprint of 5x20 cm^2 are mainly collided in the forward direction, the test modules housing the specimens to be irradiated are positioned immediately adjacent of the lithium target.

The main components of IFMIF have been classified into five subsystems: (1) Accelerator System which delivers high energy deuterons, (2) Target System which produces a stable flowing lithium jet to convert the deuterons into neutrons, (3) Test Facilities which expose, handle, and examine specimens, (4) Conventional Facilities, and (5) the Central Control System and Common Instrumentation. Figure 1 shows a bird's eye view of the cost-reduced IFMIF project. Major engineering efforts have been undertaken to establish a design that is based on largely available, proven technologies. The design developed is based on extensive reliability, availability, maintainability, and safety studies and is conceived for long-term operation with a total facility availability of at least 70%.

The lithium target that converts deuterons into neutrons and all test modules that accommodate the material test specimens are located in a common test cell. The Post-Irradiation Examination (PIE) facilities are foreseen to examine irradiated specimens. Maximum availability is achieved by two completely independent accelerator lines; the ion source, radio frequency quadrupole (RFQ) and high energy beam transport (HEBT) of one deuteron beam line are indicated.

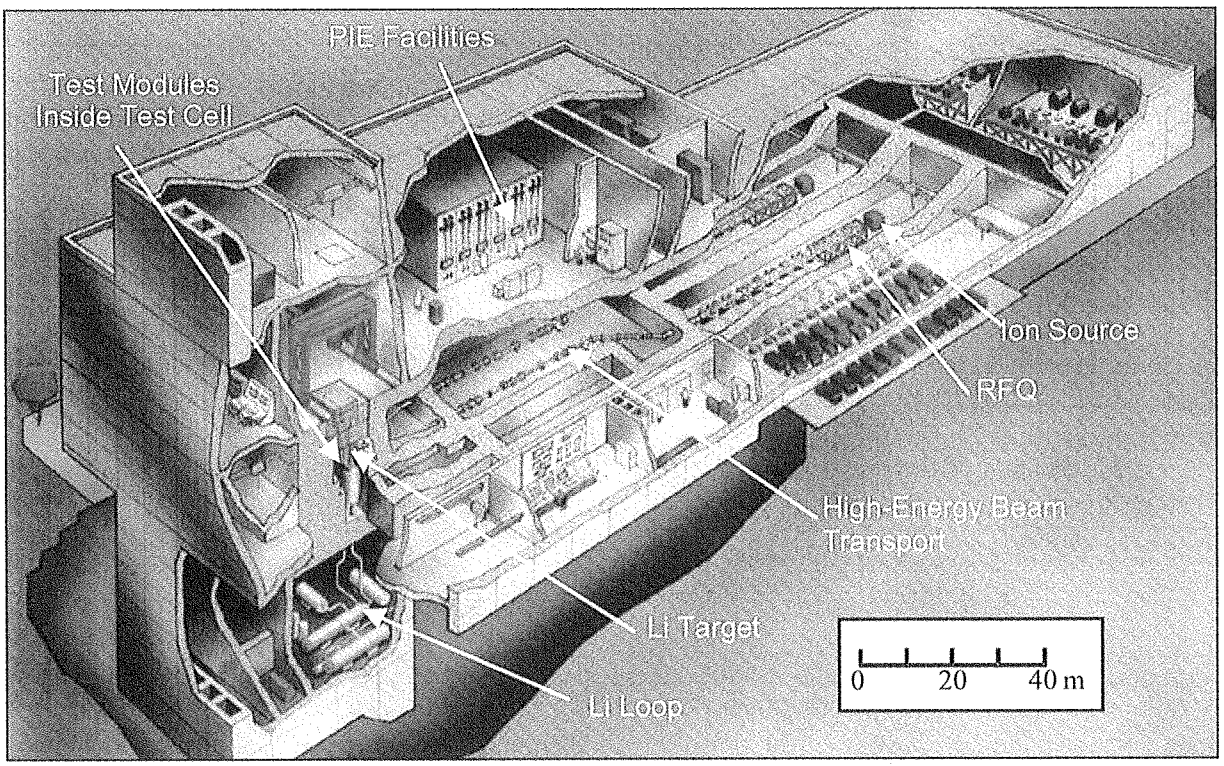


Fig. 1 Overview of the present IFMIF design showing major subsystems

5. Test Facilities

The IFMIF test cell and specimen testing areas must be capable of accommodating the wide range of environments associated with fusion reactor materials, and they have to assure system availability of about 97% during normal operation. To meet these materials testing needs, the irradiation volume downstream of the neutron-producing lithium target has been partitioned into a high-flux region with a displacement damage accumulation of about 20-55 dpa/ full power year (fpy) and an available volume of 0.5 L, a medium-flux region (1-20 dpa/fpy, 6 L), and a low-flux region (<1 dpa/fpy, >100 L). All test modules for all flux zones have to be instrumented and able to control the irradiation temperature that might vary from 250 to 1000°C in the high-flux and medium-flux regions, and range down to cryogenic temperatures in the low-flux zones.

Activities during KEP were concentrated on key engineering development items of the Test Facilities system as well as on optimization of IFMIF irradiation parameters and materials selection for use by the fusion materials community. Twenty four tasks have been conducted by the European Union and Japan, focusing on (i) reduction of the uncertainty of the neutron yield from the D-Li reaction, with a reasonably complete data evaluation up to 50 MeV, (ii) improvement in the design of helium cooled test modules that provide candidate materials with a broad temperature window, as well as flexible and safe operating conditions, (iii) further characterisation and optimisation of irradiation parameters, and (iv) several activities related to test module handling, the tritium laboratory, and waste management.

5.1 D-Li Source Term and Nuclear Data above 20 MeV

An important step has been taken for the calculation of the neutron production of the D-Li source by combining the Li(d,xn) reaction cross sections from different evaluated data files. Using this with a newly developed advanced Monte Carlo Code, the n-source yield uncertainty has been reduced from about ±35 to ±20%. Dedicated high resolution "time of flight" experiments are being performed with neutrons generated by 20-40 MeV deuterons striking a lithium target in order to further significantly reduce the yield uncertainty, to determine the neutron distribution in the test cell, and to measure the production rate for radioisotopes like ^{7}Be in a real, thick target ^{nat}Li(d,xn) reaction.

Over the KEP period, substantial effort has been devoted to preparing and releasing an intermediate energy activation file (IEAF) with 679 target nuclides from Z=1 to 84 with approximately 51,000 excitation functions for neutrons up to 50 MeV. On the basis of this library IEAF-2001 and the recent ALARA activation code, reliable activation analyses have become available for the first time. A major outcome of initial activation analyses is that for reduced-activation steels the same type of radioisotopes are produced during IFMIF and DEMO reactor exposure, with the consequence that after irradiation dose rates are comparable for equivalent neutron fluences in either facility.

5.2 Characterization of Irradiation Parameters and Test Module Development

Studies within the past few years have shown that the irradiation response of materials in both the high-flux and medium-flux test modules could be further significantly improved. These studies used the above-mentioned nuclear data libraries and advanced neutron transport calculations. In combination with thermal hydraulics and fluid dynamics calculations, a neutron reflector made of reduced activation ferritic steel has been designed for the high flux test module (HFTM). In addition, the HFTM allows specimen capsules with individual rig temperatures with practically homogeneous temperature profiles. At the same time the high-flux volume has been increased by ~20% and the flux gradients decreased by ~10%.

To optimize the neutron spectra and radiation responses for breeder ceramics, as well as for structural materials, systematic neutron transport calculations have been performed for the two medium flux test modules (MFTMs) dedicated to creep-fatigue and tritium release experiments. A major result of the neutronics calculations is, that with a proper combination of two tungsten plates acting as "neutron spectral shifters" and an additional carbon envelope acting as a "neutron reflector", the shape of the neutron spectrum in the medium flux test volume can almost perfectly match over

several orders of magnitude that for a DEMO-type helium cooled pebble bed breeding blanket. With respect to suitability criteria, IFMIF adequately meets DEMO reactor-relevant H, He, and dpa production rates as well as H/dpa and He/dpa ratios in structural materials like Fe-based alloys (Table 1). It is also a suitable test bed for ceramic breeder materials. In addition, it has been shown that with respect to the recoil energy distribution fusion relevant conditions can be achieved in IFMIF test modules over the entire recoil energy range.

As the irradiation volume of any accelerator-based neutron source is limited, the use of miniaturized specimens is mandatory for the high flux region. Rapid progress is being made by the international materials community in developing a set of miniaturized specimens with proven scaling laws. The development of online subminiature fission chambers for a quantitative determination of local neutron/gamma spectra inside the IFMIF test modules is in the final stage. The proposed program is aimed at the realization of prototype on-line neutron monitors in conjunction with meaningful irradiation tests. Two of three 8 mm diameter fission chambers have been developed, fabricated, and irradiated in a thermal fission reactor, and suitable cyclotron irradiations are scheduled. For the non-destructive verification of the structural integrity of safety relevant modules inside the test cell a micro-tomography system has been set up. The micro-tomography method is the only known tool with the potential of monitoring voids, micro-cracks and deformation in a wide range of irradiated and unirradiated materials.

5.3 Test Module Handling, Tritium Laboratory and Waste Management

The planned IFMIF remote handling system consists of several master/slave manipulators and a universal robot system with various manipulators and tools. All the operations in the test, access and test module handling cell, including the replacement of the lithium target assembly, will be carried out by the remote handling system. Therefore, detailed flow plans for all remote handling operations for the test facilities have been developed during the KEP.

The design requirements for the tritium laboratory are (i) handling, assembling/disassembling and post irradiation examination (PIE) of the tritium release test module, (ii) handling, assembling, maintenance and PIE of the lithium target, and (iii) tritium processing. During KEP the design outline of the tritium laboratory was significantly improved, the predicted amounts of gaseous, liquid and solid waste with tritium were determined, and various detritiation systems and waste management installations were outlined on the basis of national laws e.g. for air leakage. The IFMIF design outline of the tritium laboratory and tritium processing systems meets the Japanese requirement for tritium discharge into the atmosphere of less than 5×10^{-4} Bq/cm^3.

Table 1 Comparison of major irradiation parameters for reduced activation ferritic steels

Irradiation parameter, calculated for RA-steel	ITER*	DEMO HCPB blanket*	IFMIF HFTM	IFMIF MFTM-CF
Total flux, [n/(cm^{2}s)]	4×10^{14}	13×10^{14}	$(4\text{-}10) \times 10^{14}$	$(2\text{-}6) \times 10^{14}$
Displ. damage production, [dpa/fpy]	12	30	20-55	7-10
H production, [appm/fpy]	500	1200	1000-2500	300-500
He production, [appm/fpy]	120	300	250-600	70-120
H/damage, [appm/dpa]	45	40	40-50	30-50
He/damage, [appm/dpa]	11	10	10-12	8-14

* First wall structure, near mid-plane outboard position.

6. Target System

Design requirements for the lithium target system are (i) removal of the power deposited by the deuterium beams, (ii) impurity control to ensure safety with respect to the lithium hazard and tritium release from the lithium loop, and (iii) system availability of more than 95% during the lifetime of the plant. To remove the thermal power of 10 MW within a beam footprint of 5 cm x 20 cm, the liquid lithium jet in the target system has a velocity of ~15 m/s, a flow rate of 130 L/s, and an inlet temperature of 250°C. The target system consists of the target assembly, the lithium loop and the lithium purification system. Fig. 2 shows a bird's eye view of the target system with major subsystems labelled. The loop electromagnetic pump circulates the lithium through the target assembly, then through the purification and heat exchange systems. The maximum temperature of the lithium jet (bulk and free surface) can be kept below 400°C, which is below the local boiling temperature. Major impurities in the lithium are transmutation products protium, deuterium, tritium, and beryllium-7 (^{7}Be), and contamination elements like C, N, and O. For effective erosion/corrosion prevention and to avoid deterioration of the purification system, the maximum impurity concentrations (C, N and O) must be lower than ~10 wppm. The purification system uses both cold and hot traps to achieve these goals.

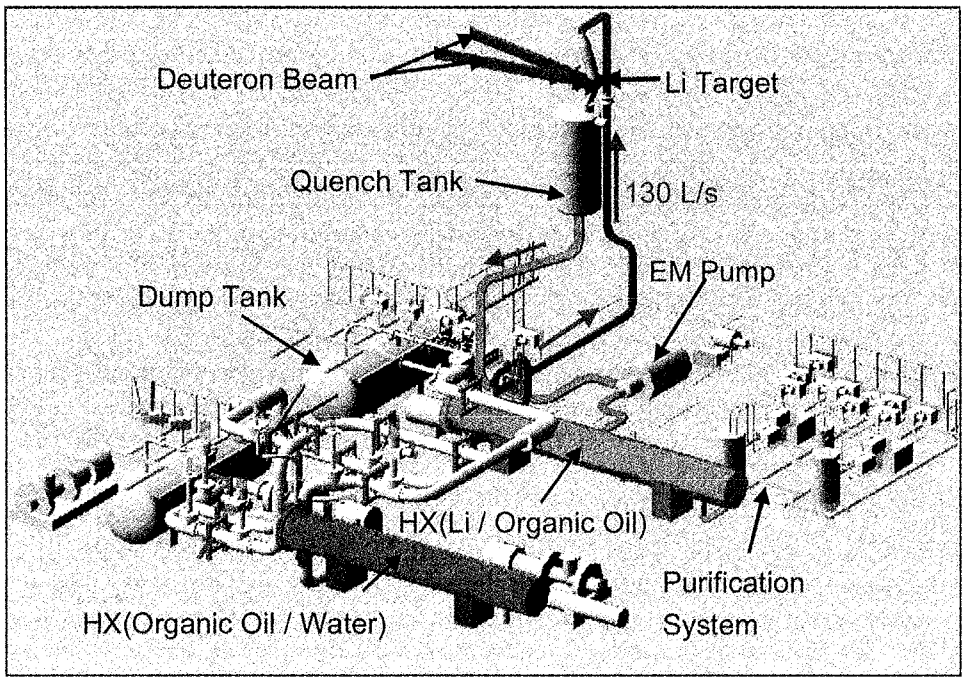


Fig. 2 Bird's eye view of the lithium target system

In the KEP activities, 19 tasks for the lithium target system have been shared by the European Union, Japan and the Russian Federation. This work was needed to reduce the key technology risk factors to reach the required power handling capacity in the target system, and to demonstrate the availability and reliability by endurance tests. Progress on these KEP tasks is summarized as follows.

6.1 Water Jet and Lithium Flow Experiments

A water jet facility with a flow velocity of up to 20 m/s was used to simulate characteristics of the liquid lithium flow. Experiments where water has the same Reynolds number as the lithium flow were used to evaluate the effects of surface roughness of the nozzle and of working pressure on the flow behavior. This showed that the working pressure is not a cause of the surface wave growth. Experiments with a nozzle with 100 μm roughness showed larger surface waves beyond a flow speed of 10 m/s than for a nozzle with 6.5 μm roughness. Measurement of velocity distributions showed that boundary layer changes from laminar flow to turbulent flow occur for an increase in velocity beyond

10 m/s. In evaluating the replaceable back wall option, one concern is that a small discontinuity in the back wall might influence the jet stability. A modification of the water jet mock-up has been used in order to measure the effect of a few parameters, such as a back wall curvature (25 cm to 45 cm) and a step at the nozzle joint (-0.1 mm to +0.1 mm). Experiments are now in progress.

Modification of the existing lithium loop has been made to evaluate the stability of lithium flow with a double reducer nozzle, and the experiment has been started. Major diagnostics are a charged coupled device (CCD) video camera, a high-speed video camera, lithium thickness monitors and a laser surface wave monitor. Initial tests were for high speed lithium flows of up to 14 m/s under cover gas conditions and 8.5 m/s under vacuum conditions. Surface observation by the CCD video camera showed that relatively calm flow without violent waves or splashing of the fluid was obtained. Further experiments are being prepared to measure surface stability, cavitation characteristics, and corrosion of the nozzle or channel walls.

6.2 Lithium Purification System and Corrosion Effects

Non-metallic impurities in the lithium are divided into two groups. The first group consists of radioactive impurities such as tritium and ^{7}Be generated by D-Li reactions. The second group includes carbon, nitrogen and oxygen that are picked up from the loop materials. Behavior of impurities (mainly C, N, O) in the primary loop, identification of the main impurities, and definition of a strategy for trapping have been completed. Basic tests of the cold and the hot traps for removal of the impurities, and the on-line monitoring (H, C, N) in stagnant lithium will be performed. Nitrogen concentration in liquid lithium can be controlled by hot trapping. An evaluation of the trapping effectiveness of advanced materials Cr, Ti, V, and V-Ti alloys has been performed. Under high nitrogen concentration (a few hundreds ppm) in lithium, nitrogen getting by Cr is more efficient than Ti and V-Ti-alloy. On the other hand, under low nitrogen concentration, the V-Ti alloy is an effective getter. Nitriding of yttrium, used in a hot trap for tritium control, was suppressed if used together with V-10Ti alloy. For impurity monitoring, on-line resistivity techniques for N; electrochemical sensors for H, O and N; diffusion meter for C; and analytical techniques could be used.

Corrosion data for materials, especially for reduced-activation ferritic/martensitic (RAF) steel, is limited. Modification of the existing corrosion loop (LIFUSE III) to add a test section is in progress. Corrosion data with a maximum velocity of 10 m/s will be obtained. A rotating sample experiment for corrosion measurements is also planned.

6.3 Thermohydraulic Stability andTransient Analysis of the Lithium Loop

The thermal-hydraulic conditions of the liquid lithium jet in the present design have been analyzed by means of the RIGEL code. Final results are temperature and velocity distributions of the jet, evaporation rate at the free surface, and pressure distribution in the jet under non-boiling conditions. The boiling margin, defined as saturation temperature - local temperature, is minimum (35°C) on the free surface just below the beam footprint. Inside the lithium flow, the boiling margin is more than 400°C due to the increase of the saturation temperature by centrifugal pressure. Analysis by a simulation code evaluated the transient thermal behavior of the loop during a beam trip or start-up of IFMIF. A key result is that without control of the heat exchanger system, the temperature at the exit of the cooler becomes less than the solidification temperature of lithium (180°C) after 380 s. However, with control of the heat exchanger system, the exit temperature is maintained above the solidification temperature.

6.4 Safety Analysis

The FMEA (Failure Modes and Effects Analysis) approach has been adopted to identify potential system failures. The outcome is the identification of relevant target-related hazards and of major initiating events for accident sequences. In particular, FMEA has identified radioactive material generated in the lithium loop (tritium and ^{7}Be) as major hazards relative to the target system, and the risk related to the liquid lithium loop operation. These results are reflected in the design and system operation: as regards the former safety issue, the majority of tritium, other radioactive materials, and

impurities are removed by trapping. With regard to the risk, the vacuum environment in the test cell and lithium cell, eventually with argon flushing, assures protection against lithium fire risk due to the lithium-air reaction. The main conclusions are that, with the plant modifications in the reduced cost version of the IFMIF design, the target safety is assured and any environmental impact is negligible.

6.5 Remote Handling System

The reference IFMIF target design is based on a replaceable backplate, to allow changeout of this component after radiation damage, and thus increase the lifetime of the whole target system. There are two design options for the back wall replacement. The first option is to move the target assembly to the hot cell area for replacement of the back wall. An yttrium aluminum garnet (YAG) laser will be used to cut the lip seals of the flanges and then a new backplate will be welded in place. The remote handling system to replace the target assembly is part of the Universal Robot System (URS) in the Test Facilities. Conceptual procedures for the target assembly transfer to the hot cell and for repair have been established. The second option is a so called "Bayonet" type backplate. With this concept the back wall is replaced without moving the target assembly, by using a remote handling device. The sliding back wall is mechanically attached to the target assembly. To check the feasibility of the concept, verification of the locking system, the sealing capability under operating conditions, and validation of the removal and installation procedures are needed. A verification test is underway using the remote handling facilities set up to test the ITER divertor remote handling. Using a dummy backplate mock-up, the basic operations of insertion, removal and locking capability have been verified.

7. Accelerator System

The IFMIF requirement of 250 mA of deuteron beam current delivered to the lithium target will be met by two 125-mA, 40-MeV accelerator modules operating in parallel. The technological approach of the reference design selected is only cautiously aggressive with respect to the beam current handling capabilities of the rf linac technology, and provides operational redundancy by allowing operation to continue at 125-mA when either of the two accelerators is temporarily removed from service for repair. Each 125-mA accelerator is designed with sufficient derating, but not with a significant upgrade capability. The IFMIF deuteron accelerators are a sequence of acceleration and beam transport stages. A CW 155-mA deuteron beam is extracted from the ECR ion source at 95 keV. A low energy beam transport (LEBT) guides the deuteron beam from the source to a radio frequency quadrupole RFQ. The RFQ bunches the beam and accelerates 125 mA to 5 MeV. The 5-MeV RFQ beam is injected through a matching section (2 cavities, 4 quadrupoles) into a room temperature, ramped-gradient Drift Tube Linac (DTL) of the conventional Alvarez type with post couplers, where it is accelerated to 40 MeV. The baseline rf power system for the IFMIF accelerator assumes the use of Diacrode technology with an output power level of 1.0 MW and a frequency of 175 MHz. Operation of both the RFQ and the DTL at the same relatively low frequency is a conservative approach to delivering the high-current deuteron beam with low beam loss in the accelerator. This will facilitate hands-on maintainability without remote manipulators. Although the present reference design is based on conventional, room-temperature rf linear accelerator (rf linac) technology, superconducting linac technology that has the potential of reaching an even higher performance and possibly lower cost is also being followed closely.

The Accelerator Facility KEP work is firmly based on the previous Conceptual Design Activity / Conceptual Design Evaluation (CDA/CDE) activities. This is especially important to note in all costing studies, where an explicit path to the comprehensive CDA Cost Estimate can always be traced.

In the KEP, the most important accomplishments for lowering construction risk and affording a rapid construction start are: (1) the selection of the electron cyclotron resonance (ECR) injector for the reference design, (2) achievement of a preliminary but detailed reference beam dynamics design

for the full accelerator indicating that the low beam loss specification can be met, and (3) the demonstration of good availability of order hundreds of hours from an operational ECR injector and from the Diacrode 1 MW rf power amplifier.

In this KEP report, the accelerator work packages are organized, as outlined in Section 3.1, in terms of major accelerator subsystems in order to relate the KEP tasks to the overall accelerator design. The KEP results are summarized briefly as follows.

7.1 Accelerator Subsystems

The accelerator begins with the ion source and low energy beam transport, which transports and matches the beam to the RFQ. The IFMIF ion injector, comprised of the ion source and the low-energy-beam-transport (LEBT), has to provide excellent beam quality, sufficiently high beam current, and high operational availability. To minimize downtime and maximize system availability, all failure-prone injector components are being designed for rapid exchange in the accelerator vault, subsequent to shutdown. Extensive operational experience with the ECR ion source type was obtained at Saclay, with several very long runs of 100-700 hours duration, with availability of >95% achieved. Institut für Angewandte Phisik (IAP) continued evaluation of multi-cusp sources and LEBTs, and operational tests of multi-cusp and ECR sources were conducted at Japan Atomic Energy Research Institute (JAERI). Operation with a D^+ beam at Commissariate a l'Energie Atomique (CEA) Saclay shows that IFMIF beam performance requirements can also be achieved with a deuterium beam. After extensive parallel developments during the CDA, CDE and KEP, the ECR ion source was selected as the reference design ion source for the IFMIF project.

The linear accelerator consists of an RFQ to 5 MeV, followed by an Alvarez-type drift-tube linac to 40 MeV. The reference design RFQ is a 4-vane type 175 MHz structure. The output energy of 5 MeV was selected for the RFQ, because it is the lowest energy allowing a F0D0 magnetic lattice in the DTL which is desirable for halo control and the consequent minimization of beam loss. The high output energy, however, necessitates a long RFQ structure of ~12.5 m. The RFQ will likely need 3 Diacrodes of 1 MW each. Within the present KEP phase, the preliminary design of the RFQ beam dynamics has been finished, with extensive simulation and sensitivity (machining) studies. Detailed design work was performed by two groups using different techniques. Both RFQ designs meet the low beam loss specifications. Further work is required to achieve final design status. It is desired to reduce beam loss still further, and extensive optimization and sensitivity studies must be done, as for any conceptual design. In another study, a formalism that has been developed permits the computation of all quantities necessary to RFQ tuning procedures.

The IFMIF reference design uses a conventional room-temperature 5-40 MeV DTL, the structure having the strongest focusing possible in this energy range, in order to achieve minimum beam loss in the accelerator. The DTL includes 5 DTL tanks (with a peak accelerating field of 1.75 MV/m) and 9 rf tubes to power them (per linac; 1 tube on Tank 1, 2 tubes on Tanks 2-5). Preliminary mechanical design and modeling of alternative quadrupole magnet cooling schemes, plus refined cost and schedule estimates, indicate full readiness for construction. Detailed design work was accomplished on the shortest, most difficult drift tube at the 5 MeV end of the DTL. The HEBT has been substantially revised from the CDA configuration; most importantly, the RF cavities used for beam energy spread control in the CDA design were removed. Preliminary simulations indicate that a suitable HEBT system can be defined.

Accelerator technology continually develops, and results achieved in other projects need to be evaluated in terms of possible advantage to IFMIF. A 4-rod type RFQ is under consideration to ascertain whether it might have cost and other advantages for IFMIF. Preliminary investigation is being made of an alternative 5-40 MeV design using a room-temperature interdigital H-mode (IH)-structure and a following superconducting crossbar H-mode (CH)-structure. In case of superconductivity the rf losses are lower, and the linac is shorter and has larger apertures. Work in other programs on superconducting spoke resonator designs also needs to be applied to IFMIF to explore potential operational and cost advantages.

7.2 Beam Dynamics Evaluation

Comprehensive end-to-end particle dynamics calculations including errors have been performed, showing that for various conditions stable solutions with low emittance growth and full transmission could be found. With DTL errors and corrections, the end-to-end transmission is expected to reach 98%. The DTL beam dynamics reference design has no particle losses. Parameters and some performance information are given in Tables 2-4.

Table 2 Main IFMIF RFQ parameters

Parameters	Values	Parameters	Values
Length	12.482 m	Synchronous phase (Φ_s)	-90°→ -40°
Frequency	175 MHz	Peak field	1.8 Kp
Voltage	130→ 101.2 kV	Copper power (+20%)	683.9 kW
Mean aperture (R_0)	6.41→ 5.16 mm	Beam power	613.1 kW
Modulation (m)	1. → 1.6	Total power	1297 kW

Table 3 Results of the IFMIF RFQ simulation

Parameters	Value
Transmission	98.5%
Output X transverse emittance	0.249 π.mm.mrad
Output Y transverse emittance	0.251 π.mm.mrad
Output longitudinal emittance	0.195 deg.MeV

Table 4 Main parameters of IFMIF DTLs

Parameters	Values	Parameters	Values
Length (5 tanks)	28.9 m	Peak field	1.3 Kp
Max. Z_sT^2	31.2 MΩ/m	Copper power (+20%)	1.503 MW
Maximum quad. gradient	75.6 T/m	Beam power	4.550 MW
Synchronous phase (Φ_s)	-45°-> -30°	Total power	6.053 MW

7.3 RF Power Subsystem

Development and testing of a 1 MW rf system was identified as the highest impact development item, as existing operating experience was for short periods (1-8 hours). Outstanding progress has been made in developing and testing a new kind of gridded tube called the Diacrode which can overcome the limitations of conventional tetrodes, mainly the RF losses, by a factor of 4. The challenging goal was to meet the reliability demonstration goal of IFMIF, namely, 1000 h at 1MW CW rf power and 175-200 MHz. Endurance tests with a TH 628 Diacrode have been performed, with over 1047 hours at full power in the range of 1010-1030 kW CW rf and 200 MHz. This shows the capability to operate stably under IFMIF-relevant conditions. Diacrode phase and amplitude modulation data were also obtained from Los Alamos National Laboratory (LANL), and an updated cost estimate of the Diacrode price. Investigations of solid-state driver amplifiers for the Diacrode were conducted, as well as rf drive loop design for up to 500 kW CW by two different groups.

7.4 Diagnostics and Beam Loss Activation

Significant progress on non-interceptive diagnostics has been made at CEA/Saclay and IAP for high intensity beams. IAP has also developed a high-power interceptive emittance measurement device. However, diagnostics for high power CW beams are not yet fully available and require continuing development.

The primary deuteron beam and the secondary neutron induced activities and the resultant dose levels were estimated by using the existing nuclear data libraries and checked with the available experimental data. The beam loss criteria required to allow hands-on maintenance throughout the lifetime of each component were examined.

7.5 Cost Evaluations

In response to widespread discussion of the benefit of having a fully operational accelerator prototype, the US team undertook a task in 2002 to define the scope and develop a cost estimate for such a program. The work incorporated the latest design information available to arrive at an updated design configuration for the IFMIF accelerator. From this configuration a prototype design was developed that meets the technical requirements set forth at the IFMIF Design Integration Meeting at Forschungszentrum Karlsruhe (FZK) in October 2001. The results of this study were finalized in early March 2002 and presented at the IFMIF Subcommittee meeting in Tokyo later that month. The estimated cost for the five year prototype program is 102 MICF including an AFI allowance of 23 MICF, where ICF: IFMIF Currency Factor = $1 in January 1996, and AFI: Allowance for Indeterminates.

As a separate task, the cost of the revised "reduced cost IFMIF" HEBT and the Diacrode-based rf system was evaluated. The expected savings over the CDA cost estimate were seen; however, the savings were not as great as assigned in the reduced cost estimate.

7.6 Transition to Accelerator Facility EVEDA

High priority items for continuing development in the next immediate phase of IFMIF include:

- Updating the IFMIF Accelerator option to use superconducting linac technology for the 5-40 MeV Linac. IFMIF evaluated superconducting linac technology thoroughly during the CDA, but did not incorporate it into the reference design, largely for cost reasons. During the intervening years, development of superconducting accelerating structures and rf drive techniques continued in several institutes. These developments offer the possibility of technical, cost and availability advantages to the IFMIF project.
- Development of an H_2^+ beam ion source to be used during commissioning studies to avoid radioactivity. It is more difficult to achieve high H_2^+ beam current than D^+; and a development program is required.
- RF drive loop tests up to 500 kW CW.
- Updating of interface requirements from users, test cell and target and conventional facilities, and application to the accelerator design as required.
- Continued design refinement.
- Continued effort to gain operating experience with a deuterium beam in the ECR injector, for application to IFMIF design.

Any complex facility is only known fully as operating experience is obtained. The experience with the operating ECR injector and the Diacrode rf amplifier has been very valuable. Although it seems clear that a full-scale prototype, designed for incorporation into the final facility, is probably unaffordable, a continued effort to test subsystems during the period preceding IFMIF construction would be worthwhile. For example, during the ECR runs, the neutron production in the LEBT rose rapidly, indicating that further optimization is necessary for the final IFMIF factory.

8. Design Integration

The Design Integration (DI) activities concentrated on the whole IFMIF facility to achieve cost reduction and to allow staged construction, and on examination of several basic issues related to facility safety and stable operation. The European Union and Japan contributed to 14 DI tasks. Basic building utilities were designed based on the analysis of material flow and these designs integrated information from the several years of previous IFMIF activities. The schedule for the IFMIF project was revised to account for the KEP results. Also, the total cost of the next phase (EVEDA) and of construction was reassessed.

8.1 Design of Buildings

The IFMIF site layout was based on the assumption that IFMIF is located within an existing nuclear facility, able to supply electric power, water, and radioactive waste treatment. The site area of about 250 m × 200 m is shown in Figure 3. There is a main building (accelerator and target/test systems), an administration building, utility buildings for electrical power and cooling water, and other structures. The main building is about 170 m × 60 m and its height is 26 m above ground and 11 m below ground. To minimize IFMIF construction cost the building height, especially the underground part, was reduced from earlier designs. The Target System, the Test Facilities and the Accelerator Vault for the first accelerator will be constructed during the first stage of a two-stage construction schedule. The accelerator with a length about 110 m is installed at ground level, and the lithium loop is mainly installed below ground level.

The target/test building design was based on Japanese seismic engineering guidelines, with requirements more severe than for the accelerator building. This results because IFMIF is estimated to produce about 7 g of tritium per year in the D-Li reaction. Stainless steel wall lining is included in the Test, Access, and Test Module Handling Cells to prevent diffusion of activated materials and lithium leakage. Material flow for the full operational life of IFMIF was analyzed in order to fix the basic concepts for materials handling. The conceptual designs of the Access Cell and Tritium Laboratory meet the needs shown by these analyses.

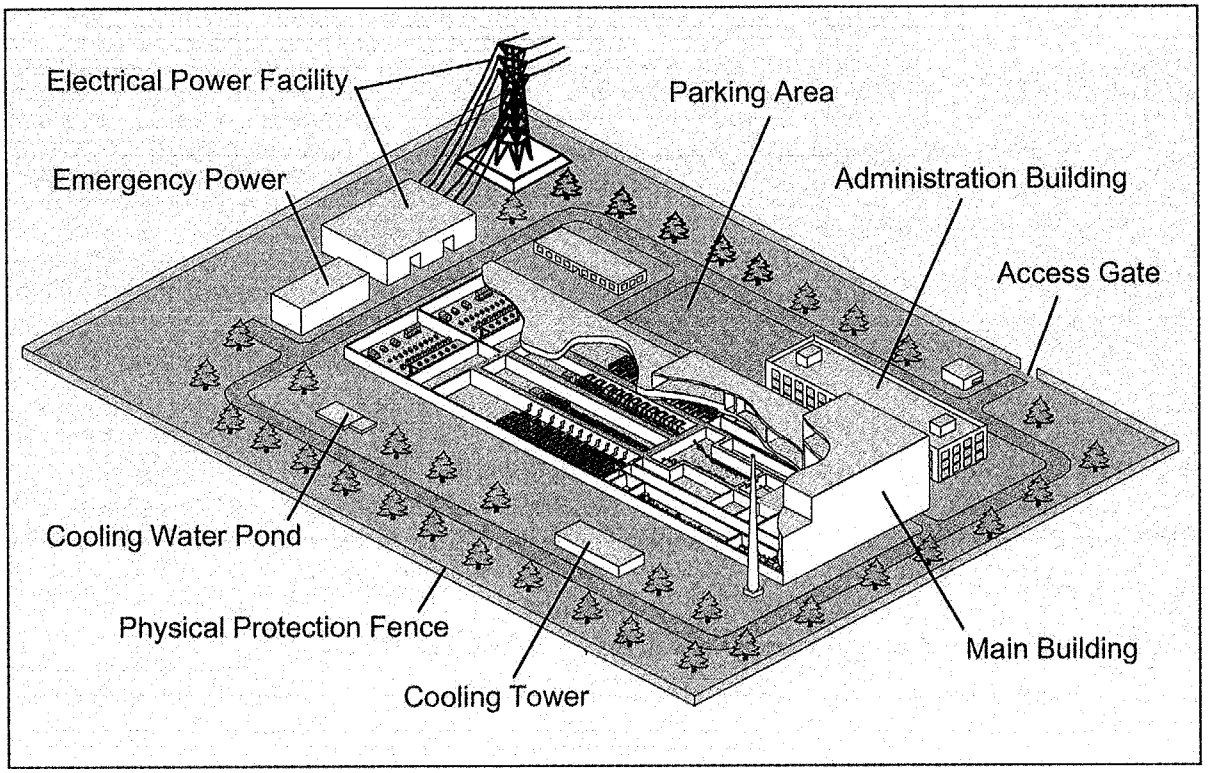


Fig. 3 IFMIF Site Layout

8.2 Design of Utilities

Utilities for the reduced cost IFMIF with two-stage construction were designed based on the assumption of a Japanese site. The heating, ventilation and air conditioning (HVAC) systems were designed as two separate systems, industrial and nuclear HVAC systems, based on the radiological risk for each area served. The areas served by the nuclear HVAC system are filled with air or argon gas at 200-400 Pa below atmospheric pressure. The required total electric power is estimated to be 50 MVA, including emergency power. Requirements for heat rejection by cooling water are 26 MW

for the Accelerator and 14 MW for the Target system. Argon gas is used to suppress lithium fires in the Test Cell and Lithium Loop Areas.

The Radioactive Waste Treatment System was designed for liquid, gaseous and solid wastes, to accommodate annual IFMIF generating rates of 7 g of tritium, 1.5 g of beryllium-7 (^{7}Be) and some other radioactive nuclides. The process for treating liquid wastes that include tritium and ^{7}Be uses storage tanks, evaporation, ion exchange and/or discharge units. Tritium is removed from tritiated argon gas by palladium permeation and hydrogen getting. Tritiated air is oxidized to tritiated water.

8.3 Radiation Shielding and Neutron Monitoring

The shield performance was calculated using a Monte Carlo computer code MCNPX with the data library LA150. Areas considered were the Test Cell, Target Interface Room, and Lithium Loop Area. Analysis took into account streaming through lithium pipes and through beam line ducts. The dose rates were also estimated at the outside of the Test Cell front wall, at the shielding plugs, and at vacuum piping pass-through structures. The results showed that a 4.3 m thick front wall was enough to limit the worker dose rate to less than 10 μSv/h, and that the current building design was appropriate for radiation shielding. A bubble type of counter was selected to monitor neutrons because it provides non-gamma, on-line, spatial and spectrum measurements. Activation of the shielding wall by the intense neutron radiation influences the design of the structure and maintenance equipment. Elements in the shielding with large cross section for activation are C, N, O and Si. Calculations for activation of these elements are used to design the shielding wall and maintenance equipment in the test cell.

8.4 Operation Flow, Central Control and Safety Analysis

To check the consistency of the IFMIF design as a neutron irradiation facility, operational flows were examined for comprehensive scenarios that included start up, normal operation, shut down, and maintenance phases of the facility lifetime. Using this operational flow analysis, the basic concepts of the central control system were designed.

The IFMIF facility was reviewed from the viewpoint of safety, with special attention to Occupational Radiation Exposure, using exposure data from an existing accelerator facility. Safety of the Accelerator and Test Facilities was analyzed using Failure Modes and Effects Analysis methods. These analyses identified key issues for safety of the IFMIF design. Quantitative analyses based on component reliability databases are needed in the next phase of the project.

8.5 Examination of Licensing, Regulation, Schedule and Cost

To ensure the feasibility of the IFMIF project, tasks relating to project management were performed. Japanese laws and regulations applicable to the IFMIF facility were examined. The main applicable laws are "The Law Concerning the Prevention of Radiation Hazards Due to Radioisotopes" and "The Fire Service Law," and include their related laws. A schedule for IFMIF construction and tasks for the Transition Phase (19 tasks in FY2003) and EVEDA (49 tasks in FY2004 – FY2008) were proposed. The draft of a new Annex for EVEDA under the current IEA Implementing Agreement on Fusion Materials was proposed and is under consideration by Parties in the IFMIF Project.

The impact of a change of staged construction from three stages in 15 years to two stages in 10 years was evaluated and found to have little effect on the total construction cost.

1. Introduction

The development and qualification of radiation-resistant, low-activation materials are key requirements for realizing the promise of fusion power. In an operating deuterium-tritium (D-T) reactor the materials are exposed to an intense neutron flux with energy of 14 MeV. A necessary tool to develop the materials is a neutron irradiation facility simulating such fusion condition. An accelerator-based neutron source using the deuteron-lithium (D-Li) stripping reaction was selected to meet this need by the International Energy Agency collaboration on fusion material (Implementing Agreement for a Programme of Research and Development on Radiation Damage in Fusion Materials) (IEA IA-FM). The International Fusion Materials Irradiation Facility (IFMIF) project was organized to develop this selected neutron source. It is an international collaboration among the European Union (EU), Japan, the Russian Federation (RF), and the United States (US) under the IEA IA-FM.

The IFMIF project started in 1995, completed the reference design through the Conceptual Design Activity (CDA) phase in 1995-96 [1], and the Conceptual Design Evaluation (CDE) phase in 1997-98 [2]. In 1999, a reconsideration of the design and a study of staged deployment were performed to reduce the IFMIF total construction cost and the required annual expenditures [3]. The 29th Fusion Power Coordinating Committee (FPCC) in January 2000 recommended proceeding to the next phase, the Key Element Technology Phase (KEP) and the preparation of a plan for continuation of the activity after KEP.

A three-year KEP began in 2000 with the objective of reducing the key technology risk factors to achieve continuous, long-time operation of each subsystem: accelerator, target, and test facilities. Systems design work, including buildings and utilities, was also part of the KEP to assure attention to operating performance and safety. All KEP work was performed on a voluntary basis by the participating countries.

After the KEP and a Transition Phase in 2003, a six-year Engineering Validation and Engineering Design Activity (EVEDA) will validate continuous stable operation of the subsystems and will produce a complete design for IFMIF.

1.1 Requirements of IFMIF

IFMIF is required to maintain stable, continuous operation with high availability for the support of materials development. It must achieve this while providing a high level of worker safety and protection of the environment. The requirements for the irradiation parameters, the operation performance and the safety conditions are summarized in the following sections.

1.1.1 Irradiation field

To simulate the D-T neutron field with energy of 14 MeV, the IFMIF provides high-energy neutrons with a broad energy peak at about 14 MeV. Deuterons from a 40 MeV accelerator are stopped in a lithium target, with neutrons produced in a stripping reaction. Specimens of candidate materials are tested under irradiation at controlled temperatures, in a neutron flux of about 10^{18} n/m^2-s, which in the case of iron-based materials corresponds to a damage production rate of 20 dpa/year (displacements per atom per year). The required irradiation test volume at each damage production rate is as follows:

> 50 dpa/y in 0.1 L
> 20 dpa/y in 0.5 L
> 1 dpa/y in 6 L

The neutron flux gradient of 10%/cm or less is needed to maintain uniform irradiation temperatures in the specimens. The ratios of the H- and He-production rates to the displacement rate in the specimens are required to be similar to those corresponding to the materials used in the typical blanket structure of the fusion reactors, for example, 10 appm He /dpa in iron-based alloys.

1.1.2 Facility operation

Operation of IFMIF must be continuous to avoid the complications of annealing effects that would occur in the case of intermittent irradiation. It is also required that long-time operation achieve

a total facility availability of 70% to reach accumulated damage levels around 100 dpa within a few years of operation. Allowing for the scheduled maintenance time of one month per year and eight hours per week, this requires system availability of 80.7 % during scheduled operation.

1.1.3 Safety

As IFMIF is an accelerator-based facility, neutron and gamma radiation are generated in the D^+ accelerators, at the lithium target, and in the test cell. Radiation levels will generally be highest during accelerator operation. Careful design of the radiation shielding is necessary to control the worker dose, for example. Transmutations and activation occur in lithium, in structures and in the atmospheres in these facilities. Typical radioactive nuclides generated in the IFMIF are tritium (^3H) and beryllium-7 (^7Be). Especially careful design is necessary for the control and treatment of tritium, to assure worker safety, public safety, and environmental protection.

Another safety issue is the fire hazard of the large amount of liquid lithium containing tritium and beryllium-7. It should be confined or suppressed for environmental safety. Also any possibility of reaction through lithium contact with water must be prevented.

1.1.4 Each subsystem

The IFMIF consists of three major subsystems: the Accelerator Facility; the Target Facility; and the Test Facilities, including the post irradiation examination (PIE) facilities. IFMIF also includes Conventional Facilities, mainly building and utilities, and the Central Control and Common Instrument (CC&CI) systems.

(1) Accelerator

The required high-energy, intense neutron field with the necessary volume is generated by a continuous wave (CW) 250 mA, 40 MeV D^+ beam on a lithium target. The beam is achieved using two 125 mA D^+ accelerators, and the two beams are transported to one 20-cm-wide by 5-cm-high footprint on the lithium target.

(2) Target

Most of the D^+ beam power is deposited as heat in the lithium target. The target removes this heat load of up to 10 MW with liquid lithium flowing at 15 m/s (range: 10-20 m/s). This high-speed free-surface flow facing the accelerator vacuum (about 10^{-3} Pa) must maintain the thickness (25 mm in case of 40 MeV deuterons) in order to stop all of the beam within the lithium.

(3) Test Facilities

The IFMIF test cell and specimen testing areas must be capable of accommodating the wide range of environments associated with fusion reactor materials. All test modules used for the different flux zones have to be instrumented and able to control the irradiation temperature that might vary in the range 250°C - 1000°C in the high-flux (> 20 dpa / full power year (fpy), 0.5 L), 250°C - 1000°C in medium-flux (1-20 dpa/fpy, 6 L) and –269°C - 500°C in the low-flux (<1 dpa/fpy, >100 L) zones.

(4) Conventional Facilities

The fundamental safety requirements for the conventional facilities of the IFMIF are radiation shielding, tritium treatment, and confinement of lithium containing radioactive nuclides. Equipment for this treatment and regulation / monitoring must be included.

1.2 The KEP Phase of the IFMIF Project

The IFMIF KEP has been carried out to reduce the risk factors of the key technology before beginning validation tests of the continuous, long-time operation of each subsystem. The KEP work during 2000-2002 was a voluntary, international collaboration among the EU, Japan, the RF and the US under Annex-II of the IEA IA-FM.

1.2.1 Implementation of KEP Tasks

The planned KEP activities were divided into IFMIF KEP Tasks, to assure clear definition and responsibility for the work. The contents of KEP Tasks were first proposed at a March 2000 meeting at Forschungszentrum Karlsruhe (FZK), and then refined at the following international technical meetings.

- Design Integration Meeting at FZK in March 2000
- Technical Meetings for Accelerator at Monterey and Los Alamos National Laboratory (LANL) in August 2000
- Technical Meetings for Target and Test Facilities at Ente per le Nuove Tecnologie, l'Energia e l'Ambiente (ENEA) Brasimone in September 2000
- Technical Meeting for Target at Institute of Physics and Power Engineering (IPPE) Obninsk in September 2000
- Design Integration Meeting in Tokyo in November 2000
- Design Integration Meeting in Knoxville in March 2001
- Technical Meetings for Target / Test Facilities / Design Integration teams, and Design Integration Meeting at FZK in October 2001
- Technical Meeting for Accelerator at FZK in January 2002
- Design Integration Meeting in Tokyo in March 2002
- Technical Meetings for Target at ENEA Frascati and IPPE in October 2002
- Design Integration Meeting in Garching in November 2002

The initial assignments and definitions of the KEP Tasks were published in August 2000 [4], identifying responsible persons, institutes in charge, schedules, and task deliverables. An Interim Report [5] on the progress in each Task up to June 2001 was compiled, and was used as the basis for review of future plans and collaborations.

The schedule for the publication of this KEP Report was approved in the Tokyo Meeting, March 2002. The progress and results of the Tasks were reviewed in the Garching Meeting, October 2002. The KEP tasks were completed and reported by the contributors in the EU, Japan, the RF and the US. Tasks for IFMIF design and for subsystem designs were conducted on the basis of a two-stage construction schedule (the first accelerator to be completed in seven years, and the second in the following three years), which was proposed and accepted at the Tokyo Meeting. The Executive Summary of the three-year KEP activity was delivered to the IEA IA-FM Executive Committee in early 2003.

1.2.2 Organization

IFMIF-KEP activities have been carried out under the direction of the Executive Committee of IEA IA-FM and the Executive Subcommittee for IFMIF. The KEP Tasks were completed by the efforts of the IFMIF Design Team and the contributors from the participating parties. The IFMIF Design Team consists of members from the EU, Japan, the RF and the US. The relationships among these organizations are shown in Fig. 1.

References

[1] IFMIF CDA Team (ed. M. Martone), IFMIF International Fusion Materials Irradiation Facility Conceptual Design Activity Final Report, ENEA Report RT/ERG/FUS/96/11 (1996).

[2] A. Möslang (ed.), IFMIF International Fusion Materials Irradiation Facility Conceptual Design Evaluation Report - A Supplement to the CDA by the IFMIF Team, FZK Report FZKA6199 (1999).

[3] Fusion Neutronics Laboratory, IFMIF International Fusion Materials Irradiation Facility Conceptual Design Activity - Reduced Cost Report - A Supplement to the CDA by the IFMIF Team, JAERI Report JAERI-Tech 2000-014 (2000).

[4] Fusion Neutron Laboratory, IFMIF International Fusion Materials Irradiation Facility Key Element Technology Phase Task Description, JAERI Report JAERI-Tech 2000-052 (2000).
[5] IFMIF International Team, IFMIF International Fusion Materials Irradiation Facility Key Element Technology Phase Interim Report, JAERI Report JAERI-Tech 2002-022 (2002).

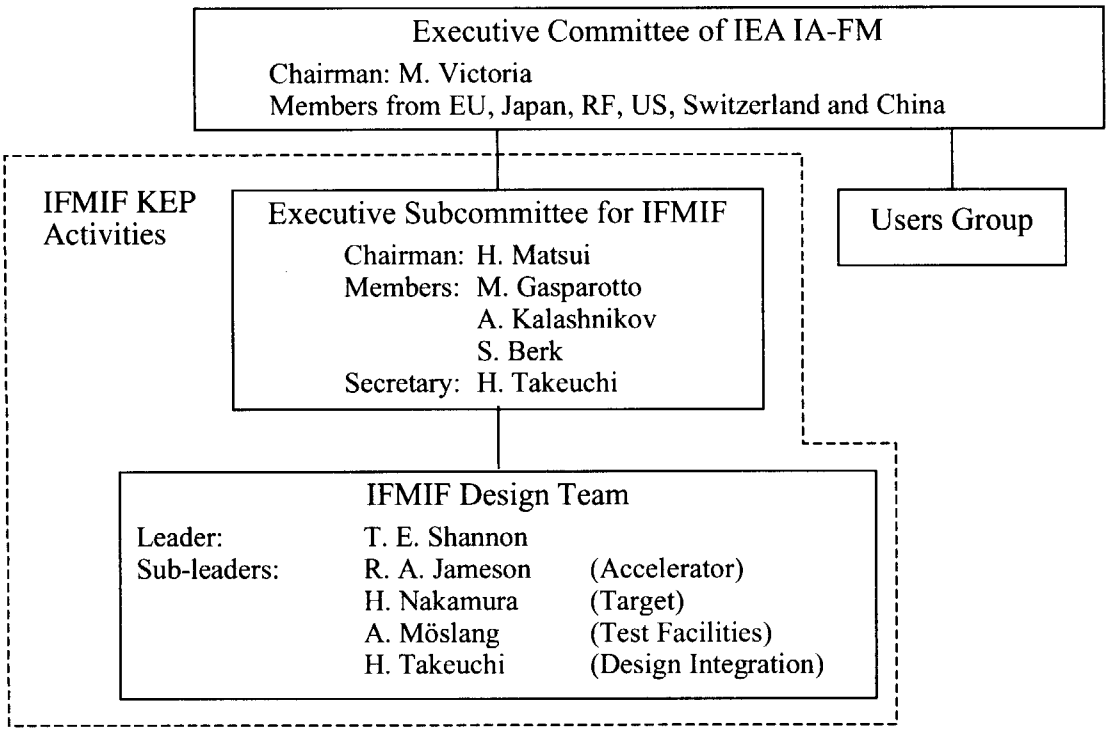


Fig. 1 Organization of IFMIF-KEP activities.

2. Outline of KEP Report

The KEP Tasks were carried out with the objective of reducing the risk factors of the key technology before beginning validation tests of continuous, long-time operation of each subsystem. The Tasks are needed to achieve a continuous wave (CW) D^+ beam with current 250 mA and energy up to 40MeV. The tasks must also establish the power handling capability (up to 10MW) of the liquid lithium target system, to achieve stable irradiation parameters on test specimens, and establish the required availability and safety conditions for the facility.

The KEP Tasks, their contents, schedule, responsibility and contributors were defined in the Task Description [1] in 2000. After publication, several Tasks were modified for efficient task completion and individual circumstances of research / development in each party. For examples, a few Target diagnostic tasks were moved from Design Integration to the Target area. Progress in these tasks through June 2001 was reported in the Interim Report [2].

Considerable progress has been made since the Interim Report, especially in experimental tasks for Accelerator, Target, and Test Facilities. Also, the tasks of Design Integration have advanced. As a result, 83 tasks (26 tasks for Accelerator, 19 tasks for Target, 24 tasks for Test Facilities and 14 tasks for Design Integration) were completed. The Tasks in each subsystem are outlined in the following sections.

2.1 Accelerator

The Accelerator system is required to deliver D^+ beams with total current of 250 mA (125 mA in each of two accelerators) and energy up to 40 MeV. The availability of IFMIF mainly depends on the Accelerator; therefore, a long lifetime is required for all components. Low beam loss is required throughout the entire accelerator and high energy beam transport (HEBT) to minimize radiation that would complicate maintenance. In the KEP work, the accelerator reference design was improved and several critical components were tested experimentally. The investigations were conducted in parallel by several parties. While the present reference design is based on conventional, room-temperature accelerator technologies, more advanced accelerator technologies like superconducting (SC) linacs are being investigated. The Accelerator Tasks directed at these issues included design, evaluation and experiments as follows:

2.1.1 Injector

Several D^+ ion sources were tested for the capability to deliver high current and long lifetime. This included tests with H^+ (and D^+) beams at Commissariat à l'Énergie Atomique (CEA) Saclay (Electron Cyclotron Resonance (ECR) type), Institut für Angewandte Physik (IAP) (volume type) and Japan Atomic Energy Research Institute (JAERI) (filament-driven multi-cusp and mirror field ECR types) as Tasks AC11. Beam emittance and noise at the entrance to the radio frequency quadrupole (RFQ) were estimated by analyses from the respective sources through the low energy beam transport (LEBT). These analyses were performed in the three institutes (AC12, AC13). As a result of the work during the KEP stage, the ECR source was chosen as the reference ion source for the IFMIF accelerator.

2.1.2 RF Source

For long-time operation and system reliability, a long-duration (~1000hr) test of the Thales Diacrode and investigation of a solid state driver amplifier were performed as Tasks AC21. RF window design to provide a basis for a future durability test was performed (AC22).

2.1.3 RFQ / DTL / HEBT

A 4-vane RFQ is the reference design. The beam dynamics design was fully developed by two groups during the KEP phase, and is now a robust preliminary design (AC33-34). Beam performance and cooling of Alvarez type drift tube linac (DTL) were investigated (AC31/32/36/37); the results show that the DTL reference design is robust. Alternative technologies for the RFQ (4-rod RFQ) and other types of DTL (Interdigital H mode DTL (IH-DTL) and SC Crossbar H mode DTL (SC-CH-DTL))

were investigated to explore if these alternative choices might offer advantages to IFMIF (AC35). Activation estimates were made for the safety analysis (AC39). Analyses of HEBT were also included (AC21).

2.1.4 Diagnostics

Non-destructive diagnostic methods for measuring beam profile and beam emittance were investigated experimentally.

2.1.5 Cost Estimation

Partial cost updating tasks were added as Tasks AC26-27, covering the revised HEBT, the Diacrode RF system, and a fully operational IFMIF prototype.

2.2 Target

The liquid lithium target, with a free surface and a maximum speed of 20m/s, must maintain the flow thickness and temperature profile during the continuous and long-time operation. The basic hydraulic behavior of the lithium flow was simulated using a water flow experiment and the thermal behavior of the lithium target and lithium loop was simulated using computer code calculations. Diagnostic methods to monitor the stability of the operation were investigated. The control of impurities, such as tritium, Be, N, C, O, etc., is necessary for radiation safety and loop integrity, and materials for impurity getter were examined. The design of a remote-handling device to work near the activated materials is needed before mockup testing.

2.2.1 Stability of Li Target Flow

Water experiments simulating the lithium flows, conducted as Tasks TG11, were used to examine the effect of the nozzle inner-wall roughness (JAERI) and the effect of steps at the back-plate joint on surface stability (ENEA). Lithium flow behavior testing in a small lithium loop has been started in Osaka University (TG13/16) with ENEA support (TG15), and another loop is under preparation at IPPE (TG12). The thermal-hydraulic stability of the lithium target was verified by numerical analysis (TG12).

2.2.2 Erosion / Corrosion and Impurity Control

The erosion / corrosion of stainless steel was evaluated by examining some parts of the Osaka loop (TG21). An experiment to select a nitrogen getter material was performed at the University of Tokyo (TG31). Other investigations and experiments were planned at ENEA (TG22/31) and IPPE (TG12).

2.2.3 Diagnostics on Target

Adaptation of ultrasonic methods to measure the lithium flow thickness was tested using an ultrasonic device on the Osaka loop (TG35). Monitors for target temperature and distortion were also investigated (TG33, TG37).

2.2.4 Safety and Loop Integrity

To examine the possibility and the effect of lithium fire, a lithium fire experiment and a compilation of lithium reaction data were performed as Tasks TG51-52. The effect of a target failure or a beam trip on the safety and the loop integrity was examined by performing a safety analysis and transient analyses (TG61, TG71).

2.2.5 Remote Handling System

The remote handling devices were designed for two options of the back wall replacement method. One option is the bulk replacement of the target assembly with a cut and weld at the lip seal by yttrium aluminum garnet (YAG) laser (TG81) and the other option is a replacement of the "Bayonet" type back-plate only (TG82).

2.3 Test Facilities

Irradiation conditions over the irradiation test volume need to be stable during the irradiation campaigns for the accurate evaluation of the irradiation effects and the efficient execution of the materials development. The uncertainty of the neutron yield and the neutron data library up to 50MeV should be reduced to predict the correct nuclear response for planning the irradiation tests. The design of the helium cooled test module should be improved to achieve precise specimen temperature control. The irradiation parameters should be optimized for the materials development plan and to account for non-full beam use at beam trip or in the staged construction. Safety concerns must be evaluated during test modules handling and for the treatment of tritium and the other radioactive wastes.

2.3.1 High Flux Test Module

To verify the integrity and the performance of the temperature control in the helium cooled High-Flux Test Module (HFTM), the HFTM was designed based on the thermal hydraulic and fluid dynamic calculations. Mock-up fabrication and thermal hydraulic testing were performed in FZK (as Task TF11) and in Centre de Recherches en Physique des Plasmas, École Polytechnique Fédérale de Lausanne (CRPP-EPFL) (TF12).

2.3.2 Neutron Distribution

Measurement of the D-Li neutron source spectrum and the production of beryllium-7 were performed at Tohoku University under condition of D^+ beam with energies of 25 and 40 MeV (TF21). The asymmetric neutron field was analyzed to evaluate the effect of one-accelerator operation (TF22). To improve the nuclear response for breeding materials in the Medium-Flux Test Module (MFTM), Monte Carlo Code for Neutron and Photon Transport (MCNP) calculations were performed to design the MFTM with added moderator/reflector materials (TF23, TF24).

2.3.3 Test Equipment

The structure to accurately install the Vertical Test Assembly 1 (VTA1) was reviewed (TF31). A prototype of micro-tomography to survey the Test Cell equipment's was fabricated and tested in National Institute for Laser, Plasma and Radiation Physics (NILPRP) (TF33). For radiation safety, an outline of the tritium laboratory was improved, and the treatment scheme for radioactive waste, especially for those containing tritium, was examined (TF34). The arrangement of the Test Cell (TF35), the transfer of heavy equipment (TF36) and the operation methods in off-normal conditions (TF38) were examined. The feasibility of the gas-cooled HFTM was investigated in a thermal-hydraulic study with 3-D numerical simulation at Kyushu University (TF39).

2.3.4 Review of the Effects of Cost Reduction and Staged Construction

The neutron flux distribution during staged construction (TF41) and the PIE equipment were examined (TF42).

2.3.5 Neutronics

To improve the D-Li neutron source term, the related data files and codes were revised at FZK (TF51), and experimental verification was carried out at Nuclear Physics Institute (NPI) (TF52). The reliability of the activation cross-section library was studied (TF53). A data library for the high-energy neutrons was created and tested (TF54, TF55). The performance of the radiation shielding was verified by calculations around the Test Cell (TF56). A sub-miniature fission chamber to be used as an on-line neutron monitor was fabricated and tested in ENEA and NPI (TF57, TF58).

2.3.6 User Specific Issues

The nuclear response for use of the first accelerator during the staged construction was calculated for different beam footprints (TF61), and plans for material tests at each stage were

reviewed (TF62). Small fracture toughness specimens were evaluated to determine size effects (TF63, TF64).

2.4 Design Integration

Design Integration (DI) activities cover the entire IFMIF to ensure that each subsystem is consistent with the needs and plans for the full facility. The IFMIF design and operation must meet the user requirements, the required availability, and safety standards. The Design Integration function assures continuing attention to these needs.

2.4.1 Diagnostics during Operation

Monitoring irradiation condition during the operation requires on-line neutron-field measurement; Task DI11 examined options for making these measurements.

2.4.2 Activation and Shielding

To prepare for the design of the maintenance equipment used around Test Cell, shield-wall elements with large activation cross-section were determined (DI21). MCNP calculations were performed to verify the performance of the bulk shield and to determine radiation streaming in the Test Cell shielding walls (DI71).

2.4.3 Conventional Facilities

Room arrangement within the Main Building was performed to assure that space needs and material flow requirements were met (DI41). The utilities, including the treatment of radioactive wastes, were reviewed to verify that the capacities of the utilities met the safety requirements (DI43).

2.4.4 Central Control and Operation Flow

The concept of the central control was examined (DI51) and the operation flows of subsystems were reviewed and compared (DI61) to check that they were consistence with IFMIF operational requirements.

2.4.5 RAM and Safety Analyses

Reliability, Availability, Maintainability (RAM) analysis (DI81), a safety analysis (DI83) and an evaluation of the worker dose (DI85) were executed to check the availability and the safety for the revised IFMIF concept.

2.4.6 Project Issues

Examination of the licensing requirements (DI91), the analysis of the schedule for the whole IFMIF project (DI93) and review of the cost estimate (DI95) were conducted to be consistent with the progress of the IFMIF project.

References

[1] Fusion Neutron Laboratory, IFMIF International Fusion Materials Irradiation Facility Key Element Technology Phase Task Description, JAERI Report JAERI-Tech 2000-052 (2000).

[2] IFMIF International Team, IFMIF International Fusion Materials Irradiation Facility Key Element Technology Phase Interim Report, JAERI Report JAERI-Tech 2002-022 (2002).

3. Results of KEP Activities

3.1 Accelerator Facilities

3.1.1 Accelerator Facilities

The IFMIF requirement of 250 mA of deuteron beam current delivered to the lithium target will be met by two 125-mA, 40-MeV accelerator modules operating in parallel. The technological approach of the reference design selected is only cautiously aggressive with respect to the beam current handling capabilities of the rf linac technology, and provides operational redundancy by allowing operation to continue at 125-mA when either of the two accelerators is temporarily removed from service for repair. Each 125-mA accelerator is designed with sufficient derating, but not with a significant upgrade capability. The IFMIF deuteron accelerators are a sequence of acceleration and beam transport stages. A cw 155-mA deuteron beam is extracted from the ECR ion source at 95 keV. A Low Energy Beam Transport (LEBT) guides the deuteron beam from the source to a Radio Frequency Quadrupole (RFQ). The RFQ bunches the beam and accelerates 125 mA to 5 MeV. The 5-MeV RFQ beam is injected through a matching section (2 cavities, 4 quadrupoles) into a room temperature, ramped-gradient Drift Tube Linac (DTL) of the conventional Alvarez type with post couplers, where it is accelerated to 40 MeV. The baseline rf power system for the IFMIF accelerator assumes the use of Diacrode technology with an output power level of 1.0 MW and a frequency of 175 MHz. Operation of both the RFQ and the DTL at the same relatively low frequency is a conservative approach to delivering the high-current deuteron beam with low beam loss in the accelerator. This will facilitate hands-on maintainability without remote manipulators. Although the present reference design is based on conventional, room-temperature rf linear accelerator (rf linac) technology, superconducting linac technology that has the potential of reaching an even higher performance and possibly lower cost is also being followed closely.

The Accelerator Facility KEP work is firmly based on the previous CDA/CDE activities. This is especially important to note in all costing studies, where an explicit path to the comprehensive CDA Cost Estimate can always be traced.

In the KEP, the most important accomplishments for lowering construction risk and affording a

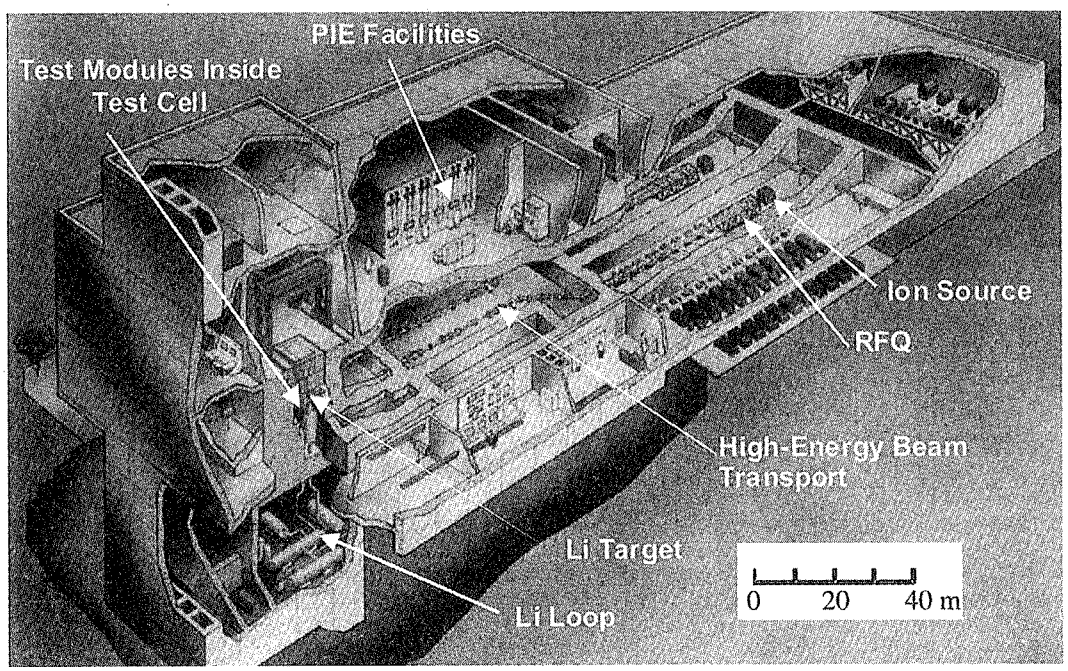


Fig. 1 Overview of the present IFMIF design with major subsystems. Maximum availability is achieved by two completely independent accelerator lines. The ion source, RFQ and HEBT of one deuteron beam line are indicated, with the second accelerator lying behind. The blue blocks indicate the high-power rf system for the accelerator.

rapid construction start are: (1) the selection of the ECR injector for the reference design, (2) achievement of a preliminary but detailed reference beam dynamics design for the full accelerator indicating that the low beam loss specification should be met, and (3) the demonstration of good availability of order hundreds of hours from an operational ECR injector and from the Diacrode 1 MW rf power amplifier.

The Accelerator Facility KEP Report is organized in sections according to the following outline, which briefly summarizes the achievements and includes some additional references.

Injector - Ion Source/LEBT/Matching to RFQ

The IFMIF ion injector, comprised of the ion source and the LEBT, has to provide excellent beam quality, sufficiently high beam current, and high operational availability. To minimize downtime and maximize system availability, all failure-prone injector components are being designed for rapid exchange in the accelerator vault, subsequent to shutdown. Extensive operational experience with the ECR ion source type was obtained at Saclay, with several very long runs of 100 to 700 hours duration, with availability of >95% achieved. IAP continued evaluation of multi-cusp sources and LEBTs, and operational tests of multi-cusp and ECR sources were conducted at JAERI.

Operation with a D^+ beam at CEA Saclay shows that IFMIF beam performance requirements can also be achieved with a deuteron beam.

After extensive parallel developments during the CDA, CDE and KEP [1], the ECR ion source is selected as the reference design ion source for the IFMIF project.

3.1.2	AC11A-EU (CEA-Saclay)	Very Long Test of ECR Ion Source
3.1.3	AC11B-EU (IAP)	Long-run Test of Multi-Cusp Ion Source
3.1.4	AC11C-JA	Test of ECR and Multi-Cusp Type Ion Sources
3.1.5	AC12A/13A/14-EU (CEA-Saclay)	ECR Source Analyses
3.1.6	AC12B-EU (IAP)	Source Analysis
3.1.7	AC13B-EU (IAP)	Low Energy Beam Transport (LEBT)
3.1.8	AC13C-JA	Test of Low Energy Beam Transport
3.1.9	AC34B-JA	Examination of Beam Matching to RFQ

Radio Frequency Quadrupole (RFQ)

The reference design RFQ is a 4-vane type 175 MHz structure. The output energy of 5 MeV was selected for the RFQ, because it is the lowest energy allowing a F0D0 magnetic lattice in the DTL which is desirable for halo control and the consequent minimization of beam loss. The high output energy, however, necessitates a long RFQ structure of ~12.5 m. The RFQ will likely need 3 Diacrodes of 1 MW each. Within the present KEP phase, the preliminary design of the RFQ beam dynamics has been finished, with extensive simulation and sensitivity (machining) studies. Detailed design work was performed by two groups using different techniques. Both RFQ designs meet the low beam loss specifications. Further work is required to achieve final design status. It is desired to reduce beam loss still further, and extensive optimization and sensitivity studies must be done, as for any conceptual design.

In another study, a formalism that has been developed permits the computation of all quantities necessary to RFQ tuning procedures.

3.1.10	AC20-US	Equipartitioned RFQ Beam Dynamics Design
3.1.11	AC34A-EU (CEA-Saclay)	Optimization of Electric Field Property in RFQ on Cold Model

Drift Tube Linac (DTL)

The IFMIF reference design uses a conventional room-temperature 5-40 MeV DTL, the structure having the strongest focusing possible in this energy range, in order to achieve minimum beam loss in the accelerator. The DTL includes 5 DTL tanks (with a peak accelerating field of 1.75 MV/m) and 9 rf tubes

to power them (per linac; 1 tube on Tank 1, 2 tubes on Tanks 2-5) [2]. Preliminary mechanical design and modeling of alternative quadrupole magnet cooling schemes, plus refined cost and schedule estimates, indicate full readiness for construction. Detailed design work was accomplished on the shortest, most difficult drift tube at the 5 MeV end of the DTL.

3.1.12	AC36-EU (CEA-Saclay)	Drift Tube Linac R&D Studies
3.1.13	AC37-US	Engineering Evaluation of the Drift Tube at 5 MeV
3.1.14	AC32-JA	Examination of Drift Tube Cooling Scheme

Study of Evolving Accelerator Technology Developments of Possible Advantage to the IFMIF Accelerator

A 4-rod type RFQ is under consideration to ascertain whether it might have cost and other advantages for IFMIF.

Preliminary investigation is being made of an alternative 5-40 MeV design using a room-temperature IH-structure and a following superconducting CH-structure. In case of superconductivity the rf losses are lower, and the linac is shorter and has larger apertures. Work in other programs on superconducting spoke resonator designs also needs to be applied to IFMIF to explore potential operational and cost advantages [3].

3.1.15	AC33B-EU (IAP)	Choice of RFQ Structure, Development of 4-rod RFQ
3.1.16	AC35-EU (IAP)	Choice of DTL Structure, and Investigation of CH-DTL

High-Energy-Beam-Transport (HEBT) System

The HEBT has been substantially revised from the CDA configuration; most importantly, the RF cavities used for beam energy spread control in the CDA design were removed. Preliminary simulations indicate that a suitable HEBT system can be defined.

3.1.17	AC21-US	Analysis of Revised IFMIF High Energy Beam Transport (HEBT) (HEBT) System

End-to-End Beam Dynamics Design

Comprehensive end-to-end particle dynamics calculations including errors have been performed, showing that for various conditions stable solutions with low emittance growth and full transmission could be found. With DTL errors and corrections, the end-to-end transmission is expected to reach 98%. The DTL beam dynamics reference design has no particle losses.

3.1.18	AC33A/38-EU (CEA-Saclay)	End to End Beam Dynamics

RF Power System

Development and testing of a 1 MW rf system was identified earlier as the highest impact development item, as existing operating experience was for short periods (1-8 hours). Outstanding progress has been made in developing and testing a new kind of gridded tube called the Diacrode which can overcome the limitations of conventional tetrodes, mainly the rf losses, by a factor of 4. The challenging goal was to meet the reliability demonstration goal of IFMIF, namely, 1000 h at 1MW cw rf power and 175-200 MHz. Endurance tests with a TH 628 Diacrode have been performed, with over 1047 hours at full power in the range of 1010-1030 kW cw rf and 200 MHz. This shows the capability to operate stably under IFMIF-relevant conditions.

Diacrode phase and amplitude modulation data were also obtained from LANL [4], and an updated

cost estimate was developed for the Diacrode.

Investigations of solid-state driver amplifiers for the Diacrode were conducted, as well as rf drive loop design for up to 500 kW cw, by two different groups.

3.1.19	AC21A-EU (CEA-Saclay)	Radio Frequency system
3.1.20	AC21B-JA	RF Power Tube Durability Test
3.1.21	AC22A-JA	Test of the RF Window

Diagnostics, Instrumentation and Control

Significant progress on non-interceptive diagnostics has been made at CEA/Saclay and IAP for high intensity beams. IAP has also developed a high-power interceptive emittance measurement device. However, diagnostics for high power cw beams are not yet fully available and require continuing development.

3.1.22	AC41A-EU (CEA-Saclay)	Diagnostics for High Power Beam
3.1.23	AC41B-EU (IAP)	Diagnostics for High Power Beams

Activation Analyses, Interfaces

3.1.24	AC39-JA	Activation of Accelerator System Components
3.1.25	AC31-JA	Estimation of Beam Loss at Various Operating Conditions

Examination of the Cost of a Fully Operational IFMIF Prototype, and Cost Update for HEBT and RF Power

In response to widespread discussion of the benefit of having a fully operational accelerator prototype, the US team undertook a task in 2002 to define the scope and develop a cost estimate for such a program. The work incorporated the latest design information available to arrive at an updated design configuration for the IFMIF accelerator. From this configuration a prototype design was developed that meets the technical requirements set forth at the IFMIF Design Integration Meeting at FZK Karlsruhe in October 2001. The results of this study were finalized in early March 2002 and presented at the IFMIF Subcommittee meeting in Tokyo later that month. The estimated cost for the five-year prototype program is 102 MICF including an AFI allowance of 23 MICF.

As a separate task, the cost of the revised "reduced cost IFMIF" HEBT and the Diacrode-based rf system was evaluated. The expected savings over the CDA cost estimate were seen; however, the savings were not as great as assigned in the reduced cost estimate.

3.1.26	AC22B-US	Cost Evaluation of Changes in the System Including the Revised HEBT and the Diacrode Based RF system
3.1.27	AC23-US	Examination of the Cost of a Fully Operational IFMIF Prototype

Transition to Accelerator Facility for EVEDA

High priority items for continuing development in the next immediate phase of IFMIF include:

- Updating the IFMIF Accelerator option to use superconducting linac technology for the 5-40 MeV Linac. IFMIF evaluated superconducting linac technology thoroughly during the CDA, but did not incorporate it into the reference design, largely for cost reasons. During the intervening years, development of superconducting accelerating structures and rf drive techniques continued in several institutes. These developments offer the possibility of technical, cost and availability advantages to the IFMIF project.
- Development of an H_2^+ beam ion source to be used during commissioning studies to avoid

radioactivity. It is more difficult to achieve high H_2^+ beam current than D^+, and a development program is required.
- RF drive loop tests up to 500 kW cw.
- Updating of interface requirements from users, test cell, target, and conventional facilities, and application to the accelerator design as required.
- Continued design refinement.
- Continued effort to gain operating experience with a deuteron beam in the ECR injector, for application to IFMIF design.

Any complex facility is only fully known as operating experience is obtained. The experience with the operating ECR injector and the Diacrode rf amplifier has been very valuable. Although it seems clear that a full-scale prototype, designed for incorporation into the final facility, is probably unaffordable, a continued effort to test subsystems during the period preceding IFMIF construction would be worthwhile. For example, during the ECR runs, the neutron production in the LEBT rose rapidly, indicating that further optimization is necessary for the final IFMIF facility.

References

[1] "CDA-Report-Table2622updated.doc", Excerpt from CDA-Report (RT/ERG/FUS/96/11) Table 2.6.2-2. IFMIF-related injector development status data, updated.
[2] R. Ferdinand, "200111IFMIFDTLdesign.doc". (This configuration in use for costing studies.)
[3] Workshop on the Advanced Design of Spoke Resonators, Los Alamos, NM, USA, October 7 and 8, 2002; http://laacg1.lanl.gov/spokewk/.
[4] IFMIF Memorandum IFMIF/RF/RAJ-20020805, "THALES Diacrode Modulation Tests for LANL", IFMIF Memo-TTE DiacLANL .pdf.

3.1.2 AC11A-EU : Very Long Test of the ECR Ion Source

(1) Brief Task Description

The task was completed in the framework of the CEA program on high-power particle accelerators supported by the IPHI demonstrator project. This project is dedicated to high power beam production (CW beam, 100 mA) [1-5].

The injector system (source and Low Energy Beam Transport) must demonstrate reliability commensurate with the maintenance schedule of the IFMIF accelerators. Low to very low spark rates have to be shown, as well as reliability in terms of source performance.

The work concentrated on verifying/improving the ECR source availability with a 100 mA cw beam for more than 4 weeks. Current, beam energy, beam noise, species fraction, beam emittance, etc. were recorded. The source ran in a proton mode to avoid activation of the existing test stand.

Contributors

Name	Party	Institute	E-mail address
R. Ferdinand	EU-FRANCE	CEA-Saclay	rferdinand@cea.fr
R. Gobin	EU-FRANCE	CEA-Saclay	rjgobin@cea.fr

(2) Introduction

SILHI ("Source d'Ions Legers Haute Intensité") is in operation at CEA-Saclay. Figures 1 and 2 show a photograph and a schematic view of SILHI. It delivered its first proton beam in July 1996. This ECR (Electron Cyclotron Resonance) source is designed to produce continuous high-intensity proton and deuteron beams. The reliability-availability of IFMIF is one of the most important goals, so the source has to be as reliable as possible. Six long run tests were done to analyze the source behavior in continuous operation.

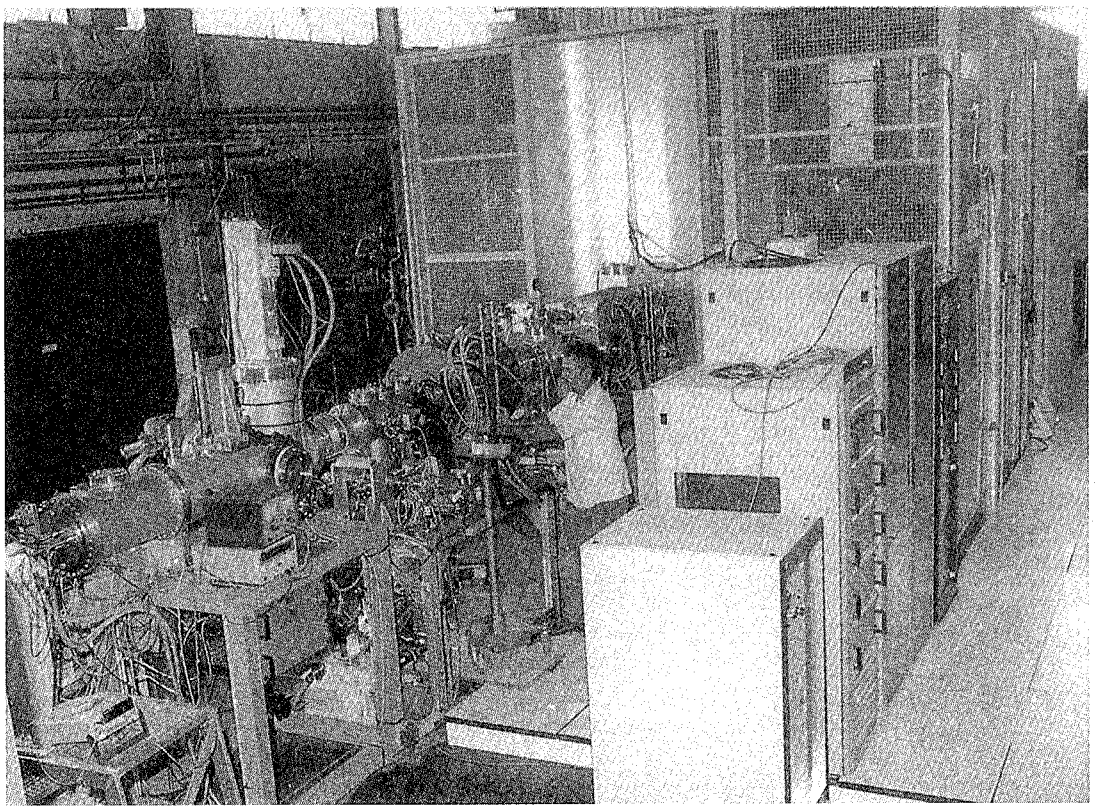


Fig. 1 SILHI ECR injector.

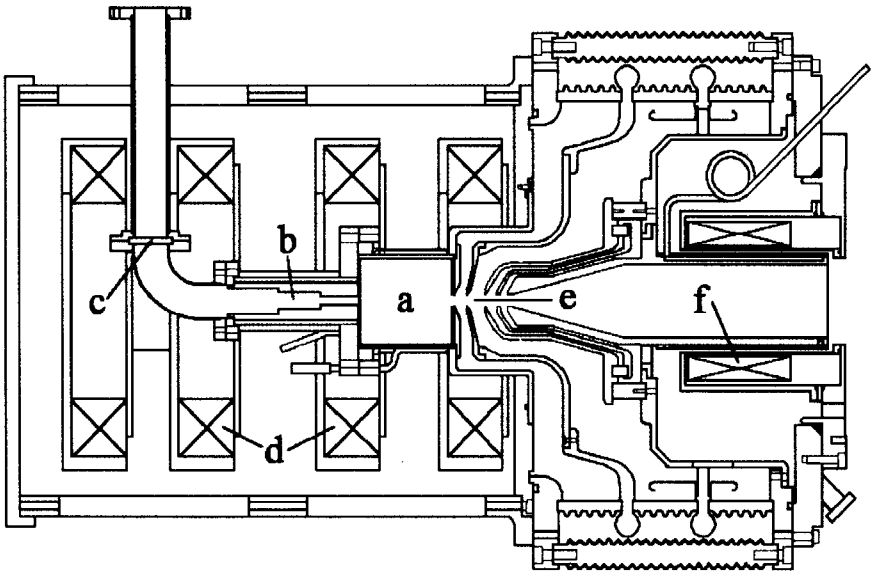


Fig. 2 Schematic of SILHI ECR ion source. a: plasma chamber; b: ridged waveguide coupling system; c: window; d: coils; e: extraction system; f: DCCT

The extraction system has been improved in the past to minimize beam losses at higher extracted beam current and the source command and control system was completely updated with the EPICS system. This new configuration allows us to extract higher intensity deuteron beam after conditioning; a second long run reliability test was performed for one month in October 2001.

Dose rates need to be estimated both during normal plant operation, "beam-on", and at "beam-off" conditions.

(3) Summary of the First Run Tests

In December 1997 the source was continuously operated for five days (103 hours) with a 100 mA CW proton beam at 80 keV. The global reliability reached 94.5 % with 53 shutdowns mainly induced by HV sparks. A second test was performed in May 1999 with a 75 mA CW beam at 95 keV, and the availability reached 98% for continuous operation of 106 hours. The beam was interrupted 24 times.

In October 1999, after improvements, a new five-day test run was done with a 75 mA extracted beam at 95 keV. Only one beam trip occurred, lasting 2.5 minutes, during the 104 hours run test; 103 hours uninterrupted running time was achieved. The reliability reached 99.96%.

(4) First Four Week Reliability Test

Long run tests often benefit the knowledge of the source behavior and component failure. A four-week run test was planned following the remote control exchange and the installation of the new extraction system.

To limit beam losses in the extraction zone, a new set of electrodes was designed and assembled. In October 2000 it allowed us to extract up to 150 mA total extracted beam with a LEBT transparency (up to the future RFQ matching point) higher than 90%.

The source was shut down for 2.5 months (mid November 2000 to end of January 2001) to completely change the remote control system. The old system, based on Visual Basic and PCs, controlled all the power supplies and was associated with a Selectron PLC for vacuum control. The SILHI source became the development test bench for the new EPICS system. It was also the only way to make a four-week run with accurate measurement of beam characteristics. It includes much better automatic recovery algorithms. At the end of January, the beam was again extracted and weeks were spent improving the control system, specifically the automatic procedures. These procedures allow us to leave the source working without an operator and allow long distance control through modem connections.

For the new long-run test, all beam characteristics were checked: beam intensity, proton fraction, emittance and beam noise. To avoid LEBT activation, the tests were conducted with protons.

The four-week run started on Monday, March 19, 2001, with the beam parameters reported in Table 1. Due to various problems, the experiment was interrupted on the morning of Monday April 9 for a complete check-up of the accelerator column. Contrary to what was expected, we were not able to obtain satisfactory source behavior. Even though this reliability test did not reach the expected results, it did yield a lot of information summarized below.

Table 1 SILHI 1st long run requirements and run test parameters.

Parameters	Requests	Run Status
Energy [keV]	95	95
Proton extracted beam [mA]	100	~ 97
Total extracted beam [mA]	110	118
Proton fraction [%]	> 90	~ 84
Extraction aperture [mm]	9	9
Extracted beam density [mA/cm²]	156	185
Forward RF power [W]	Up to 1200	1000
Duty cycle [%]	100	100
Hydrogen mass flow [sccm]	< 10	5.3
Beam noise (rms) [%]	< ± 1	± 0.95 max

Beam line contamination leads to rapid beam quality degradation. The LEBT design has to clearly take this into account.

The oxygen cleaning beam seems very efficient in improving the proton fraction but unfortunately after the cleaning, the spark rate increased. The improvement of proton fraction after ion source conditioning with oxygen plasma is similar if not identical to Los Alamos LEDA injector performance.

The automatic restart procedures were not completely adapted to all situations, especially if a spark occurs during the restart period. Improvements were made to minimize these failures. An automatic restart presently takes one minute, with a one second scan period.

The new EPICS control system allowed us to work without a local operator and to operate from a remote connection via the Internet network. Few hardware failures obligated us to come back to the source to repair. Despite this good control system, a spark during a weekend or at night implied a very long beam stop, which strongly decreased the beam availability. Better operability could be obtained with 24 h in-situ control.

The servocontrol loop, which maintains a constant extracted beam current, works well. The beam noise was never over ± 0.95 % and frequently in the ± 0.5 to ± 0.7 % range. This noise was mainly due to the 19 kHz spaced-lines transferred to the plasma from the magnetron rf switched power supply.

This four-week reliability test did not show the expected results for several reasons, including oil contamination. Compared to the 1999 tests, the main differences came from increased current and the new electrodes. With the new set of extraction electrodes, a 100 mA proton beam was transported to the future RFQ matching point and more than 150 mA total beam was extracted. The new set of electrodes increases by 10% the electric field at the surface. This may be one of the reasons for the spark rate increase. Of course, the contamination observed (carbon traces) is also very important for HV column reliability.

(5) New Long Run

Soon after the failure of the four-week run, and after improvements to the command/control system and the source itself, a new long run was started. Slightly more than a week was then available, giving about 160 h of source availability. The results shown in Fig. 3 returned to the very good results of the October 1999 test, and reflect very well the present source behavior. There is now about one spark per day. The MTBF was about 23 hours and the MTTR was about 2.5 min.

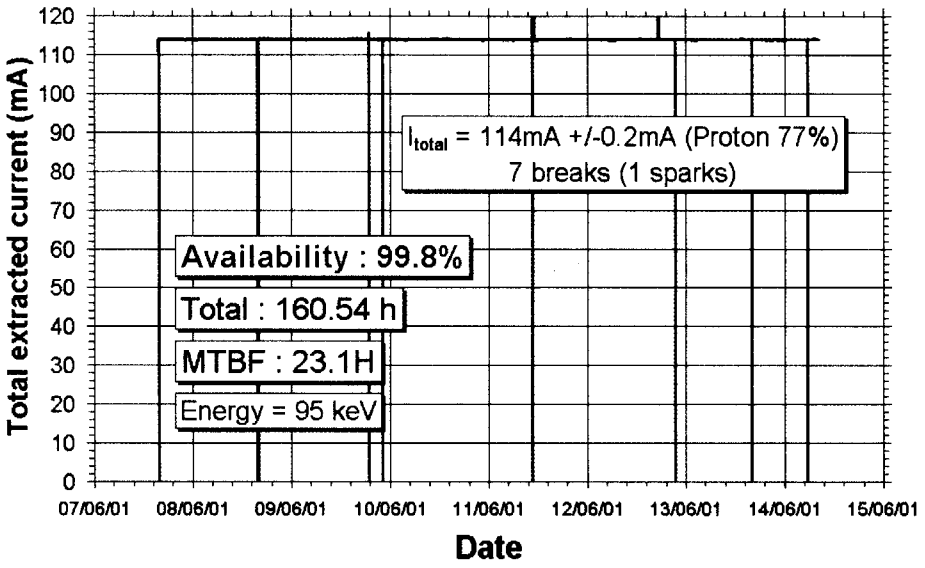


Fig. 3 Total extracted beam current during the 160h long run tests of the CEA-Saclay ECR SILHI Source.

(6) One Month Reliability Test

A four-week run test was restarted in October 2001, according to the decision taken in March 2001. The new procedures allow us to leave the source working without an operator and allow long distance control through modem connections.

The four-week run started on Monday, October 5, 2001, with the beam parameters reported in Table 2. It lasted in fact for a full month through November 6 (744 hours). There were 233 sparks recorded. The availability is equal to 95% (Fig. 4). One big problem occurred in the beginning but no special technical point was related to this breakdown. A non-foreseen stop occurred on the VME controller during the weekend and nobody was present to restart the source. The resulting downtime was 15 hours; the availability would have increased to 97% without this 15 hours down time. The beam noise was relatively stable, in the range 0.5 to 0.8% total. The proton fraction increased from 77% to 81% during the month.

Table 2 SILHI 2nd long run requirements and run test parameters.

Parameters	Requests	Run Status
Energy [keV]	95	95
Proton extracted beam [mA]	100	~ 96
Total extracted beam [mA]	110	120
Proton fraction [%]	> 90	~ 80
Extraction aperture [mm]	9	9
Extracted beam density [mA/cm²]	156	185
Forward RF power [W]	Up to 1200	800
Duty cycle [%]	100	100
Hydrogen mass flow [sccm]	< 10	5.7
Beam noise (rms) [%]	< ± 1	0.8 max

(7) Conclusion

Most probably because of oil contamination in the source, the two very long runs did not give extremely good results. The most representative source behavior was observed during the 160 hour test. We generally observed about one spark per day.

Nevertheless, IFMIF will have to take into account possible source malfunctions. The number of these can be minimized by careful design (screw pumps without oil, for example).

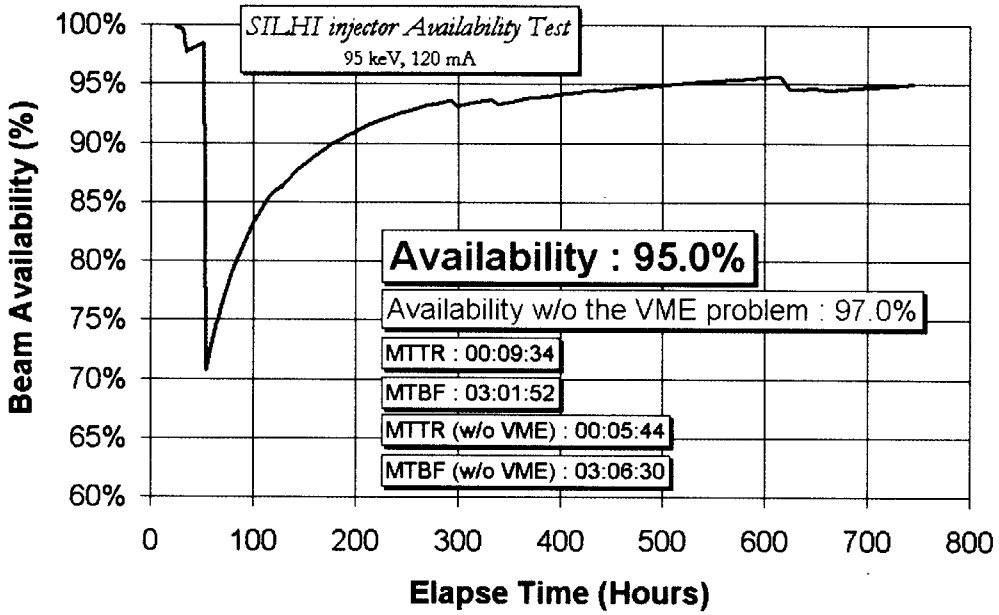


Fig. 4 Beam availability chart of the one month run test of the ECR SILHI source.

References

[1] R. Gobin, P-Y Beauvais, D. Bogard, R. Ferdinand, P. Mattéi, "Reliability tests of the high power proton source SILHI at CEA/Saclay", Third international workshop on HPPA reliability, Santa Fe, USA, May 2002.

[2] R. Gobin, P.-Y. Beauvais, K. Benmeziane, D. Bogard, G. Charruau, D. De Menezes, O. Delferrière, R. Ferdinand, A. France, Y. Gauthier, F. Harrault, J.-L. Jannin, J.-M. Lagniel, P. Mattéi, A. Sinanna, P. Ausset, S. Bousson, D. Gardes, B. Pottin, L. Celona, J.D. Sherman, "Saclay High Intensity Light Ion Source Status", EPAC 2002, La villette PARIS 2002, p.1712.

[3] R. Ferdinand, P.-Y. Beauvais, A. France, R. Gobin, J.-M. Lagniel, "Deuteron Beam Test For IFMIF", EPAC 2002, La villette PARIS 2002, p.894.

[4] R. Gobin et al., "High intensity ECR ion source (H^+, D^+, H^-) developments at CEA Saclay", ICIS2001 Conference, Rev. Sci. Instrum., 73, 922 (2002).

[5] P.-Y. Beauvais et al., "Status Report on the Saclay High Intensity Proton Injector Project (IPHI)", EPAC 2000 Proceedings, p.283.

3.1.3 AC11B-EU : Long-run Test of the Multi-cusp Ion Source

(1) Brief Task Description

The multi-cusp volume ion source under development at Frankfurt for IFMIF shall be operated in a long-term run. Source parameters (including beam current, source noise, cathode performance, etc.) are to be recorded and stable extraction and transport of the beam are to be shown. The optimum cathode arrangement is to be investigated. The source will be operated with protons to avoid activation.

Contributors

Name	Party	Institute	E-mail address
P. Beller	EU	IAP	p.beller@gsi.de
R. Hollinger	EU	IAP	r.hollinger@gsi.de
H. Klein	EU	IAP	horst.klein@iap.uni-frankfurt.de
A. Maaser	EU	IAP	andreas.maaser@O2.com
K. Volk	EU	IAP	k.volk@iap.uni-frankfurt.de
M. Weber	EU	IAP	manfred.weber@clariant.com

(2) Introduction

A new high current deuteron/proton ion source has been developed. It is a volume type source, and delivers 200 mA H^+ (corresponds to 140 mA D^+, according to the Child Langmuir law) in continuous wave operation with an H^+ fraction of about 93% [1]. Moreover, it is possible to operate this source in a high current H_2^+ beam production mode, which allows commissioning of the accelerator facility with an H_2^+ beam instead of a deuteron beam. Thus, the low beam emittance ($\varepsilon_{rms,\ 89\%,\ norm.}$= 0.042 π mm mrad at 56 mA) [2] and the low cost of the ion source make it to a promising candidate for IFMIF.

In a further step, a long-run test should be performed. Since at present our ion source test stand does not meet the safety regulations of the university (exhaust system for hydrogen), it cannot be used as it is. The necessary modifications are being performed.

The triode extraction system has an aperture with 8 mm diameter and is designed for voltages up to 55 kV. Consequently, the beam energy is 55 keV. For the following accelerator component, the RFQ, it is necessary to accelerate the 55 keV proton (deuteron) beam to 100 keV. Therefore, a new tetrode system has been designed and analyzed. In an additional step, the influence of different auxiliary gases on the H^+ fraction and the beam noise level has been investigated.

(3) Ion source Lifetime

In addition to a high current and a low beam emittance (we measured normalized 89% rms emittance of 0.042 π mm mrad), an appropriate ion source lifetime is an important requirement. The ion source lifetime is determined by the lifetime of the filament. During operation the filament is exposed to erosion by bombardment by positive ions from the plasma. For a given filament arrangement and operating gas, the lifetime is approximately inversely proportional to the duty cycle, the arc power and the arc voltage (energy of the ions). In order to obtain a long ion source lifetime, one should employ several filaments with large cross sections. As it is possible to use our ion source with up to four filaments, shown in the case of a high current H- volume source, the lifetime will be four times higher than for operation with one filament, leading to a lifetime of approximately three weeks.

(4) 100 kV Extractor

The triode extraction system used has an aperture of 8 mm diameter and is designed for voltages up to 55 kV. Consequently, the beam energy is also 55 keV. For the following accelerator component, the RFQ it is necessary to accelerate the 55 keV proton (or deuteron) beam to 100 keV. Due to the delay with the modification of our ion source test stand, a new tetrode extraction system has been designed and analyzed.

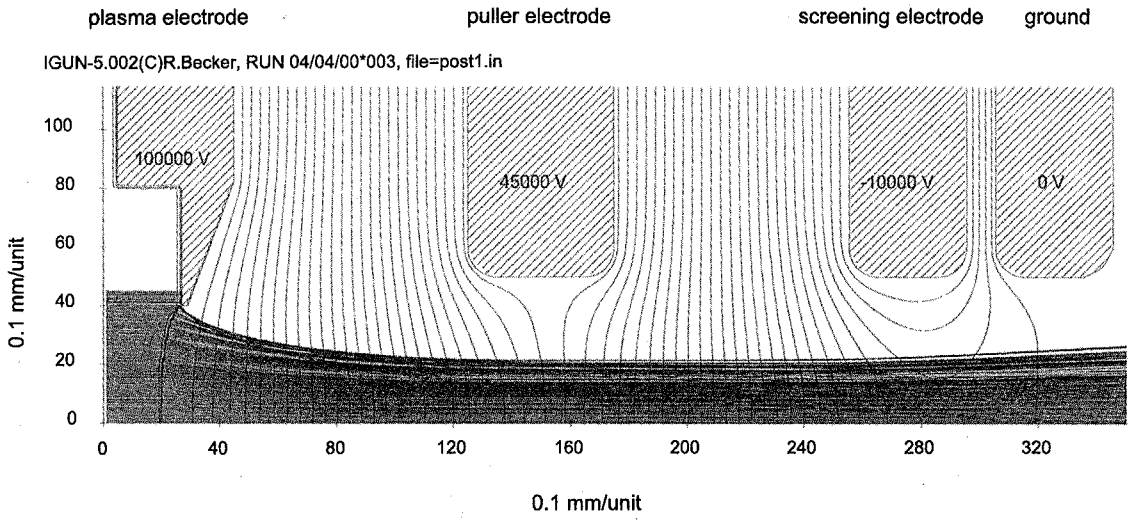


Fig.1 IGUN plot of the post accelerated 140 mA at 100 keV deuteron beam.

Figure 1 shows a schematic drawing of the tetrode system. It consists of four electrodes: plasma, puller, screening, and ground electrodes. It is different from the triode system in the use of a so-called puller electrode, installed between the plasma and screening electrodes. Other geometric parameters (aperture radius, thickness of the electrodes, aspect ratio, and gap field strength) are the same as in the experimentally proven triode system.

An important step in the design study of the extraction system is the choice of the potential of the puller electrode and the distances between puller, plasma, and screening electrodes. Both the electrical field strength and the distances between the electrodes should be carefully adapted to the proven values of the triode system. The neutral gas flow in the extraction system is responsible for voltage breakdown. Consequently, the maximum field strength in the extraction system is a function of the aperture radius, the neutral gas flow and the gap distances. For the triode system we determined a maximum field strength of 7.75 kV/mm for gap distances up to 8 mm. In the course of the design of the tetrode system, we used a more moderate gap field strength of 6.8 kV/mm. As shown in Fig. 1, the distance between plasma and puller electrodes is 8 mm with a potential difference of 55 kV. The distance between puller and screening electrodes is also 8 mm with a potential difference of 55 kV. With the computer code IGUN [3] we designed a 140 mA at 100 keV extraction system for an ion temperature of zero. The ion beam is extracted in the matched case with a radius of 2.9 mm (80%) and a divergence angle of 35 mrad at the end of the extraction system. The normalized rms-80%-emittance is 0.008π mm mrad and fulfills the IFMIF requirements.

(5) Influence of different auxiliary gases

In a second step, the influence of different auxiliary gases on the H^+ fraction and on the beam noise was investigated, in a series of experiments. The goal was to reduce the beam noise and to enhance the H^+ fraction at low arc powers. Fig. 2 illustrates the H^+ fraction as a function of the auxiliary gas pressure for different auxiliary gases. It was found that the H^+ fraction increases from 75 to above 92% by increasing the auxiliary gas pressure from 0.02 to 0.8 Pa. The effect is stronger for higher atomic mass of the auxiliary gas. Helium has little influence, xenon on the other hand has the strongest effect. Note, in all measurements, the extracted auxiliary ion fraction in the beam was below 1%.

It is assumed that the enhancement of the H^+ fraction is caused by the reduction of the mean electron energy. In contrast to electron collisions with hydrogen atoms and molecules, the cross sections for vibrational and rotational excitations of the investigated auxiliary gas atoms are higher. A higher cross section leads to a shorter mean electron path with the consequence of a higher number of inelastic collisions, resulting in a reduction of the mean electron energy as well as a reduction of the electron

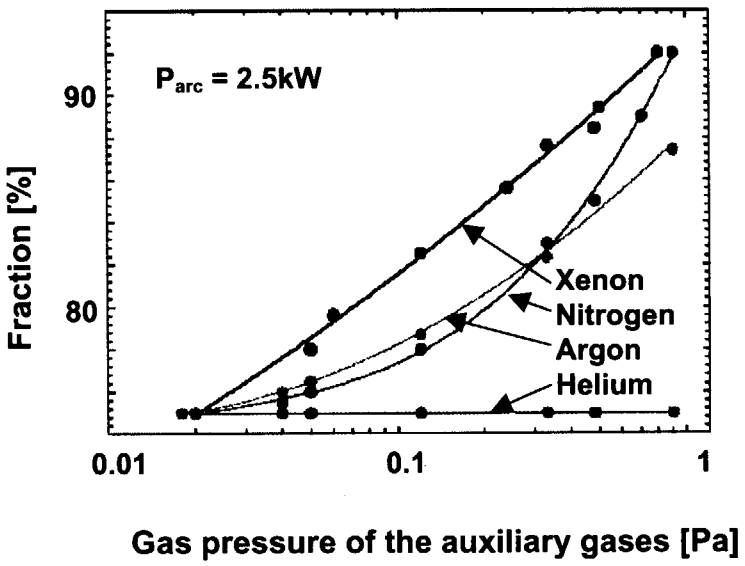


Fig. 2 H^+ fractions as function of the pressure for several auxiliary gases.

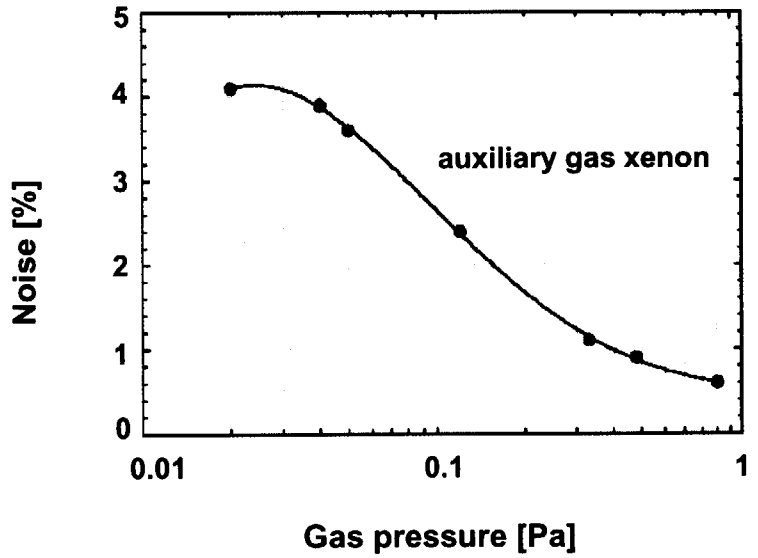


Fig. 3 Noise level as function of the auxiliary gas pressure (xenon).

temperature. From this it follows that the fraction of the generated H^+ ions rises. As shown by theoretical considerations, low energy electrons in the plasma are favorable for high H^+/D^+ fractions. Moreover, the use of a trace amount of an auxiliary gas reduces the beam noise level from 4% (without auxiliary gas) to less than 1% (with xenon, Fig. 3). Density fluctuations of the ions at the plasma sheath are coupled with density fluctuations of the electrons. As shown in basic plasma investigations with a 127° cylinder spectrometer, traces of xenon in the plasma reduce the electron temperature. This results in lower electron density fluctuations. Consequently, the ion density fluctuations are also reduced.

(6) Conclusions

With the filament arrangement used, the lifetime of the ion source was estimated to be about 100 h. As it is possible to use up to four filaments, the lifetime will be four times higher for an assembly than for a single filament.

Using the computer code IGUN, we designed a 140 mA @ 100 keV extraction system. The ion beam is extracted in the matched case with a radius of 2.9 mm (80 %) and a divergence angle of 35 mrad at the end of the extraction system. For an ion temperature of zero, the normalized rms-80 %-emittance is 0.008 π mm mrad.

Density fluctuations of the ions at the plasma sheath are coupled with density fluctuations of the electrons. As shown by basic plasma investigations with a 127° cylinder spectrometer, traces of xenon in the plasma reduce the electron temperature. This results in lower electron density fluctuations. Consequently, the ion density fluctuations and noise are reduced, too.

The investigations have shown that the multi-cusp ion source is capable of producing a 200 mA H^+ beam with good beam quality. This source can also produce a high current H_2^+ beam, which could be used to allow commissioning of the accelerator facility without any activation.

References

[1] R. Hollinger, P. Beller, K. Volk, M. Weber and H. Klein, "The Frankfurt 200 mA Proton Source", Rev. Sci. Instrum., 71, 836-838 (2000).

[2] R. Hollinger, K. Volk and H. Klein, "Measurement of the beam emittance of the Frankfurt proton source", Rev. Sci. Instrum., 73, 1027-1029 (2002).

[3] R. Becker and W.B. Hermannsfeldt, "IGUN-A program for the Simulation of Positive Ion Extraction Including Magnetic Fields", Rev. Sci. Instrum., 63, 2756-2758 (1992).

3.1.4 AC11C-JA : Test of ECR and Multi-Cusp Type Ion Sources

(1) Brief Task Description

Two types of ion sources, a multi-cusp ion source and an ECR ion source, are to be tested at 60 keV in the same test facility at JAERI (ITS-2M Test Stand) to compare the performances; e.g. efficiency, beam emittance, proton ratio, current stability, life time, gas flow rate, etc.

Contributors

Name	Party	Institute	E-mail address
K. Watanabe	Japan	JAERI	watanabe@naka,jaeri.go.jp
T. Iga	Japan	JAERI	igataka@fusion.naka,jaeri.go.jp
T. Morishita	Japan	JAERI	morishit@fusion.naka.jaeri.go.jp

(2) Introduction

Major specifications of the IFMIF ion source are listed in Table 1. Two types of ion sources are candidates for IFMIF. One is a filament-driven multi-cusp ion source; the other is an ECR ion source. The main goal of this task is to compare the characteristics of these ion sources and to provide a database for the selection of the source for IFMIF use [1]. These ion sources have been tested on the same test stand and with the same diagnostic system. Figure 1 indicates a scenario to select the ion source for IFMIF.

Table 1 Major Specification of IFMIF target.

Requirements	Specification
Ion source type	Volume or ECR
Particle Type	D^+
Output energy	100 keV
Output current	155 mA (200 mA H^+)
Species fraction	$D^+ > 90\%$
Current noise fluctuation	± 1%
Normalized rms transverse emittance (Normalized 90%)	0.2 π mm mrad (1 π mm mrad)
Duty factor	100% (CW)
Lifetime	1,000 h

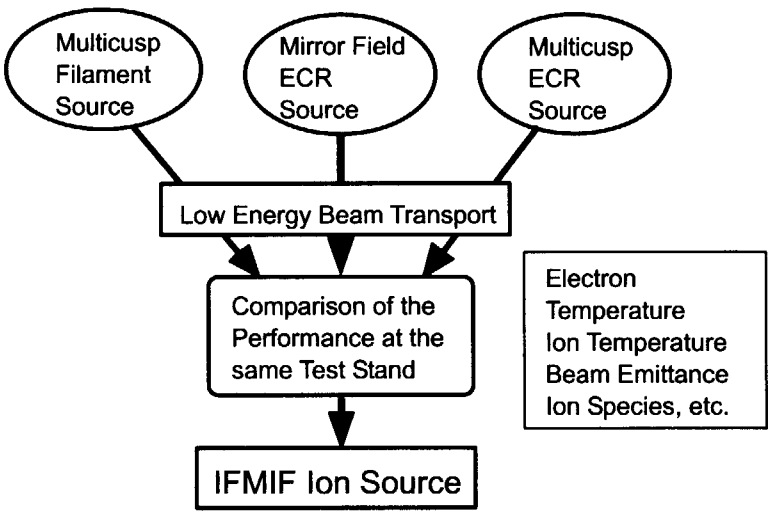


Fig. 1 Scenario to decide the type of the ion source for IFMIF.

(3) Experimental Equipment and Conditions

The experimental setup of the ITS-2M test stand at JAERI is illustrated in Fig. 2 [2]. The ion source is mounted in the vacuum chamber, which is evacuated by three turbo molecular pumps whose pumping speed is 2,000 ℓ/s. Hydrogen gas is fed to the ion source. A beam diagnostic system consists of a spectrometer for ion species measurement by Doppler shift spectroscopy, a multi-channel calorimeter for beam divergence measurement and calorimetric measurement of beam current, and an emittance scanner employing a single slit and a multi-channel detector. The maximum acceleration voltage of this test stand is limited to 60 kV.

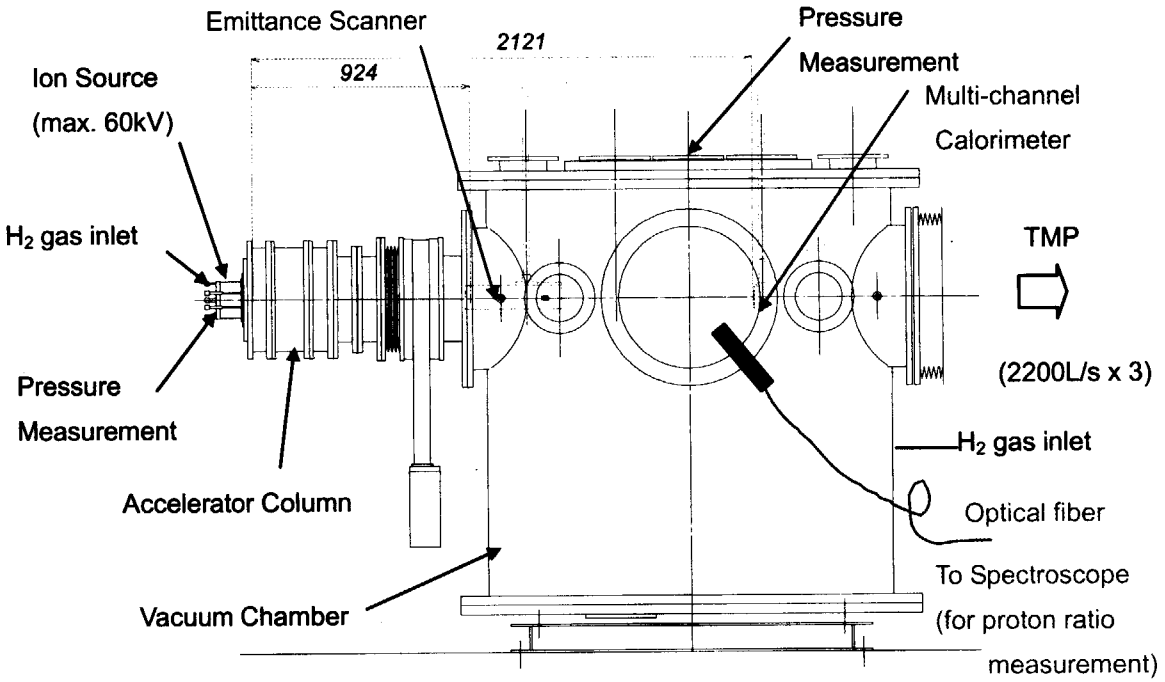


Fig. 2 Schematic drawing of the experimental setup.

A cross-sectional view of the multi-cusp ion source is shown in Fig. 3 [2]. The source consists of a plasma generator and a two-stage extraction system. The plasma generator is made of a cylindrical copper chamber whose dimensions are 120 mm diameter and 100 mm depth. Two pieces of tungsten filaments (1.2 mm in diameter) are installed from the back plate. Ten columns of permanent magnets surround the chamber, which forms a line-cusp field. A plasma electrode encloses the open end of the chamber, where 10 additional rows of magnets are installed except for the central extraction region. It is necessary to isolate the energetic primary electrons from the extraction region, to suppress generation and subsequent direct extraction of molecular ions, and thus to obtain a high proton yield. Therefore, the directions of the fields of these magnets were arranged as described in Fig.3 to generate a magnetic filter to repel the fast electrons. Additionally, filaments were bent to 45 degrees to prevent primary electrons from flowing to the extraction area. The extraction system is composed of four electrodes: plasma, gradient, suppression, and exit electrodes. The potential ratio of the gradient electrode to plasma electrode was fixed to be 64%. The diameter of the extraction aperture is 12 mm for all electrodes. In the multi-cusp ion source, the plasma generator was electrically connected to the plasma electrode potential via a resistance of 100 ohm.

A cross-sectional view of the ECR ion source is shown in Fig.4 [3]. A discharge chamber is made of a copper cylinder whose dimensions are 148 mm diameter and 280 mm depth. The same extraction system as described above was also used for this source, with some modifications. Pumping slots were added to the electrode support. The electrode support material was changed from aluminum to soft iron to reduce the stray field from source solenoids to suppress glow discharges in the

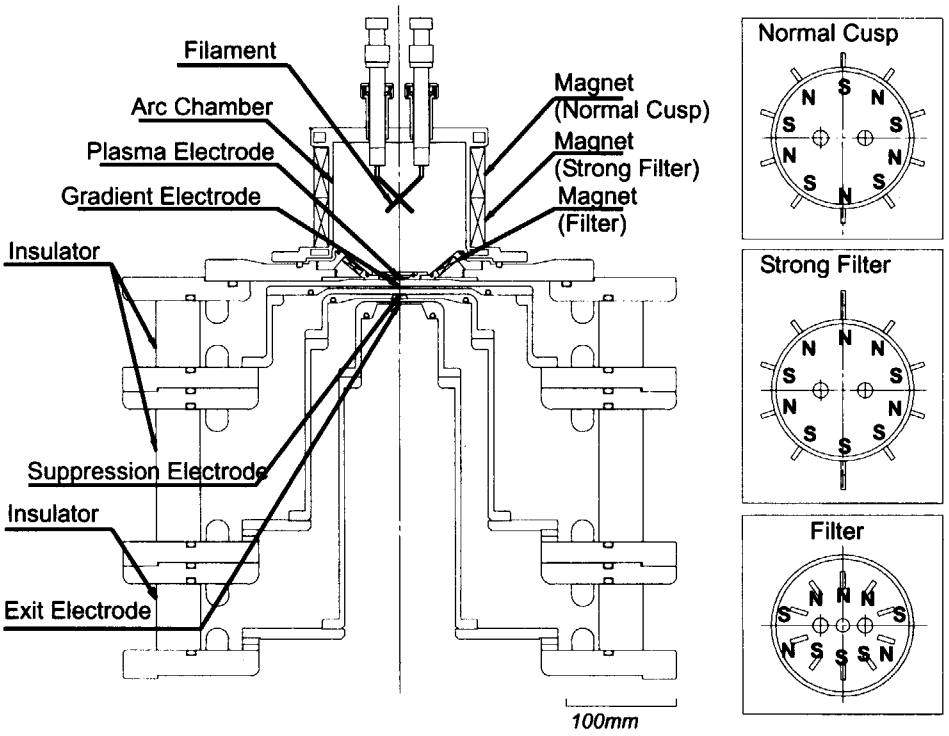


Fig. 3 Schematic cross-sectional view of the filament type ion source.

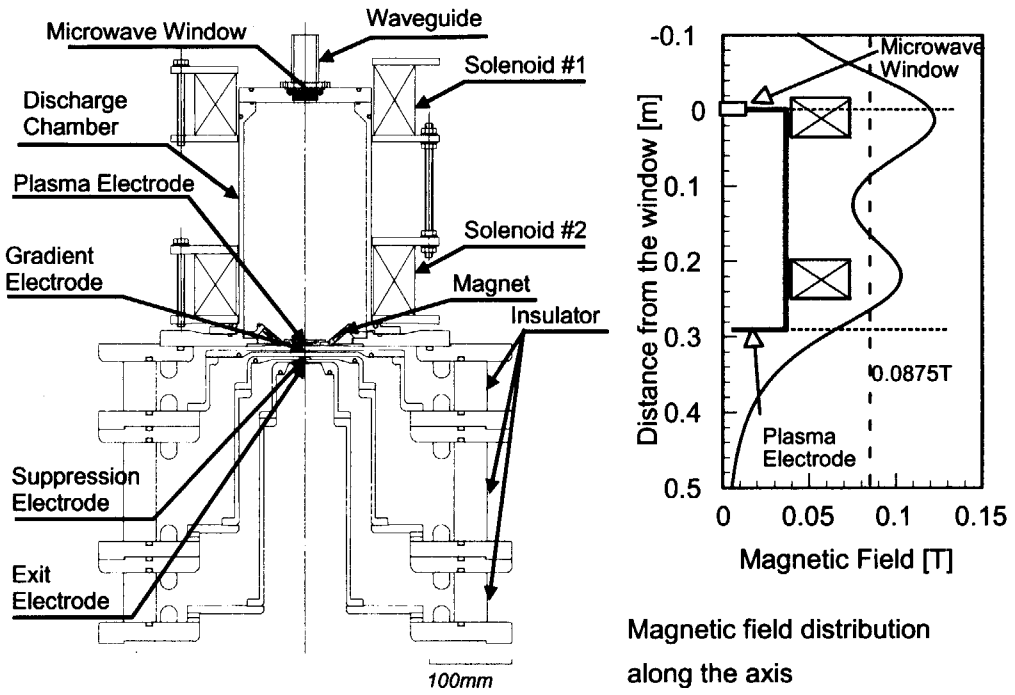


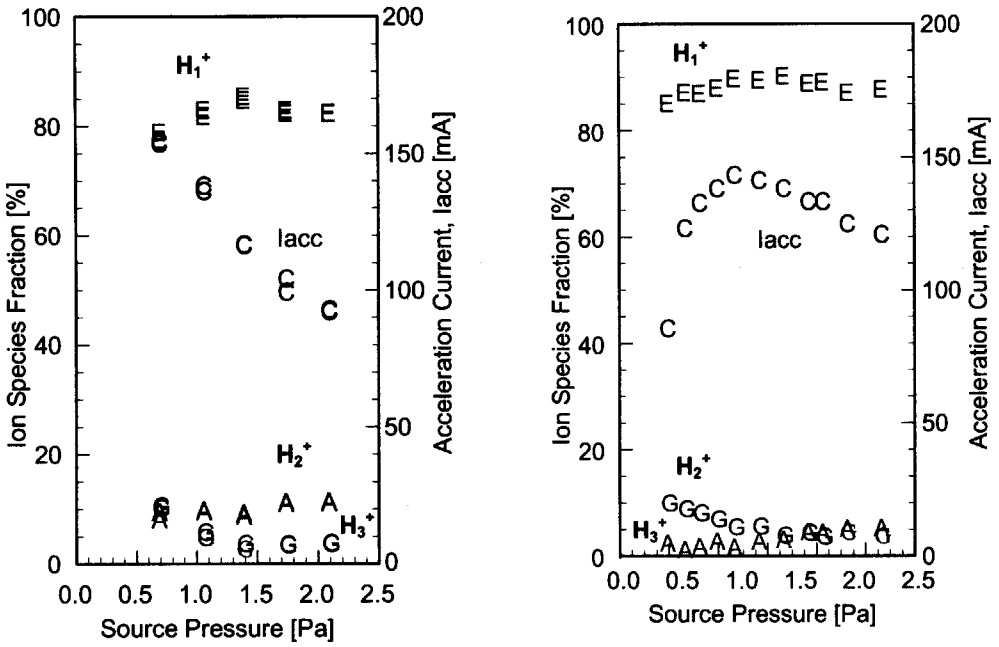
Fig. 4 Schematic cross-sectional view of the mirror field type ECR ion source.

accelerator column. The plasma electrode was electrically connected directly to the discharge chamber. Magnets surrounding the extraction aperture are arranged to form a normal cusp field. Microwave power is injected through a rectangular waveguide in the TE_{10} mode. A two-layer quartz window is installed at the end of the chamber. Two solenoid coils generate a static longitudinal magnetic field. A typical magnetic field profile along the chamber axis is also shown in Fig. 4. In this condition, three

ECR surfaces were generated along the axis of the discharge chamber.

(4) Results and discussions

Figures 5(a) and 5(b) show the dependence of ion species fraction and the acceleration current on the source pressure at a constant discharge power and an acceleration voltage for the multi-cusp ion source and the ECR ion source, respectively. For both types of ion sources, H_2^+ fraction increases and H_3^+ fraction decreases gradually with increasing source pressure, and H_1^+ fraction shows a slight peak at some source pressures. From the proton fraction point of view, the optimum source pressure for the multi-cusp ion source was about 1.4 Pa, which corresponds to gas flow rate of 0.028 Pa·m^3/s. On the other hand, the optimum source pressure for the ECR ion source ranges from 0.4 to 0.6 Pa, which corresponds to gas flow rate of 0.014 to 0.021 Pa·m^3/s , from the view points of proton fraction and acceleration current. Therefore, the gas flow rate of the ECR ion source could be reduced to about half that of the multi-cusp ion source.



(a) multi-cusp ion source (b) ECR ion source

Fig. 5 Ion species fractions and acceleration current vs. source pressure.

The ion species fraction as a function of the discharge power at constant source pressure for each source is shown in Fig. 6. The proton fraction of the multi-cusp ion source increased gradually with the discharge power and reached 90% at 5 kW. For the ECR ion source, the proton fraction reached 90% even at 1 kW, and clearly exceeded the contrast of the multi-cusp ion source.

Figure 7 shows the acceleration current as a function of the discharge power. The operating pressures were kept constant, at the optimum pressure of each source. The acceleration current increases linearly for both sources. The power efficiency of the multi-cusp ion source was about 25 mA/kW, and of the ECR ion source 86 mA/kW. The multi-cusp ion source requires at least 8 kW to extract 200 mA of H^+ beam, which corresponds to the 155 mA D^+ beam. It is undesirable for a filament-driven ion source to operate at such high power because it leads to a short lifetime of the tungsten filament. For the ECR ion source, the relatively low power of 2.5 kW is sufficient to extract the same current. These results confirmed that the ECR ion source has the advantage in power efficiency.

The dependence of beam divergence on the acceleration current (or discharge power) has been measured at several acceleration voltages. The beam divergence angle showed a minimum value at

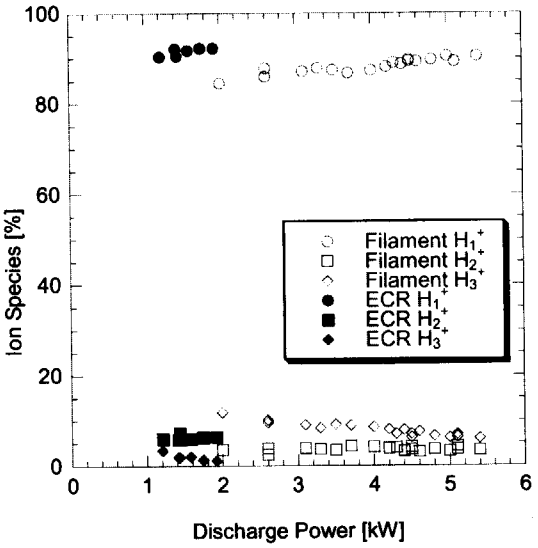


Fig. 6 Ion species fraction vs.. discharge power.

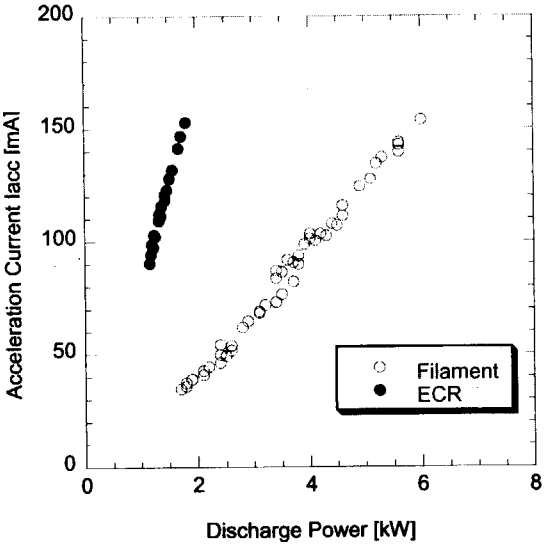


Fig. 7 Acceleration current vs. discharge power.

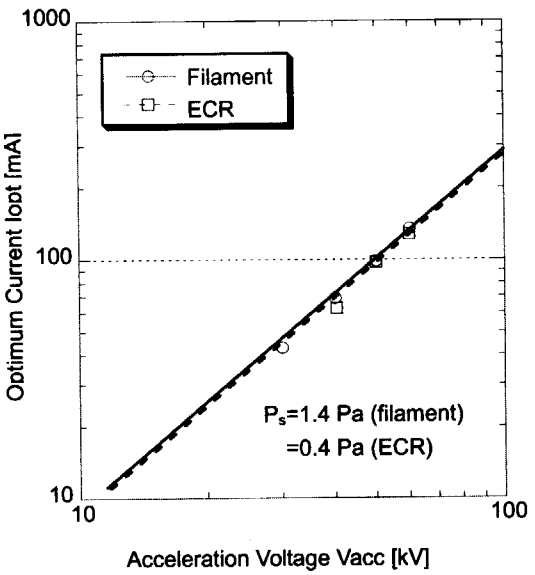


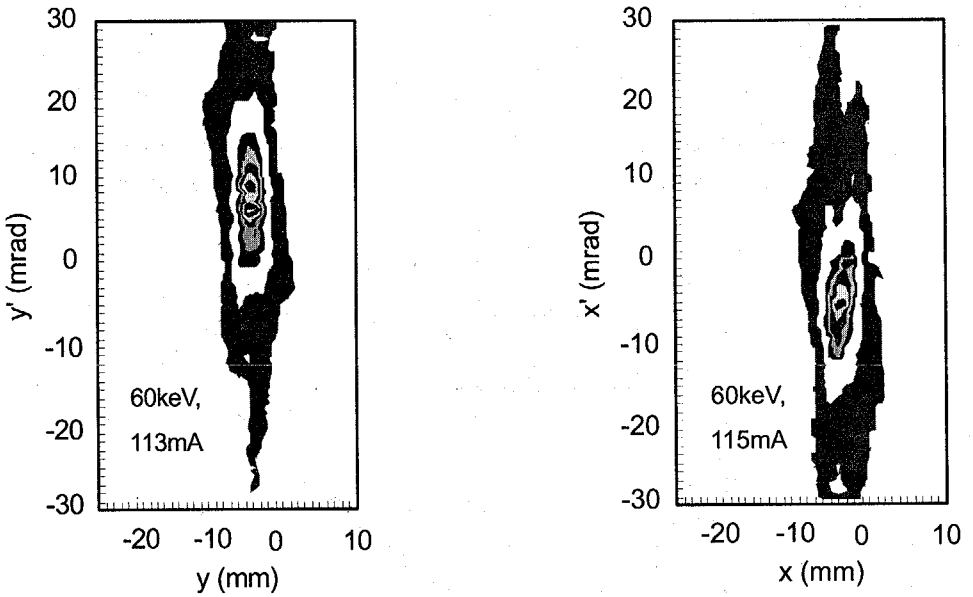
Fig. 8 Optimum acceleration current vs. acceleration voltage.

some acceleration current for each acceleration voltage. These optimum currents as a function of the acceleration voltage are plotted in Fig. 8 for both ion sources. The solid line and the broken line indicate the constant perveance according to the Child-Langmuir law. The deviation of measured values from the lines is due to the increase of the proton fraction. By extrapolation to 100 keV using the Child-Langmuir law, it is estimated that a 275 mA H^+ beam, which corresponds to a 194 mA D^+ beam, would be obtained at the rated energy in good beam optics from either of the sources.

Beam emittance was measured 924 mm downstream from the exit electrode for both sources. The transverse magnetic field was necessary to obtain the high proton yield for the multi-cusp ion source as mentioned above, and this field may increase the beam emittance. To determine the influence of the magnetic field, the beam emittance of the multi-cusp ion source was measured along two directions, parallel (y-direction) and perpendicular (x-direction) to the magnetic filter field, by rotating the ion source. Typical emittance diagrams in y- and x- directions, projected onto the source

exit, are shown in Fig. 9(a) and 9(b), respectively. While the x components of the beam seem to be a little more divergent than y components, the shapes of the diagrams are almost the same. The normalized 63%, 90%, and 100% emittance for two directions at a constant acceleration voltage of 60 kV as a function of the acceleration current are plotted in Fig. 10. It is seen that the normalized emittance has a minimum value at the optimum acceleration current. The optimum current that gives the minimum x-x' emittance was about 10% smaller than that at which y-y' emittance was minimized. The x-x' emittance was slightly larger than the y-y' emittance, especially at full emittance. However, the normalized 63% emittance in both directions are almost the same. These results confirmed that the influence of the magnetic filter on the emittance in the multi-cusp ion source is negligibly small for the beam core.

The minimum normalized y-y' emittance as a function of the acceleration voltage for the multi-cusp ion source is shown in Fig. 11. The minimum normalized y-y' emittance increases almost



(a) y-y' (parallel to the filter) (b) x-x' (perpendicular to the filter)

Fig. 9 Projected emittance diagram of the multi-cusp ion source onto the source exit.

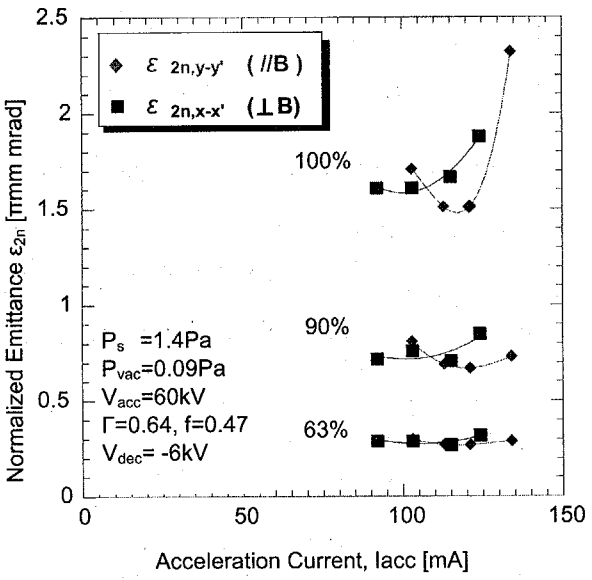


Fig. 10 Normalized emittance vs. acceleration current for the multi-cusp ion source.

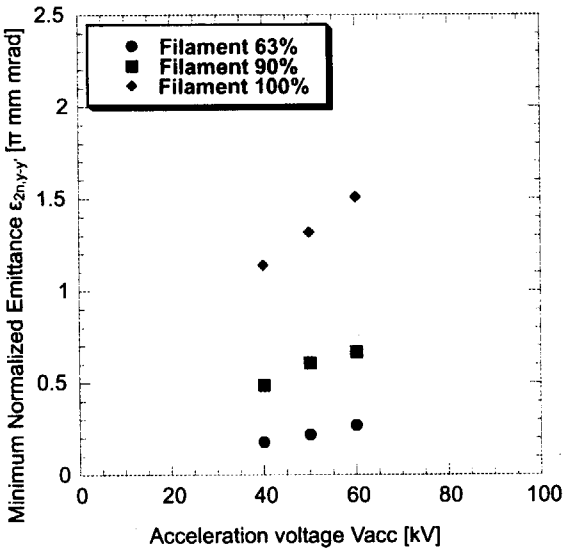


Fig. 11 Minimum normalized emittance vs. acceleration voltage for the multi-cusp ion source.

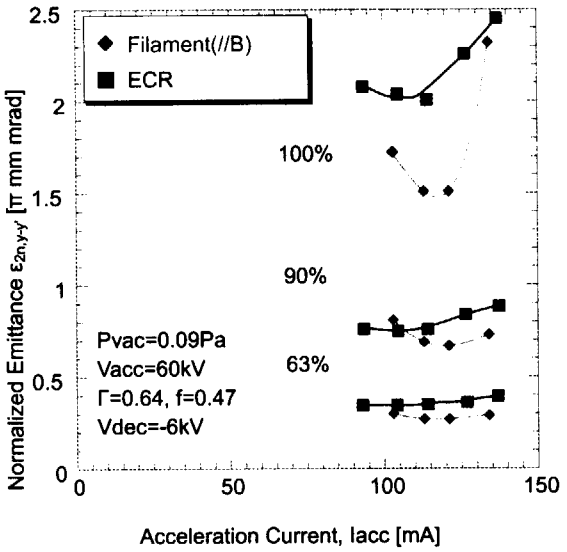


Fig. 12 Normalized emittance vs. acceleration current for the ECR ion source.

linearly with acceleration voltage, since the required arc power, which dominates the ion temperature, also increases with the acceleration voltage. The 63% normalized y-y' emittance at 60 kV was about 0.27 π mm mrad. By extrapolation, this value is estimated to become about 0.5 π mm mrad, which is 2.5 times higher than the IFMIF requirement.

For the ECR source, the beam emittance has been measured only along the y-direction, since the beam from the ECR source was axially symmetric. In Fig. 12, the normalized 63%, 90%, and 100% emittance at a constant acceleration voltage of 60 kV is plotted as a function of the acceleration current, along with the results for the multi-cusp ion source. The optimum current that gives the minimum emittance for the ECR ion source was about 17% smaller than that for the multi-cusp ion source. The minimum normalized emittance, the normalized 63%, 90% and 100% emittance for the ECR ion source were about 35%, 23%, and 13% higher than those for the ECR ion source, respectively. It is believed that these differences of beam optics and emittance arise from the strong magnetic field around the emitting surface and the acceleration gap.

During the experiment on the ECR ion source, the quartz window facing the source plasma was occasionally damaged by backstreaming electrons. This potential problem for long pulse operation can be easily solved by small modifications to the wave guide connection. It is much less of a problem than the cathode life of the filament-driven source. A four-week test run of the ECR ion source was completed at CEA-Saclay [1].

(5) Conclusions

A filament-driven multi-cusp ion source and a mirror field ECR ion source have been tested at 60 keV on the same test facility at JAERI to compare the performances; e.g. gas flow rate, proton ratio, power efficiency, and beam emittance. The presented investigation demonstrated that the power efficiency of the ECR source is more than three times that of the multi-cusp ion source, while high proton yield of 90% could be obtained for either source. Moreover, the gas flow rate of the ECR ion source was about half that of the multi-cusp ion source. The beam emittance of each source was measured. For the multi-cusp ion source, it was confirmed that the magnetic filter field does not affect the emittance; however, the emittance value was still higher than the IFMIF requirement. It was also shown that the 63% emittance of the ECR ion source is about 35% higher than that of the multi-cusp ion source. It is necessary to improve the beam emittance by optimizing the accelerator, source configuration, operation conditions, etc. These results are summarized in Table 2.

As a result of this investigation, it can be said that the ECR ion source holds greater promise for the IFMIF project than does the filament-driven multi-cusp ion source. The better performance is in efficiency, gas flow rate, and lifetime. It is assumed that the emittance can be reduced to the level of the IFMIF requirement for either source.

Table 2 Comparison of the measured performance.

Performance \ Type of ion source	Filament-driven multi-cusp	Mirror field type ECR
Gas Flow Rate [Pa m^3/s]	0.028	0.014-0.021
Proton Ratio [%]	90	92
Beam Current at optimum perveance [mA] (at 60keV)	134	128
Power Efficiency [mA/kW]	25	86
Normalized 63 % emittance [π mm mrad] (at 60keV)	0.27	0.36

References

[1] IFMIF International Team, IFMIF International Fusion Materials Irradiation Facility Key Element Technology Phase Interim Report, JAERI report, Japan Atomic Energy Research Institute, JAERI-Tech 2002-022, March 2002.

[2] T. Iga, Y. Okumura, M. Kashiwagi, "Development of a High Brightness Ion Source for IFMIF and Preliminary Test Results", JAERI Report, Japan Atomic Energy Research Institute, JAERI-Tech 2001-028, May 2001 (in Japanese).

[3] K. Watanabe, "Development of Ion Sources for IFMIF", J. Plasma Fusion Research, 78(6), (2002) 535-540 (in Japanese).

3.1.5 AC12A/13A/14-EU : ECR Source Analyses

(1) Brief Task Description

The task was completed in the framework of the CEA program on high-power particle accelerators supported by the IPHI demonstrator project [1-10]. This project is dedicated to high power beam production (CW beam, 100 mA).

The injector system (ion source and Low Energy Beam Transport) must demonstrate reliability commensurate with the maintenance schedule of the IFMIF accelerators. Low to very low spark rates have to be shown, as well as reliability in terms of source performances. Very good beam quality has to be provided in order to ensure proper beam transport to the next accelerator components. The task consists of analyzing the source performance and developing the necessary engineering. The source parameters that need to be obtained/verified are the total extracted D^+ beam current at the IFMIF extraction energy, beam emittance, beam noise, and pulsed and CW H^+ operation. It is continuing work that influences the accelerator parameter choices and could lead to cost savings. (For example, if the emittance is decreased in the RFQ, the total RFQ length could be reduced, leading to lower power consumption.).

Contributors

Name	Party	Institute	E-mail address
R. Ferdinand	EU-FRANCE	CEA-Saclay	rferdinand@cea.fr
R. Gobin	EU-FRANCE	CEA-Saclay	rjgobin@cea.fr

(2) Deuteron Performance of the ECR Source

Neutron production was predicted in the Low Energy Beam Transport (LEBT) line if operations with deuterium were conducted. Authorization to extract a pulsed deuteron beam from the CEA-Saclay ECR source SILHI was obtained in June 2001, based on experiments on the Saturne accelerator. At that time the duoplasmatron source was delivering up to 50 mA of deuterons at energy up to 500 keV (1 ms, 1 Hz) without observed neutron production. To minimize neutron production (from D,D reactions) on the IPHI test stand, the source was in pulsed running mode (2 ms/s) with lots of voluntary breaks to minimize the activation. The experiment was conducted using the 120 mA proton extraction system, and poor extraction conditions for deuterons were expected.

We observed excellent operating conditions; the SILHI source appears to be as well adapted for deuteron production as for protons. The source behavior was very close to the proton production. In an effort to extract the maximum D^+ beam, current up to 170 mA was obtained at 100 keV (267 mA/cm^2), but with an ugly shape and a lot of beam noise (Fig.1).

A more coherent set of measurements was sought in order to get a good qualification of the "normal" beam characteristics. It consists of tuning the source to good running conditions and making all possible measurements simultaneously. The results are:

- I > 130 mA (100 kV)
- $D^+ > 96$ % and $D_2^+ < 4$ %; no measurable D_3^+.
- LEBT transparency = 75 %
- rms beam noise = 1.2 % (19 kHz)

Figure 2 shows the pulse measurement through the SILHI LEBT. In blue is the DCCT measurement of the extracted beam in the accelerator column. In red is the ACCT measurement, showing a better rise time since it has a much better bandwidth (see the beam noise paragraph). It also shows that about 13% of the beam is lost by that point. This is because the extraction electrodes are adapted to a 120 mA proton beam. The last (green) curve is the beam stop measurement 4.4 m downstream from the extraction aperture. It again shows some losses and the global LEBT transparency is only 75 %. This can easily be corrected to reach 100% with the appropriate set of electrodes. The rise time of the beam stop measurement is very low because of a filter on the faraday cup.

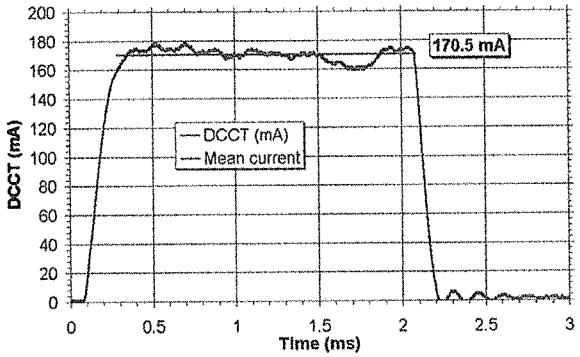


Fig. 1 Max extracted deuteron beam.

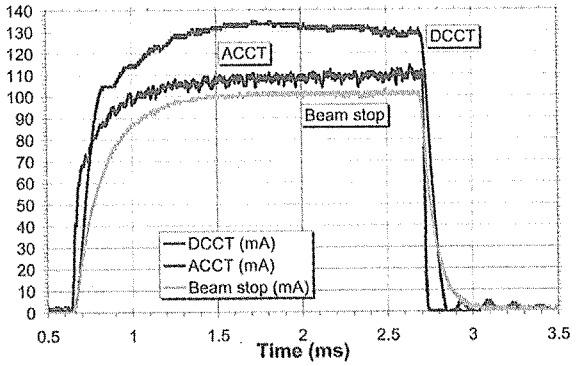


Fig. 2 130 mA D^+ beam through the LEBT.

(3) Species Fractions

The SILHI source is equipped with 3 different species fraction measurement techniques. The most useful is the Wien filter, part of the emittance measurement unit. The beam is stopped in a water-cooled copper target with a small tantalum aperture. Behind this, a Wien filter selects the species and they are analyzed on a biased wire. Figure 3 shows the measurement associated with the "coherent set of measurements" described above.

The two other techniques are a classical aperture-faraday cup measurement and a non-interceptive Doppler shift measurement.

The 96.9% D^+ species is much better that the classical 80% usually obtained in CW proton mode. In pulsed mode, the source is tuned with a lower gas pressure, allowing the species fraction to increase. Nevertheless, measurements in the pulsed proton beam show that the species fraction is always better in deuteron production (96%) than in proton production (92%). This observation is not yet understood.

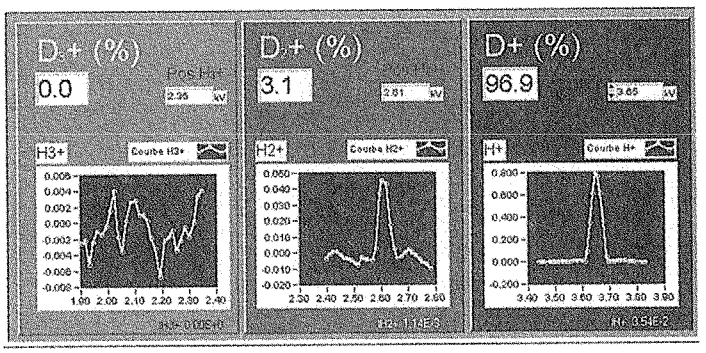


Fig. 3 Typical deuteron proportion.

(4) Beam Noise Measurements

The beam noise is measured using a 6 MHz bandwidth ACCT, located between the two solenoids (about 2 m downstream of the aperture). Depending on the source tuning (pressure, ECR solenoid setting, etc.) the rms beam noise is easily around 1.0% for good extraction conditions ($80<I_{beam}<130$ mA @ 100 keV). This noise was analyzed in detail, and is mostly due to the 19 kHz spaced lines induced by the magnetron power supply. Time raster plots are used to display long signal records versus time, and allow:

- Detection of isolated, out-of-range samples,
- Detection of minute, periodic pulses,
- Separation of multiple pulse bursts

Accelerator designers require a good quantification of the noise. They need to know not only the rms value but also the probability distribution function to which the numbers of noise random processes apply. Figure 4 shows such a probability function, and one of the important points to notice is the deviation from a symmetrical signal (left picture) and the deviation from a Gaussian signal (right picture).

Checking noise amplitude distribution allows one to:

- identify unsuspected noise sources,

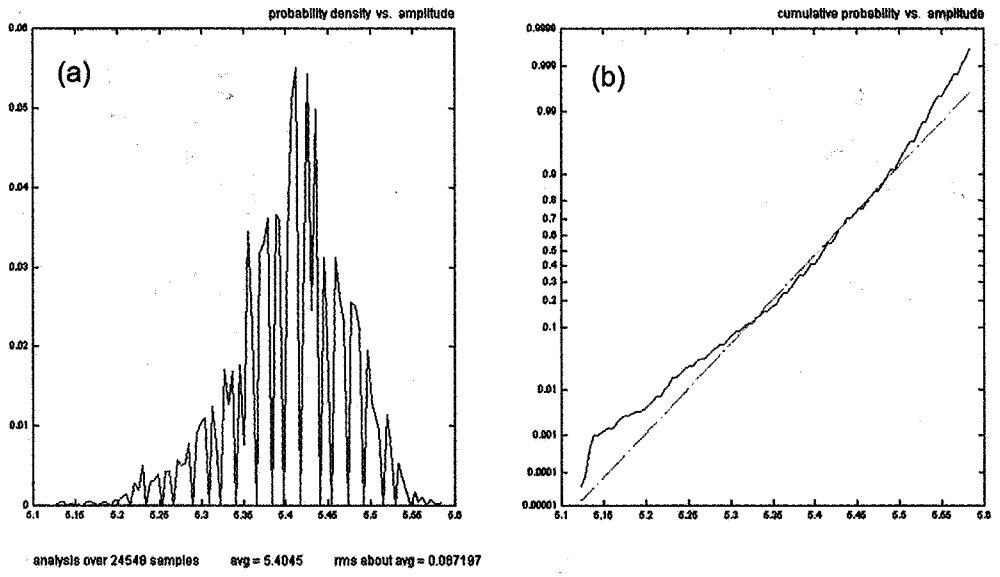


Fig. 4 (a) probability distribution function of the deuteron beam noise (1.2% in this case); (b) deviation from a Gaussian distribution represented by the green line.

- precisely tune the dynamic range of ADCs
- check the linearity of these ADCs,
- accurately quantify the signal-to-noise ratio of the measurements.

The above results give an absolute value of rms beam noise compared to a "plus or minus" value, incompatible with the non-symmetrical distribution of the noise.

(5) Activation

We ran the source in deuteron mode for two days, with an 0.2% duty cycle, and with lots of voluntary breaks to minimize the activation. During the test, high-energy neutron production was measured with a specific probe (Bertold LB 6411). The observed reaction is the (D,D) reaction at the surface of the copper target, producing 2.45 MeV neutrons. In contrast to what was expected, the activation increased quickly and linearly to 11.5 μSv/h (1.15 $mrem.h^{-1}$) after two hours (measured 60 cm from the target). The saturation level was not reached at that time, but the level was already above that allowed for workers class B at CEA.

The neutron production is highly dependant on LEBT pressure (around 2×10^{-5} torr during the test) and this is the explanation for the difference between the Saturne duoplasmatron and SILHI sources. Fortunately, the neutron production stops with the beam (no activation detected without beam) and no activation was observed close to the target after switching back to protons. It may become a serious problem for CW accelerator (IFMIF) on a mid- to long-term scale because of the species fraction (D_2^+ and D_3^+ lost on the vacuum pipe).

The observed level of neutron production forced us to run in a discontinuous mode, stopping as often as possible. Each restart of the source returns the neutron production to the previous level. The night gives only very little decrease in this production, while running for a few moments in CW proton mode heated and cleaned the surface.

(6) Emittance Measurement

The beam r-r' emittance can be measured at two different locations: 53cm and 4.4m downstream from the aperture. Because of the activation, this measurement cannot be performed during deuteron operation, but only with the proton beam. Similar results are expected in deuteron production (emittance at the source exit is mostly defined by the extraction system). At the source exit (0.53m) the beam emittance is in the range 0.155-0.175 π mm mrad rms, normalized (r, r'). More important from the RFQ point of view,

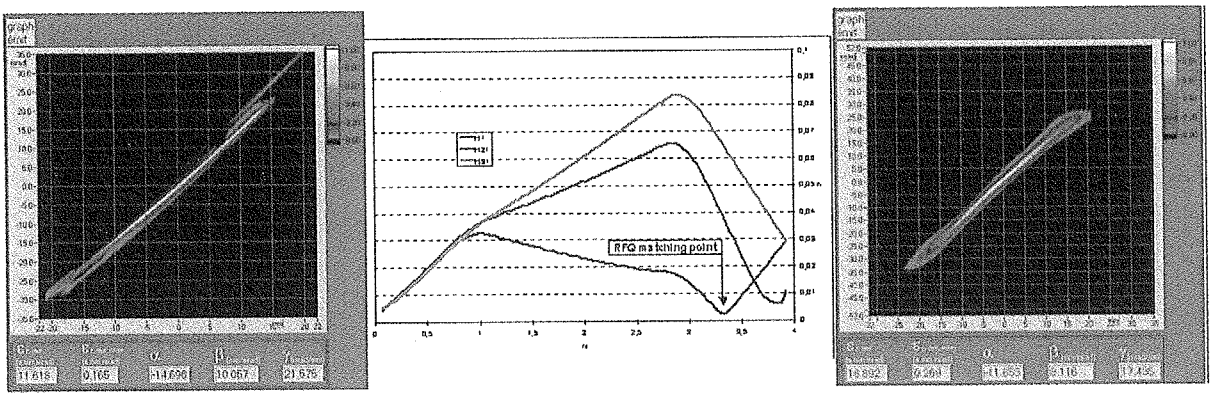


Fig. 5 Total normalised emittance of a 120mA proton beam at 95keV, left at the source exit, right at the LEBT exit. Middle is the beam envelope calculation in the measurement configuration showing a cross over before the measurement.

99% of the beam is inside 1.4 π.mm.mrad (Fig. 5).

Complete analyses of the beam emittance were done as a function of the source parameters. Extraction simulations indicated minimum emittance value for a 40 kV first gap extraction voltage, and this was confirmed by the measurements.

Beam emittance at the LEBT end depends on solenoid values and looks quite stable versus the extraction electric field configuration. It ranges at the LEBT end from 0.2 to 0.45 π.mm.mrad (r-r', rms, normalized).

(7) Space Charge Measurements

The high intensity beam induces ionization of the residual gas, leading to space charge compensation [6]. In order to easily transport and match the deuteron beam at the RFQ entrance, the compensation has to be as high as possible.

A space charge analyzer has been installed in the LEBT in order to measure the space charge compensation (SCC) of the beam. The description is given elsewhere [6] and it has been successfully used on different beams, especially on the LEDA injector (75 keV, 110 mA, CW). At Saclay, the FGA has been installed upstream and downstream of the first LEBT solenoid (64 and 170 cm from the source aperture). It provides the ion energy distribution function as well as the SCC.

(8) Upstream Results

The SCC measurements lead to values of about 98% for a beam current ranging from 60 to 100 mA. Different measures have been made as functions of beam energy, beam size, beam current and pressure.

Beam size has been modified by varying the intermediate electrode potential. The rms beam size was varied from 11 mm to 17 mm. The pressure curves were obtained by adding argon or hydrogen gas into the LEBT line. The residual gas pressure, without gas additions, was measured close to the SCC analyzer, and was about 4 10^{-5} torr of mostly H_2.

Figure 6 shows the condensed results as a function of those parameters. The SCC ratio

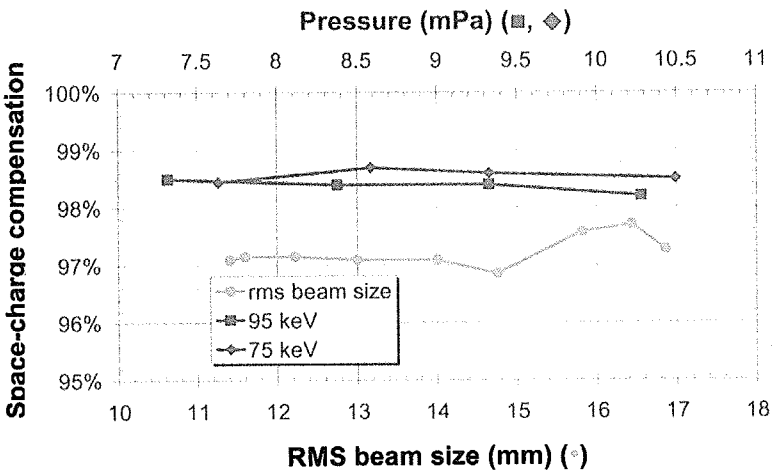


Fig. 6 SCC versus pressure, beam size and beam energy.

whatever the gas added or pressure and energy settings. Mostly the results are exactly the same as the ones obtained at LANL, and the SCC is extremely good. At this point, no variation was observed that could explain the observed emittance reduction with gas injection.

(9) Downstream Results

The LEBT solenoid 1 allows beam size changes in a large range. A crossover of a few mm can easily be achieved for the H^+ beam in front of the SCC analyzer. Even the H_2^+ becomes convergent. Depending on the settings, the SCC results changed a lot from the upstream results. Three peaks are commonly observed on the ions energy distribution curves that are attributed to the three separate beams H^+, H_2^+ and H_3^+. Analyses are much more complicated and delicate in some cases.

Beam stop influence

A beam stop (BS) can be inserted 27 cm behind the FGA. There is no suppression of the secondary electrons (electrostatic or magnetic). These electrons are free to stream off into the beam plasma and affect the SCC.

When the BS is inserted, a lot of secondary electrons are produced and the SCC is about 98%. This value decreases to about 80% without the BS and an energy increase of the residual ions is observed. This energy shift is theoretically expected as the apparent current increases. Similar results are obtained depending on how much beam current is lost on the wall (due to low LEBT solenoid settings, steering, etc.).

When the second LEBT solenoid is on, a SCC increase is observed. These observations show that the solenoids play an important role in electron confinement in the LEBT.

To achieve reliable SCC measurements it has been decided to conduct all of the following experiments with the beam stop inserted into the LEBT line. In such conditions, the number of free electrons created between the two solenoids remains almost constant for all settings.

Pressure Influence

Gas additions shows different results for this FGA location. Now the SCC increases from 89 % to 98 % with an argon increase from 4.3×10^{-5} to 8.1×10^{-5} torr which means a factor of 5 gain in the SCC (Fig. 7).

That phenomenon was NOT observed upstream of the first solenoid and could explain the emittance decrease as the argon pressure increases. Preliminary simulation using a basic model acknowledged that result, including that the Twiss parameters of the beam do not change a lot with the SCC after the solenoid.

The appearance of the H_2 and H_3 peaks in the energy distribution function could allow a rough estimate of the proton fraction (Fig. 8).

Beam size influence

At this SCC analyzer location, the rms beam size can easily be changed by a factor of 20. The results show a big change, as expected from the SCC theory in such extreme conditions.

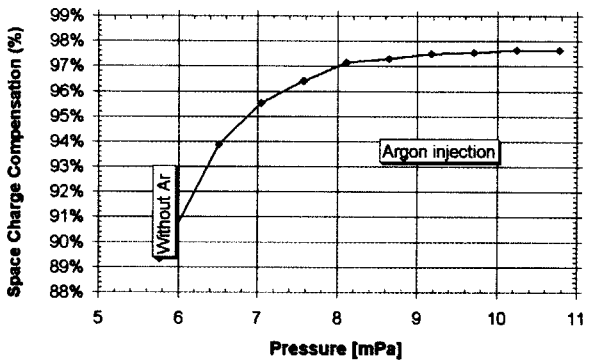


Fig. 7 SCC as a function of Argon addition in the LEBT.

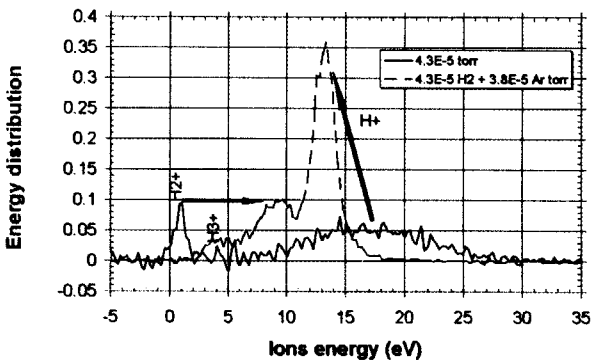


Fig. 8 130 mA D^+ beam through the LEBT of the residual ions.

This SCC collapses in the vicinity of the crossover and leads to a large emittance increase (0.7 to 1 π mm mrad rms values !) (Fig. 9).

(10) Conclusion on Space Charge Measurements

A strong dependence on the number of free electrons in the LEBT line was found, as well as a mirror effect of the LEBT solenoids on those electrons. The SCC can be much lower than expected without an electron source such as occurs at the beam stop or due to beam losses on the beam pipe or induced by a pressure increase. Low SSC leads to a strong emittance increase in the LEBT.

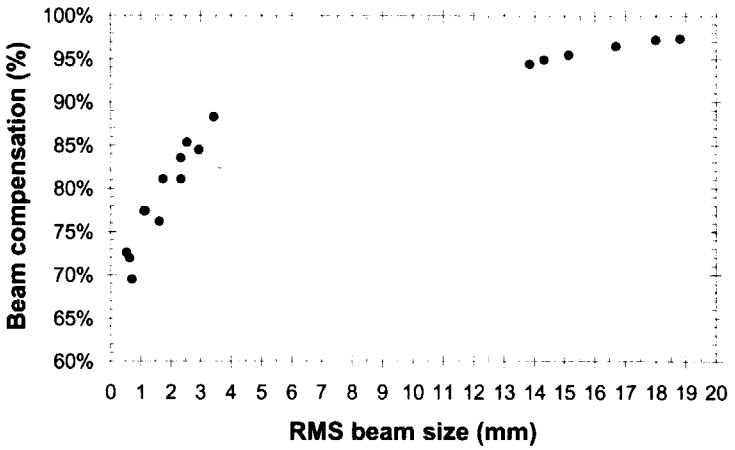


Fig. 9 SCC versus the rms beam size.

(11) SILHI Status

Table 1 contains a coherent set of parameters obtained simultaneously (except for the I_{max} quoted in bold after the total current).

Table 1. SILHI parameters obtained simultaneously (except (I max)).

Parameters \ Particles	Proton		Deuteron	
	Requests	Status	Request	Status
Energy [keV]	95	95	95	100
Intermediate Electrode [kV]	55	56	?	50
Proton, Deuteron Current [mA]	100	108	140	129
Total Current [mA] **(I max)**	110	130 **(157*)**	155	135 **(170)**
Proton, Deuteron Fraction [%]	> 90	83	> 90	96
Plasma electrode diameter [mm]	-	9	-	9
Current Density [mA/cm²]	140	204	243	212
Availability [%]	AHAP	> 99	AHAP	-
RF Forward Power [W]	< 1200	850	< 1200	900
Duty Factor [%]	100	100	100	0.2 **
H_2, D_2 Gas Flow [sccm]	< 10	5	< 10	1
Beam Noise rms [%]	2	1.2	2	1.2
rms normalized emittance [π mm mrad]	0.2 (x,x')	0.25 (r,r')	0.2	-
Total normalized emittance [π mm mrad]	1.5	1.4	1.5	

* Limited by the beam stop (power density exceeding the Faraday cup capability)

** Limited by neutron production

(12) Conclusions

SILHI showed excellent operating conditions with deuterons. The source is as well adapted for deuteron production as for protons, the behavior being very close to the proton production. Up to 170 mA of deuteron beam was extracted in a pulsed mode, and 130 mA in stable operating conditions. The neutron production in the LEBT rises rapidly to a dangerous level, and may lead to difficulties during IFMIF operation.

References

[1] R. Gobin, P-Y Beauvais, D. Bogard, R. Ferdinand, P. Mattéi, "Reliability tests of the high power proton source SILHI at CEA/Saclay", Third international workshop on HPPA reliability, Santa Fe, USA, May 2002.

[2] R. Gobin, P.-Y. Beauvais, K. Benmeziane, D. Bogard, G. Charruau, D. De Menezes, O. Delferrière, R. Ferdinand, A. France, Y. Gauthier, F. Harrault, J.-L. Jannin, J.-M. Lagniel, P. Mattéi, A. Sinanna, P. Ausset, S. Bousson, D. Gardes, B. Pottin, L. Celona, J.D. Sherman, "Saclay High Intensity Light Ion Source Status", EPAC 2002, La villette PARIS 2002, p.1712.

[3] P. Ausset, S. Bousson, D. Gardes, A.C. Mueller, B. Pottin, R. Gobin, G. Belyaev, I. Roudskoy, "Transverse Beam Profile Measurements for High Power Proton Beams", EPAC 2002, La villette PARIS 2002, p.245.

[4] R. Ferdinand, P.-Y. Beauvais, A. France, R. Gobin, J.-M. Lagniel, "Deuteron Beam Test For IFMIF", EPAC 2002, La villette PARIS 2002, p.894.

[5] P. Ausset, S. Bousson, D. Gardès, A.C. Mueller, B. Pottin, R. Gobin, G. Belyaev, I. Roudskoy, "Optical Transverse Beam Profile Measurements for High Power Proton Beams", EPAC 2002, La villette PARIS 2002, p.1840.

[6] R. Ferdinand et al., "Space-charge neutralization measurement of a 75-keV, 130-mA hydrogen-ion beam", PAC'97 Conf., Vancouver, Canada, May 12-16, 1997, p.2723.

[7] N. Rouvière, F. Dubois, R. Leplat, L. Vatrinet, R. Gobin, F. Harrault, P.A. Leroy, "Status of the Vacuum System for the IPHI Project", EPAC 2002, La villette PARIS 2002, p.2586.

[8] P-Y. Beauvais et al., "Emittance improvement of the SILHI beam by gas Injection in the LEBT", ICIS99 conference, RSI, Vol.71, n°3, June 2000, (1413).

[9] B. Pottin et al., "Optical beam profiler for high current beams", EPAC 2000, Vienna, Austria, p.960.

[10] R. Gobin et al., "High intensity ECR ion source (H+, D+, H-) developments at CEA Saclay", ICIS2001 conference, RSI, Vol.73, n°2, February 2002 (922).

3.1.6 AC12B-EU : Ion Source Analysis

(1) Brief Task Description

A 127° cylinder spectrometer will be used to measure the energy distribution from an ion source. The source will be optimized for low ion temperature and for small energy spread. With the knowledge of the ion temperature we will estimate the beam emittance. In a second step we will check the beam emittance at high currents using our slit-grid emittance measurement device.

Contributors

Name	Party	Institute	E-mail address
P. Beller	EU	IAP	p.beller@gsi.de
R. Hollinger	EU	IAP	r.hollinger@gsi.de
H. Klein	EU	IAP	horst.klein@iap.uni-frankfurt.de
A. Maaser	EU	IAP	andreas.maaser@O2.com
K. Volk	EU	IAP	k.volk@iap.uni-frankfurt.de
M. Weber	EU	IAP	manfred.weber@clariant.com

(2) Introduction

The IFMIF scenario requires a D^+ source, delivering a 140 mA deuteron beam in cw-mode with a D^+ fraction above 90% and a normalized rms-emittance of 0.2π mm mrad at the exit of the LEBT. Within the IFMIF study, the *Institut für Angewandte Physik* at the University of Frankfurt has developed a high current proton/deuteron ion source. The Frankfurt 200 mA proton source belongs to the HIEFS volume source family and meets the requirements for the IFMIF project [1]. The ion source delivers 200 mA H^+ (corresponding to 141 mA D^+) at 55 keV with an H^+ fraction of 93% in continuous wave operation [2].

As far as the plasma production processes are concerned, the use of H^+ instead of D^+ is possible because of the similarity of the atomic shells of the two ions. Consequently, the cross sections for electron collisions are also similar. A major advantage of using H^+ is that there are no D-D reactions in the Faraday cup or on the walls and hence no neutron production. For that reason, in this study for beam energies higher than 20 keV the ion source was operated with hydrogen instead of deuterium.

(3) Experimental Setup

Figure 1 shows a schematic cross-sectional view of the experimental setup. An electrostatic 127° cylinder spectrometer was used as the energy analyzer, with a relative energy resolution of 0.5%. The diameter of the entrance hole is 1 mm, and the radii of the inner and outer plates are 50 mm and 75 mm, respectively. A slit aperture of 1 mm height is installed at the exit of the spectrometer, followed by a screened Faraday cup.

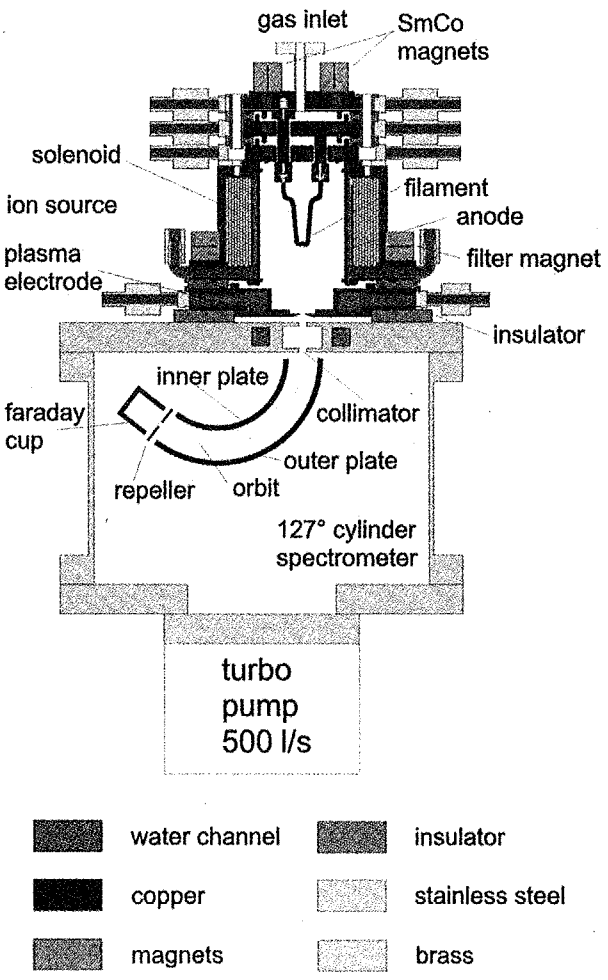


Fig. 1 Experimental setup: ion source and energy analyzer, not to scale.

(4) Ion Energy Distribution

The ion temperature was first estimated by means of the measured ion energy distributions. Figure 2 presents a typical ion energy distribution for an input power of 10 kW, gas pressure of 30 Pa and filter field strength of 15 mT. These are optimum source parameters for the extraction of a 200 mA proton beam. Moreover, in this operation mode the H_2^+ and H_3^+ fractions of the ion beam are below 4%. In order to estimate the ion temperature, a suitable Maxwellian fit for the measured ion energy distribution was calculated.

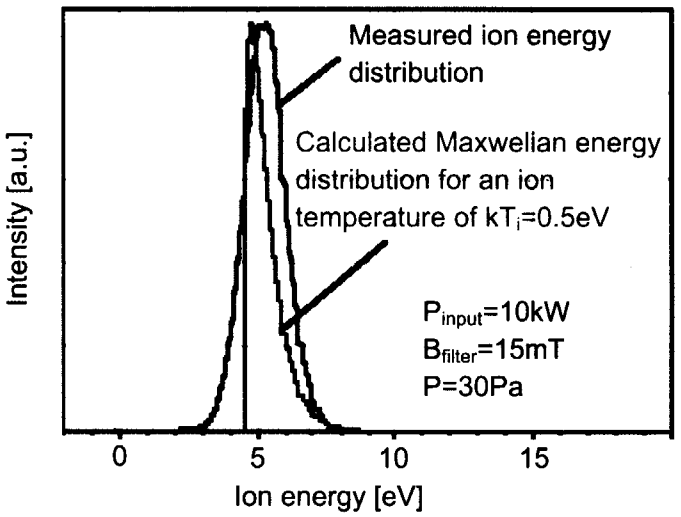


Fig. 2 Comparison of the measured and calculated ion energy distribution used to estimate the ion temperature.

Figure 2 illustrates the measured ion energy distribution and the calculated Maxwellian fit for an ion temperature of $kT_i = 0.5$ eV. The height of the Maxwellian distribution was scaled to the height of the measured distribution. A comparison of the half-height widths and the high energy tails of both measured and calculated curves shows that the ion temperature is about $kT_i = 0.5$ eV. Taking into account the two factors which are responsible for an increase in the energy spread of the measured curve (resolution of the analyzer and gradient of the plasma potential) the ion temperature can be estimated to be $kT_i < 0.5$ eV, a very low value for ion sources.

Please note that the measured mean ion energy of 5.2 eV in Fig. 2 is not the mean energy of the ions in the plasma. When leaving the plasma, the ions have to cross the plasma wall potential, leading to an energy of eU_{PW}. Within the plasma the ions have only a thermal energy distribution.

(5) Electron Energy Distribution

In Fig. 3 the influence of the gas pressure on the electron energy distribution is demonstrated. Therefore, it was also necessary to investigate the influence of the neutral gas pressure on the electron energy distributions. As the gas pressure was changed from 0 to 30 Pa, it was not possible to keep the input power constant. Consequently, with increasing gas pressure the arc current also rises. The spectra were measured during operation without the magnetic filter, in order to detect electrons emitted by the filament. The arc voltage was kept at 75 V. Figure 3 presents the result of these investigations.

The electron energy distribution can be divided into three groups according to their mean energy: high (a), middle (b), and low (c) energy electrons. Without any neutral gas (the arc is off) there are only high energy electrons with a mean energy corresponding to the applied arc voltage of 75 V. These

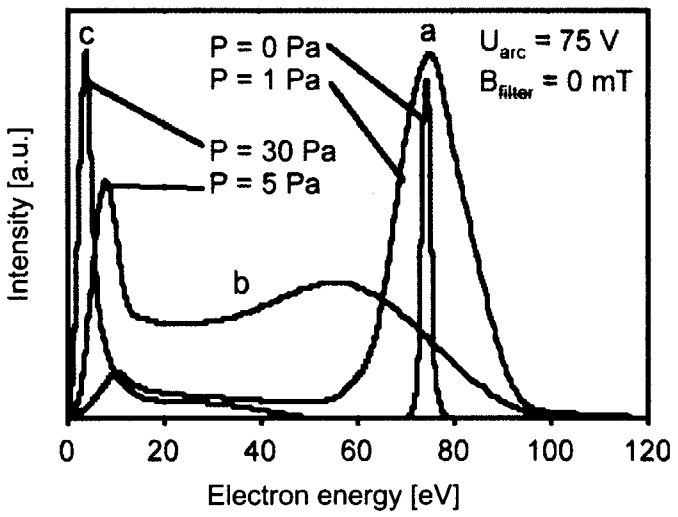


Fig. 3 Electron energy distribution as function of different gas pressures (arc current) at low input power.

electrons are generated at the filament and accelerated to the plasma chamber or plasma electrode without any interactions. In this operation mode, the mean free path length is in the range of the plasma chamber dimension.

For a glow discharge (P = 1 Pa, P_{input} = ~10 W) the energy spread of the high energy electron peak rises because of inelastic and superelastic collisions. Moreover middle (b) and so-called bulk electrons (c) are registered. These are electrons from the filament, which are decelerated due to inelastic interactions with other plasma particles generated in the plasma.

The higher the gas pressure, i.e. the arc current, the more middle energy and bulk electrons are observed. At a gas pressure of 30 Pa and an input power of about 2 kW, more than 80% of the electron population consist of bulk electrons. Only a small fraction of middle energy electrons are detected, high energy electrons are thermalized in the plasma, and filament electrons do not achieve high energies due to frequent inelastic collisions with other plasma particles.

The result is that the mean free path and the mean energy of the electrons are affected by the neutral gas pressure and the plasma density. It is remarkable that a gas pressure of 30 Pa (at the gas inlet!) reduces the electron energies to such low values, even in operation without a filter magnet. Consequently, for operation with typical arc power (10 kW) and typical source pressures (30 Pa), only a small filter field flux density is necessary to prevent the high energy tail in the energy distribution.

As a further step, the electron temperature was estimated with a Maxwellian fit as already performed in the case of the ion energy distribution. Figure 4 shows a typical measured electron energy distribution and a suitable Maxwellian fit for an assumed electron temperature of kT_e = 1.2 eV.

The low electron temperature, even in operation with full arc power, is the basis for the low ion temperature in the plasma. Otherwise the ions in the plasma are heated by means of "Coulomb heating" with hot electrons. This is a big advantage of arc discharge sources compared to ion sources with an rf coupling for plasma generation. In the later type of ion source, the electron temperature and the beam emittance are considerably higher.

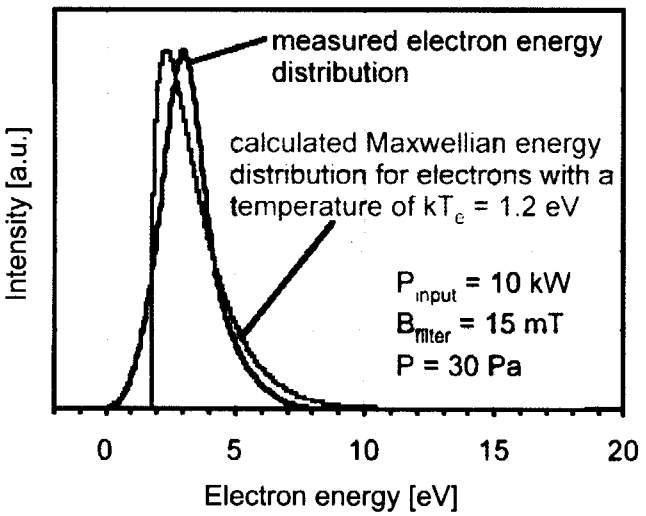


Fig. 4 Comparison of measured and calculated electron energy distribution used to estimate the electron temperature.

(6) Magnetic Filter

The magnetic filter is a key element for the production of a nearly pure proton (deuteron) beam. Therefore, it is important to investigate its influence on the ion and electron energy distribution. Figure 5 displays the electron energy distribution for three different filter field strengths. Analysis shows that the magnetic filter has two main influences. First, it reduces the electron temperature and second, in operation with optimum filter field strength, only low energy electrons (bulk electrons) are detected.

The reduction of the electron temperature can be qualitatively seen as the decrease of the energy spread with increasing filter field strength. At filter field strength of 15 mT, the energy spread of the bulk electron peak is only 2 eV, compared to an energy spread of 10 eV in operation without the magnetic filter. The influence of the filter field strength on the electron temperature was also observed in a study of the positive ion energy distribution (not presented in this paper). In operation with the optimum filter field strength, the plasma wall potential is about 0.7 V lower than in operation without the magnetic filter.

The influence of the filter field on the high energy tail of the distribution is obvious in Fig. 5. Without any filter, high energy electrons are detected with energies up to 88 eV (arc voltage = 85 V). With increasing filter field strength the area of the high energy tail decreases. That means energetic electrons

from the filament or the region around the filament are thermalized. At a filter field of 15 mT no high energy electrons are measured.

The effect of the magnetic filter can be understood in the following way. By means of the transverse magnetic field electrons are forced into curved paths. Consequently, the distance covered between two points in the plasma is increased and so is the probability of inelastic collisions with other plasma particles. Due to the higher number of inelastic collisions, the mean electron energy as well as the electron temperature is reduced. The influence of the filter is stronger for the more energetic electrons. If the electron energy drops below the lowest excitation energy, the filter has only a weak influence.

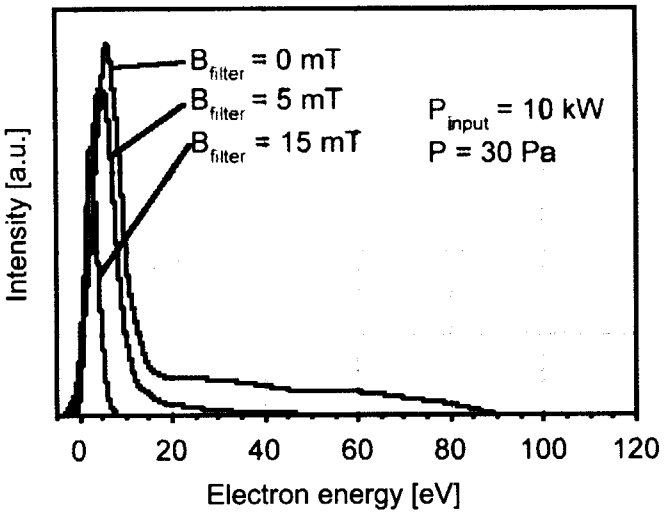


Fig. 5 Electron energy distribution for different magnetic filter field strengths.

This investigation demonstrated that a filter field flux density of 15 mT is strong enough to keep the mean electron energy below 5 eV, an optimum energy for a high proton (deuteron) yield in the plasma. Higher field strength is not useful because it would lead to beam deflection in the extraction system.

(7) Conclusions

The Institut für Angewandte Physik developed a high brilliance 200 mA proton (deuteron) source (corresponding to 141 mA D^+) for IFMIF. An H^+ fraction of 93% and current density of 400 mA/cm^2 was achieved in cw-mode operation.

In order to get optimum beam performance, basic plasma investigations have been performed on this source. An ion temperature below 0.5 eV has been derived from the measured ion energy distributions. Such a low ion temperature is an excellent basis for a low ion temperature in the beam, which is favorable to low beam emittance. An analysis of the ion and electron energy distributions for different source pressures shows that a pressure of 30 Pa is sufficient to prevent the distinctive high energy tail of the ion energy distribution.

The electron temperature in the plasma is estimated to be 1.2 eV for full source power. Consequently, there is little heating of the ions by the electrons. This is also an important precondition for low beam emittance. Furthermore, for arc powers between 5 and 10 kW, the mean electron energy in the plasma is almost constant. This guarantees optimum mean electron energy (5 – 10 eV) for plasma generation with high proton (deuteron) yield.

The influence of the magnetic filter on the electron energy distribution was studied to find the optimum filter field flux density. It was found that a filter field flux density of 15 mT is necessary to prevent a distinctive high energy tail of the electron energy distribution, an important condition for a high proton (deuteron) yield in the plasma and for small beam deflection.

References

[1] A. Möslang, IFMIF-International Fusion Materials Irradiation Facility-Conceptual Design Evaluation Report, A Supplement to CDA by the IFMIF Team, Karlsruhe, 1999.

[2] R. Hollinger, P. Beller, K. Volk, M. Weber, H. Klein, "The Frankfurt 200 mA Proton Source", Rev. Sci. Instrum., 71, Volume II, 836-838, 2000.

3.1.7 AC13B-EU : Low Energy Beam Transport

(1) Brief Task Description

A LEBT system consisting of two solenoids will be used to analyze the space charge compensation process, the transmission and emittance growth as a function of beam current, beam size, current fluctuation, and residual gas pressure. (These are believed to be the most important factors.) The behavior of the beam current, emittance, and space charge compensation is studied and measured between the ion source exit and the RFQ entrance.

Contributors

Name	Party	Institute	E-mail address
H. Klein	EU	IAP	horst.klein@iap.uni-frankfurt.de
J. Pozimski	EU	IAP	Pozimski@iap.uni-frankfurt.de
A. Jakob	EU	IAP	A.Jakob@iap.uni-frankfurt.de
O. Meusel	EU	IAP	O.Meusel@iap.uni-frankfurt.de

(2) Introduction

In the IFMIF project the low energy beam transport (LEBT) from ion source into the first RFQ is characterized by very high space charge forces. Therefore the lens system has to counteract the space charge forces without major aberration or emittance growth. Additional varying space charge forces due to current fluctuations, source noise, and rise time of space charge compensation negatively influences the low energy beam transport and the injection into the RFQ. Rotation of the emittance pattern as a function of time increases the time integrated emittance. Varying twist parameters of the emittance inhibit proper injection into the RFQ and decrease the transmission. Numerical simulations including a beam current variation of ±2 % at frequencies from 20 kHz up to 5 GHz have been performed for different transport systems.

(3) Beam transport simulation from ion source to RFQ

(3.1) Beam extraction

Simulation of the influence of varying beam current on beam extraction has been performed using the IGUN code. It was assumed that a varying plasma density in the ion source is the main cause of the current fluctuation. Figure 1 shows the triode extraction system geometry used for simulation of the trajectory plot (Fig.1) of the D^+ beam with nominal current 140 mA.

Figure 2 shows the emittance at the end of the extraction system (at ground potential) for the three different ion currents (137.2, 140, and 142.8 mA). Due to the space charge forces the beam radius and angle increase slightly with the current. The decrease of the RMS-emittance indicates that the extraction system is optimized for a slightly higher current than the nominal 140 mA.

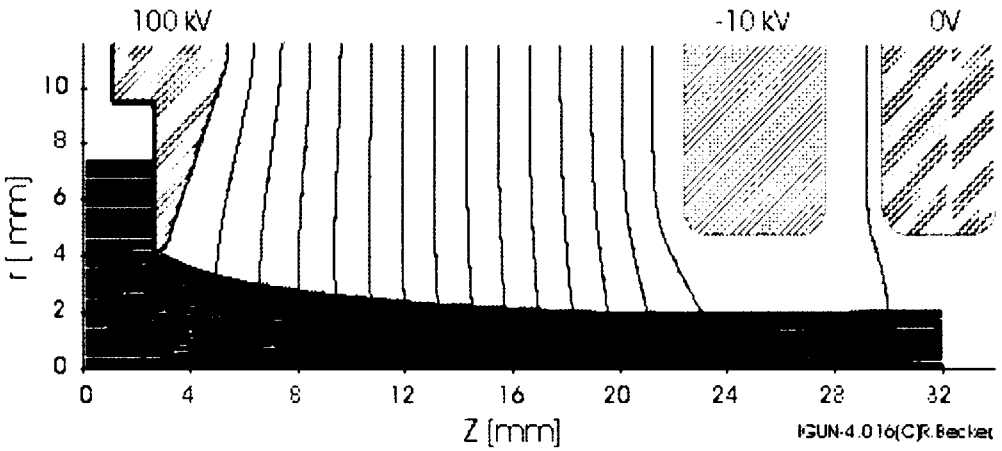


Fig. 1 Trajectory plot of the ion extraction from the ion source, calculated with IGUN.

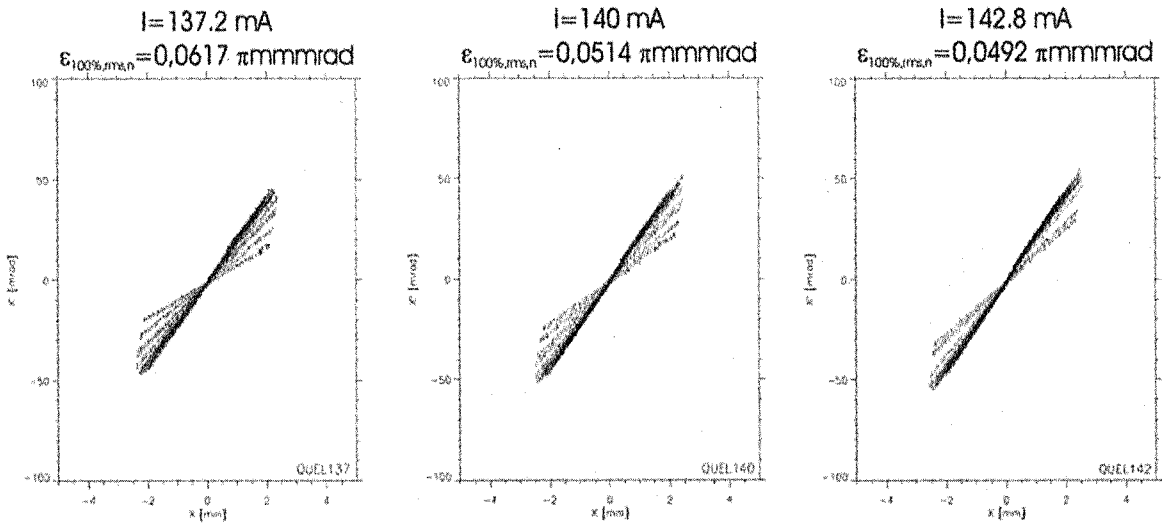


Fig. 2 Emittance at the entrance of the LEBT system for varied extracted beam currents, obtained by simulations using the computer code IGUN.

(3.2) Electrostatic (decompensated) transport

In Fig. 3 the layout of the electrostatic LEBT system used for calculating the beam transport is shown. The LEBT was kept as short as possible (Ez< 7.7 kV/mm) to reduce the influence of the space charge forces. The particular shape of the electrodes was used to flatten the field distribution and therefore reduce aberrations.

Figure 4 shows the emittance at the exit of the electrostatic LEBT for the three different cases. Due to the space charge forces the beam radius decreases slightly (1.6, 1.5, and 1.3 mm) and the envelope angle increases strongly (50, 60 and 80 mrad) with the current. This increase in angle can be explained also by the increasing space charge forces leading to a higher degree of lens filling in the last electrode and to a stronger deflection. The increase of the RMS-emittance (~ 100% between the -2% and the +2% cases of the simulation) shows the effect of higher lens aberrations due to the increased degree of lens filling.

(3.3) Conclusions:

Figure 5 shows the phase space distribution of the three cases of electrostatic beam transport. This is comparable to the effective time-integrated emittance at the entrance (left) and the exit (right) of the electrostatic LEBT. Due to the current fluctuations the RMS-emittance at source exit is slightly (12%) higher than for the nominal current. At the LEBT exit the RMS-emittance growth has already increased to 33%. The additional 21% is mostly due to the higher space charge in the 142.8 mA case. This leads to extensive redistribution due to lens

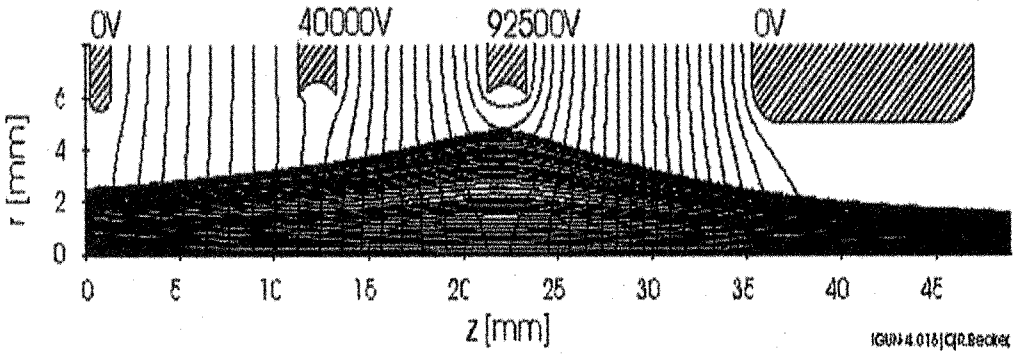


Fig. 3 Comparison of measured and calculated electron energy distribution used to estimate the electron temperature.

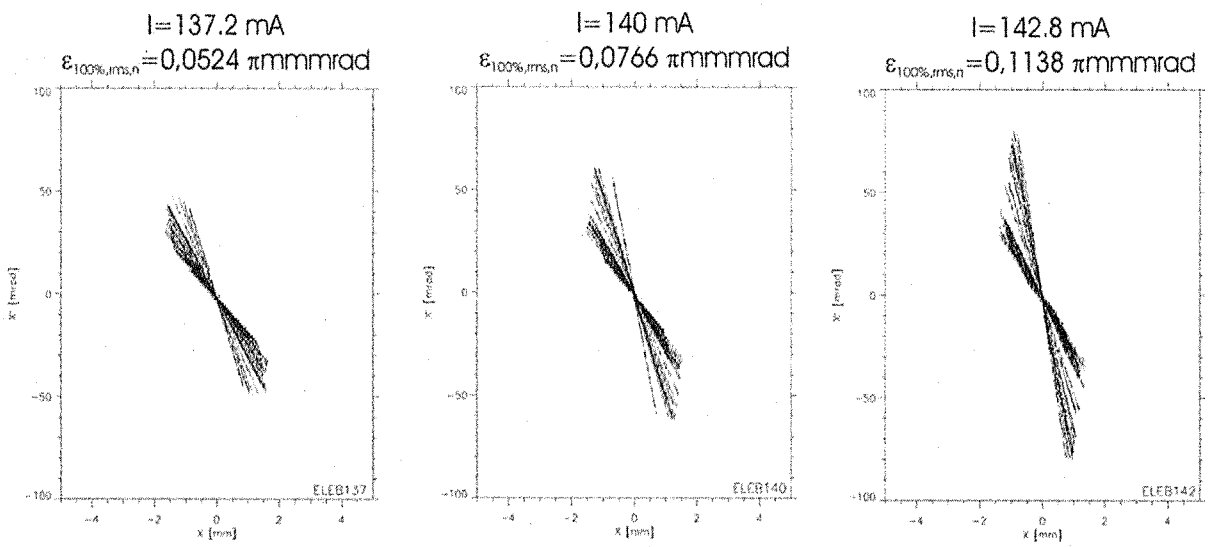


Fig. 4 Emittance at the exit of the electrostatic LEBT system (RFQ entrance) for varied extracted beam currents. The simulations have been performed using the computer code IGUN.

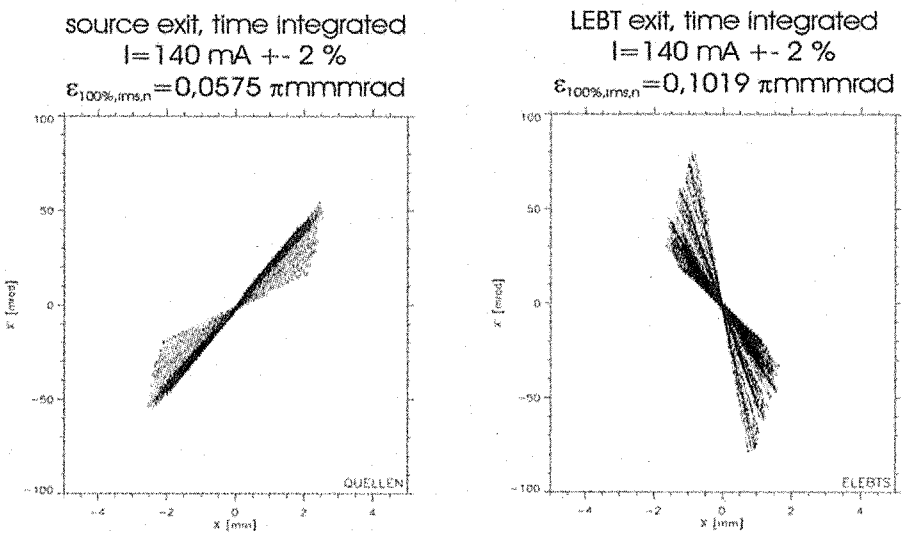


Fig. 5 Input (left) and output (right) emittance of the electrostatic LEBT obtained by simulation of three different ion currents (source noise) and superposing them for time integration.

aberrations. For a current fluctuation of ±2%, the electrostatic lens systems seem unable to meet the requirements for IFMIF.

(4) Magnetic (space charge compensated) transport

Knowledge of the time scale of the disturbance (fluctuation frequency) and the reaction time of the compensated beam plasma is necessary for simulation of the influence of varying beam current on space charge compensated beam transport [1]. From these, two frequencies can be defined. The maximum frequency (f_{max}) is given roughly by the plasma frequency (for IFMIF f_{max} ~ 0.5 GHz) and the minimum frequency (f_{min}) is defined by the production mechanisms of the compensation. Below f_{min} the compensation is adiabatic and can be neglected for beam transport properties. Above f_{max} the space charge compensation cannot follow the current disturbance.

(4.1) Measurements of the rise time of compensation.

For IFMIF f_{min} has been determined from Saclay rise time measurements at the H^+ injector [2]. Figure 6 (left) shows the development of the beam current (for a pulsed ion source) as a function of time. The rise time of the ion current (given by the ion source) can be estimated by measurement using a Faraday cup to approximately 7 μs. Figure 6 (right) shows the development of the beam potential on beam axis as a function of time for different residual gas pressures from which different theoretical rise times of compensation (2.3-10 μs) can be derived. The rising potential during the first 2-3 μs is due to the rise time of the source, the falling potentials after 3 μs is already the effect of the space charge compensation (for 100 % variation of the space charge !). As a result for IFMIF, the lower boundary frequency will be between 200 kHz > f_{min} > 20 kHz (depending on the residual gas pressure).

Therefore simulation of the low energy beam transport using the LINTRA code [3] under assumption of a two solenoid LEBT section (shown in Fig. 7) has been performed for different ion currents and for three different scenarios (f_{noise} < 20 kHz ; f_{noise} ~ 100 kHz ; f_{noise} > 500 MHz).

Figures 8 and 9 show results of simulation with the LINTRA code under the assumption of a source noise frequency of 100 kHz (space charge fluctuations are partly compensated, and the resulting variation is ±1.2%). The variation of the emittance at the exit of the magnetic LEBT section

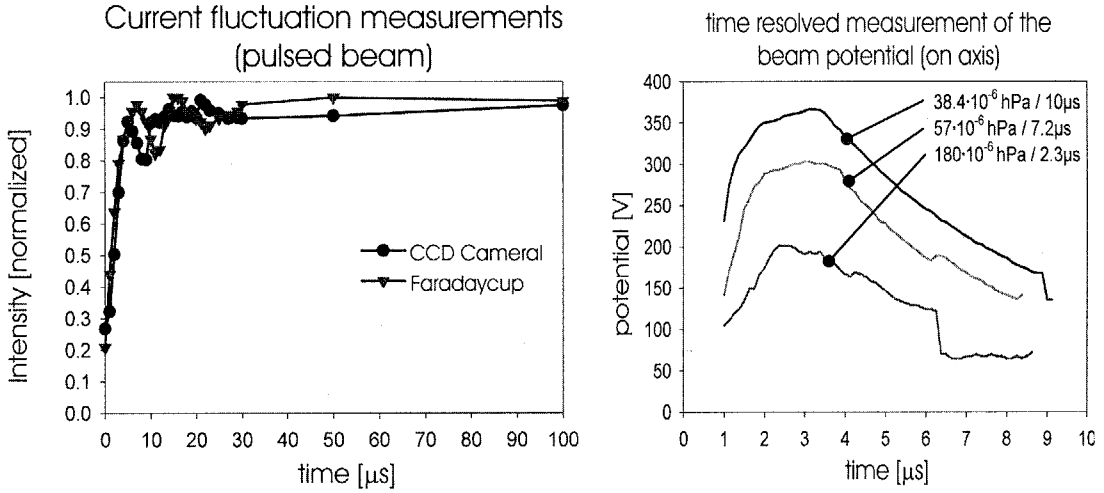


Fig. 6 Left: Ion current measurements as a function of time using a faraday cup and CCD camera measurements of a pulsed ion beam. Right : Development of the beam potential as a function of time for different residual gas pressures, determined by time resolved measurements with a residual gas ion energy spectrometer.

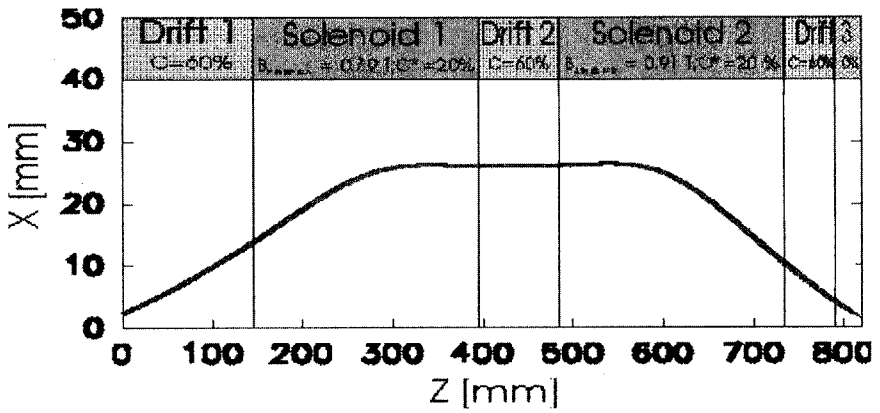


Fig. 7 Schematic drawing of the magnetic LEBT for IFMIF including beam envelope for 140 mA.

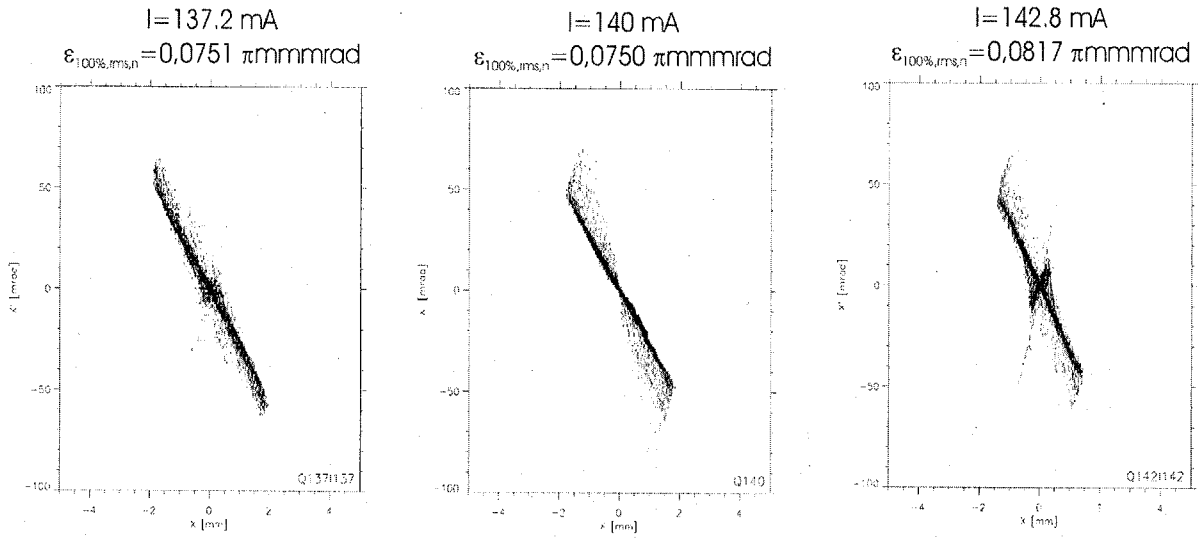


Fig. 8 Simulation of beam transport for constant space charge compensation (20 kHz < f_{noise} < 100 kHz) using entrance emittances according to Fig. 1.

is mainly influenced by the variation of the LEBT input emittance due to the varying input emittance delivered by the ion source (see Fig. 2).

(4.2) Conclusions

Measurements of space charge compensated beam transport at Saclay have shown the influence of the compensation rise time on beam transport. From those results a boundary frequency can be derived. For noise below the boundary frequency no major influence on the compensation is expected. Calculations show that even for current fluctuation of ±2% amplitude, no significant emittance growth is expected. The injection parameters for IFMIF can be fulfilled by magnetic focussing using two solenoids, even for a variation of the beam current of ±2% at any frequency.

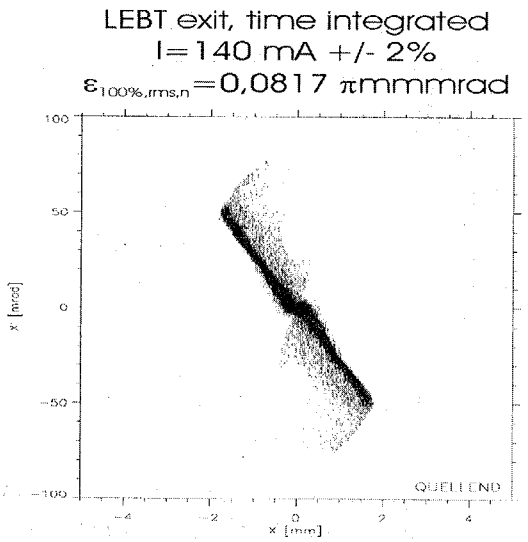


Fig. 9 Time integrated emittance gained from the simulations (see Fig. 8) of beam transport for constant space charge (100 kHz < f_{noise}) using entrance emittances according to Fig.2. using entrance emittances according to Fig.1. Left for space charge variation of +/- 1.2 % (20 kHz < f_{noise} < 500 MHz) right for a variation of +/- 2 % (500 MHz < f_{noise} < 5 GHz).

(5) Beam transport using space charge lenses (Gabor lenses)

Gabor lenses used for beam transport not only deliver strong cylinder symmetrical focussing but also totally compensate the space charge of the beam within the lens. This is valid up to the plasma frequency (app. 5 GHz). Outside the lenses the degree of compensation is reduced compared to magnetic focussing [4]. This is due to the heating of the electrons inside the lens. On the other hand, this exchange of lens electrons and compensation electrons increases the boundary frequencies for fluctuations outside the lens. A magnetic field for electron capture below 0.2 T and an electrode potential of 15 kV is necessary to fulfil the injection requirements at the RFQ entrance. Figure 10 shows the results of transport simulations

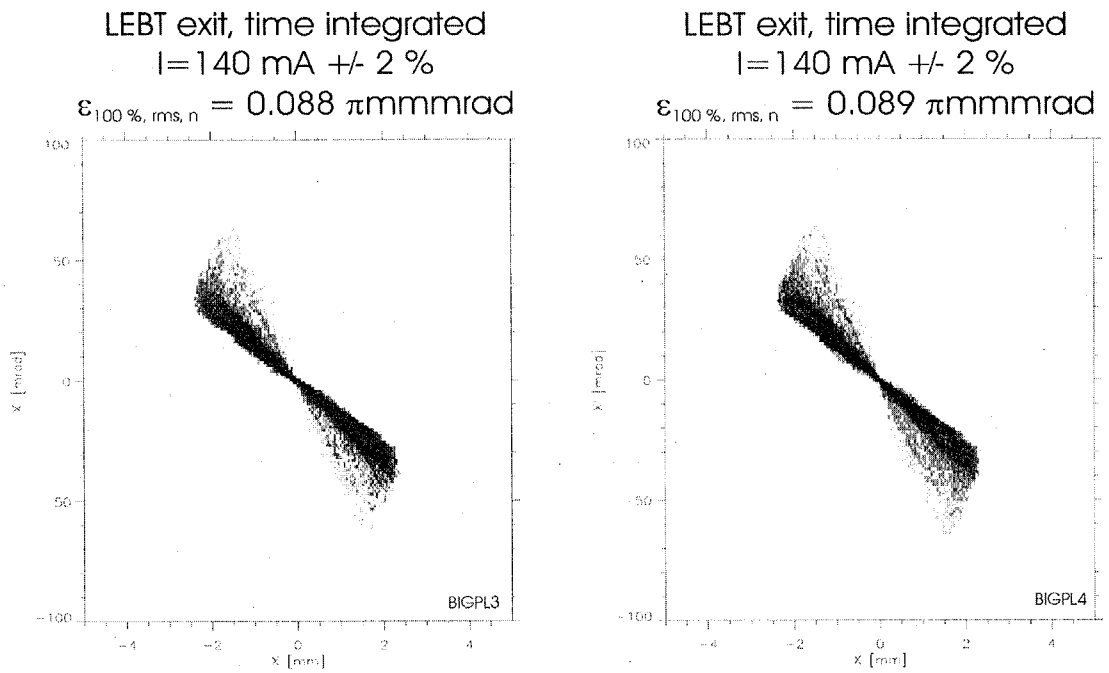


Fig. 10 Time integrated emittances gained from a simulation of beam transport (using Gabor lenses) using entrance emittances according to Fig. 1. Left for space charge variation of +/- 1.2 % (20 kHz < f_{noise} < 500 MHz). Right for a variation of +/- 2 % (500 MHz < f_{noise} < 5 GHz).

for IFMIF for a variation of beam current of ±2%. The degree of lens filling was 84 % for the chosen geometry. An overall emittance growth of 54% (0.088 π mm mrad) is forecast. The additional emittance growth due to current fluctuation is mainly caused by the variation of the input emittance. An additional emittance growth of 15% is found.

(5.1) Conclusions

For variation of the beam current of ±2%, minor changes in beam transport have been found. An overall growth of the time integrated emittance of 15% is not significant and is mostly caused by the variation of the input emittance delivered by the ion source. The injection parameters for IFMIF can be fulfilled by a LEBT system consisting of Gabor lenses, even for variation of the beam current of ±2%.

(6) Summary

The influence of current fluctuations of ±2% on low energy beam transport has been investigated numerically for three different transport systems. For electrostatic systems the largest growth of the time integrated emittance has been found (77%, at app. 50% lens filling) partly caused by the variation of the delivered source emittance and the varying space charge in the lens. Space charge compensated transport shows better results (42% for solenoids below a frequency of 100 kHz at 50% lens filling, and 54% for Gabor lenses below a frequency of 5 GHz at 84% lens filling). For compensated transport the main source of emittance growth is the variation of the source emittance. Comparison between magnetic systems and Gabor lenses shows a slightly better performance of the solenoid system, but only at very low frequencies. On the other hand the magnetic field strength is reduced by at least a factor of seven. Therefore the investment cost for Gabor lenses is approximately 50% of the solenoid solution. Both fulfil the requirements for IFMIF even at a current variation of ±2%. The beam transmission is mainly influenced by residual gas interaction (~10% depending on residual gas pressure) and not dominated by radial losses (for all cases <1%).

References

[1] R. Dölling, "Raumladungskompensation Driftender Intensiver Strahlen Niederenergetischer Ionen und Techniken zu ihrer Vermessung", Dissertation IAP, University of Frankfurt, Germany (1994).

[2] A. Jakob, P-Y. Beauvais, R. Gobin, H. Klein, J-L. Lemaire, P-A. Leroy, J. Pozimski, "Time Resolving Diagnostics of Compensation process of Pulsed Ion Beams at SILHI", Proc. 8th ICIS Conf. 1999 Kyoto, Japan, to be. Publ.

[3] J. Pozimski, O. Meusel, "LINTRA ein Computerprogramm zur Berechnung des Strahltransportes Teilkompensierter, Hochperveanter Ionenstrahlen", GrakoNews 1/99 , Graduiertenkolleg Physik und Technik von Beschleunigern, grako@ikp.tu-darmstadt.de

[4] J. Pozimski, "Untersuchungen zum Transport Raumladungskompensierter Niederenergetischer und Intensiver Ionenstrahlen mit einer Gabor Plasma Linse", Dissertation, Institut für Angewandte Physik der Johann Wolfgang Goethe Universität, 1997.

3.1.8 AC13C-JA : Test of Low Energy Beam Transport

(1) Brief Task Description

The LEBT system using solenoid coils is to be tested in the ITS-2M test stand with a 60 keV/200 mA H^+ ion beam, whose space charge is higher than the 155 mA/100 keV D^+ ion beam. The beam emittance growth exceeds the permissible value; therefore, an electrostatic LEBT system is to be tested.

Contributors

Name	Party	Institute	E-mail address
K. Watanabe	Japan	JAERI	watanabe@naka.jaeri.go.jp
T. Iga	Japan	JAERI	igataka@fusion.naka.jaeri.go.jp
T. Morishita	Japan	JAERI	morishit@fusion.naka.jaeri.go.jp

(2) Introduction

The ion beam extracted from an ion source is transported to the RFQ which accelerates the 100 keV D^+ beam to an energy of 5 MeV [1]. The LEBT transports the beam from the ion source to the RFQ with acceptable beam emittance for the RFQ. In the present experiment, performance of a LEBT using solenoid coils attached to the multi-cusp type ion source [1-3] has been investigated.

(3) Experimental equipment and conditions

The experimental setup is illustrated in Fig. 1. The LEBT was mounted between the ion source and vacuum chamber. The LEBT consists of a pair of solenoid magnet coils, each coil having 225 turns. Dimensions of the coils are 193 mm inner diameter, 266 mm outer diameter, and 108 mm thickness. Each solenoid coil can produce a magnetic field of about 0.15 T at the center with a current of 150 A. A typical magnetic field distribution in the LEBT is shown in Fig. 2.

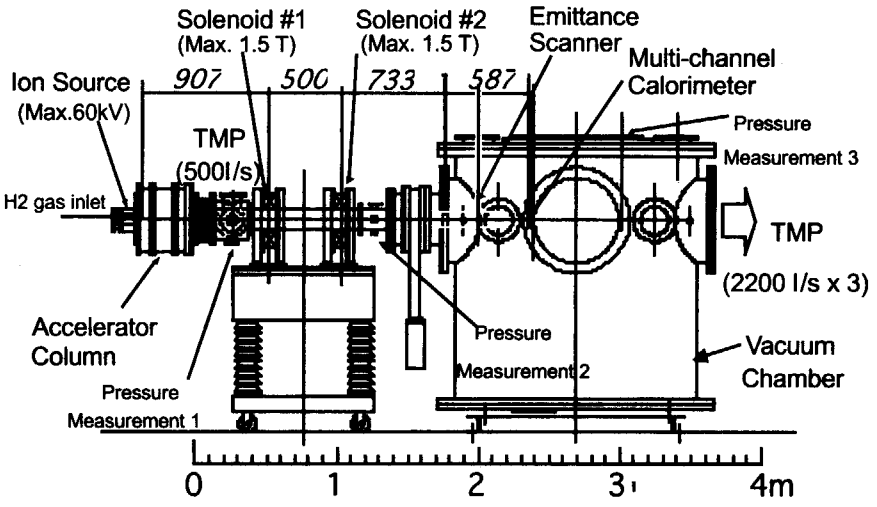


Fig. 1 Experimental setup of the LEBT.

The multi-cusp ion source used in this experiment is illustrated in Fig. 3. Dimensions of the multi-cusp plasma generator are 120 mm diameter and 122 mm depth. Two pieces of tungsten filament cathode were installed in the plasma generator. An electrostatic accelerator has a two-stage acceleration

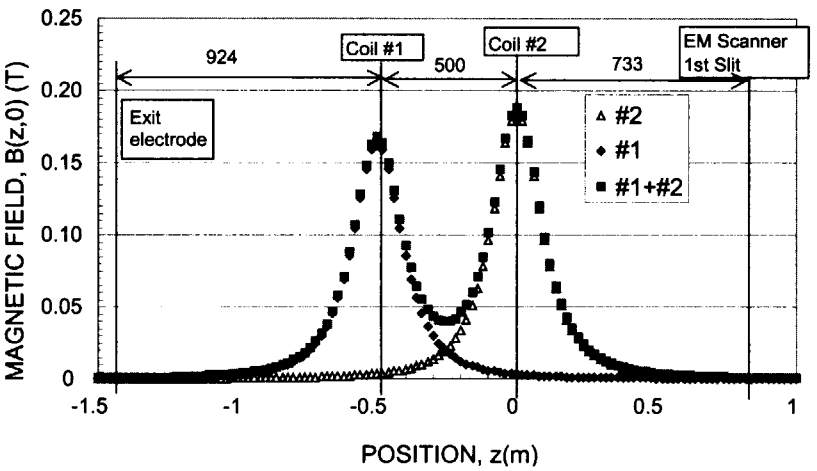


Fig. 2 Magnetic field distribution of the LEBT.

system with a single aperture of 12 mm diameter. Detailed structure of the ion source accelerator is given in task report AC11-JP.

A turbomolecular pump (TMP) with pumping capacity 500 ℓ/s was mounted between the ion source and the LEBT. The distance between the exit electrode and the first solenoid coil is 924 mm, and the distance between the two coils was 500 mm. A current transformer was installed downstream of the second magnetic coil to measure the ion beam current. An emittance scanner was installed 2140 mm from the exit electrode, And a multi-channel calorimeter was mounted 2727 mm from the exit electrode. Three TMPs (2200 ℓ/s x 3) were used for vacuum pumping. Hydrogen gas was fed to the plasma generator.

The experiment was performed at the test stand ITS-2M. This test stand can operate up to the acceleration voltage of 60 kV, and the experiments were performed at this energy level. In the experiments, gas pressure distribution in the beam line was measured; then the beam transport experiments were performed.

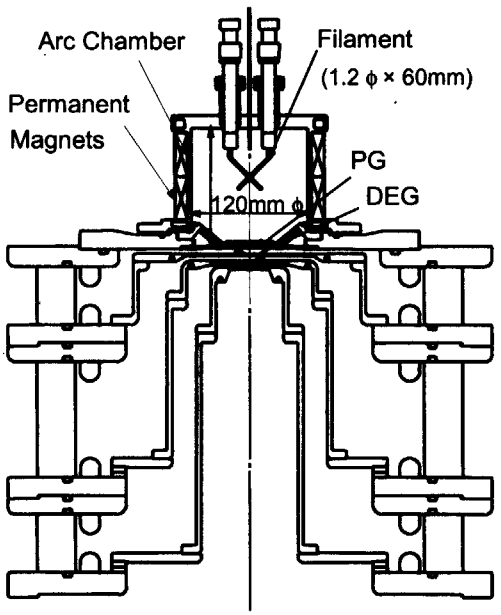


Fig. 3 Configuration of the multi-cusp ion source.

(4) Results and Discussion

Typical operating pressure of the ion source was 1.4 Pa with hydrogen. Gas pressure distribution in the beam line is shown in Fig. 4, with both calculated and measured pressures given. Good agreement was confirmed between them. The pressure distribution showed that the LEBT region is in the range of 0.003 to 0.03 Pa. A line density from the exit electrode to the exit of the LEBT was estimated to be about $1.02\times10^{15}cm^{-2}$. Neutralization efficiency of the H^+ beam for this line density was estimated to be about 10% for beam energy of 60 keV. In this pressure region the H^+ ion beam tends to diverge by space charge effects without a converging method [4].

The beam measured 2.7 m downstream from the exit electrode of the ion source is shown in Fig. 5. By increasing the magnetic field strength from 0.07 to 0.18 T, the ion beam converged from 60 mm (e-holding half width of the beam profile) to 10 mm.

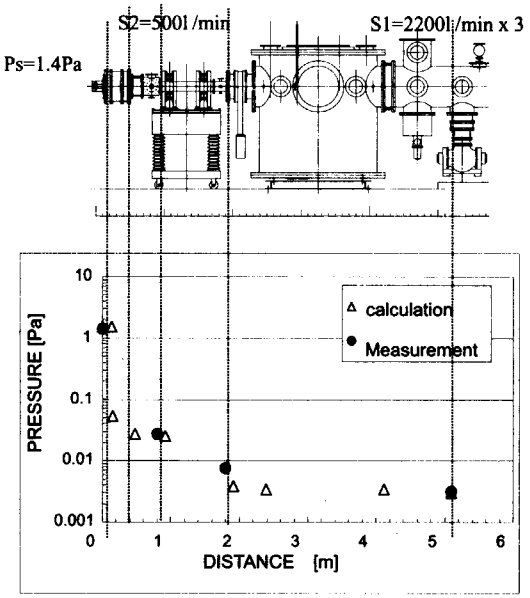


Fig. 4 Gas pressure distribution in the beam transport region.

Beam current was measured 1.5 m downstream from the ion source by using a current transformer. The measured beam current was 92 mA at energy 60 keV. By extrapolation and taking into account the same perveance of the beam to energy 100 keV, this current corresponds to a beam current of 198 mA for hydrogen, and a D^+ beam current of 140 mA. From these estimates, the space charge of the transported beam is similar to the rated beam for deuterons.

Beam emittance was measured before and after the LEBT. Figure 6(a) shows the measured emittance at the ion source exit. The beam energy was 60 keV. The beam current was varied from 103 mA to 134 mA by changing the arc discharge power in the plasma generator. The 63% emittance was about 0.27 π mm.mrad at beam current of 110-120 mA where the smallest beam divergence was observed. The 100% beam emittance showed a big variation with the beam current; however the 63% emittance did not change as much.

The beam emittance measured at the position after the LEBT is shown in Fig. 6(b). Emittance growth has been observed. The 63% emittance was 0.67 π mm.mrad. An example of the emittance diagram is shown in Fig. 7(a). Diverged component of the beam can be seen in the diagram. The beam core profile is shown in Fig.7 (b). The core of the beam component is strongly converged by the LEBT. The e-folding half width of the beam core profile was only 1.3 mm.

Diverged beam has been converged strongly by the LEBT. Though the beam core could be converged to a very small beam diameter, the emittance could not be kept in the extracted beam. One of the reasons to produce a larger emittance is believed to be due to the strong convergent the divergent beam. In this experiment, the position of the LEBT was fixed as shown in Fig. 1. The distance between the exit electrode and the LEBT coil

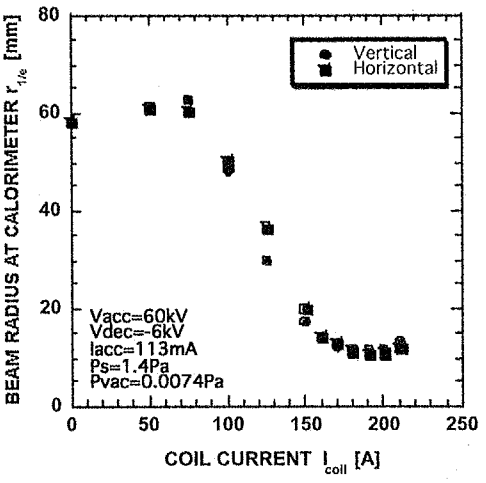


Fig. 5 Beam converging by the LEBT.

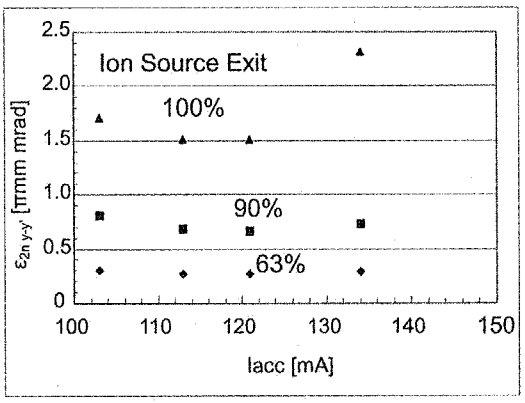
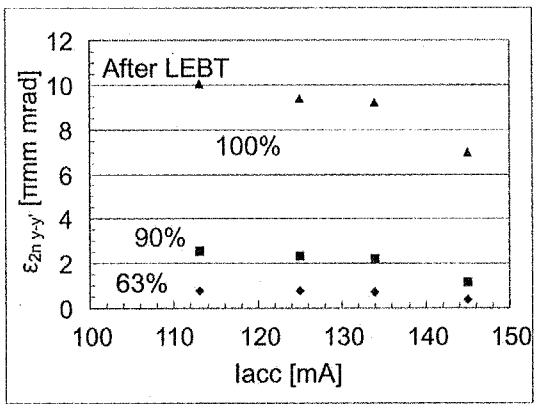
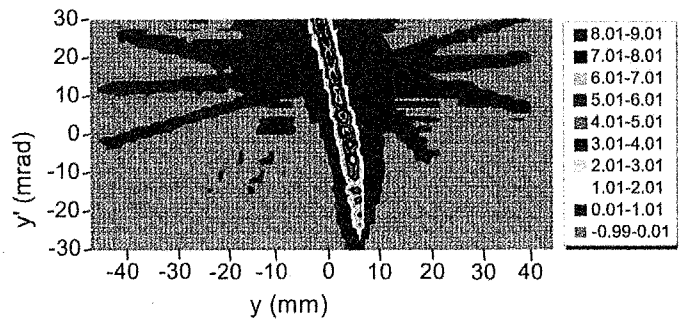


Fig. 6 (a) Beam emittance measured at the Exit of the ion source.

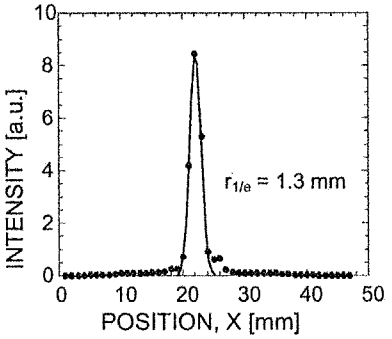


(b) Beam emittance measured after the LEBT. (Vacc=60kV, Vdec=-6kV, Ps=1.4Pa, PLEBT1=2.6x 10^{-2}Pa, PLEBT2=7.7x10^{-3}Pa, Pvac=3.2x10^{-3}Pa)



V_{acc} = 60 kV, V_{dec} = –6 kV,
P_s = 1.4 Pa, P_{LEBT1} = 0.026 Pa, P_{LEBT2} = 0.0077 Pa,
P_{vac} = 0.0032 Pa, P_{arc} = 7.6 kW

(a)



BEAM CORE PROFILE

(b)

Fig. 7 Emittance diagram and beam core profile after the LEBT.

was longer than 0.9 m. This layout produced the divergent beam down stream of the ion source, because the space charge effects of the beam are strong in the low pressure region. Some modifications of the layout which can converge the beam before diverging is required to produce smaller beam emittance.

(5) Conclusions

The low energy beam transport composed of two solenoid coils connected to the multi-cusp ion source has been tested. In the preliminary test, the beam converging by the LEBT was confirmed. The beam current up to 92 mA at 60 keV was transported by the LEBT. The space charge of this beam corresponds to the 140 mA D^+ at energy of 100 keV, which is near the rated beam space charge.

References

[1] IFMIF International Team, IFMIF International Fusion Materials Irradiation Facility Key Element Technology Phase Interim Report, JAERI report, Japan Atomic Energy Research Institute, JAERI-Tech 2002-022, March 2002.

[2] T. Iga, Y. Okumura, M. Kashiwagi, "Development of a High Brightness Ion Source for IFMIF and Preliminary Test Results", JAERI Report, Japan Atomic Energy Research Institute, JAERI-Tech 2001-028, May 2001 (in Japanese).

[3] K. Watanabe, "Development of Ion Sources for IFMIF", J. Plasma Fusion Research, 78(6), (2002) 535-540 (in Japanese).

[4] Y. Okumura, M. Araki, M. Hanada, H. Horiike, T. Inoue, T. Kurashima, S. Matsuda, Y. Matsuda, Y. Ohara, S. Tanaka, K. Watanabe, "One Ampere Volume H- Ion Source with Multi-aperture Extractor", IAEA Technical Committee Meeting on Negative Ion Beam Heating, Culham Lab., 15-17 July, 1987.

3.1.9 AC34B-JA : Examination of Beam Matching to RFQ

(1) Brief Task Description

Mock-up modules of a 175 MHz RFQ were designed and fabricated for low power measurements. In the design work, the MAFIA code was used; resonant frequencies for the operating mode and higher modes as a function of RFQ longitudinal length were analyzed. Using the mock-up module for RFQ lengths of 1.1 m and 2.1 m, the resonant frequencies were measured. The measured frequencies agree with the calculated values within 1 MHz.

Contributors

Name	Party	Institute	E-mail address
S. Maebara	Japan	JAERI	maebaras@fusion.naka.jaeri.go.jp
M. Saigusa	Japan	Ibaraki U.	saigusa@ee.ibaraki.ac.jp
S. Sazawa	Japan	Ibaraki U.	sazawa@popx.tokai.jaeri.go.jp
M. Sugimoto	Japan	JAERI	sugimoto@ifmif.tokai.jaeri.go.jp

(2) Introduction

In the 175 MHz IFMIF RFQ system, a deuteron beam of 140 mA is injected at 0.1 MeV and accelerated to the output energy of 5-8 MeV. As an RFQ longitudinal length of about 12 m will be needed, suppression of higher modes is indispensable. For this purpose, a coupled cavity technique was developed by the APT/LEDA project of LANL, where a 350 MHz RFQ with 6.7 MeV output energy was built and operated. This study addresses verification of the technical issues in the 175 MHz IFMIF RFQ system.

In the first step, it is important to establish the design method for the 175 MHz RFQ mock-up modules. The first issue is to obtain the know-how for setting the mesh size in the analysis code, in order to achieve good agreement with measured values. For this purpose, 175 MHz RFQ mock-up modules which consist of two end-plate modules and RFQ modules, were designed using the MAFIA code. The mock-up modules were fabricated for low power tests. For both modules, a simplified vane shape was designed, without longitudinal modulation.

In the design work, resonant frequencies for operating mode and higher modes as a function of RFQ longitudinal length were analyzed. In the low power tests, the resonant frequencies were measured for RFQ lengths of 1.1 m and 2.1 m, and the measured frequency were compared with the calculated values.

This report presents design of the 175 MHz mock-up module using the MAFIA code, the resonant frequency analysis for the operating mode and higher modes against RFQ longitudinal length, and the low power test results.

(3) Design of the 175 MHz RFQ mock-up module and the numerical calculations

Cross-sections of the RFQ module and a side-view of the end-plate module, which were designed using the MAFIA code, are shown in Fig. 1 and Fig. 2. The bore diameter is ϕ8 mm and the radius of the vane-tip is 4 mm. For the dimensions of the RFQ module, the resonant frequencies of the TE_{210} and TE_{110} modes calculated by the SUPERFISH code were 183.8 MHz and 179.4 MHz respectively. With this RFQ dimension, the end-plate configuration is optimized to achieve uniformity of the electric field distribution vs. longitudinal length using the MAFIA code. The optimized gap length between the end-plate and the vane edge is 4 cm, and the vane under-cut length is 7 cm. The decrease of electric field at the vane edge is 1% of the electric field in the RFQ module as shown in Fig.3.

With the RFQ module combined with the end-plate modules, the resonant frequency of the operating mode (TE_{210}) and higher modes (TE_{11n} and TE_{21n}) vs. RFQ longitudinal length were analyzed using the MAFIA code (Fig.4). For the RFQ length of 1.1 m, the resonant frequency of 186.786 MHz for the operating mode (TE_{210}) and 187.309 MHz for the dipole mode (TE_{110}) were obtained, respectively. In the 2.1 m case, frequencies of 186.438 MHz for TE_{210} and 184.386 MHz for TE_{110} were calculated. The difference frequency of TE_{210} is 348 kHz, but the difference is 2.913 MHz for TE_{110}. In the case of 2.1 m length, higher modes (TE_{211} and TE_{111}) are also shifted, to 198.518 MHz and 199.388 MHz, respectively.

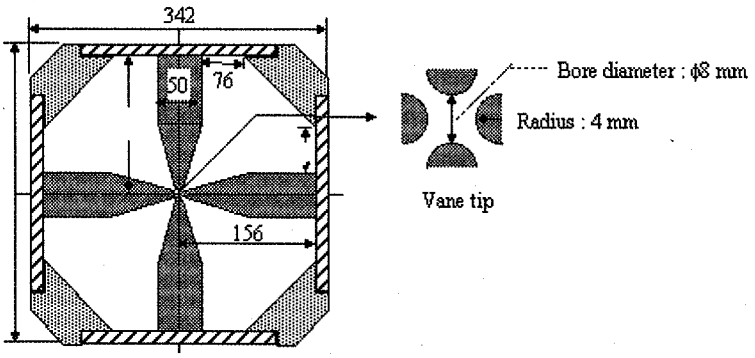


Fig. 1 Cross-section view of 175 MHz RFQ module.

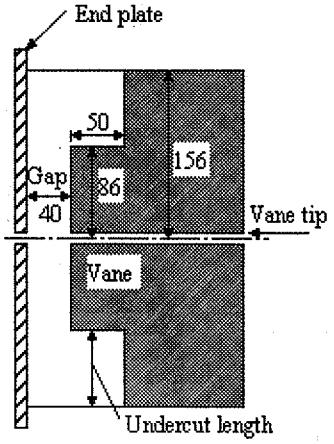


Fig. 2 Side view of end-plate module.

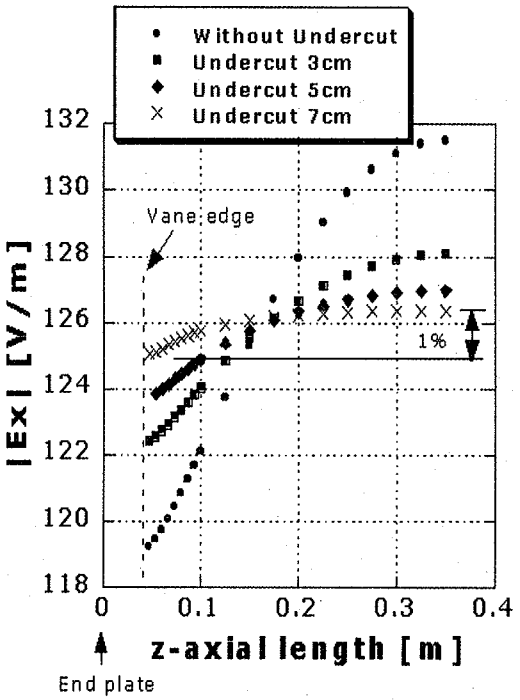


Fig. 3 Resonant frequency of operation mode (TE_{210}) and higher modes against RFQ length.

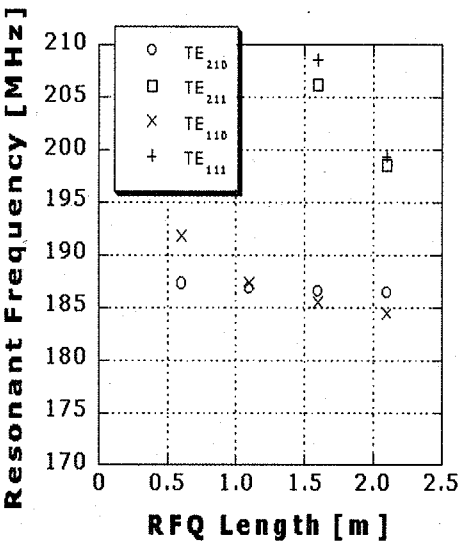


Fig. 4 Resonant frequency of operation mode (TE_{210}) and higher modes.

(4) Low power measurements

Figures 5 and 6 show photographs of the RFQ module and the end-plate module. Both modules are made of aluminum, and the modules are connected by flanges. Each RFQ module length is 1 m; the RFQ length combined with the end-plate modules are 1.1 m and 2.1 m, respectively. The resonant frequency and phase are measured in both cases.

Resonant frequency spectra which were measured by a network analyzer are shown in Fig. 7.

The solid and dotted lines show spectra for 1.1 m and 2.1 m length, respectively. In these measurements, a loop antenna of ϕ60 mm and a pick-up coil of ϕ25 mm were used. Two peaks for 1.1 m and four peaks for 2.1 m were measured. For each peak, the resonant frequency was measured in detail with a frequency resolution of 1 kHz. These measured resonant frequencies and the calculated frequencies are indicated in Table 1 and Table 2, respectively. The measured frequencies are in good agreement with the calculated values, within 1 MHz. In order to obtain good agreement with the measured values, it was found

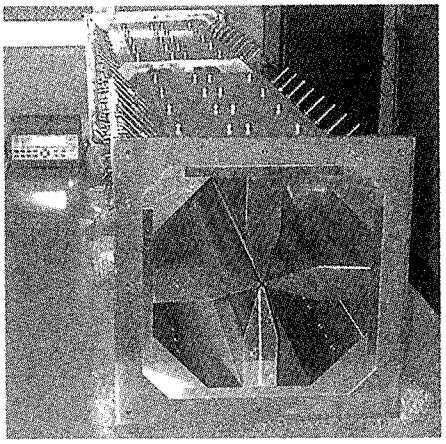


Fig. 5 Photograph of RFQ module.

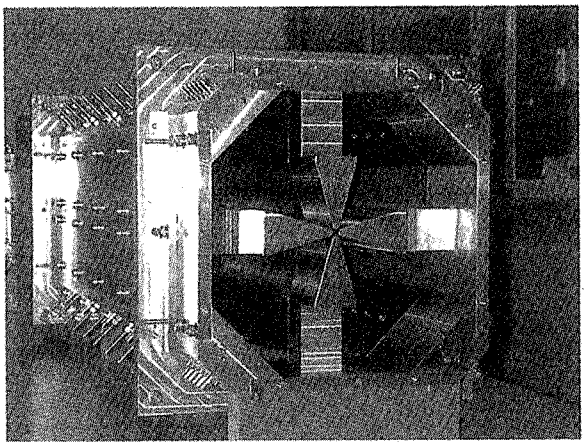


Fig. 6 Photograph of end-plate module when the end-plate is removed.

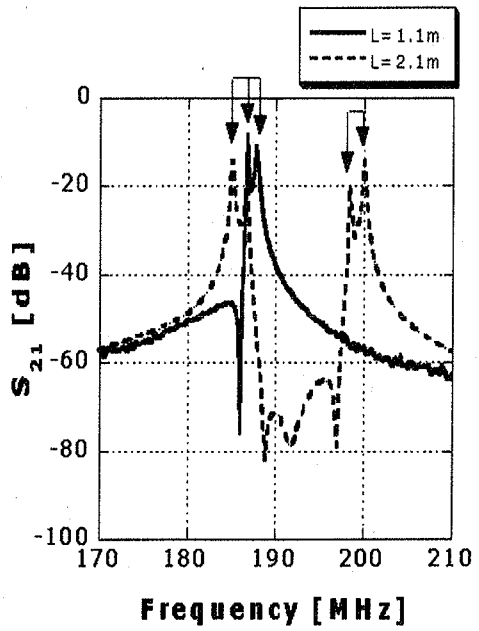


Fig. 7 Measured resonant frequency by Network analyzer.

Table 1 Resonant Frequency for RFQ length of 1.1 m (Unit: MHz).

	TE_{210}	TE_{110}
Calculation	186.786	187.309
Measure	186.781	187.724
Δf	+0.005	-0.415

Table 2 Resonant Frequency for RFQ length of 2.1 m (Unit: MHz).

	TE_{110}	TE_{210}	TE_{211}	TE_{111}
Calculation	184.386	186.438	198.518	199.388
Measure	185.138	186.758	198.464	200.023
Δf	+0.752	+0.320	+0.054	+0.612

that a mesh size not in excess of 5 mm/mesh in the z-axial direction is needed for the end-plate parts, since the boundary conditions at the end-plate parts are a complicated configuration with vane-undercut parts and a gap between the end-plate and vane-edge. For RFQ module parts, the mesh size should be 27.5 mm/mesh or less.

(5) Conclusions

RFQ mock-up modules were designed using the MAFIA code and fabricated for low power tests. Measured resonant frequencies are in good agreement with the calculated values, within 1 MHz for the first step. We also obtained the know-how to optimize mesh size in the MAFIA code. The 1 MHz difference observed in this first step is not yet satisfactory, as an accuracy at the 10 kHz level is required for RFQ design work. We plan to improve the measurement tools and the vane alignment in continuation of this work.

3.1.10 AC20-US : Equipartitioned RFQ Beam Dynamics Design

(1) Brief Task Description

Preliminary designs meeting the IFMIF RFQ beam performance requirements were completed for maximum rf voltage conditions on the RFQ vanes corresponding to 1.7 and 1.8 times the Kilpatrick Limit at 175 MHz. [1]

Contributor

Name	Party	Institute	E-mail address
R.A. Jameson	US	Consultant	rjalosalam@aol.com

(2) Design and Simulation Strategy

As part of a larger investigation, a procedure for RFQ design and simulation has been developed that is very flexible and allows many design strategies to be studied. The program is named LINACS and is programmed in Mathematica.

IFMIF RFQ designs were developed for 140 mA, 0.1-8.0 MeV deuteron RFQs with the field held at 1.7 or 1.8 Kilpatrick throughout. The design strategy sets the local vane voltage according to the KP field and the values given for the other parameters.

The design procedure begins by requiring that the beam is at an equipartitioned equilibrium [2] at the end of a shaper section. This powerful space-charge physics principle minimizes free energy in the system and avoids resonances that are the mechanism for creating beam halos that could be scraped off, causing radioactivation of the structure. At the end of the shaper, the synchronous phase is set at a few degrees from -90°, and an aperture is defined. The design proceeds from the shaper-end back to the beginning of the RFQ.

A weakened value of the focusing variable B is defined at the beginning of the shaper (end of radial matching section), resulting in a larger bore there. This procedure was adopted by Lloyd Young, who weakened the B value at the RFQ entrance in order to make the input match convergence less severe and therefore less sensitive. B is then ramped linearly to the value required at shaper-end. In this report, B at the shaper-input is 60% of the B at shaper-end.

A "porch" (section where ϕ_s=-90°) is used at the beginning of the shaper to minimize the highest energy of any lost particle. (The porch length and overall shaper length in the designs in this report may be somewhat longer than necessary, and might be made shorter after further optimization.) The length of the shaper and the parameter ramping through the shaper are then found using a set of rules based on space-charge physics principles. A standard, linear-ramp radial matching section (typically four cells) is added before the shaper. The aperture at the end of the shaper is optimized for maximum transmission.

In the main part of the RFQ, the beam is maintained at an equipartitioned condition, with eln/etn=γrmsl/rmsr=σ^t/σ^l=2 in most of the cases described. Other tune trajectories can also be tested easily, and a few are discussed.

The synchronous phase is set according to a Teplyakov/Kapchinsky principle that maintains a prescribed ratio between the longitudinal beam size and the left edge of the bucket. This ratio may vary along the RFQ. Two ratios were used in this study: lfac1 means that the longitudinal aperture factor was increased by 1.0 from its value at the shaper-end, over a length of 11.5 m. lfac0 means the longitudinal aperture factor was kept constant at its value at the shaper-end.

The transverse aperture is usually allowed to increase (linearly with β) by a factor of about two, to minimize particle losses while at the same time trying not to increase the overall length too much. Tests were made with other aperture rules, e.g., less aperture growth or constant aperture after the shaper.

The two matching equations and the equipartitioning equation are then solved to find the transverse and longitudinal rms beam sizes and the vane modulation.

The design is tested by simulation in the PTEQ code [3]. PTEQ does not include special end cells like the Crandall cell, or image charges, and multipoles were turned off. Robin Ferdinand has stressed that Saclay feels that multipoles and image charges must be included for such intense beams [4]. The more powerful codes like TOUTATIS include these effects. In some previous studies on multipoles, it

was found that with some designs, depending on the way the vanes are machined (constant radius, or radius varying with the two-term potential) transmission was significantly lower when multipoles were included. The earlier work also indicated that the main effect of multipoles is to reduce somewhat the strength of the main quadrupole focusing term. By readjusting the vane recipe for a few percent higher transverse focusing, the transmission could be restored. In the preliminary comparison of the 175 MHz results, a few percent decrease in transmission is seen by TOUTATIS compared to PTEQ. The input match is found self-consistently using the full beam.

(3) Note on Earlier CDA Results

Conceptual design work for the IMFIF RFQ preceding and during the CDA phase used different strategies from those used in this study. The strategies and results are discussed in various IFMIF reports [5].

The most important variable to determine is the rf frequency for the accelerator. The FMIT linac design used 80 MHz, consistent in those days with the required beam dynamics, mechanical constraints, and available rf power. When IMFIF studies began, it was desired to raise the frequency if possible to make the structure diameter smaller and less complicated and costly to construct. When the decision was made to fulfill the 250 mA cw requirement by constructing two parallel 125 mA accelerators, a following decision was to try to optimize the design of a 125 mA module - that is, to push in the direction of an optimum frequency for accelerating and transporting 125 mA per module, without an upgrade capability. Detailed studies, using the strategies available at that time, indicated that 175 MHz was a good upper limit for the frequency, and that ~120 MHz seemed to be at the lower limit for good beam dynamics performance with respect to transverse particle losses.

This short summary is given to set the background, but also to stress that newer methods and other things we have learned may indicate somewhat different answers, discussed in some measure below.

(4) Design Results at 175 MHZ

Design studies were performed with the RFQ design program LINACS and the RFQ simulation program PTEQ, using 5000 particles.

Three optimizations were explored in a preliminary way:

- aperture at the end of the shaper - this maximizes transmission. (Figure 1)

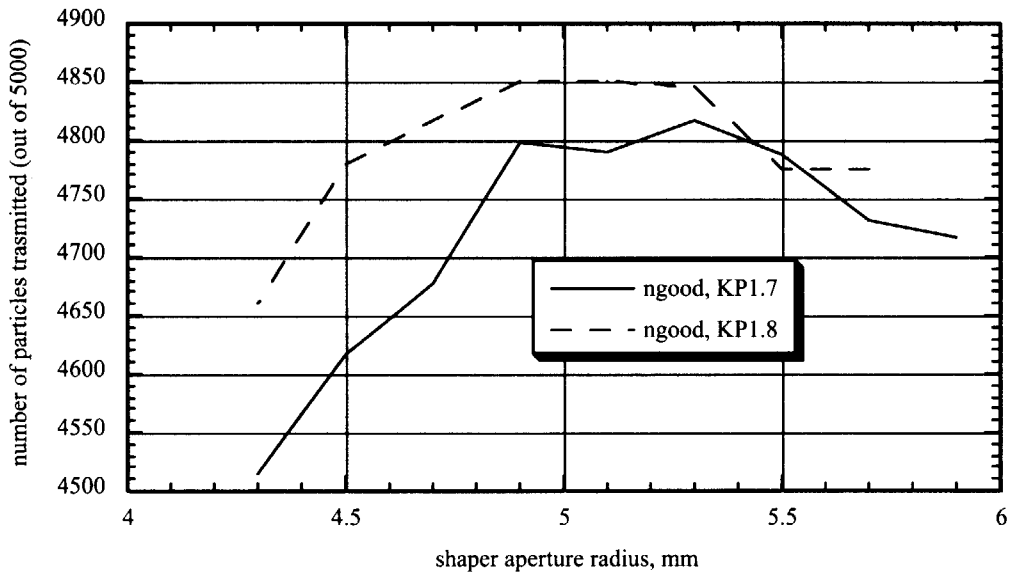


Fig. 1 Number of accelerated particles (out of 5000 initial particles) vs. aperture at the end of the shaper, as function of shaper aperture radius. The results at KP1.7 and KP 1.8 are given.

- length of shaper porch and overall shaper length - this strongly reduces the highest energy of lost particles. The shaper is rather long and 60% of the length is a -90° porch. This adds to the total length of the RFQ; further optimization might reduce the shaper length somewhat.
- optimization of total length.

Two strategies for reducing the overall length were investigated in a preliminary way:

1. Varying the prescribed growth of the aperture along the main part of the RFQ. The aperture in the main part of the RFQ is allowed to grow in this design by about a factor of two from the aperture at the end of the shaper. The resulting length at 5 MeV is about 12m. Making the aperture grow less (or, for example, keeping it constant) produced a shorter length but quickly led to more losses. Perhaps a reoptimization of the initial aperture would help.
2. Raising the injection energy, with all other parameters the same. This produced longer RFQs, as expected (Table 1.).

Table 1. Change injection energy.

Injection Energy	Length at 5 MeV	Transmission
100 KeV (a5.3)	11.7 m	4816/5000 = 96.3%
120 KeV (a5.3)	13.5 m	4875/5000 = 97.5%

It should be said here that the design length is quite sensitive to changes in many of the parameters – this sensitivity merits detailed sensitivity studies. It may be possible that some other parameter change could offset the increased length that is normally seen as the injection energy is raised.

(5) RFQ Characteristics and Aperture Factors

The RFQ characteristics and the transverse and longitudinal aperture factors achieved in 5000 particle simulations are shown in Figures 2-5.

The maximum beam size has a transverse aperture factor of about 1.3 in transverse, and a longitudinal aperture factor that increases along the RFQ.

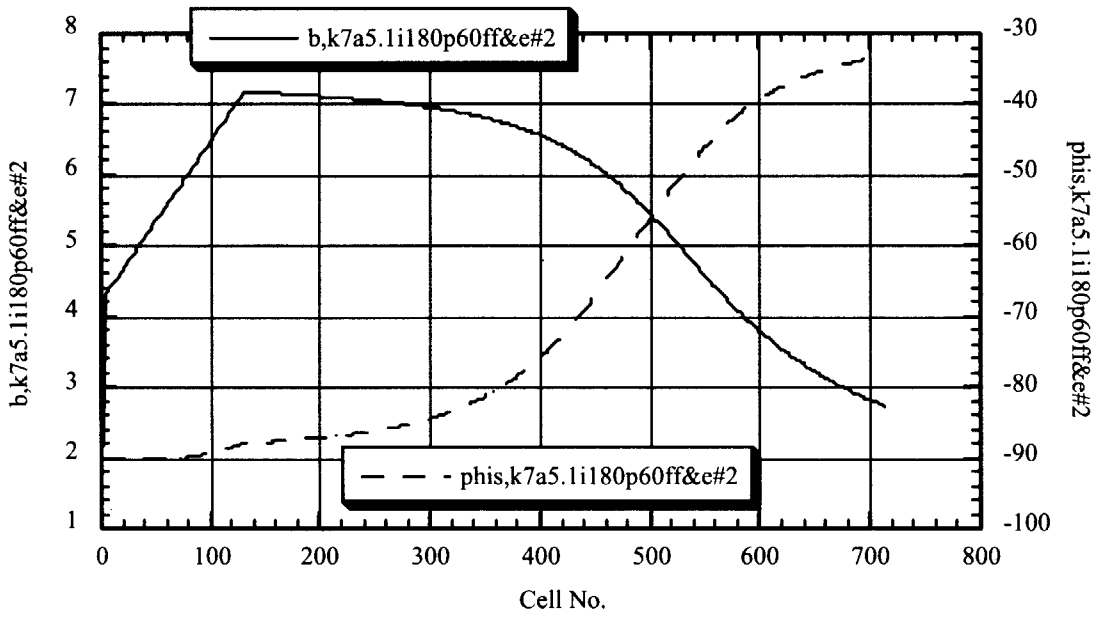


Fig. 2a B and phis as functions of Cell Number along the RFQ.

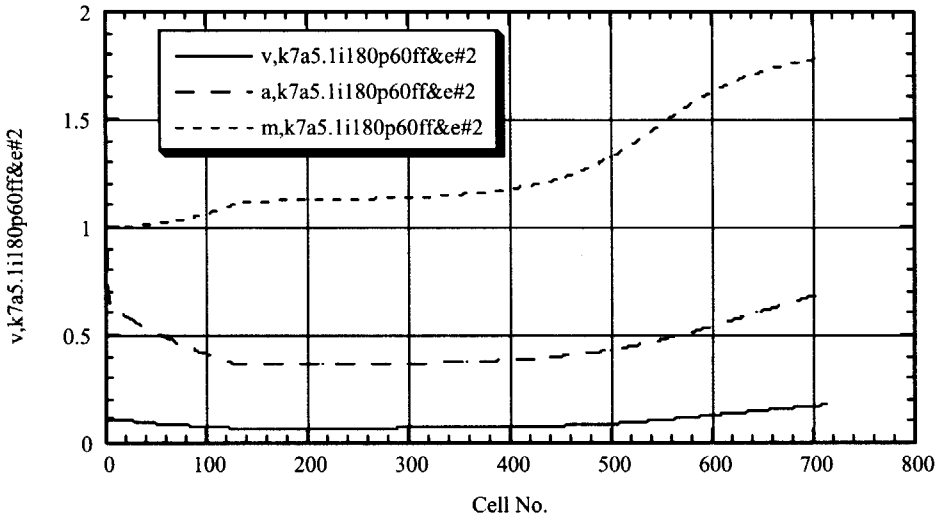


Fig. 2b Vane voltage, aperture and modulation as functions of Cell Number along the RFQ.

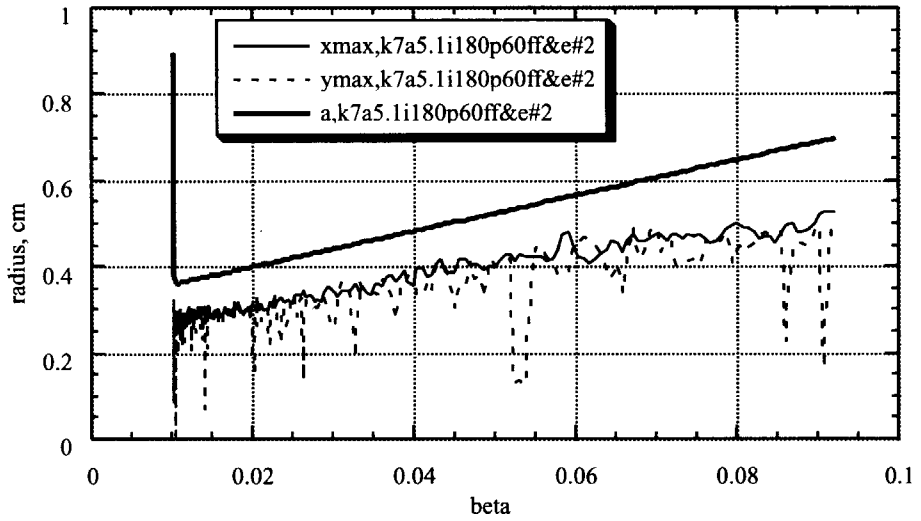


Fig. 3 RFQ aperture and maximum transverse bean size vs. beta along RFQ.

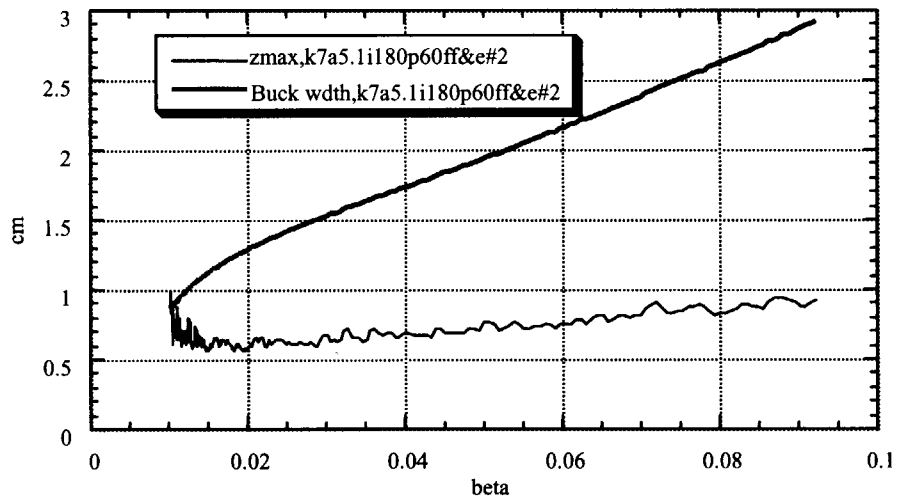


Fig. 4 Maximum longitudinal beam size and bucket width vs. beta along RFQ.

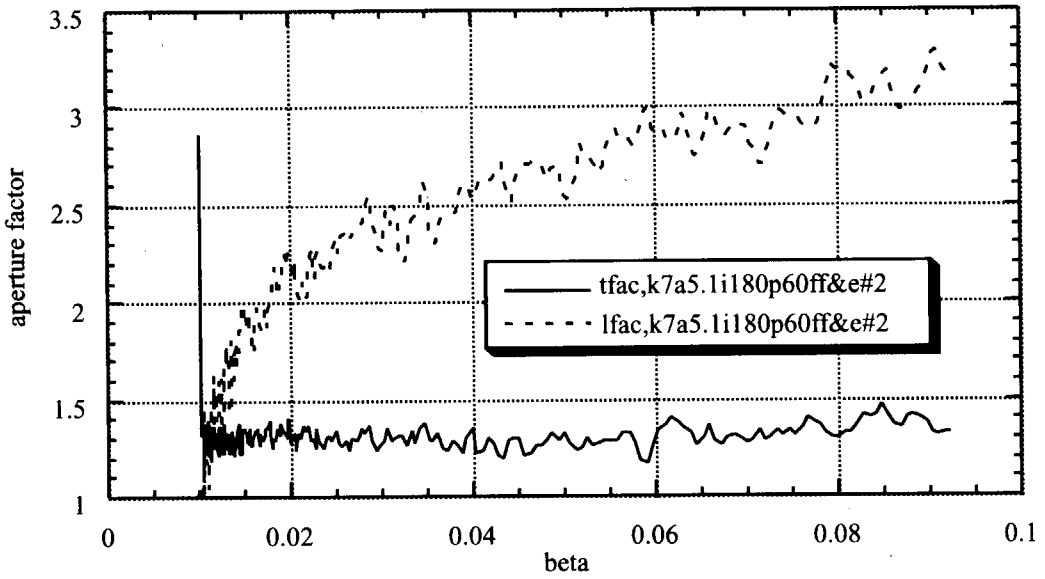


Fig. 5 Transverse aperture factor, tfac, (~constant at 1.3)) and longitudinal aperture factor, lfac, vs. beta along the RFQ. Transverse aperture factor is (aperture)/(maximum transverse beam size). Longitudinal aperture factor is (bucket width defined as one ϕs)/(maximum longitudinal beam size).

(6) Verification of 175 MHz designs by Saclay

The TOUTATIS code was used to check the transmission results. A few percent decrease in transmission is seen by TOUTATIS compared to PTEQ. Details are given in [1].

(7) Discussion of Best Results at 175 MHZ

The IPHI 100 mA proton RFQ and the KP1.7 175 MHz IFMIF designs presented appear to have similar fundamental characteristics. The vane voltage, aperture, modulation B, and phis characteristics are quite similar. In both cases, the curves are kept very smooth. The transverse focusing is tapered down, a feature found empirically to be useful in producing good beam performance by Schempp and Young in earlier work, and an intrinsic result of the exactly equipartitioned design with the given rules.

The aperture variation in the IFMIF shaper was explained above as helpful for input matching. Also, in some shaper optimization work outlined below, a better shaper aperture strategy was not found. The IFMIF aperture variation after the shaper to the end of the RFQ is similar to that of the IPHI RFQ.

The following simulation results seem particularly important:

- Good agreement on transmission was found between several codes, with the exception of some problems with PARMTEQM, which is known to be inaccurate in its space-charge computation and assumptions regarding paraxiality. The simulated transmission for KP = 1.7, quite minimal focusing, of order 96% with 5000 particles is very good. (See also comments about the effect of multipoles and image charges above.)
- A suitably long shaper and initial porch can minimize the highest energy of lost particles (to energies near the injection energy, and well below 1 MeV).
- With 5000 particles, a transverse aperture factor of about 1.3 is seen for both the IPHI and IFMIF RFQs. Saclay experience indicates that this aperture factor is "virtual" because particle loss is seen all along both RFQs when ~100,000 particles are simulated.

However, it is important that an IFMIF designs at KP=1.7 and 1.8 exist with performance at the CDA requirement of ~90% transmission.

Simulation results with 100,000 particles for the Saclay 100 mA RFQ now under construction

show transmission of greater than 99%. Saclay has indicated that their design was judged to be the best they could do in terms of total transmission, even though particles are being lost all along the RFQ in the 100,000 particle simulation, and that on this basis, they are proceeding with construction. It is probable that use of the Saclay methods for an IFMIF KP1.7 design, especially in the shaper section, would give an improved 175 MHz design. (see Sec. 3.1.11 (2))

(8) Conclusions Regarding the IFMIF KP1.7, 175 MHz Design

The IFMIF KP1.7, 175 MHz design presented here indicates performance that meets the CDA requirement. The design method is now robustly derived. The design methods and codes were verified by checking with other codes presently used by different groups for very intense light-ion beams. KP factors or 1.7 and 1.8 are considerably lower than the KP factor used in the CDA conceptual design. A KP factor = 1.8 is considered safe for the IFMIF RFQ. The performance is better at KP=1.8 than at KP=1.7, as expected, but demonstration of feasibility at KP=1.7 is important, because it indicates that some beam dynamics design margin for low beam loss exists even for the intense IFMIF beam.

However, even better beam dynamics performance is desirable for IFMIF, to be sure that beam loss is minimized.

(9) Preliminary Investigations Toward Better IFMIF RFQ Performance

The new design procedures in the LINACS and PTEQ codes are more powerful than older methods, suggesting that parameter variations studied earlier might be revisited. The full reference also reports some preliminary investigations, at KP=1.7, of the rf frequency. Shortening the RFQ length by optimal control of the bunch length is an effective strategy. Optimizing the aperture at shaper-end primarily maximizes the transmission, and a longer shaper with a -90° porch is effective in minimizing the maximum energy of any lost particle (to energies near the injection energy, and well below 1 MeV - important to minimize radioactivation.) Some possible changes of the number of radial matching cells and of the transverse focusing characteristics in the shaper were explored. RFQ designs with an equipartition unbalance showed lower transmission. Several other equipartitioned and non-equipartitioned tune variations were explored, indicating that design margin exists and that some small further increase in transmission and reduction of the maximum lost particle energy might still be achieved. The current-insensitive case was briefly explored, as well as variations in the input emittances.

The design procedure (which uses envelope equations), is completely specified by rules and seeks to make the RFQ conform to completely specified space-charge physics. In such intense RFQs, the beam is in the space-charge dominated regime and the emittance terms are small with respect to the space-charge terms. Therefore, the procedure is effective at controlling the beam size ratio (although for very good control, the envelope equations require a correction of the ellipsoidal form factor, which has been developed but is not discussed in this report). The emittances are not so well controlled; that is, although in the design program the envelope equations are solved exactly and the emittances are strictly controlled, when the designed RFQ is simulated, the emittances are not always as specified. This indicates further work is required.

(10) Conclusion

Robust RFQ designs meeting the IFMIF specifications have been developed at Kilpatrick factors of 1.7 and 1.8.

Before the RFQ design can be considered final, a great deal more work is indicated, to further explore the parameter space, to understand better the basic space-charge physics and nonlinear dynamics principles governing the beam dynamics behavior, and the sensitivity of a reference design that is otherwise judged good enough. Full design input files for the RFQ simulation code PTEQ are given in [1].

References

[1] R. A. Jameson, "SOME CHARACTERISTICS of IFMIF RFQ KP1.7 DESIGNS", IFMIF Memo RAJ-6-Sept-2000. Design report for IFMIF RFQ reference design.

[2] R.A. Jameson, "On Scaling & Optimization of High Intensity, Low-Beam-Loss RF Linacs for Neutron

Source Drivers", AIP Conf. Proc. 279, ISBN 1-56396-191-1, DOE Conf-9206193 (1992) 969-998, Proc. Third Workshop on Advanced Accelerator Concepts, 14-20 June 1992, Port Jefferson, Long Island, NY, LA-UR-92-2474, Los Alamos National Laboratory, 28 July 1992.

[3] R. A. Jameson, "A Discussion of RFQ Linac Simulation", Los Alamos National Laboratory report LA-CP-97-54, September 1997.

[4] R. Ferdinand, "Re Misalignment and IFMIF Acc", e-mail 5 July 2001.

[5] R. A. Jameson, "IFMIF RFQ DESIGN STATUS AND RELATED WORK", IFMIF Memorandum RAJ-6-Dec-2000. Summary of Saclay RFQ design, acceptance of feasible parameters for Kilpatrick Limit = 1.8 and transverse rms input emittance = 0.25 mm.mrad. This design also meets the CDA transmission requirement of ≥90%.

3.1.11 AC34A-EU : RFQ Tuning Method, Electric Field Optimization on Cold Model

(1) Brief Task Description

RFQs are powerful accelerators used to both accelerate and bunch beams. Nevertheless, the IFMIF beam power and IFMIF RFQ design complicates the RF tuning of this part of the accelerator. This task consists of using the IPHI RFQ cold model to develop the tuning method and the tools for the IFMIF RFQ RF tuning.

Contributors

Name	Party	Institute	E-mail address
R. Ferdinand	EU-FRANCE	CEA-Saclay	rferdinand@cea.fr
A. France	EU-FRANCE	CEA-Saclay	afrance@cea.fr
F. Simoens	EU-FRANCE	CEA-Saclay	fsimoens@cea.fr

(2) Studies

The building and the development of a complete RFQ tuning method [1] has implied three main parts:

(2.1) Test bench

An experimental test bench [2] has been designed and developed in order to measure the electromagnetic parameters to be tuned.

Test bench principles

The bench that measures the field distribution in the cavity is based on the perturbation method. The acquisition of the σ21 transmission coefficient phase shift is synchronized with the displacement of a bead through the four quadrants of the RFQ. The measured raw data are then converted to a quantity proportional to the electromagnetic field magnitude. The overall setup is fully computer controlled and easily transportable.

Special topics

The important efforts that have been devoted to the optimization of the signal-to-noise ratio have led to very sensitive and repetitive measurements; these characteristics are essential for accurate RFQ tuning.

The technological choices of the experimental setup are such that it can be directly applied to RFQs having geometries or working resonance frequencies different from that of the IPHI RFQ.

(2.2) Mathematical model

A comprehensive mathematical model [3] has been developed.

RFQ model principles

The RFQ is viewed as a Transverse Electric wave-guide at cutoff. The central region delimited by electrode tips is modeled by a coupled, inhomogeneous (i.e. the geometry and the cutoff frequency of the transverse section varies longitudinally) 4-wire line system. The shunt admittances are derived by stating a purely transverse propagation in the wave-guide, and series self- and mutual-inductances by stating a phase velocity equal to light velocity at infinite frequency. The voltages between electrodes are solution of a vector differential equation, which is recast into an eigen-value problem, leading to a bi-orthonormal basis and its associated inner product. The real RFQ is then viewed as a perturbation of a perfectly symmetrical RFQ, and the measured fields are expanded on the eigen-basis. End boundary conditions are of the von Neumann type, and are directly extracted from measured fields before expansion. The field perturbations are then transformed into line perturbations, such as capacitance perturbations (continuous functions of abscissa) or tuner perturbations (discrete functions), for which eigen-bases are built, following the Riesz

theorem

Different interpretations of the measured fields derived from the mathematical model

The model is able to interpret the fields measured in a real-life RFQ in terms of :

- *Mechanical errors.* This theoretical approach leads to the estimation of the distribution of the transverse disequilibria between the four quadrants [4]. This diagnosis is able to check whether the mechanical structure of the RFQ sections has been modified during the brazing operation.
- *Slug tuners commands.* The mathematical model that has been developed for the IPHI project is continuous by nature, i.e. measured voltages are expanded on a set of continuous 'voltage basis functions', perturbed line inductances are expanded on a set of continuous 'inductance basis functions', with a one-to-one correspondence between the two sets, and a convergence theorem associated with these expansions. The tuning system of the RFQ (slug tuners) is on the contrary discontinuous by nature. Unfortunately, the sampling theorem that can be naturally derived from the reproducing kernel of the functional space is not directly applicable to an arbitrary, highly irregular distribution of tuners. An original anti-aliasing filter [5] is shown to yield a stable sampling of inductance functions belonging to a particular, but useful, sub-space. **The tuning of any segmented vane RFQ with the use of slug tuners is now theoretically modeled and computed.**
- *Ends detuning corrections by plate thickness and dipole rod length adjustments.* The two ends of the RFQ and the coupling cells (connecting each segment to the next one) are viewed as unknown circuits inserted in the 4-wire line model. The full set of electrical parameters of any one circuit may be estimated from a set of measurements with various excitations of that particular circuit (excitation is varied by moving plungers some distance apart). End plate and coupling plate thickness are directly related to a few of these electrical parameters, quite suited for easy tuning. For dipole rods adjustment, a practical criterion derived from the theory has been introduced. This criterion ensures the convergence of tuning by preventing too big a discrepancy between the model and the real cavity [6].

(3) Cold Model Testing

The tuning formalism has been successfully tested on a RFQ prototype. (Figs. 1 and 2)

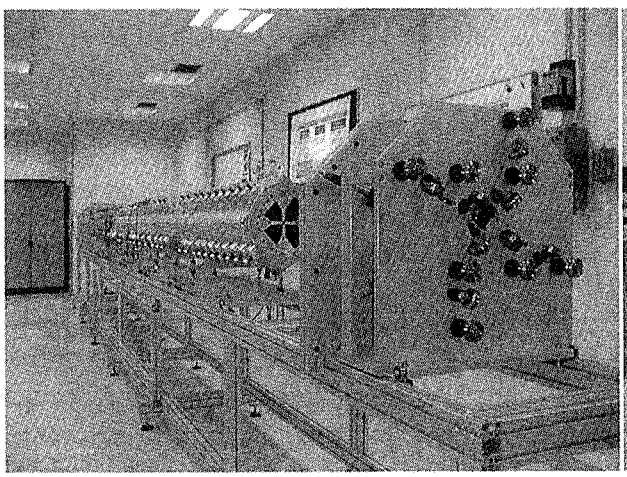


Fig. 1 6-m long IPHI cold model.



Fig. 2 Low-level analyses before brazing.

RFQ cold model

A 6-m long aluminum RFQ cold model has been designed and built. In addition to being a very efficient and essential bench to validate the tuning formalism, this prototype has given the opportunity to test the validity of 3-D electromagnetic code simulations [7]. Remember that the design of the real RFQ is based on such simulations. In particular the vane-end matching is pretty well predicted: accurate field

measurements on a 1-m long configuration showed excellent agreement vs. simulation with or without dipolar stabilizer rods.

A specific study has consisted of comparing measurements of segmented modes on the RFQ cold-model with our mathematical model and 3-D simulation results [8]. The good agreement that we have found validates our cut-off wave-guide equivalence approach.

Specifically for the RFQ tuning study, different transverse section positions selected to guide the perturbing object have been tested on our RFQ cold-model [9]. This study has led to the choice of field measurement on the bisector of each quadrant.

Different tuning procedures

1-Mechanical error diagnosis.

Tests of cold-model vane mechanical translations have demonstrated the ability to **detect displacements as small as 20 micrometers** [4]. Though being less precise than 3-D mechanical measurement probes, this diagnosis of the mechanical defects is very relevant since it can be applied inside the cavity even after brazing. It has been decided to apply this RF test to each RFQ on the factory site before and after brazing.

During 2002, the first IPHI RFQ section defects have been characterized on the factory site before and after brazing [9]. The measurement bench has been moved to the industrial site for the tests. These tests have shown that the brazing procedure had slightly modified one dipolar contribution while keeping its level very low.

2- Slug tuner commands.

The tuning slugs are highly irregularly spaced along the RFQ structure, between vacuum windows, RF wave-guide inputs, and cooling ducts. The slug tuner commands [5] have been successfully tested for many configurations of the cold prototype, as a one-meter homogeneous line with eight tuners (per quadrant), a two-meter homogeneous line with eight tuners on the first meter and four tuners on the second meter, and the same two-meter line with a capacitive coupling cell at mid-position. This last case corresponds to the fact that the IPHI RFQ is segmented, i.e. the RFQ line is divided into four 2-meter long segments, with capacitive couplings in-between.

Modulated and non-constant r0 vanes have been installed in the body of the cold-model which simulates precisely the first 2-m long segment of the real IPHI RFQ. The voltage profile has been tuned with the IHI RFQ specifications (first 2 meters) using the algorithm and only slug tuners.

For all configurations, the tuning procedure requires only a small number of iterations, and convergence is demonstrated on every component of the functional bases. Constant and variable voltage profiles have been tuned in only four steps, achieving a final relative voltage error less than 1% in every quadrant and at every longitudinal position.

3- Dipole end detuning corrections by rod length adjustments [6].

A 'quadratic shift frequency' df(n) can be computed in all RFQs. By adjusting the rod length, the measured df(n) is made equal to the nominal value. When this criterion is satisfied, tuning tests of the RFQ cold-model using only the slug tuners have perfectly converged.

4- Quadrupole end detuning corrections by plate thickness adjustments [6].

The tuning of the end regions with respect to the quadrupole mode is made by machining the thickness of the end plates. The end region mismatch is characterized by a parameter $\Omega = Lx\Delta f$, expressed in m.MHz, where L is the RFQ half-length and Δf is the difference between mismatched and matched resonance frequencies. Our model can extract Ω from as few as three measurements with different voltage excitations. These excitations are easily achieved by moving slug tuners at some distance of the end being tuned. The tests on the cold-model have shown very good agreement between the Ω sensitivity extracted from the measurements and the 3-D simulations.

(4) Conclusion

The formalism that has been developed permits computation of all quantities necessary for RFQ tuning procedures:

- plate thickness and dipole rod length adjustments (boundary regions),
- slug tuner commands.

It also generates a unique diagnosis of the mechanical defects of each single RFQ section, available for use at the factory site before and after brazing.

All these procedures have been validated with different configurations on our cold model,:

- with a constant or variable inter-electrode r0,
- in a homogeneous or inhomogeneous RFQ (i.e. with electrical parameters varying from one cell to the next),
- segmented or continuous,
- with a constant or variable accelerating voltage law,
- at different resonance frequencies of the accelerating mode, and
- with different lengths.

The rigorous mathematical model makes possible a fast convergence and a high precision tuning level. Its other important advantage is that it can be applied to all 4-vane RFQs, regardless of the resonance frequency, accelerating voltage profile, or mechanical length.

References

[1] F. Simoens, "Etude théorique et expérimentale du réglage électromagnétique d'une cavité radio-fréquence quadripolaire (RFQ) accélératrice d'un faisceau intense d'ions", Thesis of the "Pierre et Marie Curie" University, September 2002.

[2] F. Simoens, F. Ballester, A. France, J. Gaiffier, A. Sinanna, "A Fully Automated Test Bench for the Measurement of the Field Distribution in RFQ and Other Resonant Cavity", EPAC2002 Conference (Paris), June 2002.

[3] A. France, F. Simoens, "Theoretical Analysis of a Real-life RFQ Using a 4-Wire Line Model and the Spectral Theory of Differential Operators", EPAC2002 Conference (Paris), June 2002.

[4] F. Simoens, A. France, J. Gaiffier, "A New RFQ Model Applied to the Estimation of Mechanical Defaults Distribution", EPAC2002 Conference (Paris), June 2002.

[5] F. Simoens, A. France, J. Gaiffier, "A New RFQ Model applied to the Longitudinal Tuning of a Segmented, Inhomogeneous RFQ with Highly Irregularly Spaced Tuners", EPAC2002 Conference (Paris), June 2002.

[6] F. Simoens, A. France, "Tuning procedure of the 5 MeV IPHI RFQ", CEA-SACLAY, LINAC Conference (Gyungju, Korea), August 2002.

[7] P. Balleyguier, F. Simoens, "Simulations vs. Measurements on the IPHI RFQ Cold Model", EPAC2002 Conference (Paris), June 2002.

[8] F. Simoens, A. France, O. Delferrière, "An Equivalent 4-Wire Line Theoretical Model of Real RFQ based on the Spectral Differential Theory", CEA-SACLAY, LINAC Conference (Gyungju, Korea), August 2002.

[9] F. Simoens, A. France, J. Gaiffier, "Electromagnetic Characterization of the First IPHI RFQ Section", EPAC2002 Conference (Paris), June 2002.

3.1.12 AC36-EU : Drift Tube Linac R&D Studies

(1) Brief Task Description

The task was completed in the framework of the CEA program on high-power particle accelerators supported by the IPHI demonstrator project. This project is dedicated to high power beam production [1-11].

Drift tube and quadrupole analyses include cavity calculations, power deposition, and extrapolation from IPHI DTL measurements on hot models (measured power deposition, cooling, manufacturing tolerances, etc.).

Contributors

Name	Party	Institute	E-mail address
R. Ferdinand	EU-FRANCE	CEA-Saclay	rferdinand@cea.fr
P-E. Bernaudin	EU-FRANCE	CEA-Saclay	pebernaudin@cea.fr

(2) Introduction

A 4-cell short hot model of a 352 MHz drift tube linac has been built at CEA Saclay. The purpose of this model is to verify the feasibility of such a structure for cw operation with a high current beam inducing tight tolerances.

This short model includes one tank, three drift tubes of two different designs, and two magnets of different types. Their designs have been described in [1] and are summarized in Table 1.

Table 1 - Quadrupole magnets data (as calculated).

	Permendur magnet	Soft iron magnet
Integrated gradient	4.70 T	4.70 T
Transverse gradient	83.79 T/m	75.89 T/m
Magnetic length	56.09 mm	61.94 mm
Total length	48 mm	56.16 mm
Pole length (beam axis)	36 mm	42 mm
External diameter	140 mm	157 mm
Aperture diameter	16 mm	16 mm
Ampere-turns	2 750	2 317
Turns per pole	5.5 in 1 layer	9 in 2 layers
Lead dimensions	5x5 mm	5.6x2 mm
Isolation	0.25 mm per face	0.07 mm per face
Intensity	500 A	258 A
Current density	27.88 A/mm²	23.04 A/mm²
Total resistance	6.1 mΩ	15.3 mΩ
Electric power	1 524 W	1 018 W
Nominal cooling flow	1.68 l/min	(External cooling)
Water heating	13°C	
Pressure drop	6.22 bars	

The main difference between the IPHI and IFMIF DTLs is the frequency. Generally speaking, the higher frequency of the IPHI DTL is more restrictive as the dimensions are smaller, especially for the first drift tubes and magnets for which the dimensions problems are more severe. Therefore, results obtained for the IPHI DTL can be easily extrapolated to the IFMIF DTL, with an even better margin of safety. From a manufacturing point of view, dimensions are not different enough to lead to different problems and solutions. More important, both machines share the most constraining aspect, which is the cw operating mode.

(3) Magnets

The magnets [1] are made of two different materials, one uses standard soft iron, and the other uses cobalt-iron Permendur alloy. They are optimized to provide the strongest integrated transverse gradient with the smaller power dissipation, respecting a 0.5% homogeneity tolerance over the useful region (a circle of 6.5 mm radius). Their main characteristics are summarized in [2]. The cooling scheme of both magnets is different. The Permendur electromagnet leads are standard hollow copper conductors, with flowing water coolant. The soft iron magnet conductors are solid, with the cooling being external: the drift tube is flooded with water, which simultaneously cools the magnet leads and the drift tube walls. This scheme allows a slightly enlarged magnet, and also optimizes the power dissipation (two layers of conductors against only one for the other magnet), leading to power dissipation 35% lower than for the more standard magnet. However, both magnets are strongly saturated.

The manufacturing of these magnets caused no major concerns, except for the Permendur model. In this case, the passage of the leads through the yoke is very difficult, considering the conductor dimension, the high degree of saturation (even in the yoke) and the small space available. This aspect led to drift tube welding problems, and it proved necessary to cut into the yoke at the cost of a performance decrease caused by the high saturation (3% on the transverse gradient, about 2.5% on the integrated gradient). Preliminary tests showed that the cooling was adequate, especially for the soft iron (flooded) model. On the other hand, some isolation defects between conductor and ground potential were detected in both models. The reasons of these defects are different for each magnet, but in each case causes are well established and solutions identified.

The magnet gradients have been measured[1]. The results for the soft iron magnets were as planned. In the Permendur magnet case, the modifications performed on the yoke to ease the leads passage resulted in a 2.5% decrease of the integrated gradient at nominal excitation.

(4) Drift Tubes

Each magnet had a different drift tube design. The design intended for the Permendur magnet was performed by AES [2]. It is conventional, made of copper welded by the electron beam method. Coaxial stems guide the water in the drift tube where the cooling is located at the circumference only (two opposed azimuthal flows). This is the major weakness of this design, as the other drift tube surfaces are cooled by conduction only, through the thin walls of the drift tube. Another problem is the complexity of the design, especially at the flow diverter level. This diverter is the piece which transforms the coaxial water circulation of the stems into the azimuthal circulation in the drift tube. Difficult to perform welds are necessary to ensure water tightness at this level [3]. (Figs. 1 and 2)

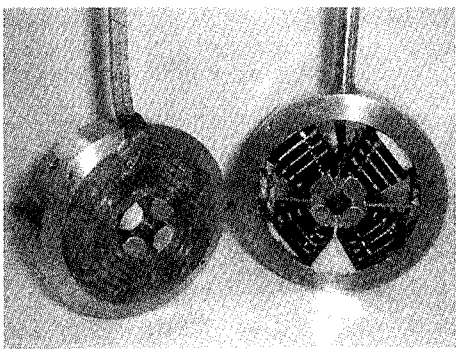


Fig. 1 The magnets manufactured for the DTL short model. Left: Permendur magnet, right: soft iron magnet.

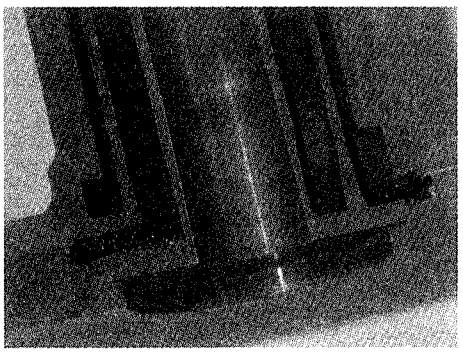


Fig. 2 Test piece showing the welds for the AES drift tube (interfaces between the three concentric stems and the drift tube two-part body).

[1] By Yorck HOLLER & al., DESY, Hamburg, Germany.

The other drift tube uses basically the same scheme (copper, coaxial stems, electron beam welding) but on a simpler scale. Since the whole drift tube is flooded, there are fewer pieces and fewer welds. The complex diverter is not used. The stem is made of only two tubes, the magnet leads being cooled by the return flow. Advantages of this solution are numerous: mainly, cooling is better as almost every surface is in direct contact with the coolant, and the mechanical design is simpler, easier to manufacture, and therefore cheaper.

Several problems were raised during the manufacturing process. The first was the one related to the yoke passage of the Permendur magnet leads, as mentioned previously. This problem forbade the welding of the diverter on the body and forced us to modify the magnet yoke to enlarge the lead passage at the expense of the magnetic performance.

Leaks appeared in both drift tube models (but more acutely in the non-flooded design) after the final machining. These leaks are related to an excessive thickness of the rough shape. An optimization of this thickness will allow to suppress this leakage problem.

(5) Tank Design

The high power density on the walls in such a cw machine makes cooling a major concern, the ultimate purpose being to minimize and control both thermal stress and expansion. Another aspect is that the tolerances for the whole machine are very tight, because of the beam intensity and the focusing type (F0D0). Therefore the tolerances are especially tight for the magnetic alignment of the quadrupoles (IPHI: ±51 μm misalignment, gradient ±0.5%, IFMIF: ±100μm, gradient ±1%). The design is further complicated by the very short space between successive drift tubes.

Despite being theoretically suitable, a full copper solution is extremely costly and should be used only when no other solution is available. The solution used for the hot model tank is a stainless steel thin (4-mm) component, which is copper-plated both inside and outside by an electrolytic process. The inner plating is obviously for electric conductivity purposes, whereas the thicker external plating is intended to enhance the thermal conductivity. With a 1-mm thick external layer, the maximum temperature increase on the tank walls is reduced by more than a factor of four. (Plating of both surfaces was done almost simultaneously.) Other technical solutions, like a thermally sprayed copper coating, have been studied. The non-welded elements of the cavity (caps and girder, see below) are full OFHC copper parts.

The mechanical design of the cavity, and especially of the apertures (vacuum pumping slot, RF coupling, girder aperture) have been optimized to minimize thermal stress. Thermal displacement has been computed and will be measured during the test phase.

Great care has also been devoted to the optimization of the stem-tank connection, which proved to be a sensitive point in previous cw DTL projects (namely Chalk River and the Los Alamos FMIT components). A flexible system based on a thin copper bellows allows mechanical adjustment of the drift tube position and orientation at any time (except around the stem axis). Mechanical tests have been performed on a bellows to ensure the vacuum tightness.

The tank design is both cheap and reliable, presenting no major difficulty. Copper plating, deposited using the acid bath technique, yielded lower measured outgasing rates and, according to literature sources, gives the best RF electrical conductivity. The length of each tank section will therefore be limited by the plating bath dimensions, the biggest ones being GSIs with a depth capacity of up to three meters. (Figs. 3 and 4)

(6) Hot Model Tests

Power tests have been limited by the inability of CERN to provide the required power (40 kW cw). Up until now, only 8 kW cw has been available (but with more than 50 kW peak power at low duty cycle).

Further work is being performed on the power amplifier in order to solve this problem. Within this power range, some results have nevertheless been obtained.

The Q factor of the cavity (21600) is 1/3 lower than the calculated *SUPERFISH* value. This result is worse than expected, but the relative effects of the cavity edges and of the various apertures (pumping, RF coupling, diagnostics) are very important. The strong influence of RF seals has been measured. (The suppression of the girder RF seal alone leads to a 15% decrease of the Q factor.)

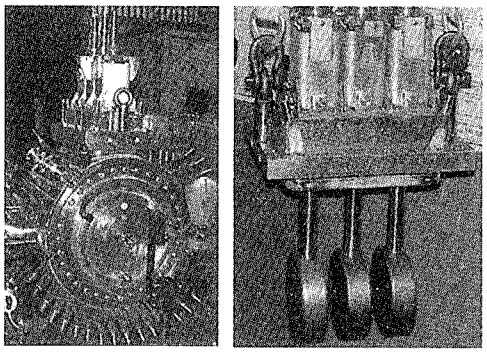


Fig. 3 Left: the hot model fully assembled. Right: girding supporting the three drift tubes.

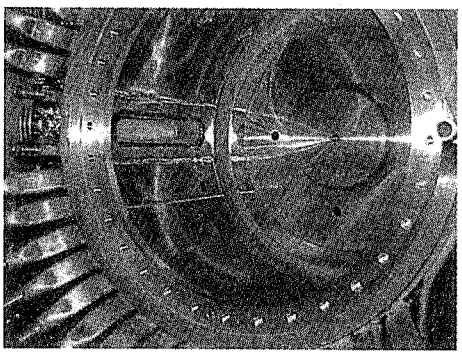


Fig. 4 Interior view of the copper-plated stainless steel tank (the aperture is the pumping slot).

The low level RF tests allowed us to measure the on-axis field and showed the benefits of the shift possibility of the drift tube positions.

Globally, no major heating has been discovered. All measured values are coherent with respect to the expected ones, at least at this level of rf power. Nevertheless, we were not able to measure any displacement, most probably because of this low level of power.

The electric field on the axis was measured during RF operation using a X-ray spectrometry measurement technique (the RF was pulsed in order to perform measurements up to 40 kW, peak power). The results of these measurements confirm that the Q factor is 1/3 lower than expected by *SUPERFISH*. The precision of the X measurements technique is estimated to be 3%.

RF conditioning was quite easy up to the available power limits (55 kW peak power, 8 kW mean power), with a good enough vacuum and very few observed multipactor levels. The nominal vacuum seal configuration (*Helicoflex* seals) has not yet been tested.

(7) Perspectives

Further tests will be carried on as soon as the RF amplifier is ready. The cavity will be tested at nominal cw power from the thermal, mechanical and vacuum point of view.

Useful information has been gathered during the manufacturing and test phases, allowing us to contemplate the construction of a cw DTL in the relatively near future. Different engineering designs for magnets and drift tubes have been operated, leading to several possible improvements.

We are also looking for solutions to relax the excessively strong tolerances imposed on the magnet alignment, mainly by increasing the beam aperture.

References

[1] "CEA-DSM-DAPNIA-SEA contribution to the IFMIF KEP phase. Step report – June 2001". DSM/DAPNIA/SEA 01/41, 35 pages.

[2] Advanced Energy Systems, Inc., "Conceptual design development of the 5 MeV drift tube for the IPHI drift tube linac - Phase I final report" (23/04/1999).

[3] P.-E. Bernaudin & al., "Design of the IPHI DTL", Proceedings of the 2001 Particle Accelerators Conference.

[4] P.-E. Bernaudin, O. Delferrière, M. Painchault, "Technical innovations for a high gradient quadrupole electromagnet intended for high power proton drift tube linacs", Proceedings of the 2001 Magnet Technology (MT-17) Conference.

[5] M. Painchault, P.-E. Bernaudin, G. Congretel, "Thermo-mechanic of a DTL vessel for the IPHI project", Proceedings of the 2002 European Particle Accelerators Conference.

[6] P.-E. Bernaudin, "Etude et optimisation d'un linac à tubes de glissement pour accélération de forts courants de protons en continu", PhD thesis of the Paris XI (Orsay) University, ref. 6975 (30/09/2002).

[7] D. Uriot, N. Pichoff & P.-E. Bernaudin, "Design of a ramped-gradient drift-tube linac", CEA internal

report ref. DSM/DAPNIA/SEA 2000/69 (12/12/2000).
[8] "2001 11 IFMIF DTL design.doc", the main parameters for 2 tank designs, IFMIF Accelerator Team document.
[9] "meeting_22102001_RDuperrier.ppt", IFMIF RFQs & DTLs, CEA developments, IFMIF Accelerator Team document.
[10] "Saclay_IFMIF_FZK.ppt", IFMIF Accelerator Team document.
[11] R. Duperrier et al., "Beams Dynamics Simulations in IFMIF Linac", EPAC 2002, Paris.

3.1.13 AC37-US : Engineering Evaluation of the Drift Tube at 5 MeV

(1) Brief Task Description

The reduced cost International Fusion Materials Irradiation Facility (IFMIF) configuration proposed by the Japan Atomic Energy Research Institute (JAERI) in 1999 shifts the transition energy between the Radio Frequency Quadrupole (RFQ) and the Drift Tube Linac (DTL) from the baseline of 8 MeV to 5 MeV. Although neither one of these two values should be considered cast in stone in the conceptual phase of the design, attention has to be paid to those details that could potentially spell trouble later on. Typical difficulties encountered in lowering the transition energy from RFQ to DTL are associated with packaging the DTL's focusing quadrupole magnets inside its drift tubes in a way that simultaneously satisfies all the physical constraints while providing the required magnetic field levels. As the particle velocity is lowered, the drift tube length is reduced in proportion. Reduced length of the drift tube requires a shorter magnet, which now may have to be stronger to compensate for the shorter length. A stronger magnet may require an increased number of turns or higher current in the conductor which, in turn, may require a heavier gauge conductor. Either way, the diameter of the magnet grows. As the outer diameter of the drift tube is limited, it is clear that we could potentially run out of material necessary to provide adequate cooling conduction paths and structural strength. Usually, the first drift tube, which is the shortest, is the most difficult, critical element. In IFMIF, the problem of packaging the quadrupole of the required size inside each drift tube is compounded by the requirement of providing adequate cooling passages to withstand the 100% duty cycle (CW) RF power and a relatively large bore needed for the 125 mA deuterium ion (D^+) current.

In order to address the potential issues that have been raised in connection with the above concerns, it has been decided that a closer look at the first drift tube is warranted. With that objective in mind, AES has developed a conceptual design of the electromagnetic quadrupole and its packaging in the first drift tube of the DTL and performed preliminary analyses necessary to identify any potential show stoppers. These analyses included a determination of the power losses on the drift tube and the associated thermal analysis to verify the performance of the cooling system. SUPERFISH and ANSYS codes, respectively, were used for these tasks. This preliminary but comprehensive examination revealed that the design is "pushed hard" but seems acceptable, although additional analyses are still necessary to cover all the bases and address all the fine points (e.g. similar analyses for selected drift tubes along the length of the DTL to verify that there is no bottleneck in another location).

Contributors

Name	Party	Institute	E-mail address
John Rathke	US	AES	john_rathke@mail.aesys.net
Tom Schultheiss	US	AES	tom_schultheiss@mail.aesys.net

(2) Geometry Development

The objective of the present analysis was to determine the feasibility of building a drift tube for CW operation in a 175 MHz DTL with 125 mA D^+ at an energy of 5 MeV ($\beta = 0.073$). The design starting point was provided by CEA Saclay (Ferdinand, et. al.) in a June 15, 2000 memorandum. This document contains a thorough treatment of beam dynamics, magnet scoping, and drift tube/tank dimensions. The cell dimensions provided in that memo were used by AES as inputs to the conceptual design of an electromagnet quadrupole and subsequent thermal analyses. As discussed later, certain modifications to the geometry described in the memo are being proposed as a result of this design and analysis effort.

The CEA Saclay IFMIF DTL design was based on the assumption that the RF power in each DTL tank is limited to 1 MW, following the RF tube specification. Within this budget, a standard 25% safety margin was applied to the power losses obtained via the SUPERFISH calculation. The resulting design parameters include: length of the N-th cell, L_N, bore radius, R_b, outer drift tube radius, R_t, inner drift tube nose curvature radius, R_i, outer drift tube nose curvature radius, R_o, radius of curvature of the nose cone to drift tube body transition, R_c, nose cone angle, α_f, gap length, g, and inner tank diameter, D (all shown in the accompanying diagram). The box in the lower right hand corner of Figure 1 explains the significance

of the individual geometric parameters of the drift tube. The outer drift tube nose curvature radius, R_o, and the drift tube nose curvature separation distance, F, control the Kilpatrick factor. The drift tube nose angle, α_f, controls the length available for the quadrupole inside the drift tube. The gap, g, and tank diameter, D, control the RF frequency. The cell center length, L_c, and gap center, g/2, control the phase of the particles coming through the gap (note that the two adjacent drift tubes are not equal in length, so that the two centers do not coincide).

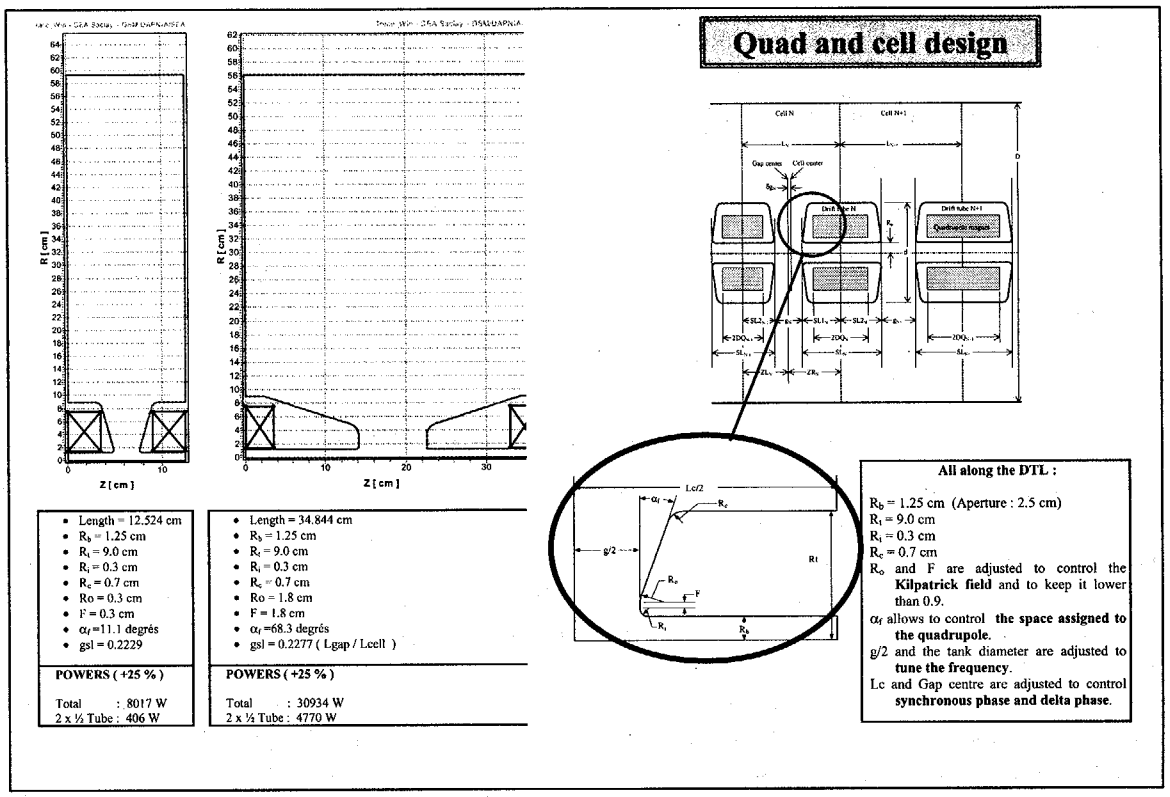


Fig. 1 Drift tube geometry specification (CEA Saclay).

(3) Electromagnetic Quadrupole Conceptual Layout

Several different EMQ design options have been considered initially by Saclay as shown in Table 1. For this study AES chose to examine the highlighted selection. A "conventional" hollow conductor cooling approach was adopted for the electromagnet as it is the most demanding from a packaging standpoint.

Using Outokumpu 6836 conductor, the quadrupole was laid out as shown in Figure 2. Six turns and 115 cm length of this conductor are required for each of the four poles of the quad. The total conductor length per quad, including the leads, is 640 cm. With the internal coolant passage diameter of 0.4 cm, the water cross section area is 0.1257 cm^2. Assuming the water flow velocity below 2 m/sec, the pressure drop is 18.81 psi per quad. The calculated water temperature change of 18.36° C and the resulting average water

Table 1 Magnet options for the IFMIF drift tube linac (CEA Saclay).

Aperture diameter (mm)	External diameter (mm)	Length without conductors	Full length (mm)	Material	Number of conductors per pole	Ni (A.t)	Gradient (T/m)	Magnetic length (mm)	Integral of gradient (T)
20	140	70 (*)	70	Fe	5.5	3437	59	75.2	4.42
20	140	70 (*)	70	Fe-Co	5.5	3437	64	75.8	4.89
25	152	58	70	Fe-Co	6.5	~5000	63	70	4.4
25	152	70 (*)	70	Fe-Co	6.5	~4700	59	75	4.4

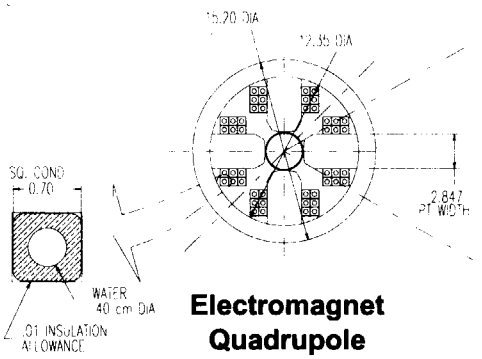
(*) With pole nose.

INPUT VALUES

DTL Parameters		Magnet Parameters			
DTL Frequency (MHz)	175	Number of Turns per Pole	6 (for NI Calculations Only)		
Tank Diameter (cm)	118.84	Conductor Length per Pole (cm)	115		
DT Clear Bore Radius (cm)	1.25	Conductor Area (cm^2)	0.3557		
Magnet Gradient (kG/cm)	5.9	Passage Diameter (cm)	0.4 with a	Water Area (cm^2)	0.1257
Inlet Water Temp (°C)	20	Water Flow Velocity (m/sec)	2		

DERIVED VALUES

Pole Tip Radius (cm)	1.35	
Conductor Length per Magnet (cm)	638.84	
Pole Tip Field (kG)	7.97	
Total Current (NI) (A)	4753.90	OK
Conductor Current (A)	792.32	
Current Density (A/cm^2)	2227.49	
		~24% > LAMPF
Coil Resistance (Ω)	0.0031	
Coil Voltage (V)	2.43	
Coil Power (W)	1927.98	
		High but OK?
Coolant Mass Flow Rate (kg/sec)	0.0251	equals 0.3977 gpm
ΔT in Water (°C)	18.36	
Avg Water Temp (°C)	29.18	
Pressure Drop (psi)	18.81	OK



Electromagnet Quadrupole Assembly

Fig. 2 Scoping calculations for the electromagnet quadrupole.

temperature of 29.18 degrees are acceptable (with inlet temperature of 20 degrees centigrade). The pole tip field of 7.97 kG, calculated at the pole tip radius of 1.35 cm, is satisfactory. The corresponding conductor current of 792 amperes results in the current density of 2227.5 A/cm^2, which is within state of the art, although 24% greater than the corresponding value at LAMPF. Coil resistance is 0.0031 Ohm and, therefore, the dissipated power is 1928 W, which is also on the high side but within state of the art. The voltage required across the conductor leads is 2.43 V.

As mentioned above, the design approach adopted in this study is the "conventional" one, consisting of an electromagnet quadrupole wound with a hollow conductor for dedicated cooling, and a completely separate cooling circuit for the drift tube body to deal with the RF induced heating of the drift tube surface. This approach is similar to the design employed in the GTA, SNS, and CWDD (Continuous Wave Deuterium Demonstrator) DTL.

An alternative approach, which has been recently proposed by CEA Saclay, floods the entire interior of the drift tube with the water coolant, thereby cooling both the electromagnet and the body of the drift tube with the same flow. Needless to say, in this case the electromagnet conductor is not hollow but solid. Since the conductor does not have to contain the cooling channel, its outer diameter can be smaller, resulting in an overall smaller magnet. Likewise, the drift tube itself can be smaller as well, since there is no need for separate cooling channels inside the drift tube walls. The only potential problem with this design is that all the elements, including the drift tube body, magnet conductor, and magnet iron are immersed in water. Since the long term effects of continuous water flow around these elements could potentially lead to problems related to corrosion, more tests are required before one can confidently baseline this approach. Since the prototype has already been built, some initial tests have already been performed and long term tests are being planned. Clearly, this design alternative has the potential for significant cost savings provided that it does not lead to increased maintenance expenditure.

(4) Geometry Modifications

Several changes to the initial design geometry are being proposed here as a result of the analyses that have been performed by AES. First of all, the drift tube diameter is increased from 18.0 cm to 19.2 cm to accommodate the cooling channels in the walls of the drift tube. This change leads to an increase of the inner diameter of the DTL tank by 0.8 cm. This results in a 6.1% increase of the wall RF power loss in the cell. Also, with increased drift tube diameter, the flat region in the center of the last drift tube (No. 117) becomes rather narrow, due to the high value of the face angle, αf, and the long length required for that drift

tube. Thus, our analysis suggests a reduction of the nose flat from 1.8 cm to 1.2 cm, and a reduction of the nose cone angle from 68.3o to 61.5o. This change results in an increase of tank diameter by 0.04 cm and an increase of power loss in cell 117 by 5.8%.

Our thermal requirements analysis for drift tube No. 117 dictates an increase in the drift tube stem diameter from 3.3 cm to 4.0 cm. This increase keeps the coolant flow velocities below 5 m/sec for this drift tube that is the worst case. The change of the stem diameter to 4.0 cm improves its stiffness by 85% and does not increase the RF power requirements by a significant amount (the corresponding RF power increases are already included in the numbers quoted above). Also, the 4.0 cm diameter stem is more closely in line with other accelerator designs in proportion to the length of the cell.

Post coupler considerations may require further changes of the drift tube geometry (see "Other Issues" later in this report).

(5) Drift Tube Detailed Design

The major characteristics of the drift tube No. 1 design can be seen in section A-A in Figure 3. The 2.5 cm interior diameter bore tube is located centrally between the quadrupole magnet's iron poles. There is a 1.0 cm clearance between the 15.2 cm OD magnet and the 16.2 cm ID drift tube body bore. This clearance is dictated by the need to insert the quadrupole leads into the stem hole during assembly. Magnet leads run within the innermost channel of the triaxial stem. The other two stems form annuli for coolant feed (outer annulus) and return (inner annulus). A special flow diverter fitting at the junction between the stem and the body of the drift tube redirects the incoming coolant flow into two counterflow cooling channels around the circumference of the drift tube (the details of the flow diverter design are presented below). The 2 cm by 0.5 cm drift tube body cooling channels are visible in cross sections C-C and D-D. The total length of the first drift tube is 9.732 cm and its outer diameter is 19.2 cm. The nose cone angle is 11.1°. The cross sections B-B, C-C, and D-D also make visible the details of the drift tube assembly and the welds. The drift tube body consists of several parts that are electron beam (EB) welded together. One can also clearly see the wavespring holding the iron yoke of the magnet within the body of the drift tube between the banking surface of the drift tube body and the end cap cover. There are also two precision locating pins in the drift tube banking surface that control the transverse location of the magnet. This scheme allows for close control of the magnet's axial position with respect to the body of the drift tube. Figure 4 shows a rendered cutaway section of drift tube 1 and Figure 5 shows an exploded assembly view.

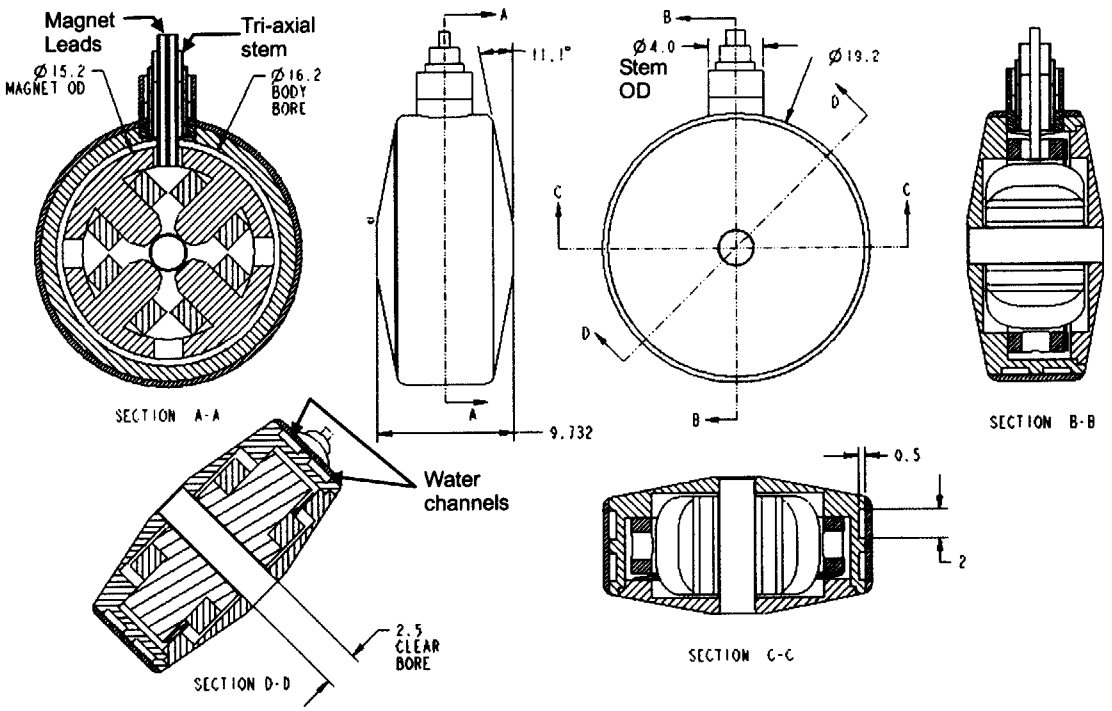


Fig. 3 Drift tube 1 conceptual design drawing.

(6) Drift Tube Assembly

Figure 6 shows the assembly sequence concept for the drift tube. The body of the drift tube is a cup shaped machined element with an opening for the flow diverter and two cooling channels running around the external circumference. The flow diverter directs the coolant flow in two directions opposite to each other (counterflow). During assembly, these channels are covered with an outer shell that is EB welded to the body. The magnet is placed within the interior cavity of the drift tube body. As the flexibility of the magnet leads is limited, the ability to insert the magnet without stressing its leads into the drift tube body

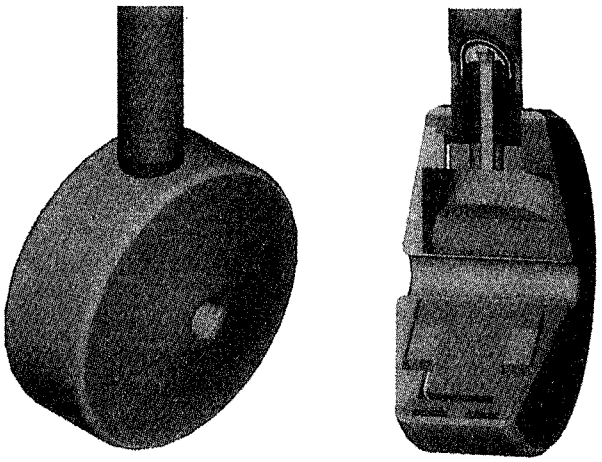


Fig. 4 Drift tube 1 cutaway.

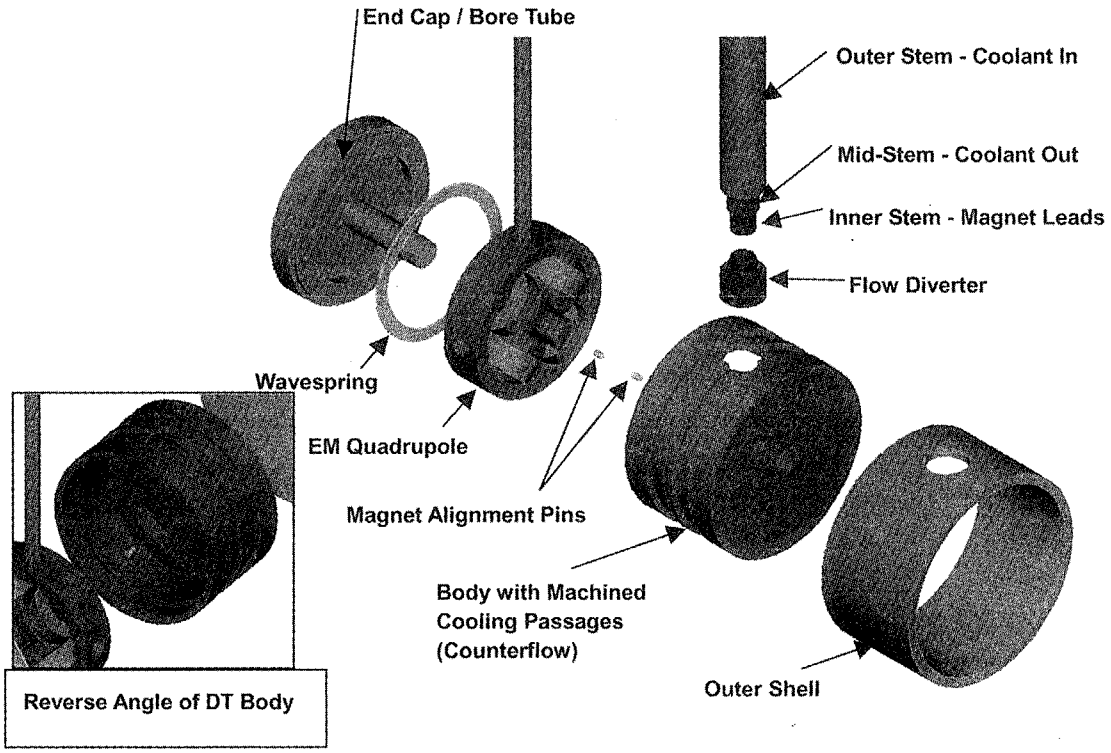


Fig. 5 Drift tube 1 exploded view.

imposes additional constraints on the geometry of the entire assembly. Once the magnet is in place, the drift tube magnet cavity is closed by means of the end cap with the attached bore tube. A wavespring and magnet alignment pins are used to hold the magnet to a known position within the body of the drift tube in both the axial and angular degrees of freedom.

The assembly of the drift tube begins with EB welding of the outer shell component to the drift tube body (step 1 in Figure 6). The photograph of the GTA drift tube assembly shows three EB welds around its circumference. Then, the two magnet alignment pins (a round pin and a diamond pin) are installed in the holes in the bottom interior face of the drift tube body. Next, the EMQ is inserted into the body with the conductor leads running through the stem opening (step 2).

After the magnet is in place, the preassembled diverter with the inner and mid stems EB welded together (step 3) is inserted over the magnet leads and welded to the body of the drift tube (step 4). This is

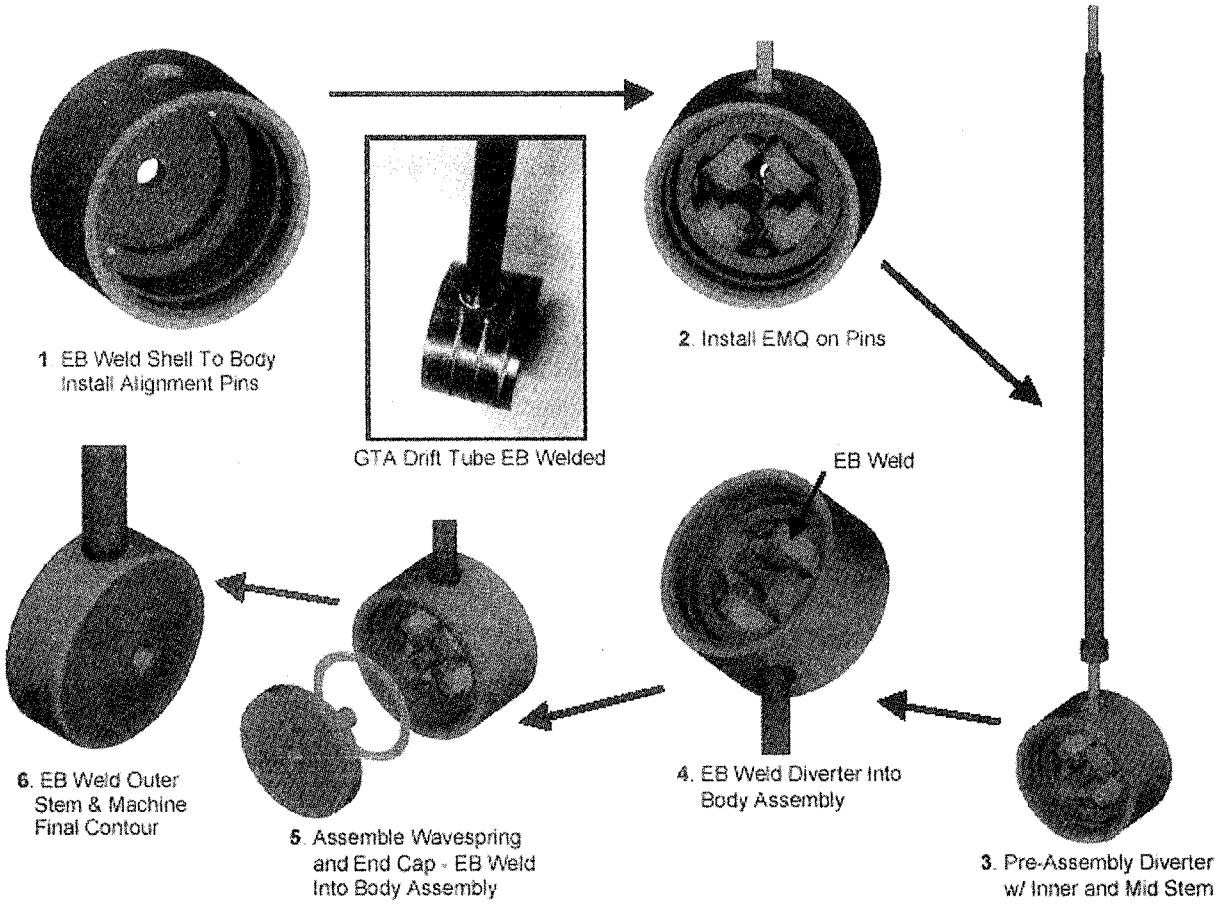


Fig. 6 Assembly sequence for IFMIF drift tube.

perhaps the trickiest part of the EB welding sequence because the diverter has to be welded to both the drift tube body and the outer shell, with the beam crossing the gap of the coolant channels.
With the diverter/stem assembly in place, the drift tube magnet cavity is closed off by placing the wavespring on top of the magnet and covering it with the end cap. Next, the two EB welds are performed: one between the cap and the drift tube body assembly on the front side and one between the bore tube and the drift tube body on the back side (step 5).

In the final step, the outer stem is EB welded to the outer shell and the diverter. Then, the final contour of the drift tube is machined (step 6).

(7) Flow Diverter Design

The geometry of the flow diverter (Figure 7) includes four cutouts that connect the inner and outer stems with the appropriate channels around the circumference of the drift tube body.

With the diverter in place as shown in Figure 8 (outer shell removed), the incoming coolant flows down from the outer stem into the right cooling channel in the clockwise direction and down into the left channel in the counterclockwise direction. After coming back to the diverter, the flow from both the left and the right channels is redirected into the inner stem and flows back up the stem.

(8) Thermal Analysis

The thermal modeling of the drift tube was performed using finite element methods with the ANSYS code. Figure 9 shows the finite element model along with the surface heat load map used to apply loads to the model. ANSYS meshing algorithms were used to generate the finite element mesh with increased element density where required for better computational accuracy.

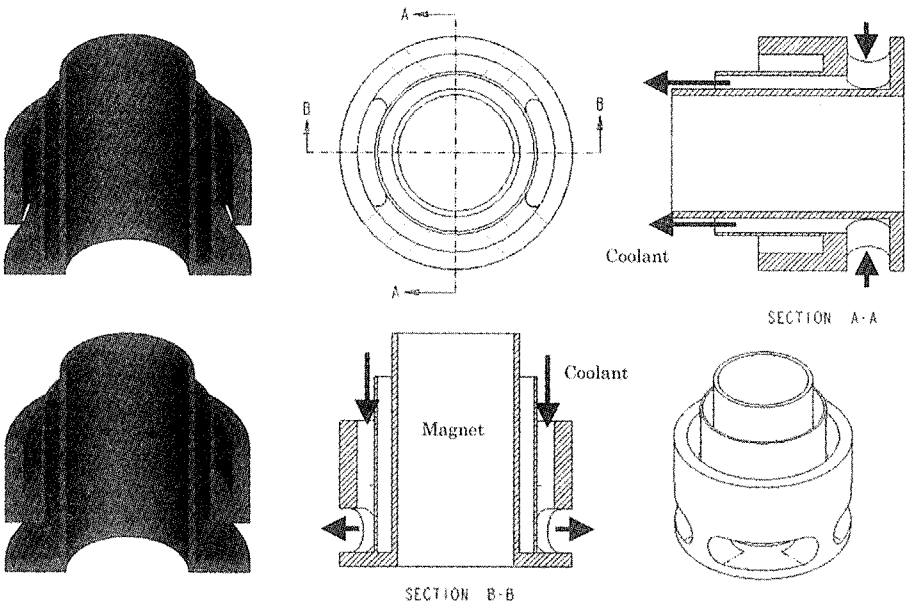
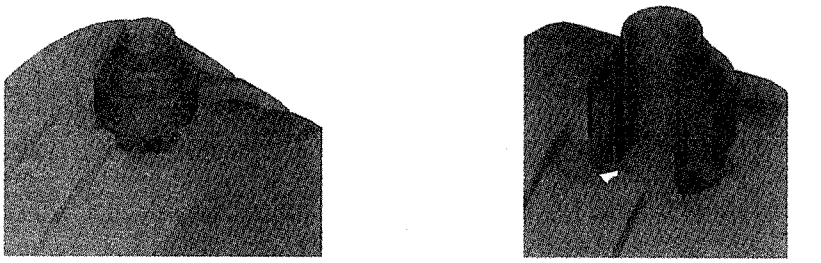


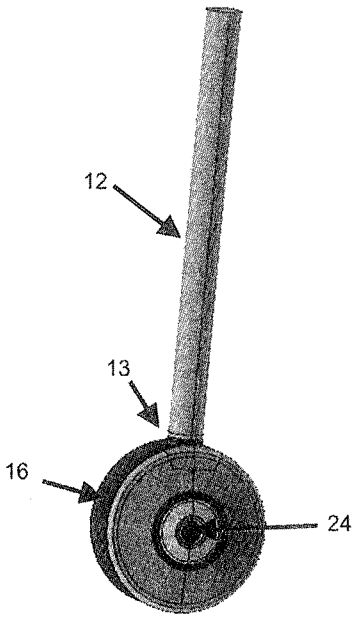
Fig. 7 Flow diverter detail.



Flow Directions
(Drift Tube Shell Removed)

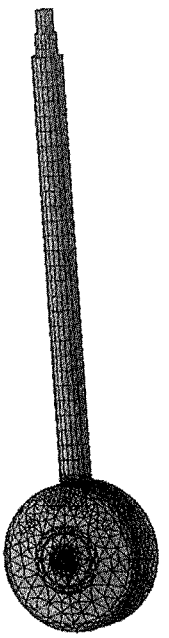
Section Cut Out of Diverter

Fig. 8 Counterflow effect of flow diverter.



Superfish Segments

Segment	Power	P/A mW/cm^2
12	247.7	807.
13	2.49	1122.
14	1.31	1178.
15	.40	1205.
16	95.	569.
17	24.4	429.
18	53.	272.
19	2.84	80.6
20	2.76	29.4
21	.0202	29.4
22	.0679	21.2
23	.0252	6.25
24	.0006	.977



Finite Element

Fig. 9 ANSYS finite element mesh and applied heat loads.

Surface power deposition loads obtained from the SUPERFISH calculation were applied over many segments of the drift tube surface as shown in Figure 10. As usual, the highest power density levels, reaching 1.2 W/cm^2, occur at the bottom of the stem, at the interface between the stem and the body of the drift tube.

The temperature distribution resulting from the power loads applied as indicated above was calculated with ANSYS under the assumption of coolant flow rate of 12 ft/sec (3.7 m/sec) in the drift tube body channels, which corresponds to a mass flow of 1.6 lbm/sec (0.73 kg/sec). An initial coolant temperature of 21° C has been assumed here. The overall coolant temperature rise is only 0.77° C. Accordingly, the effect of the coolant heat up was neglected in the finite element modeling. Similarly, the small difference between the conduction paths on the two sides of the drift tube due to the presence of the gap between the end cap and the drift tube body has been neglected as well (the EB weld does not join the flat on the bottom of the cap, only its side surface). Nevertheless, the temperature distribution is not completely symmetric because the distribution of the material is not symmetric between the two sides of the drift tube, with the cap having an additional space provided for the wavespring. The maximum temperature values, however, are the same at 22.7° C on both sides of the drift tube, near the tip of the nose cone flat.

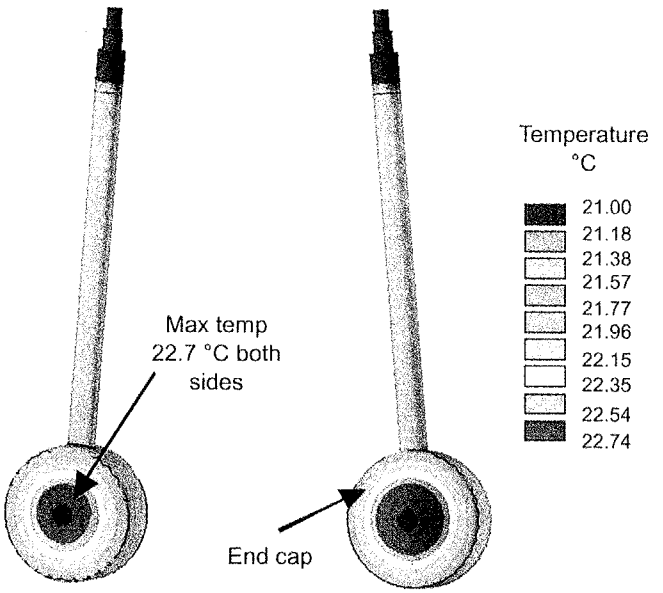


Fig. 10 Thermal results for drift tube 1.

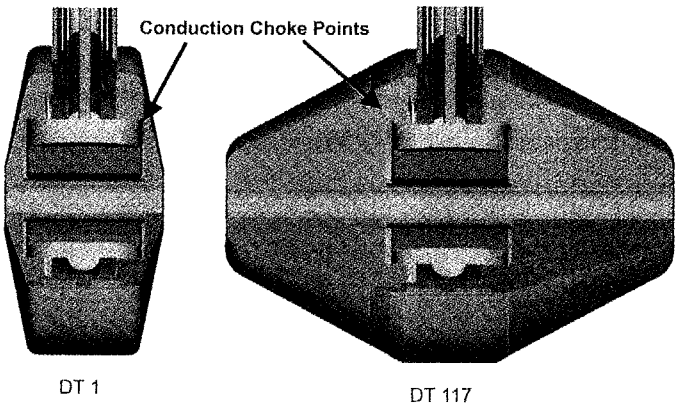


Fig. 11 Drift tube 1 compared to drift tube 117 showing much larger conduction area in DT 177.

(9) Drift Tube 117

Despite its much higher heat loads, drift tube No. 117 may not be much more difficult than drift tube No. 1. This is because the conduction "choke" in that drift tube is not nearly as bad, i.e. there is more material available for conducting the heat away from the nose cone into the cooled side surface of the drift tube body. Figure 11 illustrates this geometry.

(10) Conclusion

In summary, AES has developed a conceptual design and performed an engineering analysis of the 5 MeV drift tube for the IFMIF DTL linac as proposed in the reduced cost IFMIF concept by JAERI, using the physics data generated by CEA Saclay. The analysis results indicate that the magnet "is pushed hard but seems OK". That is, we were able to develop a concept of an electromagnet quadrupole which provides the required field levels and can be successfully packaged, assembled and cooled within the first, 5 MeV, drift tube in the first tank of the IFMIF DTL.

The engineering analysis suggested several relatively minor geometry changes to the initial physics design that are needed to accommodate the magnet and cooling passages for the "conventional" cooling

approach with the magnets cooled by water flow inside the hollow conductor and the drift tube body cooled with a separate flow within channels cut into the side surface of the drift tube body. All of these changes, however, result in a small increase in RF power losses, which may impact the overall system design.

Further work in this area is required as the physics design matures. The effect of the coolant heat up, although secondary, should be included in the analysis by adding fluid elements. Next, the transient and steady state structural deflections induced by the thermal stresses can be evaluated and the corresponding RF frequency shifts computed. Also, as mentioned before, analyses need to be performed for a number of selected drift tubes along the linac to verify that the performance is adequate all along the machine. As a minimum, drift tube No. 117 should be examined.

3.1.14 AC32-JA : Examination of the Drift Tube Cooling Scheme

(1) Brief Task Description

The Alvarez-type DTLs are assembled and aligned with the beam axis. The beam axis must be coincident with the magnetic field axis, so that the accelerating and focusing fields achieve the required beam properties. Under high-power cw operating condition, it is important to efficiently remove the heat generated in the drift tubes in order to maintain the precision alignment. The original plan was to fabricate and test a drift tube model and conduct cooling tests using that model; however, the task was modified to conduct the design study in some detail through numerical simulation. This is sufficient for initial examination of the cooling scheme for drift tubes in the IFMIF DTL. The major items covered by this task are the design of a drift tube model and numerical simulation of the of the heat load removal through the cooling channel.

Contributor

Name	Party	Institute	E-mail address
M. Sugimoto	Japan	JAERI	sugimoto@ifmif.tokai.jaerigo.jp

(2) Introduction

The baseline design of the IFMIF accelerator system employs an Alvarez-type drift tube linac (DTL) as the main accelerator. It will provide a 125 mA, 40 MeV cw deuteron beam on the flowing lithium target. The input energy to the DTL is an important parameter determining acceptance of the beam from the upstream line elements, and in matching the beam to the accelerating and focusing structure formed by the sequence of drift tubes (DT). The principle of the DTL is well established by a number of operating proton linac systems, e.g. the LANSCE linac injector of LANL. In the IFMIF-DTL, the operating frequency is 175 MHz and good output emittance, $< 0.4\ \pi$ mm mrad (transverse norm. rms) and $< 0.8\ \pi$ mm mrad (longitudinal norm. rms), is required for transfer through the high energy beam transport (HEBT). The HEBT includes a beam expander to make a flat-top 20 cm x 5 cm footprint on the target surface. The details of the DTL tanking is outside the scope of this task but, as a boundary condition, one tank would be excited by 1 or 2 of the RF power source modules with 1 MW cw output each. The outer shell diameter of all tanks would be the same to facilitate the use of common design of the interfacing equipment, including the RF system, vacuum, support and alignment mechanisms, etc. Therefore, each cavity cell in the DTL must be designed to be tuned by adjusting the geometry of the DT. The design parameters of the DT to be used in this study are described first, and the results of the thermal analysis for the specific DT are shown. As the frequency tuning of the IFMIF DTL is achieved by changing the temperature of DT cooling water, the capability of the tuning range due to the beam loading and the stability of the gap voltage are examined.

(3) Drift tube model

The parameters of the DTL cells are determined by the DTLFISH module of the SUPERFISH/ POISSON package [1]. The parameters employed follow the previous analysis by Rathke et al. [2], and are listed in Table 1. The resultant power loss distributions agree well, with a minor difference due to the mesh size treatment between the present and the former analyses. As the normalization reference for the total power dissipated in the cavity, the average electric field on the central axis of 1.75 MV/m is used, the value also used in the former analysis. The total power dissipation is 3,086 W, including the dissipation at the stem of 661W (~21%).

Table 1 Geometrical parameters of the first DTL cell.

Item	Value	Item	Value	Item	Value
Frequency	175 MHz	Cell length	12.525 cm	Tank diam.	118.0 cm
Gap length	2.792 cm	Corner rad.	0.7 cm	Inner nose rad.	0.3 cm
Outer node rad.	0.3 cm	Flat length	0.3 cm	DT rad	9.6 cm
Bore rad.	1.25 cm	Stem rad.	2.0 cm		

(4) Thermal analysis

The thermal and mechanical structure analysis was carried out using the ANSYS code. The total power dissipated in the DT is normalized to 430 W (per half of the DT cell) obtained by the cavity RF analysis described in the previous section. The cooling channel is located near the center of the outermost DT shell as shown in Fig. 1, and the channel cross section is 2 cm x 0.5 cm. The flow rate of the cooling water is assumed to be 3.7 m/s. The estimated heat transfer coefficient is 15 kW/m^2/deg for this cooling water channel. The result of thermal analysis for the case of cooling water with inlet temperature 21°C is shown in Fig. 2 and the temperature range is 21.25 ~ 22.42°C, very close to the independent analysis by Rathke [2]. The contour maps for the deformations due to the thermal expansion are shown in Fig. 3 (a) and (b) in the radial and axial directions, respectively. The resultant deviations respective to the radial and axial directions are 0.03 mm and 0.04 mm at the maximum.

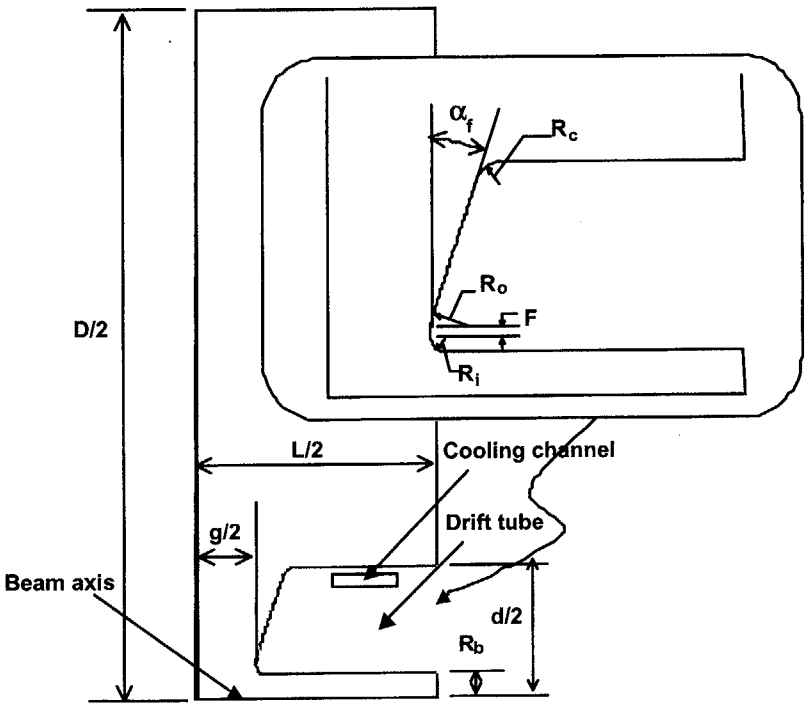


Fig. 1 Geometry of the first DT used for rf and thermal analysis.

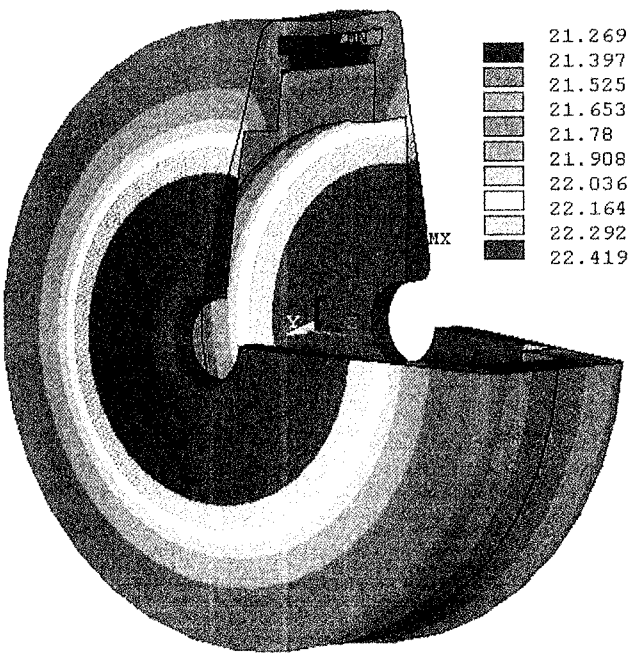


Fig. 2 Contour map of temperature distribution in the first DT.

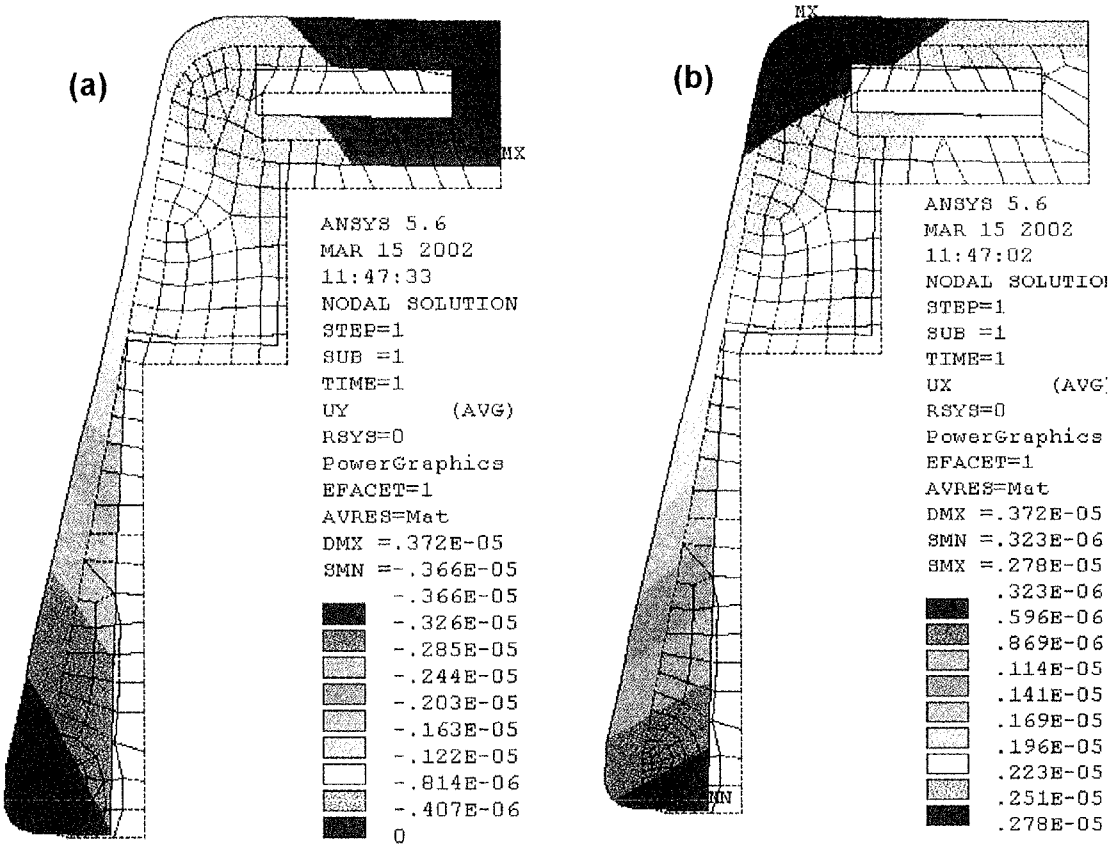


Fig. 3 Contour maps of the deformations in (a) radial and (b) axial directions.

(5) Cooling water temperature control

The frequency shift due to the thermal deformation can be deduced from the results of the RF cavity analysis and the thermal analysis. Figure 4 shows the frequency shift at the various coolant temperatures from 16 to 31°C and the gradient of the frequency shift of 1.3 kHz/deg is obtained.

The beam loading effect in the IFMIF DTL is an important issue because it is comparable to the wall loss. The reference design employs the temperature control method to retune the cavity frequency after the beam is accelerated. The frequency shift can be estimated by using an equivalent circuit model and is expressed as [3]:

$$\frac{\Delta\omega}{\omega_0} = \frac{-I_b R_c \cos\phi_b}{2V_c},$$

where $\Delta\omega=\omega_0-\omega_{rf}$, ω_0 resonance frequency (175 MHz), ω_{rf} driving frequency, I_b beam current (125 mA), Rc cavity impedance (~125Ω), ϕ_b synchronous phase (~-30deg), and V_c voltage between gaps (~100 kV). Then the results are obtained as $\Delta\omega = -6.8\times10^{-5}$ and $\Delta\omega$ = -12 kHz, corresponding to a 9.2°C coolant temperature change.

The stored energy can be expressed as:

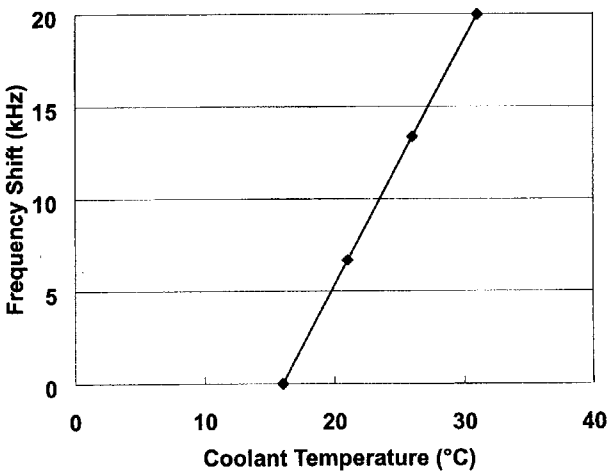


Fig. 4 Frequency shift vs. coolant temperature calculated for the first DT cell

$$U = \frac{V_c^2}{2R_c} \cdot \frac{1}{1+\left(\frac{\omega_0 L_c}{R_c}\right)^2 \cdot \left(\frac{2\Delta\omega}{\omega_0}\right)^2},$$

and the following relationships are derived:

$$U \propto \frac{1}{\Delta\omega^2 + \left(\frac{\omega_0}{Q}\right)^2}, \quad U_0 \propto \frac{1}{\left(\frac{\omega_0}{Q}\right)^2}, \quad \frac{U}{U_0} \propto \frac{1}{\Delta\omega^2\left(\frac{\omega_0}{Q}\right)^2 + 1},$$

When the SUPERFISH result of Q~9.15×10^4 is used in the above formula, the required control accuracy of the frequency to keep the gap voltage stable can be obtained as shown in Table 2. If the required stability for voltage is ~1%, the required precision of the temperature control will be 0.2°C.

Table 2 Frequency change and resultant stored energy and gap voltage deviations.

Δω (kHz)	U/U_0	V/V_0
1	0.785	0.886
0.5	0.936	0.967
0.25	0.983	0.992
0.2	0.989	0.995
0.1	0.997	0.999

(6) Conclusions

The temperature distribution and the resulting deformation of the first DT assembly of the IFMIF DTL were estimated using SUPERFISH and ANSYS codes. The absolute power dissipation is normalized to the reference design value, E_0=1.75 MV/m, so that the distribution obtained reproduces the previous results and the maximum temperature rise is 1.5°C. The frequency shift coefficient of the change in the coolant temperature is deduced, and the requirements for the range of tuning due to the beam loading and for the control precision to maintain voltage stability are estimated as ~9°C and 0.2°C, respectively.

References

[1] J. Billen and L. Young, "Poisson Superfish", LA-UR-96-1834, January 1996.

[2] J. Rathke, T. Schultheiss, M. Cole, "IFMIF Drift Tube LINAC 5MeV Drift Tube Design Study Status Report", presented at IFMIF Accelerator Team Mtg, Monterey, USA, Aug. 25-26, 200.

[3] E. Raka, "RF System Considerations for a Large Hadron Collider", in AIP Conf. Proc. 184, Physics of Particle Accelerators, Eds. Month and M. Dienes, A.I.P. New York 1989, p.288.

3.1.15 AC33B-EU : Choice of RFQ Structure, Development of the 4-rod RFQ

(1) Brief Task Description

The 4-rod RFQ structure developed at Frankfurt for a high duty factor will be adapted to meet IFMIF needs. Beam dynamics layout will accomplish small emittance and high transmission. Technical design and experimental verification of a short 4-rod RFQ to demonstrate the required cw operation capability is planned.

Contributors

Name	Party	Institute	E-mail address
A. Schempp	EU	IAP	A.Schempp@em.uni-frankfurt.de
A. Bechthold	EU	IAP	A.Bechthold@iap.uni-frankfurt.de

(2) Introduction

Investigation of the 4-rod RFQ structure has been conducted to evaluate it as an alternative solution to the complex 4-vane structure. Though power dissipation is approximately the same and current densities are higher by a factor of 2 to 3, the fields are concentrated in the resonating stem structure, which can be cooled very efficiently. The rf-coupling of this structure is stronger than the 4-vane structure; therefore, tuning sensitivity and operating stability are very high.

(3) 4-Rod RFQ Design

The design for the injector of the IFMIF accelerator consists of a high current ion source, a magnetically focussing neutralized LEBT and a 175 MHz RFQ accelerator. The RFQ accelerator has to accept a 100 keV deuteron beam of I_{in} = 140 mA and transport, bunch, and accelerate it to an energy of 5 MeV with minimum loss and emittance growth.

An important design criterion is a low Kilpatrick value, which especially for continuous (cw-) mode operation plays an important role in operational stability and accelerator down time.

All attempts for a beam dynamics design using either the standard shaper buncher and accelerator section for RFQs or versions of the modified method keeping, e.g. the phase advances constant, lead to RFQs which are much longer than standard accelerators. The reason is the need for very slow bunching and rather low accelerating gradient to maximize radial focusing and minimize losses at reasonable electrode voltages.

Our design uses the basic parameters of an electrode voltage of 120 kV starting with a focusing parameter of B = 6.2 at stable phase 90° resulting in a radial phase advance of σ = 40° at the RFQ input. These values are smoothly varied to the final values of B = 6.5 and ϕ_s = -50° resulting in an RFQ with length 127 m. The Kilpatrick value stays below 1.9.

Figure 1 shows the parameters along the RFQ. Results of PARMTEQ simulations with an input emittance of 125 π mm mrad and a waterbag distribution are shown in Fig. 2. The transmission at 140 mA input deuteron beam current is T = 94.8% with an emittance growth of $\Delta\varepsilon$ = 43.5%. Figure 3 shows the output emittances.

A feature of our design is a constant voltage along the RFQ, which results in a rather long RFQ. The accelerator section can be shortened very efficiently by using a higher electrode voltage, without touching the Kilpatrick limit, and thus make up for an

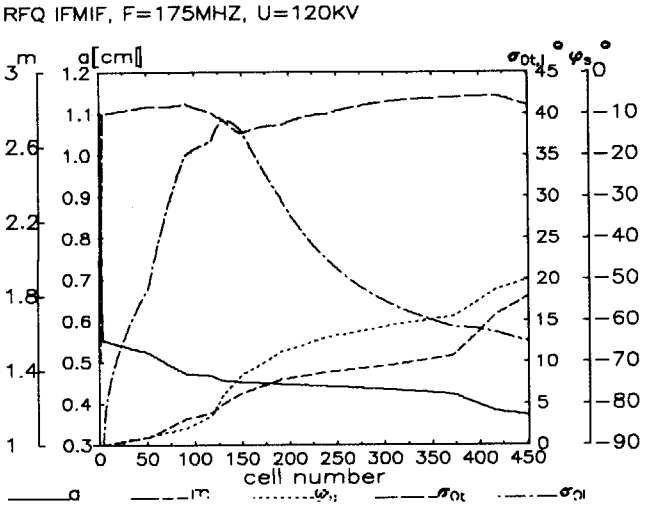


Fig. 1 RFQ Parameters.

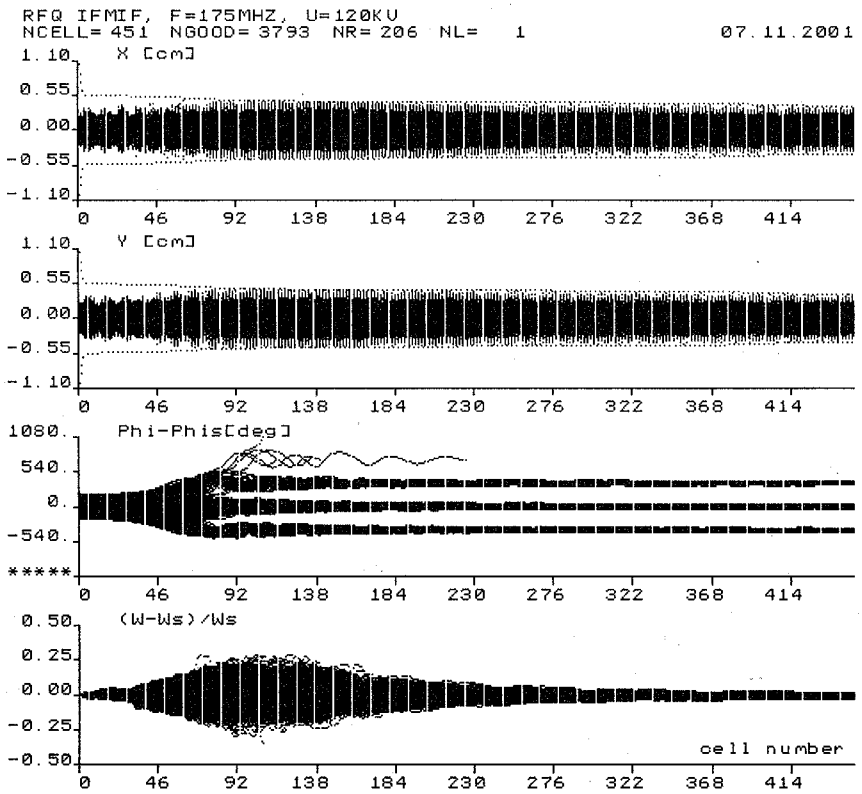


Fig. 2 PARMTEQ simulation.

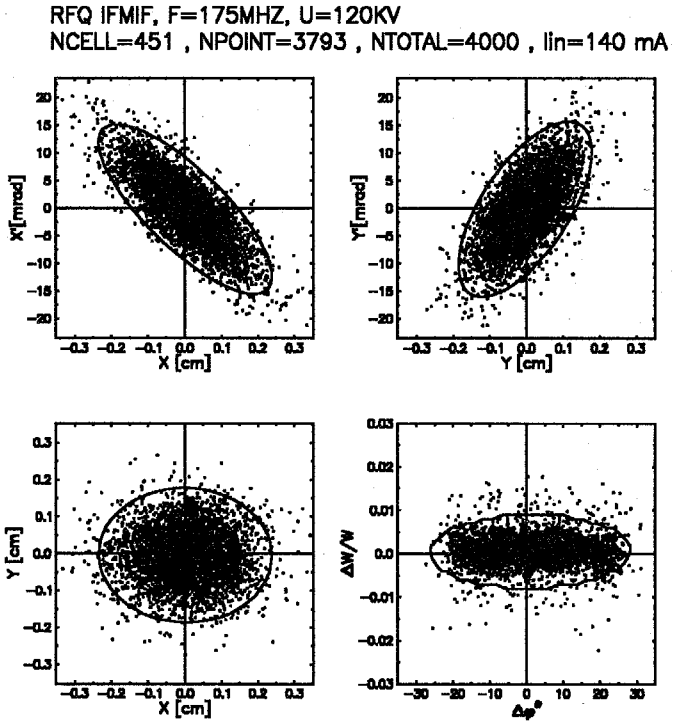
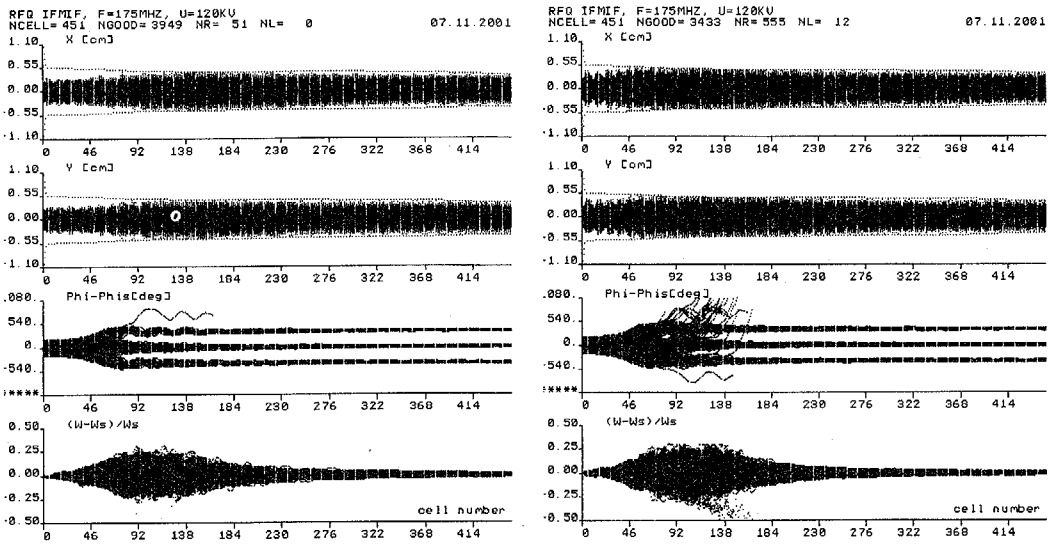


Fig. 3 Output emittance (140 mA).

excessively long bunching section. The disadvantages are extreme power losses in this part of the RFQ, which will be hard to reduce because even the average value of ~120 kW/m for our design will be very hard to build and may be a limiting factor.



(a) (b)

Fig. 4 PARMTEQ simulations for 100 mA (a) and 200 mA (b).

The particle dynamics design can be further examined by changing the design current. Our design is very robust and allows currents up to 200 mA while still achieving transmission of 86%.

Figure 4 shows the beam behaviour along the RFQ for beam currents of 100 and 200 mA, and Fig. 5 gives the transmission as a function of the input beam current. The transmission drops smoothly from 99% for 50 mA to 98% at 100 mA and 94.8% at the design input current of 140 mA. At 200 mA and even at 300 mA the transmission is as high as 86% and 70%.

The particle losses along the RFQ indicate that the major losses occur radially in the region of rapid bunching and acceleration, at energy of ~200 keV (Fig. 6). At this stage of acceleration many particles are changing to adjacent buckets as can be seen in Fig. 2. The insensitivity of our RFQ design to variation in the input emittance is shown in Fig. 7.

(4) Investigation of 4-Rod RFQ [1]

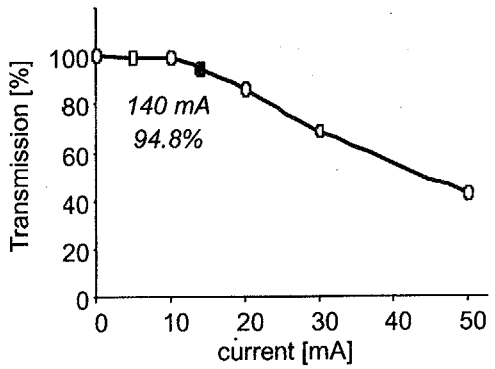


Fig. 5 Transmission as a function of the beam current.

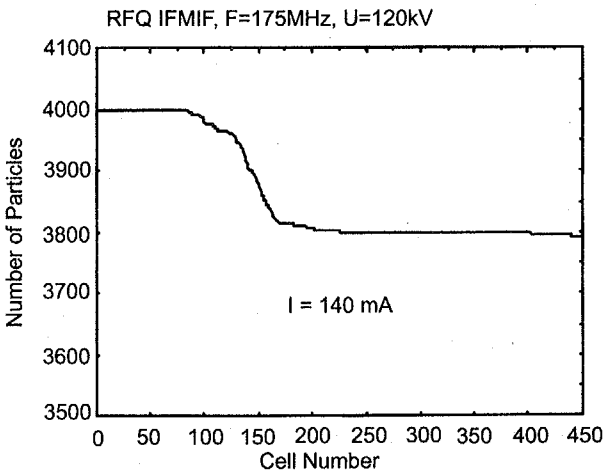


Fig. 6 Losses along the RFQ.

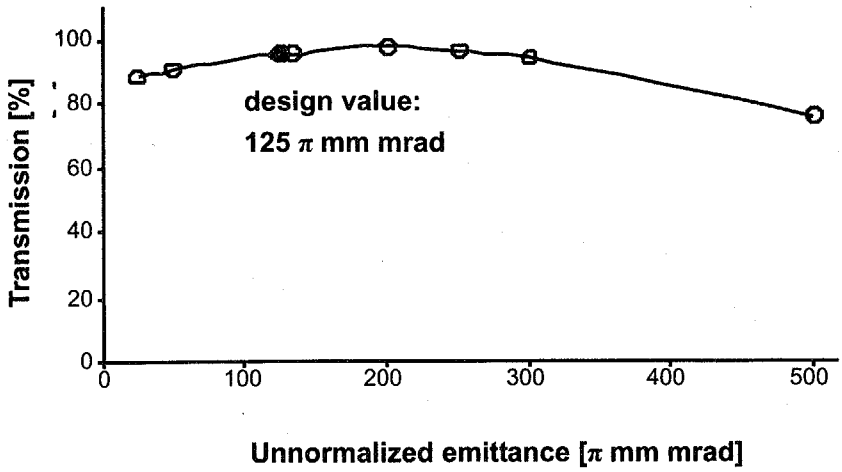
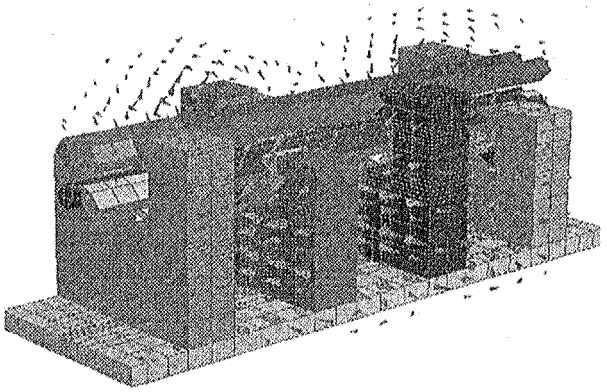


Fig. 7 Transmission as a function of the unnormalized input emittance.

Work on a cw hot model was performed to study the cw operating conditions. Due to the availability of rf-power sources we set up a short rf-resonator with four stems, a basic cell of the 4-rod RFQ. The electrodes were 32.5 cm long, and the distance and length of the stems were 85 mm and 95 mm. Each stem is separately water cooled by a feedthrough from the tank outside. The 4 electrodes were made from our standard CuCr with an internal cooling channel in the small vane shaped conductor. MAFIA calculations and experiments identify the hot spots on the electrode-stem connections, shown in Figs. 8 to 12.

Operation was without tuner by VCO control of the amplifier. After conditioning the resonator, we



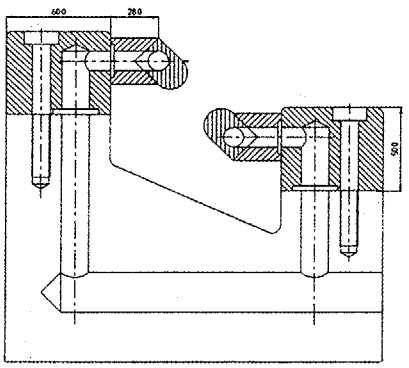


Fig. 9 Electrode cooling scheme.

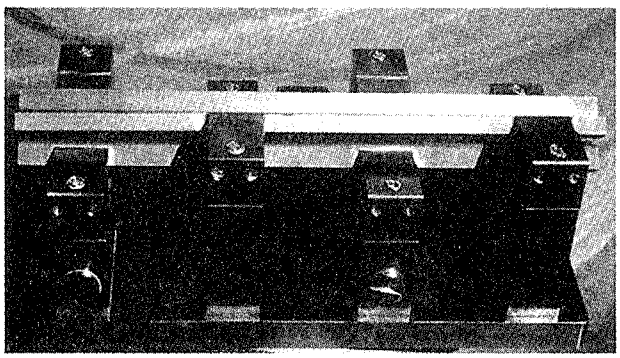


Fig. 10 View of the test model.

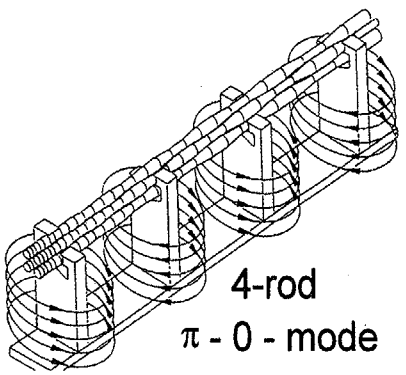


Fig. 11 Schematic of the 4-Rod RFQ insert.

could operate with the full transmitter power of 20 kW cw, corresponding to 60 kW/m, a value four times higher than previously achieved.

These tests were done with unmodulated electrodes and a number of direct water-vacuum seals. A more realistic test has been started with a resonator designed for beam operation but lower duty factor. The RFQ is 4 m long and designed to operate at a duty factor of 20%.

The alignment and tuning produced very good results. The 4-rod RFQ has an input/output energy of 35 keV/4 Mev and a resonance frequency of 200 MHz. The field flatness is within 1.5%, the $Q_0 = 3350$. The cavity has one central rf-input coupler and two sliding tuners for thermal compensation with a tune of Δf=0.55 MHz. The maximal rf input power was 250 kW.

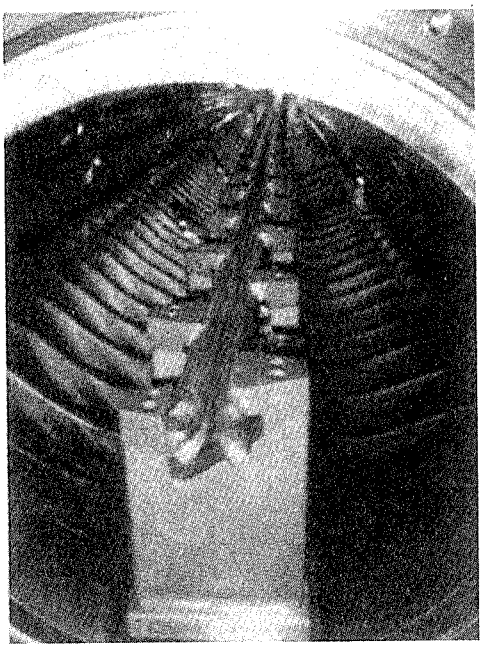


Fig. 12 View of the 4-Rod-RFQ.

(5) Conclusions

With the presented design, which is well adapted to the 4-rod structure with high Kp value and spacing, useful input emittances are between 50 and 500 π mm mrad. With further optimization of input matching, e.g. $\alpha\beta$, additional improvements can be achieved.

Depending on the general optimization priorities, this design might be modified for lower average power of the RFQ. That means lower electrode voltage, or even higher transmission or improvements in emittance.

The rf-conditioning was done to a power level of 250 kW for proton beam tests. The conditioning process was successful. It was only interrupted by melting of the rf-loop caused by a blockage of cooling water flow. The RFQ has been repaired, put back into operation, and is ready for beam tests.

Reference

[1] A. Schempp New Developments in High DC, High Currrent RFQ, LINAC2002, Gyeongyu, Korea.

3.1.16 AC35-EU : Choice of DTL Structure, and Investigation of CH-DTL

(1) Brief Task Description

Particle dynamic design is needed for an Alvarez-type DTL for IFMIF. Error studies and stability calculations must include mismatched input beams, statistic rf errors and mechanical tolerances for the Alvarez. Investigations should identify matching possibilities between RFQ and Alvarez, and verify by overall simulation of the linac (RFQ+Alvarez DTL). Alternatives can be studied through particle dynamic design of an IH-type DTL for IFMIF, and should include additional error studies and stability calculations, including mismatched input beams, statistic rf errors and mechanical tolerances for the IH-DTL. Investigations will include matching possibilities between RFQ and IH-DTL, and integrated simulation of the linac (RFQ+IH-DTL). Evaluation of superconducting (sc) options uses particle dynamic design of a sc IH/CH-DTL combination for IFMIF, with error studies and stability calculations. Matching to the sc IH/CH-DTL is evaluated using an RFQ output distribution and overall simulations (RFQ+IH/sc CH-DTL) are performed. A sc 175 MHz CH cavity is designed with MicroWave Studio based on particle dynamics calculations, and detailed analysis of the rf and sc properties of the CH cavity is carried out.

Contributors

Name	Party	Institute	E-mail address
H.Deitinghoff	EU	IAP	deitinghoff@em.uni-frankfurt.de
H.Klein	EU	IAP	horst.klein@iap.uni-frankfurt.de
H.Liebermann	EU	IAP	hlieberm@stud.uni-frankfurt.de
H.Podlech	EU	IAP	h.podlech@iap.uni-frankfurt.de
U.Ratzinger	EU	IAP	u.ratzinger@iap.uni-frankfurt.de
A.Sauer	EU	IAP	a.sauer@iap.uni-frankfurt.de
R.Tiede	EU	IAP	tiede@iap.uni-frankfurt.de

(2) Introduction

During the CDA and CDE phases of IFMIF, particle dynamics calculations were performed for a 175 MHz, 125 mA deuteron linac. The linac has to provide a 40 MeV beam with low losses and small emittance growth for the uniform irradiation of a lithium target. The accelerator consists of an RFQ injector followed by a Drift Tube Linac. The complete facility would need two 125 mA linacs in parallel operation. In a first attempt the particle dynamics layout of an Alvarez type DTL (room temperature) has been studied aiming for low rf voltages and moderate power losses in the structure due to the required cw operation. In addition, first investigations of an H-type DTL (room temperature) have been started for a further evaluation of the capability of this structure for the acceleration of high intensity beams. Results will be presented and discussed, including matching requirements to the DTL.

Since the IFMIF linac has to be operated in cw-mode, normal conducting acceleration structures have high thermal losses. A way out could be the use of superconducting cavities. One could think of short quarter-wave- or spoke-type cavities. With a chain of many of these resonators a high flexibility in the acceleration of different ion species and charge-to-mass ratios can be achieved by individual phase tuning of each resonator. In the IFMIF DTL only one ion species with a fixed velocity profile has to be accelerated. In this case multi-gap structures like H-type are more appropriate. The room temperature IH_{110}-structure already serves successfully in the field of light and heavy ion acceleration. The typical frequency range is between 30 and 300 MHz with energies up to 20 MeV/u*. Together with the KONUS (Kombinierte Null Grad Struktur) beam dynamics concept [1], which allows drift tubes to be built without quadrupoles and concentrates the transverse focusing in separate quadrupole triplets, compact and highly efficient linacs can be designed and constructed. The higher the energy, the higher the required frequency for efficient acceleration. This is met by the CH (crossbar H_{210}-mode) cavities [2]. Due to the larger diameter compared to the IH structures, frequencies up to 700 MHz and energies up to 150 MeV/u can be reached; thus, the

* Unit of particle energy per particle mass = MeV/(atomic mass unit).

CH structure shows a large potential for room temperature as well as for sc designs. CH-cavities show high mechanical and thermal robustness, provided by the crossed-stem construction. The transverse dimensions are small compared to half-wave or spoke-type cavities operated at the same frequency. For the required cw operation, the power losses are low and large drift tube apertures can be chosen to reduce the probability of particle losses. For the IFMIF DTL a combination of room temperature IH tanks with internal quadrupole triplets for the low energy part followed by a chain of superconducting CH-cavities with inter-tank focusing has been designed and multi-particle beam dynamics calculations have been performed to check the beam behavior.

(3) The Alvarez-DTL for IFMIF

Design studies have been performed for the RFQ as well as for a modular-built DTL of the Alvarez-type, which demonstrated the suitability of the reference design. Since then some critical points have been reconsidered: the transition energy between RFQ and DTL was lowered from 8 MeV to 5 MeV, to reduce the RFQ requirements. Beam dynamics calculations performed with the multi-particle program PARMILA [3] showed that the DTL is capable of handling the high current at this lower injection energy. There are no loss or packaging problems of the drift-tube-housed magnetic quadrupoles. However, a special matching between RFQ and DTL may be required. Figure 1 shows a schematic layout and Table 1

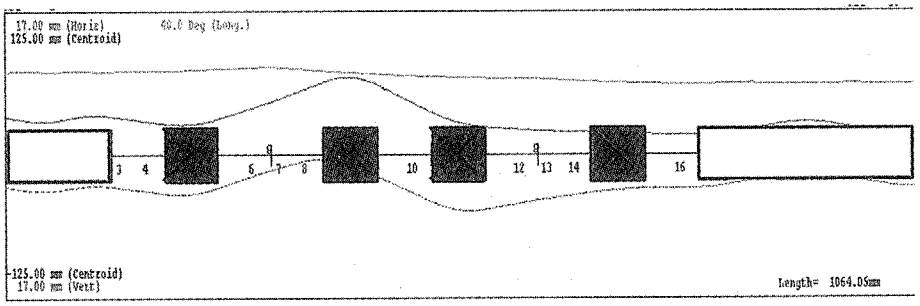


Fig. 1 Schematic layout of the MEBT for the Alvarez-DTL calculated with TRACE3D. Last focusing period of RFQ and first of Alvarez is also plotted (yellow parts).

summarizes the structure parameters for an appropriate MEBT, using the same zero current phase advances per unit length of the RFQ and Alvarez, for matching the RFQ output beam to the Alvarez-Type DTL.

Table 1 Structure parameters of the MEBT for the Alvarez-DTL.

Element	G [kG/cm]	B [T]
D-Quad	-8.227	1.31
F-Quad	7.555	1.20
D-Quad	-7.716	1.23
F-Quad	3.113	0.498
Aperture [cm]	1.6	
Length [cm]	80.6	

Another question is the ability of the high power rf amplifiers to feed the accelerator modules, including the very high beam load. In a first choice, 1 MW input power per tank was assumed for the layout of the Alvarez, leading to six tanks with 1 $\beta\lambda$ spacing between the tanks [4]. Rf power reserves are needed when the following aspects are taken into account: the calculated shunt impedances of the rf structure may be too optimistic, and some power is needed for the phase and amplitude control. Because of the cw operation, the peak surface fields are lowered to avoid sparking. Therefore different layouts of the DTL have been studied with reduced shunt impedance (-17%), lower rf input power (<0.8 MW per tank), reduced Kilpatrick factor (0.9 instead of 1.0) and rf structure losses limited to <50 kW/m. After those changes, some parameters have been reconsidered: the aperture radius in the high energy section was increased from 1.5 to 2.0 cm for higher safety margins against particle losses. The tank end walls were included in the design to get more exact total power estimates for the DTL. The inter-tank matching was improved by adjusting the first and last two quadrupoles in the last four tanks and the synchronous phase of the first and last two gaps of each module [5]. Figure 2 displays a schematic layout and Table 2 gives the structure parameters of the

optimized Alvarez-DTL.

All particle dynamics calculations showed the capability of an Alvarez DTL to handle a high current beam without beam losses, even with combined standard errors. In addition, simulation with variable end energies of the DTL between 35 MeV and 40 MeV were performed (detuning the 7th and 8th tank) with a small reduction of the quadrupole field strength. The transverse beam quality was nearly unchanged but the longitudinal quality deteriorated significantly [6].

(4) The IH-DTL for IFMIF

In the past several years IH-type DTL linacs have been successfully built and operated for the efficient acceleration of light and heavy ions, e.g. at GSI and CERN [1]. This modern type of accelerator combines high acceleration rates with a new focusing scheme called KONUS, and leads to compact accelerators. Therefore, this type has been investigated for use in high intensity machines like IFMIF. Figure 3 shows the schematic of an optimized IH–type DTL for IFMIF, and Table 3 gives the structure parameters generated with the multi-particle program LORASR [1]. In the KONUS scheme the particles are accelerated in a number of gaps with 0 degree bunch center phase, which are followed by a quadrupole triplet and rebunching cells with negative phase. In the first tank of the IH-DTL the quadrupole is still integrated into the tank; in the following nine sections we use inter-tank quadrupole triplets, for easy adjustment and maintenance of the quads.

The multi-particle simulations showed no particle losses and smooth beam behavior with moderate emittance growth [6]. A possible advantage of the IH-Type DTL could be the lower rf power consumption (IH is 30% more efficient) and shorter length (8 m shorter than the Alvarez). All beam dynamics calculations showed that the

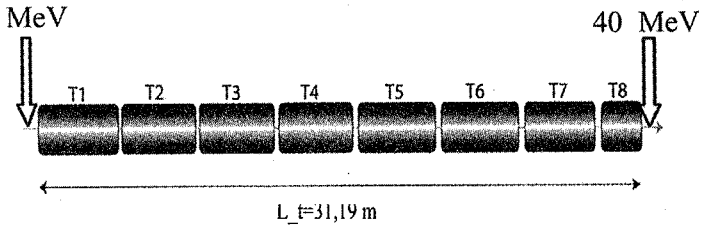


Fig. 2 Schematic layout of the Alvarez-DTL.

Table 2 Structure parameters of the Alvarez DTL for IFMIF.

Parameters	Alvarez	Uits
I design	125.0	mA
f_{rf}	175.0	MHz
N_T / N_{cell}	8 / 124	
P_{tot}	5.94	MW
$<P_{Cu+Beam/T}>$	0.750	MW
W_{in} / W_{out}	5.0 / 40.34	MeV
W_{tot}/L	1.13	MeV/m
L_{tot}	31.19	m
r_o	1.5 – 2.0	cm
$<ZT^2>$	43.14	MΩ/m
b_{Kilp}	0.90	

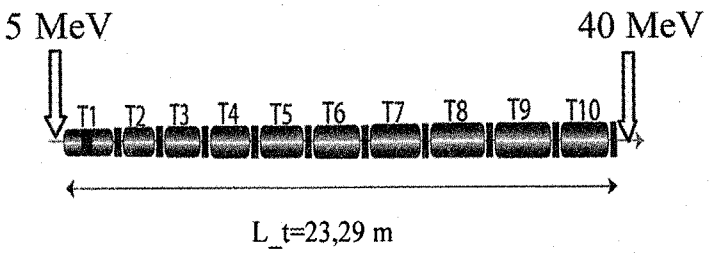


Fig. 3 Schematic layout of the IH-DTL.

Table 3 Structure parameters of the IH-DTL.

Parameters	IH	Uits
I design	125.0	mA
f_{rf}	175.0	MHz
N_T / N_{cell}	10 / 157	
P_{tot}	5.33	MW
$<P_{Cu+Beam/T}>$	0.536	MW
W_{in} / W_{out}	5.0 / 40.1	MeV
W_{tot}/L	1.50	MeV/m
L_{tot}	23.29	m
r_o	1.5 / 2.0	cm
$<ZT^2>$	94.29	MΩ/m
b_{Kilp}	0.43	

IH-DTL is capable of accelerating such high current, high intensity beams without losses. Preliminary design suggested some modifications to improve the beam quality and the performance of the IH-DTL: the number of gaps per resonator was reduced, which results in a smaller transverse beam size. With that change, the number of tanks is now 10. Furthermore, error and tolerance studies for the IH-DTL have been performed. The result was that the IH-DTL is more sensitive to errors than the Alvarez, leading to smaller aperture factors and larger emittance growth. With a special compact matching section between RFQ and IH-DTL, which provides transverse and longitudinal matching and simultaneously prepares the beam for the KONUS-dynamics (the structure parameters of the MEBT can be seen in Table 4 and the schematic in Fig. 4), it was possible to inject an RFQ output beam into the IH-DTL without particle losses. Finally, to achieve

Table 4 Structure parameters of the MEBT for the IH-DTL.

Element	G [kG/cm]	B [T]
D-Quad	-6.2	1.24
F-Quad	2.2	0.44
F-Quad	6.45	1.29
D-Quad	-6.2	1.24
F-Quad	6.45	1.29
Aperture [cm]	2.0	
Length [cm]	65.7	

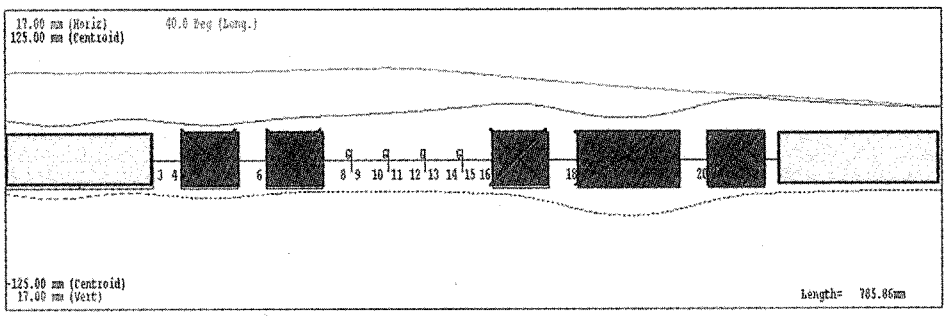


Fig. 4 Schematic layout of a MEBT for the IH-DTL calculated with TRACE3D. Last focusing period of RFQ and first of IH is also plotted (yellow parts).

variable output energy between 35 and 40 MeV, the 9th and 10th tanks of the IH were detuned and the quadrupole triplets were slightly adjusted. This leads to similar beam behavior as for the Alvarez [6].

(5) The Superconducting CH-DTL for IFMIF

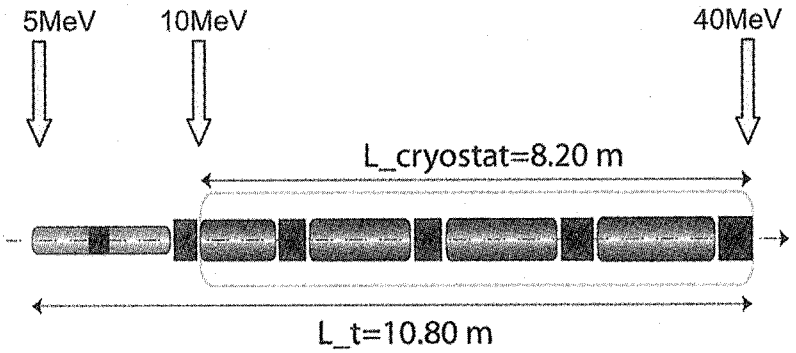


Fig. 5 Schematic layout of the sc IH-CH-DTL.

Beam dynamics design for IFMIF has been studied for a combination of a room temperature IH-section followed by a chain of superconducting 175 MHz CH-sections. Fig. 5 shows a schematic layout of the optional IFMIF linac generated with the multi-particle program LORASR. Due to beam dynamics reasons, a magnetic lens is integrated into tank 1, which has to be operated at room temperature. The other four tanks are superconducting with external lenses between them.

Table 5 shows the structure parameter of the linac generated with the multi-particle program LORASR. One important design restriction was the maximum average rf power per tank needed in the sc part. It should not exceed 800 kW (which is almost completely converted into beam power) due to rf amplifier and coupler power limits (requiring two rf couplers per tank). Therefore the effective field amplitude E_{eff} was limited to 4.1 MV/m. The cw operation mode of the IFMIF facility and the use of deuterons requires a large safety margin in the bore sizes of the accelerators to avoid losses which lead to

structure activation. Therefore we increased the bore radius of the drift tubes with the particle energy in the sc part from 2.4 cm up to 4.0 cm. Such a large increase of the linac aperture is only possible in a sc layout without a dramatic decrease in efficiency. Furthermore we reduced the maximum gap voltage to V_{gap} (max) ≤ 1.0 MV to avoid sparking and to reduce the critical electric surface fields $E_{peak.}$ [7]. Extended particle dynamics calculations were made with different scenarios, including: a) mismatch of the input beam, b) errors and tolerances of the quadrupole triplets and rf phase and amplitude of tanks, and c) using a real RFQ output distribution as input for the sc CH-DTL in combination with a compact matching section (see Table 6 for the structure parameters and Fig. 6 for the schematic of the MEBT).

The MEBT is similar to the normal conducting IH-DTL design because the first module of the linac is identical. This results in smooth beam behavior, acceptable emittance growth, and no particle loss [8].

Table 5 Structure parameters of the IH-CH-DTL.

Parameters	SC IH-CH-DTL	Uits
I design	125.0	mA
f_{rf}	175.0	MHz
N_{tank}	5 (1 NC+4 SC)	
P_{tot}	4.44	MW
$<P_{Cu+Beam/T}>$	NC: 0.690 SC: 0.740	MW
W_{in} / W_{out}	5.0 / 40.1	MeV
N_{cell} / L	73 / 10.5	1/m
r_o	NC: 1.5 SC: 2.4 – 4.0	cm
b_{Kilp}	1.00	

Table 6 Structure parameters of the MEBT for the IH-CH-DTL.

Element	G [kG/cm]	B [T]
D-Quad	-6.1	1.22
F-Quad	2.3	0.46
F-Quad	6.35	1.27
D-Quad	-6.3	1.26
F-Quad	6.35	1.27
Aperture [cm]	2.0	
Length [cm]	65.7	

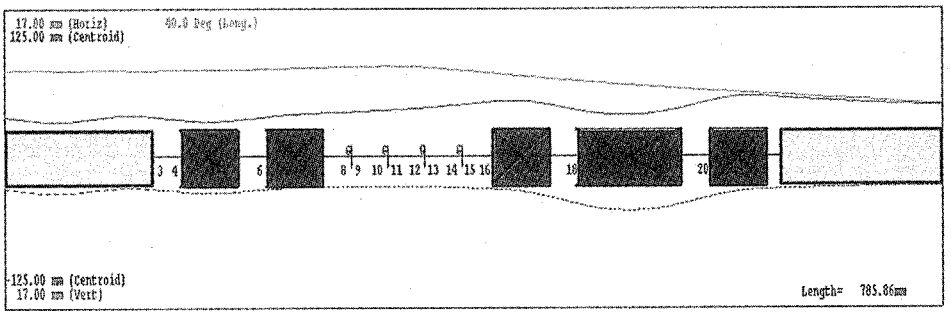


Fig. 6 Schematic layout of a compact MEBT for the sc IH-CH-DTL calculated with TRACE3D. Last focusing period of RFQ and first of IH/CH is also plotted (yellow parts).

Figures 7 - 9 show the 100% transverse and longitudinal beam envelopes along the IH/CH linac calculated with LORASR. With the structure parameters determined from multi-particle simulations, a preliminary sc CH cavity design study was made with MicroWave Studio.

Table 7 gives the parameters of the first sc 175 MHz CH resonator with a fixed beta of 0.1. Figure 10 shows a sectional view of the cavity. Preliminary optimization procedures lead to relatively low peak surface electric and magnetic fields of 38.7

Table 7 Cavity parameters of the first 175MHz sc CH-resonator.

Cavity parameters	SC CH-DTL	Uits
Beta	0.1	
Frequency	174.86	MHz
Eacc	5.35	MV/m
Epeak	38.7	MV/m
Tnk length	1.52	m
Drift tube diameter	5.0	cm
Tnk diameter	58.0	cm
Nmber of gaps	12	
Epeak / Eacc	7.23	
Bpeak / Eacc	9.17	MT/MV/m

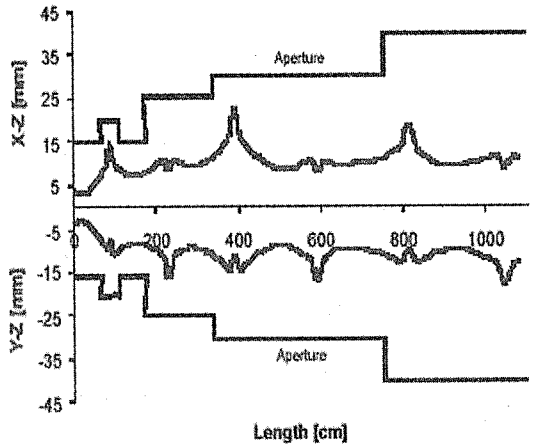


Fig. 7 100 % transverse beam envelopes along the linac.

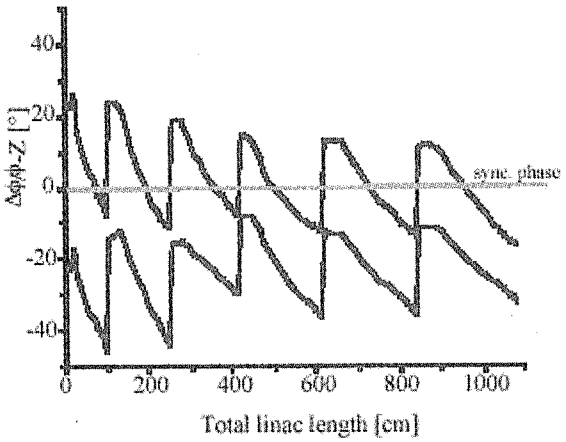


Fig. 8100 % phase width with respect to the bunch center along the linac.

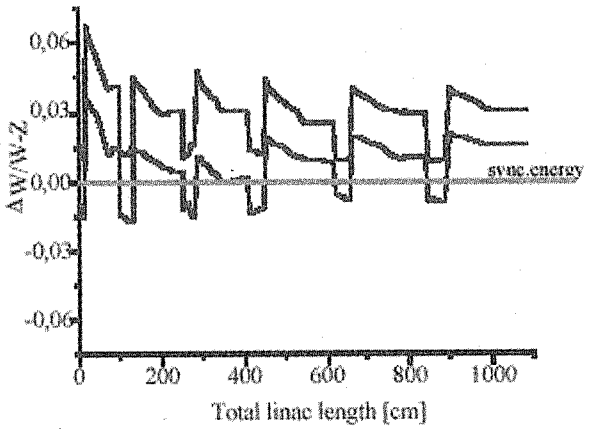


Fig. 9 100 % energy width with respect to the bunch center along the linac.

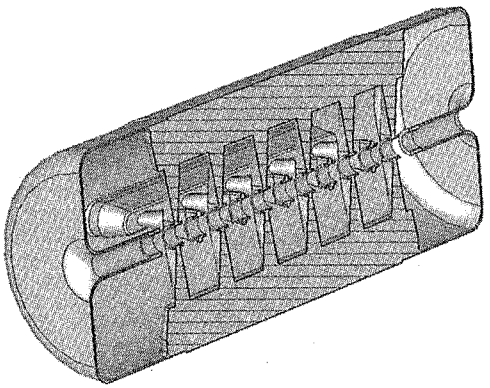


Fig. 10 View of a 175 MHz 12 gap sc CH-cavity for beta=0.1 (const).

MV/m and 49.1 mT, which are well below the theoretical BCS limits of cavities made of niobium [9].

(6) Development of the CH Structure

A copper scale model (1:2) was built at the IAP in Frankfurt in order to determine basic rf properties (see Fig. 11). The model has 18 gaps and the cell length $\beta\lambda/2$ has been kept constant with a fixed β of 0.17. The tank diameter is about 30 cm and the tank length about 1.2 m. The measured resonance frequency (350 MHz) was less than 1% lower than the frequency calculated with MicroWave Studio (352 MHz).

Measurements of the longitudinal field profile with a bead-pull setup have been performed to investigate different tuning possibilities. Figure 12 shows an example of a measured field profile along the z-axis.

A design study of a sc CH structure

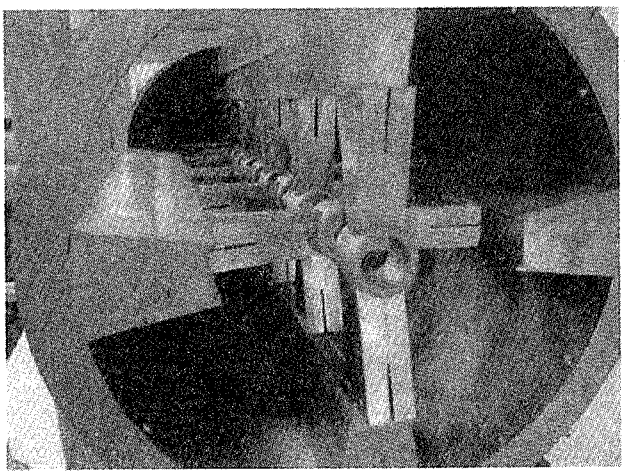


Fig. 11 Photo of the copper model of the 350 MHz CH structure.

has been made in close cooperation with industry. The assembly of the cryogenic laboratory is in progress. The cryostat has been delivered and the magnetic shielding was ordered.

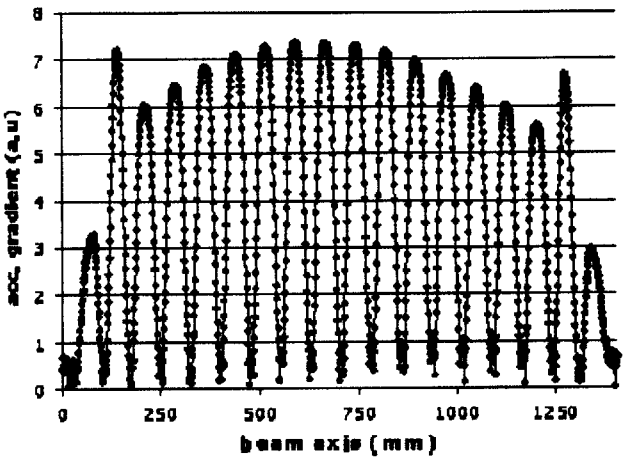


Fig.12 Measured field profile along the z-axis.

(7) Conclusions

Particle dynamics investigation of the IFMIF DTL showed robust beam behavior for the Alvarez-type DTL. Lower input energy, beam matching and lower input power per tank gave in all cases stable solutions, good emittance conservation, strong transverse and longitudinal focusing, no particle losses, and sufficiently large aperture factors even when including standard quadrupole and rf errors and mismatched input beams. Beam dynamics studies for the IH-type showed its capability for high intensity acceleration with good power efficiency. Investigations of beam stability against matching, field and quadrupole errors showed, however, that the IH-DTL is more sensitive to errors than the Alvarez, due to the KONUS-dynamics. The beam dynamics design of an Alvarez-type and an IH-type DTL for IFMIF was significantly advanced by the KEP phase activities. Integrated beam dynamics simulations for the whole linac (RFQ+DTL) were made to ensure the safety of the injector facility against losses and activation. Both structures showed, when used in combination with a special compact MEBT, no particle loss and smooth beam behavior, whereas the RFQ+Alvarez chain gave higher aperture factors and lower emittance growth. Due to the mandatory cw operating mode of IFMIF, a design with a combination of a room-temperature (rt) IH structure and a chain of superconducting (sc) CH resonators with inter-tank focusing has been completed and shown to also fulfill the requirements for a high current IFMIF DTL. The sc CH DTL section provides very high rf and acceleration efficiencies and, due to its special cell geometry, high mechanical robustness. The sc drift tube linac has a total length of only about 11 m, and the cryostat length is about 8 m. The estimated total power (including all cryostat losses) per meter of this design study is ≈1.5 kW/m (for comparison the rt linacs need ≈50 kW/m), which demonstrates the high rf efficiency of the sc CH modules. The large drift tube apertures in the sc components reduce the risk of particle losses. Intensive simulations also showed low sensitivity of the beam behavior to statistic and mechanical errors. Overall calculations from RFQ+SCCH-DTL including a compact MEBT also proved the stability of the IH/CH linac layout against possible structure activation when a realistic RFQ beam is injected. In this view, the proposed IH/sc CH-DTL combination is a promising alternative to the conventional reference layout. First on-axis field measurements of a down-scaled 350 MHz copper model of a CH cavity showed satisfying results for field flatness and mechanical stiffness. A first superconducting cavity for experimental evaluation is in preparation.

References

[1] U.Ratzinger, "Effiziente HF-Linacs für leichte und schwere Ionen", Habilitationsschrift, Johann Wolfgang-Goethe University, Frankfurt, July 1998.

[2] R.Eichhorn, U.Ratzinger, "Superconducting H-Mode Structures for Medium Energy Beams", LINAC 2000, Monterey, USA, Vol. 2 Page 926.

[3] H.Takeda, H.Billen, "PARMILA", LA-UR-98-4478, Los Alamos National Lab (LANL), Los Alamos, New Mexico, USA, November 2001.

[4] A.Sauer, H.Deitinghoff, H. Klein, "Beam Dynamics Studies For A High Current Ion Injector", LINAC 2000, Monterey, California, August 2000.

[5] A.Sauer, R.Tiede, H.Deitinghoff, H.Klein, U.Ratzinger, "Particle Dynamics Investigations For A High Current D+ DTL", PAC 2001, Chicago, USA, June 2001.

[6] A.Sauer, R.Tiede, H.Deitinghoff, H.Klein, U.Ratzinger, "Investigation Of A Normal Conducting 175

MHz Linac Design For IFMIF", EPAC 2002, Paris, France, June 2002.
[7] A.Sauer, R.Tiede, H.Deitinghoff, H.Klein, U.Ratzinger, R.Eichhorn, "Beam Dynamics Design Of A Superconducting 175 MHz CH-Linac For IFMIF", EPAC 2002, Paris, France, June 2002.
[8] A.Sauer, Ph.D thesis, in preparation.
[9] A.Sauer, H.Deitinghoff, H.Klein, H.Liebermann, H.Podlech, U.Ratzinger, R.Tiede, "Beam Dynamics Layout of H-Type Drift Tube Linacs For Intense Light Ion Beams", LINAC 2002, Gyeongju, Korea, August 2002.

3.1.17 AC21C-US : Analysis of the Revised IFMIF High Energy Beam Transport (HEBT) System

(1) Brief Task Description

The purpose of the present study was to examine the HEBT design for the Reduced Cost IFMIF [1]. This design has been substantially revised from the CDA configuration and most importantly, the RF cavities used for beam energy spread control in the CDA design were removed. Our goal in this study was to take a first look at the impact of these changes on the ability to achieve the required beam profile and homogeneity on target. Our preliminary conclusion is that it appears the RF cavities can be removed and that a suitable HEBT system can be defined. Figure 1 shows a HEBT configuration resulting from this preliminary study.

Contributors

Name	Party	Institute	E-mail address
John Rathke	US	AES	john_rathke@mail.aesys.net
Alan Todd	US	AES	alan_todd@mail.aesys.net

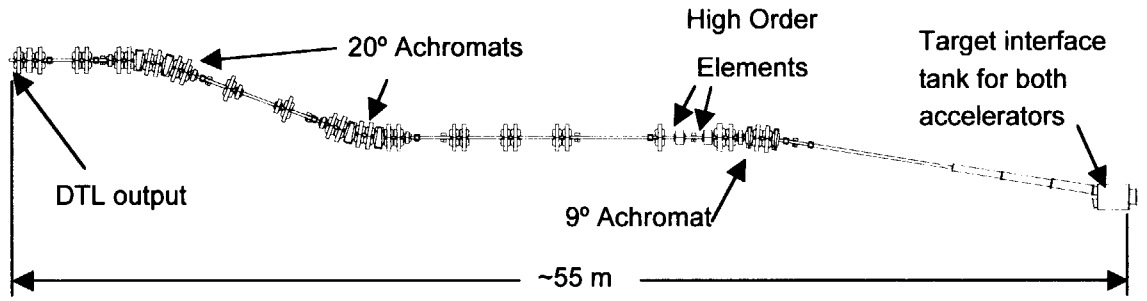


Fig. 1 Preliminary HEBT Physical Layout.

(2) Discussion

The resultant beam line conveys a 40 MeV, 125 mA beam 55 meters to the target and incorporates two twenty degree achromatic bends, FODO transport, a final focus and a final nine degree achromatic bend followed by a 17 meter drift to the target. Initial beam parameters for this analysis were provided by R. Ferdinand of CEA Saclay and are the output parameters of a candidate IFMIF DTL design [2]. The preliminary Trace 3D results are shown in Figure 2.

The twenty degree achromats are symmetric about their center allowing both Rxz and Rx'z to be simultaneously zero. The beam envelope is also symmetrized to help preserve achromaticity when space

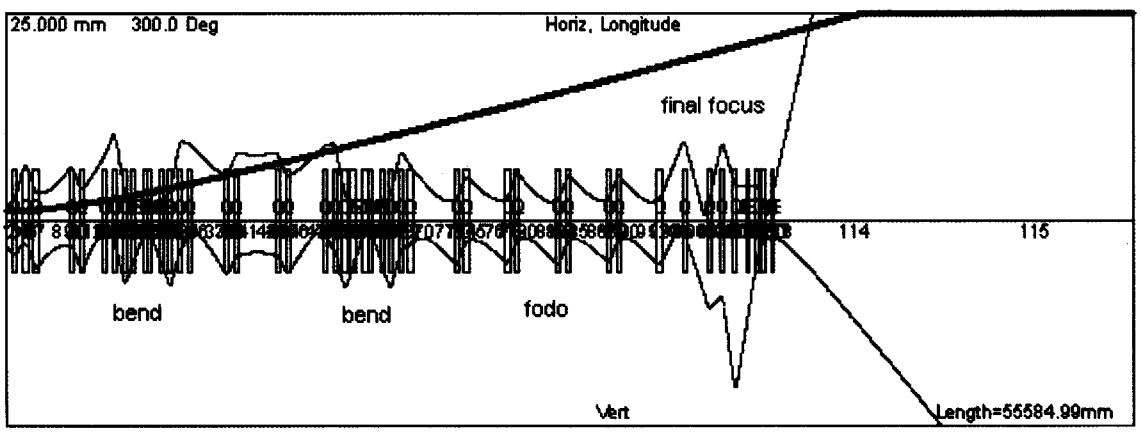


Fig. 2 Preliminary Trace 3D Results.

charge is present. Further this symmetry allows a FODO lattice to go into a DOFO lattice, different only in phase.

The transverse phase advance per cell in the FODO sections is 104.5 degrees without space charge and 51.5 degrees with a current of 125 mA. In the future, this phase advance may be reduced down to a more conventional value, below 90 degrees, by the incorporation of more focusing elements per unit length which would increase the cost. However, there is no present evidence of resulting performance degradation in the relatively short beamline.

Of note in this preliminary analysis is the larger vertical beam size of ~9 mm RMS just before the final bend. As bunches travel down the beam line they may grow longitudinally until they overlap, depending on RF bucket occupancy. When this occurs a three-dimensional space charge model no longer applies. Further, energy-spread stops growing. In the present study, only a 3D model of space charge was used and the RMS energy spread was predicted to increase from 150 keV at the DTL exit to 270 keV on target.

In developing the magnetic lattice we limited the pole tip fields of magnetic elements in the beam line to 1 Tesla. Therefore, assuming a pole tip radius ("a") of 10 cm the quadrupole magnets, with $B(r) = B_0 (r/a)$, will have a maximum allowable field gradient B_0/a on the order of 10 Tesla per meter. Octupole elements, with $B(r) = B_0 (r/a)^3$, will have a maximum allowable field gradient of 1000 Tesla/Meter^3. Further, 1 Tesla or less dipole bending magnets are limited to a minimum radius of about 1.3 meters. Here we have used 1.5 meters. A few of the beam line elements in this model exceed our nominal quadrupole maximum strength. In an iteration of the present design, these would simply be made longer and their gradient reduced at near constant strength.

Details of a final focus, up to and including the final nine-degree bend, slightly redesigned from the line of Figure 2 are shown in Figure 3. The beamline upstream of element 92 is identical to that of Figure 2. The split elements, items 94-95 and 97-98, are Trace3D placeholders for combined function elements that can apply octupole and, possibly, duodecapole fields in addition to the quadrupole field. The design achieves the goal of a 10 mm RMS beam in the nonlinear elements.

The nonlinear elements are necessary to square-off and flatten the beam. On target, the requirement is for a beam uniformly illuminating a rectangle 20 cm in width by 5 cm in height. The idea is to have two nonlinear elements, 94-95 and 97-98. The beam is sent into a waist in both, but in different transverse directions. The two waists allow independent control of each transverse direction since the octupole will most strongly effect the large beam direction.

A beam waist is produced in the center of the nonlinear elements. Normally, one avoids small waists and the associated aberration effects. Here, this is unavoidable and, in any event, the beam is spread out both in the other transverse direction and longitudinally at this point so that space charge effects should be manageable.

The ray-tracing version of a modified version of Topkark was used in the present study. Figures 4

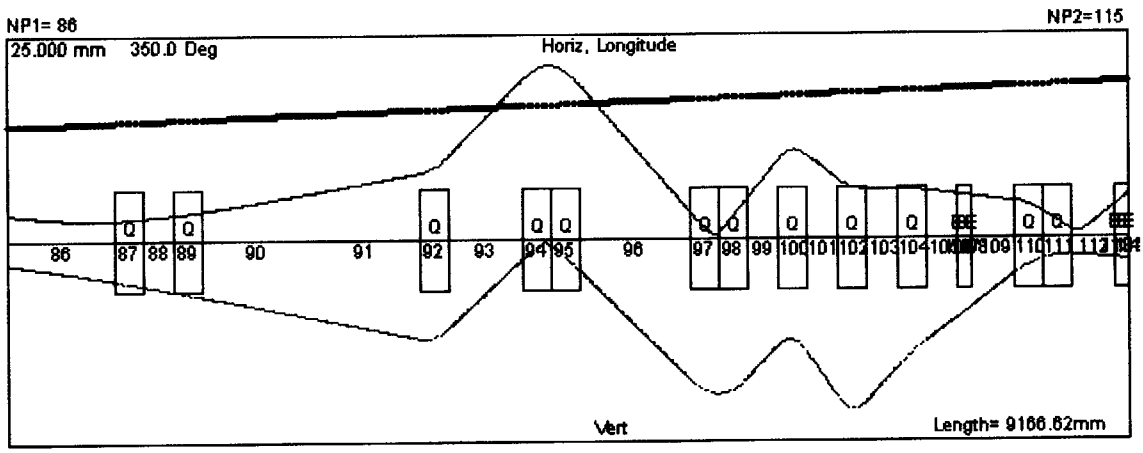


Fig. 3 Redesigned Beam Final Focus.

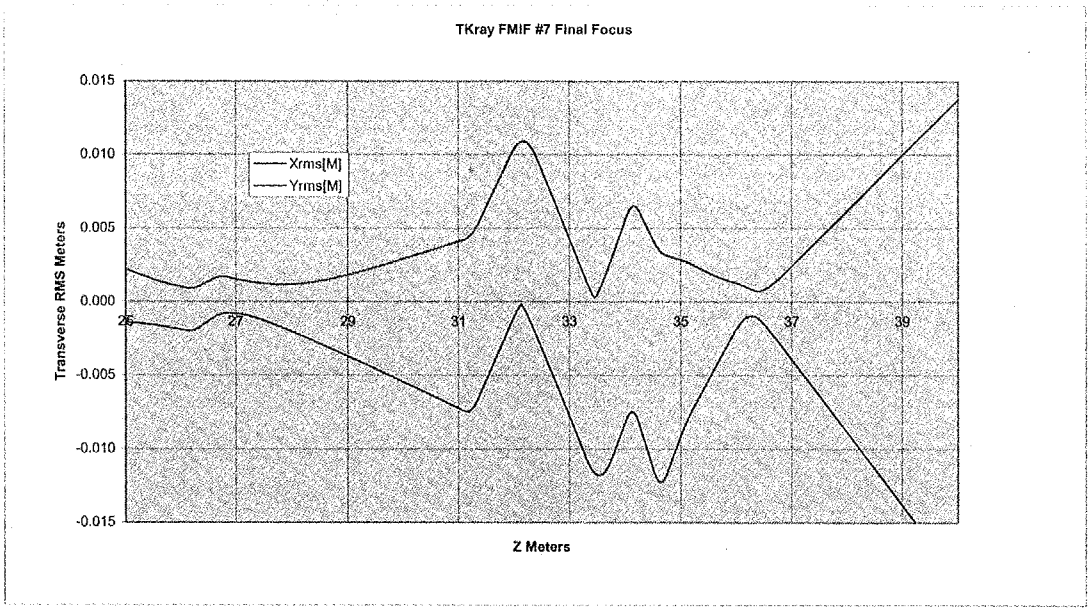


Fig. 4 TKRay Large Beam Final Focus.

- 7 were generated by this TKRay code using 10,000 particles, a Gaussian initial particle distribution, a uniform (i.e. linear) space charge model and a current of 125 mA. Figures 8 - 10 used the "generalized" space charge model. As may be seen in Figure 4, TKRay's RMS transverse envelopes are quite similar to those of Trace as expected. Figure 5 illustrates the profile with physically reasonable octupole values. The profile is not ideal in that the shoulders are still too broad.

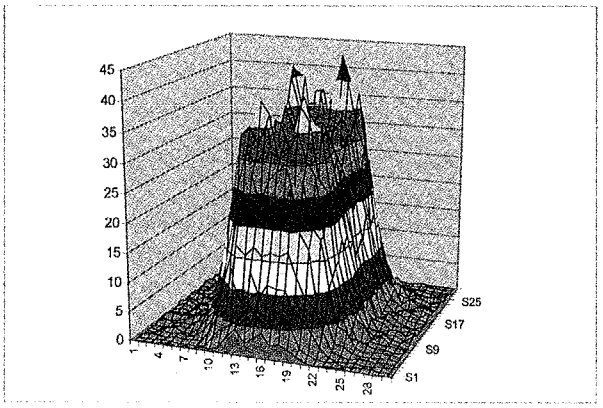


Fig. 5 Final Focus with Octupole Correction.

Profile slices, at regular intervals, of the distribution of Figure 5 are given in Figures 6 and 7 respectively. These are the

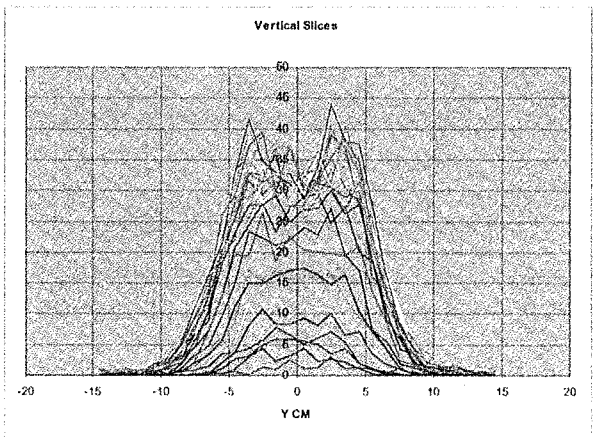


Fig. 6 Vertical Profile Slices

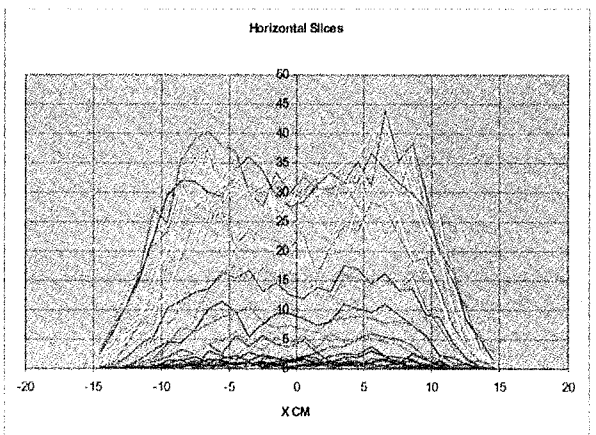


Fig. 7 Horizontal Profile Slices

results of averaging some five different runs with different random number seeds. The colors distinguish the different intervals as the slicing proceeds through the beam.

Figures 8, 9 and 10 are plots averaged over five runs using 10,000 particles and the generalized Garnett and Wangler (G-W) 3D space charge model instead of the prior linear model. The current remains 125 mA.

(3) Conclusion

This preliminary study validates the IFMIF HEBT design tools and indicates that a realistic design solution without RF cavities probably exists. Further work is needed to complete a satisfactory IFMIF HEBT design and a list of tasks for ongoing analysis is given below.

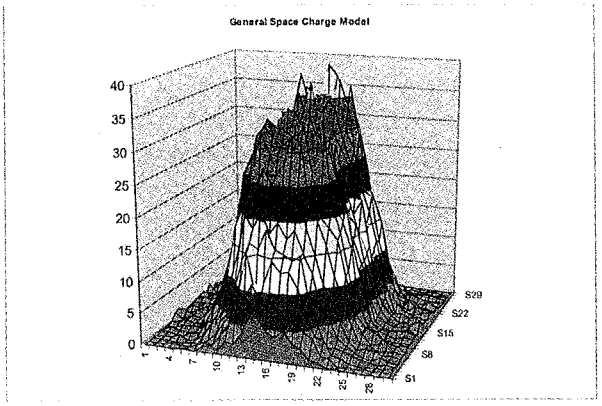


Fig. 8 Histogram, G-W Space Charge Model.

- Reduce the transverse phase advance in the FODO
- Examine the effects of increased post-nonlinear-element drift length as used in the earlier Los Alamos design [3]
- Investigate the impact of duodecapole elements on flattening and profile shoulder control
- Account properly for the bunch overlap effect on space charge
- Examine reduced beam current, field sensitivity, mismatch and misalignment tolerances.

References

[1] M. Ida (ed.), "IFMIF CDA Reduced Cost Report," JAERI-Tech 2000-014, Japan Atomic Energy Research Institute, February, 2000.

[2] R. Ferdinand, et al., IFMIF Accelerator Group Meeting, FZK, Karlsruhe, Germany, January, 2002 and Private Communication.

[3] B. Blind et al.,"High Energy Beam Transport Design", Sec. IV, "Deuteron Linac Design Studies for ESNIT/IFMIF", LA-CP-94-136, Los Alamos National Laboratory, 1994.

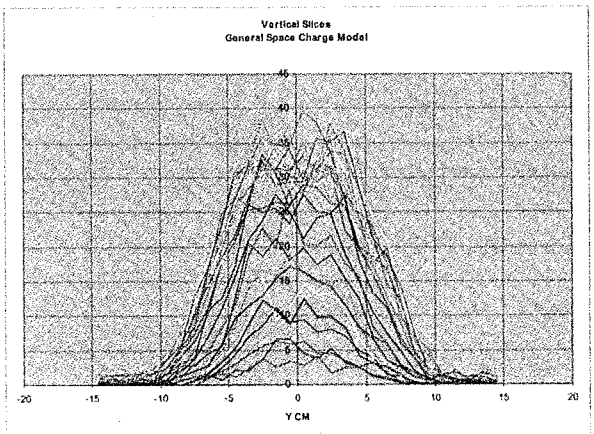


Fig. 9 Vertical Slices for G-W Space Charge Model.

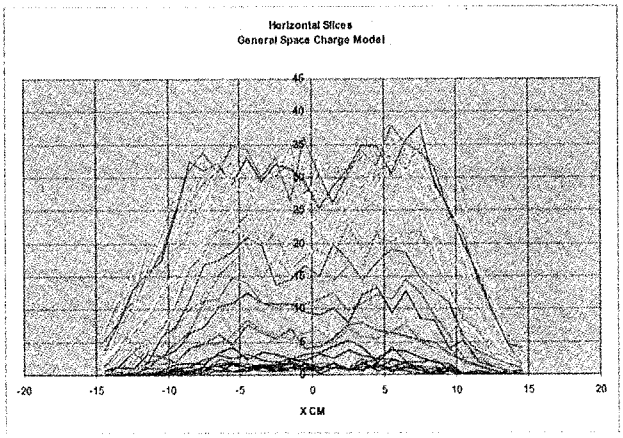


Fig. 7 Horizontal Slices for G-W Space Charge Model.

3.1.18 AC33A/38-EU : End-to-End beam dynamics

(1) Brief Task Description

The IFMIF project requires two linacs designed to accelerate 125 mA CW deuteron beams up to 40 MeV. After extraction and transport, the deuteron beams (with strong internal space charge forces) have to be bunched, accelerated and transported to the lithium target for the production of a high neutron flux. This task presents the reference design linac, which is a combination of RFQ and DTL structures. Beam dynamics end-to-end calculations with errors studies and cavity designs are detailed.

Contributors

Name	Party	Institute	E-mail address
R. Ferdinand	EU-FRANCE	CEA-Saclay	rferdinand@cea.fr
R. Duperrier	EU-FRANCE	CEA-Saclay	rduperrier@cea.fr
D. Uriot	EU-FRANCE	CEA-Saclay	duriot@cea.fr

(2) Introduction

IFMIF requires generation, by a linear accelerator, of 250 mA continuous current of deuterons at a nominal energy of 40 MeV, with provision for operation at 30 MeV and 35 MeV [1]. The basic approach is to provide two linac modules, each delivering 125 mA to a common target. This approach has availability and operational flexibility advantages.

Very low beam loss along the linac is required in order to minimize structure activation by beam-loss particles, so that maintenance can be performed without remote manipulators. This study presents the reference design for the RFQ and DTL sections of the facility. Beam dynamics with and without errors are detailed. This work is done for the fusion community and supported by the EFDA contract 2000/10.

(3) RFQ Design

The IFMIF 175 MHz RFQ is a four-vane structure. This ensures minimum power consumption compared to coaxial RFQs and better control of the cavity deformation in CW mode. The cavity, designed with BELENOS [2], has a total length of 12.482 m and is segmented in three parts. This segmentation ensures an efficient longitudinal damping of field errors [3], and introduces two resonant coupling gaps. The first gap is located at 4.161 m and the second at 8.321 m. From mechanical considerations, in particular the size of the welding/brazing furnaces, each segment is cut into four 1.04 m pieces. Figs. 1 and 2 show 3-D views of segmented RFQs [4,5]. The different parameters are summarized in Table 1, showing that the final synchronous phase is -40 deg. One may think that this value is too high and penalizes the accelerating efficiency of the structure, but this choice allows appreciable margin for the longitudinal acceptance. This point is important for of the high currents. The high voltage (130 kV to 100 kV) compensates for this high synchronous phase and allows strong focusing.

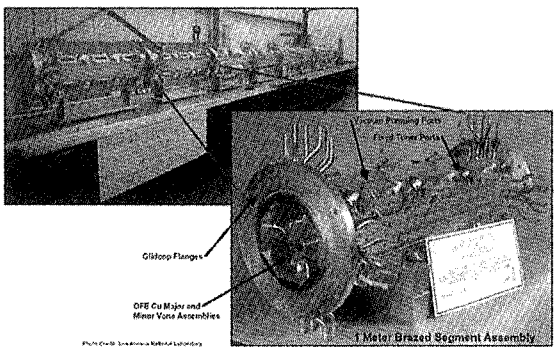


Fig. 1 LEDA RFQ.

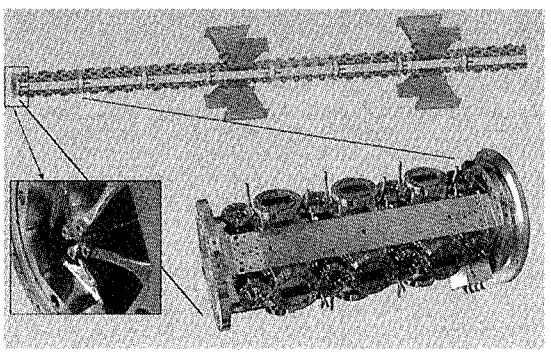


Fig. 2 IPHI RFQ.

(4) RFQ Beam Dynamics

In order to ensure the required 125 mA, a current of 130 mA is simulated in the RFQ. The input normalized rms emittance is 0.25 π mm mrad at 95 keV. These values are in agreement with the present performance of SILHI [4], the French ECR source, and the LEDA ECR source [5]. Table 2 shows the main results of simulation performed with the code TOUTATIS [6]. The output phase space distribution is plotted in Fig. 3.

Table 1 Main IFMIF RFQ parameters.

Parameters	Values
Length	12.482 m
Frequency	175 MHz
Voltage	130 → 101.2 kV
Mean aperture (R_0)	6.41 → 5.16 mm
Modulation (m)	1. → 1.6
Synchronous phase (Φ_s)	-90° → -40°
Peak field	1.8 Kp
Copper power (+20%)	683.9 kW
Beam power	613.1 kW
Total power	1297 kW

Table 2 Results of the IFMIF RFQ simulation.

Parameters	Values
Transmission	98.5%
Output X transverse emittance	0.249 π.mm.mrad
Output Y transverse emittance	0.251 π.mm.mrad
Output longitudinal emittance	0.195 deg.MeV

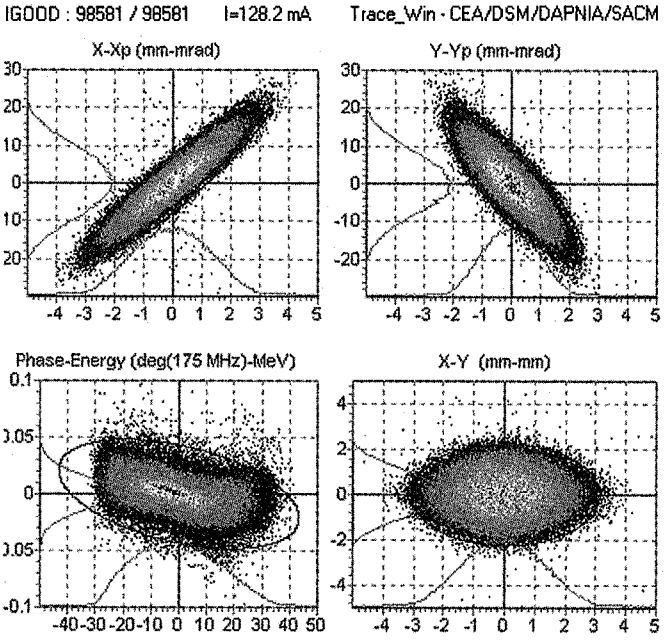


Fig. 3 IFMIF RFQ output phase space.

(5) DTL Design

The 175 MHz DTL cavities have been designed with the GENDTL code [7]. The DTL section is comprised of 10 tanks. Each cell has been computed with SUPERFISH [8]. Main parameters (phase, field law) are computed by a step-by-step transport of a reference particle, and are summarized in Table 3.

Table 3 Main parameters of IFMIF DTLs.

Parameters	Values
Total Length (10 tanks)	31.8m
Max. Z_sT^2	39.53 MΩ/m
Maximum quad. Gradient	74 T/m
Synchronous phase (Φ_s)	-45°; -35°
Peak field	1.3 Kp
Copper power (+20%)	1907.1 kW
Beam power	4550 kW
Total power	6.46 MW

(6) Beam Dynamics

Fig. 4 shows the behavior of x and phase beam distributions along the DTL tanks. No emittance growth and no loss are observed. The output current of 127 mA fills the IFMIF requirement, with a small margin.

(7) Error Studies

(7.1) Strategy

The study is decoupled, with each defect first being studied separately. For example, the sensitivity on modulation error over a range [0→M] was tested, the range [0→M] being cut into 10 steps: ten per cent of M, twenty per cent of M, ... For each step, 100 linacs are generated with a randomly distributed error. The longitudinal step in error is based on the machining step (IPHI RFQ) for each drawing. Once this first

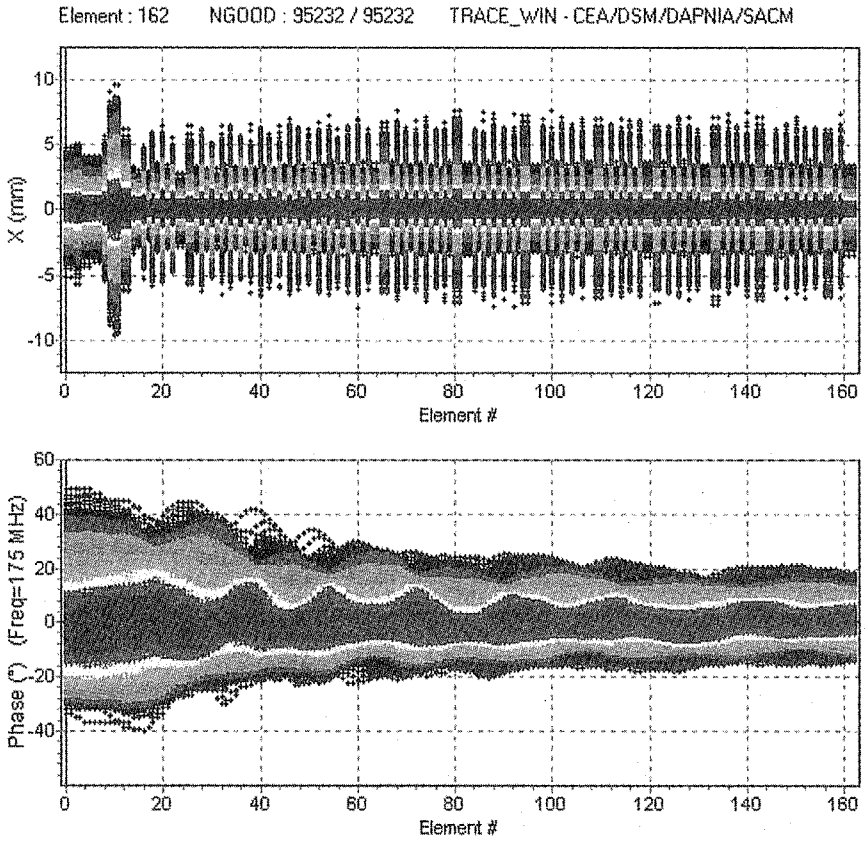


Fig. 4 X and phase beam distributions along DTL.

study is performed, it is then possible to extract from the simulation the maximum error amplitude for each defect.

Finally, all errors are combined with a maximum excursion, which had been determined in the first study. The combination is also cut into ten stages of 100 linacs. At the end, it is easy to determine the required threshold for each defect.

The GUI for error studies is TraceWin [9]. The user can easily choose error types: phase, voltage, field, segment or tank tilt, and misalignment, etc. Calculations are distributed on several computers via a client/server architecture (multi-parameter scheme) [10]. Ten PCs have been used for two weeks for the IFMIF linac study.

(7.2) Results

For the RFQ cavity, the machining defects and misalignments have been studied separately. The machining defects are simulated with incorrect transverse and longitudinal curvatures. Misalignments are segment tilts, rotations, and shifts. Fig. 5 shows emittance and loss growth with respect to a fraction of the maximum machining defect (100 μm). It can be noted that below 60 μm, the performance is stable. The study for segment misalignments shows than a 120 μm error is acceptable. The combined study decreases the tolerances to 50 μm for machining and 100 μm for misalignment.

The DTL and matching line defects are quadrupole errors (displacement and rotation in three directions, and gradients). To correct beam misalignment, a pair of steering coils are placed into the last tube of each tank and a pair of Beam Position Monitors (BPM) are placed between tanks. A first errors study gives acceptable tolerances of 100 μm for displacement, 0.25° for rotation and 1% for the gradient.

Once each component has been studied, the whole linac is simulated. Figs. 6 and 7 show the beam size for 100 runs of 10,000 macro particles without and with combined errors and corrections. The red line corresponds to 90% of the beam; the blue to 99%, etc. The black line includes all the beams. Fig. 8 shows

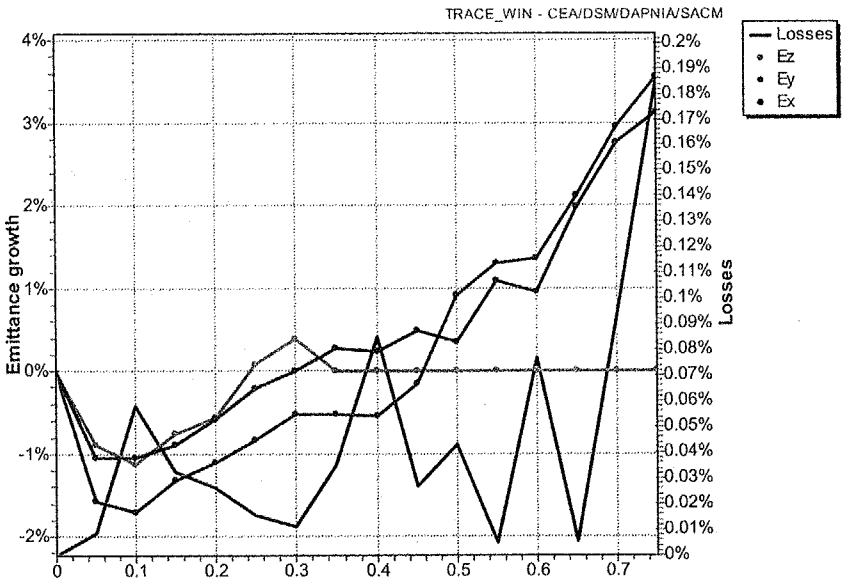


Fig. 5 Emittance and loss growth in respect to machining defect (fraction of 100 μm).

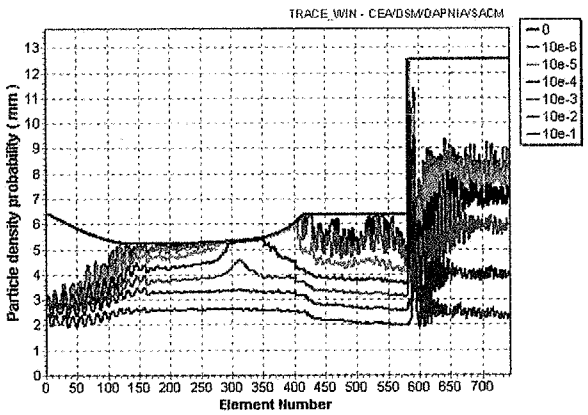


Fig. 6 Beam size along the accelerator without errors.

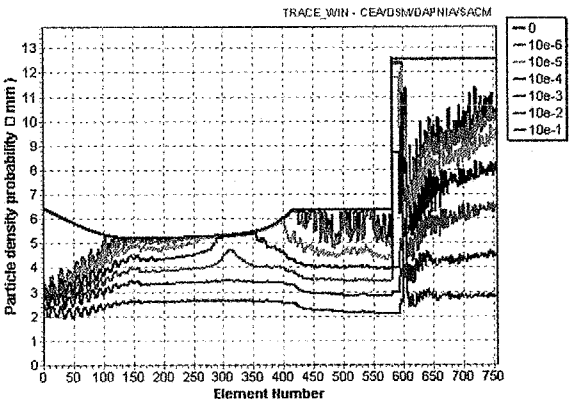
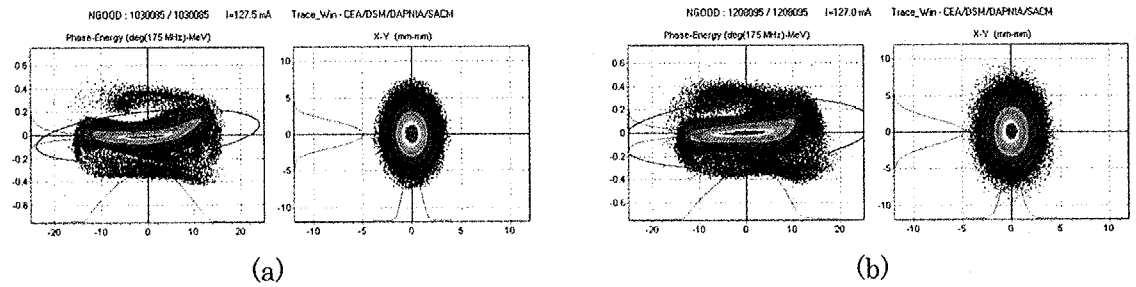


Fig. 7 Beam size along the accelerator with errors.



the output beam distribution in phase space for the two cases.

The rms emittance growth is 50% in the transverse plane and 14% in the longitudinal plane. No extra loss is observed because of the errors, due to the efficiency of the correction scheme.

(8) Conclusions and Perspective

The beam dynamics study showed no special concerns. The reference design fulfils the IFMIF requirements [11]. With errors and corrections, the transmission is expected to reach 98%. No loss occurs in the DTL section. This error study does not include input beam errors (beam mismatch, etc.), RFQ field errors, phase errors in the DTL, or BPM readout errors.

A new design is under study, using two Diacrodes in the last four DTL tanks. One RF system per linac is then saved. Overall efficiency is better, and error studies are underway (there are fewer BPM and steering coils). The results will be available before the end of 2002 and will also include all the above-mentioned error analyses (RFQ field, phase, BPM errors).

References

[1] IFMIF international team, "IFMIF key element technology phase, interim report", JAERI-Tech 2002-22.

[2] R. Duperrier, "High intensity beams dynamics in RFQs", Ph. D. thesis n°6194, Orsay, July 2000.

[3] L. Young, "Segmented Resonant Coupled RFQ", proceeding PAC 1993, Washington, D.C..

[4] P.-Y. Beauvais & al., "Status Report on the Saclay High Intensity Proton Injector Project (IPHI), EPAC 2000 Proceedings.

[5] H. Vernon Smith, Jr., J. D. Schneider, and R. Sheffield, "Low-energy demonstration accelerator (LEDA) test results and plans", PAC01, Chicago, pp 3296-3298.

[6] R. Duperrier, "TOUTATIS, a radio frequency quadrupole code", Phys. Rev. Special Topics Acc. & Beams, december 2000.

[7] D. Uriot, N. Pichoff, "GENDTL", internal report CEA/DSM/DAPNIA/SEA/2000/46.

[8] J. Billen, L. Young, "Poisson Superfish", Los Alamos internal report LA-UR-96-1834 (1996).

[9] D. Uriot, N. Pichoff, "TraceWin, Documentation", internal report CEA/DSM/DAPNIA/SEA/2000/45.

[10] R. Duperrier, D. Uriot, N. Pichoff, "Cluster pour études d'erreurs de dynamique faisceau", internal report CEA/DSM/DAPNIA/SACM/2002/21.

[11] R. A. Jameson, "IFMIF RFQ DESIGN STATUS AND RELATED WORK", IFMIF Memorandum RAJ-6-Dec-2000. Summary of Saclay RFQ design, acceptance of feasible parameters for Kilpatrick Limit = 1.8 and transverse rms input emittance = 0.25 mm.mrad. This design also meets the CDA transmission requirement of ≥90%.

3.1.19 AC21A-EU : Radio Frequency System

(1) Brief Task Description

Development and testing of a 1 MW RF system was identified as the highest impact development item. Existing operating experience was only for short periods, 1 to 8 hours. The RF amplifier power baseline of 1 MW ensures that competitive bids could be obtained from two manufacturers. Accomplishing a full-scale test of the first system would allow the remaining large procurement to be on a fixed-price basis.

This task consists of collecting information and tracking progress on the THALES Diacrode TH628 [1]. The main goal remained the 1000 h RF test, and required an upgrade of the existing test stand. The test was done using the available 200 MHz – 1 MW Diacrode, knowing that a higher frequency is generally harder to develop. This existing Dacrode could achieve the requirement without the expense of developing and buying a 175 MHz Diacrode [2].

Contributors

Name	Party	Institute	E-mail address
R. Ferdinand	EU-FRANCE	CEA-Saclay	rferdinand@cea.fr
E. Margoto	EU-FRANCE	THALES Electron devices	Eric.margoto@thales-electrondevices.com

(2) Introduction

Each IFMIF accelerator will require 11 high-power RF stations (22 total). Each station will provide 1 MW of cw RF power at 175 MHz. Together, they will be required to provide a world record level of average RF power.

The size of the RF power system makes it a major component of the IFMIF capital cost. The RF power system will also be a primary contributor to the annual operating cost. First, it dominates IFMIF electricity consumption (>40 MWe for both accelerators). Second, because several of the major RF components have limited lifetime (e.g., 10,000 hour expected lifetime for tetrode power amplifier tubes, 20,000 h expected for RF windows). The annual cost of component replacement and refurbishment will be comparable to other major elements of the operating cost.

Because all 11 RF power stations must be working for an accelerator to operate, it follows that the reliability, availability and maintainability of the individual RF power stations will be of critical importance to the achievement of IFMIF's overall availability goals. However, it is generally recognized that existing operating experience with tetrode-based RF power systems is not sufficient to provide a high level of confidence in the reliability and maintainability of RF power stations of the required power and frequency, operating in cw mode.

Validation of the design performance, reliability and maintainability of the RF power technology selected for IFMIF is a key objective. A secondary objective is the early identification of potential design improvements that will enhance the ultimate performance and availability of the IFMIF RF power system. Another objective is to reduce the cost of the RF power system by achieving a firm basis for fixing the design early in the project.

The RF tubes needed for the IFMIF accelerator are required to work at 175 MHz with 1.0 MW cw output power. Although there was no tube on the market with proved ability to provide such performances, the development work was underway and the achievement of a long test was needed to demonstrate the operational feasibility of the IFMIF RF design.

Existing operating experience is for short periods (1-8 hours). Therefore a test lasting 100 – 1000 hours would represent a decisive stage in validation of the proposed IFMIF design.

Accomplishing a full-scale test of the first system would also allow the remaining large procurement to be on a fixed-price basis.

IFMIF requirements imply a long test to ensure the quality of the design. A test of 1000 h duration is long enough to give confidence about the probable component lifetime and availability.

(3) Scope of the Contract

Thales Electron Devices has developed a new kind of gridded tubes called the Diacrode which can overcome the limitations of the conventional tetrode, mainly the RF losses. As a result, it is the first tube allowing 1 MW of cw RF power at the IFMIF frequency (175 MHz).

The scope of the contract was to assess the feasibility of an RF tube operating at relevant IFMIF conditions (175-200 MHz, 1 MW, cw). The Diacrode TH628 has been tested on an RF cavity designed also by Thales Electron Device, the cavity and the diacrode being a whole assembly.

The activities of the contract were divided into three phases. The contract was placed initially for the first phase.

First phase

Assemble the needed equipment for the test programs and install the RF sources in the test facility.

Perform operability tests, which include:

- Operation of the RF source in the range 175 MHz-200 MHz (175 MHz -0 MHz/+25 MHz), knowing that the RF losses are the main loss, and are proportional to the power 5/2 of the frequency. This frequency shift used for the test provides a safety margin in the results.
- Operation of the RF source at 1 MW ± 150 kW at 175 MHz or 900 kW ± 100 kW at 200 MHz. (Demonstration of 1 MW cw output power into a matched load.)
- Determination of the maximum RF power output and power transmission capabilities (subject to operating thermal, mechanical and electrical loads)
- Determination of system instabilities,
- Report on intermittent HV arcing in RF system, causing accelerator system shutdown.

Provide intermediate and final reports on the various phases of the specified testing.

Second phase

Perform lifetime 89 RF h test (Demonstration of continuous operation for 89 RF h at 1 MW level, cw).

Third phase

Perform lifetime 941 RF h test (Demonstration of discontinuous operation at 1 MW level, cw, for 941 RF h or up to first tube/test stand failure. Continuous operating time for each phase had to be longer than 60 h. This provided initial RAMI (Reliability, Availability, Maintainability, and Inspectability) and lifetime information. Provide a record of the maximum output RF in cw operation.)

(4) Results

The first phase was fully achieved and the first intermediate report was submitted on 26 February 2002. The test bench was modified and the operability tests were performed, reaching the full output RF power of 1030 kW.

In the second phase continuous operation at 1 MW level for 89 RF h was demonstrated. (Second intermediate report submitted on 16 April 2002.)

The third phase consisted in 12 continuous runs carried out for periods ranging from 65 h to 220 h. The conditions selected to make this test were the best ones, the cathode being cycled at each restart.

The output RF power was for most of the time in the range 1010 – 1030 kW with a few periods in the range 980 – 1050 kW. It should be noted that most of the power supplies were not regulated; therefore the RF output power was sensitive to the variation of the main supply power.

The screen grid rectifier with its crowbar was very sensitive to parasitic signals that can fire it without other reason.

Adding the second and third phases, the duration of the tests was 1061 hours. The Diacrode tube was operating at full power for 1047 h and was stopped 18 times for faults, for a total shutdown period of 14 h (availability of 98.7%).

Most of the faults were due to:

i. screen grid (10 of these)
ii. other equipment of the test facility (8 of these).

Therefore about 95% of the faults were not due to the tube. After each trip-off the tube could be restarted immediately without any difficulty and did not show any sign of degradation. None of the faults seems to have caused any internal damage to the tube. (Figs. 1 and 2)

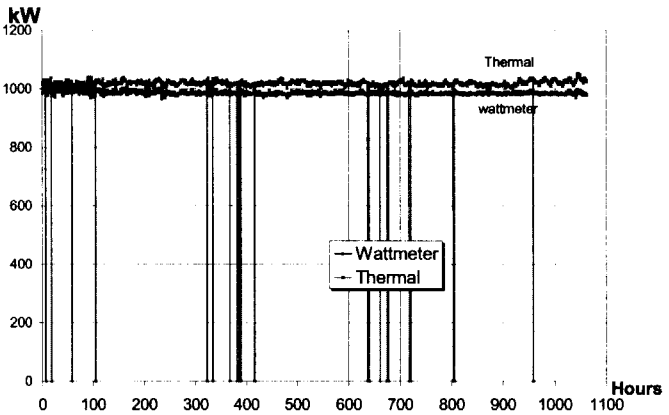


Fig. 1 RF output power DIACRODE S/N 00102.

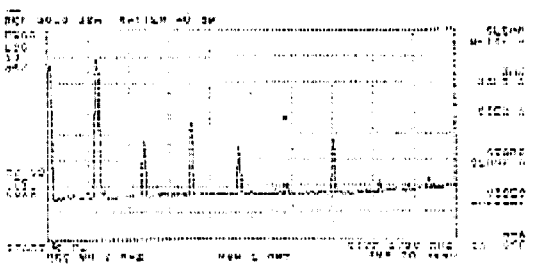


Fig. 2 Output spectrum on a calibrated probe.

(5) Conclusion

The conditions selected for this test were the best possible. The cathode was cycled at each restart. The tube was cycled in RF and temperature over short (65 h) and long periods (220 h).

The Diacrode has shown the capability to run at 200 MHz at an output power over 1000 kW with a remarkably stable operating point. This long test of 1047 h demonstrated the great improvement brought by the new design of a power gridded tube and the feasibility of an RF tube in IFMIF-relevant conditions (175-200 MHz, 1MW, cw).

In conclusion, the tests specified in the contract were successful and the Diacrode tube has shown the capability to operate at IFMIF conditions (200 MHz – 1 MW - cw) with a remarkably stable operating point.

The final report was submitted by Thales on 22 July 2002, well in advance of the contract completion date (31 October 2002).

There is at least one tube manufacturer that can provide a tube meeting the IFMIF accelerator requirements.

Thales has and may again provide cost evaluations for the IFMF program.

(6) Pulsed operation, phase and amplitude drive modulation

Closed loop control of the RF field phase and amplitude in the accelerating structures will be accomplished by drive modulation of the Diacrode. Information on the phase and amplitude modulation characteristics of the Diacrode, such as linearity, bandwidth and freedom from "glitches" (regions of the modulation transfer curves where the tube might break into oscillation or exhibit infinite gain) were required by LANL; courtesy of John Lyles, this test information has been collected and documented [3].

References

[1] EFDA Executive summary, Study contract FU 05 CT 2001 – 00135, (EFDA/00-926).
[2] THALES Electron device, IFMIF tests final report, RP 511.02.049 ChR/pv, July 15, 2002.
[3] IFMIF Memorandum IFMIF/RF/RAJ-20020805, THALES Diacrode Modulation Tests for LANL.

3.1.20 AC21B-JA : RF Power Tube Durability Test

(1) Brief Task Description

The RF power required to accelerate the beam for the IFMIF accelerator is provided by a set of RF power source modules, each of which employs a high power tube as the final amplifier to supply 175 MHz, 1 MW cw power [1]. A performance test of such a high power tube system, including multi-hour operation, was planned at the beginning of the KEP; however, performance tests using the Thales Diacrode (TH628)[2] were proposed and started as a European activity. The objective of this task was shifted to the design of the RF power source module to improve the stability and lifetime by evaluating the applicability of the solid-state power amplifier system as the intermediate power amplification stage. As the basic concept of using the solid-state power amplifier was already applied in the conceptual design study phase, the present study mainly focuses on revision of the design using the up-to-date information on the amplifier system components.

Contributors

Name	Party	Institute	E-mail address
M. Sugimoto	Japan	JAERI	sugimoto@ifmif.tokai.jaerigo.jp
S. Moriyama	Japan	JAERI	moriyama@naka.jaeri.go.jp
T. Fujii	Japan	JAERI	fujii@naka.jaeri.go.jp
T. Imai	Japan	JAERI	imai@naka.jaeri.go.jp

(2) Introduction

The reference design of the IFMIF accelerator RF system employed a power tube as the final amplifier to satisfy the power requirement of the RF power source module, 175 MHz /1 MW cw. Two candidate tubes, Thales Diacrode (TH628) and CPI Eimac tetrode (4CM2500KG) were nominated [1]. The requirements and the main parameters of the RF system derived from the conceptual design report are listed in Table 1.

Table 1 Requirements for RF power system in reference design.

Item	Specification
Frequency	175MHz
Operation mode	CW
Total power	10.3 MW (8.8 MW for Cu losses)
Maximum output power	1 MW per module
Total number of units	12 (3 for RFQ, 8 for DTL, 1 for HEBT) or 11 (same as above except no unit for HEBT)
Stability	<1% for amplitude; ± 1° for phase
Lifetime	2,156 hours (MTBF of module unit) 10,000 hours (MTBF of power tube)
Availability	95.5% (for total RF system) 99.6% (per RF power source module)
Reliability	42.3% (for total RF system) 92.8% (per RF power source module)

The availability is estimated by assuming that most components are replaced annually under the preventive maintenance policy. The block diagram of the RF power source module is shown in Fig.1. As the RF system is the major part of the accelerator system cost, and its reliability is critical for achieving the required availability of the accelerator system, >88 %, it is important to optimize the RF system design and to verify the performance of RF components, their stability, and lifetime. For the Diacrode tube, a long-run test with 200 MHz, 1MW cw output has been carried out as a European KEP activity and that tube is the primary candidate for the final amplifier. Thus the design study of the driver amplifier starts with the expected specification parameters for the Diacrode and the requirements can be derived to satisfy the

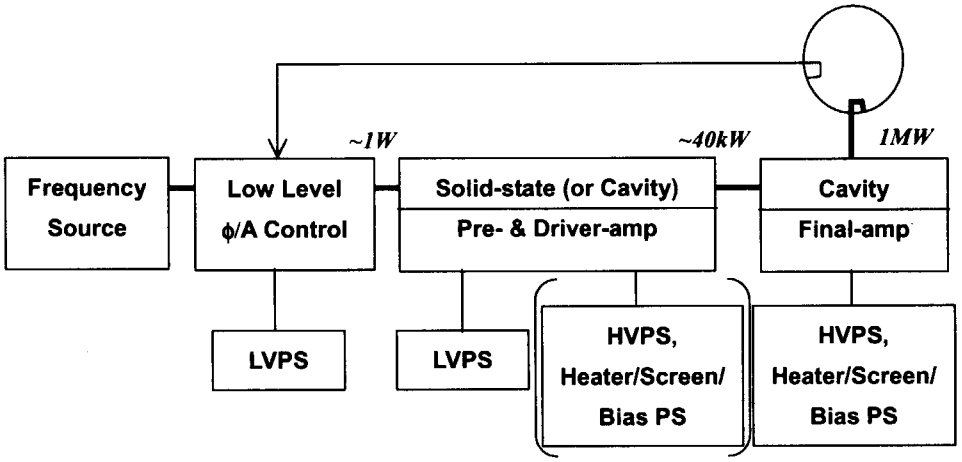


Fig. 1 Schematic diagram of IFMIF RF power source module taking into account of replacement of the driver cavity amplifier by solid-state amplifier.

input power condition to the Diacrode. In the reference conceptual design, the solid-state amplifier module with 1.5 kW output was employed and 3 kW input power for intermediate cavity amplifier with 50 kW output power was provided by combining the output power from two such modules. It is possible to improve the availability and reliability at the pre- and driver-amplifier components by replacing them with a solid sate power source module with ~40 kW cw output. The basic technology of such a power source module at ~200 MHz is available and used as the VHF television transmitter system, so the expected improvement by replacement of the intermediate amplifier with a solid-state amplifier module is investigated.

(3) Requirements for Driver Amplifier

Based on the expected performance data of the Diacrode given in Table 2, the requirement for the RF driver amplifier is derived as shown in Table 3. The differences of cascading structure types (single stage of solid-state amplifier vs. pre-driver of solid-state amplifier and intermediate driver of tetrode amplifier) affect the layout and the space occupied by the power source module. However it is assumed that either structure can be installed in the space available for the single RF module in the RF power station room. Generally, the bandwidth requirement, ~2% [3], will be achieved with little difficulty, especially for the case of single stage solid state amplifier.

Table 2 Assumed performance parameters of Diacrode.

Item	Specification
Output power	1,000 kW
Input power	32 kW
Gain	14.8 dB
Anode voltage / current	16 kV / 96 A
Screen- / control-grid voltage	1.6 kV / -0.33 kV

Table 3 Requirement of driver amplifier system.

Item	Specification
Output power	40~50 kW
Gain (Input power)	46 ~ 47 dB (1 W)
Cascading structure types: 1) Single stage of solid-state amplifier 2) Pre-driver of solid-state amplifier and intermediate driver of tetrode amplifier	Output power level: 1) >40 kW 2) ~2 kW at solid-state amp and ~50 kW at tetrode output
Bandwidth	±4MHz (~2% of operating frequency *)
Impedance	50 Ω (typ.)

*) Based on the typical operation scheme used in IFMIF (see Ref. 3)

The basic scheme of the high power solid state amplifier system is shown in Fig. 2, and the essential component is a power amplifier unit with output power of ~1 kW to be combined to the final required output power. The total number of power amplifier units needs to take into account the loss at distribution and combination of the input and output power respectively. The

margin of power for derating the full performance of the power transistors is also necessary to maintain the specified power condition during the long operating period. Practically, a margin of 0.4 dB (~10%) is required for each combining step. As a result of this criterion ~49 units (40 x 1.1^2) are required to achieve with two combining steps or ~54 units (40 x 1.1^3) for three combining steps, by assuming 1 kW power per unit. Usually the power combining at the higher power level can be achieved by the hybrid (2-part combiner), so that the practical way to obtain the 40 kW is three combining steps: (i) 7 units to make 6 kW output; (ii) combining four outputs of (i) to make 22 kW output; and (iii) providing the final 40 kW as the sum of two outputs of (ii). Figure 3 shows the schematic diagram of the above module structure.

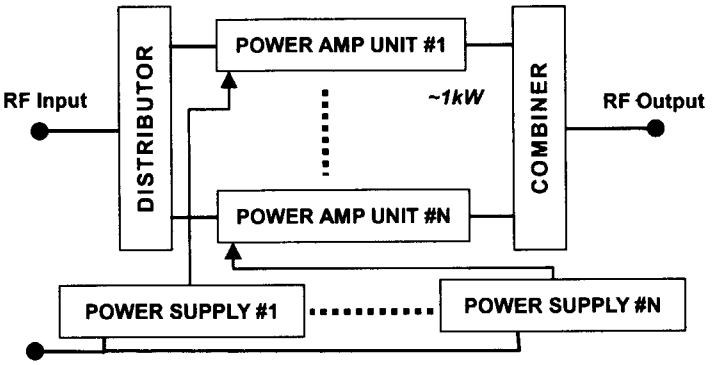


Fig. 2 Generic structure of solid state power amplifier system.

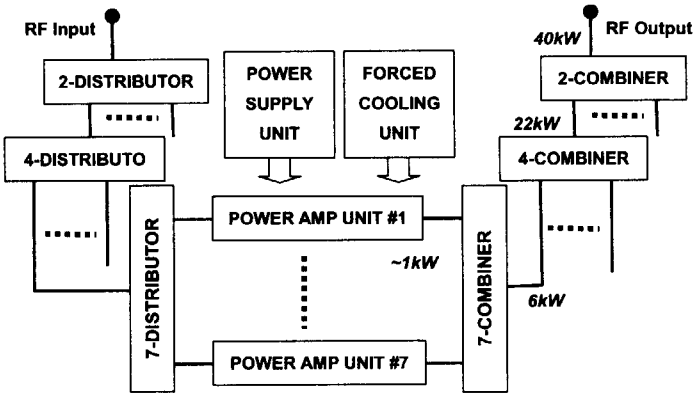


Fig. 3 Schematic diagram of 40kW solid state driver amplifier module.

The effect on the availability and reliability to the RF system due to the replacement of the tube-based driver by the solid state driver is estimated by using a model similar to that employed in the CDA report. Figure 4 shows the RAM model of the RF system, which includes the 11 RF power source units for RFQ and DTL, and the breakdown by major components in each RF power source unit. The expected improvement in reliability is marginal because it is already very good, even in the original RF system (306 hours MTBF increases to 345 hours). On the other hand, the availability is significantly improved due to the much easier replacement of a solid state driver power amplifier than replacement of a tube and its cavity.

(4) Amplifier Design

As shown in Fig. 2, the driver amplifier module consists of several power units, each of which consists of a number of power transistors with 100 W or more output. The choice of the transistor is of primary importance to design of the unit, and the output power combination method is critical to minimizing the loss of power and protecting during off-normal conditions. The cooling scheme is also important to achieve good stability of the output power. Installation of the control and power supply units must fit into the given space for each RF power source unit.

(a) Power transistor

The most important component of the solid-state amplifier system is the power transistor. Two commercially available MOS FETs (as of Oct. 2002) with capability of producing >100 W cw output are listed in Table 4 [4]. These transistors have similar characteristics, except that the gain at 200 W output level and the drain efficiency for Toshiba 2SK1310A are superior, whereas the output power per transistor for SD2932 is larger. The merits of MOS FET are: (i) high gain; (ii) wide safe operating area; (iii) no thermal runaway; (iv) large tolerance for VSWR; (v) ease of combining parallel units; and (vi) simplified bias circuit.

Table 4 Specifications of power MOS FET for solid-state power amplifier for IFMIF [4].

(October, 2002)

	Unit	2SK1310A+	SD2932+
Make		Toshiba	STMicroelectronics
Drain Source Voltage	V	100	125
Gate Source Voltage	V	± 20	± 20
Drain Current	A	12	40
Power Dissipation	W	250	500
Output Power @ 175 MHz	W	200	> 300
Gain @ 200 W (Input Power)	dB (W)	17.0 * (4.0)	16.2 (4.8) [or 15.9 (7.8) **]
Efficiency @ 200 W	%	70 *	50 [or 62 **]

*) Data given at 230 MHz

**) At 300 W output power

+) Both are packaged as common source configuration and push-pull operation with V_{DD}=50 V.

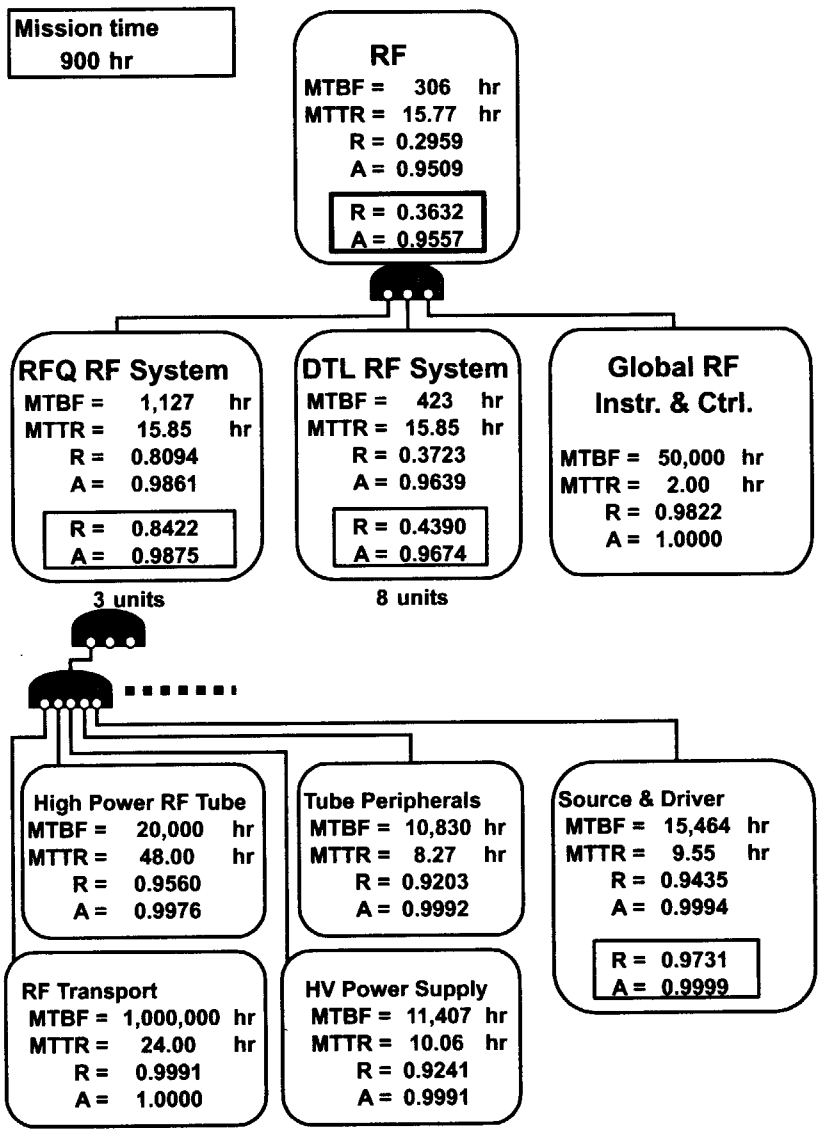


Fig. 4 RAM model of the IFMIF accelerator RF module.

(b) Power combiner

The isolator to protect against a change of load impedance is inserted before combining the output power from each pair of power transistors. The power combination can be achieved by using the simple impedance transform method.

(c) Cooling unit

The cooling requirement depends on the total conversion efficiency from AC input to RF output and the density of the packaging of the units. For the commercial broadcast transmitter, a forced-air cooling method is employed to avoid the problems related to maintenance of a liquid cooling system. For the IFMIF RF system, water cooling is possible because the cooling water system is already available.

(d) Control unit

Local control units are recommended to maintain the output power level, except for the overall RF low level control system. This is required to detect malfunctions of the amplifier module.

(e) Power supply unit

A DC power supply for V_{DD} (50 V) is required and a ~50 A switching regulator PS is available. It is recommended to use one PS unit for each power unit for easy maintenance, even though it is more expensive.

(f) Design base

The existing component design for the broadcast transmitter system is fully utilized to minimize the design effort. The derated operation is favorable for long lifetime; however, there is a large margin in the commercial design and the reduction of the margin, e.g. number of 1kW solid-state RF power modules per unit, is possible under the assumed accelerator maintenance scheme.

(5) Discussion and Conclusions

The employment of a solid state power source unit for the driver amplifier of the IFMIF RF power source module is favorable to improve the availability of the system, and it is feasible with the existing technical base. The design for commercial broadcast transmitter systems can be used for the 175 MHz, 40 kW cw output with a three-stage power combining scheme (1 kW – 6 kW– 22 kW – 40 kW). The major issue is the total cost of the initial equipment and the operation/maintenance. The cost of the solid state amplifier system is higher than the power tube system due to the power combining method using the multiple and redundant 1 kW units. This may be partly decreased by reducing the derating of the power transistor, but that would be at the expense of some loss of reliability. The space occupied by the solid state driver unit is another issue, however, the space can be reduced if a water cooling scheme is used instead of air cooling.

References

[1] M. Martone, (editor), IFMIF International Fusion Materials Irradiation Facility Conceptual Design Activity Final Report, ENEA Frascati Report, RT/ERG/FUS/96/11, November 1996.

[2] G. Clerc, J.P. Ichac, C. Robert, "A new generation of gridded tubes for higher power and higher frequencies", Proc. of 1997 Particle Accelerator Conf., Vancouver, B.C., Canada, May 12-16, 1997, p.2899.

[3] M.A. Chernogubovsky, M. Sugimoto, Nucl. Instr. and Methods A428, 263 (1999).

[4] The data sheet is available from WWW sites:
http://www.semicon.toshiba.co.jp/eng/prd/hfredevi/ft_hfredevi.html;
http://us.st.com/stonline/prodpres/discrete/rf/rf_mos.htm.

3.1.21 AC22A-JA : Test of the RF Window

(1) Brief Task Description

In the IFMIF design the RF window is a vacuum boundary in the transmission line from the RF generator (amplifier) to the RFQ and the DTL. The window has to transmit 500 kW cw at 175 MHz. The RF transmission line is assumed to be 152 mmϕ coaxial waveguide. A prototype RF window for the high power, long pulse test is designed and fabricated. In the design work, the RF characteristics and the mechanical stress are analyzed. The RF characteristics of the prototype window are checked experimentally by low power measurements.

Contributors

Name	Party	Institute	E-mail address
Shinichi Moriyama	Japan	JAERI	moriyama@naka.jaeri.go.jp
Sunao Maebara	Japan	JAERI	maebaras@fusion.naka.jaeri.go.jp
Tsuneyuki Fujii	Japan	JAERI	fijii@naka.jaeri.go.jp
Tsuyoshi Imai	Japan	JAERI	imai@naka.jaeri.go.jp
Masayoshi Sugimoto	Japan	JAERI	sugimoto@ifmif.tokai.jaeri.go.jp

(2) Introduction

The IFMIF accelerator is required to provide a 40 MeV, 250 mA deuteron beam to produce a neutron irradiation field similar to the environment at the first wall of a fusion reactor. Such a high current and high power beam can be delivered using an RF linear accelerator that will maintain good beam quality to minimize structure activation due to beam loss. The reference design employs two identical, parallel accelerators to deliver the required current. Each accelerator has the capability to handle up to 5 MW beam power. This beam power and power lost in the copper accelerator cavities need to be supplied by the RF system, which consist of many RF power source modules of 1 MW, 175 MHz output. The total power from each module is divided into 2 or 4 to be transmitted to the cavities. Each drive needs to have a window to isolate the cavity vacuum from the gas-filled transmission line.

The window consists of a ceramic disk and a coaxial waveguide with a water-cooling channel. The greatest temperature rises will appear on the ceramic disk, due to heating by dielectric loss, and on the inner conductor of the coaxial waveguide, due to heating by ohmic loss. The important design issues are the arrangement of a cooling channel for effective heat removal, and the structure to support the ceramic disk and accommodate the thermal stress.

The key part of the mechanical design is the structure of the inner conductor. In many high power rf accelerators with frequencies higher than 300 MHz, the required RF power is transmitted by rectangular waveguides from the generator to the window, and the inner conductor of the window on the generator side is mechanically free. In contrast, for IFMIF operating at 175 MHz, a large rectangular waveguide is not practical, and the transmission lines should be coaxial waveguides. The inner conductor at the window is rigidly connected to the transmission line and innovative methods are needed to minimize the thermal stress.

The key issue in the electrical design is an optimization of the shape of the inner surfaces of the coaxial waveguide near the ceramic disk. It is important to match the impedance and to avoid multipactoring discharges at the operational frequency and the transmitted power.

(3) Calculation and Design

In preliminary thermal stress analysis of the window, the conical shaped ceramic was used because the design base was the window for the ion cyclotron resonance heating (ICRH) system in nuclear fusion research. In the ICRH system, the window is used in the VSWR transmission line because of low coupling between the antenna and the plasma. The conical shape aids high voltage performance without serious multipactoring discharges for a wide range of RF voltages. The specification and the results of a thermal stress analysis for this window design are summarized in Tables 1 - 3. The results suggested that the stress at the connection between the ceramic and the inner conductor exceeds the allowable stress limit, when the

Table 1 The specifications and operational parameters for the window.

Inner diameter of the outer conductor of the coaxial wave guide	152mm
Characteristic impedance of the coaxial wave guide	50Ω
Shape of the ceramic	Cone
Input power	600kW
VSWR	~1
Frequency	175 MHz
Duty cycle	100 % (cw)
Duration	10 hours
Material	SUS304, cobar, Al_2O_3 / BeO
Pressure of the cooling water	< 10kg/cm^3

Table 2 Calculated maximum temperature of the ceramic (cooling water : 40 °C).

Flow rate of the cooling water	1m/sec	0.5m/sec
Al_2O_3	51.2°C	51.4°C
BeO	45.0°C	50.1°C

Table 3 Calculated thermal stress in the window.

	One end of coax. is free		Both ends constrained	
Flow rate of the cooling water	1m/sec	0.5m/sec	1m/sec	0.5m/sec
Al_2O_3	80MPa	80MPa	512MPa	514Mpa
BeO	80MPa	80MPa	474MPa	467Mpa

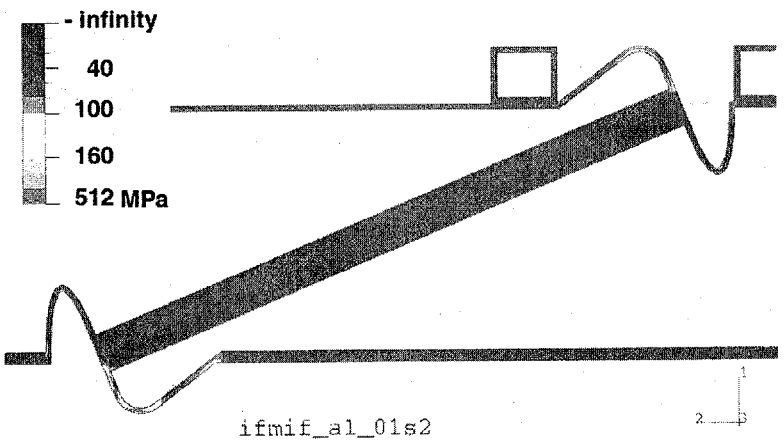


Fig. 1 Calculated thermal stress of the window with conical shaped ceramic design.

inner conductor is rigid as shown in Fig.1. It is concluded that a flexible part, such as a bellows, is needed for the inner conductor. This calculation showed that the selection of the ceramic has little effect, and we can use Al_2O_3 (which is easier to use than BeO).

After this preliminary analysis, we changed the shape of the ceramic from a cone to a disk, and the cooling channel was improved for more effective heat removal, especially at the junction of the ceramic and the outer conductor. The new design, shown in Fig. 2, is based on the E4268 window developed by KEK and Toshiba [1]. For operation at ~ 500 kW with VSWR ~ 1, the risk of breakdown is low even for the disk-shaped ceramic. In the new design, the energy loss and temperature increase of the ceramic were estimated to be 50 W and 20°C, respectively. The original E4268 made for operation at 509 and 324 MHz is

used with a rectangular waveguide, so the inner conductor is not rigid. However, for the IFMIF rigid connection to the coaxial transmission line, we need a flexible part in the inner conductor to reduce the thermal stress, even in the new design.

The reflection coefficient of the designed window is calculated by a FEM code and the result for S11 is shown in Fig. 3. It is low enough, -50.9 (VSWR< 1.006), not only at the IFMIF frequency of 175 MHz but also at 130 MHz and 200 MHz. High power RF sources for the later two frequencies can be used for testing if a 175 MHz power source is not immediately available. The probability of multipactoring discharges has been calculated using the Multipac code [2], and the result was low for transmitted power ~ 500 kW at 175 MHz.

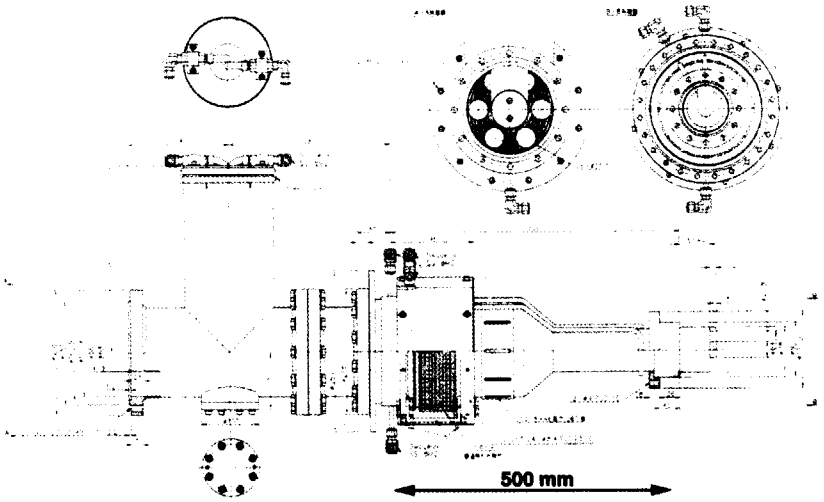


Fig. 2 A design of the coupler featuring a new disk-shaped window.

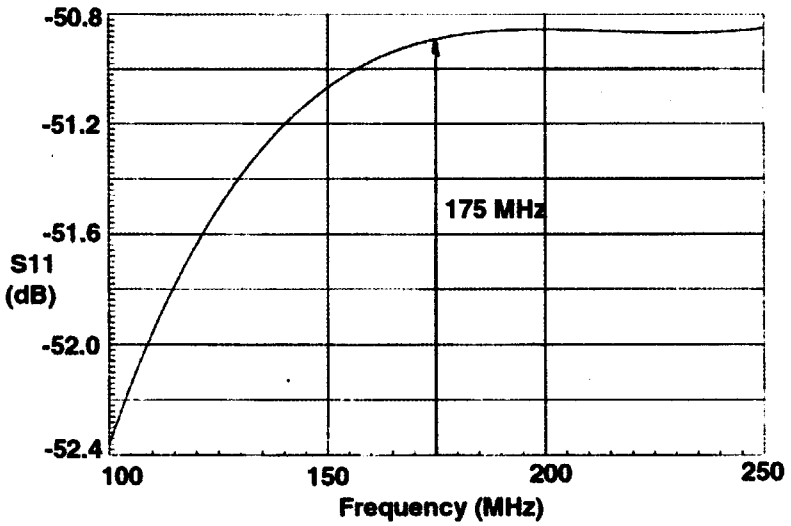


Fig. 3 The calculated reflection coefficient (plotted as S11) of the window shown in Fig. 4.

(4) Fabrication

The main parts of the prototype window, shown in Fig. 4, were fabricated for the long pulse, high power tests. The inner surface was plated with copper to reduce the ohmic loss and the ceramic disk was coated with TiN of 0.1 μm to reduce the electron yield in multipactoring discharges. The interface of the

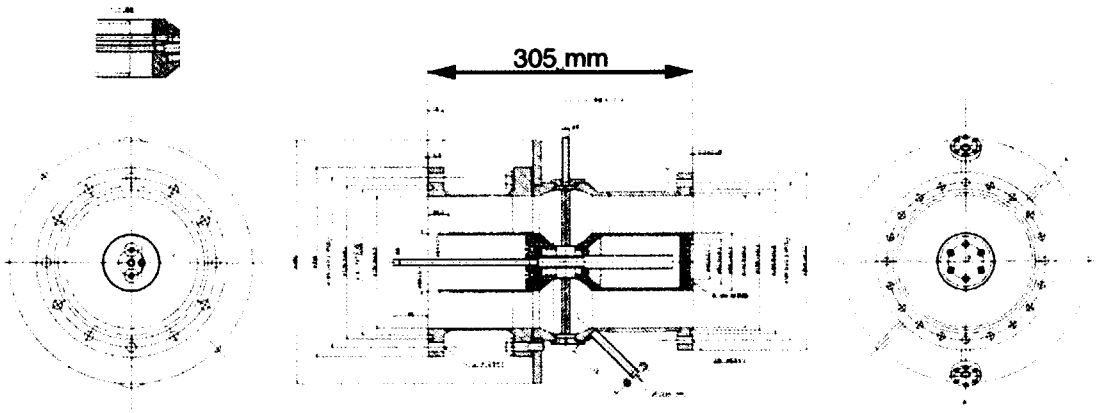


Fig. 4 Prototype window fabricated for low power measurement and high power test.

coaxial waveguide was designed to be compatible both for low power measurement and for future high power, long pulse tests. Prior to the high power test, we need to fabricate the T-junction and a quarter wave-length stub for the water inlet as shown in Fig.2, the drawing of the possible design of the whole coupler.

(5) Low Power Test

To evaluate the RF characteristics of the window, the measurements using a network analyzer are scheduled in February 2003. A pair of N-152D reducers are used on each side of the window. The insertion loss and the reflection coefficient will be measured from 130 MHz to 200 MHz, focusing on the 175 MHz frequency for the RFQ and the DTL. The relatively wide frequency range is for the possible high power tests in the JT-60 ICRF (ion cyclotron range of frequency) facility at 130MHz [3], or in the test stand for the Diacrode at 200 MHz. The results of the low power test are expected to be close to the calculations shown in Fig.3.

(6) Conclusions

An RF window was designed to feed continuous RF of 500 kW at 175 MHz to the RFQ and the DTL of IFMIF. A prototype of the RF window for high power, long pulse testing has been fabricated. The calculated RF characteristics and the mechanical stresses meet the requirements. The RF characteristic measurements will be carried out in February 2003 and agreement with the calculations is expected.

References

[1] Y. Kang., et al., Electro Magnetic Simulations and Properties of the Fundamental Power Couplers for the SNS Superconducting Cavities, Proc. of the 2001 particle Accelerator Conf., Chicago.

[2] P. Yla-Oijala, et al., MultiPac - Multipactoring Simulation Package with 2D FEM Field Solver, Proc. of the 10th Workshop on RF Superconductivity, Tsukuba, September 6-11, 2001.

[3] S. Moriyama, et al., Research and Development on the Ion Cyclotron Range of Frequency Heating System in JT-60U, Fusion Sci. and Tech., Vol.42, Nos.2/3, American Nuclear Society, 2002, pp.467-481.

3.1.22 AC41A-EU : Diagnostics for high power beams

(1) Brief Task Description

The task was completed in the framework of the CEA program on high-power particle accelerators supported by the IPHI demonstrator project [1,2]. This project is dedicated to high power beam production.

The IFMIF beam represents about 15 kW between the source and the RFQ, 625 kW before the DTL and 5 MW in the HEBT. The relatively low energy (40 MeV) means that this power is deposited in any interceptive diagnostics. New kinds of diagnostics are needed and have to be developed. Possibilities include intensified CCD analyses, spectroscopy analyses, pulsed wire scanner, laser analyses, etc. [3-8]

Contributors

Name	Party	Institute	E-mail address
R. Ferdinand	EU-FRANCE	CEA-Saclay	rferdinand@cea.fr
P. Ausset	EU-FRANCE	CEA-Saclay	ausset@ipno.in2p3.fr

(2) Introduction

Among the parameters that need to be measured for beam control, monitoring, and halo formation prevention, the transverse beam profiles are the most difficult to obtain. The large expected specific energy deposition in any interceptive monitor can lead to the destruction of the sensor and to an appreciable amount of radiation production. Therefore traditional multi-wires chambers and wire scanners are not usable under high duty factor pulsed-beam operation and obviously cannot be used for continuous beam operation.

A very attractive phenomenon that might prove useful is the production of visible light by the beam interaction with background or added gas. Transverse beam profiles of the SILHI ECR source have been measured using this phenomenon. However, several difficulties emerge in explaining the different shapes between the transverse beam profiles deduced from the elementary observation of the emitted light by a CCD camera, a grid profiler (low duty cycle operation), and a residual gas profiler. More sophisticated measurements using the Doppler effect have been used to determine the energy and the spatial extension of the different components of the beam.

Wire scanners are also used under low duty factor pulsed beam operation. Experiments have been conducted on tungsten, tantalum, titanium and carbon wires intercepting a 5 MeV proton beam delivered by the tandem accelerator at the Institut de Physique Nucléaire d'Orsay. Transverse beam profiles have been deduced from back-scattered protons, X and γ emission, and electric current collected on the wires.

(3) Optical Measurement

In the LEBT the moderately relativistic protons interact strongly with the atoms of the residual gas which is mainly hydrogen (pressure 2x10-3 Pa). A blue light, visible to the human eye, is emitted by the de-excitation of these atoms. This light was first sensed with an intensified CCD camera working in the 200 to 820 nm range.

(3.1) Fluorescence Beam Profile Measurements (FBPM) Under CW and Pulsed Mode Operation

The experiments were carried under CW and pulsed mode operation in a diagnostics box, located after the two solenoids focusing the beam in the LEBT line. Gases including N, Ne, Ar, Kr, Xe were injected into this box, in addition to the residual gas. Two intensified 16-bit CCD cameras were installed perpendicularly to the axis of the beam, in order to measure vertical and horizontal beam profiles. Specific software performed the subtraction of the background signal (without beam) to improve the signal/noise ratio, and calculation of vertical and horizontal projection and peak fitting convolution were used. It was found:

- The proton beam is, as expected, cylindrical along the LEBT
- The intensity of the emitted light depends on the nature of the gas and increases proportionally to the pressure of the gas.
- Profiles obtained by FBPM have the same geometrical shape for all gases at the same pressure (after

normalization with respect to the amplitude of the profiles). The same result is obtained by a classical grid profiler working under pulsed mode operation.
Under pulsed mode operation, the widths of the profiles measured by FBPM are larger than the widths measured by a grid profiler (Fig. 1). The width and the difference decrease as the pressure increases.

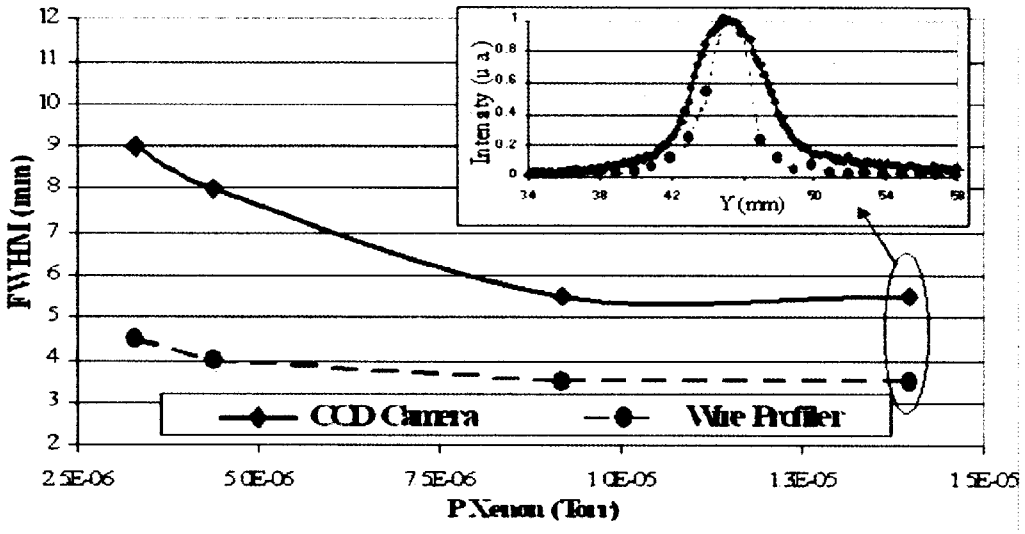


Fig. 1 Evolution of the widths of the profiles measured by a grid profiler and by FWHM with the pressure of the gas (Xenon).

(3.2) Spectroscopic Measurements

We replaced the horizontal CCD camera by a photomultiplier coupled to a scanning monochromator in order to analyze the emitted light spectrum. As expected, we found the well-known lines of the Balmer series. Previously [3], precise measurements were made and showed that the amplitude of each line is proportional to the intensity of the proton beam. The light spectrum of the other gases (N, Ar, Kr, Xe, Ne) were also recorded. Experiments were carried out with a laser absorption on specific lines of Ar (l= 811.5 nm) and Kr (811.3 nm) with the aim of measuring the transverse profiles of the beam.[3,5].

(4) Shifted Doppler fluorescence beam profile measurements

The existence of a halo surrounding the core of the beam measured by FBPM suggests that the light produced by the excited atoms of the gas does not result only from the incoming protons, but also from second step processes involved in the production of this light.

Explanation the intensity and the spatial extension of the light produced in the vessel requires consideration of several major physical processes which may contribute to the production of this light and to the broadening of the measured profiles:

- Possible delayed decay of excited atoms of the specific gas present in the vacuum vessel. (This phenomenon is well known in nitrogen.)
- Backscattered protons may also excite other atoms of the gas which lead to the production of light
- Inelastic collisions may produce electrons able in their turn to excite atoms of gas.
- Dissociation of molecules of H_2^+ and H_3^+ may occur and create excited atoms which become source of light. (Unfortunately these are produced by the source SILHI in addition to the protons.)

As we want to select only the light produced by the incoming protons delivered by the source at 95 keV, and accelerated by the RFQ, we turn to their high electronic capture cross section. A fraction of these protons capture an electron, producing an excited hydrogen atom. The typical Doppler shift effect of these very specific atoms in the frequency (or wavelength) domain will allow us to select their light

produced by de-excitation from the overall light in the vessel.

(4.1) Experimental Setup

The CCD Camera was installed in the focal plane of an imaging spectrograph equipped with a 900 gr/nm grating. The resolution was better than 0.1 nm at 500 nm. The experimental configuration was chosen to sufficiently shift (8 nm) the H_α line of the Balmer series of hydrogen.

The vertical beam profiles, according to the vertical slit orientation at the entrance of the monochromator, are deduced from the image transported to the CCD matrix of the camera.

In addition, due to the possible discrimination of the different components of the beam H^+, H_2^+ and H_3^+ because of their different Doppler shift wavelengths, this method potentially allows:

- Relative intensity measurement of the different species present in the beam.
- Measurements of the transverse profiles of the species, which contribute to the entire profile of the beam.
- Energy measurements of the different species and in particular their energy spread which is proportional to the width of the corresponding spectrum line.

(4.2) Experimental results

Identification of the different lines of the Balmer series of hydrogen was first recorded. Their corresponding Doppler shifts were checked. Second, the current in the solenoids was changed over a large range to vary the size of the beam. The full width half maximum (FWHM) of the (H_α) and its corresponding Doppler shift line H_+ component profiles were measured. A remarkable result is that the size of the halo surrounding the beam remains constant independent of the focusing conditions (Fig. 2).

The evolution of the profiles was also studied by varying the nature and the pressure of the gases introduced into the vessel: N, Ar, Kr, Xe, Ne and H. Adding gas to the vessel increases the light produced: for each component H_α, H^+, H_2^+, H_3^+ the fluorescence yield increases linearly with the pressure (up to 10^{-2} Pa), except for hydrogen. The curve shows saturation which may be attributed to an auto-absorption process, but this needs to be confirmed.

(4.3) Absorption techniques

Absorption techniques were tested using laser light. Different injected gases (krypton, argon with λ=811.5 nm) allow observation of a linear absorption with beam current and pressure. Nevertheless this technique did not give satisfactory results. As absorption was observed out of the beam, no direct profile measurement was possible. Structures inside the measurement were observed and were not clearly understood. Metastable trajectories out of the beam due to excitation by fast electrons (about 50 eV) and diffusion are probably the reason for the difficulties.

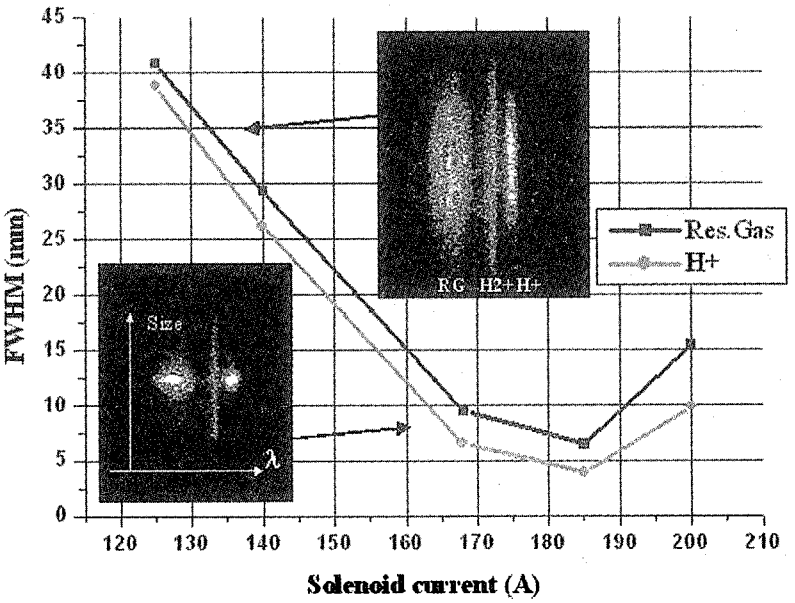


Fig. 2 FWHM of the H_α (residual gas) and its corresponding Doppler shifted line vs beam size (solenoid setting).

(5) Interceptive profile measurement methods

Accelerators are usually able to work under pulsed mode operation for machine commissioning and experimental operation. The beam average power reaches 15 kW at the entrance of the RFQ (95 keV) and 625 kW at the exit. Wire scanners are also usable under low duty factor pulsed beam operation.

(5.1) Slow Wire Scanner (SWS)

In this method, a wire is stepped in small increments through the beam. The profiles are obtained over many pulses by measuring the current flowing in the wire resulting from the secondary electrons emitted from the wire, subtracted from the protons collected by the wire. Heating of the wire is the major problem because of the large energy deposited by the beam in any intrusive sensor. A crude estimation of the attained temperature is given by solution of the heat equation: the pulse duration must remain below 300 μs and the repetition rate above 1 s in order to keep the peak temperature of a carbon fiber (30 μm diameter) below 1200 K in a 5 MeV, 100 mA, 320 mA/cm^2 proton beam. SWS are only usable under low duty factor operation.

In the case of slightly higher beam average power, the amplitude of the mechanical deformations increase and thermionic emission of electrons occurs which distorts the measurements of the true profiles. At higher beam average power and under CW mode operation any kind of fiber is destroyed.

(5.2) Fast Wire Scanner (FWS)

At high average power pulsed beam and under CW operation, the wire must go very quickly through the beam. It was found that the speed of the wire must then exceed 60 m/s to withstand the power of a CW, 5 MeV, 100 mA; 320 mA/cm^2 proton beam. Because of this high speed, a FWS is very difficult to design.

(6) Experiments with a wire scanner

Even under low duty-factor pulsed-beam, the heating of the wire of a SWS may bring out errors in the profile measurements, in particular because of the thermionic emission of electrons. In order to design a SWS, and to crosscheck the measurements of the current traditionally used in SWS, we looked for physical processes, the characteristics of which do not depend on the temperature.

Valid candidates are:

- The production of backscattered protons due to elastic collisions between the protons of the beam and the atoms of the wire.
- The production of γ (and X) rays due to the excitation or nuclear reaction of the nucleus caused by inelastic collisions between the accelerated protons and the atoms of the wire.

(6.1) Experimental Setup

Tests were carried out on the tandem accelerator at the "Institut de Physique Nucleaire d'Orsay" in a 5 MeV, 1 μA proton beam. A frame on which different wire samples were fixed can be translated through the vacuum vessel. The current flowing in the wire was measured by a current-to-voltage converter, and measuring the current of the beam with a Faraday cup.

The amplitude of the pulse delivered by the charge amplifier associated with the Si junction is proportional to the energy deposited by the backscattered protons. The transverse beam profiles are deduced by integrating the whole spectrum for each position of the wire. The same is done for the detection of the γ rays after detection with a NaI scintillator associated with a photo-multiplier. Finely, specific software was used to fit the measured profiles.

(6.2) Experimental Results

Wires of different materials and diameters were tested: W (ϕ= 100 μm and 500 μm), Ta (ϕ= 100 μm), Ti (ϕ= 125 μm, 500 μm), C (ϕ= 1 mm) and Ti wires. (ϕ= 125 μm, 500 μm).

It was first checked that the profiles measured with the different wires were similar and did not depend on the diameter of the wire. For example, the profiles deduced from the backscattered protons, the γ ray production and the current measured with the Ti wire are very similar.

The first experiments show very good agreement in the profiles measured with the different wires, independent of the physical processes involved in the measurements. The total error in the measurement of the width is on the order of 250 μm.

The profiles obtained are the results of 5 MeV particles, allowing the decorrelation of accelerated particles from background-ionized particles or non-accelerated particles coming through the RFQ. Halo measurement of real beams should be possible with this technique (providing sufficient sensibility).

(7) Conclusion

We developed specific tools for the measurement of the transverse profiles of high power proton beams:

- Traditional wire scanners work for low duty factor pulsed beam operation.
- Measurement of backscattered protons or γ-ray production are powerful tools to cross-check the measurement of the current in a wire in the temperature range of the wire below thermionic emission.
- Measurements by means of a wire scanner may also be cross-checked with Doppler fluorescence beam profile measurements.

Because of their non-destructive nature with respect to the beam, optical methods are very attractive for high power beam monitoring. We investigated and tested some specific optical diagnostics on the high intensity source SILHI:

- Direct fluorescence beam profile measurements under high average power beam pulsed mode and CW operation are valid for centroid beam position measurement. In addition, the qualitative estimate of the beam transverse profiles is possible.
- Fluorescence measurements on the Doppler shifted lines of the hydrogen Balmer series are very promising to determine the energy of the different components of the beam (H^+, H_2^+ and H_3^+). In addition, the energy spread of the beam is potentially measurable. Beam profile measurements are underway.

References

[1] "CEA-DSM-DAPNIA-SEA contribution to the IFMIF KEP phase. Step report – June 2001". DSM/DAPNIA/SEA 01/41, 35 pages.

[2] "CEA-DSM-DAPNIA-SEA contribution to the IFMIF KEP phase. Step report – June to December 2001". DSM/DAPNIA/SEA 02/09, 25 pages.

[3] B. Pottin et al., "Optical beam profiler for high current beams", EPAC 2000, Vienna, June 2000.

[4] D.Gardès et al., "Optical beam-profile monitoring developed for high intensity proton beam", presented at 14th International Symposium on Heavy Ion Inertial fusion, Moscow, May 2000. To be published in Laser and Particle Beams.

[5] B. Pottin, "Etude d'un Profileur Optique de Faisceaux Intense de Protons par Absorption Laser", These Université Paris XI, 18 Octobre 2001.

[6] P. Ausset, S. Bousson, D. Gardes, A.C. Mueller, B. Pottin, R. Gobin, G. Belyaev, I. Roudskoy, ""Transverse Beam Profile Measurements for High Power Proton Beams", EPAC 2002, La villette PARIS 2002, page 245.

[7] P. Ausset, S. Bousson, D. Gardès, A.C. Mueller, B. Pottin, R. Gobin, G. Belyaev, I. Roudskoy, "Optical Transverse Beam Profile Measurements for High Power Proton Beams", EPAC 2002, La villette PARIS 2002, page 1840.

[8] P. Ausset et al., "Beam diagnostics for high intensity accelerators", Workshop on utilisation and reliability of high power proton accelerators, Aix en Provence, France 22-24 November 1999. (N.E.A.).

3.1.23 AC41B-EU : Diagnostics for high power beams

(1) Brief Task Description

The IFMIF beam is a high power beam of D^+ ions in cw operation. For beam diagnostics the power deposition and possible activation are major concerns. Existing and new beam diagnostic devices have to be investigated and developed further. Emittance measurement devices, optical diagnostics with a CCD camera and other non-destructive methods have to be analyzed and tested. Diagnostic elements will be tested with beam in the ion source and LEBT region.

Contributors

Name	Party	Institute	E-mail address
H. Klein	EU	IAP	Horst.Klein@iap.uni-frankfurt.de
K. Volk	EU	IAP	K.Volk@iap.uni-frankfurt.de
J. Pozimski	EU	IAP	Pozimski@iap.uni-frankfurt.de
A. Jakob	EU	IAP	A.Jakob@iap.uni-frankfurt.de
O. Meusel	EU	IAP	O.Meusel@iap.uni-frankfurt.de

(2) Introduction

Beam diagnostics for IFMIF and especially the determination of the beam emittance using conventional destructive methods are difficult. The interaction between the ion beam and the measurement device produces a high amount of secondary particles which can influence the beam transport itself. Additionally, the power deposited on the emittance measurement device (for IFMIF up to 1 kW/mm^2) can lead to extensive heating of the detector itself and can destroy the device. Therefore a new conventional slit-grid emittance measurement device optimized for high power beams has been constructed, built, and tested. Additionally, the use of CCD camera measurements of the incident light emitted from interaction of beam ions with residual gas has been investigated for measurement of the spatial beam density distribution and for determination of the beam emittance.

(3) Slit-grid Emittance Measurement Device

(3.1) Detailed layout

A beam emittance measurement just behind the ion source [1] is a crucial need. Due to the high beam current (up to 200 mA at 100 keV) and the small beam radius, the thermal load on the slit is very high. Therefore a high power slit with an improved water cooling system was designed and used in the new device. Since the beam radius and angle behind the ion source are very small, a high spatial resolution is required. With the slit used, the spatial resolution of our device is 0.1 mm. The angle resolution is given by the grid wire distance divided by the slit-grid distance. The wire distance is fixed at 1 mm. As both feed-throughs are integrated in different vacuum chambers, by means of the distance between the two chambers, the angle resolution can be optimized. With a slit-grid distance of about 1 m an angle resolution of 1 mrad can be achieved. Table 1 summarizes the main parameters of our emittance measurement device.

Table 1 Parameters of the emittance measurement device.

Minimal beam diameter	~ 8 mm
Maximal beam diameter	~ 30 mm
Maximal beam current	+/- 200 mA, dc and pulsed
Increment	0.05 mm, ... 0.5 mm;
Slit height	0.1 – 0.2 mm
Measured displacement	+/- 30 mm
Thickness of wires	0.1 mm
Number of wires	60
Distance of wires	1 mm
Duty cycle	0.1 – 10 %
Pulse length	0.1 – 2 ms
Repetition rate	50 – 200 Hz

In order to measure the beam emittance of the Frankfurt proton/deuteron source, a new slit-grid device was ordered and fabricated by "PET". The measurement device was delivered, installed and tested using the ion source test stand for first calibration measurements. In Fig. 1 the different components of the device (feedthroughs

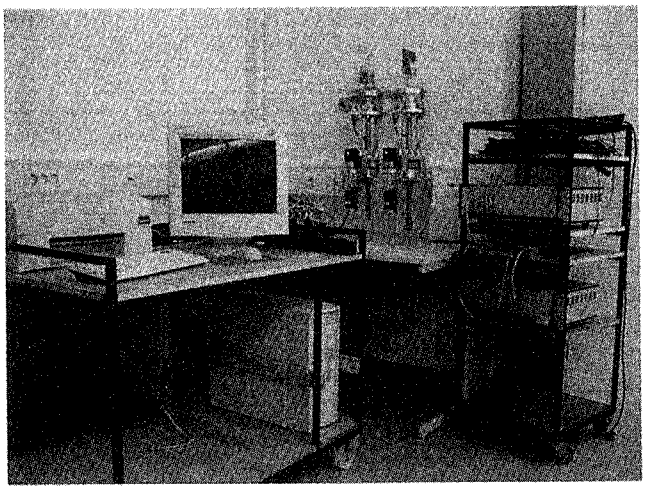


Fig. 1 Picture of the new high power emittance measurement device.

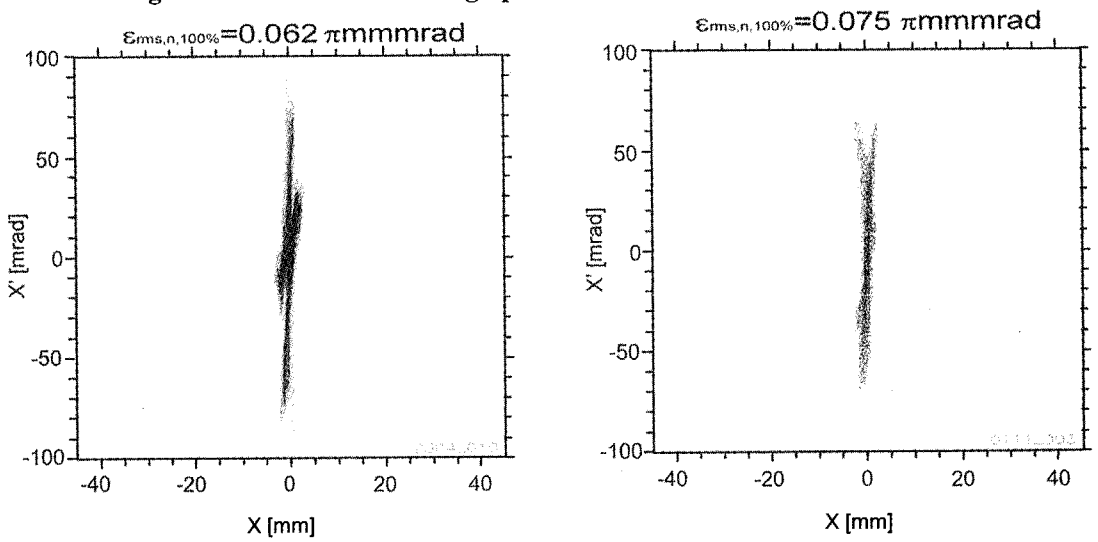


Fig. 2 Comparison between the results of the Allison emittance scanner and the new high power slit-grid emittance measurement device.

with slit and grid and the electronics) are shown.

Preliminary tests of the emittance measurement device were performed using a small ion source and two Gabor plasma lenses. The beam current was 10 mA of He^{1+} at an energy of 14 keV. Figure 2 shows the measured beam emittance behind the lenses. The normalized rms beam emittance was 0.06 π.mm.mrad.

(3.2) Conclusions

The new high power slit-grid emittance measurement device has been designed, built and successfully tested. Reference emittance measurements have been performed at low beam power (He^{+}, 10 mA, 14 keV). Comparison between the results obtained by the new high power device and the low power Allison-type emittance measurement devices shows good agreement.

(4) Non-destructive Beam Diagnostics

The determination of the beam emittance using conventional destructive methods suffers from two main disadvantages. The interaction between the ion beam and the measurement device produces a high amount of secondary particles which can influence the beam transport. In addition, the power deposited on the emittance measurement device (for IFMIF up to 1 kW/mm^2) can lead to extensive heating of the detector itself and can destroy the device. CCD camera measurements of the incident light emitted from interaction of beam ions with residual gas are commonly used for determination of the beam emittance

[2,3]. A compact low energy beam transport (LEBT) section was used to compare measurements using a conventional destructive Allison-type emittance scanner with the results gained from CCD camera measurements. The experimental set up is shown in Fig. 3.

A volume source was used to deliver 4.4 mA of He^+ at 11 keV. The solenoid (0.002 T/A; 360 A max.) was able to transport 3.7 mA of He^+ into the diagnostics chamber (85% transmission). In the diagnostic chamber a Faraday cup, the Allison-type emittance scanner, the CCD camera [4] (512 x 512 pixel, LN_2 cooled) and an absorber tank for reduction of reflected light were installed perpendicular to each other at the same longitudinal beam position. Due to the length of the emittance scanner the first slit defining the position of the emittance measurement is 38 mm in front of the common centerline (see Fig. 3). Approximately 200 mm behind the main diagnostics a residual gas ion energy analyzer [5] was installed to determine the degree of compensation.

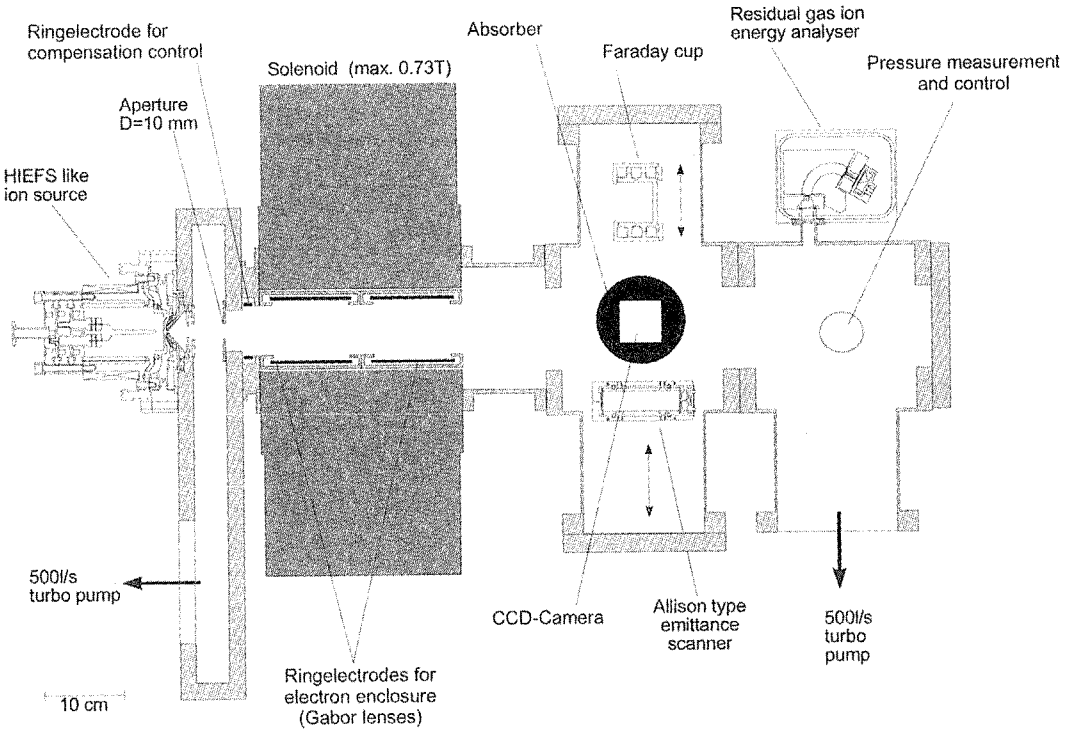


Fig. 3 Schematic drawing of the experimental setup.

Figure 4 shows the result of an emittance measurement using an Allison-type measurement device. The solenoidal field was 0.44 T (220 A) and the beam current into the Faraday cup 3.4 mA. The potential depression inside the beam was determined to be 9.9 V (compensation degree ~80 %). The beam is convergent and the envelope radius is ~6.5 mm, the convergence angle +/- 30 mrad and the normalized beam emittance (rms, 100%) is 0.011 π.mm.mrad. The corresponding CCD camera measurements show a signal-to-noise ratio of ~8.

Figure 5 shows the results of an emittance determined by calculation, using the data of the CCD measurements. The envelope radius is approximately 7 mm, the convergence angle +/- 35 mrad, and the normalized beam emittance (rms, 100%) is 0.020 π.mm.mrad. The compensation degree can be estimated from the calculations to be 80%. Comparison of emittances gained from conventional destructive measurements and from CCD camera measurements show good overall agreement of the orientation of the emittance in phase space. The values given by the calculation have slightly higher beam radius and angle (10-20% deviation). This might be caused by the higher resolution of the CCD chip compared with the conventional detector. From this, and due to the numerical errors typical of differential methods, the RMS values are greater too. The values for the compensation degree are also in good agreement with the measurements. The lower values might be explained by improper separation of space charge and emittance effects, and also explain the smaller pattern. First tests of beam diagnostics have been performed in the LEBT section at low beam power. Measurements of beam emittance and space charge compensation will

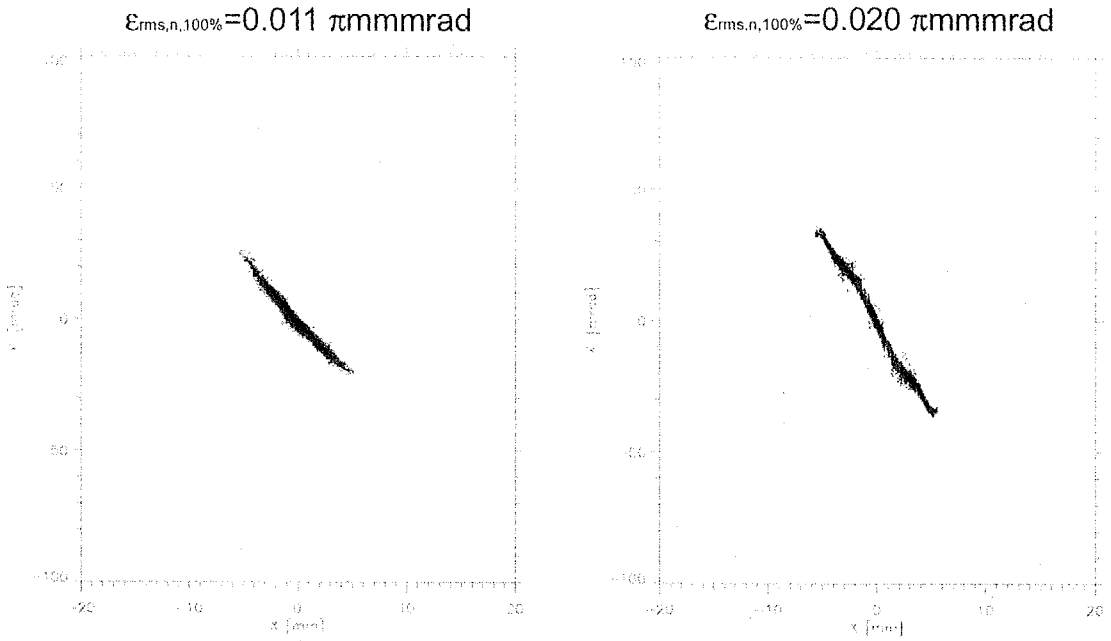


Fig. 4 Left: Beam emittance measured using an Allison measurement device.
Right: Emittance determined by calculation using a CCD camera measurement.

be performed in the near future. Transport calculations, including the results of beam potential measurements, will be continued for final optimization.

(5) Tomography of Ion Beams using a CCD Camera

Emittance measurement methods using optical measurement devices described in the literature [1,2] are only applicable for rotationally symmetrical ion beams. Computerized tomography allows determination of any beam profile. This can be done using the inverse Fourier transformation of a sufficient number of projections (>40) of the ion beam. For this purpose the CCD camera will be rotated around the ion beam (Fig. 5). The accurate distribution of the beam ion density in the space phase [3] can be univocally determined from the beam profiles measured as a function of the lateral position of the camera using convenient numerical methods of data analysis [5,6]. Using a CCD chip with 1024 x 1024 pixels one image covers over 1000 beam profile measurements along the beam axis. (The measurement covers a drift distance of ~40 mm.) Therefore this method allows determination of the beam profiles in a four-dimensional phase space. The tomographic measurement device yields a maximum of space-resolved information about the longitudinal development of the beam profile. Due to the aspect of measurement duration this method is inapplicable for time-resolved measurements. For time-resolved measurements of beam profiles in two planes, two time-synchronously-controlled CCD cameras constructed in the same way will be installed in an orthogonal arrangement.

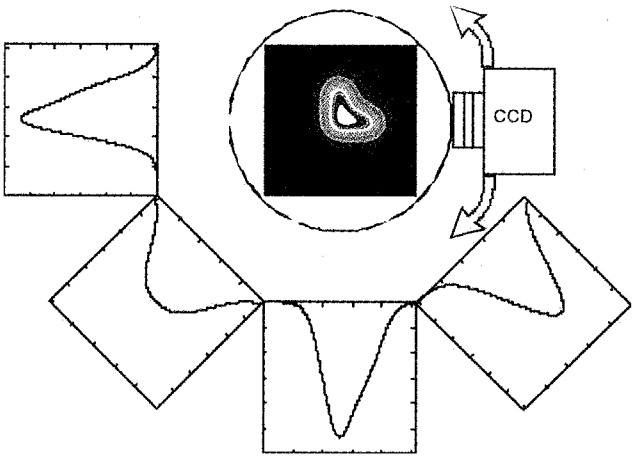


Fig. 5 Schematic drawing of the tomography set up for the determination of the density distribution of ion beams in space phase using CCD-camera images.

(6) Conclusions

The setup of the low energy beam transport line was completed and their components tested. The new conventional high power slit-grid emittance measurement device has been tested successfully at low beam power. The non-destructive optical beam diagnostics were also tested at low beam power level. A high signal-to-noise ratio was gained near the RFQ injection point, even at low power levels. The encouraging results indicate that the use of a CCD camera for the determination of beam emittance is an alternative to conventional devices at high beam power. Mathematical methods can derive most of the relevant parameters needed for beam transport using a single CCD camera image. Improvements of the computer codes used and the use of tomographic methods are planned for the future.

References

[1] P. Strehl, "Beam diagnostics", Proc. of CAS, CERN accelerator school, CERN 87-10 (1987).
[2] F. Sittinger, "Untersuchungen zu optischen Profil- und Emittanzmessungen an niederenergetischen intensiven Ionenstrahlen", Dissertation IAP, University of Frankfurt, Germany (1995).
[3] R. Dölling, "Raumladungskompensation driftender intensiver Strahlen niederenergetischer Ionen und Techniken zu ihrer Vermessung", Dissertation IAP, University of Frankfurt, Germany (1994).
[4] L. Wicke, "Untersuchungen zu Strahlprofilmessungen intensiver Ionenstrahlen mit optischen Methoden", Diploma Thesis IAP, University of Frankfurt, Germany (1998).
[5] J. Radon, "Berichte der Sächsischen Akademie der Wissenschaften", Leipzig, Math.-Phys. Kl. 69 (1917) 262.
[6] Kak, Avinash, "Principles of computerized tomographic imaging", IEEE No PC02071.

3.1.24 AC39-JA : Activation of Accelerator System Components

(1) Brief Task Description

The accurate estimation of the activity produced in the accelerator components is important to achieving the hands-on maintenance requirement specified by the conceptual design of IFMIF. The primary deuteron beam and the secondary neutron induced activities and the resultant dose levels are estimated using the existing nuclear data libraries and checked against available experimental data. The beam loss requirements to meet the hands-on maintenance criterion are examined through the lifetime of each component.

Contributor

Name	Party	Institute	E-mail address
M. Sugimoto	Japan	JAERI	sugimoto@ifmif.tokai.jaerigo.jp

(2) Introduction

In the reference design of the IFMIF accelerator system, hands-on maintenance is required during the design lifetime of about 40 years [1]. The accelerator components near where beam losses are anticipated may possibly become radioactive due to nuclear reactions between the structural materials and lost-beam particles and secondary neutrons. In particular, loss of the IFMIF deuteron beam will generate neutrons even in the low energy sections. This results in the greater importance of the activation issue in IFMIF, with 40 MeV maximum D^+, compared to proton beams with much higher energy. In Fig. 1, guidelines for beam loss at the major accelerator components are estimated from the design requirements for beam transmission up to the RFQ and the beam loss criteria tentatively borrowed from the FMIT design [2]. (These are <3 μA/m along the accelerator and the high energy beam transport line, and <10 μA at each bending magnet.) Such criteria requiring remote handling maintenance are employed to keep a safety margin for the radiation shielding. However, a value of ~3 nA/m for achieving hands-on maintenance is assigned as the goal for beam loss control in the IFMIF design. The important reactions producing radioactivity due to the beam loss at each part of the accelerator module are also summarized in Fig. 1. At the injector, about 15 mA of 0.1 MeV D^+ is lost before entering the RFQ and another 15 mA of D_2^+ and D_3^+ ions would be scraped off. Such lost ions are trapped at the surface of the equipment facing the beam and the next ions produce neutrons with ~2 MeV and tritium by the D(d,n) and D(d,p) reactions, respectively. A similar process occurs at the entrance section of the RFQ in the course of the beam bunch formation stage where ~15 mA beam is lost. The neutrons produced can activate the accelerator components when they are thermalized and

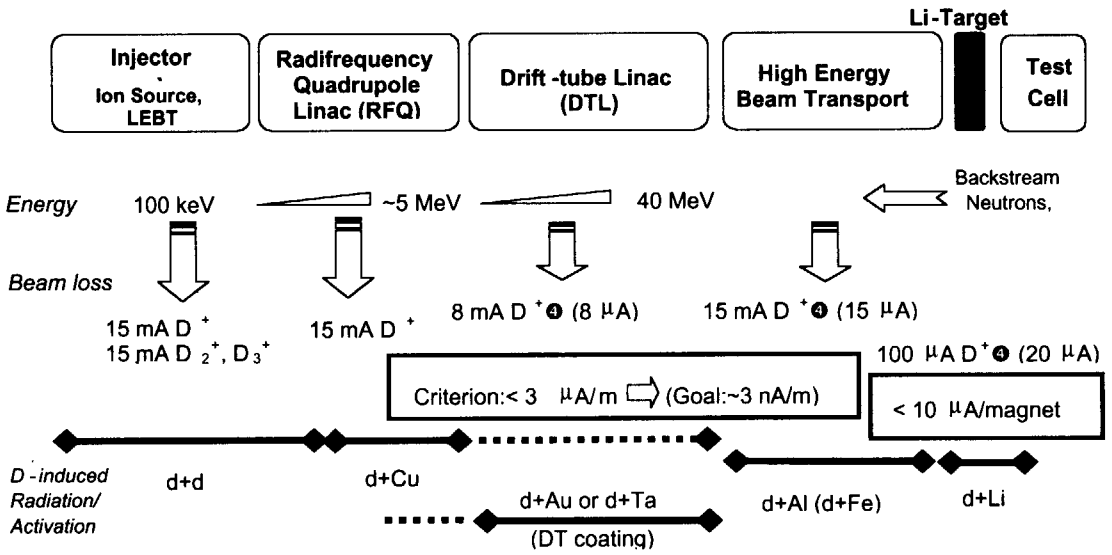


Fig. 1 Beam loss criteria and activation of materials in IFMIF accelerator components.

captured. Therefore the following approach might be effective for suppressing such activation at the injector section:

1) Set up a specific point where most of the beam loss component will be trapped;
2) Periodically or continuously replace the ion trapping materials with new materials to restrict the accumulation of deuterium on their surface; and
3) Locate a neutron absorbing material around the ion-trapping materials, to reduce the thermal neutron flux on the accelerator components.

A possible approach for the equipment where the beam energy is higher is to use some high-Z material coating on the surface to reduce the neutron production yield at the beam loss points. (Gold plating on drift tubes was proposed in the FMIT project.)

In this report, validity of the beam loss goal value is examined through calculation of the activation and the resulting dose equivalence due to the beam loss. The results of the induced activities for selected materials (copper, tantalum and aluminum) are presented for a typical beam loss condition which can be scaled to the actual conditions. The dose equivalence is derived by assuming the typical cooling down time and approach distance to perform equipment maintenance operations, such as inspection or removal for repair. Effects of the choice of material compositions for the components are also examined. Finally, the acceptable beam loss for the specified cool-down scenario is estimated.

(3) Calculation Method and Results

The primary deuteron and the secondary neutron induced activities are calculated using the IRACM code [3], which was developed to handle the isotope production yield due to the particles, n, p, d, α and some heavy ions. In this code the cross sections for n and d of the incident energy up to 150 MeV are available as ACSELAM data library. The evaluated data are mainly derived from theoretical calculations and the comparison with experimental data is necessary for the important reaction products, to confirm the reliability of the calculations. In this study, three materials (copper, aluminum, and tantalum) are selected as typical beam-facing materials in the accelerator components.

(a) Copper

Copper is the main element of the cavity walls, electrodes (vanes of the RFQ and drift tubes of the DTL), and magnets conductors in the IFMIF accelerator. It is the most important element for the production of activity with lifetime greater than several minutes, which might be a minimum threshold lifetime in considering the cool down time for the start of maintenance. The cross sections and the thick target yields for producing the activities, ^{65}Zn (half-life, $T_{1/2}$=244.3d), ^{63}Zn ($T_{1/2}$=8.5mn), ^{62}Zn($T_{1/2}$=9.2h), ^{64}Cu ($T_{1/2}$=12.7h), ^{62}Cu ($T_{1/2}$=9.7m), ^{61}Cu ($T_{1/2}$=3.3h), are compared between the ACSELAM library and the experimental data to confirm the reliability of the data library. As an example, the results for the ^{65}Zn production are shown in Figs. 2 and 3. Although the individual data in the library have a systematical discrepancy with the experiments due to the deficiencies of the theoretical model, the effect on the overall accuracy on the dose equivalence is limited because it is obtained by the integration over the energy range up to 40MeV and the summation over the various contributing reaction channels. The dose equivalence at a position 1 cm distant from the activity is estimated at various deuteron energies and cooling down times after 40 years of irradiation by a 1 μA beam on 1 cm^2 area, as shown in Fig. 4. After 10 hours cool down, the dose level would be less than 20 Sv/h and the actual dose for the workers can be easily reduced by a factor of 10^{-4} to 10^{-6} due to the attenuation of the radiation and by avoiding close approach. If the dose level of ~10μ Sv/h needs to be achieved for maintenance after 10 hours cool down, the beam loss at the high energy section should be kept below 5 to 500 nA for 40 years of operation. At beam energies ~12 MeV and ~7 MeV, the beam loss criteria are relaxed by a factor of 10 and 100, respectively.

(b) Aluminum

For aluminum, used as the main component of the beam tube/chamber, two activities, ^{22}Na

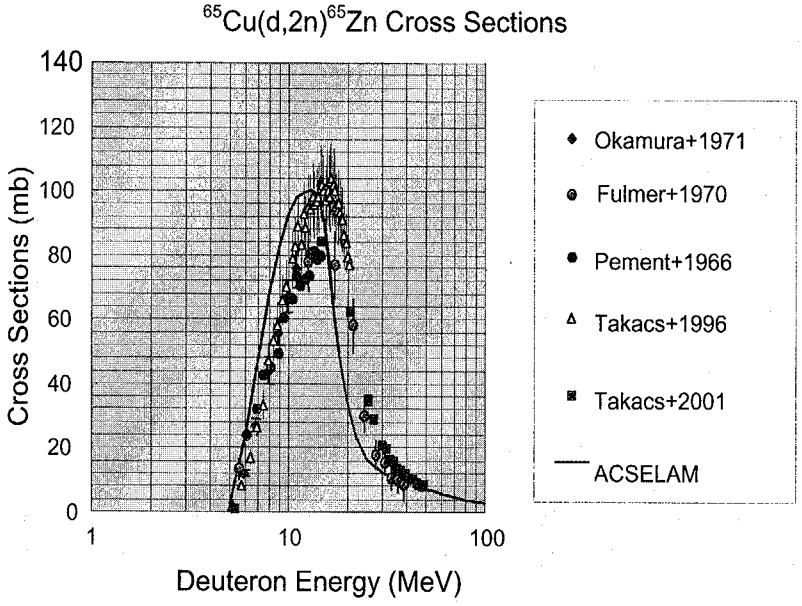


Fig. 2 Comparison of the ACSELAM data library and the experimental data for the ^{65}Cu(d,2n) ^{65}Zn reaction.

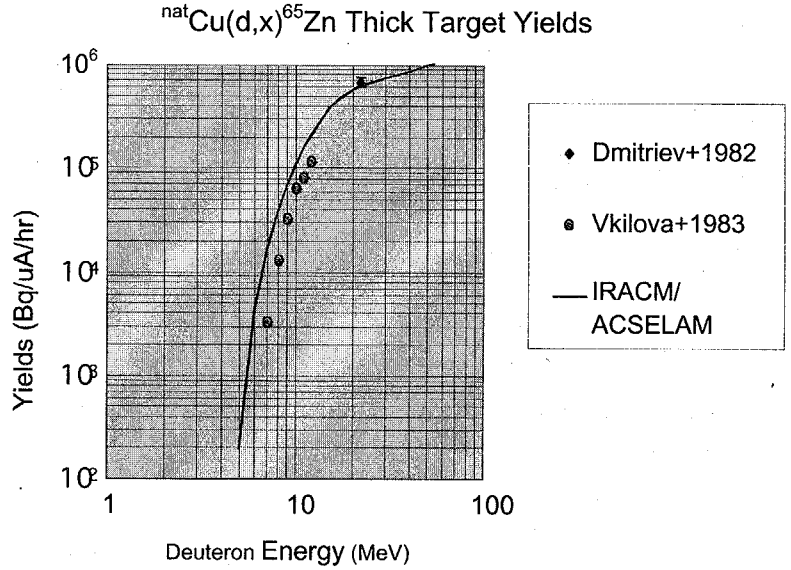


Fig. 3 Comparison of the production yield per _A-hour beam charge for thick target calculated by IRACM code (using ACSELAM library) and the experiments for 65Cu(d,2n) 65Zn reaction.

($T_{1/2}$=2.6 y) and ^{24}Na ($T_{1/2}$=15.0 h), are important from the viewpoint of maintenance on the accelerator system. The dose equivalence curves for Al are shown in Fig. 5. However, the data in the ACSELAM library for ^{27}Al(d,x)^{24}Na reaction indicated ~1 order lower than the experimental data, and it is a single contributing channel to the total dose in the cool down time ranging from 1 hour to several tens hours, so that the result should be multiplied by 10 in the energy range greater than 16 MeV. From this consideration, the dose level after 10 hours cool down is similar to the Cu case at the high energy section, so that the same beam loss criteria can be applied for Al. For the lower energy sections, the activity in Al is much less than that in Cu and the activity decays fast enough if the cool down time of ~100 h is employed.

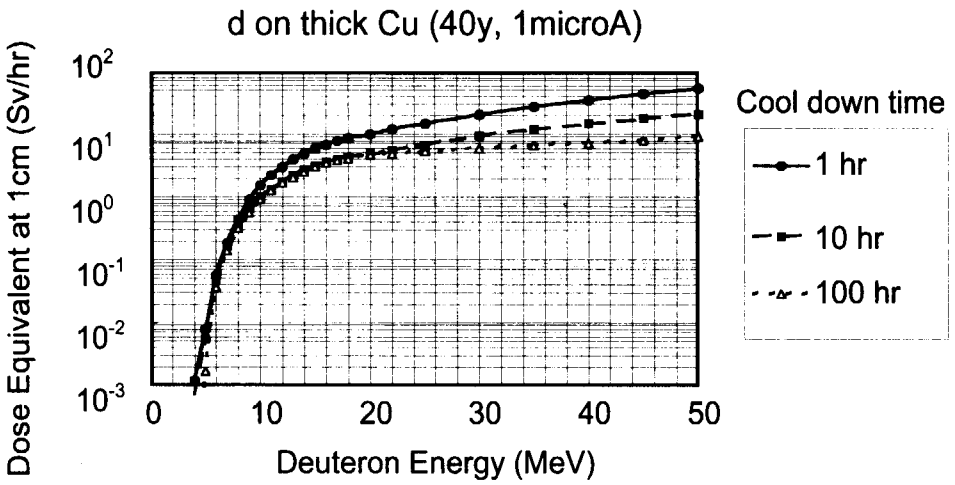


Fig. 4 Dose equivalence at 1 cm from the activity produced by 1μA beam loss for 40 years on copper calculated by IRACM code.

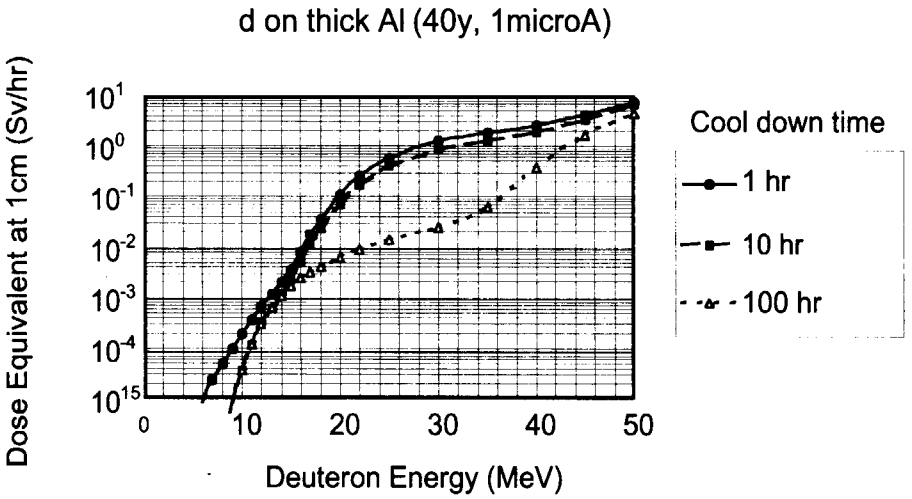


Fig. 5 Dose equivalence at 1 cm from the activity produced by 1μA beam loss for 40 years on aluminum calculated by IRACM code.

(c) Tantalum

Tantalum is a candidate material for beam slits to scrape off the beam halo component and also can be used as a coating to protect the beam facing materials to avoid the production of excessive radioactivity. Other high-Z materials, like Au, W, etc., or C, are also useful for the same purpose, but tantalum is the best from the viewpoint of lower induced activity and higher melting point. The dose curves for Ta are shown in Fig. 6 and no difference in the various cool down times (1 – 100 h) in the energy range < 40MeV is seen because the decay of activities is controlled by ^{182g}Ta ($T_{1/2}$=114.4 d). The tolerance level of beam loss on Ta is larger than Cu and Al by a factor of 10, i.e. 50 nA~5 μA for 40 years, so it is effective to use Ta for scraping off the halo component of the beam.

The results for the gold case are similar to the tantalum case with a few differences: (1) the dose equivalence of Au at energy > 20eV is about three times larger; (2) the decay of Au in the time range of 1-100 h is mainly controlled by ^{195}Hg ($T_{1/2}$=9.9 h) and ~100 h cool down time can reduce the dose equivalence by a factor of 5. The light element, like carbon, produces less activity and the decay is faster than the above elements; however, it may produce more neutrons by deuteron-induced reactions, so that evaluation of the use of C must consider the neutron-induced activation around it.

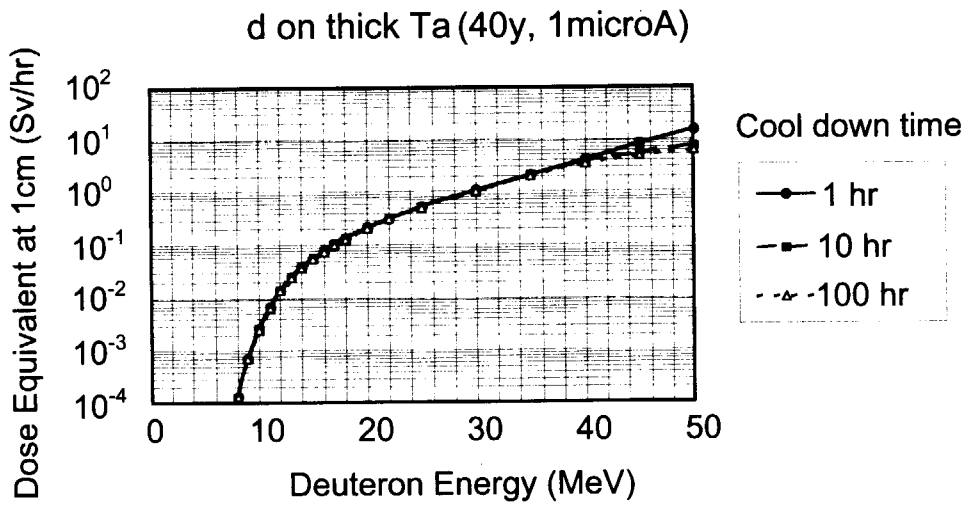


Fig. 6 Dose equivalence at 1 cm from the activity produced by 1μA beam loss for 40 years on tantalum, calculated by IRACM code.

(4) Conclusions

The reliability of the database for the calculation of activation of accelerator components is checked with some experimental data and discrepancies are found in microscopic cross sections, especially for the $^{27}Al(d,x)^{24}Na$ reaction. Discrepancies are not as critical in the case of the heavier elements for which the number of contributing channels is large and the errors can cancel out. The beam loss criteria are estimated from the calculated dose equivalence to be 5 nA at a point (or 5 nA/m) for Cu and Al (at Ed=40 MeV after 40 years of operation) by taking into account the modest value of the attenuation factor for the radiation shielding planned for use at maintenance time. For Ta, this value is relaxed to 50 nA. It is concluded that a guideline for the beam loss along the section with beam energy larger than 20 MeV is estimated to be 5 nA/m. This value can be increased to 20 and 50 nA/m in sections with energy ranges 12 to 20 MeV and 8 to 12 MeV, respectively.

References

[1] M. Martone (editor), IFMIF International Fusion Materials Irradiation Facility Conceptual Design Activity Final Report, ENEA Frascati Report, RT/ERG/FUS/96/11, November 1996.

[2] D. Liska, et al., "High-radiation-zone design of the FMIT high-energy beam transport", IEEE Trans. on Nucl. Sci., NS-28, 2812 (1981).

[3] N. Yamano, M. Fukuda, S. Tanaka, "Isotope production cross section library for use of transmutation calculation in the IRAC code system for the TIARA facility", ICRS-9: 9th Int. Conf. On Radiation Shielding, Oct. 17-22, 1999, Tsukuba, Japan.

3.1.25 AC31-JA : Estimation of Beam Loss at Various Operating Conditions

(1) Brief Task Description

Control of beam loss along the IFMIF accelerator and beam transport line components is critical to realizing hands-on maintenance of these components over the operating lifetime of the facility. Various operating modes of the IFMIF accelerator system can be identified under the specified beam conditions. Beam dynamics simulations are carried out for these operating modes to model the results.

Contributor

Name	Party	Institute	E-mail address
M. Sugimoto	Japan	JAERI	sugimoto@ifmif.tokai.jaerigo.jp

(2) Introduction

The deuteron beam generated by the IFMIF accelerator can produce neutrons even at beam energy as low as several MeV. Analysis of activation due to beam loss is very important to achieve the goal of hands-on maintenance of the accelerator equipment during its lifetime. The guideline of the maximum allowed beam loss derived from shielding calculations and adopted in the FMIT conceptual design [1] was 3 μA/m along the Drift-Tube Linear accelerator (DTL) and the High Energy Beam Transport (HEBT) beam lines, and 10 μA/m at every magnet in the HEBT; these values were also accepted in the IFMIF design [2]. Actually, these criteria are not sufficient to allow hands-on maintenance after 40 years of operation of the accelerator and it should be lowered to a new goal at 40 MeV of ~5 nA/m instead of 3 μA/m, according to the studies outlined in Sec. 3.1.24, AC39-JP. The allowed beam loss in the lower energy region is relaxed compared to 5 nA/m; however, it can be set as a design objective to keep the possible activation as low as possible. Generally, the beam loss events are not distributed uniformly but are highest near the positions of magnetic field elements, like quadrupoles in drift tubes and focusing/bending magnets in the transport lines, where the beam envelope becomes larger than that in the other regions. However, the cause of the loss events originate from the accumulation of various effects in the beam line upstream. So a cause and effects analysis of the perturbations in the related parameters is necessary to perform an accurate estimation of the beam loss events. For this purpose, a code to estimate the beam behavior in the IFMIF accelerator with enough precision needs to be developed and applied to verify the robustness of the beam quality against parameter perturbations to prevent excessive beam loss [3]. In this report, the operation patterns for the IFMIF accelerator are identified, and the issues to be solved for each operation pattern are clarified. The beam dynamics simulation code necessary to evaluate the beam loss taking into account the variation of the important parameters of beam line elements is under development and its status is described.

(3) Operation Patterns

The summary of the operational modes of the IFMIF accelerator is shown in Table 1. These are characterized by the condition of the beam properties and the state of the accelerator equipment, and the estimated frequencies of occurrence are indicated.

1) In the steady-state mode that occupies most of the operation time, the beam loss is mainly caused by the beam halo component. This continuous beam loss must be minimized through design optimization efforts, and the goal for the allowed beam loss is 50-5 nA/m along the beam path, as discussed in Sec. 3.1.24.
2) The pulsed mode operation is included in the IFMIF baseline design to suppress excessive activation during the start-up conditioning phase after a long shutdown. The average current needs to be ramped up to realize the acceptable time profile of the beam power injection into the target. This procedure will be applied after each shutdown for monthly maintenance. The typical time profile of pulsed mode is shown in Fig. 1, and the location and time span for possible beam loss in each pulse is indicated in Fig. 2. The rough estimation of loss events would be 10^{-3} (~0.1 ms x 10 pps) at maximum, so that the duration of the pulsed mode operation should be controlled within ~4 min. This meets the guideline that the additional beam loss due to the pulsed mode operation is less than 10% of the steady-state

Table 1 Operating modes of the IFMIF accelerator system.

Mode	Beam property	Equipment state	Frequency of occurrence	Comments
Steady-state	40MeV /125mA CW, 20cm W x 5cm H beam footprint	Full performance for RF power & magnetic field	88% (availability) of scheduled operation	Principal mode; Beam loss due to halo
Pulse	0~100% current, controlled by duty cycle	Controlled performance	~1 /month (after monthly scheduled maintenance)	Start-up conditioning; Current ramping is required by target system
Transient	0~100% current, uncontrolled event	Recovering from off-normal state	~100 /year *	Corresponding to beam trip events
Special (e.g. Low energy beam)	~32MeV (TBD) / 125mA (typ.)	Last RF modules are powered off	TBD (in irradiation planning)	Scheduled operation

*) For major failures, 60 hours MTBF and 6,132 hours for yearly operation time are assumed. The events with the shorter recovery times are much larger than this

beam loss (~10^{-6}).

3) The transient mode is defined as the state of the immediate recovery process from the equipment failures that cause beam trips. During this recovery process, the operation would be in either mode 1) or 2) above; therefore the contribution of this mode to the total beam loss quantity is estimated to be small if the frequency of occurrence, ~100/year, is realized in the IFMIF accelerator operation as stated in the conceptual design requirement.
4) The special mode of low energy beam operation for varying irradiation neutron spectrum is planned for separate irradiation campaigns, specific to the materials for which the softer neutron spectrum is necessary. The details of the operating conditions cannot be determined at the present stage and it is necessary to consider these after the users requirements for the irradiation condition are clearly defined.

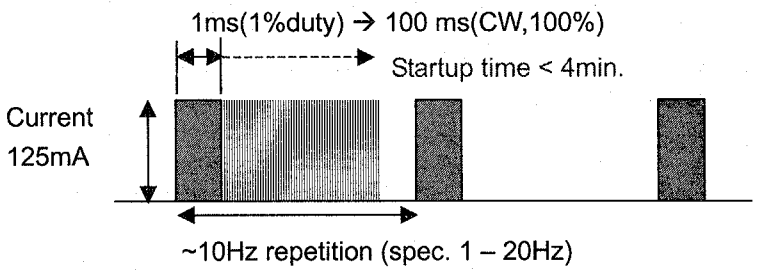


Fig. 1 Time chart of the pulsed-mode operation of IFMIF.

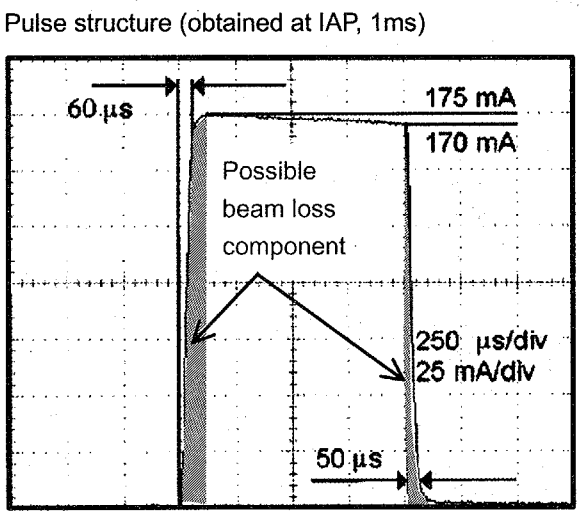


Fig. 2 Typical pulse beam obtained from the high-current ion source. The leading and trailing edges of pulses are possible sources of beam loss events because the beam properties are not well matched to the accelerator.

The cause and effects of the perturbations of the accelerator equipment are summarized in Table 2. As major causes, the status change of ion injector, cavity tuning, RF power, HEBT magnets and alignment distortion are considered. Several causes have the same effects on the accelerator system and it is important to identify the correct cause from the observed events. The detection scheme must be developed in such a way that it will clarify the problems of the equipment status and initiate automatic recovery procedures for restoring continuous operation. The thermal deformation problem of RFQ due to the RF heating is studied as an important example of the cause and effects analysis of equipment.

The heat production at the cavity surface is estimated using the SUPERFISH code [4], and the thermal/mechanical problem is solved by using the ANSYS code [5]. The calculation conditions are listed in Table 3. Two different shapes of cavity wall structure, (a) a usual octagonal shape and (b) a rectangle shape with a thick edge wall part to restrict the movement, are compared. The geometrical parameters and the obtained temperature maps for a quadrant of RFQ are shown in Figs. 3 and 4, respectively. As shown in Table 4, the calculated position movement of the vane tip for case (a) was smaller than that for case (b). The effect of unequal temperature for two 12 mm ϕ cooling channels is also considered as case (c), and the resultant movement was between those for cases (a) and (b).

It is found that the estimated deformation of the RFQ vane tips, less than 10μm, gives no prominent change to the field characteristics, and the errors introduced at fabrication and installation may be greater problems for the IFMIF RFQ. For the other components similar analyses need to be performed as a next step, to obtain the relative importance of each contributing error.

Table 2 Cause and effect of perturbations to the IFMIF accelerator equipment.

Cause	Effect	Issue
• Ion source beam current & resulting phase ellipse rotation / wobbling	• Change of cavity beam-loading & frequency tuning • Change of matching condition	Method of re-tuning process
• Thermal & mechanical motion of cavity structure	• Change of cavity frequency tuning • Change of electric & magnetic fields at beam path	Effective cooling & temperature control method; supporting structure to minimize effects
• RF power source phase & amplitude	• Change of electric & magnetic fields at beam path	Detection method for monitoring deviation from normal state
• Beam expander & final bend magnetic field	• Change of position & beam distribution pattern at target	Detection method for monitoring deviation from normal state
• Distortion of alignment axis of equipment	• Change of matching condition • Change of electric & magnetic fields at beam path	Dynamical alignment checking & adjustment

Table 3 Calculation conditions for thermal & mechanical analysis of RFQ.

Calculation conditions	Values	Comments
Maximum heating at wall	6.4 W/cm^2	Varied by multiplying factor 0.5 ~ 1.5
Cooling water inlet temperature & cooling channel diameters	40 °C 18, 12 and 6 mmϕ	Flow rate: 320 ℓ/min, Flow speed: 2 m/sec

Table 4 Results for position movement of the vane tip of the RFQ.

Calculated results	Position movement	Temperature & Stress
Case (a): usual octagonal shape	-1.3 μm at vane tip (102 μm max.)	ΔT_{max} = 29 °C σ_{max} = 5.9 MPa
Case (b): rectangle shape with thick edge wall	-6.7 μm at vane tip (126 μm max.)	ΔT_{max} = 22 °C σ_{max} = 6.0 Mpa
Case (c): same as case (a) except the inlet temperature of one of two 12 mmϕ cooling channels = 50°C	-4.4 μm at vane tip (115 μm max.)	ΔT_{max} = 29 °C σ_{max} = 6.7 MPa

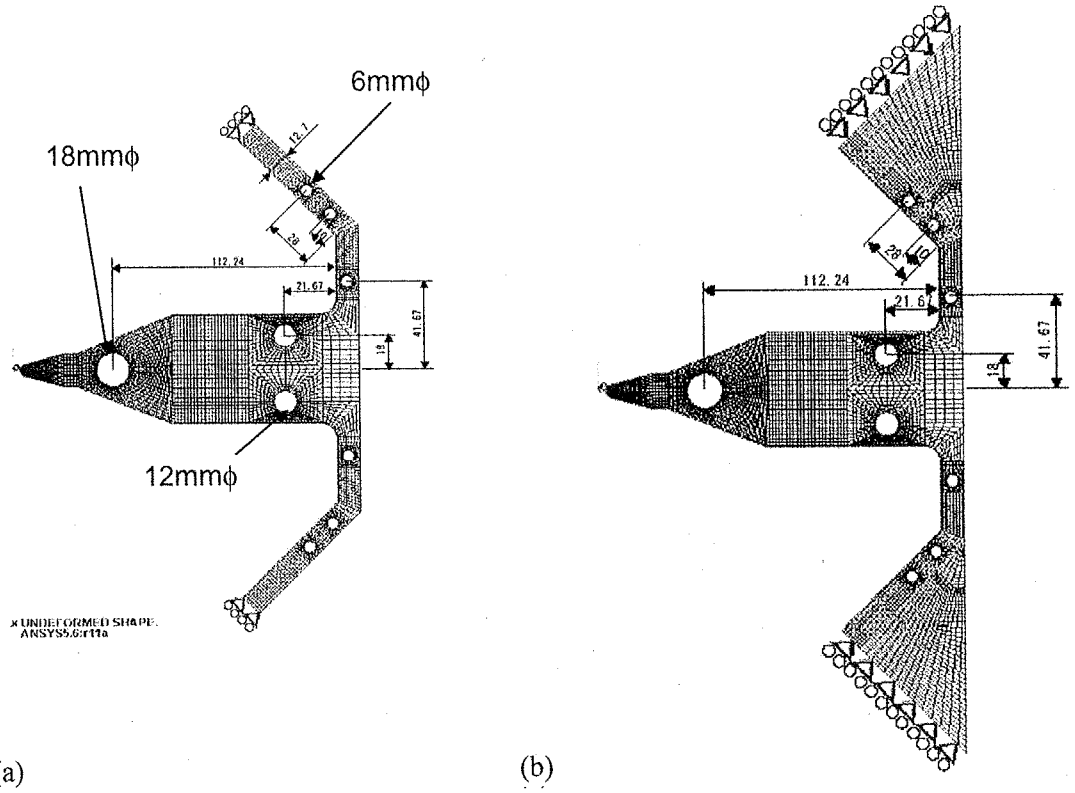


Fig. 3 Cross sectional views of a quarter of RFQ cavity:
(a) octagon with 12.7 mm wall thickness, (b) rectangle with thick edge wall

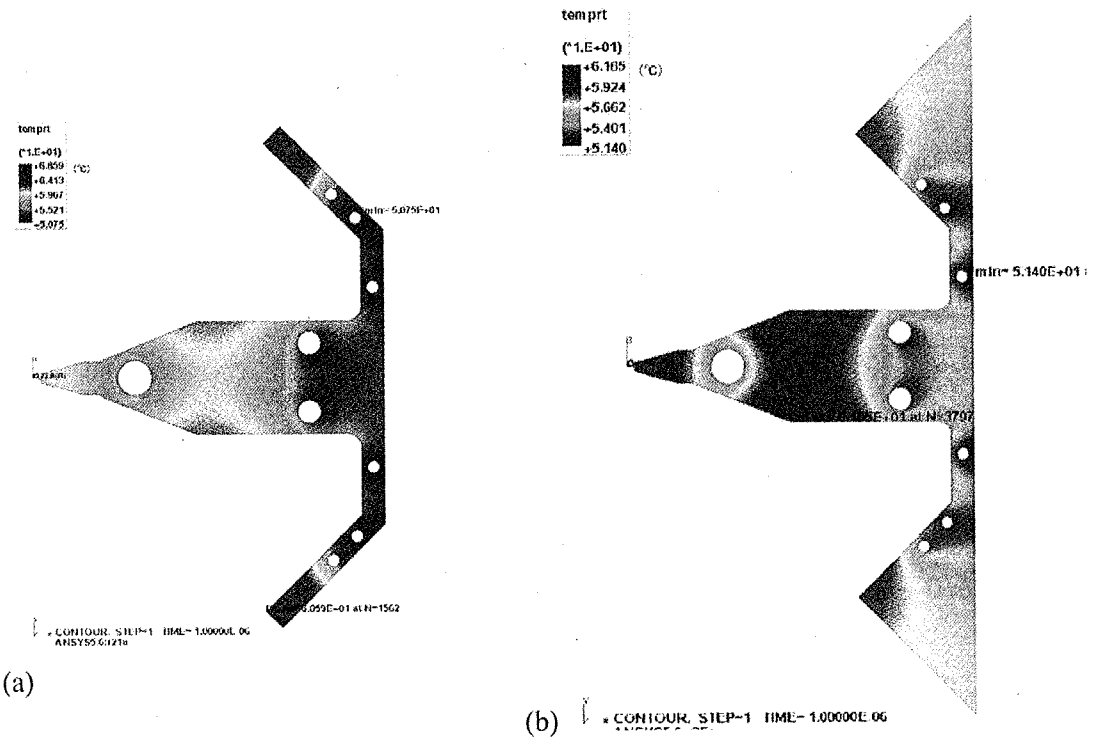


Fig. 4 Temperature maps of a quarter of RFQ cavity:
(a) octagon with 12.7 mm wall thickness, (b) rectangle with thick edge wall.

(4) Beam Dynamics Simulation

The beam dynamics simulation needs to be carried out for each operating pattern to obtain detailed information about beam loss during the operating lifetime; however, the primary concern is beam loss for steady-state operation as discussed above. A new code is under development to simulate the beam behavior through the beam line components with some imperfections, to analyze the beam loss in steady-state operation. The major features of the simulation code are: (a) initial beam generation section separated from main simulator, (b) choices for space charge force approximations (particle-in-cell using 2-D cylindrical or 3-D Cartesian cells, point-to-point Coulomb force), (c) multiple schemes to obtain the transfer map of particle coordinates through a unit of beam line elements (conventional matrix formalism, methods for integration of equation of motion), and (d) optional "blob" model for simulating particles [6] (or equivalent to "ensemble" model [7]). The beam line elements, having magnetic fields (solenoid, bend, quadrupole and higher multipole) and electric fields in RF gaps, are included as the first step. The connection between the simulation for RFQ and the present code is now in progress.

(5) Conclusions

The operation of the IFMIF accelerator can be categorized as the steady state, pulse, transient and low-energy modes. For each operational mode, the beam loss events need to be controlled by monitoring and stabilizing the critical parameters of both accelerator equipment and accelerated beam. The simulation code to take into account the perturbed conditions of beam line elements is necessary to obtain the requirements for their stability to achieve the beam loss criterion, and a new code is under development for the next stage of detailed design.

References

[1] D. Liska, et al., "High-radiation-zone design of the FMIT high-energy beam transport", IEEE Trans. on Nucl. Sci., NS-28, 2812 (1981).

[2] M. Martone, (editor), IFMIF International Fusion Materials Irradiation Facility Conceptual Design Activity Final Report, ENEA Frascati Report, RT/ERG/FUS/96/11, November 1996.

[3] M. Sugimoto, M. Kinsho, M.A. Chernogubovsky and Y. Hojo, "Impact of the beam dynamics simulation for the concept of IFMIF accelerator", Proc. of 1st Asian Particle Acc. Conf. (APAC98), KEK, Tsukuba, Japan, March 23-27, 1998, KEK Proceedings 98-10 November 1998, p614.

[4] J. Billen and L. Young, "Poisson/Superfish on PC Compatibles", Proceedings of the 1993 Particle Accelerator Conference, Vol. 2 of 5, 790-792 (1993).

[5] ANSYS Inc., http://www.ansys.com/.

[6] G. Coppa, G.Lapenta, G. Dellapiana and V. Riccardo, "Blob method for kinetic plasma simulation with variable size particles", J. Comput. Phys. 127, 268 (1996).

[7] A. Novokhatski and T. Weiland, "The model of emsemble for the beam dynamics simulation", Proc. of 1999 Particle Accelerator Conf. (Eds.: A. Luccio, W. MacKay), 2743 (2000).

3.1.26 AC22B-US : Cost Evaluation of Changes in the System Including the Revised HEBT and the Diacrode Based RF System

(1) Brief Task Description

The scope of this effort was directed at the revised High Energy Beam Transport (HEBT), the RF Coupling Loops, and the RF Power System (including transport and support equipment).

(2) Contributors

Name	Party	Institute	E-mail address
J. Rathke	US	AES	john_rathke@mail.aesys.net
T. Myers	US	AES	tim_myers@mail.aesys.net
Joe Sredniawski	US	AES	joe_sredniawski@mail.aesys.net

(3) Ground Rules and Assumptions

The linac cavity RF Resonant Control System and the RF Cooling System were not included; however, it is recommended that these also be updated in light of the most recent understanding of their requirements. The previous CDA WBS architecture has been held constant as a point of reference.

Cost comparison is based upon an assumed escalation of the costs from the CDA report [1] by 13% to cover inflation to CY2002 rates. Current hardware costs of the revised systems were determined using an updated Bill of Materials (BOM), obtaining vendor Budgetary Pricing (BP) on large dollar items, and using published catalog pricing and phone quotations on lesser dollar items. In some cases, AES engineering estimates had to be applied. As required, labor estimates of the relevant WBS elements were also revised to reflect more current thinking in terms of the technical approach. Current labor rates in ICF units under the pricing ground rule (13% escalation) are:

Project Engineering	170	ICF/hr
Engineering	122	
Fabrication	98	
Technician	98	
Craft	28	
Institutional Support	122	

All of the above hourly rates include 8% fee except the Institutional Support rate per the CDA costing guidelines.

(4) HEBT Cost Revisions

Table 1 Overall HEBT Cost Comparison.

Cost Comparison (kilo ICF) *	CDA	CY2002
WBS 4.2.3.4 (1st Accelerator)	17,992	6,277
WBS 4.2.4.5 (2nd Accelerator)	12,893	3,694

The HEBT includes all beam transport equipment (vacuum beam tubes, bellows, flanges and magnetic lattice) from the output of the DTL up to the entrance of the lithium target chamber. Also included is the associated support equipment such as the beam diagnostics, the support structure, the

vacuum system, and the various power supplies.

Responding to direction given by the Fusion Power Coordinating Committee in January 1999, JAERI led the development of a reduced cost design [1]. While the accelerators themselves remained largely unchanged from the CDA, the HEBT system changed substantially. Rather than a system capable of switching between three different target chambers, the reduced cost design provides for only a single target. Further, the CDA design employed a series of RF "buncher" cavities to control energy spread through the long transport system. The reduced cost HEBT eliminated this system. Recently, a preliminary study was conducted of this simplified beam transport system to examine the ability to deliver the properly shaped and homogenized beam profile on target (Sec. 3.1.17). Results of this study are encouraging and a revised magnetic lattice design has been produced. This new lattice was used for the cost evaluation presented here. A conceptual configuration of the revised HEBT is shown in Figure 1.

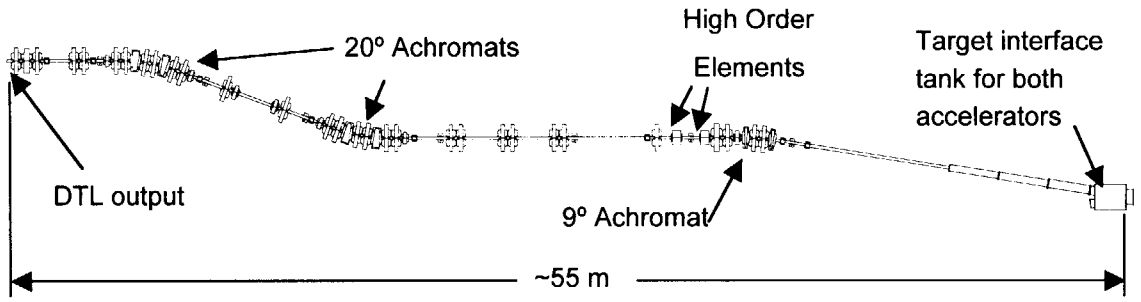


Fig. 1 Preliminary HEBT Physical Layout.

With the deletion of the buncher cavities comes the question of need for the energy spread and phase spread diagnostics. For the current cost update it is assumed that these diagnostics are not needed. If there arises some justifiable reason for either diagnostic in the future, appropriate cost updating should follow because the original approach used in the CDA may not be the most cost effective in terms of current technology. Table 2 shows a comparison of hardware costs before AFI. The largest changes are obviously due to the elimination of the RF cavities and the substantial reduction in the number of magnets. Bear in mind that the hardware costs from the CDA have been escalated by 13% over those published in reference 1. Along with these changes the required labor was also re-evaluated. The revised labor estimates are shown in Table 3.

Table 2 Comparison of Hardware Costs Before AFI.

	Accelerator #1		Accelerator #2	
Purchased Item	CDA Cost (kICF)	New Cost (kICF)	CDA Cost (kICF	New Cost (kICF)
Beam Tube, Flanges, Bellows, etc.	237	212	237	212
RF Cavities	1,819	0	1,819	0
Vacuum System	0	176	0	176
Support/Alignment Structure	328	214	328	214
Magnets	3,774	869	3,774	869
Magnet Power Supplies	1,887	556	0	556
Energy Spread Monitors	361	0	361	0
Phase Spread Monitors	170	0	170	0
Video Profile Monitor	90	97	90	97
Microstriplines	644	70	644	70
TOTAL:	9,310	2,194	7,423	2,194

Table 3 HEBT Resource Hours.

	Resource Hours	
Labor Type	Accelerator #1	Accelerator #2
Engineering	8,090	950
Drafting	4,100	580
Fabrication	3,760	3,070
Institutional Support	3,500	0
Vendor Oversight/Mfg.	2,218	1,224

(5) RF Coupling Loop Cost Revisions

This cost element includes the effort to develop production versions of the RF

coupling loops required throughout the accelerator. The coupling loop cost element does not include the RF window. The RFQ and DTL sections of both accelerators will require a total of 48 drive loops. The nose piece coaxial size will be at least 2 5/8 inch O.D. based upon scaling the required power handling (350kW max) from a design previously developed by Advanced Energy Systems. (Figure 2) Other than some possible minor geometrical differences, the same design can be used for the RFQ and the DTL. The coupling loops will have a tapered section expanding up to 9 3/16 inch uncooled coax. The matching section cavities of both accelerators will require 4 additional drive loops with power handling of up to 60kW CW maximum. The same design concept will be used for both types of loops with dimensions scaled according to power handling. The technical aspects and configuration of these RF coupling loops is described [2].

Advanced Energy Systems, Inc. conducted a bottoms-up estimate based upon a drive loop design that was developed and tested in the early 1990's. The actual drive loop and existing detailed drawings were used for current shop and material estimates. Revised labor estimates for engineering and fabrication are primarily credited for reducing cost (Table 4.).

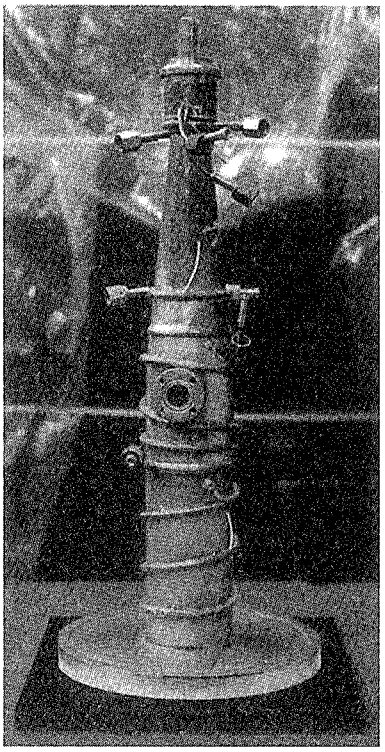


Fig. 2 250kW CW Coupling Loop Developed by AES.

Table 4 Overall RF Coupling Loop Cost Comparison.

Cost Comparison (kilo ICF) *	CDA	CY2002
WBS 4.2.3.5 (1st Accelerator)	3,492	1,852
(2nd Accelerator)	**	**

* Includes AFI of 35%

** Included in the cost for the 1st accelerator

(6) RF Power System Cost Revisions

This cost element is a top-level summary of the costs to design, fabricate, functionally test, and ship the RF power system for both accelerators. This cost element differs from the other summary level elements in that it contains separate estimates from lower level cost elements. The estimate at this level represents the top level of the RF System. It also includes administrative functions such as project management, systems engineering, project travel during the design and construction phase, report data and other miscellaneous activities not related to the specific hardware design tasks described in the lower level RF power system WBS element worksheets. These costs were more correctly aligned with scheduled project phases. The system summary costs as well as lower level costs are compared in Table 5.

(6.1) LLRF Control

This subsystem interfaces with the RF station monitor & control subsystem, and the cavity resonance control subsystem, and maintains the phasing and amplitude of the RF delivered by the high power RF amplification chain for proper RFQ, DTL, and MS operation. This subsystem also provides the RF system low level frequency source. AES's past experience delivering and costing LLRF systems was utilized to update the labor estimates. To understand the material costs, a bill of materials based upon the hardware used for the TTF system at DESY was utilized with current pricing from a recent study for an Energy Recovery Linac (ERL) proposed by Cornell University [3]. The system design uses an adaptive

Table 4 RF Power System Cost Comparison.

Cost Comparison (kilo ICF) *	CDA	CY2002
WBS 4.2.3.7 (1st Accelerator)	96,839	70,697
Project/Administrative	4,703	1,938
LLRF Control	8,927	2,464
Pre-Driver	5,867	2,772
Driver & Final Amplifier	41,307	37,377
Transport	11,676	10,538
Cavity Resonance Control	2,228	2,228
Switchgear	2,614	0
Cooling	9,447	9,447
RF Station Monitoring & Control	2,509	1,995
Integration Equipment & Services	5,042	1,938
WBS 4.2.4.6 (2nd Accelerator)	78,734	59,907
Project/Administrative	1,294	1,124
LLRF Control	7,702	2,044
Pre-Driver	5,056	2,282
Driver & Final Amplifier	36,650	33,364
Transport	8,669	9,607
Cavity Resonance Control	1,669	1,669
Switchgear	2,097	0
Cooling	8,700	8,700
RF Station Monitoring & Control	2,289	1,117
Integration Equipment & Services	3,927	0

* Includes AFI of 35% on all systems except the LLRF Control System which was increased to 50%

feed forward approach with state-of-the-art DSP technology instead of analog control. This permits more procurement of commercial components resulting in significantly less in-house fabrication than previously estimated and lower cost. Although the overall cost is significantly less than the CDA estimate, the AFI was increased to 50% based on technical risk due to lack of definition of the LLRF system design for IFMIF.

(6.2) Pre-Driver

The RF Pre-driver is a high gain, 175 MHz solid state amplifier responsible for boosting the low level RF signal source up to the 2.5 kW range needed by the driver stage of the 1MW main RF amplifier chain. This is adequate to run the drive stage tube at 50kW output for the diacrode to operate at 1MW. The single RF amplifier for the matching section cavities of each accelerator will require a 5kW pre-driver instead to run the TH781 tube at a higher output of 140kW. The Pre-driver is a commercially available self contained, air cooled, solid state amplifier designed with a digital control panel which provides for both local and remote control of the amplifier. Forward and reflected power as well as all operational control and status is provided through a GPIB/IEEE-488 interface. Also included in this estimate are the coaxial interface lines for the main power amplifier chain.

Very little if any in-house fabrication cost is associated with this element since the primary components are commercially available. The labor portion of the estimate is primarily for specification, assembly and checkout prior to shipment.

(6.3) Driver & Final Amplifier

The system uses two stages, each providing approximately 14 dB of gain to bring the total RF output up to 1.0 MW of CW power as needed by the RFQ and DTL accelerating sections of the linac. The first stage RF output will be in the range of 50kW during normal operation of the linac. For the MS section of the linac, only the 1st stage amplifier is used at a higher total output power of 140kW. This output is split and transported into two separate MS cavities. The first stage amplifier uses a TH781 tetrode (rated to 200kW CW) while the final amplifier (second stage) uses a TH628 diacrode (rated to 1MW CW). Each amplifier stage includes the driving tube and resonant cavity assembly, along with its power conditioning, monitor, control, protection, and cooling interface components. In addition, each amplifier stage is functionally supported by a fully integrated High Voltage Power Supply (HVPS) and Switchgear subsystem, complete with control and monitor functions as well as safety interlocks. The cost of these integrated subsystems is included in this cost element thereby negating the use of a separate Switchgear cost element.

Schematically, the RF Driver and Final Amplifier system looks identical to Figure 2.6.2-12 of the CDA report [1] with the exception that the HVPS subsystems will now take the 13.2kV input line directly. All power conversion will be done within the HVPS subsystems.

(6.4) Transport

Most of the elements of the RF transport system are existing production items. Exceptions to this are the circulators, the 1MW load, and the RF windows. These special items will need modest development (for the IFMIF operating frequency and power level) during the EVEDA phase of the program. A base assumption for this estimate is that all technical feasibility issues are resolved prior to any work covered by the allocations here. In addition, the cost of design and fabrication of the various transmission line structural support components is included.

Upon evaluating the suggested 9" water-cooled coax instead of the original air-cooled 19" coax, it was determined that the original 19" coax is less expensive by about a factor of 3. Furthermore, two suppliers of coax stated clearly that there would be a reliability issue with the use of water-cooled coax. Subsequently AES decided to present the revised system costs using the less expensive, all air-cooled coax. (Figure 3)

(6.5) Cavity Resonance Control System

This element was left unchanged except for cost escalation by 13% to CY2002 dollars.

Upon review of this element it was found that the design and equipment employed does not account for the state-of-the-art approach to cavity resonance control such as that used by the APT project. This will have a significant impact upon cost and this area should be re-evaluated during the EVEDA phase.

(6.6) Switchgear System

The cost of this equipment is included as part of the proposed integrated HVPS subsystems for the high power RF amplifier chain in WBS 4.2.3.7.3 and WBS 4.2.4.6.3. An experienced supplier of accelerator equipment was able to provide quotations on such an approach, thereby simplifying the RF system design.

(6.7) Cooling System

This element was left unchanged except for cost escalation by 13% to CY2002 dollars. Based upon the available new data for cooling requirements of the RF system components, it is recommended that this cost element be updated at some future time.

(6.8) Station Monitoring and Control

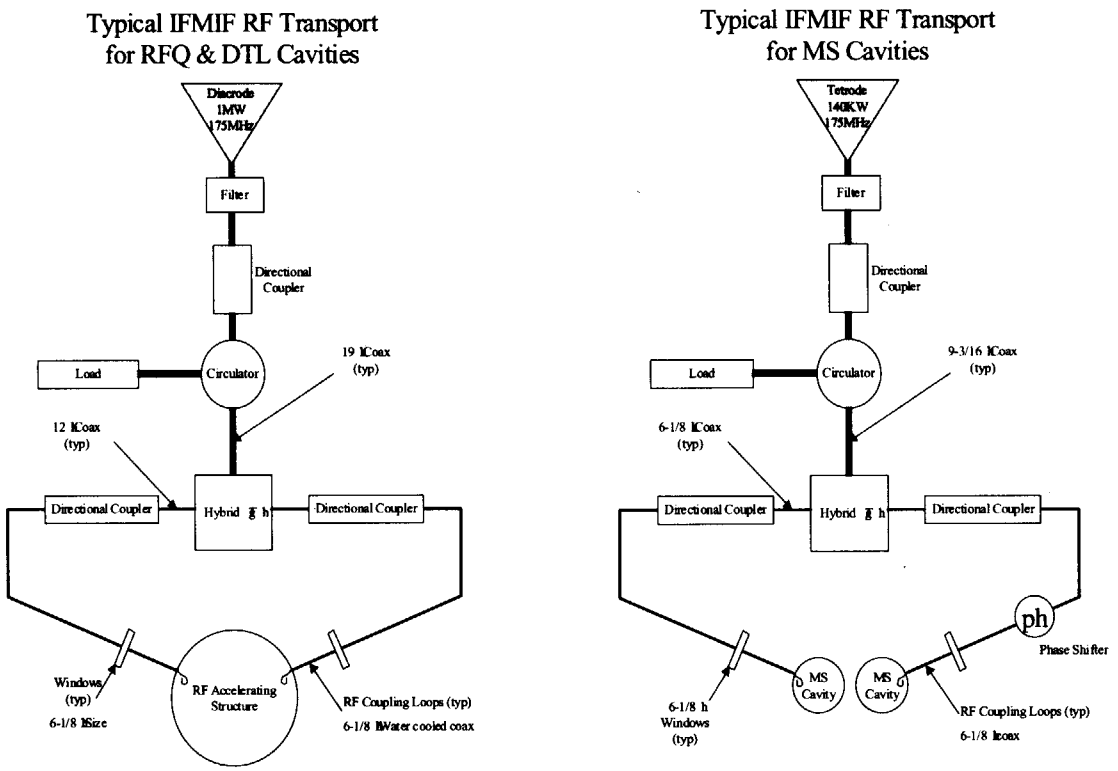


Fig. 3 RF Transmission Line Schematics.

This cost element includes the integrated control and monitoring function to maintain the proper operation of the complete RF station, and also provides remote digital information transfer to the master IFMIF control system via data bus interconnections. Also included is the local equipment safety interlock subsystem.

Each RF power system requires a local control system to simplify interaction with the main control system and to allow easy local control, independent of the main control system for testing. (Figure 4) A local control concept consisting of ControlNet Distributed Interface (DI) boxes from Group3, configured with analog and digital data acquisition and control modules is assumed for the IFMIF cost model. This simplifies integrating the controls on the HV deck with the ground level control system. For testing purposes the fiber optic loop will be connected to a controller card on a standard PC running Windows 98 or some similar operating system. The test software may be programmed in LabVIEW for testing flexibility. For normal operation, the RF controls are integrated into the main EPICS-based system by means of a VME-based controller (by Group3) for which EPICS drivers are available.

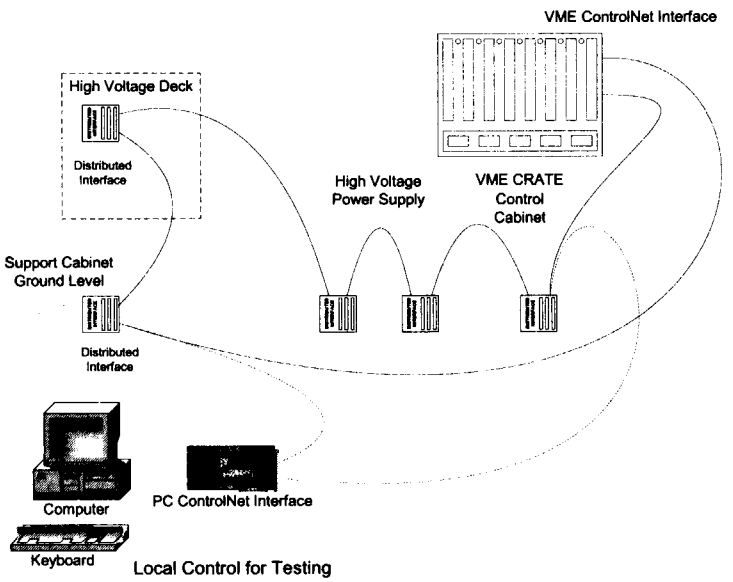


Fig. 4 Block Diagram of RF Station Monitoring and Control Subsystem.

Protection of RF station equipment from

damage due to subsystem/component faults, is provided by a separate subsystem of solid state relays and various sensors for cooling water flows, temperatures and pressures/vacuum levels related to the RF station equipment. The protection subsystem cost is included within this cost element.

(6.9) Integration Equipment and Services

This cost element includes the resources required to setup and qualification test each of the first production RF power systems (1MW for main linac, and 140 kW for MS section cavities) prior to any equipment being shipped to the IFMIF site. This worksheet also includes the special test equipment needed to install and setup the two RF stations and the respective transport elements of the IFMIF systems. Full power testing into a water load is planned. The water loads will be used from the production set of equipment. The hardware items in this task are those which are manufactured and/or used solely for the testing of the RF equipment. It is also assumed that this testing will be conducted at the RF power system manufacturer's facility thereby negating the cost of setting up an entirely new facility.

AES evaluated and revised the CDA estimate based primarily upon the change in philosophy to only test the first of each kind of RF power system at the manufacturer's site. The CDA assumed each of the 26 RF systems would be fully integrated and tested prior to shipment.. Final acceptance testing of the follow-on production systems will now occur at the IFMIF site and should be included under Commissioning. This is the most current approach being used for this kind of equipment on other accelerator projects.

References

[1] JAERI-Tech 2000-014, IFMIF Conceptual Design Activity, Reduced Cost Report, A Supplement to the CDA by the IFMIF Team, February 2000.

[2] Cole, et. al., "Design and Test Results of a 250kW (CW) RF Coupling Loop", Proceedings of the 1990 NPB Symposium.

[3] Advanced Energy Systems, Inc., "Cost Study for the Energy Recovery Linac Prototype", Cornell contract #493101, March 7, 2001.

3.1.27 AC23-US : Examination of the Cost of a Fully Operational IFMIF Prototype

(1) Brief Task Description

In response to widespread discussion of the benefit of having a fully operational accelerator prototype, the US team undertook a task in 2002 to define the scope and develop a cost estimate for such a program. The work incorporated the latest design information available to arrive at an updated design configuration for the IFMIF accelerator. From this configuration a prototype design was developed that meets the technical requirements set forth at the IFMIF Design Integration Meeting at FZK Karlsruhe in October 2001. The prototype design, design justification, and cost estimating methodology were then presented and agreed upon by the accelerator team at FZK Karlsruhe in January 2002. The cost estimate was developed during February 2002 and circulated amongst the IFMIF accelerator team for evaluation and feedback. The results of this study were finalized in early March 2002 and presented at the IFMIF Subcommittee meeting in Tokyo later that month. The estimated cost for the five year prototype program is 102 MICF including an AFI allowance of 23 MICF [1,2].

Contributors

Name	Party	Institute	E-mail address
J. Rathke	US	AES	john_rathke@mail.aesys.net
T. Myers	US	AES	tim_myers@mail.aesys.net

(2) Updating the IFMIF Accelerator Configuration

The work of defining the prototype configuration and requirements was started by first updating the overall accelerator configuration to reflect the latest work done by the IFMIF collaboration. In doing this work it was encouraging to see the striking similarity of the design solutions that have been developed at different institutions, primarily in Europe. Figure 1 shows a view of the updated accelerator configuration as it would be placed in the accelerator vault of the reduced cost IFMIF (upper vault in the figure). The figure highlights the fact that the RF hall is somewhat small but the accelerator structures themselves appear to fit well into the vault space. For comparison, the "old" (pre 2002) accelerator configuration is shown in the second accelerator vault (lower vault in the figure). The updated configuration reflects the latest machine elements including:

- Realistic layout of the injector/LEBT taken from the injector installation at the Low Energy Demonstration Accelerator (LEDA) facility at Los Alamos
- ~12.3 meter, 5 MeV RFQ typical of the Saclay and IAP designs
- 2 cavity, 4 quadrupole Matching Section (MS) system between the RFQ and DTL. Designs from IAP

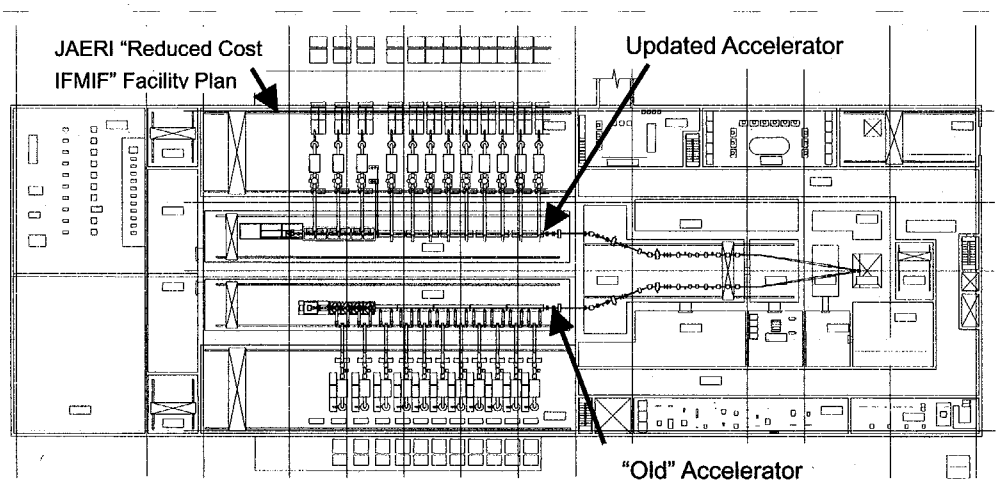


Fig. 1 IFMIF Facility Plan showing updated accelerator layout (upper vault) vs. the "old" (pre 2002) accelerator layout (lower vault).

and Saclay are very similar. Each MS cavity requires a 70 kW, 175 MHz RF source.
- 5 tank DTL system from latest Saclay design that employs 2 RF power systems per tank in tanks 2 through 5 and a single supply in tank 1. This layout is very similar to designs produced at IAP.

The HEBT in this configuration does not include updates resulting from efforts conducted under task AC21-US presented in 3.1.17. Because the HEBT is not part of the prototype this does not impact the work presented here. A perspective view of the updated accelerator in the IFMIF Reduced Cost Design vault is shown in Figure 2.

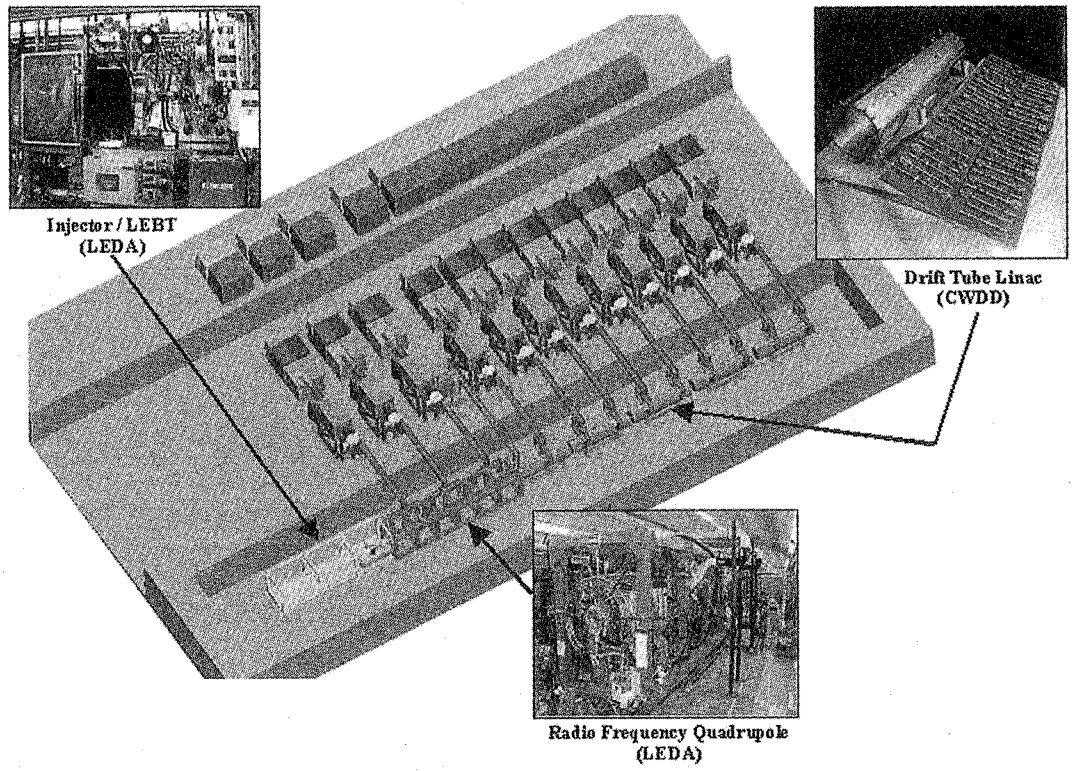


Fig. 2 Perspective view of updated linac with some design basis hardware references.

(3) Defining the IFMIF Accelerator Prototype

With the updated accelerator configuration established it was possible to define an appropriate accelerator prototype that would satisfy the following top level requirements that were agreed to by the IFMIF collaboration in October of 2001.

- Prototype to be a "full performance" accelerator up through the first tank of the DTL (8-10 MeV)
- Prototype tests are required to demonstrate high reliability and availability for the IFMIF system
- Prototype hardware will be suitable for use on the project as appropriate after testing

These three overriding requirements dictate the use of IFMIF equipment throughout the prototype such that the true operational characteristics can be demonstrated. Equipment that is available from other programs cannot properly demonstrate the performance of the integrated IFMIF system.

A further ground rule was established for performing the cost estimate of the prototype program.

The prototype will be installed and operated in a host facility that is capable of supplying infrastructure elements such as:

- Prime Power (~6.5 MW including substation, step-down transformers, power distribution)

- Shielded vault area, RF Hall, and ancillary areas (~2100 m^2 of vault, high bay with crane, shop and control room areas)
- Final heat rejection system (water & HVAC capable of ~6.5 MW)
- Support shops, RF labs, metrology physical security and radiation safety systems

A prototype accelerator system configuration that meets the above requirements is shown in Figure 3. For reference, the accelerator is shown in a with a vault and RF power hall that are the same size as the IFMIF facility. The system comprises a full performance D+ Injector and LEBT followed by the RFQ with its three, 1 MW RF Power systems. The matching section (MS) with 2 RF cavities follows the RFQ. For the prototype we have estimated 2 separate 70 kW RF power systems. This was done for expediency in performing this estimate and is not the result of a proper design process to determine the best RF sources for this application. After the MS is the first tank of the DTL with its single, 1 MW RF power system. These components and there primary subsystems represent the minimum system to satisfy the requirements of our prototype. These subsystems are the low level RF system and RF feedback/control system, the resonance control cooling systems for the RF cavities, the accelerator high vacuum system, and the minimum suite of beam diagnostics necessary for safe, stable operation. This machine, with an output energy of 9.31 MeV and a beam current of 125 mA, would be one of the most powerful accelerators in the world with average beam power of 1.16 MW.

A necessary element of the prototype system that will not be a part of the final IFMIF machine is a short High Energy Beam Transport (HEBT) system and a beam dump. The concepts for these components have been taken from the Continuous Wave Deuterium Demonstrator (CWDD) project that had a requirement for beam transport and stopping of a 80 mA CW deuterium beam. It is considered a

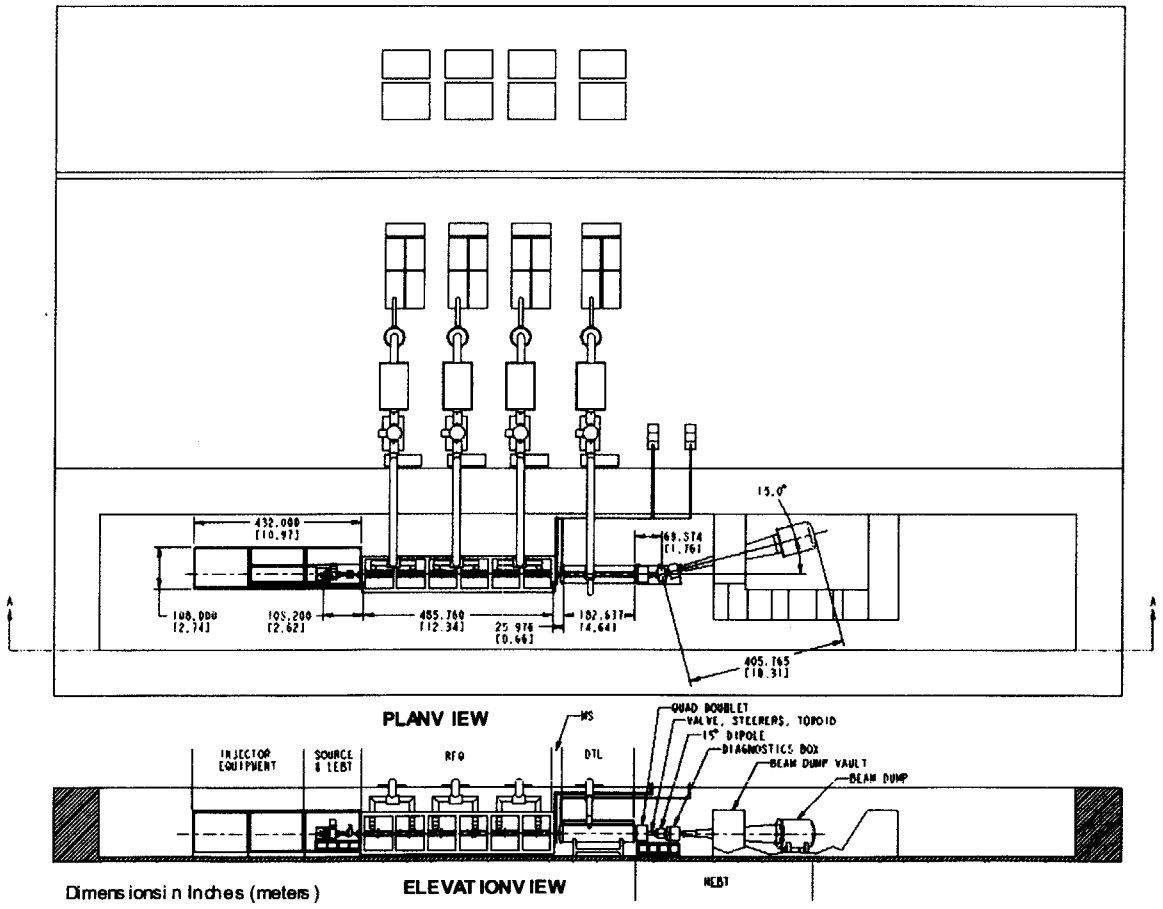


Fig. 3 Prototype Accelerator Layout (shown in IFMIF-size vault).

minimum system for this application. Figure 4 presents a perspective view of the prototype concept, highlighting each of the major elements.

The RF power requirements for each of the accelerator components was determined from the conceptual designs produced by Saclay and IAP. In both cases the RF system requirements are the same with three, 1 MW RF systems required for the RFQ and a single 1 MW RF system required for DTL tank 1. Power calculations for the Saclay RFQ design are presented in Figure 5. In this case a typical, roughly optimized, RFQ cross section consistent with the Saclay design has been analyzed in Superfish. The

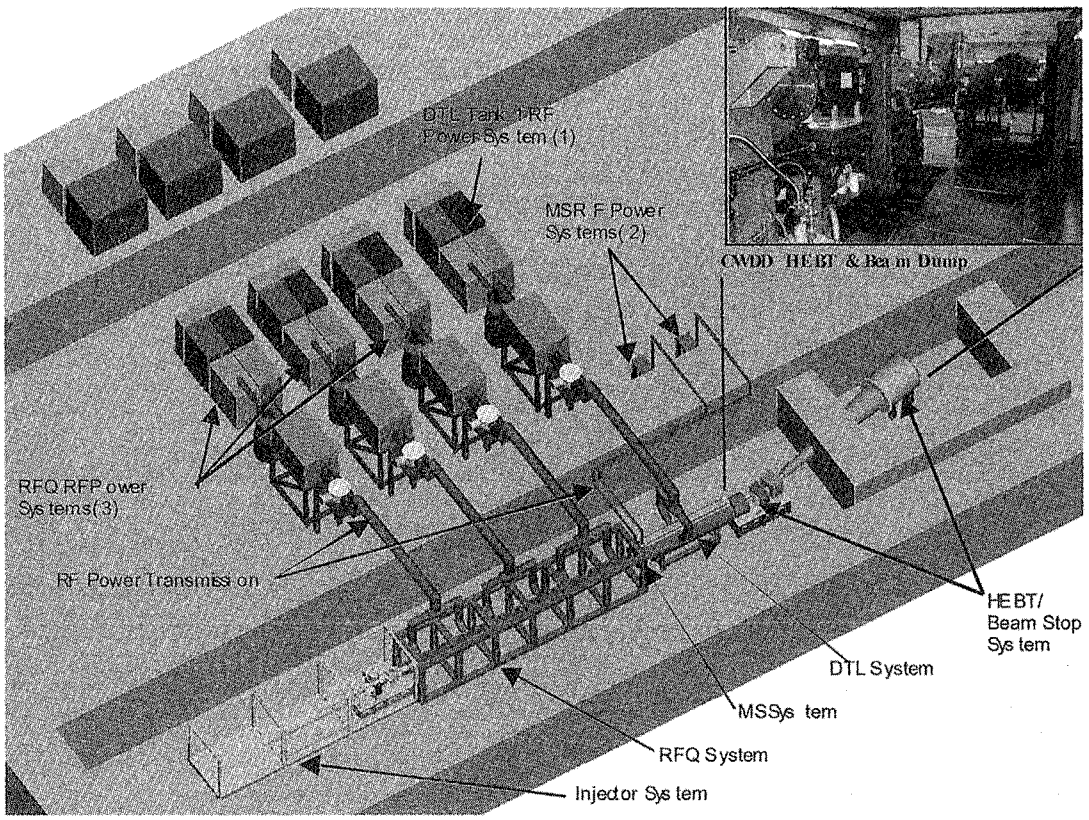
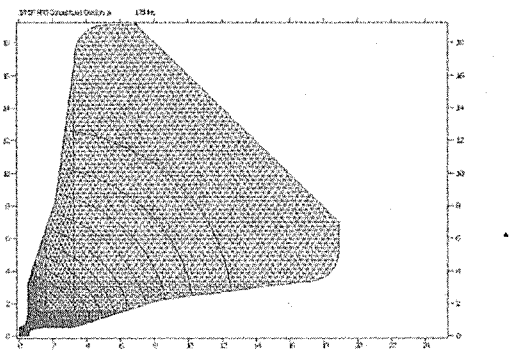


Fig. 4 Perspective view of the IFMIF Prototype Accelerator System.

SUPERFISH output summary for problem description:
IFMIF RFQ Conceptual Design a 175MHz
r0,Vg,rho,Ws,Ls,Wb,H,W= 0.561 .106 .477 2.22 0.00 3.36 19.10 7.00 Vary H
Problem file: D:\MyDocuments\IFMIF\RFQ\IFU1.AM 1-10-2002 14:58:14

All calculated values below refer to the mesh geometry only.
Field normalization (NORM = 0): EZERO = 9.44742 MV/m
Frequency (starting value = 175.000) = 174.99771 MHz
Normalization factor for E0 = 9.447 MV/m = 14722.664
Stored energy = 0.0017908 Joules/cm
Using standard room-temperature copper.
Surface resistance = 3.45126 milliOhm
Normal-conductor resistivity = 1.72410 microOhm-cm
Operating temperature = 20.0000 C
Power dissipation = 135.7888 W/cm
Q = 14500.6 Shunt impedance = 3687.439 MOhm/m
r/Q = 15.984 Ohm Wake loss parameter = 0.00439 V/pC
Average magnetic field on the outer wall = 3907.79 A/m, 2.635 W/cm^2
Maximum H (at X,Y = 19.0994,6.35179) = 3908.36 A/m, 2.636 W/cm^2
Maximum E (at X,Y = 0.33185,0.696082) = 24.333 MV/m, 1.7399 Kilp.
Ratio of peak fields Bmax/Emax = 0.2018 mT/(MV/m)
Peak-to-average ratio Emax/E0 = 2.5756



SUPERFISH Mesh – ¼ Segment

Cavity Power with 10% Field Margin = (1.21 * .1358 * 4 * 1248)/0.8 = **1025kW**
Beam Power Required = **613 kW**
Total Power = 1638 kW / 680 kW/Station = **2.41 Stations** ← **Need 3 Stations**
Beam Capability with 2 Stations = (1360 - 1025)/4.905 = **68 mA (45.6% low)**

Fig. 5 Power calculations for 175 MHz RFQ (Saclay Model).

Superfish power dissipation was then augmented assuming a requirement for at least 10% additional field capability (21% power increase). This value can be clearly justified by the experience at LEDA and many other facilities where operation at 5-10% higher field has been required. To the cavity power we have added the beam power of 613 kW to arrive at 2.4 RF power stations required. The value of 680 kW available from the RF power stations accounts for control margin, transmission losses, and coupling errors and has been agreed to by the IFMIF accelerator team.

(4) Cost Estimate for the IFMIF Accelerator Prototype Program

The accelerator prototype configuration as described above was presented to the IFMIF accelerator team at FZK Karlsruhe in January 2002. At that time the team agreed that this configuration satisfies the requirements for the IFMIF prototype and that a cost estimate for a program with this equipment is appropriate. Figure 6 summarizes the items included in the Prototype Program Cost Estimate.

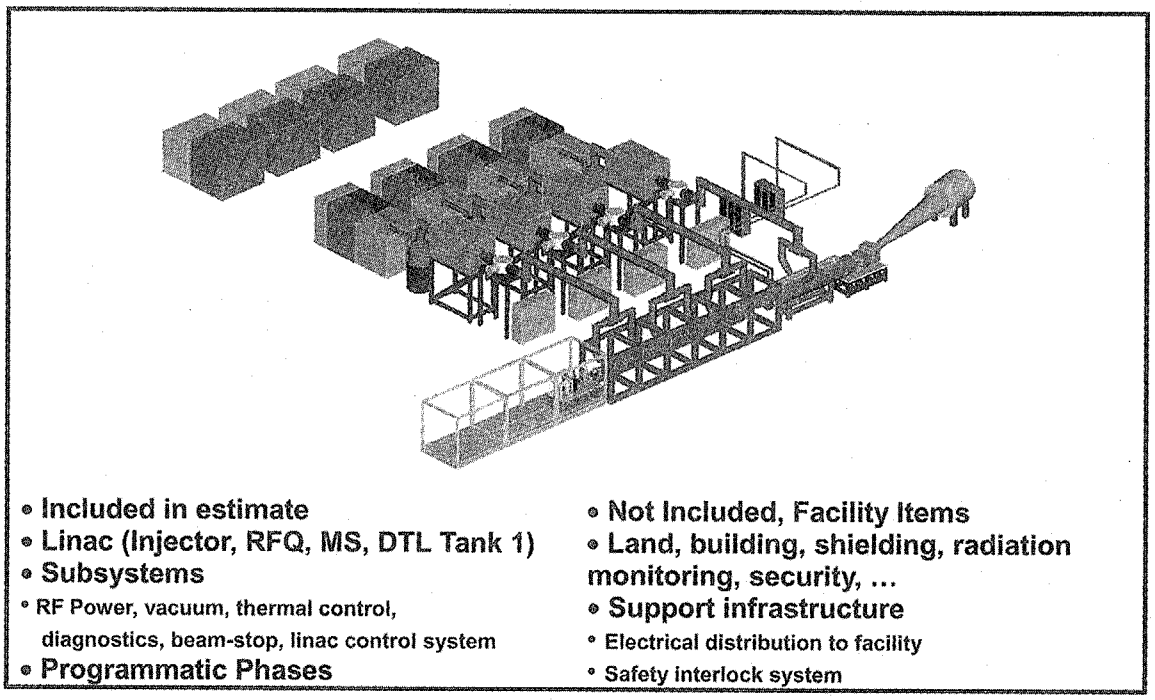


Fig. 6 Elements Included in and Excluded from Prototype Cost Estimate.

Figure 7 presents a Work Breakdown Structure (WBS) for the Prototype Accelerator Program and a cross-reference to the corresponding WBS items in the CDA cost estimate from 1996. Figure 8 presents the schedule for the prototype program that was used in generating the estimate. The CDA cost estimate was used as the basis for developing the costs for the prototype with credit given for work accomplished between 1996 and 2002. Figure 9 presents the details of the cost estimate along with the credits (expressed as a percentage of CDA) given in each area.

It must be emphasized that one goal of the prototype program is to build and operate an accelerator that is, to the greatest extent possible, the real IFMIF hardware. Further, it is expected that the hardware built under this project can be transferred to the final IFMIF facility and used "as is." This drives the requirement for the design phase of the program to be fully rigorous in all areas. Indeed, it is reasonable to view this Prototype Program as early fabrication and operation of the IFMIF front-end.

The project management and preliminary design areas of the cost estimate used only 25% of the CDA estimate for two primary reasons. First, progress has been made in areas of injector, RFQ, and DTL design since 1996 and some elements of the machine (i.e. HEBT, DTL tanks 2 thru 5) are not required for the prototype.

In the areas of accelerator final design, fabrication, and installation varying levels of credit have been used based on the individual area. These vary from 0% for the HEBT up to 100% for areas like the

Matching Section that has only recently been included in the baseline design, and 100% for the Beam Stop (includes short HEBT) that is unique to the prototype. Other percentages vary based again on progress since 1996 and/or the amount of the total system that is required for the prototype (i.e. DTL and RF Power).

The final major category of cost in the estimate is the operational set-up and commissioning including a full power test. For the purposes of this estimate the full power acceptance test was deemed to be the final element of the program at the end of 5 years and ongoing operations to build a reliability database were not considered. This category which covers a schedule period of 1.5 years with 6 to 9 months of dedicated operations has a total cost including AFI of 11.2 MICF. This can be compared to the approximate annual operating cost of LEDA at Los Alamos of approximately $15 M.

Prototype WBS	CDA WBS	WBS Name
		Prototype Design & Management
4.1	4.1.1	EVP Accelerator Project Management
4.2.1	4.2.1	Accelerator Equipment Preliminary Design (injector thru Beam Stop)
4.2.2	4.2.2	Accelerator Equipment Physics (injector thru Beam Stop)
		Prototype Accelerator
4.2.3.1	4.2.3.1	Injector System (H2+ and D+)
4.2.3.2	4.2.3.2	Radiofrequency Quadrupole System
4.2.3.3 & 4.2.3.7.4		Matching Section System (with two 70 kW RF stations)
4.2.3.4	4.2.3.3	Drift Tube Linac Tank #1 System
4.2.3.5	4.2.3.4	HEBT System
4.2.3.2 & .3	4.2.3.5	RF Drive Loop
4.2.3.2 & .3 & .4 & .5	4.2.3.6	Acc & HEBT Thermal Control Systems
4.2.3.7	4.2.3.7	RF Power System
4.2.3.6	4.2.5	Beam Dump
4.2.4	4.2.6	Accelerator System Control
4.2.3.2 & .3 & .4 & .5	4.2.7	Accelerator Support Systems
		Accelerator Installation and Checkout
4.3.1.1	4.3.1.1	Injector system
4.3.1.2	4.3.1.2	RFQ System
4.3.1.3		Matching Section System
4.3.1.4	4.3.1.3	DTL Tank#1 System
4.3.1.5	4.3.1.5	HEBT
4.3.1.6	4.3.1.6	RF Power System
4.3.1.5	4.3.1.7	Beam Dump
4.3.2	4.3.1.9	Accelerator System Control Installation & Checkout
		Operational Startup & Commisioning
4.4.6	4.3.1.8	Full Power acceptance test
4.4.1.1	7.1.1	Personnel & Overhead:Admin & OH Staff
4.4.1.2	7.1.2	Personnel & Overhead: Accelerator Operations Staff
4.4.2.1	7.2.1	Electrical Power: Prototype Accelerator
4.4.2.2	7.2.3	Electrical Power: Balance of Plant
4.4.3.1	7.3.1	Utilities: Inert Gas
4.4.3.2	7.3.2	Utilities: Deionized water
4.4.3.3	7.3.3	Utilities: Sewer / Water
4.4.4.1	7.5.1	Waste Disposal: Uncontaminated
4.4.4.2	7.5.2	Waste Disposal: Contaminated

Fig. 7 Work Breakdown Structure for Prototype Program and Corresponding WBS Items from the CDA Cost Estimate.

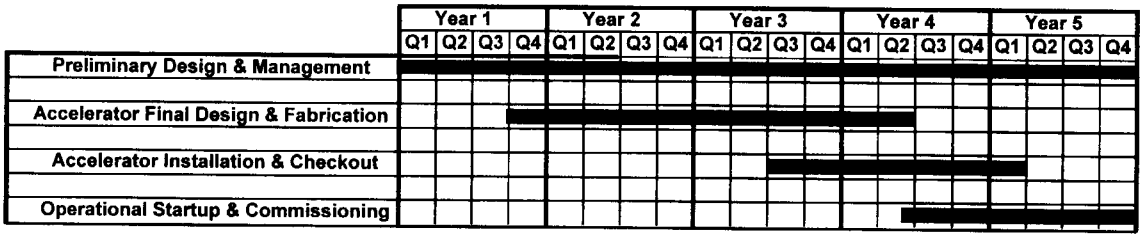


Fig. 8 Schedule for Completion of the Accelerator Prototype Program.

CDA WBS	WBS Name	%CDA Engrg	%CDA Mat'l	Cost Instit. Engrg	Cost Ind. Engrg	Cost Ind. Lab/Mat'l	Total Cost - No AFI	%AFI For Proto	AFI	Cost - Total KICF
	Prototype Design & Management									
4.1.1	IVP Accelerator Project Management	25%		0	4,506	0	4,506	25%	1,126	5,632
4.2.1	Accelerator Equipment Preliminary Design (injector thru Beam Stop)	25%		0	3,632	0	3,632	30%	1,089	4,721
4.2.2	Accelerator Equipment Physics (injector thru Beam Stop)	25%		0	1,766	0	1,766	25%	441	2,207
	Prototype Accelerator									
4.2.3.1	Injector System (H2+ and D+)	75%	50%	182	793	1,115	2,090	30%	627	2,717
4.2.3.2	Radiofrequency Quadrupole System	75%	100%	268	1,884	9,045	10,976	30%	3,293	14,269
(new)	Matching Section System (with two 70 kW RF stations)	100%	100%	688	688	1,366	2,741	30%	822	3,563
4.2.3.3	Drift Tube Linac Tank #1 System	50%	20%	337	3,515	2,947	6,798	30%	2,039	8,836
4.2.3.4	HEBT System	0%	0%	0	0	0	0	0%	0	0
4.2.3.5	RF Drive Loop	75%	25%	53	1,665	0	1,718	25%	429	2,147
4.2.3.6	Acc & HEBT Thermal Control Systems	75%	50%	0	1,568	0	1,568	30%	470	2,038
4.2.3.7	RF Power System	30%	33%	585	3,080	17,087	20,753	30%	6,226	26,979
4.2.5	Beam Dump	100%	100%	0	1,928	3,315	5,243	30%	1,573	6,815
4.2.6	Accelerator System Control	50%	25%	71	2,291	171	2,532	30%	760	3,292
4.2.7	Accelerator Support Systems	25%	25%	0	572	0	572	25%	143	714
	Accelerator Installation and Checkout									
4.3.1.1	Injector system	50%	50%	27	43	383	452	30%	136	588
4.3.1.2	RFQ System	75%	100%	20	47	741	808	30%	242	1,050
(new)	Matching Section System	100%	100%	30	72	135	237	30%	71	308
4.3.1.3	DTL Tank#1 System	75%	100%	23	54	676	753	30%	226	978
4.3.1.5	HEBT	0%	0%	0	0	0	0	0%	0	0
4.3.1.6	RF Power System	30%	30%	86	171	1,890	2,147	30%	644	2,792
4.3.1.7	Beam Dump	35%	35%	26	62	529	617	30%	185	802
4.3.1.9	Accelerator System Control Installation & Checkout	25%	25%	0	0	192	192	25%	48	240
	Operational Startup & Commisioning									
4.3.1.8	Full Power acceptance test	25%	25%	191	357	1,019	1,566	30%	470	2,036
7.1.1	Personnel & Overhead: Admin & OH Staff	100%	100%	1,714	0	700	2,414	30%	724	3,138
7.1.2	Personnel & Overhead: Accelerator Operations Staff	100%	100%	2,488	0	1,050	3,538	30%	1,061	4,599
7.2.1	Electrical Power: Prototype Accelerator	100%	100%	0	0	912	912	30%	274	1,186
7.2.3	Electrical Power: Balance of Plant	100%	100%	0	0	49	49	30%	15	64
7.3.1	Utilities: Inert Gas	100%	100%	0	0	6	6	30%	2	8
7.3.2	Utilities: Deionized water	100%	100%	0	0	6	6	30%	2	8
7.3.3	Utilities: Sewer / Water	100%	100%	0	0	110	110	30%	33	144
7.5.1	Waste Disposal: Uncontaminated	100%	100%	0	0	9	9	30%	3	12
7.5.2	Waste Disposal: Contaminated	100%	100%	0	0	0	0	30%	0	0
		Totalls ==>		6,786	28,470	43,454	78,710		23,175	101,886

Fig. 9 Cost Estimate Breakdown for the Accelerator Prototype Program All costs given in kICF.

(5) Summary

A technical specification, design configuration, and corresponding cost estimate has been generated for a prototype front end accelerator for the IFMIF project. This work was done in order to provide project management with the information necessary to make a decision as to whether the EVEDA phase of the IFMIF program could support such an undertaking.

The technical specification addressed the desires of the IFMIF user group and the resulting machine configuration was developed using the latest work by the IFMIF accelerator team. The backbone of the cost estimate was the original IFMIF estimate generated by the IFMIF team during the CDA in 1996 and appropriate factors were applied to account for the scope of the prototype program and for technical progress made in the intervening years. Finally, the complete prototype specification, configuration, and cost estimate were iterated several times by the IFMIF accelerator team prior to being finalized in March 2002.

References

[1] "Prototype Accelerator Cost Estimate", T. Myers, J. Rathke, Tokyo, Japan, March 2002, "IFMIF Prototype Cost 3-7-02.pdf".

[2] "International Fusion Materials Irradiation Facility IFMIF Prototype Accelerator Configuration Study", J. Rathke, T. Myers, Tokyo, Japan, March 2002, "IFMIF Prototype Configuration 3".

3.2 Target Facilities

3.2.1 TG11A-EU : Water Experiment at the Joint of the Replaceable Back-plate

(1) Brief Task Description

In 2000 ENEA, in the framework of the IFMIF Key Element Technology Phase, launched an R&D activity on the lithium target system of the International Fusion Materials Irradiation Facility (IFMIF). In particular, its activity is the water flow simulation experiment on the nozzle-backplate mock-up of the Li target system. The main aim of the experiment is the evaluation of the water jet stability using as relevant parameters the target back wall curvature, the precision of the joint between the nozzle and the target back plate, and its surface roughness. The test activity is carried-out on the CEF 1-2 thermal hydraulic facility at ENEA Brasimone.

Contributors

Name	Party	Institute	E-mail address
G.Dell'Orco	EU	ENEA	Giovanni.dellorco@brasimone.enea.it

(2) Introduction

In the IFMIF testing facility, the required high-energy neutron emission is produced by the stripping reaction of two D^+ beams bombarding a free surface liquid lithium jet target flowing along a concave back-wall at high speed (< 20 m/s) [1]. The stability of the lithium jet influences the neutron field and the integrity of target system. The concave back-wall was selected to increase the lithium boiling point beyond 340°C by using the centrifugal force on the jet flow.
In 2000 ENEA, in the framework of the IFMIF Key Element Technology Phase and in close co-operation with JAERI, launched a testing activity on the water jet flow simulation of the nozzle-backplate of the reference lithium target, aimed at verifying which parameters affect the free jet surface stability. ENEA, on the base of the available reference IFMIF lithium target geometry and thermal hydraulic data, has designed an experimental mock-up, called HY-JET, and has planned the related water experiment. The main aims of the test activity were focused on:

- Evaluation of the stability of the IFMIF lithium jet flow on the target by water experiments on HY-JET that simulate a double reduced nozzle and curved replaceable back plate;
- Monitoring of the cavitation occurrence near the nozzle and the orifice flow straighter of the HY-JET mock-up.

At the beginning of 2002, ENEA, on the base of the previous design of the experiments, issued a Technical Specification [2] and launched a call for tender for the fabrication of the HY-JET mock-up and the relevant modification of the ENEA CEF1-2 thermal hydraulic facility.

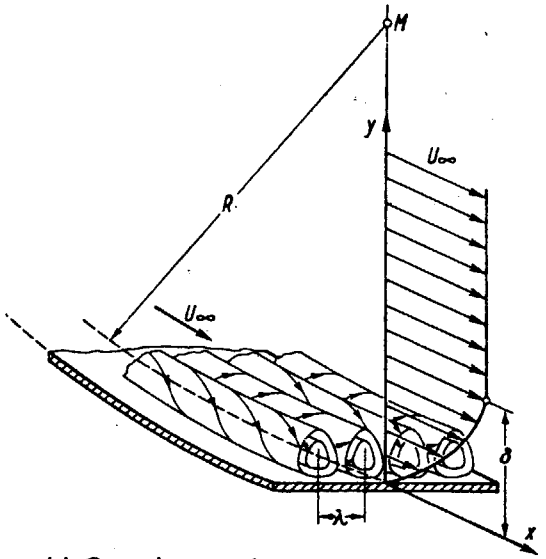
(3) Design of the experimental equipment

One-dimensional calculations, using the water/lithium hydraulic equivalence in Reynolds number, were also carried out for selecting both the hydraulic test parameters and the mock-up geometry Table 1 [3].

Table 1 Geometrical and hydraulic equivalence between IFMIF and HY-JET.

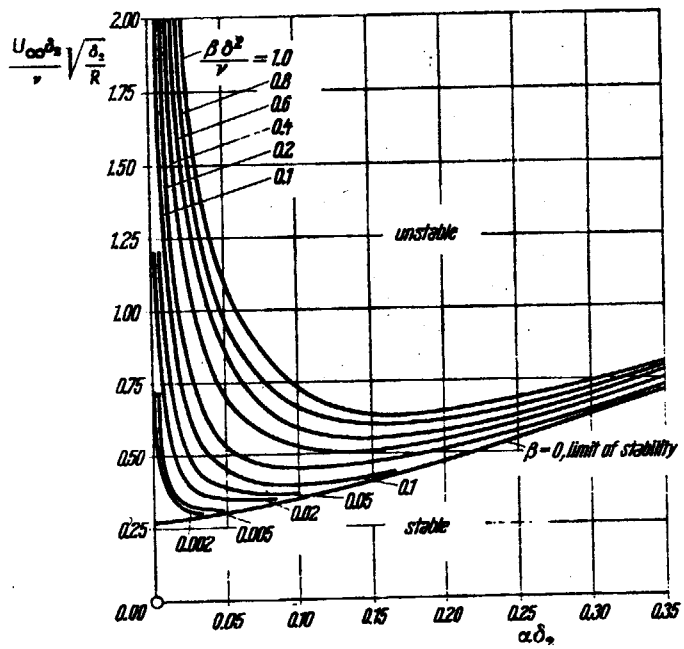
NOZZLE CROSS SECTION							
IFMIF Real scale				HY-JET MOCK-UP (Scale ratio = 0.8)			
Width [m]	Height [m]	Area [m^2]	Hydr.Diam. [m]	Width [m]	Height [m]	Area [m^2]	Hydr.Diam. [m]
0,26	0,025	0,0065	0,045614035	0,200	0,020	0,00416	0,036491228
Out. velocity [m/s]		15 (10-20)		Out. velocity [m/s]		10	
flow rate [l/s]		max.130		flow rate [l/s]		41,6	
				pressure drop [Pa]		4,99E+04	
HYDRAULIC EQUIVALENCE BETWEEN LITHIUM AND WATER							
LITHIUM				WATER			
Temperature [°C]	density [kg/m3]	dynamic viscosity [Pa s]	Reynolds number	Temperature [°C]	density [kg/m3]	dynamic viscosity [Pa s]	Reynolds number
200				0	999,8000	1,79E-03	2,04E+05
300				10	999,0000	1,31E-03	2,78E+05
400	490,0	4,20E-04	7,98E+05	20	998,2000	1,00E-03	3,64E+05
500				30	995,4000	7,97E-04	4,56E+05
				40	992,4000	6,53E-04	5,55E+05
				50	990,5000	5,47E-04	6,61E+05
				60	980,7000	4,65E-04	7,70E+05
				70	975,5000	4,11E-04	8,66E+05
				80	971,8000	3,55E-04	1,00E+06
				90	965,0000	3,17E-04	1,11E+06
				100	957,1000	2,82E-04	1,24E+06

The risk of hydraulic instability in the jet flow along the concave backplate was also evaluated by means of the Goertler similitude [4], Fig. 1. The calculated Goertler number appears high enough to suspect the occurrence of vortex instability [5], Fig. 2. This occurrence needs to be further investigated by experimental testing.



b) Goertler vortices

Fig. 1 Goertler vortices for flow along concave wall [4].



Stability curves for flow along a concave wall, as calculated by H. Goertler [46] and G. Haemmerlin [52]

δ_2 = momentum thickness; δ = boundary layer thickness; β = amplification factor from eqn. (17.24); R = radius of curvature of wall

Fig. 2 Stability curves for flow along concave wall [4].

As a design result, the experimental mock-up will simulate the reference IFMIF lithium target in smaller geometrical scale with a 200 x 20 mm free surface jet flow, Fig. 3-5. A comparison among IFMIF, Osaka and ENEA Brasimone mock-ups is shown in Table 2. In order to assure more experimental flexibilities in the selection and change of the more interesting test section parameters, the HY-JET mock-up was subdivided into the following separated flanged pieces, Fig. 5: i) flow straightener, ii) multi-hole diaphragm pressure reducer, iii) double reduced nozzle, iv) curved backplate.

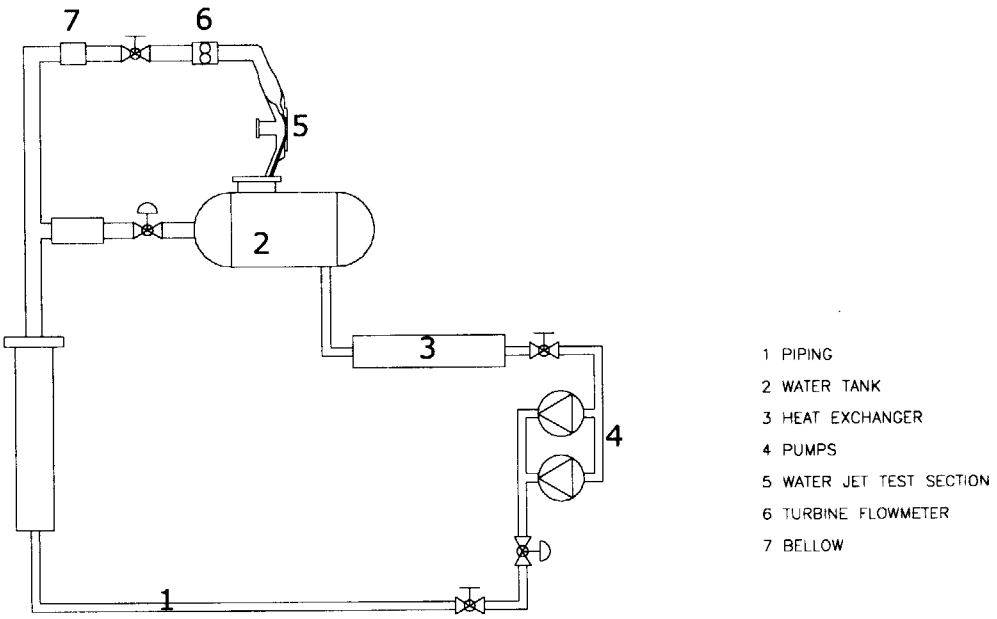


Fig. 3 Scheme of the CEF 1-2 thermal hydraulic test facility.

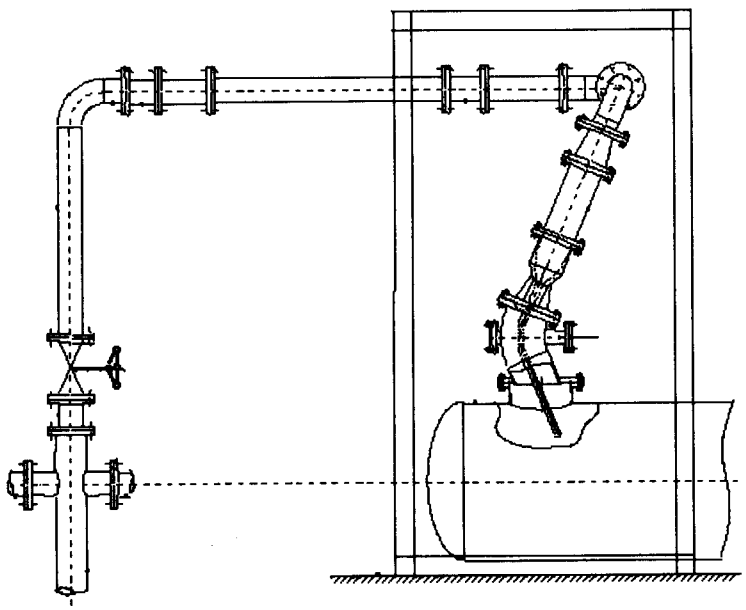


Fig. 4 Scheme of the frontal view of the HY-JET mock-up and connection to the CEF 1-2 thermal hydraulic test facility.

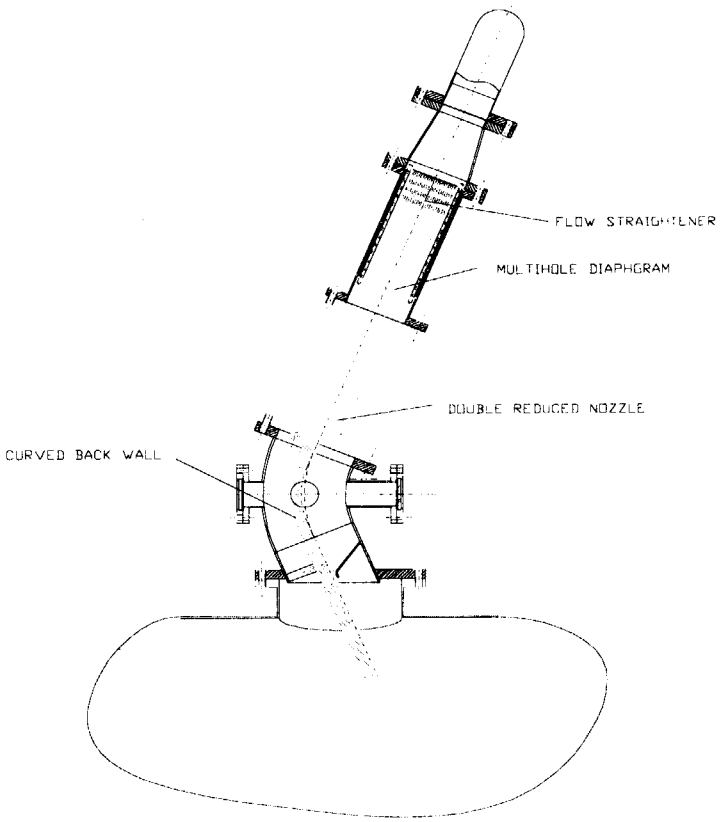


Fig. 5 HY-JET mock-up and connection to the CEF 1-2 test facility (particular).

Table 2 Comparison among IFMIF, Osaka and ENEA Brasimone mock-ups.

Parameter	IFMIF Li loop	Water Exp.(1) JAERI	Water Exp.(2) JAERI	Osaka Li loop	Water Exp. ENEA
Nozzle Geometry	Double Reducer Nozzle	Double Reducer Nozzle	Double Reducer Nozzle	Double Reducer Nozzle	Double Reducer Nozzle
Back wall Geometry	Concave (R=250 mm)	Concave (R=250 mm)	Straight	Straight	Concave (R=250-450 mm)
Jet Thickness (mm)	25	20	10	10	20
Jet Width (mm)	260	240	100	70	200
Li/water Speed (m/s)	20	20	20	15	10-20
Flow Rate (l/s)	130	96	20	10.5	30-80
Vacuum Condition (Pa)	10^{-3}	10^{5}	10^{4} - 10^{5}	100-1000 (TBC)	Pressure $5x10^{5}$ (Pa)
Nozzle Material	304L	acrylic resin	acrylic resin	304 SS	304L SS

Both the flow straightener and the multi-hole diaphragm pressure reducer, Fig. 6, were designed to assure a proper matching with the pressure drop available in the CEF 1-2 thermal hydraulic experimental facility [3]. The reference IFMIF lithium jet flow will be simulated by a double reduced nozzle and a curved target backplate. The nozzle, Fig. 7, was designed by the following correlations derived from the Shima model [6]:

$$2\pi x / De = (R + 1) \tanh^{-1}(\cos\theta) + 1/2\,(R - 1) \ln[2\,(1 - \cos 2\theta)] + [((2(R+1))^{0.5} - (R + 1)] \cos\theta ;$$

$$2\pi y / De = \pi + (R - 1)\,\theta + [((2(R+1))^{0.5} - (R + 1)] \sin\theta ;$$

with $R = Di / De$, $0 < \theta < \pi$, Di = inlet nozzle width at $\theta = \pi$, De= outlet nozzle width at $\theta = 0$.

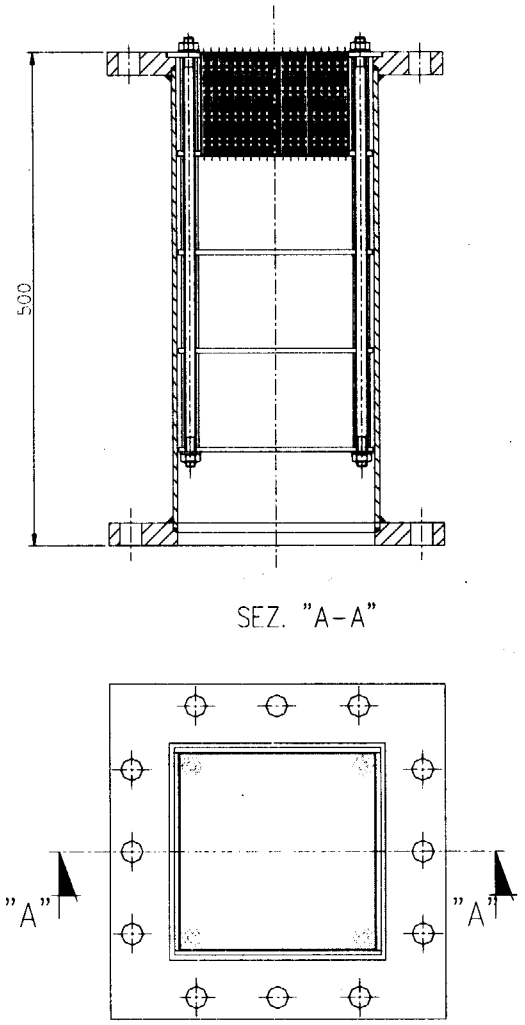


Fig. 6 Multi-hole diaphragm pressure reducer of the HY-JET mock-up.

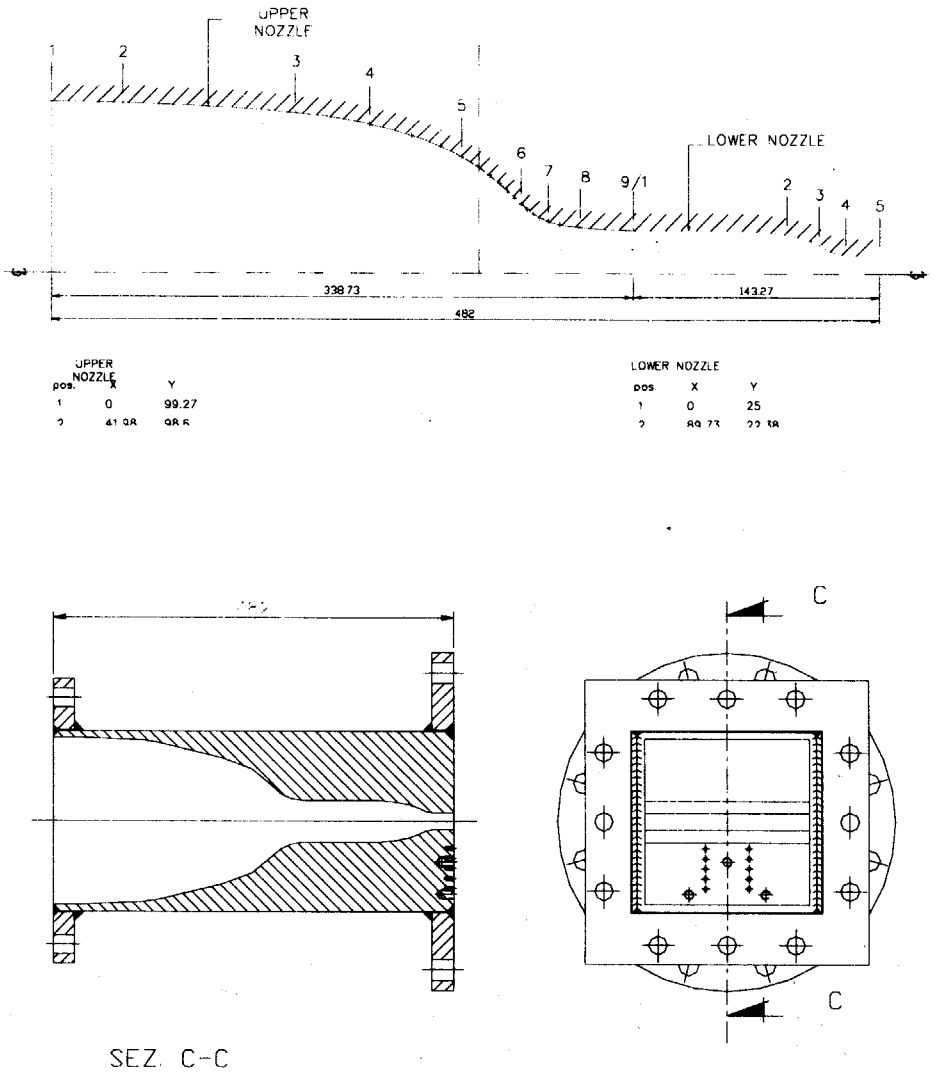


Fig. 7 Double reduced nozzle of the HY-JET mock-up.

The curved backplate, Fig. 8, designed with reference to the IFMIF target, is flanged to the nozzle; therefore it is interchangeable with different radius. The experimental test matrix was obtained, according to the reference assumption [7], varying the water jet flow velocity on the mock-up when the following test parameters are assumed as fundamental: i) nozzle shape, ii) jet thickness, iii) back wall curvature; iv) surface roughness, v) precision of the joint between the nozzle and the target back plate.

The basic selection of the experimental parameters is the following: i) backplate curvature: 250-450 mm; ii) tolerance of the joint between the nozzle and the target backplate: ± 0.1 mm; iii) backplate surface roughness: 1 – 10 μm.

The hydraulic instability waves will be monitored by optical penetrations located on the front and lateral sides downstream of the free surface jet flow, Fig. 5, and it will be recorded by a high-speed camera. The monitoring of the cavitation occurrence, close to the nozzle and the flow straightener/ multi-hole diaphragm pressure reducer, will also be performed during the water jet tests by means of the CASBA-2000 ENEA patented equipment [8].

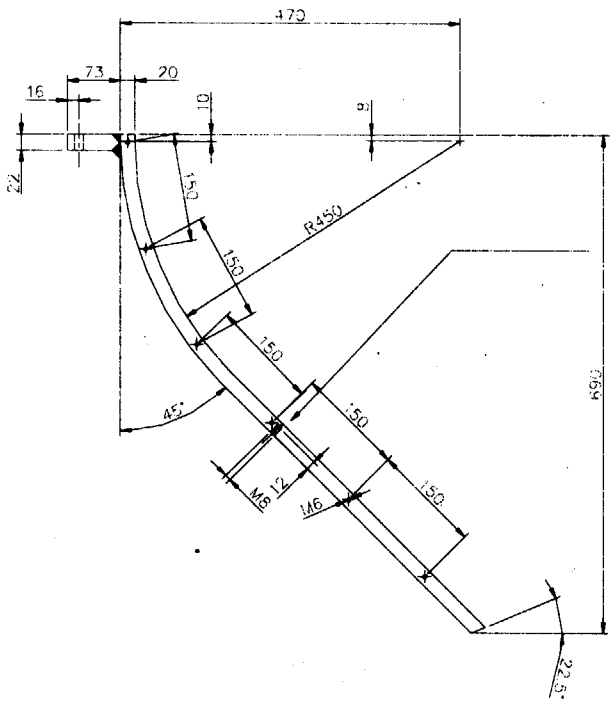


Fig. 8 Curved backplate of the HY-JET mock-up.

(4) Conclusion

The ENEA testing activity on the water jet flow simulation of the nozzle backplate of the reference lithium target was started in 2000. The design of the test and Technical Specification [2] related to the mock-up was finished at the beginning of 2002. The mock-up manufacturing and the relevant water loop modification were finished in Dec. 2002. The tests will start in Jan. 2003 and will be completed by mid 2003.

References

[1] M.Martone, (editor), IFMIF International Fusion Materials Irradiation Facility Conceptual Design Activity Final Report, ENEA Frascati Report, RT/ERG/FUS/96/11, November 1996.

[2] G. Dell'Orco, F. Desideri, Specifica tecnica per la fornitura di una sezione di prova denominata HY-JET e modifiche all'impianto CEF1-2, ENEA Int. Report, IM-G-S-001, Mar. 2002

[3] G. Dell'Orco et al., Li-Target Tasks Deliverables 2-3, IFMIF Meeting on 2001 Monitoring and 2003 Tasks, Karlsruhe, 30 January - 1 February, 2002

[4] H. Schilchting, Boundary-Layer Theory, Mc Graw-Hill Book Company, 1968, pp. 506-508

[5] B.Riccardi, M.Martone, C.Antonucci, L.Burgazzi, S.Cevolani, D.Giusti, G.Dell'Orco, C.Fazio, G.Miccichè, M.Simoncini, Activities on IFMIF Lithium Target at ENEA, 22nd Symposium on Fusion Technology, 9 – 13 September, 2002 , Helsinki, Finland

[6] H. Nakamura, K. Itoh, Y. Kukita, M.Ida, Y. Kato, H. Maekawa, Water Experiment of high-speed, free-surface, plane jet along concave wall, 8th International Topical meeting on nuclear Reactor Thermal Hydraulic (NURETH-8), 30 Sept. – 4 Oct., 1997, Kyoto, Japan

[7] M. Ida, H. Nakamura, H. Nakamura, K. Ezato, H.Takeuchi, Thermal-hydraulic Characteristics of IFMIF Liquid Lithium Target, ISFNT-6, 8-12 Apr. 2002, San Diego, USA

[8] D. Tirelli, CASBA 2000–Operating Manual, Demo Center, Modena - Italy, September 2002

3.2.2 TG11B-JA : Examination of the Lithium Target Free Surface Behavior under Low Pressure

(1) Brief Task Description

The IFMIF liquid Li Target flows at high speeds, up to 20 m/s. Furthermore, the free surface covers a large area, 260 mm wide and 350 mm in the flow direction. The stability of the Li jet influences the neutron field and the integrity of the Target system. The free surface behavior in the flow direction influences the stability of the high-speed, broad jet under high vacuum conditions. The free surface behavior is simulated in a low pressure water experiment. The experiment at JAERI uses horizontal water flow with a 100 mm-wide free surface water jet. The equipment has been modified to produce a free surface under low pressure condition. Waves on the free surface are observed using a high-speed camera under various jet velocity conditions, and the length and amplitude of surface waves are measured.

Contributors

Name	Party	Institute	E-mail address
M.Ida	Japan	JAERI	ida@ifmif.tokai.jaeri.go.jp
Hideo Nakamura	Japan	JAERI	nakam@lstf.tokai.jaeri.go.jp
Hiroshi Nakamura	Japan	JST	nakamura@metaljetp.com
K.Ezato	Japan	JAERI	ezatoku@fusion.naka.jaeri.go.jp
Hiroo Nakamura	Japan	JAERI	nakamurh@fusion.naka.jaeri.go.jp

(2) Introduction

IFMIF is an accelerator-based D-Li neutron source designed to simulate the neutron irradiation field in a fusion reactor. After the IFMIF Conceptual Design Activity (CDA)[1] in 1995-96 and the Conceptual Design Evaluation (CDE)[2] in 1997-98, the IFMIF project proceeded to the next phase: the Key Element Technology Phase (KEP)[3] to reduce key technology risk.

In the IFMIF target, free surface liquid Li flows at speeds up to 20 m/s to remove the heat load of up to 10 MW (1 GW/m^2). This heat is generated by D^+ beams with energies up to 40 MeV and currents up to 250 mA. The stability of the flow surface affects the neutron field and irradiation conditions. Furthermore, significant flow fluctuations may affect flow integrity and long-term operating stability of IFMIF. Therefore, flow stability is a main issue for the IFMIF target system, and was evaluated in the KEP.

Water flow experiments have been employed to simulate IFMIF liquid Li flow because the kinematic viscosity of water at 20°C (1.01 x 10^{-6} m^2/s) and Li at 250°C (0.98 x 10^{-6} m^2/s) are similar. Both flows are nearly equal in Reynolds number under common conditions of geometry and flow velocity. (Li average temperature is increased from 250°C to 285°C by 250 mA beam heating.) The validity of a double reducer nozzle to generate high-speed flow without separation was confirmed in the CDA[4] through water experiments using a nearly full-scale nozzle. Measurements of velocity and pressure in a nozzle region, including boundary layers in a water flow experiment, are useful for designing a Li flow experiment. Thermal-hydraulic analyses of the Li target stability showed that the heated Li flow would not boil [5], because the Li boiling point increases with the pressure induced by the centrifugal force in flow along the concave wall. After these experimental and analytical investigations, the main concern has shifted to the hydraulic stability of the free surface. In the water flow experiments performed previously, smooth 2D and 3D wave regions were observed on the free surface from the nozzle exit to downstream, and they depended on the average velocity [6]. Significant instability of the free surface should be avoided to ensure reliable IFMIF operation. Therefore, the effects of nozzle condition on the surface instability should be clarified to determine the target nozzle design.

This report describes water experiments performed at the Japan Atomic Energy Research Institute (JAERI) to clarify the effects of the inner wall roughness of the upstream nozzle on behavior of the surface waves. The results will be used to develop nozzle manufacturing specifications for subsequent

Li flow experiments. Results of Li flow experiments will be utilized for the design and manufacture of the IFMIF target. The Li flow experiments planned as a collaboration between the National Institute for Fusion Science and JAERI, involving a modification of an existing Li test facility at Osaka University, is also described. The experiments will investigate the characteristic behavior of flowing liquid Li.

(3) Experimental equipment and conditions

Previous water flow experiments showed that the main cause of surface waves was boundary layer formation along the nozzle inner wall upstream of the free surface [6]. Growth of the surface wave depended on flow velocity [5,6]. Another possible cause was the pressure of the cover gas at the free surface. The water experiments in the CDE [6] were performed under a pressure of 0.1 MPa.

The water experiments in KEP were performed at JAERI using two types of test sections to investigate the effect of nozzle wall roughness on free surface stability. One nozzle had an inner wall roughness of 6.3 μm and the other a roughness of 100 μm. Figure 1 shows a schematic of a test section made of acrylic resin. The test section was placed horizontally to make free surface observations convenient. The effect of gravity on the wave amplitude was negligible for high-speed (10-20 m/s) flow, according to a linear stability analysis of surface waves[4]. This analysis also showed that the effect of centrifugal force on surface stability was not significant for water and Li flows. Therefore, straight test sections have been employed to investigate such surface behavior. Through the double reducer nozzle, a water flow with a thickness of 100 mm and a width of 100 mm is reduced to a thickness of 10 mm and a width of 100 mm. A flow straightener composed of a honeycomb and multi-hole-diaphragms was installed upstream of the nozzle. To maintain test conditions of water viscosity which influences the velocity distribution in the boundary layer, the water temperature was roughly controlled by regulating city water flow. Differences between pure and city water did not affect the velocity measurement efficiency.

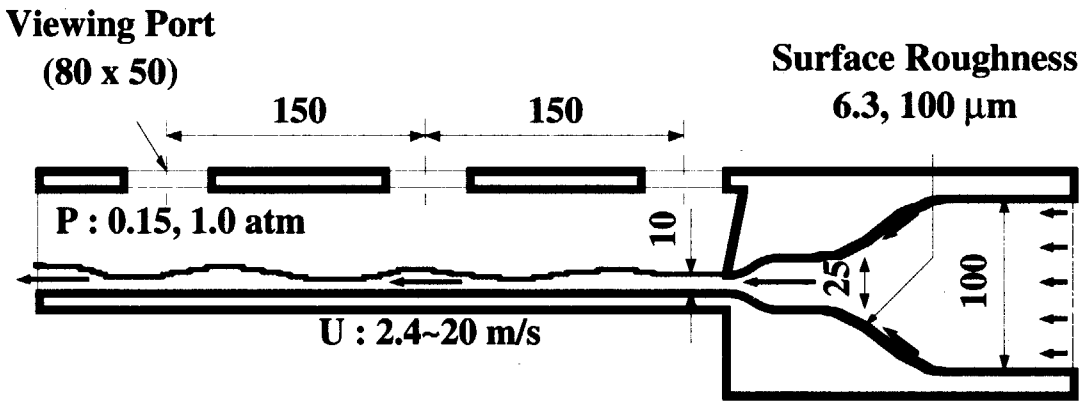


Fig. 1 Schematic cross section of test section for water experiments.
(High-speed water flow is generated through a double reducer nozzle at the right side, and flows left with free surface. This test section is made of acrylic resin for observation using a high-speed digital camera and velocity measurement using LDV.)

The average flow velocity at the nozzle exit ranged from 2.4 to 20 m/s in the experiments. The velocity distribution at the nozzle exit was measured using an argon laser source (Spectra Physics, Model 168-06) and a Laser Doppler Velocimeter (LDV, Aerometrics RSA-2000). Measurements with a resolution of 0.01 mm were performed near the wall on the free surface side to obtain data in the boundary layer. Behavior of the free surface was observed using a high-speed digital camera at

locations near the nozzle exit and 150 mm downstream from the exit. The latter location corresponds to the bottom of the footprint of the D^+ beam in IFMIF. The cover gas (air) pressure at the free surface ranged from 0.015 to 0.1 MPa to investigate the effect of cover gas pressure on growth of the surface waves. The surface behavior at 0.015 MPa was observed through acrylic windows, although the windows were sometimes misted by splash or vapor from the water surface.

(4) Results and discussions

The effect of cover gas pressure on the surface wave growth was found to be insignificant by comparing results from 0.1 MPa and 0.015 MPa experiments. These experiments were the first comparing the effects of cover gas pressure. An air stream was found to flow along the flow surface. This behavior lessened, even at a pressure of 0.1 MPa, the Kelvin-Helmholtz instability caused by velocity difference between gas (air) and liquid (water). This result is useful for planning Li flow experiments, where a test section is to have a gas (Ar) phase in a closed, limited volume nearly equal to that in the water experiments. Subsequent Li experiments can thus be performed under gas-covered conditions, which is advantageous to avoid cavitation in experiments using an electromagnetic pump (EMP). The result also suggests that surface waves may occur even on the IFMIF target under a near-vacuum condition of $1x10^{-3}$ Pa. Therefore, the behavior of the surface wave should be clarified for continuous long-term operation of the IFMIF target system. Utilizing the above result, the rest of the experiments were performed under a cover gas pressure of 0.1 MPa, and the surface behavior was observed without the acrylic windows. The experiments were performed using smooth (wall roughness : 6.3 μm, defined as a height between the highest and the lowest points) and rough (100 μm) wall nozzles and varying flow velocity. Figure 2 shows the dependence of the surface behavior on the speed of the water flow.

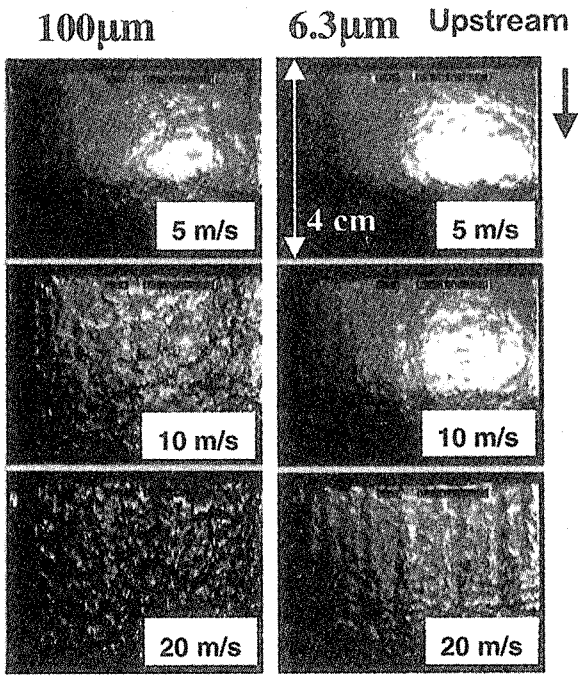


Fig. 2 Free surfaces observed at viewing ports 150 mm downstream from nozzle exit, which corresponds to of the bottom of the IFMIF beam footprint.

The wall roughness of the reducer nozzle was found to promote interfacial instability, especially at a speed of 10 m/s or more in the rough wall nozzle case. The velocity range of 10-20 m/s corresponds to IFMIF operations. This result suggests that the rough wall nozzle may be not acceptable for IFMIF operation. More exact investigations of the surface behavior of Li flow will be performed in subsequent Li flow experiments. The cause and growth of surface waves can be understood in connection with the boundary layer at the nozzle exit. Figure 3 shows velocities near the walls at the nozzle exit. The boundary layer thickness decreases with increasing mean velocity in the smooth wall nozzle. At a mean velocity of about 20 m/s, the boundary layer thickness is about 0.08 mm (defined at a velocity 90% of the mean velocity). However, in the rough wall nozzle, the boundary layer thickness increases in the high velocity range of 10-20 m/s, while it decreases in the low velocity range up to 5 m/s. In the case of 20 m/s, the thickness is about 0.26 mm. A characteristic change was observed in the boundary layer in the rough wall nozzle above 5 m/s.

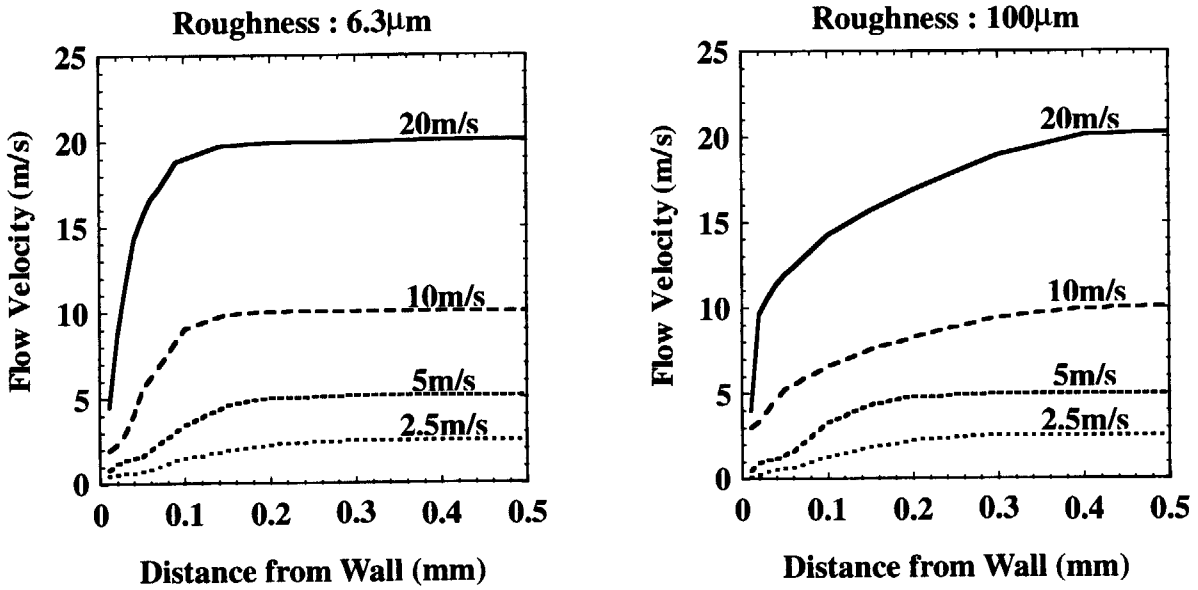


Fig. 3 Velocity distribution near wall.
(The left and the right graphs show velocities at the exit of the smooth and the rough wall nozzles, respectively. The boundary layer thickness decreases with increasing mean velocity in the smooth wall nozzle, while the thickness increases in the rough wall nozzle in the velocity range above 5 m/s.)

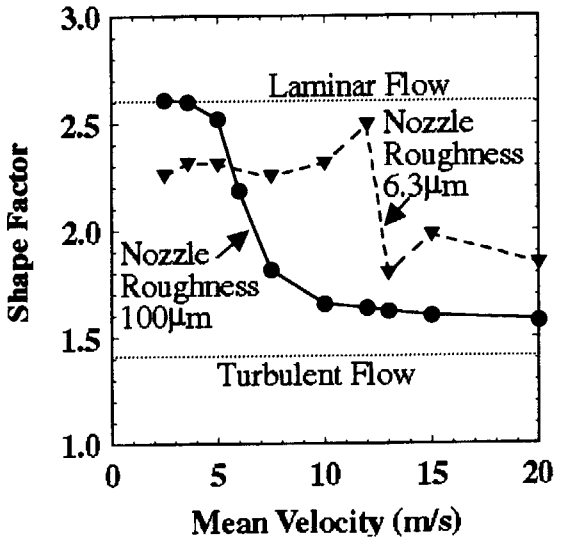


Fig. 4 Characteristic change of boundary layer. (The change of boundary layer flow from laminar to turbulent occurs at higher velocity in the smooth wall nozzle case, while it occurs at lower velocity in the rough wall nozzle case.)

The shape factor, H12, is given as $H12 = d_1 / d_2$, where d_1 and d_2 are displacement thickness and momentum thickness of the boundary layer, respectively. Laminar and turbulent flows give $H12 = 2.6$ and $H12 = 1.4$, respectively, for fully developed flow between parallel plates. Significant changes in H12 were observed at about 5-10 m/s for the rough wall nozzle and at roughly 10-15 m/s for the smooth wall nozzle. Therefore, it can be summarized that laminar and turbulent boundary layers cause relatively stable and unstable behavior on the free surfaces, respectively. Furthermore, the These results show that the surface wave growth mainly depends on the nozzle surface roughness. The nominal value of 6.3 μm (surface roughness defined in JIS B-0601) is easily achieved by machining. This roughness is to be applied to the manufacturing specification of a nozzle made of stainless steel for use in the subsequent Li flow experiments. These results will also provide a guideline on replacement frequency for IFMIF target assemblies, because nozzle wall roughness increases due to corrosion and erosion of the stainless steel by flowing Li.

(5) Conclusions

Water experiments have been performed featuring the parameters necessary to realize lithium flow experiments being planned. The following conclusions were obtained.

i) The effect of cover gas pressure on interfacial wave growth at a high-speed free surface jet was insignificant for the range of pressure 0.015 to 0.1 MPa.
ii) Interfacial wave growth mainly depends on the nozzle inner wall roughness, affecting the development of a boundary layer on the wall, especially when the average jet flow speed is high. It is necessary to confirm wave growth behavior for flowing Li which has a far larger surface tension than water.

References

[1] M. Martone (editor), IFMIF International Fusion Materials Irradiation Facility Conceptual Design Activity Final Report, ENEA Frascati Report RT/ERG/FUS/96/11 (1996).
[2] A. Möslang (editor), IFMIF International Fusion Materials Irradiation Facility Conceptual Design Evaluation Report, FZK Report FZKA6199 (1999).
[3] M. Ida et al. (editor), IFMIF International Fusion Materials Irradiation Facility Key Element Technology Phase Task Description, JAERI-Tech 2000-052 (2000).
[4] H. Nakamura et al., Proc. 8th Int. Topl. Mtg. Nuclear Reactor Thermal-Hydraulics (NURETH8) vol. 3, p. 1268, Kyoto, Japan, September 30 – October 4, 1997.
[5] M. Ida et al., Preliminary analyses of Li Jet Flows for the IFMIF Target, JAERI-Research 97-030 (1997).
[6] K. Ito et al., Fusion Technology 37 (2000) 74.

3.2.3 TG12A-EU : Jet Flow Stability Analysis

(1) Brief Task Description

The liquid lithium jet of the IFMIF target is hit by a D+ beam with energies up to 40 MeV and currents up to 250 mA (125 mA × 2 beams), corresponding to a heat load up to 10 MW. In order to remove this amount of power, the liquid lithium flows at high speeds, up to 20 m/s. Due to the strong nonuniformity of the power deposition profile in the beam direction, the temperature increase in the lithium jet is also nonuniform and the design must guarantee that no lithium boiling occurs in the jet. Also, the jet flows under very low pressure, to enable the physical connection with the beam accelerator. As a consequence, the lithium evaporation at the jet free surface, depending on the lithium temperature, has to be evaluated, in order to design the devices controlling the accelerator low pressure region. The evaluation of the lithium temperature distribution in the jet and the evaporation rate at the free surface are then basic issues in the IFMIF target design.
Such an analysis was performed at ENEA by using the RIGEL code [5], developed in the frame of the IFMIF-CDA phase, and referring to the target design and features adopted in the frame of the KEP.

Contributors

Name	Party	Institute	E-mail address
S. Cevolani	EU	ENEA	cevolani@bologna.enea.it
D. Giusti	EU	ENEA	giusti@bologna.enea.it
R. Tinti	EU	ENEA	tinti@bologna.enea.it

(2) Introduction

With respect to the reduced cost IFMIF concept and the staged deployment suggested during the CDE-phase, some target scenarios, described in the following, have to be considered in more detail. Altough an international decision on whether they are "reference cases" is pending, they had to be used during the KEP as relevant guidelines. Such cases are concerned with the different irradiation conditions: in addition to the full performance condition (10 MW, 40 MeV, 250 mA). Following the three-stages construction proposal, the facility would start with 50 mA, be upgraded to 125 mA and finally achieve the full performance of 250 mA. For 50 and 125 mA current there are two options: option one consists in leaving the beam footprint size constant and reducing the beam current density on the target; option two consists in reducing the beam footprint size and keeping the beam current density constant [4].

(3) The Jet Thermohydraulic features and the RIGEL code

In the IFMIF Target System the lithium is in liquid state in order to remove the big amount of power, up to 10 MW, deposited by the D penetration into Li. The lithium flows downstream in the form of a jet from a rectangular nozzle, and finally falls into a recovering tank. Notwithstanding the high flow velocity, up to 20 m/s, there is some risk of lithium boiling in the jet. This is particularly true in the beam direction, where the power deposition profile has the Bragg type shape, as shown in figure 1. Moreover, in order to avoid the presence of a window between the target and the accelerator, the jet operates in a rarefied atmosphere (the vacuum chamber), as necessary for the correct operation of the accelerator. This very low pressure increases the boiling risk. For increasing the lithium pressure, the jet is not straight but curved, as imposed by a curved wall (the back plate). In this way, some centrifugal pressure is produced in the jet and the boiling risk is reduced. Boiling of lithium can thus be avoided, but it is still necessary to verify if the adopted flow velocity and wall curvature are sufficient for that purpose. Such a verification can be performed by means of a calculation of the 3D temperature distribution in the lithium jet. As mentioned, the jet free surface is facing a chamber directly connected with the accelerator. From this surface some evaporation occurs, depending both on

chamber pressure and lithium free surface temperature. The evaporation poses a problem with respect to the vacuum contamination. As a consequence, the evaporation rate also has to be evaluated.

With respect to the thermal hydraulics, the analysis of the IFMIF jet requires the determination of the 3D velocity, pressure and temperature distributions within a turbulent, curved and asymmetric jet with strongly nonuniform internal heating. In order to treat this problem, in the frame of the IFMIF-CDA the ENEA-RIGEL computer code has been developed [5]. The leading concept in the development of the RIGEL code was to build up a problem oriented, simple and easily used code. The RIGEL code takes into account all the effects relevant for the case of interest. This way, the necessary physical models are simplified and reduced in number, and the code becomes easy to handle and fast running on a personal computer. The RIGEL code was succesfully employed both in the CDA and in the CDE phases.

(4) Analyses, Results and Discussion

Table 1 reports five possible IFMIF operating conditions to be investigated with respect to jet thermal flow stability. [4]. The adopted power deposition profiles are those shown in figures 1 and 2 [6].

Table 1 Considered cases [4].

Case	Beam Power [MW]	Beam Current [mA]	Beam Footprint			Beam Current Density [mA/cm^2]	Priority
			Width [cm]	Height [cm]	Area [cm^2]		
1	10	250	20	5	100	2.5	High
2	5	125	20	5	100	1.25	Medium
3	2	50	20	5	100	0.5	Low
4	5	125	10	5	50	2.5	High
5	2	50	4	5	20	2.5	High

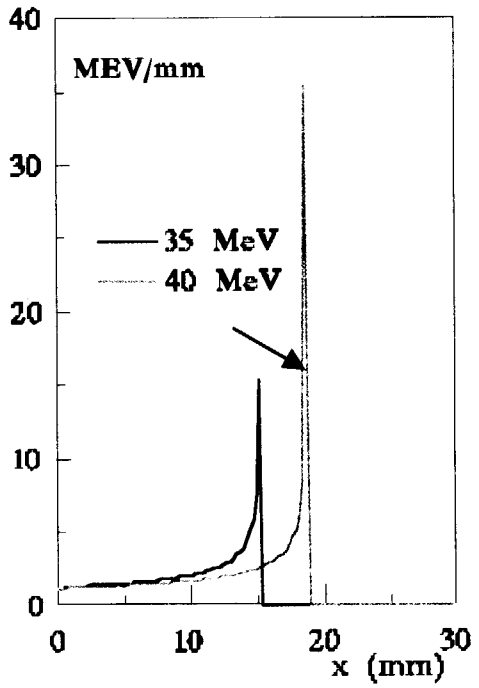


Fig. 1 Power deposition in the jet along the beam direction different beam energy. [7]

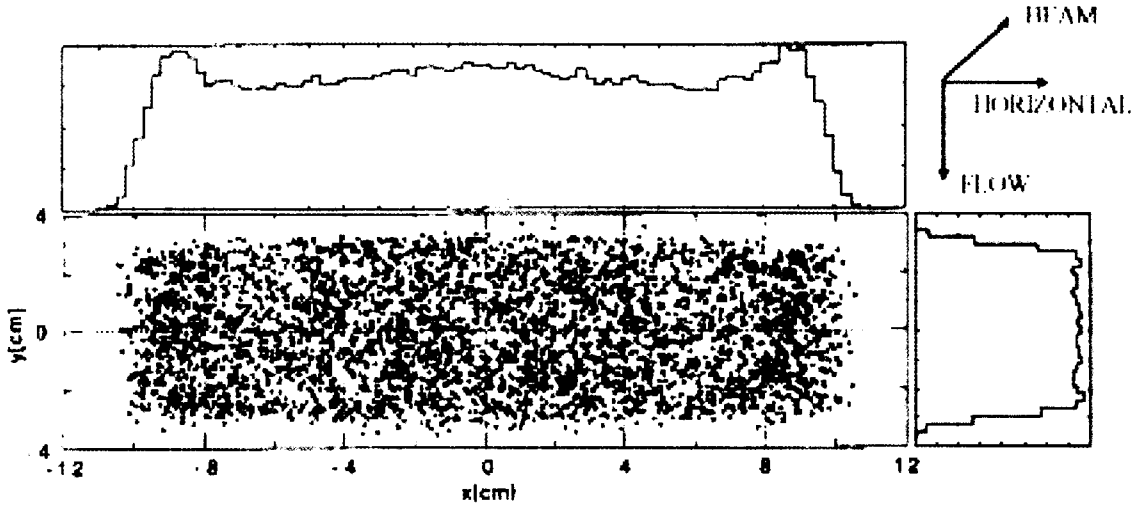


Fig. 2 Power deposition in the jet along the flow and transversal directions [1].

1) Case-1. The analysis of the calculation results [7] demonstrates the stability of Li jet from a thermal-hydraulic point of view. As can be seen from figures 3 to 6, the jet is everywhere quite far from boiling, see for example figures 4 and 5. It has to be pointed out that figure 4 shows the situation within the jet: the first point on the left does not represent the free surface temperature, but the first calculation mesh point. It is interesting to notice that, in spite of the rather sharp temperature rise corresponding to the Bragg-like power deposition peak, see figure 3, the minimum boiling margin within the jet (fig.4) takes place close to the free surface and not in correspondence to the power deposition peak. This result shows that the curved back-wall is effective in inducing a centrifugal pressure able to increase the local saturation temperature in the bulk.

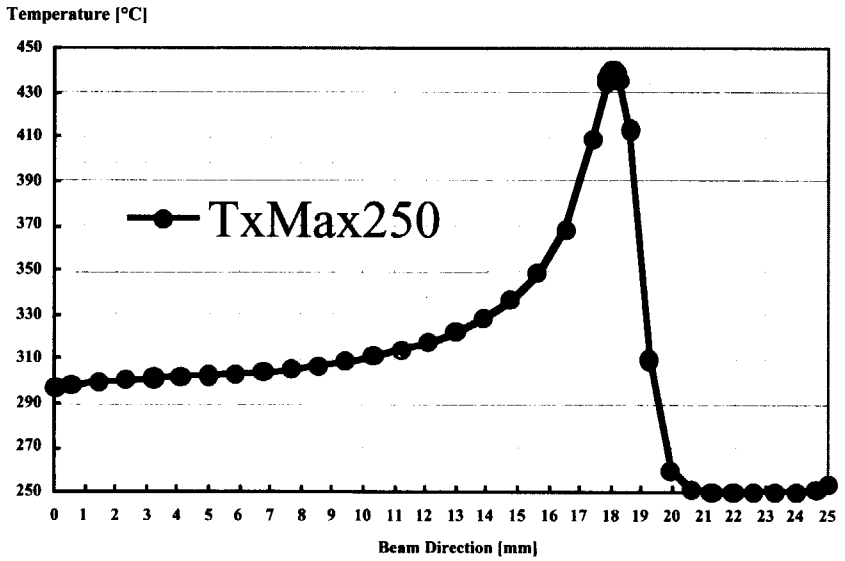


Fig. 3 Temperature distribution within the jet along the beam direction.

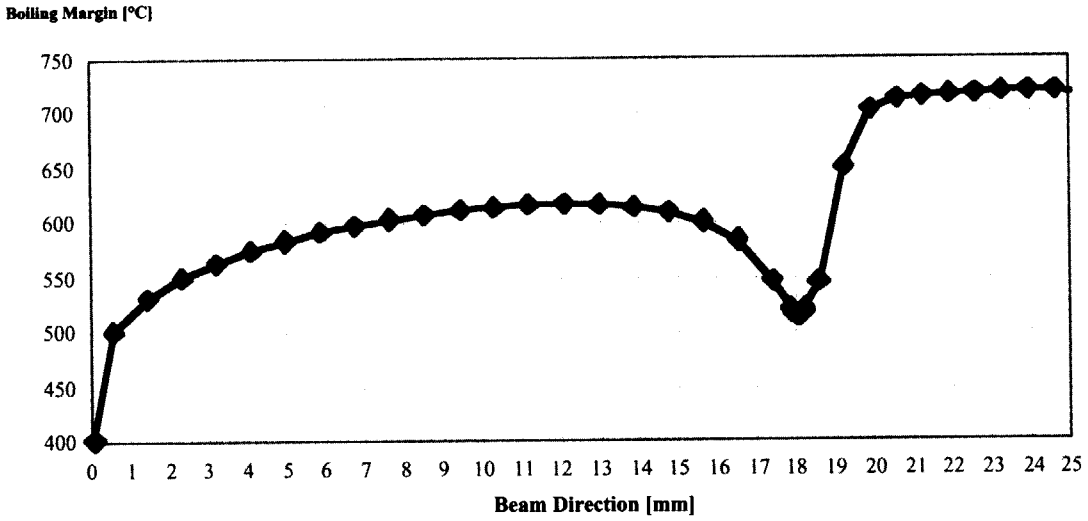


Fig. 4 Boiling margin within the jet along the beam direction.

The situation is different on the free surface, where no effective overpressure can be induced by the centrifugal load.

From figure 5, where the free surface temperature and boiling margin are plotted together along the jet flow direction, it is possible to realise that the boiling margin on the free surface (35°C) is much lower than the one in the bulk close to the free surface (400°C). The evaporation rate was conservatively estimated to be 16 grams/year. Finally, the strong effect of curvature radius was investigated. Two values have been taken into account (474 and 250 mm). The results of this analysis are presented in figure 6. They show that both radii fullfil the design needs.

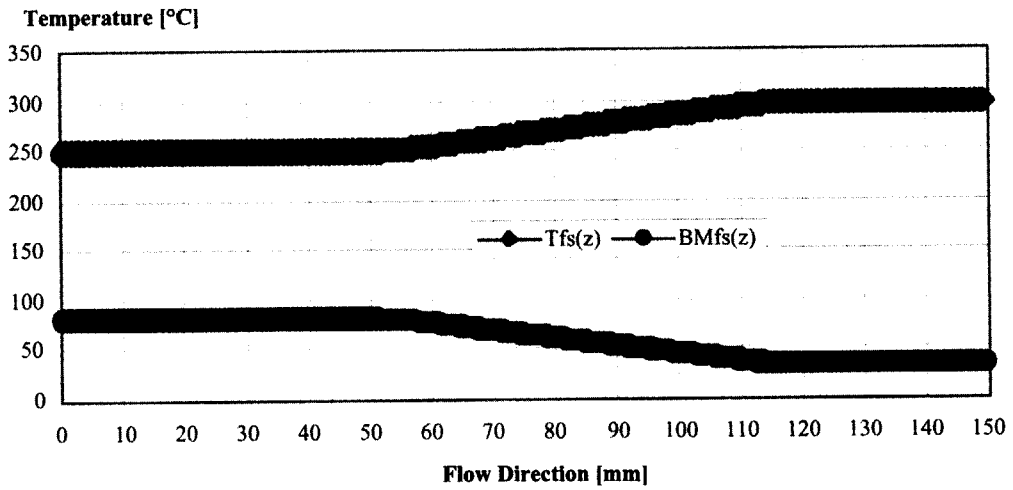


Fig. 5 Temperature and boiling margin on the jet free surface along the flow direction.

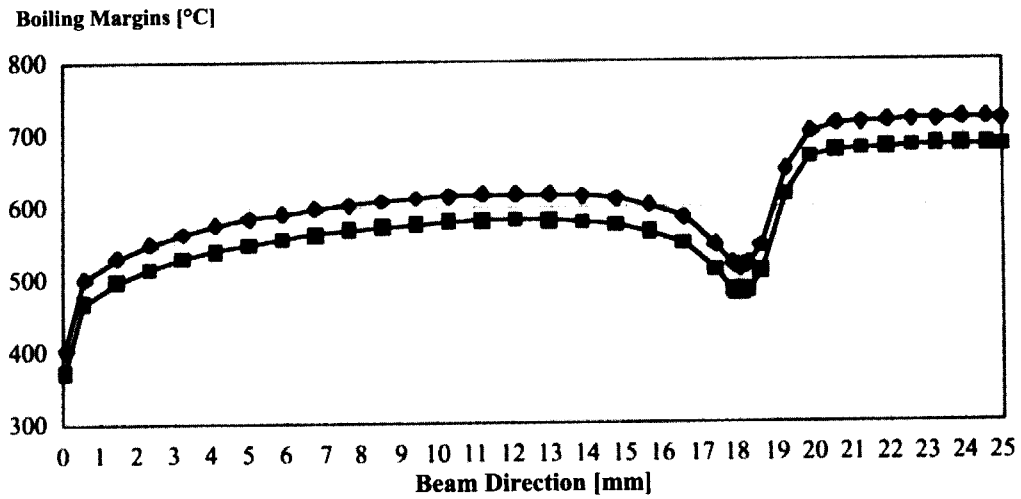


Fig. 6 Effect of the back plate curvature radius on the boiling margin. (◆ R=250 mm; ■ R=474 mm)

2) Cases 2,3,4,5. The analyses of the remaining cases given in Table 1 were also performed. The results are shown in Table 2. As expected, all these cases give rise to more conservative jet operation conditions in terms of maximum temperatures, boiling margins, and evaporation rates.

Table. 2 Main Results of the Analyses.

IFMIF KEP	Tmax Bulk [°C]	Tmax FS [°C]	Min BM Bulk [°C]	Min BM FS [°C]	Evap. Rate [g/yr]
Case 1	441.17	297.30	402.99	35.21	16.2
Case 2	346.35	273.64	426.50	58.87	5.87
Case 3	288.80	259.45	428.69	73.05	3.61
Case 4	347.8	274.00	426.14	58.51	5.92
Case 5	289.37	259.60	429.69	72.91	3.62

(5) Conclusions

The KEP reference operating conditions of the IFMIF lithium target jet have been analysed by means of the RIGEL computer code. The following conclusions can be drawn:

1) The jet temperatures are relatively far from the lithium boiling point for all the examined cases. The minimum value for the boiling margin (35) is found to occur at the jet free surface.
2) The evaporation rate at the free surface has been evaluated for all the cases; the maximum value is 16 g/y.

References

[1] M.Martone, (editor), IFMIF International Fusion Materials Irradiation Facility Conceptual Design Activity Final Report, ENEA Report, RT/ERG/FUS/96/11, November 1996.

[2] A.Möslang, (editor), IFMIF International Fusion Materials Irradiation Facility Conceptual Design Evaluation Report, FZK Report, FZKA6199, January 1999.

[3] M. Ida, et al. (editor), IFMIF International Fusion Materials Irradiation Facility Key Element Technology Phase Task Description, JAERI Report, Japan atomic Energy Research Institute, JAERI-Tech 2000-052, August 2000.

[4] A. Möslang, Memo of February 23, 2001

[5] S. Cevolani, RIGEL, a Computer Code for the Thermal Hydraulic Analysis of Liquid Lithium Jets, ENEA report CT.FBC.00003 (1995)

[6] S. Cevolani, D. Giusti, R. Tinti, IFMIF Lithium Jet Design Parameters Review - a Novel Input File for RIGEL, ENEA report CT.SBD.00009 (2001)

[7] S. Cevolani, D. Giusti, R. Tinti, IFMIF Lithium Target Design - First Evaluations, ENEA report, CT.SBD.00010 (2002)

3.2.4 TG12B-JA : Design of the Lithium Test Loop

(1) Brief Task Description

A stable lithium jet is the most critical requirement of IFMIF target performance. Jet stability depends on several factors, including the flow straightener, nozzle, diffuser, backwall/nozzle transition, jet length, interaction with surrounding medium, and temperature [1]. Extensive testing of FMIT target prototypes were conducted in the FMIT project using lithium working fluid [2]. Similar testing of IFMIF target configurations will be needed because of significant differences in the design and operation of the IFMIF target system.

Design of the lithium loop mockup will be based on the results of the water jet [3,4] and lithium loop experiments [5]. Validated simulation models of the water and lithium experiments will be applied to analysis of the lithium flow. Thermal and structural analysis will also be done. Diagnostics of lithium temperature, surface waves and evaporation will be designed for the mockup loop. Transient behavior of the lithium loop will also be included.

Contributors

Name	Party	Institute	E-mail address
H. Nakamura	Japan	JAERI	nakamurh@fusion.naka.jaeri.go.jp
M. Ida	Japan	JAERI	ida@ifmif.tokai.jaeri.go.jp

(2) Results

Parameters of the proposed prototype Li loop are selected to be the same as in IFMIF except for the jet width. Considering the effects of the side wall on surface behavior in the center region of the Li 15 cm from the nozzle exit, 10 cm is selected as the width of the prototype Li loop nozzle. Comparison of the cross section of the nozzles in the several loops considered is shown in Fig.1. The parameters of the FMIT mockup Li loop, the water experiments, the Osaka Li loop (KEP), the prototype Li loop (for EVEDA) and the IFMIF Li loop are summarized in Table 1.

In the FMIT project, two types of full scale mockup nozzles (Mark I, Mark II) were tested. Mark I is a symmetric nozzle and Mark II is an asymmetric nozzle. Both are single reducer nozzles. In these experiments, surface waves (called wakes) were observed. The origin of the wake is believed to be surface roughness or deposition of corrosion products at the nozzle exit. Detailed geometry of these nozzles is not known, so reproduction of the FMIT nozzle is difficult.

For IFMIF, a double reducer nozzle based in Shima's model has been proposed to provide uniform velocity at the nozzle exit. This model is obtained for uncompressed perfect fluid. Therefore, this fluid has no viscosity nor inertial momentum. Reliable fabrication of this nozzle is possible because the geometry can be defined by an equation.

The water experiment at JAERI has been used to check the flow stability of the double reducer nozzle with the same Reynolds number as Li (250 °C). Although surface waves with amplitude less than 1 mm were observed, the performance of this nozzle was found to be acceptable. However, validation of Li flow with the same nozzle as the water experiment is needed, since the surface tension of Li is 5 times that of water. Therefore, a small Li loop experiment at Osaka University is now under consideration. However, to validate the IFMIF nozzle performance and continuous operation of the Li loop, a prototype Li loop experiment is needed. The Shima nozzle is based on an uncompressed perfect fluid. To extrapolate the small nozzle with a 1 cm height to the IFMIF nozzle with a 2.5 cm height, validation in the prototype Li loop experiment is essential. The Li flow width of the prototype Li loop will be 10 cm, selected in consideration of the effect of the side wall on surface behavior in a center region at 15 cm from the nozzle exit. A schematic view of the prototype Li loop is shown in Fig.2, and a flow diagram for the Li loop is shown in Fig.3.

References

[1] Hiroo Nakamura, et al., Status of lithium target system for international fusion materials irradiation facility (IFMIF), Fusion Eng. and Des. 58-59(2001)919-923.

[2] R.Kolowith, et al., Experimental Lithium System Final Report, Hanford Engineering Development Laboratory Report, HEDL-TME-84-29(1985).

[3] Hideo Nakamura et al., Experimental and analytical studies on high-speed plane jet along concave wall simulating IFMIF Li target flow, J.Nucl. Mater. 258-263 (1998) 440-445.

[4] K. Itoh et al., Free-surface Shear Layer Instabilities on a High-speed Liquid Jet, Fusion Technology, 37 (2000) 74-88.

[5] H.Horiike, et al., 22nd Symposium on Fusion Technology, Helsinki, 9-13 September 2002 (to appear Fusion Eng. and Des.).

[6] Hiroo Nakamura, et al., 22nd Symposium on Fusion Technology, Helsinki, 9-13 September 2002 (to appear Fusion Eng. and Des.).

Table 1 Comparison of the FMIT mockup Li loop, the Osaka Li loop, the EVEDA prototype Li loop, and the IFMIF loop.

Parameter	FMIT Full Scale Mockup ELS [2]	Water Experiment Phase-1[3]	Water Experiment Phase-2[4]	Osaka Li loop (KEP) [5]	Prototype Li loop (EVEDA)	IFMIF Li loop [6]
Nozzle Geometry	Single Reducer Nozzle	Double Reducer Nozzle	Double Reducer Nozzle	Double Reducer Nozzle	Double Reducer Nozzle	Double Reducer Nozzle
Back wall Geometry	Concave (R= TBC cm)	Concave (R=25 cm)	Straight	Straight	Concave (R=25 cm)	Concave (R=25 cm)
Jet Thickness (cm)	1.9	2.5	1	1	2.5	2.5
Jet Width (cm)	10	24	10	7	10	26
Li Speed (m/s)	17	17	20	15	20	20
Flow Rate (l/s)	40	TBC	TBC	13	50	133
Purification System	Cold trap, Hot trap	—	—	Cold trap	Cold trap, Hot trap	Cold trap, Hot trap
Impurity (N_2:wppm)	100	—	—	>1000	10	10
Vacuum Condition (Pa)	10^{-3}	10^{5}	10^{4} - 10^{5}	100-1000 (TBC)	10^{-3}	10^{-3}
Nozzle Material	304 SS	acrylic resin	acrylic resin	304 SS	RAF	RAF
Operating Period	9000 hrs	TBC	TBC	500 hrs (TBC)	>5000 hrs	20 years

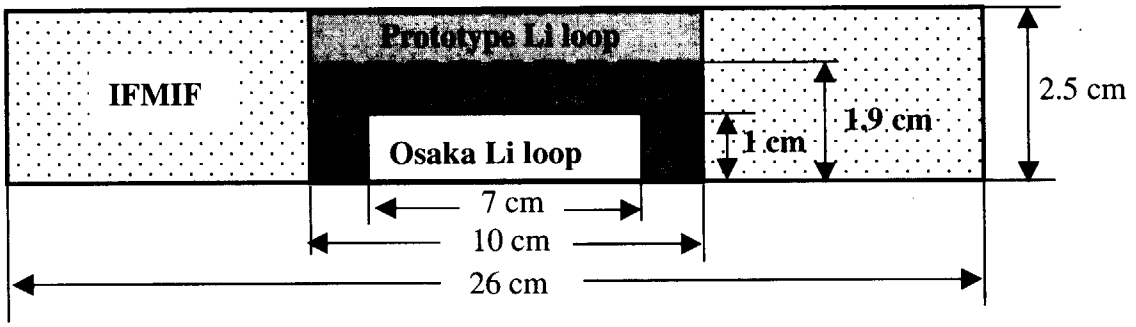


Fig. 1 Comparison of the cross sections of the nozzle exit for the different lithium loops.

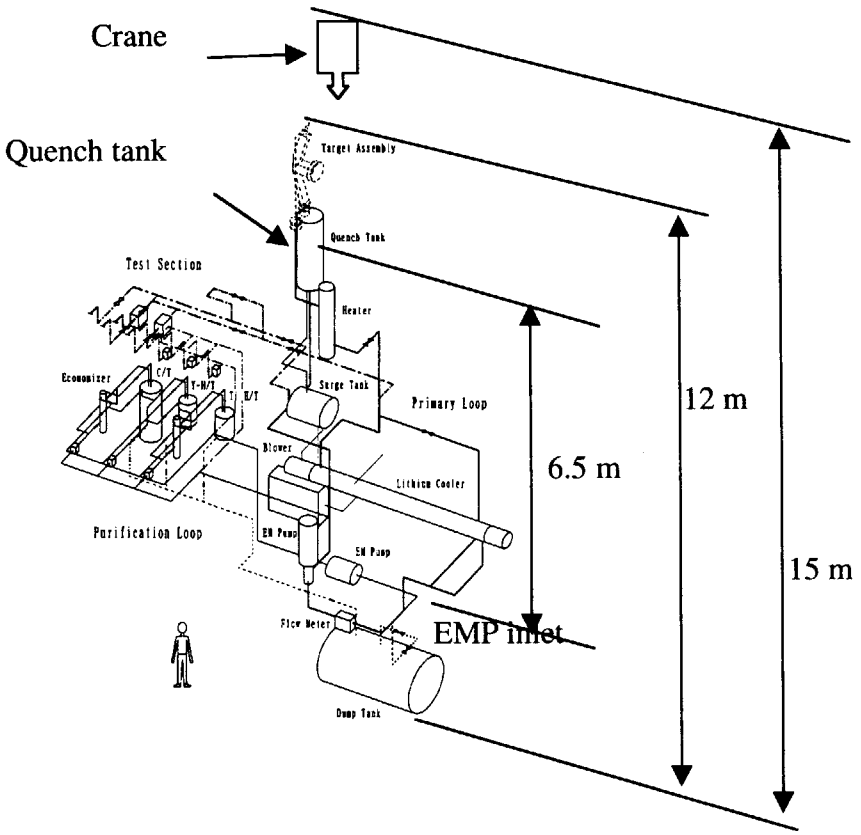


Fig. 2 Schematic view of the prototype Li test loop.

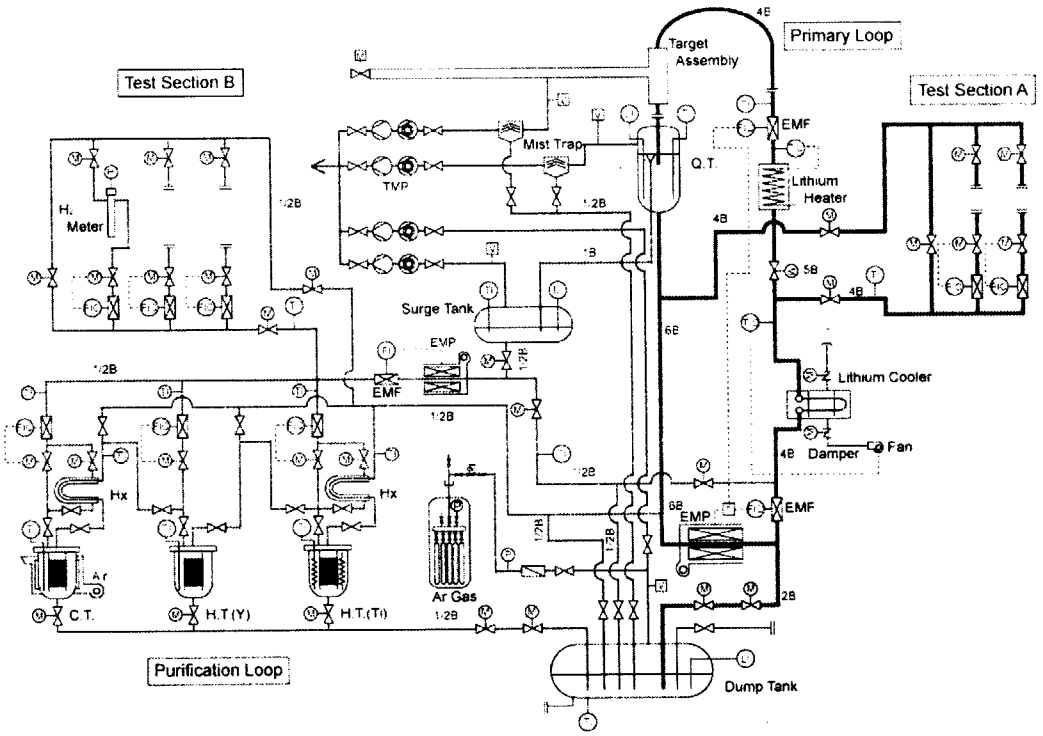


Fig. 3 Flow diagram of Li engineering test facility.

3.2.5 TG12C-RF : Status and Plans for Water and Lithium Experiments

(1) Brief Task Description .

Research and development on a lithium neutron target for IFMIF are carried out in the SSC RF-IPPE with ISTC financial support (project # 2036). The work commenced June 1, 2002, and the duration of the project is 3 years. The title of the project is "The thermal-hydraulic and technological investigations for validation of the project of lithium circulation loop and neutron lithium target for IFMIF".The project pursues two main purposes: i) Research on hydrodynamic stability of a plane, high-speed lithium jet with a free surface flowing along the concave back wall of a target assembly. ii) Development of technological aspects of the lithium circulation loop to provide long lifetime in the IFMIF installation (up to 20 years).

Contributors

Name	Party	Institute	E-mail address
N.Loginov	Russian Federation	IPPE	loginov@ippe.obninsk.ru
V.Chernov	Russian Federation	IPPE	chernovv@bochvar.ru
V.Fedotovsky	Russian Federation	IPPE	
V.Shishulin	Russian Federation	IPPE	
A.Mikheyev	Russian Federation	IPPE	
V. Morozov	Russian Federation	IPPE	
M.Arnol'dov	Russian Federation	IPPE	
J.Aksyonov	Russian Federation	IPPE	
L.Berensky	Russian Federation	IPPE	

(2) Introduction

Research and development on a lithium neutron target for IFMIF are carried out in the SSC RF-IPPE with ISTC financial support (project # 2036). The work commenced June 1, 2002, and the duration of the project is 3 years. The title of the project is "The thermal-hydraulic and technological investigations for validation of the project of lithium circulation loop and neutron lithium target for IFMIF".

The project manager is N.Loginov. The foreign collaborator of the project is the Japan Atomic Energy Research Institute (JAERI).

The project pursues two main purposes:

1. Research on hydrodynamic stability of a plane, high-speed lithium jet with a free surface flowing along the concave back wall of a target assembly.
2. Development of technological aspects of the lithium circulation loop to provide long lifetime in the IFMIF installation (up to 20 years).

To reach these purposes it is necessary to solve a number of complex problems, namely:

- The calculated and theoretical analysis of the physical phenomena and factors that affect the hydrodynamic stability of a jet (invariance of the jet form and dimensions in time, its continuity, wave generation at the free surface, etc.) Some results of this analysis will be tested in experiments with a water jet.
- Experimental investigations of lithium jet stability in diminished hydrodynamic IFMIF target models to optimize construction and to obtain the required stability.
- Experimental determination of lithium evaporation rates at the jet free surface and vapor transfer in the vacuum system, check of jet thermodynamic stability (boiling conditions, cavitation, foaming

and splashing).

- Experimental study of corrosion, erosion and other physicochemical processes that affect the long-lived serviceability of the target and the loop.
- Experimental investigation and justification of lithium purity, and required methods, devices and instruments for its control and monitoring.
- Preparation of technological, methodological and design recommendations for creation and maintenance of the target and IFMIF lithium loop on the basis of the experimental investigations.

The status of the work and plans for the rest of the ISTC project are briefly explained below.

(3) Preparation for hydraulic research with a water jet

The SSC RF-IPPE now has results from some of this work:

1.1 The water facility (WF) is ready for research (main parameters of the facility: pressure pump head – 2.5 MPa, water flow rate – 75 m^3/hour).

1.2 The mock-up target assembly (WM) designed for experiments with a water jet is under way. The WM construction includes the pressure head chamber, the upper vibration reducer, the flow straightener, the two-stage convergent channel such as a Shima nozzle, a curvilinear tray with radius of curvature 250 mm, drain channel, a lower vibration reducer, and the quench tank.

The facility provides for installation of devices intended for experimental research on the influence of design parameters on hydrodynamic stability of the jet, and wave and splash generation in both steady state and transient modes (start-up and shut-down).

Plug-in elements of the Shima nozzle edge will be used to evaluate changes in radius, roughness and wettability. Influence of these factors on generation of surface waves will be determined. Results of hydraulic testing of the WM mock-up will be used to optimize design of the lithium target assembly (TA).

1.3 Procedures and measurement instrumentation for the water jet hydrodynamic parameters in the WM and vibration parameters of the mock-up are developed:

- measuring edge velocity of a jet at Shima nozzle outlet – by means of Pitot tube and the special device for its three-coordinate motion,
- measuring thickness of the jet at different distances from Shima nozzle outlet – by means of the electrocontact probe and the device for its three-coordinate motion,
- measuring statistical performances of waves at the jet surface (wavelength, wave amplitude, rate of wave propagation) – by means of a probe with two electrocontact sensors and devices for three-coordinate motion,
- visual observation, photography and video recording of the jet surface.

The possibility of measuring turbulent performances of the jet (intensity and spectrum of turbulent fluctuations) by means of a film thermoanemometer and special instrumentation is also being considered. Vibration detectors on the WM are provided for measuring the natural vibration characteristics. An electrodynamic vibrator will be used to obtain forced vibrations of the channel (and jet) and to investigate its influence on the jet stability.

The needed equipment and instruments have been acquired. It is planned to start water experiments in December 2002 and to finish in February 2003. After that, the performance of the lithium TA will be verified by experiments on the water facility.

(4) Preparation for experiments with a lithium jet

Within the framework of the ISTC project # 2036 in the SSC RF-IPPE the lithium test facility (LTF-M, a modification of the existing LTF) is designed and will be constructed to carry out experimental investigations needed to validate IFMIF lithium circulation loop and lithium neutron target. The facility created includes two lithium loops – the hydrodynamic (main) loop and the technological

loop. These can be used either separately or jointly.

The experimental TA is installed in the main loop in order to evaluate the hydraulic performances and stability of a high-speed free surface lithium jet, flowing against a concave wall. The main loop contains an MHD pump for lithium circulation, a magnetic flowmeter, a heater and cooler to control the circulating coolant temperature, a quench tank, a dump, a feed tank, liquid metal valves, and filters. The quench tank is placed after the TA and intended to reduce the jet kinetic energy, to separate gases from lithium, accommodate lithium volume changes, and to provide stable lithium pressure at the pump inlet.

The technological loop includes a pump and some parallel branches through which lithium can be pumped. In each branch a magnetic flowmeter and experimental technological equipment are placed. Feed, dump and compensating tanks, a device for adding lithium, and backup bypass pipes are provided for the loop.

Experimental technological equipment includes instruments for monitoring impurity concentration and apparatus for purification of lithium. Gas impurities will be measured in the compensating tank. Remote handling, safety, and measuring systems will be designed and fabricated.

Design parameters of the main loop of the LTF-M facility:

- Flow rate of lithium – up to 40-50 m^3/hour,
- Volume of lithium in the loop– up to 200 liters,
- Material of the loop –austenitic X18H10T stainless steel (similar to SS304),
- Pump head – up to 0.6 MPa,
- Temperature of lithium – 220-300°C (short-term – up to 450°C),
- Diameter of piping in the loop – 80 mm,
- Height of the loop – up to 13 m,
- Height of lithium column at pump input – up to 10 m,
- Power of the main heater – up to 50 kW.

Design parameters of a technological loop:

- Flow rate of lithium – up to 10 m^3/hour,
- Material of the loop and main units – X18H10T stainless steel (similar to SS304),
- Pump head – up to 0.8 MPa,
- Temperature of lithium – 200-600°C,
- Lithium volume in the loop – up to 50 liters,
- Up to five experimental sections can be installed simultaneously in the technological loop.

The data acquisition, data storage, and control system – i.e. measuring-handling system (MHS) – are based on personal computers. A separate server is provided for the database. The software for the MHS, adapted to requirements of experiments, is being developed now. By means of the MHS it will be possible to start and stop lithium circulation through the TA (both normal and emergency modes), operate at steady state, operate the lithium purification system, etc.

Design of the experimental TA, the lithium jet parameters, and measuring devices are directed at meeting the needs of the IFMIF project and also the experiments with the lithium jet testing at Osaka.

The TA contains the same basic elements as in the IFMIF target assembly design, but its dimensions are smaller. The lithium flow rate in LTF-M (about 50 m^3/hour) is less by an order of magnitude than in IFMIF loop. Lithium enters into the flow straightener, then into the nozzle, a concave wall tray, drainage channel and quench tank. From the quench tank lithium is piped to the main pump.

The flow straightener and the nozzle construction and design are similar to IFMIF. They differ only in dimensions. The tray jet cross-section is geometrically similar to IFMIF.

Above the tray is the sealed target chamber for optical observations, measuring lithium jet parameters and location of other measuring devices. Additional experimental sections can be connected to

the target chamber to study evaporation of lithium and vapor transport along a vacuum cavity. The chamber is connected to the inert gas system and vacuum system of the facility. It allows research at different pressures above the lithium jet. The drainage channel connected to the tray is to move lithium from target assembly to the quench tank. The drainage channel and the quench tank construction and dimensions have to provide both minimum lithium drops and spray in the target chamber for stable pump operation in all modes of lithium circulation. The quench tank is also connected to the gas-vacuum system of the facility.

The target assembly key parameters:

- lithium flow rate – up to 40-50 m^3/hour,
- tray back wall geometry - concave, R=250 mm,
- lithium jet thickness at the nozzle outlet – 8 mm,
- jet width – 80 mm,
- cross section averaged jet velocity at the nozzle outlet – up to 20-22 m/s,
- nozzle and tray material – X18H10T stainless steel (similar to SS304),
- nozzle geometry – double reducing Shima nozzle,
- pressure above the jet free surface – 0.15 MPa-10^{-3}Pa,
- lithium temperature at the nozzle inlet – 230-300°C, short-term – up to 450°C.

The following parameters will be measured during research on lithium jet hydrodynamics and stability:

- amplitude and length of waves on the free surface (jet longwise and edgewise),
- jet thickness (jet longwise and edgewise),
- velocity distribution at jet surface (jet longwise and edgewise),
- velocity distribution in jet thickness and width,
- vibrations.

For general application of experimental data on jet stability it is necessary to research variation in all parameters. Planned variables for initial experiments are: lithium velocity at the nozzle outlet, lithium temperature at the nozzle inlet, environment pressure in the target chamber, and vibrations in the target assembly.

To obtain experimental data on target assembly the following main measuring instrumentation will be used:

- high-speed video camera and a digital photographic camera (for analysis of the jet surface),
- electrocontact sensor (for measuring amplitude and length of waves, and the jet thickness),
- ultrasonic sensor (measuring the jet thickness),
- thermocouples,
- sensors of acceleration (measuring vibration).

Other methods of diagnostics of lithium flow will also be considered: electromagnetic transducers (measurement of local velocity, electric contact resistance, wettability), laser diagnostics (for measuring of lithium velocity at the jet surface), etc. Some of the above measuring devices were already used in experiments with lithium jets (in FMIT project and in experiments in Osaka) and showed their serviceability; other ones are at the development stage.

Research will clarify the circumstances which influence the free surface lithium jet hydrodynamic stability, and develop recommendations for IFMIF.

(5) Preparation for experiments on lithium evaporation from the jet surface

Experimental research on lithium evaporation from the jet free surface will be conducted on a specially constructed test section, which is a model of a part of the accelerator beam tract. The test section will be connected to the mock-up of TA. The lithium vapor flow rate from the jet free surface and distribution of lithium deposition along the test section during ~500 hours will be measured. The research will be carried out at fixed jet parameters: temperature of 250-300°C, jet velocity of 10-20 m/s, and vacuum of ~10^{-3} Pa.

(6) Research on interactions of the lithium jet with structural materials

The analysis of available literature data on the behavior of impurities in lithium and steel, corrosion in lithium loops, erosion and cavitation affect of the moving medium on a solid surface, on solubility and thermodynamic activity of different impurities in lithium, on wetting of different materials by lithium, and on liquid metal adsorption effects is now underway.

This analysis will give a clearer picture of the effects of moving lithium on steel as a function of the type and concentration of impurities, temperature, and interaction time. This will improve the experimental tasks.

Experimental research on wetting of austenitic steel by lithium will be carried out by both " the method of drop" and under dynamic conditions in new and existing lithium loops. The data are needed to determine the best preparation and procedures for stable loop operation.

Corrosion and erosion tests of X18H10T stainless steel (SS304 type) will be carried out by the method of rotating disk at the special installation, and then in the target loop.

Outgassing of the steel of the LTF technological loop is being studied before filling with lithium. The composition and amount of emitting gases are measured. Experiments using "the method of drop" are planned to begin in January 2003, and at the installation with rotating disk by June 2003. It is planned to have lithium velocity near rotating disk up to 20 m/s.

The wettability of stainless steel with lithium will be studied by means of electromagnetic sensors of contact resistance. The sensors will be installed both into piping and at the back wall of the mock-up target.

(7) Development of lithium technology

Development of lithium technology includes the following:

1. Studying sources and removal of impurities, including radioactive impurities; studying behavior of tritium in circulating lithium; studying processes of outgassing from lithium flowing through the target; studying thermodynamics of the "lithium/impurities/structural material/inert gas" system.
2. Development of methods and devices for purification of lithium (cold traps, chemical traps). It is proposed to use getters insoluble in lithium as well. It is also proposed to study methods of lithium purification to remove sodium and potassium. The special attention will be given to methods of purification of lithium from tritium.
3. Development of methods and devices for monitoring impurity content in lithium. Methods to be developed include: sampler-distiller, plug indicator, and diffusion sensor for monitoring hydrogen (tritium). Also, electrochemical cells for monitoring oxygen and other impurities (electrical indicator of impurities) will be tested.

The recommendations on the optimum system of devices and methods of monitoring and purification of lithium for IFMIF project will be the result of the work.

The existing LTF – technological loop – will be used for the work. It has the following main units: MHD pump,

electrical heater, compensating tank, cold trap, sampler – distiller, plug indicator, feed and dump tanks.

The facility has systems for monitoring impurity content in inert gas (mass spectrometer,

chromatograph). Further the facility will be supplied with a number of other devices for monitoring impurity content (diffusion sensor of hydrogen, the oxygen electrochemical cell, and so on).

This facility will be used to carry out the main operations on development and modification of methods and devices for monitoring and purification of liquid lithium. Experimental adjustment of the sampler-distiller has started. Degassing of the loop is underway. After completion of degassing, the loop will be filled with lithium, and checkout of equipment and experiments will begin (December 2002).

(8) Conclusion

The authors briefly describe their intentions and plans. The program is open to suggestions and proposals which will be taken into account during execution of the project, within the framework of the technical and financial rules and limitations of the ISTC.

3.2.6 TG13-JA : Modification and Verification of an Existing Lithium Loop

(1) Brief Task Description

High speed lithium flow was demonstrated under free surface conditions using the Lithium Loop facility at Osaka University. The purpose of the project is to determine the hydrodynamic stability of free surface lithium flow at velocities up to 15m/s. A horizontally aligned test channel, as well as other auxiliary equipment, was installed on the loop. The modification was completed by the middle of 2002. Preliminary result shows that the design of the nozzle and the test channel are successful in producing high speed free surface flow of lithium.

Contributors

Name	Party	Institute	E-mail address
H.Horiike	Japan	Osaka University	horiike@eie.eng.osaka-u.ac.jp
T.Iida	Japan	Osaka University	chernovv@bochvar.ru
S.Inoue	Japan	Osaka University	inoue@eie.eng.osaka-u.ac.jp
S.Miyamoto	Japan	Osaka University	miyamoto@eie.eng.osaka-u.ac.jp
N.Yamaoka	Japan	Osaka University	yamaoka@nucl.eng.osaka-u.ac.jp
I.Matsushita	Japan	Shinryoh High Technologies Ltd.	Izuru__matsushita@kbg.kobe.mhi.co.jp
T.Muroga	Japan	NIFS	muroga@nifs.ac.jp
T.Tanaka	Japan	NIFS	teru@nifs,ac.jp
M.Ida	Japan	JAERI	ida@ifmif.tokai.jaeri.go.jp
Hideo Nakamura	Japan	JAERI	nakam@lstf.tokai.jaeri.go.jp
Hiroo Nakamura	Japan	JAERI	nakamurh@fusion.naka.jaeri.go.jp
K.Ara	Japan	JNC	ara@oec.jnc.go.jp
M.Hirabayashi	Japan	JNC	mhirarin@oec.jnc.go.jp

(2) Introduction

High-speed lithium flow is necessary to remove the high heat load deposited by the IFMIF beam[1]-[3]. High speed is required to control the surface temperature and prevent the spill of fluid into the accelerator. Lithium has a high boiling temperature, 1615 K at 1 atmosphere and 617 K at 1.0 mPa. This value is marginal for the beam line vacuum for stable accelerator operation. Use of a beam window is impractical, therefore the lithium jet flow has to be located in the same space as the accelerator. (That is, the lithium jet "sees" the accelerator vacuum.) Thus a stable free surface is required to avoid significant heating of the target back wall by deuteron penetration, to suppress excessive vaporization of lithium into the beam line, and to assure stable generation of neutrons.

Liquid sodium was studied extensively in fast breeder reactor research from the 1970s. The research was carried out in many countries and in many sodium facilities. A few lithium loops were also constructed in the past, mainly related to space power system research around the world. Lithium flow with a free surface was first studied at the Hanford Engineering Development Laboratory for FMIT design[4]-[5], and were supplemented by water flow experiments with the same target geometry. Two shapes of reducer nozzle were tested to get stable jet flow on a concave back-wall with minimum surface roughness. An asymmetric reducer nozzle was finally developed for a small beam footprint (10 mm x 30 mm at FWHM) at about 20 mm from the nozzle exit at the beam center.

In the design of IFMIF, a wider target of 280 mm was required to accept the larger beam footprint of 50 x 200 mm. The location of the beam center was moved downstream to reduce neutron damage to the nozzle, and there is a concern that the flow might be less stable due to large-amplitude interfacial waves. To satisfy these, a symmetric nozzle with double reducer shape has been designed. Water flow experiments were conducted and the superior stability of the new nozzle design was confirmed[6]-[7]. However, water flow does not simulate effects of the high surface tension of

lithium, wall wetting, and the erosion and corrosion of the structures on the surface stability. Thus, the lithium jet flow experiment was initiated at Osaka University.

(3) System Design and Construction

(3-1) Lithium Circulation Loop

The lithium loop at Osaka was originally constructed for heat transfer and pressure drop studies in a magnetic field[8]. The loop consists of 2 inch 304 stainless steel tubing, an ALIP type electromagnetic pump (EMP), an air cooled module, an expansion tank and an electromagnetic flow meter. The maximum flow rating of the EMP is 0.5 m^3/min at 0.4 MPa head and 0.8 m^3/min at 0.3 MPa. A connected loop was equipped with a cold trap for lithium purification and preliminary operation to reduce the oxide contents was the first task of the experimental schedule. Table 1 shows the outline of the loop, and Fig. 1 the schematic diagram.

Table 1 Major specifications of the Osaka lithium loop.

EMP	ALIP 500*l*/min, 0.5MPa
	Max. velocity at test section: 6.3 m/sec
Magnet	DC, Max. *B:* 0.8T
	Pole faces: 500 x 250 mm
	Inter pole gap: 175 mm
Heater pin	10mm diameter, 1 mm thickness, 306SS
	Heat flux: Max. 2.5 MW/m^2
Test section	52.7 mm I.D., 60.5 O.D, SS304
	Operating temp. 300~550 °C
Nozzle	70mm width 10mm high
Open channel	- 100cm long
Buffer tank	270 liter
Cold trap	6*l*/min, operating temp. >220 °C
Evacuation	Dry pump down to 15Pa

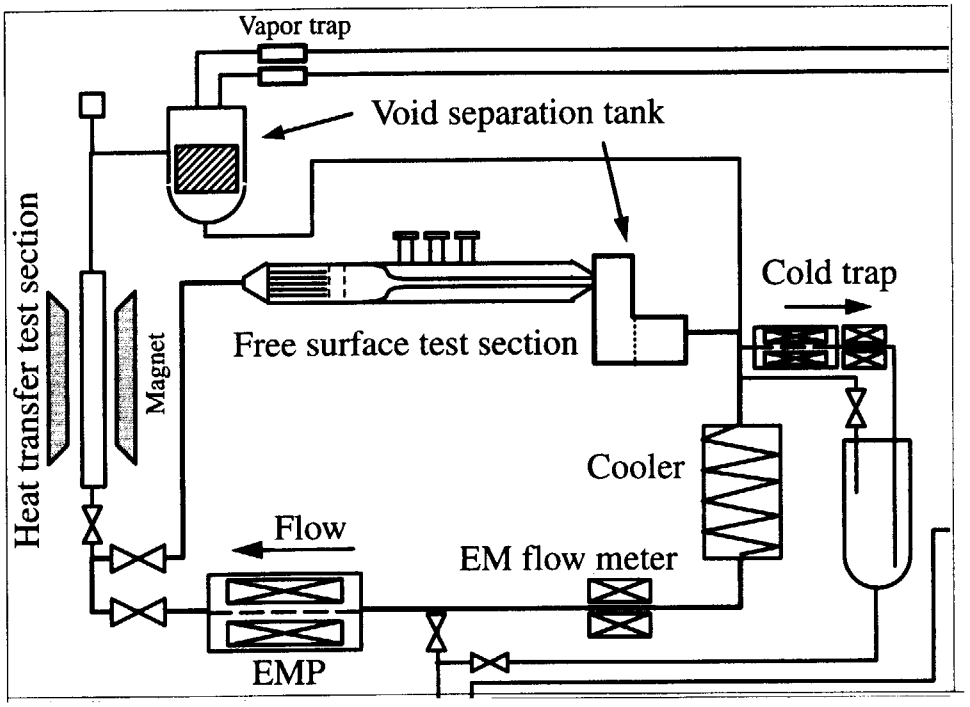


Fig.1 Schematic diagram of the Osaka lithium loop.

(3-2) Loop Modifications and Procedures [9]

To study free surface flow, an open channel test section with a surrounding test chamber, a gas liquid separation buffer tank, and switching valves were installed. The test channel is placed in the horizontal direction for ease of setup and diagnostics. The experimental operation is much easier in a horizontal channel, if large variations in the velocity are planned, from stagnant to more than 15m/s. It is estimated that effects of gravity on flow stability can be neglected for the high-speed flow.

The dump tank was replaced to accommodate a larger inventory of 440 liter. The heart of the system lies in the nozzle, so it was designed and fabricated very carefully. Its shape is two-dimensional, precisely symmetric, with two-step contraction, which reduces the cross section from 100 mm high x 70 mm wide to 10 mm x 70 mm. It was designed based on hydrodynamic theory, and the water experiment[7]. The parts are shown before assembly. in Figs.2 to 4. The fluid is supplied through a circular cross section 2B tube, then passes through an expander and straightener of four perforated plates. Just upstream of the nozzle inlet, two tubes with pneumatic valves were attached for drainage and gas extraction. The cross section and view of the test chamber are shown in Figs.5 and 6.

Gas bubble entrainment is a problem in individual facility design. In order to reduce the lithium inventory, the present loop was designed to be low in height. The height from the gas liquid separation tank to the pump inlet is 4 m. This head is very small, so a 1/2.5 size model of the separator was constructed and the performance was studied using water. As a result, the need for a centrifuge buffer tank combined with bubble combiner panels was determined. This structure works well and in the preliminary test, velocity of up to 14 m/s and flow rate of 576 liters per min under pressurized argon gas was easily obtained. This was limited by the slider transformer and could be increased in the future.

Major objectives of the modifications were to enable cavitation tests of the EMP and tests of the nozzle. The modifications required test of a gas/liquid separator design and provision of a free surface test section, a preheating system, modified power supply and control system, a diagnostic window with clear-view design, diagnostic equipment, a dump tank, vacuum system, and gas feed system. A photograph of the whole facility is shown in Fig.7. An electric contact sensor and ultrasonic sensors are included for the measurement of flow thickness, in addition to visual observations with a TV camera and a high-speed camera.

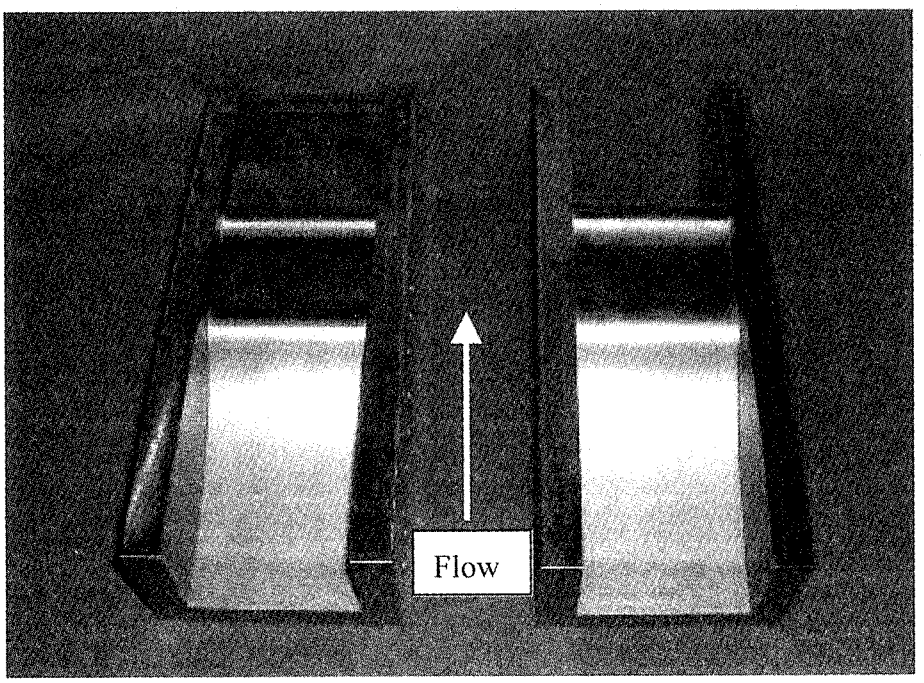


Fig.2 Nozzle parts just before assembly.

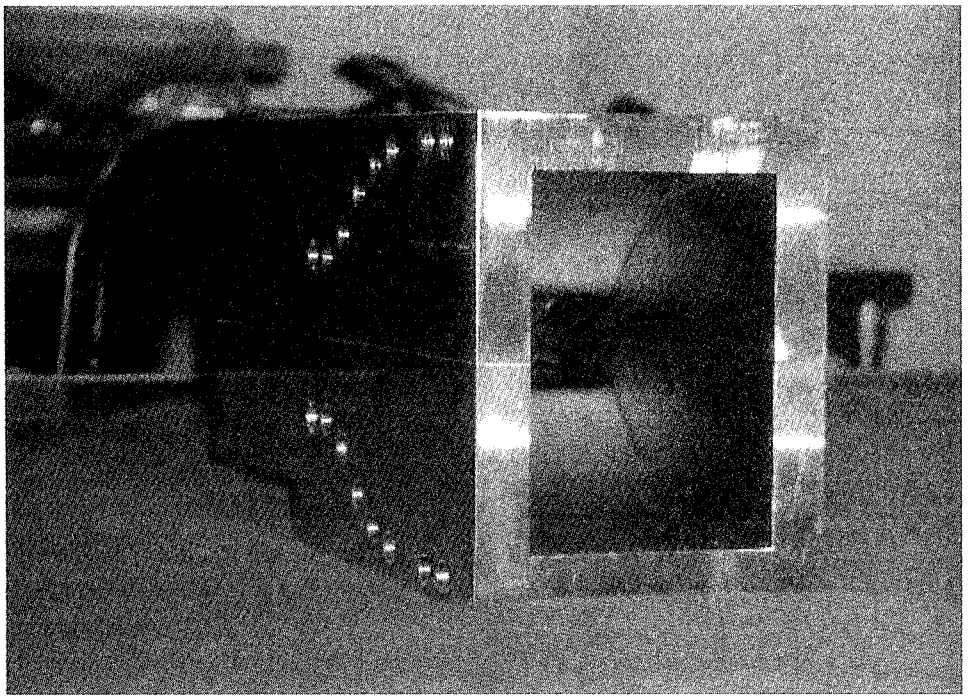


Fig.3 Nozzle unit seen from the upstream side.

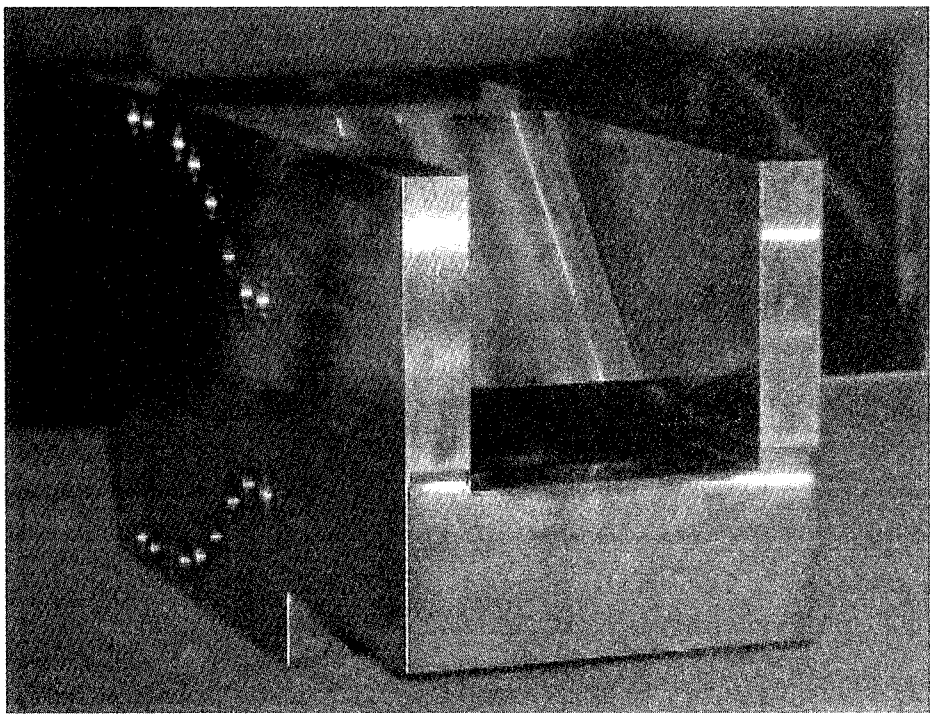


Fig.4 Nozzle unit seen from the downstream side.

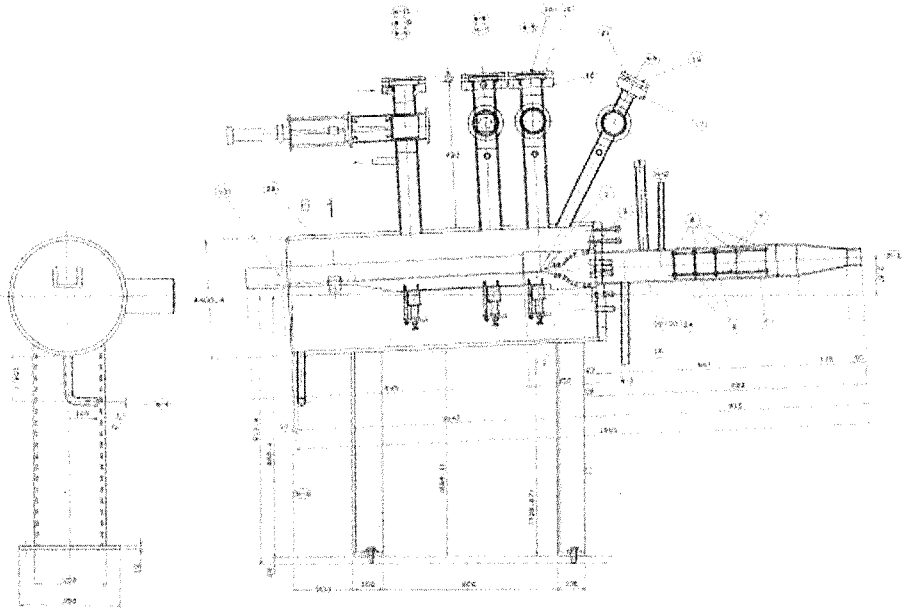


Fig.5 Cross sectional view of the test chamber.

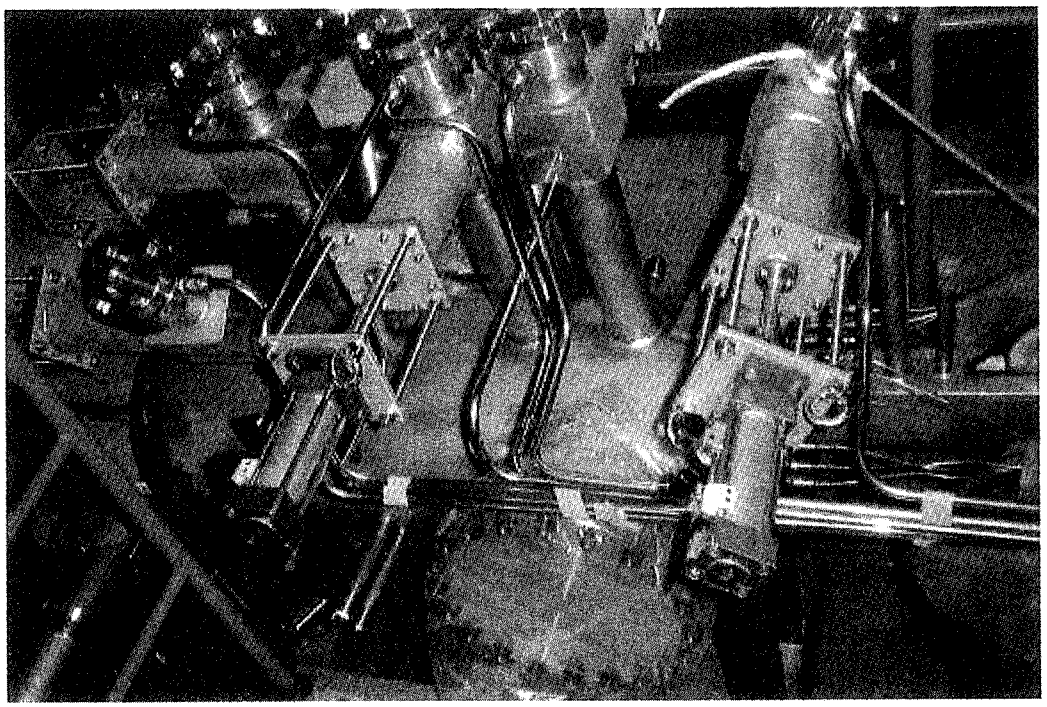


Fig.6 View of the test chamber before adding thermal insulation.

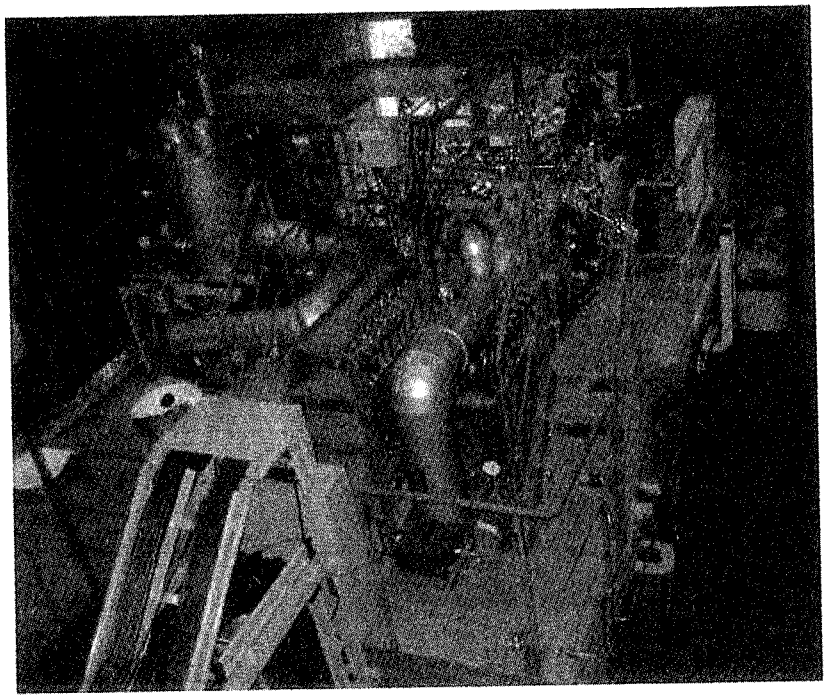


Fig.7 View of the loop facility.

(3-3) Operation

While system pressure can be reduced to 15 Pa, flow testing is generally performed at a pressure of 0.15 MPa under argon. This allows the inner surfaces of the window glass to be continuously swept by the gas flow to help maintain clear viewing. Under evacuated condition, the glass is guarded by a pneumatic shutter that is opened temporary for observation. The temperature was kept at approximately 300^0C in order to avoid freezing of the lithium if the temperature accidentally dropped below the freezing point of 186^0C.

(4) Experimental results and discussion

With lithium circulating through the loop, free surface flow of near zero to 14 m/s was obtained under pressurized cover gas, and 8.5 m/s in 0.029 MPa, and 4.3 m/s in vacuum. Some observed flow surfaces are indicated in Fig.8. Photos in the left hand column and those in the center were taken by a conventional CCD camera, which was mounted on the second and third ports from right hand side. (The ports are shown in Fig.5.) The right hand side column shows photos taken by the high-speed camera at 4500 pictures per second. The center column shows the view from the third port, which corresponds to the beam center planned in IFMIF. The other columns show the view from the second port, which directly views the nozzle edge. The illuminating light was provided from the first port, which directly sees the nozzle edge, 30 degrees inclined from the upstream side. The lower half of these photos are shiny and the upper halves dark, because the light coming into the upper half region is reflected out of the viewing area. At both sides of the circular region, we can barely identify the sides of the channel walls (70 mm apart). In the case of 4.9 m/s flow, the wake-like crest of waves are seen to develop from both side walls to the center region of the channel at an inclined angle, and the surface is covered with characteristic cross stripes. Careful observation showed that the contact line of lithium with the side wall was not smooth, leaving some spot-like patterns on the boundary. This is probably because wetting of the wall by lithium was not complete when these photos were taken. Above 10 m/s velocity, the angle of the wake to a side wall became smaller and the lattice patterns were difficult to

identify with conventional cameras. On the region near the wall, a rise of the surface along the flow direction was observed. The width of these steps became smaller with an increase in the flow velocity, so these might be due to the sum of wave amplitude from the walls.

As shown above, lithium flow was found to be relatively calm, and neither violent waves nor splashing of the fluid were observed. This validates the present nozzle design. This nozzle was manufactured based on a table of the curvature and surface finish specifications provided to the vendor, so the reproducibility of fabrication was considered to be automatically demonstrated.

Further experiments are being prepared for measurement of surface wave height, cavitation, evaporation characteristics, and any corrosion of the nozzle or channel walls.

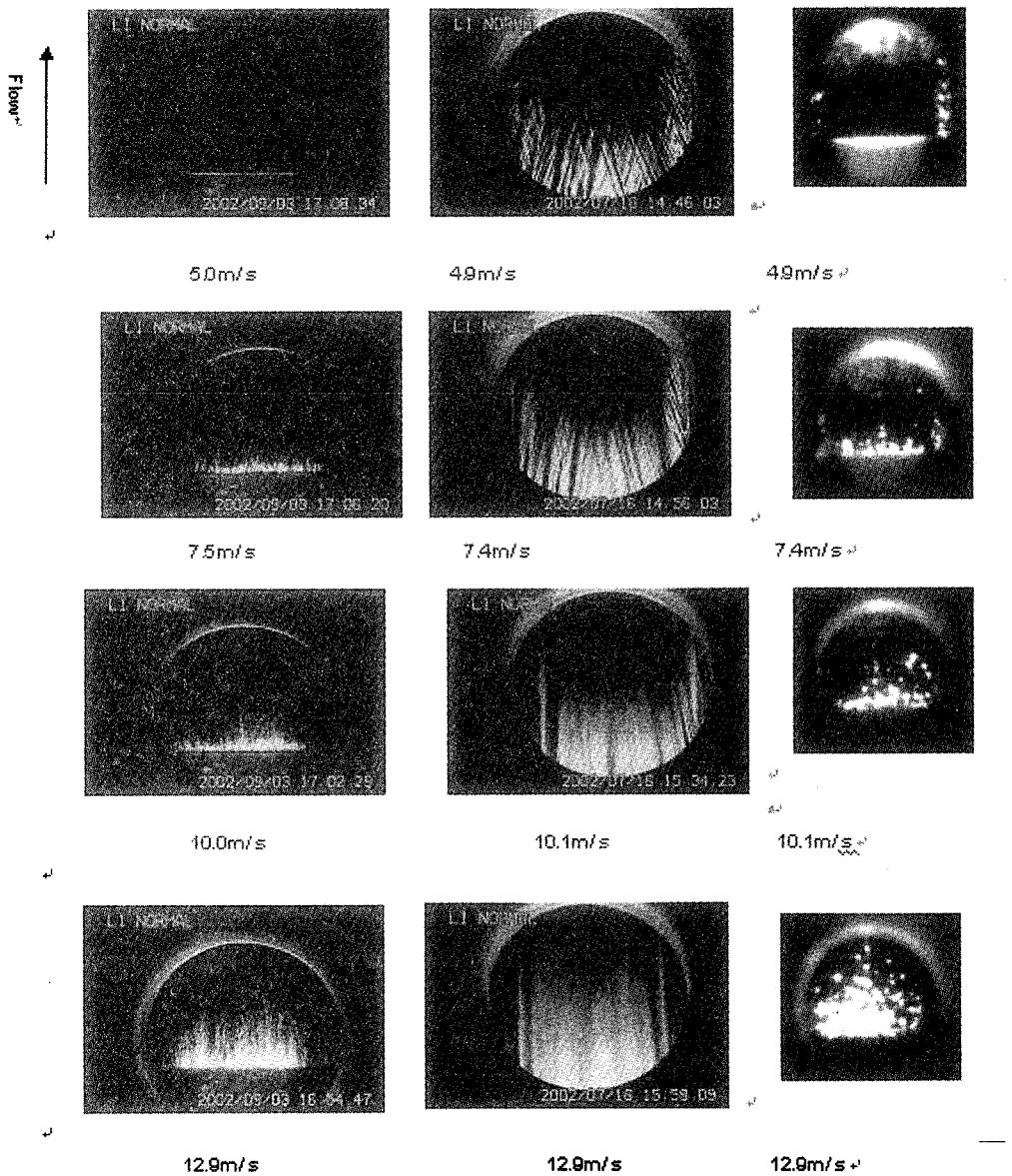


Fig.8 Surface condition of the lithium flow in various velicities. (Left:Ultra Sonic Signals, Center:CCD Video, Right:Fast Camera)

(5) Summary

The lithium loop facility at Osaka University was modified to perform free surface jet flow experiments for IFMIF target design. Through the modifications various key features for future system design were obtained, including nozzle fabrication, gas bubble entrainment, cavitation, and wetting issues. In the experiment lithium flow up to 14 m/s was obtained under a cover gas and 8.5 m/s under vacuum conditions. Surface observations showed relatively calm flow, with neither violent waves nor splashing of the fluid. Further experiments are being prepared for measurement of surface stability, evaporation, cavitation characteristics, and possible corrosion of the nozzle or channel walls.

References

[1] H.Matsui, et al., Proc. 10th Int. Conf. On Fusion Reactor Materials, Baden-Baden, 14 - 19 October 2001. paper 09.PL.3.

[2] H. Nakamura, et al., Status of lithium target system for international fusion materials irradiation facility (IFMIF), Fusion Eng. and Design, 58-59 (2001) 919-923.

[3] Fusion Neutron Laboratory, IFMIF Key Element Technology Phase Task Description, Laboratory report, JAERI, JAERI-Tech 2000-052, August 2000.

[4] R. R. Miles et al., Improved Liquid Lithium Target for the FMIT Facility, HEDL Report, HEDL-SA-2721-FP (1982).

[5] J. A. Hassberger et al., Comparison between measured and predicted performance of a high speed free surface liquid jet flowing along a curved wall, Nuclear Technology Fusion 4 (1983) 433-438

[6] Hideo Nakamura et al., Experimental and analytical studies on high-speed plane jet along concave wall simulating IFMIF Li target flow, J. Nucl. Materi. 258-263 (1998) 440-445.

[7] M. Ida et al., Thermal-hydraulic characteristics of IFMIF liquid lithium target, 6th International Symposium on Fusion Nuclear Technology, Apr. 7-12, 2002, San Diego, California, USA (ISFNT-6), To be published in Fusion Engineering and Design

[8] N.Uda et al., Forced Convection Heat Transfer and Temperature Fluctuations of Lithium under Transverse Magnetic Field, J.Nucl.Sci.Tech., 38, 11(2001) 936-943

[9] H.Horiike et al., Lithium Free Surface Flow Experiment for IFMIF, Proc. 22nd Symposium on Fusion Technology (SOFT 22), 16-20 Sept. 2002 Helsinki Finland

3.2.7 TG15-EU : Support of Japanese Tests for Cavitation Conditions at EMP and at the Joint of the Replaceable Back Plate

(1) Brief Task Description

Since 2000, in the frame of Key Element Technology Phase, ENEA has launched an R&D activity on the lithium target system of the International Fusion Materials Irradiation Facility (IFMIF). One of the modifications for the cost reduction of the lithium loop is the reducing of the loop height and the relevant static pressure but, in this case, the risk of cavitation onset in the target system becomes real. In this frame, Osaka University has planned cavitation tests in the Li loop with collaboration between JAERI and ENEA. Objective of the ENEA activity, among others, is the sharing of its expertise for the evaluation and experimental monitoring of the occurrence of cavitation during lithium flow tests to be carried out in Japan. During these tests, the cavitation will be detected by ENEA CASBA-2000 accelerometer equipment. The results will give an evaluation of the actual cavitation risk and the new requirements for further experiments in dynamic simulation.

Contributors

Name	Party	Institute	E-mail address
G. Dell'Orco	EU	ENEA	giovanni.dellorco@brasimone.enea.it

(2) Introduction

In the IFMIF testing facility, the required high energy neutrons are produced by reaction of two D^+ beams with a free surface liquid lithium jet target flowing along concave back-wall at high speed (> 20 m/s) [1]. The lithium height in the experimental loop and its relevant static pressure, the high flow velocities and the presence of several devices for the flow control and the pressure reduction increase the risk of cavitation onset in the target system. Special attention has to be paid to the primary pump, the flow straightener, the nozzle and their interconnections where the local increases of velocity or the flow separations could promote the emission of cavitation vapour bubbles. This could produce large jet instability and disturbance of the neutron field in the D^+ beams-lithium target zone. The successive bubble re-implosions, in the higher pressure liquid bulk, could activate material erosion and transport of activated particles. For those reasons, the cavitation risk must be avoided along the whole lithium target circuit. During 2001 ENEA, in the frame of IFMIF Key Element Technology Phase, initiated a co-operation with JAERI for the monitoring of the lithium experimental facility at Osaka University against the risk of cavitation occurrence near the electromagnetic pump, the orificed multi-holes flow straighter and the nozzle of a straight mock-up. The cavitation noises will be detected and analysed by the patented ENEA CASBA-2000 accelerometer equipment, Fig. 1.

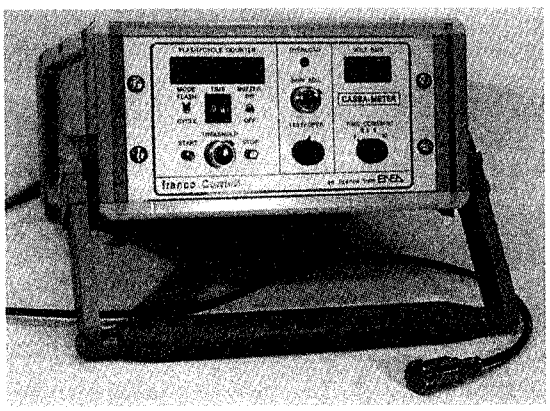


Fig. 1 CASBA-2000 and its accelerometer sensor.

(3) CASBA-2000 Accelerometer

The CASBA-2000 accelerometer was developed and patented by ENEA [2] for monitoring bubble re-implosions due to cavitation or boiling phenomena. The CASBA acoustic detection of bubble re-implosions is based on vibration frequency spectra obtained from an accelerometer operating in its non linear resonance region, Fig. 2 [3].

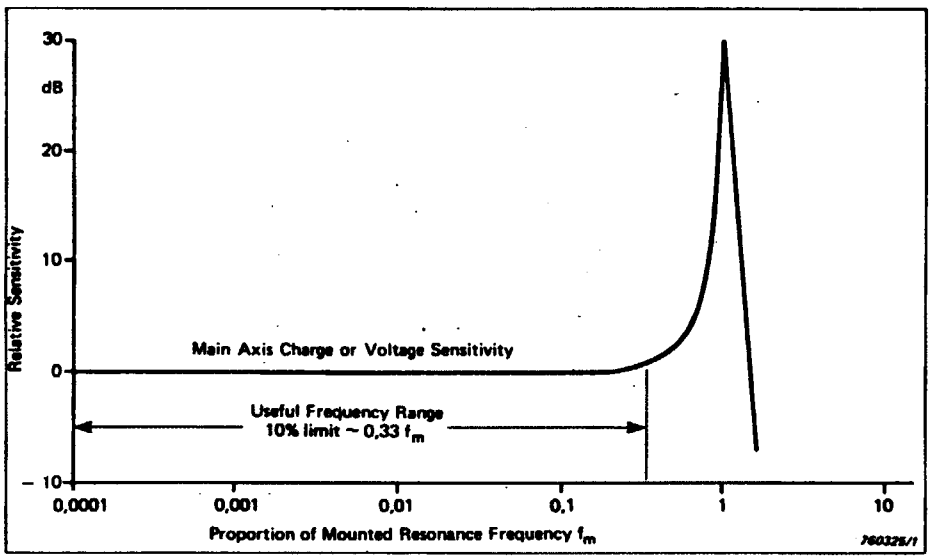


Fig. 2 Sensitivity vs. frequency of a piezoelectric accelerometer.

Various experimental studies have shown that the onset of cavitation generates a white noise (i.e., a flat power spectral density in the whole frequency range) with a possible exception for the very early onset phase when fast pulse rise fronts are emitted at a frequency of about some tens kHz. The CASBA accelerometer has a resonant frequency of 40 kHz, much higher those generated by mechanical or hydrodynamic vibrations. Therefore, it magnifies the bubble noise emissions at a frequency close to its resonance. The CASBA signal processing, as reported in the flow chart of Fig. 3, includes:

- a piezoelectric accelerometer transducer with a resonance frequency of 40 kHz;
- a fixed band pass filter (around 40 kHz and 50 dB/octave) on the resonance response of the transducer;
- a special signal amplifier for the implosion shock pulses;
- a true-rms voltmeter;
- a time constant to set the duration signal integration;
- an adjustable amplitude threshold.

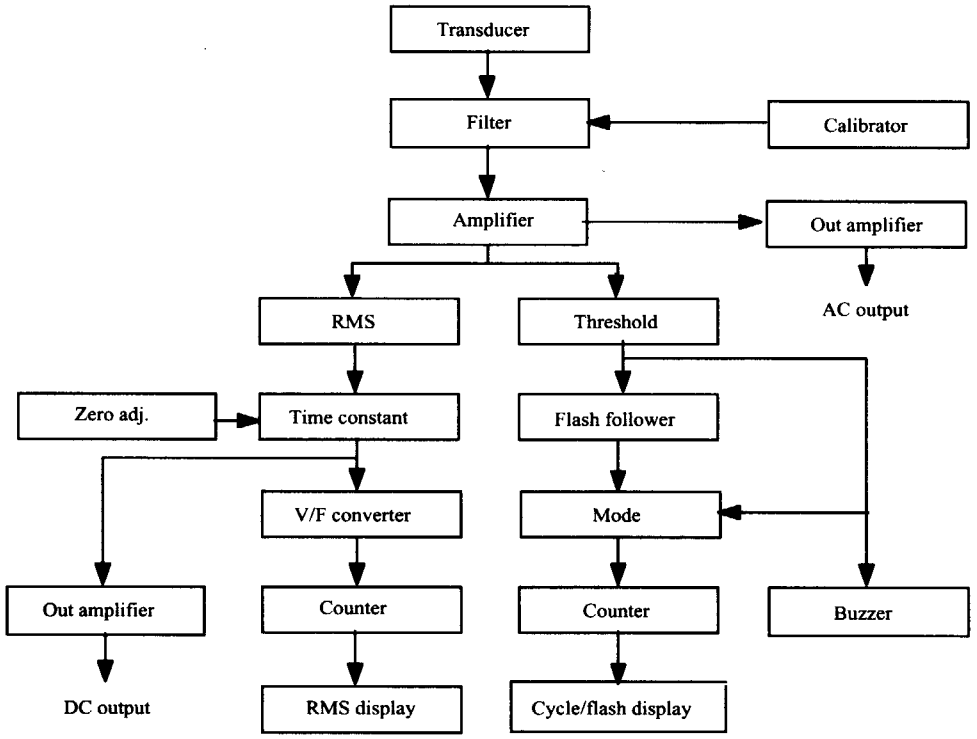


Fig. 3 CASBA meter flow chart.

The CASBA dynamic response of the bubble implosion onset was tested to be greater than other common systems. In fact, tests on cavitation of pumps have demonstrated the CASBA greater capacity to detect the noise inception in advance of pressure head drop monitoring or visual bubble growing, Fig. 4 [4]. Different comparison was performed in subcooled boiling two-phase flow between CASBA detection and thermocouple measurement with the evidence of a faster and better phenomenon monitoring, Fig. 5 [5].

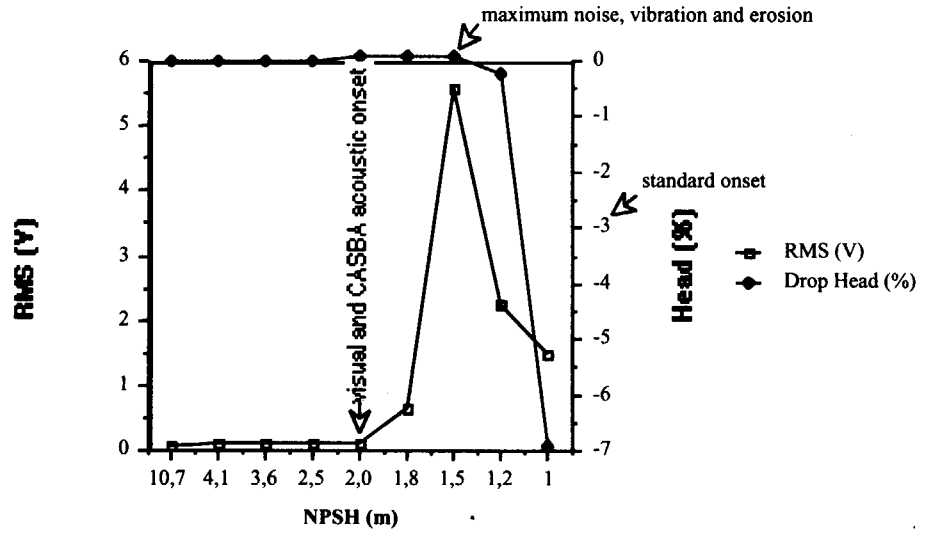


Fig. 4 Pump cavitation detection in "EPOCA" test.

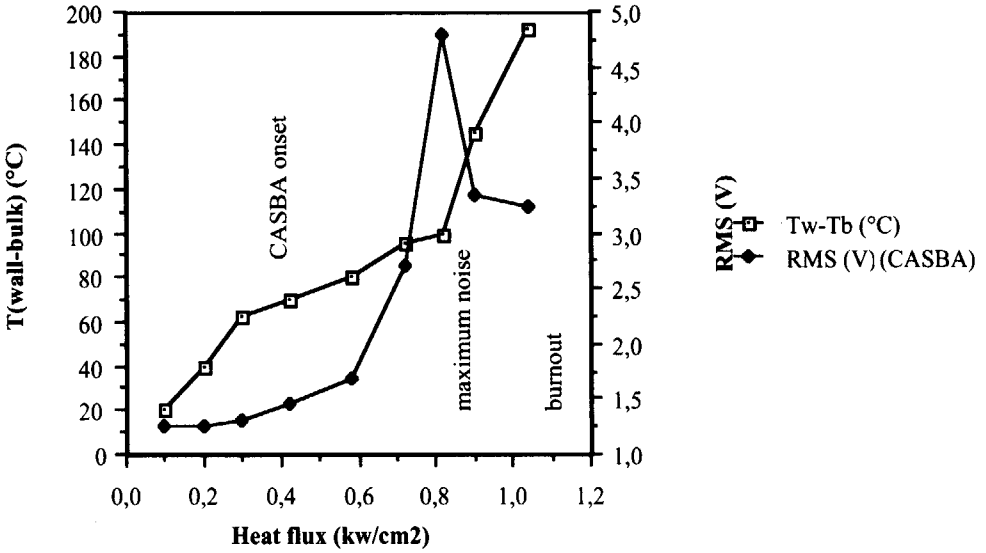


Fig. 5 Subcooled boiling detection in divertor tubes .

(4) Support of the Japanese Tests

In the frame of the co-operation with JAERI, during the preparation of the tests and the loop modification of the Osaka University Lithium facility, ENEA has furnished solutions for mounting the CASBA gages onto the existing pipe lines.

ENEA has also carried-out some preliminary calculations on the Japanese test section, using cavitation simulation, concerning the prediction of which component are at risk to initiate cavitation phenomenon [6] during nominal operation.

The cavitation index utilized to estimate this occurrence was defined as:

$$\sigma = (P_s - P_v)/P_d$$

with P_s= static pressure in the cavitation zone of the component;
P_v= vapour tension in the fluid at operating temperature;
P_d= 0.5 ρ V^2 or dynamic pressure in the cavitation zone of the component;
ρ= density of the fluid at operating temperature.

These calculations have evidenced the lowest cavitation index was found at the fourth multi-hole diaphragm of the pressure reducer, Table I [7], with a very probable zone of incipience of cavitation [6]. Therefore, during these tests, the effective occurrence of cavitation will be investigated by a CASBA transducer mounted in proximity to the zones of probable risk: i) the electromagnetic pump (EMP); ii) the flow straightener/multi-hole diaphragm pressure reducer; iii) the joint of replaceable backplate, Fig. 6. However, by the end of 2002 ENEA will preliminary determine the cavitation occurrence in the HY-JET test facility at Brasimone, close to the higher risk zones as previous indicated.

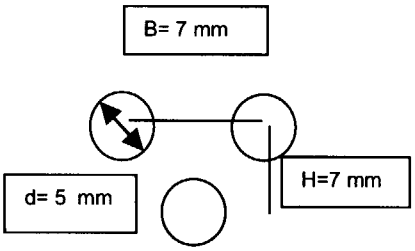
Table 1 Cavitation similitude at Osaka lithium loop.

Nozzle cross section

Base [m]	Height [m]	Surface [m^2]	Lithium velocity [m/s]
0,07	0,01	0,0007	15

Flow straightener cross section

Base [m]	Height [m]	Surface [m^2]
0,1	0,07	0,007



Flow straightener triangular surface (see sketch above)

Base B [m]	Height H [m]	Surface [m^2]
0,007	0,007	0,0000245

Flow straightener tube surface

tube diameter [m]	Surface [m^2]
0,005	9,817E-06
Flow straightener cross surface [%]	Lithium flow rate [m3/s]
40,07133487	0,0105
Flow straightener free cross surface [m^2]	Lithium velocity in the holes [m/s]
0,002804993	3,743324
	Lithium duct velocity [m/s]
	1,5

Cavitation similitude

Diaphragm number	4
Lithium density (kg/m3)	490
Lithium static pressure at inlet (Pa)	1,00E+05
Lithium vapour tension (Pa)	1,30E+02
Lithium dynamic pressure inside hole (Pa)	3,43E+03
Cavitation number in the duct	181,170068
K factor for local pressure drop	8,187605323
DP Diaphragm (Pa)	2,81E+04
Cavitation number at 1° Diaphragm	20,90308769
Cavitation number at 2° Diaphragm	12,71548237
Cavitation number at 3° Diaphragm	4,527877049
Cavitation number at 4° Diaphragm	-3,659728274

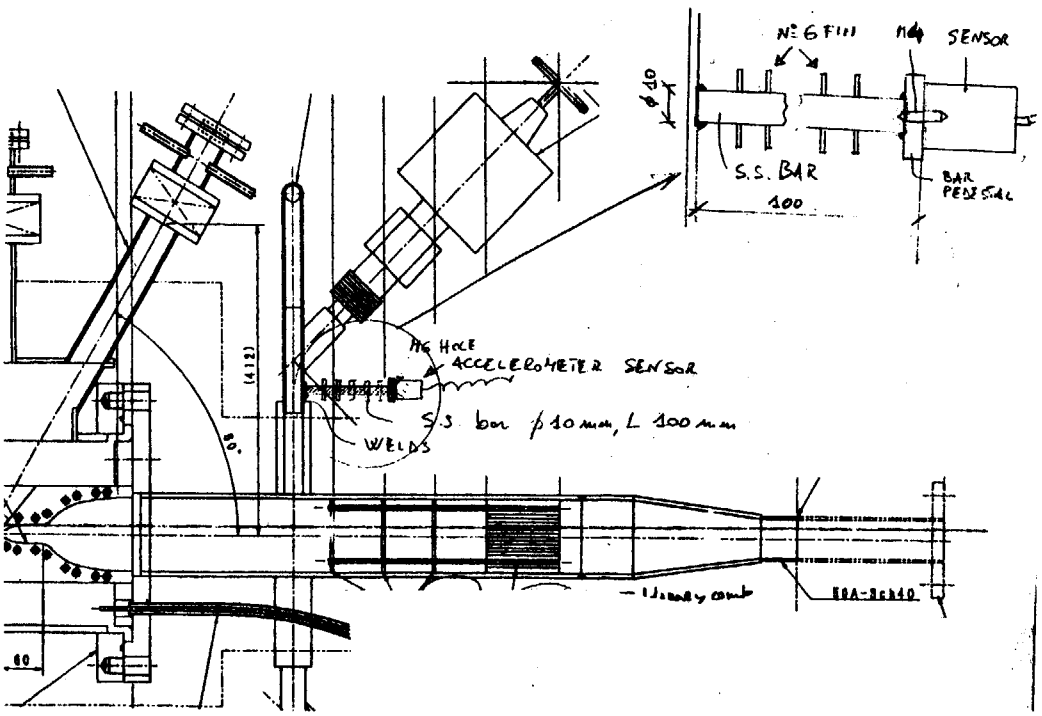


Fig. 6 Scheme of the CASBA-2000 sensor mounting on the Osaka University lithium test facility.

(5) Conclusion

The ENEA activity in support of Japanese tests for the cavitation noise detection in the Osaka University Lithium facility was started in 2000. The cavitation tests will start at the end 2002 on the ENEA Brasimone HY-JET test facility and will continue at the Osaka University. This activity will continue beyond 2002 presumably up to July 2003.

References

[1] M.Martone, (editor), IFMIF International Fusion Materials Irradiation Facility Conceptual Design Activity Final Report, ENEA Frascati Report, RT/ERG/FUS/96/11, November 1996.

[2] D. Tirelli, P. Gori: "Instrument for the Measurement of the Cavitation or Boiling Rate in a Liquid", USA Patent Number 5,074,150.

[3] D. Tirelli, Development and Testing of On Line Detection Systems for Cavitation, Subcooled Boiling and Leaks in NPP Components, ENEA Internal Report, November 1996

[4] J. Biscarel, J. M. Dorey, J. Mc Knight, D. Tirelli: "European Fast Reactor. Common Report: EPOCA Test", ENEA Internal Report.

[5] G. Dell'Orco: "Thermal-hydraulic Experimental Studies about One-side Heated Tubes", Specialists' Workshop on High Heat Flux Component Cooling, Cadarache (France), September 22-24, 1993.

[6] F. G. Hammitt, Cavitation and Multiphase Flow Phenomena, McGraw-Hill International Book Company, 1980, pp. 100-117

[7] G. Dell'Orco et al., Li-Target Tasks Deliverables 2-3, IFMIF Meeting on 2001 Monitoring and 2003 Tasks, Karlsruhe, 30 January - 1 February, 2002

3.2.8 TG16-JA : Cavitation Verification in a Small Lithium Loop

(1) Brief Task Description

High speed lithium flow was demonstrated under free surface condition using the Lithium Loop facility at Osaka University. Cavitation charactersitics are a key feature of loop operation, since it determines the stable operating region of the system. This report gives preliminary results of a study of cavitation in a free surface lithium loop. The preliminary experiments included lithium flow rates up to 14 m/s under a pressurized cover gas and 8.5 m/s under vacuum. It was shown that the flow characteristics generally agree with the design estimates of the pressure changes throughout the loop tubing system.

Contributors

Name	Party	Institute	E-mail address
H.Horiike	Japan	Osaka University	horiike@eie.eng.osaka-u.ac.jp
T.Iida	Japan	Osaka University	chernovv@bochvar.ru
S.Inoue	Japan	Osaka University	inoue@eie.eng.osaka-u.ac.jp
S.Miyamoto	Japan	Osaka University	
N.Yamaoka	Japan	Osaka University	yamaoka@nucl.eng.osaka-u.ac.jp
I.Matsushita	Japan	Shinryoh High Technologies Ltd.	Izuru__matsushita@kbg.kobe.mhi.co.jp
T.Muroga	Japan	NIFS	muroga@nifs.ac.jp
T.Tanaka	Japan	NIFS	teru@nifs,ac.jp
M.Ida	Japan	JAERI	ida@ifmif.tokai.jaeri.go.jp
Hideo Nakamura	Japan	JAERI	nakam@lstf.tokai.jaeri.go.jp
Hiroo Nakamura	Japan	JAERI	nakamurh@fusion.naka.jaeri.go.jp
K.Ara	Japan	JNC	ara@oec.jnc.go.jp
M.Hirabayashi	Japan	JNC	mhirarin@oec.jnc.go.jp

(2) Introduction

High-speed lithium flow is necessary to remove the high heat load generated in the IFMIF target[1]-[3]. Lithium has a boiling temperature of 1615 K at 1 atmosphere and 617 K at 1.0 mPa. This value is marginal beam line vacuum for stable accelerator operation. Therefore a target with a stable free surface is required and has to be carefully designed. It is also important to maintain a stable jet to avoid significant heating of the target back wall by deuteron penetration, to suppress excessive lithium vaporization, and for stable neutron generation.

Lithium flow with free surfaces was first studied in the Hanford Engineering Development Laboratory for the FMIT design[4],[5]. An asymmetric reducer nozzle was selected for a small beam footprint whose axis was located about 20 mm from the nozzle exit.

In the design of IFMIF, the beam cross sectional area was much larger than in FMIT and the location of the beam axis was moved downstream to reduce neutron damage to the nozzle. To satisfy this goal, a symmetric nozzle with double reducer shape was designed[6],[7]. A lithium jet flow experiment was initiated at Osaka University to validate this design. The present report describes cavitation measurements conducted during the test.

(3) System Design and Construction

(3-1) Lithium Circulation Loop

The lithium loop at Osaka [8] consists of 2 inch 304 stainless steel tubing, an ALIP type electromagnetic pump (EMP), an air cooled module, an expansion tank and an electromagnetic flow meter. The maximum flow rating of the EMP is 0.5 m^3/min at 0.4 MPa head and 0.8 m^3/min at 0.3 MPa, with a 440 liter lithium inventory. Table 1 shows the parameters of the loop, and Fig. 1 the

schematic diagram. Details of the construction are presented in 3.2.6 and in a separate report[9].

Table 1 Major specifications of the Osaka lithium loop.

EMP	ALIP 500*l*/min, 0.5MPa
	Max. velocity at test section: 6.3 m/sec
Magnet	DC, Max. *B:* 0.8T
	Pole faces: 500 x 250 mm
	Inter pole gap: 175 mm
Heater pin	10mm diameter, 1 mm thickness, 306SS
	Heat flux: Max. 2.5 MW/m^2
Test section	52.7 mm i.d., 60.5 o.d., SS304
	Operating temp. 300~550 °C
Nozzle	70mm width 10mm high
Open channel	- 100cm long
Buffer tank	270 liter
Cold trap	6*l*/min, operating temp. >220 °C
Evacuation	Dry pump down to 15Pa

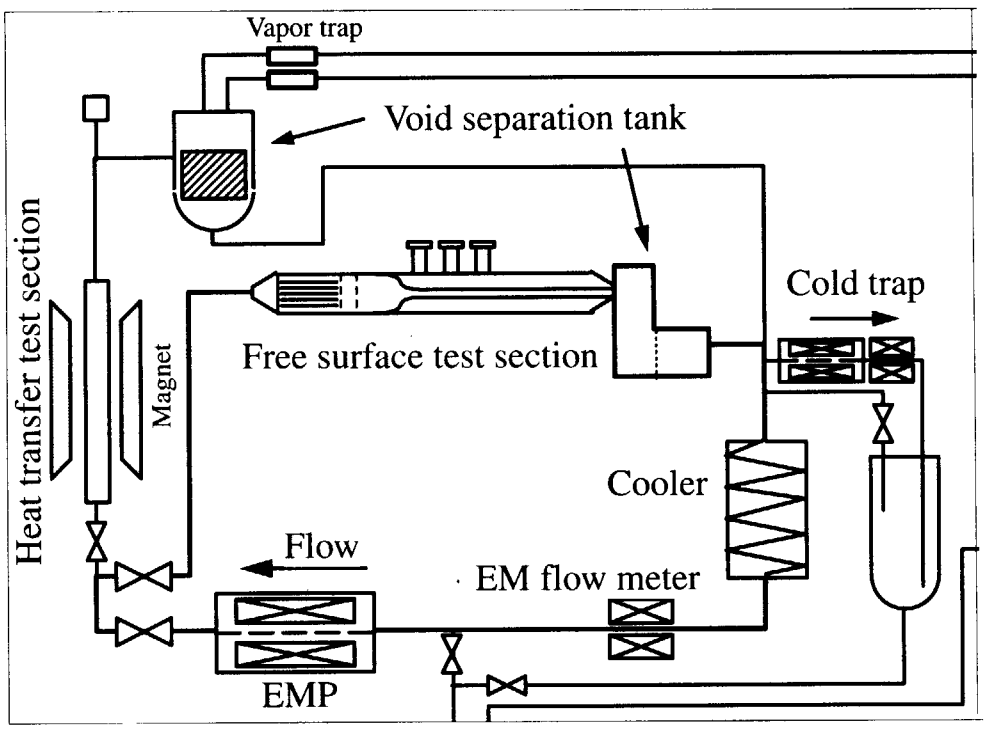


Fig.1 Schematic diagram of the Osaka lithium loop.

(4) Entrainment of Gas

Entrainment of gas bubbles is a problem related to individual facility design. In order to reduce the loop volume and lithium inventory, the present loop was designed for a low height. The height difference from the gas liquid separation tank to the pump inlet is 4 m. This head is small considering the density of Li, so a model liquid vapor separator of 1/2.5 size was constructed and performance studied using water and nitrogen gas.

The test was carried out with a separator tank made of clear plastic through which we can observe the behavior of bubbles and make measurements with a volume meter. The result is that the centrifuge buffer tank combined with bubble combiner panels gave the best performance in separating the bubbles from water flow, and was selected for the loop modification. In Fig.2 the cross sectional view is indicated, and a photograph of the component is shown in Fig.3. This structure works well and in the preliminary test flow velocity up to 14 m/s and flow rate of 576 liter per min under pressurized argon gas was obtained. However, it is still unknown if very small bubbles, of size less than say 0.5 mm, could be produced in lithium and this cannot be determined in the water experiment.

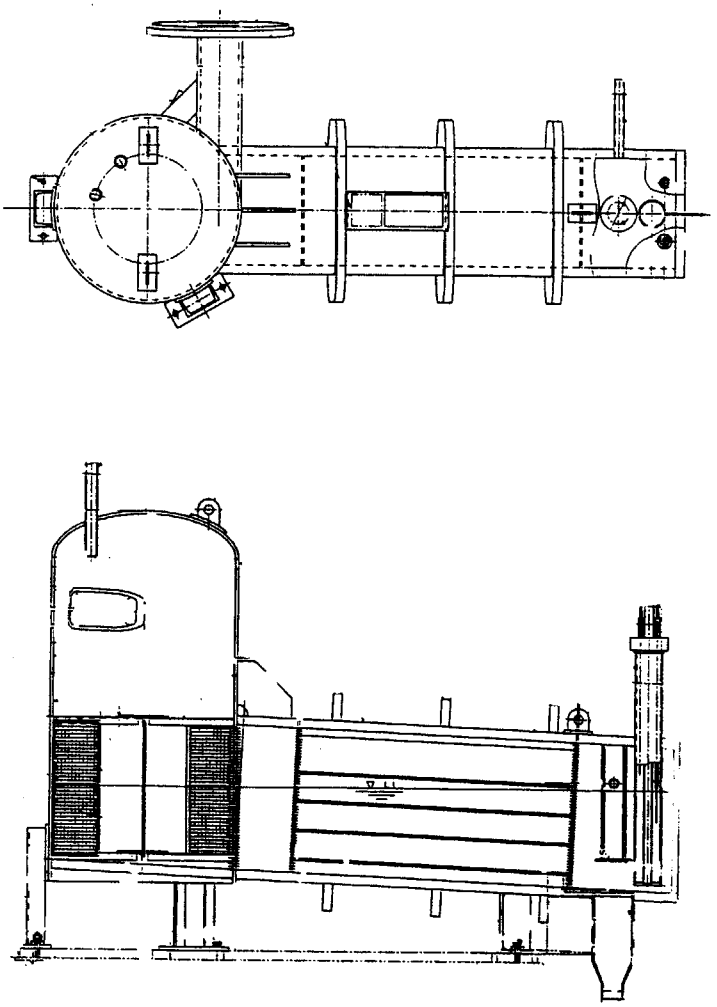


Fig.2 Cross sectional view of the gas liquid separation tank.

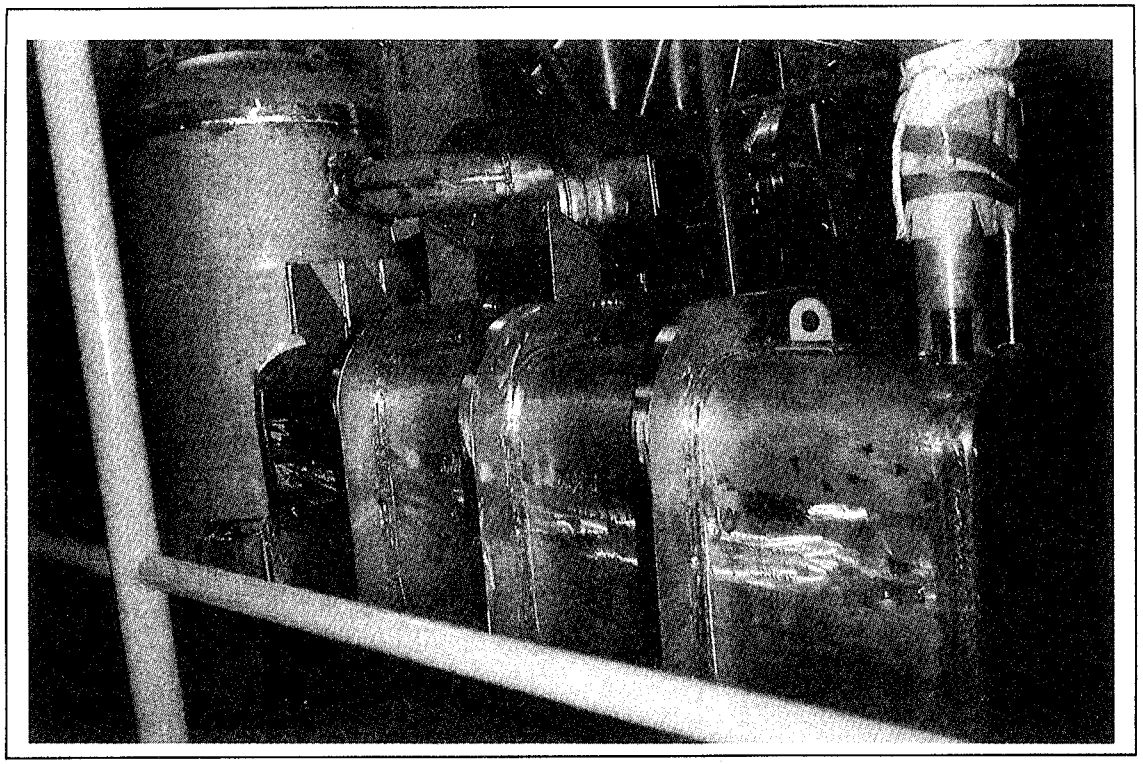


Fig.3 Photograph of the gas liquid separation tank.

(5) Experimental results

The results of cavitation measurements under vacuum are indicated in Fig.4. The two plots indicate the initiation points of cavitation, which was obtained by gradually increasing the flow rate under fixed system pressures of 0 and 0.029 MPa. The zero pressure case means the loop volume was evacuated to the minimum pressure achieved by a dry pump and then sealed. The "zero" pressure is believed to be approximately 50 Pa.

The dotted line in Fig. 4 shows the calculated value of the pressure drop between the outlet of the separator tank and the inlet of the EMP, based on the standard design curves and shape data for water properties, not lithium. The left hand side of the curve starts from -0.02 MPa, corresponding to the gravity head of 4 m lithium. The experimental plot falls slightly lower than the design line, and is reasonable in view of the conservativeness in the estimate. The deviation between dotted and solid lines includes ambiguities in the estimate of the onset of cavitation. It can be concluded that cavitation takes place when the differential pressure at the pump inlet goes below zero to some extent. The present result shows that the cavitation initiation could be estimated from careful estimation of the pressure drop values between the free surface and pump inlet.

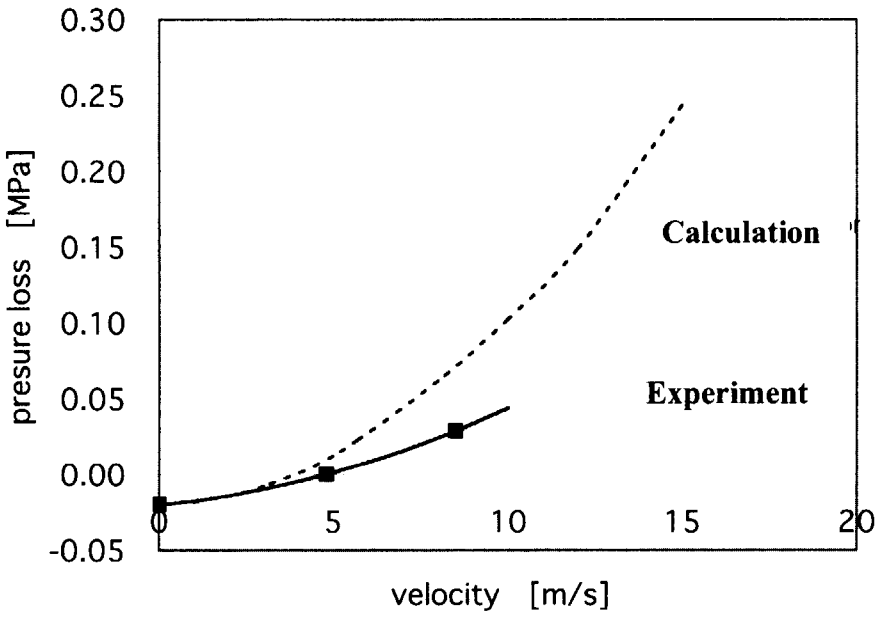


Fig.4 Cavitation characteristics of the present loop. The vertical shows the pressure drop and the horizontal flow velocity. (Label: insert pressure drop units in ordinate)

(6) Summary

The lithium loop facility at Osaka University was modified to perform free surface jet flow experiments for the IFMIF target design. Through the modification work, various key factors for design were obtained, including entrainment of gas bubbles and cavitation. In the experiment, lithium flow rates up to 14 m/s were obtained under a cover gas and 8.5 m/sec under vacuum. Caviation was observed at two pressures, and the result nearly agreed with the curve drawn from a pressure drop estimate. It can be concluded that cavitation takes place when the differential pressure at the pump inlet goes below zero to some extent. Surface observations showed relatively calm flow, with neither violent waves nor splashing of the fluid. Further detailed experiments to measure cavitation characteristics are planned in cooperation with ENEA.

References

[1] H.Matsui, et al., Proc. 10th Int. Conf. On Fusion Reactor Materials, Baden-Baden, 14 - 19 October 2001. paper 09.PL.3.

[2] Hiroo Nakamura, et al., Status of lithium target system for international fusion materials irradiation facility (IFMIF), Fusion Eng. and Des. 58-59(2001)919-923.

[3] Fusion Neutron Laboratory, IFMIF Key Element Technology Phase Task Description, Laboratory report, JAERI, JAERI-Tech 2000-052, August 2000.

[4] R. R. Miles et al., Improved Liquid Lithium Target for the FMIT Facility, HEDL Report, HEDL-SA-2721-FP (1982).

[5] J. A. Hassberger et al., Comparison between measured and predicted performance of a high speed free surface liquid jet flowing along a curved wall, Nuclear Technology Fusion 4, (1983) 433-438

[6] Hideo Nakamura et al., Experimental and analytical studies on high-speed plane jet along concave wall simulating IFMIF Li target flow, J.Nucl. Mater. 258-263 (1998) 440-445.

[7] M. Ida et al., Thermal-hydraulic characteristics of IFMIF liquid lithium target, 6th International Symposium on Fusion Nuclear Technology, Apr. 7-12, 2002, San Diego, California, USA (ISFNT-6), To be published in Fusion Engineering and Design

[8] N.Uda et al., Forced Convection Heat Transfer and Temperature Fluctuations of Lithium under Transverse Magnetic Field, J.Nucl.Sci.Tech., 38, 11(2001) 936-943

[9] H.Horiike et al., Lithium Free Surface Flow Experiment for IFMIF, Proc. SOFT 22, 16-20 Sept. 2002 Helsinki Finland

3.2.9 TG21-JA : Measurement of Stainless Steel Erosion/Corrosion in a Lithium Loop

(1) Brief Task Description

Erosion and corrosion of stainless steel (SUS304) in contact with liquid lithium had been investigated for the IFMIF target system. Verification of the erosion and corrosion of the SUS304 in liquid lithium was performed in a liquid metal circulating experimental device, the forced lithium loop at Osaka Univversity. Part of the SUS304 loop tubing was evaluated after lithium circulation for 186 hours, and the results compared with former studies.

Contributors

Name	Party	Institute	E-mail address
Hiroshi Horiike	Japan	Osaka Univ.	horiike@eie.eng.osaka-u.ac.jp
Akihiro Suzuki	Japan	NIFS	asuzuki@nifs.ac.jp
Ken Kurosaki	Japan	Osaka Univ.	kurosaki@nucl.eng.osaka-u.ac.jp

(2) Introduction

IFMIF is a Deuteron-Lithium neutron source to simulate the neutron irradiation field in a fusion reactor. Deuteron ions accelerated to 40 MeV with total current 250 mA bombard a lithium target system. The target system removes the heat load of 10 MW by a flow of liquid lithium at velocity up to 20 m/s in a circulating coolant loop.

Because liquid lithium can dissolve metallic and nonmetallic elements at high temperatures, lithium could corrode the loop tubing and the back-wall materials. In addition, the liquid lithium flows at such a high rate in the IFMIF target system that erosion phenomena could occur, inducing mass reduction of the materials and deposition of corrosion/erosion products. Thus, the study of corrosion and erosion of the structural material is an important task to reduce mechanical degradation of the target and predict any safety issues with the loop system.

Many basic studies of liquid lithium compatibility with SUS304, a structural material candidate for IFMIF target system, have been performed. The corrosion rate reaches a steady-state value after an initial transient period and is insensitive to temperature in the range up to 773 K [1]. The initial transient period is characterized by rapid dissolution of nickel in the alloy, resulting in rapid changes in surface composition [2]. This is due to the high solubility of nickel in liquid lithium compared to the other metallic elements. The surface of the alloy develops a dimpled, sponge-like appearance because of formation of a ferritic layer [3]. Moreover, the rapid changes include dissolution of chromium from the alloy. Because the dissolution rate of the chromium depends on the nitrogen impurities in the liquid lithium [4], formation of a ternary nitride (Li_9CrN_5) corrosion product is likely during the corrosion process [5]. The mass loss from SUS304 decreased as the ratio of the square or cube of the nitrogen concentration in the lithium [6]. Grain boundaries of the alloy are preferentially attacked due to the rapid dissolution of nonmetallic elements in the alloy [7]. The corrosion at grain boundary is largely enhanced by high nitrogen and high carbon concentration in the lithium [8]. The flow rate of liquid lithium also affects the mass decrease. Increase of the lithium flow rate from 0.1 m/s to 2.4 m/s results in one order of magnitude larger mass decrease rate [9]. No effect of liquid lithium flow rate on erosion was found for flow rates up to ~15 m/s. Therefore, observation of the structural material in actual lithium loops, especially in high speed loops, is needed to estimate effects of corrosion and erosion in the IFMIF target system.

In this report, measurements of the erosion and corrosion of the SUS304 in the forced lithium loop at Osaka University are given and compared with former studies. A section of the SUS304 tubing of the loop was cut out after lithium circulation for 186 hours and corrosive behavior determined by Scanning Electron Microscope (SEM), Energy Dispersion Spectroscopy (EDS), X-ray photoelectron spectroscopy (XPS), surface roughness measured with a digital microscope, and X-ray diffraction (XRD).

(3) Measurements of erosion / corrosion in the loop tubing

Figure 1 shows optical microscope images of the surfaces of the SUS304 tubing before and after corrosion in the Osaka lithium loop. After the lithium exposure, the scratches on the polished surface of the SUS304 have disappeared. This is believed to be due to the slight dissolution of material and/or transformation of the surface caused by the initial rapid mass decrease. In Fig. 1, severe corrosion at grain boundaries is also observed. This may show a relatively large amount of nitrogen is dissolving in the liquid lithium., The only nonmetallic impurity control system, a cold trap in the loop, theoretically cannot decrease the nitrogen impurity content below about 1500 wppm.

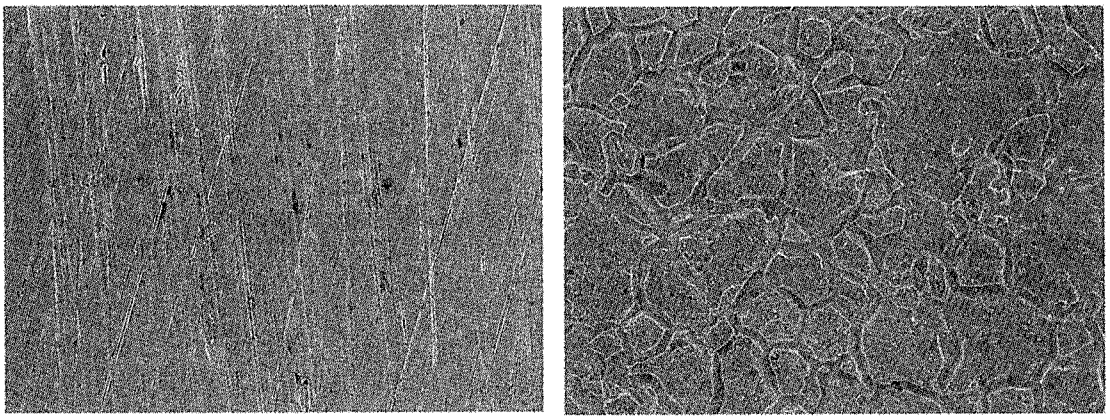


Fig.1 Optical microscope images of tubing (left) before the lithium corrosion and (right) after corrosion.

Figure 2 shows an SEM image of the SUS304 surface after the lithium corrosion. In addition to the relatively large water-saturated lithium lumps remaining on the surface, a lot of sub-micron holes in the bulk are observed, showing a spongy structure of the surface layer. The thickness of this spongy layer was observed by SEM images of the cross section and found to be less than 1 micrometer. The Ref. [9] reported that the spongy layer thickness reached a steady-state value of 10 micrometers after the corrosion liquid lithium for 1000 to 2500 h. In the case of the total corrosion time of 185 h for the present observation, this suggests that the corrosion process has not yet reached steady state, but is still in the initial transient period.

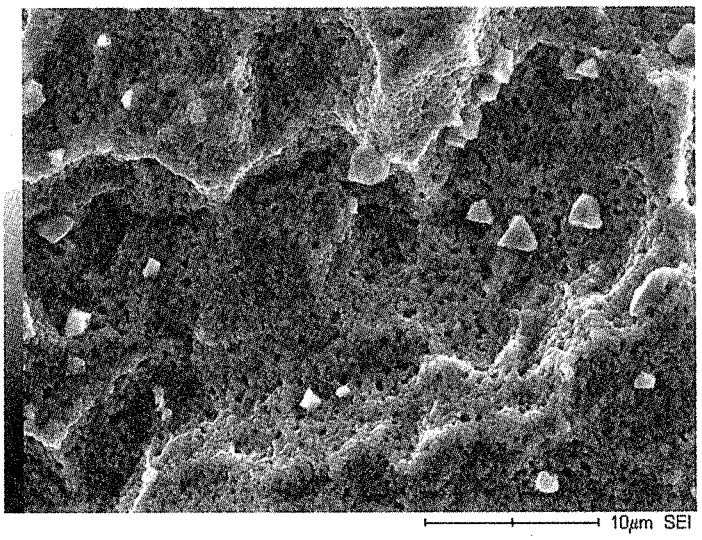


Fig. 2 SEM image of the SUS304 surface after the lithium corrosion.

XRD measurements of the surface after the lithium corrosion are shown in Fig. 3. In addition to a peak of the austenitic steel fcc lattice, peaks from the ferritic bcc lattice are observed. This is because the decrease of chromium and nickel in the SUS304 is accompanied by the steel transformation to ferrite. Both the fcc and bcc structures are observed because the corrosion/depletion layer is thinner than the penetration depth of the Xrays.

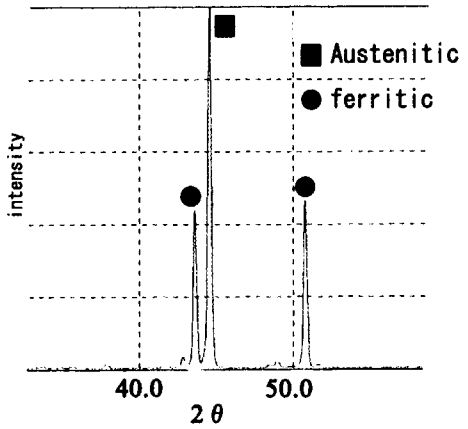


Fig. 3 XRD peaks of the SUS304 surface after the lithium corrosion.

Table 1 shows the ratio of iron, chromium, and nickel determined by EDS and XPS analyses of the surface of the SUS304 after the lithium corrosion. In both analyses, the ratios of chromium and nickel to iron are dramatically decreased. Additionally, XPS, analyzing only a few atomic layers on the surface, shows much smaller amounts of chromium and nickel than EDS, which averages information over about one micrometer depth below the surface. This result indicates a steep depth gradient in the concentration of chromium and nickel. Thus, the relatively high nitrogen concentration induces the dissolution of chromium, and the reduction of chromium and nickel occurs in the initial transient period of the forced loop operation.

Table 1 Ratios of iron, chromium, and nickel by EDS and XPS analysis on the SUS304 surface after the lithium corrosion

SUS304 samples	Analysis method	Iron (wt %)	Chromium (wt %)	Nickel (wt %)
before lithium corrosion	EDS	72.6	18.3	9.1
after lithium corrosion	EDS	82.1	12.5	5.4
after lithium corrosion	XPS	92.9	3.8	3.3

The surface roughness of the SUS304 after the lithium corrosion is shown in Fig, 4. The figure shows large roughness on the surface of the specimen. Table 2 shows arithmetical mean deviation of the surface, Ra, and root-mean-square deviation, RMS, of two samples located in different parts of a tubing bend. The surface roughness of the sample located in the outer part of the tubing has a little larger deviation than the inner part. However, the difference is small. The sample located in the outer part of the bent tubing faced about 1.25 times higher flow rate of liquid lithium than the sample at the inner part. The mean flow rate during the loop operation was -0.7 m/s, and the maximum was -2.3 m/s. From Ref. [10], the difference of mass decrease rate of the samples is estimated to be less than 10%. Therefore, no definite proof of dependence on the lithium flow rate was obtained.

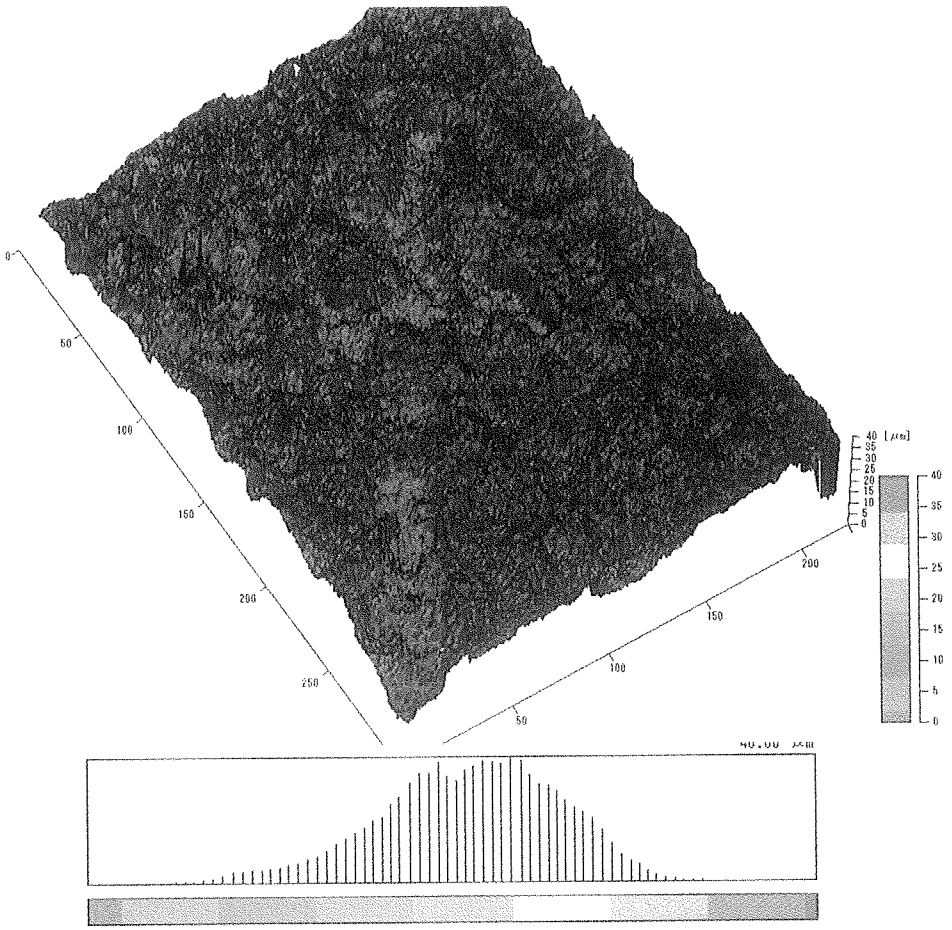


Fig. 4 Surface roughness of the SUS304 after the lithium corrosion.

Table 2 Deviation of the two sample surfaces located on different parts of a tubing bend after the lithium corrosion.

SUS304 samples	Ra (μ m)	RMS (μ m)
Inside part of bent tubing	2.53	3.19
Outside part of bent tubing	2.79	3.64

(4) Conclusion

Measurements of the erosion and corrosion of the SUS304 in a forced lithium loop at Osaka University were compared with the former studies. Severe corrosion at grain boundaries and large dissolution of chromium at the surface were observed. This may show that a relatively large amount of nitrogen is dissolved in the liquid lithium of the forced loop. Dissolution of chromium and nickel results in the formation of a thin spongy ferrite layer. The surface roughness of the sample located in the outer part of the tubing has a little larger deviation than the inner part. However, no definite proof of dependence on the lithium flow rate was obtained. Thus, the SUS304 in a forced lithium loop shows similar erosion and corrosion behavior to that in earlier pot and loop experiments.

References

[1] O. K. Chopra and D. L. Smith, J. Nucl. Mater., 141 (1986) 584.
[2] G. A. Whitlow, et al., J. Nucl. Mater., 85-86 (1989) 283.
[3] J. Qian, J. Chen, et al., J. Nucl. Mater., 179-181 (1991) 603.
[4] P. F. Tortorelli, J. Nucl. Mater., 155-157 (1988) 722.
[5] I. E. Schreinlechner and P. F. Sather, J. Nucl. Mater., 155-157 (1988) 736.
[6] R. J. Schalager, et al., J. Nucl. Mater., 57 (1975) 312.
[7] R. Anderson and H. Stepher, NEPA-1652 (1950).
[8] J. A. Reeves, etal., Nucl. Tech., 30 (1976) 385.
[9] F. Casteels, et al., Trans. Internal. Struct. Mech. React. Technol., (1979).
[10] D. G. Bauer et al., CONF-800401, (1981) 13.

3.2.10 TG22/31A-EU : Lithium Corrosion and Chemistry

(1) Brief Task Description

The construction of the IFMIF loop and target requires the development of suitable systems and materials able to operate in flowing Li. Even if the envisaged operating temperatures within the target and in the loop are relatively low, both the effect of corrosion/erosion and liquid metal chemistry has to be controlled and assessed. Indeed, as in the case of sodium, lithium corrosion is strongly influenced by the presence of non-metallic impurities in the liquid metal. Those impurities, especially N and C, are able to form Li-compounds which can increase the corrosion effects on steels. This phenomenon, in addition to the elemental dissolution, can create problems for the structural materials. Thus the development of a Li purification strategy, including monitoring and removal systems and evaluation of the corrosion rate of different materials (namely steels) in conditions relevant for the IFMIF loop and target, is mandatory and will be studied in the framework of this task.

Contributors

Name	Institute	Party	e-mail address
C. Fazio	ENEA	EU	concetta.fazio@brasimone.enea.it
G. Scaddozzo	ENEA/Politecnico di Torino	EU	giuseppe.scaddozzo@brasimone.enea.it
A. Bailey	ENEA/University of Nottingham	EU	pcxasb@nottingham.ac.uk

(2) Introduction

The International Fusion Materials Irradiation Facility (IFMIF) has been proposed to test and qualify fusion reactors materials under high energy neutron irradiation. For this purpose a high intensity neutron source based on a deuteron beam impinging on a liquid lithium target has been selected as the basic concept of the IFMIF. The lithium target system has two subsystems; the target assembly itself providing a stable Li jet, and the lithium loop for the removal of the deposited heat. The mean lithium temperature in the loop will be of the order of 250-300°C. It could be foreseen that in these operating conditions liquid metal corrosion/erosion phenomena on structural materials could occur. Further, as it has been recognised in the past, corrosive effects of some structural materials (i.e. steels, vanadium alloys) could be enhanced by the presence of non-metallic impurities in the liquid Li. Due to this aspect, the reference design of the IFMIF loop foresees also ancillary systems for the monitoring and control of those impurities. The impurities that may affect the corrosion rate are mainly nitrogen, carbon, oxygen and hydrogen. Nevertheless, some synergetic effects of hydrogen and carbon content in the alkali metals on the corrosion of steels have also been described. As far as safety issues are concerned, hydrogen isotopes such as tritium are produced in the IFMIF target, both by the direct reaction between the deuteron beam and the Li jet and by the capture of low energy back scattered neutrons by Li-6. Since tritium has a relevant toxicity, tritium monitoring and control in the main Li loop will be mandatory.

Concerning the correlation between the oxygen level in the liquid lithium and the corrosion enhancement of structural materials, such as steels, it could be reasonably foreseen that there will be little effect. If vanadium alloys are used, then an effect of oxygen activity in the liquid metal on the corrosion rate of the V alloy could be supposed. Anyway, the oxygen monitoring and control in the flowing liquid lithium of the IFMIF main loop is relevant for hydraulic issues, since the oxygen could react with lithium to form solid lithium oxides which could cause plugging of the pipes.

Usually a relative high chemical activity of carbon in liquid lithium could give rise to corrosion phenomena through an exchange reaction of this element. For instance the carburization - decarburisation of stainless steels affects the chemical activity of chromium in the steel. Due to the decarburisation process occurring on grain boundary areas, the depletion of chromium by alkali metals corrosion will be enhanced. Synergetic effects of carbon and nitrogen dissolved in the liquid lithium on the corrosion enhancement were also described. Thus the monitoring and control of carbon in the

lithium loop is mainly related to the compatibility of structural materials. On the other hand the lithium carbide has a negative free energy of formation and plugging due to the formation of this compound could also be envisaged.

Concerning nitrogen, liquid lithium could dissolve considerable amounts of this element. The main effect of the dissolved nitrogen is the corrosion rate enhancement of steels or vanadium alloys due to the formation of stable ternary nitride (Li – M – N). For instance, for chromium-bearing steels, the preferential corrosion mechanism pass through the formation of the complex nitride Li_9CrN_5 if the chemical activity of nitrogen in the liquid lithium satisfies the thermodynamic criteria to form the complex nitride. Since the solubility of nitrogen in Li is effectively high, it could be understood that the mentioned criteria is easily reached.

(3) Literature review

The solubility of the non-metallic elements in liquid lithium is a relevant parameter to establish the control methods to be applied to the IFMIF facility. In literature the solubility data available for oxygen, carbon and nitrogen are:

Log[O](wppm) = 6.992 - 2896/T(K) [1]
Log[C](wppm) = 7.459 - 3740/T(K) [2]
Log[N](wppm) = 7.597 - 2098/T(K) [3]

In Table 1 the solubility of the three elements at different temperature are reported. As far as the hydrogen solubility, controversial data are available [4].

Table 1 Solubility data of O, N and C in liquid lithium given in wppm.

Temp. (°C)	Oxygen	Nitrogen	Carbon
200	7.4	1450.4	0.4
300	86.7	8621.2	8.5
400	488.5	30172.8	79.8
500	1760.2	76365.8	417.5
600	4728.3	156240.2	1496.0
700	10366.6	275919.3	4123.0

Together with the solubility data, the lithium compounds free energy of formation are relevant for the most suitable trapping method to be chosen for controlling the impurities in liquid lithium. These data are available in the JANAF tables [5], and in Fig. 1 they are reported vs. the temperature.
The first step for the selection of the most promising non-metallic impurities Monitoring And Control (MAC) techniques was to perform a literature review in order to summarize the state of the art [6]. As is well known, monitoring methods could be of the on–line or laboratory types and the control methods are mainly trapping techniques. For the IFMIF purposes on–line methods are most suitable and several techniques could be available for each type of impurity previously mentioned. The available methods were described in a report by the University of Nottingham, which collaborates in the frame of this task with ENEA [6]. The report gives a thorough description and evaluation of the methods as well as their pros and cons, also taking advantage of the sodium technology. A summary of the most promising monitoring and controlling methods for each element follows.

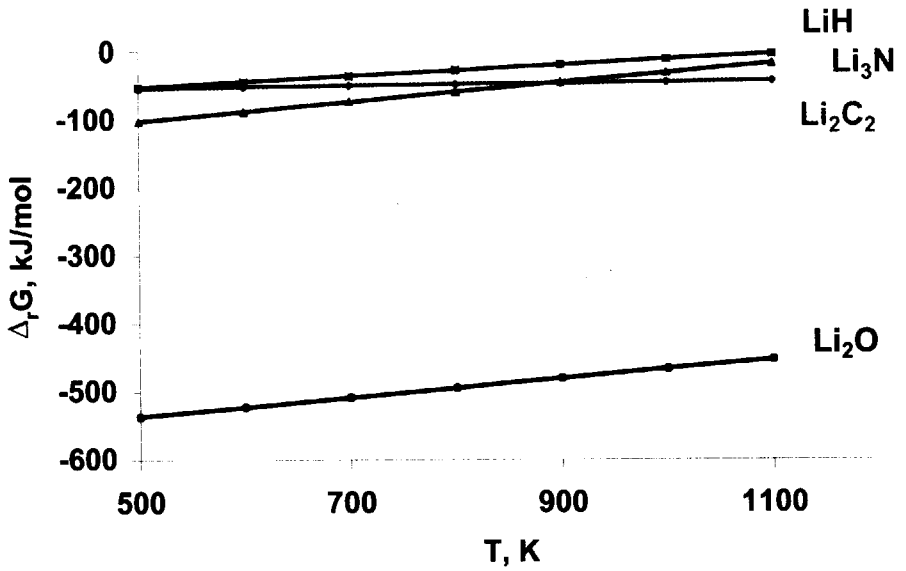


Fig. 1 Free energy of formation of Li compounds. (Data taken from JANAF Table [5])

a) Hydrogen

a-1) Monitoring

The two on-line methods considered for monitoring hydrogen are the electrochemical method and the direct pressure measurement. For the electrochemical method, a sensor was developed for Na applications which was based on the (CaH_2, $CaCl_2$) solid electrolyte and Li/LiH as reference electrode. It could be assumed that similar sensors work also in Li. Concerning the direct pressure measurement, this method is based on the use of niobium or niobium-zirconium membranes, and the application of a quadrupole mass analyser on-stream. The hydrogen permeates through the Nb base membrane into a calibrated vacuum chamber, and the pressure increase in the chamber will be measured and related to the hydrogen concentration in the liquid metal through the Fick equation:

$$J = D/L \cdot c_{H(Li)}$$

were J is the hydrogen flux, D is the hydrogen diffusion coefficient through the Nb based membrane, L is the thickness of the membrane, $c_{(H)Li}$ is the hydrogen concentration in lithium. The direct pressure measurement method has been envisaged to be the most suitable technique and its development is an ongoing activity. The experimental activities will be performed with Nb and Nb-Zr alloy with different amounts of Zr. The selection of the most suitable Nb – Zr alloy will be based on its compatibility with the liquid metal and on its hydrogen diffusion behaviour. Literature data on the compatibility of Nb and Nb-1Zr with liquid lithium are available and are reported in Table 2 [8-10]. These data were obtained for high temperature and show a good compatibility of the Nb based alloys with the liquid metal. Thus, the preliminary compatibility test of the Nb or Nb-1Zr membrane in liquid lithium will be performed in order to confirm the literature data and to analyze the compatibility of the membrane with higher Zr content. In addition the hydrogen diffusivity data on the Nb and the Nb-Zr alloys will be measured with the gas-gas UHV method [7].

a-2) Control

The reference method for the control of hydrogen in liquid lithium is the cold trapping method even if the potential of using zirconium, yttrium or lanthanum hot traps could be explored.

Table 2 Corrosion rate at high temperature of Nb and Nb-1Zr in liquid lithium [8-10].

T (°C)	ΔT (°C)	Time (hr)	Li velocity (m/s)	Corrosion rate (μm/yr)
1100	200	10,000	3-6	negligible
1200	200	1,550	3-4	negligible
1297	179	3,000	0.05	7.5
1073-1143	~10	500	48.5	120
1330	200	500	3-4	1000

b) Oxygen

b-1) Monitoring

The two methods taken into account were the electrochemical and the amalgamation methods. Since the amalgamation method is not an online one, the development has been focussed on the electrochemical one. An oxygen sensor using Yttria Doped with 7.5 mol % Thoria (YDT) as solid electrolyte and In/In_2O_3 as reference electrode has been envisaged. The electrochemical scheme of the sensor is:

$$O \text{ in } Li \parallel ThO_2 \text{ and } 7.5\% \text{ mol } Y_2O_3 \parallel In, In_2O_3$$

The electromotive force measured with the sensor is related to the oxygen activity in the liquid metal by the Nernst equation:

$$|\Delta E| = \frac{RT}{nF} \ln \frac{a_{Oref}}{a_{[O]}}$$

and the first step of this activity will be the evaluation of the compatibility of the ceramic with the liquid metal in order to assess the influence of the chemical reaction:

$$Li(N) + ThO_2 \rightarrow ThN + Li_2O$$

which depends on the N content in the liquid lithium.

b-2) Control

Concerning oxygen control, on the basis of the solubility data reported in Table 1 cold trapping has been proposed for removing oxygen from lithium. Hot trapping might be also a feasible method using Ta or La.

c) Carbon

c-1) Monitoring

Development of a carbon diffusion meter based on the designs used for sodium systems could be the reference method for measuring carbon concentration.

c-2) Control

Carbon levels appear to be controlled by cold trapping due to its solubility in liquid lithium at the operating temperature (see Table 1). In addition the application of hot trapping using zirconium, yttrium or titanium could provide a useful option and should be examined.

d) Nitrogen

d-1) Monitoring

The use of electrochemical monitoring, using a molten salt LiCl-LiF-Li_3N system, could be considered as reference system for nitrogen monitoring. As a backup solution the resistivity technique has been taken into account. This method is based on the fact that a liquid metal solution containing impurity elements has a higher electrical resistivity than the pure liquid metal. Thus, the difference in resistivity between the solution and pure liquid metal at constant temperature is proportional to the concentration of the impurities in the liquid metal. A disadvantage of the method is that it is not specific to a particular impurity. For instance, nitrogen and hydrogen isotopes have much higher solubilities and can change the resistivity to a much greater extent with respect to oxygen and carbon. If one is present in a known concentration, the other can be monitored using the resistivity technique. Hence, using a resistivity meter coupled with a hydrogen permeation meter would allow both hydrogen and nitrogen to be monitored in liquid lithium solution.

d-2) Control

As far as the control of nitrogen in flowing liquid metal is concerned, cold trapping could not be taken as a reference method due to the high solubility of N in liquid Li at low temperatures (see Table 1) Hot trapping has been pointed out as the most effective, having either zirconium or titanium as a getter as shown in Fig. 2.

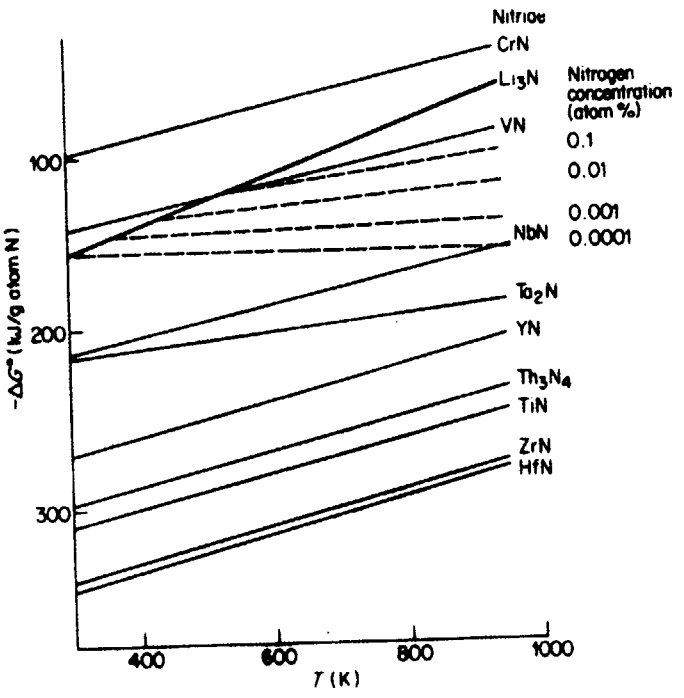


Fig. 2 Free energy of formation of nitrates for N hot trapping.

(4) Corrosion testing

The final goal of this task is to evaluate the corrosion of austenitic steels in liquid Li with a well known chemical composition in terms of non-metallic impurities. The corrosion phenomena expected could be of the following types:

- uniform leaching of steel elements such as Cr with a consequent transformation to ferrite;
- intergranular penetration with a consequent weakening of the structure;
- interstitial element transfer;

In addition, the deposition of solid products could cause hydraulic problems and are related to safety issues. The solid products might be formed due to the presence of non-metallic impurities in the liquid metal, i.e. oxide formation, dissolution of metallic elements from the structural materials, or ternary compound formation from liquid metal and steel elements. It is evident that to avoid any mechanical and geometrical change of the structural material of the IFMIF loop and to operate in a safe condition, monitoring and control methods should be well validated. The final goal of this task is to validate the MAC techniques developed and calibrated. The validation will be performed on the LIFUS III loop, properly designed for this aim. In Fig. 3 a schematic of the Loop is shown. The loop has a figure eight configuration, and test sections are foreseen both in the cold leg and in the hot leg. The maximum allowable temperature in the hot leg will be 450°C and the test sections, in which cylindrical steel specimens will be tested in order to assess the corrosion rate, were designed in order to reach about 10 m/s of liquid Li velocity in them.

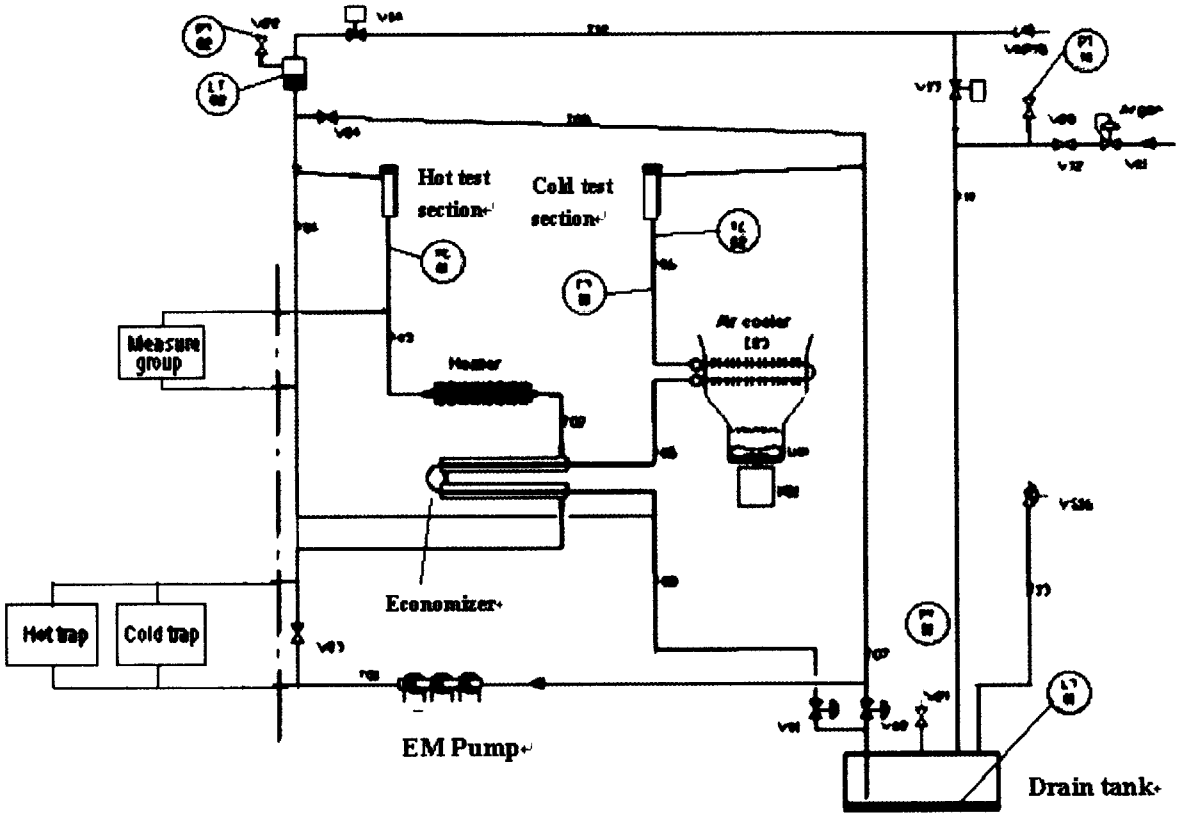


Fig. 3 Diagram of LIFUS III loop.

References

[1] T. B. Lindemer et. al. J. of Nuc. Mater, 100 (1981) 178.
[2] R. M. Yonco, et. al., J. Nucl. Mater. 138 (1986) 117.
[3] R. M. Yonco, et. al., J. Nucl. Mater. 57 (1975) 317.
[4] P. F. Adams, et. al., J. Less-Common Metals, 46 (1976) 325.
[5] NIST-JANAF Thermochemical tables, J. of Physical and Chemical Reference Data, Monograph 9 AMC, Maryland, 1998.
[6] C. Fazio, ENEA Brasimone Report, IM-AR-001, 07/05/2002.
[7] E. Serra, G. Benamati, Mater. Sci. Technol. 14 (1998) 573.
[8] A. J. OVERMAN, et al, LCRE Non Nuclear System test, Final Report PWAC-402, Part IV, Pratt and Whitney Aircraft, Middletown, Connecting (October 1965).
[9] L. G. HAYES, Corrosion of Niobium-1Zr Alloy by Lithium at High Velocities, JPL Technical Report 32-1233 (December 1,1967).
[10] References: M. S. FREED, Corrosion of Columbian Base and Other Structural Alloys in High Temperature Li, PWCA-3555 (June 30,1961).

3.2.11 TG31B-JA : Control of Nitrogen Impurity in Lithium by Hot Trapping

(1) Brief Task Description

Impurities in IFMIF liquid lithium include accumulated nuclear reaction products of the facility operation and impurities from the cover gas and structural materials. Among these impurities, nitrogen and hydrogen are difficult to remove by cold trapping methods. If yttrium is used as a getter material for tritium, nitriding of the yttrium surface can prevent tritium being absorbed. The purpose of the present study is to develop a method to control nitrogen concentration in lithium by hot trapping.

Contributors

Name	Party	Institute	E-mail address
Satoru Tanaka	Japan	Univ. Tokyo	s-tanaka@q.t.u-tokyo.ac.jp
Takayuki Terai	Japan	Univ. Tokyo	tera@q.t.u-tokyo.ac.jp
Toshiaki Yoneoka	Japan	Univ. Tokyo	yoneoka@q.t.u-tokyo.ac.jp
Takeo Muroga	Japan	NIFS	muroga@nifs.ac.jp
Akihiro Suzuki	Japan	NIFS	asuzuki@nifs.ac.jp

(2) Introduction

The compatibility of structural materials with liquid lithium is affected by non-metallic impurities such as nitrogen in lithium. If the nitrogen concentration in lithium is high, a precipitate of lithium nitride could erode tubing materials. One of the purposes of the present study is to control the nitrogen concentration down to 10^{-3} mass% in liquid lithium by the method of hot trapping. The accurate analysis of nitrogen at concentrations below 5_10^{-3} mass% is difficult. Therefore, we are forced to evaluate the possibility of gettering under this low nitrogen concentration from the experimental data with initial nitrogen concentrations in molten lithium from 10^{-2} to 10^{-1} mass%. In this method, materials for nitrogen gettering are immersed in liquid lithium. Metals which easily form nitrides and have high compatibility with lithium are the candidate getter materials [1]. Getter metals used in the present study were titanium, vanadium, an alloy of these two metals, and chromium. Fig. 1 shows that titanium nitride has a high stability compared with lithium nitride (Li_3N). Vanadium nitride is also stable in liquid lithium when the nitrogen concentration in lithium is above 10^{-4} mass%. This figure shows that the affinity of titanium for nitrogen is larger than that of vanadium. However, the diffusion coefficient of nitrogen in vanadium is larger by three orders of magnitude than that in titanium at 800K [2,3], because the crystal structure of vanadium is bcc and that of titanium is hcp. Therefore, vanadium was a candidate getter material even though the affinity for nitrogen is not large. Alloys of titanium and vanadium may combine the merits of titanium's large affinity for nitrogen and vanadium's large nitrogen diffusivity, so a V-Ti alloy was evaluated. Chromium is known to form a ternary nitride with lithium. This nitride is stable at 800 K when the nitrogen concentration in lithium is higher than 10^{-3} mass% [4]. Hence, chromium is a candidate nitrogen getter for high nitrogen concentrations in lithium.

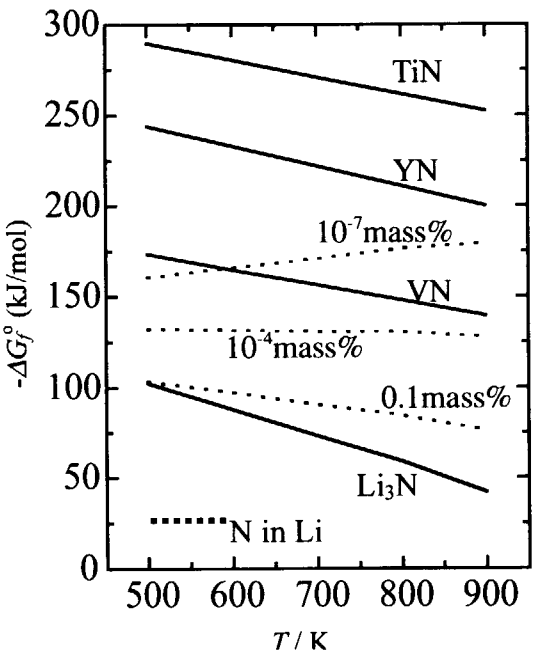


Fig. 1 Stability of nitride of various metals.

Yttrium is a candidate material for tritium gettering in lithium. Fig. 1 shows that yttrium nitride has higher stability than nitrides of all

other metals except titanium. Nitriding of yttrium surfaces will prevent tritium from being absorbed. Therefore, one purpose of the present study is to investigate the behavior of nitrogen in a system using both V-Ti alloy and yttrium getters in liquid lithium. Details of the experimental results are given in our previous papers [5,6].

(3) Experimental Setup

The purity of the titanium, vanadium, chromium, and yttrium used was greater than 99.9%. Alloys V-5at%Ti, V-10at%Ti and V-15at%Ti were made from the two elements using a plasma arc-melting furnace. The Ti, V, Y and V-Ti getter materials were tested as plate. The size of the titanium and vanadium plates was 1x10x50 mm^3, the alloys 0.6x10x40 mm^3 and the yttrium 1x10x25 mm^3. The chromium was tested as rod 1.5x4x30 mm^3. The mass of lithium in each test was 12 or 25 g, and the purity greater than 99.9%. The concentration of nitrogen impurity in the as-received lithium was about 10^{-2} equivalent to $5x10^{-3}$ mass%. In most experiments the Sievert's method was used to increase the nitrogen concentration to about $3.7x10^{-2}$ mass%.

Changes of nitrogen concentration in the liquid lithium due to gettering was measured by the ammonia method, in which nitrogen in lithium was converted to ammonia by a hydrogenation reaction with nascent hydrogen formed by the reaction of lithium with water [7]. The amount of ammonia in the aqueous solution was measured by an ammonia sensor. About 0.6 g of lithium was sampled at predetermined periods to measure the nitrogen concentration. In this case, the measurement error of the ammonia method was evaluated to be $+/-3x10^{-4}$ mass%.

All loading operations of specimens into a stainless steel pot were carried out inside a glove box filled with high purity argon. Lithium pieces, nitrogen getter materials, yttrium specimens, a molybdenum crucible with 48mm inside diameter and 69mm height, a furnace for melting lithium, and a stainless steel pot were prepared in the glove box. Lithium was melted in the molybdenum crucible within the furnace, at about 500 K, then getter materials were immersed in the liquid lithium. In the case of yttrium experiments, the yttrium specimen and the V-10at%Ti alloy were both immersed in the same lithium. The molybdenum crucible was then loaded into the stainless steel pot. A lid made of vanadium or tantalum was placed on the crucible to exclude impurities. During the immersion test, high purity argon flowed through the pot at the rate of 5 ml/min. This experimental apparatus is shown in Fig. 2. The experimental temperatures were 673 to 873 K and the immersion periods were 0.26 Ms (3 days) to 2.8 Ms (32 days). After the immersion test, getter materials and the yttrium specimens were taken out of the liquid lithium in the argon glove box. Lithium that adhered to the getter material was removed by reaction with methanol and water. For the yttrium specimens, lithium on the surface was evaporated at 773 K in vacuum in order to prevent the yttrium from reacting with water vapor, oxygen and nitrogen in the atmosphere.

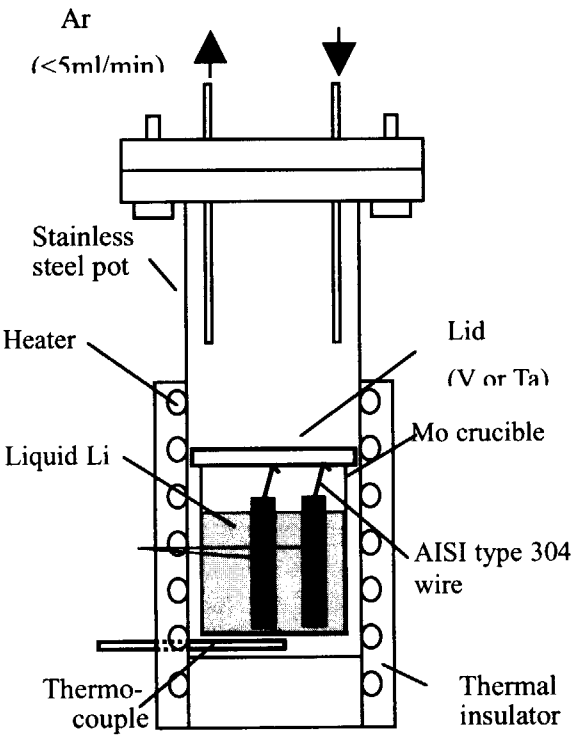


Fig. 2 Experimental apparatus.

(4) Results and Discussion

(4-1) Nitrogen gettering for low nitrogen concentrations in liquid lthium

Preliminary and screening investigations were carried out using the lithium with low nitrogen concentration. The nitrogen concentration in getter materials that were immersed in liquid lithium for 2.5 to 2.8 Ms were measured by a nitrogen/oxygen analyzer and estimated from the mass change before and after immersion. Both results are almost the same. The increments of average nitrogen concentration calculated from the mass changes are shown in Fig. 3. The nitrogen concentration in the titanium and vanadium plates tested at 673 and 773 K was found to be little changed. The nitrogen concentrations in titanium and the V-5at%Ti and V-10at%Ti alloys tested at 823 K increased. In spite of the lower initial nitrogen concentration in lithium for the case of V-10at%Ti than for the case of titanium, the increase of nitrogen in V-10at%Ti was larger than in titanium. The V-10at%Ti alloy at 823 K has a larger nitrogen gettering effect than the other materials tested.

Titanium nitrides (TiN and Ti_2N) formed on the surface of the titanium plate tested at 823 K for 2.8 Ms. Moreover, several XRD peaks of titanium were found to be shifted, indicating a lattice expansion. This shows the nitrogen was dispersed in titanium by diffusion and formed a solid solution. It should be noted that an expansion was not found in all lattice directions, just in some specific ones. However, when the surface of this titanium plate was polished to 2μm depth, peaks due to the titanium nitride and the broadening of the peaks disappeared.

On the surface of the V-10at%Ti alloy that was immersed at 823 K for 2.8 Ms, a VN-TiN (nitride of titanium and vanadium) layer was formed as shown in Fig. 4b. In addition, broad peaks of the V-Ti-N solid solution were also confirmed. Fig. 4c shows that, when the surface of this alloy was polished to remove 4 mm, peaks of the VN-TiN layer disappeared and only those of the nitrogen solid solution remained. When the surface was polished to remove 8 μm, all shifted and broad peaks nearly disappeared and the XRD peaks were identical to the sharp initial patterns shown in Fig. 4a.

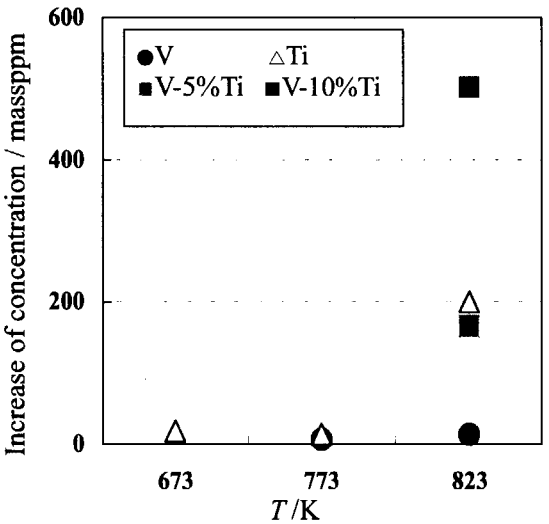


Fig.3 Nitrogen concentration change in getter materials from mass change.
The initial nitrogen concentration
: 100 mass ppm for V&Ti
50 mass ppm for V-Ti alloys

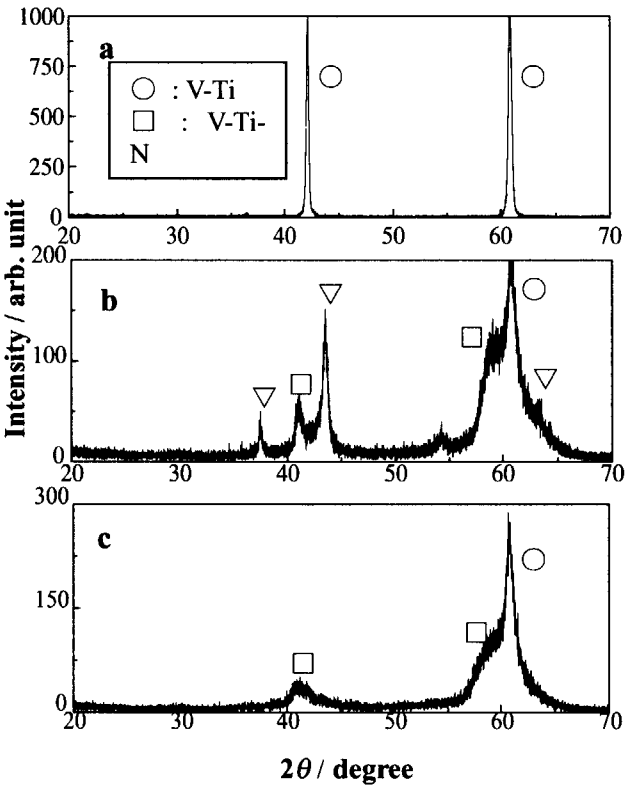


Fig. 4 XRD results of the V-10at%Ti alloy.
(a) as-received (annealing at 823K, for 1.5Ms),
(b) after immersion at 823K, for 2.8Ms,
(c) after polished by 4μm,
V-Ti-N : nitrogen solid solution in alloy
VN-TiN : nitride layer of titanium and vanadium

(4-2) Nitrogen gettering experiments for high nitrogen concentrations in liquid lithium

Prior to nitrogen gettering experiments, the nitrogen concentration in liquid lithium was increased to about 3.7×10^{-2} mass% by the Sievert's method. Three V-10at%Ti alloy plates (surface area 24 cm^2) or six chromium rods (20 cm^2) were immersed in liquid lithium. Using the square root of the immersion time of gettering materials at 823 K, experimental results are shown in Fig. 5. In this figure, the nitrogen concentration in the liquid lithium shows a linear relationship to the square root of the immersion time. It indicates that a diffusional process is involved in the nitrogen gettering. This figure shows that the nitrogen gettering rate of chromium was larger than that of the V-10at%Ti alloy for nitrogen concentration higher than 10^{-2} mass%. At this condition of 823 K and about 0.4 Ms (that is, 5days and $t^{1/2}$=0.63), the V-10at%Ti alloy reduced the nitrogen concentration from the initial 3.7×10^{-2} mass% to 2.1×10^{-2} mass%, while chromium reduced to 1.8×10^{-2} mass%. However, these rates seem to be somewhat slow.

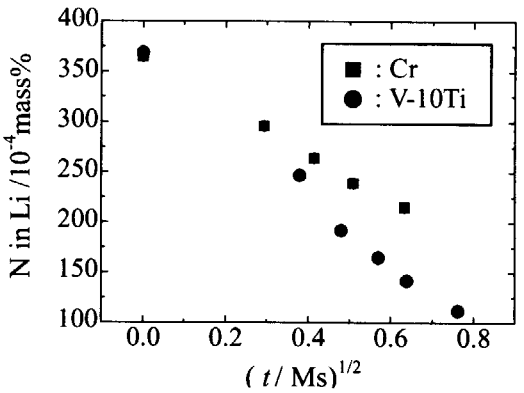


Fig. 5 Change of nitrogen concentration in liquid lithium.

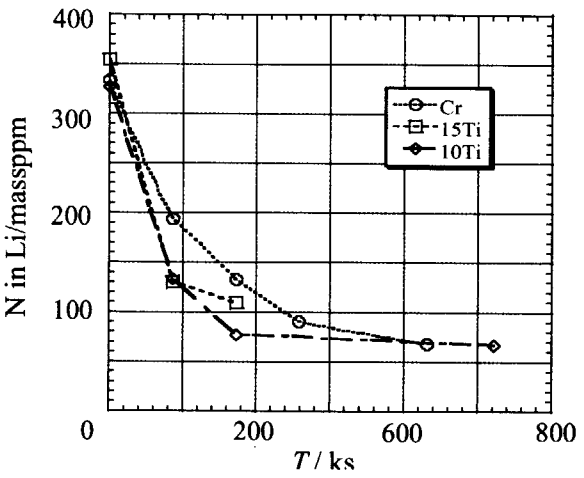


Fig. 6 Change of nitrogen concentration in liquid lithium.

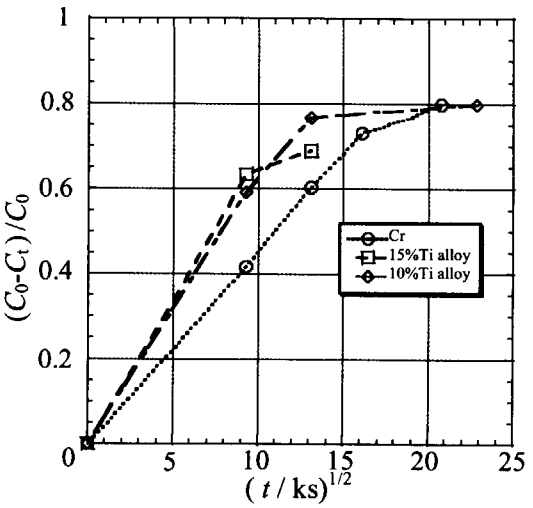


Fig. 7 Relations of time and normalized rates of nitrogen uptake by getter materials.

C_0:Initial nitrogen concentration of lithium,
C_t:nitrogen concentration at t>0

To increase the rate, tests at 873 K were carried out. The specimens were chromium, V-10at%Ti, and V-15at%Ti alloy. The results are shown in Fig. 6. The two V-Ti alloys reduced nitrogen from the initial 3.7×10^{-2} mass% to below half that value in 86.4 ks (1day). This rate is much large than that at 823 K. However, the rate decreased for longer times. On the other hand, chromium reduced nitrogen to 60% of the initial concentration in the initial 86.4 ks and continued to reduce nitrogen for longer times. The decrease in nitrogen concentration is reflected in the mass gain of the getter materials and the data are plotted against the square root of time in Fig. 7. The line for chromium is almost straight to 259 ks and seems then to saturate. The line for V-10at%Ti alloy also follows a straight line to 173 ks. These parabolic relationships show that the rate determining process is diffusion in the getter material or nitride layer formation in chromium. The diffusing specie is believed to be nitrogen in the case of V-10at%Ti alloy and chromium in the case of chromium. On the other hand, in the case of V-15at%Ti

alloy, the initial rapid increase suddenly slowed down after 86.4 ks, and the behavior of V-10at%Ti after 173 ks is similar. The mechanism of this slowdown seems to be the formation of nitrides of vanadium and titanium. When these nitrides completely cover the surface, the nitrogen uptake slows due to the rate of nitrogen diffusion in the nitride.

(4-3) Limit of nitrogen gettering by chromium

Six chromium specimens were immersed in liquid lithium with initial nitrogen concentration 1.15×10^{-2} mass%, and the change in nitrogen concentration in lithium was measured by the ammonia method. Results of this experiment are shown in Fig. 8. The nitrogen gettering rate of the chromium slows below 7×10^{-3} mass% nitrogen concentration, and seems to approach a limit of about 6.5×10^{-3} mass%. The reason for this limit is believed to be the instability of the ternary nitride of chromium and lithium below this nitrogen concentration.

If the nitrogen concentration in lithium is near the solubility limit, the ternary nitride of chromium and lithium is known to be stable. Juza and Haug heated Li_3N and Cr_2O_3 to high temperature, and reported that ternary nitride ($Li_9Cr(VI)N_5$) was actually formed [8]. In other work at about 773 K, stainless steel was immersed in liquid lithium in which nitrogen concentration was 5×10^{-3} to 10^{-2} mass% [9,10]. The chromium content of the stainless steel was decreased by the immersion. Barker et al. showed from thermodynamic considerations that the ternary nitride is stable at 800 K, if nitrogen concentration in liquid lithium is higher than 10^{-3} mass% [4].

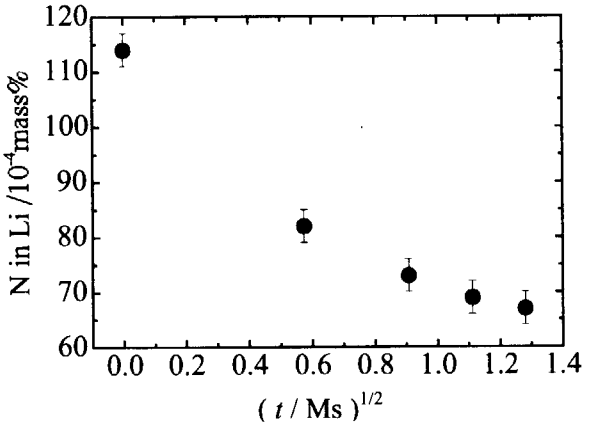


Fig. 8 Change of long-term nitrogen concentration in liquid lithium using chromium getter.

As mentioned earlier, nitrogen gettering by chromium reached a limit at about 6.5×10^{-3} mass% nitrogen in lithium in our experiment. Comparing this to the results of previous works, the limit is reasonably explained by the stability of the ternary nitride.

The composition of the ternary nitride was evaluated as follows. In each chromium immersion experiment, mass decrements of nitrogen in lithium were calculated from the change in nitrogen concentration in liquid lithium. The mass decrements of the chromium specimens were measured after dissolution of the ternary nitride by pure water. From these results, the atomic ratios of the mass loss of the chromium getter to that of nitrogen in lithium were calculated. These results and the initial nitrogen concentration in the liquid lithium for each experiment are shown in Table 1. The solubility of chromium in liquid lithium at 823 K is not large enough to influence these results [11]. Hence the mass decrements of nitrogen and chromium were equal to the mass of the ternary nitride. From this data, the atomic ratio was found to be Cr:N=3:5, except for one point where the ratio of 4:9 probably results from the large measurement error. Therefore, three chromium atoms were found to trap five nitrogen ions in the ternary nitride that was formed in these experiments.

The aqueous solution in which the ternary nitride was dissolved was analyzed by ion chromatography, but chromium (6+) ion could not be confirmed. In the measurement by absorption spectrophotometry, prior to the measurement, chromium specie in that solution was oxidized to chromium (6+) ion. After that, absorption peak of chromium (6+) ion was confirmed by an adsorption spectrophotometry. Therefore, the valence state of chromium in the ternary nitride was believed to be +3. From these results and the requirement of the electrical neutrality of this compound, the formula of the ternary nitride that was formed in these experiments is believed to be $Li_6Cr(III)_3N_5$.

Table 1 Mass decrements of chromium in getter and nitrogen in lithium after the immersion experiment.

Initial nitrogen concentration in lithium /10^{-4}mass%	Mass decrement of Cr*/mg	Mass decrement of N**/mg	Atomic ratio of the decrement Cr:N
527	17.21	7.62	3:5
446	15.54	7.00	3:5
369	14.10	6.43	3:5
166	2.11	1.30	4:9

* Measurement error: 0.02mg
** Measurement error: 0.125mg

(4-4) Nitriding of yttrium

In one experiment, an yttrium specimen was immersed in liquid lithium for 0.5 Ms without V-10at%Ti alloy. After immersion, XRD measurement showed yttrium nitride on the surface of the specimen. This result is shown in Fig. 9-a. During this experiment, the nitrogen concentration in the lithium decreased from $5x10^{-3}$ to $4x10^{-3}$ mass%. This shows that nitrogen in lithium was absorbed by the yttrium specimen to form yttrium nitride. In the second experiment, both the yttrium specimen and V-10at%Ti alloy were immersed in lithium. XRD measurement of the yttrium specimen surface, shown in Fig. 9-b, has smaller peaks of the yttrium compared with the result in Fig. 9-a. In addition, nitrogen solid solution was found on the V-10at%Ti alloy surface by the XRD measurement, and the nitrogen concentration in the liquid lithium decreased from $5x10^{-3}$ to $3.5x10^{-3}$ mass% during this experiment. This shows that the nitrogen in the lithium was mainly absorbed by the V-10at%Ti alloy, not by the yttrium specimen, and nitriding of the yttrium was controlled by the V-10at%Ti alloy. This is explained by thermodynamics, Fig. 1, showing the stability of yttrium nitride is lower than titanium nitride. The conclusion is that yttrium used with V-10at%Ti in lithium can effectively absorb tritium.

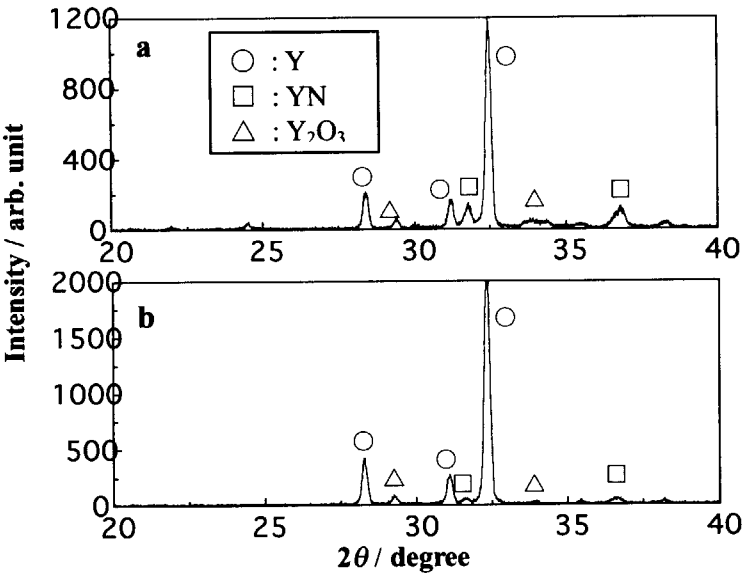


Fig. 9 XRD observation of the yttrium surface.
(a) immersed without V-10at%Ti alloy
(b) immersed with V-10at%Ti alloy

(4-5) Evaluation of the gettering capability of the V-Ti alloys and Cr

The goal of this study is to control the nitrogen concentration to 10^{-3} mass% in lithium by hot trapping, and to evaluate gettering at this low nitrogen, using experimental data with initial nitrogen concentration in lithium from 10^{-2} to 10^{-1} mass%.

Based on these experimental results, an effective method to decrease nitrogen concentration from initial high values (above $3x10^{-2}$ mass%) is as follows. First, chromium is used as getter to decrease nitrogen to about 10^{-2} mass%; then V-Ti alloy is used to decrease to 10^{-4} mass% level. The gettering rate of V-10%Ti alloy was slower than expected at 823 K, but would be more rapid if

immersion temperature was increased to about 873 K. Also, the nitrogen concentration in commercial lithium is about $5x10^{-3}$ mass%, and if this is used with a low nitrogen structural material contacting molten lithium, nitrogen control to $<10^{-3}$ mass% by V-Ti alloy is feasible.

The optimum concentration of titanium in the V-Ti alloy may be 7 to 10 mass%, to avoid the formation of a blocking surface nitride layer observed at higher titanium concentrations and high nitrogen concentrations in initially impure lithium.

(5) Conclusions

Nitrogen control in lithium by hot trap methods was evaluated for temperatures 673 to 873 K and times 0.26 Ms to 2.8 Ms

1) For low nitrogen concentrations in lithium, V-Ti alloys are effective nitrogen getters at 823 K and 873 K.

2) Nitrogen picked up by the V-Ti alloy was mainly in solid solution in the alloy.

3)For high nitrogen concentrations in lithium, gettering by chromium is more effective than by V-Ti alloys.

4) Gettering by chromium at about 850 K reached a limit at $6.5x10^{-3}$ mass% nitrogen in lithium.

5) Nitriding of yttrium in lithium was suppressed by immersion with V-10at%Ti alloy.

References

[1] K. Natesan, Influence of Nonmetallic Elements on The Compatibility of Structural Materials with Liquid Alkali Metals, J. Nucl. Mater, **115** (1983) 251-262.

[2] Metals Data Book, 3rd Edition, Japan Institutes of Metals, Maruzen, Tokyo (1993) 24.

[3] R. Farraro and R. B. McLellan, The Diffusion of Interstitial Solute Atoms in Body-Centered Cubic Metals, Mater. Sci. Eng. **39** (1979) 47-55.

[4] M. G. Barker, P. Hubberstey, A. T. Dadd and S. A. Frankham, The Interaction of Chromium with Nitrogen Dissolved in Liquid Lithium, J. Nucl. Mater, **114** (1983) 143-149.

[5] Toshiharu Sakurai, Toshiaki Yoneoka, Satoru Tanaka, Akihiro Suzuki and Takeo Muroga, Control of Nitrogen Concentration in Liquid Lithium by the Hot Trap Method, J. Nucl. Mater, in print.

[6] Toshiharu Sakurai, Toshiaki Yoneoka, Satoru Tanaka, Akihiro Suzuki and Takeo Muroga, Control of Nitrogen Concentration in Liquid Lithium by Hot Trapping, Fusion Engineering and Design, in print.

[7] R. J. Schlager, D. L. Olson and W. L. Bradley, Analytical Determination of Nitride Nitrogen in Lithium Coolants, Nucl. Tech, **27** (1975) 439-441.

[8] V. R. Juza and J. Haug, Herstellung und Eigenschaften der Ternären Nitride von Chrom, Molybdän und Wolfram der Zusammensetzung Li_9MeN_5, Z. Anorg. Chem, **309** (1961) 277-282.

[9] O. K. Chopra and D. L. Smith, Influence of Temperature and Lithium Purity on Corrosion of Ferrous Alloys in a Flowing Lithium Environment, J. Nucl. Mater, **141-143** (1986) 584-591.

[10] O. K. Chopra and D. L. Smith, Corrosion of Ferrous Alloys in a Flowing Lithium Environment, J. Nucl. Mater, **133&134** (1985) 861-866.

[11] H. W. Leavenworth and R. E. Cleary, The Solubility of Ni, Cr, Fe, Ti and Mo in Liquid Lithium, Acta. Metal, **9** (1961) 519-520.

3.2.12 TG33-JA : Diagnostic System for Target Temperature

(1) Brief Task Description

The IFMIF Li target is designed to produce an intense flux of high energy neutrons (2 MW/m^2) with 10 MW of deuteron beam deposition, which corresponds to a heat load of 1 GW/m^2. The temperature of Li at the inlet of the target nozzle is 250°C, and thermohydraulic analysis shows that the maximum temperature in the Li flow is about 400°C. Measurement of the position of the deuterium beams and of the temperature of Li free surface is necessary for stable and safe operation of the target system. In the IFMIF CDA, an infrared camera was selected to monitor the beam footprint on target and the Li surface temperature. In this task the configuration of the infrared camera system has been determined, without significant change of the existing design of the camera and target systems.

Contributors

Name	Party	Institute	E-mail address
H.Nakamura	Japan	JAERI	nakamurh@fusion.naka.jaeri.go.jp
K. Shimizu	Japan	MHI	katsusuke_shimizu@kind.kobe.mhi.co.jp
M. Ida	Japan	JAERI	ida@ifmif.tokai.jaeri.go.jp

(2) Design Requirement

Two deuterium beam lines are focused on the Li free surface of the IFMIF target with a foot print 20 cm wide x 5 cm high. The cross section and plan view of the target assembly are shown in Figs. 1 and 2, respectively.

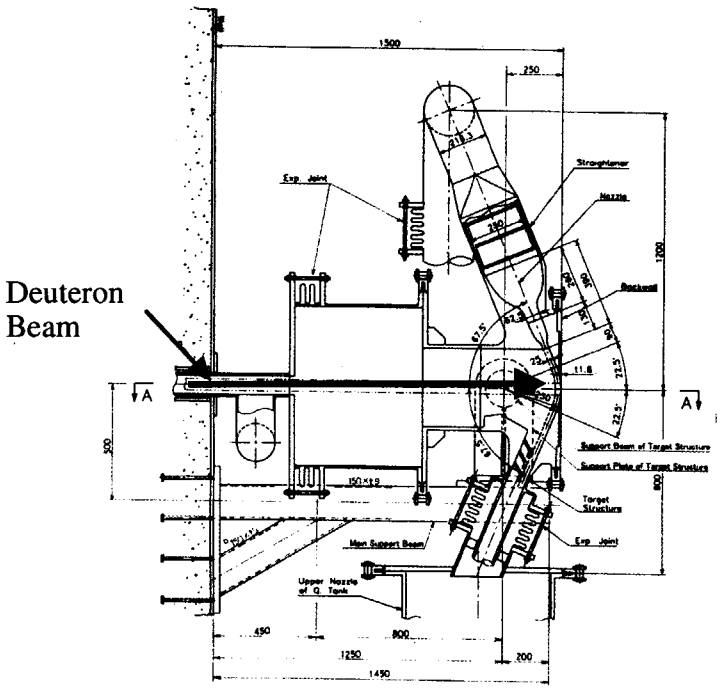


Fig.1 Cross section of Li the target assembly.

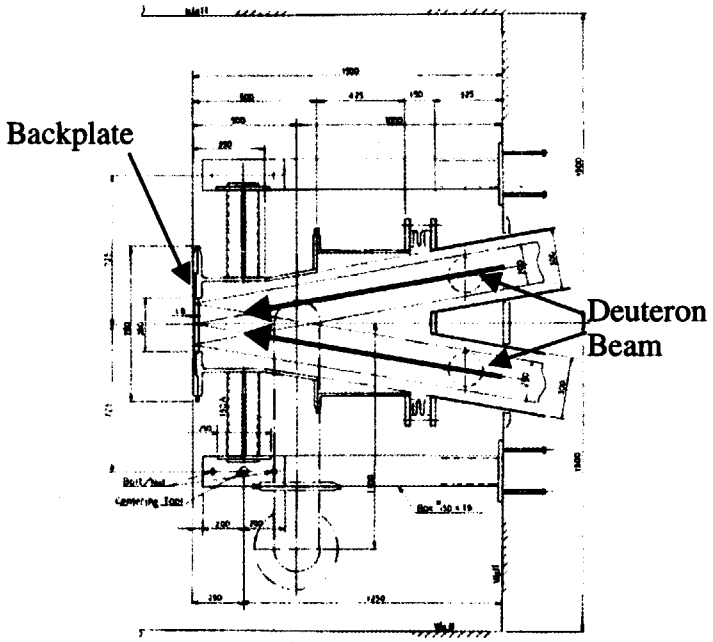


Fig.2 Plane view of the Li target. assembly

Basic design requirements for the temperature measurements are as follows;

- Diagnostics Object : Li target
- Range of Temperatures : 200℃ - 400℃
- Accuracy of Temperature Measurement : 5℃
- Diagnostics Area : 24 cm wide x 6 cm high
- Accuracy of Spatial Resolution : 1 mm
- Accuracy of Time Resolution : 0.1 ms (line scan), 10ms (2D scan)
- Temperature at the IR Camera : Room temperature
- Pressure at the Monitor : 1 atmosphere
- Radiation Environment : 7.9×10^{-4} μSv/hr

(3) Evaluation of Infrared Camera System

(3-1) Radiant intensity

Spectral emissivity (ε) of the Li target is given by $\varepsilon=36.5(\rho/\lambda)^{0.5}$ where ρ is resisitivity ($=9.4 \times 10^{-6}$ Ωm) and λ is wave length (μm). The spectral emissivities for 200-400℃ are as follows.

Wave length	Spectral emissivity, ε
2.0 μm	0.133 - 0.152
2.5 μm	0.119 - 0.136
5.0 μm	0.084 - 0.096

According to an equation for radiant energy, a wave length with the maximum radiant energy is given by the following equation.

$$\lambda \cdot T = 2898\ (\mu m \cdot K) \quad (1)$$

In a temperature range 200 - 400℃, the range of wave lengths with maximum emission energy is 4 – 6 μm. In the CDE study, 5 μm is selected as the wave length of the measurement. However, at this wave length, light absorption is expected by H_2O (6 μm). Therefore, the wave length for the measurement is selected to be 2 – 2.5 μm to prevent the light absorption. Radiant intensity is given by $\varepsilon \cdot W \cdot \Delta\lambda$ where $\Delta\lambda$ is band width of wave length (=1 μm). The radiant intensities at each temperature are shown as follows.

Temperature (℃)	Emissivity	Radiant emission ($W/cm^2/\mu m$)	Radiant intensity (W/cm^2)
200	0.119	$1.98x10^{-3}$	$2.36x10^{-4}$
300	0.128	$1.65x10^{-2}$	$2.11x10^{-3}$
400	0.136	$7.36x10^{-2}$	$1.00x10^{-2}$

(3-2) Sensitivity and spatial resolution

Candidate infrared sensors for the camera are PbS, InSb and HgCdTe. Sensitivity of the sensor is defined by specific detectivity (D*).

$$D^*=(A_d\Delta f)^{0.5}/NEP\ [cmHz^{0.5}W^{-1}] \quad (2)$$

where NEP is noise equivalent power (W), A_d is the sensitive area of the detector (cm^2) and Δf is the frequency band width of the circuit. Typical values are in the range 10^{10} to 10^{12}. Noise level in the detector (N: W/cm^2) is defined by NEP/A_d.

$$N= (\Delta f /A_d)^{0.5}/ D^* \quad (3)$$

Therefore, the sensitivity of measurement (S/N) is obtained by the following equation.

$$S/N=P/N=P \cdot D^* \cdot (A_d/\Delta f)^{0.5} \quad (4)$$

where P is a power on the detector and is given as follows.

$$P=(\varepsilon \cdot W \cdot \Delta\lambda) \cdot S_T \cdot (S_1/2\pi L^2) / (A_d K) \quad (5)$$
$$=(\varepsilon \cdot W \cdot \Delta\lambda) \cdot S_T \cdot (S_1/(2\pi L^2 \cdot A_d)) \cdot K \quad (5a)$$

where S_T is viewing area on the target, S_1 is aperture area at L and K is transmission efficiency.

Here, S_T is replaced by $\pi d^2/4$ where d is the diameter of the viewing area on the Li target. Using equation (4) and (5a), the diameter (d) can be shown as follows.

$$d=((S/N)/C)^{0.5} \cdot L \quad (6)$$

$$C==(\varepsilon \cdot W \cdot \Delta\lambda) \cdot S_1 \cdot K \cdot D^* /(8(A_d\Delta f)^{0.5}) \quad (7)$$

Here, D* is $3x10^{11}$, S_1 is 28 cm^2, K= 0.2 and Δf is 100. Equation (6) is written as follows.

$$d=((S/N)^{0.5}/C^{0.5}) \cdot L \quad (8)$$

For reliable measurement, a minimum value of S/N is 10. Spatial resolution (d) can be defined

by equation (8). Dependence of the spatial resolution on the distance between the Li target and the sensor is shown in Fig. 3 for different temperatures. To achieve spatial resolution of 1 mm, L should be less than 2 m at 200℃, 6.5 m at 300℃ and 9 m at 400℃. Near the target assembly, a diagnostic port with a vacuum window will be attached. The light will be transported to the infrared camera through an optical pipe or an optical fiber.

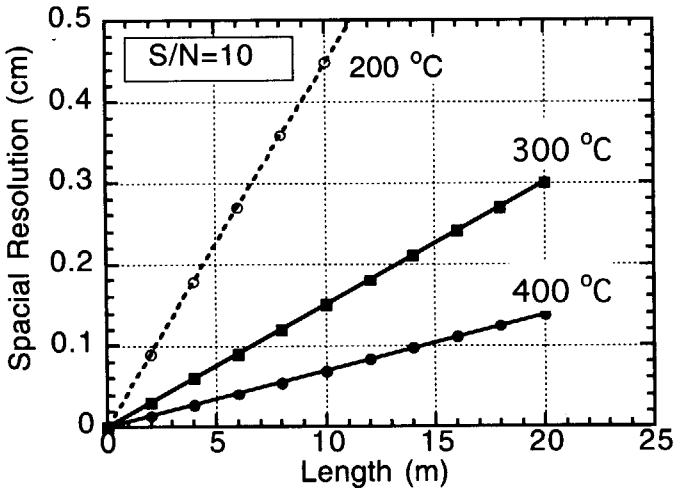


Fig.3 Dependence of spacial resolution of the IR camera system on distance between the Li target and the sensor.

(4) Layout of the Infrared Camera System

Figure 4 shows the cross section and plan view of the IFMIF building. The Li target assembly is located in the test cell room, isolated by the shield wall. Pressure inside the beam line and the Li target assembly is 10^{-2} to 10^{-3} Pa. The infrared light through the vacuum window is transferred to the infrared camera by an optical pipe or an optical fiber. The IFMIF infrared camera system is divided into the following components;

- Diagnostic port
- Focusing lens
- Optical pipe or optical fiber
- Infrared camera
- Control system

In the case of the optical fiber concept, layout of the fiber has more flexibility than the optical pipe because the focusing lens can be located about 5 m behind the shield. However, effects of neutron irradiation on the fiber characteristics needs to be evaluated. Based on the existing layout of the accelerator and the Li target of IFMIF, four options of the optical pipe concept (Case-1 to Case-4) are compared.

i) Case-1 (Fig. 5):

New optical pipe is attached between the accelerator beam lines to measure the Li surface temperature. At the end of the straight optical pipe, a mirror is attached to bend the infrared

light to the infrared camera located in the utility room. The distance from the Li target to the infrared camera is about 30 m.

ii) Case-2 (Fig. 6):

To shorten the light path, the mirror is moved from the beam transport room to a radiation isolation room as shown in Fig. 4. Although the basic concept is similar to Case-1, the distance from the Li target to the infrared camera is reduced to about 17 m.

iii) Case-3 (Fig. 7):

The optical pipe gives a straight line of sight as shown in Fig. 5. The infrared camera is located at the end of the optical pipe. Distance from the Li target to the infrared camera is about 23 m.

iv) Case-4 (Fig. 8):

The optical pipe gives a straight line of sight as shown in Fig. 6. The infrared camera is located in the radiation isolation room at the end of the optical pipe. Distance from the Li target to the infrared camera is about 12 m.

Comparing the four cases, Case 4 has the shortest length of optical pipe. Further study is needed to evaluate the effects of neutron irradiation on the optical pipe.

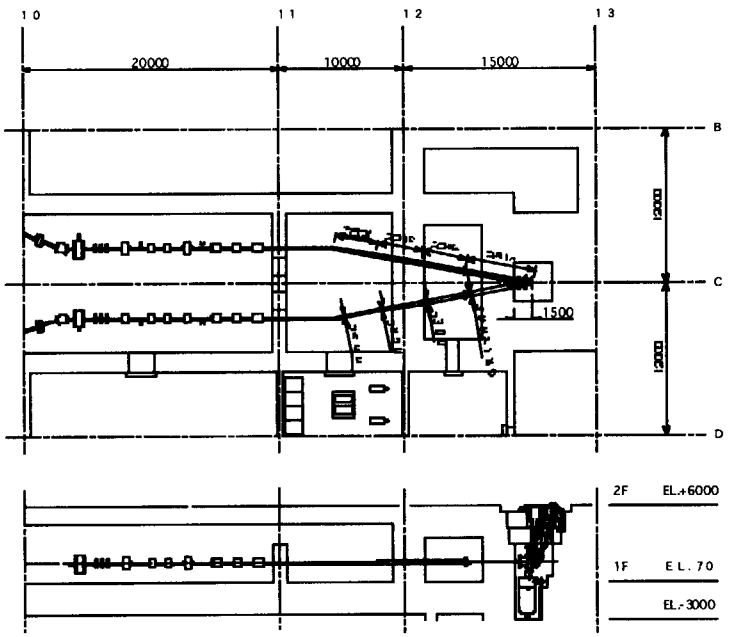


Fig.4 Cross section and plane view of the IFMIF building.

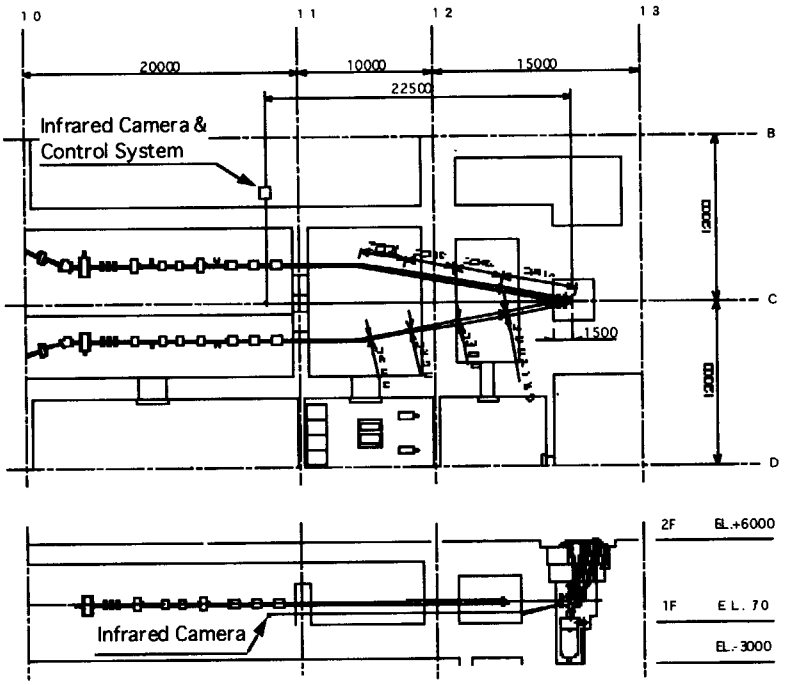


Fig.5 Layout of the Infrared camera system (Case-1).

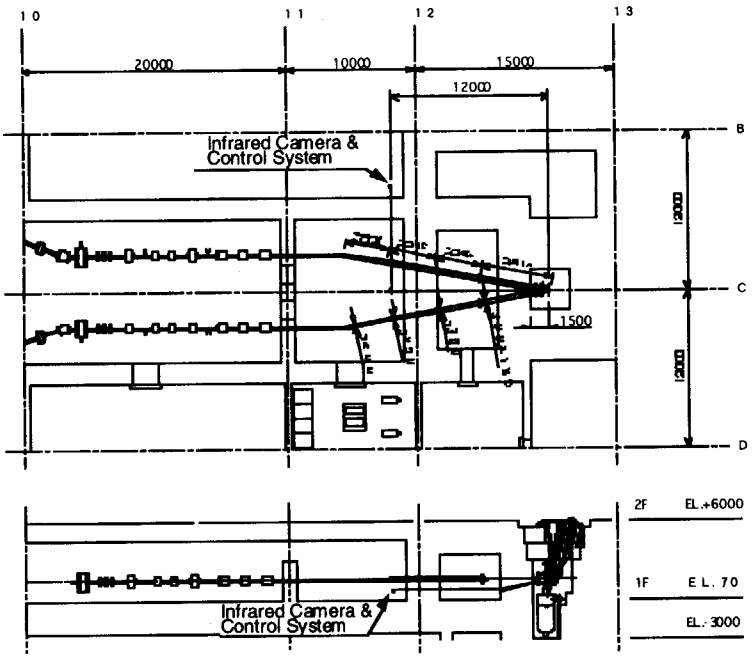


Fig.6 Layout of the Infrared camera system (Case-2).

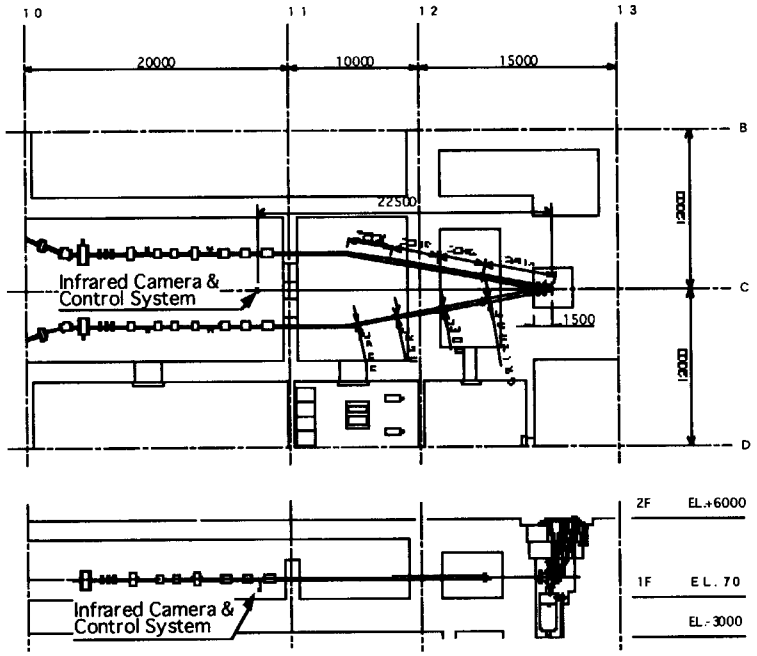


Fig.7 Layout of the Infrared camera system (Case-3).

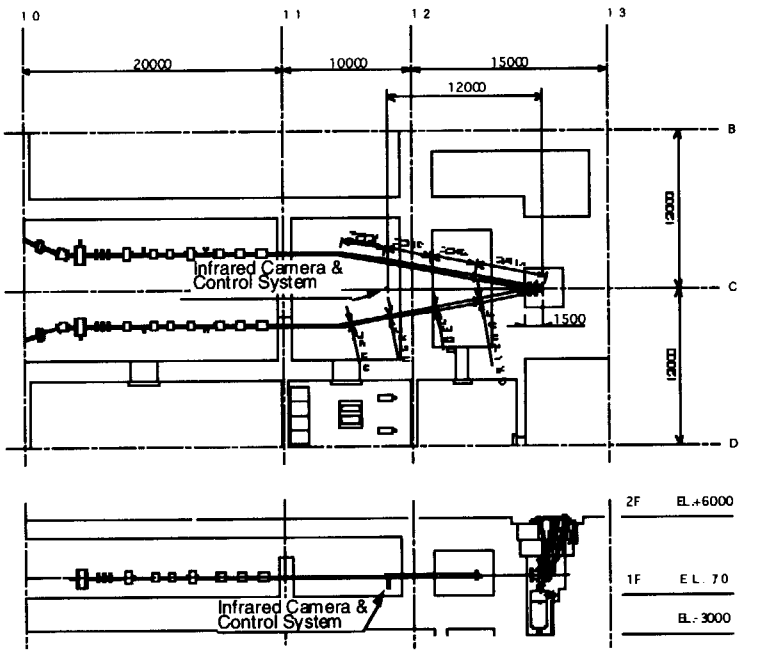


Fig.8 Layout of the Infrared camera system (Case-4).

(5) Summary

In the temperature range 200 - 400℃, candidate infrared camera sensors are PbS, InSb and HgCdTe. For transport of the light, optical pipes and optical fibers were evaluated. To achieve spatial resolution of 1 mm, L should be less than 2 m at 200℃, 6.5 m at 300℃ and 9 m at 400℃. In the case of the optical fiber concept, layout of the fiber has more flexibility than the optical pipe. However, effects of neutron irradiation on the fiber optical characteristics need to be evaluated. Comparing the four options of the optical pipe concepts, Case 4 (Fig. 8) is the most promising option with the shortest length. Further study is needed to evaluate the effects of neutron irradiation on the optical pipe.

3.2.13 TG35-JA : Design and Test of a Jet Thickness Monitor

(1) Brief Task Description

The IFMIF lithium (Li) target is designed to produce an intense flux of high energy neutrons (2 MW/m^2) with a heat load of 10 MW (1 GW/m^2.) The required thickness of the Li flow is 25 mm in case of 40 MeV deuterons, where the beam power is deposited at about 20 mm from the entrance surface. The target thickness must be monitored during operation, and for stable neutron irradiation conditions, the amplitude of surface waves on the Li jet should be less than 1 mm. In the FMIT project [1], an electrical conductivity probe system was the primary device for measuring the jet thickness and mapping the contours of the surface of the jet. In this task, the design of an electrical conductivity probe system for IFMIF and installation on the Osaka Li loop are described.

Contributors

Name	Party	Institute	E-mail address
Hiroo Nakamura	Japan	JAERI	nakamurh@fusion.naka.jaeri.go.jp
Hideo Nakamura	Japan	JAERI	nakam@lstf.tokai.jaeri.go.jp
H.Horiike	Japan	Osaka University	horiike@eie.eng.osaka-u.ac.jp

(2) Design Requirement

The design requirements of a Li thickness monitor based on the electrical conductivity probe system are as follows;

- Accuracy of position setting : ±0.01 mm
- Stroke of the probe pins : 30 mm
- Number of probe pins : 4
- Control of the thickness monitor : To be controlled by control system
- Structural material : Stainless steel 304
- Insulator material : Good compatibility with Li
- Maximum temperature : 400℃ at probe pins
- Range of working pressure : -0.1 MPa to 0.59 MPa
- Permissible He leak rate : 1x10^{-5} Pam^3/s

(3) Design of the thickness monitor

The concept of a thickness monitor based on the electrical conductivity probe system is shown in Fig. 1. The monitor has four pins to measure the amplitude of surface waves on the Li flow. This thickness monitor measures the contour of the Li surface by detecting electrical contact between the probe pins and the Li surface. The pins are insulated with MgO. The thickness monitor is inserted by a cylinder driven by an electrical motor. The stroke of the probe pins is 30 mm with an accuracy of position setting of ±0.01 mm. The length of the thickness monitor between the vacuum flange and the top of the cylinder is about 60 cm. The diameter of the vacuum flange is 15 cm. The monitor is controlled remotely by an ASTNEX, control system (Yokokawa Electric Co.).

(4) Installation and testing of the thickness monitor

Two thickness monitors and one spare have been fabricated. Fig. 2 shows photographs of the thickness monitor attached to a diagnostics port of the Li loop. Fig. 3 shows a magnified view of the probe head of the thickness monitor. Functional test of the drive mechanism has been performed. Measurements of the Li thickness and amplitude of the surface waves on the Li flow are planned in early 2003.

Reference

[1] R.Kolowith et al., "Experimental Lithium System Final Report", HEDL-TME-84-29 (1985).

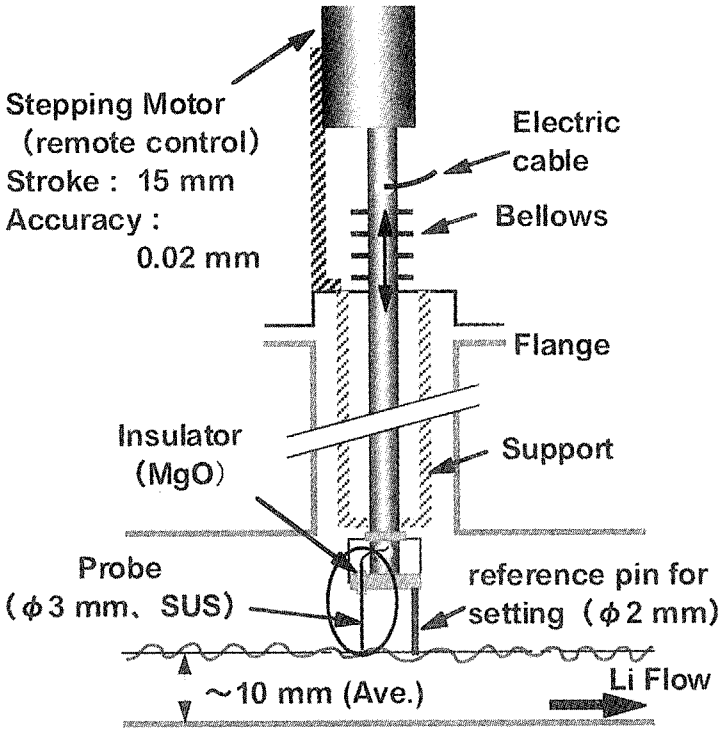


Fig.1 Concept of the thickness monitor.

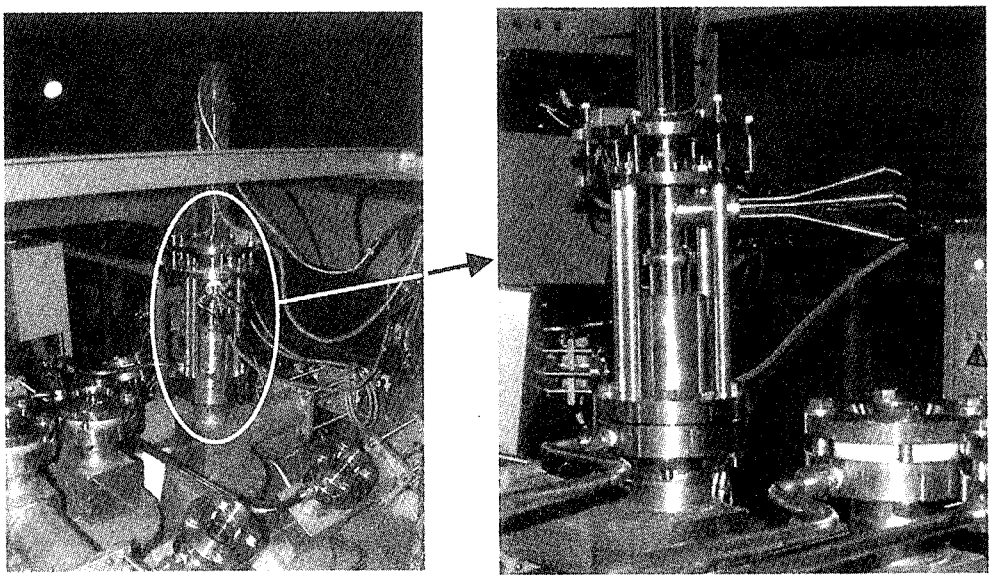


Fig.2 Photographs of the thickness monitor (left : overview of the monitor, right : magnified view of the thickness monitor).

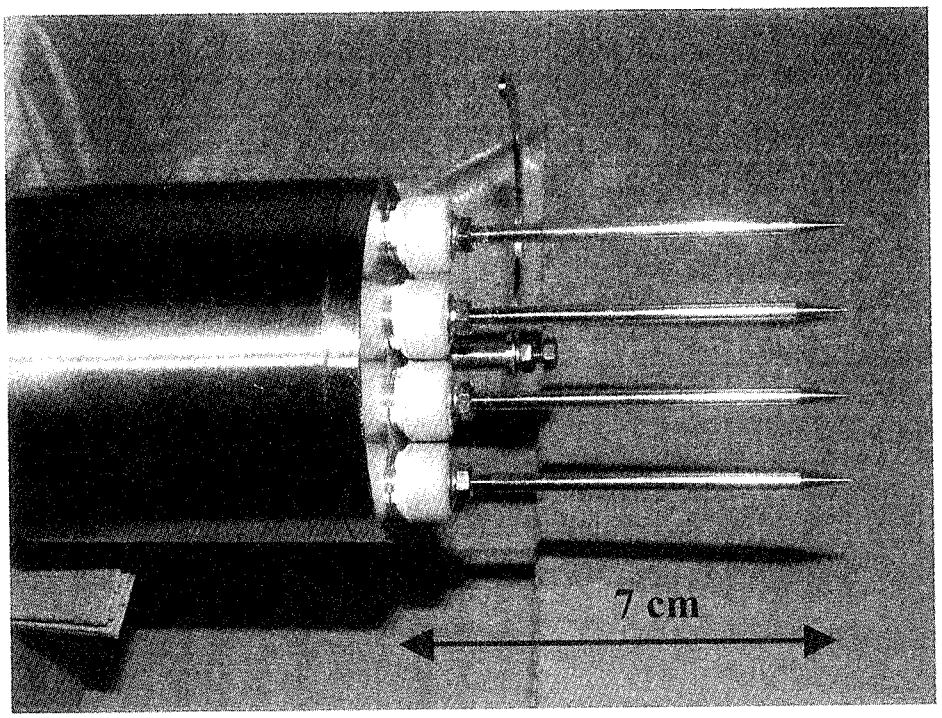


Fig.3 Probe head of the thickness monitor.

3.2.14 TG37-JA Design of a Target Distortion Monitor

(1) Brief Task Description

The IFMIF back wall and the target assembly near the back wall will be deformed by the intense neutron irradiation. This distortion affects the neutron irradiation field and the target integrity. The distortion must be monitored, to predict needed replacement of the back wall and target assembly. An accurate prediction will increase the availability and decrease the operating cost of IFMIF. Therefore, this task will design the distortion measurement methods for the back wall and the target assembly.

Contributors

Name	Party	Institute	E-mail address
H.Nakamura	Japan	JAERI	nakamurh@fusion.naka.jaeri.go.jp
M. Ida	Japan	JAERI	ida@ifmif.tokai.jaeri.go.jp
H. Ise	Japan	KHI,	ise_h@khi.co.jp

(2) Design Requirements

The cross section of the target assembly is shown in Fig. 1. In the IFMIF, the target assembly will be installed with an accuracy of ± 0.5 mm. Since the back wall will be made of RAF steel and will experience neutron irradiation of about 50 dpa per full operating year, it is designed for replacement every 11 months. Therefore, the backwall distortion should be monitored periodically, to confirm the replacement requirement. Basic design requirements of the distortion monitor are as follows;

- Diagnostics Object : Backwall, Target assembly
- Accuracy of Measurement : ± 0.1 mm
- Distance from the monitor to the target : 15 m
- Temperature at the monitor : Room temperature
- Pressure at the monitor : 1 atmosphere
- Monitoring frequency : at each Li dump
- Radiation environment : 7.9×10^{-4} μSv/hr

(3) Selection of Distortion Monitor

Conventional distortion monitors are divided into contact type monitors and non-contact type monitors. IFMIF requires a non-contact monitor, and these are classified into the following three types.

- Eddy current sensors;
  Accuracy is 0.8 μm with a range of 2 mm. The accuracy strongly depends on geometry and flatness of the diagnostic surface. 3D measurement is difficult.
- Ultrasonic sensors;
  Accuracy is 0.1 mm with a range of 80 – 300 mm. 3D measurement with high accuracy is difficult. Diameter of spot at 100 mm is 15 mm.
- Laser sensors;
  Accuracy is 1 μm with a range of ± 5 mm. 3D measurement is possible with a two-axis drive mechanism. Diameter of spot at 30 mm is 30 μm. Measurement a long distance from the target is possible.

Based on this comparison, the laser sensor is selected as the distortion monitor for the IFMIF target. Specifically, the frequency modulation (FM) laser radar system MV-200 (Metric Vision Co., USA) is selected for the IFMIF target distortion monitor. Typical specifications are as follows;

- Distance to point of measurement : 1 m – 60 m
- Accuracy of measurement : ± 0.1 mm at 10 m,
  ± 0.6 mm at 60 m

(4) Arrangement of the Distortion Monitor

Figure 2 shows cross section and plan views of the IFMIF building. Access to the FM laser radar is necessary for maintenance. Therefore the candidate locations of the FM laser radar are the radiation isolation area or the utilities area shown in Fig. 2. In Case A, the FM laser radar is located at a bend in the beam line in the radiation isolation area as shown in Fig. 3. A monitoring port will be attached to the beam line. In this case, the distance from the FM laser radar to the backwall is 21.5 m and then the accuracy of the measurement is 0.22 mm, above the IFMIF specification. In Case B, the FM laser radar is located close to the target in the radiation isolation area as shown in Fig. 4. In this case, a removable mirror will be attached to the beam lines, the distance from the FM laser radar to the backwall is 17.5 m, and the accuracy of the measurement is 0.18 mm. This is still slightly above the IFMIF specification. To satisfy the IFMIF specification, the FM laser radar needs to be located closer to the target than in Case B. A possible solution may be to locate the FM laser radar in the storage cell (Fig. 5). In this case, neutron irradiation effects on the mirror attached to the beam line need to be assessed.

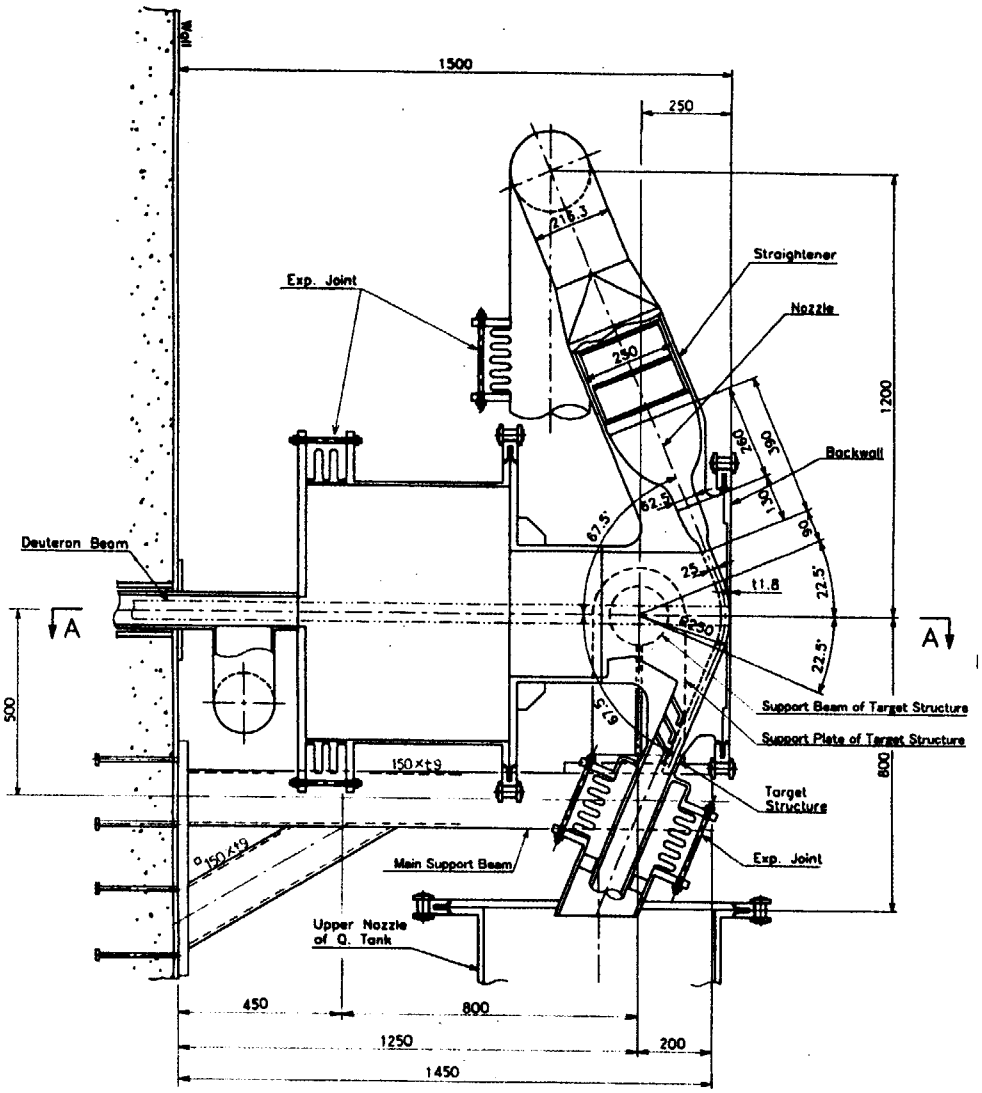


Fig. 1 Cross section of the IFMIF target assembly.

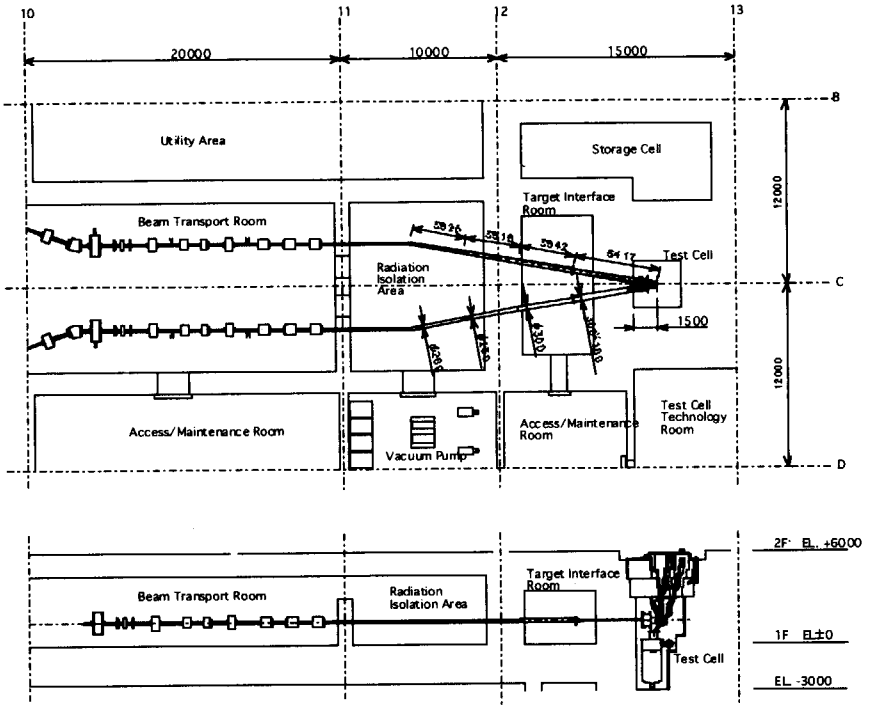


Fig.2 Cross section and plane view of IFMIF building.

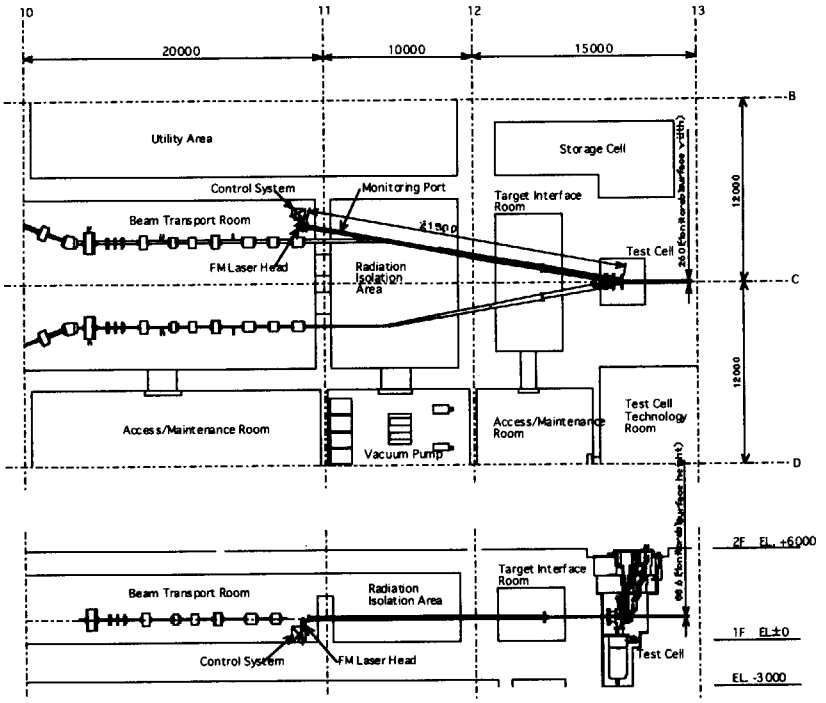


Fig.3 Location of FM laser radar (Case A).

(5) Summary

The distortion of the target assembly and back wall are measured by an FM laser radar system (MV-200, MetricVision Co.,USA) with a spatial resolution of 0.18 mm at 17.5 m and 0.22 mm at 21.5 from the Li target. To satisfy the IFMIF specification, the suggested location of the FM laser radar is in the storage cell. Neutron irradiation effects on the mirror attached to the beam line need to be assessed for this monitor layout.

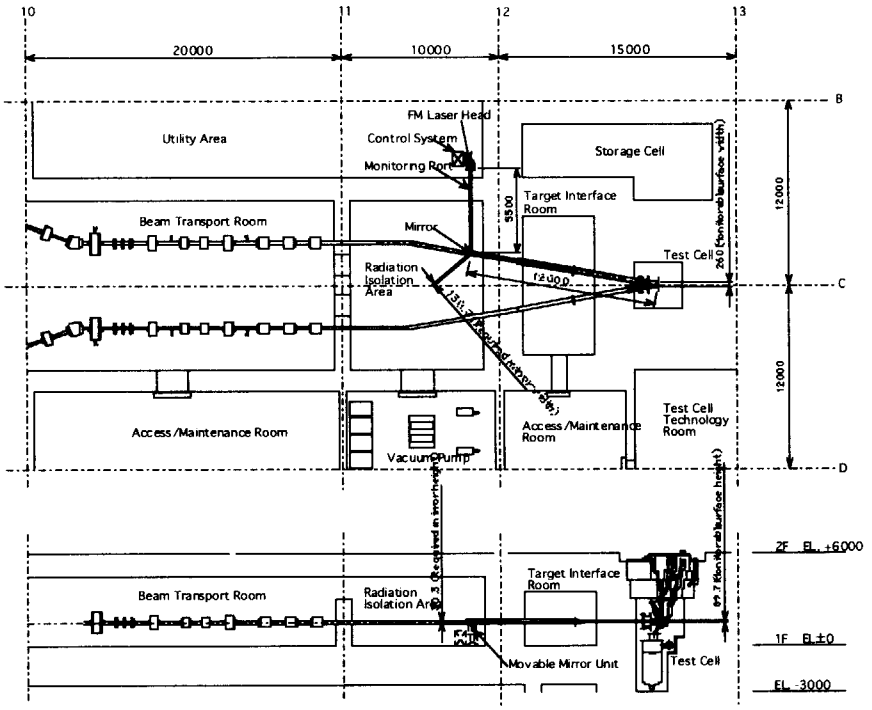


Fig.4 Location of FM laser radar (Case B).

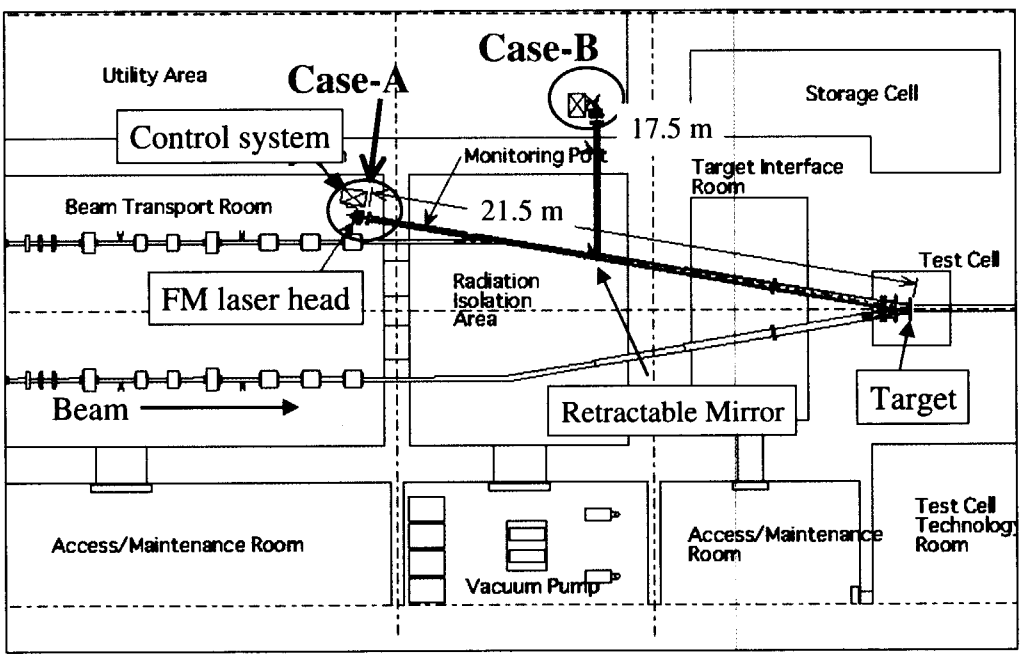


Fig.5 Plane view of the IFMIF building showing the locations of FM laser radar (Cases A and B).

3.2.15 TG51/52-JA : Collection of Lithium Reaction Data, and Characteristics and Suppression of Lithium Fires

(1) Brief Task Description

Lithium fires were studied experimentally using small amounts of Li and gas feed systems. The temperature of the Li pool was measured by a thermocouple and it was demonstrated that Li fires can be extinguished by argon gas, but not by nitrogen. However, nitrogen gas is shown to be partially effective in suppressing the burning Li pool temperature.

Contributors

Name	Party	Institute	E-mail address
H. Horiike	Japan	Osaka Univ.	horiike@eie.eng.osaka-u.ac.jp
N. Uda	Japan	Osaka Univ.	
S. Inoue	Japan	Osaka Univ.	inoue@eie.eng.osaka-u.ac.jp
N. Yamaoka	Japan	Osaka Univ.	yamaoka@nucl.eng.osaka-u.ac.jp
K. Miyazaki	Japan	Osaka Univ.	k1.miyazaki@ehdo.go.jp

(2) Introduction

Alkali metals such as sodium and lithium are very good heat transfer media, with high heat transfer coefficient and high heat capacity. But these materials are well known to react with water or oxygen, generating heat and hydrogen. This property has led to various combustion accidents in reactors and test plants using these materials. Therefore, methods to extinguish liquid metal fires are very important in the design of sodium reactors or lithium facilities like IFMIF.

Studies of methods to extinguish sodium fires were carried out in several laboratories, including Cadarache, Karlsruhe [1] and Japan [2, 3]. Our experiments [4] showed that a sodium pool begins to burn at about 250°C in air, and reached 800-850°C maximum temperature. These studies showed the effectiveness of blowing inert gas like nitrogen in extinguishing fires. However, lithium is known to react with nitrogen gas or sand, which are used as fire extinguishers on several fire types including sodium [5-8]. In the present report, lithium properties are discussed and experiments on extinguishing lithium fires are described.

(3) General Characteristics of Lithium

Properties of lithium can be understood by comparing with those of sodium, potassium, and NaK.

1) They all burn in air and generate reactive aerosols with strong alkalinity [9]

$$2Na + 2H_2O = 2\,NaOH + H_2 + 88.2\ kcal$$
$$2K + 2H_2O = 2KOH + H_2 + 92.8\ kcal$$
$$2Li + 2H_2O = 2LiOH + H_2 + 106\ kcal$$
$$3Li + 1/2N_2 = Li_3N + 47.5\ kcal$$

Thus careful fire prevention is required; otherwise the hydrogen gas generated might explode.

2) These materials react with concrete. Protective liners or catch pans are necessary to avoid direct contact. Lithium generates more energy than sodium or potassium in the reaction so it requires thicker protective plates. A concrete wall will lose thickness in a lithium fire much quicker than in a sodium fire.

3) Sodium does not react with nitrogen, but lithium does. It is reported that fire residues from a lithium loop fire at Argonne National Laboratory were analyzed and found to consist of about half oxides and half nitride [5]. Therefore, lithium fires cannot be extinguished by nitrogen gas, but require argon or helium. In any case, closed compartment structures should be effective, combined with inert gas suppression systems.

4) Dry sand is a very good extinguisher for sodium fires, but even very dry sand reacts with lithium.

5) Lithium is more difficult to ignite than is sodium at similar temperatures. Once it burns, however, lithium generates much higher flame temperatures than sodium and the fire is more difficult to extinguish. This is probably because lithium has a higher melting point, higher boiling point and generates larger reaction heat. A piece of sodium dropped in a water pool begins to burn instantly because the surface melts, but a piece of lithium in water usually does not begin to burn because the melting point is higher than the boiling point of water.
6) Thermal insulation materials have to be carefully selected to avoid reaction with any spilled or leaking alkali metals.
7) Many ordinary salts are heavier than lithium and tend to sink in lithium. This means that, for most solids used on lithium fires, the fire continues as reaction salts sink and new surface of lithium appears.

Extinguishers for lithium fires were studied at ANL [5]. The results showed that carbon powder was the best solid fire extinguisher. The reason is that carbon does not react with lithium, generates no gas or smoke, and it floats and spreads to cover the surface of the lithium pool. Li_2CO_3 was not recommended because it showed some reactivity with lithium. Experience at Osaka University shows that NaCl can also be used as an extinguisher.

(4) Lithium Fire Experiment

Experiments on lithium fires were conducted with various conditions of combustion and suppression of the fire.

a) Experimental

The experimental set up is indicated in Fig. 1. The system consisted of a gas feed system, a combustion chamber, and an exhaust gas scrubber. The gas feed system was made of a very large plastic balloon and air intake, and gas bombs of nitrogen, argon, and oxygen. In the bottle, there were a heater, humidity conditioner, fan and monitors for humidity, temperature and oxygen concentration. After the gas content was set in the balloon, the gas was fed by a blower though a flow control valve. Approximately 80 liter per min gas flow rate was obtained. The combustion chamber, made of transparent plastic sheet and steel angles, was 120 cm wide, 120 cm long and 180 cm high. The gas was exhausted from a nozzle located at the top of the chamber. The lithium sample of 40-50 g was put on a stainless steel pan of 19.8 cm long, 13.7 cm wide and 3.5 cm deep. This pan was surrounded by a rectangular cylinder 23.3 cm wide, 29 cm long and 50 cm high, as shown in the right hand part of Fig. 1. The experiment was set on a bed of sand to ensure thermal insulation and air tightness. The top of the cylinder consisted of two plates to adjust the open area. Lithium temperatures were measured by an Inconel sheathed thermocouple of 4.8 mm diameter. The sample was heated by an electric heater until burning initiated and then the heater was switched off. Typical samples are shown in Fig. 2.

b) Results

Photographs of lithium and sodium burns are compared in Fig. 3. The approximate temperature when this was taken is indicated; this was measured by a thermocouple, seen standing vertically in the center of the pans. Note that the lithium fire is much brighter than sodium. The temperature evolution in time is indicated in Fig. 4. These four samples ignited at around 200°C to 400°C as shown by the rapid temperature rise at around 100 seconds. The variable parameter is the distance of the thermocouple from the bottom of the pan. As the depth of the Li pool was estimated to be approximately 5 to 10 mm, these data show that temperatures in the pool and flame were uniformly very high. It is noted that the maximum temperature went up to 1150°C which is much higher than the sodium fire where the highest temperature was 750°C [4].

The pool and flame temperatures were measured as a function of gas composition. The temperature evolution is shown in Fig. 5 as a function of the oxygen content. Run number of R101 denotes ordinary air and R118 pure Nitrogen. The present data were taken by circulating ordinary air until the lithium begins to burn, and then the gas with adjusted composition was blown in. This

explains why the temperature in run R107 did not go very high, as the adjusted gas blow was too early in this case. It is noted from this figure that, with introduction of nitrogen, the flame temperature could be suppressed below 900°C, but the fire was not extinguished by nitrogen. It is observed that greater temperature decreases resulted with increases of nitrogen concentration; therefore, it can be concluded that the fire is suppressed but not extinguished by nitrogen.

The effect of argon was also evaluated, and the data is shown in Fig. 6. This shows that argon is very effective in extinguishing lithium fires. In the case of 100% Ar gas, the flame temperature did not go above 500°C. This means that the fire was immediately extinguished by Ar gas. Also, gas with 10% Ar could suppress the fire temperature below 750°C.

c) Conclusion

Lithium fires were studied extensively in comparison with sodium fires. It is noted that the lithium shows much higher fire and flame temperatures than sodium. This may be due to the higher melting point and larger reaction heat. Lithium is well known to react with nitrogen, so this gas cannot be used as an extinguisher. Argon gas was demonstrated to be very effective in extinguishing lithium fires

References

[1] Huber et al., Nucl. Eng. Design **35** (1975) 155-162.
[2] O. Miyake et al., J. Nucl. Sci. Tech. **28** (2) (1991) 107-121.
[3] S. Ohno, K. Kawada, N. Miyahara, Study on Sodium Leak Fire, Donen Gihoh (PNC Technical Report) 92 (1994) 18-37.
[4] K. Miyazaki, S. Inoue and H.Horiike, J. Nucl. Sci. Tech **41** (10) (1999) 1084-1091.
[5] V. A. Maroni et al., Analysis of the October 5, 1979 Lithium Spill and Fire in the Lithium Process Test Loop, ANL report ANL-81-25, Argonne National Laboratory, Dec. 1981.
[6] D. W. Jeppson, Interactions of Liquid Lithium with Various Atmosphers, Concretes, and Insulating Materials and Filtration of Lithium Aerosols, Hanford Engineering Development Laboratory HEDL-TME 79-7 UC 20 June 1979.
[7] T. K. Gil and M. S. Kazimi, The Kinetics of Liquid Lithium Reaction with Oxygen-Nitrogen Mixtures, MIT report MIT PFC/PR-86-1, 1986.
[8] D. S. Bernet and M. S. Kazimi, The Consequence of Lithium Fires in the Presence of Steam.
[9] D. W. Jeppson, J. L. Ballif, W. W. Yuan, and B. E. Chou, Lithium Literature Review Lithium's Properties and Interactions, Hanford Engineering Development Laboratory Report HEDL-TME 78-15 UC-20, April 1978.

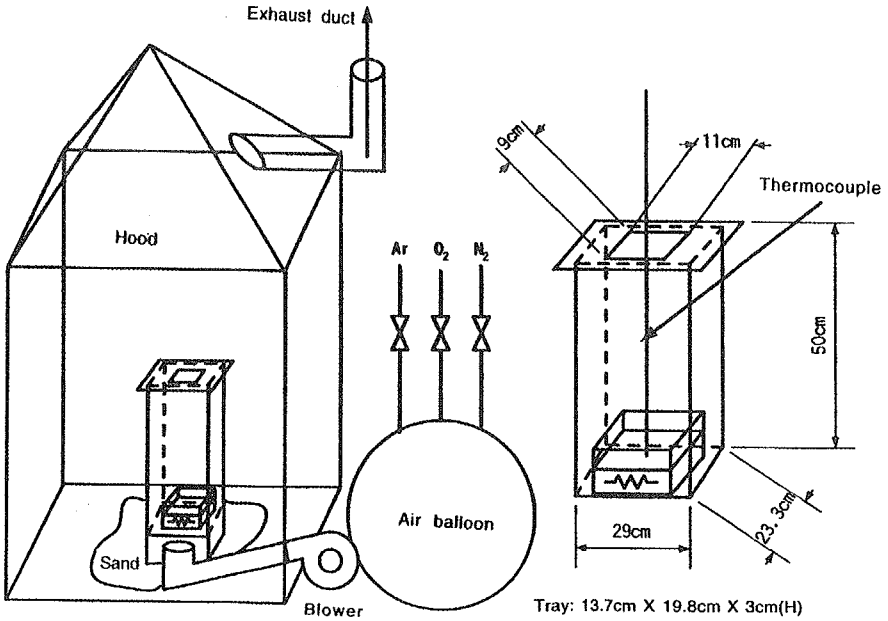


Fig. 1 The experimental set up.

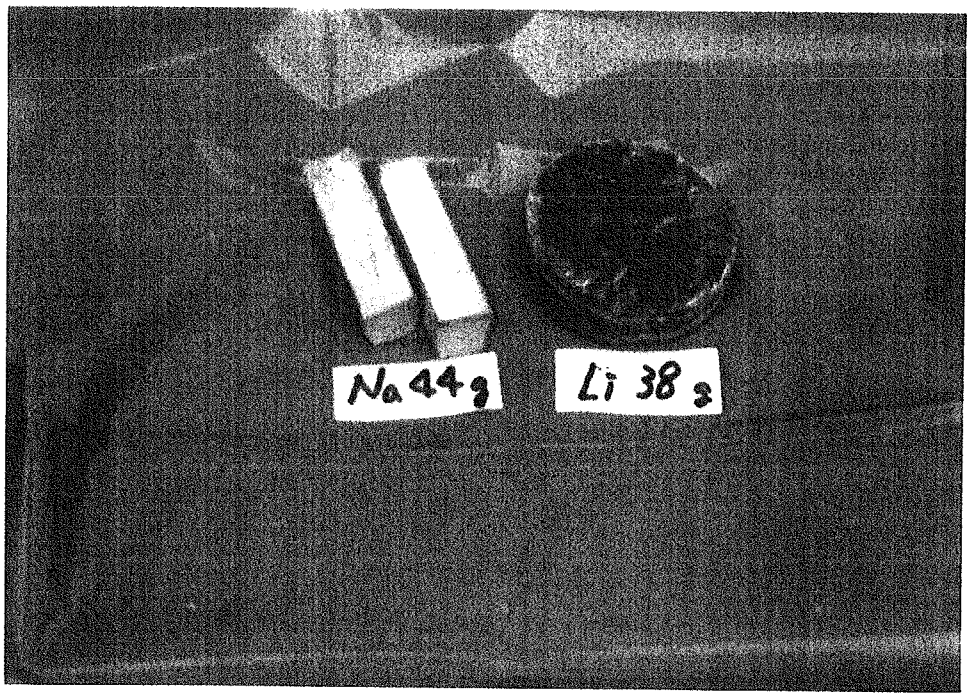


Fig. 2 Samples of Lithium (right) and Sodium (left).

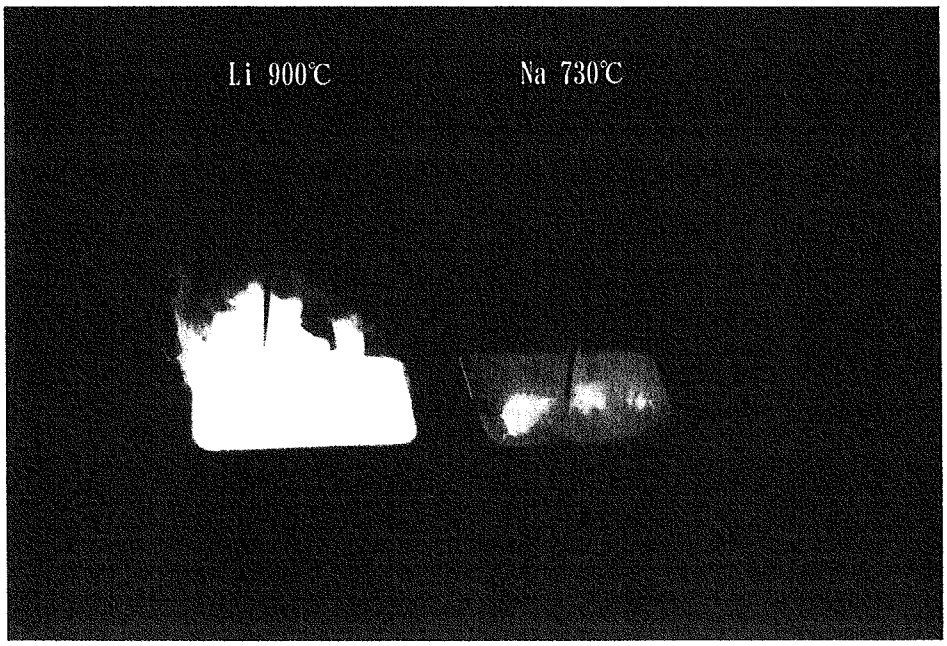


Fig. 3 Burning Lithium (left) and Sodium (right).

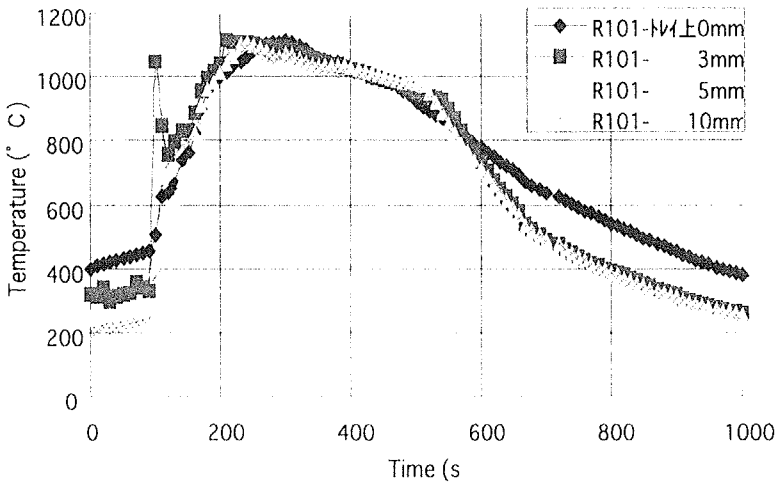


Fig. 4 Temperature evolutions in a lithium pool during burning. (The abscissa is time in seconds and the ordinate the temperature in the lithium pool measured at 0, 3, 5, and 10mm from the bottom of the pan.)

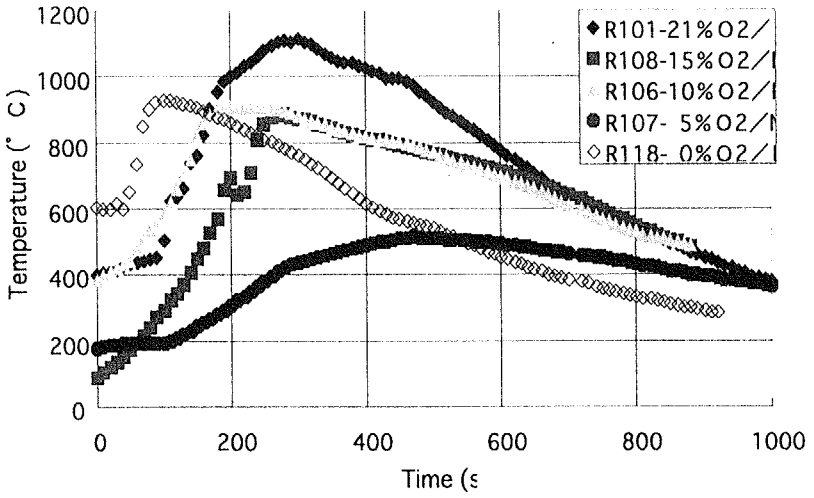


Fig. 5 Temperature evolution as a function of nitrogen gas concentration. (The abscissa is time in seconds and the ordinate the temperature in the lithium pool, for oxygen concentrations of 0 to 21% in nitrogen gas.)

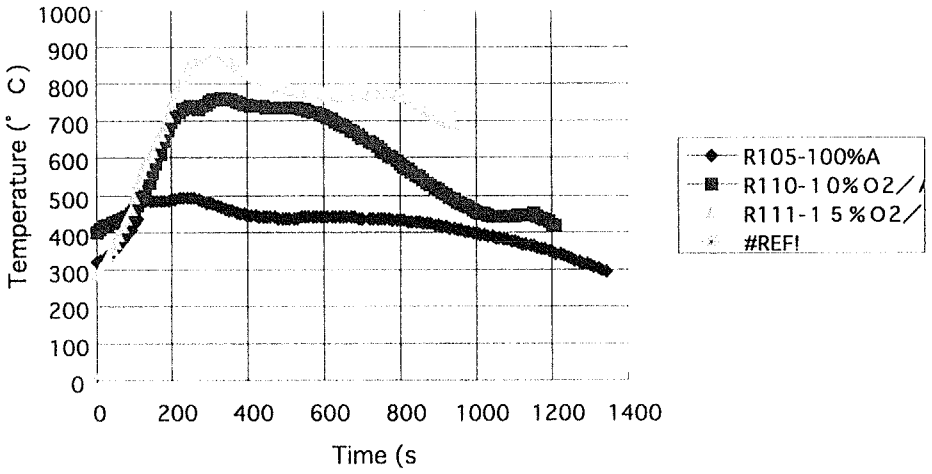


Fig. 6 Temperature evolution as a function of argon gas concentration. (The abscissa is time in seconds and the ordinate the temperature in the lithium pool, for oxygen concentration of 0 to 15% in argon gas.)

3.2.16 TG61A/71-EU : Lithium Target Safety Analysis and Thermal Transient Analysis of Target Lithium Loop

(1) Brief Task Description

The present task consists of two main subtasks. The first concerns the lithium target safety review, in light of the reduced cost design revisions, and includes the hazard analysis adopting the FMEA (Failure Modes and Effects Analysis) methodology which is oriented towards detailing on a component-by-component basis with all of the possible failure modes and identifying their effects on the plant.
Moreover the systems analysis is performed in order to assess, from a probabilistic standpoint, the reliability of the lithium target system, applying the fault tree technique.

The second task pertains to the thermal hydraulic transient analysis of the target lithium loop, including operational and accident transients. A lithium target loop model is developed, using the RELAP5 Mod3.2 thermal hydraulic code, which has been modified to include specific features of IFMIF itself, particularly the use of lithium and organic oil as the primary and secondary coolants, respectively.

Contributor

Name	Party	Institute	E-mail address
L. Burgazzi	EU	ENEA	burgazzi@bologna.enea.it

(2) Li Target Safety Analysis

Safety analysis review has been performed applying the FMEA (Failure Modes and Effects Analysis) approach in order to identify the potential failures inducing an accident in the plant or simply a stop in the operating phase, with reference to the reduced cost design version: the outcome of the present analysis is the identification of relevant target-related hazards and the identification of major initiating events of accident sequences.
The main conclusions are that, in the light of plant modifications submitted in the reduced cost version of the design, target safety is assured and environmental impact is negligible: potential target-related hazards due to tritium production and lithium operation are very low because target facilities are designed both to reduce the accident probability and, in the unlikely event of an accident, to eliminate any subsequent release to the environment.

In particular, FMEA has identified as major hazards relative to target system radioactive material generation in the lithium loop (tritium and Be-7), the main products of nuclear interaction between deuterons and liquid lithium, and the risk related to the liquid lithium loop operation. These results are reflected in the design and system operation. As regards the former safety issue, the majority of the tritium and other radioactive materials and impurities are removed by trapping and kept under control by the impurity monitoring loop. With regard to the latter, vacuum condition of the test cell and the confinement from outside, combined with the controlled argon gas atmosphere of the lithium cell, assure the countermeasures against lithium fire risk due to lithium-air reaction; moreover, the floors and the walls of the lithium cells are covered with steel liners to prevent lithium concrete reactions. All lithium components (tanks, lines, valves and valve bonnets, etc.) are provided with leak detectors. In addition to the lithium fire control system, oxygen meters are used to monitor the oxygen concentration in the argon gas. Lastly the lithium inventory has been reduced from 21 to 9 m^3, thus resulting in a reduction of the consequences of an accidental lithium-air or lithium-water reaction.

In addition, the study has pointed out any safety interfaces with test facilities and accelerator facilities. In fact, some of the events result in excess evaporation of the lithium that would diffuse to the beam line vacuum, therefore causing an effect of poor vacuum and contamination of the beam. The beam duct is evacuated by the differential pumping system and the beam vacuum system and the exhaust ducts are provided with moisture traps to trap the lithium vapors. A backwall rupture accident results in a lithium spill in the test cell. The vacuum environment in the test cell atmosphere eliminates the possibility of lithium-air reaction and also reduces the ingress of lithium into the beam line during

such an event. Other barriers to withstand lithium propagation into the accelerator, if such an event or a loss of vacuum accident occurs, are provided by the fast acting valves, which are required to immediately isolate the target from the accelerator after an emergency beam shutdown, and the gate valves placed out of the test cell shield wall, which constitute the physical interface between the accelerator and target.

Moreover the analysis has identified as reliability-critical areas, where modification to the design could be required to reduce the probability of failure. The reliability-critical items are as follows: main lithium target cooling systems, the purification loop, the cold trap cooling system and the vacuum differential pumping system. The reliability of these subsystems is accomplished in lithium target safety analysis, as a further step in the system analysis.

Lastly the analysis has provided a set of Postulated Initiating Events, that is off-normal events that could result in hazardous consequences for the plant, together with the total frequency and the list of component failures which could induce the Postulated Initiating Event. (A set of elementary accident initiators is grouped under each Postulated Initiating Event, taking into account the similarity of accident development in terms of mitigating features and possible consequences.) This assures the complete list of major initiating events of accident sequences, helpful to the further accident sequence quantification phase, to be accomplished in the frame of the Design Integration task regarding the safety analysis and assessment for IFMIF plant.

The events are classified by event likelihood of occurrence, according to Table 1. The overall set of Postulated Initiating Events identified by the FMEA is reported in Table 2. [1]

The Postulated Initiating Events are categorized into two broad classes. The first addresses the events related to the loss of function - including loss of flow in the target Li loop, loss of flow in the cold trap cooling loop, loss of Li purification and loss of heat sink – which imply the faults of components designed to assure the required function. The second class pertains to the events related to coolant leak/spill – as Li LOCA, Li spill in the Test Cell, Organic LOCA and Water LOCA – which involve the rupture of the primary boundary of the coolant carrying components.

Table 1 Event sequence categorization.

Event Category	Event Description	Event Frequency
I	Operational Events	More than one per year
II	Likely Events	$1\sim10^{-2}$/y
III	Unlikely Events	$10^{-2}\sim10^{-4}$/y
IV	Extremely Unlikely Events	$10^{-4}\sim10^{-6}$/y
V	Hypothetical Sequences	Less than 10^{-6}/y

Table 2 List of identified Postulated Initiating Events.

Event Code	Event Description	Category
LF	Loss of flow in the Target Li loop	II
LFCT	Loss of flow in the Cold Trap cooling loop	II
LH	Loss of heat sink	II
Li-LOCA	Lithium LOCA	II
LP	Loss of Li purification	II
LS1	Lithium spill in the Test Cell	III
LTR1	Li-Organic Cooler tube rupture	III
LV-B	Loss of vacuum in the beam line	II
Or-LOCA	Organic LOCA	III
W-LOCA	Water LOCA	III
Ar-LOCA	Argon LOCA	III
N/S	Not Safety relevant initiator	II

(3) Reliability Analysis

A systems analysis has been performed in order to evaluate the reliability of the target facility. The fault tree technique is adopted in the analysis to identify potential failure modes affecting the system during normal operation and to assess the system probability of failure.

The construction of an IFMIF fault tree is based on system success/failure criteria and pertains to the system modeling phase. The system model requires the identification of the relative boundaries and interfaces between relevant parts of IFMIF and includes components required for system operation, support systems required for actuation and operation of the system components (electrical power distribution system, vacuum system, water supply, control system), and other components that could degrade or fail the system.
In addition, the system model includes the relevant and possible failure modes for each component required for system operation. These include both component independent failures and dependent failures, that is, failure of one component causing some other component in the system to be unavailable (e.g. support systems) and common cause failures among similar components.

The system model building and reliability assessment are made with the support of Risk Spectrum® PSA Professional, a PC software package that performs risk and reliability analysis based on fault trees and event trees. [2] The component failure rate data necessary for reliability assessment are selected from available data bases which are judged applicable.
The underlying success criteria in fault tree construction is the availability of the whole target facility which can be attained through the availability of each system whose failure in the requested mission contributes singularly to the loss of the target.
Therefore, fault tree models are constructed for each relevant target system as previously identified, and are listed below:

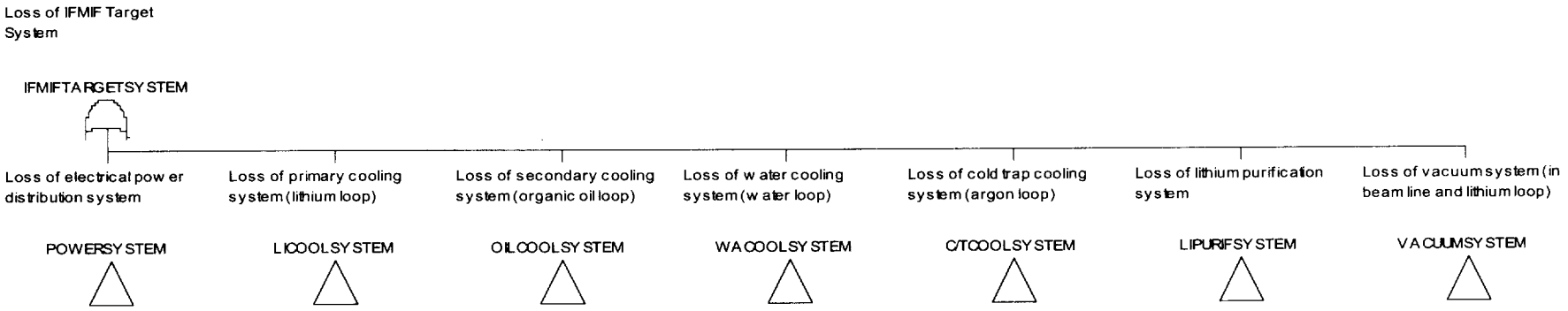
- Loss of Primary Cooling System
- Loss of Secondary Cooling System
- Loss of Water Cooling System
- Loss of Cold Trap Cooling System
- Loss of Lithium Purification System
- Loss of Lithium Target Vacuum System
- Loss of Electrical Power Distribution System

All the fault trees and the expected results are reported in [3]: in Figs. 1 and 2 the fault trees relative to the whole target system and to the primary cooling system respectively are shown. The final result of the plant fault tree analysis in terms of IFMIF Target System probability of failure over a week mission time is: Q_{TOT} = 1.29E-01. The contributions of evaluated systems are summarized in Table 3. From the table it is inferred that each relevant subsystem (i.e. cooling systems, vacuum system and purification system) contributes singularly almost equally to the 20% for the overall value.
Concerning the system architecture, it is considered that lack of sufficient redundancies for components, as valves and pumps, involves relatively high probabilities of failure. The results of an important analysis performed by RISK SPECTRUM at "component level", in order to identify most contributors to the reliability value, show that: [3]

- lithium heaters are the most critical components for probability of failure of the lithium cooling system (91.45%) and of the overall plant (19.34%);
- 3 kV breaker unavailability is predominant in failure of the electrical power system (72.78%);
- cold trap, yttrium and titanium getters are predominant in failure of the purification system (60.45%) and mist traps in the vacuum system (54%).

Table 3 List of contributors to Target unreliability.

System	Probability of failure: Q_i	$(Q_i/Q_{tot}) * 100$ (%)
Vacuum system	2.79E-02	20.48
Primary cooling system (lithium loop)	2.72E-02	20.00
Lithium purification system	2.50E-02	18.35
Water cooling system	2.15E-02	15.78
Secondary cooling system (organic oil loop)	1.68E-02	12.32
Cold trap cooling system (argon loop)	1.09E-02	8.00
Power system	6.91E-03	5.07



LEGEND:

Basic event: basic initiating fault event that requires no further development

OR gate: output event occurs if at least one of the input events occurs

AND gate: output event occurs if all input events occur simultaneously

Transfer event: the event is transferred to the relative fault tree (i.e. Loss of electrical power distribution system, Loss of primary cooling system etc.). This is used as a matter of convenience to avoid extensive duplication in the fault tree

Fig. 1 IFMIF Lithium Target System – Fault tree analysis.

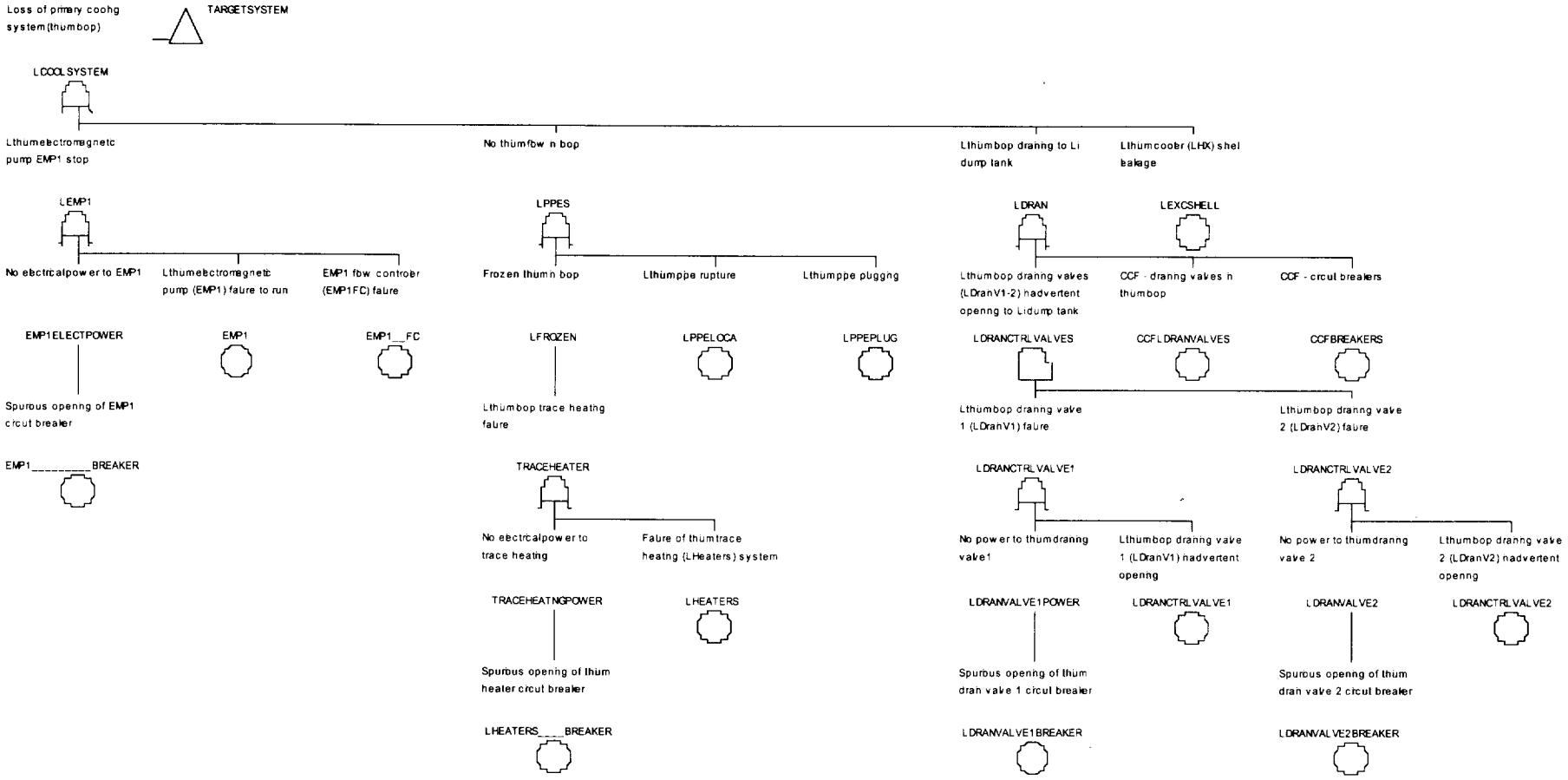


Fig. 2 Primary cooling system (lithium loop) fault tree.

(4) Transient Analysis of Lithium Loop

The thermal hydraulic code RELAP5 Mod3.2 has been utilized for the simulation of the three main circuit loops of the facility, in order to analyze the global thermal hydraulic behavior of the plant:

- in steady conditions at full power
- in the operational transients of start-up and shut-down
- in accident conditions

The IFMIF target facility nodalization has implied the reproduction, by means of a series of volumes and junctions suitable for the numerical calculations, of the following circuits:

- the primary circuit (lithium cooled)
- the secondary circuit (organic oil cooled)
- the tertiary circuit (water cooled), only the part related to the organic cooler

At first a plant steady state condition at full power has been simulated and the results showed a generally good stability of IFMIF and a good agreement with the specified conditions for the facility at 10 MW power as shown in Table 4. [4]

The shut-down and start-up operational transients have been simulated in a model consisting of five main phases. The initial condition is a 10 MW power steady state, then a shut-down power ramp takes the plant to zero power to reach a new steady state. A start-up power ramp takes the plant again to full power and to a new steady condition. As shown in Fig. 3, during the start-up phase, power provided by the accelerator passes from 0 MW to 10 MW in 120 s and a symmetric power ramp has been chosen for the shut-down phase, passing from 10 MW to 0 MW in 120 s.
It has been demonstrated that the plant answers well to simulated transients and is able to reach new steady conditions in a short time after a power ramp is implemented. In particular, at zero power steady state the system reaches an equilibrium condition in which Li and oil are at the same temperature (around 520 K), the organic cooler is completely by-passed, and the electrical heaters come into operation to compensate for the heat losses. [5]

Target inlet and outlet temperatures are shown in Fig. 4, while in Fig. 5 the lithium cooler oil inlet and outlet temperatures are shown.

Finally, the following transients in accident conditions have been evaluated:

1. Beam trip (10→0 MW on target)
2. Beam trip of one accelerator (10→5 MW on target)
3. Loss of organic circuit, due to pump failure
4. Loss of heat sink, due to loss of the water circuit (pump stop)

1. This incident resulting from the loss of both accelerators is characterized by a power reduction from full power steady state to zero power in 10 μs (Fig. 6). At the end of the transient, the target system has to reach the zero power steady state condition as soon as possible, in order to allow a new start-up. Target inlet and outlet temperatures are shown in Fig. 7, while in Fig. 8 the lithium cooler oil inlet and outlet temperatures are shown. [6]

2. In this incident resulting from the loss of one accelerator (1 out of 2), the beam power varies from full power to 5 MW in 10 μs (Fig. 9). As the beam power is reduced to 50%, the lithium, oil and water flow rates have to reduce to half the nominal values to keep the same Target inlet and outlet temperature difference (50 K), required by the IFMIF specifications.
   Target inlet and outlet temperatures are shown in Fig. 10, while in Fig. 11 the lithium cooler oil inlet and outlet temperatures are shown. [6]

3. After the pump stops in 1 s, the beam is immediately shutdown on low oil flow-rate signal (80%). The temperature of the lithium decreases to the specified (standby) value (around 523 K), while the temperature of the organic oil increases to the same value, as shown in Figs. 12 and 13, the heaters come into operation to compensate for the heat losses and the EMP and water pump continue operating and all oil flows through the by-pass line.

4. After the pump stops in 2 s, the beam is immediately shutdown on low water flow-rate signal (80%). The plant reaches a new steady state condition in which the temperatures of lithium and oil equalize at a value around 523 K, as shown in Figs. 14. The heaters compensate for the heat losses, the EMP and organic pump are kept in operation at nominal rates, and the organic cooler is completely by-passed.

Table 4 Main parameters of the 10 MW steady state.

Quantity	Value	Units
PRIMARY CIRCUIT		
Target pressure	280[1]	Pa
Target power	10	MW
Target inlet temperature	522.8	K
Target outlet temperature	572.6	K
Target flow-rate	48.38	kg/s
Quench Tank pressure	17.3	kPa
Quench Tank temperature	572.6	K
Quench Tank lithium level	6.63[2]	m
EMP inlet pressure	46.75	kPa
Lithium Cooler inlet temperature	572.5	K
Lithium Cooler outlet temperature	522.9	K
Total pressure losses in the primary circuit	0.068	MPa
Primary circuit heat losses to environment	91	kW
SECONDARY CIRCUIT		
Expansion Tank pressure	0.157	MPa
Pump inlet pressure	0.228	MPa
Lithium Cooler Inlet plenum temperature	472.7	K
Lithium Cooler Outlet plenum temperature	492.5	K
Li-Cooler logarithmic aver. temp. difference	63.95[3]	K
Organic Cooler Inlet plenum temperature	492.5	K
Organic Cooler Outlet plenum temperature	467.6	K
Organic Cooler flow-rate	182.6	kg/s
Organic Cooler valve area/nominal area	0.8	-
By-pass temperature	492.4	K
By-pass flow-rate	47.4	kg/s
By-pass valve area/nominal area	0.2	-
Secondary circuit total pressure losses	0.12	MPa
Secondary circuit heat losses to environ.	50	kW
TERTIARY CIRCUIT		
Water inlet pressure	0.294	MPa
Water inlet temperature	305	K
Water outlet temperature	310	K
Water flow-rate	472	kg/s
Organic Cooler log. aver. temp. difference	172.3[4]	K

[1] Average value (pressure higher than the specified one due to numerical problems of the code).
[2] Level from the EMP inlet level.
[3] Calculated for a counter-current flow heat exchanger.
[4] Calculated for a counter-current flow heat exchanger.

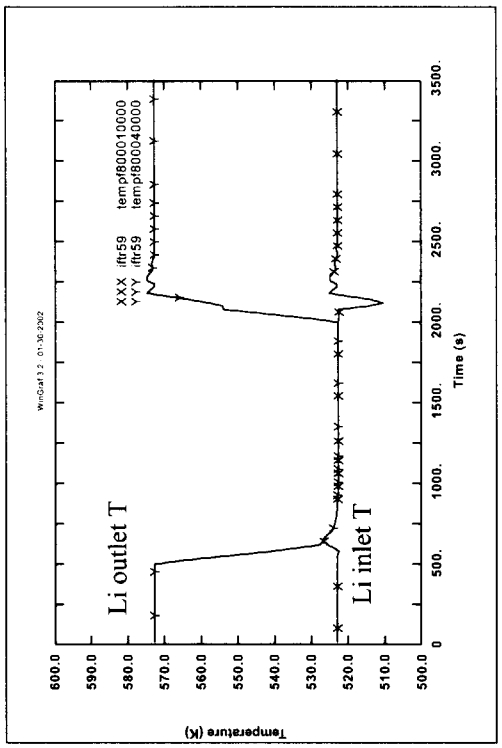


Fig. 4 Target inlet and outlet lithium temperature (start-up and shut-down).

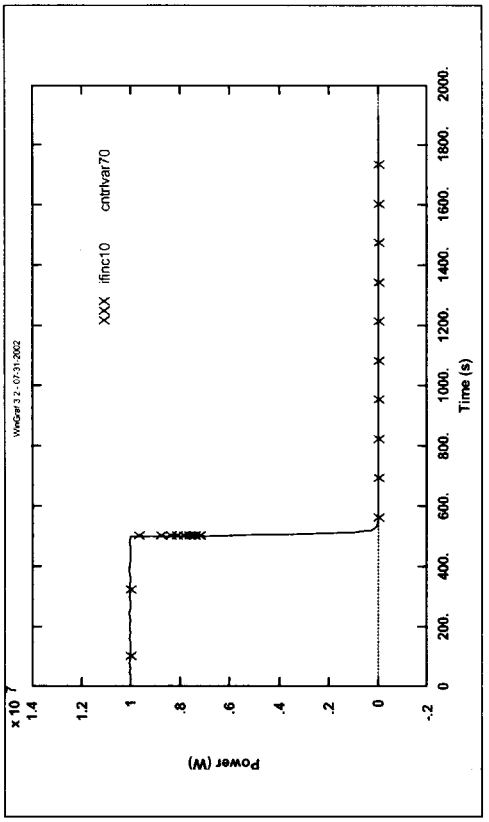


Fig. 6 Target power (beam trip).

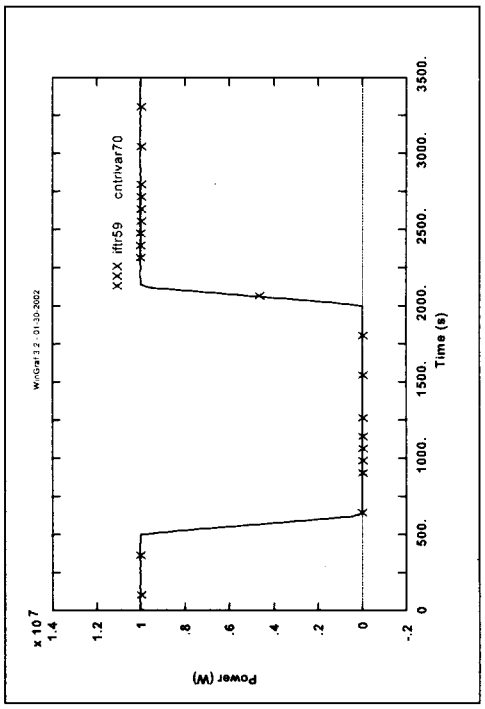


Fig. 3 Target power (start-up and shut-down).

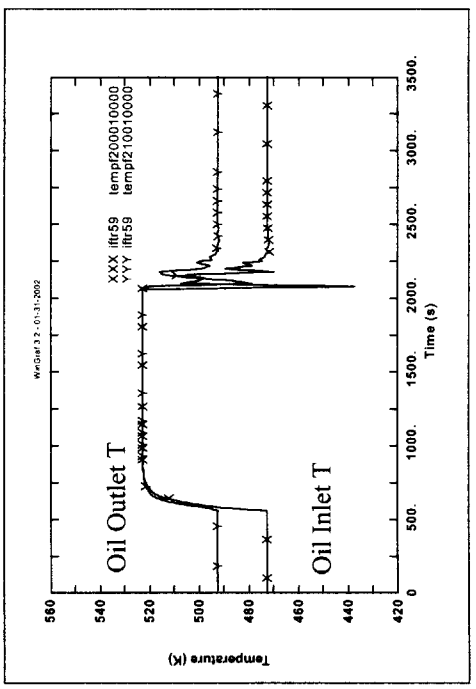


Fig. 5 Lithium cooler oil inlet and outlet temperature (start-up and shut-down).

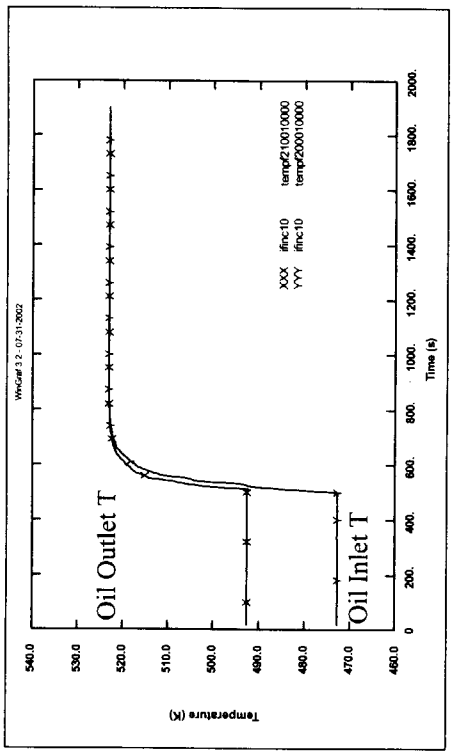


Fig. 8 Lithium cooler oil inlet and outlet temperature (beam trip).

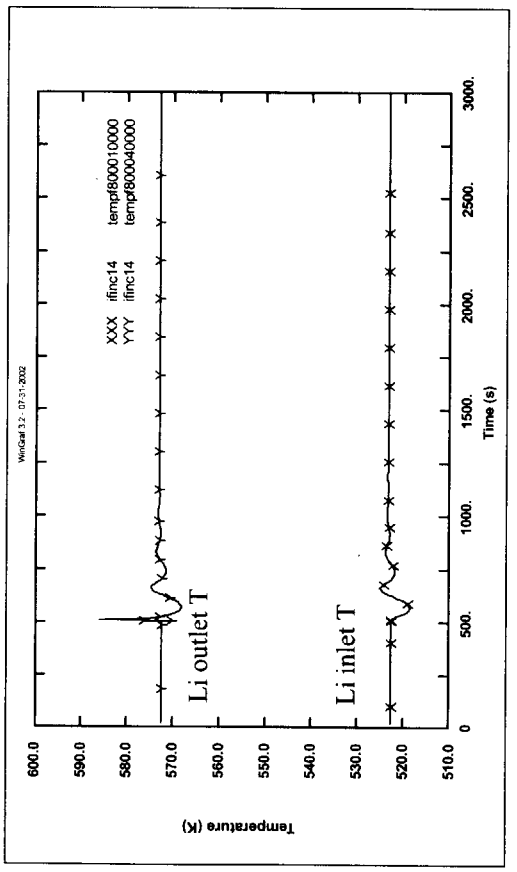


Fig. 10 Target inlet and outlet lithium temperature (one accelerator beam trip).

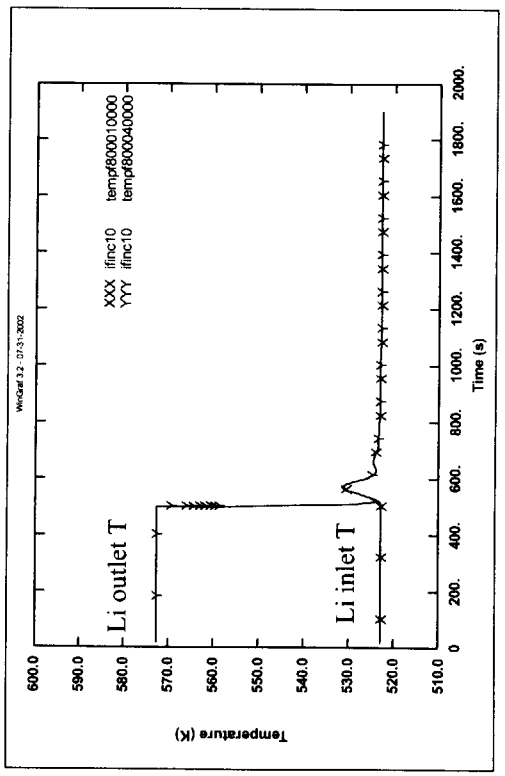


Fig. 7 Target inlet and outlet lithium temperature (beam trip).

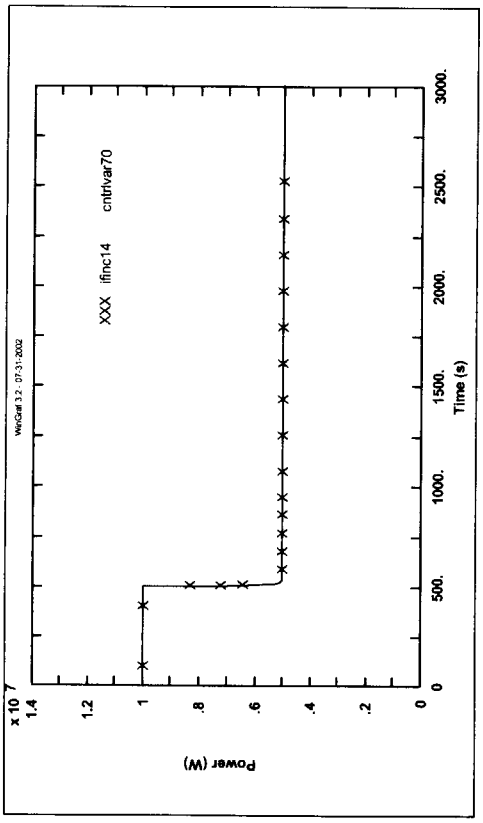


Fig. 9 Target power (one accelerator beam trip).

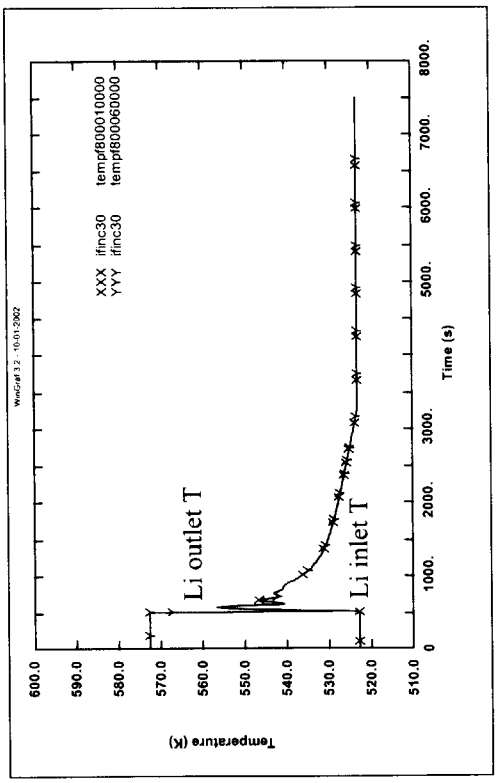


Fig. 12 Target inlet and outlet lithium temperature (organic pump trip).

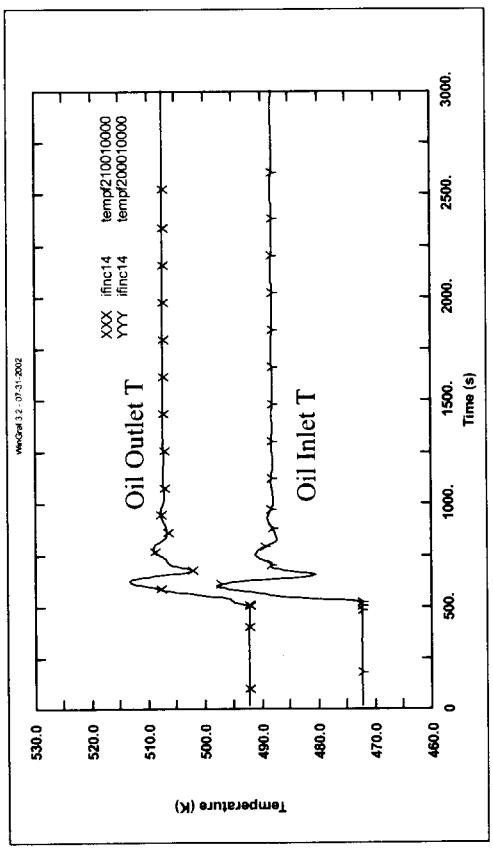


Fig. 11 Lithium cooler oil inlet and outlet temperature (one accelerator beam trip).

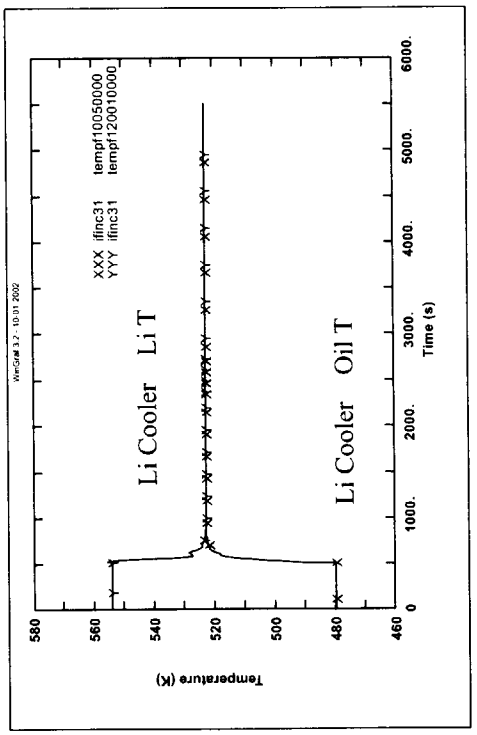


Fig. 14 Lithium Cooler oil and lithium temperature (loss of heat sink).

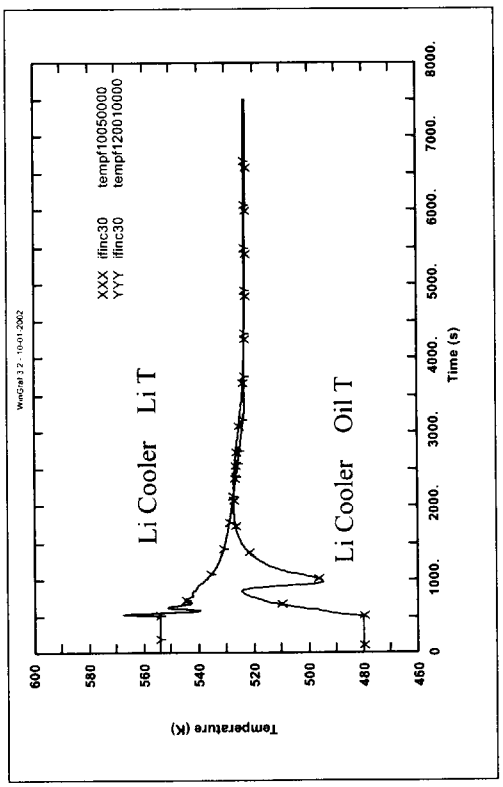


Fig. 13 Lithium Cooler oil and lithium temperature (organic pump trip).

(5) Conclusions

Safety analysis review points out that, in light of plant modifications submitted in the reduced cost version of the design, target safety is fulfilled and environmental impact is negligible, as assessed in the CDA phase. In addition, a detailed fault tree model, used for systems analysis, reveals a target system unavailability figure near 1.0E-1, derived from the single contributors of the apportioned subsystems.

Transient thermohydraulic analysis of the plant through RELAP5 Mod3.2 simulation shows that:

- results comply with the expected conditions of IFMIF facility during full power conditions,
- plant response to the operational startup and shutdown transients is satisfactory,
- the plant answers well to the simulated accident transients and is able to reach new steady state conditions in a short time, under safe conditions.

References

[1] ENEA Report CT-SBA-00010 "Lithium Target Safety Analysis Review: Failure Mode and Effect Analysis of Lithium Target", July 2001

[2] "Risk Spectrum® PSA Professional Version 1.20 - User's Manual", RELCON AB, December 2000

[3] ENEA Report FIS-P127-002 "IFMIF Lithium target system Analysis", June 2002

[4] ENEA Report QT-ESI-00032 "IFMIF: Nodalisation for RELAP5 mod3.2 code and 10MW power steady state calculations", November 2001

[5] ENEA Report XSIET-P127-002 "IFMIF start-up and shut-down operational transient simulation with the RELAP5 Mod3.2 code", June 2002

[6] L. Burgazzi et al. "IFMIF Thermal-Hydraulics Analysis", Proceedings of the International Conference Nuclear Energy for New Europe, Kranjska gora, Slovenia, Sept. 9-12, 2002

3.2.17 TG61B-JA : Transient Behavior of the Lithium Loop

(1) Brief Task Description

The IFMIF target loop system consists of the primary lithium (Li) loop, a secondary organic oil loop and tertiary water loops. Every loop, especially the Li loop, must be controlled to keep the temperature constant. The objective of this task is to evaluate transient thermal behavior of the Li loop in an accidental beam trip or during startup of IFMIF operations.

In the IFMIF Li target, most of the deuteron beam power is converted to heat and the average temperature of Li increases from 250°C to 285°C in case of 10 MW beam power and 20 m/s lithium flow velocity. This heat is removed by the target heat removal system, which consists of the primary Li loop, the secondary organic loop, the tertiary water loop, and the cooling tower. The secondary organic loop using alkyl diphenyls is provided to avoid any possibility of direct contact of Li and water.

The integrity of the Li loop requires that the Li temperature be high enough to maintain smooth flow during steady operation and also under transient conditions. The startup and shutdown of the Li loop are scheduled transient conditions, when the Li is circulated without beam heating. Furthermore, there will be unexpected beam trips of the IFMIF accelerators. For a long duration beam trip, full operation of the heat removal system would cause an unacceptably large decrease of Li temperature. Therefore, the transient behavior of Li and control methods for the Li temperature must be examined.

The transient temperatures and flow rates are simulated using the reactor transient code RETRAN. While the original RETRAN dealt only with water, it has been modified by JAERI to deal with Li and the organic oil. Transient behavior is examined first, for the cases of no control at startup, shutdown, one beam trip, and two beam trips. The transient behavior of the Li loop and the organic oil loop are simulated for these cases. Next, control by changing flow rates at the electromagnetic lithium pump and the organic pump or by use of heaters are examined as methods of keeping the Li temperature within the acceptable range.

Contributors

Name	Party	Institute	E-mail address
Hiroo Nakamura	Japan	JAERI	nakamurh@fusion.naka.jaeri.go.jp
M. Ida	Japan	JAERI	ida@ifmif.tokai.jaeri.go.jp
H. Kakui	Japan	IHI Co., Ltd.	YE0929@ihi.co.jp

(2) Introduction

IFMIF is an accelerator-based D-Li neutron source to produce an intense flux of high energy neutrons (2 MW/m^2) and a sufficient irradiation volume (500 cm^3) for testing candidate materials for ITER and DEMO[1]. To realize such conditions, a 40 MeV deuteron beam with current of 250 mA is injected into liquid Li flowing with a speed of 20 m/s. The major function of the Li target system is to provide a stable Li jet for production of neutrons [2],[3]. The Li target system consists of the target assembly and the Li loop. During operation the averaged surface heat flux on the flowing Li is 1 GW/m^2. The Li loop electromagnetic pump circulates the Li to and from the target assembly through the impurity purification system and the heat exchanger system. The IFMIF target loop consists of the primary Li loop, secondary organic oil loop, and tertiary water loops. Every loop, especially the Li loop, must be controlled to keep the temperature constant. The objectives of this task are to evaluate the transient thermal behavior of the Li loop during an accidental beam trip and during the transient behavior at startup of IFMIF operations.

(3) Model and Calculation Conditions

Figure 1 shows the flow diagram of the IFMIF Li loop treated in this transient analysis. The Li loop consists of the primary Li loop, secondary organic oil loop and tertiary water loops. Calculations

have used APSS-IFMIF developed by IHI Co., Ltd. In this piping model, thermal insulation layers and heaters are included under the following conditions.

- Ambient temperature : 20°C
- Thermal transfer coefficient of insulation : 10 Kcal/m^{2}hr°C
- Surface temperature on the insulation layer : 40°C
- Minimum temperature of Li at exit of Li cooler : 250°C
- Minimum temperature of organic coolant at inlet of the organic cooler : 200°C

The U tube type heat exchanger is modeled as a double pipe type heat exchanger with a correction factor for the thermal transfer coefficient. Temperature of the tertiary water at inlet of the organic cooler is constant. In a model of the electromagnetic pump, the pressure is modeled as a function between pipes.

In this model, the Li temperature at the exit of the Li cooler is controlled to 250°C by PI control with Gain P=0.1, Integration time I=500 s, Time constant T=100 s. In this model, the ratio of the flow between the secondary organic cooler and the by-pass line is controlled. Also, the flow rate in the tertiary water loop heat exchanger is controlled.

Calculation of the beam shutdown and startup cases have been analyzed for three beam current cases: 250 mA, 125 mA and 50 mA. In the case of beam shutdown, a control valve in the organic loop by-pass line is opened and water flow to the heat exchanger in the tertiary water loop is reduced when the temperature of the Li at the exit of the Li cooler falls below 250°C.

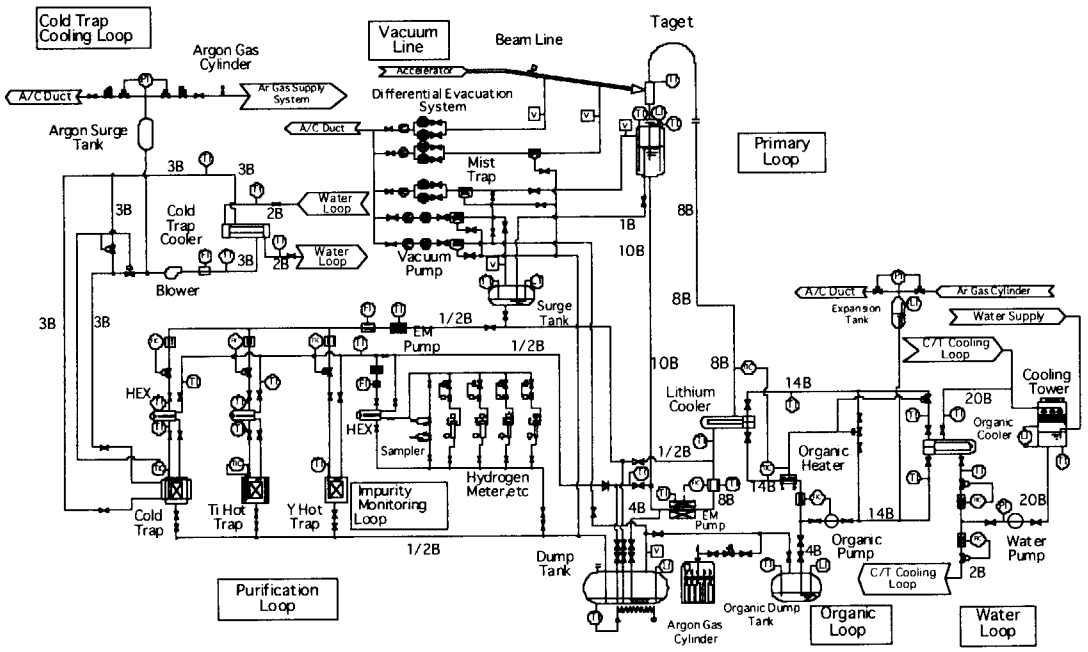


Fig. 1 Flow diagram of the IFMIF Li loop.

(4) Results

In Figs. 2 and 3, typical results for the 250 mA case are shown. Fig. 2 shows the result of the beam shutdown without control of the heat exchanger system. In this case, the organic loop and the tertiary water loop are in operation during the beam shutdown, and the temperature of Li at the exit of the Li cooler falls below the solidification temperature of Li (180°C) after 380 s. Therefore, temperature control of the organic loop and the tertiary water loops are necessary. With control of the heat exchanger system in the organic loop and the tertiary water loop, the temperature of Li at the exit

of the Li cooler is maintained at 226°C, well above the solidification temperature of Li (180°C) after 450 s as shown in Fig. 3.

Figure 4 shows the result of the beam startup from zero to 250 mA with temperature control of the organic loop and the tertiary water loops. As a result, temperatures of the Li cooler and the organic cooler reach steady state after 1000 s.

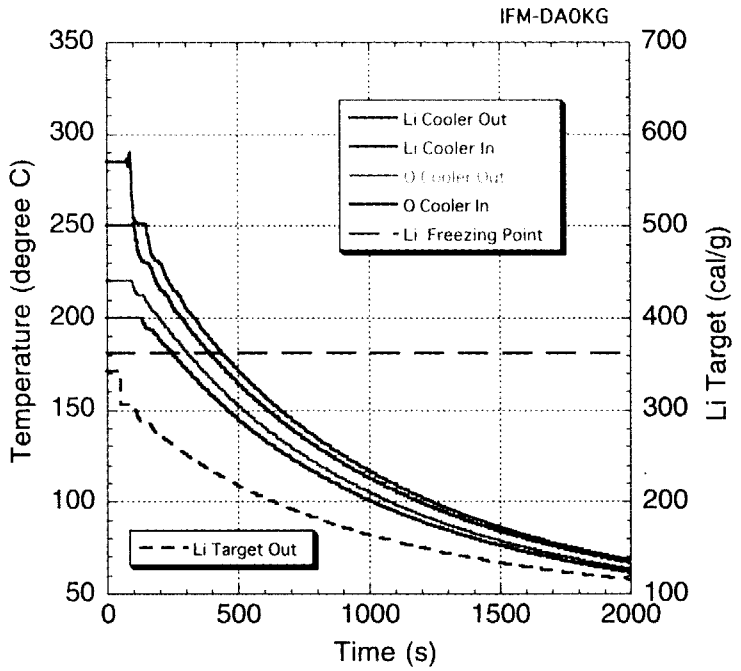


Fig. 2 Temporal behavior of the temperatures of the Li cooler and the organic cooler for the case of a beam shutdown from 250 mA to zero without control of the Li cooler and the organic cooler.

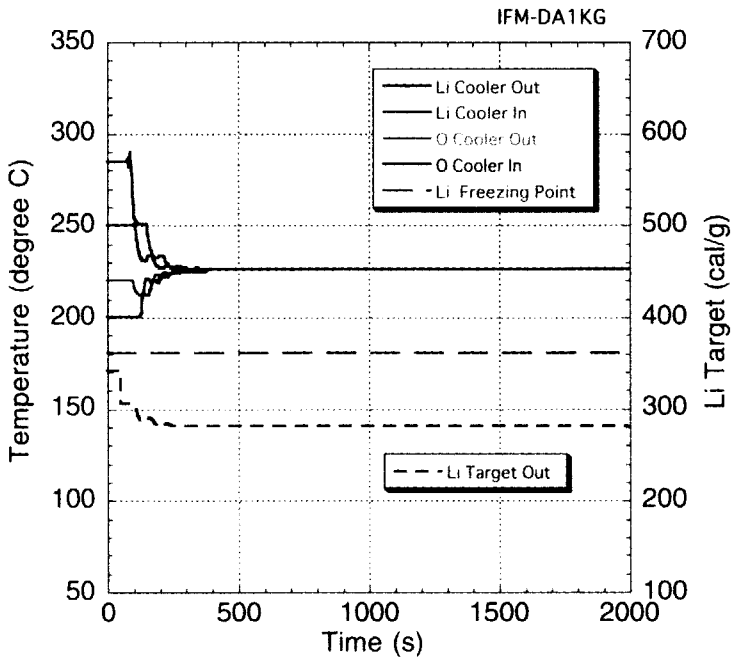


Fig. 3 Temporal behavior of the temperatures of the Li cooler and the organic cooler in case of a beam shut down from 250 mA to zero with control of both the Li cooler and the organic cooler.

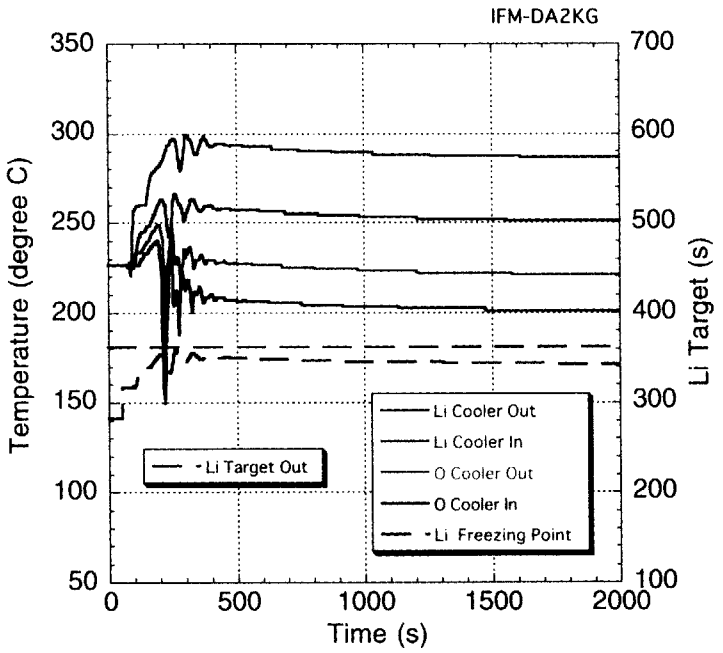


Fig. 4 Temporal behavior of the temperatures of the Li cooler and the organic cooler in case of a beam startup from zero to 250 mA with control of both the Li cooler and the organic cooler.

(5) Conclusion

With temperature control of the secondary organic loop and the tertiary water loops, the Li temperature can be maintained above the solidification temperature of 180°C in case of the beam shutdown from the maximum beam current of 250 mA.

References

[1] H. Matsui, et al., Proc. 10th Int. Conf. On Fusion Reactor Materials, Baden-Baden, 14 - 19 October 2001. paper 09.PL.3 (to appear in J. Nucl. Mater.).

[2] Hiroo Nakamura, et al., Status of lithium target system for international fusion materials irradiation facility (IFMIF), Fusion Eng. and Des. **58-59**(2001) 919-923.

[3] M. Ida, et al., Proc. 10th Int. Conf. On Fusion Reactor Materials, Baden-Baden, 14 - 19 October 2001(to appear in J. Nucl. Mater.).

3.2.18 TG81-JA : Design of a Remote Handling Device for Target Back Wall Replacement

(1) Brief Task Description

Since the back wall of the IFMIF target is used under the most severe conditions of neutron irradiation, about 50 dpa/y, it must be designed for exchange by a remote maintenance system. There are two design options for the back wall replacement. The first option is to remove the entire target assembly including the back wall and move it to a hot cell area for back wall replacement. The second option is to replace the back wall with the target assembly in place, using a remote handling device.
This task report considers the first option, and the design of a remote handling arm for welding, cutting, and assembling of the back wall and target assembly. The procedure for disconnecting the target assembly from the target cell and moving it to the maintenance cell is developed and devices used in this procedure are identified.

Contributors

Name	Party	Institute	E-mail address
H.Nakamura	Japan	JAERI	nakamurh@fusion.naka.jaeri.go.jp
M. Ida	Japan	JAERI	ida@ifmif.tokai.jaeri.go.jp
H. Kakui	Japan	IHI	YE0929@ihi.co.jp
T. Yamamura	Japan	IHI	toshio_yamamura@ihi.co.jp

(2) Design Requirements

The target assembly is connected to the main lithium pipe, quench tank and accelerator vacuum duct by flanges. The cross section of the target assembly is shown in Fig. 1. These flanges are designed as lip sealing structures, selected to avoid lithium leaks. As the first step in the removal process, the lip seals are cut remotely using a YAG laser cutting machine.

The general design requirements of the remote handling system are as follows:

i) The remote handling arm must be attached to the Universal Robot of the test facilities.

ii) The remote handling arm shall have capabilities for replacement of the target assembly in the target and test cell room by cutting and welding of the lip seals.

iii) The accuracy of assembling the target is ±0.5 mm.

iv) Weight of the target assembly for remote handling is about 970 kg.

v) The target assembly must be transferred from the target and test cell room to the tritium hot cell for replacement of the back wall.

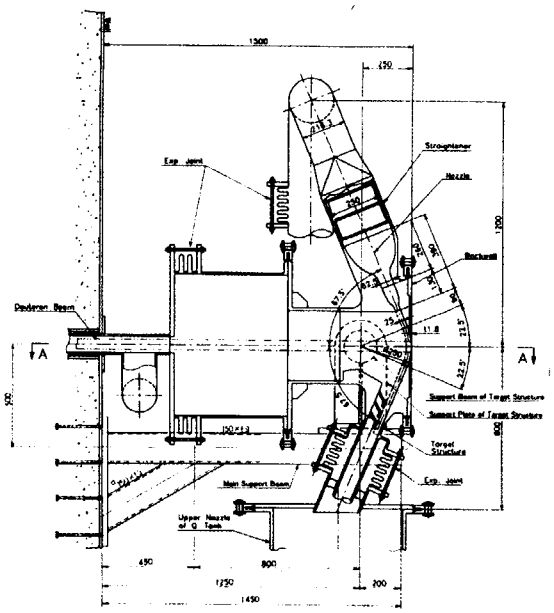


Fig. 1 Cross section of the target assembly.

(3) Remote Handling Arm

The remote handling arm is attached to the lowest part of the universal robot by a "Gripper" as shown in Fig. 2. The remote handling arm consists of a Combined Manipulator, a Lifter, and a Main

Manipulator. The main manipulator is capable of handling 200 kg and has six degrees of freedom for fine adjustment of movement. The lifter, attached to the side of the combined manipulator, is used for moving heavy components, for transfer of components from the maintenance hall, and for movement in the vertical direction. A YAG laser assembly for remote cutting and welding is shown in Fig. 3. It consists of a rail flange for positioning the cutting and welding assembly, a laser torch, and an electric motor system for moving around the flange seal and for positioning the laser torch.

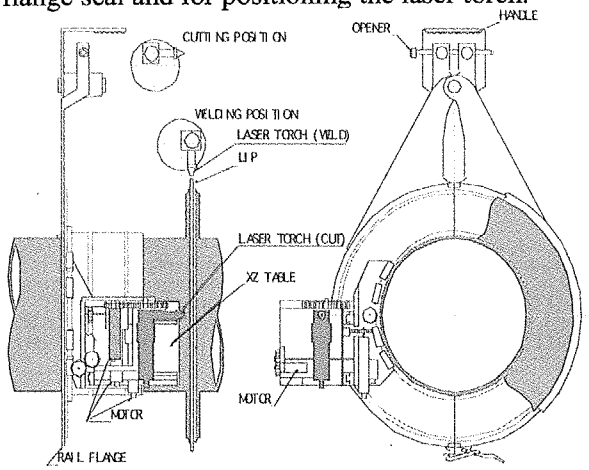


Fig. 3 YAG laser assembly for cutting and welding of lip seals.

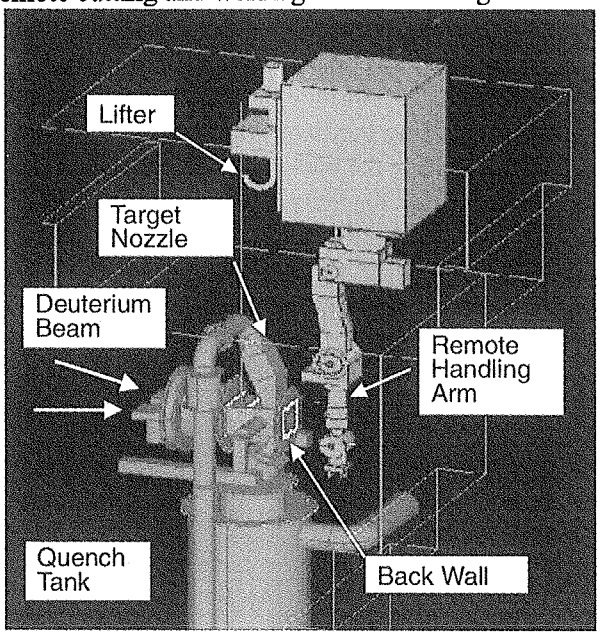


Fig. 2 3D view of the target assembly and the remote handling system.

(4) Procedure for Transfer of the Target Assembly

Transfer of the target assembly from the target cell to the maintenance cell and replacement of the back wall in the maintenance cell is divided into the following five steps.

① Release the target assembly from the main lithium loop, the accelerator beam duct, and the quench tank.

② Transfer the target assembly from the target cell to the floor of the access cell.

③ Install the target assembly into a container that will prevent leakage of any radioactive material, including tritium and Be-7

④ Transfer the target assembly container, from the access cell to the maintenance cell, through the radiation shielding hatches between cells.

⑤ Replace the back wall using the remote YAG laser cutting and welding machine.

A more detailed description on each procedure is given below.

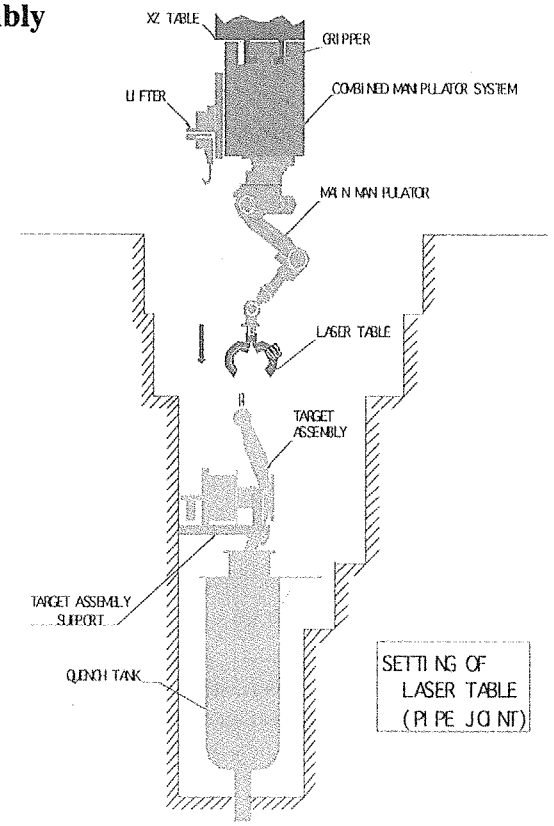


Fig. 4 Devices for removing the target assembly from the target cell to the access cell.

4-1) Remove the Target Assembly from the Target Cell

The target assembly is connected to the main lithium pipe, the quench tank and the accelerator vacuum duct by flanges. These flanges use lip sealing structures to prevent lithium leaks. As the first step, the lip seals are cut remotely using the YAG laser cutting machine. The robot system for replacing the target assembly consists of the combined manipulator, with the main manipulator, lifter, and XZ-stage gantry crane for replacing test devices.

i) YAG laser assembly for cutting and welding

The YAG laser assembly for remote cutting and welding is shown in Fig. 3. It consists of a rail flange for positioning the cutting and welding assembly, a laser torch, and an electric motor for moving around the seal flange and positioning the laser torch.

ii) Moving the target assembly

Moving the target assembly from the target cell to the access cell is accomplished using the laser table attached to the remote handling arm, as shown in Fig. 4.

4-1-1) The procedure for releasing the target assembly from the accelerator beam duct is as follows. The concept of this procedure is shown in Fig. 5.

a. Hold the laser table and move it to the flange of the beam duct using the gripper.
b. Fit the laser table to the beam duct using an electric wrench.
c. Cut the lip weld using the YAG laser.
d. Move the laser table from the position of the beam duct.

4-1-2) Procedure for releasing the target assembly from the lithium inlet pipe (Fig. 6).

a. Hold the laser table and move it to the flange of the lithium inlet pipe using the gripper.
b. Fit the laser table to the inlet piping near the flange using an electric wrench.
c. Cut the lip weld using the YAG laser.
d. Move the laser table from the inlet pipe.

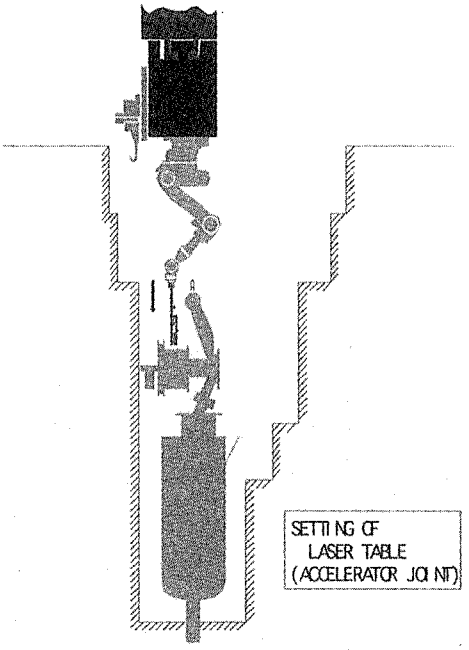


Fig. 5 Procedure to release the target assembly from the accelerator beam duct.

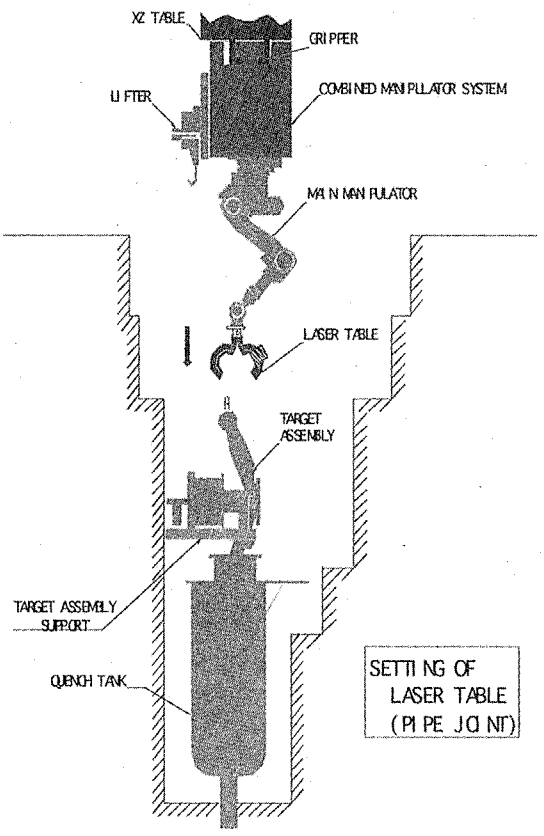


Fig. 6 Procedure to release the target assembly from the lithium inlet piping.

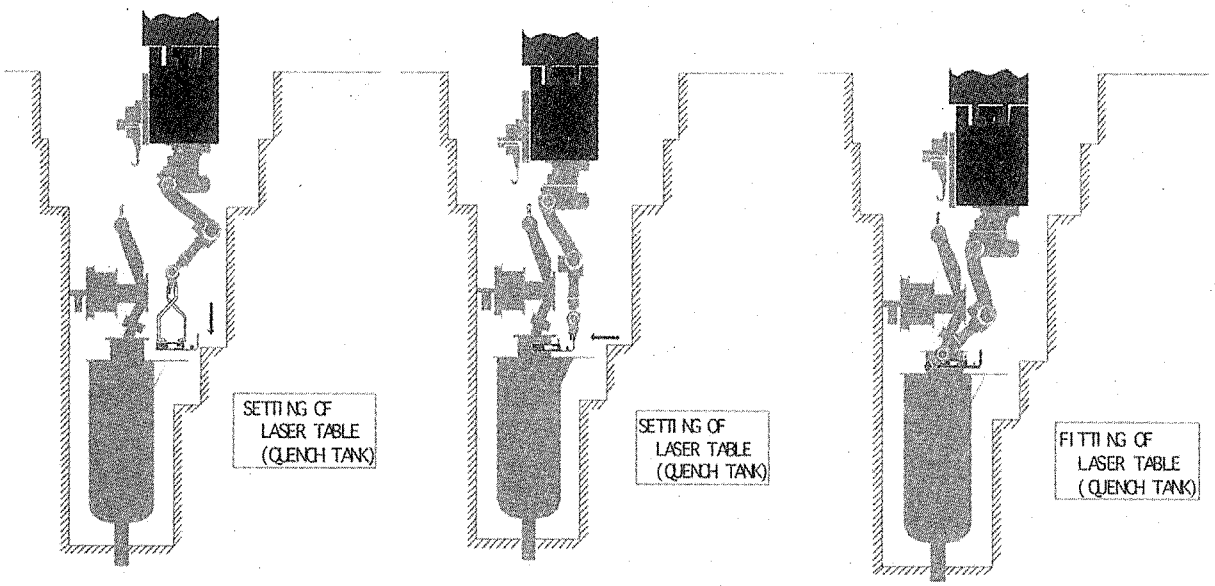


Fig. 7 Procedure to disconnect the target assembly from the quench tank.

4-1-3) Disconnecting the target assembly from the quench tank (Fig. 7).

a. Hold the laser table and move it to the flange of the quench tank using the gripper.
b. Fit the laser table to the flange using an electric wrench.
c. Cut the lip weld using the YAG laser.
d. Move the laser table from this flange.

4-1-4) Moving the target assembly from the target cell to the access cell (Fig. 8).

a. Connect the hook of the lifter on the combined manipulator to the eye-bolt of the target assembly, using the adapter
b. Disconnect the target assembly from the support structure using an electric wrench.
c. Lift the target assembly from the target cell to the access floor using the lifter and manipulator fittings on the combined manipulator.
d. Move the target assembly from the target cell to the access cell.

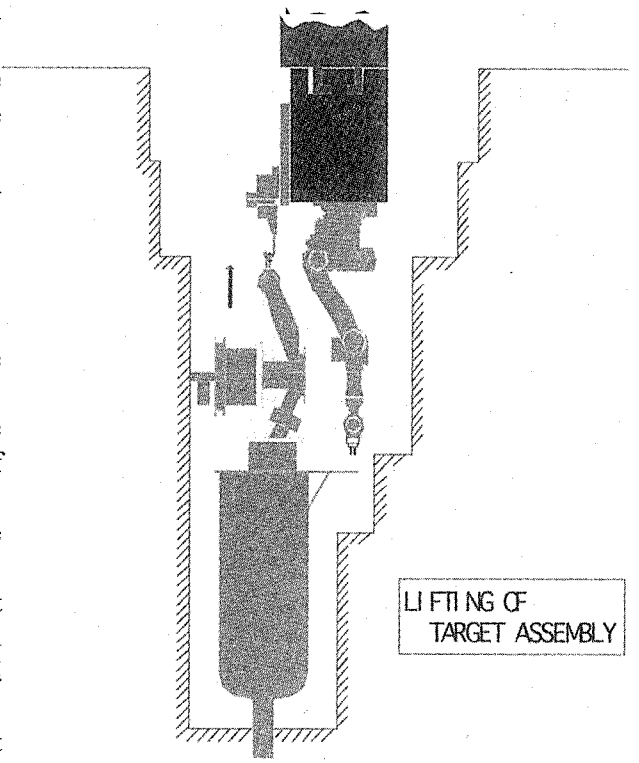


Fig. 8 Moving the target assembly from the target cell to the access cell.

4-2) Transportation of the Target Assembly from the Access Cell to the Maintenance Cell

The target assembly is carried from the target cell to the access cell, transported to the maintenance cell, and it's back wall replaced there. This section outlines the procedures and devices used for these operations.

4-2-1) Procedures for transportation

i) Removal from the target cell and setting into the container box

The target assembly is lifted from the target cell by the manipulator and gantry crane and installed in the container box to avoid spreading radioisotopes produced by the deuterium bombardment of lithium. A cover is put on this container box and bolted closed remotely, using an electric wrench.

ii) Transportation of the container box from the access cell to the maintenance cell

Container box is placed on a set of rollers for translation and transfer to the maintenance cell. The procedure for (i) and (ii) is shown in Fig. 9.

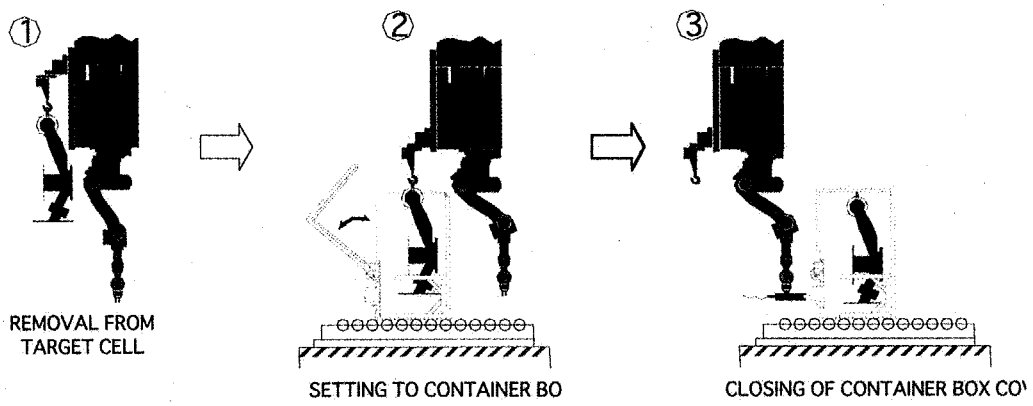


Fig. 9 Procedure for moving the target assembly from the access cell to the maintenance cell.

4-2-2) Replacement of the back wall

i) In the maintenance cell, the container box is opened and the target assembly moved to the base of the welding machine, using the crane and manipulator in the maintenance cell. Remote handling of the target assembly in the maintenance cell is shown in Fig. 10.

ii) The back wall is cut from target assembly and replaced with a new back wall using the remotely operated YAG laser cutting and welding machine. The YAG laser cutting and welding system for replacing the back wall is shown in Fig. 11.

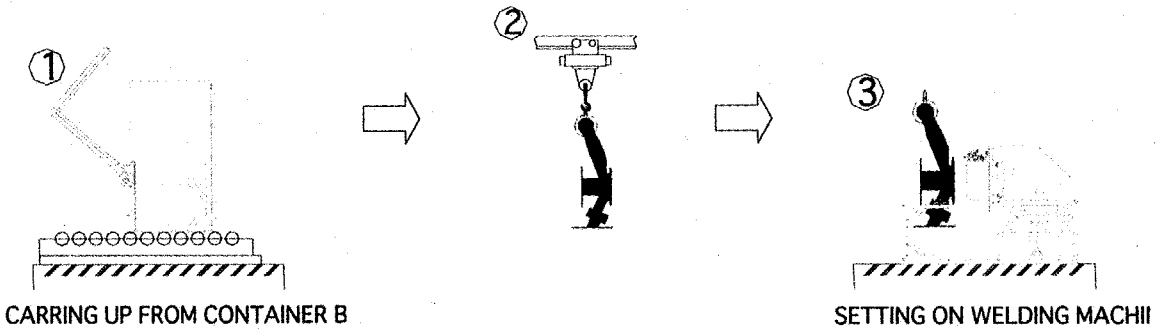


Fig. 10 Remote handling of the target assembly in the maintenance cell.

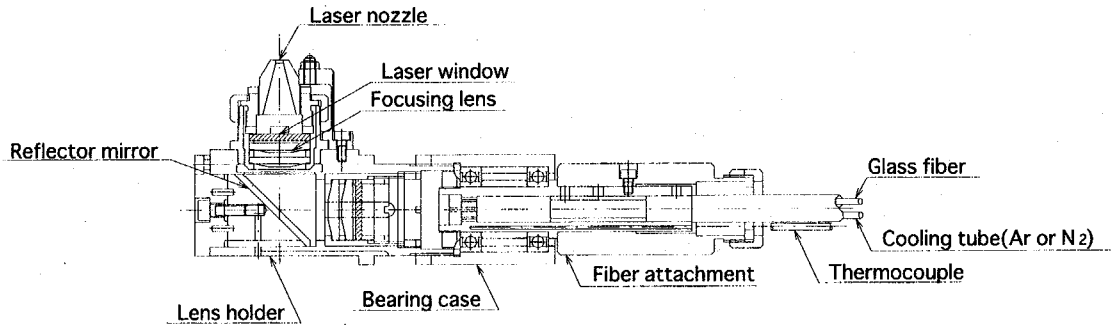


Fig. 11 YAG laser cutting and welding system for replacing the back wall.

3.2.19 TG-82-EU : Detailed Design, Fabrication and Remote Handling Test of the Removable Back-plate

(1) Brief Task Description

The reference IFMIF lithium target design foresees the use of a replaceable backwall in order to improve component reliability and lifetime, and to reduce the disposal of irradiated material. During the CDA phase ENEA has proposed a replaceable back-plate concept based on the so called bayonet concept. This task deals with the design, manufacturing, testing and remote handling of bayonet back-plate mockups. The activity involves ENEA Association and Italian companies.

Contributor

Name	Party	Institute	E-mail address
G. Micciché	EU	ENEA	gioacchino.micciche@brasimone.enea.it

(2) Introduction

The reference IFMIF target design is based on the concept of a replaceable backwall. The backwall is the component most heavily exposed to the high neutron flux, and so its lifetime is expected to be very short (approximately a few months).The replaceable backwall concept, first proposed during the 1st IFMIF-CDA Technical Workshop, held July 18-21 1995 in Tokai (JA), allows significant reduction of both the target substitution time and the quantity of irradiated material for disposal, and was aimed at improvement of the plant duty factor, with related cost reduction. The back-plate design proposed by ENEA (the so-called bayonet back-plate concept) was introduced at the 2nd Design Integration meeting in May 1996, and has a major advantage for RH operations in that it can be replaced without removing the Vertical Target Assembly (VTA). The experimental activities are aimed at validating the overall concept, developing the back-plate design, and mockup of the remote handling operation required to remove and replace the back-plate.

The remote handling activities are performed at the ENEA Research Centre using an experimental hot-cell facility equipped whit the necessary special equipment and tools.

(3) Design and Fabrication of the Back-plate Mock-up

The back-plate mockup is shown in Figs. 1a-1b-1c. It consists of a stainless steel AISI 316 plate that can be inserted or removed from the frame by means of a manipulator with a dedicated interface. The back-plate mockup is approximately 55 cm square with 15 cm deep sidewalls and weighing about 60 kg. The frame will be manufactured from the same material as used for the back-plate. A pair of pins (upper and lower on the back-plate) guides the back-plate and protects the gasket from damage during insertion. As can be seen in Fig. 1 the back-plate is locked in place by a system of skates and bolts at the end of its travel. The locking system consists of three skates mounted in upper, lower and lateral positions on the frame, and six bolts in the remaining side. Each skate, as shown in Fig. 1b, is by a structure with six triple bearings on six parallel axes. Each bearing axis comprises three wheels: the external ones pushing on the back-plate while the central one runs on the inclined plane. These locking systems provide a force up to 7.5 Tonnes on the gasket that seals the edge and maintains the required vacuum gradient between the target chamber (10^{-3} Pa) and the test cell (10^{-1} Pa). The gasket ensures a maximum leak rate of 10^{-10} Pa $*m^3$ /sec, and it is fitted into a circular groove between the front face of the back-plate and its matching surface on the permanent target structure. The gasket characteristics are given in Table 1 together with the main mock-up components. The radius of the backwall curvature has been calculated at 250 mm. This value allows optimum coupling between the backwall and the nozzle (inlet-outlet), while minimizing the discontinuities to improve stability of the lithium jet [1]. The reference requirements for the test equipment design are given in Table 2. Figure 2 shows a 3D model of the back-plate. Preliminary tests have been carried out to validate the mechanical concept, in particular the locking system (Fig. 3), and have given positive results. The tests involved a section that reproduces one side of the mock-up, where locking and

unlocking operations were carried out with the test section maintained at 300°C. During the tests, the external locking torque applied and the resulting load on the back-plate were measured.

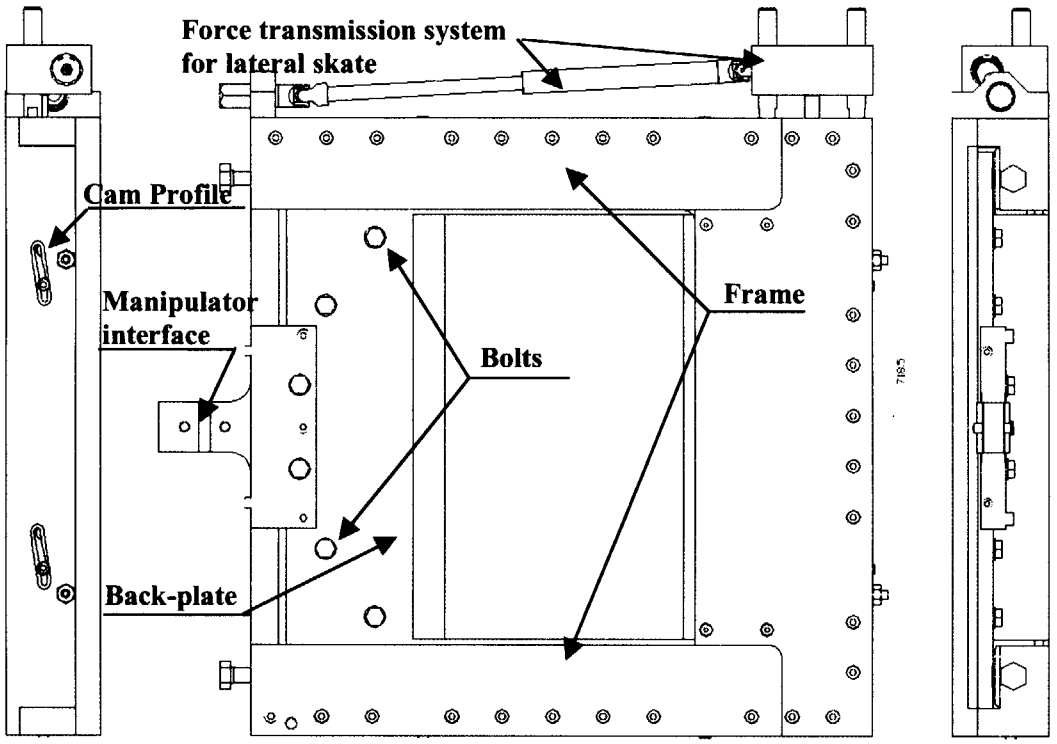


Fig. 1a General view of back-plate mock-up design.

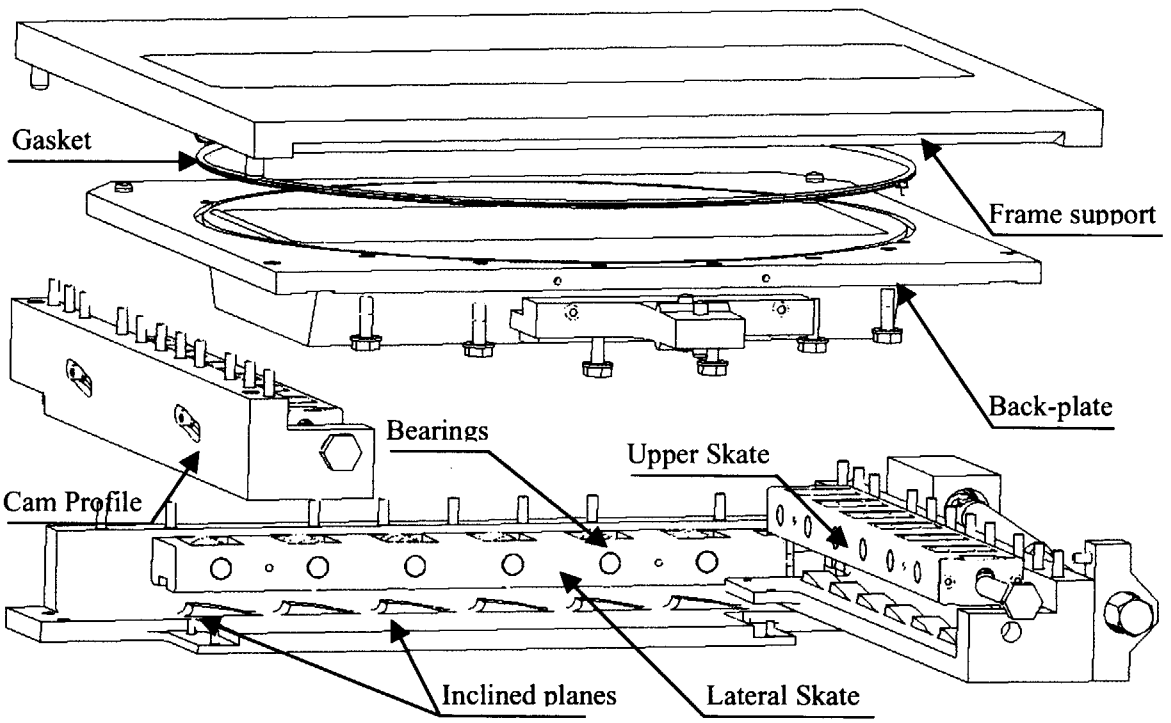


Fig. 1b Main components of replaceable back-plate mock-up.

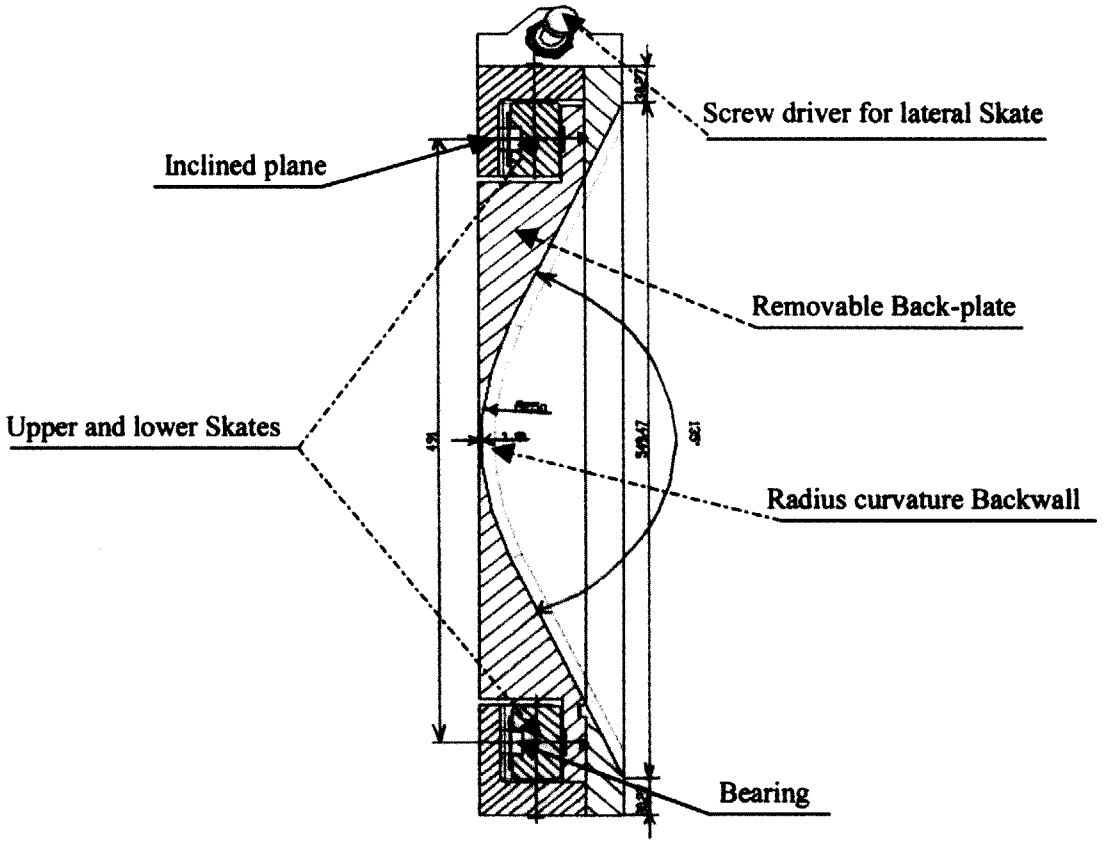


Fig. 1c Lateral view of back-plate mock-up.

Table 1 Main components characteristic.

Back-plate	Stainless steel AISI 316L, 60 kg (weight) 55 cm (width) x 55 cm (Height) x 15 cm(depth)
Frame mock-up	Stainless steel AISI 316L , 70 kg (weight) 71,85 cm (Height) x 61,5 cm (width) x 9,5 cm(deep)
Skate	Stainless steel AISI 316 L bearings INA STO15 and INA NATV15
Metallic Gasket	ARMCO / SS 304 L / NIMONIC 90 Ø488.90 x Ø498.30 x 4.7/4.6 mm.

Table 2 Reference requirements.

Vacuum in the target chamber	10^{-3} Pa
Vacuum outside the target chamber	10^{-1} Pa
Leak rate	10^{-11} Pa * m^3/sec
Lithium inlet/outlet temperature	250 °C / 300 °C
Temperature peaks	Up to 400 °C
Tightness force required	32 Tonnes
External Torque for bolt	11 Nm

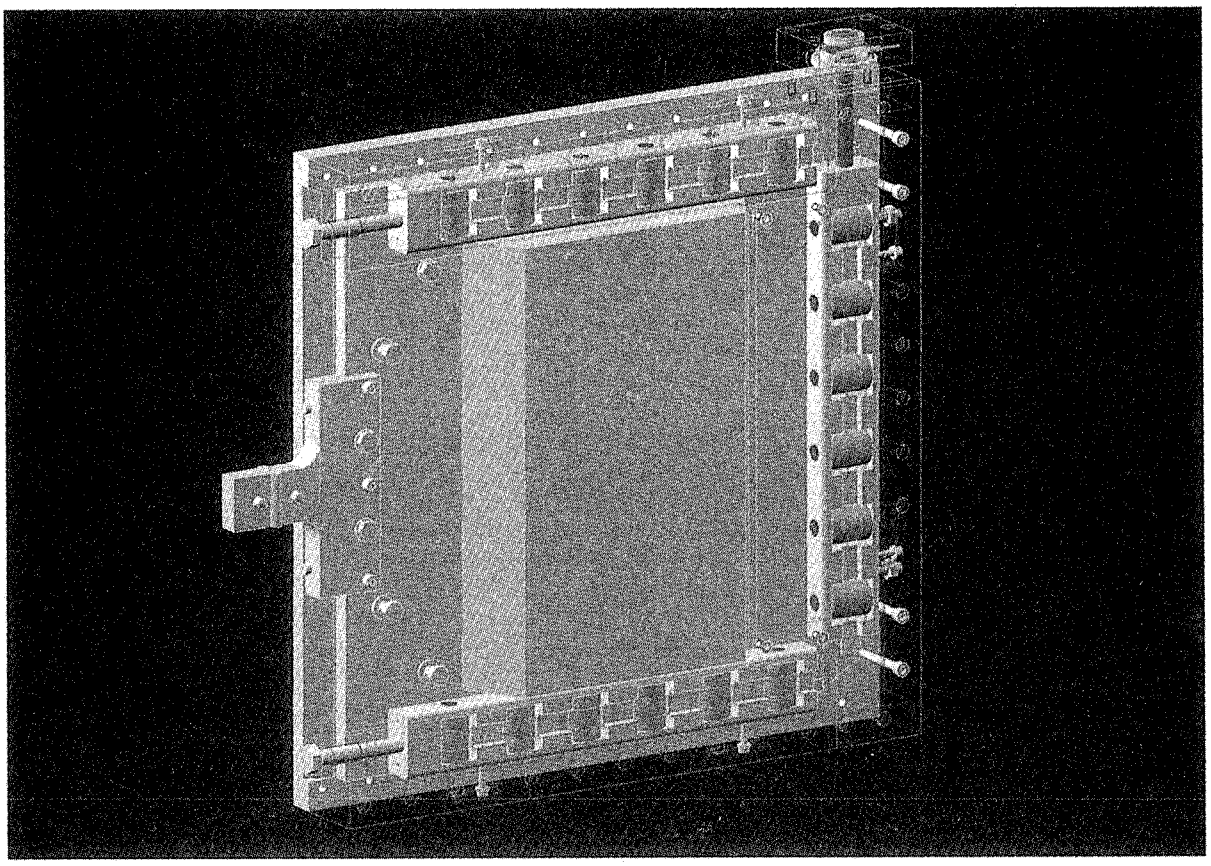


Fig. 2 3D Back-plate model under construction.

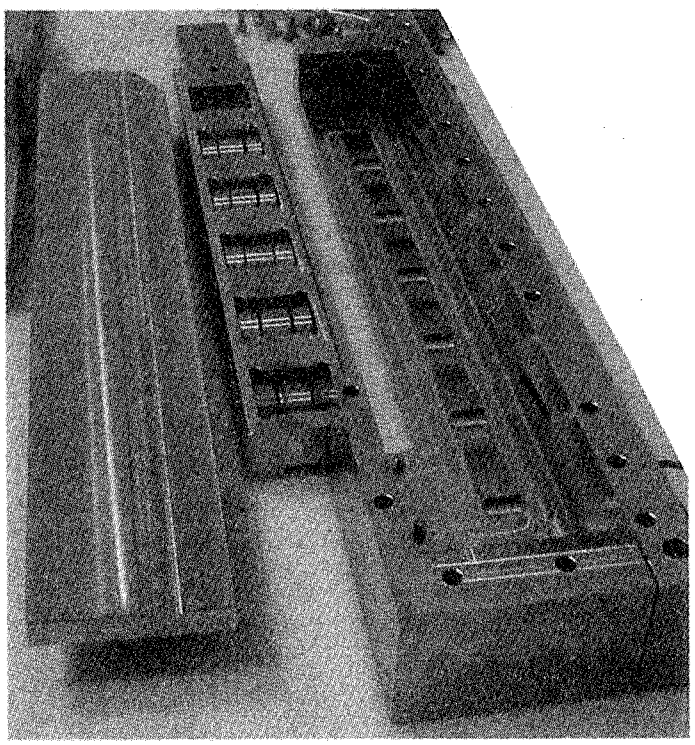


Fig. 3 Detail of the locking system.

(4) Test Facility and Remote Handling Activity

The remote handling activities are being performed by using the existing facility at the ENEA Brasimone Research Centre, which is well suited to carry out the feasibility trials needed to replace the IFMIF back-plate. The RH arrangement foresees a separation of the hot cell simulating area from the operator area by an opaque screen to enable relevant remote operations, i.e. no direct vision is possible [2]. The dimensions of the hot cell simulating area have been reduced by screens to 3x1 m^2 with height 2.5 m. The back-plate replacement requires the complete bolting/unbolting of the three skate systems and associated bolts. The time to complete these operations is estimated at two days [1]. The RH procedures were defined and tested using a dummy back-plate (see next paragraph), and were centered on the basic sequence required to remove and install the back-plate.

Although these operations may seem simple, the limited space around the mock-up represents a major problem. The dummy is a simplified back plate mock-up, with the same dimensions, weight and center of gravity as the original. Fig. 4 shows the experimental insertion trials of the dummy back-plate, and each step is reported in Table 3. The time required to execute these operations was measured. The trials also checked the ability of each component to perform its task – in particular the interface between the back-plate and the manipulator arm was optimized to give the best coupling – and to characterize the working range of the equipment.

Table 3 Sequence of demo back-plate insertion.

Use of:

In the Hot Cell

- heavy manipulator;
- light manipulator (slave arms);
- special tools

In the operator area

- main control panel;
- light manipulator (master arms);
- viewing system;
- recording system;

Precondition:

- the frame is empty;
- the interface between the back-plate and the manipulator gripper is fitted;

Sequence of principal actions:

- put the back-plate in front of the frame in a working position, ready to insert the back-plate;
- insert the **BP** into the frame;
- rotate each **SAW** to clamp the back-plate;
- tighten the screws on the left-side of the back-plate.

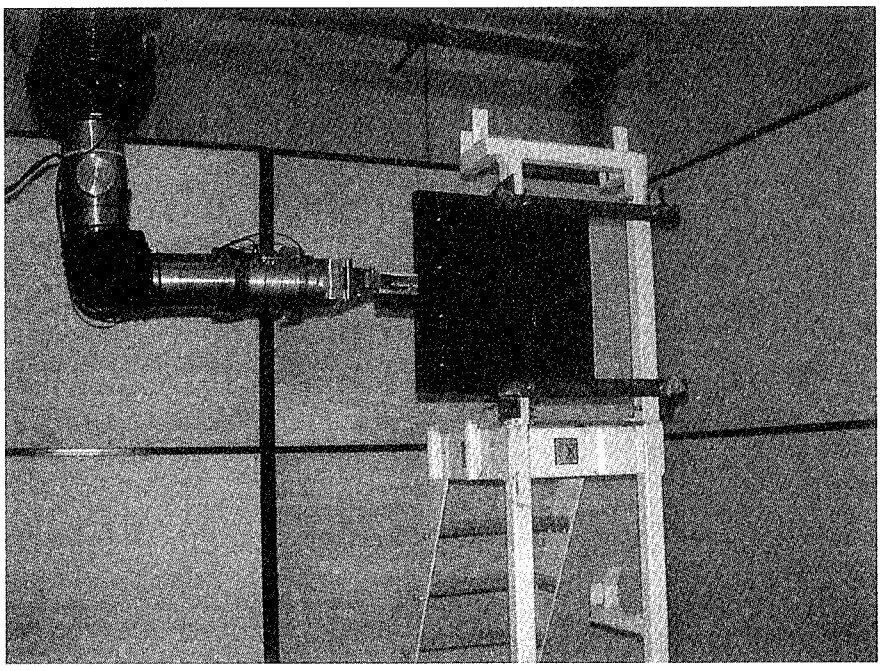


Fig. 4 Trials with dummy back-plate.

(5) Conclusions

A mockup of the IFMIF target back-plate, based on the bayonet concept, has been fabricated. This will enable remote handling trials to take place in the ENEA Brasimone Research Centre hot-cell mockup facility, with a view to evaluating the remote replaceability of the back-plate. Some preliminary quantitative tests on the locking system of the mock-up have given good results and indicate that the design will achieve its intended objective.

A number of simple trials have also been carried out successfully on a dummy back-plate mockup to gain some early impressions of the viability of the remote handling principles, procedures and time required to exchange it.

References

[1] M. Martone,(editor), IFMIF International Fusion Material Irradiation Facility Conceptual Design Activity Final Report, ENEA Frascati Report , RT/ERG/FUS/96/11, November 1996.

[2] G. Micciché, M.Muzzarelli, C.Antonucci, Target assembly with removable backwall and related remote handling equipment.

3.3 Test Facilities

3.3.1 TF11/12-EU : Helium-cooled High Flux Test Module: Design Improvement, Fabrication of Sub-assembly and Thermal Hydraulics Testing

(1) Brief Task Description

Providing a test module for specimen irradiation temperatures between about 250 and 1000°C is one of the most challenging design requirements for the IFMIF Test Facilities. The successful development of a He-cooled test module will provide for any material a broad range of possible irradiation temperatures, simultaneous irradiation of rigs having different temperatures, as well as flexible and safe operating conditions.

As a first step, a fundamental re-evaluation of the existing reference design was performed, including (1) detailed thermal hydraulics and fluid dynamics calculations and (2) FE-optimized design of an improved test module mockup that can be equipped with a representative number of rigs. The thermal hydraulic calculations take into account potential irradiation induced creep and swelling as well as the nuclear decay heat and beam-off times. An evaluation of whether the nuclear decay heat could replace very complicated electrical heaters during beam-off periods was also attempted. In a second step an assessment of manufacturing processes for specimen encapsulation, piping, and active ohmic heating elements was done together with a validation of heat transfer and pressure loss calculations. Finally, in a third step, construction and fabrication of one test module mockup and an adequate number of specimen capsules was done using a reduced activation ferritic/martensitic steel. The fabrication was also necessary to validate assembly, disassembly and precise positioning of capsules, rigs and specimens.

Contributors

Name	Party	Institute	E-mail address
V. Heinzel	EU	FZK	Volker.heinzel@irs.fzk.de
S. Gordeev	EU	FZK	Gordeev@irs.fzk.de
U. Fischer	EU	FZK	ulrich.fischer@irs.fzk.de
S. Simakov	EU	FZK	simakov@irs.fzk.de
A. Möslang	EU	FZK	anton.moeslang@imf.fzk.de

(2) Introduction

The reference design of the IFMIF, described in the CDA report [1], envisages a High Flux Test Module (HFTM) with 27 rigs. The rigs house capsules which enclose the material specimens to be irradiated. The rigs have an almost square cross section. Due to the irradiation with neutrons and gamma radiation, the specimens and the structural materials exhibit an internal volume heating. The rigs are cooled with helium flowing upward at the outside of the rig walls. The gap inside the rig and between the capsule walls acts as thermal insulation. The capsule is surrounded by electric heaters. These keep the capsule and specimens at constant temperatures independent of nuclear heat spatial distribution and fluctuation.

The rigs are positioned in a container. The inlet section to the container has to distribute the helium evenly to all gaps within the rigs. According to the preceding nuclear analysis, reflector elements were arranged lateral to the container. Steel extensions of the rigs provide an axial reflector.

The redesign of the HFTM aims at "maximum space and flexibility for the specimens" which means on the other hand "minimum space for heater, coolant channels and structural material". The nuclear volume heating causes temperature gradients within the specimen and the structural material. The heat transfer from the specimen via the capsule and the rig walls to the helium with variation of the heat transfer coefficient in the helium channel and the increase of the helium temperature along the channel creates a complex temperature distribution. In addition, the nuclear heat density has a spatial distribution. The rig design and the layout of the electric capsule heaters have to cope with and minimize the temperature differences within the specimen stack.

(3) Spatial Distribution of the Nuclear Heat Density

The nuclear calculations indicate an overall power of $P_{nucl,av}$ = 7 kW. The power density in the volume for the specimens is about 25 W/cm^3 at maximum and 14 W/cm^3 on average. (The power release within the reflector is not considered in the following analysis.) For a first survey of the helium cooling, we assume a balance of power density and power shape with electric heaters and reserves of additional 20% for heat release in the structural components and the container, an overall power of P_{total} = 15 kW has to be removed. We further limit the temperature increase for the helium flowing along the rigs to ϑ = 30°C so that the resulting axial temperature gradient for the specimens is small. This leads to a helium mass flow rate of $\dot{m}$ = 96 g/s. For a rig arrangement like that of the reference design, a gap between the rigs of δ = 1 mm and a helium pressure of 0.2 MPa results in a helium velocity of about c_{He} = 300 m/s. The Reynolds number is about Re = 9000 [2].

Fig. 1 shows the power distribution results of the nuclear calculation [3]. The figure also depicts the geometry of the HFTM of the reference design. However an earlier nuclear calculation required an extension of the HFTM in the axial direction of about 80 mm for optimal exploitation of the neutron beam. From Fig. 1 we can take the power density gradients in all three dimensions. Only at the beam entrance side does the power density vary within about 15% in the x-direction for 80 mm and in z-direction for about 15 mm. In the y-direction the power declines by a factor of 3 within the region of interest. As this is the region with the highest power density our detailed analysis of the temperature field in the rigs and the heat removal mainly concentrated on this position in the container.

(4) Rigs with Chocolate Plate like Cross Section

The design analysis started from the reference design with rigs of almost squared cross sections. The reasons for the transition to chocolate plate like cross section are given before the new design is presented.

(4.1) Rig design with squared cross section

The temperature distribution within the specimen volume of a squared rig was calculated with the code PERMAS for the highest power density at the beam entrance position. Only with a

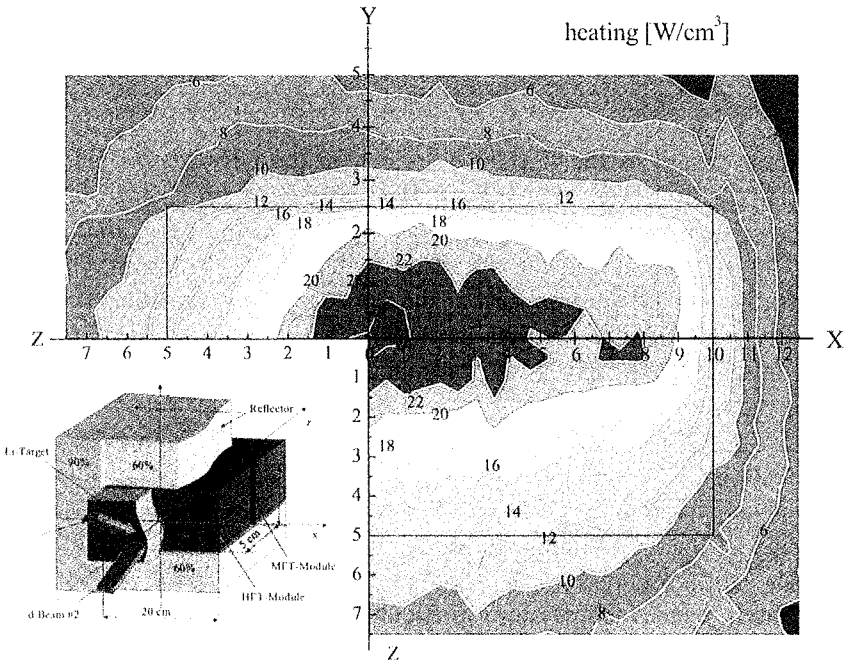


Fig. 1 Heat production in and around the HFTM with EUROFER steel reflector of 10 cm thickness (bottom). Black lines show geometrical boundaries of the reference test module (20×5×5 cm^3).

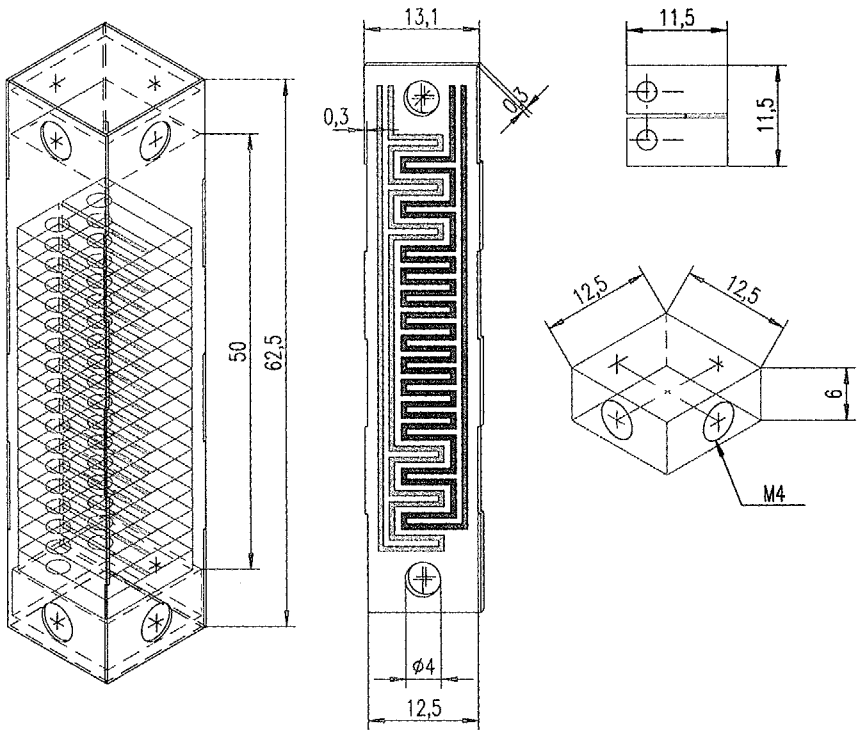


Fig. 2 Open capsule with flat heater plates.

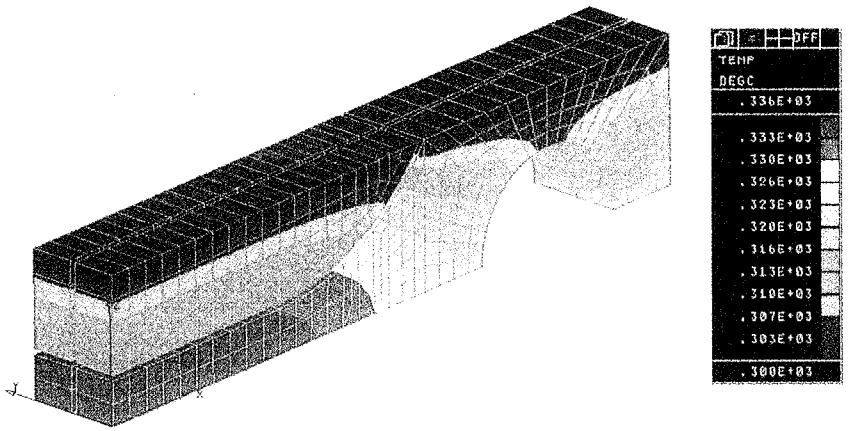
temperature control or heat removal from all 4 rig sides could the temperature variation can be kept below 10°C. This entails a cooling gap on the four sides of the rigs and for temperature control at beam shutdown situation electric heaters on all four surfaces of the capsule.

In section 3 the nuclear power density gradient in the axial direction was addressed. Additional heaters are necessary in order to balance the power and to prevent an axial temperature gradient. To achieve such a power distribution with electric jacket wire heaters as usually applied would require too much space. Therefore, less space-consuming flat plate heaters were suggested. A design is shown in Fig. 2. Two heaters are embedded in a ceramic carrier. They can be arranged so that they balance the nuclear heating as well as create an appropriate power distribution without a nuclear contribution. A promising development on the basis of AlN-ceramic with heating elements of TaC is being investigated in collaboration with a ceramic manufacturer.

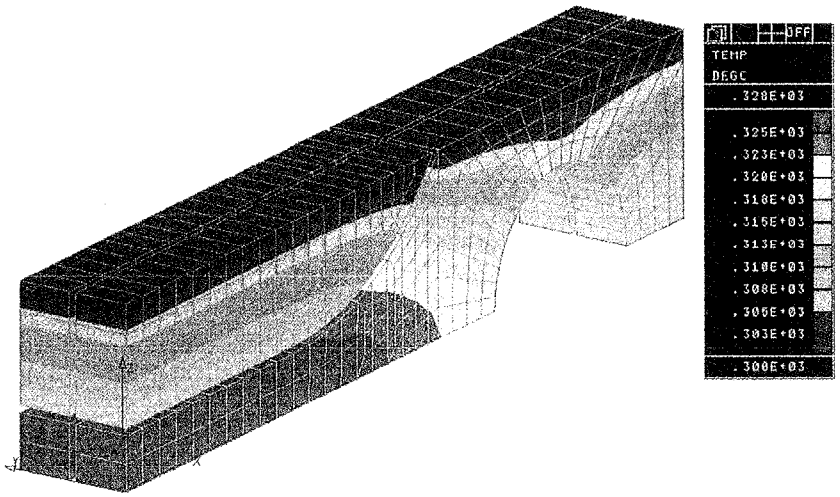
(4.2) Heat transfer from specimen to specimen to capsule wall

Specimens inserted into the capsule will fill up the space according to their shape. This will alter the nuclear power release on the one hand. This may be mitigated by using filler pieces. On the other hand, the power must be transported across the boundary from specimen to specimen and finally to the capsule wall. However, the heat transfer can hardly be defined or guaranteed in practice if the gaps are filled by a gas. This is demonstrated in Fig. 3, where the gap width was changed from 0.02 (top) to 0.01 mm (middle). The lower figure shows the temperature distribution for a gap filled with sodium. The temperature variation falls to 15 C compared to 36°C in the upper case.

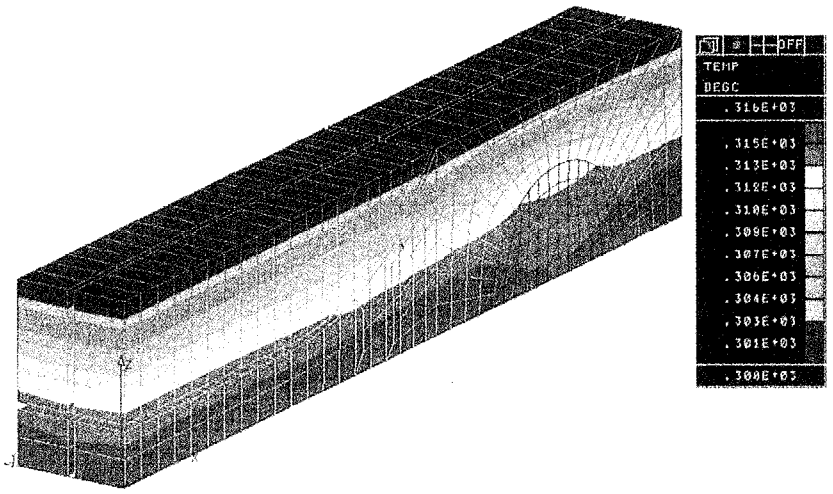
Supplemented by further analysis, the results led to the decision that the capsules have to be filled with sodium. Nuclear calculations showed that the small amount of sodium in the capsules had no impact on the neutron flux or the power generated. The use of the eutectic alloy Na/K in order to simplify the handling is still under discussion. Capsules filled with a liquid metal preclude the open boxes with flat heater plates as shown in Fig. 2. Therewith, electric heaters of the jacket wire type have to be used. Independently, however, the development of flat ceramic heaters is continued for use in capsules in positions with lower power density.



He gap of 0.02 mm between the specimen and a steel filler peace



He gap of 0.01 mm between the specimen and a steel filler peace



Gap between the specimen and the steel filler peace filled with Na
The nuclear power is 28 W/cm^3, the cooling temperature 30°C.

Fig. 3 Temperature distribution in a specimen for stress analysis together with a steel filler piece, calculated with the code PERMAS for a volume heating rate of 28 W/cm^3; the gap between the filler peace and the specimen is filled with helium at a width of 0.02 mm (top), 0.01 mm (middle) and filled with sodium (bottom).

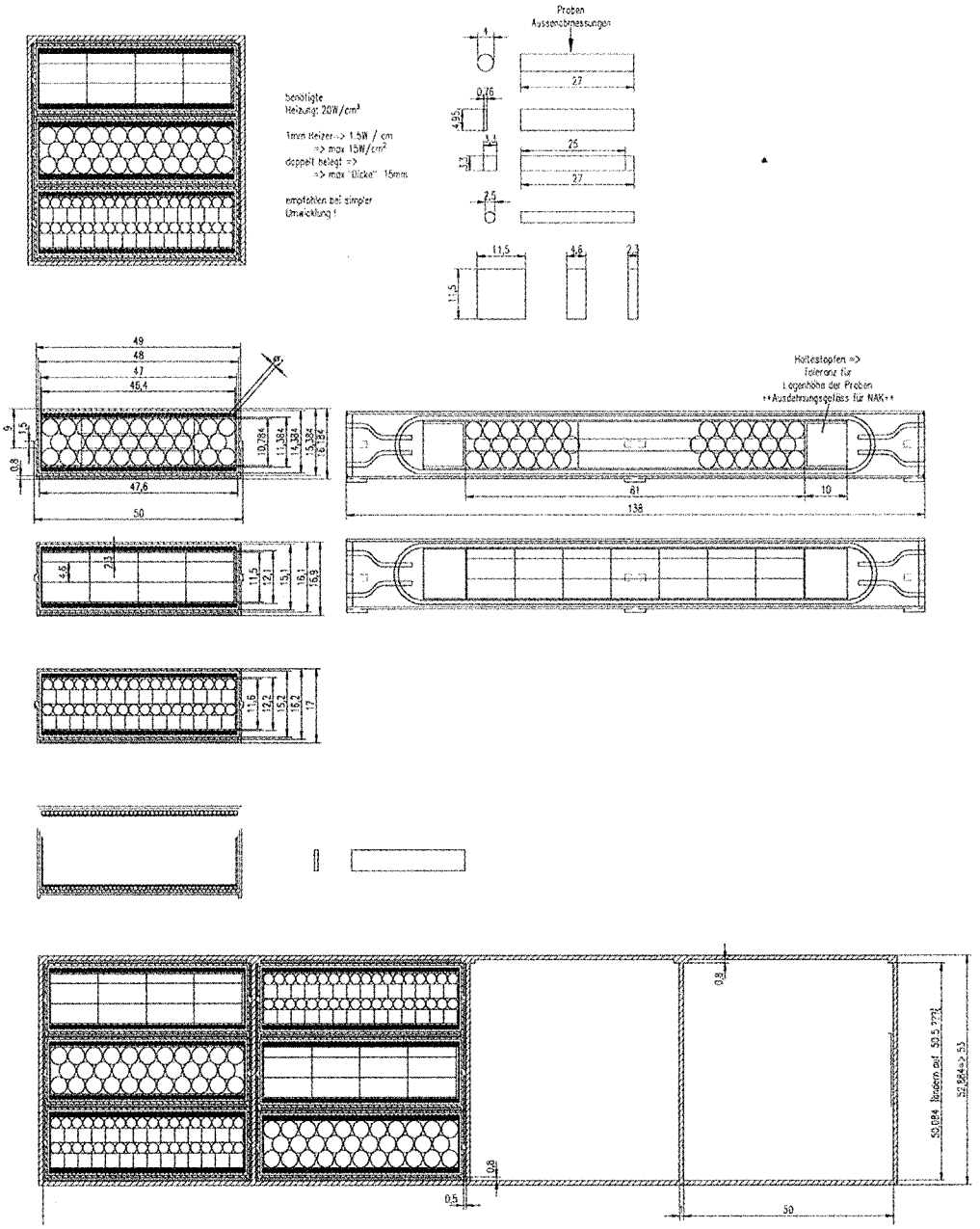


Fig. 4 Rigs with chocolate plate-like cross section installed in the container which is subdivided into four compartments; the specimen types are depicted at right top; studies with specimen arrangements are shown on the left side; the container with compartments and rigs is presented below.

(4.3) Chocolate plate rigs design

Smaller width of the specimen volume, the need for wire heaters, and the need for reduced space for the wire heaters led to the decision to analyse rigs with a chocolate-plate-like cross section. The wish to keep individual rigs independent at different temperature levels caused the subdivision of the container into four compartments filled with 3 rigs each. The major contour dimensions of the specimen are shown in Fig. 4 (top right). Different arrangements of the specimen within the capsules were studied Fig. 4 (left). It was found that the more completely the space was used for a maximum number of specimens, the less flexibility in changing specimen types or in the option of preserving a certain position for an individual specimen.

Mainly two rig types were analysed in detail, with some variants each. Fig.4 (middle right)

shows the variant with wire heaters wound vertically around the capsule. The axial inner length of the capsule to hold the specimen stack is 81 mm. The length in horizontal or x-direction (see Fig.4) is 46.4 mm and the width 10.74 mm. The capsule is closed by weld seals at both ends. The seam is located at an extension of the capsule wall and therewith removed from the high flux area. (An expansion volume for the sodium still has to be added to this design.) Additional axial heaters may be installed in the hat-like end closures of the capsules. Spacer pins with low heat conduction secure the position in the rigs. On one side of the rig spacer pads keep the distance to the container wall or the next rig. These form the helium channel with only one manufacturing tolerance.

The electric wire heaters are embedded in grooves on the capsule. Caps with a comb-like outer surface are fixed to the end closure hats. They extend the heater positioning grooves so that the heater wires can be wound like a coil around the capsule ends.

(4.4) 2D thermal analysis of the chocolate rig with variable gap between capsule and rig walls

As noted earlier, the electric heaters on the capsules have to control the temperatures of the specimen at different temperature levels during beam operation, as well as during short beam-off periods. They have to supplement the nuclear power and cope with the nuclear power variation in the axial direction. During beam-off periods this non-uniform power contribution is not present.

In order to advance with one heater coil, we analysed a design where the gap between capsule and heater was varied in axial direction. It increases step wise from the specimen stack midplane to the upper and lower stack ends, thus providing a step wise increase of the thermal barrier between capsule and rig. The 2-D simulation with PERMAS assumes a constant helium temperature and heat transfer coefficient on the outside of the rig.

For comparison, Fig. 5a presents a reference design with a constant axial gap width. With nuclear heating only, the relative temperature difference in the specimen stack amounts to 127°C. If the gap width is enlarged in 3 steps, the temperature difference is reduced to 14°C. However, for the beam-off situation a temperature difference of 64°C occurs, whereas the constant gap width has a relative temperature variation of only 7°C (Fig. 5b). Fig. 5c demonstrates that a heater system with incrementally differentiated heater power in the axial direction is indispensable.

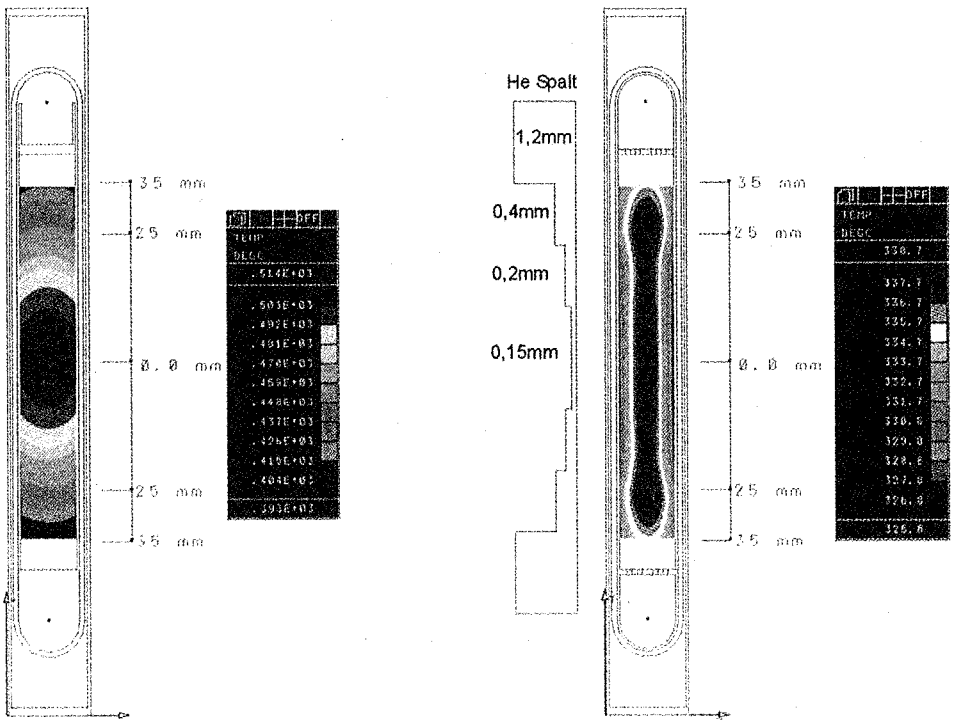


Fig. 5a Specimen capsule with constant (left hand side), and variable (right hand side) He gas gap between specimens and inner capsule wall. Only nuclear heating is taken into account.

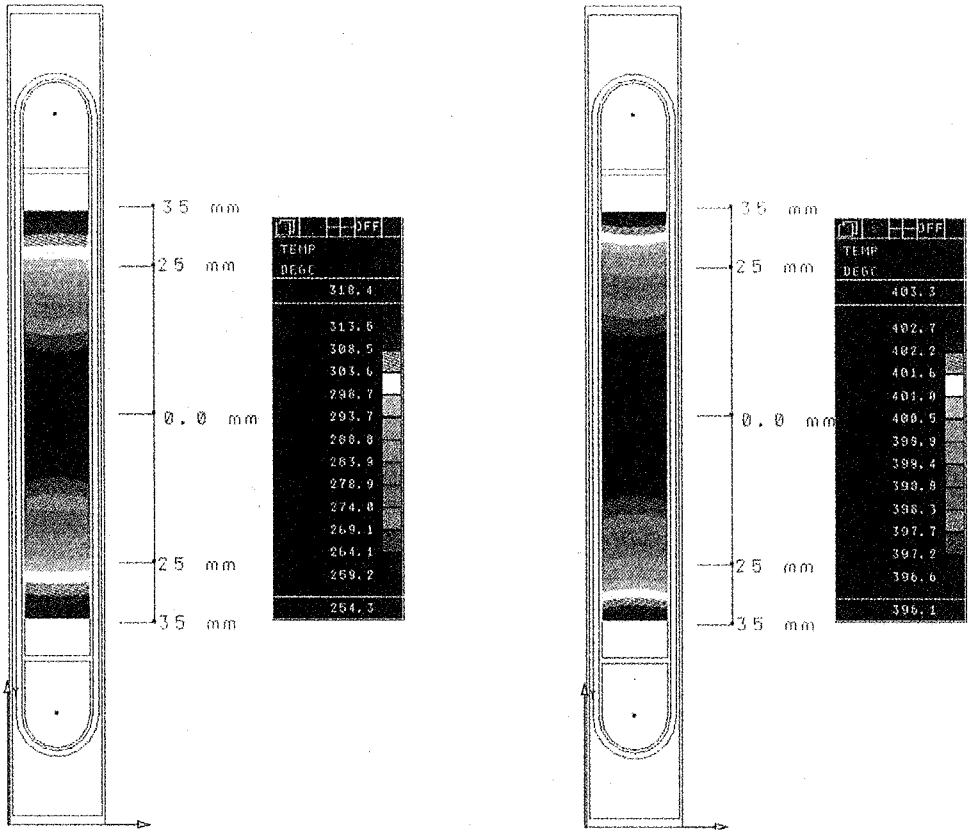


Fig. 5b Only electrical heating with ohmic wires (150 W/m) is taken into account. Left side: variable gas gap from the middle (0.15 mm, 0.2 mm, 0.4 mm, 1.2 mm). Right side: constant He gas gap of 0.5 mm.

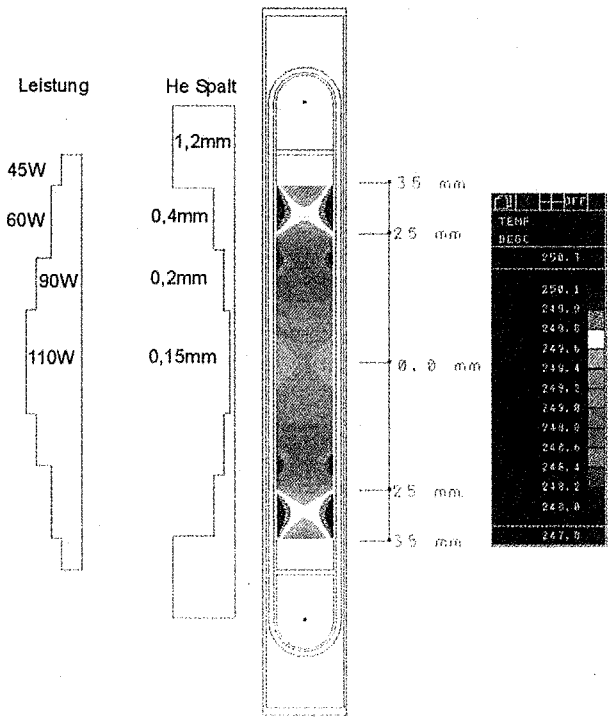


Fig. 5c Capsule/rig-design with variable He gas gap width between capsule and rig walls and variable power distribution of electric heater.

(4.5) 3D calculations of the temperature distribution in rig and capsule with 3 axial heater coils and constant gap between capsule and rig walls

The jacket wire heaters are wound in horizontal groves on the capsules. They are subdivided into a lower, middle and upper heater. The simulations were carried out with the code STARCD. This

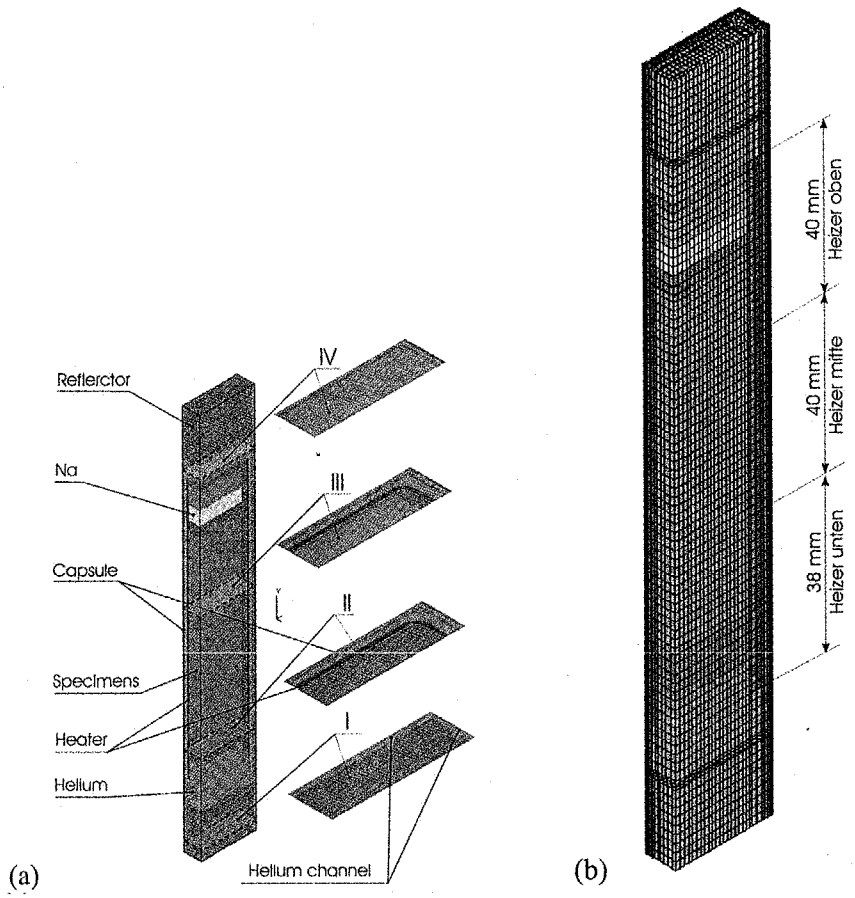


Fig. 6 (a) model used for the simulation with STARCD.
(b) model with the electric heaters for the 3D simulation with STARCD.

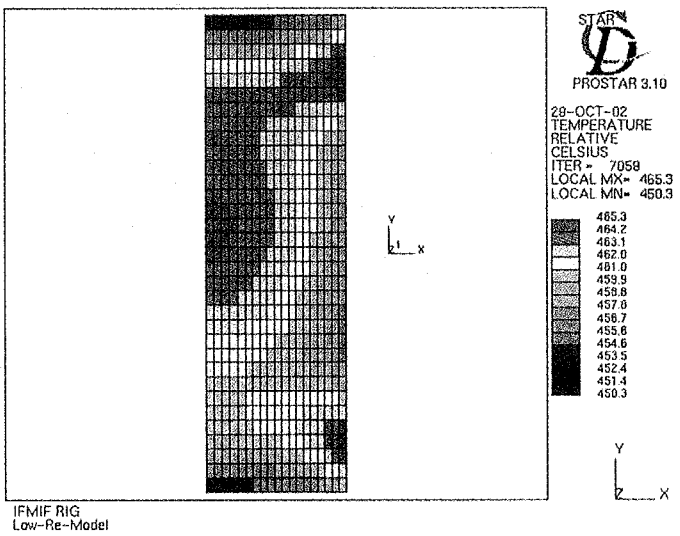


Fig. 7 Temperature distribution in the specimen stack with nuclear heating and additional electric heater power; with an adapted power distribution of the three electric heaters the temperature can be kept within a tolerance of 15°C over a stack height of 66 mm.

CFD code calculates the major parameters of the helium flow, such as heat transfer to the helium and gas pressure. Several design variants were analysed. The computer model for one example is shown in Fig. 6a. More details and the position of the electric heaters are given in Fig. 6b. An example of the temperature distribution in the specimen stack with nuclear heating and additional electric heater power is shown in Fig.6b. With an adjustable power distribution of the three electric heaters the temperature can be kept within a tolerance of 15°C over a stack height of 66 mm.

This optimization will be continued. The main parameters are the capsule wall thickness, heater axial subdivision and heater power distribution, gap width between capsule and rig, as well as the channel cross section at the outer side of the rig. As can be taken from Fig. 7, the temperature can be held within about 15°C over the specimen stack for a wide range of temperatures by an appropriate arrangement and power distribution in the electric heaters. However there remains a small zone with larger temperature deviations. This deviation can be reduced by additional heaters. These heaters on the other hand will require additional space. It has to be carefully considered whether the specimens in those regions are rejected or some specimens are removed in order to give space for additional heaters.

(5) ITHEX Experiments for Validating the Heat Transfer and Pressure Loss Simulation Calculation

Tests in the ITHEX experimental facility are designed for the validation of the heat transfer and pressure loss simulation calculations in the helium channels. The test section has an annular channel geometry shown in Fig. 8. It is heated from both sides. Electric jacket wire heaters are used as they are envisaged for the IFMIF HFTM.

The channel walls are made from two co-axial shells. The heaters are embedded into grooves of one shell. After installation of thermocouples and insertion in the second shell the space between the shells is filled by a braze filler material. The development of the brazing procedure is now complete and the final test section can be made. The installation of the heater was also an exercise for the milling manufacturing of the parallel grooves with a small inclination angle and the winding of the heater.

It was planned to install the ITHEX test section into the helium loop of the former Dual-Beam facility at FZK. The reactivation of this loop revealed that the pump created pressure fluctuations with which the flow meter could not cope. Therefore, tests with side channel compressors and a new mass flow meter were carried on in order to build a new but much smaller loop (Fig. 9).

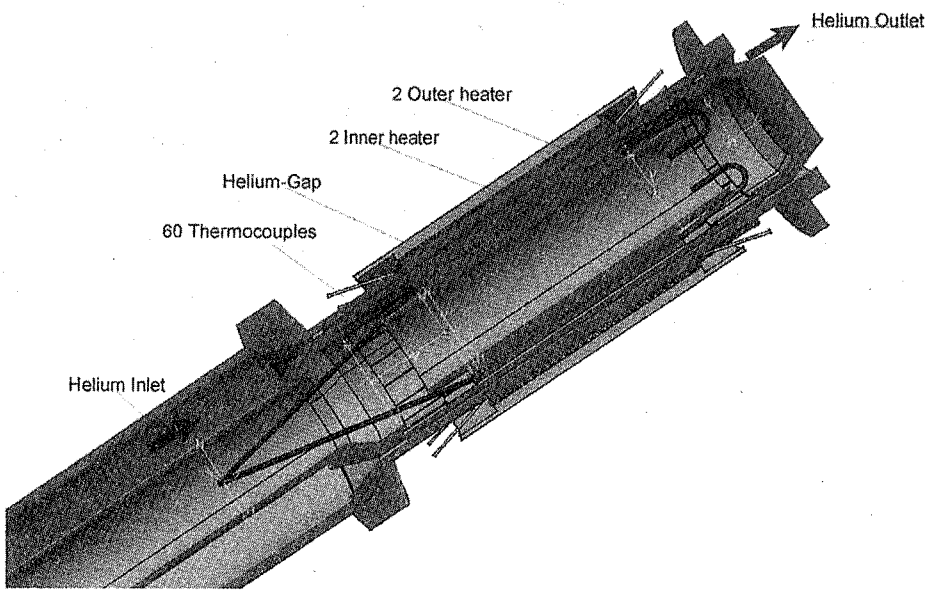


Fig. 8 ITHEX test section designed using CATIA V5.

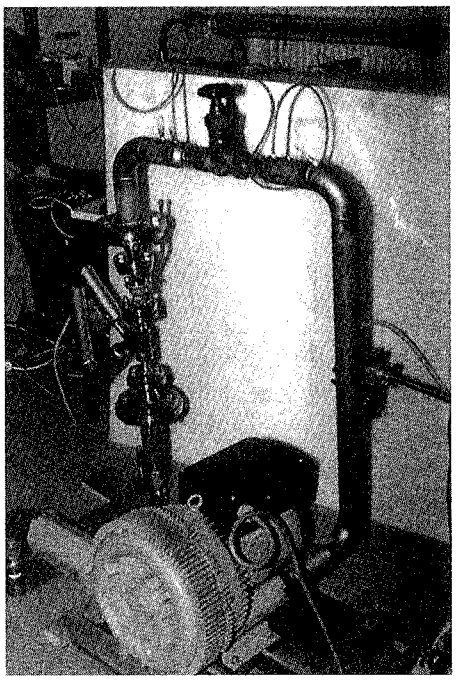


Fig. 9 He-loop for ITHEX with a side channel compressor and a coriolis mass flow meter.

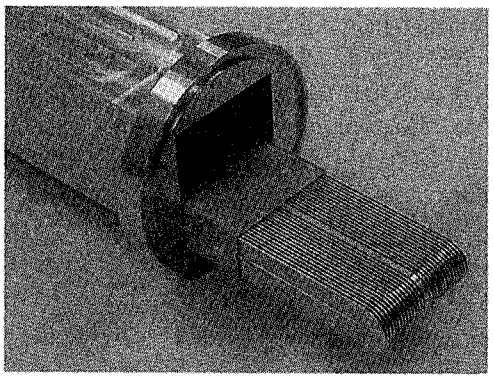


Fig. 10 Manufacturing test of capsule, rig and container; the outer surfaces and the grooves on the capsule surface are milled; all hollow spaces are spark eroded; the container has a flange on both sides; the wall thickness is 1mm; the components are made from solid stock which was annealed before milling and spark erosion.

(6) Proving Manufacturing Technologies

The crucial manufacturing technologies for the HFTM design are milling of the grooves for the wire heater, winding of the heater wires, and the spark erosion of the capsule, rig and container. Fig. 10 shows the result of the test for manufacturing technologies. The quality control revealed that those technologies were successful and can be used for the HFTM.

References

[1] M. Martone (Ed.), IFMIF International Fusion Materials Irradiation Facility, Conceptual Design Activity, Final Report, IFMIF CDA TEAM, ENEA Frascati, Report ENEA-RT/ERG/FUS/96-11, December 1996.

[2] S. P. Simakov, U. Fischer, V. Heinzel, U. v. Möllendorf; International Fusion Materials Irradiation Facility (IFMIF) Neutron Source Term Simulation and Neutronics Analysis of the High Flux Test Module; FZKA 6743; July 2002.

[3] V. Heinzel, U. Fischer, B. Dolensky, S. Gordeev, K. Schleisiek, S. P. Simakov, V. Slobodtchouk, E. Stratmanns; Lay-out Activities for the IFMIF high flux test module; ISFNT-6, San Diego, USA; April 7-12, 2002.

3.3.2 TF21-JA : Neutron Spectrum and ^{7}Be Production in Li(d,n) Reactions at 25 and 40 MeV

(1) Brief Task Description

To improve the data accuracy of the neutron emission spectrum for the Li(d,n) reaction and the radioactivity (^{7}Be, ^{3}H, etc) accumulation in the lithium target in IFMIF, we have measured the neutron emission spectrum and the production of ^{7}Be for thick lithium targets at 25 MeV and 40 MeV deuteron energy at the Tohoku University AVF cyclotron (K=110) facility.

Neutron spectra were measured with the time-of-flight method at ten laboratory angles by using a beam deflection system and a well-collimated time-of-flight channel detector. Induced radioactivity was measured by detecting the gamma-rays from ^{7}Be with a pure Ge detector.

The present result of neutron emission spectra covers most of the energy range down to ~0.8 MeV and clarified the neutron spectrum and the angular dependence of the yield. The results for ^{7}Be production were much larger than predicted by the recent codes.

Contributors

Name	Party	Institute	E-mail address
M. Baba	Japan	Tohoku Univ.	babam@cyric.tohoku.ac.jp
M. Hagiwara	Japan	Tohoku Univ.	hagi@cyric.tohoku.ac.jp
M. Sugimoto	Japan	JAERI	sugimoto@ifmif.tokai.jaeri.go.jp

(2) Introduction

For the design and operation of the neutron production target of IFMIF, detailed knowledge is required on the energy-angular neutron emission spectrum of the ^{7}L (d,n) reaction, and the radioactivity (^{7}Be, ^{3}H, etc) production in the target [1]. The neutron flux and spectral data are required for precise evaluation of neutron irradiation effects, and the radioactivity accumulation is of concern for the safe management of the target system. Work was done on these subjects in the course of the FMIT project, but the status of the data is not good enough, as shown by marked differences among experimental data [2-6].

To improve the data accuracy of the neutron energy-angular distribution and the predictability of the radioactivity production in the IFMIF ^{7}Li target, we have carried out experiments on the neutron emission spectrum of the ^{7}Li(d,n) reaction and the radioactivity induced in the target using the AVF cyclotron (K=110) at the Tohoku University Cyclotron and Radioisotope Center (CYRIC) [7].

This paper presents the experiments on 1) the neutron emission spectra and 2) the production of radioactive nuclide, ^{7}Be, of the Li(d,n) reaction for 25 MeV and 40 MeV deuterons. The neutron spectra were measured with the time-of-flight (TOF) method at ten laboratory angles between 0- and 90- or 110-deg using a beam deflection system and a well-collimated TOF channel. The amount of ^{7}Be produced in the lithium target was measured by counting the gamma-rays from ^{7}Be using a pure Ge detector.

Experimental results for 25 MeV deuterons are presented; however, the analysis of 40 MeV data is not finished. The results are compared with other experimental data and calculations.

(3) Experiments

Figure 1 illustrates the layout of target room No. 5 in CYRIC where the experiment was carried out. A deuteron beam accelerated by the AVF cyclotron was transported to the target room No. 5 which is equipped with a beam deflection system and a neutron TOF channel detector as shown in Fig. 1. The beam deflection system changes the incident angle of the beam onto the target from –5- deg to 145-deg and enables angular distribution measurement without changing the detector setup. The neutron flight channel is 44-m-long.

The target was a metallic plate of elemental lithium. Care was taken on the chemical purity of the lithium target: The target was prepared by mechanical pressing of a lithium ingot under argon atmosphere to avoid oxygen contaminant and the lithium ingot was cleaned up thoroughly prior to the

pressing to avoid carbon contamination. The lithium target was 7.5 mm thick to stop the incident beam of 25 MeV deuterons. The size of the target was about 2 cm x 4 cm which is sufficiently larger than the deuteron beam spot, about 5 mm in diameter. It was set in a remotely controllable target changer without a backing together with a beam viewer of aluminum oxide. The support frame was isolated from the ground to read out a beam charge induced on the target. Also, the target frame was surrounded by a copper mesh biased at –300 V to suppress secondary electron emission from the target.

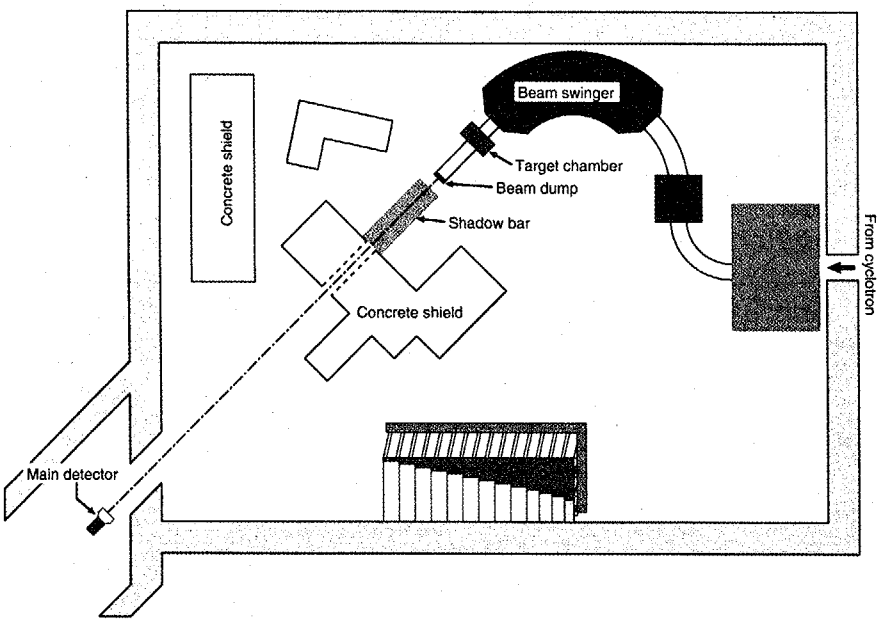


Fig. 1 The layout of target room No. 5 at CYRIC.

The target chamber was shielded with 1 m thick concrete walls having a beam channel for collimators to reduce neutron and gamma-ray backgrounds. Iron collimators, 10-cm-diam, were inserted into the beam channel to collimate neutrons from the target.

Emitted neutrons were detected with an NE213 scintillation detector, 14-cm-diam × 10-cm-thick or 2"-diam × 2"-thick equipped with pulse-shape-discrimination (PSD). The larger and smaller detectors were placed about 11 m and 3.5 m from the target, respectively (Fig. 1). The shorter flight path was used to measure the low energy part of the neutron spectrum.

The frequency of the deuteron beam was reduced to about 2 MHz by using a beam chopper, to avoid frame-overlap of the TOF spectrum. This enables measurement of the neutron spectrum down to ~0.6 MeV with a flight path near 3.5 m.

The TOF, PSD and pulse-height data were collected event by event as three-parameter data for off-line analysis [8].

Typical pulse width was 1-1.5 ns FWHM, and the beam current on the target was in the range of 0.5 to 5 nA. The beam current was digitized and recorded by a mullti-channel scaler for normalization of the neutron TOF spectrum and the ^{7}Be production measurement. The TOF data were obtained at ten angles 0, 5, 10, 15, 20, 25, 30, 40, 60, 90 deg.

The activity of ^{7}Be accumulated in the lithium target was measured by detecting the 477 keV gamma-rays produced in the decay of ^{7}Be. The lithium target bombarded by the deuteron beam during the neutron spectrum measurement was measured with a pure Ge detector (EURICIS MESURESE GPC50 – 195-R) and a multi-channel analyzer.

(4) Data Analysis

Neutron TOF spectra gated by a PSD signal and a lower pulse-height bias were converted into energy spectra taking account of the effect of relativity.

As a second step, the spectra were divided by the detector efficiency and the solid angle to convert into differential yields. The efficiency versus energy curves of detectors were obtained by calculations using a revised version of the Monte Carlo code SCINFUL [9] that was verified by Meigo to be accurate within ±5% up to 80 MeV [10]. The spectra were normalized by the integrated beam current. The neutron spectrum data was corrected for the effects of neutron attenuation in the target and in the air between target and detectors.

The induced ^{7}Be activity was determined from the gamma-ray counts by the pure Ge detector and the decay constant. The efficiency of the Ge detector was determined by calculation using the Monte Carlo code EGS 4 [11]. The calculated results were confirmed at several energy points with standard gamma-ray sources.

(5) Results and Discussion

Li(d,n) neutron spectra

The present results for the Li(d,n) neutron spectrum for 25 MeV deuterons are shown in Fig. 2 and Fig. 3. The data are given as the neutron spectrum per unit solid angle and microCoulomb. The present results provide neutron spectra over almost the entire range of neutron energy owing to the utilization of the beam chopper and the low-threshold neutron detector. The data will contribute greatly to reducing uncertainty in the source term of IFMIF. The experimental spectra are divided into two parts; a high-energy tail region probably due to direct stripping reactions, and a main peak region, centered around 10 MeV which is expected as a main neutron source in IFMIF. The present data clearly show the shape and angular dependence of the neutron spectrum including the high-energy tail.

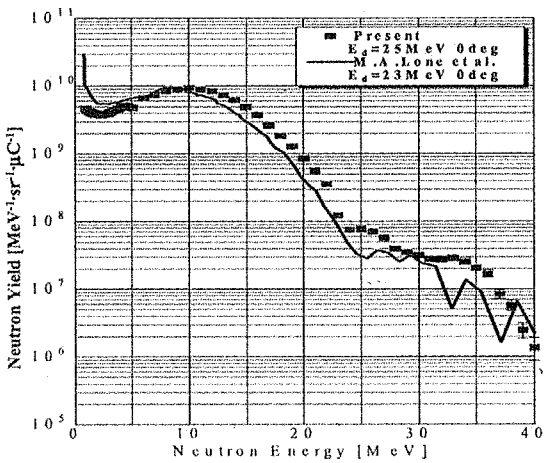


Fig. 2 Comparison of the present Li(d,n) spectrum at 25 MeV and 0-deg. with those by Lone et al [3] at 23 MeV and 0-deg.

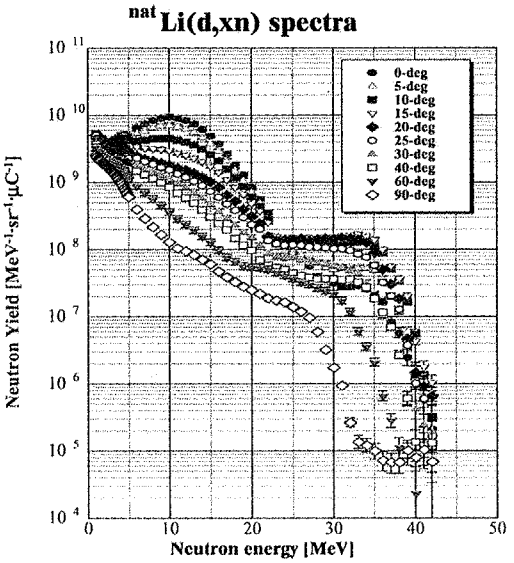


Fig. 3 The present results on the angular dependence of the Li(d,n) neutron spectrum with a thick target at 25 MeV.

In Fig. 2, the present data at 0-deg are compared with the experimental data by Lone et al at 23 MeV and 0-deg. [3]. The data of Lone et al are in agreement with the present data in most energy regions if the difference in incident energy is taken into account. However, the data by Lone et al are systematically higher below ~5 MeV and in the high-energy tail region. The large neutron yield in the

low energy region in Lone et al' s data seems improbable because of very strong recoil effects in the Li(d,n) reaction. In the high energy tail region, the data by Sugimoto [12] at 32 MeV are closer to the present data rather than those by Lone et al. Establishment of the neutron spectrum in this energy region is important because neutrons in the high energy tail will cause much more damage due to large helium production cross-sections and the higher energy of primary-knock-on atoms.

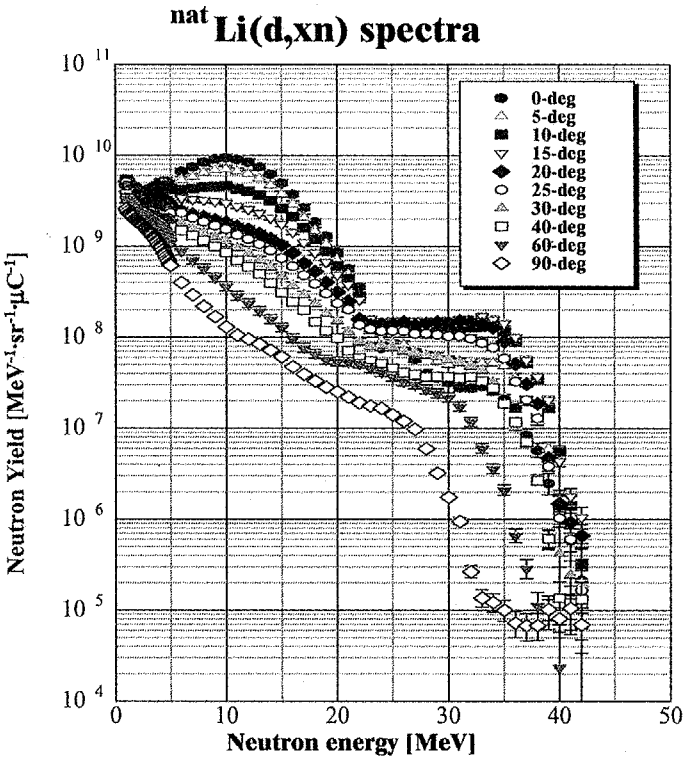


Fig. 4 The present results of the Be(d,n) neutron spectrum with a thick target at 25 MeV.

The yield intensity of the high-energy tail is maximum near 20-deg, while the total neutron yields has a maximum at 0-deg. The former measurement is in agreement with Sugimoto [12] and can be interpreted as a result of the angular momentum effects in the $^{7}L(d,n_{0,1})^{8}Be$ reaction. Therefore, to reduce the influence of high-energy neutrons and obtain higher intensity irradiation field, neutrons at angles close to 0-deg will be preferable.

Figure 4 shows the neutron spectrum data for the Be(d,n) reaction with a thick target which were taken concurrently with the Li(d,n) data as a reference. The data show a similar structure in the mid energy peak region but no high-energy tail.

^{7}Be activity

The measured ^{7}Be activity was compared with other experimental data and the calculation by the code IRAC [11] used for activity assessment of accelerator components. Figure 5 shows the comparison of the present results, other experimental data [14,15] and the calculation using the IRAC code. These values are for thick targets. Above 15 MeV, experimental data are very few but the present results at 25 MeV apear to be consistent with the data near 22 MeV [15] and at 40 MeV [16], but are substantially higher that the IRAC calculation. The production of ^{7}Be *via* the (d,n) reaction on elemental lithium will be mainly due to the ^{7}Li(d,2n) and the ^{6}Li(d,n) reactions. Figure 6 shows the comparison of the experimental data and IRAC calculation for the ^{7}Li(d,2n) reaction cross-section. It is apparent that the IRAC code underestimates the ^{7}Li(d,2n) cross-sections and this may be a principal reason for the underestimation by the IRAC code of the ^{7}Be production rate through the Li(d,n) reactions. Similar underestimation is reported even for the new code [9].

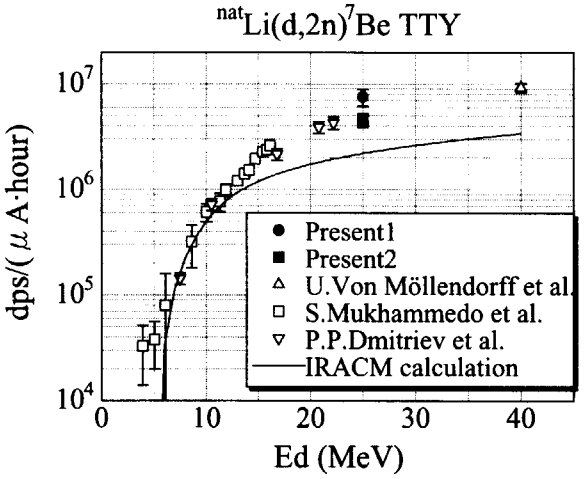


Fig. 5 The status of the cross section data for the ^{7}Li(d,2n) ^{7}Be reaction.

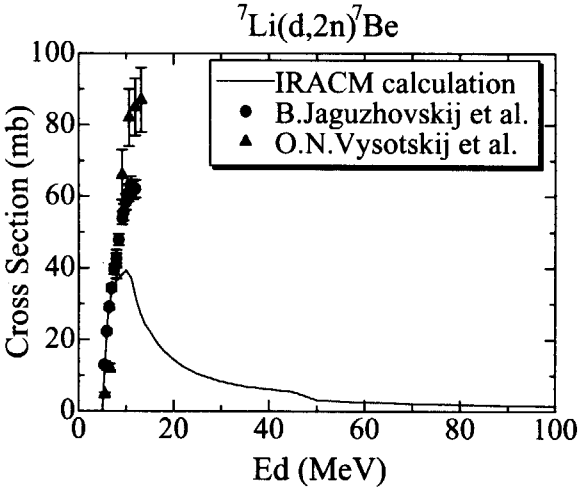


Fig. 6 The status of the cross section data for the ^{7}Li(d,2n) ^{7}Be reaction.

(6) Conclusion

The present experiment provided data on (1) the energy and angular distribution of neutron production, and (2) the ^{7}Be production rate *via* the (d,n) reaction on thick elemental lithium at 25 MeV and 40 MeV using the K=110 AVF cyclotron at Tohoku University CYRIC.

1) In the spectrum measurement, almost the entire spectrum could be observed clearly, including the high-energy tail. The data provided the basis to establish the shape and angular dependence of the Li(d,n) neutron spectrum.
2) The experimental values for the ^{7}Be production rate were much smaller than expected by the IRAC code, probably due to underestimation of the ^{7}Li(d,2n) reaction by the code.

In summary, the present results will provide a firm database for the design and the operation of the IFMIF neutron field.

References

[1] IFMIF CDA TEAM, IFMIF Conceptual Design Activity Final Report edited by Marcello Martone, Report 96.11, ENEA, Dipartimento Energia, Frascati (1996)
[2] K. A. Weaver et al.: Nucl. Sci. Eng., 52, (1973) 35
[3] M.A.Lone et al.: Nucl. Instrum. Methods, 143 (1977) 331
[4] M. J. Saltmarsh et al.: Nucl. Instrum. Methods, 145 (1977) 81
[5] H. I. Amols et al., Med. Phys. 4 (1977) 486
[6] C. E. Nelson et al., Phys. Med. Biol., 23 (1978) 23
[7] http://www.cyric.tohoku.ac.jp
[8] M. Ibaraki et al., Nucl. Sci. Technol., 35. (No.12) (1998) 843
[9] J. K. Dickens, ORNL-6436, Oak Ridge National Laboratory, 1988
[10] S. Meigo Nucl. Instrum. Methods in Physics Research A 401 (1997) 365
[11] W.Nelson, H.Hirayama, D.W.O.Rogers, "The EGS4 Code System" SLAC-265, Stanford University, Stanford (1985)
[12] M.Sugimoto (Japan Atomic Energy Reaserch Institute), Private communication
[13] A.Yu.Konobeyev, Yu.A.Koriovin, P.E.Pereslavtsev, U. Fischer , U.Möllendorff; Nucl. Sci.Eng.,139 (2001) 1
[14] S.Tanaka et al. Proc. of 8th Int. Conf. On Radiation Shielding, Arlington, Apr. 1994, Vol.2, (American Nuclear Society, 1994) pp.965
[15] EXFOR system: OECD/NEA http://www.nea.fr
[16] U.Von Möllendorff, H.Feuerstein and H.Giese, Proc. 20th Symp., on Fusion Technology (Marseille, France, 7-11 Sept.1998) pp.1445

3.3.3 TF22-JA : Analysis of Asymmetry in the Neutron Irradiation Field

(1) Brief Task Description

The IFMIF neutron flux distribution is formed by two beams. The neutron flux is calculated to show the effect of unbalanced beam intensities on the neutron flux distribution in the loading material, assumed for the purpose of calculation to be uniformly composed of Fe 50% and void 50%. The gradient of neutron flux is little affected by the unbalance of beam intensities, although the neutron flux varies in proportion to the total intensity of beams. Therefore, the unbalance of beam intensities will not be a limitation on the materials irradiation experiments.

Contributors

Name	Party	Institute	E-mail address
M. Sugimoto	Japan	JAERI	sugimoto@ifmif.tokai.jaeri.go.jp
T. Yutani	Japan	JAERI	yutani@ifmif.tokai.jaeri.go.jp

(2) Introduction

The neutron irradiation field of IFMIF is required to be distributed with flux gradient less than 10%/cm, which is adequate for the small specimens used in experiments. However, the 40-MeV deuterons interact with lithium and generate neutrons with a forward peaked distribution, and the beam footprint is large (20 cm width by 5 cm height) compared to the specimen size (~cm). Furthermore, the two deuteron beams enter the lithium target with 20 degrees opening angle to the surface of the target, and the intensity of each beam may be varied independently, depending on the operating conditions, such as beam failure and planned beam-off time. Therefore, the asymmetry of the irradiation field needs to be examined.

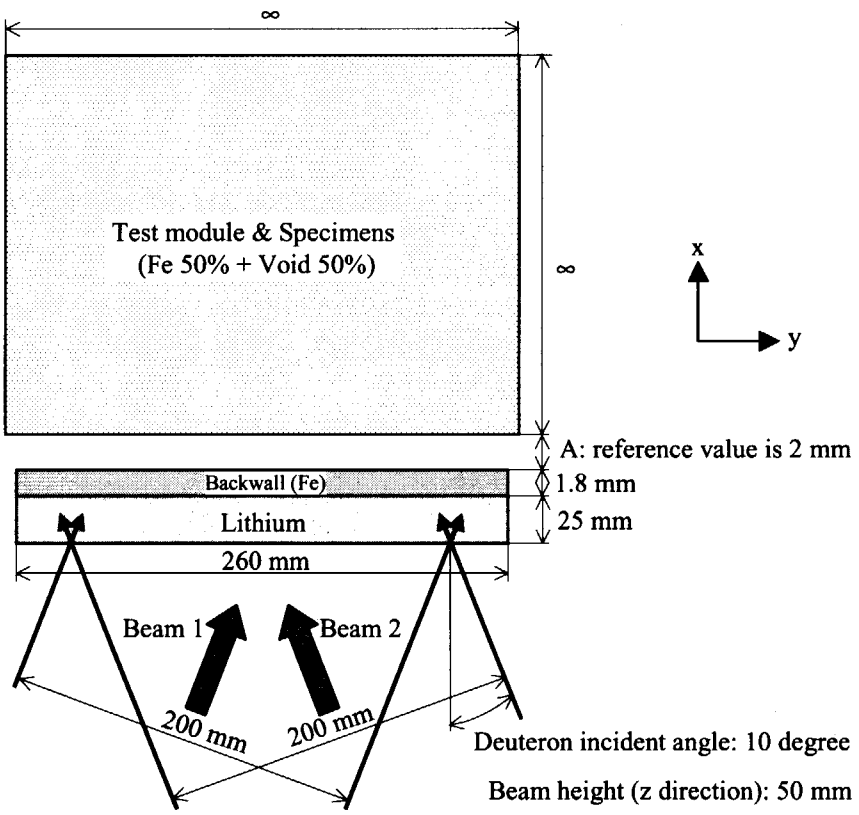


Fig. 1 Neutron flux calculation model.

(3) Calculation Model and Method

The calculation configuration is shown in Fig. 1. Two 40-MeV deuteron beams enter the lithium target with 20 degrees opening angle (10 degrees to the y-z plane normal). Each beam is uniformly distributed over a footprint of 20 cm width x 5 cm height (z direction) and has 1 cm tails at top and bottom. The thickness of the lithium stream and steel backwall are 25 mm and 1.8 mm respectively on the basis of the design of a recent target system. The loading material (test module and specimens) in the high flux test module is assumed to be uniformly composed of Fe 50% and void 50%, and its size is infinite. The reference value for the distance between backwall and loading material is 2 mm, and will be accurately set by the remote handling system in IFMIF. The calculation cases are as follows.

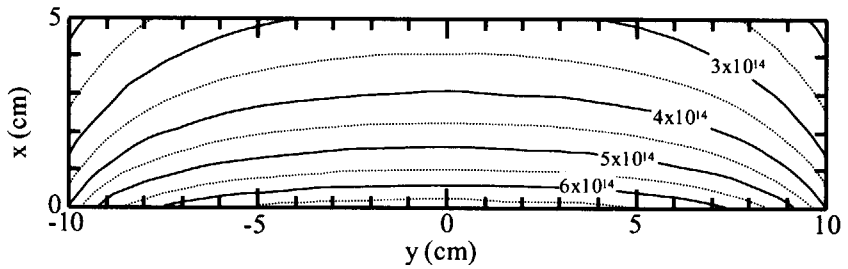
- Case 1 (reference)
  Beam current: beam 1 - 125 mA, beam 2 - 125 mA
  Distance between backwall and loading material: 2 mm
- Case 2
  Beam current: beam 1 - 125 mA, beam 2 - 125 mA
  Distance between backwall and loading material: 5 mm
- Case 3
  Beam current: beam 1 - 125 mA, beam 2 – 62.5 mA
  Distance between backwall and loading material: 2 mm
- Case 4
  Beam current: beam 1 - 125 mA, beam 2 - 0 mA
  Distance between backwall and loading material: 2 mm

The source neutrons energy and angular distributions from the d+Li reaction are deduced from the analysis of the existing measurements, for energies up to the incident deuteron energy of 35 MeV. The neutron flux at each point is estimated by assuming the continuous slowing down of deuterons along the injection direction and a simplified range vs. energy formula fitted to the stopping power calculated by SRIM2000. The multiple scattering effects are neglected for the sampled area near the target region. The resultant response map consisting of flux per unit cell at each sampled points over the calculation area for the line source based on the pencil-like beam is superimposed by a given beam distribution pattern. The above method is necessary to suppress the numerical noise to derive the flux gradients. Therefore the absolute values of the flux and the irradiation volumes obtained have some uncertainties, and they should be renormalized to the results of detailed Monte Carlo calculations. The source model also has some ambiguities about the precise shape of energy spectra and the newly available result of d+Li measurement at 40 MeV will be used to refine the model later.

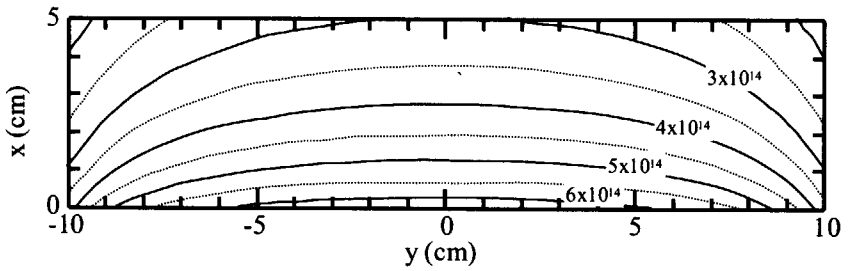
(4) Neutron Flux Distribution

Figure 2 shows the contour plots of neutron flux for the region of 5 cm x 20 cm on the central x-y plane of the specimen irradiation region. Figure 3 shows the volumes giving the neutron flux above the specific level in the specimen irradiation region. These volumes are large, because they include volumes of the outside of the high flux region (5 cm depth x 20 cm width x 5 cm height). As shown in Fig. 4 especially the neutron fluxes in the z direction are comparatively high around the high flux region.

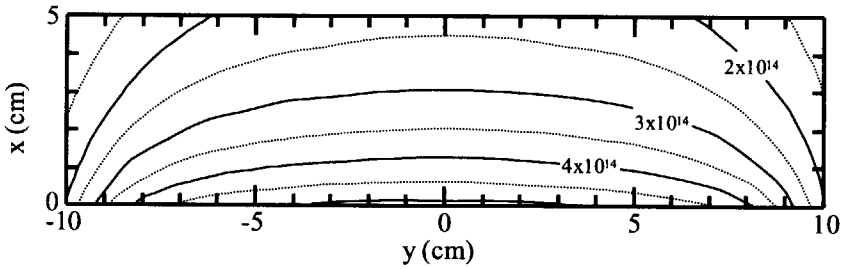
As the distance between backwall and loading material increases, the highest neutron flux of the specimen irradiation region is reduced. When the distance is varied from 2 mm (reference) to 5 mm the maximum neutron flux is reduced by 7 %, corresponding to a gradient of about 20%/cm and the volume having neutron flux above $2x10^{14}$ n/cm^2/s is reduced by 5%. (Neutron flux of $2x10^{14}$ n/cm^2/s is equivalent to 17 dpa/fpy in Fe, if the value of dpa cross section for Fe in IFMIF is estimated to be 2.7 b*keV.).



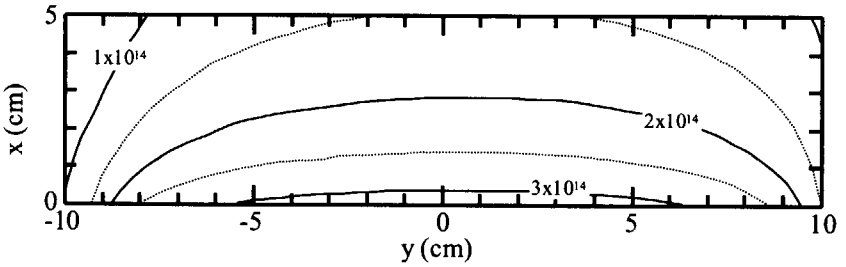
(a) Case 1 (Reference case. Beam 1 current is 125 mA and beam 2 current is 125 mA. Distance between backwall and loading material is 2 mm.)



(b) Case 2 (Beam 1 current is 125 mA and beam 2 current is 125 mA. Distance between backwall and loading material is 5 mm.)



(c) Case 3 (Beam 1 current is 125 mA and beam 2 current is 62.5 mA. Distance between backwall and loading material is 2 mm.)



(d) Case 4 (Beam 1 current is 125 mA and beam 2 current is 0 mA. Distance between backwall and loading material is 2 mm.)

Fig. 2 Contour plot of neutron flux (n/cm^2/s) for the region of 5 cm x 20 cm on the central x-y plane of the specimen irradiation region.

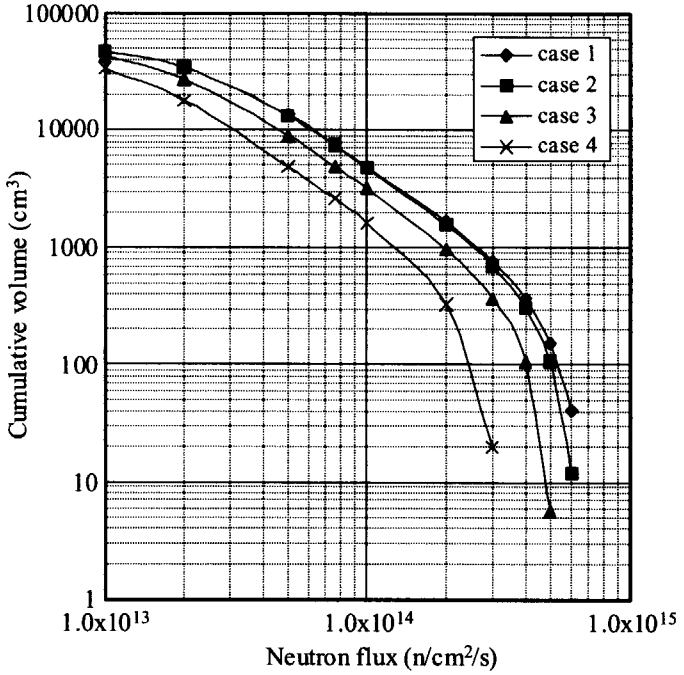


Fig. 3 Volume over specific neutron flux in the specimen irradiation region

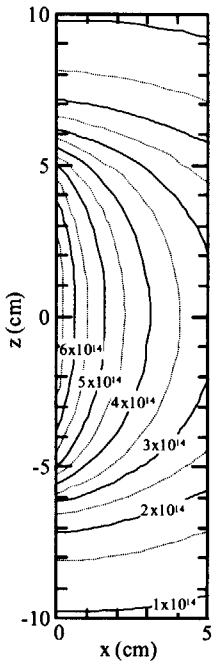


Fig. 4 Contour plot of neutron flux (n/cm²/s) on the central x-z plane of the specimen irradiation region

As the current of beam 2 is lowered from the rating value (125 mA), the neutron flux is reduced in accordance with the decrease of total current and the symmetry of the neutron distribution is only slightly disturbed. When the current of beam 2 is 62.5 mA and 0 mA the neutron fluxes are reduced to 75% and 50% of the reference case, respectively. These are shown in Fig. 2 (c) and (d).

(5) Neutron Flux Gradients

The contour plots of neutron flux gradients of x direction and y direction for the region of 5 cm x 20 cm on the central x-y plane of the specimen irradiation region are shown in Fig. 5 and 6, respectively. The contour plots of neutron flux gradient in the z direction on the central x-z plane of the specimen irradiation region are shown in Fig. 7.

The neutron flux gradient in the x direction exceeds 10%/cm at any case, and the gradient at the beam edge exceeds 20%/cm, which is approximately equal to the decrease of neutron flux produced by increasing the distance between the backwall and the loading material. However, the neutron flux gradient in the y direction is less than 10%/cm inside the range of y from -8 cm to 8 cm. This zone receives little effect of the change of beam current, and little effect of changes in the distance between backwall and loading material. It is shifted about 1 cm in the positive y direction when one beam is shut down. The neutron flux gradient in z direction is less than 10%/cm in the high flux region (-2.5 cm ~ 2.5 cm in the z direction) at any case.

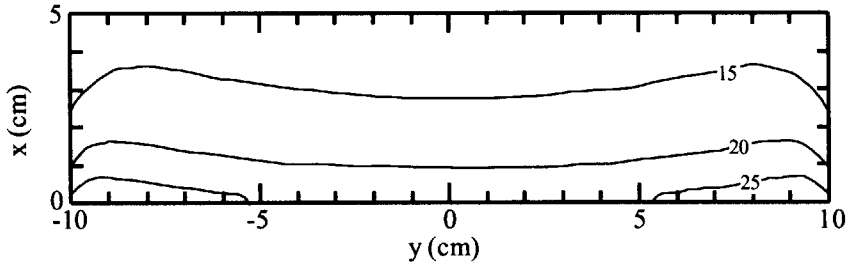
(6) Conclusion

The neutron flux distribution is calculated in the specimen irradiation region composed of Fe 50% and void 50%. Variables are the distance between backwall and loading material and the balance of intensity of the 2 beams.

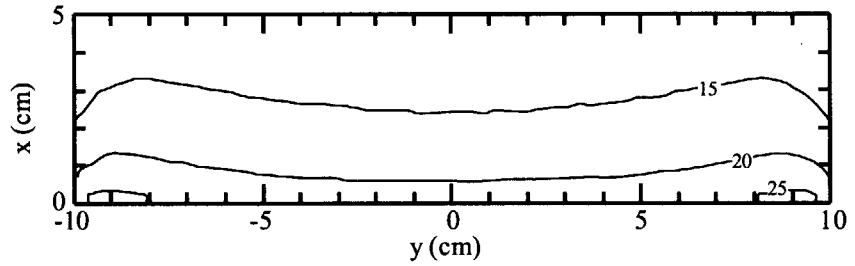
The maximum neutron flux in the specimen irradiation region is reduced at the rate of about 20%/cm, as the distance between backwall and loading material is increased. Therefore, it is desirable to keep this distance as short as possible, to efficiently use the limited irradiation volume.

The neutron flux is reduced in proportion to the decrease of total beam current, as the current of

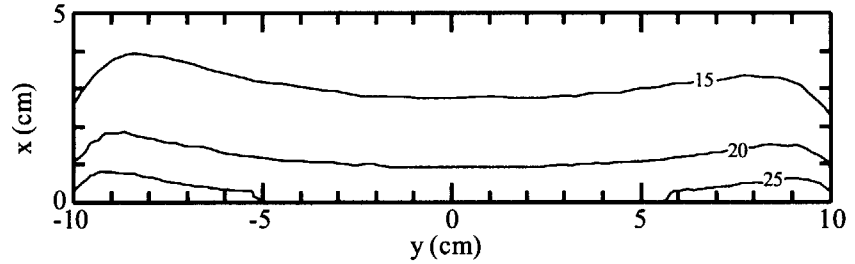
one beam is lowered. However, the neutron flux gradient is little affected. Therefore, the imbalance in beam current will not limit the materials irradiation programs.



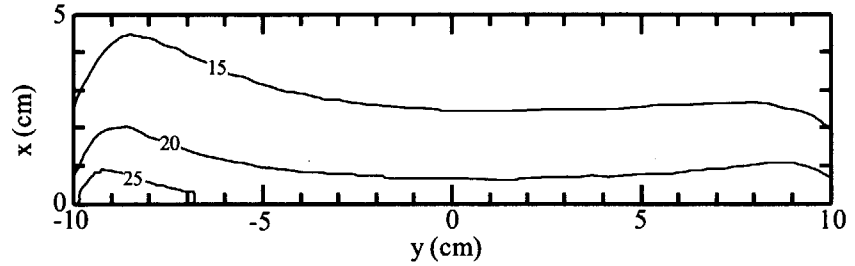
(a) Case 1 (Reference case. Beam 1 current is 125 mA and beam 2 current is 125 mA. Distance between backwall and loading material is 2 mm.)



(b) Case 2 (Beam 1 current is 125 mA and beam 2 current is 125 mA. Distance between backwall and loading material is 5 mm.)

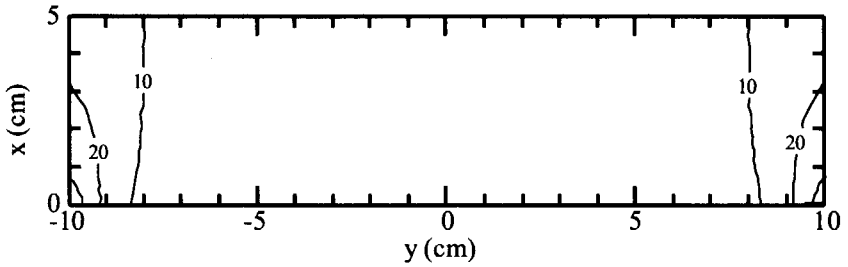


(c) Case 3 (Beam 1 current is 125 mA and beam 2 current is 62.5 mA. Distance between backwall and loading material is 2 mm.)

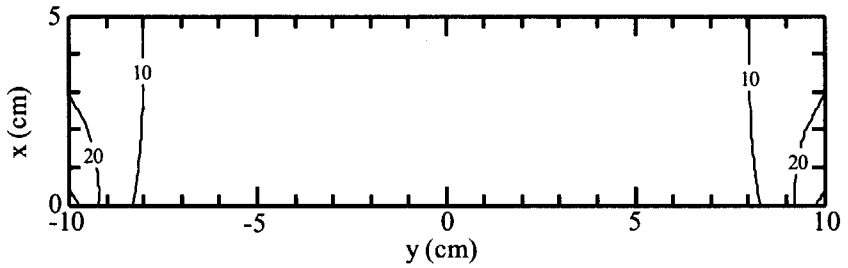


(d) Case 4 (Beam 1 current is 125 mA and beam 2 current is 0 mA. Distance between backwall and loading material is 2 mm.)

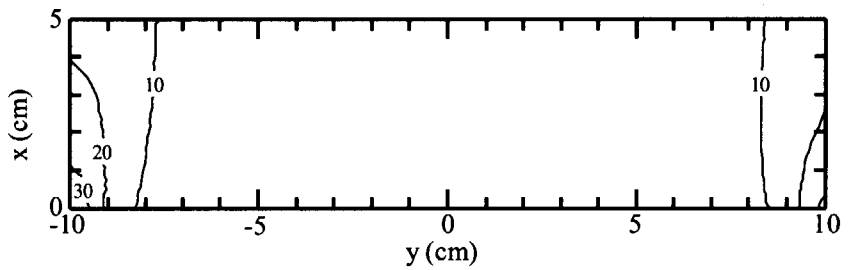
Fig. 5 Contour plot of neutron flux gradient (%/cm) of x direction for the region of 5 cm x 20 cm on the central x-y plane of the specimen irradiation region.



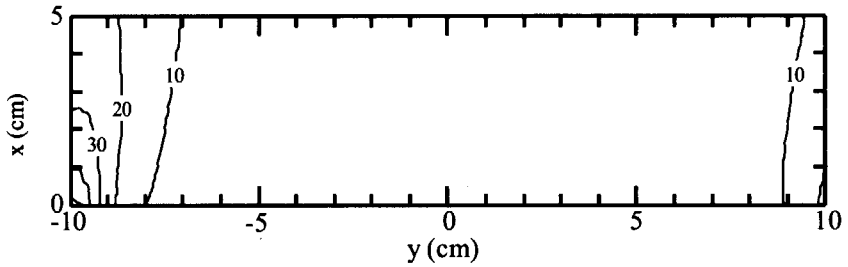
(a) Case 1 (Reference case. Beam 1 current is 125 mA and beam 2 current is 125 mA. Distance between backwall and loading material is 2 mm.)



(b) Case 2 (Beam 1 current is 125 mA and beam 2 current is 125 mA. Distance between backwall and loading material is 5 mm.)



(c) Case 3 (Beam 1 current is 125 mA and beam 2 current is 62.5 mA. Distance between backwall and loading material is 2 mm.)



(d) Case 4 (Beam 1 current is 125 mA and beam 2 current is 0 mA. Distance between backwall and loading material is 2 mm.)

Fig. 6 Contour plot of neutron flux gradient (%/cm) of y direction for the region of 5 cm x 20 cm on the central x-y plane of the specimen irradiation region.

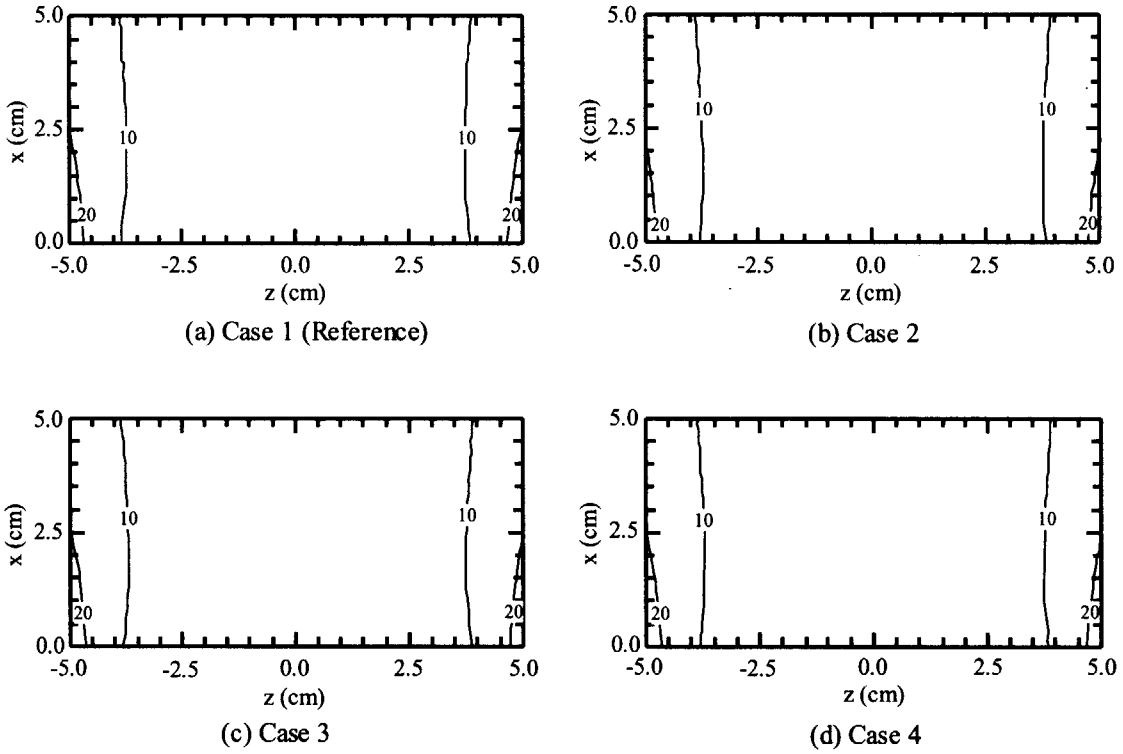


Fig. 7 Contour plot of neutron flux gradient (%/cm) of z direction on the central x-z plane of the specimen irradiation region.

3.3.4 TF23/24-EU : Performance Improvement of the Medium Flux Test Module by Neutronics Calculations and Revised Design

(1) Brief Task Description

The objective of task TF23-EU is to further improve the neutron spectrum and the irradiation conditions in the high and medium flux volumes of the test cell. Although the general data like H, He and dpa production already reflect DEMO-relevant irradiation conditions in the high flux volume, there is reasonable hope to further improve the irradiation conditions by adapting also the spectral distribution of the primary knock-on atoms. This distribution depends strongly on the neutron spectral distribution. The latter can be modified by an additional neutron moderator/reflector module that might become part of an existing test module. It is expected that a successful development of such a module will also improve the irradiation conditions for in-situ tritium release experiments on breeder ceramics in the medium flux region.

The objective of task TF24-EU is to integrate a neutron moderator and a neutron reflector into an existing test module in order to further improve the neutron spectrum and the irradiation conditions in the high and medium flux volume of the test cell. Based on the results of neutronics calculations, a technically feasible concept must be developed that is also compatible with the major features of the existing reference design. It is expected that the coolant for this moderator/reflector component can be supplied by the Vertical Test Assembly (VTA) of the involved test module.

Contributors

Name	Party	Institute	E-mail address
A. Möslang	EU	FZK/IMF-1	anton.moeslang@imf.fzk.de
P. Vladimirov	EU	FZK/IMF-1	pavel.vladimirov@imf.fzk.de

(2) Introduction

IFMIF is proposed as an intense neutron source to test fusion reactor materials under relevant irradiation conditions. It should provide a proper neutron spectrum with sufficiently high damage production rates to also allow accelerated testing within an appropriate volume. The primary goal of the present study was to select, on the basis of neutron transport calculations, a suitable design of the IFMIF medium flux test module (MFTM) for a proper irradiation response of ceramic breeder materials. On the basis of systematic screening studies of different material combinations and test module shapes, it was shown that the IFMIF neutron spectrum could be adjusted to nearly match DEMO reactor conditions by a combination of tungsten plates serving as spectral shifter and carbon coating of the test modules acting as neutron reflector. In addition, damage code calculations confirmed that IFMIF provides, over the entire energy range, DEMO reactor relevant primary knock-on atom (PKA) spectra, which governs the damage morphology and, hence, mechanical properties of many irradiated materials. For Li_4SiO_4 enriched with in ^6Li, neutron spectra, gas production and damage rates are presented and compared with those of a helium cooled pebble bed blanket of a fusion DEMO reactor. Finally, an outline for an improved design is also being proposed that takes into account the neutronics calculations and the related neutron spectral shifter and neutron reflector requirements.

(3) Suitability of IFMIF MFTM Irradiation Conditions for Structural Materials

Previous extensive Monte Carlo simulations [1,2] have clearly shown that the IFMIF irradiation conditions for iron-based structural materials fit quite well those of a DEMO power reactor. In particular, it was shown that with a proper selection of spectral shifter material and design configuration, IFMIF provides DEMO reactor relevant H, He and dpa production rates as well as perfectly matched H/dpa and He/dpa ratios in structural materials. A major result of the screening study is that the integration of two 30 mm thick tungsten plates at the front and back of the IFMIF creep-fatigue test module very effectively levels the high energy neutrons peaked around 12-16 MeV and, at the same time, notedly increase the neutron population in the range $5x10^{-3}$ to $5x10^{-1}$ MeV [1]. Between

10^{-2} and 10^{-1} MeV the neutron flux increase is more than fourfold. This spectral shifter effect is most pronounced immediately behind the W-plates, that is, in the test module dedicated to in-situ tritium release experiments on Be and ceramic breeder materials.

These neutron transport calculations also revealed that a replacement of tungsten, e.g by iron or nickel based alloys, would have only a very moderate spectral shifter effect. A substitution of tungsten by silicon carbide or graphite would increase the high energy part (>3MeV) of the neutron spectrum by about 50% and 80%, respectively, mainly due to elastic scattering but would have practically no "spectral shifter" effect.

The usual way to characterize a PKA spectrum is to use the cumulative damage production function W(T), which represents the fractional damage energy created by PKA recoils with energies below a given energy T. This function reflects the damage morphology, as low energy PKAs produce mainly isolated Frenkel pairs while high energy PKAs generate atomic collision cascades. With a proper combination of tungsten and graphite, the W(T) function inside the high flux test module follows that of a DEMO reactor blanket over the entire PKA energy range, as Fig. 1 shows.

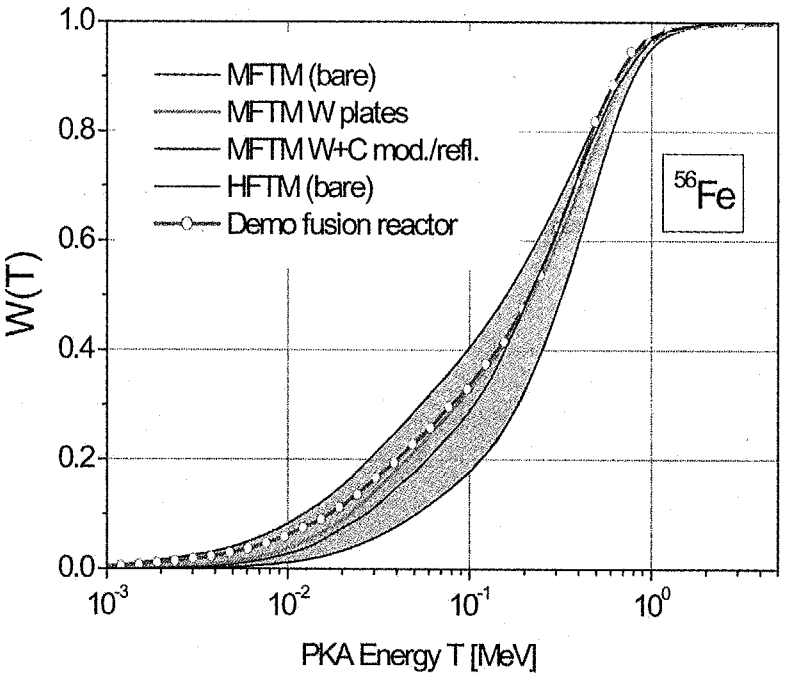


Fig. 1 Damage production function for the HCPB blanket of the fusion DEMO reactor in comparison with IFMIF HFTM and various design variants for MFTM (hatched area).

(4) Results and Discussions

Optimization of MFTM irradiation conditions for breeder ceramics

A major requirement of breeder blanket design development is to achieve an appropriate tritium production rate throughout the blanket lifetime. Presently lithium-based ceramics (e.g., Li_2O, $LiAlO_2$, $LiSiO_4$, Li_2TiO_3, $LiZrO_3$) are candidate materials for pebble bed blankets. The isotope ^6Li is more effective for this purpose as the cross section of the $^6Li(n, t)^4He$ reaction is very high and increases at low energies as $\sim E^{-1/2}$. Therefore the low energy tail of the neutron spectrum at tritium release module position should have sufficient flux intensity to achieve DEMO relevant tritium production rates.

It was found in our studies that the population of epithermal neutrons in the former IFMIF MFTMs was not sufficient to properly match helium cooled pebble bed (HCPB) blanket relevant tritium production rates. In order to meet this additional requirement, the MFTM design of the CDA phase (1995-1996) was improved based on systematic neutron transport studies with the aim of softening the IFMIF neutron spectrum in the MFTMs. The related neutron spectra were calculated by means of Monte Carlo code MCNP4c [3] using several realistic geometry models of the facility.

To optimize the neutron spectra and radiation responses for breeder ceramics, the test modules were encased in neutron moderator/reflector materials. Several materials were screened to obtain higher tritium production rates in the MFTM [4]. The results depend on the thickness of the surrounding material. The best results up to now were obtained by an additional carbon jacket of 25-30 cm attached to the MFTMs and the low flux test module. Such a carbon "coating" significantly increases

the population of epithermal neutrons and thus greatly improves the tritium production rates for breeding ceramics. For example, below 10^{-2} MeV, the flux increase is more than two orders of magnitude.

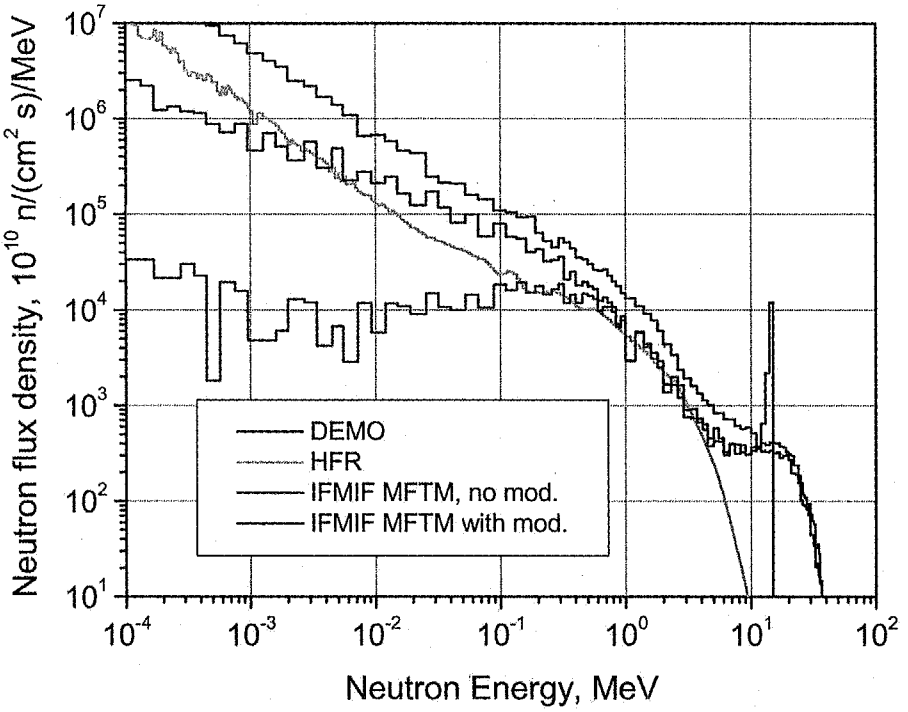


Fig. 2 Neutron spectra of the former IFMIF MFTM design (1996), and the new design with integrated W moderator and graphite reflector (2002), and comparison with the mixed spectrum reactor HFR and the HCPB blanket of a fusion DEMO reactor.

Figure 2 shows typical neutron spectra of the HCPB DEMO blanket [5] and the HFR in comparison with various spectra in an IFMIF medium flux test modules. A major result of the neutronics calculations is that with two tungsten plates acting as "spectral shifter" and additional carbon coatings acting as "reflector", the shape of the neutron spectrum in the medium flux test volumes closely follows that of a DEMO-type HCPB breeding blanket over several orders of magnitude.

Comparison of radiation responses

The results on radiation damage, gas production rates and gas-to-dpa production ratios were obtained for several design variants. In the following we will consider only four major variants (see Table 1).

The overall intention was to increase the flux at the tritium release module (TRM) position, necessary to reach DEMO relevant doses in reasonable times, while keeping the low energy part of the spectrum high enough for sufficient tritium production. Obviously these goals are mutually exclusive. Therefore an acceptable compromise must be found.

The radiation responses for these design variants are summarized in Table 2.

With respect to gaseous transmutation

Table 1 Description of the major design variants.

Variant	Description
1	Basic variant with W plates and carbon jacket around MFTM. Both MFTMs (CFTM and TRM) are present.
2	Same as item 1, but with entire TRM shifted by 3 cm upstream
3	Both W plates moved together and CFTM removed
4	Same as previous, but with entire TRM shifted by 3 cm upstream

products, the implementation of moderators and reflectors significantly improves the helium and tritium production, by a factor of 7.5 and 22.6, respectively in the MFTM of IFMIF, but has only a moderate effect on the less-relevant proton and deuteron production (see Table 3). On the other hand, the mixed spectrum reactor HFR with its overwhelming density of low energetic neutrons has comparatively high T and He production rates coming from the ^{6}Li(n, t) ^{4}He reaction, but due to the lack of higher energy neutrons a negligible H and D production. Compared to orthosilicate, meta-aluminate has generally smaller gas/dpa rates in all neutron sources investigated, mainly due to stoichiometric differences with respect to the lithium content.

Table 2 Radiation response in lithium orthosilicate† in the tritium release module for major design variants.

Variant	Damage‡, dpa/fpy	H, appm/fpy	D, appm/fpy	T, appm/fpy	He, appm/fpy	T/dpa, appm/dpa	He/dpa, appm/dpa
1	6.8	26.0	36.7	$1.68\cdot10^{4}$	$1.69\cdot10^{4}$	$2.47\cdot10^{3}$	$2.49\cdot10^{3}$
2	6.8	39.7	54.8	$1.16\cdot10^{4}$	$1.18\cdot10^{4}$	$1.70\cdot10^{3}$	$1.72\cdot10^{3}$
3	12.8	46.6	63.9	$3.20\cdot10^{4}$	$3.22\cdot10^{4}$	$2.51\cdot10^{3}$	$2.52\cdot10^{3}$
4	12.4	72.1	97.1	$2.03\cdot10^{4}$	$2.05\cdot10^{4}$	$1.64\cdot10^{3}$	$1.66\cdot10^{3}$

Although the T and He production rates and, consequently, corresponding gas to dpa ratios could be significantly increased for breeder materials in the MFTM of IFMIF, the ratios are about those for DEMO reactor at the MFTM creep fatigue test module (CFTM), while for the MFTM, TRM and HFR these ratios are too high.

The high number of low-energy neutrons in the HFR spectrum give high tritium and helium production and damage rates (the most part of which is produced by tritium and helium recoils). While the time to reach a DEMO relevant dose for irradiation in HFTM is about that for DEMO reactor itself, the dose rate for MFTM is about a factor of two lower.

To increase the neutron flux, other design variants were considered. One option is to shift the TRM upstream to get it as close as possible to the CFTM. The allowed shift is 3 cm. The other option would be to temporarily remove the entire creep fatigue test module, move both tungsten moderator plates together, and shift the tritium release module upstream by another 3 cm. The neutron flux distribution and neutron responses were calculated for these variants to get the optimal solution.

We used for the evaluation of the entire PKA spectrum the cumulative damage production function W(T) described above. For ceramic breeder materials irradiated in a HCPB DEMO reactor blanket, this damage production function W(T) continuously increases over about two orders of magnitude with increasing PKA energy, revealing a broad energy spectrum of recoils. A specific feature of breeder ceramics is the sudden increase around 2 MeV caused by an additional contribution coming from nearly monoenergetic tritium (2.6 MeV) and α-particles (2.0 MeV) emitted in the ^{6}Li(n,t)α reaction (see Fig. 3). Except of a small range (0.8-3 MeV), over the whole PKA spectrum DEMO specific recoil energy distributions can be adjusted in breeder ceramics irradiated in the present MFTM layout of IFMIF.

In contrast to lithium containing ceramics, the W(T) function in fusion structural materials continuously increases without steps. The hatched area in Fig. 1 shows that the HFTM of IFMIF perfectly meets DEMO reactor conditions in iron based alloys over the entire PKA energy range, as the shape of the W(T) function can be adjusted by using an appropriate combination of W-moderator and C-reflector. On the other hand, the PKA spectrum of the HFR is too soft by about an order of magnitude.

† Lithium isotope enrichment: 30at% ^{6}Li and 70at% ^{7}Li.

‡ Threshold displacement energies used for damage calculation: 10 eV for Li, 25 eV for Si and 30 eV for O.

Table 3 DPA and gas production in Li_4SiO_4[†] irradiated in the medium (MFTM CFTM) and high flux (HFTM) test volumes of IFMIF, in a typical position of the mixed spectrum reactor HFR, and in a HCPB DEMO reactor blanket [5][‡].

Irradiation parameter	Demo reactor	HFR position F8	MFTM no moder.	MFTM W+C moderator	HFTM W+C moderator
Total flux, 10^{14} n/cm^2/s	11.94	3.83	1.54	4.84	10.09
Damage, dpa/fpy	27.5	57.8	4.77	11.87	30.59
H, appm/fpy	330	2.6	216.1	142.9	607.3
D, appm/fpy	509	40.3	242.6	200.2	927.4
T, appm/fpy	$1.82\cdot10^4$	$1.86\cdot10^5$	$3.62\cdot10^2$	$4.22\cdot10^3$	$3.21\cdot10^3$
He, appm/fpy	$1.95\cdot10^4$	$1.86\cdot10^5$	$1.02\cdot10^3$	$4.71\cdot10^3$	$5.38\cdot10^3$
H/dpa	12.0	0.0	45.3	12.0	19.9
D/dpa	18.5	0.7	50.8	16.9	30.3
T/dpa	$6.65\cdot10^2$	$3.22\cdot10^3$	$0.76\cdot10^2$	$3.56\cdot10^2$	$1.05\cdot10^2$
He/dpa	$7.12\cdot10^2$	$3.22\cdot10^3$	$2.14\cdot10^2$	$3.97\cdot10^2$	$1.76\cdot10^2$

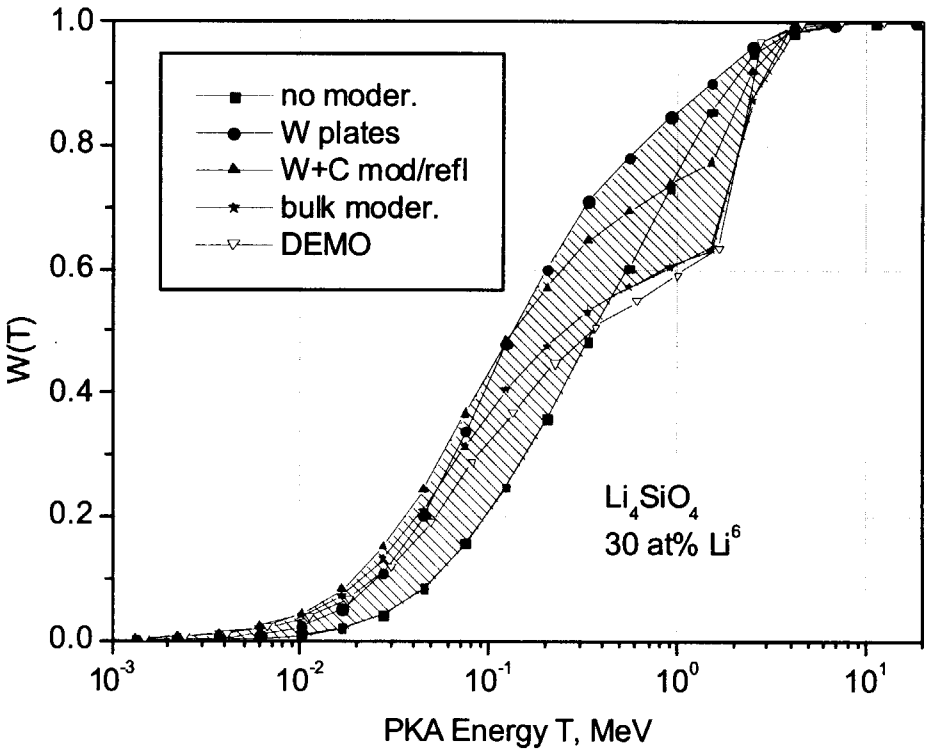


Fig. 3 Damage production function W(T) in Li_4SiO_4 for the MFTM of IFMIF (closed symbols) in comparison with HCPB DEMO blanket.

[†] The following lithium isotope enrichment assumed: 30at% ^{6}Li and 70at% ^{7}Li.
[‡] Threshold displacement energies used for damage calculation: 10 eV for Li, 25 eV for Si and 30 eV for O.

(5) Design Outline of Medium Flux Test Modules

In order to accommodate the neutron spectral shifter (or moderator) and the neutron reflectors, the original design of the MFTMs needed substantial design modification. The selected design tried to integrate both the creep-fatigue and the tritium release test modules into a carbon jacket and to position a single, 60 mm thick tungsten plate between the test modules. W acts as effective neutron spectral shifter and graphite as neutron reflector. Figure 4 shows an exploded view of all medium flux sub-test modules.

The design of the tritium release test module had earlier been significantly improved by FZK and is now integrated into a graphite shield that effectively reflects the lower energy neutrons, in order to significantly improve the tritium production, mainly via the $^{6}Li(n,t)$ reaction. The design improvement have been mainly driven by the above-mentioned design considerations, by the requirements to effectively use the available volume of 6 *l*, and to allow the simultaneous irradiation of both in-situ test modules. Figures 5 and 6 show that tritium release test module with helium gas coolant ducts, piping for sweep gas, instrumentation, and specimen arrangement.

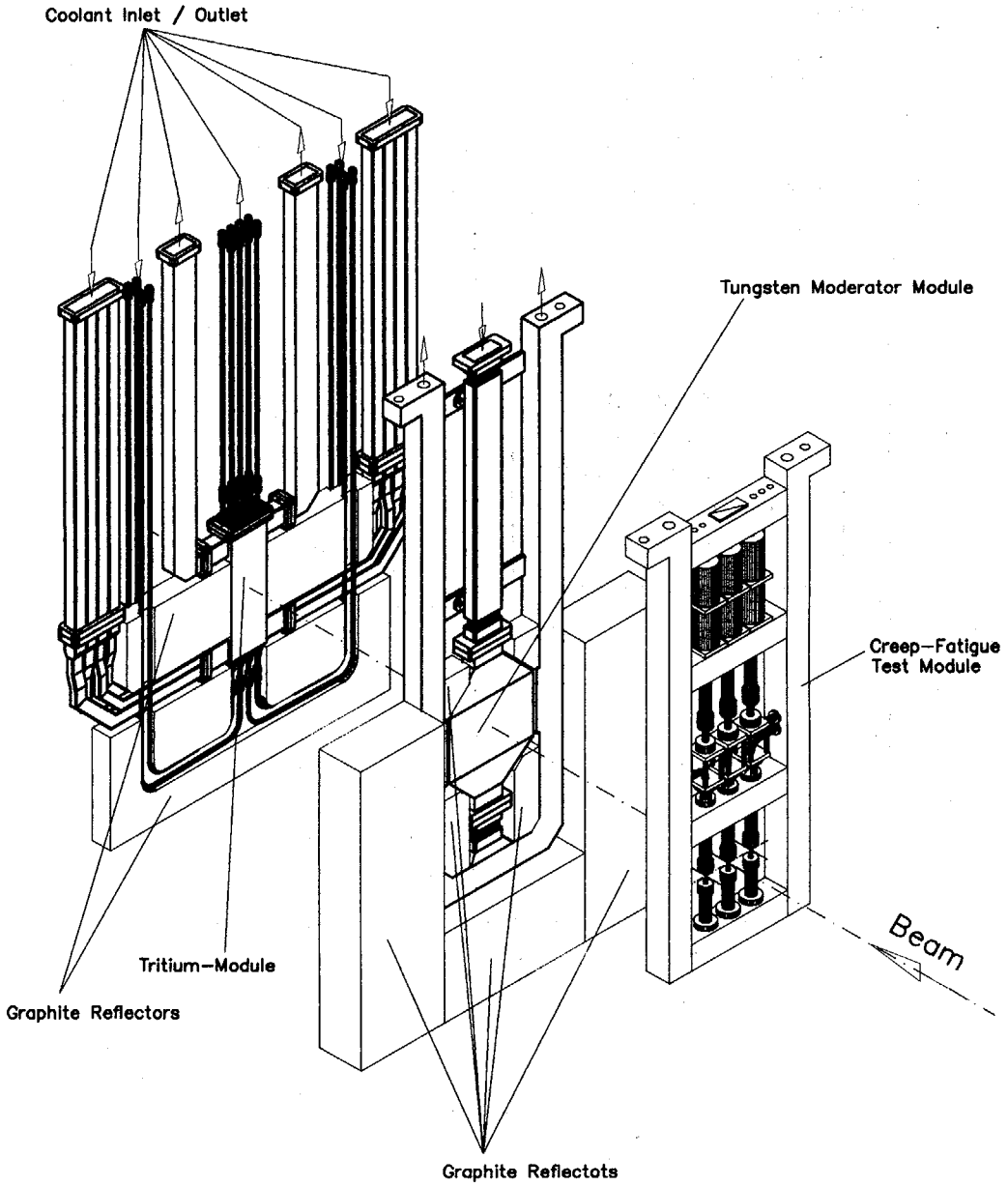


Fig. 4 Exploded view of all medium flux sub-modules.

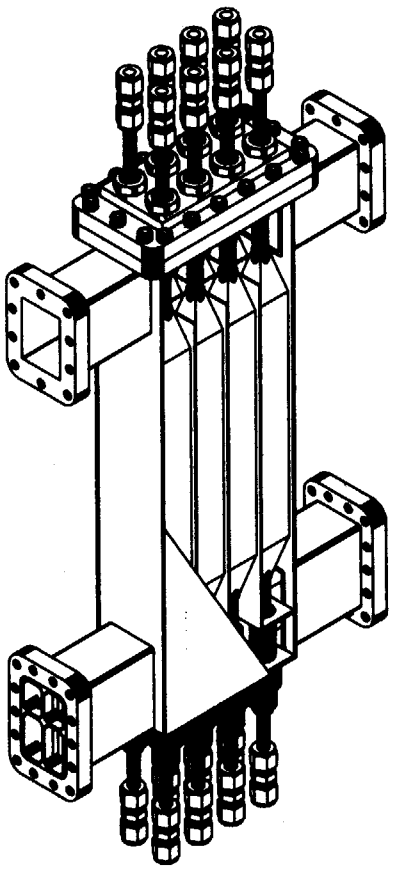


Fig. 5 Tritium module with 8 individual rigs for in situ tritium release experiments on ceramic breeder materials.

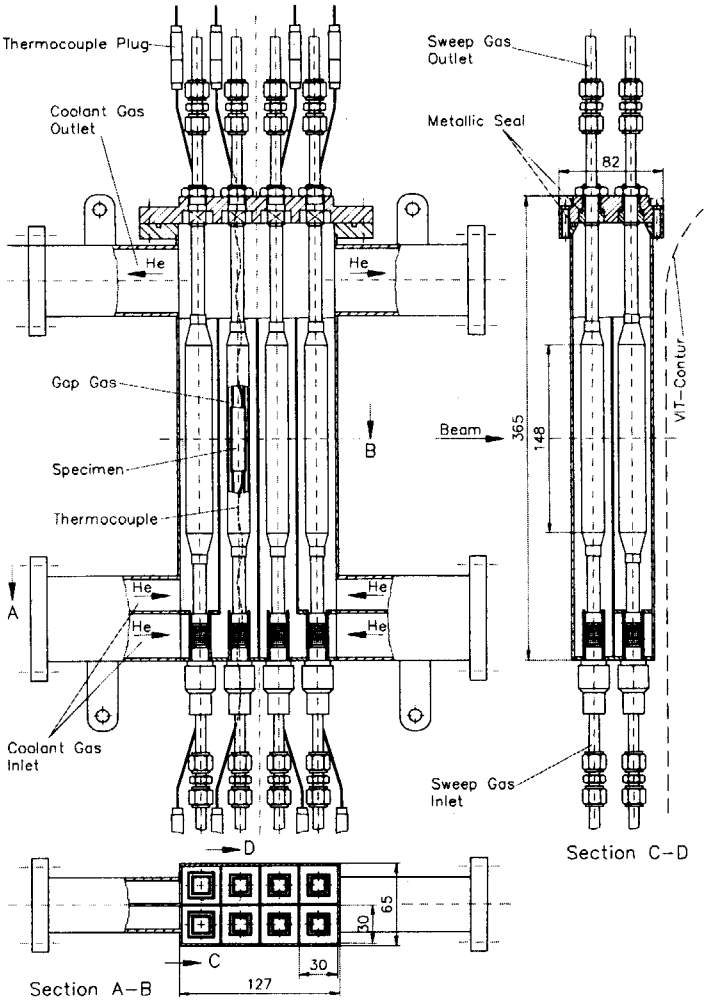


Fig. 6 Front view (left), elevation view (right) and cross section (bottom) of the tritium release test module for ceramic breeder materials.

The tritium release test module is divided into parallel coolant sections with independent control of the helium coolant flow. The specimen temperature is controlled during the test campaign by balancing the internally generated heat in the specimen, the coolant gas flow, and heat generated by ohmic heating wires. Similar to the high flux test module, the regulation will be flexible to set different temperature for different specimen materials inside a coolant section, and accommodate the geometrical and physical modification during the irradiation campaign. In particular, it should be capable of coping with varying levels of heat generation due to ion beam modulation.

(6) Conclusions

- The displacement damage of breeder ceramics is significantly affected by low energy neutrons due to the production of high energy tritium (2.6 MeV) and helium (2.0 MeV) recoils through the $^{6}Li(n,t)\alpha$ reaction.
- Gas to dpa production ratios for a MFTM surrounded by a thick graphite jacket (W+C bulk) are surprisingly close to those of a DEMO reactor, while gas and dpa production rates are smaller by a factor of two than DEMO reactor specific values.
- Variants with increased damage production rate (v3-v4) produce significantly higher gas to dpa ratio for hydrogen and deuterium than DEMO.

- In structural materials, the recoil energy distribution now perfectly meets DEMO reactor conditions in all test modules of IFMIF, while in ceramic breeder materials this distribution has become very similar to that of a DEMO reactor HCPB blanket.
- Substantial design improvements in the medium flux position allow the simultaneous irradiation of creep-fatigue and a tritium release test modules and in addition the integration of both a W plate acting as neutron spectral shifter and a graphite jacket acting as neutron reflector.

(7) Future Development

- Calculations will be performed with a beryllium moderator replacing the graphite in order to further increase the low- and high-energy parts of the MFTM neutron spectrum.
- The geometry model of the facility should be updated according to the recent drawings (see Fig. 4-6). The effect of proposed changes on neutronics and materials response under irradiation will be analyzed. Proposed design and construction material selection will be adjusted based on the neutronics analysis.

References

[1] E. Daum, How to improve IFMIF neutron spectrum, J. Nucl. Mater. 283-287 (2000) 1001.
[2] M. Martone (Ed.), IFMIF – International Fusion Materials Irradiation Facility – Conceptual Design Activity, Final report ENEA-RT/ERG/FUS/9611, Dec. 1996.
[3] F. Briesmeister (ed.), MCNP – a general Monte Carlo N-particle transport code, version 4B, LA-12625M, March 1997; ENEA-RT/ERG/FUS/9611, Dec. 1996.
[4] Yu. Lizunov, A. Möslang, A. Ryazanov, P. Vladimirov, New Evaluation of Displacement Damage And Gas Production For Breeder Ceramics under IFMIF, Fusion and Fission Neutron Irradiation, ICFRM-10, 14-19 Oct. 2001, Baden-Baden, Germany, accepted for J. Nucl. Mater.
[5] U. Fischer, S. Herring, A. Hogenbirk, D. Leichtle, Y. Nagao, B.J. Pijlgroms, A. Ying; Comparison of nuclear irradiation parameters of fusion breeder materials in high flux fission test reactors and a fusion power demonstration reactor; J. Nucl. Mater. 280 (2000) 151

3.3.5 TF31-JA : Vertical Test Assembles

(1) Brief Task Description

The heavy Vertical Test Assemblies (VTAs) must be positioned to ensure that the test modules are accurately aligned (±1 mm) relative to the neutron source because the gradient of neutron flux is large. Although VTAs can be handled accurately by the Universal Robot system, they may not be accurately positioned due to several reasons, including bowing due to the difference of thermal expansion. Distortion of the VTA due to the difference of thermal expansion is calculated by finite element methods, and review of the structure of VTA is carried out. The thermal deformation of VTA seems not to be an obstacle for the installation. The VTA may be precisely installed using guide pins.

Contributor

Name	Party	Institute	E-mail address
T. Yutani	Japan	JAERI	yutani@ifmif.tokai.jaeri.go.jp

(2) Introduction

The Vertical Test Assemblies are heavy (>5 tons), because they include the concrete shielding arranged in a stair-step configuration. These VTAs must be positioned to ensure that the test modules are accurately aligned (±1 mm) relative to the neutron source (Target Assembly) and to each other. Satisfying this requirement needs the remote handling system to accurately handle the heavy weight. The proposed remote handling system is the Universal Robot system, based on a gantry-type crane with a combined manipulator system. This system may handle VTAs accurately. However, the test modules may not be accurately aligned. If the concrete shielding is not fabricated accurately, VTAs will be inclined after setup. Also the distance between target assembly and test module and between test modules will be changed by the bowing of test modules due to the differences of temperature and swelling rate during irradiation. Therefore, the structures of VTAs need to be modified.

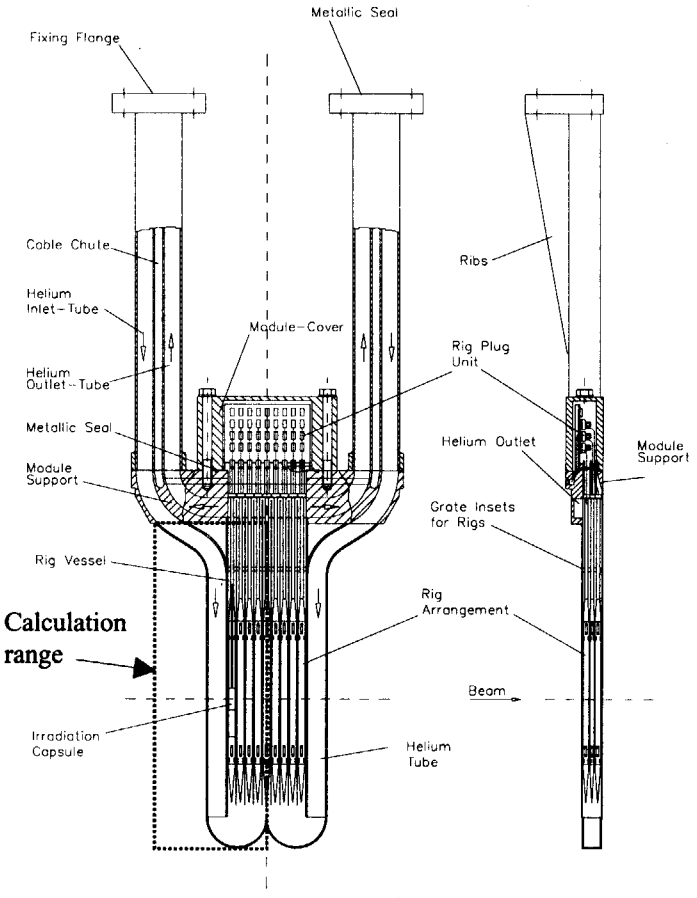


Fig. 1 Helium gas cooled high flux test module.

(3) Thermal Deformation of Test Modules

When irradiation is started, nuclear heating raises the temperature of VTAs and other items in the test cell. Of particular concern, test modules may deform by the difference of thermal expansion, because the neutron flux of the side facing the beam differs from that of the opposite side. The deformation of the test module needs to be known for the examination of the installation method of VTA1. An approximate determination of the deformation of the test module VTA1 was carried out. The

calculation conditions are based on the results [1] of FZK design and analyses of a helium gas cooled high flux test module.

The test module that was proposed by FZK is shown in Fig. 1. The cross section of a rig vessel is shown in Fig. 2 [2].

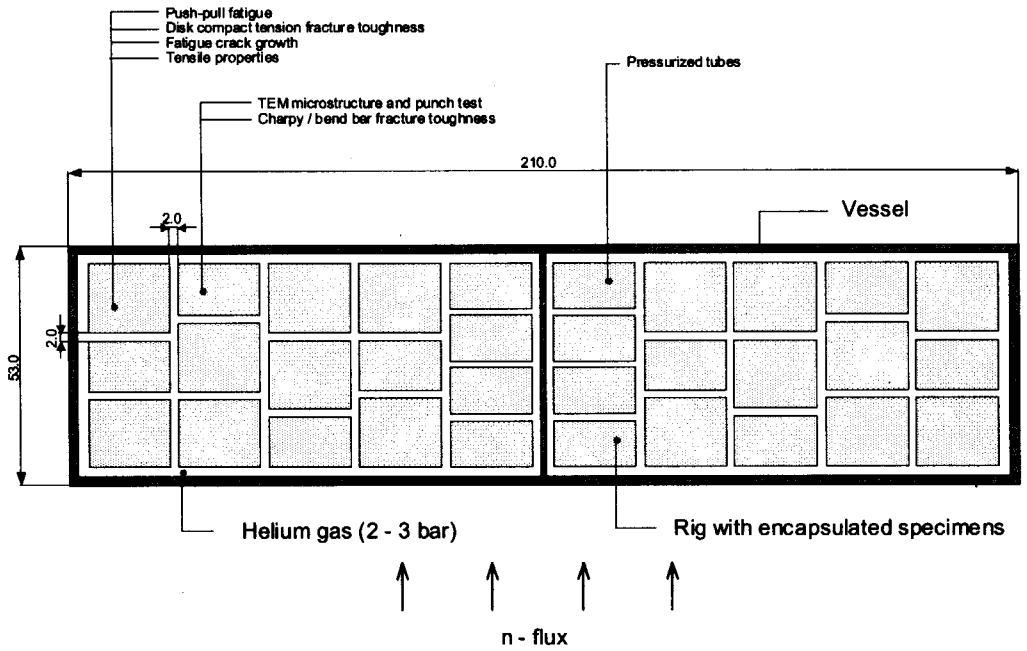


Fig. 2 Cross section of the HFTM rig vessel.

The condition of the He coolant flow is as follows.

- Pressure: 0.25 MPa
- Average temperature: 336 K
- Mass flow: 0.21 kg/s

Heat transfer coefficient of 1500 W/m^{2}K for rig vessel wall is given by

- Cross section area: $S=0.05x0.002x12+0.2x0.002x4=2.8x10^{-3}$ m^3
- Periphery length: $L=0.05x12+0.2x4=1.4$ m
- Equivalent diameter: $d_e=4S/L=4x2.8x10^{-3}/1.4=8.0x10^{-3}$ m
- Velocity: $u=0.21/(2.2x2.8x10^{-3})=33$ m/s
- Reynolds number: $R_e=\rho u d_e/\eta=2.2x33x8.0x10^{-3}/30.3x10^{-6}=1.9x10^4$
- Prandtl number: $P_r=C_p\eta/\lambda=5.19x30.3/238=0.66$
- Nusselt number: $Nu=0.22xR_e^{0.8}xP_r^{0.5}=0.22x(1.9x10^4)^{0.8}x0.66^{0.5}=47$
- Heat transfer coefficient: $h=(\lambda/d_e)N_u=238x10^{-3}x47/(8.0x10^{-3})=1500$ W/m^{2}K

Similarly, the heat transfer coefficient of the helium tube becomes 620 W/m^{2}K.

The finite element method calculations for the lower part (rig vessel and He tube) of the test module were carried out using the above-mentioned heat transfer coefficient. Temperature distributions in the rig vessel and He tube are shown in Fig. 3. This simple model is the lower part of test module and half of structure shown in Fig. 1. (The neutron beam runs opposite to the Z direction in this figure.) In order to conservatively evaluate thermal deformation, it is assumed that the front wall and the back wall in the range of 20 cm of axis direction have nuclear heating rates of $40x10^6$ W/m^3 and $18x10^6$ W/m^3 respectively. Other parts of the wall receive a small amount of nuclear heating, on the order of $5x10^4$ W/m^3. The hot spot is limited to the irradiated area and the temperature of unirradiated walls is almost constant at 336 K, the temperature of the He gas. Thermal expansion of the rig vessel and He tube in the beam direction is shown in Fig. 4. The vertical walls bend in the beam direction (opposite of Z-direction

in the figure) because of the difference of nuclear heating between the front and back walls. The total bowing from the wall surface reaches 1.1 mm. This value should not be an obstacle to installation of VTA1. However, detailed examination may be necessary in the future, because the heat deposition in the VTA components is expected to be complicated.

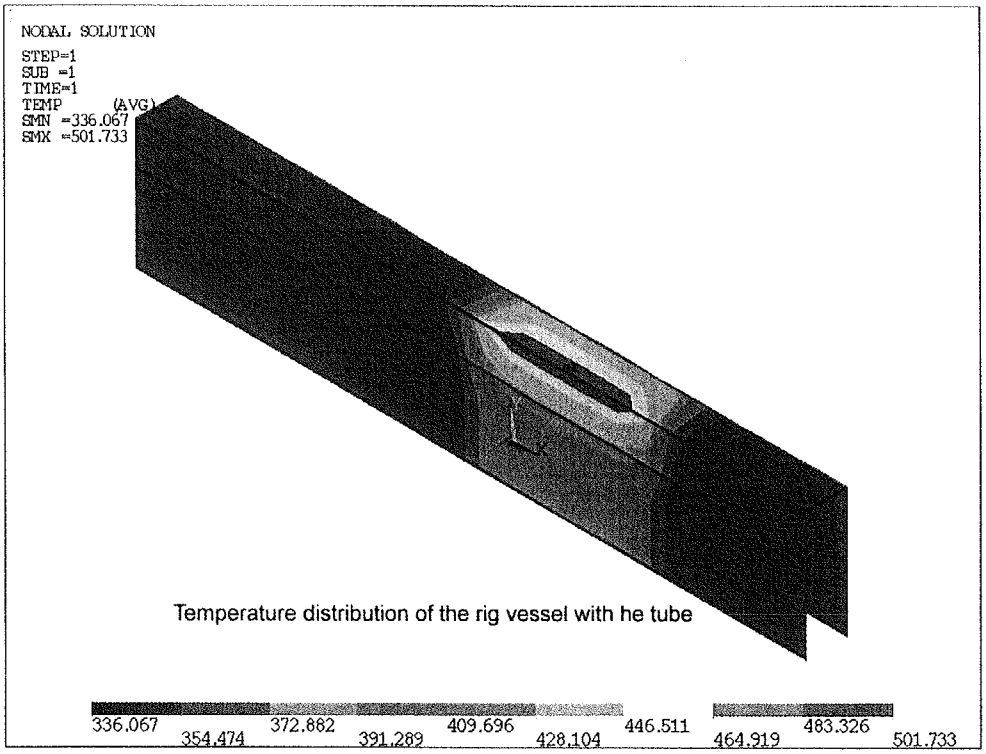


Fig. 3 Temperature distribution of the rig vessel and He tube.

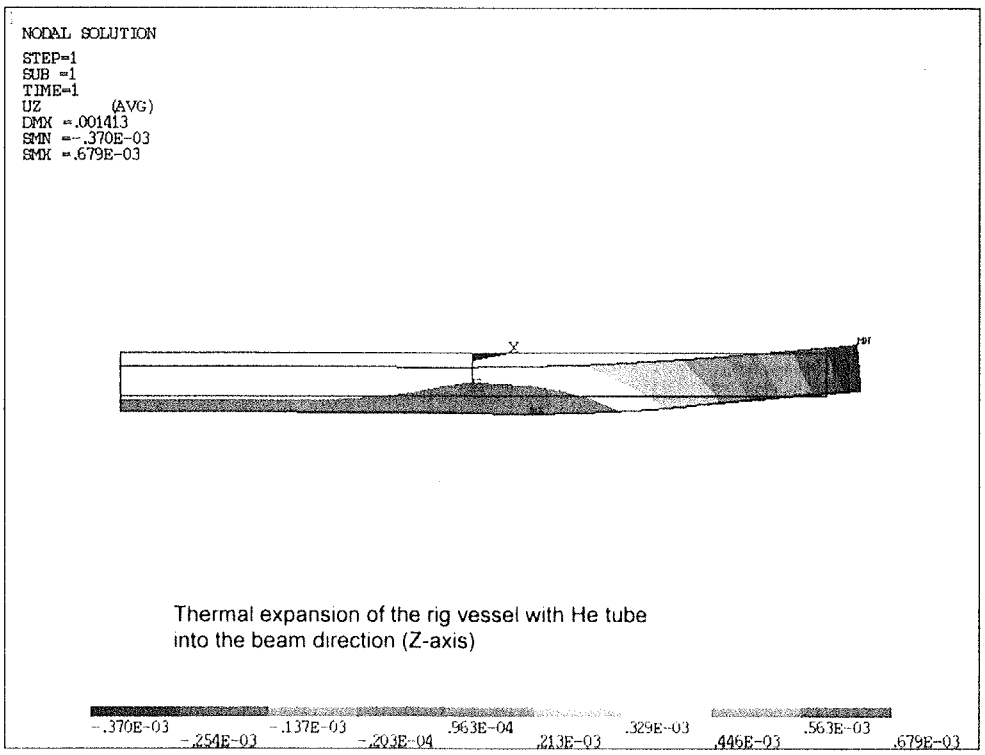


Fig. 4. Thermal expansion of the rig vessel and He tube.

(4) Installation Method for the Vertical Test Assembly

There may be several methods to precisely install the test module. One method is to install the test module along a guide. (Two places of the test cell and test cell cover are assumed as the places to set up the guides.) In the case of setting up guides in the test cell, the installation of the target assembly needs to be taken into account. In the recent design for the target system, the target assembly will be installed repeatedly in the same position, using guides that consist of two rectangular tubes extending in the beam direction from the beam-side wall of the test cell. The interval between the two rectangular tubes is about 1.5 m. If these tubes can be used as the guides for test module installation, the distance between the test module and target assembly will be set to maintain the desired value during irradiation. However, it seems difficult to use these pipes, since the length of the test module in the direction perpendicular to the beam direction is more than 1.5 m. The cross section of the test module should be smaller than (200 mm x 1250 mm) at the lower end of the shielding body.

Therefore, another method using guides is proposed. The requirements of this method are as follows.

- VTA needs to be installed precisely in the test cell cover.
- The test cell cover needs to be installed precisely in the test cell.
- The connection position of the test module to the shielding body needs to be adjustable.

The installation procedures for the test cell cover and VTA1 are shown in Fig. 5. The three lower faces of stair steps on the shielding body face the steps on the test cell covers. The premise of this method is that the VTA and lower test cell cover are kept level while they are lowered by the universal robot. VTA1 may be stably supported by the lower test cell cover in the place of lower face of the 2nd stair for shielding body, because the facing area is largest. And there is enough space in this part to hang guide pins from the shielding body and to make insertion holes for guide pins in the lower test cell cover. VTA1 may be installed accurately in the lower test cell cover by inserting pins into the holes. In this method, VTA has only to have adequate rigidity to support itself and avoid oscillation during transport, because it does not contact other equipment during installation. However, the contact surface needs to be machined precisely, because the guide pins are not able to completely restrain the movement of VTA1 after VTA1 is released from the universal robot.

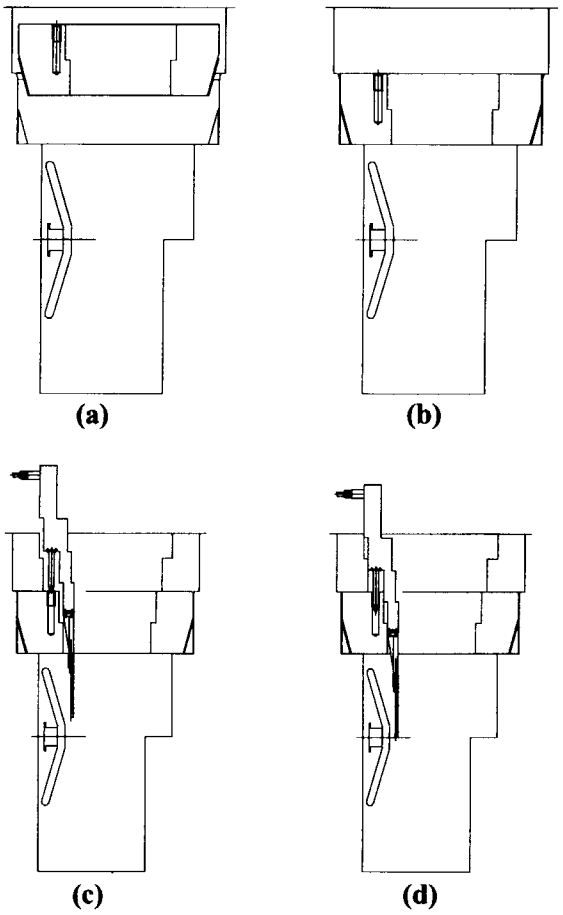


Fig. 5 Installation procedures of test cell cover and VTA1.

The upper part of the insertion hole with a bushing is shown in Fig. 6. The bushing is pressed into the insertion hole. The gap between bushing and guide pin is 0.1-0.2 mm to prevent galling and frictional resistance. In order to prevent galling and scratching of bushing at the insertion of pins, the bushing must be made of material different from that of the pin and its surface must be hardened. When VTA1 is lowered, the insertion of the pin into the hole must be started before the lower end of the shielding body is below the middle stair of the lower test cell cover, to avoid collision of the

shielding body with the lower test cell cover. Therefore, the length of pin needs to be about 800 mm. The position of the pin is adjusted in accordance with the position of the bushing, and is fixed by a dowel pin.

The lower test cell cover also must be installed repeatedly in the test cell with high accuracy. The method of using a taper is adopted, because the diameter of the guide pins will become large and machining may be difficult, if the same method as the installation of VTA1 is adopted. Tapers of lower test cell cover and test cell ensure the accurate positioning of the lower test cell cover. The backlash and gap of tapers must be eliminated by shim adjustment at the first assembling.

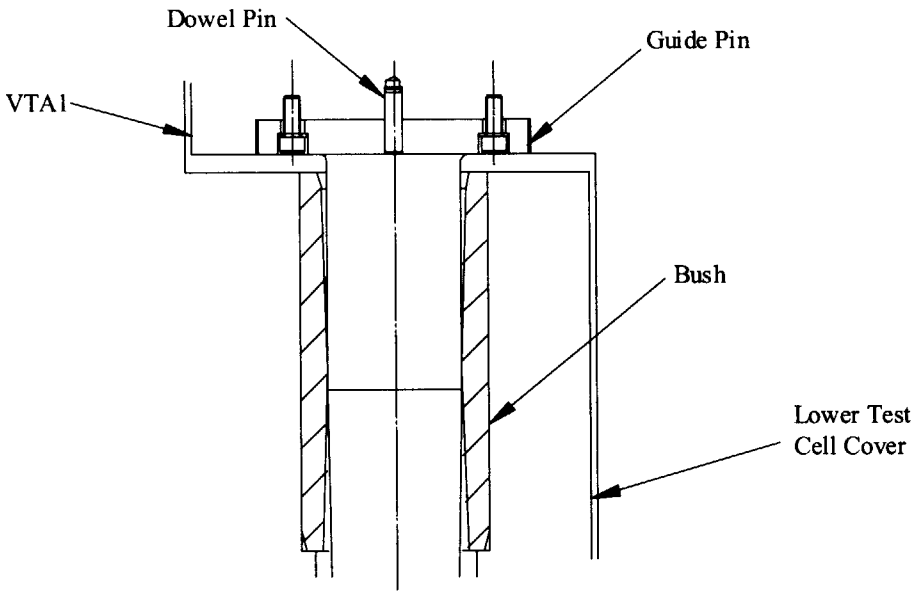


Fig. 6 The upper part of insertion hole with bushing.

Although the test module is repeatedly installed in the same position by the above-mentioned method, it is difficult to hold the distance between the test module and the target assembly to the desired value. It will be necessary to adjust the position of the test module to the shielding body, on the basis of the relative position between the target assembly and lower test cell cover that is measured beforehand by Universal Robot. The connection of the test module to the shielding body is shown in Fig. 7. The conditions to use this method are as follows.

Two tubes are contained within the shielding body.

- Two helium tubes for inlet and outlet gas and many wires for thermocouples and electric heaters are contained within each tube.
- Helium tubes can be slightly moved horizontally at the lower end part of the shielding body.
- The helium pipes are connected to holes bored in the floating plate.

The floating plate attached to the lower

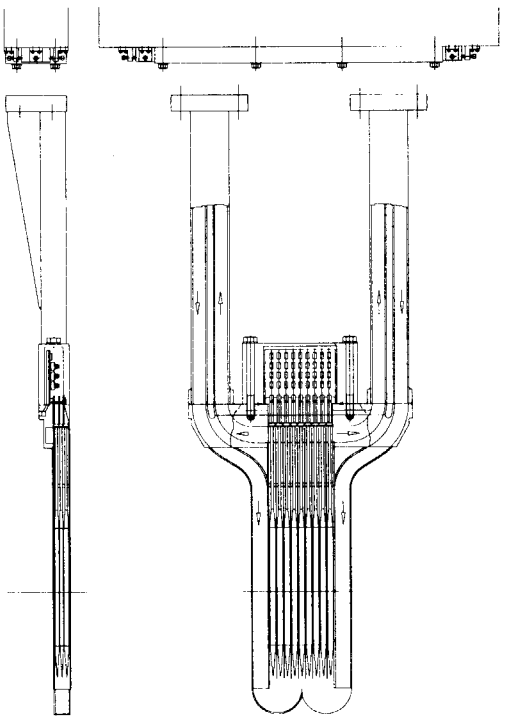


Fig. 7 The connection of the test module to the shielding body.

end of the shielding body can be moved in two horizontal directions using set screws. Then, the test module is adjusted to have the desired distance between test module and target assembly.

The periscope of the remote handling system will monitor operations inside the test cell when VTA1 is installed by this method. If the test module is not installed in the appropriate position, the position of test module can be adjusted after taking out VTA1. The distance between the test module and target assembly at the installation of VTA1 needs to be decided by allowing for the thermal expansion of the target assembly and lower test cell cover which supports VTA1. The advantages of this method are 1) there is little probability that VTA1 will collide with other devices at the installation of VTA1 and 2) the probability is low of stress due to contact between the target assembly and VTA1 during irradiation.

(5) Summary

When irradiation is started, a test module may be distorted by differential thermal expansion. The deformation of the test module is calculated by finite element methods for the evaluation of possible effects on the installation method of VTA1. The total bowing of the test module into the beam direction reaches 1.1 mm, and seems not to be an obstacle to installation of VTA1.

To install the test module precisely, the method to installing the test assembly along a guide is examined. VTA1 may be installed precisely in the lower test cell cover by inserting pins hanged from shielding body of VTA1 into the holes on the lower test cell cover. The distance between the test module and target assembly is held to the desired value by adjustment of the connection position of the test module to the shielding body.

References

[1] A. Moeslang (Ed.), "IFMIF International Fusion Materials Irradiation Facility, Conceptual Design Evaluation Report, A Supplement to the CDA by IFMIF TEAM", FZKA 6199 (1999).

[2] G. Schmitz, A. Moeslang, "Helium Cooled High Flux Test Module Task 1", IFMIF-CDE Test Facility Workshop, Karlsruhe July 7-9 1997.

3.3.6 TF33-EU : Development of Microtomography System

(1) Brief Task Description

A non-destructive, powerful analysis of all safety relevant devices inside the highly activated test cell is urgently needed. Due to its penetration ability and contrast mechanism, the X-ray microtomography is the only known tool that could meet these requirements. This technique has the ability of monitoring voids, micro-cracks and flaws in activated and completely assembled rigs, test modules and the Li-target back-wall.

A cone-beam X-ray microtomographic system has been constructed at the National Institute for Laser, Plasma and Radiation Physics (NILPRP), Bucharest-Magurele, Romania. The system consists of an open type microfocus X-ray source, a 3D micrometric translation and rotation samples manipulator and a 2-D X-ray detection system based on a large area image intensifier and fast-scan CCD. The selection of optimum tomographic configuration and components is based on test measurements of miniaturized sample mock-ups carried out on existent tomographs as well as on fully 3-D Monte Carlo simulations of X-ray radiation generation and transport. Currently, system calibration and tuning work are in progress. Planned future work is extensive NDT inspection of fusion materials miniaturized samples using the transmission microtomography system in order to establish the reference design for microtomography system for IFMIF environment conditions.

Contributor

Name	Party	Institute	E-mail address
I. Tiseanu	EU/Romania	NILPRP	tiseanu@alpha2.infim.ro

(2) Introduction

Computed tomography is widely used in the medical community and is receiving increased attention from industrial users including electronics, aviation, advanced materials research, casting and other manufacturing areas. Computed tomography systems are usually configured to take many views of the object in order to build a 3-D model of its internal structure. 2-D slices through this volume can be viewed as images, or the 3-D volume may be rendered, sliced, thresholded and measured directly. Amplitudes of the volume elements (or voxels) are proportional to the X-ray linear attenuation of the material at that position and therefore dependent only on material properties and not on the shape of the object.

X-ray microtomography is the only known tool that can meet the requirements of monitoring voids, micro-cracks and flaws in activated and completely assembled rigs, test modules and the Li-target backwall.

The microtomographic systems have to fulfill rather difficult design constraints such as:

- high space resolution requirements;
- wide range of material densities and attenuation coefficients;
- capable to overcome limited access angle problems.

According to the main needs of the fusion materials community we considered two main types of samples: low density materials such as ceramics and light metallic alloys and high-density metals. In the later category, most representative are steel samples.

The evaluation of optimum tomographic configuration suitable for the IFMIF test cell was carried out by test measurements on existing tomographs and through 3-D Monte Carlo simulations of X-ray radiation generation and transport.

Following the evaluation procedure a cone-beam X-ray microtomographic system has been constructed at NILPRP. The system consists of an open type microfocus X-ray source, a 3-D micrometric translation and rotation sample manipulator and a 2-D X-ray detection system based on a large area image intensifier and fast-scan CCD.

(3) Experimental Equipment

A general view of the microtomography system is presented in Fig. 1. The main components

are: the open type microfocus X-ray source, the 2-D X-ray detection system and the micrometric sample manipulator. The X-ray source is mounted on a manually adjustable positioning support. The X-ray detection system is mounted on a micrometric translation axis supported by a manually adjustable positioning device. The whole tomographic system lies on an optical table which is placed inside a lead shielded cabinet. Two Dual Athlon, 2GHz networked workstations are used for the data acquisition and control and for the 3-D tomographic reconstructions and visualizations.

The designed targets of spatial resolution, magnification, and reduction of beam hardening can be optimally satisfied by a combination of image intensifier detection system and an open type 160 kVp X-ray source. These specifications are synthetically presented in Table 1. A few comments on key components are in order:

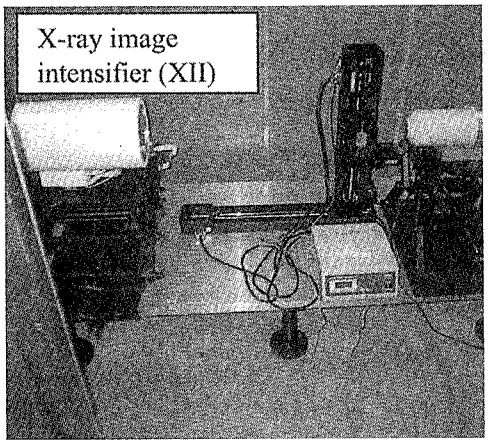


Fig.1 Fully 3-D cone-beam X-ray computer tomograph.

X-ray source

The system is provided with an open type 160 kV microfocus X-ray source manufactured by Phoenix|X-ray. Its main applications list includes typical inspection tasks in the automotive, aerospace, steel and electronics industries and industrial and medical computer tomography. At a feature recognition down to 1 μm, the minimum object-focus distance is 0.4 mm to provide highest geometrical magnifications at short focus-detector distances. Consequently this ensures a reasonable longitudinal dimension of the tomographic system: a distance of 1000 mm from the beryllium window to image intensifier input window would guaranty a magnification factor of about 2000. Another advantage consists in its replaceable filament. A small manual adjustable table was constructed in order to adjust the vertical and transversal position of the X-ray source.

Detection system

The detection system is based on a SIRECON 17-2 HDR-M X-ray image intensifier, manufactured by Siemens Medical Solutions. It is a large diameter (169 mm useful entrance field and 20 mm output window) imaging tube that converts low contrast images into visible light images. For image acquisition a 10 bit analog frame grabber IMAQ PCI-1409 from National Instruments is used. Due to a newly developed CsI input phosphor screen the X-ray image intensifiers provide high DQE (detection quantum efficiency) of 65% and high-quality images with good resolution and contrast (the modulation transfer function is less than 1% for 0.1 Lp/mm). The image intensifier is coupled with a CCD-Compact-Camera. The distortion of the lens has deliberately been selected to obtain compensation of the image intensifier distortion. The reduction in distortion for the total imaging chain (image intensifier + lenses + CCD) is in the range 3 to 7% depending on the reproduction scale. The detector is placed on a manually adjustable table with vertical and transverse positioning. Alternatively, the transverse position of the detector can be adjusted using a computer controlled micrometric motorized stage.

Micrometric manipulators

An essential component of a microtomograph system is the micrometric manipulator. Motorized stages are combined to assure a maximum degree of freedom in sample positioning for both tomography and high magnification radiography. The sample manipulator includes two translation and one rotation axis in order to realize an X-Z-θ assembly. The X stage has a relatively long travel distance (500 mm) for implementation of the magnification degree of freedom. Its positional repeatability is better than 10 microns. It is placed along the axis between the X-ray source and the detection system (X axis). The Z axis is used for sample elevation control and has a travel distance of

Table 1 MICROTOMOGRAPHIC SYSTEM: Overall Performances.

Items	Specifications
Microfocus X-ray source Max. high voltage: Max power: 20 W Feature recognition: 1 μm Min object-focus distance: X-Ray cone:	 160 kVp 20W 1 μm 0.4 mm 170°
Detector elements	512x512 or 1024x1024 (maximum)
Micrometric manipulator	- X stage, Z stage, θ stage - travel 500 mm, loading capacity 30 kg - travel 300 mm, loading capacity 6 kg - accuracy 0.03°, loading capacity 20 kg
Magnification Factor	< 2000
Source-Detector Distance	1000 mm typical
Source-Object Distance[1)]	>0.5mm typical
Spatial Resolution[2)]	≅10μm
Density Resolution	>0.5%
Digital Output[3)]	10 bits
Scanning Time[4)]	< 10min. (720 angle)
3D Reconstruction Time[5)]	< 2min. (256x256, 256lines) <5min. (512x512, 256lines) <20min. (1024x1024, 512 lines)
Effective Area of Detector	169x169 mm^2
Probe Dimensions	Diameter <40 mm; Height <500 mm
Projection Number	360 ; 720
Scan Method	Cone beam CT (<512lines)
Full scan Short Scan	360deg. 180deg.+1/2 fan angle
Output data format	Uncompressed 16 bits integer
Geometry Calibration Program	Center of Rotation
Alignment	Vertical & Horizontal

1) Minimum distance from X-ray focus to the object is 0.4 mm.
2) Mainly limited by stage control accuracy.
3) Digital output from frame grabber NI – PCI-1409.
4) Assuming 0.5sec./angle and stage motion.
5) Based on Dual Athlon, 2 GHz PC.

300 mm and positional repeatability better than 5 microns. The *Z* axis has a large enough loading capacity (6 kg) to support the rotary stage as well as the sample itself. The reinforced motorized rotary stage has a positional accuracy 0.03° or less and positional repeatability 0.01° or less.

The motorized stages are computer controlled simultaneously by a single control unit via a serial RS232 (or USB) port by a Mark-204 (Sigma-Koki, Japan) stage controller. Trigger output signals make it possible to synchronize the stage movements with external measuring devices as image acquisition. Additionally, a joy pad (control pad) is provided for manual operation, memory settings, and programming.

Optical table

The dimensions of the optical table are 1890 x 800 mm with a height of 300 mm above the

ground level and the possibility of a vertical adjustment of ±30 mm. It is provided with a rectangular screw hole matrix which allows the precise mounting of the microtomograph components.

X-ray shielding cabinet

The X-ray cabinet was designed and manufactured in our laboratory in accordance with the ionizing radiation safety regulations and is rated for continuous operation in normal working environments. In the calculations the weekly dose limit of 0.02 mSv is used, as derived from the dose limit for the general public (1 mSv/year). The X-ray shielding cabinet is made of steel and lined with lead with maximum 6 mm thickness on the front side of the cabinet and minimum 4 mm for the side facing the room wall and the ceiling. The lead shielding is covered by aluminium plates. Special attention was paid to solving the problem of the overlap of the lead sheath at joints, corners, penetrations, floor and door.

The X-ray cabinet is provided with a key-activated control to ensure that X-rays will not be generated when the key is removed. The door of the cabinet X-ray system has two safety interlocks.

For collision avoidance the inside of the cabinet is continuously watched by a video camera and it is provided with fans for extracting excess heat.

Image acquisition and 3-D reconstruction

Image acquisition and motorized stage control programs are developed on the base of National Instruments LabView Virtual Instruments.

The 3-D reconstruction is achieved by a generalized Feldkamp-type cone-beam algorithm cast in the filtered back projection framework. Specifically, the Feldkamp-type reconstruction consists of two processes: (1) filtration, and (2) back projection. In the filtration process, horizontal projection profiles are ramp-filtered in the Fourier domain after zero padding. In the back projection process, an image volume is reconstructed by back projecting filtered data along X-ray paths with appropriate weights.

The image acquisition, 3-D reconstruction and results visualization are performed on two networked Dual Athlon, 2GHz workstations. The reconstruction software is implemented such that the reconstruction time roughly matched the acquisition time so that at the end of the measurement a 3-D volume rendered image is available.

(4) Results and Discussions

According to Bio-Imaging Research, world leading manufacturer of tomographic facilities, current industrial CT systems cost from 400,000 USD to over 2 million USD. While the commercial products are very nice general-purpose instruments they might not be satisfactory to address the main challenges of the microtomography analysis of the fusion material samples i.e. the intense beam hardening effects associated with high-density materials samples. These challenges were identified and described in detail in [1,2]. Since our total budget is slightly higher than half of the minimum sum quoted above, we have to consider a compact low energy (low power) microtomographic facility [3].

According to the main needs of fusion materials community, we considered two main types of samples: low density materials such as ceramics and light metallic alloys and high-density metals. In the later category most representative are steel samples. Individual miniaturized samples and complex structures of individual samples were investigated and detailed results are presented elsewhere [3].

Low density materials

Obviously, the most important low-density materials relevant to fusion application are ceramic tritium breeders. Figure 2 shows the images reconstructed for two high voltages for a relatively large channelled ceramic sample at low magnification. One can say that this is a satisfactory result showing accurately the structural integrity. Since the pre-filtering was insufficient (thicker pre-filters would reduce too much the flux) the higher voltage measurement displays higher beam hardening effects (apparently lower density in the inner part of the image).

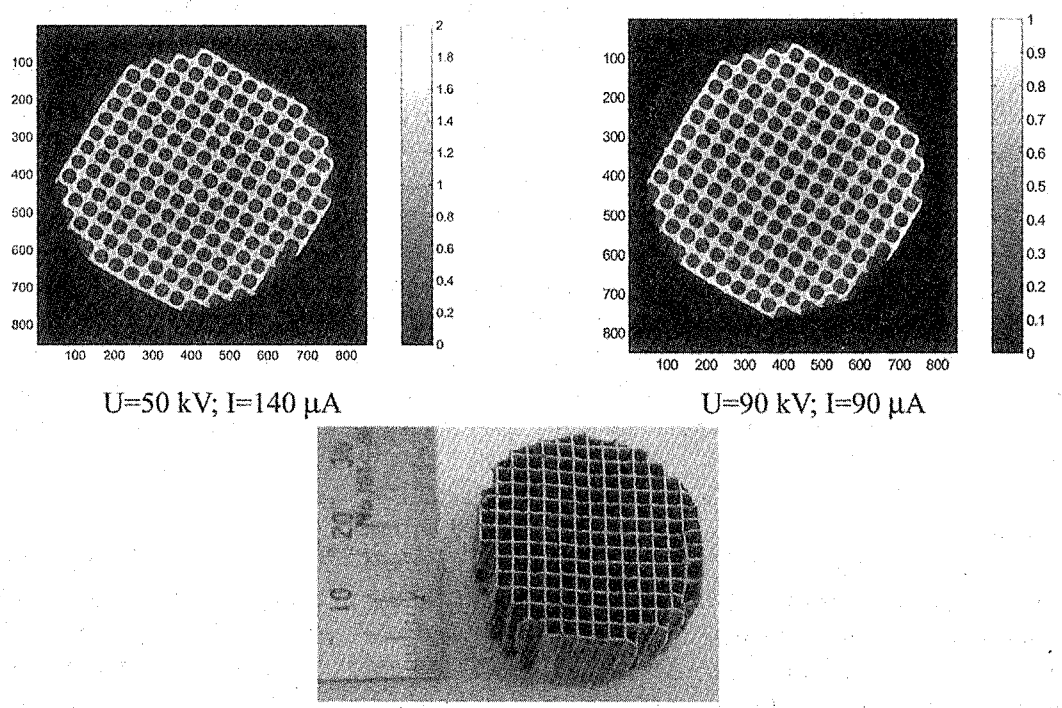


Fig. 2 Reconstruction images of ceramic structure. The size of the hole is 1.5 mm and the wall is 0.25 mm thick. Magnification = 1.2.

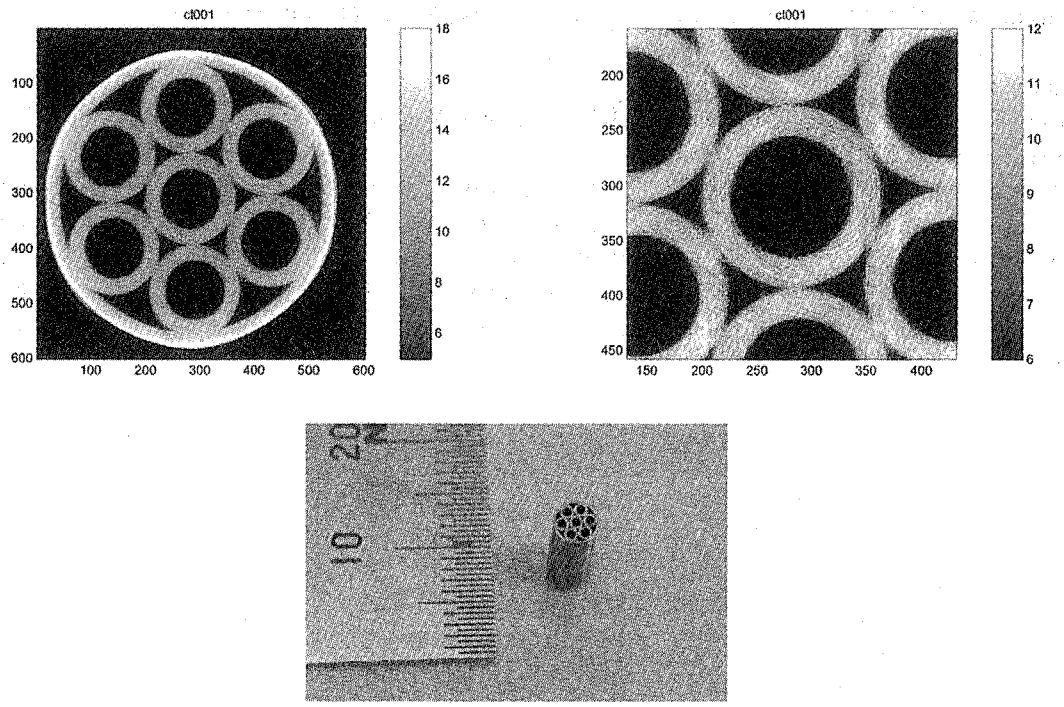


Fig. 3 Reconstruction image of an SUS bundle (U=90 kV; I=90 μA, Magnification 7.1). Exterior diameter of the outer pipe is 5 mm, wall is 0.25 mm thick. Magnification = 1.2.

High density materials

Most relevant high-density metallic materials are composed of steel and similar alloys. As an example we present a reconstruction of a structure composed of SUS 316. Figure 3 represents the reconstructed cross section of a SUS bundle of 7 pipes of 1 mm interior diameter enclosed in an outer

pipe of 5 mm exterior diameter. All pipe walls are 0.25 mm thick. One remark is that beam hardening effects are very strong with the attenuation coefficient of the center pipe, more than 80% lower than the attenuation coefficient of the outer pipe. In the left picture one shows a zoomed image of the pipe welding.

Design considerations extracted from test measurements:

- A compact low energy (low budget) microtomographic facility performs adequately only in measurements which require low magnification (i.e. low space resolution) and for relatively low density materials as ceramics and light metal alloys.
- In most of the measurements involving high-density individual samples or structures, most relevant for the fusion materials community, such an instrument performs rather unsatisfactorily.

Based on these considerations we included in our new system a relatively high energy (max 160 kVp) open type microfocus X-ray source and an X-ray image intensifier. This configuration allows us to reduce the beam hardening artifacts and at the same time to achieve very large magnification factors (up to 2000).

(5) Conclusions

The newly developed tomography system will allows us to provide the fusion materials community with a unique instrument for NDT inspection of individual miniaturized samples as well as for verification of irradiation capsule integrity. In the process of using this facility for extensive NDT inspection of fusion material miniaturized samples, the main goal was to establish the reference design for transmission microtomography system for IFMIF environment conditions. An effort will also be made to develop new methods to cope with the challenging problem of beam hardening in high density materials. Fully 3-D Monte Carlo radiation transport simulations, combined with validation experiments, represent our main tools in approaching these problems. In addition, new inspection configurations will be investigated in order to visualize irradiation capsules integrity.

References

[1] I. Tiseanu, Micro-tomography for IFMIF, Technical Meeting on IFMIF Test Facility System September 20 2000, ENEA-Brasimone, Italy.

[2] I. Tiseanu, M. Ganciu, F. Gherendi, M. Iacomi, N.B. Mandache, M. Nistor , Tomographic test measurements for miniaturized fusion material samples, Interim Report 04/2001, National Institute for Lasers, Plasma and Radiation Physics.

[3] I. Tiseanu, C. Sauerwein, M. Simon, M. Misawa, High-Resolution X-ray Tomography for Nuclear Applications and Research, Annual Meeting of Nuclear Technology, May 2002, Stuttgart, Germany.

3.3.7 TF34-JA : Tritium Laboratory and Tritium Processing

(1) Brief Task Description

Gaseous, liquid, and solid materials contaminated by tritium are generated during IFMIF operation, and these materials need to be processed appropriately. Also, an airtight hot cell is required to perform post irradiation examination (PIE) of the activated/tritium contaminated materials such as irradiated ceramic breeder materials. To meet these needs, a tritium processing method is designed on the basis of the evaluation of tritium sources and generation rates. The tritium laboratory for PIE of the activated/tritium contaminated materials is also evaluated.

Contributor

Name	Party	Institute	E-mail address
T. Yutani	Japan	JAERI	yutani@ifmif.tokai.jaeri.go.jp

(2) Introduction

In the IFMIF tritium is generated in reactions between the 40 MeV deuterons and the lithium (Li). It is also generated in the tritium release test of ceramics breeders [1]. Moreover, the high-energy and a small fraction of the deuteron beam that is lost in the accelerator produce tritium. The gaseous, liquid, and solid materials contaminated with tritium need to be processed appropriately. An airtight hot cell (tritium hot cell) which has the capability of handling materials that have high activity and tritium contamination is necessary, to perform PIE on irradiated ceramic breeder materials. The backwall of the lithium target assembly will be exposed to the highest neutron flux, and the lithium target assembly must be exchanged periodically or repaired. The maintenance of the lithium target assembly must be carried out in the tritium hot cell.

(3) Tritium Source

The sources of tritium in IFMIF are shown schematically in Fig. 1. The main tritium source is the reaction in the lithium target assembly:

$$D + {}^{7}Li \rightarrow T + {}^{6}Li \quad (1)$$

The production rate of tritium due to this reaction will be about 7 g/year. Most of the tritium will be trapped by an yttrium trap in the lithium purification loop, and the remainder, 0.65 appm in the Li at steady state (total of 4.41×10^{14} Bq), will be distributed throughout the lithium in the loop components made of 316 stainless steel. (In this design all components are assumed to be 316 stainless steel, although a part of the components will be made of a low activation steel). Small amounts of the tritium will escape from the liquid lithium and permeate through 316 stainless steel boundaries. The tritium in the liquid lithium adheres to the inner surface of the components in accordance with the distribution coefficient between liquid lithium and 316 stainless steel. Then, the tritium diffuses through the wall and leaks out. The tritium concentration $C_{T\text{-}316}$ of the inner surface is given by

$$C_{T-316} = C_{T-Li} \times K_d \quad (2)$$

where $C_{T\text{-}Li}$ is the tritium concentration in liquid lithium and K_d is the distribution coefficient. Because K_d between 316 stainless steel and lithium is unknown, the estimated value for 304 stainless steel is used as follows.

$$\ln K_d = 2.52 - 7500/T \quad (3)$$

Where T is temperature (K). The flux of tritium from the outer surface of metal at steady state is given approximately by

$$J(L) = D(T)\left(\frac{C(0) - C(L)}{L}\right) \quad (4)$$

where J(L) is the diffusion flux of tritium from the outer surface of metal of thickness L, D(T) is the diffusion coefficient at temperature T, C(0) is the tritium concentration at the inner surface of metal, and C(L) is the tritium concentration at the outer surface of metal. Then, the diffusion flux from the

316 stainless steel is as follows.

$$J(L) = 1.07x10\text{-}16\ (g/m2/s) \quad (5)$$

A leak rate is obtained by multiplying J(L) and the total surface area of all components. The lithium loop components will be installed in two areas, the test cell where the lithium target assembly and the quench tank are installed, and the lithium loop area where the remaining components are installed. The leak rates of tritium to the lithium loop area is $1.1x10^{4}$ Bq/h ($3.1x10^{-11}$ g/h) and to the test cell area $2.3x10^{3}$ Bq/h ($6.55x10^{-12}$ g/h). However, a safety factor of about 10 is used for the lithium loop area to be conservative in the evaluation. Thus, the leak rate of tritium to the lithium loop area becomes $1x10^{5}$ Bq/h.

Tritium release tests of ceramic breeder materials such as Li_2O and Li_2ZrO_3 will be conducted using an in-situ tritium release test module. The generation reaction for tritium is

$$n+{}^{6}Li \rightarrow T+{}^{4}He \quad (6)$$

In this module, specimens in the shape of pebbles are loaded into the specimen holders and helium gas containing up to 1000 ppm hydrogen flows through each holder to sweep out released tritium[2]. The tritium concentration in helium is assumed to be 1000 Bq/cc. The total flow rate of helium is 1000 cc/min (0.06 m^3/h) so, if there are five specimen holders, the tritium release rate becomes $6x10^{7}$ Bq/h.

The high-energy neutron generated within the accelerator (by the reaction between a small escaped fraction of the deutron beam and the accelerator components) reacts with the nitrogen and oxygen in the air around the accelerator and with cooling water as follows.

$$\begin{aligned} n+{}^{14}N &\rightarrow T+{}^{12}C \\ n+{}^{16}O &\rightarrow T+{}^{14}N \end{aligned} \quad (7)$$

Another source of tritium is the high energy neutrons produced in the target reacting with the elements in the components and the wall in the test cell as follows.

$$\begin{aligned} n+{}^{56}Fe &\rightarrow T+{}^{54}Mn \\ n+{}^{58}Ni &\rightarrow T+{}^{56}Co \\ n+{}^{12}C &\rightarrow T+{}^{10}B \end{aligned} \quad (8)$$

The tritium quantities produced by equations (7) and (8) are assumed to be small, although the estimates are only approximate because the uncertainties in the nuclear reaction data for high energy neutrons are large.

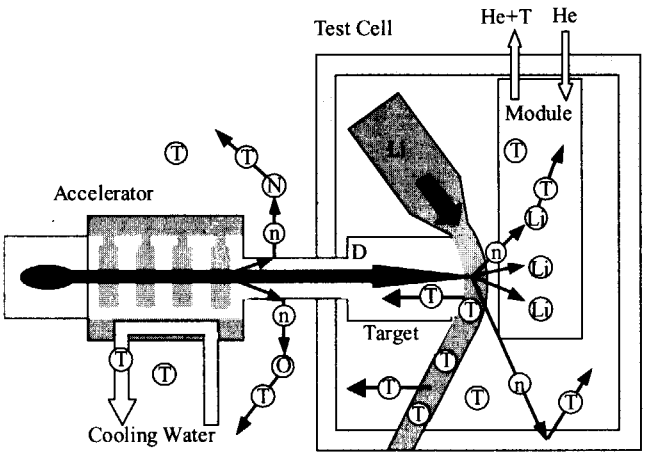


Fig. 1 Schematic identification of tritium sources.

The measurement of the tritium inventory in the irradiated ceramic breeder materials, handling of the lithium target assembly, and other operations will be carried out in the tritium hot cell. The tritium discharge rate in the tritium hot cell is assumed to be $6x10^{7}$ Bq/h, the same as the tritium release rate in the in-situ test module.

(4) Tritium Processing

The final disposal of the tritium will not be carried out in IFMIF. Also, the tritium processing will be conducted using established technology. A processing flow diagram for gases containing tritium is shown in Fig. 2. The exhausts from the lithium loop area, the in-situ tritium release test module and the tritium hot cell, and the vacuum exhaust from the test cell, etc. will be discharged through the stack after they have been continuously detritiated to below one tenth of the regulatory limit. The exhausts from other areas where tritium contamination is possible are detritiated by the temporary exhaust detritiation system for air whenever tritium is detected or before the start of maintenance operations.

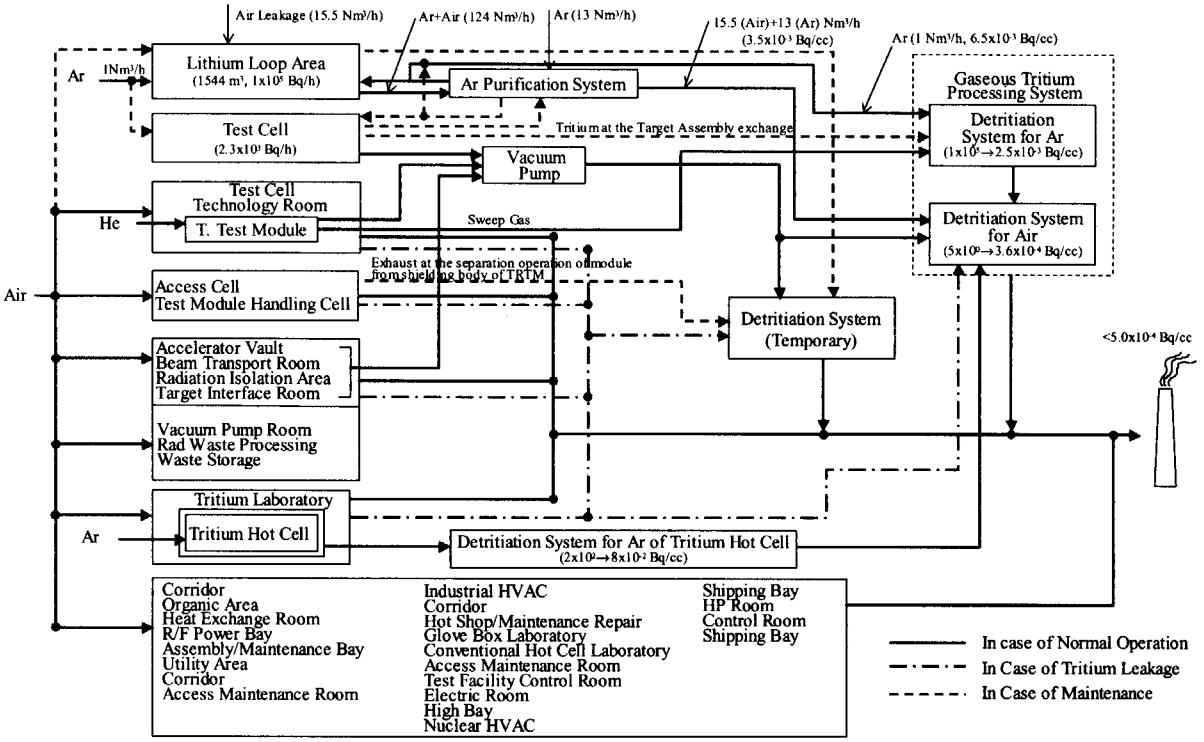


Fig. 2 Flow chart for the processing of gases containing tritium.

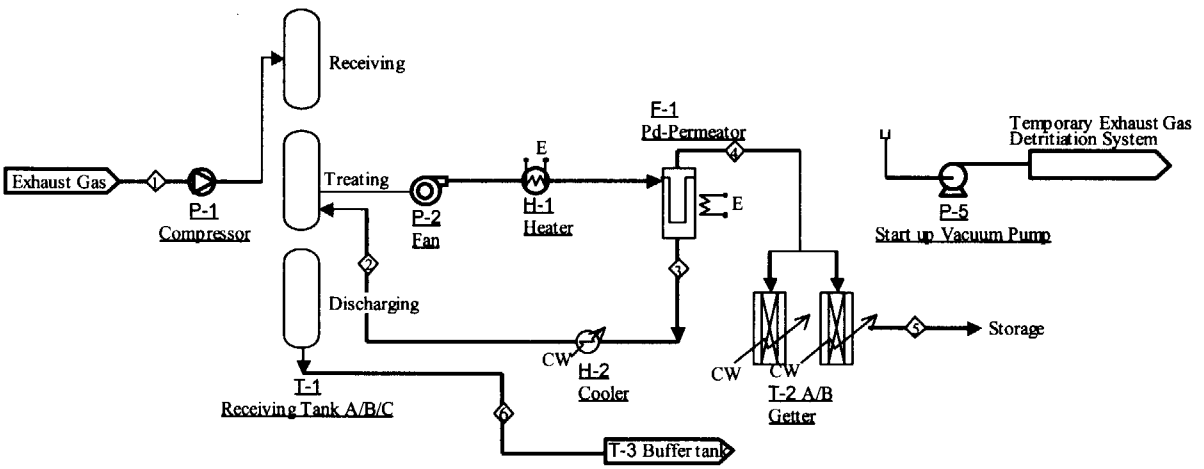


Fig. 3 Flow chart of the exhaust detritiation system for tritium contaminated Ar gas.

Since lithium reacts intensly with oxygen, nitrogen, water, carbon dioxide etc, the lithium loop area is filled with argon (Ar) to eliminate the possibility of combustion in the event of a lithium leak.

The lithium loop area is kept at negative pressure to prevent uncontrolled releases of the tritium. Also, any air component in the Ar gas needs to be eliminated and discharged, because any air could leak to the lithium loop area. The leak rate of air into the lithium loop area is assumed to be 1.0 vol%/h, entering through the epoxy lining of the interior walls, and through the seals placed to maintain air-tightness, e.g., seals of feedthroughs for cables or pipes. The circulation rate of Ar gas to eliminate air by the Ar purification system depends on the level to which the oxygen and nitrogen concentrations are to be regulated. In order to make a conservative evaluation, the regulatory value for oxygen is assumed to be 2 wt% (selected as half of that in the sodium coolant loop area of the fast reactor in Japan). The regulatory value for nitrogen is assumed to be 7 wt%, which is the nitrogen concentration when the oxygen concentration in Ar gas becomes 2 wt%. Then, the required circulation rate is about eight times the air leak rate. Figure 3 shows the flow chart for the exhaust detritiation system for tritium contaminated Ar gas during normal operation.

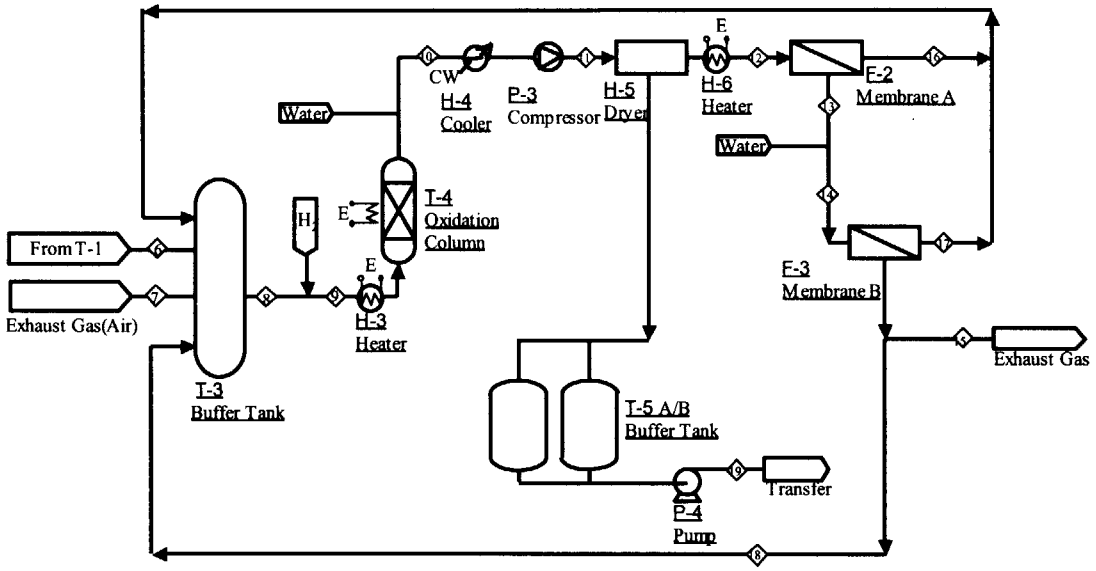


Fig. 4 Flow chart for the exhaust detritiation system for tritium contaminated air.

A pressure swing absorption (PSA) method will be adopted to eliminate oxygen and nitrogen. In this method, replacement Ar gas of 10-20% of the atmosphere processed is necessary as a purge gas. The atmosphere discharged from the Ar purification system is processed in the exhaust detritiation system for tritium contaminated air. In order to adjust the pressure in the lithium loop area, part of the Ar gas (1 Nm^3/h) that is purified by the Ar purification system is discharged, and new Ar gas supplied. The discharged Ar gas is processed by the exhaust detritiation system for tritium contaminated Ar. Subsequently, this gas is processed to below one tenth of the regulatory value by the exhaust detritiation system for tritium contaminated air. The tritium hot cell will be filled with Ar gas at negative pressure. The concentration of oxygen and nitrogen will be controlled by supplying new Ar gas, because the air leak rate of the cell may be lower than that of the lithium loop area. Argon gas discharged from the cell will be processed in the exhaust detritiation system for tritium contaminated Ar gas of the tritium hot cell, because it includes air and unknown tritiated chemical species.

The detritiation systems are as follows.

1) Exhaust detritiation system for tritium contaminated Ar gas. In this system the tritium in the exhausted Ar gas is separated from other gases by a Paladium permeation system and is absorbed by a tritium getter alloy that is used to occlude hydrogen gas as shown in Fig. 3.
2) Exhaust detritiation system for tritium contaminated air. A flow diagram for the exhaust detritiation system for tritium contaminated air is shown in Fig. 4. The tritiated species in

the exhaust gas is oxidized to tritiated water using an oxidation catalyst at high temperature. Tritiated water in the exhaust gas is condensed and collected. The tritiated water in the remaining exhaust gas is removed through the membrane separators.

3) Exhaust detritiation system for triated Ar gas from the tritium hot cell. This is fundamentally the same method as the exhaust detritiation system for triated Ar except for processing to remove impurities by zirconia.
4) Temporary exhaust gas detritiation system. This is fundamentally the same method as the exhaust detritiation system for tritium contaminated air.

Liquid waste with tritium contamination will come from the cooling water of the accelerator, PIE (polishing, etching and cleaning operation) and decontamination in the tritium laboratory, and tritiated water generated in the exhaust detritiation system for tritium contaminated air. These will be discharged after dilution by an evaporator. The concentrated liquid is temporarily stored or solidified, if necessary.

Highly activated solid wastes with tritium contamination will be generated in the test cell, the tritium hot cell, the lithium loop area and the exhaust detritiation system for tritium contaminated Ar gas. These wastes include pieces of the in-situ tritium release test modules, tested specimens of ceramics breeder materials, lithium target assembly, traps, and spent getters. These will be stored in the waste storage cell. The spent ion-exchange resin, materials solidified with concrete, paper and rags used in controlling the contamination, etc. will be placed in containers and stored in an existing storage facility on the site, a facility that is not part of IFMIF.

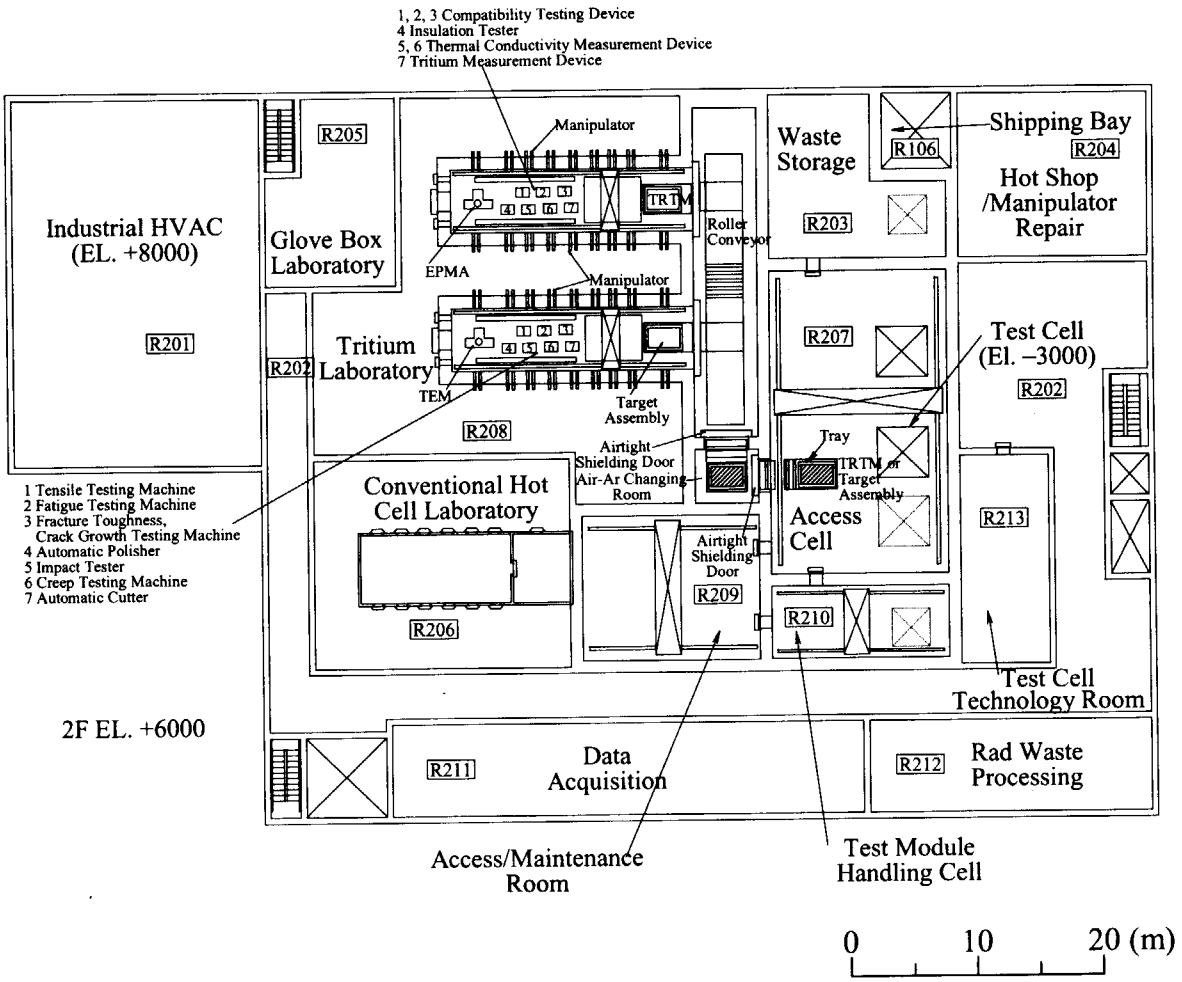


Fig. 5 Plan view of the second floor of the IFMIF building, showing the tritium laboratory.

(5) Tritium Laboratory

A PIE facility is located in the second floor of the IFMIF building. It includes the tritium laboratory with the capability to handle various forms of tritium contaminated materials generated in the operation of IFMIF. Figure 5 shows a plan view of the second floor. This layout will be reconsidered according to the detailed design of Tritium Handling Hot Cells and other PIE facilities.

The test cell contains vertical test assemblies (VTAs), the lithium target assembly, etc[1]. The VTA supports the modules used for the in-situ tritium release test module and other irradiation experiments. After irradiation, the VTA is lifted into the access cell located above the test cell and the module is separated from the VTA using a remote handling system. The in-situ tritium release test module with a weight of about 100 kg is packaged to prevent tritium leakage and is transported to the tritium hot cell via an Ar-gas/air exchange room using the roller conveyors. The lithium target assembly with a weight of about 1000 kg is transported to the tritium hot cell by the same method. The PIE for the in-situ tritium release test module will include the retrieval of specimens from the module and reloading the irradiated specimens, ceramography observation, SEM observation, thermal conductivity measurement, tritium measurement, etc. Therefore, equipment for assembly/disassembly, optical microscopy, SEM, thermal conductivity measurement, tritium measurement, etc. will be installed.

Dedicated equipment including a welder are necessary for the maintenance of the lithium target assembly. The backwall of the lithium target assembly will be regularly tested for damage because it is exposed to the highest neutron flux. Therefore, various equipment (machines for tensile testing, fatigue testing, fracture toughness testing, crack growth testing, creep testing, etc.) will be installed.

The airtight tritium glove box, to analyze small pieces of ceramic breeder materials or low gamma-ray activity ceramic breeder materials, was included in the tritium laboratory in the CDA[1]. However, the activities of ceramic breeder materials is expected to be too high to handle in the glove boxes, even if their sizes are small. Therefore, the glove boxes are eliminated, and the function of the Tritium Handling Hot Cell is expanded to include the analysis of small pieces of ceramic. The tritium hot cell consists of two lines as shown in Fig. 5 and has the capability of handling the in-situ tritium release test module and the lithium target assembly simultaneously.

(6) Conclusions

The tritium processing methods are designed on the basis of the evaluation for the tritium sources and the tritium generation rates. The main tritium source is the D-Li reaction in the litium target. Most of the tritium will be trapped by the yttrium trap, and the remainder will be distributed in the liquid lithium. The main concern for processing is the gaseous tritium released into the lithium loop area due to permeation from the liquid.

The tritium hot cell in the tritium laboratory has the capability of handling materials such as irradiated ceramic breeder materials and the irradiated lithium target assembly that have high activity and tritium contamination.

The future issues to be addressed include the detailed evaluation of the tritium leak rate from liquid lithium, examination of the capacity of the exhaust detritiation system during maintenance, evaluation of the radioactivity due to high energy neutrons, and regulations for allowed concentrations of O_2 and N_2 in the lithium loop area.

References

[1] IFMIF-CDA Team (Ed.) M.Martone, "IFMIF Conceptual Design Activity, Final Report," ENEA Frascati Report, RT/ERG/FUS/96/17 (1996).

[2] IFMIF Team (Ed.) A.Moeslang, "IFMIF Conceptual Design Evaluation Report," Forschungszentrum Karlsruhe report, FZKA 6199, January 1999.

3.3.8 TF35-JA : Arrangement of the Test Cell System

(1) Brief Task Description

The equipment installed in the test cell, access cell and test module handling cell require various pipes and wires for the signal, power and coolant connections. These need to be connected through the shielding walls to the related systems located outside the cells, without allowing radiation leaks or presenting obstacles to the operation of equipment. The arrangement of the test facilities must take into account the irradiated material flow. Therefore, examination of the arrangement of piping and wiring and of the irradiated material flow was carried out. The result was to show that the piping and wiring from the equipment can be connected with the related systems, and the test cell facilities are arranged so they do not obstruct the flow of irradiated material.

Contributor

Name	Party	Institute	E-mail address
T. Yutani	Japan	JAERI	yutani@ifmif.tokai.jaeri.go.jp

(2) Introduction

Test equipment such as the vertical test assembly (VTA) is equipped with various signal lines, power cables, and coolant lines. Also, the cooling system, instrumentation equipment, vacuum pumping, and surveillance systems outside the cells are connected to components in the test cell. The piping and wiring for these systems need to be arranged in the optimum way. Furthermore, the test cell and its surrounding area must be arranged to take into account the flow of irradiated material.

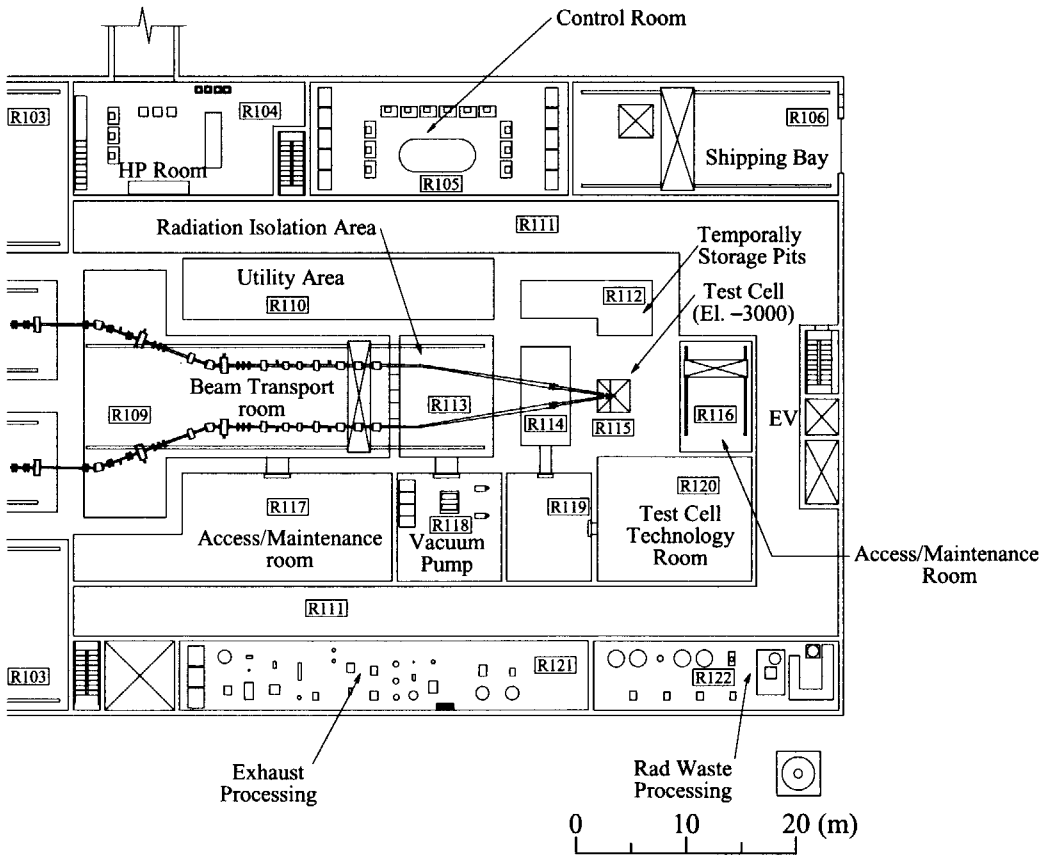


Fig. 1 Plan view of test cell and its surrounding area on 1st floor.

(3) Arrangement of Piping and Wiring

The control systems, vacuum pumps and gas supply systems etc. for the test cell, access cell and test module handling cell and for the equipment installed in these cells will be located outside the cells. Many pipes and wire must be connected to the control systems, vacuum pumps and/or gas supply systems etc. Finally, most of those are linked to the central control systems. However, the installation and location of systems with which these pipes and wire are connected are important for the arrangement of the test cell and the surrounding area. Table 1 shows the expected piping and wiring for the test cell, access cell, test module handling cell and equipment in these cells. The plan view of the test cell and its surrounding area on the first floor is shown in Fig. 1. The plan view of the second floor is shown in Fig. 2. (Note: Some differences between Fig. 1 and 2 need to be coordinated after KEP.)

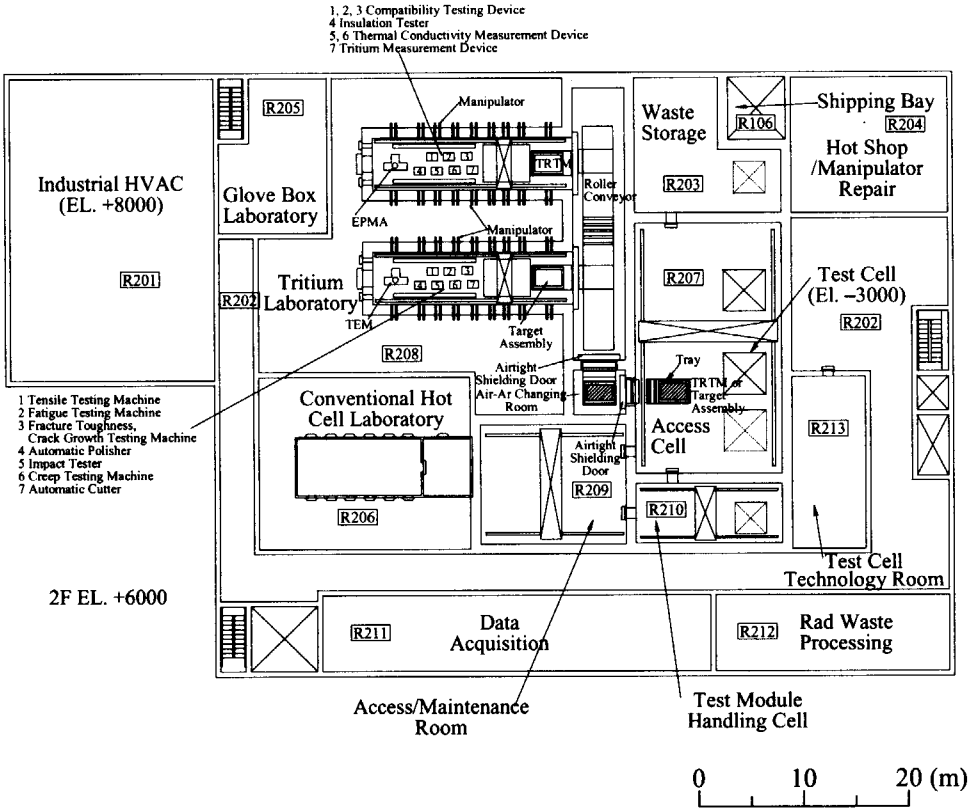


Fig. 2 Plan view of 2nd floor.

The test cell technology room on the first floor, adjacent to the test cell, houses equipment such as vacuum pumps, He gas cooling system, Ar gas supply system, control units, etc. The vacuum lines, He gas coolant piping, Ar gas supply piping, and signal lines for surveillance systems for the test cell are connected with related equipments in the room. The vacuum line piping and electric heater/ thermocouple wiring of heat insulating material for the lithium target assembly and quench tank that are housed in the test cell are also connected with related equipment in the room. When accelerators are operating, personnel access to the test cell technology room may be restricted or impossible because of neutron streaming through piping and wiring.

The test cell technology room on the second floor adjacent to the access cell and test module handling cell houses the He gas cooling system for test cell cover and equipment for irradiation experiments (He cooled high flux test module, in-situ creep-fatigue test module, in-situ tritium release test module and vertical irradiation tube). Personnel access to this room may be possible during operation of the accelerators. The piping and wiring from the access cell to the test cell technology

room must pass below the rail of the gantry crane of a universal robot to allow operation of the universal robot. Figure 3 shows the elevation view of the test cell and the surrounding area that is drawn on the basis of the position of the deuteron beams. The upper end of the upper test cell cover is located about 55 cm below the floor level of access cell. (The exact distance depends on the thickness of the shielding ceiling of the beam transport room and the radiation isolation area.) The piping and wiring can pass below the rail by using this difference in level.

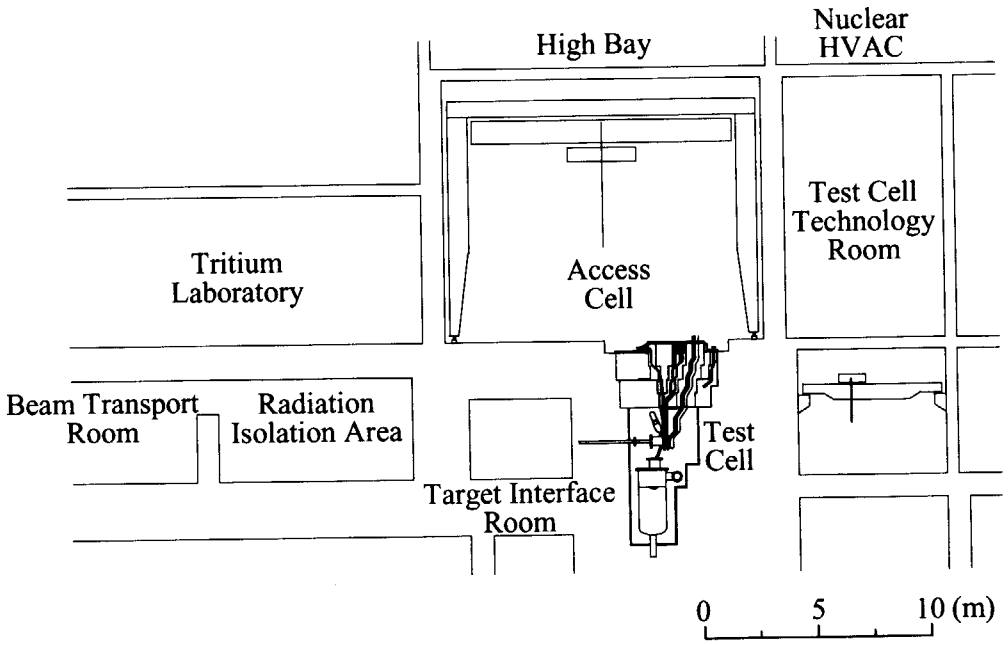


Fig. 3 Elevation section view of test cell and its surrounding area.

Operation of the universal robots in the access cell and test module handling cell is conducted from the operating area (R202). The cable and wiring for each universal robot are taken to the operation area at location above the top of each universal robot. The wiring for access cell and test module handling cell are taken to the operation area at locations above the top of each universal robot or under the rail of the universal robots.

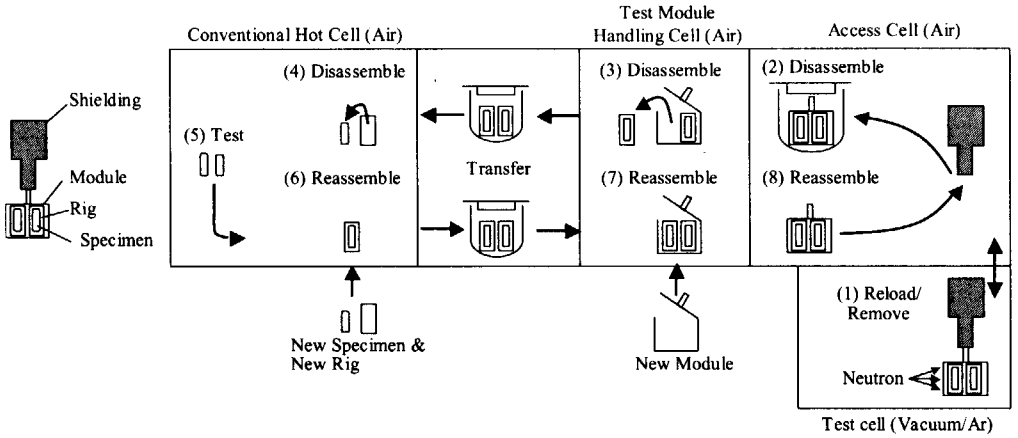
(4) Irradiated Material Flow

The irradiated material flow from the test cell to the post irradiation examination (PIE) facilities is shown schematically in Fig. 4. This figure is modeled on VTA 1 with the He cooled high flux test module and VTA 2 with the in-situ tritium release test module.

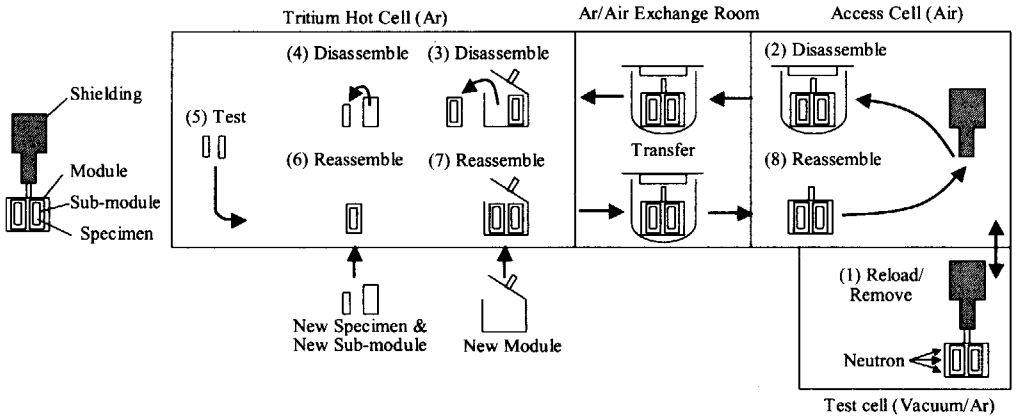
PIE for most high activity materials irradiated in the high- and medium-flux regions (except for the tritium contaminated and tritium containing materials) will be performed in the conventional hot cell or shielded glove box laboratory. Some testing of moderate activity materials irradiated in the medium- and low-flux regions may also be performed in these rooms. The material flow to the shielded glove box laboratory is not shown in Fig. 4. PIE of tritium contaminated and tritium containing materials is performed in the tritium hot cell.

A test assembly removed from the test cell is disassembled in the access cell (disconnection of the test module from the shielding body). The test module without contamination of tritium is disassembled in the test module handling cell (removal of rigs from test module). If the test module can be reused, the rigs are removed from the test module in the access cell, without removing the test module from the shielding body. The access cell and test module handling cell are separated by a concrete shielding wall. The test module is moved through the shielding door between the access cell and test module handling cell. Personnel access to the access cell is possible by putting components

with shielding attached (such as the VTA) into the storage pits in the access cell and by moving other activated material into the test module handling cell.



(a) Flow of materials that is not contaminated with tritium.



(b) Tritium contaminated and containing material flow.

Fig. 4 Irradiated material flow from test cell to PIE facilities

Irradiated rigs in a container (or shielded cask) are moved from the test module handling cell to the conventional hot cell through an access/maintenance room (R209) using a rig transporter on the universal robot system. Whether or not the access/maintenance room is shielded has not been decided. Personnel access to the access cell and test module handling cell is through the access/maintenance room. The maintenance and repair of contaminated equipment that can be moved from the hot cells are conducted by hands-on operation in the access/maintenance room, and this room is also used to store equipment when it is not being used in the hot cells.

The specimens are removed from the rigs arriving at the conventional hot cell before testing. Some testing of small volume specimens is performed in the shielded glove box laboratory. Small volume specimens in a shielded small vessel can be moved by hand from the conventional hot cell to the shielded glove box laboratory.

It is likely that irradiation rigs and test modules may not be able to reach the full goal fluences of the specimens, because they are exposed to a higher neutron flux than the specimens. Therefore specimens must be repeatedly reencapsulated into new rigs and new test modules. Also, new specimens are installed in the rigs to fill the space that was occupied by specimens removed for PIE.

Therefore, the mix of irradiated and new specimens will be installed in new rigs in the conventional hot cell by remote handling. The assembled rigs are moved from the conventional hot cell to the test module handling cell and are installed in a new test module. The test module is connected to the shielding body in the access cell (reassembly of the VTA). The VTA is stored in the storage pit until installed for the next irradiation.

The tritium contaminated and containing materials such as the in-situ tritium release test module and lithium target assembly are handled in a similar way in the tritium hot cells.

The in-situ tritium release test module that is packaged to prevent the leakage of tritium is disassembled in the access cell, and then is moved from the access cell to the tritium hot cells through an Ar/air exchange room by using the roller conveyors. When the roller conveyors are not used, these are stored where they do not interfere with the operation of universal robot or the movement of the shielding door.

The tritium hot cells consist of airtight cells with two lines: one for PIE of the in-situ tritium release test module and materials tests containing tritium (to be designed in the future); the other for the repair and maintenance of the lithium target assembly. These cells are filled with Ar gas to process unknown tritiated chemical species and to eliminate the possibility of lithium combustion. Several PIE tests such as the measurement of tritium inventory and observation of microstructure are performed for specimens that are removed from the in-situ tritium release test module and its sub-modules. When specimens are to be re-irradiated, they are installed into new sub-modules/modules in the tritium hot cells. The lithium target assembly is handled in the same way. (Its details may be described in other KEP task report.)

The highly activated solid wastes like tested irradiated specimens, irradiated test modules and irradiated lithium target assemblies will be generated by IFMIF operation. These are put into containers and stored in the waste storage cell (R203) next to the access cell.

(5) Summary

Examination of the arrangement of piping and wiring and of the flow of irradiated materials was carried out. The piping and wiring from the equipment in the test cell, access cell and test module handling cell can be connected with the related systems installed in the test cell technology room on the first floor or second floor, or in the operating area. The test cell facilities are arranged so they will not interfere with the irradiated material flow.

The pipes and wires of the test cell and of the equipment installed in the cell are connected to related systems in the test cell technology room that is adjacent to the test cell on the first floor. The piping and wiring from the access cell to the test cell technology room on the second floor must pass below the rail of the gantry crane of a universal robot so it does not prevent operation of the universal robot. Operation of universal robots in the access cell and test module handling cell are conducted from the operating area.

Materials without tritium contamination are moved in a container to the conventional hot cell through the access/maintenance room, using the transporter. Small volume specimens in a shielded small vessel are moved by hand from the conventional hot cell to the shielded glove box laboratory. Tritium contaminated and containing materials that are packaged are moved to the tritium hot cells through the Ar/air changing room using the roller conveyors

Table 1 Piping and wiring for the test cell, access cell, test module handling cell, and equipment installed in these cells.

Equipment/ room	Pipe /wire	Installation room	Installation room of related system
Test cell	Vacuum line piping	Test cell	Test cell technology room (1F)
	He gas coolant piping	Test cell	Test cell technology room (1F)
	Ar gas supply piping	Test cell	Test cell technology room (1F)
	Signal line for surveillance system	Test cell	Test cell technology room (1F)
Test cell cover	He gas coolant piping	Access cell	Test cell technology room (2F)
Target assembly, Quench tank	Vacuum line piping	Test cell	Test cell technology room (1F)
	Electric heater/ thermocouple wiring for heat insulating material	Test cell	Test cell technology room (1F)
He cooled high flux test module	He coolant piping	Access cell	Test cell technology room (2F)
	Thermocouple wirings	Access cell	Test cell technology room (2F)
	Electric heater wirings	Access cell	Test cell technology room (2F)
In-situ creep-fatigue test module	Signal line wiring	Access cell	Test cell technology room (2F)
	Coolant piping	Access cell	Test cell technology room (2F)
In-situ tritium release test module	He sweep gas line piping with heater	Access cell	Test cell technology room (2F)
	He coolant piping	Access cell	Test cell technology room (2F)
	Vacuum line piping	Access cell	Test cell technology room (2F)
	Thermocouple wirings	Access cell	Test cell technology room (2F)
Vertical irradiation tube	Tubes	Access cell	Test cell technology room (2F)
Universal robot	Power cable	Access cell, Test module handling cell	Operating area
	Signal line wiring	Access cell, Test module handling cell	Operating area
Access cell	Wiring for lighting	Access cell	Operating area
	Signal line for surveillance system	Access cell	Operating area
Test module handling cell	Wiring for lighting	Test module handling cell	Operating area
	Signal line for surveillance system	Test module handling cell	Operating area

3.3.9 TF36-JA : Transfer of Heavy Equipment (Examination of Universal Robot System)

(1) Brief Task Description

Heavy equipment such as a Vertical Test Assembly must be accurately aligned to the neutron source, to irradiate specimens to high fluence as fast as possible. Some of the equipment will become highly activated. The remote handling system and operational flow to handle these items are examined. The remote handling system consists of a large universal robot system and other equipment. The large universal robot system is based on a gantry crane equipped with movable tables with positioning accuracy better than 1 mm. This system will cover almost all of the operations expected in the irradiation field.

Contributor

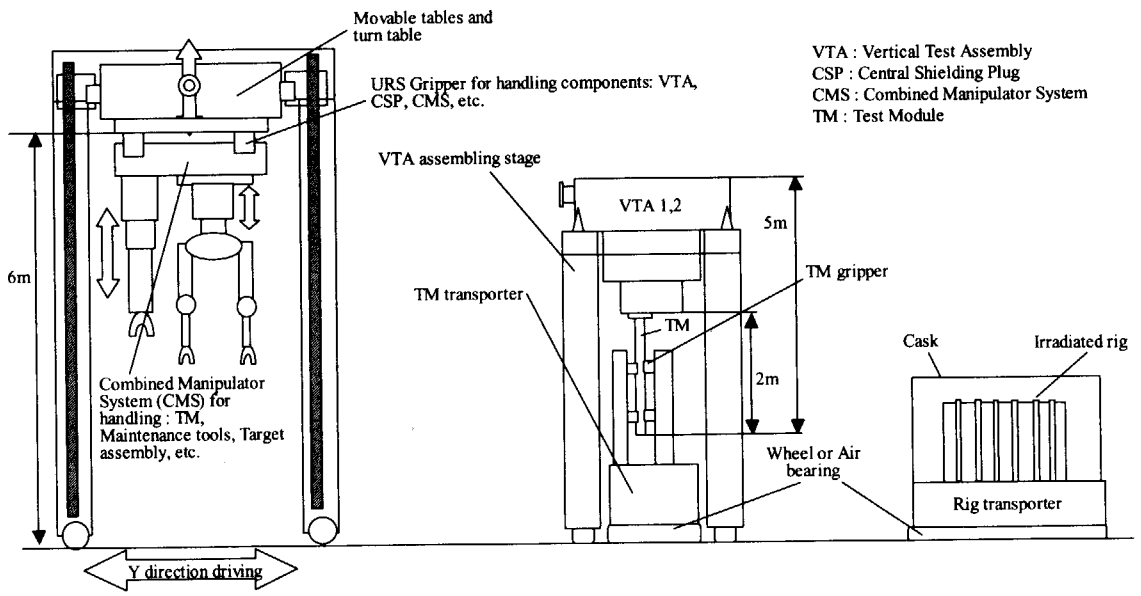
Name	Party	Institute	E-mail address
T. Yutani	Japan	JAERI	yutani@ifmif.tokai.jaeri.go.jp

(2) Introduction

The irradiation equipment in IFMIF such as the Vertical Test Assembly (VTA) is heavy (>5 tons), because it includes a shielding body of concrete arranged in stair-step [1]. In order to irradiate specimens to high fluence as fast as possible, the test module that is the specimen holding section of the VTA must be accurately aligned to the neutron source (lithium target assembly). This is because the neutron flux gradient in the direction of the beam is large. Therefore, the heavy equipment needs to be positioned accurately (±1mm) by the remote handling system.

(3) Remote Handling System

The remote handling system for the access cell and the test module handling cell (located over the test cell) can cover almost all of the operation expected in these cells. This system is composed of a large universal robot system for the access cell, a small universal robot system for the test module handling cell, a test module transporter and a rig transporter, as shown in Fig. 1 [2].



(a) Large & Small Universal Robot System with CMS (combined Manipulator System) for Access and Test Module Handling cells

(b) Test Module Transporter

(c) Rig Transporter

Fig. 1 Remote handling system.

The large universal robot system is composed of a gantry crane for transportation in the Y direction and manipulators with several degrees of freedom. The gantry crane is equipped with movable tables for X, Y and Z (vertical) directions, a turntable, and a gripper. The manipulators are connected to the gripper. The test module transporter covers the waste storage cell, the access cell, and the test module handling cell. The rig transporter can travel between the test module handling cell and PIE hot cell.

The requirements of the remote handling system in the access cell are as follows.

- Routine VTA removal and reloading operations
- Removal and exact insertion of shielding plug, vertical irradiation tube (VIT), and removal of the test cell cover
- Routine VTA assemble and disassemble operations
- Replacement of the lithium target assembly
- Any maintenance operations in the access and test cells, including cleanup of Li contamination.

Some of above-mentioned requirements are for the transfer of heavy equipment that are carried out by the gantry crane of the large universal robot system. The gantry crane is shown in Fig. 2. It has 5 mm positioning accuracy and 50 t handling/transportation capacity (the handling capability of the gripper is 30 t). Its working space in X, Y and Z direction is respectively 13 m, 30 m and 6 m. The positioning accuracy of each movable table is better than 1 mm.

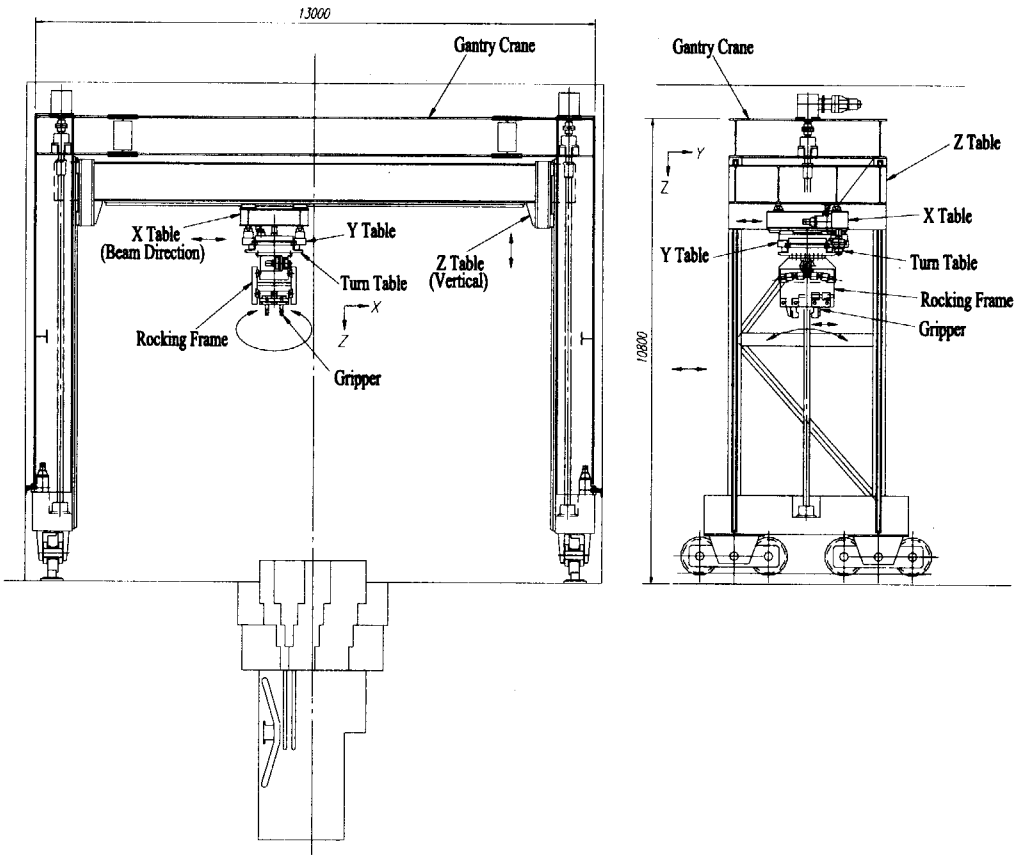


Fig. 2 Gantry crane of large universal robot system.

The handling procedure for the heavy equipment using the gripper is shown in Fig. 3. The four hook-shaped grips, of which two are movable, hold the equipment. Inserting the wedges prevents the

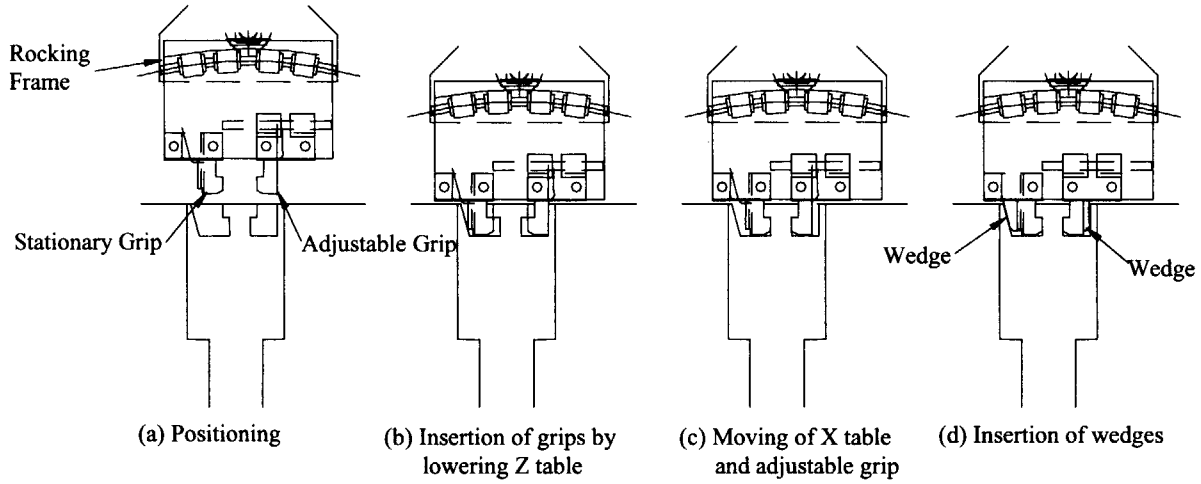


Fig. 3 Handling procedure of heavy equipment by gripper.

bending of the grips due to the bending moment that occurs during the lifting of equipment. When the thin equipment such as VTA1 is raised it might not be possible to insert all four grips because the grips are large. In such a case, the sidewall of VTA1 can be gripped by the stationary grips as shown in Fig. 4.

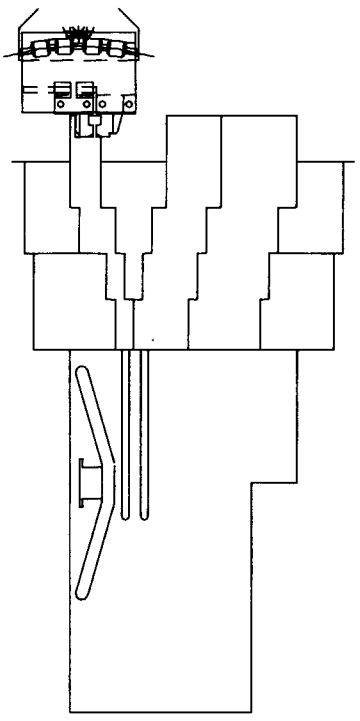


Fig. 4 Handling of VTA1.

When the gripper is not located over the center of gravity of equipment, the equipment is kept vertical using the rocking frame. An alternative method to maintain the desired orientation of the equipment is to attach counter-weights to the equipment. However, even in such case use of the rocking frame may be necessary. When the test cell cover is handled, it is lifted using the lifting attachment. The upper test cell cover and lower test cell cover should be designed to be two pieces each, because their weight may exceed the gripper handling capability, even though they were reduced in size for the reduced cost IFMIF.

(4) Operational Flow in the Test Facilities

A flow plan of all remote handling operations for the test facilities is shown in Fig. 5. Two sets (label #1 and #2) of VTA1, VTA2 and central shielding plug are provided to reduce the downtime due to the disassembling/assembling operations on the VTAs. After completion of irradiation, removal of the vacuum seal plate from the test cell, disconnection of pipes and cables from the VTAs, and connection of temporary cooling systems to the VTAs are normally conducted as hands-on operations. These operations can be conducted by the large universal robot, if necessary in the case of contamination. If only a short cooling period of the specimens is expected, the connection of the temporary cooling system to VTA will be not necessary, but in that case the disconnection of pipes and cables from VTA cannot be

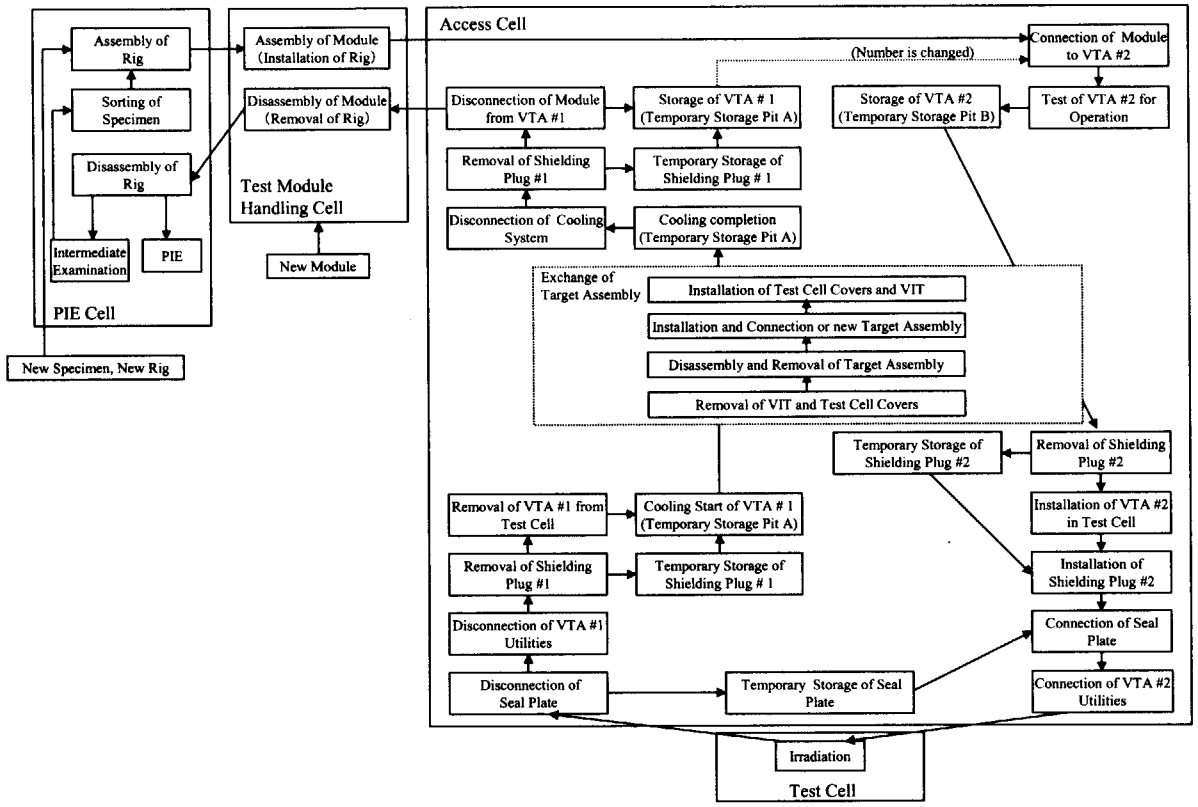


Fig. 5 Flow plan of remote handling operations for the test facilities.

conducted until the completion of specimen cooling by the VTA cooling system.

The central shielding plug and VTAs are removed from the test cell by the gantry crane, with the central shielding plug put into a temporary storage pit and the VTA put into temporary storage pit A. The elevation section view of the test cell and temporary storage pits are shown in Fig. 6. Temporary storage pit B is for another set of VTAs. Personnel access to the access cell is possible because the parts of the VTAs that have high activity are shielded. The operation of the gantry crane is still possible because the VTAs are housed in the pits.

When the lithium target assembly needs to be replaced, the VIT and removable test cell covers are removed from the test cell by the gantry crane. The removable test cell covers are put on the temporary storage area (the floor of the access cell). The remote handling system for the replacement of the target assembly is held by the gripper of the gantry crane.

The installation of another set of VTAs in the test cell is started before the disassembling of the VTAs, although it does depend on the specific irradiation plan. After the completion of specimen cooling by the temporary cooling system, the test module is disconnected from the VTA (shielding body) by the manipulators connected to the gripper. The test module, if not contaminated by tritium, is moved to the test module handling cell by the test module transporter with capacity of 0.1 t. The rigs are removed from the test module by the small universal robot in the test module handling cell. The rigs are moved to the conventional hot cell (PIE cell) using the rig transporter. The remote handling operations in the PIE cell are carried out by another system, which will be examined in the detailed design of test modules as a future task.

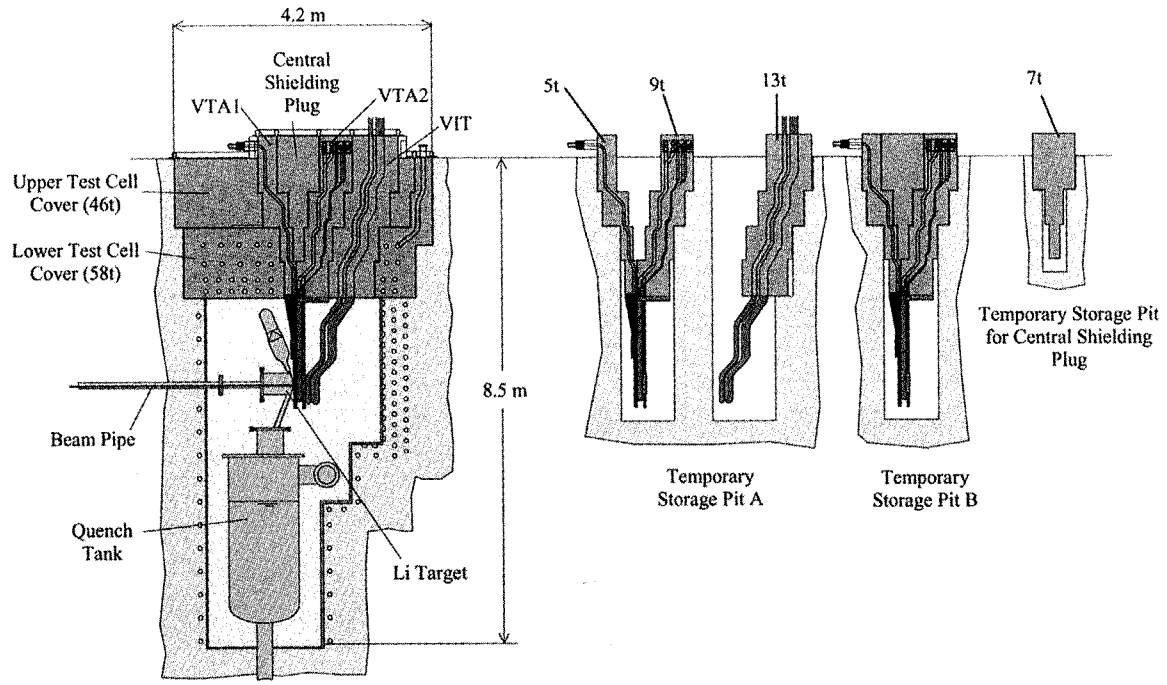


Fig. 6 Elevation section view of the test cell and temporary storage pits.

(5) Summary

The remote handling systems and operational flow were examined to determine whether they can accurately handle the heavy equipment such as a Vertical Test Assembly. The remote handling system is composed of the large and small universal robot systems, test module transporter, rig transporter, and other elements. The large universal robot system for the access cell that is located over the test cell can handle the heavy equipment in the test cell. It is composed of the gantry crane with movable tables and manipulators with several degrees of freedom. The gripper that holds the heavy equipments is better than 1 mm in positioning accuracy in the x, y and z directions and has 30 t handling capacity. This system will cover almost all of the operations expected in the test cell, access cell and test module handling cell.

References

[1] M. Martone (Ed.), "IFMIF International Fusion Materials Irradiation Facility, Conceptual Design Activity, Final Report, IFMIF CDA TEAM", ENEA Frascati, Report ENEA-RT/ERG/FUS/96-11 (1996).

[2] Fusion Neutronics Laboratory (Edited by M. Ida et al.), "IFMIF International Fusion Materials Irradiation Facility, Conceptual Design Activity, Reduced Cost Report, A Supplement to the CDA by the IFMIF TEAM", JAERI-Tech 2000-014 (2000).

3.3.10 TF38-JA : Operation Methods for Off/Normal Conditions of IFMIF

(1) Brief Task Description

IFMIF operation in off/normal conditions influences the irradiation behavior of material. Thus the operating methods during off/normal conditions need to be examined on the basis of the understanding of irradiation damage and experience with existing radiation facilities. The irradiation behavior of materials can be affected by the low temperature irradiation that occurs during facility startup. The temperature control in IFMIF is required to raise the specimen from below 0.3 T_m to the irradiation temperature within 10 minutes of startup, to avoid any significant neutron fluence at temperatures below the specified temperature for the experiment.

Contributors

Name	Party	Institute	E-mail address
T. Yutani	Japan	JAERI	yutani@ifmif.tokai.jaeri.go.jp
H. Nakamura	Japan	JAERI	nakamurh@fusion.naka.jaeri.go.jp

(2) Introduction

The specimen temperatures need to be maintained constant during irradiation, because temperature variation can affect the irradiation behavior of materials. The IFMIF Helium Cooled High Flux Test Module for the irradiation of blanket structural materials will have an electric heater to supplement nuclear heating and have a helium gas cooling system. However, the specimen might not be maintained at the target (irradiation) temperature at startup and shutdown of the accelerators and also during any beam-off transients. To minimize such situations, the temperature control mode of the specimen during off-normal conditions should be determined.

(3) Review of Existing Experimental Data

In irradiation experiments in conventional fission reactors, the specimens are maintained at the target temperature by controlling the thermal conductivity of a gas layer by changing the composition and/ or pressure of the gas layer to compensate for the fluctuation of nuclear heating rate and/ or cooling capability. However, the specimens may be irradiated at temperatures lower than the target temperature during startup and shutdown of the reactor. In the Japan Materials Testing Reactor (JMTR), the material receives a displacement damage of about 0.01 dpa during the startup period [1]. It seemed that this pre-irradiation at low temperature during the reactor startup might affect subsequent evolution of the radiation-induced microstructure in materials. To evaluate this, irradiation rigs that could control the specimen temperatures by electric heaters as well as by changing the conductivity of the gas layer were developed for JMTR [1]. In the experiment using this irradiation rig, the specimen temperature is raised to the target temperature before reactor startup and is lowered after the reactor is shut down. Irradiation rigs that could vary the specimen temperature during the irradiation were also developed for JMTR and for the High Flux Isotope Reactor (HFIR) [2, 3]. The effect of temperature variation has been investigated using these irradiation rigs. That the low temperature irradiation in the early stage of an experiment is especially important has become fairly obvious by the results of neutron irradiations in JMTR and the ion irradiations. The examples of the effect are as follows [4].

1) Increase in defect cluster density

Defect clusters (loops and voids) are formed during pre-irradiation at low temperatures, even if this period is short, and the clusters grow during the subsequent irradiation at higher temperatures. The result is that the density of defect clusters is higher than that of defect clusters formed by irradiation only at the higher, constant temperature.

2) Effects of accumulation of very small defect clusters

The fine defect clusters that are formed by vacancies with low mobility accumulate in the matrix of a material during the low temperature irradiation. The microstructural evolution, such as the

formation and growth of interstitial atom loops and formation of dislocation networks, is retarded substantially, because the fine defect clusters decompose and discharge free vacancies during the subsequent irradiation at the high temperature.

3) Stability of precipitates

When a material that forms a stable precipitate during high temperature irradiation is irradiated at a lower temperature in the early stage of irradiation, a number of fine precipitates form and they disappear during the subsequent irradiation at high temperature because of their instability. Therefore, the material loses any effects of the precipitates, such as void swelling resistance.

(4) Requirements on IFMIF Operation

Based on the existing data from fission reactor experiments, it is important to avoid irradiation at temperatures lower than the target temperature. If low temperature irradiation is unavoidable, the time must be kept short as much as possible.

The probable operating conditions of the accelerators during startup and shutdown of IFMIF are as follows.

- The time for accelerator startup is desired to be more than 1 minute.
- The time for accelerator shutdown is short.
- Two accelerators are started up separately, though they may be done at the same time.
- Two accelerators can be shut down at the same time.

The times for startup and shutdown are short in comparison to fission reactor operation. (The time for the startup of JMTR ranges from less than a few hours to more than a few days, and the time for shutdown is more than 1 hr [1]). The short time of low temperature irradiation may be acceptable in normal IFMIF operations.

The accelerators will be accidentally shut down due to various causes, in addition to the shutdowns for maintenance, although the probability that both accelerators are shut down simultaneously is very low. When one accelerator is shut down, and the downtime is expected to be short, the irradiation will be continued using only the other accelerator. The nuclear heating rate which depends on the accelerator power will fluctuate substantially during the irradiation in IFMIF. Therefore, the heater needs to have enough capacity to compensate for these fluctuations.

There will be a great many interruptions in the IFMIF neutron irradiation for material specimens to achieve the target displacement per atom. Since there is also a concern with recovery of irradiation damage that may occur if the specimens are maintained at the high temperature without the neutron irradiation, the following tentative requirements are set for temperature control of the specimen at restart and shutdown. This is expected to avoid both low temperature irradiation accumulation and high temperature irradiation recovery.

- The specimen temperature must be raised from below 0.3 T_m to the irradiation temperature within 10 minutes at start of irradiation. In the case of F82H ferritic/martensitic steel, 0.3 T_m is about 500 K.
- When both beams shut down, the specimen temperature must be reduced below 0.3 T_m within 10 minutes.

(5) Operating Method

1) Normal Operation

The temperature of specimens is controlled by nuclear heating and electric heaters. When the specimen temperature is higher than the desired temperature, it may be lowered by adjustment of the flow rate and/or pressure of the coolant. An example of the control mode for normal conditions is shown in Fig.1. The two accelerator beams are turned on separately. Each accelerator is turned on after the specimens are maintained at the target temperature by the electric heaters, and the electric heater is

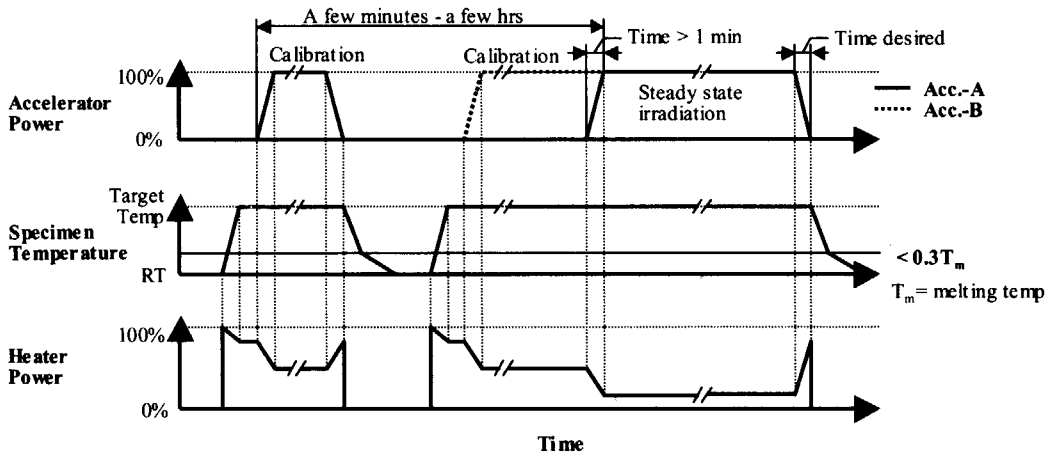


Fig. 1 Example of Temperature Control Mode in Normal Conditions (1).

turned off after both accelerators are shut down. In this case, the electric heater must have enough capacity to raise the specimen to the target temperature within 10 minutes, so that the specimens are not irradiated at lower temperature than the target temperature during the startup. Also, the test module cooling system must have the capacity to lower the specimens to the temperature less than $0.3T_m$ within 10 minutes.

Another control mode is shown in Fig. 2. The heater is turned on after the beam power reaches 100%, and it is turned off just after beam-off. The capacity of the heater is reduced from the mode shown in Fig.1, although then a short low temperature irradiation time is inevitable. However, higher cooling

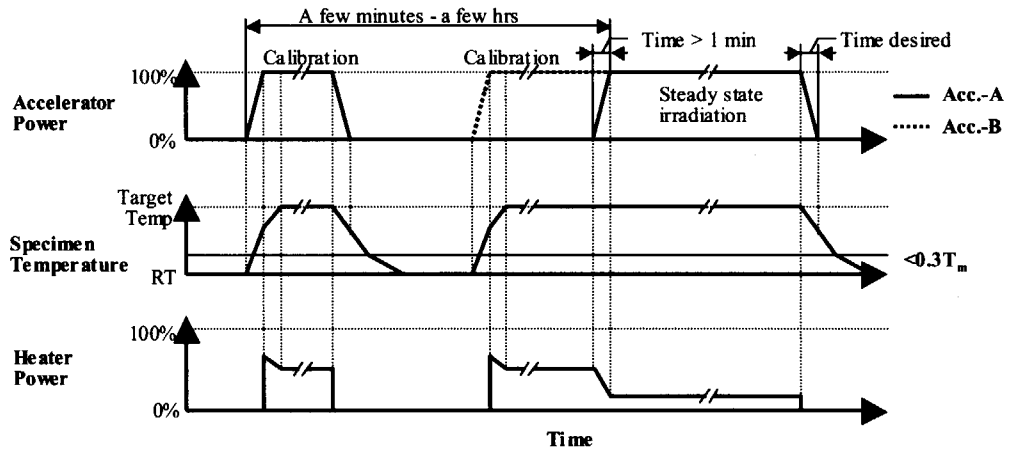


Fig. 2 Example of Temperature Control Mode in Normal Conditions (2).

capacity is necessary.

Other temperature control modes may exist. Which mode is most appropriate should be judged from the result of related tasks (TF11-EU, TF12-EU and TF39-JA).

2) Off-normal operation

Beam shutdowns due to various causes are unavoidable. If one beam is off, the irradiation can be continued with other beam. The irradiation behavior of the material will not be seriously affected,

although the neutron flux drops to about half. For instance, no significant difference has been observed in the irradiation behavior of material that has been irradiated in two positions of HFIR, the reflector position and the target position, although the neutron flux of the former is about half of that of the latter. The control mode for one beam-off is shown in Fig. 3. For one beam-off time up to several hours, the specimen is maintained at the target temperature by raising the heater power. If the beam-off time is longer, the specimen temperature will be controlled by adjustment of flow rate and/or pressure of the coolant as well as by raising heater power.

When both beams are off, the specimen temperature must be lowered below 0.3 T_m within 10 minutes.

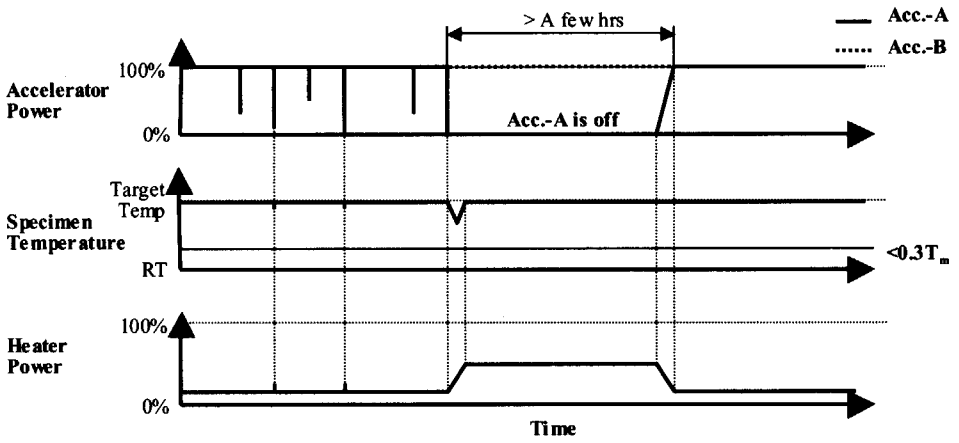


Fig. 3 Example of Temperature Control Mode in Off-normal Conditions.

(6) Summary

The irradiation behavior of materials is affected by the low temperature irradiation during startup, according to the review of existing irradiation effects observed in fission reactor experiments. The effects are an increase of defect cluster density, and related effects.

In order to avoid the low temperature irradiation, the temperature control in IFMIF is required to raise the specimen to the target temperature from below 0.3 T_m within 10 minutes at startup. Also, the specimen temperature must be lowered below 0.3 T_m within 10 minutes complete beam shutoff.

Temperature control modes that meet the above requirements were examined. Which mode is most appropriate will be judged from the result of related tasks.

References

[1] M. Narui, T. Sagawa, Y. Endo, T. Uramoto, T. Shikama, H. Kayno and M. Kiritani, J. Nucl. Mater. 212-245, 1645 (1994).
[2] M. Narui, H. Kurishita, H. Kayno, T. Sagawa, N. Yoshida and M. Kiritani, J. Nucl. Mater. 212-245, 1665 (1994).
[3] A. L. Qualls and T. Muroga, J. Nucl. Mater. 258-263, 407 (1998).
[4] T. Muroga and M. Narui, Journal of Plasma and Fusion Research 76, 349 (2000).

3.3.11 TF39-JA : Feasibility Study of the Gas Cooled High Flux Test Module

(1) Brief Task Description

Long-term temperature control of irradiation experiments is a key issue of IFMIF design, because temperature critically affects the irradiation response of all materials. Basically, test specimens should be kept at a prescribed constant temperature through the irradiation period, and they must be quickly cooled down in case of any unexpected beam cut-off in order to retain their property changes. In the present conceptual design of the test modules, the temperature control is accomplished by use of helium gas cooling and ohmic heating.

We performed a series of numerical simulations in 3-D, based on the test module design that was originally proposed, and found three unfavorable features arising from the current configuration. These are: difficult temperature monitoring; non-uniform temperature distribution in specimens; and poor cooling performance. We now proposed a modified design of the test module that can overcome the problems and report here the results of numerical and experimental examination of this newly proposed test module design.

Contributors

Name	Party	Institute	E-mail address
Akihiko Shimizu	Japan	Kyushu Univ.	shimizu@ence.kyushu-u.ac.jp
Takehiko Yokomine	Japan	Kyushu Univ.	yokomine@ence.kyushu-u.ac.jp
Yukinobu Watanabe	Japan	Kyushu Univ.	watanabe@aees.kyushu-u.ac.jp
Shinji Ebara	Japan	Kyushu Univ.	ebara@ence.kyushu-u.ac.jp
Yukihiro Yonemoto	Japan	Kyushu Univ.	yonemoto@aees.kyushu-u.ac.jp

(2) Introduction

In the high flux test region of the IFMIF test module, test specimens are housed in capsules with gas gaps and irradiated for long times, must be kept at the set temperature (which will be in the range 250 to 1,000°C) because irradiation characteristics of materials are strongly dependent on temperature. During the irradiation, although it is assumed that perturbations of the beam causes some changes in nuclear heating, acceptable changes in the temperature fluctuation in specimens should be less than 1%. In addition to these small beam changes, the temperature control system must accommodate: (1) rapid increases in nuclear heating at beam start-up (2) heating rate changes for one beam-off and (3) loss of nuclear heating at two beam shutdown by accident or maintenance. With regard to conditions (1) and (3), a specific goal has been proposed by JAERI, that immediate heating up or rapid cooling down to $0.3T_m$ should be achieved within 10 minutes.

The most challenging position for temperature is in the high flux test region, because of the severe heat load. Moreover, the test module must avoid high pressure to avoid damage to the module structure.

(3) Analysis of the Previous Test Module Design and Proposed New Design Concept

Firstly, we examined the cooling performance of the test module originally proposed in IFMIF-KEP. Calculations were performed in a three dimensional system by using the ANK turbulence model for flow and thermal fields[1,2]. The inlet Reynolds number of flowing He coolant was varied in the range 3,400 to 185,000, which corresponds to inlet pressure conditions ranging from 0.1 to 0.9 MPa. Specific nuclear heating was assumed to be 5W/g for both specimens and rig wall structural materials. Specimen and rig wall materials were SS and that of the capsule was optional, either DS-Cu or SS.

Figure 1 shows the calculation domain used in our study. From the numerical results, in spite of choice of capsule materials, the maximum temperature of specimens can be kept at 550K, which is the most severe requirement for cooling, when the Reynolds number is 68,000, inlet pressure 0.5 MPa and inner gap width 0.1mm. Some examples of the temperature in specimens during start-up are shown in Fig. 2(a) while Fig. 2(b) shows temperatures in rapid cool down from steady state conditions.

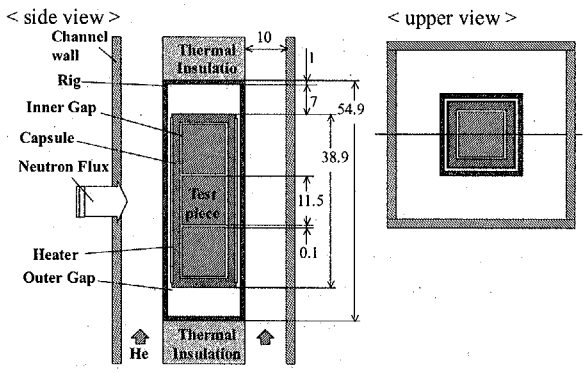
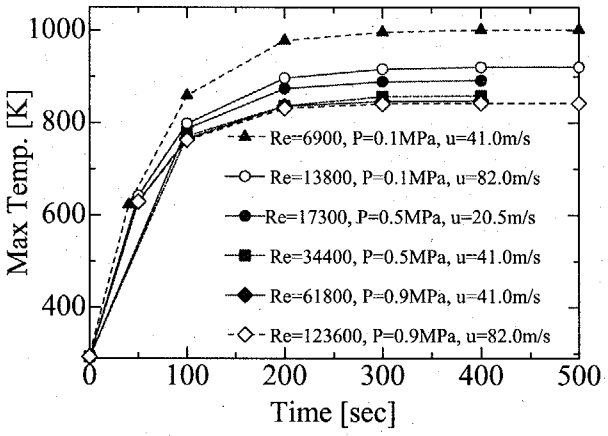
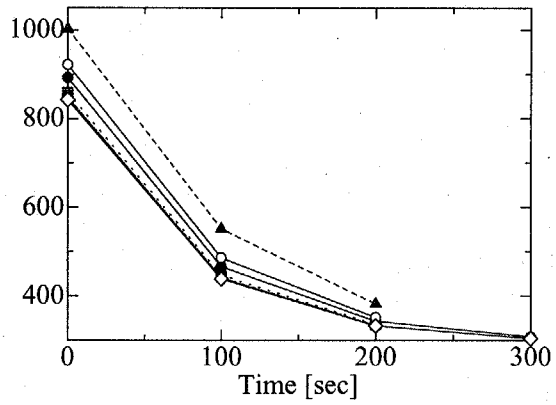


Fig. 1 Calculation model for the previous design.



(a) At start-up



(b) At shut down

Fig. 2 History of temperature at start-up and shutdown.

These data were obtained by adopting SS capsule material and the inner and outer gap width of 0.5mm. From Figs. 2, we can see that the required conditions at start-up and shutdown that heating up or cooling down to 0.3Tm within 10 minutes are adequately satisfied. Nevertheless, it is also found that the lowest achievable irradiation temperature is about 840K. There would be a lower limit of specimens temperature if unlimited flow velocity of coolant could be available. This limit originates from thermal resistance between specimens and cooling channel, and the thermal resistance is determined by dimensions and arrangement of the irradiated unit. Because the dual gaps are filled with a gas phase of poor thermal conductivity, the thermal resistance is very large. In other words, the cooling is extremely limited by the gaps.

In addition to the above disadvantage, two inconvenient features due to the configuration were clear from the numerical results. First, there is a non-uniform temperature distribution inside the specimens, due to the volumetric nuclear heating. Our numerical results indicate that there are temperature difference of 40 K and more in the specimens, although the maximum temperature can be kept at 550 K.

Second, a large uncertainty in measurement of specimen temperature may appear in the design. If the thermocouples (T/Cs) are buried in the capsule to monitor the temperature of specimens, a large uncertainty in temperature measurement is inevitable due to the change of gap conditions during the experimental and to the accuracy of the location of T/C. Fig. 3 shows the estimate of uncertainty of temperature measurement. In the calculations, the effective gap conductance, λ_{gap}, is defined as a function of parameter f, $1/\lambda_{gap} = (1-f)/\lambda_{SPECIMENS} + f/\lambda_{He}$, where f means the volume fraction of occupation of gas (helium) in the gap. When $f=1$, the gap is filled with gas only, but f can change, for example, due to swelling. The case of $f=0$ corresponds to the case in which the gap is completely filled by swelling material. In Fig. 3 the relative location of T/C means the change of position from the location where T/C is buried originally. The change in location of T/C can be caused by swelling of the capsule and positioning error. As shown in Fig. 3 small changes of the volume fraction or the location of T/C cause large differences between actual specimen temperature and those estimated from T/C which is assumed to stay at the original position.

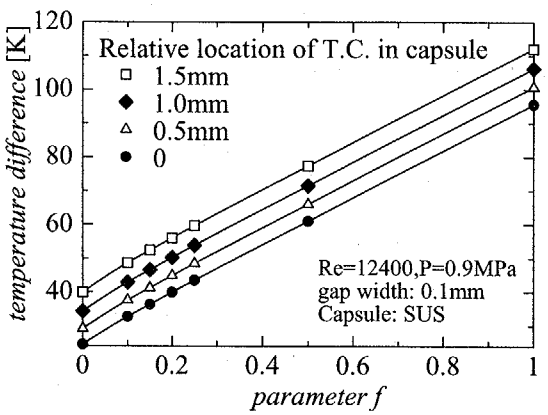


Fig. 3 Estimation of uncertainty of temperature measurement.

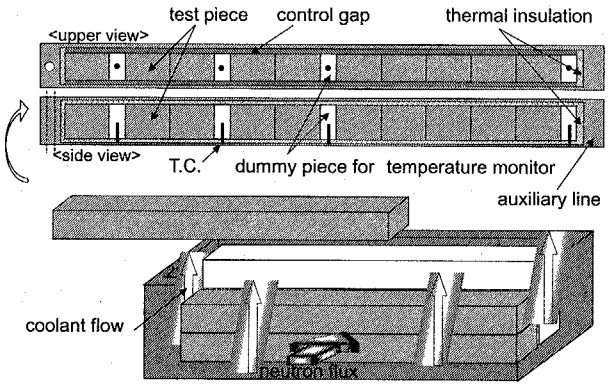


Fig. 4 New design of test module.

From the numerical results, it is concluded that drastic change in design of the test module is needed in order to obtain uniformity of temperature of specimens, to improve the reliability of temperature measurement, and to relieve the coolant flow condition, especially the high inlet pressure. Our team proposed a new concept for the test module and specimen arrangement.

Fig. 4 shows the new design of test module that we propose. The new design has some improved features, including the followings; In the current design, temperature of specimens is estimated from capsule temperatures that are measured directly by T/Cs buried in it and may change due to the installed location of T/Cs and the changes in gap conditions as mentioned above. In the new design, however, temperature of specimens is measured directly by monitoring a few dummy pieces in the specimen array. The current design has two gaps between specimens and the cooled surface. They work as insulating layers due to large thermal resistance of the gas phase, and causes deterioration of cooling performance. In our design, enhancement of cooling is achieved by removing the rig wall and outer gap. In addition, the long irradiated unit is expected to realize a two-dimensional temperature profile in the row of specimens, so that a uniform temperature distribution in each specimens can be obtained.

In addition to these design modifications, a fine mesh is inserted in the gap between specimens and capsule walls so that the influence of uncertainty of the gap width on specimens temperature can be reduced and uncertainty of the contact between specimens and the capsule can be excluded. From now on, the gap between the specimens and the capsule is called 'the control gap'.

(4) Numerical Simulation for the New Design

Calculations were performed to confirm that the expected improvements were realized in the new design of the test module. The system configuration and dimensions under consideration are illustrated in Fig. 5. Considering the symmetry of the system, only a one-quarter region of the module was simulated. The specimens are surrounded by insulation except for the control gap. This makes heat flow mainly in one direction, the y-direction in Fig. 5. The control gap is filled with a flexible porous matrix, composed of SS and helium to accommodate the uncertainty of contact due to swelling. The effective thermal conductivity of this material mix is estimated by the geometric mean,

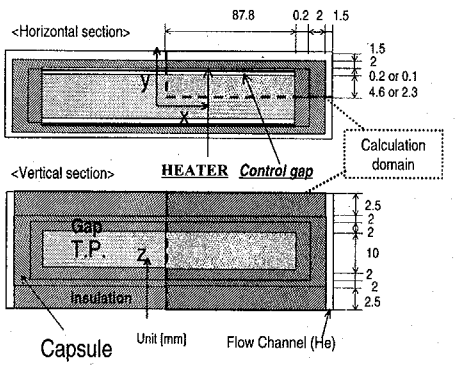
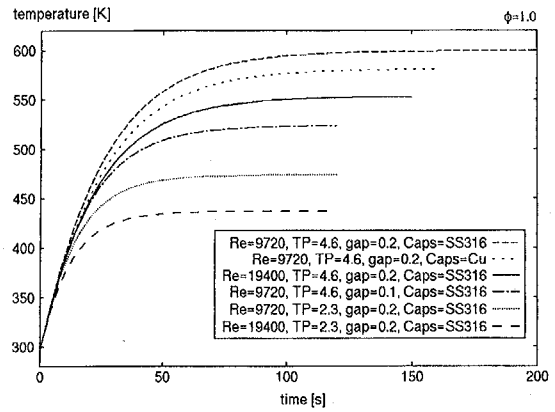
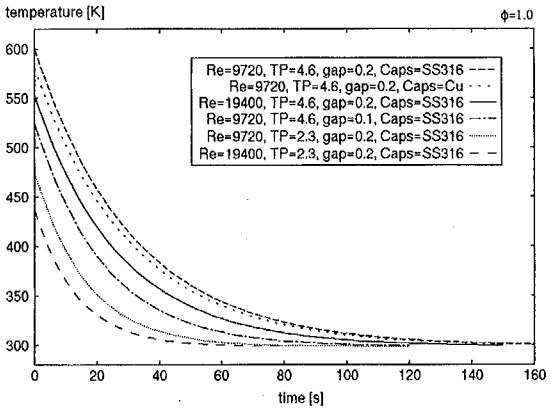


Fig. 5 Numerical system for new design.



(a) At start-up



(b) At shutdown

Fig. 6 History of temperature for various parameters.

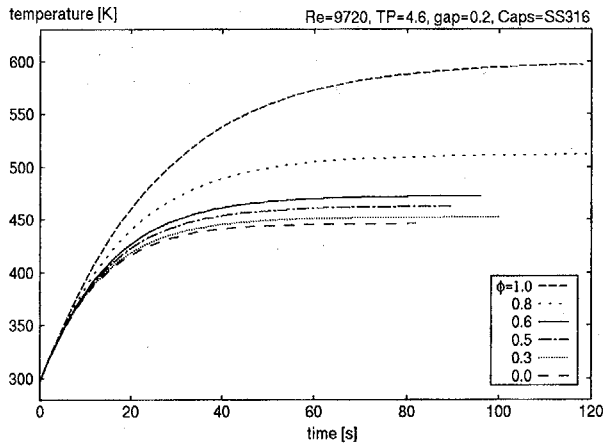


Fig. 7 History of temperature for various porosity cases.

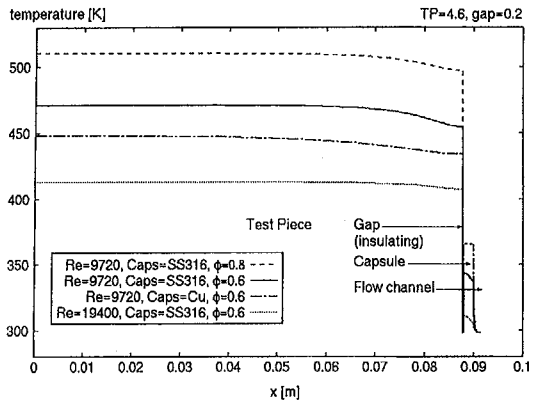
expressed as $k_{eff} = k_{SS}^{(1-\phi)} k_{He}^{\phi}$, where ϕ is the porosity of the matrix[3]. A heater to compensate for variation in nuclear heating is located on the gap side of the capsule.

In the calculation, the conjugate heat transfer problem between solid and fluid with turbulent flow was solved using ANK turbulence model, similar to the former simulation. The specimen material was SS and that of the capsule was either DS-Cu or SS. To determine the effect of thickness of specimens and the width of the control gap, 4.6 and 2.3 mm were selected as specimen thickness, and 0.2 and 0.1 mm were width of the control gap. Two kinds of fully developed turbulent flow, Re=9,270 and 19,400, corresponding to flow velocity of 79.5 m/s and 159.0 m/s respectively, were provided for the inlet conditions of coolant flow. The porosity in the control gap was varied from 0.0 to 1.0.

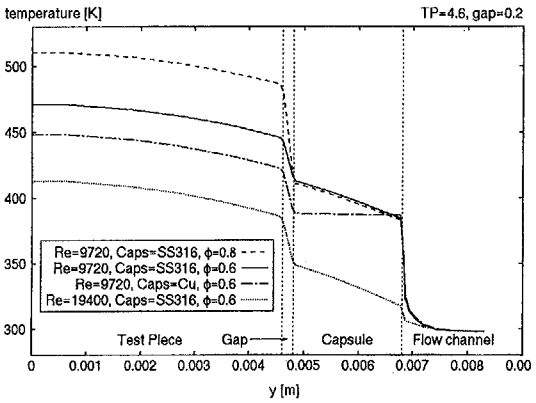
(5) Numerical Results and Discussion

Fig. 6 shows maximum temperature histories at startup and shutdown for all variables except porosity. For all data, porosities were fixed at 1.0. The figure clearly indicates adequate cooling performance to satisfy the conditions required at start-up and shutdown. The lowest irradiation temperature, 523 K, is quite easy to achieve, even though the case with porosity of 1.0 is the hardest to cool. Fig. 7 gives temperature histories for various porosity cases with Re=9,720, specimen thickness of 4.6 mm, control gap width of 0.2 mm and a SS capsule. Obviously, the specimen temperature is significantly affected by the porosity of the control gap.

In Fig. 8, temperature profiles in the x- and y-directions are shown for several different cases. Fig. 8(a) shows good uniformity of specimen temperature in the x-direction, with larger Reynolds number improving the uniformity. As shown in Fig. 8(b), if the specimen thickness is fixed, namely, the nuclear heat generated is the same, then the temperature of the capsule surface is determined by flow conditions. The higher the flow velocity, the lower the surface temperature. The temperature profiles in the specimens are almost the same though their levels are different because of the capsule material and the conditions of the control gap. Fig. 9 illustrates the 3-dimensional distribution of temperatures in specimens, corresponding to the case drawn in solid line in Fig. 8. It is easy to see the



(a) In x-direction



(b) In y-direction

Fig. 8 Temperature profiles on symmetric axises.

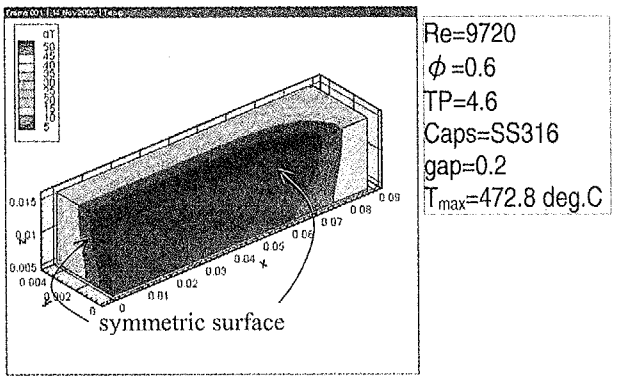
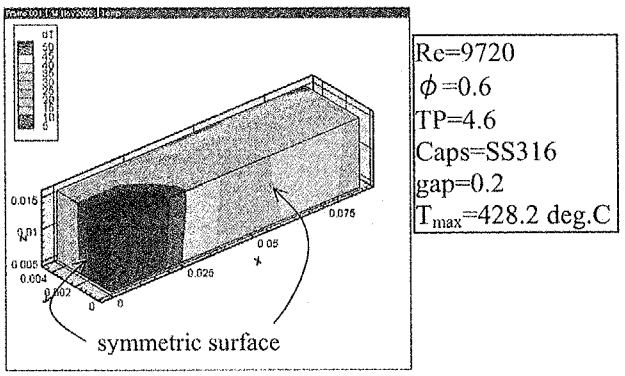
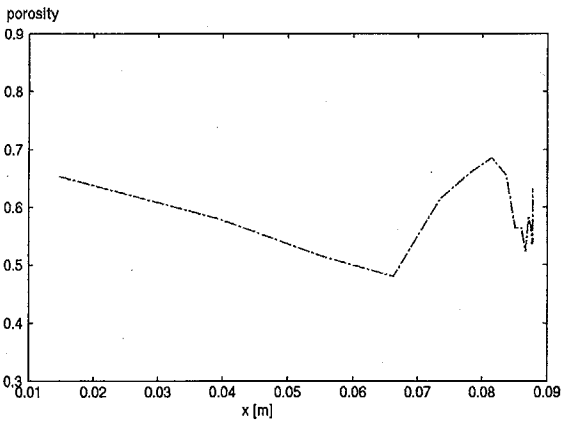


Fig. 9 Temperature difference distribution in T.P.



(a) Temperature difference



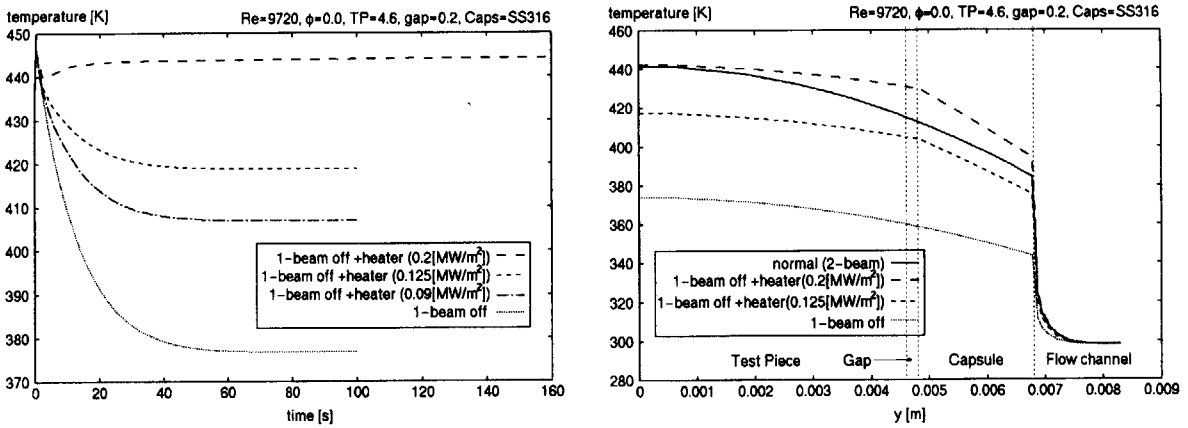
(b) Porosity profile

Fig. 10 Temperature difference distribution in T.P. for random porosity case and porosity profile.

uniform temperature distribution in the span-wise direction.

The results discussed above were obtained for the constant porosity cases. Fig.10(a) shows the distribution of temperatures in specimens calculated for a random porosity case. All parameters except porosity were the same as those of Fig.9. The porosity was assumed a function of x only, and its distribution was supposed to follow the form of the normal distribution with mean porosity of 0.6 and standard deviation of 0.01 shown in Fig.10(b). The uniformity of temperature in the spanwise direction is easily destroyed by the random porosity of the control gap.

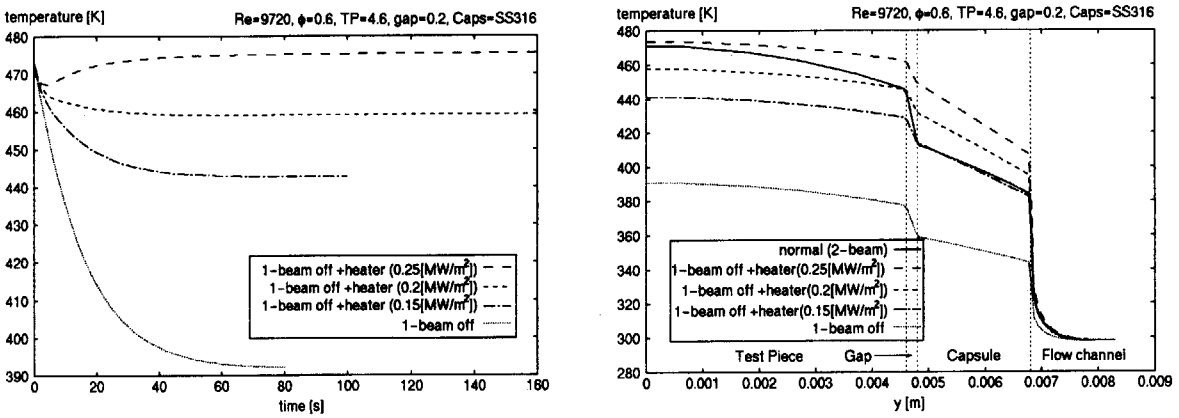
Fig.11 shows data corresponding to the one beam-off scenario for Re=9720, porosity of 0.0, specimens thickness of 4.6 mm, and SS capsule. The heater power was given as a certain heat flux and the condition of one beam-off was expressed by reducing the volumetric heating to half of the 5W/g reference value. In Fig.11(a), maximum temperature histories for one beam-off with and without heater use are depicted. In this figure, a single beam is cut off at 0s and each simulation starts from the steady state temperature that had been reached in normal (2-beam) irradiation. Temperature profiles at steady state in the y-direction of the data for the one beam-off scenario are compared with that of the normal (2-beam) case in Fig.11(b). The heater is at y=0.0048 in this figure. When the heater power is



(a) History of temperature **(b) Temperature profile in y-direction**

Fig. 11 Results of 1 beam-off case for porosity of 0.0.

0.2 MW/m^2, temperature close to the steady state value can be recovered within 20 s and maintained for single beam operation. It should be also noted that in the one beam-off condition, the temperature difference in the y-direction becomes smaller than that of the 2-beam case. This is inevitable because of the difference in volumetric heating between the two cases. Fig. 12 illustrates the one beam-off data for porosity of 0.6. Heater power of 0.25 MW/m^2 is required to keep the temperature level at the steady state. This power is larger than that required in the case for porosity of 0.0. The reason why required heater power is different among different porosity cases is clearly indicated in Fig. 12(b). A large porosity causes a temperature difference in the control gap to increase. The heater has to compensate for a portion of this large temperature difference to keep the temperature at the steady state condition.



(a) History of temperature **(b) Temperature profile in y-direction**

Fig. 12 Results of 1 beam-off case for porosity of 0.6.

In order to estimate the influence of beam fluctuation on specimen temperature, calculations of transient temperature profiles were performed for various cases. The beam fluctuation is expressed as a fluctuation in heat generation. We use a sine function as the fluctuation in time, with amplitude 10% of the nuclear heating in 2-beam irradiation. Fig. 13 shows temperature histories for diverse cases together with the fluctuation of the volumetric heating. In the figure, the steady state is maintained before t/T=0, and the fluctuation begins at t/T=0. Three cycles of fluctuation, T_{bf} were used in the calculations and they were determined by the specimen thickness, L, and the thermal diffusivity of SS, α. The cycles were set at $1/4*L^2/\alpha$, L^2/α, and $4*L^2/\alpha$, and they were about 1.3, 5.2 and 21.0 s, respectively. The abscissa in Fig. 13 is normalized for each cycle.

From Fig. 13, temperature fluctuation strongly depends on the cycle. Other factors, including

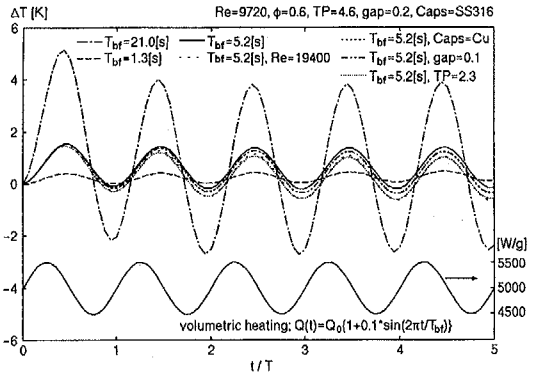


Fig. 13 Temperature deviation for beam fluctuation case.

the gap width, the capsule material and so on, have only a slight effect. The maximum cycle length of 21.0 s in the simulation is considered to be sufficiently long, and that results in maximum temperature difference from steady state of about 4 K, within the acceptable temperature fluctuation. This shows that a perturbation of beam power of about 10% does not require any extra measures to control specimen temperatures.

(6) Preliminary Experimental Confirmation

Experimental Apparatus and Conditions

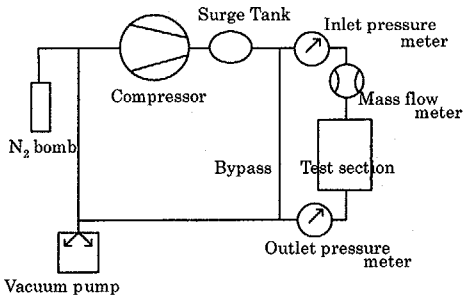


Fig. 14 An illustration of experimental loop.

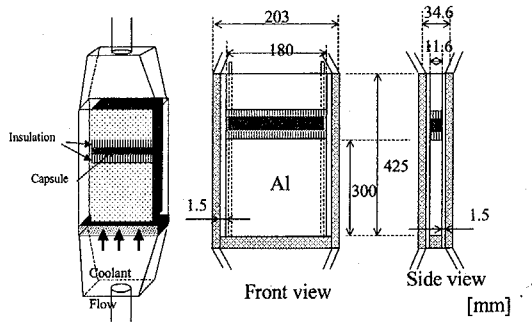


Fig. 16 Test section.

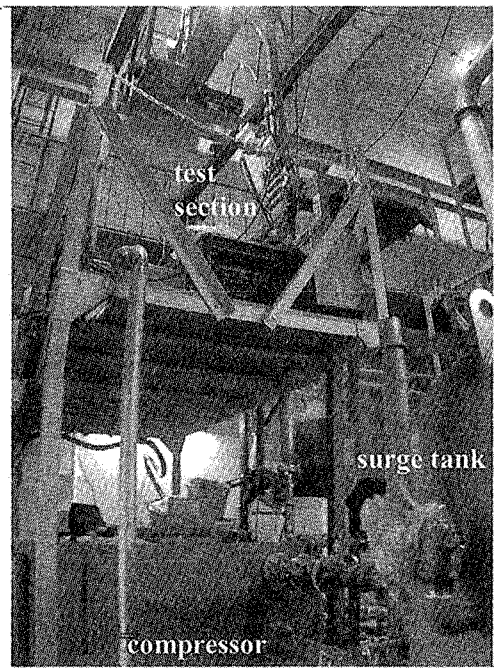


Fig. 15 Photographic view of experimental setup.

We conducted a series of experiments using the gas loop illustrated in Fig. 14. Fig. 15 shows a photographic view. The loop consists of a compressor, a surge tank with a volume of 1.8 m^3, nitrogen reservoir, a vacuum pump and a test section. The mass flow rate of gas is measured at the inlet of the test section, and gas pressure and temperature are measured at the inlet and the outlet of the test section. The test section is a square duct including a capsule and aluminum blocks, illustrated in Fig. 16. Insulating boards are inserted between the capsule and the aluminum blocks. All parts are fixed on both sides by SS shafts. The flow channel in the test section is a dual

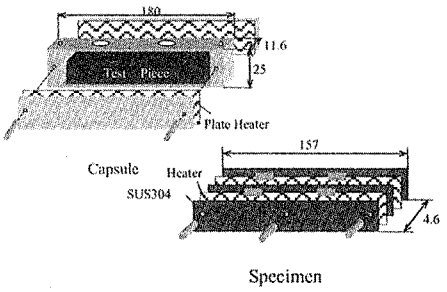


Fig. 17 Capsule and specimen in preliminary experimental run.

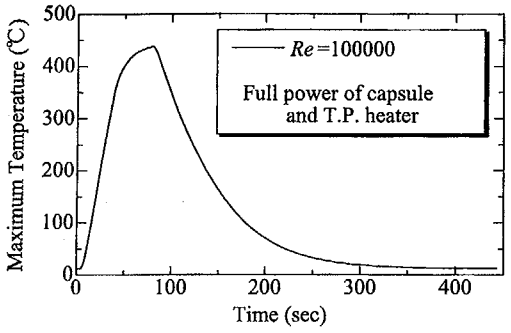


Fig. 18 History of maximum temperature at full heating.

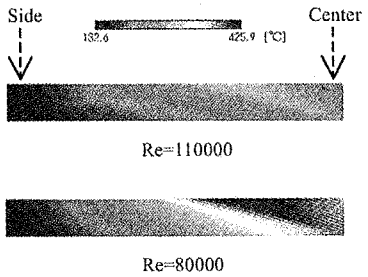


Fig.19 Temperature distribution on T.P. surface without capsule heating.

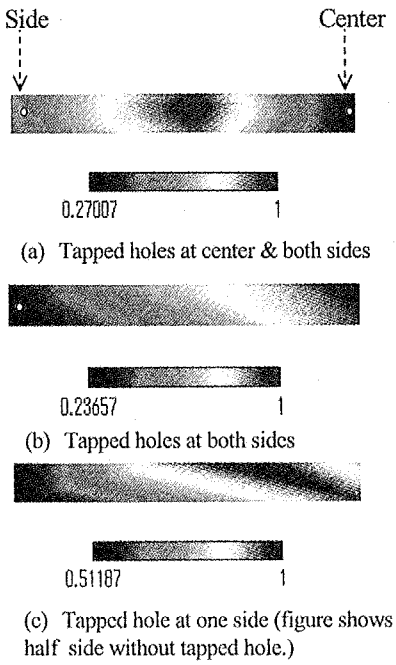


Fig.20 Temperature distribution on T.P. surface influenced by tapped holes.

square channel with a width of 1.5mm. Fig.17 shows a capsule holding specimens. The capsule consists of SS plates, SS blocks and two plate heaters (each 376 W) and the heaters are installed on the side walls of the capsule. Specimens are sandwiched by three SS plates (157x11x1 mm) and two plate heaters (each 159 W). The thickness of 4.6 mm is the thickest size of proposed specimens listed in IFMIF-KEP.

For temperature measurement we used K-type T/Cs with a sheath diameter of 0.25 mm. They were placed only on one side of the specimen surface due to symmetry. Nitrogen gas was used as coolant and the pressure was raised to 0.5 MPa. Dimensionless groups such as Nusselt number are used to apply data obtained using N_2 to model He coolant. The main parameters of this experiment were heater power and Reynolds number (defined at the inlet of the test section, based on averaged velocity and equivalent diameter of the flow channel).

Extraction of Problems

The preliminary experiments identified some issues to be solved with the new experimental apparatus. First, the nuclear heating of the capsule material was not adequately simulated with this experiment. Fig. 18 shows the temperature with full heating. The rate of temperature rise was too fast to continue the experimental run and all heaters were turned off at 80 s because of their temperature limit of 600 degrees C. In the numerical simulation where the configuration was similar to the experiment, adequate cooling performances were confirmed. But this performance is limited to the condition where the SS capsule wall itself generates heat. In the experiment, however, the nuclear heating was imitated by electric heaters made of insulating material, and heat transfer in the capsule was significantly different than in the case of the IFMIF capsule. Therefore, it is difficult to obtain an exact relationship with respect to the cooling performance, such as a correlation of specimen temperatures with Reynolds numbers in the experiment.

Second, the temperature distribution was non-uniform. Fig.19 shows the temperature distribution of the specimen surface for the cases that Reynolds numbers are 80,000 and 110,000, without use of the capsule heaters. It is seen that the non-uniformity of the temperature distribution of the specimens is mitigated by increasing Reynolds number. However, the temperature difference is still large and the temperature is extremely low at the

edge of the specimens. The reason for this large non-uniformity of temperature is believed to be insufficient contact between specimens and the bottom SS capsule plate. Fig. 20 show that the temperature distribution depends on the structure of plate heaters. In this experiment, heaters were held by screws in tapped holes at side(s) and/or center. The position of the tapped holes is center and both sides in case (a), both sides in case (b) and one side only in case (c). It is found that the structure of the plate heater drastically influences the temperature distribution of specimens surface. These results can lead to improvement of the capsule design and specimen configuration to solve these problems.

In the next section, using the results above, we will concentrate on the temperature distribution in specimens.

(7) Experiment for Uniformity of Temperature Distribution in Specimens

Improvements in Capsule and Specimens

Fig. 21 illustrates a revised design of the capsule and specimen loading. The capsule consists of insulation and SS plates. This time, the SS block at both sides and the bottom plate of the capsule were replaced by insulation to make heat flow one-dimensional. The specimen package consists of SS plates, plate heaters and Cu plate. Cu plate was cut into pieces (2x11x14.5 mm) for fear of irregular contact between specimens and the bottom plate. Metal mesh was inserted into gaps, which was expected to improve contact between the specimens and the capsule and accommodate any swelling. The metal mesh is made of stainless fiber (SS 316L, Tomoegawa Paper Co., Ltd.). Its porosity is 86% (catalogue value). The specimens are sandwiched by the capsule wall screwed to the side blocks. Temperature measurement was by T/Cs inserted into Cu pieces. The measurement area was half side only similarly to the preliminary experiment.

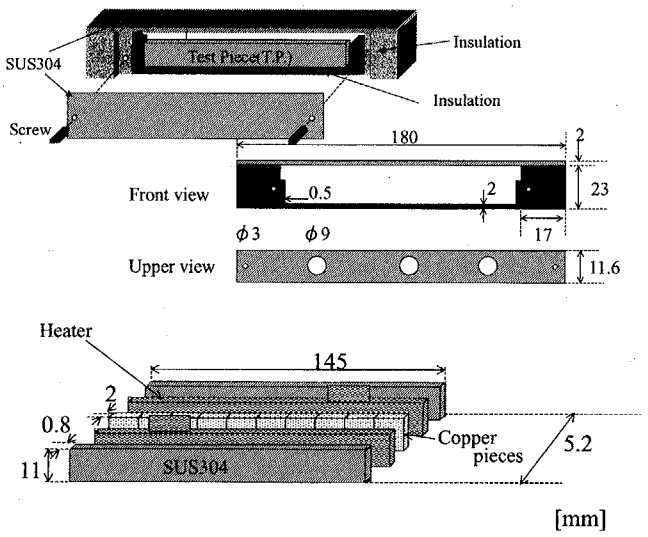


Fig. 21 Revised capsule and specimen.

Experimental Results and Discussion

Fig. 22 shows the temperature distribution in specimens in the new system. The maximum temperature difference becomes smaller than in the former experiment, but does not satisfy the 1% of the maximum temperature criterion. In this figure, temperature peaks at the center, because of the method of fixing specimens. Both sides of the capsule wall, where the wall was held by screws, were in good contact with the specimens through the mesh. The center of the wall, however, was not fastened and was not in good contact with the inside, with high porosity near the center of the capsule wall. The high porosity corresponds to large thermal resistance; therefore the temperature at the center rose.

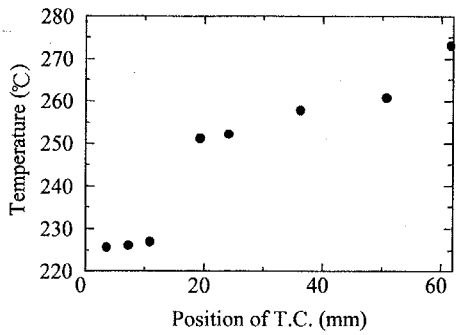
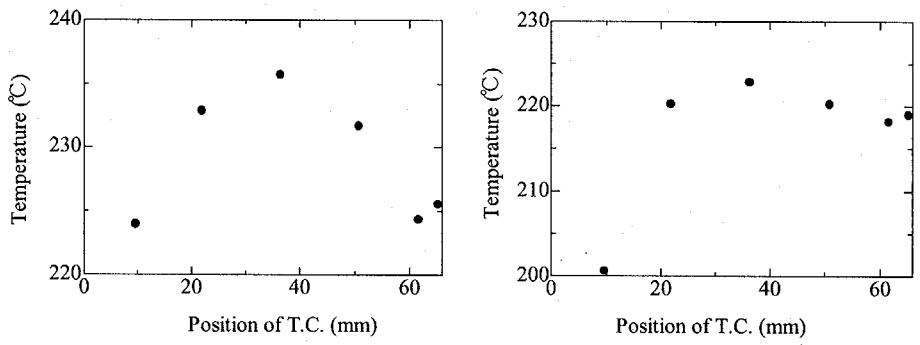
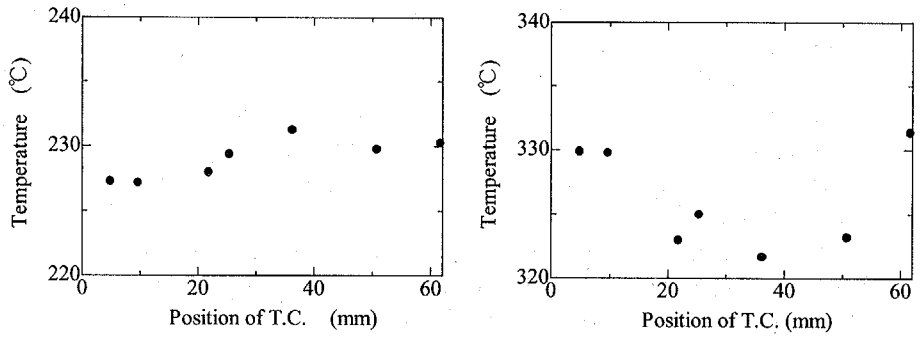


Fig. 22 Temperature distribution in specimen in new design.

Next, we located some screws on the capsule wall, shown in Fig. 23. The left-hand figure in Fig. 23(a) shows the results when the capsule wall had a screw at the center. As might be expected, the temperature is reduced at the center by improving the thermal contact there. The right-hand figure is



(a) Screw at center



(b) Screw at center and between side and center

Fig. 23 Temperature distribution in specimen (capsule wall has some screws).

the result when we have slightly displaced a piece which had been located in the side end of the specimens. This suggests that slight displacement of specimens influence the temperature distribution. Then, screws were added to the capsule wall at the positions where temperature peaks appeared in case (a). Uniformity of temperature distribution was achieved, satisfying the temperature difference within 1%, shown in the left-hand figure of Fig. 23(b). But at temperatures higher than about 300 degrees C, it was impossible to confirm the uniformity as shown in the right-hand figure. This probably is because the SS plate in the capsule changed its shape due to thermal stresses, and the plate altered contact conditions between Cu pieces and the plates, and among the pieces. Finally, we fixed each piece with screws as shown in detail in Fig. 24. Fig. 25 shows the results of the fixed-piece-case. In the left-hand

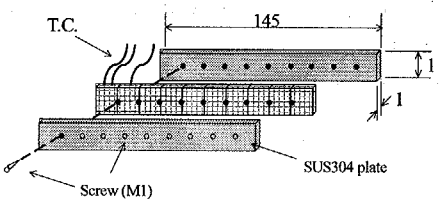


Fig. 24 Fixation of specimen.

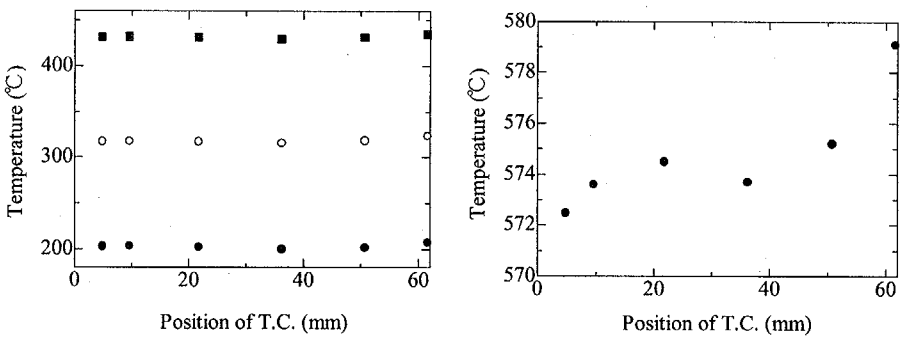


Fig. 25 Temperature distribution of specimen fixing Cu pieces.

figure, uniformity of temperature distribution is compared for different temperature levels. This fixed-piece result satisfies the condition of temperature difference within 1%, even at high temperatures, as shown in the right-hand part of the figure.

The experiment shows that the uniformity of temperature distribution in specimens is realized in the proposed design of the test module. Also, a small displacement of specimens and the gap condition (such as contact among pieces and contact between capsule and specimens) has a strong influence on the temperature distribution in the specimens.

(8) Conclusion

We proposed a new concept for the IFMIF test module that is expected to improve the achievable temperature, the uniformity of temperature in specimens, and the cooling performance. Calculations were performed for various cases corresponding to assumed scenarios for temperature control during IFMIF operation. The cooling performances of the new design were examined numerically for diverse conditions and good results were obtained.

In the proposed system, uniform specimen temperature distributions in span-wise direction can be realized and the cooling performance is greatly enhanced. This leads to better performance of the irradiation capsules and more accurate measurement of the temperature of each specimen. A series of numerical simulations indicate that the effect of the conditions of the control gap on specimen temperatures is very large, and that the key to temperature control is the gap condition.

A mock-up experimental facility was made based on the new design and experiments for temperature control were conducted. From the results, the uniformity of temperature in specimens with temperature difference within 1% was validated. Also in the experiment, the gap conditions were shown to markedly affect the temperature in the specimens.

References

[1] K.Abe, T.Kondoh and Y.Nagano, A New Turbulence Model for Predicting Fluid Flow and Heat Transfer in Separating and Reattaching Flows-I. Flow Field Calculations, In. J. Heat Mass Transfer 37 (1994)139-151.

[2] K.Abe, T.Kondoh and Y.Nagano, A New Turbulence Model for Predicting Fluid Flow and Heat Transfer in Separating and Reattaching Flows-II. Thermal Field Calculations, In. J. Heat Mass Transfer 38 (1995)1467-1481.

[3] S. Kakac et al.(eds.), Convective Heat and Mass Transfer in Porous Media, Kluwer Academic, Netherland, 1991.

3.3.12 TF41-JA : Optimization of Staged Construction

(1) Brief Task Description

IFMIF construction is planned in two stages (125 mA → 250 mA). Two deuteron beams enter a lithium target with 20 degrees opening angle (each beam enters with the angle of 10 degrees to the surface of target), completely overlapping with a beam footprint 20 cm wide x 5 cm high. However, only one accelerator will be operated in the first stage. It is necessary to optimize the beam size and incident beam angle for the first stage, and then to determine the distribution and gradient of the neutron flux. It is concluded that the best beam size during first stage operation is 10 cm wide x 5 cm high, with the beam incident angle 10 degrees.

Contributors

Name	Party	Institute	E-mail address
M. Sugimoto	Japan	JAERI	sugimoto@ifmif.tokai.jaeri.go.jp
T. Yutani	Japan	JAERI	yutani@ifmif.tokai.jaeri.go.jp

(2) Introduction

The full capability of the IFMIF neutron irradiation field will be achieved in a staged construction. At the start of the Key Element Technology Phase the planned staging was: (i) 1 beam with ~50mA, (ii) 1 beam with 125mA, and (iii) 2 beams with 250 mA total. In the final configuration, two deuteron beams enter a lithium target with 20 degrees opening angle, and completely overlap with a beam footprint 20 cm wide x 5 cm high. As the neutron flux is proportional to the total beam current, a possible way to increase the neutron flux on the specimens is to reduce the beam size in stages (i) and (ii).

The conceptual design recently changed, with the staged construction compressed to two stages (125mA → 250mA) with the operating starts scheduled for 2016 and 2019 for the two stages. It is still possible to change the beam size for the first stage of operation, and the incident direction can also be changed from 10 to 0 degree. The effects on the distribution and gradient of the neutron flux due to the different options for the beam footprint size and the entering angle are examined to determine the optimal irradiation field during first stage operation.

(3) Calculation Model and Method

A calculation configuration is shown in Fig. 1. In full operation two deuteron beams enter the lithium target with 20 degrees opening angle (10 degrees to y-z plane). Each beam has energy of 40 MeV, current of 125mA, and uniform distribution 20 cm wide x 5 cm high (z direction) with 1 cm tails at top and bottom. In stage one only one deuteron beam (beam 1), with energy 40 MeV and current 125mA, enters the lithium target with incident angle of 0 or 10 degrees. Also it has uniform distribution of 10 or 20 cm wide x 5 cm high and has 1 cm tails at top and bottom. The thickness of the lithium jet and steel backwall are 25 mm and 1.8 mm respectively on the basis of the recent design of the target system. The loading material (test module and specimens) in the high flux test module is assumed to be uniformly composed of Fe 50% and void 50%, and of infinite size. The distance between backwall and loading material is 2 mm and will be accurately set by the remote handling system in IFMIF. The calculation cases are as follows. (The numbering of the cases is continued from Task TF22-JA.)

- Case 1 (reference)
  two beams with 20 degrees opening angle, 200 mm beam width
- Case 4
  one beam with incident angle 10 degrees, 200 mm beam width
- Case 5
  one beam with incident angle 0 degree, 200 mm beam width
- Case 6
  one beam with incident angle 0 degree, 100 mm beam width

- Case 7
  one beam with incident angle 10 degrees, 100 mm beam width

(The calculation method is described in Task TF22-JA.)

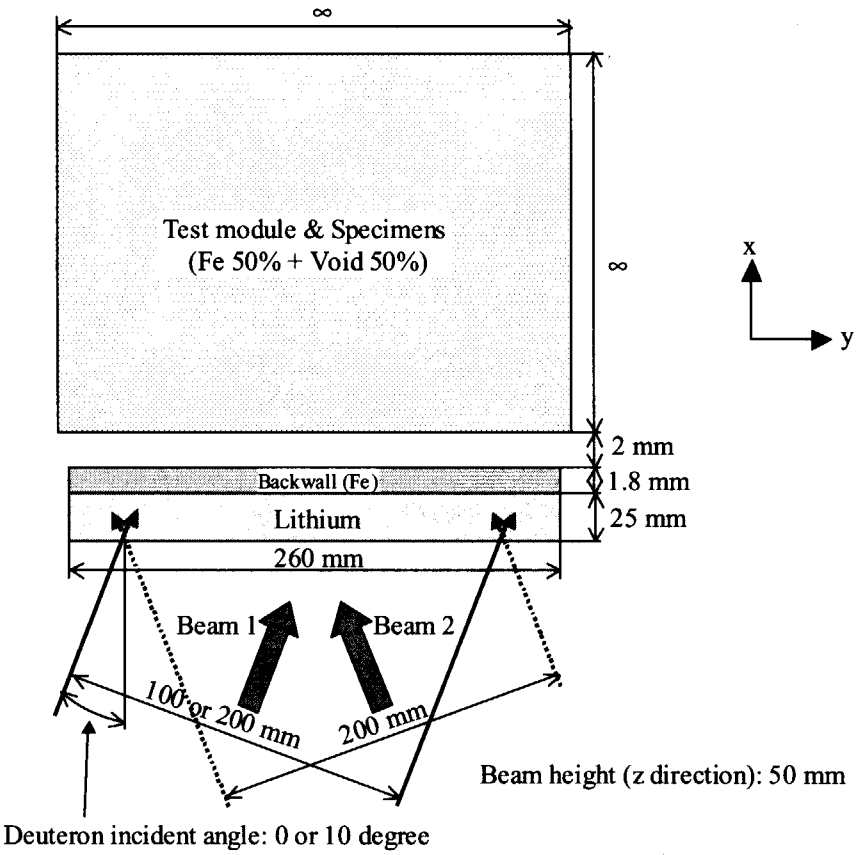
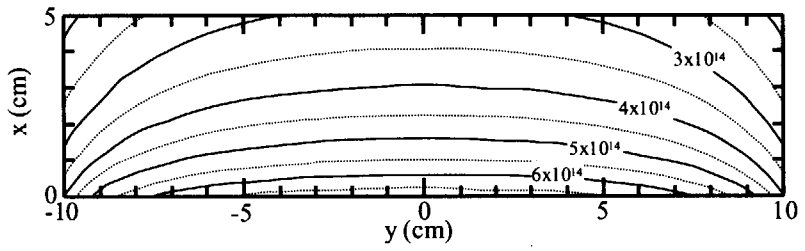


Fig. 1 Neutron flux calculation model.

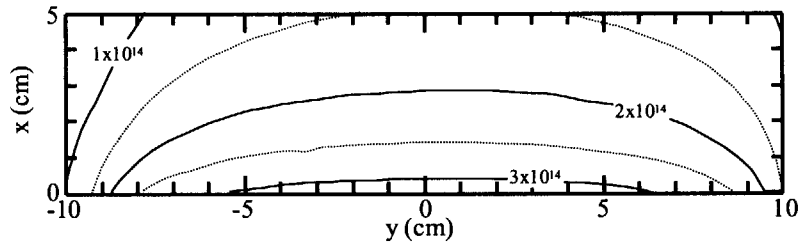
(4) Neutron Flux Distribution

Figure 2 shows the contour plots of neutron flux for the region of 5 cm x 20 cm on the central x-y plane of the specimen irradiation region. Figure 3 shows the space volumes giving the neutron flux above the specific level in the specimen irradiation region.

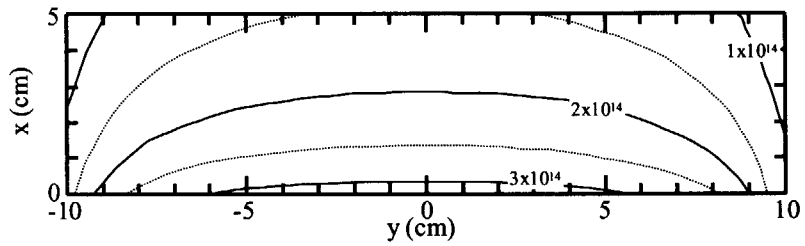
IFMIF construction is planned in two stages (125 mA →250mA). Two accelerators operate in the second stage, when each beam size is 200 mm (width) x 50 mm (height), and that is Case 1. The beam width of 100 mm (Case 6 and 7) or 200 mm (Case 4 and 5) will be selected for the first stage, when only one accelerator is operated. Also, the beam incident angle of 0 degree (Case 5 and 6) or 10 degrees (Case 4 and 7) will be selected.



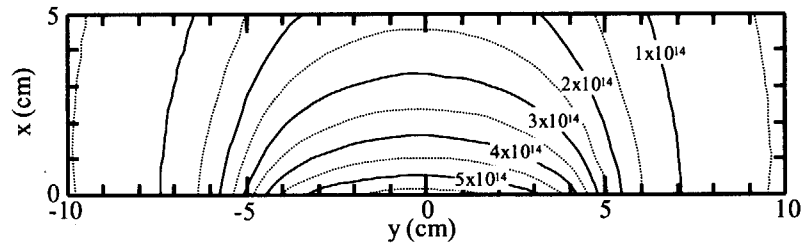
(a) Case 1 (Reference case, 2 beams, 20 degrees opening angle, 200 mm beam width.)



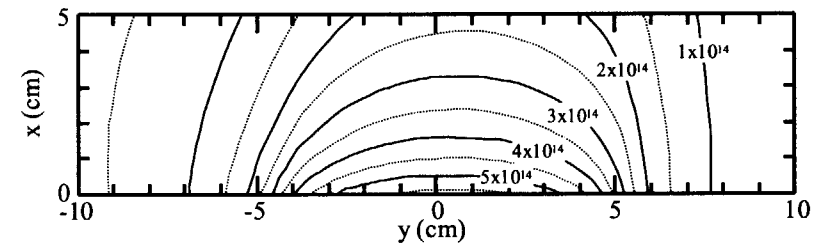
(b) Case 4 (1 beam, 10 degrees incident angle, 200 mm beam width.)



(c) Case 5 (1 beam, 0 degree incident angle, 200 mm beam width.)



(d) Case 6 (1 beam, 0 degree incident angle, 100 mm beam width.)



(e) Case 7 (1 beam, 10 degrees incident angle, 100 mm beam width.)

Fig. 2 Contour plot of neutron flux (n/cm^2/s) for the region of 5 cm x 20 cm on the central x-y plane of the specimen irradiation region.

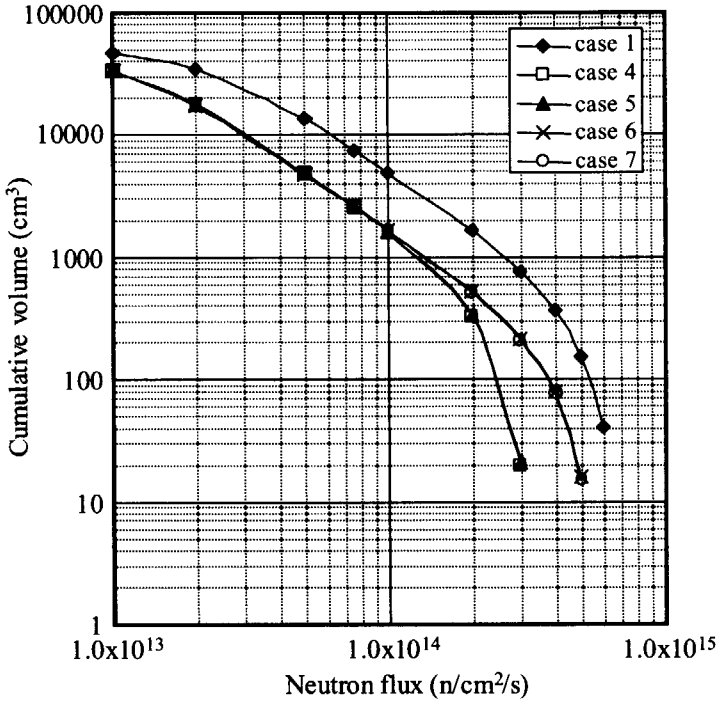


Fig. 3 Volume over specific neutron flux in the specimen irradiation region.

When the beam width is 200 mm the neutron flux is reduced to about half of that of the reference case. The neutron flux inside the range -5 to 5 cm in the y direction reaches about 80% of the reference case if the beam width is 100 mm. At beam widths of 200 mm and 100 mm, the volumes with neutron flux above $2x10^{14}$ $n/cm^2/s$ are reduced to 20% and 30% that of the reference case, respectively. (A neutron flux of $2x10^{14}$ $n/cm^2/s$ is equivalent to 17 dpa/fpy, if the value of the dpa cross section for Fe in IFMIF is estimated to be 2.7 b*keV.) However, these volumes are little affected by the beam incident angle. Therefore, the best beam size is 10 cm wide x 5 cm high during first stage operation.

(5) Neutron Flux Gradients

Contour plots of the neutron flux gradients of the x direction and y direction for the region of 5 cm x 20 cm on the central x-y plane of the specimen irradiation region are shown in Fig. 4 and 5, respectively. The contour plots of neutron flux gradient of z direction on the central x-z plane of the specimen irradiation region are shown in Fig. 6.

All neutron flux gradients in the x direction inside the region having a relatively high neutron flux (>$1x10^{14}$ $n/cm^2/s$) exceed 10%/cm. When the beam incident angle is 0 degree the neutron flux gradient in y direction is less than 10%/cm in the range -8 cm to 8 cm (for 200 mm width) and -3 cm to 3 cm (for 100 mm width) in the y direction. When the beam incident angle is 10 degrees these ranges are shifted about 1 cm to the positive side of y direction. The neutron flux gradient in the z direction is less than 10%/cm in the high flux region (-2.5 cm ~ 2.5 cm in the z direction) at any case. Therefore, the beam incident angle of 10 degrees is not a significant concern to the materials irradiation program.

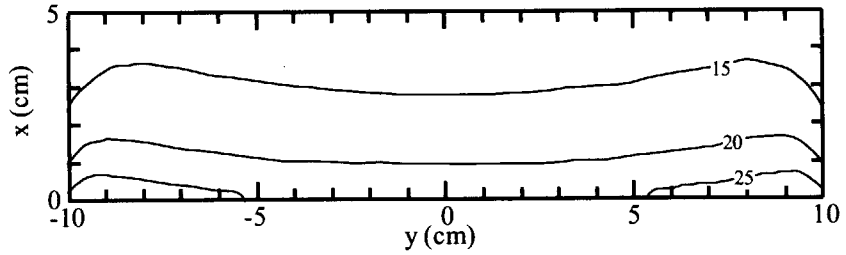
(6) Conclusions

The effects on the distribution and gradient of the neutron flux due to the difference of beam size and incident angle were examined to optimize the beam size and incident angle of beam during the first stage of IFMIF operation.

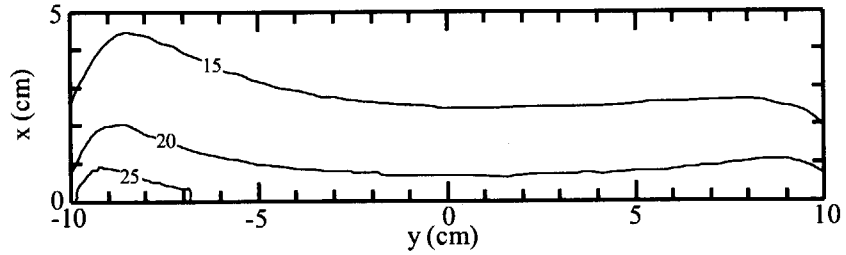
The neutron flux is reduced to about half of that of two beams (the second stage), if the beam width is 200 mm, the same as it will be in the second stage. When the beam width is 100 mm the neutron flux is about 80% of what it will be in the second stage.

The volume having neutron flux above a specific level is little affected by the difference of beam incident angle. However, the neutron flux gradient is slightly affected.

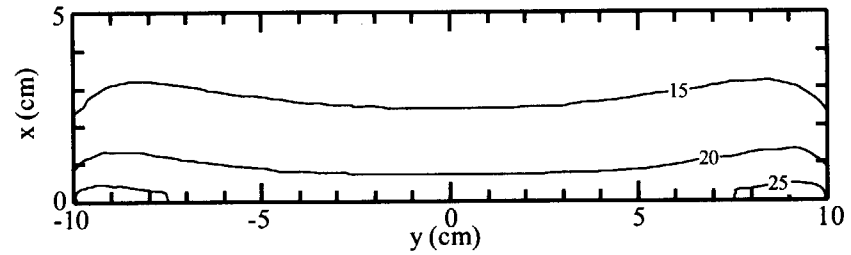
The best beam size during the first stage is 10 cm wide x 5 cm high, because the neutron flux is nearly equal to that of second stage operation when the effective irradiation volume will be larger than that of the first stage operation. The beam incident angle of 10 degrees, the same value as in the second stage, will have little effect on the irradiation program.



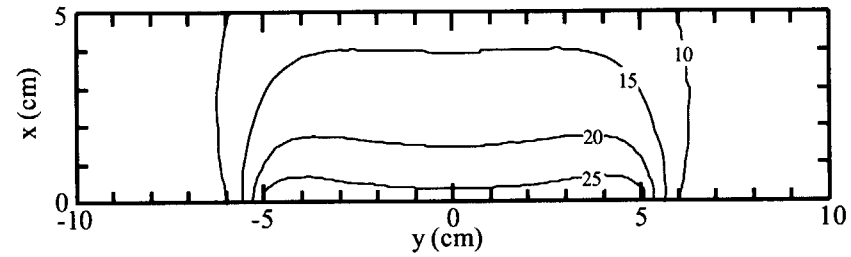
(a) Case 1 (Reference case, 2 beams, 20 degrees opening angle, 200 mm beam width.)



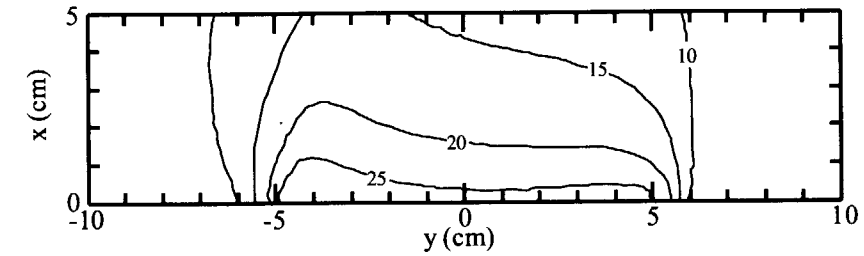
(b) Case 4 (1 beam, 10 degrees incident angle, 200 mm beam width.)



(c) Case 5 (1 beam, 0 degree incident angle, 200 mm beam width.)

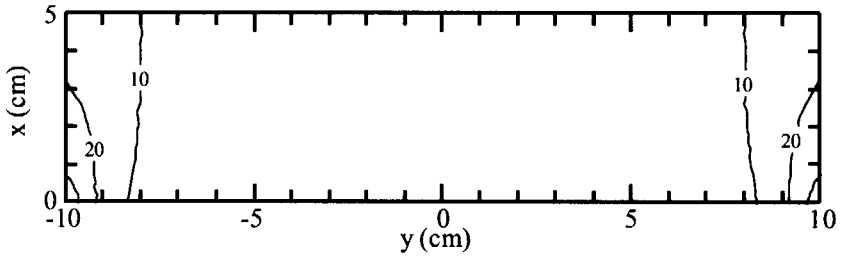


(d) Case 6 (1 beam, 0 degree incident angle, 100 mm beam width.)

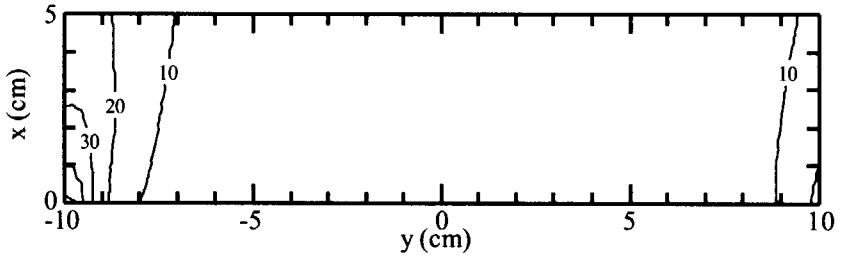


(e) Case 7 (1 beam, 10 degrees incident angle, 100 mm beam width.)

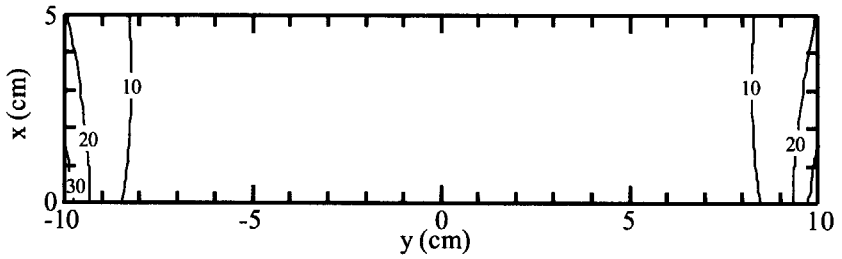
Fig. 4 Contour plot of neutron flux gradient (%/cm) of x direction for the region of 5 cm x 20 cm on the central x-y plane of the specimen irradiation region.



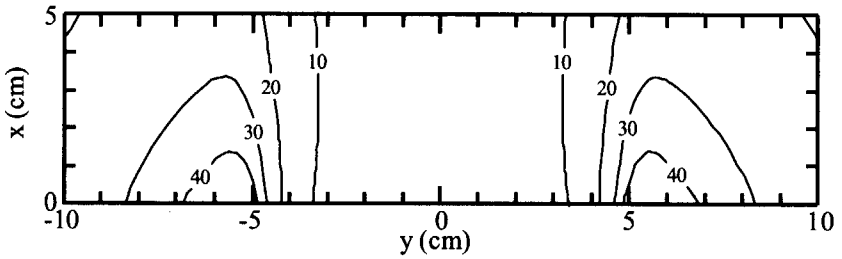
(a) Case 1 (Reference case, 2 beams, 20 degrees opening angle, 200 mm beam width.)



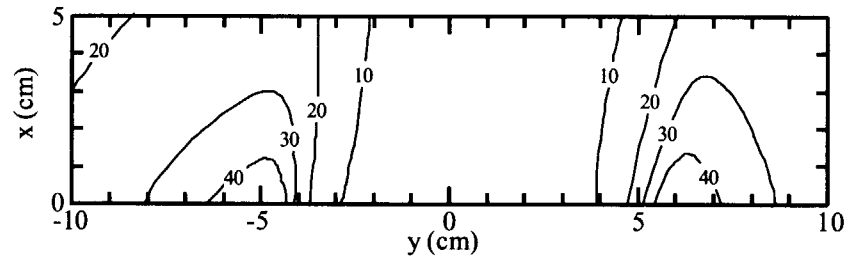
(b) Case 4 (1 beam, 10 degrees incident angle, 200 mm beam width.)



(c) Case 5 (1 beam, 0 degree incident angle, 200 mm beam width.)

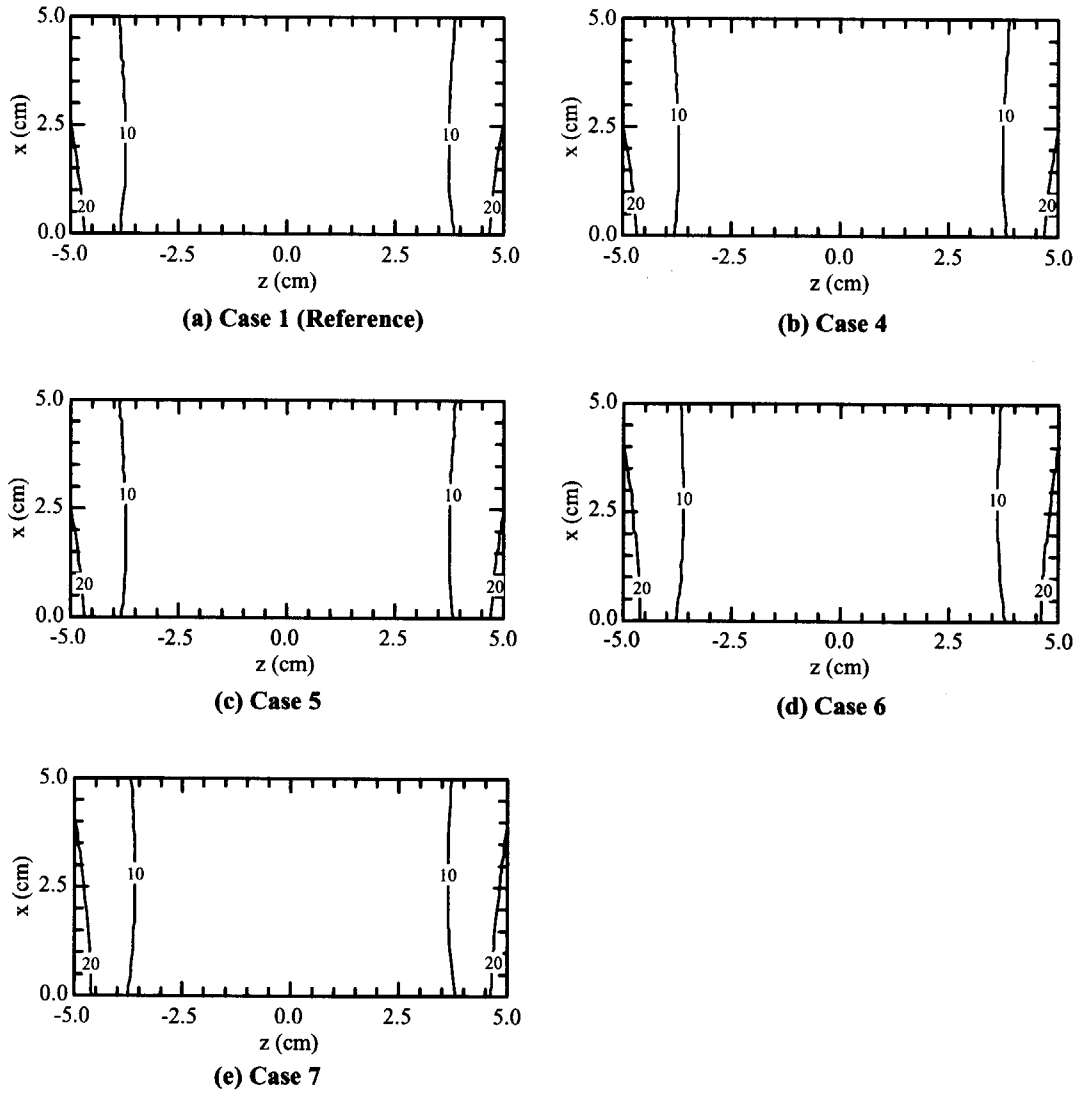


(d) Case 6 (1 beam, 0 degree incident angle, 100 mm beam width.)



(e) Case 7 (1 beam, 10 degrees incident angle, 100 mm beam width.)

Fig. 5 Contour plot of neutron flux gradient (%/cm) of y direction for the region of 5 cm x 20 cm on the central x-y plane of the specimen irradiation region.



(a) Case 1 (Reference)

(b) Case 4

(c) Case 5

(d) Case 6

(e) Case 7

Fig. 6 Contour plot of neutron flux gradient (%/cm) of z direction on the central x-z plane of the specimen irradiation region.

3.3.13 TF42-JA : PIE Facility

(1) Brief Task Description

IFMIF construction is planned in two stages (125 mA →250 mA). The irradiation tests and post irradiation examination (PIE) tests will be planned to coordinate with the staged construction. The items of PIE testing are reviewed to provide the equipment for PIE during the construction phase. There is no significant difference in the PIE requirements between the first and second stages. However, duplicate test equipment may not be necessary during the first stage.

This task focuses on the examination of facilities needed for specimens without tritium contamination. The examination of the facilities that handle specimens containing tritium is carried out in task TF34-JA.

Contributor

Name	Party	Institute	E-mail address
T. Yutani	Japan	JAERI	yutani@ifmif.tokai.jaeri.go.jp

(2) Introduction

IFMIF will be constructed in two stages (125 mA →250 mA). There will be differences in the number of irradiated specimens and/or the neutron flux between first stage and second stages. Therefore, the PIE items and specimens to be tested during the first stage might differ from requirements with full facility operation. Also, the equipment for PIE needs to be provided and installed during the construction phase.

The layout of the PIE facilities also needs to be reviewed in consideration of the material flow, since the design of the main building that houses the PIE facility has been modified from that of the CDA phase.

(3) PIE Test Items and Equipment

In the present plan, the operating period of the first stage is about three years. Although the beam size of the first stage is not yet decided, it will probably be half that of the second stage, because of the users desire to reach high fluences as soon as possible. As a result, the beam size is assumed to be half that of the second stage. A fluence of at least 50 dpa will be achieved during operation in the first stage, although IFMIF may not be operated smoothly due to early failures and interruptions for work on the second stage. The specimens from the high flux test module will be taken out more than once in reaching this fluence for interim testing and evaluation.

There is no significant difference in PIE test items between the first and second stages. Thus, the equipment for all kinds of PIE must be provided in the first stage, although some equipment may be added or removed according to future progress in development of fusion materials. The candidate materials will be investigated in various kinds of tests (tensile test, fracture toughness test, push-pull fatigue test, impact test, measurement of profile of pressurized tube creep specimen, optical microscopy, transmission electron microscopy, etc.). The equipment to carry out these PIE tests are reviewed on the basis of examination on the CDA phase [1]. A radioactivity level of the specimens is estimated to be of the order of 10^{10} Bq/cc from calculation results on the ITER-FEAT, so all mechanical tests will need to be carried out in the hot cells (i.e., conventional hot cells). However, some small volume specimens, such as TEM specimens (volume 0.002 cc), may be handled with hands-on operation in the shielded glove box.

The disassembly/assembly of the test modules of VTA1 and VTA2, except for the in-situ tritium release test module, is conducted in the test module handling cell using a small universal robot. The disassembly/assembly of the rig, which holds capsule in the high flux test module, will be conducted in the conventional hot cells, although they may be done in the test module handling cell. They will not involve the PIE equipment.

The equipment for the conventional hot cells and shielded glove box laboratory are shown Tables 1 and 2 respectively.

Table 1 PIE test equipment for conventional hot cells.

Equipment	Number (Specification)	Purpose
Cutter	1	Disassembly of rig and capsule
Welder	1	Assembly of rig and capsule
NaK processing equipment	1 (cutter, kerosene)	Disassembly of capsule with NaK
NaK pouring equipment	1	Assembly of capsule with NaK
Universal testing machine	3 (10 kN load cell, 20-1000°C, vacuum)	Tensile test, fracture toughness test
Fatigue testing machine	3 (Inert gas/vacuum, aqueous/liquid metal)	Push-pull fatigue test, fatigue crack growth test, corrosion fatigue test
Slow strain rate testing machine	2 (aqueous/liquid metal)	Slow strain rate test
Compact Charpy impact tester with thermostat	1	Charpy impact test
Equipment for measurement of specimen dimension	1 set	Measurement of specimen dimensions before and after mechanical test
Periscope	1	Observation of specimen appearance
Laser profilometer	1	Measurement of profiles of pressurized tube creep specimens
Diamond saw, grinder, mechanical polisher, electro polisher, etc.	1 set	Specimen preparation for optical microscope, SEM, TEM
Optical microscope	1	Optical microscopy
Microhardness tester	1	Hardness test
SEM	1	Fractography
Furnace	3 (Vacuum/inert gas)	Annealing of specimens
Other equipment	As needed (TBD)	Measurement of magnetic property of specimen, electric insulation of heater, electromotive force of thermocouple, etc.
Shielded storage containers	1 set (Computerized specimen identification system)	Storage of irradiated specimens

Table 2 PIE test equipment for shielded glove box laboratory.

Equipment	Number (Specification)	Purpose
Grinder, electro polisher	1 set	Specimen preparation for TEM
Immersion density equipment	1	Precision density measurement for TEM disks
SEM	1	Scanning electron microscopy, elemental analysis
TEM	1	Transmission electron microscopy, elemental analysis
Ge and Si-Li gamma ray spectrometer	1	Activation analysis
Temporary vacuum storage grids	1 set	Storage of TEM specimens

In the conventional hot cells, the needed number of universal testing machines, fatigue testing machines and slow strain rate testing machines may be one of each kind for the first stage of IFMIF operation, because the specimen number is half that in the second stage. The equipment added to the list compiled in the CDA phase of IFMIF design is as follows.

- NaK processing equipment and NaK pouring equipment

- Compact Charpy impact tester
- Equipment for measurement of specimen dimension and periscope
- Microhardness tester
- Scanning electron microscope (SEM)
- Equipment for measurement of electric insulation of heaters and electromotive force of thermocouples

In the present design for the high flux test module, He gas fills the gap between specimen and specimen holder. Thermocouples are attached to the specimen holder, and specimen temperatures may not be accurately estimated from the value of the thermocouple, because the uncertainty of heat transfer coefficient of the gas gap is large. In order to solve this problem, users recently proposed the use of NaK in this gap. Then, NaK processing equipment and NaK pouring equipment are necessary. The kerosene will be used to process NaK. The need for a compact Charpy impact tester was overlooked in the CDA phase. The equipment for measurement of specimen dimensions and a periscope are indispensable for the mechanical testing. The microhardness tester can be installed in the conventional hot cells because it is not difficult to automate. In the CDA design, SEM and transmission electron microscope (TEM), which are expensive, were planned to be located in the tritium laboratory to minimize the cost of the PIE facilities. However, the users may need to observe the fracture surfaces of specimen as soon as possible after the mechanical test, and the SEM needs to be located in the conventional hot cells. A focused ion beam system might be needed for TEM specimen preparation. Also, PIE test equipment for damage evaluation of electric heaters and thermocouple may be important.

The equipment to prepare specimens for optical microscopy and the microhardness tester (diamond saw, grinder, mechanical polisher, electropolisher) is eliminated from the list of equipment for the shielded glove box laboratory, and relocated to the conventional hot cells. In accordance with the above-mentioned plan on the CDA phase, the SEM and TEM will be located in the tritium laboratory at the first stage. However, an additional SEM and TEM may need to be located in the shielded glove box laboratory at the second stage. Furthermore, other equipment (e.g. scanning tunneling microscope) may become necessary as additional needs and instrumentation improvements are identified.

(4) Layout

The plan view of PIE facilities is shown in Fig. 1.

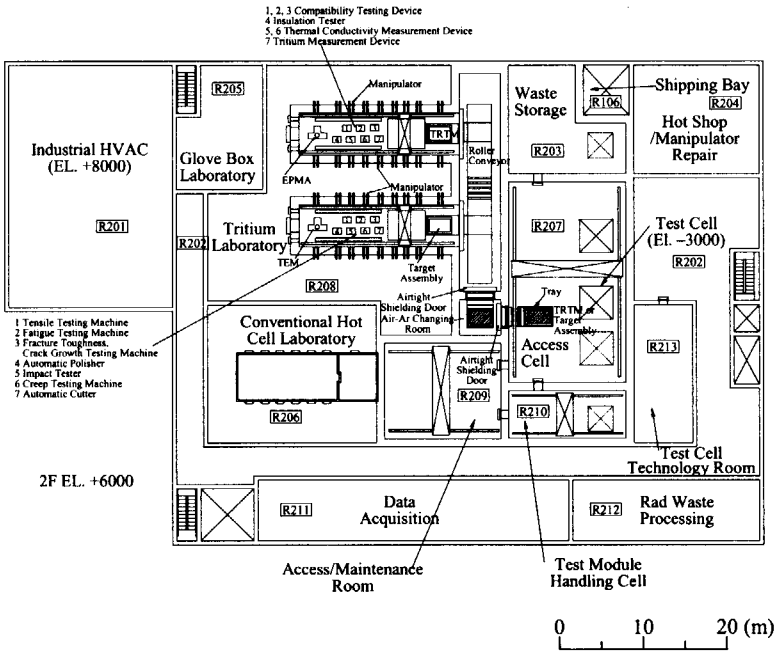


Fig. 1 Plan view of Test Facilities.

The layout of this facility must take into account the flow of irradiated material, and that will be considered now. The specimen holding rigs from the high flux test module will be transferred in a cask from the test module handling cell to the conventional hot cells using the rig transporter of universal robot system, passing through an access/maintenance room. Other non-tritiated materials are transferred by the same method. The access/maintenance room is located between the conventional hot cells and the test module handling cell (and access cell). The personnel access to the test module handling cell and access cell is through this room. The maintenance and repair of contaminated equipment that can be transferred from the hot cells are conducted by hands-on operation in the access/maintenance room. Also, equipment for the hot cells are sometimes temporarily stored in this room.

Tritium-containing materials such as the in-situ tritium release test module and lithium target assembly are transferred from the access cell to the tritium hot cells via an Ar/air changing room using the roller conveyors. The small volume TEM and SEM specimens are moved in a shielded small vessel that can be handled by personnel, from the conventional hot cells to the shielded glove box or tritium hot cell.

The main building that houses the accelerator system, target system and test facilities was revised since the CDA design. At that time, the area of the post irradiation examination facilities was enlarged from that of the CDA phase. In the KEP phase, the area for the tritium laboratory also needed to be enlarged, because the function of the tritium laboratory increased. Although the area for the conventional hot cells can be nearly equal to that of CDA phase, the area for the shielded glove box laboratory becomes about half. The precision equipment will be installed in the shielded glove box laboratory in the future. It may be necessary that the shielded glove box laboratory be located in some other area to avoid the vibrations generated by operation of the universal robot and other heavy equipment. Its location should be examined in the next phase of the IFMIF project.

(5) Summary

IFMIF construction is planned to occur in two stages (125 mA →250 mA). The requirements of PIE testing are reviewed to assure that the equipment for PIE is included and phased into the construction plan.

There are no significant differences in the PIE test types required in the first and second stages of IFMIF operation, because a fluence of 50 dpa is expected to be achieved during the first stage. Although the equipment for all kind of PIE tests must be provided in the first stage, the necessary number of systems for each type of test can probably be kept to one, since the number of specimens will be small. The probable types of PIE test needed in the first stage are the tensile test, fracture toughness test, push-pull fatigue test, impact test, measurement of profile of pressurized tube creep specimens, optical microscopy, transmission electron microscopy, etc.

Equipment for the handling of NaK has been added to respond to the recent requirement from users.

Reference

[1] M. Martone (Ed.), "IFMIF International Fusion Materials Irradiation Facility, Conceptual Design Activity, Final Report, IFMIF CDA TEAM", ENEA Frascati, Report ENEA-RT/ERG/FUS/96-11 (1996).

3.3.14 TF51-EU : D-Li Reaction Source Term – Data Evaluation and Code Development

(1) Brief Task Description

The D-Li neutron source term is of primary importance for calculating the neutron flux, the spectrum and the nuclear responses in the IFMIF Test Cell. The uncertainty in the total neutron yield is directly transmitted into the neutronic response calculated for the test modules. The objective of Task TF-51-EU is to provide the computational tools and data required for the simulation of D-Li source neutrons in the transport calculation.

During KEP, a suitable methodology for the evaluation of D + ^{6,7}Li double-differential cross-section data has been established and a first set of data files has been prepared in accordance with standard nuclear data format rules. The evaluated data include cross-sections for all reaction channels up to 50 MeV deuteron energy as well as energy-angle distributions for the neutrons emitted through the various ^{6,7}Li(d,xn)-reactions. State-of-the-art nuclear reaction models have been applied for the evaluation making use of available ^{6,7}Li + D experimental cross-section data.

The Monte Carlo code McDeLicious was developed to simulate in the transport calculation the neutron generation on the basis of the evaluated D + ^{6,7}Li cross-section data. The McDeLicious approach was tested against available experimental thick Lithium target data. It was shown that the resulting total neutron yield as well as the neutron angle-energy spectra can be predicted with considerably better accuracy than with previously available approaches. The accuracy of the angular yield spectra, however, needs to be further improved.

Contributors

Name	Party	Institute	E-mail address
U. Fischer	EU	FZK	ulrich.fischer@irs.fzk.de
S. Simakov	EU	FZK	simakov@irs.fzk.de
Yu. A. Korovin	EU	INPE	korovin@iate.obninsk.ru
A. Yu. Konobeyev	EU	INPE	
P. E. Pereslavtsev	EU	INPE/FZK	pereslavtsev@irs.fzk.de
U. v. Moellendorff	EU	FZK	moellendorff@irs.fzk.de

(2) Background

In the IFMIF lithium target, neutrons are generated through the D-Li stripping reaction and various other nuclear Li(d,xn) reactions. The neutron source generation must be represented accordingly in the neutron transport calculation.

This requires developing a suitable D-Li source term model which ideally should be integrated to a standard Monte Carlo neutron transport code such as MCNP [1]. The McDeLi code [2] has been previously developed as an extension to MCNP with the capability of representing the neutron source term on the basis of a built-in semi-empirical D-Li reaction model. McDeLi can handle two beams impinging onto the lithium target taking into account different beam directions and a spatially varying intensity distribution. Deuteron slowing down in the lithium is described according to the well established empirical model of Ziegler et al. [3]. The McDeLi Li(d,xn) reaction model considers as neutron producing reactions deuteron stripping and deuteron absorption followed by the formation of a compound nucleus with subsequent neutron emission. Adjustable parameters of the Li(d,xn) reaction model were obtained through numerical fits to experimental angle-energy distributions of neutron yields from thick lithium targets, bombarded by 32 and 40 MeV deuterons. Extensive testing of the McDeLi code against available experimental data over the full deuteron energy range from 5 to 50 MeV has shown that McDeLi fails to reproduce the experimental data below 30 MeV incident deuteron energy [4]. The high energy tail above 40 MeV cannot be reproduced either since the semi-empirical reaction model does not take into account exothermic reactions.

To overcome these drawbacks, a new approach was established during KEP with the objective to replace the semi-empirical Li(d,xn) reaction model of McDeLi by a complete description of the deuteron interactions with the lithium nuclei through the use of evaluated D + ^{6,7}Li cross-section data.

(3) Evaluation of D + ^{6,7}Li Cross-section Data

A new methodology has been developed to enable the evaluation of nuclear cross-sections for the interaction of deuterons with lithium isotopes up to 50 MeV deuteron incidence energy based on diffraction theory, a modified intra-nuclear cascade model and standard evaluation techniques [5]. Following this approach, a complete set of evaluated cross-section data was prepared for the reaction system D + ^{6,7}Li. The evaluated data include cross-sections for all reaction channels up to 50 MeV deuteron energy (Table 1) as well as energy-angle distributions for the neutrons emitted through the various ^{6,7}Li(d,xn)-reactions. Cross sections are shown in Fig. 1 as function of the incident deuteron energy for the total and the elastic D + Li reaction as well as the production of secondary particles (n, p, d, t, α, γ). A complete set of D + ^{6,7}Li cross-section data was prepared in standard ENDF-6 data format and processed with the ACER module of the NJOY99 code [6] for use in Monte Carlo transport calculations.

Table 1 Deuteron–lithium reaction channels open up to 50 MeV incident deuteron energy with associated Q values and threshold energies. Neutron producing channels are displayed in bold.

D+ ^{7}Li			D + ^{6}Li		
Reaction Products	Q, MeV	Threshold, MeV	Reaction Products	Q, MeV	Threshold, MeV
γ + ^{9}Be	16.696	0	2α	22.372	0
n + 2α	**15.122**	**0**	γ + ^{8}Be	22.281	0
n + ^{8}Be	**15.031**	**0**	p + ^{7}Li	5.0254	0
α + ^{5}He	14.232	0	**n + ^{7}Be**	**3.381**	**0**
d + ^{7}Li	0	0	p +t + α	2.558	0
p + ^{8}Li	-0.192	0.247	**n +^{3}He + α**	**1.795**	**0**
t + ^{6}Li	-0.993	1.278	^{3}He + ^{5}He	0.905	0
n +p + ^{7}Li	**-2.225**	**2.863**	t + ^{5}Li	0.593	0
d +t + α	-2.467	3.175	d + ^{6}Li	0	0
2n + ^{7}Be	**-3.869**	**4.979**	2d + α	-1.474	1.968
^{3}He + ^{6}He	-4.482	5.769	**n +p + ^{6}Li**	**-2.225**	**2.969**
n + p + t + α	**-4.692**	**6.038**	**n + p + d + α**	**-3.699**	**4.937**
...	...	...	...	...	...

(4) Monte Carlo Code McDeLicious

The Monte Carlo code McDeLicious [7] was developed to simulate in the transport calculation the neutron generation on the basis of the evaluated D + ^{6,7}Li cross-section data. To this end, the tabulated D + ^{6,7}Li cross section data (including the angular and energy distributions) are processed from the ACE data files prepared by NJOYY/ACER. With these data available, the generation of D-Li source neutron can be sampled in the Monte Carlo calculation. First

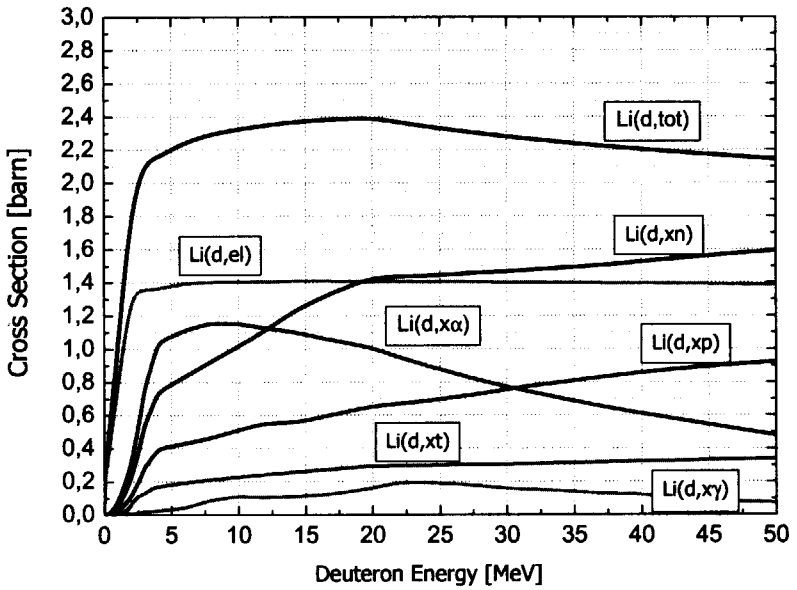


Fig. 1 D + Li(nat) reaction and production (n, p, d, t, α, γ) cross sections as a function of the incident deuteron energy.

the deuteron track length is sampled taking into account the total D-Li interaction cross sections. Next the interaction probability with either of the ^{6}Li or ^{7}Li nuclides is calculated according to the associated macroscopic cross sections for the given deuteron energy. Eventually the energy and angle of the generated neutron and photon are sampled. This information together with the coordinates of the D-Li interaction in the lithium target cell is further used for transporting the generated neutrons and photons in the Monte Carlo calculation. The procedure described has been integrated to the McDeLi code by replacing the routines describing its semi-empirical Li(d,xn) reaction model. The resulting McDeLicious Monte Carlo code is thus a further enhancement to McDeLi with the new ability to sample the generation of D-Li source neutrons and photons from tabulated D + ^{6,7}Li cross-section data as provided on an ACE formatted data file.

(5) Testing and Validation of the McDeLicious Approach

Numerical tests were performed to make sure McDelicious calculations describe correctly the D-Li source neutron generation. To this end, the angular energy spectra calculated by McDeLicious for a thin (0.1 mm) lithium target were compared to the double-differential data stored on the D + Li data files. The incident deuteron energy was selected to coincide with an energy point given on the ENDF data file (e. g. 40 MeV). In this way, the double-differential cross-section data could be derived from the original ENDF data without any further processing. The angular neutron and photon yield spectra calculated by McDeLicious for the specified deuteron energy were finally converted to double-differential cross-sections. Good agreement was found between the data stored on the original ENDF data file and those calculated by the Monte Carlo McDeLicious code using the data processed by NJOY/ACER [8].

The McDeLicious approach was extensively tested against available experimental thick lithium target data including recent results that became available with Task TF52-EU (P. Bem et al., NPI Rez) for 17 MeV deuterons [7, 8, 9]. Calculated and measured total neutron yields are compared in Fig. 2 as a function of incident deuteron energy. Fig. 3 shows a comparison for forward neutron yields where a significant number of experimental data are available. Calculated angular neutron energy spectra are compared to the experimental data of Sugimoto [10] (Fig. 4) and Mann [11] (Fig. 5) at 32 and 40 MeV incident deuteron energy, respectively. There are included calculation results obtained with the semi-empircal D-Li reaction model of McDeLi and the ISABEL intra-nuclear cascade model of the high energy particle Monte Carlo code MCNPX 2.1.5 [12]. It is revealed that McDeLicious can predict both the

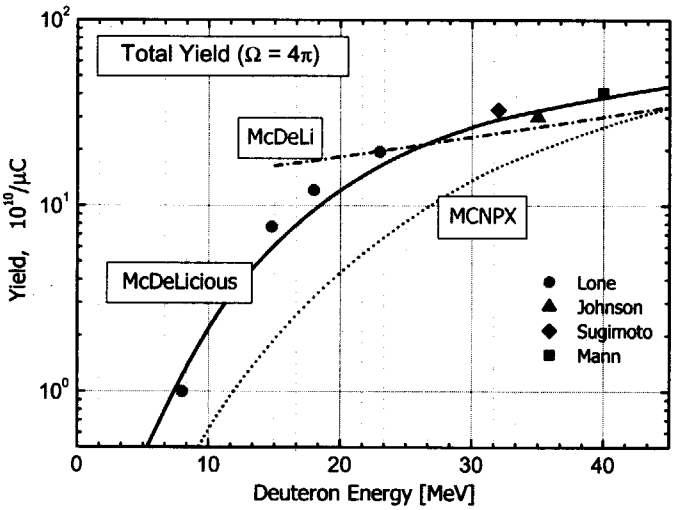


Fig. 2 Thick lithium target total neutron yields as a function of incident deuteron energy.

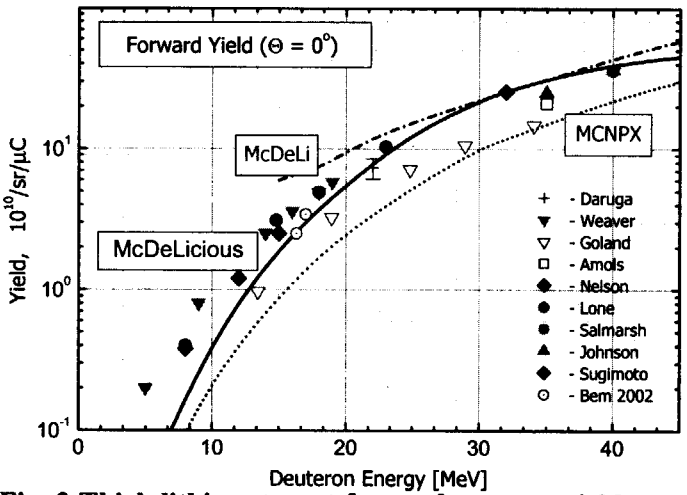


Fig. 3 Thick lithium target forward neutron yields as a function of incident deuteron energy.

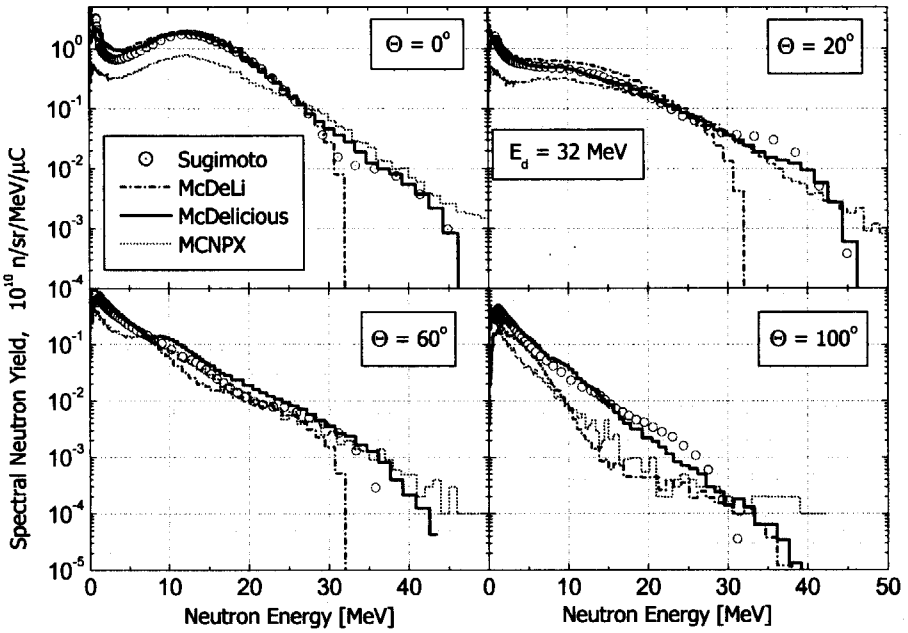


Fig. 4 Thick lithium target neutron yield spectra at 32 MeV incident deuteron energy.

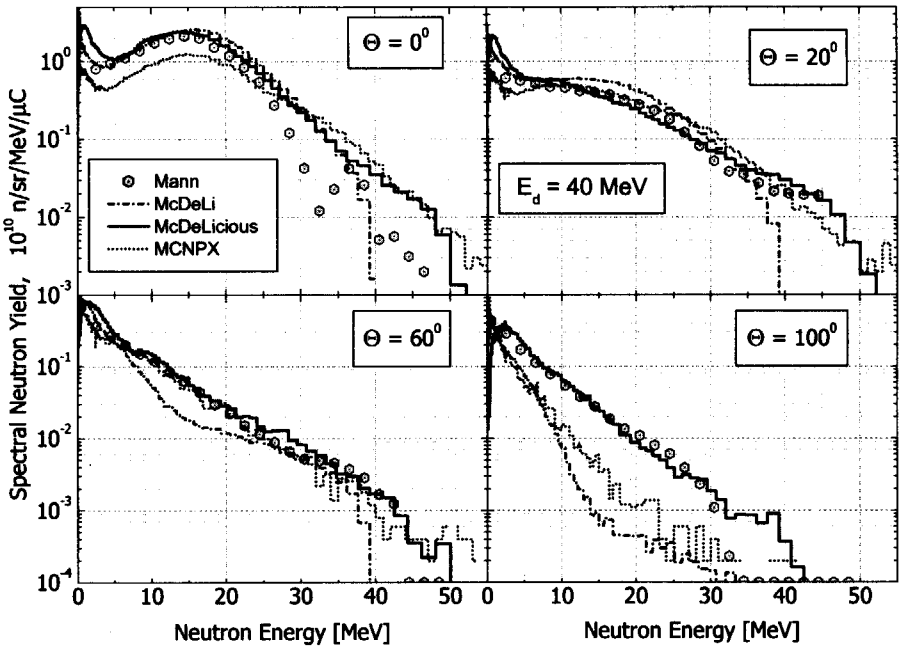


Fig. 5 Thick lithium target neutron yield spectra at 32 MeV incident deuteron energy.

neutron yields and the angular energy spectra with considerably better accuracy than McDeLi and MCNPX. This is also observed for the new angular yield spectra measured by Bem et al. at 17 MeV incident deuteron energy (Task TF52-EU).

The accuracy of the angular yield spectra, however, needs to be further improved. With the McDeLicious approach, this can be achieved in a straightforward way through the updating of the D+^{6,7}Li data evaluations by using improved nuclear models and parameters and by taking into account new thin and thick lithium target measurements currently underway at NPI Rez and JAERI as part of ongoing IFMIF tasks.

References

[1] J.F. Briesmeister (ed.), MCNP - A General Monte Carlo N-Particle Transport Code, Version 4C, Los Alamos National Laboratory, Report LA-13709-M, April 2000.
[2] P. P. H. Wilson, Neutronics of the IFMIF Neutron Source: Development and Analysis, Forschungszentrum Karlsruhe, Wissenschaftliche Berichte FZKA 6218, January 1999.
[3] J.F. Ziegler et al., The Stopping and Range of Ions in Solids, Pergamon Press, 1985.
[4] S. P. Simakov, U. Fischer, U. v. Möllendorff, Testing and updating of the McDeLi Monte Carlo Code, Forschungszentrum Karlsruhe, Interner Bericht IRS Nr. 15/00, FUSION Nr. 161, Oktober 2000.
[5] A. Yu. Konobeyev, Yu. A. Korovin, P. E. Pereslavtsev, U. Fischer and U. von Möllendorff, Developments of methods for calculation of deuteron-lithium and neutron-lithium cross sections for energies up to 50 MeV, Nuclear Science and Engineering 139 (2001) 1-23.
[6] R. E. MacFarlane: The NJOY Nuclear Data Processing System, Version 91, Los Alamos National Laboratory, Report LA-12740-M (1994).
[7] S.P. Simakov, U. Fischer, U. von Möllendorff, I. Schmuck, A.Yu. Konobeev, Yu. A. Korovin, P. Pereslavtsev, Advanced Monte Carlo procedure for the d-Li neutron source term based on evaluated cross sections files, 10th Int. Conf. on Fusion Reactor Materials (ICFRM-10), Baden-Baden, 14-19 Oct. 2001.
[8] S. P. Simakov, U. Fischer, V. Heinzel, U. v. Möllendorff, International Fusion Material Irradiation Facility (IFMIF): Neutron Source Term Simulation and Neutronics Analyses of the High Flux Test Module, Forschungszentrum Karlsruhe, Wissenschaftliche Berichte FZKA 6743 (Juli 2002).
[9] U. Fischer, S. P. Simakov, A. Konobeyev, P. Pereslavtsev, P. Wilson , Neutronics and Nuclear Data for the IFMIF Neutron Source, 6th International Symposium on Fusion Nuclear Technology (ISFNT-6), San Diego, Calif., April 7-12, 2002.
[10] M. Sugimoto, JAERI, Double differential neutron yields from Li(d,n) experiments, private communication, 1995.
[11] F.M. Mann, F. Schmittroth, L.L. Carter. Neutrons from d+Li and the FMIT irradiation environment, Report HEDL-TC-1459, Richland, 1981.
[12] L. S. Waters (Ed), MCNPX User's Manual Version 2.1.5, available from http://mcnpx.lanl.gov.

3.3.15 TF52-EU : D-Li reaction Source Term – Experimental Verification of Neutron Yield

(1) Brief Task Description

The D-Li neutron source term is of prime importance for calculating the neutron flux, the spectrum and the nuclear response in the IFMIF Test Cell. The uncertainty in the total neutron yield is directly transmitted into the neutronic response calculated for the test modules. The objective of Task TF52-EU is to provide experimental data required for the validation of the D-Li neutron source term simulation model developed in the framework of Task T51-EU.

Measurements of thin and thick Li target yield data were performed to this end at the Nuclear Physics Institute (NPI) Řež, employing the upgraded cyclotron-based Fast Neutron Facility (FNF). The spectral distribution of neutrons emitted from a thick lithium target bombarded by 17.0 MeV deuterons was measured at five detector angles (0, 30, 60, 75 and 120 degrees). The spectral distribution of the zero-degree double-differential (thin target) neutron yields at 17 MeV incident deuteron energy was obtained by the difference of the thick target yield data for 17.0 and 16.32 MeV. The experiments of NPI Řež were complemented by measurement of the neutron spectrum and yield and the tritium and Be-7 production in lithium, performed at the Karlsruhe cyclotron using 40 MeV deuterons impinging on a thick lithium target.

Contributors

Name	Party	Institute	E-mail address
P. Bém	EU	NPI	bem@ujf.cas.cz
V. Burjan	EU	NPI	
M. Götz	EU	NPI	
J. Novák	EU	NPI	
V. Kroha	EU	NPI	
E. Šimečková	EU	NPI	
J. Vincour	EU	NPI	
U. Fischer	EU	FZK	ulrich.fischer@irs.fzk.de
S. Simakov	EU	FZK	simakov@irs.fzk.de
U. v. Moellendorff	EU	FZK	moellendorff@irs.fzk.de

(2) Background

In the IFMIF lithium target, neutrons are generated through Li(d,xn) reactions. These processes are simulated in the neutron transport calculations on the basis of evaluated D + ^{6,7}Li cross-section data (Task TF51-EU). Experimental data are required both for the evaluation of the cross-section data (thin lithium target yield spectra) and the validation of the source term simulation in the transport calculation (thick lithium target yield spectra).

Only a few independent measurements of neutron yield spectra from the deuteron bombardment of thick lithium targets are available (see review [1]). These experiments were performed at a few deuteron energies between 5 and 40 MeV and covered secondary neutron energies above 1 MeV. Only one experiment is available on neutron yield spectra for thin lithium targets [2]. Moreover, the existing experimental data scatter to a large extent, thus demonstrating the need for further experiments with improved accuracy.

In the framework of Task TF52-EU, a 17 MeV deuteron beam from the NPI variable-energy cyclotron U-120M was used to measure neutron yield spectra from the D+Li reaction at different angles (0, 30, 60, 75 and 120 degrees). Pulse-height distributions were measured with a liquid-scintillator detector and unfolded to determine the energy distributions of the neutron yields. The shadow bar technique was used to determine the room neutron background. The computational analysis was performed at FZK using the McDeLicious code [3] with evaluated D + ^{6,7}Li cross-section data.

(3) Setup of Experiment

The beam passed through a collimator-free beam guide and was centered at the target of the

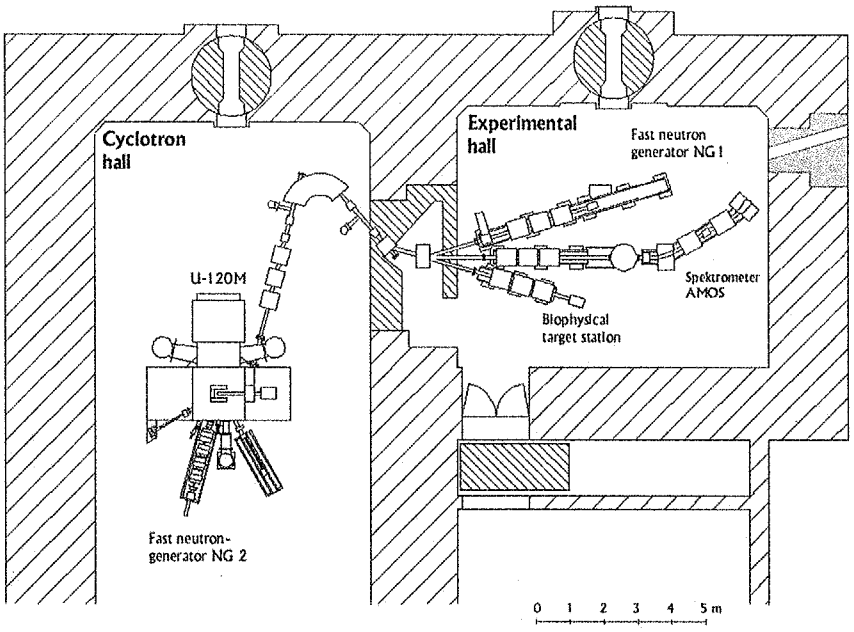


Fig. 1 Schematic layout of the NPI fast neutron facilities with variable energy cyclotron U-120M and the NG1 and NG2 target stations.

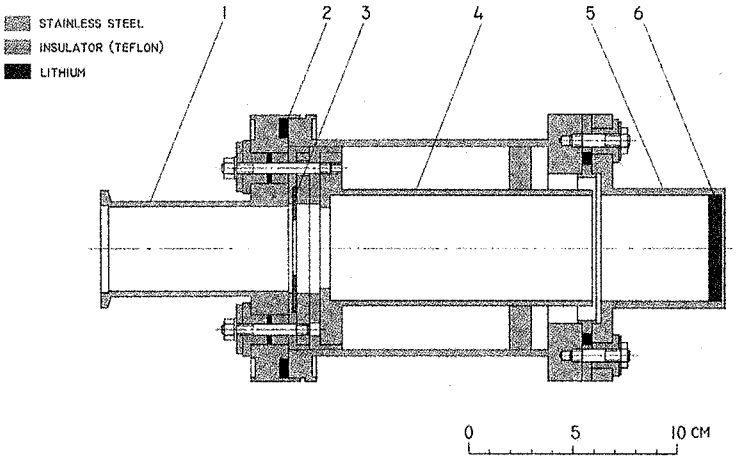


Fig. 2 Design sketch of the Li-target housing. 1 - slit-free beam guide, 2 - silicon seal, 3 - insulated tantalum slit of 24 mm diameter (allows alignment of the beam with the center of the Li-disc), 4 - repelling electrode (-600 V) for suppressing the secondary electrons, 5 - Faraday-cup, 6 - Li-disc target. Vertical and horizontal dimensions of the beam spot on the Li-target lie inside 5 and 8 mm, respectively.

NG1 target station (see Fig. 1). The thick lithium target of 40 mm diameter was composed of 1.5 mm metallic foils (density 0.534 g/cm^2) pressed into a stainless steel chamber (wall thickness 2 mm) in an argon atmosphere. The other dimensions of the target assembly can be taken from Fig. 2. For beam charge monitoring, the target was electrically insulated and equipped with secondary electron suppression by a repelling electrode biased to -600 V.

The angular distribution of the spectral neutron yield has been measured in open geometry. To subtract the room neutron background, the conventional shadow bar method has been employed. For neutron spectrometry, the scintillator pulse-height unfolding technique was utilized. A cylindrical

NE213-equivalent liquid scintillator, BICRON BC501A, with 4.5 cm diameter and 4.5 cm length was used as the neutron detector. It was encapsulated in a bubble free aluminium container and optically coupled to a Hamamatsu R329-02 photomultiplier tube (PMT). To cover the dynamic range of the registered neutron energies from 1.5 to 35 MeV, pulse-height spectra were registered at two values of the PMT supply voltage (1550 and 1850 V) in every irradiation. The pulse height spectra were calibrated up to 12 MeV by the standard gamma ray sources PuBe, ^{60}Co and ^{137}Cs and, in addition, by the known gamma lines from the thermal neutron capture in iron. Employing these reference energy points, the linearity of the PMT gain in the relevant dynamic range was tested for the PMT supply voltage varied between 1200 and 2000 V.

A multi parameter data acquisition system, augmented by the neutron gamma discrimination technique was used. Pulses from the detectors were collected in an external buffer, which was transferred to the on-line computer. List mode registration of the pulse height and monitoring events in the external buffer provided full information about the event history and permitted us to perform dead time and systematic error corrections [4].

(4) Data Processing and Results

An off-line Gaussian analysis was performed for the neutron and photon peaks in the two-dimensional (pulse shape vs. pulse height) spectra. Due to different room background conditions at the various detector positions, a complete discrimination between neutrons and photons was achieved for neutron energies above a minimum varying from 1.8 to 3.5 MeV. The proton recoil pulse-height spectra were unfolded using the GRAVEL procedure of PTB Braunschweig [5]. The neutron response functions and the efficiency of the scintillator detector were calculated with the Monte Carlo code SCINFUL-R [6] for the neutron energy range from 1.5 to 40 MeV, assuming the detector geometry specified by the producer. For generating the response matrix, the calculated response spectra were folded with a Gaussian distribution to account for finite resolution [7].

The uncertainties in the data consist of several components. The statistical uncertainty data generated during the de-convolution process account for pulse height statistics, background subtraction uncertainty and the uncertainty due to the (n,γ) discrimination procedure. The uncertainty of the detector efficiency is estimated to be less than 4-6% [6]. The beam charge on the target was determined with an uncertainty less than 2%. The beam current dependent correction for dead time (amounting up to 8%) was estimated to contribute less than 1% uncertainty. The quadratic summation of these contributions was interpreted as the uncertainty of the yield scale factor. No numerical corrections for the attenuation of the measured neutron flux were performed.

The zero-degree neutron yields from the Li(d,xn) reaction at deuteron energies of 17.0 and 16.32 MeV are shown in Fig. 3. The neutron yields from the D+^{7}Li reaction at 15 – 19 MeV (taken from Ref. 1) are also shown. These data were determined using a Stilbene neutron detector and the time-of-flight (TOF) technique. The overall agreement of the present results and the TOF data is satisfactory. The angular dependence of the measured spectral yield is displayed in Fig. 4. Except for the integral yield data, no angle-dependent spectra have been reported previously in the deuteron energy range under investigation.

Fig. 5 shows the neutron spectrum for a "thin" Li target. It was obtained by the difference of the spectral yield for E_d = 17.00 and 16.32 MeV. The dominant part of the spectra corresponds mainly to the deuteron stripping reaction. For the first time the cross-section value of 0.5 b/sr was obtained by integrating the spectrum over the energy range of the deuteron stripping reaction (neutron energy from the unfolding bias to the kinematical limit). The "effective" Li layer thickness was extracted from the energy difference using the stopping power data. In Fig. 6 the measured data are compared with the only available cross section data from the TOF measurement at Tashkent [2]. Due to the narrow time window in this TOF experiment, neutrons from the stripping process were not detected.

In Figs. 3, 4 and 6, the experimental data are compared to calculations performed at FZK with the McDeLicious, McDeLi and MCNPX codes. It is indicated that further improvement of the neutron source term is required. With the McDeLicious approach, this can be achieved by updating the D + ^{6,7}Li cross-section data evaluation. It is also noted that the contribution of the ^{7}Li(d,n)^{8}Be (E* = 2.9

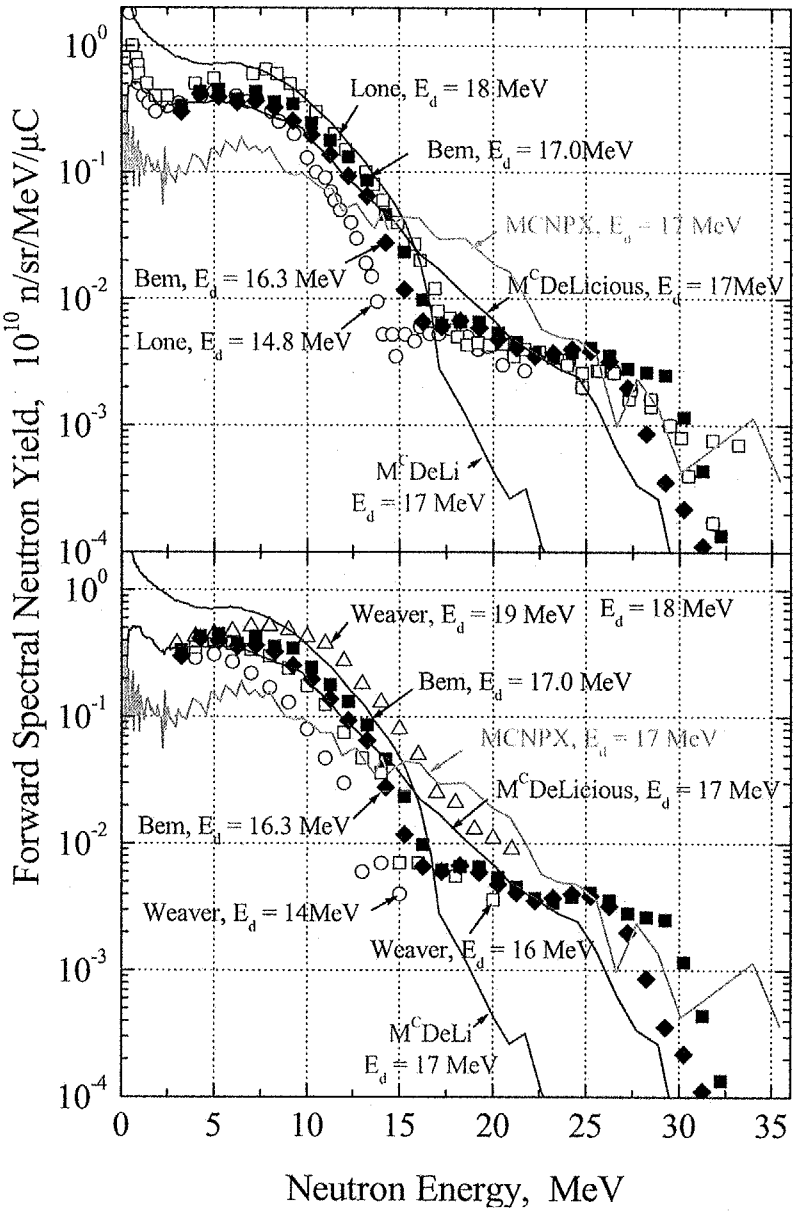


Fig. 3. Zero-degree spectral neutron yield measured at 17.0 MeV and 16.32 MeV deuteron energy. Present data are compared with experimental data of Lone (top) and Weaver (bottom). Curves correspond to the calculations using the McDeLicious, McDeLi and MCNPX Monte Carlo codes.

and 16-17 MeV) reaction channels to the D+Li double-differential neutron cross-section cannot be reproduced in the forward direction by the calculations (Fig. 5).

(5) Measurement of Neutron Spectrum, Neutron Yield, and Tritium and Beryllium-7 Production in the Lithium Target

As part of a cyclotron experiment at FZK simulating several nuclear features of IFMIF, the neutron spectrum and yield were measured [8]. This measurement had to rely on activation foil dosimetry, because other techniques were not available in the given experimental conditions at the cyclotron. Such a method is inherently of limited precision, as it requires the numerical de-convolution of the spectrum from a set of measured reaction rates. On the other hand, it measures the spectrum and yield averaged just over the transverse area of the foil sandwich. As long as, e.g., a material activation sample has the same dimensions and position, it will be exposed to the same neutron field. This was

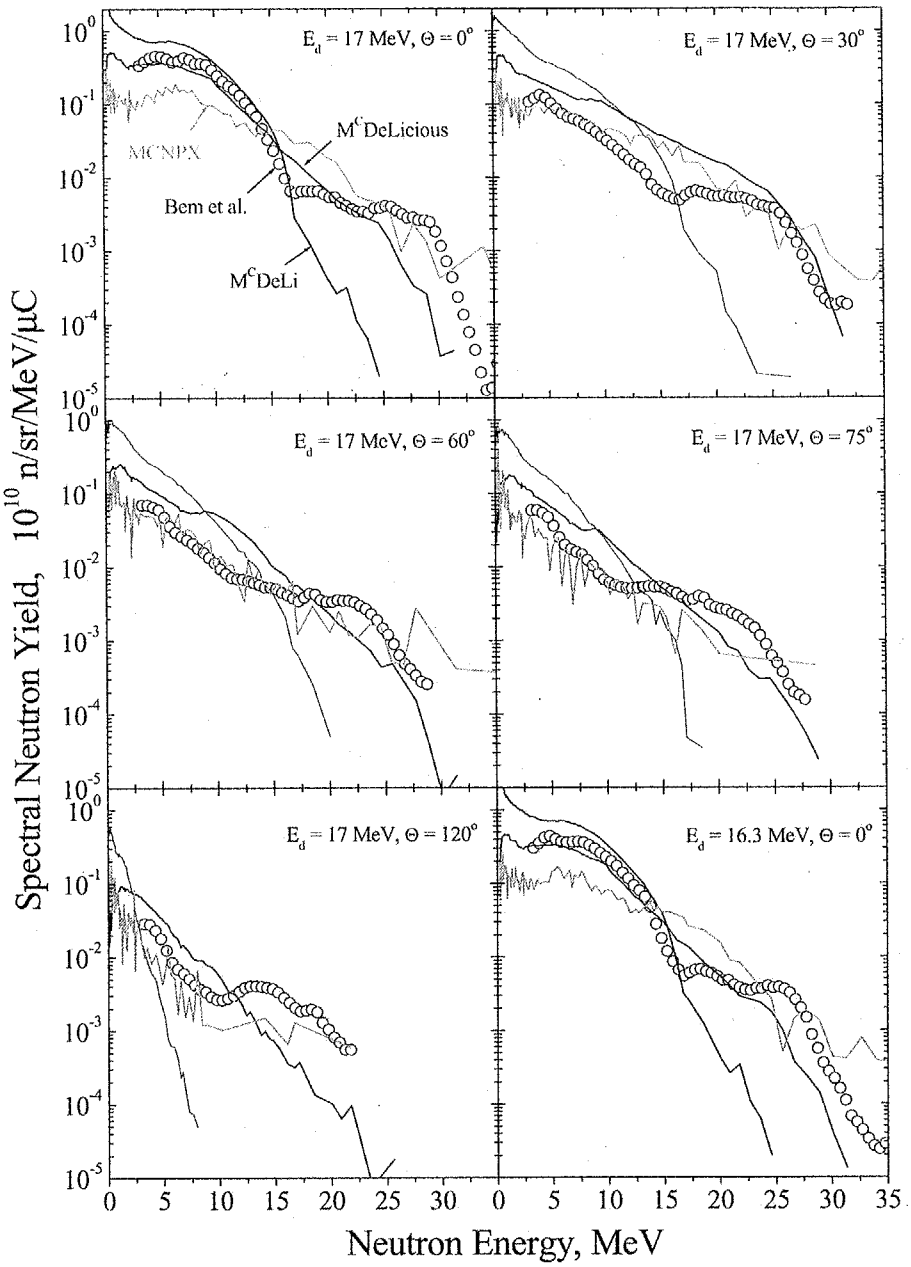


Fig. 4 Angle-dependent neutron yield spectra at 17.0 MeV and zero-degree yield spectra at 16.32 MeV compared to the M^CDeLicious, M^CDeLi and MCNPX calculations.

important in the present case, because such neutron-induced activation tests were made within the same experiment (see Task TF54-EU).

Foil sandwiches were arranged at the lithium target in two different positions, denoted Centre and Side [8, 9]. Both of the positions were on the outside of the 1.1 mm thick downstream wall of the steel container holding the lithium. The Centre position covered a 5 mm by 5 mm square region around the forward direction of the incident deuteron beam, while the Side position was shifted from that axis laterally by 7 mm. The positions are thus similar to positions immediately at the IFMIF target backplate; however, in contrast to IFMIF, the deuteron beam spot in the present experiment was very small, roughly circular with about 2.5 mm diameter, i.e., smaller than the foil areas.

As the upstream container wall had to be penetrated by the deuteron beam, an extra measurement with an empty container was made to estimate the neutron yield from this steel wall. Applying a corresponding correction to the gross yield, we obtain for the neutron yield from an open-surface thick

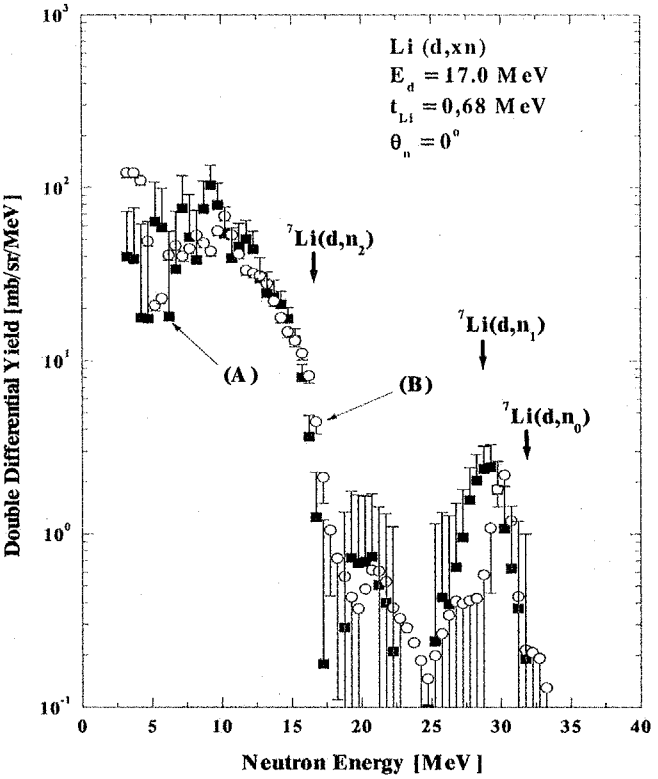


Fig. 5 Zero-degree double-differential yields for the Li(d,xn) reaction at 17 MeV obtained from the difference of yield spectra measured at 17 and 16.32 MeV.
(A) - difference of neutron spectra, (B) - unfolded difference of pulse-shape spectra.

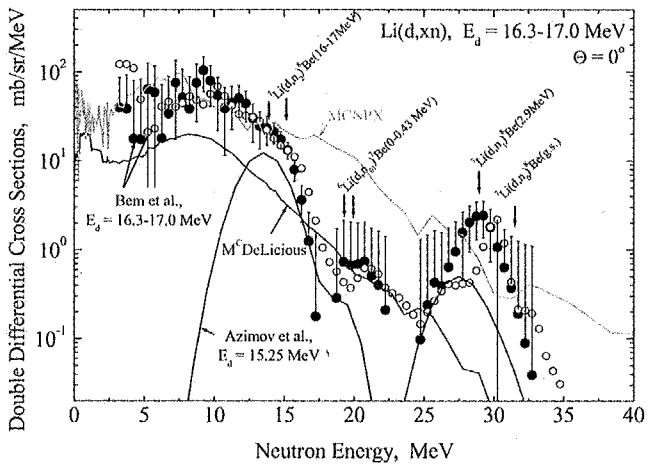


Fig. 6 Zero-degree double-differential yield for the Li(d,xn) reaction at 17.0 MeV. Comparison of present results with the cross section data of ^{7}Li(d,n)^{8}Be reacton at 15 MeV (Azimov) and MCNPX and McDeLiCious calculations.

lithium target (as in IFMIF) irradiated by 40 MeV deuterons 1.26×10^{11} n cm^{-2}s^{-1}μA^{-1} ± 12% in the Centre position and 2.61×10^{10} n cm^{-2}s^{-1}μA^{-1} ± 12% in the Side position. The quantity interesting for IFMIF analyses, the total specific neutron yield integrated over all emission directions, in neutrons per microampere or neutrons per deuteron can be inferred by fitting suitable model calculations to these integral values.

The spectra measured in the two positions are shown in Fig 7. The uncertainty of either spec-

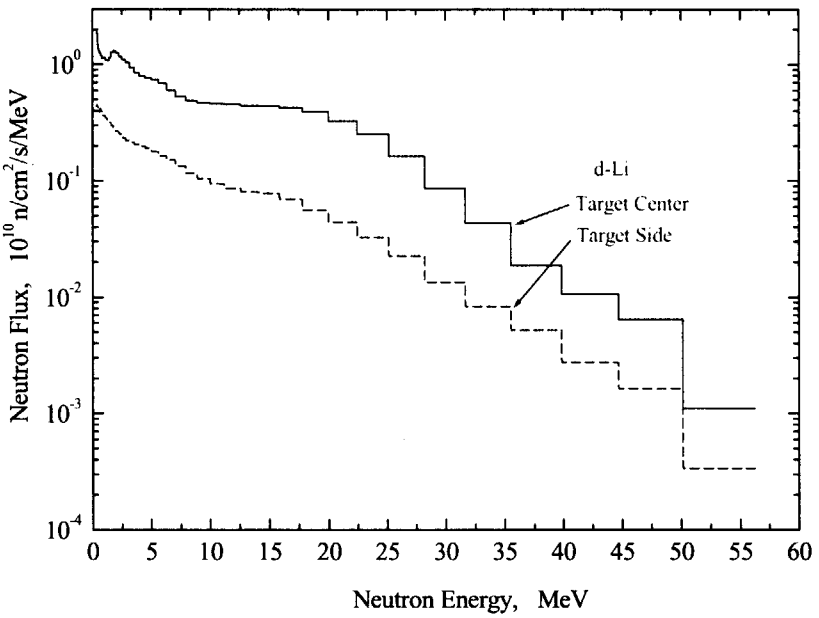


Fig. 7 D-Li neutron spectra measured in the 'Centre' and 'Side' positions of the FZK cyclotron experiment (40 MeV deuteron energy).

trum, referred to calculations of threshold neutron reaction rates, is estimated at ±10% [9].

The same experiment was exploited to determine, after the irradiations, the quantities of tritium and beryllium-7 produced in the lithium target. These are the only radionuclides with half lives longer than a few seconds that can originate from 40 MeV deuterons and pure lithium (neglecting a very small yield of beryllium-10, a beta ray emitter of 1.6×10^6 year half life). Note that the preliminary results reported earlier [10] are superseded by the new, higher ones given below.

The tritium was measured by releasing it from the target at several hundred °C within a quartz tube through which a gas stream of 95% Ar + 5% H_2 was flowing at 50 ml/min. The gas was subsequently oxidized in passing through a CuO bed. The resulting H_2O+HTO gas was absorbed in a molecular sieve. The molecular sieve was periodically changed and eluted with water. This water was then analyzed for tritium in an automated liquid scintillation system (Beckman Instruments LS 6000TA). The result, after correcting for decay and for the neutron background produced in the steel target wall, is 2.78 ± 7% tritons per 100 deuterons incident on the lithium which corresponds to 6.85 g ± 7% tritium per IFMIF full power year. If all the tritium were produced by D+Li-7 reactions, the effective production cross section per Li-7 atom averaged over deuteron energy (0...40 MeV) would be 297 mb ± 7%.

The Be-7 yield was determined by measuring (after a suitable cooling time, but prior to destroying the target for the tritium measurement) the 478 keV γ ray line from the irradiated target with a γ spectrometer. Experimental details are again found in Ref.[8]. After applying corrections for deuteron loss in the steel target wall as well as gamma ray absorption in the steel wall and in the lithium, the result for the Be-7 yield is 0.322 ± 12% Be-7 atoms per 100 deuterons incident on the lithium, corresponding to 1.85 g ± 12% Be-7 per IFMIF full power year. If all the Be-7 were produced by the ^{6}Li(d,n)^{7}Be reaction, the effective production cross section per Li-6 atom averaged over deuteron energy (0...40 MeV) would be 426 mb ± 12%.

References

[1] S. P. Simakov, U. Fischer, V. Heinzel, U. v. Moellendorff, International Fusion Material Irradiation Facility (IFMIF): Neutron Source Term Simulation and Neutronics Analyses of the High Flux Test Module, Forschungszentrum Karlsruhe report FZKA 6743 (2002).

[2] S.A.Azimov et al., Nucl. Phys. (USSR), **22**(1975)225.

[3] S.P. Simakov, U. Fischer, U. von Moellendorff, I. Schmuck, A.Yu. Konobeev, Yu. A. Korovin, P. Pereslavtsev, Advanced Monte Carlo Procedure for the D-Li Neutron Source Term Based on Evaluated Cross Sections Files, 10th Int. Conf. on Fusion Reactor Materials (ICFRM-10), Baden-Baden, 14-19 Oct. 2001.
[4] P. Bém et al., Proc 9th International Seminar on Interaction of Neutrons with Nuclei: "Neutron Spectroscopy, Nuclear Structure, Related Topics", 23-26 May 2001, JINR Dubna, pp. 465-472.
[5] M. Matzke, "Unfolding of Pulse Height Spectra: The HEPRO Program System", Report PTB-N-19, ISSN 0936-0492, ISBN 3-89429-543-0, Phys.-Techn. Bundesanstalt, Braunschweig, 1994.
[6] S. Meigo, Nucl. Instr. and Meth. **A 401** (1997) 365 and private communication.
[7] M. Tichy, H. Klein and J. Pulpan, "Calibration of an NE-213 Scintillator", Report PTB-7.2-92-1, Braunschweig, 1992.
[8] U. von Moellendorff, F. Maekawa, H. Giese and H. Feuerstein, A Nuclear Simulation Experiment for the International Fusion Materials Irradiation Facility (IFMIF), Forschungszentrum Karlsruhe report FZKA 6764 (2002).
[9] F. Maekawa, U. von Moellendorff, M. Wada, P. P. H. Wilson and Y. Ikeda, Determination of neutron spectra formed by 40-MeV deuteron bombardment of a lithium target with multi-foil activation technique, Fus. Eng. Des. **51-52** (2000) 815-820.
[10] A. Moeslang (ed.), International Fusion Materials Irradiation Facility Conceptual Design Evaluation Report, Forschungszentrum Karlsruhe report FZKA 6199 (1999).

3.3.16 TF53-JA : Reliability Study of the Activation Cross Section Library

(1) Brief Task Description

The reliability of the available cross-section data for the neutron-induced activation reactions relevant to IFMIF, especially the Test Cell equipment and shielding wall, is examined. The existing data libraries containing the cross-section data in the region of 20 to 60 MeV are surveyed and compared with the available experimental information. Recommendations for improvement of the data set are derived to enhance the reliability level of calculations of the production of radioactivity and nuclear heating in IFMIF.

Contributor

Name	Party	Institute	E-mail address
M. Sugimoto	Japan	JAERI	sugimoto@ifmif.tokai.jaeri.go.jp

(2) Introduction

Activation of the test cell equipment and shielding wall is a primary concern for maintenance of IFMIF, to protect the maintenance equipment from the radiation and contamination by radioactive materials. To evaluate this activity, the neutron induced reaction data up to ~60 MeV is needed and its reliability is important in designing the equipment, especially including devices sensitive to radiation damage. The evaluated neutron data up to 20 MeV are well covered in the existing libraries. The reliability of these libraries generally meets the requirement and is not considered in this study. The available data in the higher energy region are limited to a few libraries: IEAF-2001 [1], ACSELAM [2], REAC*3 [3] and ENDF/B VI [4], and most of these evaluated data (except for REAC*3 in the range of 20 – 60 MeV) were generated by various versions of the ALICE code [5]. This may cause similar results without changing the sensitive input parameters or applying normalization factors. Comparison among the available evaluations is made for several typical reactions to first clarify the level of agreement. The elements include Li, C, O, and Fe, which have primary importance in the Test Cell area. The required accuracy of the cross sections is around 30%, so that the cross sections to produce the activation of these elements are considered in this study.

(3) Cross Sections for Selected Isotopes

(a) Li-7

The important radioisotope produced by ^{7}Li+n reactions is tritium and the production cross sections are normally investigated through an α-production channel (^{7}Li(n,nα)^{3}H) up to 20 MeV. The available data libraries and the experimental data are compared in Fig. 1. In the energy region 15 – 60 MeV, the difference between the general library (ENDF/B and JENDL) and the activation libraries (REAC3 and IEAF-2001[1]) is found and the uncertainty of the cross sections above 20 MeV is greater than 50%.

(b) C-12

The neutron induced activation reactions for ^{12}C have threshold energies higher than 20 MeV and no data are given in the usual general libraries. The reaction ^{12}C(n,2n) ^{11}C is the most probable channel below 60 MeV, with ~20 mb maximum cross section (Fig.2). The activation libraries employ the higher cross sections at all range and the difference is a factor of 2 or more. The other two reaction channels, ^{12}C(n,x) ^{3}H and ^{12}C(n,x) ^{7}Be, have smaller cross sections, estimated as < 10 mb at the maximum values. The activation libraries give very large cross sections for tritium production with scattered results of the excitation, and the difference reaches an order of magnitude for the extreme case (Fig. 3). On the other hand, the data for ^{7}Be production are very similar (Fig. 4).

---

[1] The data given in the file have constant cross sections above 8 MeV and the correct excitation curve might be similar to the result of REAC3.

(c) O-16

Two reactions that produce ^{3}H and ^{14}C are important for the (n,^{16}O) interactions in the IFMIF environment. In Fig.5 the data libraries and the experimental data are compared and a large difference is seen among them. The tritium production cross sections of the carbon and nitrogen at the maximum are ~10 and ~20 mb, respectively, and two experimental results support this trend. For ^{14}C production, the similar situation can be seen in Fig. 6; however, the cross sections are smaller than for the tritium production by about a factor of 5.

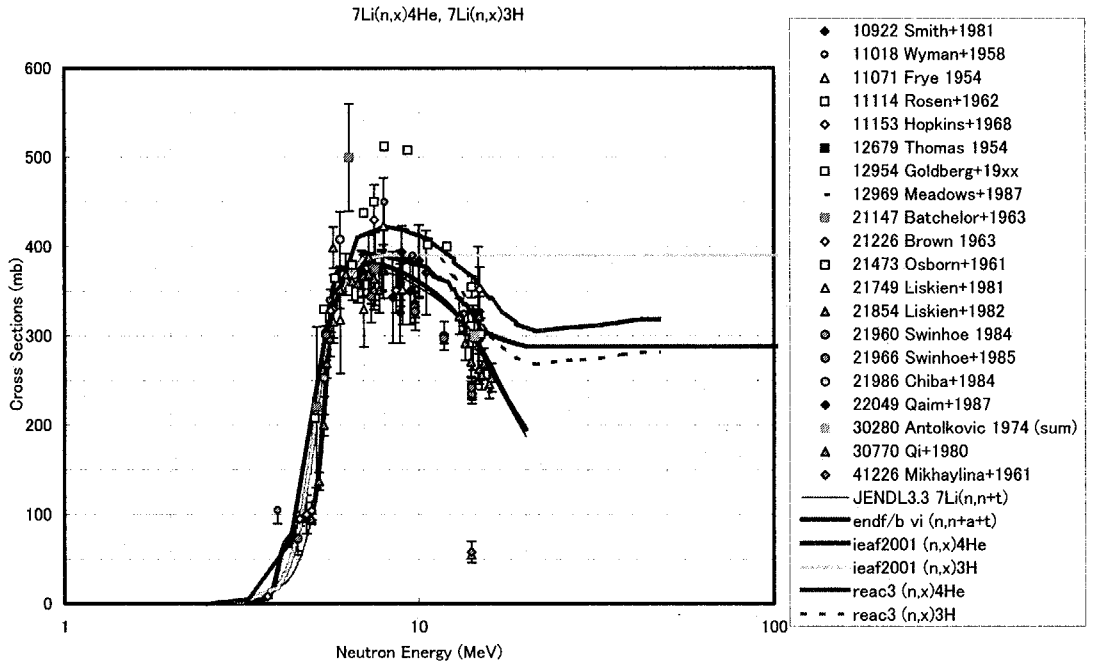


Fig. 1 Comparison among the data libraries for ^{3}H production by n+^{7}Li.

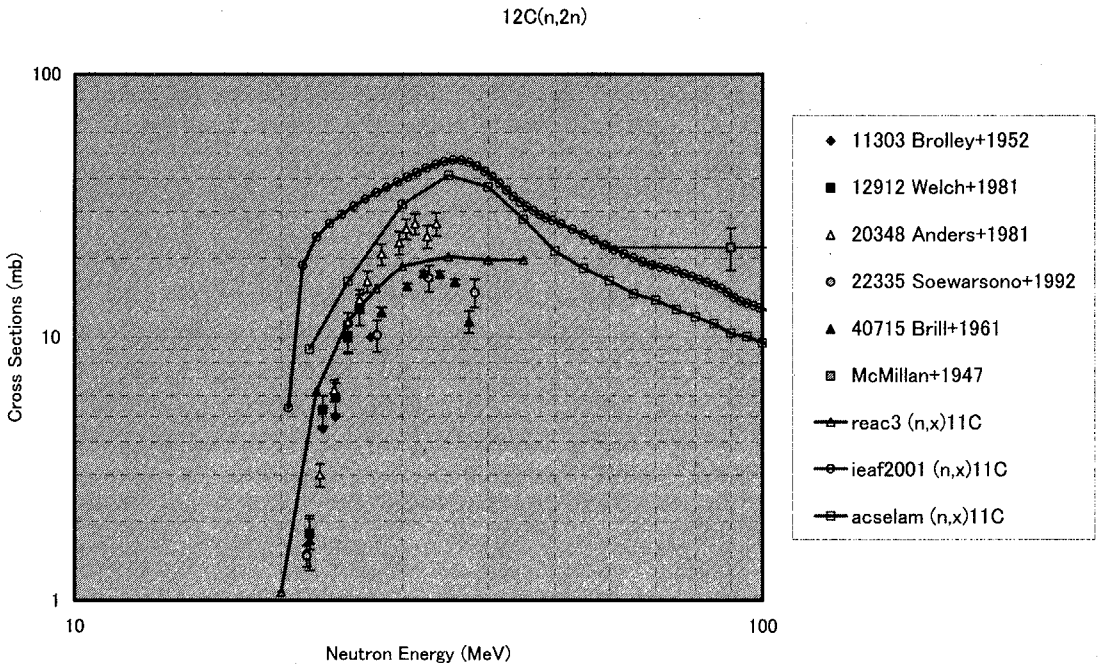


Fig. 2 Comparison among the data libraries for ^{11}C production by n+^{12}C.

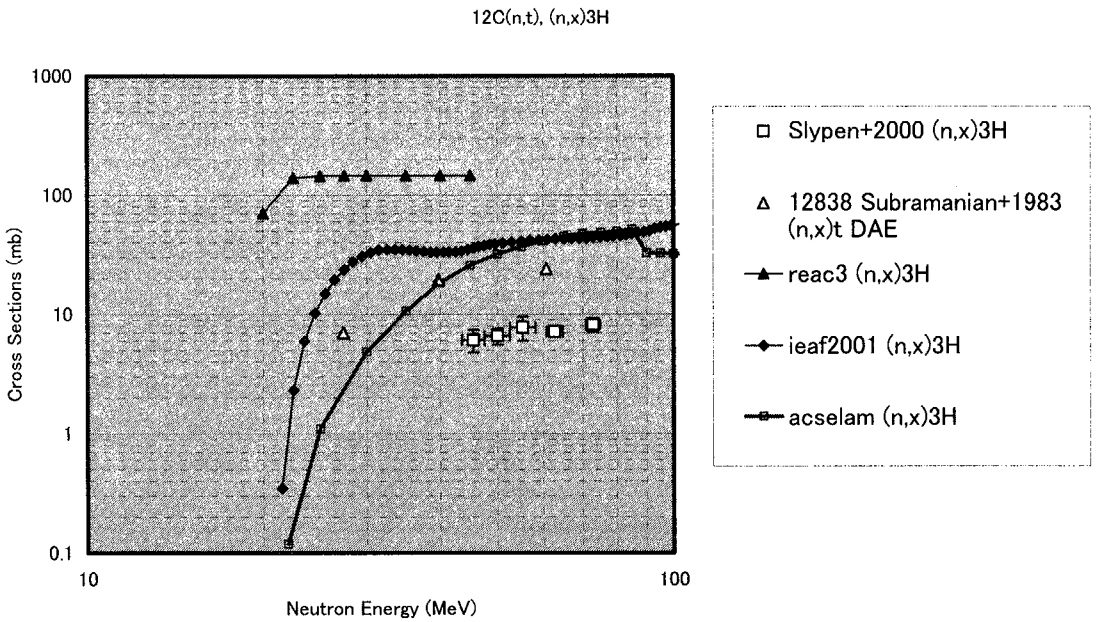


Fig. 3 Comparison among the data libraries for ^{3}H production by n+^{12}C.

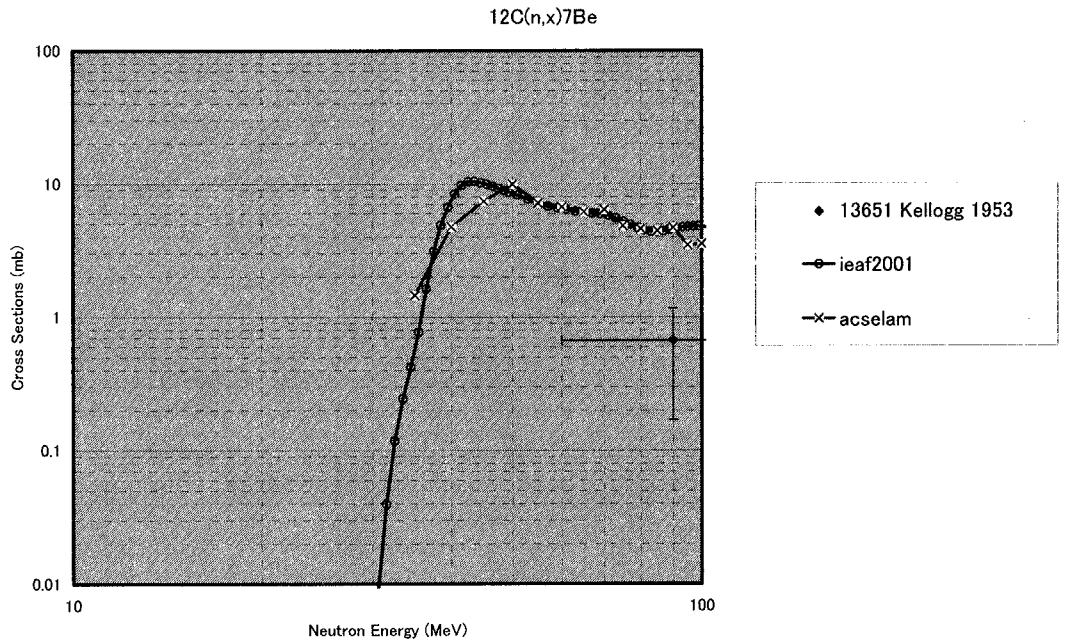


Fig. 4 Comparison among the data libraries for ^{7}Be production by n+^{12}C.

(d)Fe-56

The production of two important radioisotopes, ^{3}H and ^{54}Mn, are correlated if the majority of them originate from the $^{56}Fe(n,t)^{54}Mn$ reaction channel. As shown in Fig. 7, this is true up to ~20 MeV where the multi-particle emission channels, (n,nd) and (n,2np) open. The tritium production of REAC*3 library is too high at the higher neutron energy region, ~40 MeV, and is not consistent with the other libraries. For the ACSELAM library, the cross sections below 20 MeV are too low to reproduce the experimental data. The result is that the IEAF-2001 library is the most reliable up to 60 MeV. For the ^{54}Mn production three libraries are relatively consistent, though the magnitudes are different by about a

factor of 6 at the maximum (~40 MeV).

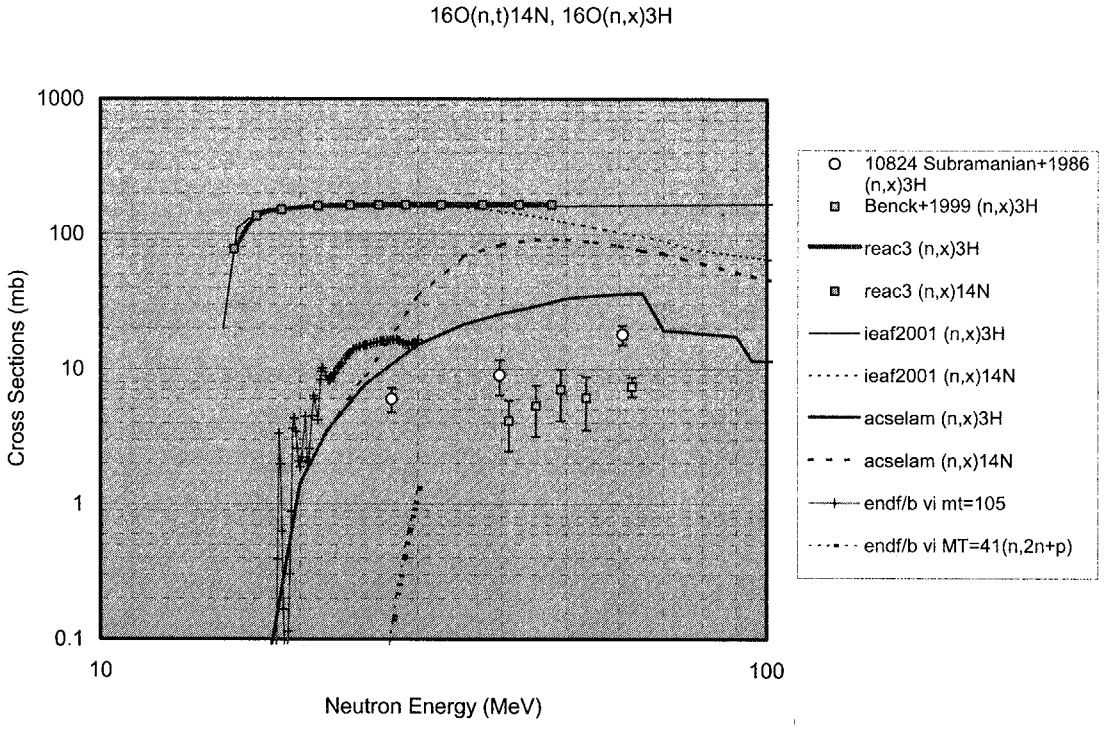


Fig. 5 Comparison among the data libraries for ^{3}H production by n+^{16}O.

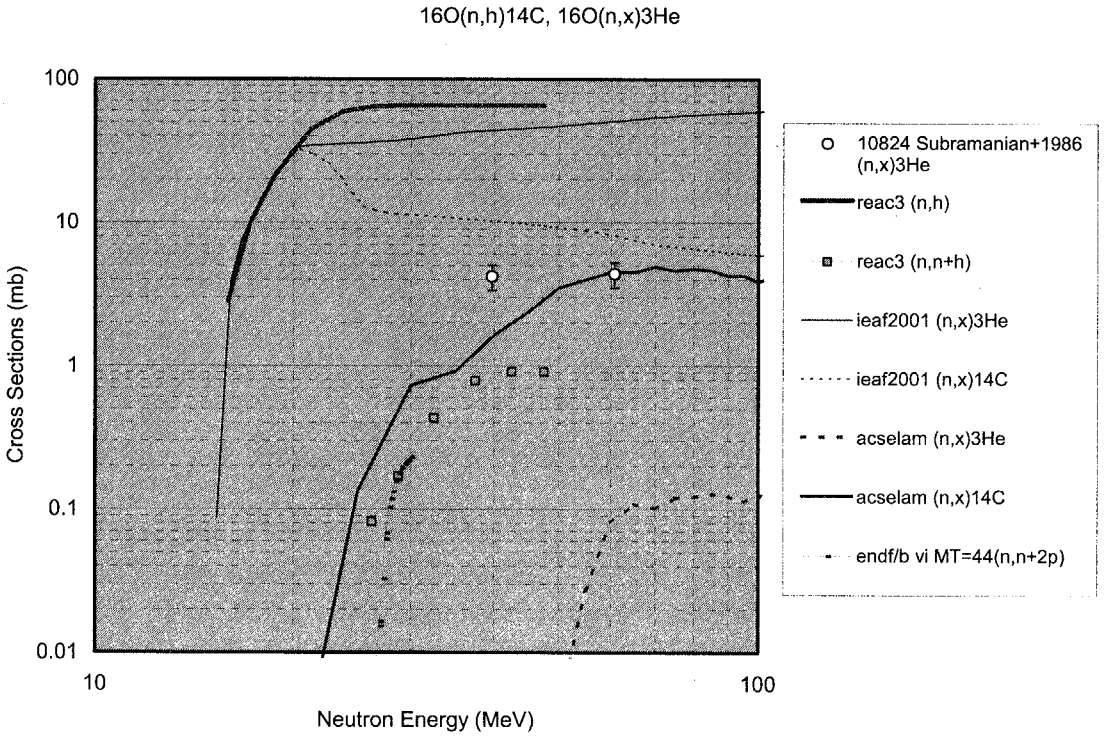


Fig. 6 Comparison among the data libraries for ^{14}C production by n+^{16}O.

(4) Recommendations for Improving Reliability

After the publication of the IEAF-2001 library, the completeness of the cross-section data set is much improved and the overall accuracy of the estimations, such as of the summary dose, meets the requirements for standard cases. However, this comparative survey of a small number of isotopes, which were selected from the list of important neutron induced radioisotopes produced in the IFMIF environment, indicates that inconsistencies can be found among the libraries and the experimental data. Improvement in the reliability can be achieved by the following scheme:

(a) Accumulate additional experimental data focused on the 20 – 60 MeV region, which may not require using monoenergetic neutron sources because most of the reactions considered have a threshold energy of around 10 MeV; (e.g. use activation stack foil experiments with a ^{9}Be(d,n) source at various incident deuteron energies)

(b) Review the systematic rules used to fill the incomplete region where no experimental data are available; (the rules for the different reaction channels should be consistent)

(c) Apply the theoretical calculations with different approaches to the same reaction channel to avoid methodical biasing.

It is also recommended to produce a thorough compilation of all data and evaluations, for independent review that will qualify the results.

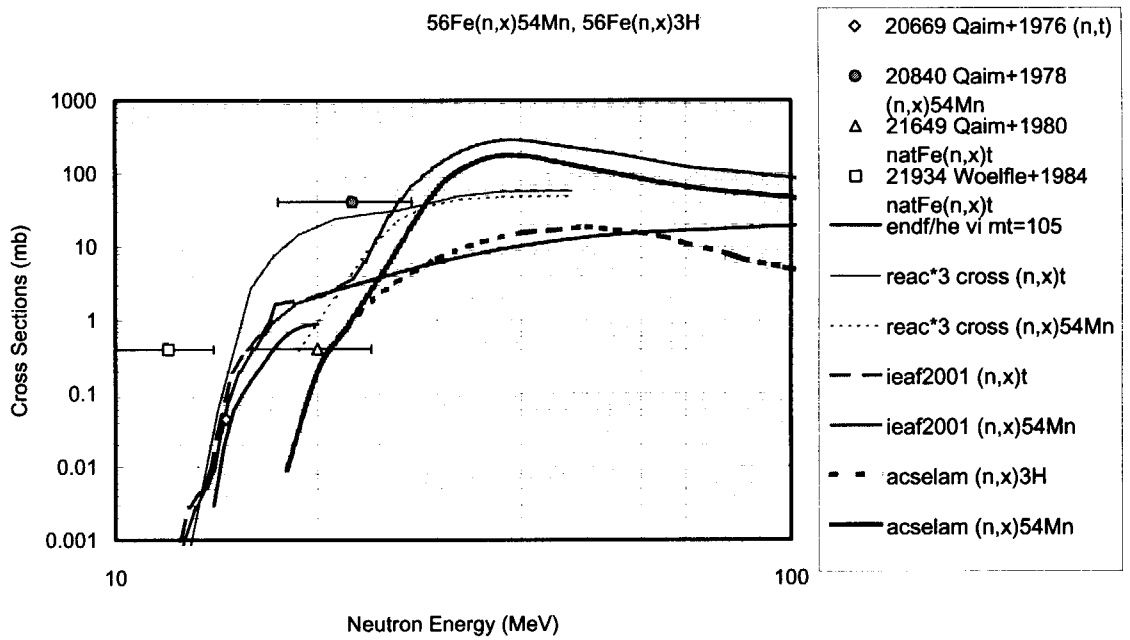


Fig. 7 Comparison among the data libraries for ^{54}Mn and ^{3}H production by n+^{56}Fe.

(5) Conclusion

The activation cross sections for neutron energies above 20 MeV were gradually completed to the level that no critical data are lacking to perform dose or heating estimates. The consistency among the available library data was checked for several radioisotopes important in IFMIF, and the consistency is not yet satisfactory. It is recommended that work in the next phase verify and revise the data set, including the accumulation of additional experimental data and review of the evaluation processes.

References

[1] Yu. Korovin, A. Konobeyev, P. Pereslavtsev, U. Fischer, U.v. Möllendorff, "Intermediate Energy Activation File IEAF 2001", Int. Conf. Nuclear Data for Science and Technology (ND2001), October 7-12, 2001, Tsukuba, Japan. (http://www.nea.fr/abs/html/nea-1656.html)

[2] N. Yamano, M. Fukuda, S. Tanaka, "Isotope production cross section library for use of transmutation calculation in the IRAC code system for the TIARA facility", ICRS-9: 9th Int. Conf. On Radiation Shielding, Oct. 17-22, 1999, Tsukuba, Japan.

[3] F.M. Mann, D.E. Lessor, "REAC*3 Nuclear Data Libraries", Proc. for Int. Conf. on Nuclear Data for Science and Technology, Jülich, Germany (May 1991). (http://www.nea.fr/abs/html/ccc-0443.html)

[4] V. McLane (Ed.), "ENDF-102 Data Formats and Procedures for the Evaluated Nuclear Data File ENDF-6", BNL-NCS-44945, July 1990. (http://www.nndc.bnl.gov/nndcscr/documents/endf/endf102/).

[5] M. Blann, "Recent progress and current status of preequilibrium reaction theories and computer code ALICE", SMR/284-1, ITCP Workshop on applied Nuclear Theory and Nuclear Model Calculations for Nuclear Technology Applications held in Trieste, Italy (February-March, 1988).

3.3.17 TF54-EU : Evaluation of Neutron Cross-section Data in the 20-50 MeV Range; Intermediate Energy Activation File

(1) Brief Task Description

The objective of Task TF54-EU is to provide nuclear cross-section data required for neutron transport and activation calculations of IFMIF. Neutron cross-section data must be available over the whole energy range of IFMIF which extends up to about 55 MeV neutron energy. In particular there is a need for neutron cross sections above 20 MeV which is the upper energy limit of the standard nuclear data libraries.

The focus of the evaluation effort during the KEP was on the generation of a complete activation data library, the Intermediate Energy Activation File 2001 (IEAF-2001), and the preparation of general purpose neutron cross-section data files for the light mass nuclides ^{6,7}Li and ^{9}Be for use in Monte Carlo transport calculations.

Contributors

Name	Party	Institute	E-mail address
U. Fischer	EU	FZK	ulrich.fischer@irs.fzk.de
S. Simakov	EU	FZK	simakov@irs.fzk.de
Yu. A. Korovin	EU	INPE	korovin@iate.obninsk.ru
A. Yu. Konobeyev	EU	INPE	
P. E. Pereslavtsev	EU	INPE/FZK	pereslavtsev@irs.fzk.de
U. v. Moellendorff	EU	FZK	moellendorff@irs.fzk.de
P. P. H. Wilson	EU	UW/FZK	wilsonp@engr.wisc.edu

(2) Background

Nuclear cross-section data must be provided over the whole neutron energy range of IFMIF, from 55 MeV down to thermal neutron energy. Such data must be evaluated for a variety of nuclides important for neutron transport calculations. They must include all data types and reactions which are required to calculate the important nuclear responses. For activation calculations, a full set of data for all potential target nuclides must be available. To allow the preparation of working libraries for use with state-of-the-art transport and activation codes, complete data sets must be prepared in accordance with standard nuclear data format rules.

During CDA and CDE general purpose cross-section data files were prepared for selected important nuclides, including ^{1}H, ^{56}Fe, ^{23}Na, ^{39}K, ^{28}Si, ^{12}C, ^{52}Cr, ^{51}V, up to 50 MeV incident neutron energy to enable Monte Carlo transport calculations for IFMIF [1,2]. Other important general purpose data files for isotopes including ^{16}O, ^{14}N, ^{27}Al, ^{28,29,30}Si, ^{31}P, ^{40}Ca, ^{50,52,53,54}Cr, $^{54,56,\ 57,58}$Fe, ^{58,60,61,62,64}Ni, ^{63,65}Cu, ^{93}Nb, ^{182,183,184,186} W were adopted from the LANL-evaluation of 150 MeV cross-sections [3] and were processed with the ACER module of the NJOY code [4] for use with McDeLi/McDeLicious Monte Carlo calculations.

A major task for KEP was (1) to provide general purpose neutron cross-section data files for the light mass nuclides ^{6,7}Li and ^{9}Be, to enable neutronic calculations for the medium flux test module, and (2) to prepare an activation data library to enable activation and decay heat calculations for the test modules.

(3) Evaluation of n + ^{6,7}Li and n + ^{9}Be Cross-section Data

By making use of the methodological approach developed for the evaluation of the D + ^{6,7}Li reaction system [5], general purpose cross-section data files have been prepared for the n + ^{6,7}Li and the n + ^{9}Be reactions according to standard ENDF-6 format rules. The upper energy limit has been increased to 150 MeV to permit the utilization of these data files for other high energy applications. The n + ^{6,7}Li data files were processed with NJOY/ACER for use in Monte Carlo transport calculations. They are being applied to neutronics calculations of the Medium Flux Test Module with the McDeLi/ McDeLicious code (Task TF23-EU).

(4) Intermediate Energy Activation File (IEAF-2001)

Activation calculations for the IFMIF D-Li neutron source require (i) a complete activation data library containing all target nuclides that may be present in the materials to be irradiated and taking into account all activation and transmutation reactions that may occur over the whole neutron energy range from 55 MeV down to thermal energy, and, (ii) an activation code capable of handling the many open reaction channels. Substantial effort has been devoted over the KEP period to preparing a complete activation data library for intermediate energy applications. The Intermediate Energy Activation File IEAF-2001 has been developed as a collaboration of Forschungszentrum Karlsruhe and the Institute of Nuclear Power Engineering, Obninsk, as part of KEP Task TF-54EU [6]. The activation code "*ALARA* (Analytical and Laplacian Adaptive Radioactivity Analysis)", previously developed at the University of Wisconsin-Madison as an advanced computational tool for simulating induced activation in nuclear facilities [7], has the ability to handle the IEAF-2001 activation cross-section data in a straightforward way.

The IEAF-2001 library includes 679 target nuclides from Z=1 (hydrogen) to 84 (polonium) with neutron induced reaction reactions from 10^{-5} eV to 150 MeV incident neutron energy. The total number of reaction channels with activation cross-section data is 134,431. The European Activation File EAF-99 [8] served as the basis for the activation cross-section data below 20 MeV neutron energy. Threshold reaction cross-sections were evaluated on the basis of geometry dependent hybrid exciton and evaporation models taking into account the pre-equilibrium emission of clusters (d, t, ^{3}He, α) and γ-rays. A new computational approach based on diffraction theory and a modified intra-nuclear cascade model was employed to evaluate the cross-sections for the light nuclei up to Z = 12 [5].

The IEAF-2001 data library has been prepared in standard ENDF-6 data format making use of the MT=5 (neutron, anything) option with the excitation functions stored in file section MF=3 and the product nuclide vectors in MF=6. A 256 group GENDF-formatted (groupwise ENDF) working library has been generated with the GROUPR-module of NJOY. IEAF-2001 was made available on CD-ROM to the NEA data bank, Paris, and to RSICC, Oak Ridge, for further dissemination [9]. The IEAF-2001 CD-ROM contains both the pointwise (ENDF) and the groupwise (GENDF) data files for use with any activation code capable of handling an arbitrary number of reaction channels; codes such as "*ALARA*".

(5) Testing and Validation of IEAF-2001 Activation Data

Testing and validation of the IEAF-2001 data library is mandatory to ensure reliable results of the activation calculations. First application tests have been performed to demonstrate its applicability and suitability for IFMIF activation analyses [10]. Table 1 shows the afterheat and activity calculated for the high flux test module (made of the low activation steel Eurofer) after an irradiation of 5 full power years.

Table 1 Total afterheat power and activity inventory of the IFMIF high flux test module (HFTM).

Cooling Time	shutdown	1 h	1 d	30 d	1 y	5 y	10 y	100 y	1000 y
Activity[10^{14} Bq]	22	20	16	15	10	3.3	0.94	$2.8\ 10^{-4}$	$7.2\ 10^{-6}$
Afterheat power[W]	244	172	51	41	19	1.0	0.10	$7.1\ 10^{-5}$	$4.6\ 10^{-6}$

Recently, detailed IEAF-2001 validation analyses were started on the basis of activation calculations with the "*ALARA*" code [11]. The validation procedure comprised several steps, including various benchmark calculations and computational analyses of integral activation experiments. In the first step, ALARA activation calculations for the low activation steel Eurofer were benchmarked against activation calculations with the "*FISPACT*" code [12]. Since "*FISPACT*" is not capable of using IEAF-2001 cross-section data, an irradiation in the first wall neutron spectrum of a fusion DEMO reactor was considered so as to enable the use of the European Activation File EAF-99 with "*FISPACT*". The same EAF-99 data have been adopted in the IEAF-2001 library for the energy range below 20 MeV. Satisfactory agreement was found for the calculated activity inventories, the decay heat production and the contact dose rate (Fig. 1). Thus there is consistency between "*ALARA*"/IEAF-2001 and

"*FISPACT*"/EAF-99 activation calculations for the energy range below 20 MeV.

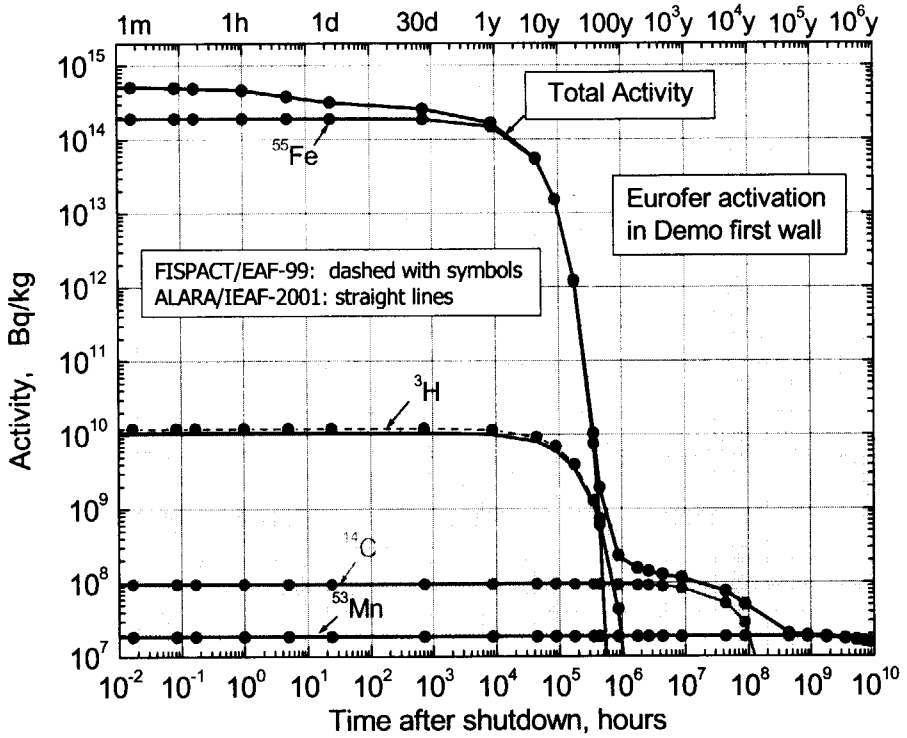


Fig. 1 Eurofer irradiation in the DEMO reactor first wall: Comparison of the activity inventories calculated with ALARA/IEAF-2001 and FISPACT/EAF-99.

The second step was devoted to the testing of the IEAF-2001 data against an integral activation experiment performed previously at FZK [13,14]. Samples of SS-316 steel, F82H steel, pure vanadium, and V-4Ti-4Cr alloy were activated in an IFMIF-like neutron field produced by a 40-MeV deuteron beam on a thick lithium target. The samples were irradiated for 2 hours with a neutron flux density between 4.10 and 4.27 × 10^{11} n cm^{-2} s^{-1}, depending on the sample. Gamma spectrometry was performed on each of the samples after 6 to 7 different cooling time intervals, ranging from 1 hour to 150 days. As an example, the results of the activation analyses for pure

Table 2 C/E (calculation/experiment) ratios for the radioactivity induced by irradiating vanadium in a white D-Li neutron source. There are included the half-lives $T_{1/2}$ and the dominant reaction pathways with the associated reaction thresholds E_{thr}.

Nuclide ($T_{1/2}$)	C/E	Dominant Pathways (E_{thr})
^{47}Ca (4.5 d)	0.81 ± 0.22	^{51}V(n,pα) ≈ 100% (11.7 MeV)
^{46}Sc (84 d)	0.77 ± 0.04	^{51}V(n,2nα) = 97.8% (21.3 MeV)
^{47}Sc (3.4 d)	0.17 ± 0.01	^{51}V(n,nα) ≈ 99.6% (10.5 MeV)
^{48}Sc (44 d)	1.07 ± 0.06	^{51}V(n,α) ≈ 99.7% (2.1 MeV)
^{48}V (16 d)	1.07 ± 0.24	^{51}V(n,4n) ≈ 93.3% (32.6 MeV) ^{50}V(n,3n) ≈ 6.7% (21.3 MeV)
^{51}Cr (28 d)	(0.41 ± 0.04)10^{-3}	^{54}Fe(n,α) ≈ 68.4% (0 MeV) ^{56}Fe(n,2nα) ≈ 31.6% (20.0 MeV)
^{92m}Nb (28 d)	1.32 ± 0.36	^{93}Nb(n,2n) ≈ 94.6% (8.9 MeV) ^{92}Mo(n,p) ≈ 4.9% (0 MeV)

vanadium are shown in Table 2. Satisfactory agreement between the "*ALARA*"/IEAF-2001 activity results and the experiment was found for all product nuclides except ^{47}Sc and ^{51}Cr. To resolve the ^{47}Sc discrepancy the ^{51}V(n,nα) reaction cross-section needs to be updated. For the ^{51}Cr, it was found that sequential charged particle reactions (SCPR) such as ^{51}V(n,xp) ⇒ ^{51}V(p,n)^{51}Cr play an important role in generating ^{51}Cr from ^{51}V. The "*ALARA*" code is presently not capable of handling the SCPR mechanism and needs to be updated to meet this need.

The third step of the IEAF-2001 data testing was devoted to comparative analyses of the activation and transmutation of Eurofer steel irradiated in the IFMIF high flux test module (HFTM) and in a fusion DEMO reactor first wall (FW). Fig. 2 shows the calculated activity inventories as a function of the decay time. It is noted that the D-Li and the D-T neutron irradiation fields produce the same radioactive nuclides. The activity is dominated by ^{55}Fe during the first year after irradiation, by ^{3}H in the time interval up to one century, and by ^{14}C and ^{53}Mn at longer times. The magnitude of the nuclide activities, however, is larger for the irradiation in IFMIF, in particular for tritium by two orders of magnitude. This is the result of the harder D-Li neutron spectrum and the high energy thresholds of many activation reactions such as the dominant tritium production reaction in iron (^{56}Fe(n,t)^{54}Mn with a reaction threshold of 12.1 MeV). The elemental transmutations induced in Eurofer steel during irradiation are compared in Fig. 3. It is noted that the transmutation of the main constituents of Eurofer, including iron and chromium, is not significant. The inventory of other elements such as Ti, V and Mn, however, increases by 5-20% per irradiation year in FW/DEMO and by 10-30% in HFTM/IFMIF. These elements are minor constituents of Eurofer and are produced during irradiation by (n,p) and (n,α) reactions of Cr and Fe, the main constituents of the steel. The large fraction of high energy neutrons in the IFMIF spectrum accounts for the higher transmutation rate of these elements in comparison with the D-T fusion spectrum. Similar reasons explain the different transmutation behaviour of elements such as B, Co, Ta, and W.

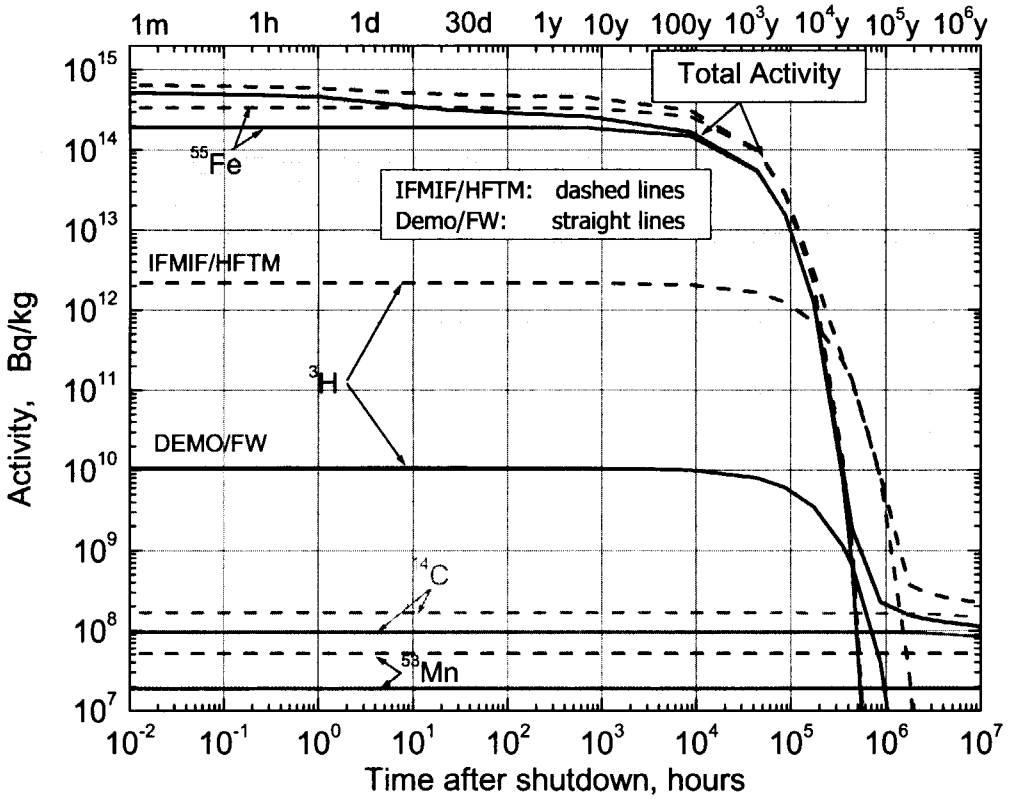


Fig. 2 Eurofer irradiation in the DEMO reactor first wall (FW) and the IFMIF high flux test module (HFTM): Comparison of activity inventories calculated with ALARA/IEAF-2001.

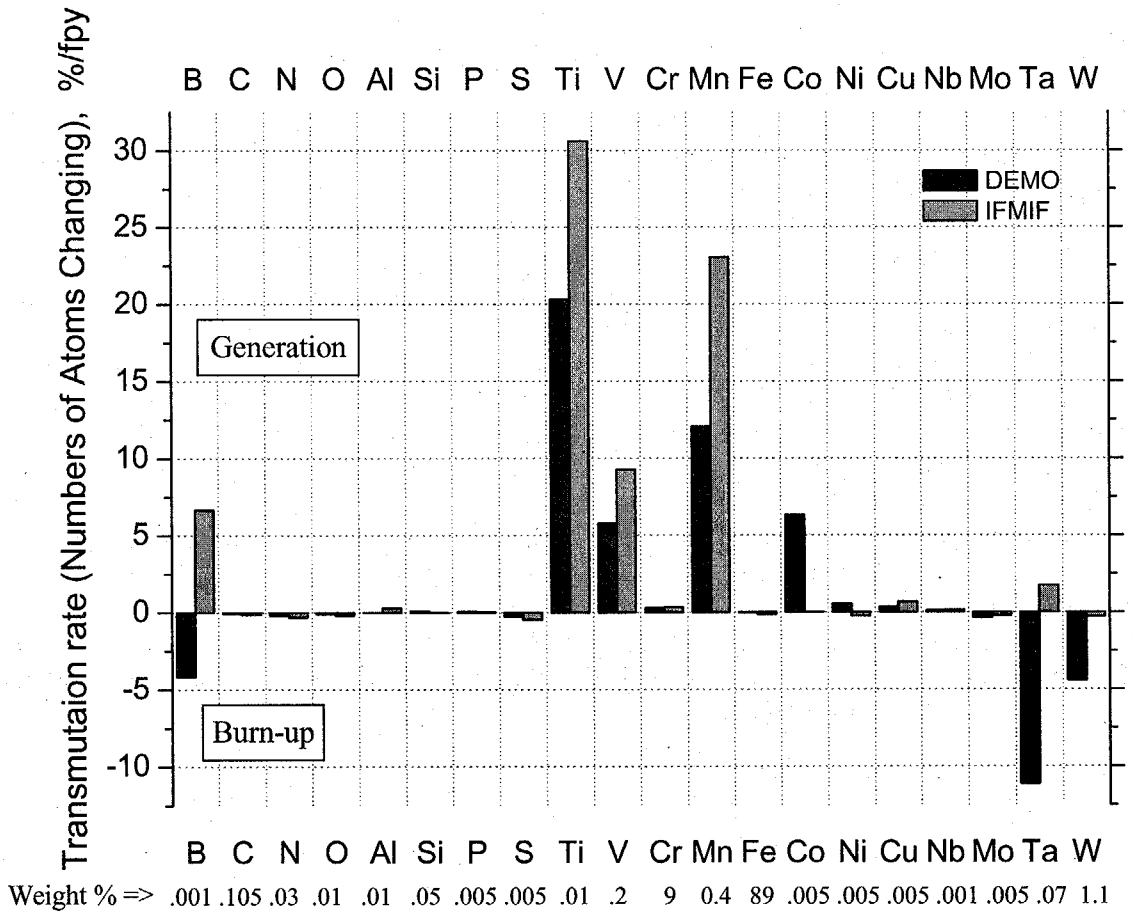


Fig. 3 Eurofer irradiation in the DEMO reactor first wall (FW) and the IFMIF high flux test module (HFTM): Comparison of transmutation rates calculated with ALARA/IEAF-2001.

References

[1] U. Fischer, P. Pereslavtsev, S. P. Simakov, Intermediate Energy Cross-Section Data for the IFMIF Neutron Source, Status Report, EFF-DOC-784, May 2001 (*available from the NEA Data Bank, Paris, at http://www.nea.fr/html/dbdata/ projects/effdoc.html*).

[2] U. Fischer, S. P. Simakov, A. Konobeyev, P. Pereslavtsev, P. Wilson , Neutronics and Nuclear Data for the IFMIF Neutron Source, 6th International Symposium on Fusion Nuclear Technology (ISFNT-6), San Diego, Calif., April 7-12, 2002.

[3] M.B. Chadwick, P.G. Young et al., Cross-Section Evaluations to 150 MeV for Accelerator-Driven Systems and Implementation in MCNPX, Nucl. Sci. Eng. 131 (1999), 293.

[4] R. E. MacFarlane: The NJOY Nuclear Data Processing System, Version 91, Los Alamos National Laboratory, Report LA-12740-M (1994).

[5] A. Yu. Konobeyev, Yu. A. Korovin, P. E. Pereslavtsev, U. Fischer and U. von Möllendorff, Development of methods for calculation of deuteron-lithium and neutron-lithium cross sections for energies up to 50 MeV, Nuclear Science and Enginering 139 (2001) 1-23.

[6] Yu. Korovin, A. Yu. Konobeev, P.E. Pereslavtsev, U. Fischer, U. v. Möllendorff, Intermediate Energy Activation File IEAF 2001, Int. Conf. Nuclear Data for Science and Technology (ND2001), October 7-12, 2001, Tsukuba, Japan.

[7] P. P. H. Wilson and D. L. Henderson, ALARA: Analytical and Laplacian Adaptive Radioactivity Analysis, Volume I, Technical Manual, University of Wisconsin, Report UWFDM 1080, January

1998.
[8] J.-Ch. Sublet, J. Kopecky and R. A. Forrest: The European Activation File: EAF-99 cross section library, UKAEA Fusion, Report UKAEA FUS 408, December 1998.
[9] U. Fischer, D. Leichtle, U. v. Möllendorff, I. Schmuck, A. Yu. Konobeyev, Yu. A. Korovin, P.E. Pereslavtsev, Intermediate Energy Activation File IEAF-2001, NEA data bank programme library, package NEA-1656/01 (2001), RSICC Oak Ridge, DLC-217/IEAF-2001 (2002).
[10] U. Fischer, P.P.H. Wilson, D. Leichtle, S.P. Simakov, U. von Möllendorff, A. Konobeev, Yu. Korovin, P. Pereslavtsev, I. Schmuck, Application of the IEAF-2001 Activation Data Library to Activation Analyses of the IFMIF High Flux Test Module. 10th Int. Conf. on Fusion Reactor Materials (ICFRM-10), Baden-Baden, 14-19 Oct. 2001.
[11] U. Fischer, S. Simakov, U. v. Möllendorff, P. Pereslavtsev, P. Wilson, Validation of activation calculations using the Intermediate Energy Activation File IEAF-2001, 22nd Symposium Fusion Technology (SOFT-22), Helsinki, September 9-13, 2002.
[12] R. A. Forrest and J.-Ch. Sublet, FISPACT 99: User Manual, UKAEA Fusion, Report UKAEA FUS 407, December 1998.
[13] U. von Möllendorff, F. Maekawa, H. Giese, P. Wilson, Experimental test of structural materials activation in the IFMIF neutron spectrum, Fusion Engineering and Design 51-52 (2000) 919-924.
[14] U. von Möllendorff, F. Maekawa, H. Giese and H. Feuerstein, A nuclear simulation experiment for the International Fusion Materials Irradiation Facility (IFMIF), Forschungszentrum Karlsruhe report, FZKA 6764, October 2002.

3.3.18 TF55-EU : Neutron Data above 20 MeV – Neutron Transport Benchmark Tests

(1) Brief Task Description

The evaluation of neutron cross-section data up to about 55 MeV neutron energy is performed as part of Task TF54-EU. Validation of the evaluated nuclear data is required to ensure they provide reliable results when applied in IFMIF neutronics design calculations. This can be achieved through integral experiments and their computational analyses.

The objective of Task TF55-EU is to provide the experimental data base for the validation of iron cross-section data used in neutron transport calculations for the IFMIF high flux test module. A suitable benchmark experiment has been conducted using a 20 cm thick iron slab at the Fast Neutron Facility of NPI Řež with an IFMIF-like white neutron source spectrum extending up to 35 MeV. The spectra of neutrons from both the bare source and transmitted through the iron slab were measured using the pulse height technique and analysed by means of neutron transport calculations with the MCNP-4C Monte Carlo code using iron cross-section data provided by Task T54-EU.

Contributors

Name	Party	Institute	E-mail address
P. Bém	EU	NPI	bem@ujf.cas.cz
V. Burjan	EU	NPI	
M. Götz	EU	NPI	
J. Novák	EU	NPI	
V. Kroha	EU	NPI	
E. Šimečková	EU	NPI	
J. Vincour	EU	NPI	
U. Fischer	EU	FZK	ulrich.fischer@irs.fzk.de
S. Simakov	EU	FZK	simakov@irs.fzk.de
U. v. Moellendorff	EU	FZK	moellendorff@irs.fzk.de

(2) Background

The IFMIF neutron source reaction D(40 MeV)+Li produces a white neutron spectrum which extends up to about 55 MeV. The evaluation of neutron cross-section data up to about 55 MeV neutron energy for neutron transport calculations is performed as part of Task TF54-EU. Validation of the evaluated nuclear data is required to ensure they provide reliable results when applied in IFMIF neutronics design calculations. In particular there is a need for validating the neutron cross-section data above 20 MeV where experimental data are scarce. Validation is achieved through integral experiments with a white IFMIF-like neutron source and computational analyses using the tools and data applied to IFMIF design calculations.

A suitable benchmark experiment on iron, the major constituent of the high flux test module, has been performed at the Fast Neutron Facility of NPI Řež using the NG1 target station (see TF52-EU, Fig. 1). The $D_2O(^3He,xn)$ reaction at 40 MeV incident energy was employed to produce an IFMIF-like white neutron source spectrum extending up to 35 MeV neutron energy.

Previously, high-yield emission of fast neutrons with a broad energy spectrum from the deuteron break-up reaction on ^3He target nuclei had been observed. The observed Gaussian spectral distribution of these neutrons was attributed to a mixture of final states of the neutron/proton and the target nucleus. Therefore, the same spectrum shape had to be expected for the inverse reaction $D(^3He, np)^3He$. On the basis of simple theoretical considerations, a mean energy of 15 MeV and a high energy tail extending up to about 35 MeV were estimated for the zero degree neutron yield in irradiation of a D target by a 40 MeV ^3He beam. A strongly forward-directed neutron emission had to be expected due to the higher mass of the projectile. These characteristics strongly favored the use of the $D_2O(^3He,xn)$ reaction for simulating the IFMIF source neutron spectrum. No experimental thick-target neutron yield data exist for this reaction so far. Thus the measurement of the $D_2O(^3He,xn)$ neutron yield spectra was required for later use in the computational analyses. Extensive calculations were performed at FZK to

assist in the design of the experiment.

(3) Experimental Arrangement

The benchmark measurements were performed on an external beam line of the variable energy cyclotron U-120M at the Nuclear Physics Institute Řež. The ^{3}He ion beam accelerated to 40 MeV was centered on the 40 μm molybdenum entrance foil. The heavy water (target) was contained in a 3 cm dia × 1 cm stainless steel chamber. The beam current on the target was kept below some tens of nA to minimize dead time corrections.

The neutron energy and angular distributions from the $D_2O(^3He,xn)$ source were measured at 0°, 10°, 20°, 30°, 60° and 90°. For the benchmark measurements, a 20 cm thick cylindrical iron slab with a diameter of 80 cm was placed 30 cm away from the neutron source in the beam direction. The experimental arrangement is shown schematically in Fig. 1. The slab was manufactured from type 11373 steel, which is 99% iron. Neutron spectra were measured at 340 cm from the neutron source at 0° and 20°. To decrease the background radiation level, the detector was surrounded by a polyethylene and iron shield in a configuration optimized by Monte Carlo calculations performed at FZK. To subtract the room neutron background, the conventional method with a 60 cm long iron-polyethylene shadow bar has been employed.

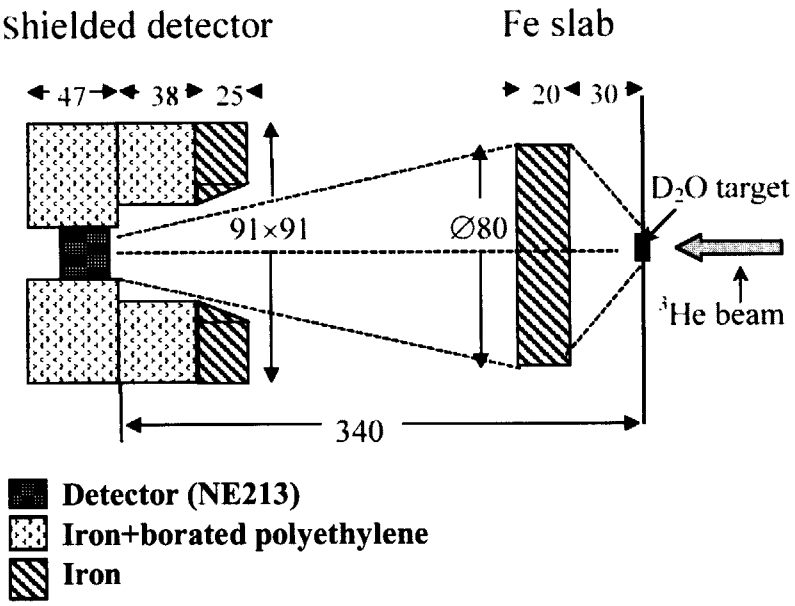


Fig. 1 Experimental arrangement for the measurement of neutron transmission spectra for an iron slab with shielded detector (sizes are given in cm).

(4) Data Acquisition and Processing

The fast neutron spectrometer is described elsewhere in detail (see Ref.[1,2] and Task TF52-EU report), thus only the main characteristics are repeated here.

The neutron detector, a liquid scintillator (NE213, 4.5dia×4.5 cm^2), was able to register neutrons in the energy range 1.8 to 35 MeV by the pulse height technique. The apparatus spectra were calibrated up to 7.6 MeV using γ-rays from ^{60}Co, ^{137}Cs, and PuBe sources and from the capture of thermal neutrons in iron. The fast neutron spectrometer was operated with two-dimensional n-γ discrimination hardware. List mode registration of pulse-height and monitoring events in an external buffer provided full information about the event history and permitted the performance of dead time and systematical error corrections [2]. By employing off-line Gaussian analysis of the two-dimensional pulse height spectra, a complete discrimination between neutrons and photons was achieved above the recoil proton energy of 3.5 MeV. The neutron spectra were obtained by applying the standard pulse height unfolding technique available with the GRAVEL procedure [3]. Detector response and efficiency were calculated using the Monte Carlo code SCINFUL-R [4].

The uncertainties of the data consist of several components. The statistical uncertainty data generated during the de-convolution process account for pulse height statistics, background subtraction uncertainty, and the uncertainty due to the (n,γ) discrimination procedure. The uncertainty of the detector efficiency is estimated to be less than 4-6% [6]. The beam charge on the target was determined with an uncertainty less than 2%. The beam-current-dependent correction for dead time (amounting up

to 8%) was estimated to contribute less than 1% uncertainty. The quadratic summation of these contributions was interpreted as the uncertainty of the yield scale factor.

(5) Experimental Results and Computational Analysis

In Fig. 2, the measured angular distribution of spectral neutron yields from the ^{3}He-D_2O neutron source is shown. The pronounced Gaussian-like shape of the energy spectra with a maximum at about 15 MeV and extending up to 35 MeV neutron energy is evidence of forward emitted neutrons as a result of the deuteron break-up process. In Fig. 3, the zero-degree spectrum is compared with the neutron spectra of the IFMIF source reaction D(40 MeV)+Li, as calculated by the McDeLicious code [5]. Fig. 4 compares the angular dependence of the integrated neutron yield of the ^{3}He-D_2O and the D(40 MeV)+Li reaction. The shape of both the spectra and the angular dependence of the yield are found to be rather similar. Therefore, the $D_2O(^3He,xn)$ reaction was selected as a suitable neutron source for the simulation of the IFMIF D-Li source spectrum. The absolute neutron yield of the D-Li reaction, however, exceeds the yield of the ^{3}He-D_2O reaction by two orders of magnitude at the same incident beam energy and current.

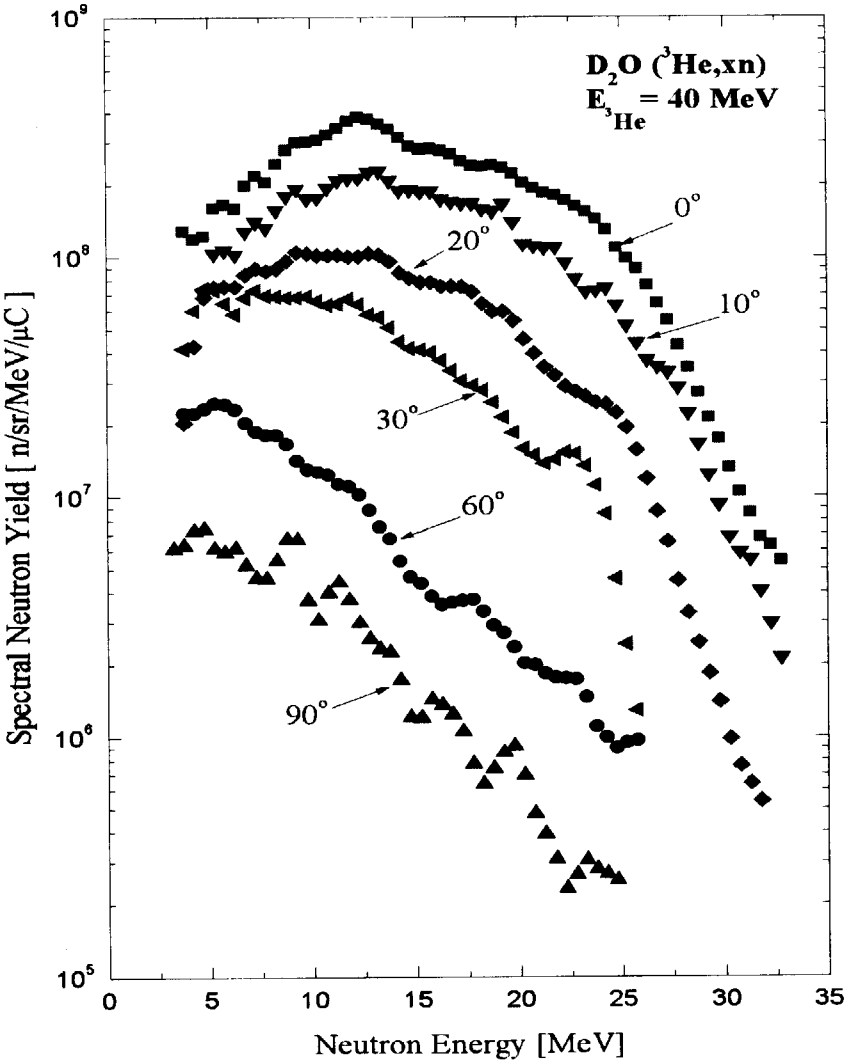


Fig. 2 Angular distribution of spectral neutron yields from the reaction $D_2O(^3He,xn)$ at 40 MeV incident deuteron energy.

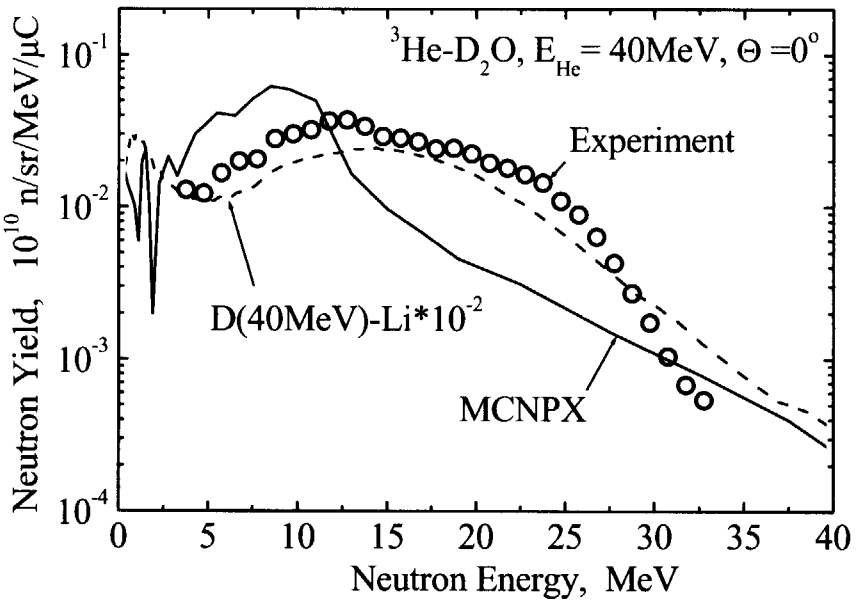


Fig. 3 Spectral neutron yields at 0° from a thick D_2O target irradiated by 40 MeV ^{3}He-ions: o – experiment, solid curve – MCNPX calculation. For comparison: dashed curve – 0° spectral yield (multiplied by 10^{-2}) from a thick Li target bombarded by 40 MeV deuterons as calculated by the McDeLicious code [3].

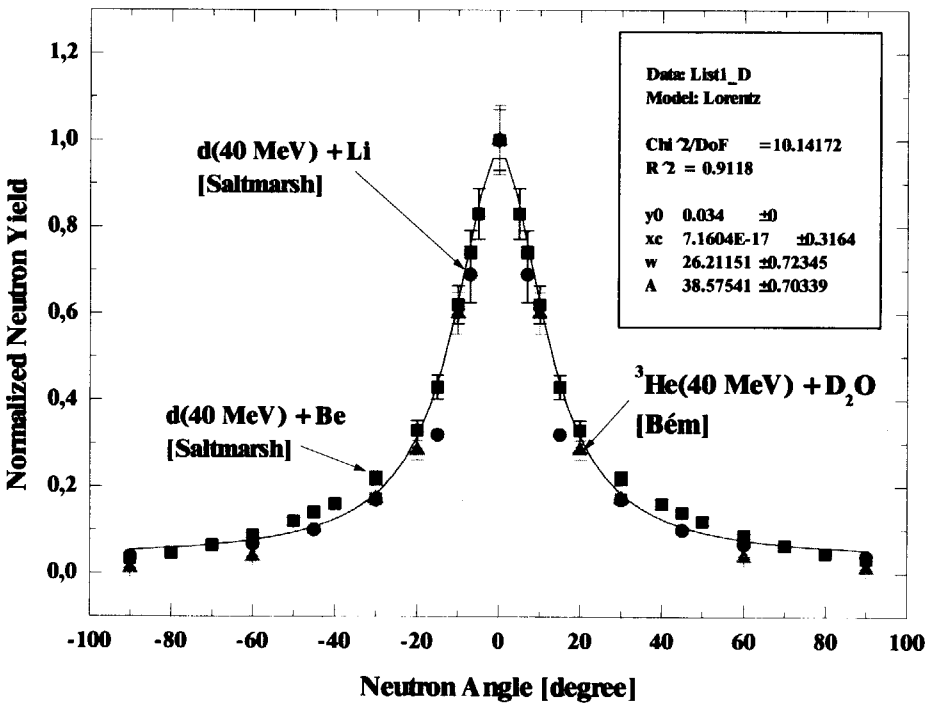


Fig. 4 Angular dependence of integrated neutron yields from the reaction $D_2O(^3He,xn)$ compared with data from the D(40 MeV)+Li and D(40MeV)+Be reactions. The experimental data from the EXFOR database are fitted with a Lorentz function.

The computational analysis of the benchmark experiment was performed with the MCNP-4C Monte Carlo code [6] and iron cross-section data provided by Task T54-EU (INPE/FZK) as well as data from the LANL 150 MeV evaluations [7]. A detailed three-dimensional geometry model was devised to accurately represent the iron slab, the detector shield, and the experimental hall. The neutron

source distribution was modeled on the basis of the measured double-differential angle-energy neutron yields obtained for the bare heavy water target. Calculated and experimental neutron transmission spectra are compared in Fig. 5 for detector angles of 0 and 20°. For the 20° yield spectra, good agreement is observed for the INPE/FZK and LANL-150 iron data in the energy range below 15 MeV. In the higher energy domain 15 to 35 MeV, the FZK/INPE evaluation satisfactorily represents the experimental results, whereas the LANL-150 data overestimates them by up to 50%. A trend to overestimating the transmission spectra with both iron data evaluations is observed for the 0° yield spectra above about 5 MeV neutron energy.

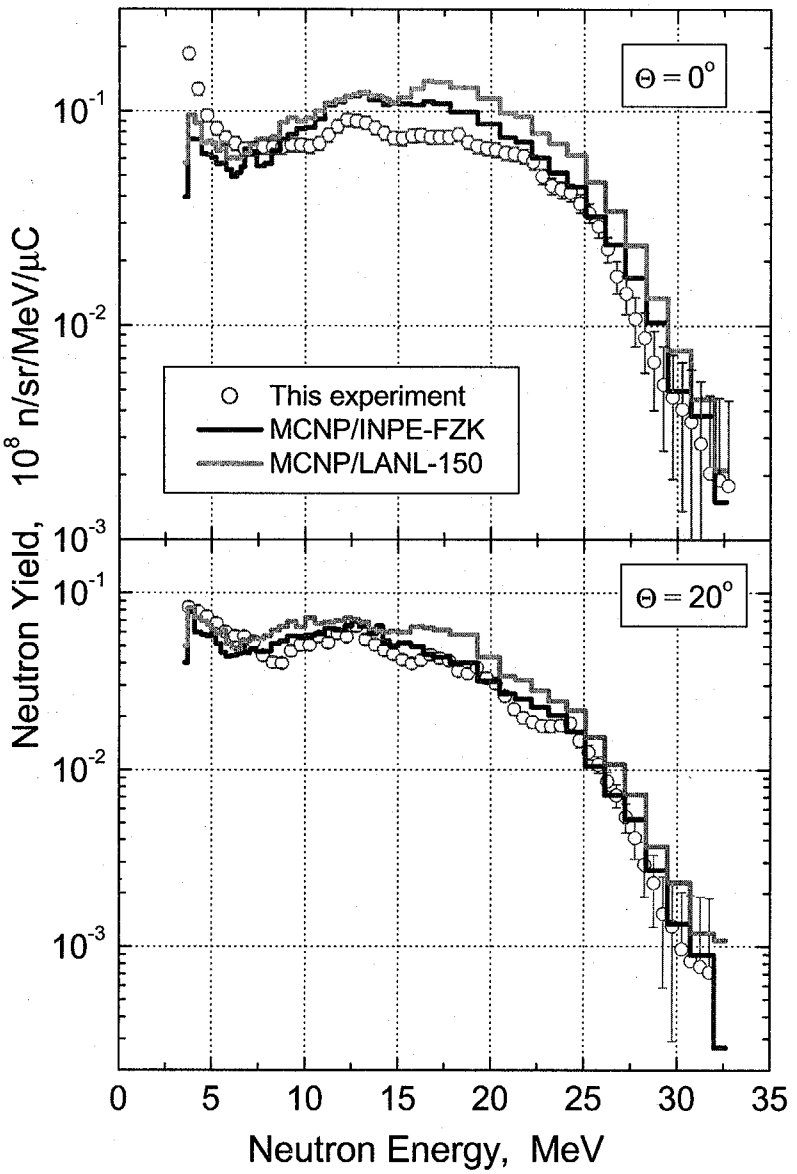


Fig. 5 Energy spectra of neutrons transmitted through 20 cm thick iron slab as recorded at 0° (top) and 20°(bottom): o – experiment, curves – MCNP4C calculation with INPE/FZK (red) and LANL iron data (green).

(6) Conclusions

The spectral yields of neutrons from a thick heavy water target bombarded by 40 MeV ^{3}He ions were measured. The comparison of the ^{3}He-D_2O and D-Li neutron producing reactions showed very similar energy-angular distributions at the same incident beam current and energy. Thus the suit-

ability of the ^3He-D_2O reaction for simulating the IFMIF source neutron spectrum in transport benchmark experiments was demonstrated.

The spectra of neutrons from a ^3He-D_2O source transmitted through a 20 cm iron slab were measured and compared with Monte Carlo transport calculations based on the INPE/FZK and LANL-150 iron data evaluations. The analysis has shown that the INPE/FZK iron evaluation satisfactorily reproduces the measured neutron transmission spectra up to 35 MeV whereas the LANL-150 iron evaluation gives an overestimation above 15 MeV by up to 50%.

A continuation of the benchmark experiment is required to improve the experimental accuracy and extend the neutron energy range down to about 0.1 MeV. This will employ a neutron collimator assembly and a Stilbene scintillator with high sensitivity.

References

[1] S.P. Simakov, U. Fischer, U. von Moellendorff, Forschungszentrum Karlsruhe, Bericht IRS-Nr. 15/00 - FUSION-Nr. 161, October 2000.

[2] P. Bém, V. Burjan et al., Nucl. Instr. Meth., **A425** (1999) 522-528.

[3] M. Matzke, "Unfolding of Pulse Height Spectra: The HEPRO Program System", Report PTB-N-19, ISSN 0936-0492, ISBN 3-89429-543-0, Phys.-Techn. Bundesanstalt, Braunschweig, 1994.

[4] S. Meigo, Nucl. Instr. and Meth. **A 401** (1997) 365 and private communication.

[5] S.P. Simakov, U. Fischer, U. von Moellendorff, I. Schmuck, A.Yu. Konobeev, Yu. A. Korovin, P. Pereslavtsev, Advanced Monte Carlo Procedure for the D-Li Neutron Source Term Based on Evaluated Cross Sections Files, 10th Int. Conf. on Fusion Reactor Materials (ICFRM-10), Baden-Baden, 14-19 Oct. 2001.

[6] J.F. Briesmeister (ed.), MCNP - A General Monte Carlo N-Particle Transport Code, Version 4C, Los Alamos National Laboratory, Report LA-13709-M, April 2000.

[7] M.B. Chadwick, P.G. Young et al., Cross-Section Evaluations to 150 MeV for Accelerator-Driven Systems and Implementation in MCNPX, Nucl. Sci. Eng. 131 (1999), 293.

3.3.19 TF56-EU : Nuclear Safety and Shielding

(1) Brief Task Description

In the framework of IFMIF project [1] the ENEA-Bologna group was committed to perform shielding calculations for various Test Facility rooms and cells. This activity required the setting up, production and application of new computational tools and data libraries for shielding analysis (deterministic approach) and activation calculations to contribute to the definition and establishment of shielding design criteria and to assess the radiological protection related to beam-on and beam-off operational phases. In particular, IFMIF production of a considerable fraction of the neutrons at energies above 20 MeV implied the following activities [2]:

- production of a new group-wise radiation transport library [3], "Vitenea-IEF", extended over 20 MeV (up to150 MeV for neutrons and 100 MeV for gamma-photons) for deterministic Sn codes;
- production of the ANITA-IEAF activation code package [4] (code and libraries) able to handle the numerous reaction channels for neutron energies over 20 MeV (up to 150 MeV).

The main characteristics of both Vitenea-IEF library and ANITA-IEAF activation code package are given in the next sections.

For qualification and calibration purposes a set of preliminary calculations of the dose rate outside the Test Cell concrete walls via the Sn Scale-Enea [2] shielding analysis sequence, with the new intermediate energy coupled 256n-49γ multi-group cross-section library Vitenea-IEF, was performed.

Two different concrete shielding-cooling design solutions have been considered. One approach utilizes an array of coolant passages embedded in the concrete shielding. Gaseous helium would remove the neutron heating deposited in the concrete. This approach is referred to as Standard. The alternate approach uses a separate stainless steel thermal shield placed between the liner and the concrete shield. This approach is referred to as Thermal Shield. Various analyses have been performed by considering, for example, different directions from beam axis and concrete wall thickness. The preliminary total dose rate values for normal plant operation (beam-on phase), in the forward direction, are:

9.15 (μSv/h)(for Standard case) and **1.26 (μSv/h)** (for Thermal Shield case).

Application of the ANITA-IEAF code package to the neutron exposure characterization and to radioactive inventories, for the SS-316 liner of the Test Cell area, is described.

Contributors

Name	Party	Institute	E-mail address
D.G. Cepraga	EU	ENEA	dangilio@bologna.enea.it
G. Cambi	EU	Bologna University	dangilio@bologna.enea.it
M. Frisoni	EU	Athena s.a.s.	dangilio@bologna.enea.it

(2) Introduction

The IFMIF is an accelerator-based D-Li neutron source to simulate the neutron irradiation field in a fusion reactor. After the IFMIF Conceptual Design Activity (CDA) in 1995-96 and the Conceptual Design Evaluation (CDE) in 1997-98, the IFMIF project proceeded to the next phase: the Key Element Technology Phase (KEP) to reduce key technology risk.

The ENEA was committed to perform shielding calculations of various Test Facility rooms and cells in order to investigate the accessibility of the IFMIF rooms during and after accelerator operation and the compliance with dose limits inside and outside the facility. For that purpose, the neutron and gamma shields both of the Test Cell and of the entire facility have to be defined. To establish the appropriate shielding, evaluation of the gamma and neutron dose rates in various IFMIF rooms and cells is required.

Dose rates need to be estimated both during normal plant operation, "beam-on", and at "beam-off" conditions.

During normal plant operation the main contributors to the dose rate outside the Test Cell are:

1) neutrons emerging from the lithium target due to the interaction of the primary deuteron beam with the target itself;
2) gammas, so called prompt gammas, generated by neutron induced nuclear reactions (for example, n-γ) in the materials of the Test Cell walls;
3) gammas generated by the neutron induced activation and subsequent decay of the materials contained in the Test Cell walls (so called decay gamma sources).

During the beam-off phase the contribution to the dose rate is due only to the decay gamma sources generated by the material radioactivity.

As a first guess for calibration purposes, it was planned to perform the evaluation of the dose rate outside the Test Cell shielding walls during plant operation, due to the a) and b) contributions, through a coupled n-γ Sn Scale-Enea transport calculation.

These calculations required the production of the new intermediate energy group-wise transport library, "Vitenea-IEF", extended above 20 MeV, in Ampx format.

The decay gamma sources calculation required the production of the ANITA-IEAF activation code package (code and libraries) able to handle the numerous reaction channels for neutron energies over 20 MeV.

(3) The Vitenea-IEF Library

Vitenea-IEF is a new intermediate energy coupled 256-neutron and 49-gamma-ray multi-group cross-section library in Ampx format, suitable for Sn radiation transport codes.

The library was obtained by processing the LANL evaluated files of ENDF/B-VI Release 6 and FZK/INPE files via the NJOY-AMPX-SCALE code systems.

The library contains the following materials/isotopes: H-1,H-2, C, O-16, Al-27,Si-28,Si-29, Si-30, P-31, Ca, Cr-50, Cr-52, Cr-53, Cr-54, Fe-54, Fe-56, Fe-57, Ni-58, Ni-60, Ni-61, Ni-62, Ni-64,Cu-63, Cu-65, Nb-93, W-182, W-183, W-184, W-186, Pb-206, Pb-207, Pb-208 from ENDF/B-VI Release 6 and K-39, Li-6, Li-7, V-51 from FZK/INPE Nuclear Data.

The inclusion in the library of the ENDF/B-VI materials together with those made available by FZK makes it possible to handle most materials, including the lithium target, stainless steel, and concrete planned to be used in IFMIF.

The following options in the NJOY processing were applied.

For neutrons:

- 256-group energy structure up to 150 MeV (standard 175-group Vitamin-J structure to 19.64 MeV and 81 groups above; constant energy bins of 1 MeV and 2 MeV were used for the energy domains 20-50 MeV and 50-150 MeV, respectively);
- weighting function: thermal + 1/E + flat
- temperatures: 300 K, 600 K, 900 K, 1500 K;
- 10 values of background cross sections: 10^{10}, 1000, 300, 100, 30, 10, 3, 1, 0.1, 10^{-6} (Bondarenko method for the resonance self-shielding treatment);
- maximum Legendre expansion order for scattering matrices: 6

For gammas:

- 49-group energy structure up to 100 MeV (standard 42-group Vitamin-J structure to 50 MeV and 7 groups above; constant energy bins of 5 MeV and 10 MeV were used for the energy domains 50-70 MeV and 70-100 MeV, respectively);
- weighting function: flat over the entire energy range;
- maximum Legendre expansion order for scattering matrices: 8

The production of the library required the development of a new Smiler code, which converts the NJOY output from GENDF to AMPX format, in collaboration with the ORNL group of the

Ampx-2000 system, in order to let it manage the nonstandard ENDF format lumped MT=5 cross section structure contained in the evaluated files for neutron energies over 20 MeV.

In order to perform the dose rate calculations by Sn method, a new file, containing the group-wise neutron and gamma fluence to ambient dose equivalent conversion factors, was produced. It was obtained by integrating the neutron and gamma point-wise factors available in literature (ICRP-74 and Ferrari-Pelliccioni evaluation [5]) on the same weighting functions and group structures previously described, converted to Ampx format and included in the Vitamin-IEF library.

(4) The ANITA-IEAF activation code package

The new ANITA-IEAF activation code package traces back to the ANITA-2000 code (OECD-NEA-1638, RSICC CCC-606). It is able to manage the many reaction channels open for neutron energies higher than 20 MeV and up to 150 MeV.

The code computes the radioactive inventories of materials exposed to continuous or stepwise neutron irradiation,. It provides activity, isotope nuclide density, decay heat, biological hazard, clearance index and decay gamma ray sources, in the 42 standard Vitamin-J energy structure, at shutdown and at different cooling times.

The code package (Fig. 1) is provided with a complete data base that includes neutron activation data library, decay, hazard and clearance data library, and gamma library.

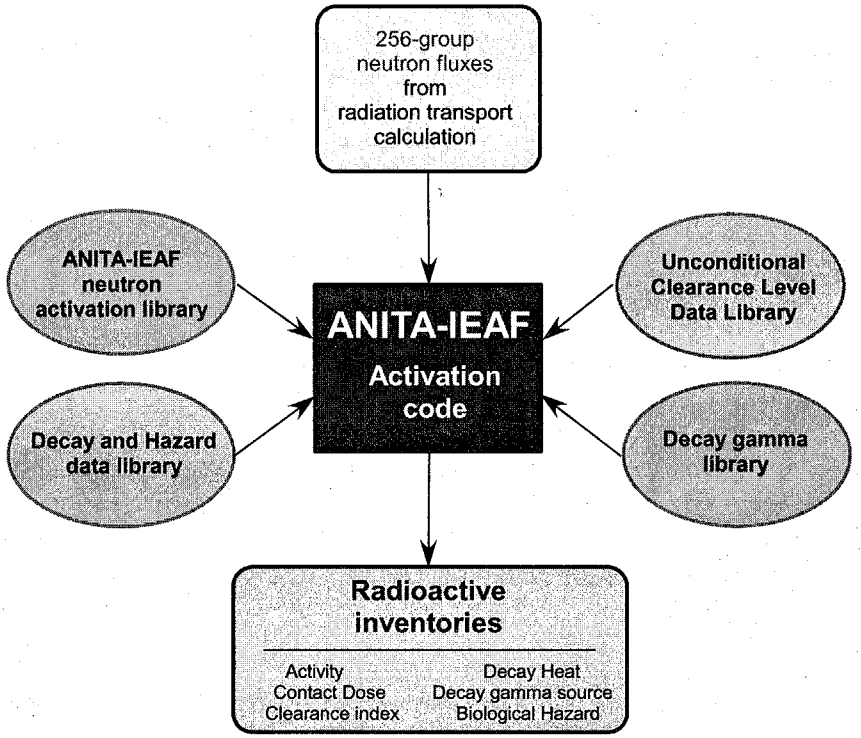


Fig. 1 ANITA-IEAF activation code package.

(4.1) New Anita-IEAF activation library

The Anita-IEAF activation library has been derived from the FZK IEAF-2001 activation library [6]. However, that library contains neutron activation cross sections (for 679 nuclides), in Gendf format, not suitable to be used in Anita code. In IEAF-2001 library the neutron activation cross sections for each nuclide are identified in the MF=3, MT=5 structure by the recoil nucleus produced. This is due to the fact that for neutron energies greater than 20 MeV many reaction channels open, which don't correspond well to defined MT numbers in the standard ENDF6 format notation. So far, a fixed reaction table, as required in Anita code, has been created by associating to every recoil nucleus, characterized by a well known difference in charge Z and mass A, a nonstandard MT number.

(4.2) Anita-IEAF Decay, Hazard and Clearance Data Library

This library contains the information describing the decay properties of unstable nuclides useful for the calculations performed by ANITA-IEAF. This file has been completely updated. It contains the following data for 1840 nuclides:

- The decay data have been taken from the Fusion Evaluated Nuclear Decay Data Library FENDL/D-2.0.
- The Annual Limit of Intake (Bq) by ingestion or inhalation for the public or workers (ALI) quantities is obtained from the ICRP-72.

- The clearance level data. They are the "unconditional clearance levels" (Bq/g), based on IAEA-TECDOC-855.

(4.3) Anita-IEAF Gamma Library

This data base contains gamma ray spectra emitted by the radioactive nuclei (1390 isotopes) in the Vitamin-J 42-γ energy group structure. The data of the library are based on the FENDL/D-2 evaluated decay data file (gamma radiation spectra).

(5) Results, Discussions and Conclusions

(5.1) Dose rate calculation outside the Test Cell concrete shielding walls

For qualification purposes of the codes and the new data libraries, a set of preliminary calculations of the dose rate outside the Test Cell concrete walls via the Scale-Enea shielding analysis sequence using the Vitenea-IEF library was performed. These calculations represent a check of the consistence of the cross sections of the Vitenea-IEF library and in the same time the results are the first preliminary "solid numbers" of the dose rates outside the Test Cell. The calculations are related to the normal plant operation, (beam-on phase) where the dose rates are due to neutrons and prompt gammas.

Geometrical configuration, material compositions, and neutron source

The geometrical layout was modeled in order to maintain the real equivalent volumes of the various regions of the Test Cell (lithium target, back plate, High Flux Test Module, Test Cell vacuum room, shielding walls etc.). This choice assures that the total collision densities are preserved in the various zones.

The IFMIF Test Cell modeled in the calculations contains:(1) Lithium target (24 cm x 6 cm x 3 cm ,volume = 432 cm^3); (2) Back plate; (3) High Flux Test Module-HFTM (20 cm x 5 cm x 5 cm, volume = 500 cm^3); (4) Test Cell vacuum room (300 cm x 250 cm x 300 cm) that encloses the test module and the lithium target; (5) neutron and gamma concrete shielding system (two different design solutions, see the details in the following).

The first design utilizes an array of coolant passages embedded in the concrete shielding. Gaseous helium would remove the neutron heating deposited in the concrete. In this case a concrete shielding, consisting of concrete 80%, plus He 20% for cooling, thickness 100 cm, and concrete 100% up to a total thickness of 310 cm, was placed after the test cell vacuum room. This approach will be referred to as **Standard** in the following.

The second design solution uses a separate stainless steel thermal shield that is placed between the liner and the concrete shield. This arrangement reduces the neutron heat load to the concrete shielding to a level that can be tolerated with only edge cooling of the concrete, i.e. no internal cooling required. Gaps of 10 mm thickness are provided between the test cell liner and the test cell thermal shield and between this and the concrete shield. A thickness of 20 mm of SS-316 as thermal shield plus concrete 100% up to a total thickness of 310 cm after the test cell vacuum room were used in the calculations. This approach will be referred to as **Thermal Shield** in the following.

The following material compositions were chosen: a) lithium target: lithium natural isotopic abundance; b) back plate: stainless steel SS-316 LN-IG; c) High Flux Test Module : Eurofer; d) liner and thermal shield: stainless steel SS-316 LN-IG; e) biological shield: concrete.

Neutron Source

To perform the coupled n-γ transport calculation **an angle- and group-dependent boundary neutron source** was used. In this case, one specifies not a source but a flux condition on the boundary. The energetic neutron source distribution, due to the interaction of the primary **40 MeV deuteron beam on Li-target**, calculated by **Oyama** based on the **Serber** model has been produced in the same group structure of the Vitenea-IEF library.(see Fig. 2).

A total neutron source strength of 1.1×10^{17} n/s^{-1} was used to normalize the calculations.

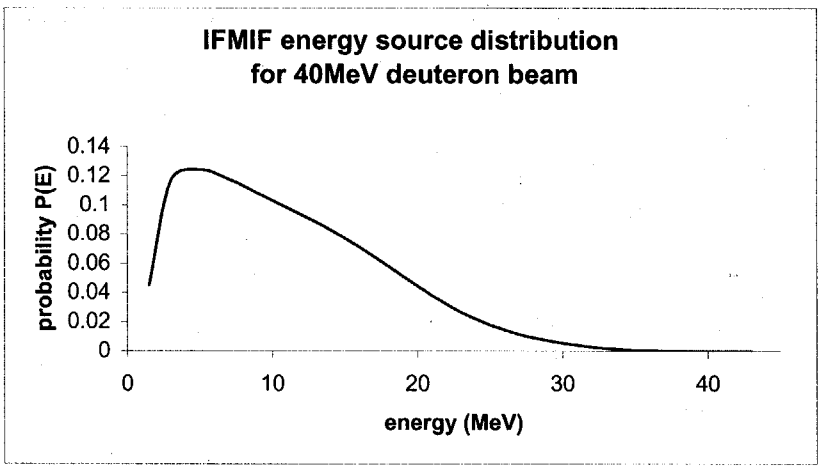


Fig. 2 Neutron energy source distribution for 40 MeV deuteron beam.

Dose rate results

The neutron and gamma dose rate calculations were performed for the two different concrete shielding design solutions, Standard and Thermal Shield, defined previously. For each, different calculations were performed in order to simulate the real 3-D Test Cell geometrical configuration (volumetric collision density conservation) and to take into account that the real neutron source is not isotropic, but peaked in the forward direction. Six different dose rate calculations were performed, in particular:

Standard configuration:

a) "Lateral Wall case"- a concrete shielding, consisting of concrete 80%, plus He 20% for cooling, thickness 100 cm, and concrete 100% up to a total thickness of 310 cm placed around the test cell vacuum room was considered. The corresponding dose rates can be considered as those out of the "lateral" walls of the Test Cell (not forward direction forced neutron source);

b) "Frontal Wall case"-the same concrete shielding of case a) was considered but a forward direction forced neutron source has been applied. The corresponding dose rates can be considered as those out of the "frontal" wall of the Test Cell. The total dose rate due to both neutrons and gammas vs. distance from the inner concrete shielding surface is shown in Fig.3;

c) "Ceiling 1 Wall case"-the thickness of the concrete shield is 210 cm. The corresponding dose

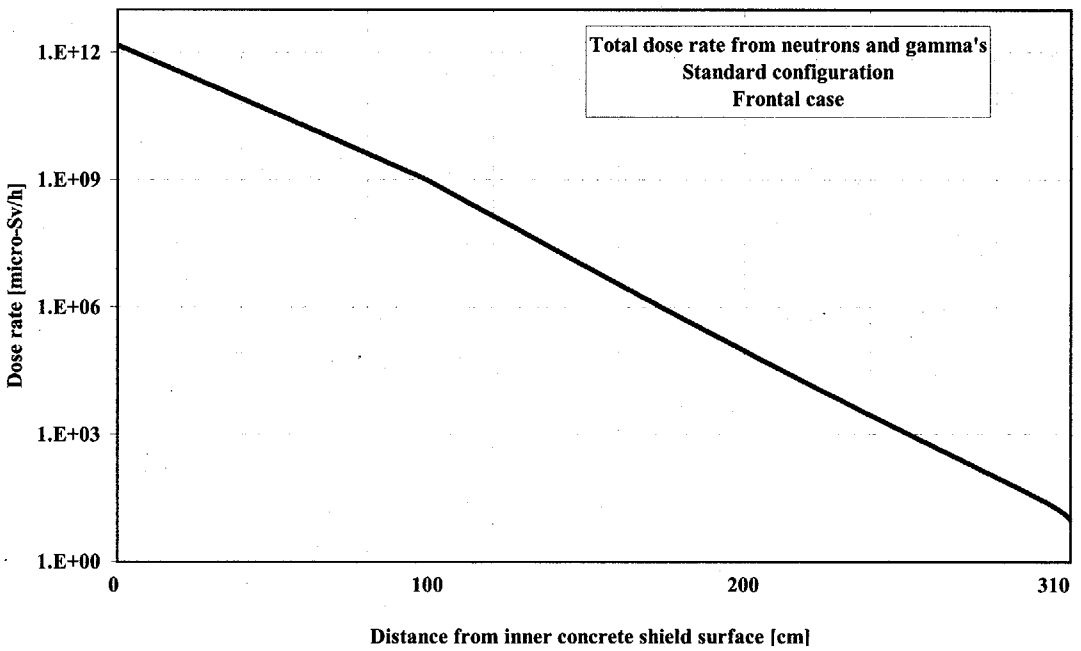


Fig. 3 Total dose rate inside concrete shielding.

rates can be considered as those out of the "ceiling" and "floor" walls of the Test Cell;

d) "Ceiling 2 Wall case"-the thickness of the concrete shield is 250 cm. Cases c) and d) are an example of testing the effectiveness of the shielding properties of concrete.

Thermal Shield configuration

The concrete shielding system consists of: I) void gap 10 mm, II) stainless steel Thermal Shield 20 mm; III) void gap 10 mm, IV) helium gap 10 mm, V) concrete 100% up to a total thickness of 310 cm.

e) "Lateral Wall case"- The corresponding dose rates can be considered as those out of the "lateral" walls of the Test Cell ;

f) "Frontal case"-same geometrical configuration of case e) but a forward direction forced neutron source has been applied. The corresponding dose rates can be considered as those out of the "frontal" wall of the Test Cell.

Results and discussion

The detailed dose rate results for cases from a) to f) are shown in Table 1, both for the standard and the thermal shield configuration. The following remarks can be made:

- neutron and gamma dose rates for both cases a) and b) (standard configuration) are lower than the recommended limit (10μSv/h);
- cases c) and d) (standard configuration) corresponding to two different wall thickness in the up and down directions show high dose rates; these are due to the reduced thickness of the shielding that reduce its effectiveness (see Fig. 2);
- cases e) and f) (thermal shield configuration) appear to be more effective than the Standard one;
- detailed results analysis points out that the total contribution to the dose rate outside the concrete shielding wall due to the neutrons with energy higher than 20 MeV and gammas with energy higher than 50 MeV is about 11% for the Standard configuration, Frontal case b). These results show the importance of taking into account the higher energy neutron in the IFMIF facility as done using the Vitenea-IEF transport library.

The 1-D deterministic calculations appear to be a powerful method to obtain reliable results in short computing times, useful to assess the shielding efficiency, via parametric and sensitivity studies.

To obtain the safety margins for the IFMIF design of the shielding structure three-dimensional calculations (both MCNP Monte Carlo family code and DOORS deterministic Sn family code, in order to guarantee a complete Q.A. process) will be performed.

Table 1 n and γ dose rates outside the shielding walls.

		Lateral (a)		Frontal (b)		Ceiling1 (c)		Ceiling2 (d)	
Standard configuration	Position	Dose n (μSv/h)	Dose γ (μSv/h)	Dose n (μSv/h)	Dose γ (μSv/h)	Dose n (μSv/h)	Dose γ (μSv/h)	Dose n (μSv/h)	Dose γ (μSv/h)
	Surface	3.56	3.91	4.36	4.79	1.94E+4	1.02E+4	5.57E+2	4.13E+2
	1 m	2.01	2.65	2.47	3.24	9.82E+3	6.05E+3	2.62E+2	2.60E+2

		Lateral (e)		Frontal (f)	
Thermal shield configuration	Position	Dose n (μSv/h)	Dose γ (μSv/h)	Dose n (μSv/h)	Dose γ (μSv/h)
	Surface	1.85E-1	8.39E-1	2.26E-1	1.03
	1 m	1.05E-1	5.77E-1	1.28E-1	7.07E-1

(5.2) IFMIF Test Cell steel liner activation

As an application and test of the ANITA-IEAF code package, an activation calculation was performed for the SS-316 liner. The neutron flux in 256 group structure calculated with the Scale-Enea shielding analysis sequence was used. A continuous 5-year irradiation scenario has been applied. Table 2 lists the specific activity, with the most relevant isotope contributing, at IFMIF plant shut down.

The contribution of the neutrons with energies higher than 20 MeV to the activation characteristics has been estimated. In particular, a difference of about 15 to 23% results in the specific activity (Bq/g) out to three years cooling time.

These calculations show the importance of taking into account the higher energy neutrons in IFMIF facility as done in ANITA-IEAF package.

Table 2 Isotope specific activity of the Test Cell steel liner at the end of beam-on phase.

	ACTIVITY (Bq/cm^3)	PERC %
Mn 56	3.66E+09	2.97E+01
Fe 55	2.66E+09	2.16E+01
Cr 51	1.95E+09	1.58E+01
Co 58	1.10E+09	8.90E+00
Mn 54	5.57E+08	4.52E+00
Co 57	4.74E+08	3.84E+00
Co 58ml	4.68E+08	3.80E+00
Co 60ml	1.98E+08	1.61E+00
Co 60	1.74E+08	1.41E+00
V 52	1.50E+08	1.22E+00
Mo 99	1.50E+08	1.22E+00
Tc 99ml	1.32E+08	1.07E+00
Cu 64	1.28E+08	1.03E+00
V 49	5.16E+07	4.18E-01
Al 28	3.64E+07	2.95E-01
Ni 57	3.63E+07	2.94E-01
Mo101	3.26E+07	2.65E-01
Tc101	3.26E+07	2.65E-01
Fe 59	3.10E+07	2.52E-01
Cr 55	2.74E+07	2.22E-01
Mn 52ml	2.44E+07	1.98E-01
Co 56	2.43E+07	1.97E-01
Cu 66	2.31E+07	1.88E-01
Ni 63	2.11E+07	1.71E-01
Fe 53	1.87E+07	1.51E-01
Ni 65	1.76E+07	1.43E-01
Mn 57	1.24E+07	1.01E-01
Sum	1.22E+10	
Total	1.23E+10	

References

[1] M.Martone, (editor), IFMIF International Fusion Materials Irradiation Facility Conceptual Design Activity Final Report, ENEA Frascati Report, RT/ERG/FUS/96/11, November 1996.

[2] M. Frisoni, D.G. Cepraga, G. Cambi, New Computational Tools and Data Libraries for IFMIF Shielding Calculations, EFDA Task No. TW0-TTMI-003, IFMIF Task No. TF56-EU, ENEA FUS-TN-SA-SE-R-34, June 2002.

[3] D.G. Cepraga, G. Cambi, M.Frisoni, Fusion Material Transmutation and Activation Analysis Induced by Fast Neutrons: a) Vitenea-IEF radiation transport library, b) ANITA-IEAF Activation code package, IEA International Workshop on Fusion Neutronics, September 5, 2002 – Dresden, Germany.

[4] D.G. Cepraga, M. Frisoni, G. Cambi, ANITA-IEAF: a code package for performing fusion material transmutation and activation analysis induced by intermediate energy neutrons, 22nd Symposium on Fusion Technology SOFT, September 9 - 13, 2002 - Marina Congress Center, Helsinki, Finland.

[5] A. Ferrari and M. Pelliccioni, On the Conversion Coefficients from Fluence to Ambient Dose Equivalent, Radiat. Prot. Dos., Vol.51, N.4, pag.251,1994.

[6] U.Fischer, D.Leichtle, A.Konobeyev, Yu. Korovin, U.v.Mollendorf, P.Pereslavtsev, I.Schmuck, Intermediate Energy Activation File 2001 (IEAF-2001), Forschungszentrum Karlsruhe, Technik und Umwelt, Interner Bericht, IRS-Nr.10/01- FUSION-Nr. 179, August 2001; U.Fischer, D.Leichtle,U.v.Mollendorff and I.Schmuck, ZZ-IEAF-2001, Intermediate Energy Activation File, NEA-1656/01.

3.3.20 TF57/58-EU : Sub-miniature Fission Chambers – Development, Construction and Experimental Tests.

(1) Brief Task Description

The task consists of the development of prototype on-line neutron monitors for IFMIF and their testing in an IFMIF-like neutron field provided by the upgrade of the NPI (Nuclear Physics Institute) cyclotron-based Fast Neutron Facility (Rez, near Prague, Czech Republic). In parallel, integral tests on activation foils selected for IFMIF neutron dosimetry can also be performed. As the NPI cyclotron can accelerate protons up to 37 MeV, the p(37 MeV)+D_2O breakup reaction is used in order to simulate the IFMIF D(40 MeV)+Li neutron spectrum. Preliminary experiments and theoretical evaluations had shown that this reaction provides a Gaussian shaped neutron spectrum, with mean neutron energy of ~14 MeV and maximum energy in excess of 30 MeV. A neutron emission rate up to ~$1x10^{12}$ n/s/sr is expected using the negative-ion extraction mode of the cyclotron.

Contributors

Name	Party	Institute	E-mail address
B. Esposito, M. Angelone, A. Pensa	EU	ENEA-Frascati	esposito@frascati.enea.it
C. Blandin, J.P. Hudelot	EU	CEA-Cadarache	christophe.blandin@cea.fr
P. Bém, V. Burjan, V. Kroha, J. Novák, E. Simecková, J. Stursa and F. Vesely	EU	NPI-Rez	bem@ujf.cas.cz

(2) Development of Sub-miniature Fission Chambers and Monitors

The task of studying the necessary instrumentation for neutron/gamma flux and neutron spectrum measurements in the IFMIF HFTM, assigned to ENEA-Frascati, started in the CDA phase [1] and continued in the CDE and the KEP phases. CEA-Cadarache collaborated with ENEA in the last two phases through a study of the modifications required to adapt available sub-miniaturized fission chambers for the monitoring of the neutron flux in various positions within the HFTM [2,3,4] and then with the detailed final design of the chambers suitable for IFMIF [5,6]. According to the results of such activity [6,7], the optimum miniaturized chambers for IFMIF application should have either ^{238}U or ^{237}Np as fissile coating; these chambers should have a diameter of 1.5 mm, a fissile mass of 0.528 mg and an argon gas pressure of 2 atm.

Due to the low expected neutron emission at the NPI cyclotron (~1×10^{12} n/s/sr), following meetings with Czech and French experts, the decision was taken to build prototype miniaturized fission chambers of larger diameter (8 mm instead of 1.5 mm) since the 1.5 mm diameter chambers would detect a very low current signal (much below the nA range), which would probably be masked by noise. Therefore, three 8 mm diameter fission chambers (^{238}U, ^{237}Np, and no fissile deposit) were produced at CEA–Cadarache in 2001, tested in the MINERVE thermal reactor (^{238}U and ^{237}Np only) and sent to NPI during March 2002. These chambers having larger diameter, greater fissile material content and higher argon pressure were expected to have a total increase in signal of a factor ~30 with respect to the 1.5 mm diameter chambers. The IFMIF-like neutron spectrum can be measured using a set of activation foils suitable to the IFMIF neutron spectrum energy range: the comparison of the spectral measurement performed with an independent spectrometer (BC-501 liquid scintillator-based) will provide information on cross sections of some activation reactions to be used in IFMIF dosimetry in the high neutron energy range (above ~20 MeV). Foils planned for use in the experiment are Al, Ti, Mn, Fe, Co, Ni, Y, Zr, Nb, Rh, Lu, Au.

(3) The Simulation of IFMIF Neutron Spectrum at NPI Fast Neutron Facility

Search for IFMIF-like neutron source reaction

The IFMIF neutron source reaction D(40 MeV)+Li produces a white spectrum with mean energy of 14 MeV and a high energy tail up to 50 MeV. Therefore, the response of- and radiation effects on IFMIF neutron monitors are to be investigated at relevant neutron energies. As deuterons can be accelerated up to 18 MeV only (and protons up to 37 MeV) on the NPI cyclotron, other reactions had to

be selected in order to simulate the D+Li IFMIF neutron spectrum. Previous experimental investigations [8] had indicated the D(p,n)2p reaction as the most suitable candidate. Measured neutron yield data of the p+D (thin gas target) reaction show a Gaussian-like spectral shape of the break-up process and a noticeable high-energy group (Fig.1(a)), corresponding to the final state interaction. Simple theoretical considerations applied to available cross section data have permitted prediction of the energy dependence of the spectral yield (Fig.1(b)) and the $E_n \sim 0.45\ E_p$ dependence for the mean neutron energy. For a 35 MeV, 20 μA proton beam, possible for the NG2 target station, a neutron emission of about $3x10^{12}$ n/sec/sr and a mean neutron energy of 14 MeV could be deduced.

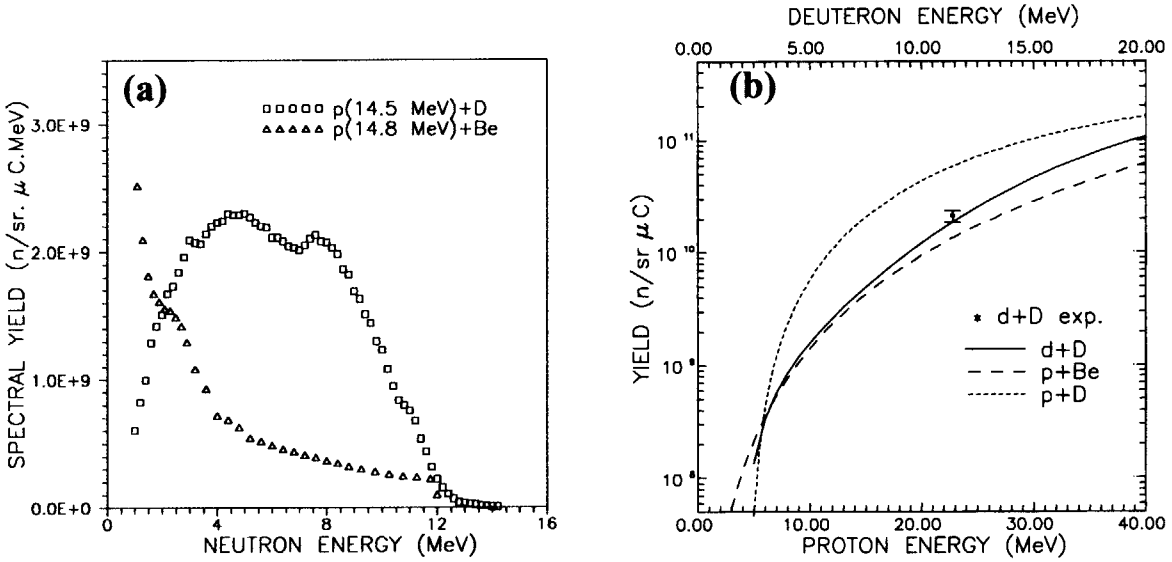


Fig. 1 (a) Zero-degree neutron yield spectra for the D(p,n)2p reaction measured using the 14.5 MeV proton beam of the NPI cyclotron; relevant data of the Be(p,xn) reaction [EXFOR database] are also shown for comparison; (b) calculated thick-target zero-degree neutron yield from D and Be targets as a function of incident particle energy.

High-power neutron target station NG2

Due to target considerations (heat dissipation of 800 W beam power), heavy water instead of D-gas was preferred as the target medium. A new beam-line, vacuum system, beam-diagnostic system and a specially designed D_2O-flowing target station have been developed and installed at the negative-ion beam extractor of the cyclotron (Fig.2). The loss of beam intensity was limited to 10% or less, and further improvements are under consideration. This leads to an acceptably low level of unwanted neutrons in the vicinity of the target. The spot size of the uncollimated beam on the target could be adjusted within 8 to 20 mm in diameter. Both the long- and short-time fluctuation of the beam intensity are less than 5%.

Neutron spectra

The contribution of the proton reaction on oxygen to the neutron yield could not be correctly calculated due to lack of relevant data. Instead, the p+D_2O reaction was investigated experimentally. The measurement of the angular distribution of the spectral neutron yield at 24 MeV and of the zero-degree spectral yield at 37 MeV incoming proton energy were carried out employing the shadow-bar method in an open-geometry arrangement. Liquid scintillator-detector techniques (BC-501) with two-dimensional n-γ discrimination hardware and a multiparameter data-acquisition system have been used. Special care was given to safe operation of the detector (phototube) hardware operating in the gamma and electromagnetic fields of the accelerator.

The resulting neutron spectra are shown in Fig. 3. The measured mean neutron energy of 13.9 MeV and the neutron emission of $9x10^{11}$ n/sr/s (for 37 MeV/20 μA proton beam) deviate only slightly

from the predicted values for the pure p+D reaction, in accordance with the assumed low neutron yield from the accompanying p+O interaction.

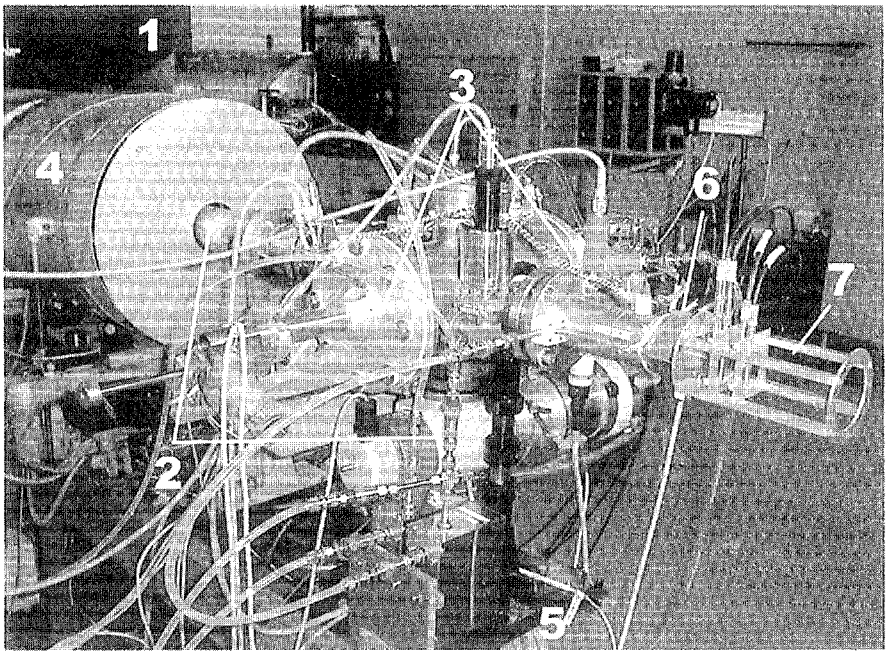


Fig. 2 NPI cyclotron-based fast neutron facility, NG2 target station: (1) cyclotron, (2) beam guide and vacuum system, (3) beam-diagnostic hardware, (4) quadrupole lenses, (5) beam-guide support, (6) heavy-water flowing target chamber, (7) holder for irradiated samples (sub-miniature fission chambers in actual positions).

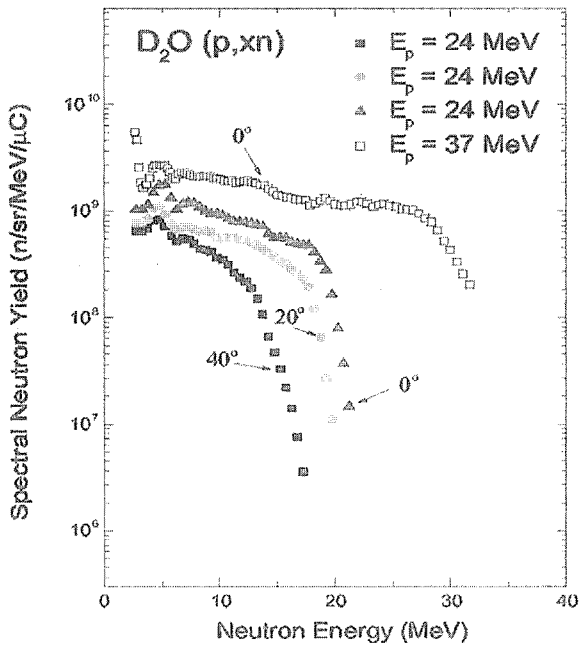


Fig. 3 Neutron spectra from NG2 target station: angular distribution of spectral yield at 24 MeV and zero-degree spectral yield at 37 MeV incoming proton energy.

Data were measured in point-like geometry (long detector-target distance): in order to extrapolate these observables to the vicinity of the target (i.e. the location of the irradiated samples), an integration of observables over target and sample dimensions was performed, utilizing simple theoretical considerations about the energy and angular dependence of data [8]. The results, i.e. the dependence of the neutron flux and the neutron mean energy vs. distance between the target and the position of the sample, are shown in Fig. 4 and Fig. 5.

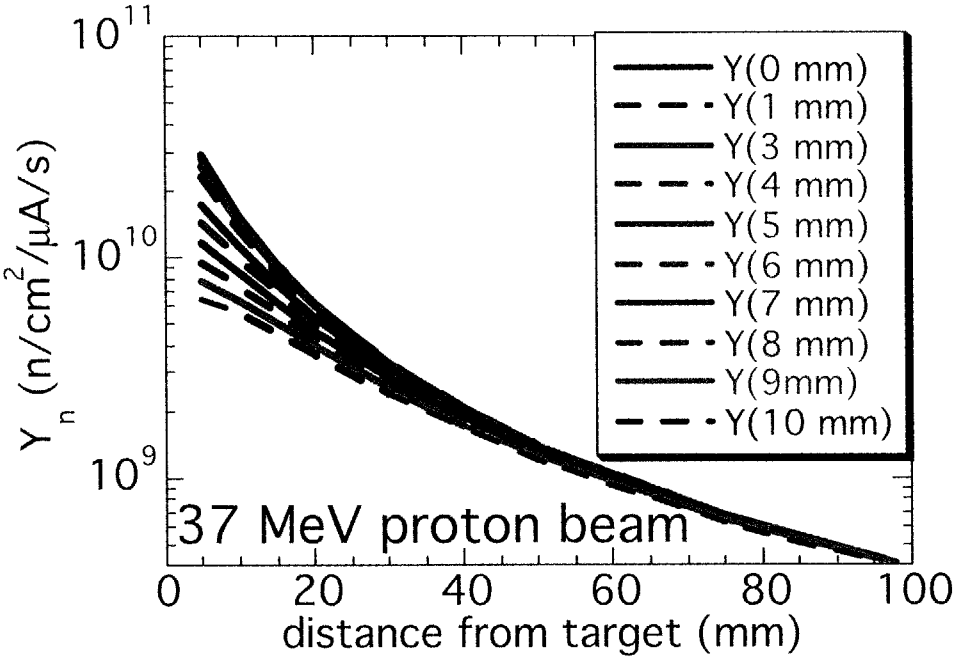


Fig. 4 Calculated neutron flux vs distance between end of target and position of the sample (y is the radial coordinate perpendicular to the beam axis).

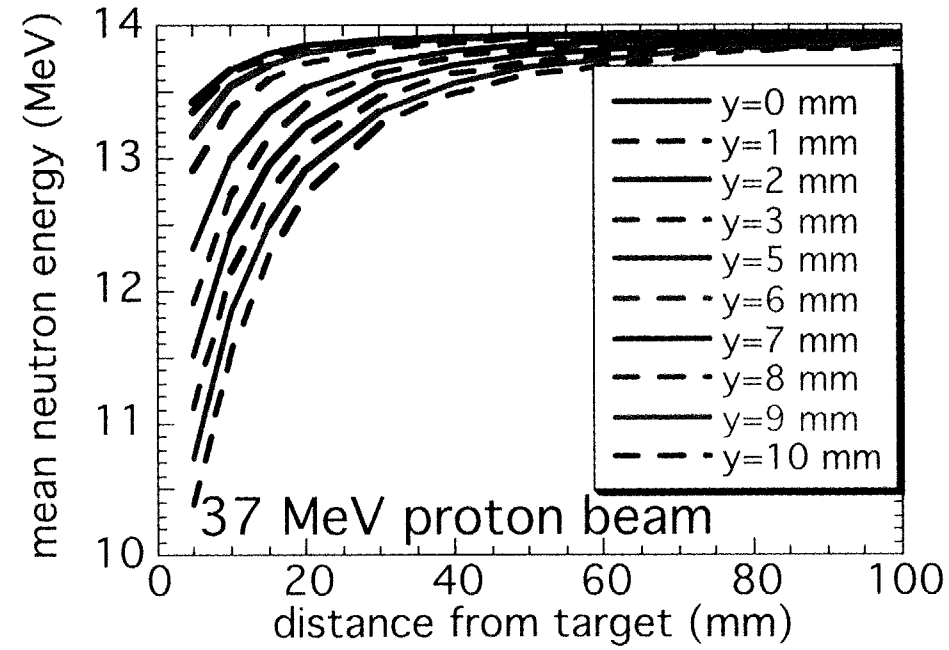


Fig. 5 Calculated neutron mean energy vs distance between end of target and position of the sample (y is the radial coordinate perpendicular to the beam axis).

As can be seen, the numerical values of both observables (reaching $5x10^{11}$ n/cm^2/s/20 μA and 12.8 MeV, respectively) strongly reflect the integration procedure for a sample of 1 cm diameter at a distance of 5 mm and only deviate slightly from point-like geometry data for distances above 50 mm. These calculations will be benchmarked employing activation-foil measurements with point-like data from scintillators as assumed neutron spectra in the deconvolution procedure.

(4) Experimental Tests

The experiment was carried out in July 2002, due to a delay in obtaining the fission chambers export license from CEA (France) to NPI (Czech Republic). Three and a half days (July 22nd-25th) were devoted to the experiment, with cyclotron maintenance carried out at night. The personnel consisted of 2 scientists from CEA, 1 scientist and1 technician from ENEA, plus local NPI scientists and technicians (for operation of the cyclotron and experiment setup). The cyclotron was operated with a proton beam at a fixed energy of 37 MeV. Fig.4 and Fig.5 show the calculated neutron flux and neutron mean energy as a function of the distance between the end of target and the position of the sample (coordinate *x*): the various curves in the figures correspond to different distances of the sample from the axis of the primary proton beam (coordinate *y*). The cyclotron produces a pulsed neutron emission: the *macrostructure* corresponds to one burst every ~6.6 ms (duration of burst ranging from 0.2 to 2 ms – typically ~1 ms, i.e.: filling of ~15%), while the *microstructure* corresponds to one burst every ~70 ns (duration of burst 3 ns). Both testing of a) fission chambers and b) activation foils were tried in the experiment.

a) *Fission chambers*:

The details of the chambers (see sketch in Fig.6) used in the experiment are as follows:

1) ^{238}U miniaturized fission chamber with 10.82 ± 0.03 mg of fissile deposit (2 mg/cm^2), argon pressure 9 atm, (serial number 2130 [9]); the purity of ^{238}U is characterized by the following ratios: ^{234}U/^{238}U=0.000003±0.000001 and ^{235}U/^{238}U=0.000359±0.000002.

2) ^{237}Np miniaturized fission chamber with 9.0±0.3 mg of fissile deposit (2 mg/cm^2), argon pressure 9 atm; fissile material purity 100% (serial number 2131 [10]);

3) miniaturized fission chamber without fissile deposit ("No Deposit" in the following), argon pressure 9 atm (serial number 2136 [11]).

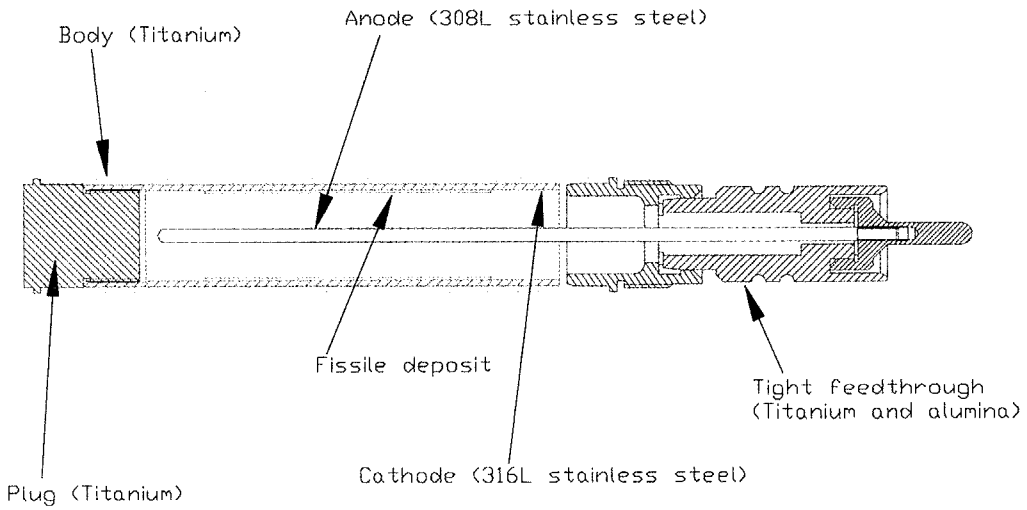


Fig. 6 Schematic cross section of miniaturized fission chamber.

All detectors and related electronics (amplifiers, cables, data acquisition chain) needed for the experiment have been prepared by CEA (pulse and current mode electronics and pulse mode acquisition system) and by ENEA (a second pulse mode acquisition system plus a current mode acquisition system based on National Instruments PCI card and LabVIEW dedicated software). Various measurements at different cyclotron beam currents were performed both in pulse and current mode fission chamber

operation. Data were collected for all available fission chambers (^{238}U, ^{237}Np, No Deposit) and for a cable not connected to any chamber ("Cable" in the following) in order to monitor noise. After some preliminary testing it was discovered that the ^{237}Np chamber was broken and therefore no data will be shown for such chamber. The arrangement of the holders of the fission chambers with respect to the target is shown in Fig.7. The scheme of electronic and acquisition chains and the overall layout of the experiment is shown in Fig.8. For the majority of acquisitions almost simultaneous monitoring of beam current level was available by means of the second pulse mode acquisition system.

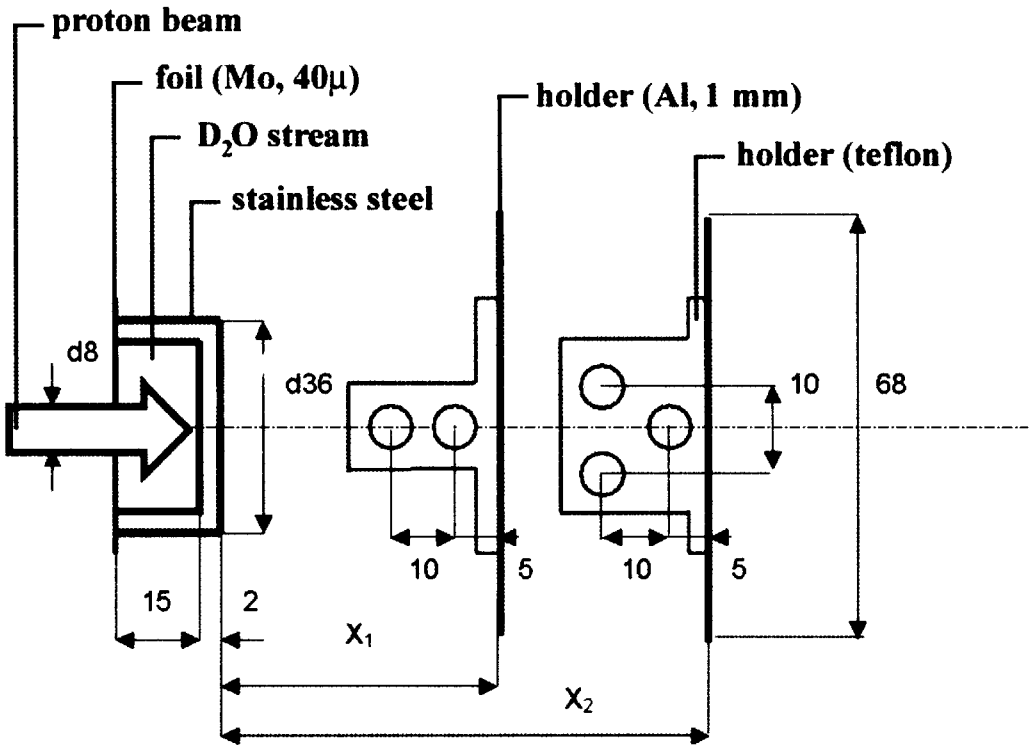


Fig. 7 Schematic cross section of target and fission chamber holders (all dimensions in mm).

Standard RG 59B/U organic cables were used throughout the experiment for all connections: a) in pulse mode: between fission chambers, preamplifiers and acquisition system; b) in current mode between fission chambers, I/V converter and acquisition system.

b) *Activation foils*

A stack of various dosimetry foils (Co, Au, Mn, Rh, Lu, Y and Zr) was mounted on the target for a preliminary test on the third day of the cyclotron run, but due to malfunctioning of the target cooling system during this dedicated run, the proton beam was directed on the stack of foils causing its destruction. In this stage, it was decided to postpone further testing to subsequent runs. However, due to the flood in the Czech territory in August 2002 (which struck the NPI territory and partly destroyed the cyclotron hardware), the cyclotron operation - and consequently the activation-foil tests - are expected to be restored at the beginning of 2003.

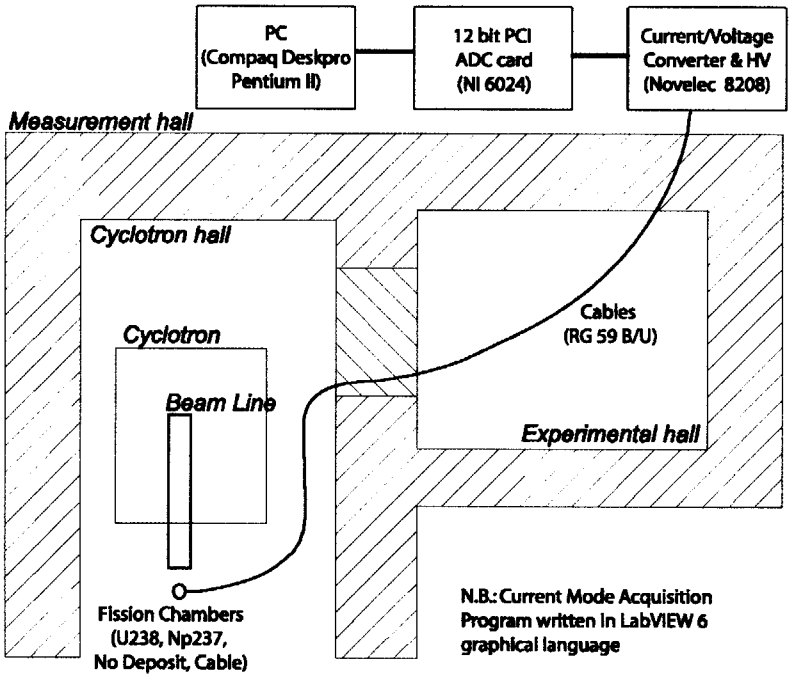


Fig. 8 Fission chamber current mode experiment layout.

(5) Results and Discussions

The analysis of the data from the experiment is still under way; preliminary results concerning the current mode tests (valid data acquired on July 24, 2002) are described below.

The sampling of the current mode acquisitions was at 100 kHz. A scan of the fission chamber current mode signal at different chamber voltages was performed for various levels of nominal cyclotron beam current (0.1, 0.5, 1, 1.2 and 5 μA). The first set of current mode data was acquired in the following configuration (*position 1*): ^{237}Np, ^{238}U and No Deposit on the first holder (having three slots) located at a distance from the target x_2=24 mm (left: ^{237}Np, right: ^{238}U, back: No Deposit); Cable on second holder (having two slots) at position x_1=54 mm. The distance of the ^{238}U fission chamber from the target was therefore x=9 mm (see Fig.7). In a subsequent run, the ^{238}U and ^{237}Np chambers positions were exchanged (*position 2*) in order to check any asymmetry of the neutron emission in the y coordinate (due to possible misalignments of the primary proton beam). No particular difference in the signal of the ^{238}U chamber at the same level of beam power was observed after this exchange, thus indicating an overall symmetry of the neutron emission with respect to the center of the target. Finally, the No Deposit and ^{237}Np chamber positions were also exchanged (*position 3*). Two last acquisitions (*position 4*) were made in the same configuration as *position 3*, but with the first holder at a distance x_2=134 mm from the target: in these acquisitions the cyclotron was functioning, but a beam dump produced zero beam current on the fission chambers.

The acquired data show the presence of a high level of noise: Fast Fourier Transform (FFT) with the Hanning window function has been used in order to clarify which frequencies are related to noise and signal (see the power spectra – square of the magnitude of the complex spectrum - in Fig.9). Spectrograms have also been produced, showing the behavior of various frequency components in time (Fig.10). By cross-checking the Cable, No Deposit and ^{238}U signals, it is found that frequencies above 10 kHz are certainly due to noise: this is proved by the fact that in the measurements in *position 4*, the FFT power spectrum shows that the frequencies related to the pulsed cyclotron beam (e.g. 150 Hz) disappear, whereas frequencies above 10 KHz still persist. Consequently, all current mode data have been filtered with a bandpass filter (low pass with cut at 10 kHz). Typical results are shown in Fig.11 and Fig.12 where the raw data (red) are overlaid to the filtered data (blue); in these figures a 1 V signal corresponds to a measured fission chamber current of 1 μA.

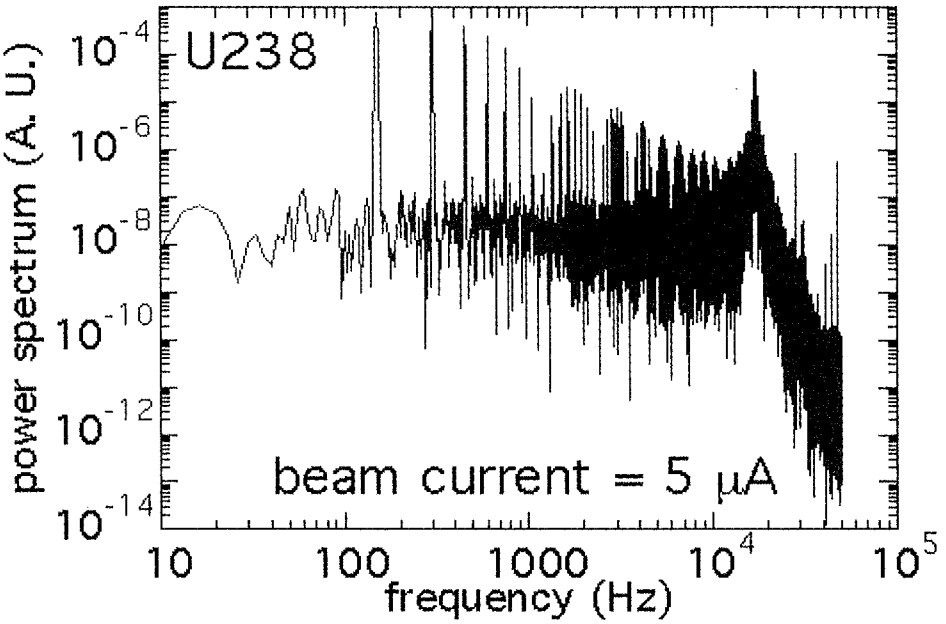


Fig. 9 Power spectrum of signal (^{238}U current mode).

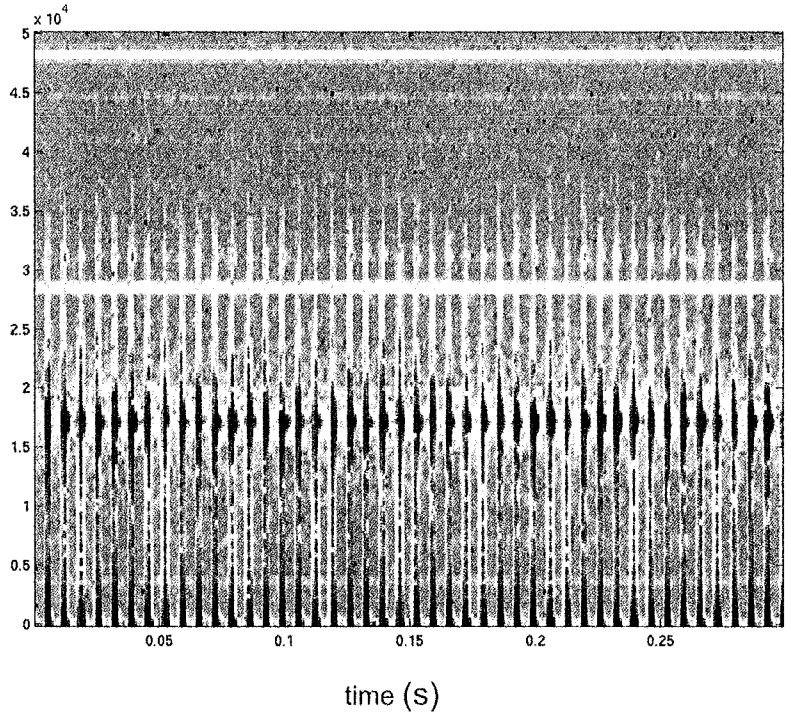


Fig. 10 Spectrogram showing current mode noise components during ^{238}Uchamber irradiation at 5 μA beam current.

After subtraction of the noise, a plot was produced showing the linearity of the ^{238}U signal with the cyclotron beam current: in Fig.13 the RMS value of the ^{238}U signal (average over the whole acquisition interval, typically 300 ms) is plotted vs the measured beam current (the chamber voltage in these measurements was set at300 V). The results indicate that the ^{238}U chamber correctly measures the fast neutron emission from an IFMIF-like source. Another interesting point is the comparison of the signals between the ^{238}U and the No Deposit chambers in this neutron field: in Fig.14 are shown the

signals when these two chambers are located in the experimental configuration at the same distance from the target (*position 3*, beam current =1.2 μA). The No Deposit chamber detects a signal about 5 times lower than the signal from the ^{238}U chamber, the Cable signal being negligible (≤ 5 mV). The reason for such a high level of signal has to be investigated in detail, but it is due to the gamma-ray field in the vicinity of the target.

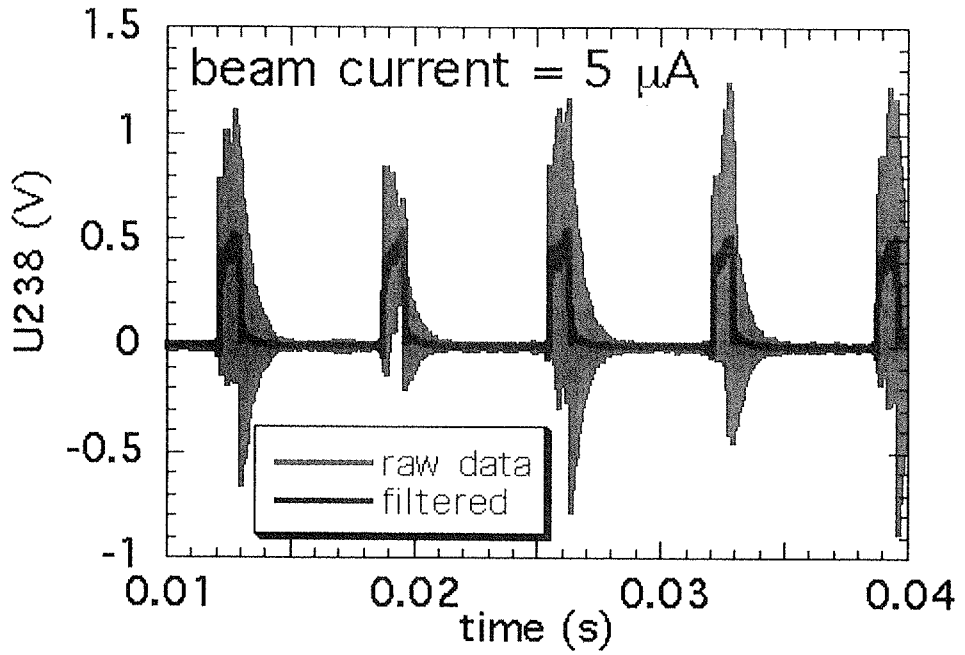


Fig. 11 ^{238}U fission chamber current mode signal (5 μA beam current, holder in position 1).

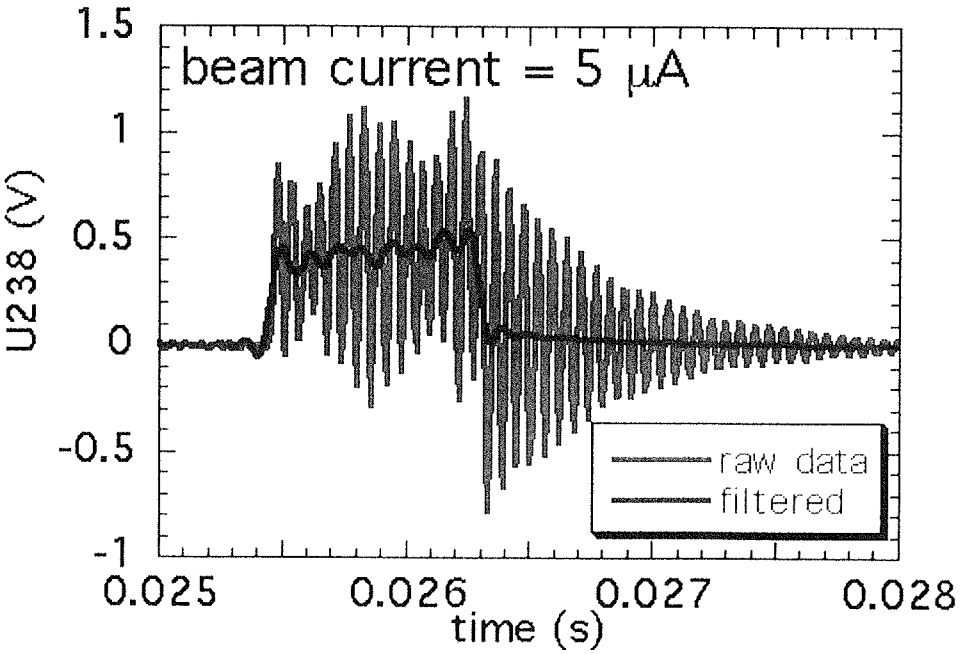


Fig. 12 Detail of ^{238}U fission chamber current mode signal (5 μA beam current, holder in position 1).

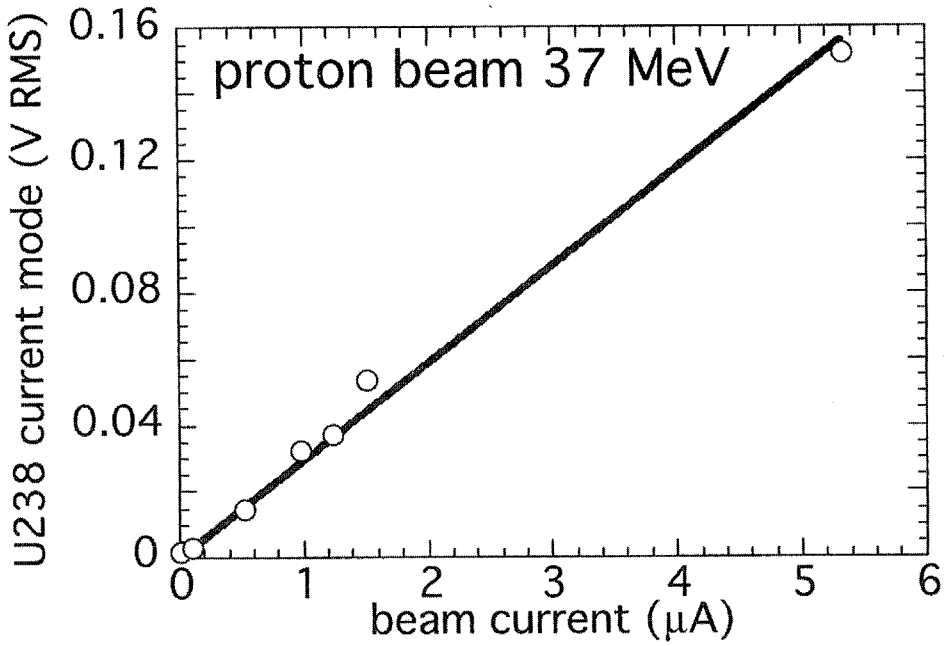


Fig. 13 Linearity of ^{238}U current mode signal with beam current (fission chamber HV=300 V).

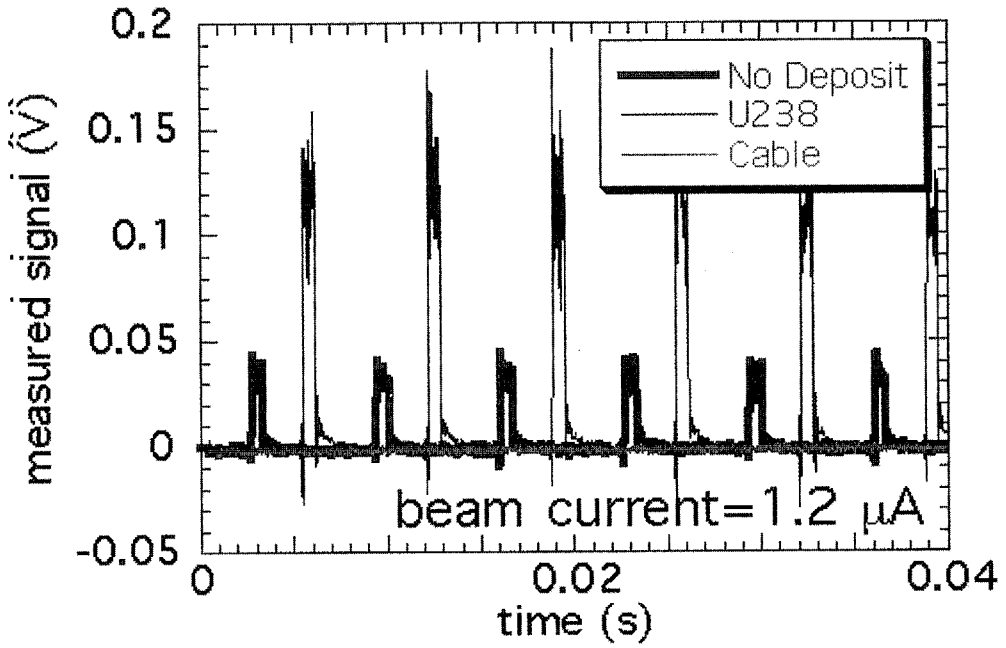


Fig. 14 Comparison of ^{238}U, No Deposit and Cable current mode signals (HV=300 V): note that ^{238}U

(6) Conclusions

The predicted neutron flux characteristics of the NPI NG2 heavy-water target station have been experimentally proven: 1) the white spectral distribution with neutron mean energy of 13.9 MeV (for a detector threshold of 2.6 MeV) and energy range up to 32 MeV is a good simulation of the IFMIF neutron spectrum; 2) for a proton beam current of 20 μA, the zero degree integral yield of $9x10^{11}$ n/sr/s leads to a flux density of ~$5x10^{11}$ n/cm^2/s at 5 mm foil-to-target distance: the mean energy is about 12.6 MeV in this case.

The experiment performed at the NPI cyclotron has demonstrated that the current mode operation of the 8 mm diameter ^{238}U miniaturized fission chambers for measuring the fast neutron flux in an IFMIF-like environment is possible; therefore the use of the planned sub-miniaturized fission chambers (1.5 mm diameter) should be feasible in IFMIF. The preliminary results of the irradiation experiment indicate the linearity of the measured current mode ^{238}U signal with the cyclotron beam current (i.e. with the neutron emission). The chamber used in the experiment has 8 mm diameter and 10.82 mg of fissile material; it detects a current of about 0.15 μA in a fast neutron field of roughly $1x10^{10}$ n/cm^2/s. The No Deposit chamber also detects a signal in the same environment at a level about 5 times lower (the signal being due to gamma-ray interactions). No useful tests of the ^{237}Np chamber were possible, as this chamber was found to be broken (possibly having been damaged during shipment). Pulse mode data (with spectral analysis) for the ^{238}U chamber have also been obtained in the experiment, but have not been analyzed yet: these data will be useful for absolute calibration of the cyclotron neutron source. However, it is foreseen that, due to the high neutron fluxes, only current mode measurements will be possible in IFMIF. No activation foil measurements have been performed in the present experiment, but they are scheduled for future cyclotron operation.

References

[1] M. Martone, (editor), IFMIF International Fusion Materials Irradiation Facility Conceptual Design Activity Final Report, ENEA Frascati Report, RT/ERG/FUS/96/11, December 1996.

[2] B. Esposito, Define Design Concept for Dosimetry, 1996 Final Report, ENEA Frascati Report, ENEA-ERB5004 CT 960061, NET/96-419, April 1997.

[3] B. Esposito, L. Bertalot, L. Petrizzi, Y. Kaschuck, G. Bignan, C. Blandin, A. Lebrun, J.P. Trapp, G. Maruccia, Activation Foils and Real-Time Neutron/Gamma Detectors-Neutronics Task 13, IFMIF CDE 1999 Final Report, ENEA-Frascati Report, NET/97-452, 1999.

[4] C. Blandin, S. Chauffriat, H. Recroix, J.P. Trapp, Etude preliminaire de faisabilite de detecteurs pur le suivi en ligne du flux de neutrons de haute energie dans l'installation IFMIF (International Fusion Materials Irradiation Facility), CEA Cadarache Technical Note, SSAE/LSMR/99/0014, 1999.

[5] B. Esposito, L. Bertalot, G. Maruccia, L. Petrizzi, Y. Kaschuck, G. Bignan, C. Blandin, S. Chauffriat, A. Lebrun, H. Recroix, J.P. Trapp, Results from the CDE phase activity on neutron dosimetry for the IFMIF test cell, Fusion Eng. and Design **51-52** (2000), 331-338.

[6] C. Blandin, Sub-miniature fission chamber design for the International Fusion Materials Irradiation Facility (IFMIF), CEA Cadarache Technical Note, SSAE/LSMR/00/0060, November 2000.

[7] C. Blandin and B. Esposito, Design of sub-miniature fission chambers for the IFMIF high flux test module, ENEA Frascati Report, ERB5005 CT990059 EFDA/99-506, November 2000.

[8] P. Bém, V. Burjan, F. Cvachovec, M. Gotz, V. Kroha, E.Yu. Nikolskii, E. Simecková, J Vincour, Fast neutrons from thick deuterium target irradiated by 15.8 MeV protons and 14.1MeV deuterons, Nucl. Instr. and Meth. in Phys. Research **A 425** (1999) 522-528.

[9] C. Blandin, S. Breaud, N.2130 Chamber: manufacturing report, CEA Cadarache Technical Note, NT SCCD 2001-074, August 2001.

[10] C. Blandin, S. Breaud, N.2131 Chamber: manufacturing report, CEA Cadarache Technical Note, NT SCCD 2001-075, August 2001.

[11] C. Blandin, S. Breaud, N.2136 Chamber: manufacturing report, CEA Cadarache Technical Note, NT SCCD 2001-076, August 2001.

3.3.21 TF61-EU : Recalculation of Nuclear Response for Different Beam Footprints

(1) Brief Task Description

The design modifications of the IFMIF reduced cost option with different deployment strategies consider different variants of the beam footprint, the beam current, the number of beams, as well as their spatial orientation. Another design modification was introduced by integrating a neutron reflector around the test module to improve the irradiation conditions for the material test samples. In addition, new computational tools and nuclear data were recently developed to increase the accuracy of the neutronics calculations. These changes necessitated performing a complete reevaluation of the irradiation parameters and the nuclear responses for the different test materials that will be irradiated in the High Flux Test Module (HFTM) of IFMIF.

Contributors

Name	Party	Institute	E-mail address
U. Fischer	EU	FZK	ulrich.fischer@irs.fzk.de
S.P. Simakov	EU	FZK	simakov@irs.fzk.de
A. Möslang	EU	FZK	anton.moeslang@imf.fzk.de

(2) Introduction

Detailed neutronics calculations were carried out for the full performance option of IFMIF with two 125 mA deuteron beams during CDA and CDE [1, 2]. The recent cost reduced option [3] with staged deployment scenarios considers the employment of one 50 mA or 125 mA deuteron beam during the IFMIF starting phase and various beam footprints to get sufficient irradiation volume and neutron flux intensity for meaningful materials testing. In addition, a neutron reflector surrounding the HFTM was proposed to improve the irradiation conditions by increasing the damage production rate and decreasing the spatial gradients [4].

New computational tools and nuclear data were continuously developed during CDA, CDE and KEP, resulting in (i) the McDeLicious Monte Carlo code [5,6] which makes use of D-Li evaluated cross sections [7] for the neutron source simulation (KEP Task TF51-EU), and (ii) the high energy neutron cross-section data [8,9] which form the basis for the neutron transport and nuclear response calculations (KEP Task TF54-EU).

In the framework of Task TF61-EU a complete reevaluation of the three-dimensional distribution of the neutron and photon fluxes, the hydrogen and helium gas transmutation production, the displacement damage and the nuclear heating has been carried out. In the following, a brief task description is given, the calculation methods applied are outlined, and an overview is provided of the main results of the irradiation parameters and nuclear response.

(3) Variations of the Deuteron Beam Configurations

It is most likely that IFMIF will start operation with one accelerator delivering one deuteron beam to the lithium target (Table 1). At this phase only one 50 mA beam current will be available for a few years (Starting Stage I), followed by a stepwise increase up to 125 mA (Starting Stage II). The deuteron beam will be oriented along the symmetry axis perpendicular to the lithium jet surface. For the full performance operation phase two 125 mA beams vertically declined by 10 degrees from the symmetry axis are foreseen in the reference design. The cost reduced option suggests the accelerator allocation at one level. This means the two deuteron beams will be declined in a horizontal plane [3].

Different beam footprints are considered for these stages: 20×5 cm^2 as reference for the full performance operation, and reduced (in horizontal direction) footprints of 10×5 cm^2 or 4×5 cm^2 during the IFMIF deployment phases. For the sake of illustration, the relative beam density distributions on the lithium target surface are shown in Figs. 1 and 2 for two extreme cases. The beam profile for the full performance IFMIF operation mode is based on the simulation of the accelerator optical system [10]. It was linearly reduced along the horizontal axis to get the beam density distribution for the smaller beam footprints.

Table 1 Scenarios of IFMIF concept deployment and main neutronics parameters (given the accelerated deuteron energy of 40 MeV).

Deployment Stage / Parameter	Starting I			Starting II	Full Performance	
	Option 1	Option 2	Option 3			
Beam/Accelerator Options						
Number of Beams/Accelerators	1				2	
Beam Orientation	Perpendicular to the Lithium Jet				Horizontal	Vertical
Each beam current, mA	50	50	50	125	125	125
Beam power, MW	2	2	2	5	10	10
Beam footprint (width × height), cm^2	20 × 5	10 × 5	4 × 5	20 × 5	20 × 5	20 × 5
Beam density, mA/cm^2	0.5	1.0	2.5	1.25	2.5	2.5
Li target backplate: n-flux, dpa and heat generation in the center						
n-flux, $10^{14}/cm^2/s$	2.8	4.9	9.0	7.1	14.5	14.2
Displacement rate, dpa/fpy	12	22	42	31	63	62
Nuclear heating, W/cm^3	6.1	10	19	15	31	29
HFTM: Irradiation parameters and nuclear heating (*)						
n-flux, $10^{14}/cm^2/s$	2.6 – 1.1	4.4 – 1.6	8.0 – 2.3	6.6 – 2.7	13.3 – 5.5	12.8 – 5.1
γ-flux, $10^{14}/cm^2/s$	0.9 – 0.7	1.4 – 1.0	2.3 – 1.3	2.2 – 1.7	4.4 – 3.3	4.2 – 3.3
Nuclear heating, W/cm^3	4.9 – 2.8	8.5 – 4.3	15 – 6.4	12 – 6.9	25 – 14	24 – 13
HFTM: Radiation induced effects in Eurofer(*)						
Displacement rate, dpa/fpy	11 – 4.2	20 – 6.6	38 – 10	28 – 11	57 – 21	55 – 20
Volume (dpa > 20/fpy), cm^3	0	0	40	100	524	514
Volume (dpa > 40/fpy), cm^3	0	0	0	0	102	90
H production, appm/fpy	500 – 200	910 - 340	1800 - 580	1250 – 490	2550 – 1000	2420 – 1000
He production, appm/fpy	110 – 41	200 - 70	390 – 120	270 – 103	560 - 210	520 – 190
HFTM: Radiation induced effects in Vanadium(*)						
Displacement rate, dpa/fpy	13 – 4.7	22 – 7.4	40 - 12	32 – 12	62 – 23	62 – 22
Volume (dpa > 20/fpy), cm^3	0	11	49	149	645	640
Volume (dpa > 40/fpy), cm^3	0	0	2	0	145	135
H production, appm/fpy	220 – 100	420 – 160	830 – 290	570 – 260	1150 – 470	1100 – 470
He production, appm/fpy	39 – 18	72 – 29	140 - 50	98 – 45	200 - 80	200 - 80

(*) *The given maximum and minimum values correspond to the center points at the front and the back surface of the HFTM, respectively.*

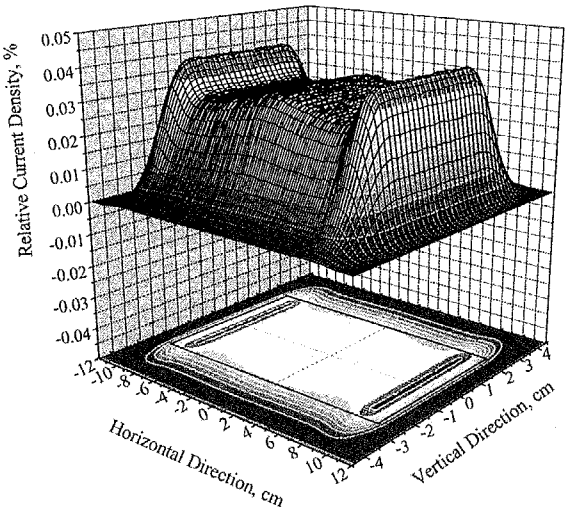


Fig. 1 Three-dimensional (top) and contour plot (bottom) presentation of the IFMIF deuteron beam profile. The box on the projection plane shows the front plate contour (20×5 cm^2) of the HFTM.

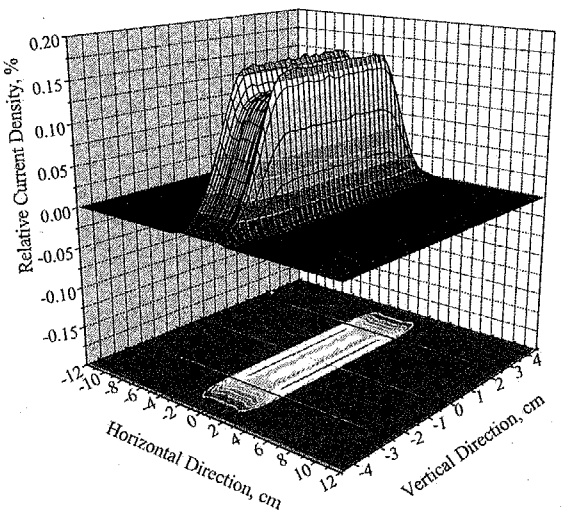


Fig. 2 The same as Fig. 1, but for the beam profile for the reduced beam footprint 4×5 cm^2.

The beam configuration options are summarized in Table 1. The three footprint options considered for the Starting Stage I correspond to the increase of the beam current density from 0.5 mA/cm^2 to 2.5 mA/cm^2 as the footprint area is horizontally compressed. The transition from the Starting Stage II to the Full Performance phase results in an increase of the beam density from 1.25 mA/cm^2 to 2.5 mA/cm^2 due to the use of the second accelerator.

(4) Computational Tools and Data

The neutron-photon transport calculations and nuclear responses evaluations have been performed with the Monte Carlo code McDeLicious [5,6]. This is a further enhancement to the McDeLi code [2] with the new ability to sample the neutron and photon generation of the D-Li source from tabulated ^{6,7}Li(d,xn) and (d,xγ) double-differential cross section data developed in the framework of KEP Task TF51-EU. The McDeLicious approach was validated against measured energy-angular yields from the thick lithium target bombarded by deuterons with energies up to 40 MeV (see Task report TF51-EU).

Two sources of evaluated neutron cross-section data were used for the neutron-photon transport calculations and the nuclear responses: the LANL-150 (14 elements, up to 150 MeV) [9] and the INPE/FZK data evaluations (cross sections for 10 elements up to 50 MeV neutron energy) [8].

The calculations have shown differences of no more than 10% in the average nuclear responses due to the different cross-section data evaluations. Validation analyses of experimental benchmarks are presently underway with the objective to check and improve the data evaluations.

The computational model used for neutronic analyses takes into account the essential features of the IFMIF source and the test modules, i.e., geometry configuration and material specifications. As an example, Fig. 3 displays a sketch of the model used in the analyses for the full performance stage with two vertically orientated deuteron beams. It comprises the lithium target (a 26×2.5×20 cm^3 box filled with Li at density 0.512 g/cm^3), the Eurofer target back plate (26×0.18×20 cm^3), the high flux test module (20×5×5 cm^3 box, filled with Eurofer at 80% of nominal density) and reflector slabs around the HFTM (10 cm thick Eurofer plates at reduced density to account for cooling channels).

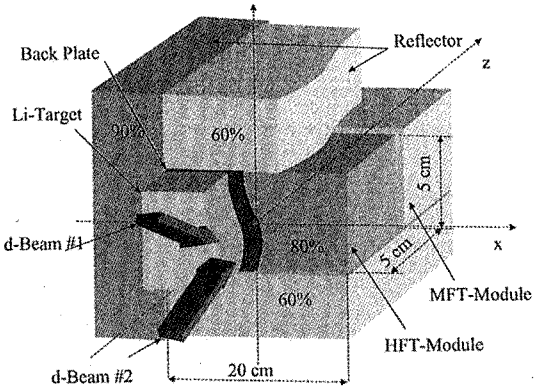


Fig. 3 Geometry and material distribution model for the Monte Carlo simulation: X-axis -horizontal direction; Y-axis - vertical direction; Z-axis - forward direction away from the target.

To get three-dimensional distributions of nuclear responses, the space of the HFTM and the surrounding reflector was divided into a regular lattice with small cubic segments of size 0.5×0.5×0.5 cm^3. The neutron and photon fluxes, nuclear heating, dpa, and gas production rates were calculated as 3-d arrays, each quantity being averaged over the volume of the small cubic segment.

(5) Results of the Neutronics Re-evaluation

The results of the calculations are summarized in Table 1. They show the main irradiation parameters and the nuclear responses calculated for Eurofer and vanadium with different deuteron beam profiles and currents. There are maximum and minimum values which correspond to the centre points at the front and back surfaces of the High Flux Test Module, respectively. The results generally show that the irradiation parameters and responses are proportional to the beam current density. The highest values of the irradiation parameters, which the lithium target back plate made of Eurofer must withstand, are also included in Table 1.

For the characterization of the irradiation volume, the space available for displacement damage exceeding a specified level was assessed. The data presented in Table 1 show that the irradiation volume available for the minimum displacement damage level of ≥20 dpa/fpy depends on both the current and density of the deuteron beam. It is noted that a relatively higher damage accumulation can be achieved in the Starting Stage I at the expense of the available irradiation volume with the reduced beam footprint configuration (Option 3).

As mentioned above, the spatial distributions were calculated for all neutron responses and stored as a 3-dimensional array. For a better understanding these data were visualized in the form of 2-d contour plots on three planes of the Cartesian coordinate system (X-axis: horizontal direction, Y – axis: vertical direction, Z – axis: deuteron downstream beam direction, see Fig. 3 and inserts in Figs. 4-9). Figs. 4 – 9 display contour maps for the dpa rate in Eurofer for the different deuteron beam/footprint configurations considered. The contour maps allow assessment of the size and shape of the 3-d irradiation volume which is available for a specified damage displacement level. To achieve 20 dpa/fpy level, for example, 4×6×2 cm^3 and 19×5×1.5 cm^3 rectangular test modules should be considered for the Starting Stage I (4×5 cm^2 beam footprint, 50 mA current) and Starting Stage II (20×5 cm^2; beam footprint, 125 mA current), respectively.

For the Full Performance Stage the two options for the beam orientations in vertical and horizontal planes were investigated. As shown in Figs. 8 and 9 and Table 1, the resulting differences are comparatively small. The reason is supposed to be the rather small declination angle, which means

that both options are geometrically close to the configuration, with one beam impinging perpendicularly on the target surface.

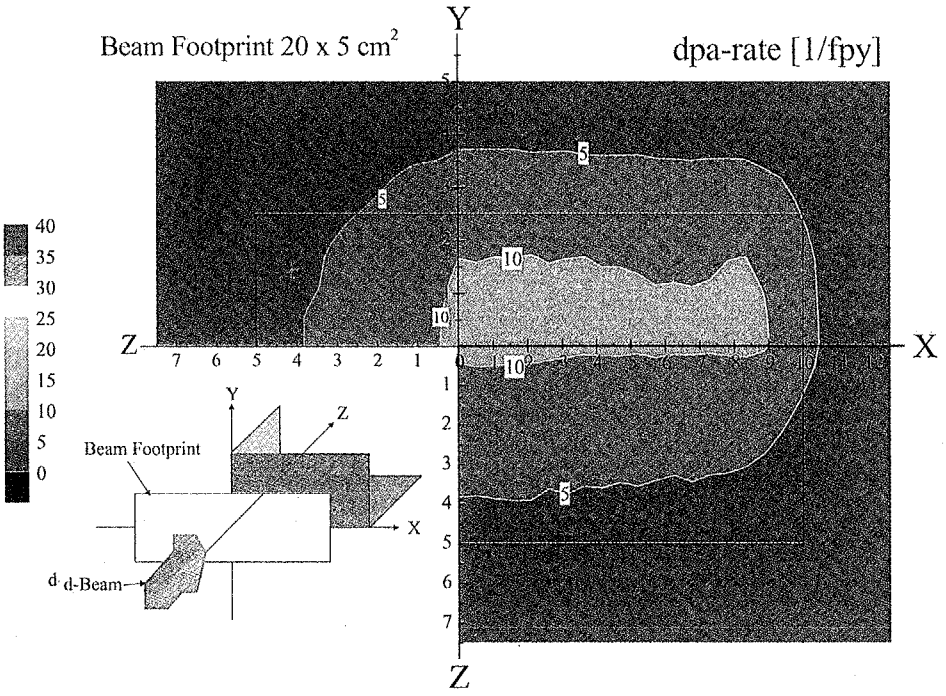


Fig. 4 Spatial distribution of the displacement damage rate induced in Eurofer for the case of one 50 mA d-beam with footprint 20×5 cm² (deployment Starting Stage I, Option 1).

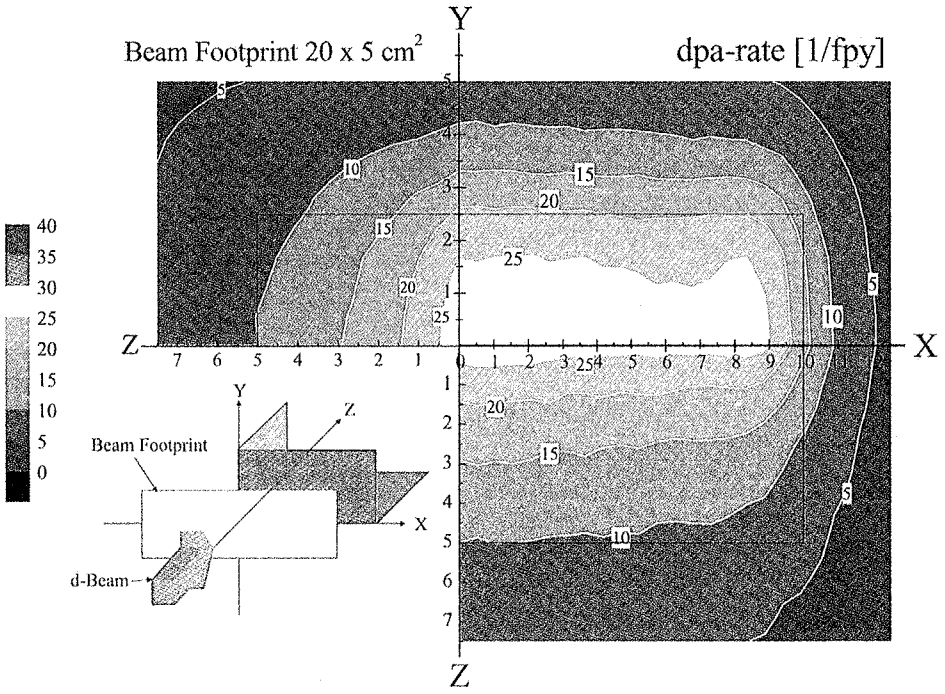


Fig. 5 Spatial distribution of the displacement damage rate induced in Eurofer for the case of one 125 mA d-beam with footprint 20 × 5 cm² (deployment Starting Stage II).

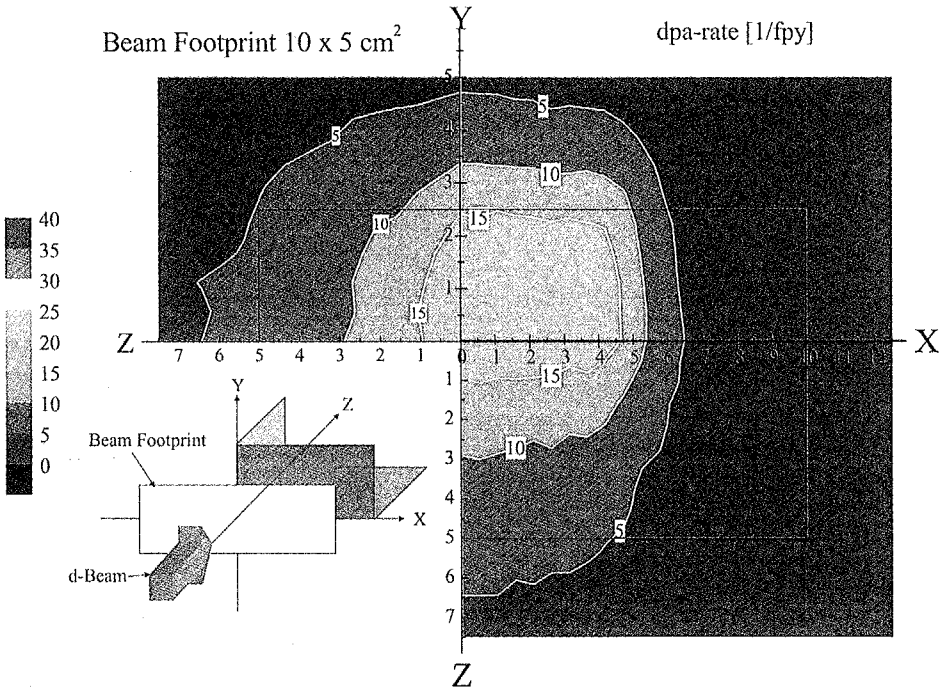


Fig. 6 Spatial distribution of the displacement damage rate induced in Eurofer for the case of one 50 mA d-beam with footprint 10×5 cm².(deployment Starting Stage I, Option 2).

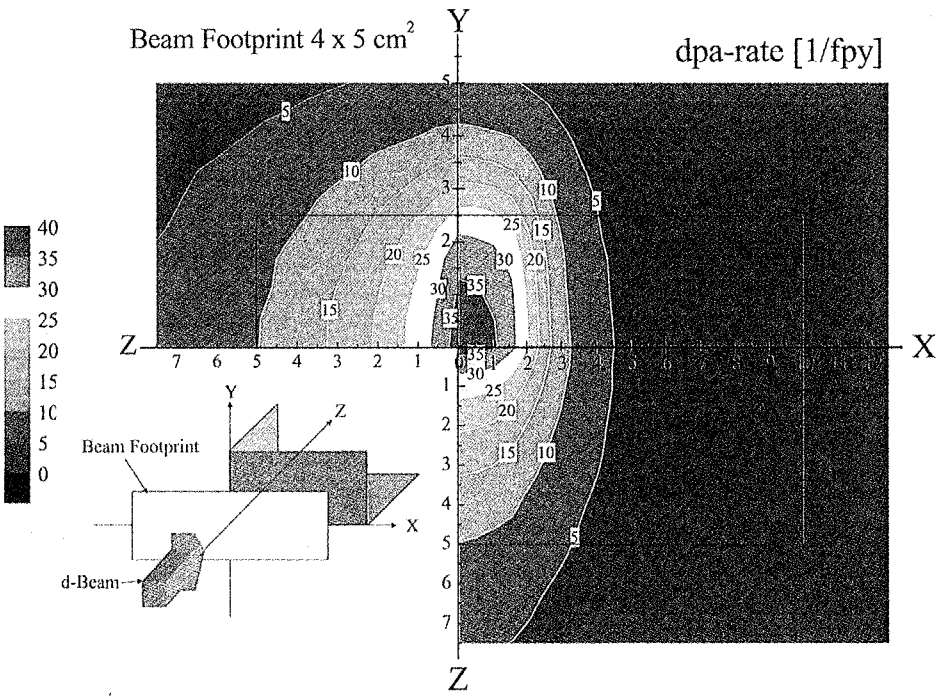


Fig. 7 Spatial distribution of the displacement damage rate induced in Eurofer for the case of one 50 mA d-beam with footprint 4 × 5 cm² (deployment Starting Stage I, Option 3).

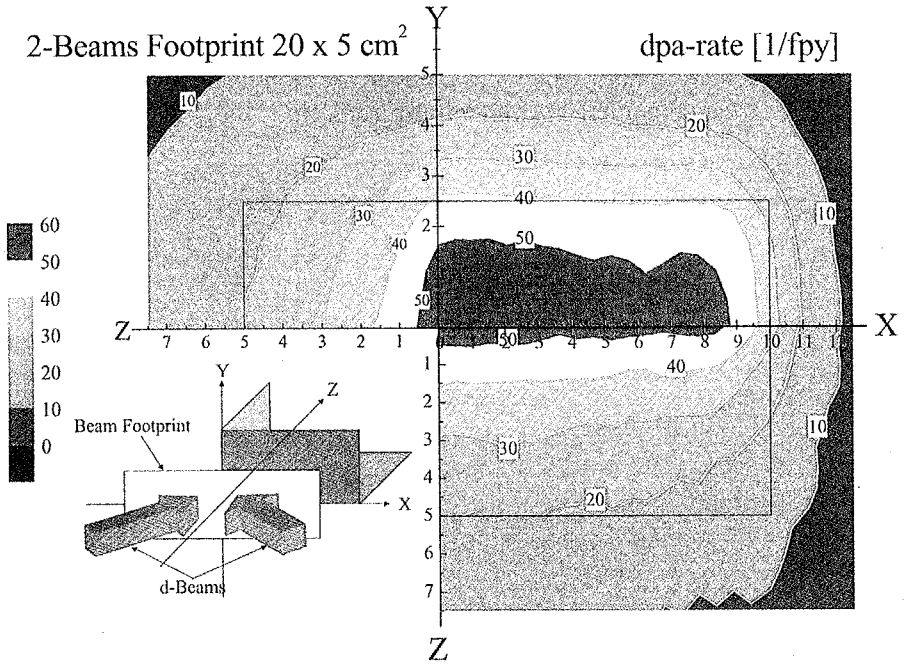


Fig. 8 Spatial distribution of the displacement damage rate induced in Eurofer for the case of two 125 mA d-beams (horizontal declination) with a footprint 20 × 5 cm² (full performance stage).

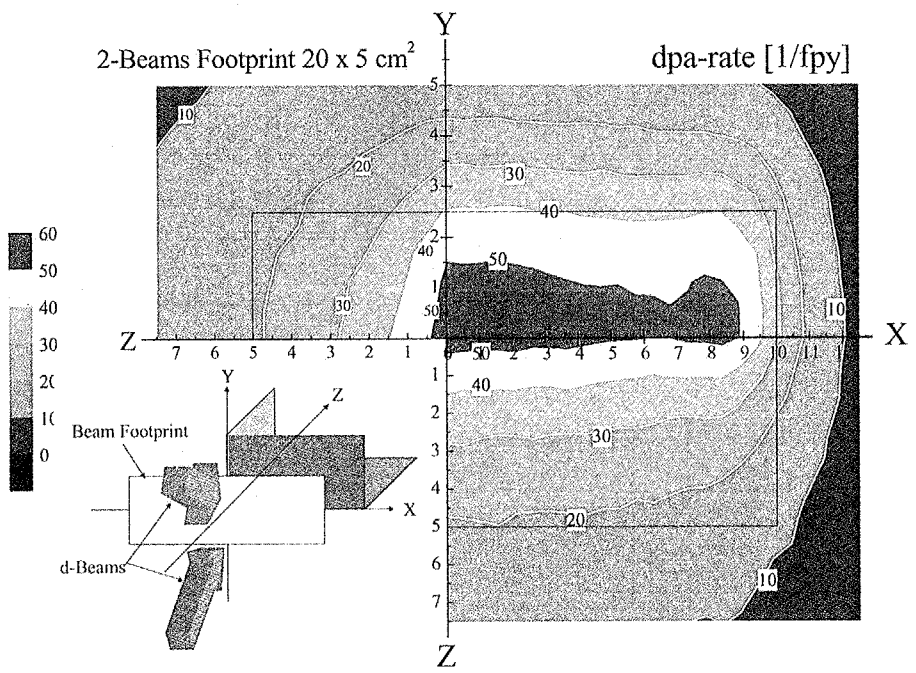


Fig. 9 Spatial distribution of the displacement damage rate induced in Eurofer for the case of two 125 mA d-beams (vertical declination) with a footprint 20 × 5 cm² (full performance stage).

In addition to the absolute values of the nuclear responses in the test module, their spatial gradients are of great importance. For example, Fig. 10 shows the dependence of the displacement damage rate versus the horizontal, the vertical and the beam downstream directions. It is seen that the relative gradient near the test module edges is practically independent of the beam footprint sizes: along the beam and vertical directions it amounts to 25%/cm; along the horizontal direction it is around 50%/cm.

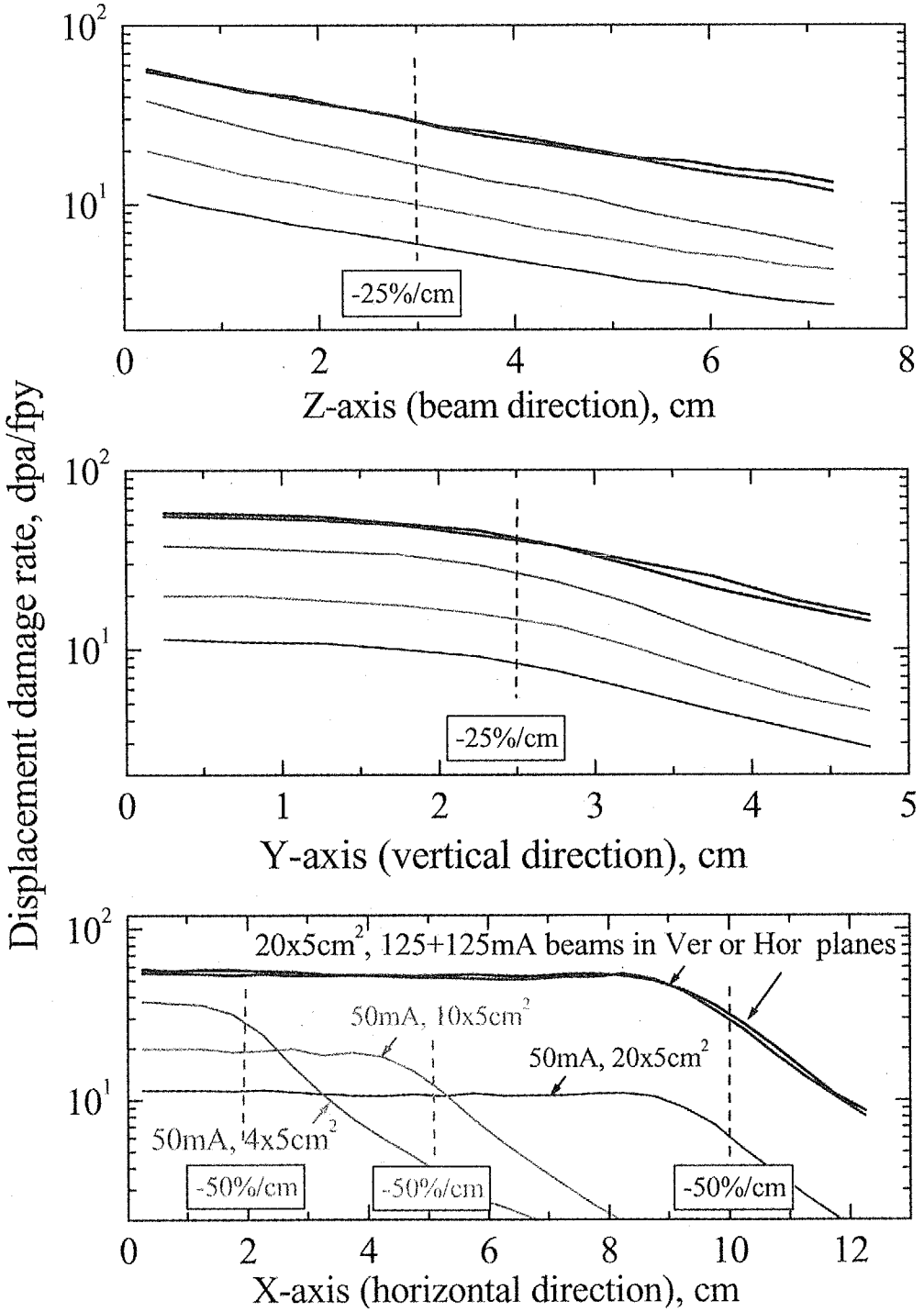


Fig. 10 Displacement damage rate produced in Eurofer as a function of three coordinates for different beam currents and footprints. Vertical dashed lines indicate the position of the corresponding HFTM box edges, values in the frames – relative gradients near these points.

(6) Summary and Conclusions

The energy deposition, the neutron and photon flux, the gas and heat production, and the displacement damage rates have been reevaluated for the IFMIF high flux region for the full performance operation and the intermediate deployment stages. Variations of the beam current, the number of beams, the beam orientation, and a neutron reflector around the HFTM were considered. The three-dimensional spatial distributions provided for the nuclear responses in the HFTM allow assessment of the actual shape and the irradiation volume in which specified dpa rates and gradients can be reached.

The analysis has shown that an accelerated displacement damage accumulation during the starting stages is achievable with a higher beam current density or reduced beam footprints. The latter option, however, results in a reduced irradiation volume. The horizontal and the vertical orientations of the deuteron beams do not show significantly different result for the nuclear responses calculated for the HFTM. This was shown for the full performance operation of IFMIF.

References

[1] E. Daum, U. Fischer, A.Yu. Konobeev et al., Neutronics of the High Flux Test Region of the International Fusion Materials Irradiation Facility (IFMIF), Report FZKA 5868, Karlsruhe, 1997.

[2] P.P.H. Wilson, Neutronics of the IFMIF neutron source: Development and Analysis, Report FZKA 6218, Karlsruhe 1999.

[3] E. Daum, K. Ehrlich, U. Fischer et al, FZK Contribution to IFMIF Test Faciltity Optimisation and Cost Reduction, Forschungszentrum Karlsruhe, Interner Bericht, Mai 2000.

[4] V. Heinzel, B. Dolensky, U. Fischer et al., Design Optimization of the IFMIF High Flux Test Module, 10th International Conference on Fusion Reactor Materials (Baden-Baden, October 2001).

[5] S.P. Simakov, U. Fischer, U. von Möllendorff et al., Advanced Monte Carlo procedure for the IFMIF d-Li neutron source term based on evaluated cross section data, 10th International Conference on Fusion Reactor Materials (Baden-Baden, October 2001).

[6] S.P. Simakov, U. Fischer et al., International Fusion Materials Irradiation Facility (IFMIF): Neutron Source Term and Neutronics Analyses of the High Flux Test Module, Report FZKA 6743, Karlsruhe, 2002.

[7] A.Yu. Konobeev, Yu.A. Korovin et al., Development of methods for calculation of n+Li and d+Li cross sections for energies up to 50 MeV, Nucl. Sci. and Eng. 139(2001)1-23.

[8] Yu.A. Korovin, A.Yu. Konobeev, P.E. Pereslavtsev et al., Evaluated nuclear data files for accelerator driven systems and other intermediate and high energy applications. Nucl. Instr. and Meth., A463(2001)544.

[9] M.B. Chadwick, P.G. Young et al., Cross-Section Evaluations to 150 MeV for Accelerator-Driven Systems and Implementation in MCNPX. Nucl. Sci. Eng., 131(1999)293.

[10] L. Bruhwiler, Non-uniform IFMIF beam profile, Northrop-Grumman Corp., private communication, May 1996.

3.3.22 TF62-JA : Review of the Concept for Materials Testing in IFMIF

(1) Brief Task Description

In the CDA phase of IFMIF it was planned to operate with current of 250 mA from the beginning. However, the IFMIF plan is now for construction in two stages (125 mA→250 mA), and therefore the irradiation plan must be reviewed. The main purpose of stage one operation is the performance confirmation of selected structural materials for ITER test blanket modules. In the second stage, the focus will shift to the acquisition of engineering data for design and licensing of a demonstration plant for power generation. The irradiation matrix to achieve these purposes was examined. Since it would take much too long to acquire the necessary data using only IFMIF, the model used in planning is based on using fission reactor irradiations in combination with IFMIF.

Contributors

Name	Party	Institute	E-mail address
T. Yutani	Japan	JAERI	yutani@ifmif.tokai.jaeri.go.jp
H. Nakamura	Japan	JAERI	nakamurh@fusion.naka.jaeri.go.jp
K. Shiba	Japan	JAERI	shiba@jmpdsun.tokai.jaeri.go.jp

(2) Introduction

In the CDA phase of IFMIF, materials irradiation tests were planned assuming that IFMIF would be operated with current of 250 mA from the beginning [1]. The plan now is for IFMIF to be constructed in two stages (125 mA→250 mA) [2]. Maximum efficiency in use of the irradiation tests, with limited volume and operation time, requires a thorough review of the purposes of the tests and the irradiation matrices to meet these needs.

(3) Purpose of Irradiation Tests in IFMIF

The development of power generation blankets and materials for fusion systems must be accelerated to match the fast track approach proposed to demonstrate the feasibility of fusion. A near-term need is to test several test blanket modules in ITER. The purpose of the first ITER tests is the demonstration of the power generation and tritium breeding in the fusion reactor environment. In the next steps, high performance blanket modules will be tested to demonstrate that fusion power will be an economically attractive energy source. Figure 1 shows the fusion blanket/materials development plan being followed in Japan. IFMIF construction is planned in two stages (125 mA→250 mA), with first stage operation scheduled to start in 2016 and the second stage in 2019.

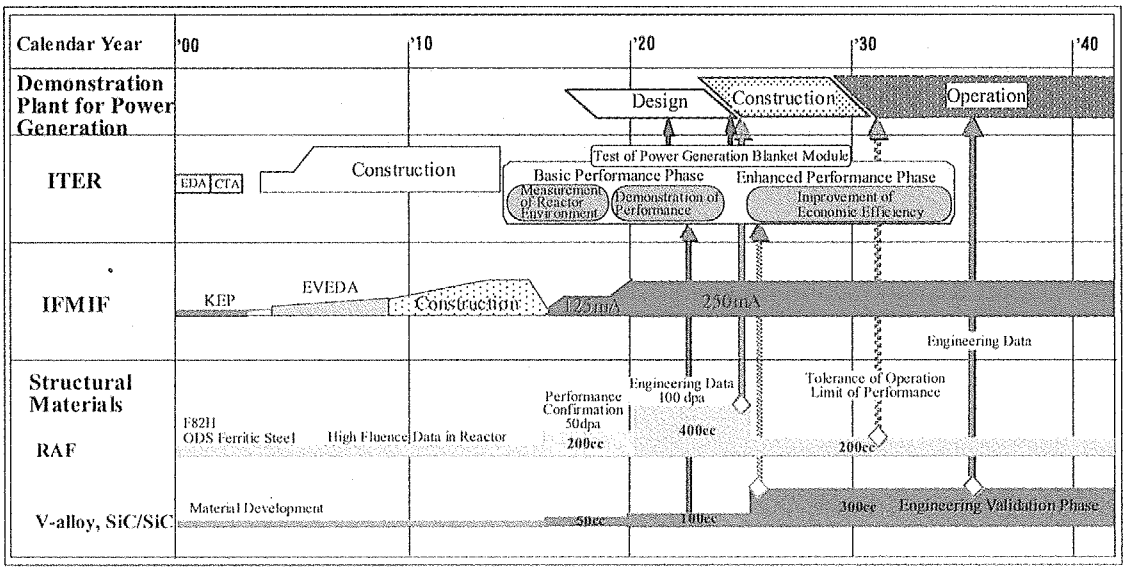


Fig. 1 Fusion blanket/material development plan in Japan.

Assuming that the deuteron beam intensity in first stage operation is kept the same as in the second stage, then the irradiation volume with flux above 20 dpa/fpy is about a half that for full operation. Fluence of at least 50dpa will be achieved during the first stage, even though IFMIF may not operate smoothly due to early failures and the installation of second stage equipment. The purposes of irradiation tests planned for the first stage are as follows:

1) Performance confirmation of selected structural materials for test blanket modules to be tested in ITER.
2) Development of advanced structural materials for the DEMO reactor.
3) Study of high fluence irradiation effects produced in materials by fusion neutrons.
4) Measurement of tritium release behavior of ceramic breeder materials.

Purpose 1) is the most important, because the structural materials for test blanket modules are likely to become the leading candidate for the power generation demonstration plant. Also, the same materials will be irradiated to fluences over 100 dpa in the second stage of IFMIF for acquisition of engineering data. Microstructural observations, tensile tests, impact tests, fatigue tests, fracture toughness tests, fatigue crack growth tests and creep tests (i.e. profile measurements on pressurized tube creep specimens) will be conducted in post irradiation examination (PIE). Also, in-situ creep/fatigue tests in the medium flux region are important. Low activation ferritic steels, vanadium alloys and SiC/SiC composite materials are under development as promising candidates. Low activation ferritic steels with oxide dispersion strengthening are the leading candidate for the test blanket modules, selected on the basis of the results of irradiation tests using fission reactors.

Vanadium alloys and SiC/SiC composite materials are advanced materials that have higher strength than ferritic steels at high temperatures. The performance blanket modules made of these materials need to be tested in the latter phase of ITER, because their development is important to make fusion reactor power economically competitive . To prepare for this use in ITER test modules, vanadium alloys and SiC/SiC composite materials need to be irradiated in the first stage of IFMIF operation to confirm their performance.

In comparison with fission reactor irradiation, the helium production rate and the primary knock-on atom energy are higher in IFMIF irradiations. The effect of these differences on the swelling, mechanical properties and microstructural evolution needs to be quantitatively determined. The effects of irradiation on materials have been examined by fission reactors, accelerated particle beams, etc, but it is necessary to have a more quantitative understanding of the effects. That knowledge base will be used for modeling irradiation damage and microstructural evolution to establish the interrelationships between the 14 MeV fusion neutron irradiation and fission reactor irradiation. Therefore, purpose 3) is also important.

The irradiation behavior of lithium-based ceramic breeder materials such as Li_2O has been investigated using fission reactors, e.g. the BEATRIX-II collaborative tests. The results demonstrated good tritium release performance up to 5% Li burnup. However, tritium release performance needs to be evaluated in higher burnup ranges by irradiation in the medium flux region of IFMIF, to confirm that the materials can be used in the power generation demonstration plant.

The irradiation volume with flux over 20 dpa/fpy in the second stage of IFMIF operation will be about 500 cc. The purposes of irradiation tests in stage two IFMIF are as follows.

1) Acquisition of engineering data for design and licensing of a demonstration power generation plant.
2) Study of high fluence irradiation effects produced in materials by fusion neutrons.
3) Blanket element performance validation tests (tritium release behavior, tritium breeding performance, compatibility of breeder/neutron multiplier /coolant, etc.).

The acquisition of engineering data is the main purpose of full performance IFMIF operation. The emphasis will be on low activation ferritic steels and the advanced materials, vanadium alloys and

SiC/SiC composite materials. The low activation ferritic steels involved will include some of the specimens from purpose 1) of the first stage, which will continue to be irradiated up to fluences of 80-100 dpa. The irradiation volume for advanced materials will be about 100 cc at the start of second stage, and increase to about 300 cc several years later. Also the research of purpose 2) will be continued to support material developments.

The tritium breeding rate increases, as neutron energy decreases, and it is important to increase the neutron flux for improvement in tritium production rates in IFMIF experiments. The reaction ^{9}Be(n, 2n) with the high-energy neutrons (over 2.5 MeV) is used to multiply the neutron numbers. Spectral tailoring by moderator materials is investigated in EU KEP tasks to increase the number of low energy neutrons in the medium flux region for the irradiation of ceramics breeder materials. The neutron spectrum in the low neutron flux region may also be modified to be similar to the environment of a fusion blanket by using moderators. With those changes, these regions will be used for blanket element irradiation tests to verify behavior before blanket designs are finalized. Other blanket element irradiation tests may involve tests for tritium release behavior, tritium breeding performance, compatibility of breeder/neutron multiplier /coolant, etc.

(4) Irradiation Test Matrix

Irradiation tests of structural materials will be performed in the IFMIF high flux region, with a volume of 500 cc, using a helium-cooled high flux test module. Small specimens are used to make maximum efficient use of this limited volume. To achieve the purposes that are mentioned in paragraph (3), properties of the structural materials that must be evaluated in the high flux region are as follows.

1) Tensile properties
2) Fatigue properties (fatigue life)
3) Fracture toughness
4) Fatigue crack growth properties (fatigue crack growth rate)
5) Impact properties (ductile to brittle transition temperature; DBTT)
6) Creep under irradiation
7) Microstructure and swelling

The irradiation matrix for one condition of one structural material is shown in Table 1, to acquire accurate engineering data related to the needed properties. Because data from small specimens vary widely, the multiplicity of each specimen is comparatively large. The volumes needed for each specimen set include the space occupied by specimen containers, and are taken from the CDA report [1]. In the CDA phase, the irradiation matrix was planned on the assumption that a NaK-cooled high flux test module might be used [1, 3]. This module has three chambers, each thermally controlled at a different temperature by a separate liquid metal (NaK) loop. Specimens were encapsulated in packets that were stacked in the chambers. Each packet contains one to six specimens of the same type, except for TEM disk packets (which contained up to 80 specimens). The main problem with this module was that irradiation at temperatures over 650°C was difficult. To solve this problem, a helium-cooled high flux test module that may be used for irradiation at temperature from 250 to 1000°C is under development. The helium-cooled high flux test module consists of a number of rigs containing the encapsulated specimens. The specimen will be kept at constant temperature by electric heaters attached to the capsules. In this stage, available volumes are unknown, because methods for encapsulating specimens are under examination. However, it is necessary to know how many specimens can be installed in the helium-cooled high flux test module. Therefore, volumes for the case of the NaK-cooled high flux test module are used in this matrix development. The volume occupied by specimens for each irradiation condition is 37.38 cc. This volume increases by about 50% to account for space for coolant. The result is that nine irradiation conditions can be simultaneously included in the 500 cc high flux region.

Table 1 Irradiation matrix for one condition of one structural material.

Specimen	Multiplicity	Occupied volume* (cc)	Comment
Tensile	16	4.64	Duplicate specimens tested at different temperatures and strain rates
Push-pull fatigue	16	9.28	Duplicate or triplicate specimens tested at different strain ranges
Fracture toughness	8	10.8	Tested at different temperatures and strain rates
Crack growth	8	6.3	Duplicate specimens tested at different temperatures
Charpy	6	3.08	Tested at 6 temperatures
Creep	8	2.88	Specimens loaded to 8 different gas pressures
TEM disk	10	0.4	
Total		37.38	

* Include space occupied by specimen container.

The present candidate materials are the low activation ferritic steels, the vanadium alloys and SiC/SiC composite materials. Irradiation conditions needed for the study of low activation ferritic steels are shown in Table 2. The steel types are a low activation ferritic steel such as F82H and an oxide dispersion strengthened steel. Also, welded/joined regions as well as base material need to be included because they seem to have different properties. The irradiation temperatures are 300, 450 and 550°C for low activation ferritic steel, and 450 and 550°C (or a higher temperature) for oxide dispersion strengthened steel. If a minimum of three dose levels are evaluated, then there are 30 irradiation conditions. In addition, each vanadium alloy and each SiC/SiC composite material may need more than 27 irradiation conditions (3 materials, 3 temperature levels and 3 dose levels).

Table 2 Irradiation conditions for low activation ferritic steels.

Material*	Temperature levels**	Dose levels	Total
LAF1	3	3	9
LAF2	3	3	9
ODS1	2	3	6
ODS2	2	3	6
Total			30

* LAF1 is low activation ferritic steel base metal, LAF2 is weldments of low activation ferritic steels, ODS1 is oxide dispersion strengthened steel base metal, and ODS2 is welded/joined sections of oxide dispersion strengthened steels.
** LAF1 and LAF2 are irradiated at 300, 450 and 550 °C, and ODS1 and ODS2 are irradiated at 450 and 550 °C.

Even if the maximum target dose is only 100 dpa, more than 30 years of IFMIF operation are necessary to satisfy all the above-mentioned irradiation conditions. This seems to be an unrealistic plan. Further reduction in the irradiation matrix and further miniaturization of small specimens may be necessary to meet the needs of a fast track program. To reduce the number of tests and conditions, the results of models based on irradiation data from fission reactor and accelerator particle beam experiments can be used to guide the development of irradiation matrices. These models and non-IFMIF data may also be used to reduce the number of candidate materials to be tested in IFMIF.

(5) Summary

With the change in the IFMIF plan to stage construction (125 mA→250 mA), review of test purposes and irradiation matrices were needed, to assure efficient use of the limited volume in

irradiation tests and limits on operating time.

Several test blanket modules need to be tested in ITER, to demonstrate the power generation and tritium breeding in a fusion reactor environment and to show that fusion energy will be economically attractive. The main purpose of irradiation tests in IFMIF stage one operation is to confirm the performance of selected structural materials for the ITER test blanket modules. In the second stage of IFMIF operation, the primary goal is the acquisition of engineering data for design and licensing of a demonstration plant for fusion power generation. Also, the study of the effects of high fluence fusion neutron irradiation on fusion materials is important.

An irradiation matrix to achieve these goals is examined. More than 30 years are necessary to acquire all data for three candidate material systems (low activation ferrite steels, vanadium alloys and SiC/SiC composite materials) based only on use of IFMIF. Because this seems to be unrealistic, the use of models based on fission reactor experiments, further miniaturization of specimens, and other measures are necessary to guide the most efficient use of the valuable space in IFMIF.

References

[1] M. Martone (Ed.), "IFMIF International Fusion Materials Irradiation Facility, Conceptual Design Activity, Final Report, IFMIF CDA TEAM", ENEA Frascati, Report ENEA-RT/ERG/FUS/96-11 (1996).

[2] M. Ida, H. Nakamura, M. Sugimoto, T. Yutani, H. Takeuchi (Ed.), "International Fusion Materials Irradiation Facility Conceptual Design Activity, Reduced Cost Report, A Supplement to the CDA by the IFMIF Team", JAERI-Tech 2000-014 (2000).

[3] Proceedings of the IEA-Technical Workshop on the Test Cell System for an International Fusion Materials Irradiation Facility, Karlsruhe, July 3-6, 1995; Editors: A. Moeslang, R. Lindau, FZK-Bericht 5633, (September 1995).

3.3.23 TF63-JA : Small Specimen Test Technology - Development of Fracture Toughness Testing with Miniaturized Specimens

(1) Brief Task Description

The objective of this task is to develop small specimen test technology to evaluate fracture toughness of several millimeter thick plates of structural materials, as well as to maximize the use of limited irradiation volume in IFMIF. Three-point bending (3PB) specimens with 7.0, 5.0 and 3.3 mm thickness and compact tension (CT) specimens with 25.4 (1CT), 12.7 (1/2CT) and 6.35 mm (1/4CT) thickness were prepared from a Japanese low activation ferritic steel, JLF-1. Elastic-plastic fracture toughness tests by the unloading compliance method at room temperature and plane-strain fracture toughness tests at 77 K were conducted in general accordance with ASTM standards, together with plane-strain FEM analysis. Since each of the 3PB and CT specimens has advantages, emphasis is placed on the reliable fracture toughness evaluation including the determination of the actual J-value for crack initiation for the 3PB specimens and on the effect of specimen size on fracture toughness for the CT specimens.

Contributors for 3PB Specimens

Name	Party	Institute	E-mail address
Hiroaki Kurishita	Japan	Tohoku University	kurishi@imr.tohoku.ac.jp
Takuya Yamamoto	Japan	Tohoku University, Now, UCSB	yamataku@engineering.ucsb.edu
Takuya Nagasaka	Japan	NIFS	nagasaka@nifs.ac.jp
Arata Nishimura	Japan	NIFS	nishi-a@LHD.nifs.ac.jp
Takeo Muroga	Japan	NIFS	muroga@ms.nifs.ac.jp
Shiro Jitsukawa	Japan	JAERI	jitsukawa@ifmif.tokai.jaeri.go.jp

Contributors for CT Specimens

Akihiko Kimura	Japan	Kyoto University	kimura@iae.kyoto-u.ac.jp
Yudai Kato	Japan	Kyoto University	katoh@iae.kyoto-u.ac.jp
Kazunori Morishita	Japan	Kyoto University	morishita@iae.kyoto-u.ac.jp
Ryuta Kasada	Japan	Kyoto University	r-kasada@iae.kyoto-u.ac.jp
Hirotsugu Kubo	Japan	Kyoto University	h-kubo@iae.kyoto-u.ac.jp
Minoru Narui	Japan	Tohoku University	narui@imr.tohoku.ac.jp
Yutaka Kohno	Japan	Muroran Inst. Technology	kohno@mmm.muroran-it.ac.jp
Hisashi Serizawa	Japan	Osaka University	serizawa@jwri.osaka-u.ac.jp

(2) Introduction

Fracture toughness is a key engineering property of structural materials. The first wall and blanket of a fusion reactor are thin wall structures, several millimeters thick. Furthermore, irradiation volumes available in IFMIF [1, 2] are limited to approximately 500 cc for displacement damage above 20 dpa/year. This volume of 500 cc corresponds to that occupied by only six standard compact tension (CT) specimens or two standard 3-point bending (3PB) specimens for fracture toughness testing. Overcoming these limitations requires miniaturization of fracture toughness test specimens.

Previous specimen miniaturization for fracture toughness testing has mainly concentrated on the CT specimen, because the load-line displacement can be correctly measured with a clip gage for the CT specimen, but not for the 3PB specimen. J-integral values obtained from the 3PB specimen might include the effect of local deformation in regions of the specimen in contact with loading and supporting pins, and thus would be overestimated. However, as shown in Table 1, the 3PB specimen has many advantages over the CT specimen. Therefore, it is desirable to develop test techniques for reliable evaluation of fracture toughness using miniaturized 3PB specimens.

Table 1 Comparison of 3PB and CT specimens.

	3PB specimen	CT specimen
Data precision	fair	good
Data availability	fair	good
Specimen miniaturization	good	fair
Specimen preparation	good	fair
Specimen setting	good	fair
Control of testing condition	good	fair

Another concern with the evaluation of fracture toughness using miniaturized specimens is loss of validity of the fracture toughness value because of the decrease in specimen thickness. Therefore, it must be determined how the fracture toughness depends on specimen thickness.

In this study 3PB miniaturized specimens with thickness 7.0, 5.0 and 3.3 mm were tested using J and parameters K for the opening mode (Mode I) loading. Tests were conducted at room temperature and 77 K. The data were combined with plane-strain FEM analysis, aiming at developing miniaturized test techniques for reliable fracture toughness evaluation. For full-sized and sub-sized CT specimens with 25.4 (1CT), 12.7 (1/2CT) and 6.35 mm (1/4CT) thickness, the elastic-plastic fracture toughness tests are conducted at room temperature to evaluate the effect of specimen size on J-value. The Japanese low activation ferritic steel JLF-1 [3] was used because it is a candidate first wall and fusion blanket material and fracture toughness data on this alloy is limited [4].

(3) Experimental

(3.1) Material

The reduced activation ferritic steel JLF-1 was used for this research. A 300 kg heat of JLF-1 was produced, as 30 mm thick plate with composition, in weight percent, 0.098 C, 0.05 Si, 0.5 Mn, 0.002 P, 0.004 S, 8.92 Cr, 2.00 W, 0.20 V, 0.098 Ta, 0.0149 N, 0.0001 B, and balance iron. The plate was normalized at 1323 K for 1 hr (AC) and tempered at 1053 K for 1 hr (AC). The plate segments were provided to each research group, including Kyoto University, Tohoku University and NIFS. Two plates were TIG-welded with JLF-1 weld filler metal.

(3.2) Specimens and test methods

(3.2.1) 3PB specimen

Four types of 3PB specimens and one type of tensile specimens were machined from the plate of JLF-1 base metal. Figure 1 shows the configuration of the 3PB specimens having the following dimensions, where B is the thickness, W is the width and L is the length: 7 mm^B x 10 mm^W x 45 mm^L, 5 mm^B x 5 mm^W x 25 mm^L, 3.3 mm^B x 5 mm^W x 25 mm^L, and 3.3 mm^B x 3.3 mm^W x 18.3 mm^L. The original crack length, a_0, was controlled between 0.50W and 0.58W and the side grooves to be 0.4B to increase the constraint for the high fracture toughness of JLF-1 [4]. The dimensions of tensile specimens are 0.5 mm^B x 4 mm^W x 16 mm^L with a gage section of 0.5 mm^B x 1.2 mm^W x 5 mm^L.

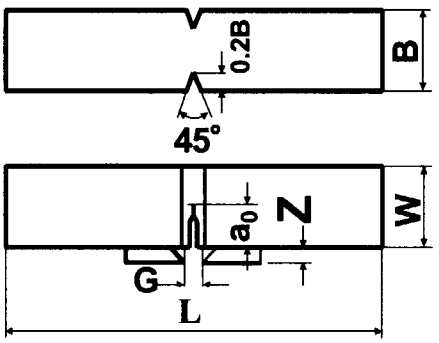


Fig. 1 3PB specimen configuration.

A fatigue testing machine (Shimadzu Servopulser with 50-kN capacity and 5-kN shear-type load cell) was installed in the Oarai Irradiation Experimental Facility of IMR at Tohoku University and used to introduce a well-defined crack and perform fracture toughness tests. For pre-cracking, control of stress intensify factor, ΔK, was most effective in introducing a well-defined fatigue pre-crack, where ΔK was controlled from the initial value of 20 $MPam^{1/2}$ to the final value of approximately 12 $MPam^{1/2}$. A temperature control bath, 3PB test fixtures with different spans, and miniature clip gages with working

ranges of 2.0 and 1.5 mm were designed to perform fracture toughness tests at and below room temperature. Figure 2 shows a photo of a test fixture with a 3PB specimen and a clip gage. In the figure, the clip gage was seated on an attachable knife edge (Z = 1 and G = 2 mm) that had been cemented to the notched side. However, such an attached knife edge would not be safe for higher-temperature irradiation because of loss of adhesion of the cement. Therefore, for the 3PB specimens with 10 and 5 mm width, the knife edge was machined on the notched side of each specimen (Z = 0 in Fig. 1).

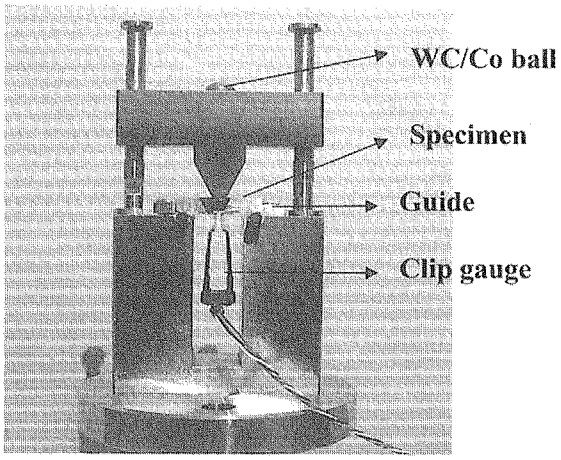


Fig. 2 Test fixture for 3PB specimen.

Elastic-plastic fracture toughness tests by the single specimen method at room temperature and plane strain fracture toughness tests at 77 K were conducted in general accordance with ASTM standards [5, 6] at a cross-head speed of 0.013 mm/s and in some cases at 13 mm/s. A program for the unloading compliance method for testing the 3PB specimens was developed and used. Tested specimens were heat tinted and fractured at 77 K to measure the initial and final crack lengths. Fracture surface observations showed that fractures occurred mainly in the plane-strain condition, even at room temperature. Therefore, two dimensional plane-strain FEM analyses with 1274 8-node elements was used, assuming that the crack-tip radius is 1 μm and the pre-crack does not grow. Tensile tests were conducted at room temperature and 77 K at initial strain rates of 1×10^{-3} and $10\ s^{-1}$.

(3.2.2) CT specimens

Specimen size effects on the fracture toughness were investigated using the following geometries of CT specimens, shown in Fig. 3:

a) 1CT-specimen (W=50.8 mm, B=25.4 mm)
b) 1/2t-1CT-specimen (W=50.8 mm, B=12.5 mm)
c) 1/2CT-specimen (W=25.4 mm, B=12.5 mm)
d) 1/4CT-specimen (W=12.7 mm, B=6 mm)

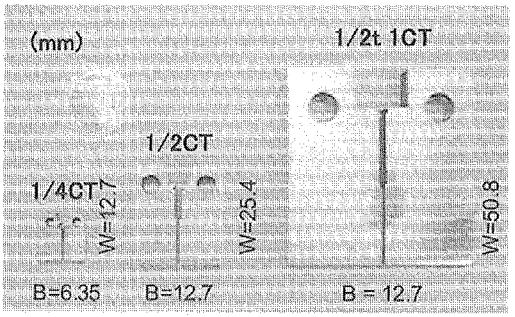


Fig. 3 CT specimens for fracture toughness measurement with different geometries.

The ASTM standard prescribes geometries for CT specimens, which are summarized in Table 2 with the main geometries of the CT specimens. All specimens selected in this work satisfied the requirements.

Table 2 Requirements for the geometry of fracture toughness specimens and the judgment for each size of specimen.

Specimen Size	W	B	a_0	Side Groove	Judgment
ASTM E1820-99a	2=< W/B =< 4		0.45W-0.70W	<0.25B	
1CT	50.8	25.4	29.60	0.2B	OK
1/2t 1CT	50.8	12.7	29.60	0.2B	OK
1/2CT	25.4	12.7	14.70	0.2B	OK
1/4CT	12.7	6.35	7.85	0.2B	OK

Prior to the fracture toughness testing, fatigue pre-cracks were introduced in all specimens until the final K value was 21.7, 21.4 and 20.1 MPa$\sqrt{m}$ for 1CT, 1/2CT and 1/4CT specimens, respectively.

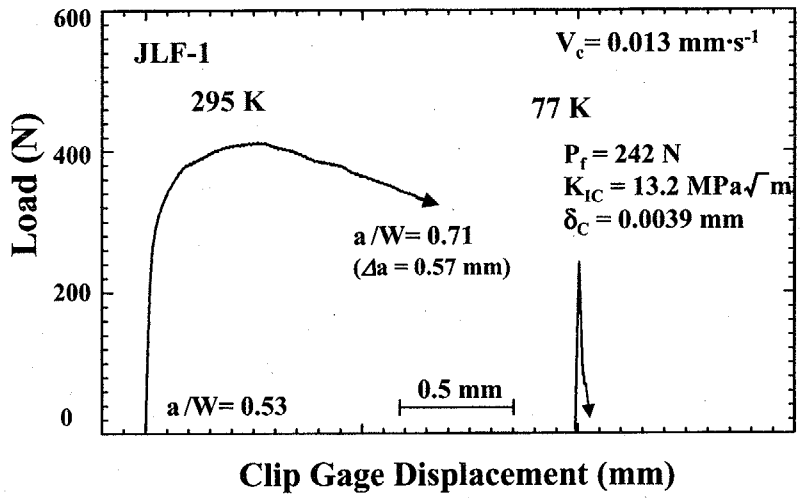
Elastic-plastic fracture toughness (JQ) tests were carried out by means of the compliance method following the ASTM standard test method E813 (E1820-99a).

Tensile specimens were produced in accordance to the JIS which defined the specimen gage length and diameter as 40 mm and 6.25 mm, respectively. The tensile tests were carried out on an Instron-type machine at a cross-head speed of 0.1 mm/min at room temperature.

(4) Results and Discussion

(4.1) 3PB specimens.

Figure 4 shows an example of the load versus clip-gage displacement records measured at 295 and 77 K at 0.013 mm/s for the smallest specimen, 3.3 mm^B x 3.3 mm^W and the fracture surfaces of tested specimens of JLF-1 base metal. The figure shows that even in this miniature specimen the pre-crack extends at both test temperatures and the fracture mainly occurs in the plane-strain condition. The tests with dynamic loading at 13 mm/s gave essentially the same result. As seen from the figure, at 77 K the miniaturized 3PB specimen fractured in a completely brittle manner and the plane-strain fracture toughness, K_{IC}, was estimated to be 13 $MPam^{1/2}$. Table 3 lists the values of K_{IC} measured for four types of 3PB specimens, which satisfy the criterion of B, $W\text{-}a_0 > 2.5(K_{IC}/\sigma_{YS})^2$, where σ_{YS} is the 0.2% off-set static yield strength measured in this study. The values of K_{IC} lie in the range 13-16 $MPam^{1/2}$ regardless of specimen size, indicating that K_{IC} does not show appreciable dependence on specimen size.



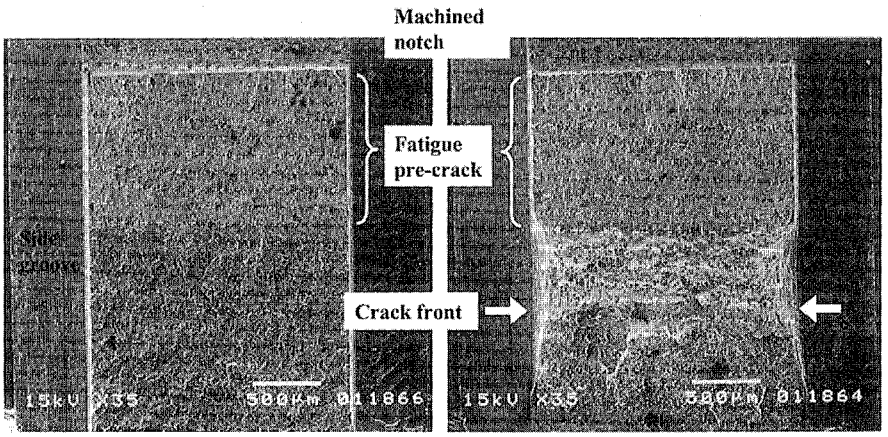


Fig. 4 Load-displacement records and fracture surfaces for pre-cracked 3PB specimens with 3.3 mm^B x 3.3mm^W of JLF-1 tested at 295 K (right) and 77 K (left) at 0.013 mm/s.

Table 3 Plane-strain fracture toughness, K_{IC}, at 77 K for four types of 3PB specimens of JLF-1.

	B (mm)	W (mm)	W-a_0 (mm)	P_f (kN)	K_{IC} (MPam$^{1/2}$)	B, W-a_0 > 2.5 $(K_{IC}/\sigma_{YS})^2$
1	7.0	10.0	4.70	1.080	16.4	satisfied
2	5.0	5.0	2.25	0.475	15.2	satisfied
3	3.3	5.0	2.45	0.370	15.7	satisfied
4	3.3	3.3	1.57	0.242	13.2	satisfied

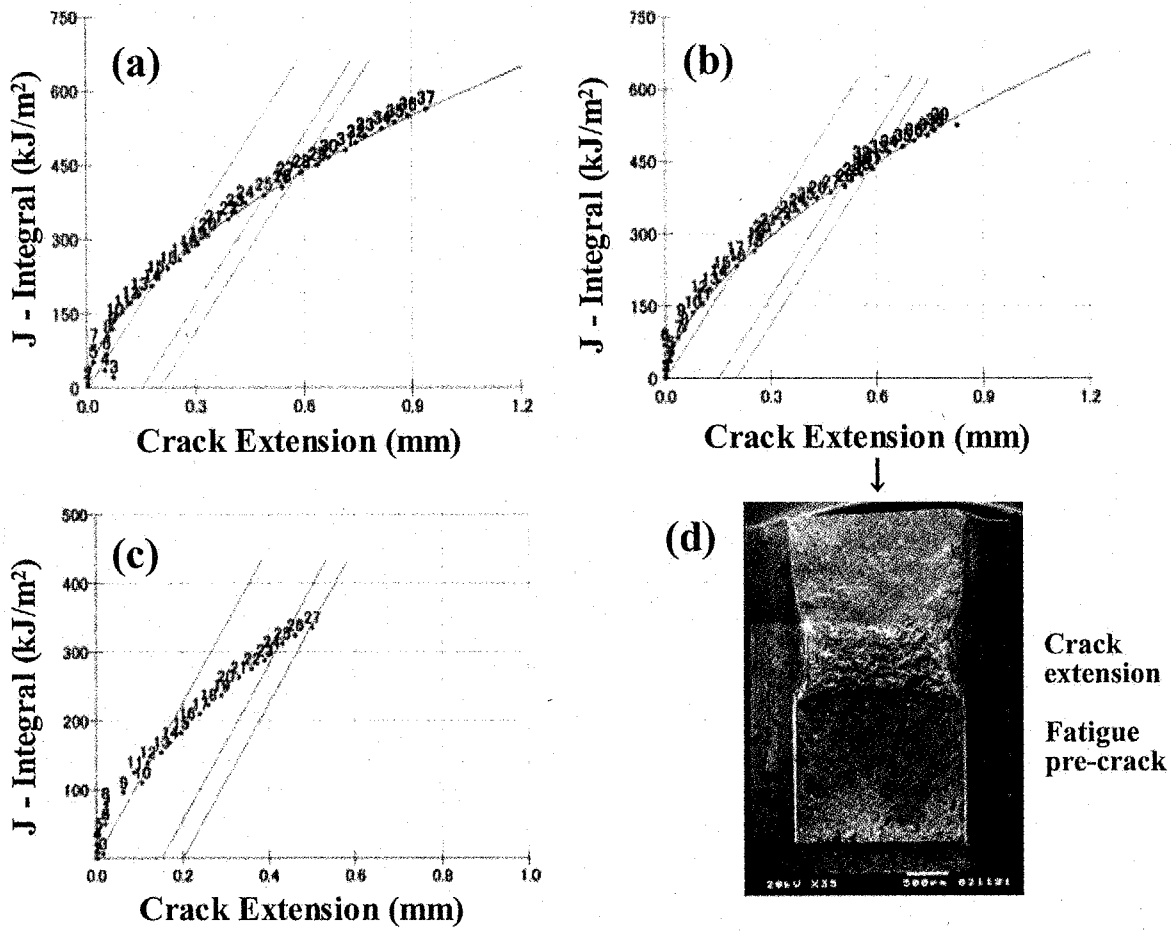


Fig. 5 Examples of J-integral versus crack extension curves for 3PB specimens with (a) 7.0 mm^B x 10 mm^W, (b) 3.3 mm^B x 5.0 mm^W and (c) 3.3 mm^B x 3.3 mm^W and (d) fracture surface of (b) of JLF-1 tested at room temperature.

At room temperature, on the other hand, slow, stable crack extension is observed. Thus, the unloading compliance method was applied to measure J-integral for JLF-1. Figure 5 shows J-integral versus crack extension curves for three types of specimens: 7.0 mm^B x 10 mm^W, 3.3 mm^B x 5.0 mm^W and 3.3 mm^B x 3.3 mm^W. The number of data points in the figure is the sequence number of unloading. The blunting line is the calculated one defined by $2\sigma_F\Delta a$ (σ_F is the flow stress and 570MPa). According to ASTM standards, the J value is defined as the intersection of the J-R curve with the 0.2 mm offset line. However, it should be noted that the initial part of the J-R curve is much steeper than the calculated blunting line. Therefore, a straight line was fitted by eye through the initial portion of the data and a

second line was drawn parallel to the first but offset by an amount corresponding to a crack extension of 0.2 mm [7]. The candidate toughness value J_Q was determined by the intersection of the data with this offset line.

On the other hand, it is obvious from the figure that clear jumps in the crack extension occur about at data point number 7 – 9, which may correspond to the onset of pre-crack extension. Therefore, in this study the value of J_{IN}, defined here as the J-value at the onset of pre-crack extension, was determined from the intersection of the straight line and a linear approximation of the data falling between approximately 0.1 and 0.3 mm of crack extension. For such J_{IN} values the effect of local deformation of specimen regions in contact with loading and supporting pins during testing may be negligible, because the J_{IN} value is obtained from the very initial part of the J-R curves and the contact regions are already hardened by loading for fatigue pre-cracking (which requires larger load than that for fracture toughness testing).

The values of J_Q and J_{IN} are listed in Table 4, together with J_Q^{ASTM} estimated according to ASTM standards. No significant differences in J_Q and J_{IN} between the specimen sizes are recognized, although the J_Q value for the 3.3 mm x 3.3 mm specimen is appreciably lower than the others.

Since the above determination of J_{IN} by the compliance method is difficult to apply to dynamic tests and to tests of highly irradiated specimens with less ductility, another approach was taken to estimate J_{IN}, and is described below.

Table 4 Elastic-plastic fracture toughness test results on differently sized 3PB and CT specimens of JLF-1 base metal at room temperature.

Specimen type	W (mm)	B (mm)	B_N (mm)	a_0 (mm)	J_Q^{ASTM} (kJ/m^2)	J_Q (kJ/m^2)	J_{IN} (kJ/m^2)
3PB	10.0	7.0	4.2	5.18	431	251	117
3PB	5.0	5.0	3.0	2.89	467	273	123
3PB	5.0	3.3	2.0	2.82	443	261	116
3PB	3.3	3.3	2.0	1.84	336	222	103
CT	50.8	25.4	20.3	29.60	486	---	---
CT	50.8	12.7	10.2	29.60	492	---	---
CT	25.4	12.7	10.2	14.70	502	---	---
CT	12.7	6.35	5.1	7.85	435	---	---

In this approach, first static or dynamic 3PB loading is conducted for a pre-cracked 3PB specimen to measure the load versus load-line and clip gage displacement records. Next, the tested specimen was heat tinted and fractured at 77 K. The original and final crack lengths, a_0 and $a_0+\Delta a$, and the effective specimen thickness, t^*, for the plane-strain fracture to occur; can be measured on the fracture surface. Then, plane-strain FEM analysis is applied to reproduce the measured load-displacement record. Finally, the measured record and the FEM curve are compared.

The FEM analysis assumes no extension of pre-crack and thus the curve obtained by FEM should reproduce the measured record up to the point where the pre-crack starts to extend. Above that point, the FEM curve should go higher than the measured record. Therefore, we can say that the pre-crack may start to extend at the point where appreciable deviation of the FEM curve from the measured record starts to occur. This means that the area, A, under the load-displacement record (more correctly the load versus load-line displacement record) up to the deviation point is related to J_{IN} for crack initiation by

$$J_{IN} = 2A/b_0B_N, \quad (1)$$

where b_0 is the original ligament size ($b_0 = W - a_0$) and B_N is the net specimen thickness.

Figure 6 shows the comparison of load-displacement curves calculated by the plane-strain FEM analysis with the measured record for the 5 mm^B x 5 mm^W specimen tested at 286 K and 0.013 mm/s. Here, *t was assumed to be 2.48 mm so that the FEM curve can well reproduce the measured record. It should be noted that the value of 2.48 mm is quite close to the thickness for the fracture to occur in the

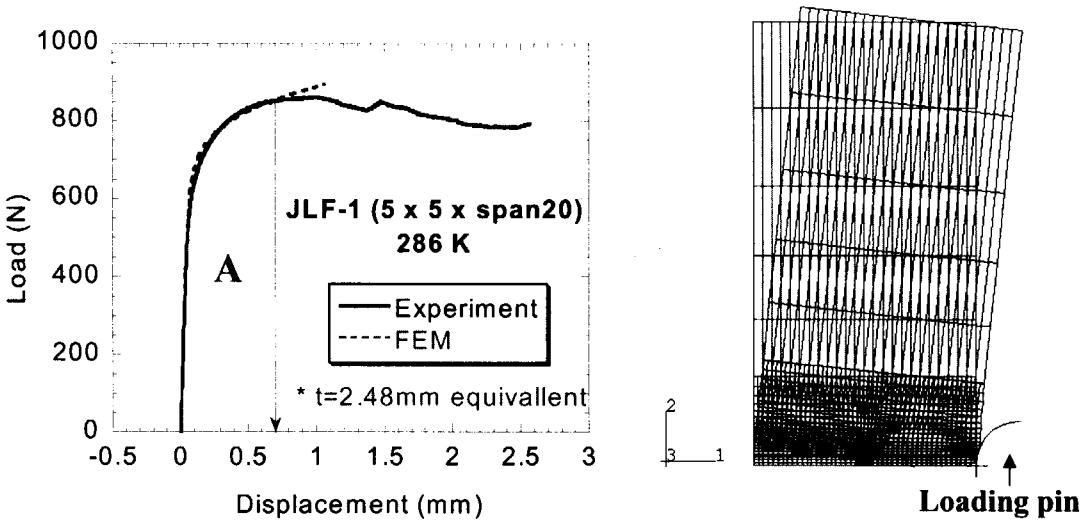


Fig. 6 Comparison between the load-displacement curves obtained by plane-strain FEM analysis and by experiment for 3PB specimen with 5 mm^B x 5 mm^W of JLF-1 tested at 286 K and 0.013 mm/s.

plane-strain condition, approximately 2.5 mm, determined by the fracture surface examination. Comparison of the two curves shows that there is a good agreement until the displacement reaches about 0.7 mm, and above 0.7 mm appreciable deviation of the FEM-curve from the measured one clearly occurs. Calculation of the area marked as A in the figure and substitution of the calculated value for A in eq. (1) gives the J_{IN} value of approximately 130 kJ/m^2, which is nearly equal to the value of J_{IN} shown in Table 4. Further study to demonstrate the validity of this approach is now in progress.

(4.2) CT specimens

(4.2.1) Tensile properties

Stress-strain curves of base metal and weldments are shown in Fig. 7, which indicate that both the yield and tensile stress are larger in weldment than in base metal, while the total elongation is smaller in the weldments. This feature is very similar to the effects of irradiation which cause hardening and ductility loss. The numerical values are summarized in Table 5.

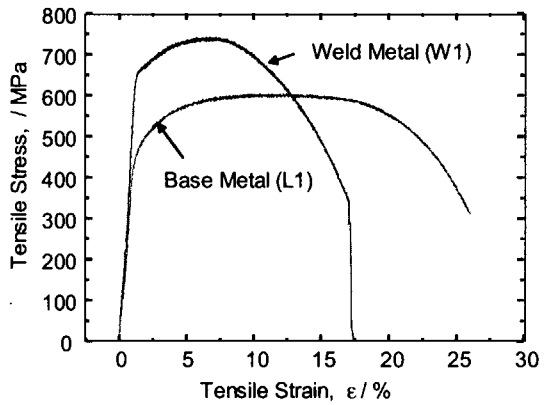


Fig. 7 Stress strain behavior of base metal and weld deformed at RT at a deformation rate of 0.1mm/min.

Table 5 Numerical data of the tensile test results of JLF-1 steel. L1 and W1 stand for base metal and weld.

ID	Y.S[MPa]	T.S.[MPa]	Eu [%]	Et [%]
L1	448	605	9.5	25.3
W1	639	743	5.3	16.5

(4.2.2) Size effects on fracture toughness

Typical examples of J-Δa curve of 1CT, 1/2CT and 1/4CT specimen are shown in Fig. 8. The fracture toughness, J_Q, was defined as the J value at Δa = 0.2 mm. In the figure, the fracture toughness values, J_Q, are 503, 505 and 435 kJ/m^2 for 1CT, 1/2CT and 1/4CT specimen, respectively. They show almost no size dependence of the fracture toughness among 1CT, 1/2t-1CT and 1/2CT specimens. A smaller fracture toughness, however, was obtained for the 1/4CT specimen.

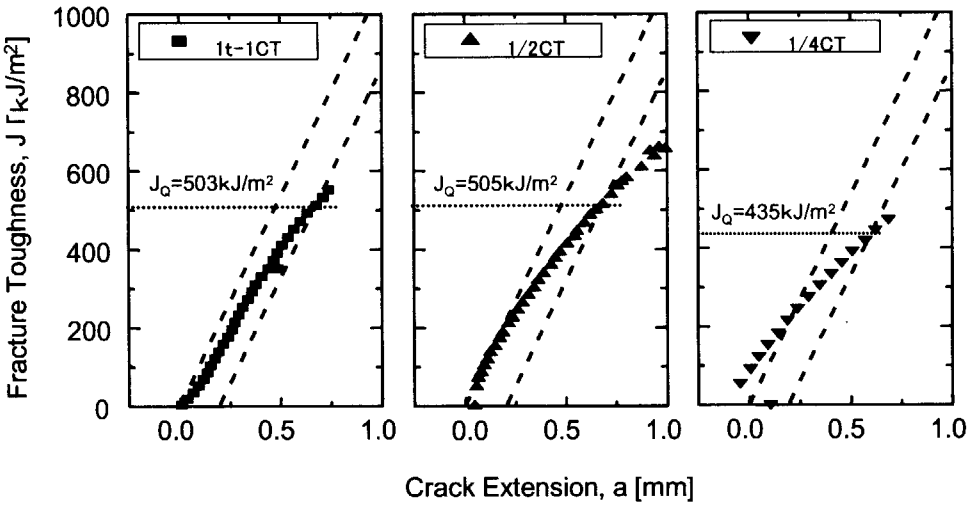


Fig. 8 The load displacement curves of JLF-1 base metal obtained with different size of specimens. The J_Q was defined to be the fracture toughness at Δa = 0.20mm.

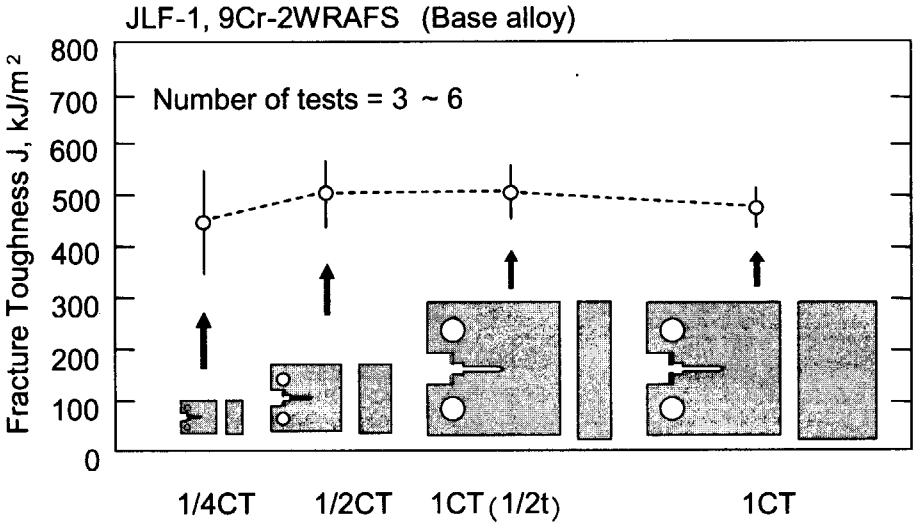


Fig. 9 The dependence of the J_{1C} of JLF-1 base metal on the specimen size.

Among the J_Q values obtained, which were the average of three or six data for each size specimen, all the values were invalid, as shown in Table 6, according to the following validity criteria:

$$B \text{ and } b_0 > 25J_Q / \sigma_Y \quad (2)$$

However, the reduction of fracture toughness coupled with hardening, which will be induced by high dose neutron irradiation, may reduce the specimen thickness that satisfies equation (2). Assuming that the irradiation-induced reduction of fracture toughness and irradiation hardening is 40% and 300MPa, respectively, the minimum thickness required for a valid value is estimated to be 9 mm, indicating that even after neutron irradiation, the fracture toughness obtained with using 1/4CT specimen will still be invalid.

Table 6 Fracture toughness obtained with use of different specimen geometries and valid-invalid evaluation.

Specimen size	J_Q (kJ/m^2)	B and b_0 (mm)	$25J_{IC}/\sigma_Y$	Valid/invalid
1CT	486	25.4	27.12	invalid
1/2t-1CT	492	12.7	27.46	invalid
1/2CT	502	12.7	28.01	invalid
1/4CT	435	6.4	24.27	invalid

Since the first wall thickness is estimated to be less than 5 mm for a ferritic steel-water fusion blanket system, fracture toughness evaluation of thin plate is believed to be inevitable. However, the fracture toughness values of JLF-1 steel were always invalid without irradiation hardening. This requires that new valid/invalid criteria be established for thin specimens to provide a valid database of fracture toughness of fusion blanket structural materials.

(5) Comparison of Test Results for the 3PB and CT Specimens

The elastic-plastic fracture toughness test results obtained from the 3PB and CT specimens are listed in Table 4. Only the J_Q^{ASTM} values can be compared between the 3PB and CT specimens and are discussed here from the engineering viewpoint. The J_Q^{ASTM} values obtained from the miniaturized 3PB specimens were shown to be much higher than the J_Q or J_{IN} values for crack initiation.

The comparison shows that the J_Q^{ASTM} from the 3PB specimens are appreciably lower than those from the CT specimens. This is opposite to the prediction that J-integral values obtained from the 3PB specimens might be an overestimate. The reason for the lower J_Q^{ASTM} value of the 3PB specimens is not clear at present. Nishimura et al. showed that the J_Q^{ASTM} value of JLF-1 base metal is 419kJ/m^2 for the 1CT specimen and 431 kJ/m^2 for the 1/2CT specimen [4].

(6) Conclusions

For the miniaturized 3PB specimens of JLF-1 steel with thickness of 7.0, 5.0 and 3.3 mm, elastic-plastic fracture toughness tests by the unloading compliance method at room temperature and plane-strain fracture toughness tests at 77 K were performed to develop test techniques for reliable evaluation of fracture toughness. Size effects were also investigated in CT specimens, to measure the room temperature fracture toughness of JLF-1. The results are as follows.

1) The elastic-plastic fracture toughness tests for the 3PB specimens gave J_Q values ranging between 222 and 273 kJ/m^2 and J_{IN} values of 103 to 123 kJ/m^2. J_{IN} is defined as the J value for crack initiation. The plane-strain fracture toughness tests gave K_{IC} of 13-16 MPam$^{1/2}$.
2) Another method to estimate J_{IN} is proposed, based on the finding that the plane-strain FEM analysis can reproduce the measured load-displacement record until the pre-crack starts to extend. The method is applicable to static and dynamic tests and also to heavily irradiated materials with less ductility.
3) Almost the same values of fracture toughness, J_Q, are obtained for 1CT, 1/2t-1CT and 1/2CT specimens, while a smaller value is obtained for 1/4CT specimens.
4) A simple estimate of fracture toughness for irradiated specimens suggests that the minimum specimen thickness of the CT specimen will be 9 mm to get a valid fracture toughness value.

Finally, these results show significant progress toward reliable evaluation of fracture toughness using miniature specimens. Since the 3PB specimen has many advantages over the CT specimen, efforts should be continued to establish test techniques for reliable fracture toughness evaluation using the miniaturized 3PB specimens.

References

[1] T.Kondo, IFMIF, Its Facility Concept and Technology, J. Nucl. Mater., 258-263 (1998) 47-55.
[2] K.Noda, K.Ehrlich, S.Jitsukawa, A.Moslang and S.Zinkle, Users' Requirements for IFMIF, J. Nucl. Mater., 258-263 (1998) 97-105.
[3] A.Kohyama, Y.Kohno, K.Asakura and H.Kayano, J. Nucl. Mater., 212-215 (1994) 684-689.
[4] A.Nishimura, N.Inoue and T.Muroga, J.Nucl. Mater., 258-263 (1998) 1242-1247.
[5] ASTM E813-89, Standard Test Method for J_{IC}, A Measure of Fracture Toughness, Annual Book of ASTM Standards, (1991).
[6] ASTM E399-90, Standard Test Method for Plane-Strain Fracture Toughness of Metallic Materials, Annual Book of ASTM Standards, (1990).
[7] D.J.Alexander, J.E.Pawel, M.L.Grossbeck, A.F.Rowcliffe and K.Shiba, ASTM STP 1270, D.S.Gelles, R.K.Nanstad, A.S.Kumar and E.A.Little, Eds., 1996, 945-967.

3.3.24 TF64-EU : SSTT – Fracture Toughness Specimen Development

(1) Brief Task Description

It has been recognized that the fracture toughness degradation of the tempered martensitic steels under neutron irradiation has to be well understood and quantified in order to safely manage the operation conditions of a fusion reactor. One of the most challenging issues regarding the development of miniaturized specimens for IFMIF is the possibility of extracting reliable fracture toughness data from small specimens. It is then necessary to develop solid experimental techniques and theoretical methods that account for the size and geometry effect on fracture toughness. As far as the mechanical testing is concerned, the fracture toughness data will be mainly obtained from sub-sized compact tension specimens and bend bars for which loss of constraint happens rapidly. It is then necessary to develop techniques and modeling that properly account for such loss of constraint. Since the whole process of macroscopic failure is a complicated one that involves multiscale phenomena, it is necessary to understand the link between the different mechanisms taking place at various length scales resulting in a complex process of fracture. This requires supplementing the mechanical testing by, for example, fractography, finite element simulation, profilometry of the fracture surface by confocal microscopy, fracture reconstruction etc. In this report, we mainly report on the fracture reconstruction technique applied to the 0.2T CT specimens of T91 tempered martensitic steel and focus in the lower transition region where the specimens fail by quasi-cleavage and where we applied a confocal microscopy/fracture reconstruction technique in order to follow the sequence of events leading to fracture. Two fracture reconstruction examples are presented along with their corresponding load-displacement curves. Other development activities are also briefly reported.

Contributors

Name	Party	Institute	E-mail address
Philippe Spätig	Switzerland	CRPP	philippe.spatig@psi.ch
Raul Bonade	Switzerland	CRPP	raul.bonade@psi.ch

(2) Introduction

Advanced tempered martensitic steels are leading candidate materials for fusion reactor structural components due to their resistance to void swelling and good balance of physical and mechanical properties. Despite these good properties, the main drawback of the tempered martensitic steels lies in their fracture mode transition, namely from ductile tearing mode with high toughness values at high temperature to cleavage mode with low toughness values at low temperature. Since the materials surrounding the plasma chamber in a fusion reactor will be highly irradiated by energetic neutrons and other types of radiation, a degradation of their overall mechanical properties induced by the radiation environment will occur. The degradation of the fracture toughness properties is reflected in an upward shift of the transition temperature between the brittle and ductile modes of fracture as well as in a decrease of the fracture toughness value in the ductile mode. These facts may seriously limit the use of the tempered martensitic steels in fusion applications. It is therefore of primary importance to characterize both the fracture properties in the unirradiated condition and to assess the degradation of these properties as a function of the neutron dose, the irradiation temperature, the flux, and so on, in order to safely operate the fusion reactor. It is well known that fracture toughness is a material property only under specific conditions, among which the plastic zone size has to be much smaller than the specimen and crack dimensions. The nuclear heating and irradiation volume limitations in IFMIF prevent irradiating a significant number of fracture specimens whose dimensions fulfill the ASTM size requirements. Thus, mainly sub-sized bend bars and compact tension specimens will be irradiated, for which constraint loss will occur. Provided that a good understanding of the fracture process is available, it is possible to correct the fracture data obtained on small specimens that are affected by constraint loss. This mainly requires an understanding of the micro-mechanisms of fracture and its relation to the macroscopic fracture. Based upon a fracture reconstruction technique originally developed at the University California Santa Barbara [1,2] we performed a series of fracture

reconstructions on 0.2T CT specimens of T91 martensitic steel and tried to gain some insights into the whole fracture process of cleavage. Here, we briefly describe the procedure of this fracture reconstruction technique and how we implemented the algorithms developed at the University California and illustrate with examples the most important information we can deduce from it.

(3) Experimental Equipment and Conditions

The mechanical testing was carried out on a modified vanadium-niobium-stabilized martensitic steel. The alloy is close to the ASTM designation T91 (Fe-8.26Cr-0.1C-0.95Mo-0.2V-0.075Nb). It was normalized for 2.5 h at 1343 K and tempered for 4.75 h at 1038 K. The tests were carried out on fatigue pre-cracked, 20% side-grooved, small compact tension specimens, with crack length a to specimen width W ratios of about a/W $\doteqdot$ 0.5 and a specimen thickness (B) to width ratio of B/W = 0.5 (B = 5.0 mm; 0.2T CT). Static tests, at a ram displacement rate of about 4 μm/s, were carried out under displacement control on a servohydraulic load frame at temperatures ranging from 77 to 188 K. Temperature control was provided by either a liquid-nitrogen-cooled alcohol bath or a regulated N_2 gas environment. Test and analysis procedures to determine K_{JC} or K_Q, representing valid small scale yielding elastic-plastic toughness and large scale yielding toughness, respectively, were based on ASTM Standard Practice E813 and E1921-97, where the specimen geometry can also be found.

The fracture reconstruction technique was used to determine the sequence of events leading to fracture. It uses the topographic maps of the two conjugate fracture surfaces. The topographic maps are measured with a confocal scanning laser microscope 1LM21. The optics of the microscope are configured to provide a very shallow depth of focus so that only the points on the focal plane can be imaged. In order to determine the height of a given point on the surface, the specimen is moved up and down at a fixed focal length. The maximum intensity of a pixel of the surface is then recorded and corresponds to the height of that specific point of the surface. In order to get a precise topography map over a significant fracture area (several mm^2), it necessary to assemble smaller confocal fields, whose characteristic dimensions are about 200 μm x 300 μm. A computer-controlled stage is used to horizontally move the specimen in order to acquire in sequence the series of confocal fields. The confocal fields are taken in such a way that they overlap over the four adjacent ones on a strip of about 10 μm so that the assembling can be accurately made. Finally, the height of a given point of the surface is represented by a gray level ranging from 0 to 255. The resolution in the horizontal plane is about 0.3 while the vertical resolution between two gray levels depends evidently on the height difference between the lowest and highest point of the surface area investigated. For the specimens studied here, it was possible to build the topographic maps with a vertical resolution of the order of 1 μm. The last step before running the fracture reconstruction itself consists of computational overlap and match of the conjugate surfaces. The difference between the two surfaces is calculated and set to zero on the pre-cracked area. Finally, the surfaces are separated by an amount corresponding to the crack tip opening displacement. At a given crack tip displacement, spots on the surfaces where the profiles cross each other correspond to material separation and can be flagged. Thus, the nucleation and evolution of the damage preceding the macro-crack initiation can be followed and the critical crack tip opening displacement determined.

The analysis programs were taken from the original codes developed at the University California Santa Barbara. However, they had to be modified and adapted to our own acquisition equipment. Furthermore, modifications of the code were necessary to recompile all the libraries and routines to make them compatible with the computer platform we used, namely a Macinstosh computer running under Mac OSX system.

(4) Results and Discussion

1) Fracture reconstruction

The 0.2T CT fracture test results obtained on the T91 steel are shown in Figure 1 where the fracture toughness-temperature curve is presented. It is important to note that all the specimens failed by a quasi-cleavage fracture mode. The data plotted on the figure have to be interpreted as an effective

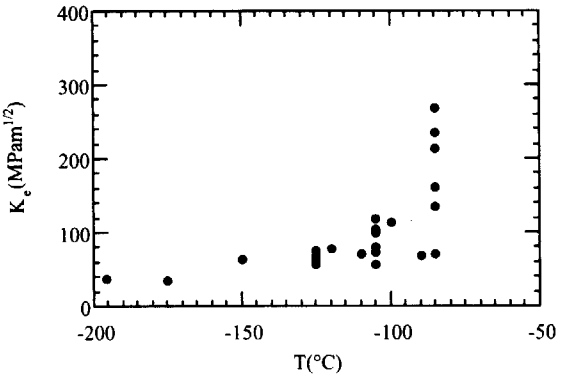


Fig. 1 Fracture toughness–temperature curve for T91 steel, measured on 0.2TCT specimens.

static fracture toughness, K_e, which intrinsically depends on the metallurgical state, loading rate, and specimen size and geometry factors. Only for restricted conditions (plane strain, mode I of loading, and much smaller plastic zone than the characteristic specimen dimensions), can K_e be considered as a material property. For the 0.2T CT geometry used here, the K_e data are reasonably valid up to about 100 MPa m$^{1/2}$ [3] where in-plane constraint is maintained. Constraint loss is primarily associated with plasticity encompassing a large fracture of the uncracked ligament. The few data points lying above 200 MPa m$^{1/2}$ underwent extensive loss of constraint; even out-of-plane constraint loss was observed by optical microscopy observations of the specimens whose fracture toughness is higher than 200 MPa m$^{1/2}$. The issues of loss of constraint can be mitigated by assessing the local properties at the crack tip that do not depend on the deformation level. This can be done by evaluating locally the stress/strain fields by finite element analysis in order to define a critical condition for cleavage. Further in this modeling, it is also important to understand how the macro-crack responsible for the failure of the specimen is initiated and evolved as a function of the local stress/strain field. In order to obtain some insight into that process, the fracture reconstruction was applied and two analyses are given in detail below.

Two different specimens were selected for fracture reconstruction: one, tested at T = -105°C,

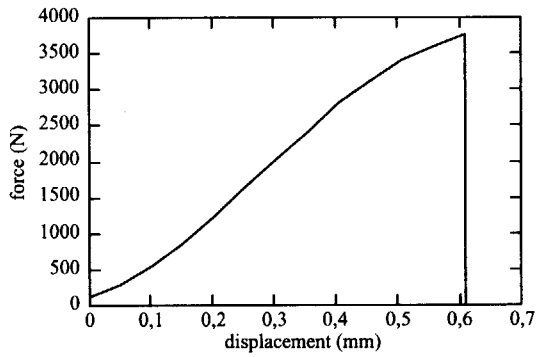


Fig. 2 Load-displacement curve, 0.2T CT specimen tested at T = –105°C.

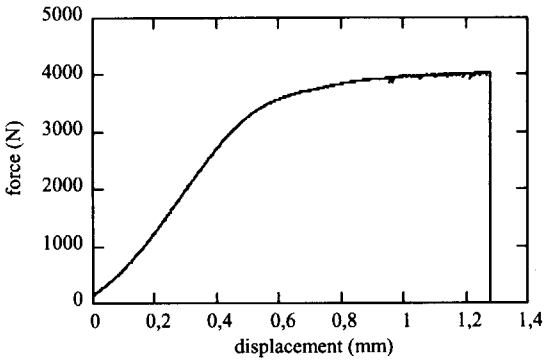


Fig. 3 Load-displacement curve, 0.2T CT specimen tested at T = –85°C.

which exhibited an almost completely elastic loading and failed at 118 MPa m$^{1/2}$, and one at T = -85°C whose loading curve was elastic-plastic and failed at 270 MPa m$^{1/2}$ after having undergone a significant loss of constraint. The two respective load-displacement curves are reported in Figure 2 and 3. The fracture reconstruction sequences are given in Figure 4 and 5. The δ-value indicated below each field is the crack tip opening displacement; the black areas correspond to the spots where the material is separated while in the white ones the material is still intact. In Figure 4, it can be seen that the crack does not propagate and that the initial damage appears for δ equal to about 20 μm. The damage zone size increases with δ and it is very important to emphasize that the damage initiated ahead of the crack tip. This observation is well revealed on the fields corresponding to δ = 28 μm and 32 μm where a white strip separates the crack tip from the damage process zone in which micro-cracks nucleate. Increasing δ above 36 μm leads to a full separation between the two surfaces. Hence, the critical opening displacement for that specific specimen is of the order of 40 μm. Interestingly, the same qualitative sequence of events occurs for the tougher specimen. In this second case, however, the damage initiates between δ = 220 μm and 230 μm. It should be noted that, in this last case, an important crack blunting is taking place which results in an overall crack tip advance of about 200 μm.

Above δ = 230 μm the crack continues to blunt and the damage zone containing the bridged micro-cracks increases until all the micro-cracks coalesce into a large macroscopic and unstable crack. This happens for a critical crack tip opening displacement of about 260 μm.

Values of the critical opening displacements obtained from fracture reconstruction can be used to recalculate the fracture toughness using the following relation [4]:

$$K_\delta = \sqrt{2E'\delta_c^*\sigma_y}$$

where E' is the plane-strain Young modulus, δ^*_c is the critical crack tip opening displacement and σ_y is the yield stress. A good agreement between the values of K_δ and those of K_e (determined from the mechanical tests) was found. The results are summarized in the Table 1.

Table 1 Fracture toughness as measured from the critical opening displacement obtained from fracture reconstruction K_δ or from the mechanical test K_e

T = - 105°C	δ_c^* =	K_δ = 106 MPa $m^{1/2}$	K_e = 118 MPa $m^{1/2}$
T = - 85°C	δ_c^* = 260 μm	K_δ = 264 MPa $m^{1/2}$	K_e = 270 MPa $m^{1/2}$

2) Other activities

In the framework of this task, different geometry of sub-sized fracture specimens of EUROFER97 were machined and pre-cracked. Namely, there were 0.4T CT, 0.2T CT, 0.1T bend bars and KLST Charpy specimens pre-cracked at a/w = 0.5. A capsule was prepared to be irradiated up to 0.5 dpa at T = 350°C in the experimental reactor at KFKI-Budapest. The corresponding clevises and three point bending fixtures were developed.

(5) Conclusions

In order to better understand the effect of specimen size/geometry on fracture toughness, the technique of fracture reconstruction was used. A scanning laser confocal microsope 1LM21, with a computer controlled stage, was used to acquire a series of small confocal fields from the two conjugate fracture surfaces, which are later assemble into large fracture areas. The topography of the fracture surfaces is represented by 256 gray levels. After a careful computational alignment of both surfaces on top of each other, they are separated by a given displacement reflecting the crack tip opening displacement. Following the overlapping of the surfaces, it is possible to determine the evolution of damage nucleation of micro-crack as a function of the crack tip opening. Two examples were given for 0.2T CT specimens of T91 martensitic steel; one with a level of in-plane constraint well maintained, and another exhibiting a huge amount of constraint loss. It was possible to localize at which crack tip opening the damage ahead of the crack tip appeared and to relate the critical opening to fracture toughness. Good agreement was found with the fracture toughness data obtained from the mechanical tests. It was emphasized that the information, which is deduced from the fracture reconstruction, is of primary importance in the development of local criterion for cleavage and in the modeling of the fracture toughness-temperature curve.

References

[1] K. Edsinger, PhD Thesis – Fracture Reconstruction and Advanced Micromechanical Modeling of Structural Steels, University of California Santa Barbara (1995).

[2] G. R. Odette, K. Edsinger, G. E. Lucas, E. Donahue, Developing fracture assessment methods for fusion reactor materials with small specimens, Small Specimen Test Techniques, ASTM STP 1329, W. R. Corwin, S. T. Rosinski and E. van Walle, Eds. American Society for Testing and Materials, (1998), 298-327.

[3] P. Spätig, G. R. Odette, E. Donahue, G. E. Lucas, Constitutive behavior and fracture toughness properties of the F82H ferritic/martensitic steel, J. Nucl. Mater. **283-286** (2000) 721-726.

[4] C. F. Shi, Relationship between J-integral and crack opening displacement for stationary and extending cracks, J. Mech. and Phys. of Solids, 29 (1981) 305.

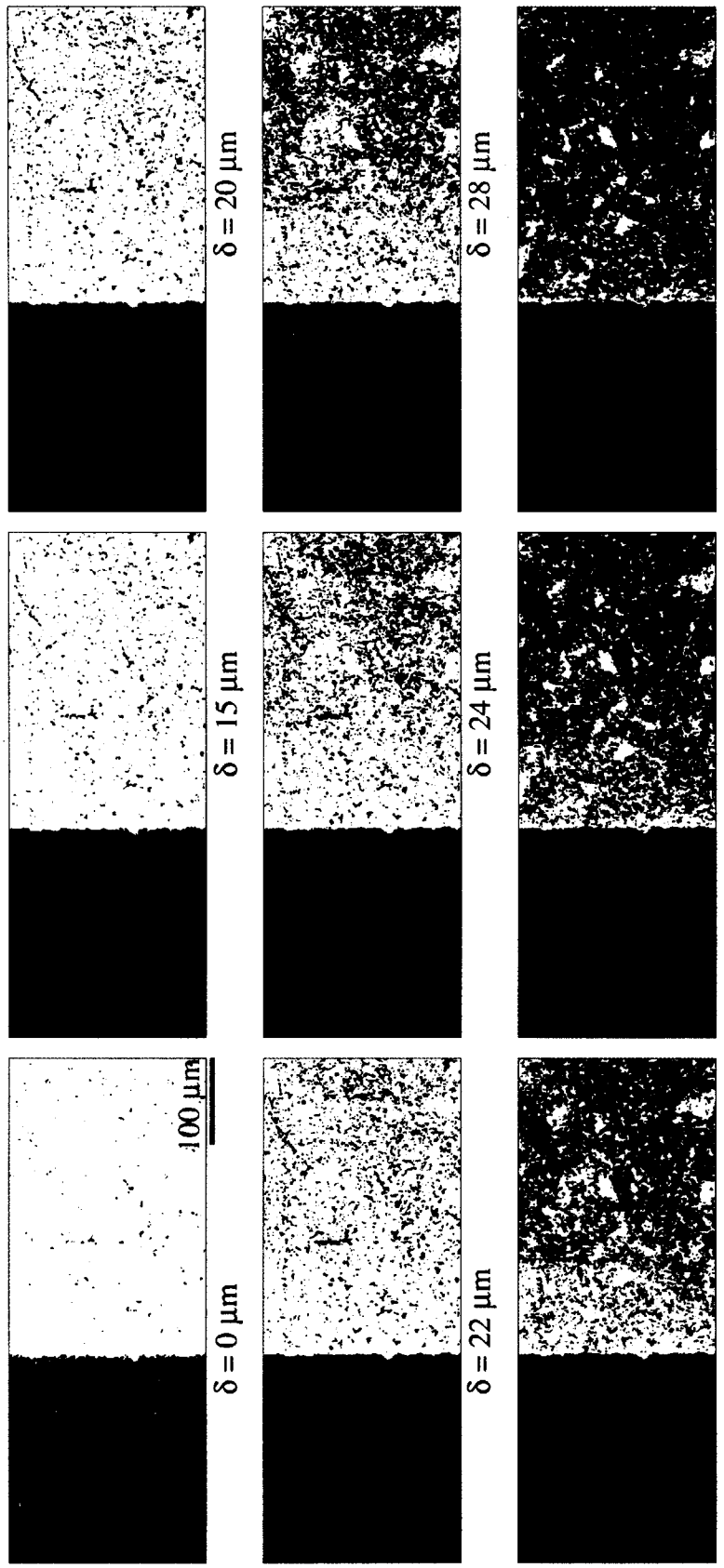


Fig. 4 Example of FR, 0.2T CT specimen of T91 at T=-105°C exhibiting a limited amount of plastic deformation before failure.

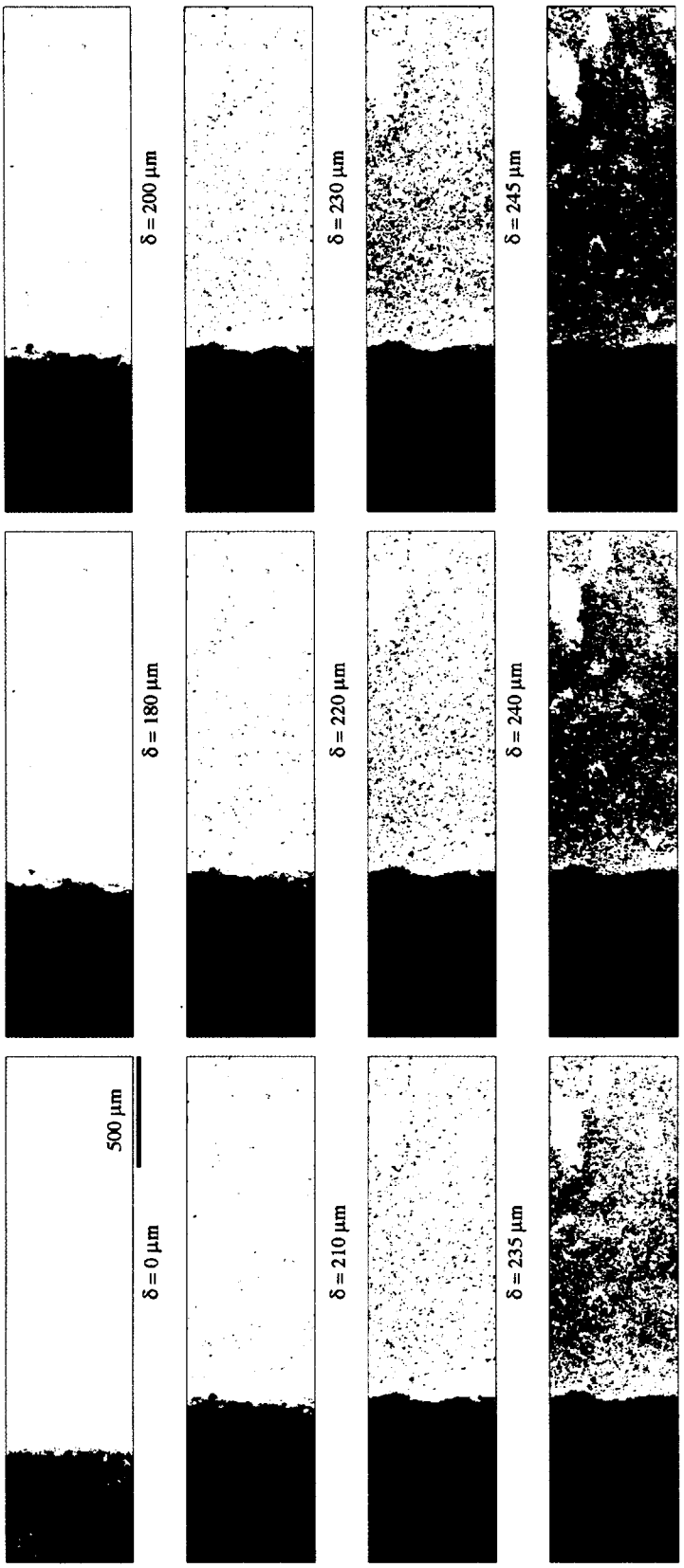


Fig. 5 Example of FR, 0.2T CT specimen of T91 at T=-85°C exhibiting a large amount of plastic deformation before failure.

3.4 Design Integration

3.4.1 DI11-JA : Diagnostics for the Spatial Distribution of Neutrons

(1) Brief Task Description

On-line information on the neutron irradiation field, such as flux intensity distribution and energy spectra, is essential for control of the quality and distribution of the ion beam on the target. In the past several monitoring methods, including a multi-foil activation detector, a miniaturized fission chamber, a nuclear heating detector (like a gamma thermometer), a moving activation wire detector, etc., were proposed and described in the IFMIF conceptual design. In this task, the feasibility of these candidate methods is examined and the possible arrangements of the diagnostic system in the test cell area are investigated. The recent progress on neutron measurement techniques also encourages the consideration of two other types of active neutron detectors, bubble detector spectrometer and activation counter, to monitor the spatial and spectral distribution of the neutron field. Therefore, the possible use of these two methods is included in the investigation.

Contributors

Name	Party	Institute	E-mail address
M. Sugimoto	Japan	JAERI	sugimoto@ifmif.tokai.jaeri.go.jp
H. Takeuchi	Japan	JAERI	takeuchi@fnshp.tokai.jaeri.go.jp
T. Yutani	Japan	JAERI	ida@ifmif.tokai.jaeri.go.jp

(2) Introduction

The on-line characterization of the fluence and the spectrum of the neutron irradiation field in IFMIF is important diagnostic information for predicting the malfunction or deterioration of the performance of the ion beam accelerator and the lithium target as the data are also needed to qualify the irradiation test results. The goal of the accuracy for neutron fluence is tentatively ~15% in the range between 5 and 20 MeV, and ~30% for neutron energies outside this range, based on guideline given in the FMIT design study (see Table 1).

Table 1 Requirements for neutron spectrum measurement in IFMIF.

Neutron energy range (MeV)	Accuracy of measured fluence* (%)	Comments
< 3	30 – 60	Small effect on the total fluence
3 – 5	20 – 40	Relatively low intensity portion of energy spectrum
5 – 10	10 – 20	Major influence on the neutron response of irradiated samples; It is enough to only measure a few energy points in this region;
10 – 15	10 – 20	
15 – 20	10 – 20	
20 – 25	10 – 20	
25 – 30	20 – 40	Relatively low intensity portion of energy spectrum
> 30	40 – 80	Penetrability and damage energy are high

*) The values were initially given as the requirements for the characterization of irradiation field at the commissioning stage of FMIT, however, they can be applicable to IFMIF commissioning and normal operation.

In the IFMIF CDA study, neutron monitoring inside the test assembly using multi-foil activation techniques and a miniaturized fission chamber was investigated [1]. Two additional methods, the gamma-thermometer and the activation wire, were proposed in the CDE phase [2] as possible on-line monitors/spectrometers (see Table 2). However, these concepts are hard to include as sensors integrated into the test equipment and to operate as reliable on-line monitors. The gamma-thermometer is relatively thick, 15 mm or more, and it is better used at back positions to avoid occupying valuable space near the target/test assembly. It also cannot be too close to the target position because of the high flux gradient along the beam direction. The activation wires inside the test assembly have low reliability because the replacement of the wire is impossible without removing and

reassembling the test module. An overall monitor of the neutron field at the test modules will be performed indirectly by measuring the nuclear heat that needs to be removed by the coolant system.

In the FMIT project three types of spectrometer were selected [3]: liquid organic scintillator, two-detector short-path TOF, and magnetic spectrometer. However, they need a lot of space for equipment to measure with enough accuracy and low background. (An extra dosimetry cell might be required to deliver the neutron beam into the low-background area from the test cell through a collimation system.) The characteristics of these methods are also compared in Table 2.

Two other possible candidate systems for the intense and high-energy neutron environment of IFMIF are the damage detector and the activation counter described in a recent textbook [4]. The applicability of these two detector types is discussed in the following section.

Table 2 On-line neutron detection methods applicable for beam diagnostics on IFMIF.

Method	Principle	Comments
Gamma-thermometer	To detect the rise of temperature due to the nuclear heating induced in the stainless steel needle; at the top of the needle thermocouple is attached and copper base board is used as heat sink;	• Produced heat is sensitive to the neutron spectrum; • Background heat from the external radiation source needs to be controlled precisely; • It can be useful for checking the overall neutron flux distribution at the commissioning stage.
Activation wire	To measure the radioactivity produced in the wire-shaped sample that is periodically extracted from monitoring position in the test cell area;	• Reliable extraction of the wire from the test cell to the outer measurement station is hard to implement under the irradiation test; • It is easier to implement together with the irradiation test using the rabbit tube by attaching a set of activation foils.
Liquid organic scintillator	To measure the scintillation light output caused by the interaction between the neutrons and liquid organic materials	• Sensitivity to γ-rays is high and the n-γ discrimination method is difficult to apply under the high flux environment. • The use under the high counting rate is limited. • It can be used to monitor the leaked or penetrated neutrons through the pipes or shields of test cell.
Two-detector short-path TOF	To measure the neutron energy by using time-of-flight method with supplying the start timing signal generated by the collision event in the first detector	• It requires a space for TOF measurement, which influences the energy resolution. • The background of γ-rays can be separated efficiently.
Magnetic spectrometer	To analyze the energy of the charged particles generated by neutron induced reactions	• The size of measurement system becomes large generally depending on the required resolution. • Accuracy of energy is the highest.
Bubble detector	To measure the bubbles formed from supercritical droplets by the thermal spikes due to recoil atoms or charged particles produced by fast neutrons	• Neutron energy threshold is controllable by changing the droplet size. • Insensitive to γ-rays. • Total measurable fluence is limited by the density of droplets.
Activation counter	To measure the radiation due to the decay of the radioactivity produced by neutrons	

(3) Neutron Detectors

(a) Bubble Detector

The bubble detectors were developed from the request to improve the neutron response of damage-track detectors like CR-39 below ~1MeV. They use the stored energy in superheated liquid droplets, dispersed in a non-active media of polymer or gel. Charged particles produced by the neutron collisions generate bubble numbers proportional to the released energy in the medium. The bubble detectors have no sensitivity to gamma radiation below photoneutron emission threshold energy. They also can be used as a neutron spectrometer [5], because the minimum energy required for bubble

formation can be changed by controlling the difference of the vapor pressure of the superheated liquid and the pressure around the droplet. Bubble chambers as passive personal neutron dosimeters are already available commercially, using optical readers for counting the number of bubbles. As an active detector, the bubble density is measured by ultrasonic methods [6] or acoustic detection methods. These methods can be extended to position-sensitive detection by using sensors attached at each end of a long pipe containing bubble detectors. The schematic view of a typical bubble detector is shown in Fig. 1. The main issue with use in the IFMIF neutron environment is limitation of dynamic range, i.e. maximum neutron dose (or fluence) measurable with sufficient accuracy. As the number density of bubbles reaches the limit where the bubbles strongly overlap, the density measurement is difficult.

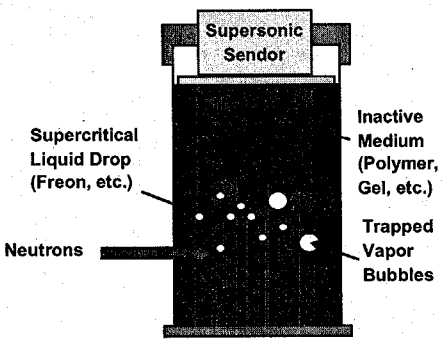


Fig. 1 Schematic view of typical bubble detector. [4]

(b) Activation Counter

An activation counter can normally be applied to measure a pulsed neutron source by counting the decaying radiation (β or γ) from the accumulated radioactivity produced by the neutron burst. In the case of non-intermittent neutron source like IFMIF (the average time duration between the bursts is ~3 ns), the separation of the decay events from background by measuring the time dependence is impossible, and it is important to select an activation reaction insensitive to low energy neutron and gamma ray background. The criteria for selection are: (i) decay constant short enough to make flux-time history measurement possible but long enough to avoid counting loss due to the detection dead-time and pile-up effects, i.e. lifetime of less than a few seconds; and (ii) competing reaction channels do not produce excessive background events. Several candidate reactions are shown in Table 3 and the optimal combination of several activation reactions needs to be established for various energy spectra at each location in the test cell. It also requires a precise determination of the reaction cross sections up to ~60 MeV, covering the IFMIF neutron spectra.

Table 3 Neutron induced reactions applicable for activation counter use in IFMIF.

Reaction	Radioactivity	Half-life	Threshold energy
^{9}Be (n,α) ^{6}He	β- 3.51MeV	0.807 s	~2 MeV
^{16}O (n,p) ^{16}N	γ 6.13MeV	7.13 s	10.2 MeV
^{19}F (n,α) ^{16}N	β- 4.3, 10.42MeV		~3 MeV
^{23}Na (n,α) ^{20}F	γ 1.63MeV	11 s	~7 MeV
	β- 5.40MeV		
^{12}C (n,p) ^{12}B	β- 13.37MeV	0.02 s	~14 MeV

A possible structure of the activation counter is schematically shown in Fig. 2. As the Test Cell area is evacuated to ~0.1Pa during operation, it is necessary for the counter to be in a vacuum to reduce the nuclear heating. The size of the detectors must be small enough to avoid flux perturbation and for easy set-up through access holes in the Test Cell shielding wall.

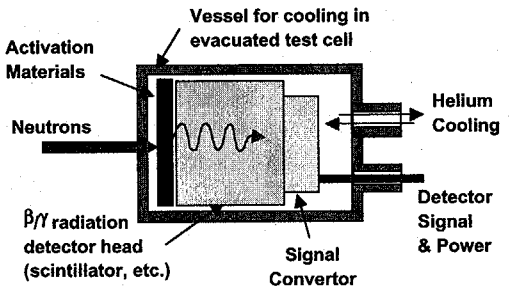


Fig. 2 Schematic view of activation counter.

(4) Detector Arrangement

Placement of the neutron detectors in the test cell will be carried out using a remote handling system that allows little interference with the target assembly and test assembly modules. The access methods for this purpose are categorized as:

(a) Vertical access using a stalk through the Test Cell ceiling;
(b) Horizontal access through the Test Cell wall on the beam entry side (or on the left- or right-hand side).

The possible access routes to the Test Cell are shown in Fig. 3. For the vertical access method the remote handling system in the Access Cell can be used for the installation of the detector assembly. The position of the access hole is restricted to the area near the side walls of the Test Cell to avoid interference with the Test Cell ceiling plugs. On the other hand, for the horizontal access method no existing remote handling equipment is available in the current design. However, the interference with target and test assembly modules can be minimized and the detector position is also controllable by extending the horizontal support arm. Both access methods require a sealing mechanism to maintain the vacuum in the Test Cell.

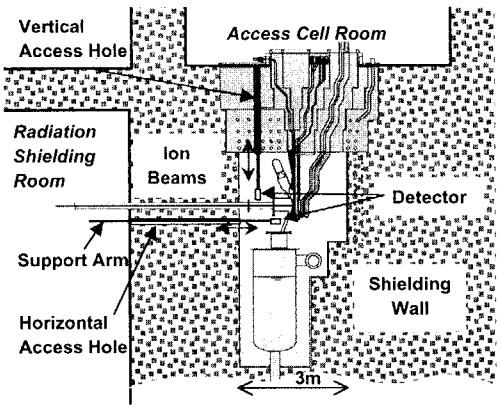


Fig. 3 Possible arrangement of on-line neutron spectrometers in the Test Cell.

(5) Conclusion and Discussion

This survey of various neutron spectrometers applicable for IFMIF shows that every measurement method has some drawbacks and a combination of several methods is necessary to meet the accuracy requirement. As the general rule, the absolute integral fluence will be calibrated by using off-line methods, such as a multi-foil activation technique, and the time-dependent flux/spectrum will be measured using the relative methods described above. Two methods, bubble detector and activation counter, are investigated for use as a compact spectrometer, and the technical issues are identified to develop these methods as the neutron monitors for IFMIF. The detector arrangement in the Test Cell is considered and two access methods, using the vertical and the horizontal holes, are proposed. Either method requires some modification of the present conceptual design.

References

[1] M. Martone, (editor), IFMIF International Fusion Materials Irradiation Facility Conceptual Design Activity Final Report ENEA Frascati Report, RT/ERG/FUS/96/11, November 1996.
[2] A. Möslang, (editor), IFMIF International Fusion Materials Irradiation Facility Conceptual Design Evaluation Report, FZK Report, FZKA6199, January 1999.
[3] J. L. Fuller, "A review of active neutron-spectrometry methods for the energy range of 1 to 50 MeV", Hanford Engineering Development Laboratory Report, HEDL-TME 82-9, January 1983.
[4] G. F. Knoll, "Radiation Detection and Measurement", Ch. 19, Third Ed., John Wiley & Sons, Inc. 2000.
[5] H. Ing, Rad. Meas. 33, 275 (2001).
[6] D. Ponraju, et al., Rad. Meas. 30, 471 (1999).

3.4.2 DI21-JA : Selection of Elements Having Large Cross Section for Activation

(1) Brief Task Description

Every element included in the structure, equipment, and buildings of IFMIF can be activated due to interactions with the primary ion beam, secondary neutron, or gamma rays. The criteria for the selection of important radioactive nuclei are investigated and elements most important for control of the dose rate at the maintenance time are identified.

Contributors

Name	Party	Institute	E-mail address
M. Sugimoto	Japan	JAERI	sugimoto@ifmif.tokai.jaeri.go.jp
H. Takeuchi	Japan	JAERI	takeuchi@fnshp.tokai.jaeri.go.jp
M. Ida	Japan	JAERI	ida@ifmif.tokai.jaeri.go.jp

(2) Introduction

The accurate estimation of the induced radioactivity in the equipment and building materials associated with the IFMIF operation is crucial to predicting the radiation dose levels during operation and maintenance. An important step is to recognize what elements or isotopes have the largest contribution to the total radiation dose, so that use of these elements can be minimized. Generally, there are two distinct origins of the radioactivity in the equipment of IFMIF:

(a) the primary charged particle beam induces activation of materials near the beam path and target material, and

(b) the secondary neutral particles induce activation throughout the entire facility.

The "primary beam" of the IFMIF is either deuteron ($^2H^+$, d) or molecular hydrogen ($^1H_2^+$), where the latter is used during the tune-up process at machine startup [1]. The radioactivity related to source (a) is strongly correlated with the accelerator design and the operation scheme, so all materials directly facing the beam are important and to be treated in the separated study. The "secondary" particles for source (b) are the neutrons and gamma rays produced by the nuclear reactions in the "primary" source regions, e.g. lithium target, moveable beam dump for beam tuning, accelerator and target system components hit by beam-loss particles. Other secondary particles are outside the scope of this study. In the following section, criteria are developed to select the isotopes that will produce induced activity by interaction with high-energy neutrons, gamma rays and deuterons. The hydrogen beam ($^1H_2^+$) is not considered because the maximum energy is half of that of deuteron, ~20MeV, and generally the induced activity is much less than that produced by the deuterons. Also the total beam operation time for hydrogen beam is very limited so that the contribution to the total activity production is negligible.

(3) Isotope Selection Method

The following criteria are applied to select the elements that might contribute significantly to total radioactivity levels.

(a) The half-life of resultant activity is larger than 0.1 s.

(b) The allowed activity level at shutdown is less than 10^8 Bq/kg, where that activity is reduced to clearance level one hour after shutdown. The clearance level data are taken from EAF-99 library [2], which was defined in IAEA publications for several isotopes or calculated by the following formula for the others isotopes.

$$L_i = \min\left\{\frac{1000}{E_{\gamma,i} + 0.1 \times E_{\beta,i}}, \frac{D}{e_i^{inh}}, \frac{D}{e_i^{ing} \times 10^2}\right\}$$

where $E_{\gamma,i}$ is the effective photon emission energy (MeV); $E_{\beta,i}$ is the effective beta decay emission energy (MeV); D = 20 mSv/y is the dose limit for radiation workers; e_i^{inh} is the effective dose

equivalent from inhalation (Sv/Bq) and e_i^{ing} is the effective dose equivalent from ingestion (Sv/Bq).

The plot of the allowed activation limit vs. the atomic number is shown in Fig. 1 and the numerical values for some important radioisotopes are listed in Table 1. This criterion excludes the short-lived isotopes so that the criterion (a) is also satisfied for all isotopes selected here.

(c) The parent isotopes that may produce the radioactive isotopes selected by (b) are considered. Tritium production is possible for all elements with atomic number > 2, and it must be treated separately.

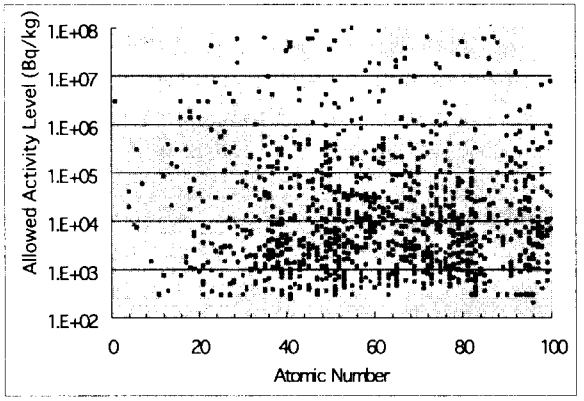


Fig. 1 Activity level of radioisotopes at shutdown satisfying the clearance level after one hour cooling.

For neutron-induced activation, the range of the parent isotopes is surveyed by adding up to five nucleons to the residual radioisotopes based on the assumption that the average binding energy of nucleon to the nucleus is about 8 MeV and the possible maximum excitation energy of the compound nucleus is 40 MeV. The typical reaction channels to produce the important isotopes are given in the last column of Table 1.

The corresponding reaction list for gamma-ray induced activity is limited to add up to two nucleons by taking into account of maximum excitation energy would rarely exceed 20 MeV after the gamma-ray absorption. The list of the reactions that have the cross sections of several mb or larger at Eγ~20MeV is given in Table 2.

The similar reaction list for deuteron-induced activation can be derived also, but the materials bombarded by deuterons are limited to the target lithium (including impurity elements); beam line component mainly made of aluminum, steel, and alumina ceramics; and the beam defining apertures typically made of tantalum. The reaction list for these materials is shown in Table 3.

Table 1 List of important isotopes contributing to neutron activation in IFMIF.

Isotope	Clearance level (Bq/kg)	Decay constant (1/sec)	Allowed activity level (Bq/kg)	Typical neutron induced reactions
H-3	3.0×10^{6}	1.77×10^{-9}	3.0×10^{6}	X(n,t)
Be-7	2.0×10^{4}	1.50×10^{-7}	2.0×10^{4}	X(n,^{7}Be)
Be-10	4.0×10^{4}	1.37×10^{-14}	4.0×10^{4}	^{9}Be(n,γ); ^{10}B(n,p); ^{12}C(n,h)
C-11	9.5×10^{2}	5.66×10^{-4}	7.3×10^{3}	^{12}C(n,2n); ^{14}N(n,nt)
C-14	3.0×10^{5}	3.83×10^{-12}	3.0×10^{5}	^{14}N(n,p); ^{16}O(n,h)
N-13	9.3×10^{2}	1.16×10^{-3}	6.0×10^{4}	^{14}N(n,2n)
F-18	9.9×10^{2}	1.05×10^{-4}	1.4×10^{3}	^{19}F(n,2n)
Na-22	3.0×10^{2}	8.44×10^{-9}	3.0×10^{2}	^{23}Na(n,2n)
Na-24	3.0×10^{2}	1.29×10^{-5}	3.1×10^{2}	^{23}Na(n,γ); ^{27}Al(n,α)
Mg-27	1.0×10^{3}	1.22×10^{-3}	8.1×10^{4}	^{27}Al(n,p); ^{28}Si(n,2p);
Mg-28	7.1×10^{2}	9.22×10^{-6}	7.3×10^{2}	^{31}P(n,ph)
Al-26	3.7×10^{2}	3.05×10^{-14}	3.7×10^{2}	^{27}Al(n,2n); ^{28}Si(n,t);
Al-29	6.8×10^{2}	1.76×10^{-3}	3.9×10^{5}	^{32}S(n,ph)
Si-31	1.6×10^{4}	7.35×10^{-5}	2.1×10^{4}	^{31}P(n,p); ^{32}S(n,h)
Si-32	1.5×10^{5}	6.66×10^{-11}	1.5×10^{5}	^{35}Cl(n,ph)
Ar-41	7.5×10^{2}	1.05×10^{-4}	1.1×10^{3}	^{40}Ar(n,γ); ^{41}K(n,p)
K-42	2.3×10^{3}	1.56×10^{-5}	2.4×10^{3}	^{41}K(n,γ)
K-43	1.0×10^{3}	8.68×10^{-3}	1.0×10^{3}	^{43}Ca(n,p)
K-44	3.9×10^{2}	5.22×10^{-4}	2.6×10^{3}	^{44}Ca(n,p)

K-45	5.1×10^{2}	6.67×10^{-4}	5.6×10^{3}	^{48}Ti(n,ph)
Ca-47	9.1×10^{2}	1.77×10^{-6}	9.2×10^{3}	^{48}Ti(n,2p)
V-47	9.3×10^{2}	3.55×10^{-4}	3.3×10^{3}	^{50}Cr(n,nt)
V-48	3.4×10^{2}	5.03×10^{-7}	3.4×10^{2}	^{50}Cr(n,t); ^{51}V(n,4n)
V-50	9.2×10^{2}	1.48×10^{-25}	9.2×10^{2}	^{50}Cr(n,p); ^{51}V(n,2n); ^{52}Cr(n,t)
Cr-48	2.3×10^{3}	8.94×10^{-5}	2.4×10^{3}	^{50}Cr(n,3n)
Cr-49	9.0×10^{2}	2.76×10^{-4}	2.4×10^{3}	^{50}Cr(n,2n)
Mn-51	9.2×10^{2}	2.50×10^{-4}	2.3×10^{3}	^{54}Fe(n,nt); ^{55}Mn(n,5n)
Mn-52	2.9×10^{2}	1.44×10^{-5}	2.9×10^{2}	^{54}Fe(n,t); ^{55}Mn(n,4n)
Mn-52m	3.9×10^{2}	5.48×10^{-4}	2.8×10^{3}	^{54}Fe(n,t); ^{55}Mn(n,4n)
Mn-54	3.0×10^{2}	2.57×10^{-8}	3.0×10^{2}	^{54}Fe(n,p); ^{55}Mn(n,2n); ^{56}Fe(n,t)
Fe-52	1.3×10^{3}	2.33×10^{-5}	1.4×10^{3}	^{54}Fe(n,3n); ^{56}Fe(n,5n)
Fe-59	3.0×10^{3}	1.80×10^{-7}	3.0×10^{3}	^{58}Fe(n,γ); ^{59}Co(n,p); ^{62}Ni(n,α)
Co-55	4.9×10^{2}	1.10×10^{-5}	5.1×10^{2}	^{58}Ni(n,nt)
Co-56	2.8×10^{2}	1.04×10^{-7}	2.8×10^{2}	^{58}Ni(n,t)
Co-58	3.0×10^{3}	1.13×10^{-7}	3.0×10^{3}	^{58}Ni(n,p)
Co-60	3.0×10^{2}	4.17×10^{-9}	3.0×10^{2}	^{59}Co(n,γ); ^{60}Ni(n,p); ^{62}Ni(n,t)
Co-62m	3.6×10^{2}	8.31×10^{-4}	7.2×10^{3}	^{59}Co(n,γ); ^{60}Ni(n,p); ^{62}Ni(n,t)
Ni-56	5.8×10^{2}	1.32×10^{-6}	5.8×10^{2}	^{58}Ni(n,3n)
Ni-57	5.1×10^{2}	5.40×10^{-6}	5.2×10^{2}	^{58}Ni(n,2n); ^{60}Ni(n,4n)
Ni-65	1.6×10^{3}	7.65×10^{-5}	2.1×10^{3}	^{64}Ni(n,γ); ^{65}Cu(n,p)
Cu-60	2.5×10^{2}	4.74×10^{-4}	1.4×10^{3}	^{63}Cu(n,4n)
Cu-61	1.2×10^{3}	5.65×10^{-5}	1.5×10^{3}	^{63}Cu(n,3n)
Cu-64	4.9×10^{3}	1.52×10^{-5}	5.2×10^{3}	^{63}Cu(n,γ); ^{65}Cu(n,2n)
Y-84m	2.4×10^{2}	2.89×10^{-4}	6.8×10^{2}	–
Y-85	7.5×10^{2}	7.19×10^{-5}	9.7×10^{2}	^{89}Y(n,5n)
Y-85m	7.1×10^{2}	3.96×10^{-5}	8.2×10^{2}	^{89}Y(n,5n)
Y-86	2.8×10^{2}	1.31×10^{-5}	2.9×10^{2}	^{89}Y(n,4n)
Y-87	2.2×10^{3}	2.40×10^{-6}	2.2×10^{3}	^{89}Y(n,3n)
Y-87m	3.2×10^{3}	1.50×10^{-5}	3.4×10^{3}	^{89}Y(n,3n)
Y-88	3.7×10^{2}	7.53×10^{-8}	3.7×10^{2}	^{89}Y(n,2n)
Lu-177m	5.7×10^{3}	5.01×10^{-8}	5.7×10^{3}	^{181}Ta(n,nα)
Lu-178m	9.1×10^{2}	5.00×10^{-4}	5.5×10^{3}	^{181}Ta(n,α)
Hf-177m2	8.3×10^{2}	2.25×10^{-4}	1.9×10^{3}	^{180}W(n,α); ^{181}Ta(n,4np)
Hf-178m2	8.1×10^{2}	7.09×10^{-10}	8.1×10^{2}	^{180}W(n,h); ^{181}Ta(n,nt); ^{182}W(n,nα)
Hf-179m2	1.1×10^{3}	3.20×10^{-7}	1.1×10^{3}	^{180}W(n,2p); ^{181}Ta(n,t); ^{182}W(n,α)
Hf-180m	9.9×10^{2}	3.50×10^{-5}	1.1×10^{3}	^{181}Ta(n,d); ^{182}W(n,h); ^{183}W(n,α)
Hf-181	1.8×10^{3}	1.89×10^{-7}	3.4×10^{2}	^{181}Ta(n,p); ^{182}W(n,2p); ^{184}W(n,α)
Hf-182	3.4×10^{2}	5.03×10^{-7}	1.8×10^{3}	^{183}W(n,2p); ^{184}W(n,h); ^{186}W(n,nα)
Hf-182m	1.0×10^{3}	1.88×10^{-4}	2.0×10^{3}	^{183}W(n,2p); ^{184}W(n,h); ^{186}W(n,nα)
Hf-183	1.2×10^{3}	1.81×10^{-4}	2.3×10^{3}	^{184}W(n,2p); ^{186}W(n,α)
Hf-184	3.4×10^{3}	4.67×10^{-5}	4.0×10^{3}	^{186}W(n,h)
Ta-171	5.2×10^{2}	4.96×10^{-4}	3.1×10^{3}	^{186}W(n,2p)
Ta-180m	1.9×10^{3}	1.2×10^{-23}	1.7×10^{3}	^{180}W(n,t); ^{181}Ta(n,4n); ^{182}W(n,2nt)
Ta-182	7.7×10^{2}	7.00×10^{-8}	7.7×10^{2}	^{181}Ta(n,γ); ^{182}W(n,p); ^{183}W(n,d)
Ta-183	3.1×10^{3}	1.58×10^{-6}	3.1×10^{3}	^{183}W(n,p); ^{184}W(n,d); ^{186}W(n,nt)
Ta-184	5.9×10^{2}	2.21×10^{-5}	6.4×10^{2}	^{184}W(n,p); ^{186}W(n,t)
Ta-185	4.1×10^{3}	2.36×10^{-4}	9.6×10^{3}	^{186}W(n,d)

Table 2 List of important isotopes contributing to gamma ray activation in IFMIF.

Isotope	Typical gamma-ray induced reactions	Isotope	Typical gamma-ray induced reactions
C-11	^{12}C(γ,n)	N-13	^{14}N(γ,n)
F-18	^{19}F(γ,n)	Na-22	^{23}Na(γ,n)
Al-26	^{27}Al(γ,n)	V-50	^{51}V(γ,n)
Cr-49	^{50}Cr(γ,n)	Mn-54	^{55}Mn(γ,n)
Ni-57	^{58}Ni(γ,n)	Cu-64	^{65}Cu(γ,n);
Y-88	^{89}Y(γ,n)	Ta-180m	^{181}Ta(γ,n)

Table 3 List of important isotopes contributing to neutron activation in IFMIF.

Isotope	Typical deuteron induced reactions	Isotope	Typical deuteron induced reactions
H-3	X(d,t)	Be-7	^{6}Li(d,n); ^{7}Li(d,2n); ^{12}C(d,hα)
C-11	^{12}C(d,t); ^{14}N(d,nα)	C-14	^{14}N(d,2p); ^{16}O(d,2pd)
N-13	^{12}C(d,n); ^{14}N(d,t); ^{16}O(d,nα)	Na-22	^{27}Al(d,tα)
Na-24	^{27}Al(d,pα)	Mg-27	^{27}Al(d,2p)
Al-26	^{27}Al(d,t)	Al-28	^{27}Al(d,p)
V-48	^{50}Cr(d,α); ^{52}Cr(d,2nα)	V-50	^{52}Cr(d,2p); ^{52}Cr(d,α); ^{53}Cr(d,nα)
Cr-48	^{50}Cr(d,2nd)	Cr-49	^{52}Cr(d,nd)
Mn-51	^{54}Fe(d,nα)	Mn-52,m	^{52}Cr(d,2n); ^{54}Fe(d,α)
Mn-54	^{54}Cr(d,2n); ^{56}Fe(d,α); ^{57}Fe(d,nα)	Fe-52	^{56}Fe(d,2nd)
Fe-59	^{58}Fe(d,p); ^{62}Ni(d,pα)	Co-55	^{58}Ni(d,nα)
Co-56	^{56}Fe(d,2n); ^{58}Ni(d,α)	Co-58	^{58}Fe(d,2n); ^{58}Ni(d,2p); ^{60}Ni(d,α)
Co-60	^{60}Ni(d,2p); ^{62}Ni(d,α); ^{63}Cu(d,pα)	Co-62m	^{62}Ni(d,2p); ^{64}Ni(d,α); ^{65}Cu(d,pα)
Ni-56	^{58}Ni(d,2nd)	Ni-57	^{58}Ni(d,2np)
Ni-65	^{64}Ni(d,p); ^{65}Cu(d,2p)	Cu-61	^{62}Ni(d,2n); ^{63}Cu(d,2nd)
Cu-64	^{63}Cu(d,p); ^{64}Ni(d,2n); ^{65}Cu(d,nd)	Lu-178m	^{181}Ta(d,pα)
Hf-177m2	^{180}W(d,pα)	Hf-178m2	^{181}Ta(d,nα)
Hf-179m2	^{181}Ta(d,α); ^{182}W(d,pα)	Hf-180m	^{181}Ta(d,pd); ^{182}W(d,2pd); ^{183}W(d,pα)
Hf-181	^{181}Ta(d,2p); ^{183}W(d,2pd); ^{184}W(d,pα)	Hf-182	^{184}W(d,2pd)
Hf-183	^{186}W(d,pα)	Hf-184	^{183}W(d,2pd)
Ta-180m	^{180}W(d,2p); ^{181}Ta(d,nd); ^{182}W(d,α); ^{183}W(d,nα); ^{184}W(d,2nα)	Ta-182	^{181}Ta(d,p); ^{182}W(d,2p); ^{183}W(d,pd); ^{184}W(d,α); ^{186}W(d,2nα);
Ta-183	^{183}W(d,2p); ^{184}W(d,pd); ^{186}W(d,nα);	Ta-184	^{184}W(d,2p); ^{186}W(d,α);
Ta-185	^{186}W(d,pd);		

(4) Production of Activated Material

(a) Neutron Induced Activity

The neutron spectra produced by deuteron bombardment depend on the bombarded materials and incident deuteron energy. So it is convenient to assume a set of typical neutron spectra to represent the overall characteristics of induced activity at every area in IFMIF.

The neutron spectra from D-Li source reaction are used as the reference, and those obtained at the three typical emission angles, 0-, 90-, and 180-deg are shown in Fig. 2. The variation of the mean energy as a function of the emission angle is given in Fig. 3. For other elements, the nature of the angle-dependent neutron spectrum is similar to that for lithium, except that the total production yield of neutrons and the detailed shape of the energy / angular dependence are different according to the specific properties of each nuclei.

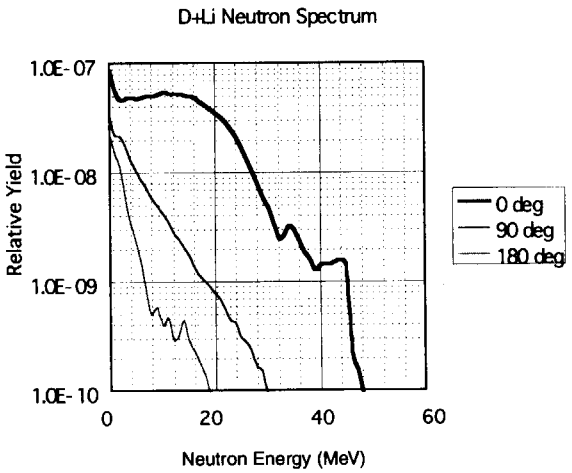


Fig. 2 Typical neutron spectra for lithium bombarded by 40 MeV deuterons at the neutron emission angles, 0-, 90-, and 180-deg.

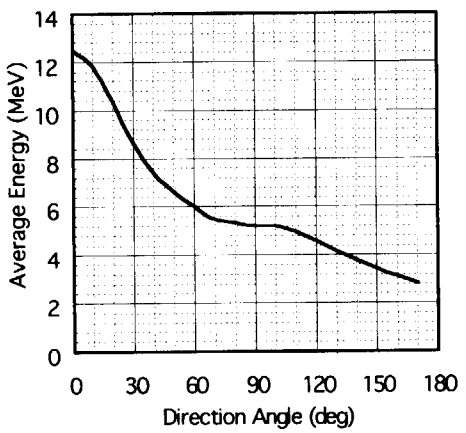


Fig. 3 Average energy of Li+d neutron spectra at various direction angles

Therefore, the following three energy groups are identified as the reference spectra in this study:

Group 1: highest energy region, mean energy ~10 MeV or more,
e.g. target backwall, test modules, front wall of test cell shield;

Group 2: middle energy region, mean energy ~5 – 10 MeV,
e.g. side-walls of target assembly, side wall of test cell shield, high energy beam transport line components bombarded by beam-loss deuterons;

Group 3: lower energy region, mean energy ~2 – 5 MeV,
e.g. beam pipes connected to target assembly, back wall of test cell shield, injector and linear accelerator components bombarded by beam-loss deuterons.

Table 4 Neutron-induced activation cross sections for important radioisotopes.

Radio-isotope	Material isotope	Threshold energy	Cross sections (mb)		
			Group 1	Group 2	Group 3
^{3}H	^{12}C	20.5MeV	σ_{max} < 10	–	–
	^{14}N	4.3MeV	20	20	–
	^{16}O	15.4MeV	σ_{max} < 20	–	–
	^{27}Al	11.3MeV	σ_{max} ~20	–	–
	^{28}Si	16.7MeV	σ_{max} < 10	–	–
	^{56}Fe	12.1MeV	σ_{max} (15~60)	–	–
	^{63}Cu	8.3MeV	σ_{max} ~20	–	–
	^{65}Cu	8.8MeV	σ_{max} ~20	–	–
	^{181}Ta	4.9MeV	σ_{max} ~20	–	–
^{7}Be	^{12}C	27.4MeV	σ_{max} < 10	–	–
^{11}C	^{12}C	20.3MeV	σ_{max} ~20	–	–
	^{14}N	24.4MeV	σ_{max} < 10	–	–
^{14}C	^{14}N	(-0.7MeV)	50	20	~30 (resonance region)
	^{16}O	15.5MeV	σ_{max} < 4	–	–
^{13}N	^{14}N	11.3MeV	σ_{max} ~10	–	–
^{22}Na	^{23}Na	13.0MeV	σ_{max} ~150	–	–
^{24}Na	^{27}Al	3.2MeV	130	30	–
^{27}Mg	^{27}Al	1.9MeV	100	80	10
^{26}Al	^{27}Al	13.5MeV	σ_{max} ~300	–	–
	^{28}Si	16.7MeV	σ_{max} ~20	–	–
^{41}Ar	^{41}K	1.8MeV	50	25	5
^{43}K	^{43}Ca	1.1MeV	100	140	90
^{44}K	^{44}Ca	5.0MeV	40	1	–
^{54}Mn	^{56}Fe	12.1MeV	σ_{max} (50~300)	–	–
^{65}Ni	^{65}Cu	1.4MeV	20	10	–
^{61}Cu	^{63}Cu	20.1MeV	σ_{max} ~200	–	–
^{64}Cu	^{63}Cu	(-10.1MeV)	2	35	50
	^{65}Cu	10.1MeV	σ_{max} ~1000	–	–

The cross sections to produce some important radioisotopes are obtained from the existing data libraries and the available experimental data for each group, and the results are given in Table 4. The values are rough estimates and their uncertainties are about 30% for reactions having cross section larger than 100 mb and exceed 50% for those having smaller cross sections. The σ_{max} in the table indicates that the reaction cross section is rising in the 20-60 MeV region and only the maximum value is given as guidance. The tritium production is relatively insensitive to the materials except for carbon and silicon whose threshold energies are very high. The main production of ^{3}H, ^{7}Be, $^{11,14}C$ will occur in the group 1 area except for nitrogen. The ^{24}Na and ^{27}Mg in aluminum are produced in the lower energy groups so that the use of aluminum components in the high neutron flux area should be restricted if remote maintenance in not available. The content of Na, K and Ca in the shielding concrete is particularly important in estimating the total dose for maintenance operations. A large discrepancy among the data libraries is found for the ^{54}Mn production in iron and it is necessary to determine the

most probable evaluation. The activation of copper will occur at every place where copper is used and neutrons are produced, so the neutron production should be controlled to the minimum level achievable in copper component zones.

(b) Gamma-ray Induced Activity

The most important reactions in this category are (γ,n) in the viewpoint of cross sections below Eγ~20MeV as listed in Table 2. The high-energy gamma rays are produced by the fast neutron collisions rarely and a possible source is neutron capture at thermal energy or ^{6,7}Li(d,γ) at the target. Therefore, carbon or other elements contained in the shielding wall and the elements used as structural materials, such as Al, V, Cr, Ni, and Cu, in the target assembly or the test modules. For both cases, neutron-induced activation is taking place at the same time, and the contribution to the total activity by gamma rays is usually a small fraction of the total.

(c) Deuteron Induced Activity

Deuteron energy up to 40 MeV is considered in IFMIF and the integrated yield of the activity production in the thick target material is important. In the typical case, the activity produced by deuterons is an order of magnitude higher than that produced by protons with the same energy, and is similar to the level of activity produced by neutrons with the same energy. Consequently, the result of the neutron-induced activation can be used as an estimate of the deuteron-induced activity, and multiplied by an adjustment factor. Tritium production through (d,t) reactions in the materials is more probable than the (n,t) reactions, and can be estimated using a higher multiplication factor with the neutron tritium production case.

(5) Conclusions and Discussion

The important elements that contribute to the total radioactivity in IFMIF are surveyed and the reaction list is identified to be used in further study and detailed evaluation of the expected dose during maintenance. The selection of radioisotopes is based on the clearance data, and neutron-, photon- and deuteron-induced channels are considered. For the neutron-induced activation cross sections, enough data are available to derive the quantitative comparison of the importance among the possible contributing elements. On the other hand, photon- and deuteron-induced activities are investigated only qualitatively in this stage, mainly due to the paucity of reliable data. It is recommended that systematical experimental research be initiated to verify the theoretical estimations of activation and to improve the data libraries.

References

[1] M. Martone, (editor), IFMIF International Fusion Materials Irradiation Facility Conceptual Design Activity Final Report, ENEA Frascati Report, RT/ERG/FUS/96/11, November 1996.

[2] R. A. Forrest and J-Ch. Sublet, "The European Activation File: EAF-99 biological, clearance and transport libraries", UKAEA FUS 410 (1998).

3.4.3 DI41-JA : Design of Buildings

(1) Brief Task Description

IFMIF building design is performed in parallel with the subsystem design. Building and site layout for the reduced cost, staged IFMIF were designed during the KEP.

The site area is about 250 m × 200 m. The IFMIF facilities mainly consist of Administration Building and Main Building for Accelerator, Target, and Test Facilities. The area of the Main Buildings is about 170 m × 60 m. The building height is 26 m aboveground and 11 m underground. For reduction of IFMIF construction cost, the building height, especially the underground part, was reduced. The accelerator with a length about 110 m is installed on the ground floor, and the lithium loop is mainly installed below ground level. The Target/Test Building, which is a part of the Main Building, was designed to meet Japanese seismic engineering guidelines. Furthermore, stainless steel linings are included in the Test Cell, Access Cell and Test Module Handling Cell to control activated materials and lithium leakage. The seismic class depends on assumed accident scenarios and applicable regulations, thus depend on the specific IFMIF site location. The design to meet this regulation is being evaluated in task DI91. Detailed design was performed for the Access Cell and Tritium Laboratory. Two lines of handling/experiment equipment are installed in the Tritium Laboratory to handle Tritium Modules and Target Assembly.

The results of this task are reported in the following sections, along with progress in subsystem designs.

Contributors

Name	Party	Institute	E-mail address
M. Ida	Japan	JAERI	ida@ifmif.tokai.jaeri.go.jp
T. Yutani	Japan	JAERI	yutani@ifmif.tokai.jaeri.go.jp
M. Takeda	Japan	JAERI	mtakeda@popx.tokai.jaeri.go.jp
H. Takeuchi	Japan	JAERI	takeuchi@fnshp.tokai.jaeri.go.jp

(2) Site Layout

This design assumes that IFMIF is located within an existing nuclear research facility that is surrounded by an exclusion boundary and is able to supply services such as electric power and water. The IFMIF buildings consist of a Main Building (Accelerator Building and Target / Test Building), an Administration Building and others. The site measures 200 m by 250 m. The site area, originally assumed to be about 10 ha, has been reduced to 5 ha through redesign for cost reduction. The following facilities will be provided in this area:

- Accelerator Building,
- Target and Test Building,
- Administration Building,
- Electrical Switchyard,
- Emergency Power Area,
- Cooling Tower Area,
- Cooling Water Blowdown Pond, and
- Others (Access Gate, Parking Area, Warehouse)

The site layout is shown in Fig. 1. Construction planned for phase two of the project is shown as "expansion area" in the figure.

(3) Buildings

This section describes designs on buildings those house and support three major subsystem facilities (Accelerator, Target, and Test Facilities). The Main Building that houses these facilities is designed in accordance with radiation-protection requirements. The building layout is shown in Figs. 2 through 6.

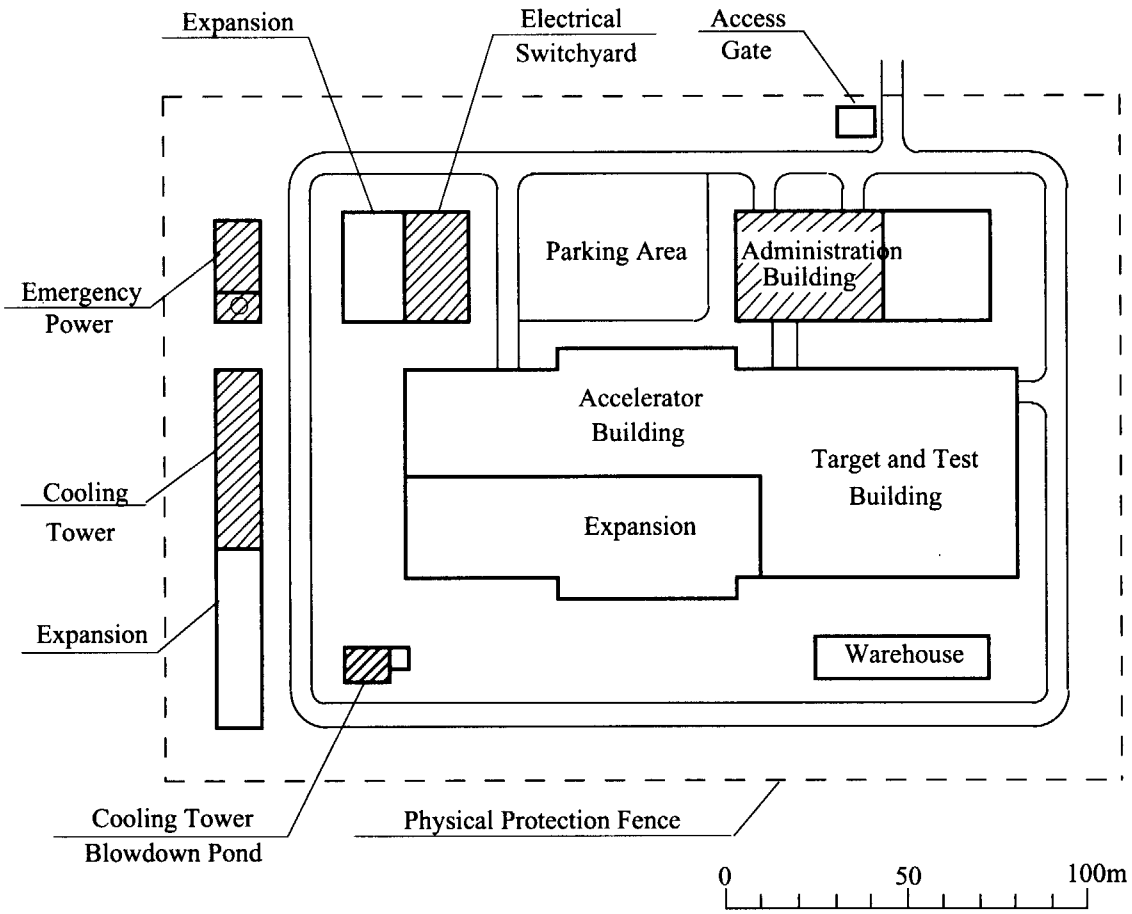


Fig. 1 Site layout.

(a) Accelerator Building

The Accelerator Building consists of the accelerator vault, RF power bay, assembly maintenance bay, heat exchange room and shipping bay. The Accelerator Building is constructed to accommodate the staged deployment, namely only the structure to house the first Accelerator is erected in stage one, and the building sections for the second Accelerator are deferred until the second stage of the project. The Accelerator Building is a reinforced concrete structure and is anchored to bedrock. Exterior walls, floors, and roof of the Accelerator Building will be waterproof to preclude seepage of water.

The dimensions of the accelerator vault are determined by the maintenance approach. Personnel access to the vault will be allowed after shutdown, with a reasonable activity decay (cool down) time to be determined. Local shielding and portable shielding will be used as required.

For maintenance functions, bridge cranes (one each) are installed in the RF Power Bays (R103) and the Shipping Bay (R102). A hoist crane is installed in the Accelerator Vault (R108). The Accelerator Building must be constructed according to the standards related to earthquake, wind load and soil condition.

(b) Target and Test Building

The Target and Test Building is the main building other than the Accelerator Building. The Target and Test Building includes beam transport rooms, the Test cell, the Access cell, the Tritium laboratory, a radioactive waste processing room, the Control room, a health physics room, etc. The Target and Test Building is a reinforced concrete structure and is anchored to bedrock. Exterior walls, floors, and roof of the Target and Test building will be waterproof to preclude water seepage.

In the lithium loop area, lithium leaks must be assumed during the loop lifetime, which could result in a possible fire through Li/air reactions. Therefore, the lithium loop area must be designed to guarantee no combustion in the event of a leak. This can be achieved by the use of confinement of the lithium loop area combined with a containment structure to exclude the outside atmosphere and a system to provide a controlled argon gas atmosphere. In the Lithium loop area, leaked lithium is caught and detected in troughs under the piping. Personnel access for inspection and maintenance is permitted after shutdown and draining of the lithium to the dump tank and replacing the argon gas with an air atmosphere.

The lithium target and all test assemblies will be accommodated in the Test Cell without any barrier between the lithium target back-wall and the test assemblies. The Test Cell is about 3 m wide, 3 m long, and 6 m high. These values were determined with consideration of the size and arrangement of the target assemblies and quench tank, and the needed working space for remote handling. The Test Cell provides adequate shielding from neutron and gamma radiation to protect personnel and equipment in the adjacent areas. Along the top of the Test Cell, a removable concrete shielding plug protects the equipment of the adjacent area. In order to maintain a pressure of 0.1 Pa in the Test Cell during normal operation of the facility, the entire inner surface is covered by a reduced activation ferritic steel liner. The liner also provides lithium containment to minimize risk in case of lithium leak.

During replacement of the Test assemblies and the Target, tritiated argon (Ar) gas will be discharged from the Test Cell. The Test Cell will be flooded with Ar before starting maintenance operations. Tritium will be discharged from components of the Target assembly during the cutting and removal operation, and the tritium concentration in the Ar atmosphere may be high. The atmosphere of the Test Cell is also circulated to monitor and control the impurity level in the Ar gas, and is kept at negative gage pressure to prevent uncontrolled releases of tritium to the Access Cell. The exhaust tritiated Ar gas will be processed in the Gaseous Waste System, described in Section 3.4.4. Helium cooling pipes are installed in the walls of the Test Cell to remove the heat generated by neutrons.

Lithium is very reactive with concrete, air, water, carbon dioxide, and nitrogen. Therefore, a stainless steel drip tray will catch any leaking liquid lithium from the loop components in the Lithium loop area (R001) and Trap area (R002) where leaks must be assumed. Epoxy paint will be used in the following areas: Organic area (R004), Radioactive waste processing room (R122), Exhaust processing room (R121), Vacuum pump room (R118), Beam transport room (R109), Radiation isolation area (R113), Target interface room (R114), Access/Maintenance room (R209), Lithium loop area (R001), and Trap Area (R002). Areas where stainless steel lining is used on all surfaces are: Test Cell (R115) (reduced activation ferric steel), Access cell (R207), Storage cell (R112), and Test module handling room (R210). For maintenance purposes, bridge cranes are installed in the Access cell, Test module handling room, Access/Maintenance room shipping bay and high bay.

(c) Other Buildings

The other buildings include the administration building, the electrical switchyard, the emergency power and the cooling tower. The administration building is about 40m × 30m in the first stage of the project and will be expanded in the second stage. This building includes office area, reception and visitor control areas and workshop areas.

(4) Fire Protection

The structure of the IFMIF will be noncombustible. Concrete and steel will be the main materials used for the structure. The lithium loop will be separated from other parts of the facility by shielding doors. An interior partition within the building will separate process areas, work areas and laboratories to limit the spread of any fires that do start. The IFMIF will be equipped with smoke detection systems and fixed type fire extinguishers. The smoke detection system will be installed in all rooms that can have personnel access. The fixed type fire extinguishers will be installed in the Electrical Room and RF power bay.

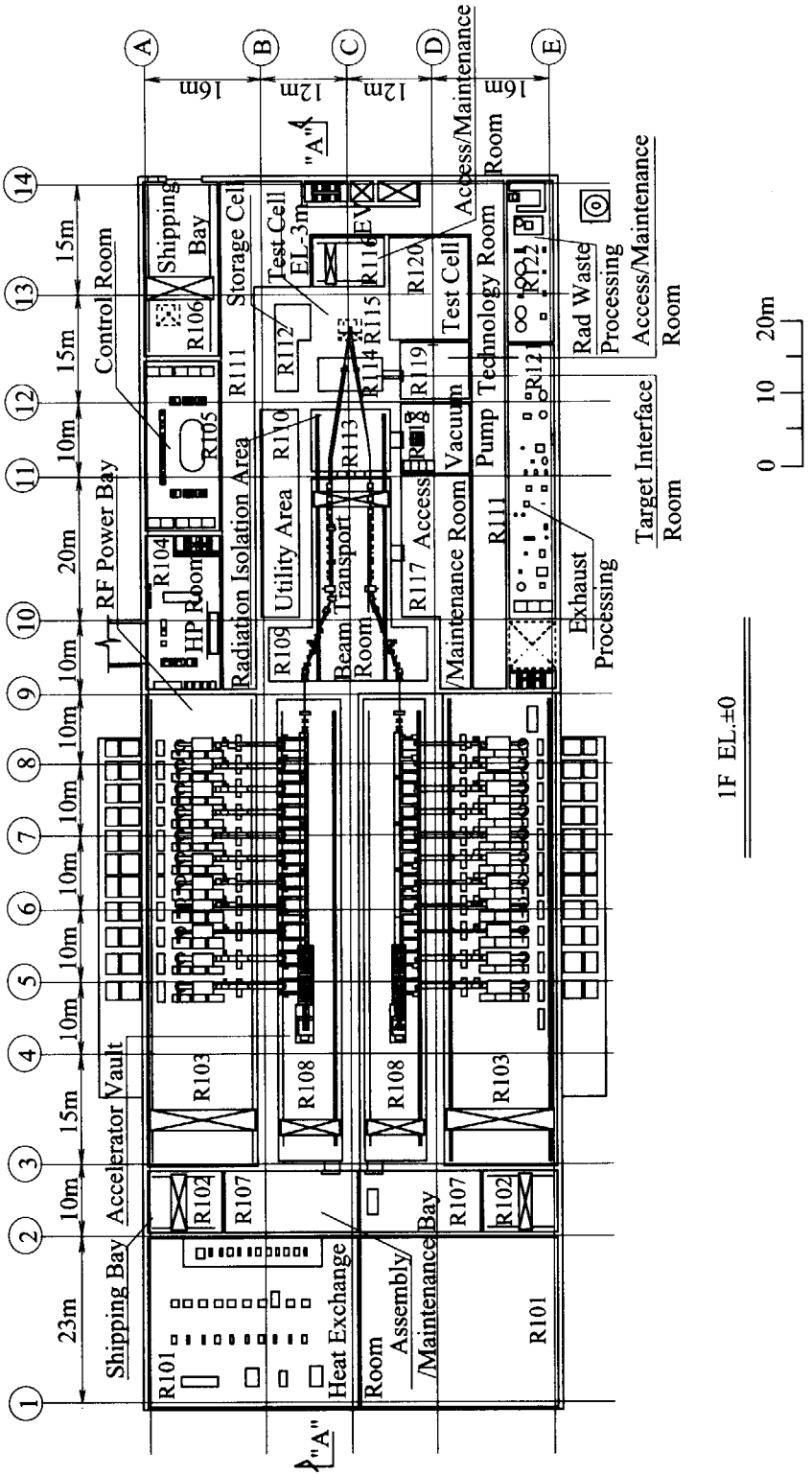


Fig. 2 Plan view of the Main Building, first floor (1F).

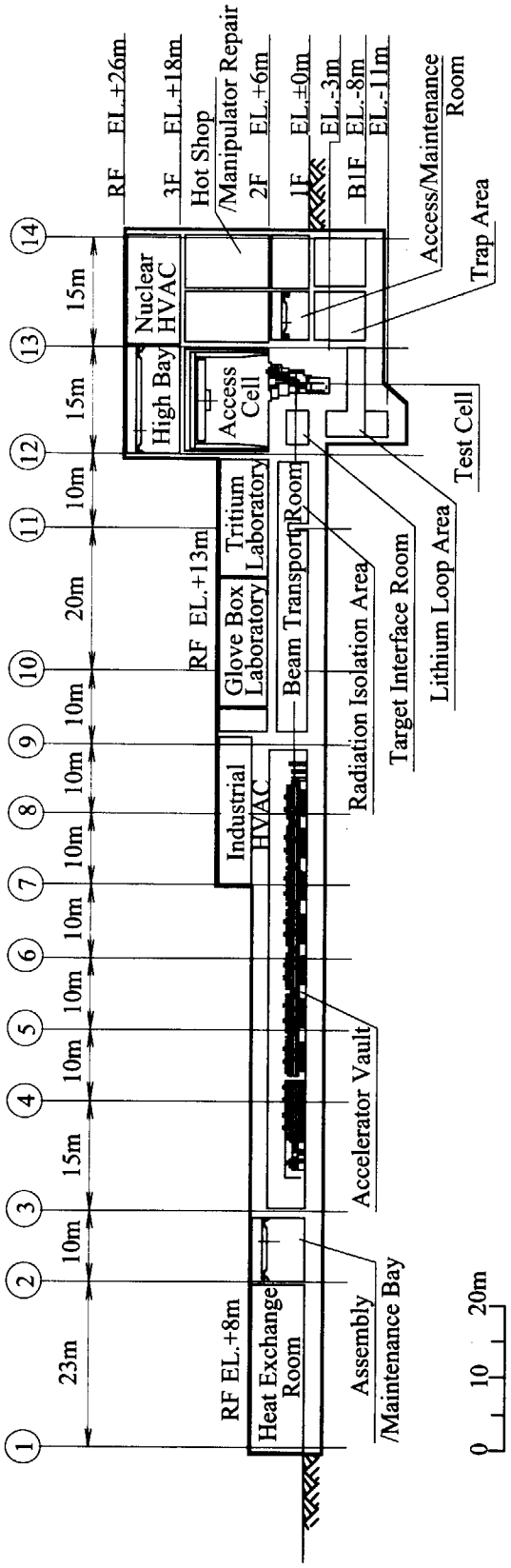


Fig. 3 Elevation view of the Main Building.

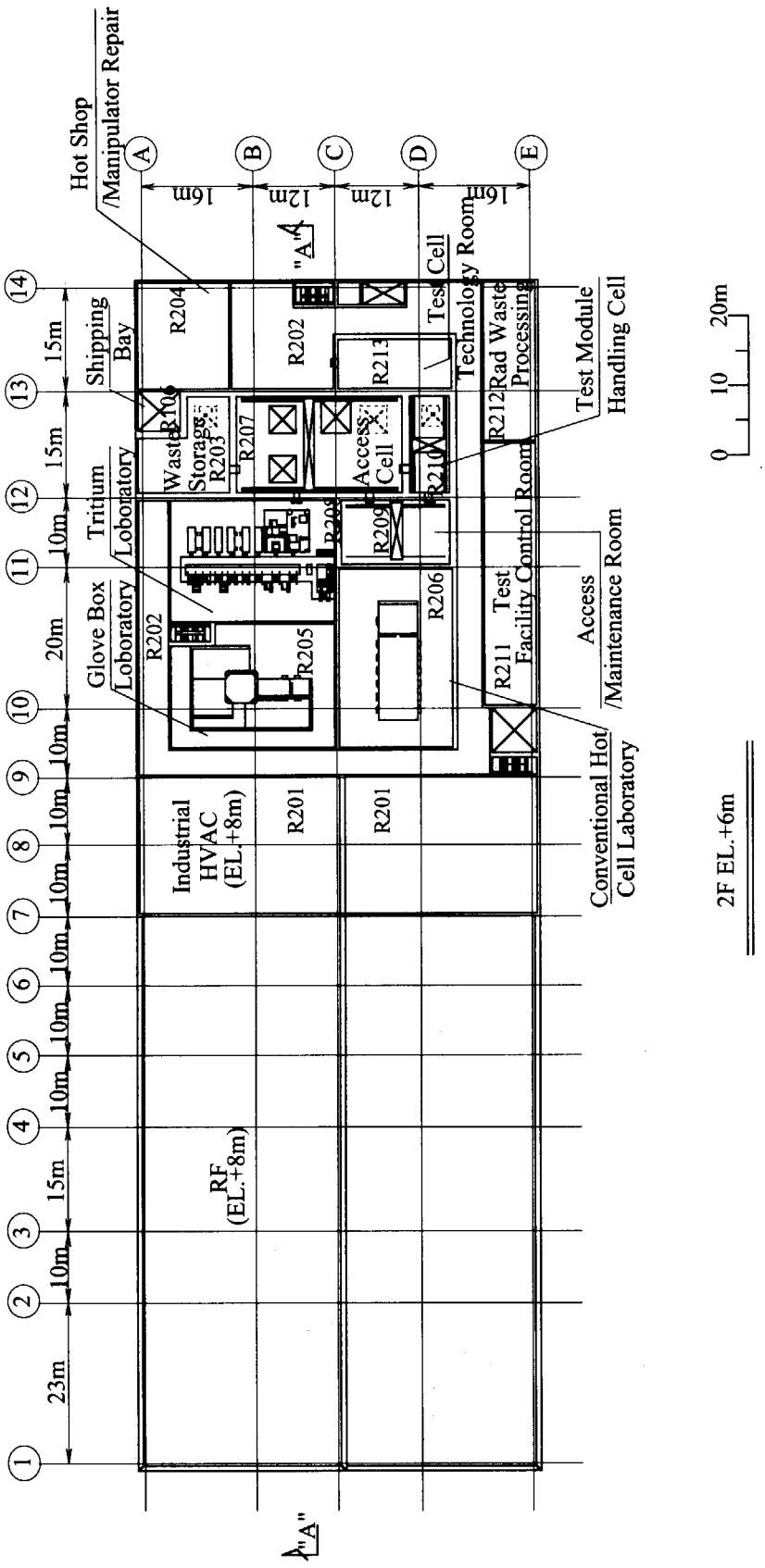


Fig. 4 Plan view of the Main Building, second floor (2F).

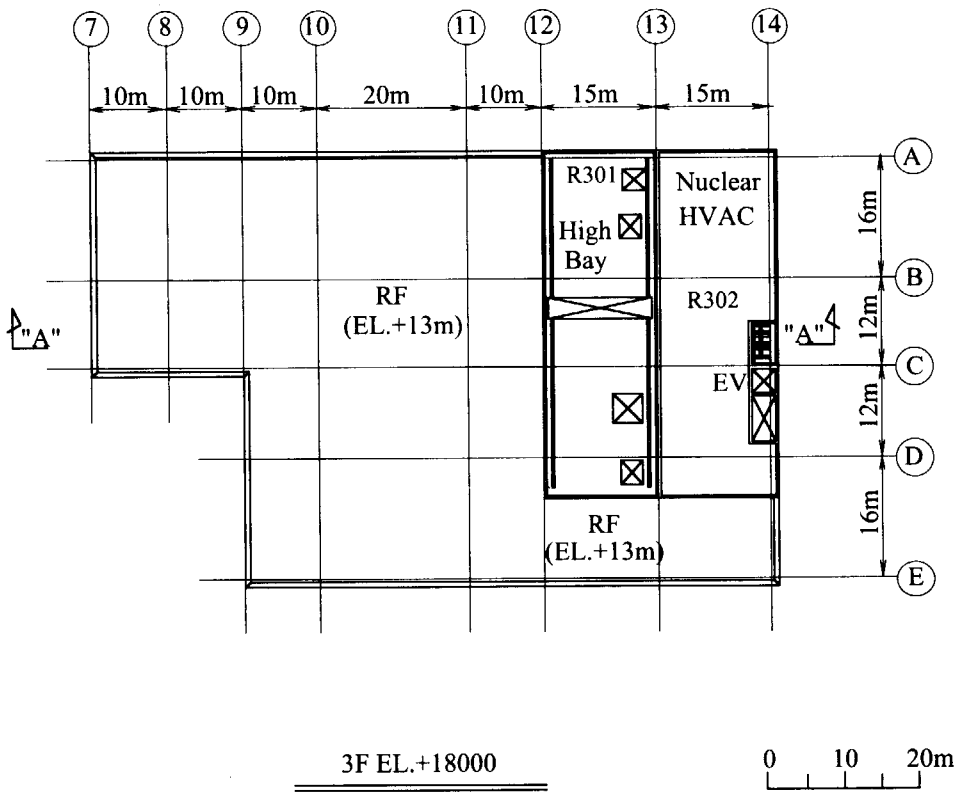


Fig. 5 Plan view of the Main Building, third floor (3F).

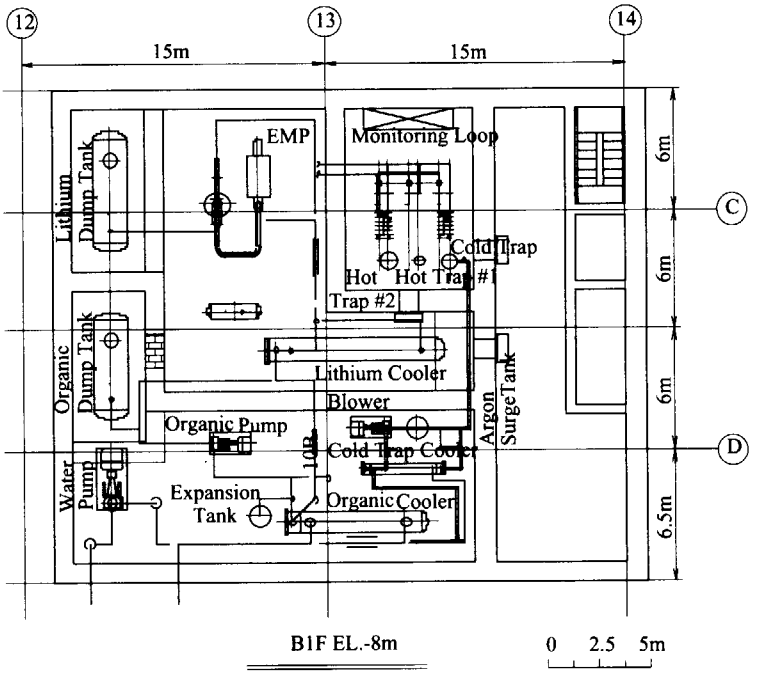


Fig. 6 Plan view of the Main Building basement (B1F).

(5) Summary

The IFMIF site area is about 250 m × 200 m. The IFMIF facilities mainly consist of the Administration Building and the Main Building for Accelerator, Target, and Test Facilities. The area of the latter buildings is about 170 m × 60 m. In the first stage of construction, one accelerator vault is constructed for the first accelerator. The Target and the Test Cell are also constructed in the first stage. The RF power supplies are installed outside this building. The building height is 26 m aboveground and 11 m underground. To minimize IFMIF construction cost, the building height, especially the underground part, was reduced. The accelerator with a length about 110 m is installed on the ground floor, and the lithium loop is mainly installed at the underground level. The Target/Test Building, which is a part of the Main Building, was designed to meet Japanese seismic engineering guidelines. Furthermore, stainless steel linings in the Test Cell, Access Cell, and Test Module Handling Cell reduce concerns about activated materials and lithium leakage.

The seismic class depends on assumed accident scenarios and applicable regulations, thus, depends on the specific IFMIF site location. Detailed design was performed for the Access Cell and Tritium Laboratory. Two lines of handling/experiment equipment are installed in the Tritium Laboratory. One is used for Tritium Modules and the other for Target Assembly. The Target Assembly line includes provision to handle the target back-wall and to have pieces of the back wall tested as irradiated specimens. More detail of this design is being reported as a task under Test Facilities.

3.4.4 DI43-JA : Design of Utilities

(1) Brief Task Description

Utility design is conducted in parallel with the subsystem designs. Utilities for the reduced cost, staged IFMIF were designed during the KEP.

The heating, ventilation and air conditioning (HVAC) system was designed for two categories; industrial and nuclear HVAC systems were separated based on radiological risk. The areas of nuclear HVAC system are filled with air or argon with pressure 200-400 Pa lower than the atmospheric pressure. The required total electric power is 50 MVA, including emergency power. The supplied voltage is 66 kV at the boundary of the assumed IFMIF site. The required capacities for heat rejection by cooling water are 26 MW for the Accelerator system and 13 MW for the Target system. The water temperature is controlled in the range 30-35°C. Gas supply systems were examined for argon (Ar), helium (He), compressed air and nitrogen (N_2). A radioactive waste system was designed for treatment of liquid, gaseous and solid wastes including tritium, beryllium-7 and other radioactive nuclides.

This task included the following work, completed along with the progress in subsystem design.

Contributors

Name	Party	Institute	E-mail address
M. Ida	Japan	JAERI	ida@ifmif.tokai.jaeri.go.jp
T. Yutani	Japan	JAERI	yutani@ifmif.tokai.jaeri.go.jp
H. Takeuchi	Japan	JAERI	takeuchi@fnshp.tokai.jaeri.go.jp

(2) HVAC System

The IFMIF HVAC system treats air and Ar gases. Argon is used in areas where leakage or an exposure to lithium may occur or where large amount of tritium release may occur. Detritiation on Ar is easier and requires smaller equipment than would air. A few pressure levels were employed to confine highly activated atmospheres. Conditions of lower pressure are used in areas of higher activation to prevent high-activation gas flow toward low-activation areas. The HVAC system is composed of two systems based on radiation zoning. An industrial HVAC System serves areas with no radiological risk. A Nuclear HVAC System, serves potentially radioactive areas. Based on the radiation zoning and atmospheric condition, the two HVAC Systems serve areas as follows;

(a) Industrial HVAC System

The HVAC system for non-active areas will provide environment control and the removal of heat generated by operating equipment. Areas not subject to radiological risks are ventilated in accordance with normal industrial ventilation practice; these areas are once-through ventilated at a flow rate ranging from 2 to 5 replacements/hour, depending on the heat load. The following areas are not subject to radiological risk and are therefore equipped with an industrial HVAC system; Control room, Health physics room, and Shipping bay. The total volume served by the industrial HVAC system is 4500 m^3 and the required flow rate is around 15,000 m^3/h.

(b) Nuclear HVAC System

The Nuclear HVAC system serves the Accelerator Building and the Target and Test Building, providing a safe and comfortable environment for personnel. The spread of activated air within the buildings is controlled through the use of differential pressures, so that air flows from potentially low contamination to high contamination areas. The atmosphere is continuously monitored for gamma activity and tritium, and is kept at negative gauge pressure (in the range 20-50 Pa) with respect to the adjacent operating areas and to the external atmosphere. This will prevent any uncontrolled release of radioactivity.

The Lithium Loop Area, the Test Cell, and the purged Ar in the hot cell and the Tritium Laboratory will be ventilated and exhausted through the Exhaust Gas Treatment System. Hot cells in

the Tritium Laboratory will also be kept in an Ar atmosphere. The hot cells will be ventilated through a circulating ventilation system in the Tritium laboratory. The exhausted gas, at negative gauge pressure, will be processed in the Exhaust Gas Treatment System. The configuration of the nuclear HVAC system is shown in Fig. 1. The room and cell conditions are shown in Table 1. The outside temperature and humidity for summer and winter will depend on the IFMIF site location, and the Nuclear HVAC System size will be determined according to these conditions.

HVAC I-1 serves potentially high contamination areas that are the Access cell and the Test Module Handling Cell. Local HEPA (high-efficiency particulate air) filters are located adjacent to the cell. The total volume served by the HVAC I-1 system is 4800 m^3 and the required flow rate is around 5000 m^3/h. The enclosure atmosphere is kept at –400 Pa (gage) (i.e. 400 Pa lower than 1 atm). If tritium is detected, the air intake valve is closed and the exhaust gas is sent to the temporary exhaust detritiation system.

HVAC I-2 serves areas related to liquid lithium. During operation, Ar gas is maintained as the atmosphere in the lithium area. The total volume is 1500 m^3 and the required flow rate (air) during maintenance operation is around 4500 m^3/h. The enclosure atmosphere is kept at –300 Pa (gage).

HVAC I-3 serves the Test cell. During operation, the pressure is maintained at 0.1 Pa in the Test Cell. For maintenance, the pressure will be increased to –400 Pa (gage) of Ar atmosphere.

HVAC I-4 serves potentially contaminated areas such as the accelerator vault and beam transport room. The total volume is 4,000 m^3 and the required flow rate is around 15,000 m^3/h. The enclosure atmosphere is kept at –300 Pa (gage). In case tritium is detected, the air intake valve is closed and exhaust gas is sent to the temporary exhaust detritiation system.

HVAC II serves areas such as the heat exchange room and tritium laboratory that are less contaminated and exceed 0.3 mSv/week. The total volume is 67,000 m^3 and the required flow rate is around 240,000 m^3/h. The enclosure atmosphere is kept at –200 Pa (gage). The atmosphere from the High bay and Assembly/Maintenance bay is not processed, and access to and from these areas is controlled.

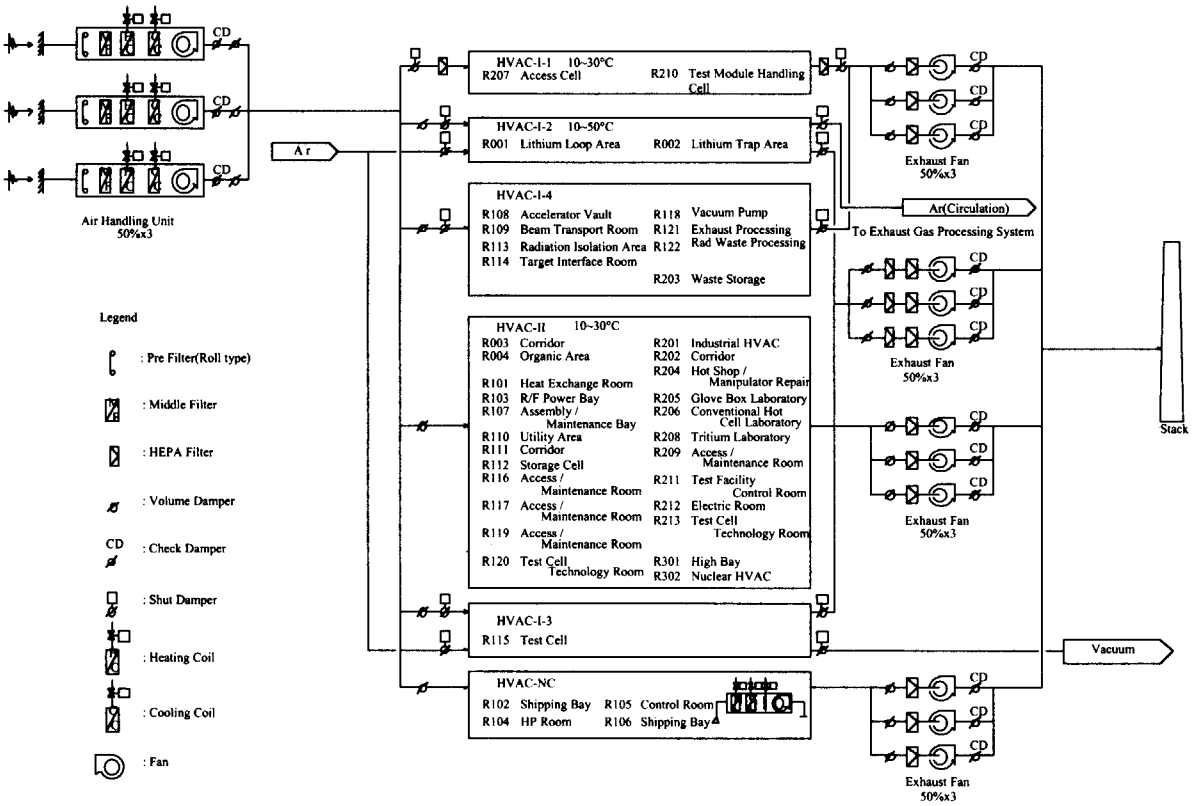


Fig. 1 Block diagram of HVAC systems.

Table 1 Room design condition.

Room No.	Room Name	HVAC ID	Area m2	Vol. m3	Maintenance Temp. CDB	Maintenance Pressure mmH2O	Operation Temp. CDB	Operation Pressure mmH2O
R001	Lithium Loop Area	I -2	200	1,134	10-50	-30	NC	-30
R002	Lithium Trap Area	I -2	59	410	10-50	-30	NC	-30
R003	Corridor	II	146	1,022	10-30	-20	10-30	-20
R004	Organic Area	II	144	1,008	10-30	-20	10-30	-20
R101	Heat Exchange Room	II	674	5,057	10-30	-20	10-30	-20
R102	Shipping Bay	NC	90	673	22-26	-10	22-26	-10
R103	R/F Power Bay	II	1,015	5,584	10-30	-20	10-30	-20
R104	HP Room	NC	200	1,098	22-26	-10	22-26	-10
R105	Control Room	NC	241	1,325	22-26	-10	22-26	-10
R106	Shipping Bay	NC	249	1,367	22-26	-10	22-26	-10
R107	Assembly / Maintenance Bay	II	311	2,330	10-30	-20	10-30	-20
R108	Accelerator Vault	II	574	3,156	10-30	-20	10-30	-20
R109	Beam Transport Room	II	394	1,774	10-30	-20	10-30	-20
R110	Utility Area	II	157	862	10-30	-20	10-30	-20
R111	Corridor	II	939	5,165	10-30	-20	10-30	-20
R112	Storage Cell	II	48	265	10-30	-20	10-30	-20
R113	Radiation Isolation Area	II	94	421	10-30	-20	10-30	-20
R114	Target Interface Room	II	41	142	10-30	-20	10-30	-20
R115	Test Cell	I -3	30	106	10-50	-40	NC	0.1Pa
R116	Access / Maintenance Room	II	65	358	10-30	-20	10-30	-20
R117	Access / Maintenance Room	II	230	1,266	10-30	-20	10-30	-20
R118	Vacuum Pump	I -4	93	509	10-30	-30	10-30	-30
R119	Access / Maintenance Room	II	76	416	10-30	-20	10-30	-20
R120	Test Cell Technology Room	II	158	866	10-30	-20	10-30	-20
R121	Exhaust Processing	I -4	215	1,183	10-30	-30	10-30	-30
R122	Rad Waste Processing	I -4	129	707	10-30	-30	10-30	-30
R201	Industrial HVAC	II	573	2,577	10-30	-20	10-30	-20
R202	Corridor	II	955	8,647	10-30	-20	10-30	-20
R203	Waste Storage	I -4	143	1,645	10-30	-30	10-30	-30
R204	Hot Shop / Manipulator Repair	II	195	2,243	10-30	-20	10-30	-20
R205	Glove Box Laboratory	II	326	2,116	10-30	-20	10-30	-20
R206	Conventional Hot Cell Lab.	II	417	2,708	10-30	-20	10-30	-20
R207	Access Cell	I -1	336	3,864	10-30	-40	10-30	-40
R208	Tritium Laboratory	II	410	2,663	10-30	-20	10-30	-20
R209	Access /Maintenance Room	II	140	907	10-30	-20	10-30	-20
R210	Test Module Handling Cell	I -1	81	926	10-30	-40	10-30	-40
R211	Test Facility Control Room	II	271	2,040	10-30	-20	10-30	-20
R212	Electric Room	II	162	1,863	10-30	-20	10-30	-20
R213	Test Cell Technology Room	II	116	1,328	10-30	-20	10-30	-20
R301	High Bay	II	656	4,921	10-30	-20	10-30	-20
R302	Nuclear HVAC	II	690	5,175	10-30	-20	10-30	-20

(3) Electrical System

The Electrical Power System transforms the grid voltage in order to meet the level specifically required for each facility load and distributes the power to each load. The main distribution voltages are 22 kV for the RF power source and the HEBT, 6.6kV for the high capacity (300 kW) equipment, and 420 V for the low capacity equipment.

IFMIF requires approximately 50 MVA of electrical power, which will be brought from a Substation (outside of IFMIF) to the site. The supply voltage is 66 kV. The normal electrical power line diagram is shown in Fig. 2. The IFMIF will require automatic switching to emergency power on loss of normal electrical power. The emergency system must provide power for fire and radiation detection and alarm systems, the Nuclear HVAC system, key instrument and control systems, and Uninterruptible power supply (UPS) system batteries.

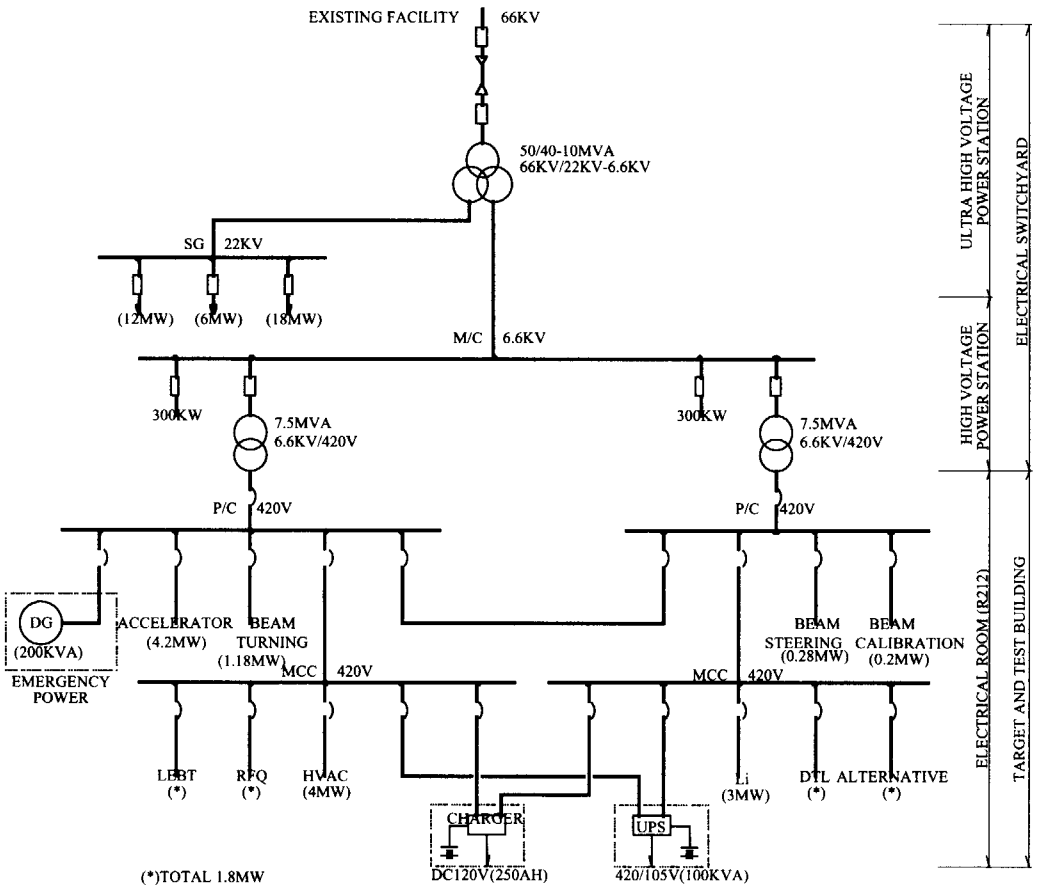


Fig. 2 Block diagram of electric power system.

(4) Cooling Water System

An overall heat rejection capacity of approximately 26 MW and 13 MW is provided for the accelerator and the target systems respectively. Cooling water is supplied at temperatures of 30℃ and 35℃. The Accelerator cooling water will be completely isolated in closed systems, consisting of cooling jackets on the accelerator and a primary intermediate heat exchanger. Heat from the primary circuit will be transferred to secondary loops in the heat exchanger, in order to reduce the risk of leakage of activated products. Demineralized water is used for the primary cooling. Helium gas will be supplied to the buffer tanks of the primary cooling loop. Piping and components are made entirely of austenitic stainless steel to reduce the generation of activated corrosion products. All cooling water will be filtered and demineralized in order to maintain conductivity of less than 1 μ S/cm^2.

Equipment is adopted for periodic sampling and analysis of the water for control of the activated corrosion products and tritium content. The secondary loop water is connected to chiller units and the cooling tower. The system configuration is shown in Fig. 3. Cooling capacity is shown in Table 2. In addition to the above systems, cooling water will be supplied to the helium gas cooling systems, which provide circulating gas to cool liners and covers of the Test Cell and the Vertical Test Assemblies (VTAs). The gas coolant will be maintained at a low pressure and is transported in ducts from the technology room to the Test Cell and the Access Cell.

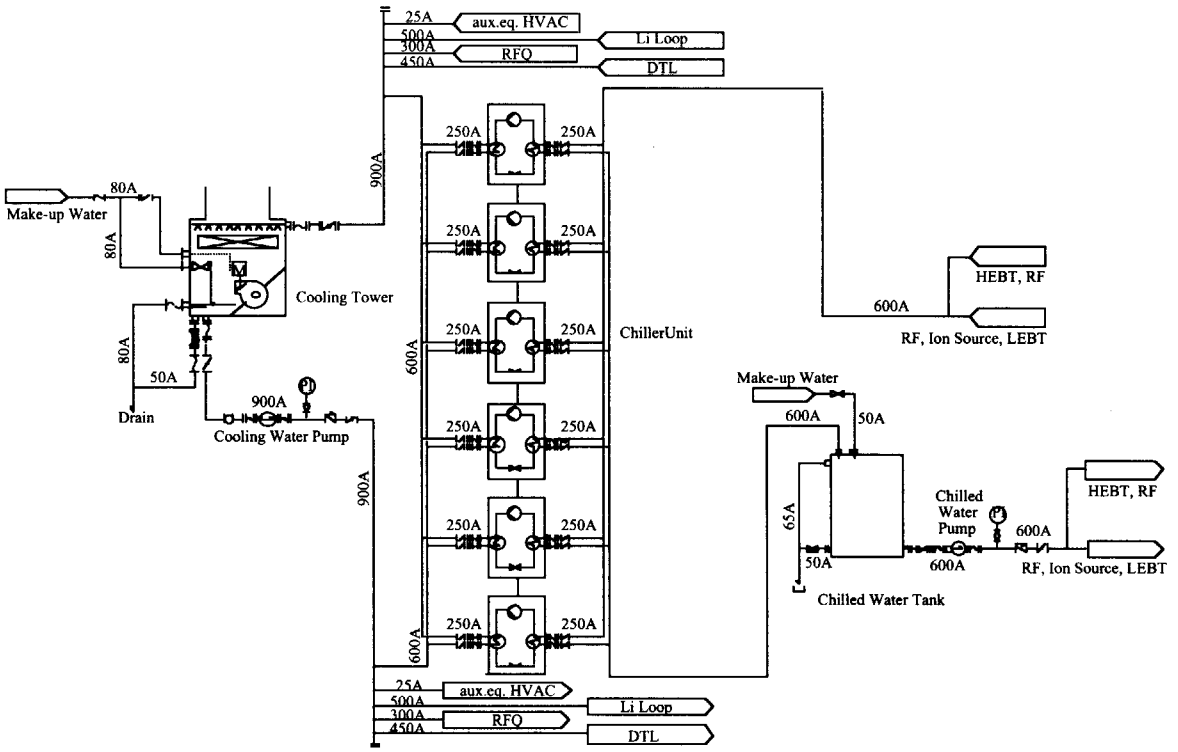


Fig. 3 Block diagram of cooling water system.

Table 2 Capacity of cooling system (MW).

			Supply Temp.	Summation external loop	Summation internal loop
Accelerator	RF	Non-radioactive	30/50℃	–	16.72
	Ion Sauce、LEBT	Non-radioactive	30/50℃	–	0.6
	RFQ	Non-radioactive	35/38℃	–	2.24
	DTL	Radioactive	35/38℃	–	5.6
	HEBT、RF	Radioactive	30/50℃	–	1.36
	aux. eq. HVAC	–	-	0.02	–
Li Loop		–	-	13	–
Summation				13.02	26.52
		Chiller Unit			18.68
		Cooling Tower		39.54	

(5) Service Water System

The industrial water supply for sanitary, process, and fire systems for IFMIF will be supplied by the existing site. The system will provide 70 m^3/h (560 m^3/day assuming 8h operation a day) for sanitary and process uses. The Japan Refrigeration and Air Conditioning Industry Association has

issued guidelines on the quality of supply water for refrigeration and air conditioning components as JRA GL-02-1994. The guidelines for cooling water and chilled water are shown in Table 3. Primary cooling water for the Accelerator will be treated by a demineralizer located in the Utility Area. Requirements of the demineralizer are 10 L/min capacity and maintaining conductivity of 1 μ S/cm^2.

Table 3 Guideline of supply water for refrigeration and air conditioning components (JRA GL-02-1994).

			Guideline			
			Cooling Water		Chilled Water	
			Circulating Water	Supply Water	Circulating Water	Supply Water
Standard	pH	-	6.5~8.2	6.0~8.0	6.8~8.0	6.8~8.0
	Conductivity	μS/cm	≦800	≦300	≦400	≦300
	Cl^-	mg/L	≦200	≦50	≦50	≦50
	SO_4^{2-}	mg/L	≦200	≦50	≦50	≦50
	M alkalinity	mg$CaCO_3$/L	≦100	≦50	≦50	≦50
	Total hardness	mg$CaCO_3$/L	≦200	≦70	≦70	≦70
	Ca hardness	mg$CaCO_3$/L	≦150	≦50	≦50	≦50
	SiO_2	mgSiO_2/L	≦50	≦30	≦30	≦30
Reference	Fe	mg/L	≦1.0	≦0.3	≦1.0	≦0.3
	Cu	mg/L	≦0.3	≦0.1	≦1.0	≦0.1
	S^{2-}	mg/L	Not Detected			
	NH_4^+	mg/L	≦1.0	≦0.1	≦1.0	≦0.1
	Cl	mg/L	≦0.3	≦0.3	≦0.3	≦0.3
	Free Carbon Dioxide	mgCO_2/L	≦4.0	≦4.0	≦4.0	≦4.0
	Stability Index	-	6.0~7.0	-	-	-

(6) Central Vacuum System

A vacuum system will be provided for the Accelerator and Target areas. The vacuum system is composed of turbomolecular, mechanical booster, and dry rotary pumps. The manifold is evacuated by a series of pumps that discharge exhaust at atmospheric pressure. The pumps should be oil-free systems to prevent contamination by tritiated oil. It is anticipated that the effluent will contain lithium vapor/aerosol and tritium and thus requires processing before being released to the environment. The assemblies that are exposed to the beam should be evacuated in order to maintain the vacuum in the range of 0.1 mPa. The beam transport system will also be evacuated, and the exhaust will contain tritium as a product of the reactions in the beam line. The Test Cell should always be evacuated to maintain the vacuum in the range of 0.1 Pa. The vacuum system for the Lithium target is not included in this system. The vacuum system configuration is shown in Fig. 4.

(7) Gas Supply System

Argon (Ar) gas, helium (He) gas, compressed air and liquid nitrogen (N) are used to operate IFMIF.

(a) Argon Supply Unit

The liquid Ar storage vessel and evaporator are located outside of the Target and Test Building. Within the Target and Test Building, the supply line is branched to provide gas to the following services: Ar purge (Lithium system), low-pressure Ar service, and the fire protection Ar flood gas system for lithium fire protection.

(b) Helium Supply Unit

The He gas storage cylinders outside of the Target and Test Building are inter-connected by a manifold. The gas is delivered to the following services: He purge (primary cooling loop), the Test Cell wall cooling systems, and Test Assembly cooling systems.

(c) Compressed Air Unit

An air compressor and storage tank supplies compressed air with pressure of 10 kg/cm^2 (gage) and rate of 10 Nm^3/h (i.e. 10 m^3/h at 0°C) throughout the facility. The compressed air system is located in the Target and Test Building Utility Area.

(d) Nitrogen System

In order to meet the requirements of various system e.g. central vacuum system, a liquid nitrogen system will be provided for the supply of dry inert gas.

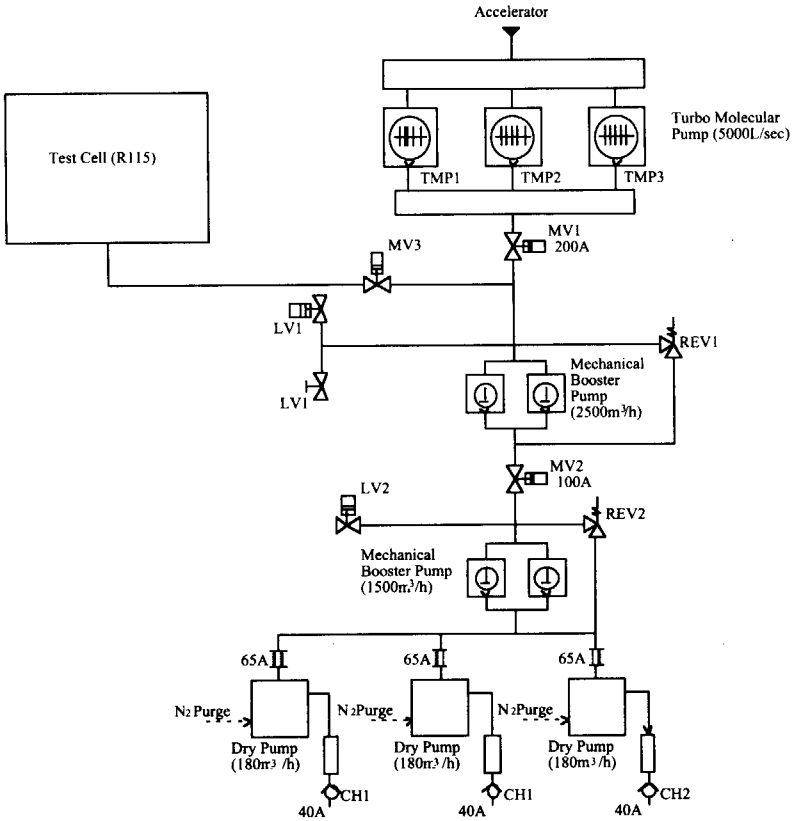


Fig. 4 Block diagram of vacuum system.

(8) Liquid Radioactive Waste Treatment System

The liquid radioactive wastes are generated mainly in the primary cooling loops of the Accelerator, the Target Assemblies, and the Lithium loop. These wastes, as well as other radioactive waste derived from operation of the plant, will be processed by the waste treatment system. A small fraction of the deuteron beam current will be lost and will bombard the accelerator drift tubes and other components, giving rise to the production of high-energy neutrons along the length of the accelerator. Radioactive liquid waste from cooling water activated by the neutrons will mainly contain tritium and short-lived nuclides (Be-7, etc). The Cooling System will be connected to the storage tank for draining. The volume of radioactive liquid waste originating in cooling water is 50 m^3/year. Its activity needs to be determined.

A relatively small amount of liquid contaminated waste is generated in polishing, etching and cleaning operations. Lithium hydroxide is estimated to be the major chemical component in water. The activity of the above mentioned liquid waste will be 0.4-40 Bq/ cm^3 and volume 15 m^3/year. It might contain Li_2O, Al_2O_3, C, HNO_3, Picric Acid, HF, Ethyl alcohol, Lactic acid and/or NaOH. The units to process these liquid radioactive wastes are as follows.

(a) Liquid Waste Storage Unit

Liquid wastes from primary cooling water and decontamination systems will be collected in one of two 10 m3 storage tanks. Sampling and analysis of the liquid waste is conducted before treatment.

(b) Liquid Waste Evaporation Unit

After neutralization, the water is routed to the evaporator for reducing the waste volume. Evaporation capacity is 150 kg/h. The reduced volume liquid with concentrated radioactive wastes is temporarily stored in a concentrated liquid waste tank before sending to the solid waste treatment system.

(c) Ion exchange Unit

An ion exchange unit further improves the water quality. The capacity of this unit is 150 kg/h.

(d) Storage before Discharge Unit

Most of the treated water is re-circulated to minimize release to the environment. Excess water within allowable activity level is discharged to the environment. The guideline for the total activity concentration in discharged water is 4.0×10^{-4} Bq/cm^3, except that tritium is controlled to 6 Bq/ cm^3.

(9) Gaseous Radioactive Waste Treatment System

During IFMIF operations, tritium (^{3}H) is produced in the lithium target, and air is activated around the linac and beam transport system. To meet safety and licensing requirements of the host country, the system design must include confinement, isolation and treatment of the radioactive gases. The main concern in this section is gaseous tritium released in the Li Loop Area / Trap Area (Ar filled) and the Test Cell Room (kept at 0.1 Pa during operation). Argon gas pressure is kept lower than 1 atm (=101.3 kPa), and the gas is circulated and detritiated. Tritium containing gases are treated by detritiation systems in the Exhaust Gas Treatment System before final treatment for discharge through the stack. Radioactive gases other than tritium can be treated by the Nuclear HVAC.

(a) Exhaust Detritiation System for Ar Gas

Tritium will be produced in the lithium target by deuteron and neutron reactions with Li-6 or Li-7 at a rate of about 3.0×10^{15} Bq/y. Most of the tritium in the lithium loop will accumulate in the yttrium trap, and the remainder of the tritium, which is 5.0×10^{14} Bq/y, will be confined in the lithium loop components. A small amount of the tritium will escape from the components due to permeation at the stainless steel boundaries. The release rate of the tritium to the Lithium Loop Area/Trap Area will be approximately 5.0×10^{8} Bq/h based on conservative assumptions.

The Lithium Loop Area/Trap Area is filled with Ar gas that is circulated at a low flow rate for impurity monitoring and control, thereby eliminating the possibility of lithium combustion in the event of a leak. The atmosphere of the area is continuously circulated to monitor and control the purity of the Ar gas, and is kept at negative pressure (gage) to prevent uncontrolled releases of the tritium.

The discharge rate will be determined by the air-tightness of the areas. Epoxy paint lining will be applied to the Lithium Loop Area/Trap Area, and treatment conducted to achieve air-tightness, for example, by sealing feedthroughs for cables or pipes. When the leak rate of the area is assumed to be 1.5 vol%/day, the discharge rate to maintain negative gage pressure is 1 m^3/h. The tritium concentration in the discharged gas will be 5.0×10^{2} Bq/cm^3. It is assumed that the concentration of tritium in the feed gas for this system is 1.0×10^{5} Bq/cm^3 considering the safety margin.

A simplified flow diagram of this system is shown in Fig. 5. After the exhausted gas is heated up to 400 ^{0}C and compressed to 700 kPa, the tritium gas in the exhausted argon gas is removed by a circulating palladium permeation system, in which hydrogen isotopes can permeate through the palladium membrane to separate them from other gases. A tritium getter alloy, which is used to occlude hydrogen gas, absorbs the tritium and the alloy is moved to the Storage Cell. The rest of the discharged Ar gas is mixed with air and treated as mentioned below.

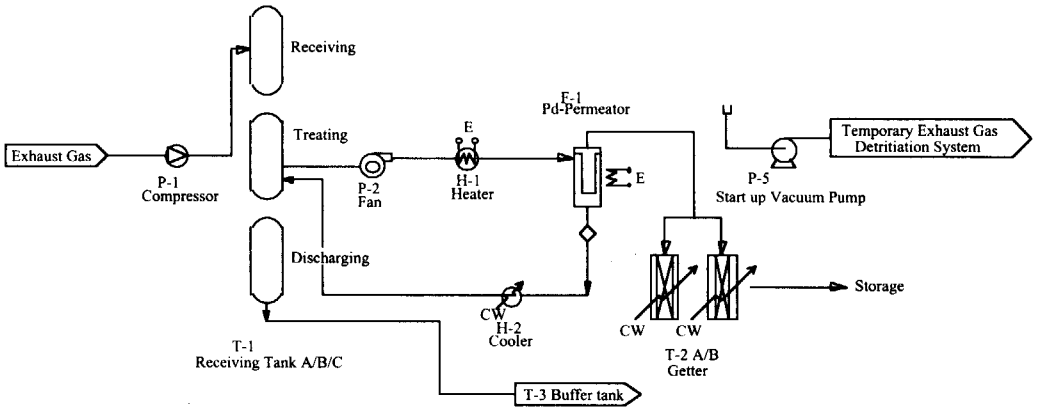


Fig. 5 Block diagram of exhaust detritiation system for argon gas circuit.

(b) Exhaust Detritiation System for Air

The vacuum exhaust from the target, quench tank and beam lines, and the Test Cell evacuation exhaust, contain tritiated gas. The tritium is removed from exhaust effluence by the air exhaust detritiation system. It is assumed that the concentration of tritium in the feed gas for this system is 5.0 Bq/cm^3 and the flow rate is 19 m^3/h. The exhaust gas is mixed with the discharged Ar gas from the Exhaust Detritiation System for Argon Gas, and a flow rate of 20 m^3/h is treated in this system.

The exhaust gas is carried into the oxidation system, and the tritiated species in the exhaust gas is oxidized to tritiated water using an oxidation catalyst at high temperature, for example, 500℃. Tritiated water in the exhaust gas is condensed and collected in a buffer tank. The tritiated water in the remaining exhaust gas is removed through two membrane separators. At the outlet of a membrane separator system, the tritium gas concentration in the exhaust gas is measured. The exhaust gas is released into the atmosphere via the Nuclear HVAC if the concentration is lower than 5.0x10^{-4} Bq/cm^3. The tritiated water stored in the buffer tank is discharged after dilution or solidified, if necessary.

(c) Temporary Exhaust Gas Detritiation System

This system is operated for management of gas exhaust during maintenance operations. Most of the gas is air with the possibility of low-level tritiated water vapor contamination. The amount of temporary exhaust gas is estimated to be 100 m^3/h, and is fed through the flexible ventilation ducts from various areas of the facility where maintenance operation will be performed. This system will be operated when the tritium concentration of the maintenance area is above the concentration limit of 8.0x10^{-2} Bq/cm^3 in the working atmosphere, which is one tenth of the Japanese regulatory limit. Accordingly, it is assumed that the tritium concentration of the feed gas for this system is 0.1 Bq/cm^3.

Any tritiated water separated by membranes is discharged after dilution or is solidified, if necessary. At the outlet of the membrane separator system, the tritium gas concentration in the exhaust gas is monitored, and the exhaust gas is released into the atmosphere via the Nuclear HVAC, if the concentration is lower than 5.0x10^{-4} Bq/cm^3.

(10) Solid Radioactive Waste Treatment System

Solid radioactive wastes generated by IFMIF operation will consist largely of spent ion-exchange resins, the Lithium Target assemblies, the test assemblies, the paper and rags used in controlling contamination, and air filters. Spent ion-exchange resins and concentrated liquid waste will be solidified after drying. Paper, rags and air filters in containers will be sent to the existing storage facility near the IFMIF.

Highly irradiated solid wastes will be generated at the Test Cell and during the analysis and testing of irradiated specimens. The wastes include the Target Assemblies, irradiated specimens and specimen holders. The most radioactive solid waste will be the Target Assembly. Concentration of

radioactive nuclide in the Target Assembly base plate is roughly estimated from calculation results for the separable first wall of ITER-FEAT. The typical isotope concentrations in the Target Assembly are $1.2x10^9$ Bq/cc of V-49, $2.1x10^{11}$ Bq/cc of Fe-55, $7.9x10^9$ Bq/cc of Co-58 and $4.1x10^8$ Bq/cc of Ni-63. This estimation was performed based on the assumption that austenitic steel SS316L is the material of the whole target assembly. This assumption will give larger values of activation and thus more conservative estimates than if ferritic steel or a vanadium alloy is employed as the materials of the target back-wall. (A technique has not been proven yet to weld these alternate backwall materials to an austenitic structure and thus allow their use.) These highly irradiated solid wastes will be placed in containers and then stored in the Waste Storage Cell.

(11) Summary

Utilities were designed with the assumption of a Japanese site for IFMIF. The heating, ventilation and air conditioning (HVAC) system was designed for two categories; industrial and nuclear HVAC systems, selected on the basis of radiological risk. The areas of nuclear HVAC system are filled with air or argon (Ar) with pressure 200-400 Pa lower than the atmospheric pressure.

The required total electric power is 50 MVA, including emergency power. The supplied voltage is 66 kV at the boundary of the IFMIF site. Required heat rejection capacities of the cooling water system are 26 MW for Accelerator system and 13 MW for Target system. The water temperature is controlled in a range 30-35°C. Gas supply systems were examined for Ar, helium (He), compressed air (10 kg/cm^2 (gage)) and nitrogen (N_2). Argon gas is used in the Test Cell and lithium loop areas etc. Helium gas is used for cooling of the test assemblies and the Test Cell walls.

Radioactive waste systems were designed for liquid, gaseous and solid wastes. The liquid waste including tritium and Be-7 is treated through storage tank, evaporation and ion exchange units etc. Tritiated Ar gas is treated through palladium permeation cells and hydrogen getters. Tritiated air is oxidized into tritiated water.

3.4.5 DI51-JA: Examination of Central Control and Common Instruments

(1) Brief Task Description

Operation of IFMIF requires that the whole facility be controlled with consistency among the Accelerator, Target, Test Facilities, Utilities, Radiation Control and Access Control subsystems. Furthermore, for the reduced cost IFMIF, the cost of Central Control and Common Instruments (C.C. & C.I.) was reduced mainly by eliminating the second target and test cell included in the CDA. The C.C. & C.I. is also affected by the staged construction of IFMIF. The design of C.C. & C.I. must be examined and revised to meet these conditions.

Conceptual design of the C.C.&C.I. was performed in the CDA. In KEP, the C.C.&C.I. concept was reviewed and examined. For this task, suitable locations of subsystem controllers and guideline on access control were emphasized. This task was performed in parallel with the task for operational flow (DI61).

Contributors

Name	Party	Institute	E-mail address
M. Ida	Japan	JAERI	ida@ifmif.tokai.jaeri.go.jp
H. Takeuchi	Japan	JAERI	takeuchi@fnshp.tokai.jaeri.go.jp

(2) General Concept of the Central Control System

Recent remarkable advances have been made in the technology fields of hardware and software for process and control equipment. Therefore, the basic concepts for equipment operating methods and management of facilities require evaluation of configurations in the central control system. Redesign and improvements are rarely restricted by conditions of the hardware configuration.

As an example related to the installation location of process and control equipment (console box and others), it is generally desirable to concentrate the equipment into one location, for the following reasons;

- Common utilization of information
- Minimization of personnel needs for continuous operation

However, the concentration may increase distance between the control equipment and controlled components, and it may bring the following concerns;

- Increased work load on the operating crew during inspection tours of the controlled components
- Possible increased wiring costs

This requires that the methods of central control be examined to evaluate the trade-off between control methods and construction and operating costs.

(3) Concept of Central Control and Related Equipment for IFMIF

Figure 1 shows a schematic of the central control system for IFMIF. The control system will be designed to provide a high degree of reliability. The mean time to repair control system components will be minimized. The deuteron accelerators, lithium target and test cell will be controlled together during accelerator operation. The facilities for post irradiation examination will be controlled independent of the accelerator and other facilities most of the time.

It is too difficult to install all process and control equipment in only one room in the IFMIF Main Building. Therefore, the control equipment is divided into four categories and installed in four rooms as follows;

(a) Accelerator, Target and Test Facilities

Control equipment for the Accelerator, the Target and the Test Facilities (except for remote handling equipment) are installed in the Control Room (R105). The controls for these systems are interconnected through interlocks, etc. Most of the facility operating personnel will work in this room. For example, operation of the accelerator requires 92 people (distributed over four shifts), out of the

total of 183 IFMIF operations personnel [1]. This concentration results since availability of IFMIF depends mainly on the accelerator [2]. With a sufficient number of personnel available, most accelerator failures may be recovered with only a short downtime. A server computer and three local control stations for the three subsystems will be installed in this room.

(b) Utilities

Control equipment for utilities will be installed in the Test Facility Control Room (R211). This will control equipment located on all three floors of the IFMIF Main Building. The Test Facility Control Room is located on the second floor, and this location is suitable for the inspection tour of the controlled components. In an alternate design, the utility controllers may be installed in the main Control Room (R105) for optimization of the operation crew.

Utility control requires a server computer and three local control stations. The first station controls equipment for the electric power supply; the second station controls equipment for HVAC, cooling water, vacuum and detritiation systems; and the third station controls equipment for waste treatment and the tritium laboratory.

(c) Remote Handling for the Test Cell

Process and control equipment for remote handling operations in the Test Cell is installed in the Test Cell Technology Room (R213) adjacent to the Access Cell (R207). The local control station in this room is used only during maintenance, to control the remote handling equipment.

(d) Access Control and Radiation Protection

Access control is required during all operation of IFMIF accelerators. Process equipment for Access Control and Radiation Protection is installed in the Health Physics Room (R104). A local control station in this room runs equipment for access control and radiation protection. These control doors, card readers, area monitors, and similar equipment.

(4) Access System

(a) Radiation Protection

IFMIF requires a large number of personnel for operation and maintenance, and they must be protected from harmful levels of radiation. At the same time, many types of radiation and radioactive nuclides are generated in IFMIF. The major source of direct radiation in IFMIF will be materials bombarded by deuterons or neutrons in the lithium target and the test assemblies. These materials will emit beta and gamma radiation. It is anticipated that low energy (18.6 keV) beta particles emitted by tritium will be important to internal exposure, but they will be stopped relatively effectively by piping and structural materials. Special provisions such as shielding, distance, and time limitations will be required to limit gamma radiation dose and internal exposure to acceptable levels. Basic criteria for radiation exposure control in the IFMIF will be:

- Limits on whole body dose of 100 mSv/5years (and a maximum of 50 mSv/y). Whenever practical, this will be accomplished by shielding which limits the whole body dose rate to less than 0.2 mSv/week in continuously or frequently worked areas.
- Limits on eye exposure to less than 150 mSv /year and on other tissue exposure to less than 500 mSv/y.
- Limit for tritium concentration in air in work areas to 0.07 Bq/cm^3.

(b) Radiation Zoning

Radiation Zoning shall be used for control of personnel exposure. If IFMIF is constructed in Japan, all areas will be divided into the following three zones based on Japanese regulations and JAERI standards.

- First grade control area
  This area will have radiation exposure risk exceeding the value published in Science and Technology Administration Notice 15 in 1988.
- Second grade control area
  This area will have radiation exposure risk exceeding 300 μSv/week and not come under the first grade control area.
- No control area
  This area will have low radiation exposure risk and will not require the first or second grade controls.

(c) Radiation Monitoring

A Radiation Monitoring System, fitted with alarms, will be installed in areas where radiation levels may exceed allowable limits. All areas in which radioactivity is present will be provided with air sampling or air monitoring systems, with appropriate alarms installed to warn of dangerous levels of airborne activity. Areas equipped with such systems will include the Lithium loop and the Test cell.

(5) Summary

The concept of C.C.&C.I. was reviewed and examined based on the concepts developed in the CDA. Suitable locations of controllers for Accelerator, Target, Test Facilities, Utilities, Remote Handling, Access Control and Radiation Protection were examined. Also the guidelines on access control were examined. This task was performed and will be refined in parallel with the task for operational flow (DI61).

References

[1] M. J. Rennich, (editor), IFMIF International Fusion Materials Irradiation Facility Conceptual Design Activity Cost Report, ORNL Report, ORNL/M-5502, December 1996.
[2] M. Martone, (editor), IFMIF International Fusion Materials Irradiation Facility Conceptual Design Activity Final Report, ENEA Frascati Report, RT/ERG/FUS/96/11, November 1996.

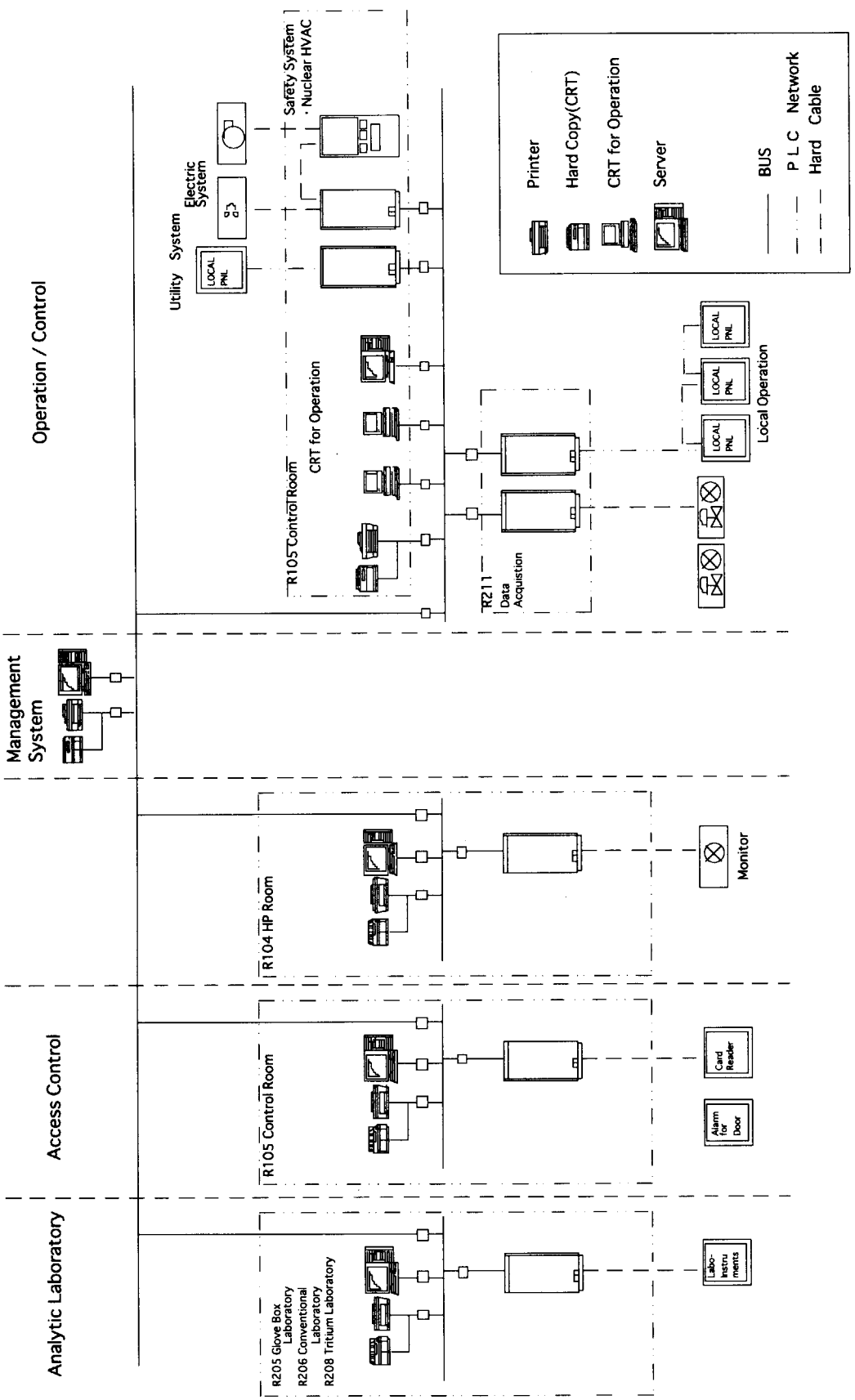


Fig. 1 Concept of central control.

3.4.6 DI61-JA : Check of Consistency and Analysis of Operations Flow in IFMIF

(1) Brief Task Description

The design of IFMIF must assure continuous flow of operations from one subsystem to the next, with consistency across interfaces between the accelerator, target, test facilities, and other subsystems. Also, the IFMIF operational flow from startup to shutdown to maintenance to restart must be considered. This task checks these requirements in parallel with the progress of other IFMIF design work.

In KEP, the operations flow was examined for each subsystem of the Accelerator, the Target, the Test Facilities (including remote handling) and the Utilities (including radiation control and access control). This flow was compared and examined to check the consistency among these subsystems.

Contributors

Name	Party	Institute	E-mail address
M. Ida	Japan	JAERI	ida@ifmif.tokai.jaeri.go.jp
H. Takeuchi	Japan	JAERI	takeuchi@fnshp.tokai.jaeri.go.jp

(2) Operations Flow

Operational flow of each subsystem was examined and summarized, as shown in Table 1, to check consistency among all subsystem flows. These operations of the Accelerator, Target, and Test Facilities are based on the CDA design [1], except for the flow of operations during maintenance. To check consistency, operating modes of all facilities at a same time are arranged on the same line of Table 1. The deuteron accelerators, the lithium target and the test cell must all be operating during IFMIF irradiation runs. (This is the mission of IFMIF, which is designed to be in operation 70 percent of the time.). Facilities for post irradiation examination must be operated independent of the irradiation facilities, and will also be in use most of the time. The remote handling systems are operated mainly during maintenance. Other utilities, such as Heating, Ventilation and Air Conditioning (HVAC), cooling water, electric power, waste treatment and radiation control / access control, are operated (or available) continuously.

(a) Accelerator Facility

During start up, the RF power is adjusted, then the deuteron beams are calibrated as pulsed beams at low power. After that, the beams are injected into the lithium target. Most failures that occur in IFMIF operation will be in the accelerator. However, most of the accelerator failures will be short-time failures, with quick return to power. In consideration of the accelerator failures, eight hours per week are allotted for recovery or maintenance in the IFMIF schedule.

(b) Target Facility

At IFMIF start up, the lithium dump tank is heated and the lithium is melted, then the loop piping is heated. After that, the liquid lithium is circulated without beams, then with beams during normal operation. At shut down, lithium circulation for two days is estimated to be necessary to remove the decay heat of the target assembly. For maintenance in the Lithium Loop Area, a change in the cover gas from argon gas to air is necessary.

(c) Test Facilities

The Test Cell is kept under vacuum pressure of 0.1 Pa during irradiation and is filled with argon gas during maintenance. Setup of the Test Cell requires the following operations: Target Assembly installation by the Remote Handling Device, removal of the Remote Handling Device, installation of the Test Modules by the Universal Robot System, and Cell Ceiling closure by welding of the seal cover. After that, the Test Cell is evacuated to a pressure of 0.1 Pa. The temperatures of all test modules must be carefully controlled to maintain the specified irradiation conditions of the test specimens in the assemblies. The remote handling device is used mainly during maintenance

operations. At the start of maintenance, the test cell cover is removed, then the test assemblies are removed. After that, the target assembly is separated using the welding / cutting device and removed. The test assemblies and the target assembly are transferred to the Tritium Laboratory.

(d) Utilities

The HVAC System, Cooling Water System, Electric Power System, Liquid / Solid Radioactive Waste Treatment System, Detritiaton System for buildings, and Radiation Control / Access Control Systems are nearly always in normal operation. Vacuum System is operated to meet the needs of the Test Cell. The Tritium Laboratory is operated as needed for PIE. The Detritiaton System for laboratories is continuously operated during the irradiation. The Liquid / Solid Radioactive Waste Treatment System and Tritium Laboratory are operated only during the daytime shift.

(3) Summary

The design and operation of IFMIF was checked for consistency of operations flow of all subsystems. It was found that the IFMIF design is basically appropriate at this stage. In the next phase, IFMIF operations flow must be checked in parallel with progress in the design of all subsystems, and any required design modifications made to assure IFMIF operations consistency.

References

[1] M. Martone, (editor), IFMIF International Fusion Materials Irradiation Facility Conceptual Design Activity Final Report, ENEA Frascati Report, RT/ERG/FUS/96/11, November 1996.

Table 1 Operation flow of IFMIF sub-systems (1/3).

		Accelerator	Target	Test Facilities	
				Remote Handling	Test Cell
Operation Flow	Stop	Maintain Vacuum	Stop	Operation	Stop
	Start Up	Main Power On Instrumentation On RF On Adjustment of RF Frequency, Current Ion Source On Adjustment with Low Energy Pulse Beam Switch to Target Transition to Continuous Operation Transition to Full Power	Preparation *Dump Tank Heating Start *Pipe Heating *Purification On Circulation On-Beam Operation	Operation Stop	Maintain Vacuum Test Cell Cooling VTA Heating VTA Temperature Control Irradiation Start
	Normal Operation	Normal Operation Short-term Stop, Maintenance (~8hr/w)	Normal Operation	Stop, Maintenance	Normal Operation
	Shut Down	Holding at Low Power with Decreased Pulse Rate (Ion Source Off) (RF Off) (Instrumentation Off) (Main Power Off)	Semi-Operation *Purification Off *Removal of Decay Heat (2day) Operation Stop *Pump Stop *Dump Stop	Operation Stop	VTA Heating Stop Confirmation of VTA Cooling VTA Cooling Stop Test Cell Cooling Stop
	Maintenance	(Holding at Vacuum or Atmosphere)	Air Filling in Li Loop Area Direct Maintenance by Worker Ar Gas Filling	Installation of Remote Handling in Access Cell VTA Removal, Disassembly Transfer of Specimen to Tritium Lab. Transfer of Test Cell Cover Back-wall Cutting Transfer of Back-wall to Tritium Lab. Back-wall Assembly, Attachment Attachment of Test Cell Cover VTA Attachment Sealing of Test Cell Removal of Remote Handling	Ar Gas Filling Maintain Vacuum
Operation Feature		Heavy Requirement on Control to Short-term Stop in Normal Operation	Light Requirement on Control in Normal Operation	Light Requirement on Control in Maintenance	Heavy Requirement on Control Corresponding to Beam Current in Normal Operation
Normal Operation Pattern		Continuous	Continuous	No Operation	Continuous
Importance for Safety		Impotant (Isolation Valve to Li Target)			
Local Process Panel					

Table 1 Operation flow of IFMIF sub-systems (2/3).

		Utilities			
		(HVAC)	Cooling Water	Electric Power	Vacuum
Operation Flow	Stop	Continuous Operation or Stop	Continuous Operation or Stop	Continuous Operation	Maintain Vacuum
	Start Up	Normal Operation	Normal Operation	Normal Operation	Maintain Vacuum *Accelerator Maintain Vacuum *Test Cell *Piping of Li Loop
	Normal Operation	Normal Operation	Normal Operation	Normal Operation	Normal Operation
	Shut Down	Normal Operation	Normal Operation	Normal Operation	Normal Operation Vacuum Pumping Stop Test Cell Piping of Li Loop
	Maintenance	Normal Operation	Normal Operation (usually), Cooling Stop, Maintenance (depending on maintenance status of other sub-system)	Normal Operation	Maintain Vacuum or Maintenance (Maintenance corresponding to maintenance plan of accelerator)
Operation Feature		Light Requirement on Control in Normal Operation	Light Requirement on Control in Normal Operation	Light Requirement on Control in Normal Operation	Light Requirement on Control in Normal Operation
Normal Operation Pattern		Continuous	Continuous	Continuous	Continuous
Importance for Safety		Important			
Local Process Panel		for Nuclear HVAC		Power Supply Panel	

Table 1 Operation flow of IFMIF sub-systems (3/3).

		Liq.&Sol. Radiation Waste Treatment	Tritium Laboratory (PIE)	Detritiation (Laboratory)	Detritiation (Building)	Radiation Control, Access Control
Operation Flow	Stop	Continuous Operation or Stop	Examination Continuing	Continuous Operation	Continuous Operation or Stop	Normal Operation
	Start Up	Normal Operation	Examination Continuing	Normal Operation This operation is always required during the examination.	Normal Operation	Normal Operation
	Normal Operation	Normal Operation	Examination Continuing	Continuous Operation	Normal Operation	Normal Operation
	Shut Down	Normal Operation	Examination Continuing	Continuous Operation This maintenance is to be realized by switching two sets of detritiation system or maintenance after the examination.	Normal Operation	Normal Operation
	Maintenance	Normal Operation	Examination Continuing Specimen Transfer to PIE	Normal Operation This operation is kept because of specimen transfer in IFMIF maintenance.	Normal Operation This maintenance is posible after tritium treatment of other facilities. Exhaust air treatment is always operated for treatment of exhaust from laborotory.	Normal Operation
Operation Feature		Most process is done locally.	Most process is done locally.	Light Requirement on Control in Normal Operation	Light Requirement on Control in Normal Operation	Light Requirement on Control in Normal Operation
Normal Operation Pattern		Daytime	Daytime	Continuous	Continuous	Continuous
Importance for Safety						
Local Process Panel		Local Process Panel	Local Process Panel			

3.4.7 DI71-JA : Verification of the Design of Radiation Shielding

(1) Brief Task Description

The materials and thickness of radiation shielding influence the construction cost of IFMIF buildings. Especially important are the weight and volume of shielding plugs on Test Cell, as they influence the specifications for the Universal Robot System (URS) in the Access Cell. Therefore, requirements of these walls and plugs must be clarified.

In this task, the adequacy of the Test Cell wall thickness was verified by a computer code MCNPX [1] with data library LA150 [2]. The neutron flux and dose rate were calculated for locations as follows;

- Neutron Flux in Test Cell (to be used for estimation of activation)
- Dose rate outside of the Test Cell front wall and at the shielding plugs (bulk shielding performance)
- Dose rate at the exit of penetrations for vacuum piping (estimate of neutron streaming)
- Neutron flux in the Lithium Loop Area by streaming through piping penetrations (to be used for estimate of activation)
- Neutron flux in the Target Interface Room by streaming through beam ducts (to be used for estimate of activation)

Contributors

Name	Party	Institute	E-mail address
M. Ida	Japan	JAERI	ida@ifmif.tokai.jaeri.go.jp
M. Sugimoto	Japan	JAERI	sugimoto@ifmif.tokai.jaeri.go.jp
H. Takeuchi	Japan	JAERI	takeuchi@fnshp.tokai.jaeri.go.jp

(2) Calculation Conditions

(a) Calculation Code and Data Library

The calculations were executed employing the Monte Carlo code MCNPX [1], which can deal with neutrons with energy up to 50 MeV. The cross section library used was LA150 [2].

(b) Geometry

The arrangement of shielding walls and plugs around the Test Cell and components in the Test Cell are shown in Fig. 1. The size of the Test Cell is 3 m x 3 m x 6 m. The Front Wall between Test Cell and Access / Maintenance Room has a thickness of 4.3 m. The shielding plugs on Test Cell have thickness of 2.4 m. Penetration holes were taken into consideration through three walls as follows:

- Back Wall: Beam ducts (outer size 0.3 m x 0.1 m, x 8 mm thick)
- Side Wall: vacuum piping (12B, Sch40 i.e. outer diameter 318.5 mm, inner diameter 297.9 mm)
- Bottom Wall: Li piping (8B/10B, Sch40 i.e. outer diameters 216.3 / 267.4 mm, inner diameters 199.9 / 248.8 mm) covered with 0.15 m thermal insulation.

(c) Modeling of Materials

The shielding wall and plug materials were treated as heavy concrete for simplicity, while the shielding plugs consist of heavy concrete, steel, and void regions. The composition of the heavy concrete is shown in Table 1 [3]. Regions of liquid lithium, stainless steel piping and the thermal insulation were conservatively treated as void regions, since there was no data for lithium in the cross section library and composition of the thermal insulation was not specified.

Table 1 Composition of heavy concrete.

Element	Weight Ratio (w%)	Atom Density (1/(b-cm))
H	0.3116	6.328E-03
O	33.09	4.233E-02
Si	2.578	1.879E-03
Ca	7.11	3.631E-03
Mg	0.9348	7.872E-04
Al	2.351	1.783E-03
S	0.1416	9.040E-05
Fe	47.48	1.740E-02
Ti	5.439	2.325E-03
Cr	0.17	6.692E-05
Mn	0.1983	7.388E-05
V	0.3116	1.252E-04

(Density : 3.4g/cc)

For a conservative estimation, target, test assemblies, quench tank and liquid lithium were also ignored.

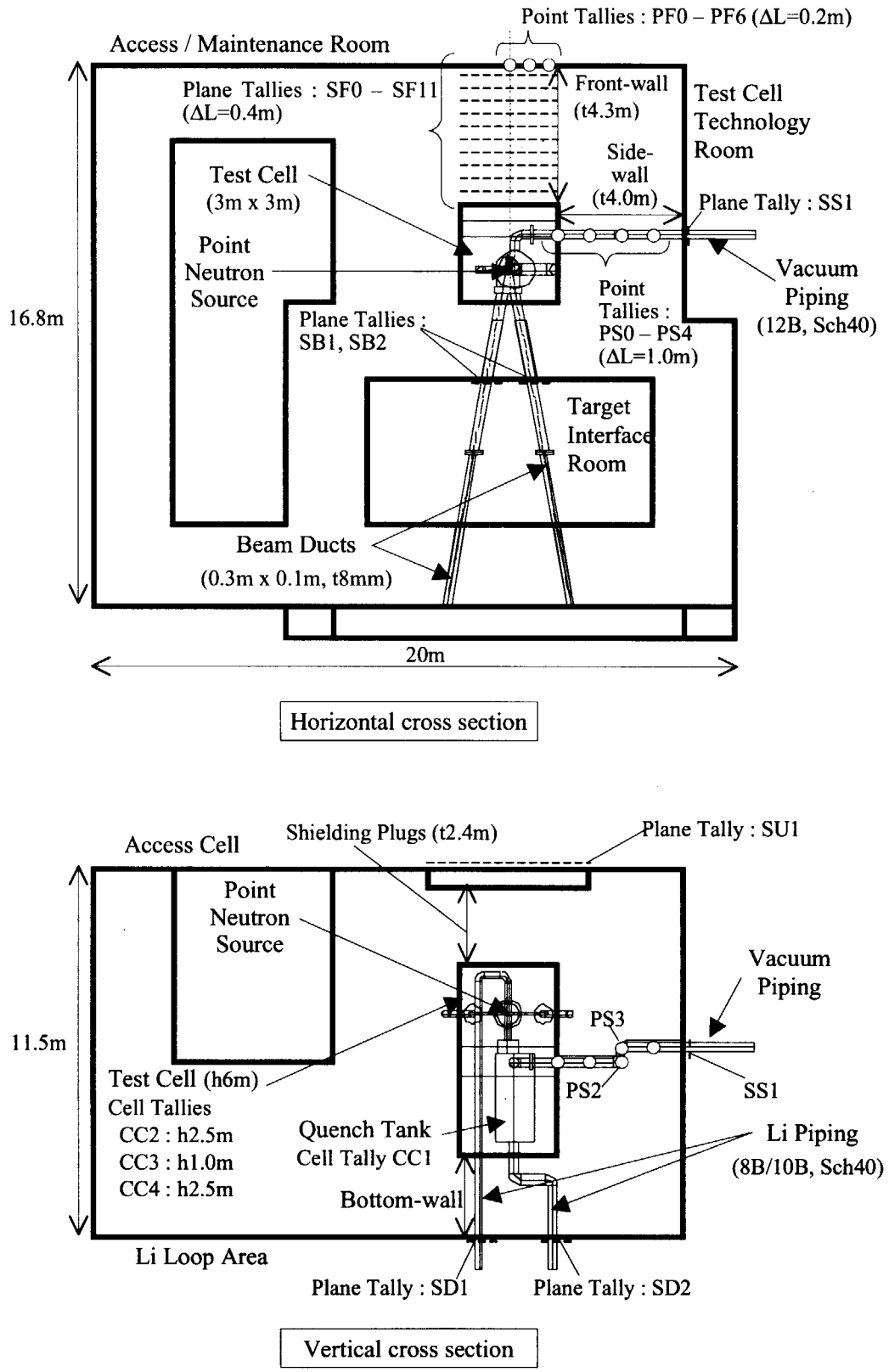


Fig. 1 Calculational model for radiation shielding calculations.

(d) Neutron Source

For simplicity, a point neutron source was assumed at the intersection of the two deuteron beams. For the deuteron beam energy of 40 MeV and current 250 mA, the neutron spectrum up to 50 MeV in steps of 1 MeV and spatial distribution 0° - 175° (0° is the direction toward the Front Wall) in steps of 5° were input. A typical spectrum is shown in Fig. 2. In the direction 0 – 5° (toward the Front Wall), the maximum neutron yield per energy of 7.5×10^{-5} neutrons / MeV / deuteron is given at neutron energy of 14 – 15 MeV. In the directions 90 – 95° (approximately toward the shielding plugs, Side Walls and Bottom Wall) and 170 – 175° (nearly toward the Back Wall), most neutrons have low energy, around 1 – 2 MeV. The total yields is about 0.06 neutrons / deuteron.

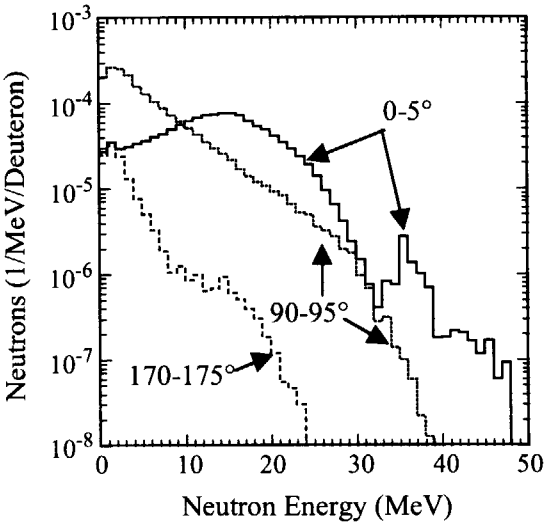


Fig. 2 Spectra and spatial distribution of source neutrons.

(e) Conversion Factors for Dose Equivalence

Conversion factors for the dose equivalence of neutrons were applied depending on the energy range of neutron as shown in Table 2 [4]. The conversion factors were calculated in MCNPX with interpolation from the data shown in Table 3 [5].

Table 2 Conversion factor for dose equivalent (neutron).

En	Cn	En	Cn	En	Cn
2.00E+03	4.52E+00	9.00E+01	1.65E+00	2.46E+00	1.43E+00
1.00E+03	3.74E+00	8.00E+01	1.62E+00	2.02E+00	1.34E+00
9.00E+02	3.46E+00	7.00E+01	1.59E+00	1.65E+00	1.23E+00
8.00E+02	3.23E+00	6.50E+01	1.57E+00	1.35E+00	1.13E+00
7.50E+02	3.05E+00	6.00E+01	1.55E+00	1.11E+00	1.02E+00
7.00E+02	2.88E+00	5.50E+01	1.54E+00	9.07E-01	9.14E-01
6.50E+02	2.70E+00	5.00E+01	1.54E+00	7.43E-01	7.66E-01
6.00E+02	2.53E+00	4.50E+01	1.55E+00	4.98E-01	5.94E-01
5.50E+02	2.38E+00	4.00E+01	1.58E+00	3.34E-01	4.49E-01
5.00E+02	2.26E+00	3.50E+01	1.61E+00	2.24E-01	3.36E-01
4.50E+02	2.14E+00	3.00E+01	1.62E+00	1.50E-01	2.38E-01
4.00E+02	2.05E+00	2.75E+01	1.64E+00	8.65E-02	1.45E-01
3.75E+02	1.99E+00	2.50E+01	1.66E+00	3.18E-02	9.00E-02
3.50E+02	1.94E+00	2.25E+01	1.69E+00	1.50E-02	6.70E-02
3.25E+02	1.89E+00	1.96E+01	1.74E+00	7.10E-03	5.65E-02
3.00E+02	1.84E+00	1.75E+01	1.77E+00	3.35E-03	5.23E-02
2.75E+02	1.79E+00	1.49E+01	1.78E+00	1.58E-03	5.12E-02
2.50E+02	1.75E+00	1.35E+01	1.79E+00	4.54E-04	5.18E-02
2.25E+02	1.72E+00	1.22E+01	1.80E+00	1.01E-04	5.34E-02
2.00E+02	1.70E+00	1.00E+01	1.79E+00	2.26E-05	5.44E-02
1.80E+02	1.70E+00	8.19E+00	1.77E+00	1.07E-05	5.42E-02
1.60E+02	1.70E+00	6.70E+00	1.74E+00	5.04E-06	5.34E-02
1.40E+02	1.70E+00	5.49E+00	1.70E+00	2.38E-06	5.15E-02
1.20E+02	1.70E+00	4.49E+00	1.62E+00	1.12E-06	4.77E-02
1.10E+02	1.69E+00	3.68E+00	1.59E+00	4.14E-07	3.02E-02
1.00E+02	1.68E+00	3.01E+00	1.55E+00	1.00E-10	-

En : Upper limit of neutron energy (MeV)
Cn : Conversion factor ((mSv/h)/(1/cm2/s))

Table 3 Conversion factor for dose equivalent (γ).

Eg	Cg
1.00E+01	2.38E+01
8.00E+00	1.99E+01
6.00E+00	1.60E+01
4.00E+00	1.20E+01
2.00E+00	7.49E+00
1.00E+00	4.48E+00
8.00E-01	3.73E+00
6.00E-01	2.91E+00
5.00E-01	2.47E+00
4.00E-01	2.00E+00
3.00E-01	1.51E+00
2.00E-01	1.00E+00
1.50E-01	7.52E-01
1.00E-01	5.17E-01
8.00E-02	4.40E-01
6.00E-02	3.78E-01
5.00E-02	3.57E-01
4.00E-02	3.38E-01
3.00E-02	3.00E-01
2.00E-02	2.05E-01
1.50E-02	1.25E-01
1.00E-02	4.85E-02

Eg : Gamma energy (MeV)
Cg : Conversion factor (pSv-cm2)

(f) Detection of Calculation Results (Tally)

Tallies, which are virtual detectors in the MCNP calculation model, were installed in the model of the test cell as shown in Fig. 1. The results from the tallies correspond to dose rate and neutron flux. Four cell Tallies (CC1 : Quench tank, CC2 : Upper part of Test Cell, CC3 : Middle part, CC4 : Lower part) were installed in the Test Cell to obtain the neutron flux to be used for estimation of activation in the Test Cell. Seven point Tallies (PF0 – PF6) were installed at the beam level on the outside of the Front Wall with spacing of 0.2 m to estimate dose rates in the Access / Maintenance Room. Twelve plane Tallies were installed in the Front Wall with spacing 0.4 m in the thickness direction (but with the outer one 0.3 m, since wall thickness is 4.3 m) to estimate shielding performance depending on the wall thickness. Five point Tallies (PS0 – PS4) were installed along the vacuum piping in the Side Wall with spacing of 1 m (but with the space between PS2 and PS3 0.5 m). A plane Tally (SS1) with the same section as that of the wall penetration was installed at the exit of the hole on the Side Wall. These (PS and SS) were installed to estimate dose rate due to neutron streaming toward the Test Cell Technology Room. Two plane Tallies (SB1, SB2) with the same cross section as that of the wall penetration were installed at the exits of the holes on the Back Wall to estimate neutron streaming toward the Target Interface Room. A plane Tally (SU1) with the same cross section as that of the Test Cell was installed above the shielding plugs to estimate the dose rate in the Access Cell. Two plane Tallies (SD1, SD2) with the same cross section as those of wall holes were installed at the exits of the holes on the Bottom Wall to estimate neutron streaming toward the Lithium Loop Area.

(3) Results

The MCNPX calculations were executed with 120,000 Histories, which is the number of source neutrons generated in MCNP. The calculation results are as follows;

(a) Neutron Spectrum in the Test Cell

Calculated neutron spectra are shown in Fig. 3. Except for neutrons with energy more than 30 MeV, the calculation of the neutron flux was accurate, since the relative errors were less than 0.1 recommended as the guideline on statistical error for cell Tally. While the averaged neutron flux in Test Cell was 1.2×10^{12} neutrons/cm^2·s, the fraction of high-energy neutron above 40 MeV was 0.1%.

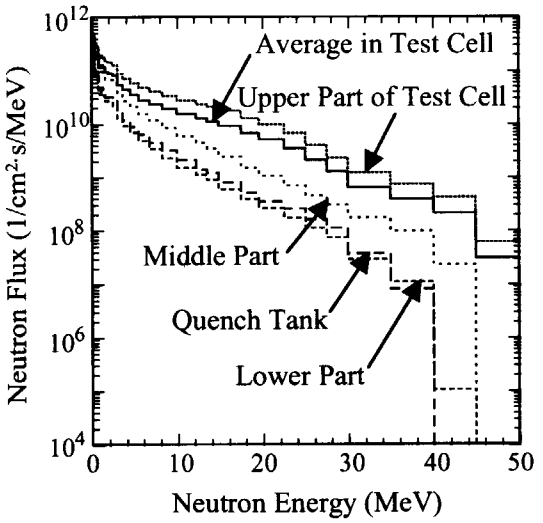


Fig. 3 Neutron spectra in the Test Cell.

(b) Shielding with Front Wall

The dose equivalent rate at the beam level on the outside of Front Wall is shown Table 4. The maximum value given at the point Tally PF0, which is located directly downstream from the neutron source, was 0.65 μSv/h. This value is far below 10 μSv/h, which had been defined as the limit for occupational exposure.

The effect of wall thickness on radiation shielding is shown in Table 4 and Fig. 5. The 4.3 m design thickness of the Front Wall is appropriate. This Front Wall has shielding performance of 10^{-12}. The minimum thickness must be about 4.0 m to reduce the dose equivalent rate to less than 10 μSv/h. According to the spectrum at point Tally PF0 shown in Fig. 4, the dose equivalent rate mainly depends on neutrons with energy less than 22.5 MeV.

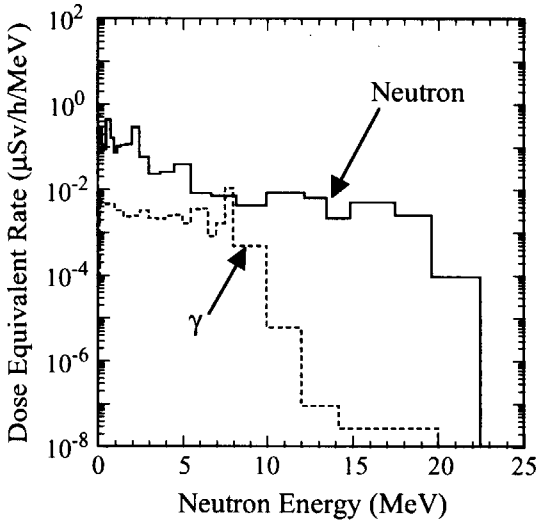


Fig. 4 Neutron and gamma spectra at PF0 on Front Wall.

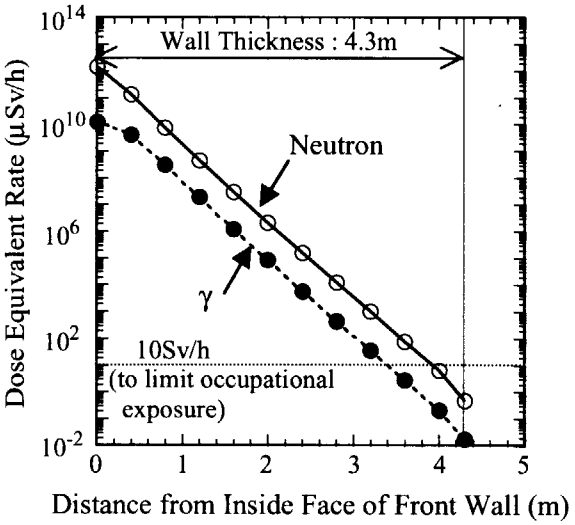


Fig. 5 Dose equivalent rate as a function of the Front Wall Thickness.

Table 4 Dose equivalent rate.

Wall	Tally and Location	Neutron Dose Rate (μSv/h)	Relative Error	Gamma Dose Rate (μSv/h)	Relative Error	Total (μSv/h)
Front Wall	PF0 : 0.0m	6.26E-01	0.215	2.61E-02	0.129	6.52E-01
	PF1 : 0.2m	5.43E-01	0.175	2.50E-02	0.117	5.68E-01
	PF2 : 0.4m	6.14E-01	0.166	3.59E-02	0.165	6.50E-01
	PF3 : 0.6m	4.58E-01	0.158	3.17E-02	0.232	4.89E-01
	PF4 : 0.8m	5.32E-01	0.252	1.64E-02	0.125	5.49E-01
	PF5 : 1.0m	3.41E-01	0.228	1.95E-02	0.236	3.61E-01
	PF6 : 1.2m	1.84E-01	0.177	1.25E-02	0.149	1.97E-01
	SF0 : 0.0m (Test Cell)	1.40E+12	0.005	1.25E+10	0.008	1.41E+12
	SF1 : 0.4m	1.34E+11	0.016	3.96E+09	0.013	1.38E+11
	SF2 : 0.8m	7.41E+09	0.028	3.03E+08	0.018	7.72E+09
	SF3 : 1.2m	4.45E+08	0.044	1.84E+07	0.031	4.63E+08
	SF4 : 1.6m	2.95E+07	0.064	1.20E+06	0.048	3.07E+07
	SF5 : 2.0m	2.14E+06	0.081	8.30E+04	0.066	2.22E+06
	SF6 : 2.4m	1.59E+05	0.101	5.98E+03	0.084	1.65E+05
	SF7 : 2.8m	1.22E+04	0.121	4.45E+02	0.107	1.26E+04
	SF8 : 3.2m	9.65E+02	0.139	3.53E+01	0.124	1.00E+03
	SF9 : 3.6m	7.90E+01	0.157	2.80E+00	0.143	8.18E+01
	SF10 : 4.0m	6.38E+00	0.170	2.18E-01	0.160	6.60E+00
	SF11 : 4.3m (Access /Maintenance Room)	4.95E-01	0.192	1.80E-02	0.172	5.13E-01
Shielding Plug	SU1	8.14E+00	0.226	3.24E-01	0.189	8.46E+00
Side Wall	PS0 : 0m, FL	4.52E+11	0.016	5.07E+09	0.028	4.57E+11
	PS1 : 1m, FL	6.38E+09	0.061	3.37E+08	0.255	6.72E+09
	PS2 : 2m, FL	7.49E+08	0.081	5.46E+07	0.304	8.04E+08
	PS3 : 2m, FL+0.5m	2.41E+07	0.320	7.87E+06	0.459	3.19E+07
	PS4 : 3m, FL+0.5m	6.01E+05	0.237	2.31E+05	0.395	8.33E+05
	SS1 : 4m, FL+0.5m	5.63E+04	0.292	2.27E+04	0.443	7.90E+04
Bottom Wall	SD1 : 8B Pipe	1.56E+08				
	SD2 : 10B Pipe	5.90E+09				
Back Wall	SB1 : Beam Duct	2.83E+10				

(c) Shielding with Shielding Plugs

The dose equivalent rate at 0.6 m above the shielding plugs is shown in Table 4. The calculated dose equivalent rate of 8.5 μSv/h is less than the limit of 10 μSv/h. However, in the simplified calculation model, the shielding plugs were assumed to be made of only heavy concrete and ignoring the existence of tubes in the plugs. Therefore, more realistic modeling is needed for more precise estimation of this radiation shielding and the adequacy of the plug design.

(d) Influence of Vacuum Piping

The dose equivalent rate in the vacuum piping is shown in Table 4 and Fig. 6. The calculated dose equivalent rate fell from 4.6×10^{11} μSv/h to 7.9×10^{4} μSv/h through the bend in the piping. This reduction of 10^{-7} is not as large as that (10^{-12}) at Front Wall. The dose equivalent rate 7.9×10^{4} μSv/h on the outside of Side Wall was far higher than the limit of 10 μSv/h. Therefore, more shielding measures should be considered. Bends in the piping are expected to have reducing performance of about $10^{-1.5}$ per 90 degree bend. According to the spectrum on the inside (PS0) and outside (SS1) of the Side Wall, shown in Fig. 7, there were few high-energy neutrons above 20 MeV.

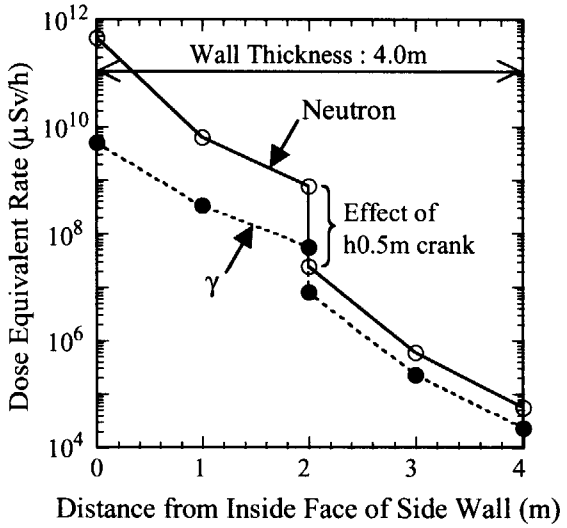


Fig. 6 Dose equivalent rate in vacuum piping.

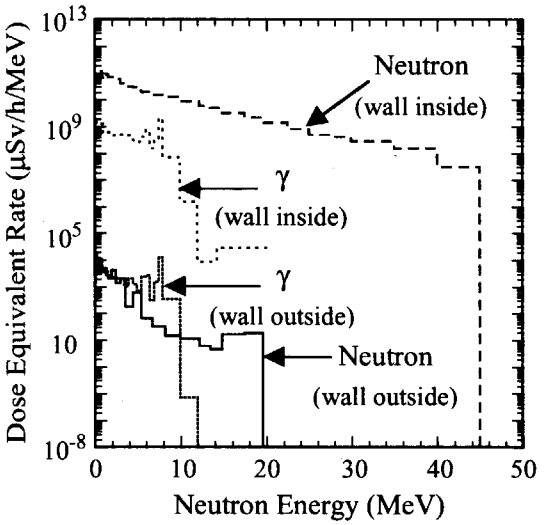


Fig. 7 Neutron and gamma spectra inside and outside of the Side Wall.

(e) Neutron Streaming toward the Lithium Loop Area

Dose equivalent rates outside the Bottom Wall, due to neutron streaming through two wall penetrations for lithium pipes 8B and 10B, are shown in Table 4 and Fig. 8. The dose equivalent rate due to the larger hole (SD2) was about 40 times greater than that due to the smaller hole (SD1), even though the larger penetration had two 90 degree bends. As shown in Fig. 8, this calculation needs to be more precise, especially about the high-energy region.

(f) Neutron Streaming toward the Target Interface Room

Dose equivalent rates outside the Back Wall, due to neutron streaming through two wall penetrations for beam ducts, are shown in Table 4 and Fig. 9

(4) Summary

Through MCNP calculations, the adequacy of wall thickness of the Test Cell was verified. The 4.3 m thickness of the Front Wall was enough to limit the Dose to less than 10 μSv/h in the areas with worker access during operation. The effects of streaming through wall penetrations on dose rate in non-access area were estimated. These results will be utilized in equipment designs.

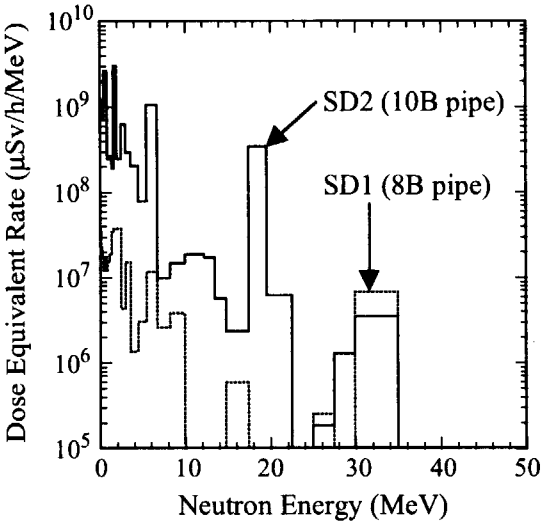


Fig. 8 Neutron spectra under the floor.

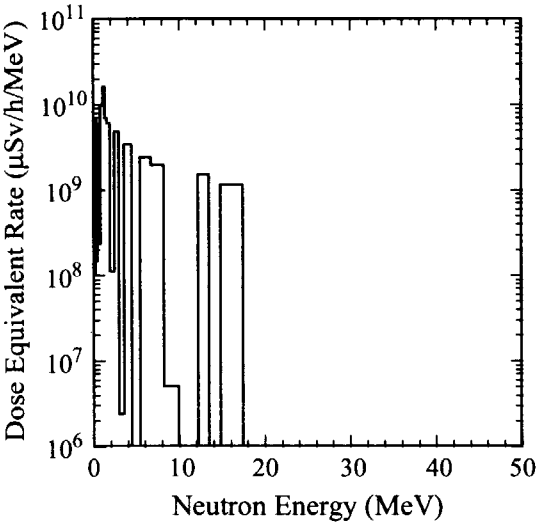


Fig. 9 Neutron spectrum outside of the Back Wall.

References

[1] MCNPX version 2.1.5, CCC-705, RSIC Computer Code Collection, Oak Ridge National Laboratory (1999).

[2] M. B. Chadwick, et al., Cross-Section Evaluation to 150 MeV for Accelerator-Driven Systems and Implementation in MCNPX, Nucl. Sci. Eng., 131, 293 (1999).

[3] 180002-28500003-01 Calculation for shielding design -around the reactor- (in Japanese), Design of JRR-3 reactor in JAERI, March 2nd (1988).

[4] Y. Sakamoto and Y. Yamaguchi, Dose Conversion Coefficients in the Shielding Design Calculation for High Energy Proton Accelerator Facilities, JAERI-Tech 2001-042 (2001).

[5] Manual for shielding calculations on radiation facilities 2000 (in Japanese), Japanese Nuclear Safety Technology Center (2000).

3.4.8 DI81-JA : RAM Analysis for the Rationalized IFMIF Design

(1) Brief Task Description

IFMIF performance measures such as Reliability, Availability and Maintainability (RAM) may have been changed with the reduced cost, staged construction design for IFMIF. Especially, availability of 80.7% must be achieved during scheduled operating time to keep the availability of 70% per year including scheduled maintenance time. Therefore RAM analyses need to be performed again for the newer design of IFMIF.

The most critical IFMIF sub-system in holding the high availability is the accelerator. The configuration of the drift tube linac (DTL) was changed through the redesign. Therefore, in KEP, RAM for the Accelerator System was revised based on the data of mean time between failure (MTBF) or failure rate and mean time to repair (MTTR). These data for IFMIF components were the same as used in the CDA analysis.

Three cases of accelerator configuration corresponding to those before and after the redesign were examined, using a revised calculational method to obtain correct values of MTBF. As a result, the change in the number of DTL tanks did not cause a significant change in availability. Employing a repair strategy using common spare parts in the DTL, the required availability (88%) of the accelerator will be achieved.

Contributors

Name	Party	Institute	E-mail address
M. Ida	Japan	JAERI	ida@ifmif.tokai.jaeri.go.jp
H. Takeuchi	Japan	JAERI	takeuchi@fnshp.tokai.jaeri.go.jp

(2) Required Availability

Operation of IFMIF must be continuous to avoid the complications of annealing effects that would occur in the case of intermittent irradiation. It is also required that long-time operation achieve a total facility availability of 70% to reach accumulated damage levels around 100 dpa in a few years of operation. This requires the following operation time per year.

Required operation time = 0.7 × 24 h/d × 365 d/y = 6132 h/y

Allowing for the scheduled maintenance time of one month per year and eight hours per week, scheduled maintenance/operation time per year is as follows.

Scheduled maintenance time = 24 h/d × 31 d/m × 1 m/y + 8 h/w × 52 w/y = 1160 h/y

Scheduled operation time = 24 h/d × 365 d/y − 1160 h/y = 7600 h/y

This requires system availability of 80.7 % during scheduled operation, determined as follows.

System availability = 6132 h/y ÷ 7600 h/y = 0.807

To achieve this availability of IFMIF: $A_{IFMIF} = 0.807$ is the product of the availability of all subsystems. The subsystem availability is allocated: $A_{TF} = 97.5\%$, $A_{TG} = 95.0\%$, $A_{AC} = 88.0\%$, $A_{CF} = 99.5\%$ and $A_{CC} = 99.5\%$ for Test Facilities, Target System, Accelerator System, Conventional Facilities and Central Control & Common Instruments (CC&CI). The availability of the Accelerator System is the most critical among the IFMIF subsystems.

(3) Main Changes of IFMIF due to Rationalization of the Design

In 1999 the IFMIF design was revised to reduce construction cost, and the cost was re-estimated [1]. At the same time, a staged deployment concept was introduced. In 2002, this concept was changed from three-stage construction (D^+ beam current: 50 mA → 125 mA → 250 mA) to two-stage (125 mA → 250 mA). This change does not bring any change of availability of the full IFMIF. The removal of the Energy Dispersion Cavity (EDC), the buncher cavities and the related RF power sources, and the RF transport will not affect IFMIF availability, since there is adequate temperature margin to avoid Li boiling at the point of maximum energy deposition. (With removal of EDC, the standard deviation of the D^+ energy decreases to about 0.2 MeV (from 0.5 MeV with the EDC) and the peak energy deposition is estimated to increase to about 1.5 times that with the EDC operating. This

sharp peak raises the temperature of Li, for example to about 730°C, in the case of a flow velocity of 10 m/s. However, the boiling point of Li is 988°C and this provides adequate margin. [2] The cost reduced design also had a change of DTL configuration. The number of DTL tanks was reduced from eight to five. This RAM analysis was performed mainly with consideration of this DTL change.

(4) Calculation Methods for Reliability, Availability, MTBF and MTTR of the System

(a) Definitions

Generally, MTBF: T is defined:

$$T \equiv \int_0^\infty t\left(-\frac{dR}{dt}\right)dt = -[tR]_0^\infty + \int_0^\infty Rdt = \int_0^\infty Rdt \tag{1}$$

where, R = Reliability, t = time. As assumed in RAM analysis of the CDA, Reliability: R of "One Part" is given as an exponential function:

$$R = e^{-Ft} \tag{2}$$

where, F = failure rate. With equations (1) and (2), MTBF: T = 1/F. Availability: A is given as follows:

$$A = \frac{T}{T+\tau} \tag{3}$$

where, τ = MTTR. Values of F and τ for every "One Part" are shown in Table 2.

(b) Subsystem Consisting of Only Working Parts

In case of "Subsystem: S1" consisting of m_1-working-parts with common values F, T, τ and no spare parts, the subsystem failure rate: F_1, MTBF: T_1, Reliability: R_1 and Availability: A_1 are given as follows:

$$F_1 = m_1 F \tag{4}$$

$$T_1 = \frac{1}{F} = \frac{T}{m_1} \tag{5}$$

$$R_1 = R^{m_1} = e^{-m_1 Ft} = e^{-F_1 t} \tag{6}$$

$$A_1 = \frac{T_1}{T_1+\tau} = \frac{(T/m_1)}{(T/m_1)+\tau} \tag{7}$$

(c) Subsystem Consisting of Working and Spare Parts

In case of "Subsystem: S2" consisting of m_2-working-parts and p_2-spare-parts, the subsystem Reliability and Availability are given in the same way as that in CDA. [3]

$$R_2 = e^{-m_2 Ft}\left\{\sum_{k=0}^{p_2}\frac{(m_2 Ft)^k}{k!}\right\} = e^{-F_2 t}\left\{\sum_{k=0}^{p_2}\frac{(F_2 t)^k}{k!}\right\} \tag{8}$$

$$A_2 = \frac{\{(p_2+1)/m_2\}T}{\{(p_2+1)/m_2\}T+\tau} \tag{9}$$

Having spare parts on hand improves reliability, availability, and MTBF of subsystem. For example, in the case of one spare part (i.e. p_2=1), unavailability (1-A_2) decreases to about half and MTBF doubles according to equations (1), (8) and (9).

(d) System Consisting of Subsystems

In the case of a "System" consisting of n-subsystems: S1, S2, ..., Sn, the system Reliability: R_S and Availability: A_S are simply given as follows:

$$R_S = \prod_{i=1}^{n} R_i \tag{10}$$

$$A_S = \prod_{i=1}^{n} A_i \tag{11}$$

where, R_j and A_j are to be calculated based on equations (8) through (11). Calculation of system MTBF: T_S is a bit more complex. To get correct values of T_S, a calculational method was revised as follows. According to equations (1), (8) and (10), the System MTBF: T_S is given as follows:

$$T_S = \int_0^\infty \prod_{i=1}^{n} \left[e^{-F_i t} \left\{ \sum_{k=0}^{p_i} \frac{(F_i t)^k}{k!} \right\} \right] dt = \frac{1}{F_S} \int_0^\infty e^{-x} \left[\prod_{i=1}^{n} \left\{ \sum_{k=0}^{p_i} \frac{1}{k!} \left(\frac{F_i}{F_S} x \right)^k \right\} \right] dx \tag{12}$$

where, System failure rate: Fs is given as follows:

$$F_S = \sum_{i=1}^{n} F_i \tag{13}$$

Using a function g(x):

$$g(x) = \prod_{i=1}^{n} \left\{ \sum_{k=0}^{p_i} \frac{1}{k!} \left(\frac{F_i}{F_s} x \right)^k \right\} = \sum_{j=0}^{\left(\sum_{i=0}^{n} p_i \right)} c_j x^j \tag{14}$$

equation (12) is given as follows:

$$T_S = \frac{1}{F_S} \int_0^\infty e^{-x} g(x) dx = \frac{1}{F_S} \sum_{j=0}^{\left(\sum_{i=1}^{n} pi \right)} \left\{ \int_0^\infty e^{-x} c_j x^j dx \right\} = \frac{1}{F_S} \sum_{j=0}^{\left(\sum_{i=1}^{n} pi \right)} \left\{ j! c_j \right\} \tag{15}$$

finally, in this analysis, T_S was calculated according to equations (14) and (15). According to equation (3), system MTBF: τ_S is given as follows:

$$\tau_S = T_S \left(\frac{1}{A} - 1 \right) \tag{16}$$

In cases where the whole system consists of a more complex hierarchy of structures such as "System", "Primary Subsystem", "Secondary Subsystem", "Tertiary Subsystem" and "Parts"; then R_S, A_S, T_S and τ_S are given by equations (10), (11), (12) and (16), respectively. Table 2 shows such T_S and τ_S.

(5) RAM Analysis of the DTL Configuration

In this Task, three RAM analyses were completed. Case-A, -B and –C analyses were performed for three different DTL configurations. As shown in Table 2, the DTL system consists of three subsystems of DTL Tank, Diagnostics, and Drift Tube & Quadrupole Magnets. The subsystem of the DTL Tank consists of Cavity, Drive loop, Ion pump, Support structure, and Cooling system controller. Table 1 summarizes configurations and number of parts (m = number of working parts, p = spares) for the three cases.

The configurations of the DTL Tanks are each different. Furthermore, the number of Drive loops and Ion Pumps are different in each of the three cases. Case-A corresponds to an eight-tank configuration, the original CDA design. Each Tank has 1 cavity, 2 Drive loops, 2 Ion pumps, 1 Support structure, and 1 Cooling system controller as working parts. The tank has 1 Drive loop and 1 Ion pump as spare parts.

Cases-B and C correspond to the five-tank configuration adopted in the reduced cost design. In Case-B, each Tank has 2 or 4 Drive loops and 4 Ion pumps as working parts. The number of other working parts per tank are the same as in Case-A. The tank has 1 Drive loop and 1 Ion pump as spare parts.

In Case-C, the number of working parts are the same as those in Case-B. However, the repair strategy is different from those in Case-A and -B. The five tanks share 2 Drive loops and 1 Ion pump as common spare parts.

Table 1 Configuration of DTL Tanks.

			Tank-1	Tank-2	Tank-3	Tank-4	Tank-5	Tank-6	Tank-7	Tank-8
Case-A	Drive loop	m	2	2	2	2	2	2	2	2
		p	*1*	*1*	*1*	*1*	*1*	*1*	*1*	*1*
	Ion pump	m	2	2	2	2	2	2	2	2
		p	*1*	*1*	*1*	*1*	*1*	*1*	*1*	*1*
Case-B	Drive loop	m	2	4	4	4	4			
		p	*1*	*1*	*1*	*1*	*1*			
	Ion pump	m	4	4	4	4	4			
		p	*1*	*1*	*1*	*1*	*1*			
Case-C	Drive loop	m	2	4	4	4	4			
		p	*2*							
	Ion pump	m	4	4	4	4	4			
		p	*1*							

(a) RAM Analysis Results for Case-A (Eight Tanks)

Table 2 shows all results for Case-A. The input conditions were failure rates of each part, system-configuration/ hierarchy-structure, and repair strategy (number of spare parts etc.). The outputs were Reliability, Availability, MTBF and MTTR of higher hierarchies such as systems and subsystems. The reliability values correspond to a mission time of 168 h (i.e. one week). The ECR type Ion source was selected, since this type has the most promising reliability in this stage. (The details of ion-source performance are described in the Accelerator Sections in this Report.) Spare parts were given to Drive loops/Pumps/RF stations in RFQ/DTL systems, since these parts have relatively higher failure rates and/or large number of parts. For the RFQ/DTL RF stations, there are no spare parts, but spare subsystems are provided. In such case, equations (8) and (9) are still applicable in treating each subsystem as one part. A summary for Case-A is shown in Fig. 1. The Availability of the Accelerator Module (i.e. one accelerator with 125 mA beam) is 87.6%, which is slightly lower than the required value of 88%. The availability of the DTL is more critical than that for the Injector, RFQ, DTL, HEBT and RF Systems.

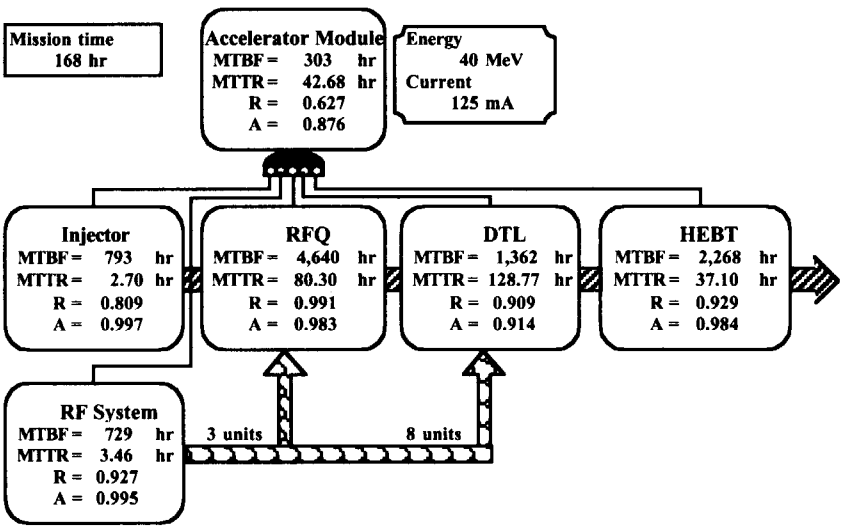


Fig. 1 Summary of RAM in Case-A.

Table 2 RAM Results of Case-A.

System	Subsystem	Assembly	Number of Parts		Failure Rate (1/hr)		MTBF (hr)	MTTR* (hr)	MTTR factor*	Steadystate Availability	Mission Reliability
			Working	Spare	One Part	Total					
Injector			1			1.26E-03	7.93E+02	2.70E+00	3.41E-03	9.97E-01	8.09E-01
	Ion source (ECR)		1			9.99E-04	1.00E+03	1.98E+00	1.98E-03	9.98E-01	8.45E-01
		RF source	1		2.00E-05	2.00E-05	5.00E+04	1.00E+00	2.00E-05	1.00E+00	9.97E-01
		RF window	1		9.75E-04	9.75E-04	1.03E+03	2.00E+00	1.95E-03	9.98E-01	8.49E-01
		Solenoid magnet	2		2.00E-06	4.00E-06	2.50E+05	2.00E+00	8.00E-06	1.00E+00	9.99E-01
	Ion source (common)		1			1.13E-04	8.83E+03	5.32E+00	6.03E-04	9.99E-01	9.81E-01
		Extractor	1		1.14E-05	1.14E-05	8.77E+04	4.00E+00	4.56E-05	1.00E+00	9.98E-01
		Gas supply (flow controller)	1		4.17E-05	4.17E-05	2.40E+04	2.00E+00	8.33E-05	1.00E+00	9.93E-01
		HV power supply	1		1.00E-05	1.00E-05	1.00E+05	2.40E+01	2.40E-04	1.00E+00	9.98E-01
		TM pump	1		5.00E-05	5.00E-05	2.00E+04	4.00E+00	2.00E-04	1.00E+00	9.92E-01
		Support structure	1		2.00E-07	2.00E-07	5.00E+06	1.68E+02	3.36E-05	1.00E+00	1.00E+00
	LEBT		1			1.50E-04	6.69E+03	5.49E+00	8.22E-04	9.99E-01	9.75E-01
		Focusing solenoid (upstream)	1		2.00E-06	2.00E-06	5.00E+05	4.00E+00	8.00E-06	1.00E+00	1.00E+00
		Focusing solenoid (downstream)	1		2.00E-06	2.00E-06	5.00E+05	8.00E+00	1.60E-05	1.00E+00	1.00E+00
		Steering magnet#1	1		2.00E-06	2.00E-06	5.00E+05	4.00E+00	8.00E-06	1.00E+00	1.00E+00
		Steering magnet#2	1		2.00E-06	2.00E-06	5.00E+05	3.00E+00	6.00E-06	1.00E+00	1.00E+00
		Magnet power supply	4		2.00E-06	8.00E-06	1.25E+05	1.00E+00	8.00E-06	1.00E+00	9.99E-01
		Gas neutralization system	1		4.17E-05	4.17E-05	2.40E+04	1.00E+00	4.17E-05	1.00E+00	9.93E-01
		TM pump	1		5.00E-05	5.00E-05	2.00E+04	4.00E+00	2.00E-04	1.00E+00	9.92E-01
		Diagnostics	1		4.17E-05	4.17E-05	2.40E+04	1.20E+01	5.00E-04	1.00E+00	9.93E-01
		Support sturcture	1		2.00E-07	2.00E-07	5.00E+06	1.68E+02	3.36E-05	1.00E+00	1.00E+00
RFQ			1			4.92E-04	4.64E+03	8.03E+01	1.73E-02	9.83E-01	9.91E-01
		Cavity	3		2.00E-07	6.00E-07	1.67E+06	4.38E+03	2.63E-03	9.97E-01	1.00E+00
		Drive loop	12	1	1.25E-05	1.50E-04	1.33E+04	1.44E+02	1.08E-02	9.89E-01	1.00E+00
		TM pump	6	1	5.00E-05	3.00E-04	6.67E+03	2.40E+01	3.60E-03	9.96E-01	9.99E-01
		Support structure	1		2.00E-07	2.00E-07	5.00E+06	1.68E+02	3.36E-05	1.00E+00	1.00E+00
		Cooling system controller	1		4.17E-05	4.17E-05	2.40E+04	4.00E+00	1.67E-04	1.00E+00	9.93E-01
DTL			1			2.09E-03	1.36E+03	1.29E+02	9.46E-02	9.14E-01	9.09E-01
	DTL Tank		8			1.54E-03	2.10E+03	1.54E+02	7.34E-02	9.32E-01	9.44E-01
		Cavity	1		2.00E-07	2.00E-07	5.00E+06	4.38E+03	8.76E-04	9.99E-01	1.00E+00
		Drive loop	2	1	5.00E-05	1.00E-04	2.00E+04	1.44E+02	7.20E-03	9.93E-01	1.00E+00
		Ion pump	2	1	2.50E-05	5.00E-05	4.00E+04	2.40E+01	6.00E-04	9.99E-01	1.00E+00
		Support structure	1		2.00E-07	2.00E-07	5.00E+06	1.68E+02	3.36E-05	1.00E+00	1.00E+00
		Cooling system controller	1		4.17E-05	4.17E-05	2.40E+04	4.00E+00	1.67E-04	1.00E+00	9.93E-01
	Diagnostics		8	1	4.17E-05	3.33E-04	6.00E+03	2.40E+01	4.00E-03	9.96E-01	9.98E-01
	DT & Quads		1		1.00E-06	2.17E-04	4.61E+03	7.23E+01	1.57E-02	9.85E-01	9.64E-01
		DT	1		1.00E-06	1.00E-06	1.00E+06	7.20E+01	7.20E-05	1.00E+00	1.00E+00
		DT chain w/o failures torelable	97	0		9.70E-05	1.03E+04	7.20E+01	6.98E-03	9.93E-01	9.84E-01
		Quad magnet	1		1.00E-06	1.00E-06	1.00E+06	7.20E+01	7.20E-05	1.00E+00	1.00E+00
		Quad chain w/o failures torelable	120	0		1.20E-04	8.33E+03	7.20E+01	8.64E-03	9.91E-01	9.80E-01
RF System			1			3.27E-03	7.29E+02	3.46E+00	4.74E-03	9.95E-01	9.27E-01
	RFQ RF station		3	1		8.87E-04	2.25E+03	5.29E+00	2.35E-03	9.98E-01	9.90E-01
			1			2.96E-04	3.38E+03	1.59E+01	4.69E-03	9.95E-01	9.52E-01
		High Power Tube	1		5.00E-05	5.00E-05	2.00E+04	4.80E+01	2.40E-03	9.98E-01	9.92E-01
		HPTP	1			9.23E-05	1.08E+04	8.27E+00	7.64E-04	9.99E-01	9.85E-01
		RF Transport	1			1.00E-06	1.00E+06	2.40E+01	2.40E-05	1.00E+00	1.00E+00
		Source & Driver	1			6.47E-05	1.55E+04	9.55E+00	6.17E-04	9.99E-01	9.89E-01
		Circulator	0							1.00E+00	1.00E+00
		HVPS	1			8.77E-05	1.14E+04	1.01E+01	8.82E-04	9.99E-01	9.85E-01
	DTL RF station		8	1		2.37E-03	8.46E+02	1.98E+00	2.35E-03	9.98E-01	9.39E-01
			1			2.96E-04	3.38E+03	1.59E+01	4.69E-03	9.95E-01	9.52E-01
		High Power Tube	1		5.00E-05	5.00E-05	2.00E+04	4.80E+01	2.40E-03	9.98E-01	9.92E-01
		HPTP	1			9.23E-05	1.08E+04	8.27E+00	7.64E-04	9.99E-01	9.85E-01
		RF Transport	1			1.00E-06	1.00E+06	2.40E+01	2.40E-05	1.00E+00	1.00E+00
		Source & Driver	1			6.47E-05	1.55E+04	9.55E+00	6.17E-04	9.99E-01	9.89E-01
		Circulator	0							1.00E+00	1.00E+00
		HVPS	1			8.77E-05	1.14E+04	1.01E+01	8.82E-04	9.99E-01	9.85E-01
	Global RF Control		1			2.00E-05	5.00E+04	2.00E+00	4.00E-05	1.00E+00	9.97E-01
		Master Oscillator	1		1.00E-05	1.00E-05	1.00E+05	2.00E+00	2.00E-05	1.00E+00	9.98E-01
		Phase Reference Distribution	1		1.00E-05	1.00E-05	1.00E+05	2.00E+00	2.00E-05	1.00E+00	9.98E-01
HEBT			1			4.41E-04	2.27E+03	3.71E+01	1.64E-02	9.84E-01	9.29E-01
	Low Activity Room		1			3.35E-04	2.99E+03	3.22E+01	1.08E-02	9.89E-01	9.45E-01
		(Assembly)	1			1.60E-05	6.25E+04	2.40E+01	3.84E-04	1.00E+00	9.97E-01
		electromag	2		2.00E-06	4.00E-06	2.50E+05	2.40E+01	9.60E-05	1.00E+00	9.99E-01
		electrical PS	1		2.00E-06	2.00E-06	5.00E+05	2.40E+01	4.80E-05	1.00E+00	1.00E+00
		cooling	1		1.00E-05	1.00E-05	1.00E+05	2.40E+01	2.40E-04	1.00E+00	9.98E-01
	Qaudrupole	(Chain)	11			1.76E-04	5.68E+03	2.40E+01	4.23E-03	9.96E-01	9.71E-01
		(Assembly)	1			1.40E-05	7.14E+04	2.40E+01	3.36E-04	1.00E+00	9.98E-01
		electromag	1		2.00E-06	2.00E-06	5.00E+05	2.40E+01	4.80E-05	1.00E+00	1.00E+00
		electrical PS	1		2.00E-06	2.00E-06	5.00E+05	2.40E+01	4.80E-05	1.00E+00	1.00E+00
		cooling	1		1.00E-05	1.00E-05	1.00E+05	2.40E+01	2.40E-04	1.00E+00	9.98E-01
	Dipole	(Chain)	2			2.80E-05	3.57E+04	2.40E+01	6.72E-04	9.99E-01	9.95E-01
		(Assembly)	1			1.40E-05	7.14E+04	2.40E+01	3.36E-04	1.00E+00	9.98E-01
		electromag	1		2.00E-06	2.00E-06	5.00E+05	2.40E+01	4.80E-05	1.00E+00	1.00E+00
		electrical PS	1		2.00E-06	2.00E-06	5.00E+05	2.40E+01	4.80E-05	1.00E+00	1.00E+00
		cooling	1		1.00E-05	1.00E-05	1.00E+05	2.40E+01	2.40E-04	1.00E+00	9.98E-01
	Octupole	(Chain)	2			2.80E-05	3.57E+04	2.40E+01	6.72E-04	9.99E-01	9.95E-01
		(Assembly)	1			1.40E-05	7.14E+04	2.40E+01	3.36E-04	1.00E+00	9.98E-01
		electromag	1		2.00E-06	2.00E-06	5.00E+05	2.40E+01	4.80E-05	1.00E+00	1.00E+00
		electrical PS	1		2.00E-06	2.00E-06	5.00E+05	2.40E+01	4.80E-05	1.00E+00	1.00E+00
		cooling	1		1.00E-05	1.00E-05	1.00E+05	2.40E+01	2.40E-04	1.00E+00	9.98E-01
	Duodecapole	(Chain)	2			2.80E-05	3.57E+04	2.40E+01	6.72E-04	9.99E-01	9.95E-01
	Beam Tube	ion pump	1		2.50E-05	2.50E-05	4.00E+04	6.00E+01	1.50E-03	9.99E-01	9.96E-01
	Vacuum	(Ion pump chain)	3			7.50E-05	1.33E+04	6.01E+01	4.51E-03	9.96E-01	9.87E-01
	High Activity Room		1			1.06E-04	9.43E+03	5.20E+01	5.51E-03	9.95E-01	9.82E-01
	Dipole	(Assembly)	1			1.40E-05	7.14E+04	4.46E+01	6.24E-04	9.99E-01	9.98E-01
		electromag	1		2.00E-06	2.00E-06	5.00E+05	4.80E+01	9.60E-05	1.00E+00	1.00E+00
		electrical PS	1		2.00E-06	2.00E-06	5.00E+05	2.40E+01	4.80E-05	1.00E+00	1.00E+00
		cooling	1		1.00E-05	1.00E-05	1.00E+05	4.80E+01	4.80E-04	1.00E+00	9.98E-01
		(Chain)	1			1.40E-05	7.14E+04	4.46E+01	6.24E-04	9.99E-01	9.98E-01
	Qaudrupole	(Assembly)	1			1.40E-05	7.14E+04	4.46E+01	6.24E-04	9.99E-01	9.98E-01
		electromag	1		2.00E-06	2.00E-06	5.00E+05	4.80E+01	9.60E-05	1.00E+00	1.00E+00
		electrical PS	1		2.00E-06	2.00E-06	5.00E+05	2.40E+01	4.80E-05	1.00E+00	1.00E+00
		cooling	1		1.00E-05	1.00E-05	1.00E+05	4.80E+01	4.80E-04	1.00E+00	9.98E-01
		(Chain)	3			4.20E-05	2.38E+04	4.46E+01	1.87E-03	9.98E-01	9.93E-01
	Beam Tube	ion pump	1		2.50E-05	2.50E-05	4.00E+04	6.00E+01	1.50E-03	9.99E-01	9.96E-01
	Vacuum	(Ion pump chain)	2			5.00E-05	2.00E+04	6.00E+01	3.00E-03	9.97E-01	9.92E-01

* MTTR : including response time. MTTR factor : MTTR/MTBF

(b) RAM Analysis Results for Case-B (Five Tanks, Some Spare Parts for Each Tank)

Table 3 shows DTL results for Case-B. Results for systems other than the DTL (Injector, RFQ, HEBT and RF System) are the same as those in Case-A. Because of the increased number of working Drive loops (16 in Case-A →18 in Case-B) and Ion pumps (16→20), the availability of the DTL was slightly decreased from that in Case-A. A summary of Case-B is shown in Fig. 2. The availability of the Accelerator Module is 87.2%, still slightly lower than the required value of 88%.

Table 3 RAM Results of Case-B.

System	Subsystem	Assembly	Number of Parts		Failure Rate (1/hr)		MTBF (hr)	MTTR* (hr)	MTTR factor*	Steadystate Availability	Mission Reliability
			Working	Spare	One Part	Total					
DTL			1			2.16E-03	1.43E+03	1.42E+02	1.00E-01	9.09E-01	9.26E-01
	DTL Tank		1			2.42E-04	8.95E+03	8.50E+01	9.49E-03	9.91E-01	9.93E-01
		Cavity	1		2.00E-07	2.00E-07	5.00E+06	4.38E+03	8.76E-04	9.99E-01	1.00E+00
		Drive loop	2	1	5.00E-05	1.00E-04	2.00E+04	1.44E+02	7.20E-03	9.93E-01	1.00E+00
		Ion pump	4	1	2.50E-05	1.00E-04	2.00E+04	2.40E+01	1.20E-03	9.99E-01	1.00E+00
		Support structure	1		2.00E-07	2.00E-07	5.00E+06	1.68E+02	3.36E-05	1.00E+00	1.00E+00
		Cooling system controller	1		4.17E-05	4.17E-05	2.40E+04	4.00E+00	1.67E-04	1.00E+00	9.93E-01
	DTL Tank		4			1.37E-03	2.41E+03	1.65E+02	6.85E-02	9.36E-01	9.69E-01
		Cavity	1		2.00E-07	2.00E-07	5.00E+06	4.38E+03	8.76E-04	9.99E-01	1.00E+00
		Drive loop	4	1	5.00E-05	2.00E-04	1.00E+04	1.44E+02	1.44E-02	9.86E-01	9.99E-01
		Ion pump	4	1	2.50E-05	1.00E-04	2.00E+04	2.40E+01	1.20E-03	9.99E-01	1.00E+00
		Support structure	1		2.00E-07	2.00E-07	5.00E+06	1.68E+02	3.36E-05	1.00E+00	1.00E+00
		Cooling system controller	1		4.17E-05	4.17E-05	2.40E+04	4.00E+00	1.67E-04	1.00E+00	9.93E-01
	Diagnostics		8	1	4.17E-05	3.33E-04	6.00E+03	2.40E+01	4.00E-03	9.96E-01	9.98E-01
	DT & Quads		1		1.00E-06	2.17E-04	4.61E+03	7.23E+01	1.57E-02	9.85E-01	9.64E-01
		DT	1		1.00E-06	1.00E-06	1.00E+06	7.20E+01	7.20E-05	1.00E+00	1.00E+00
		DT chain w/o failures torelable	97	0		9.70E-05	1.03E+04	7.20E+01	6.98E-03	9.93E-01	9.84E-01
		Quad magnet	1		1.00E-06	1.00E-06	1.00E+06	7.20E+01	7.20E-05	1.00E+00	1.00E+00
		Quad chain w/o failures torelable	120	0		1.20E-04	8.33E+03	7.20E+01	8.64E-03	9.91E-01	9.80E-01

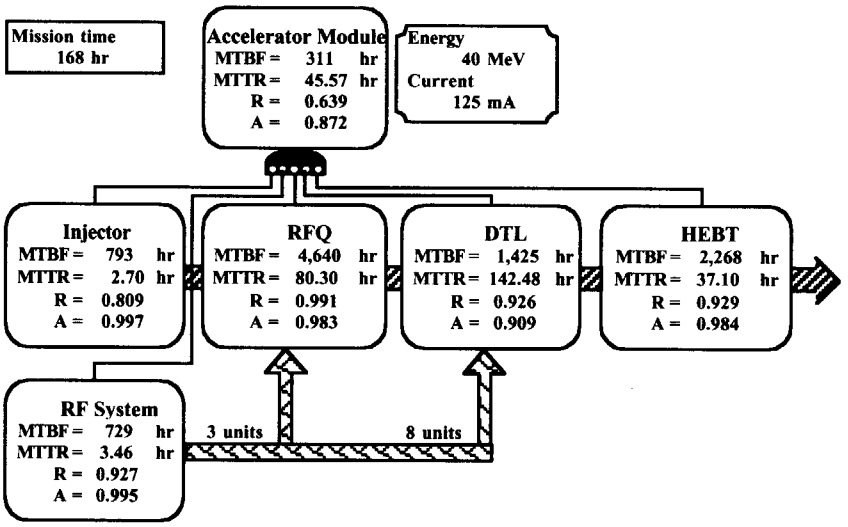


Fig. 2 Summary of RAM in Case-B.

(c) RAM Analysis Results for Case-C (Five Tanks, Common Spare Parts Shared by All Tanks)

To increase DTL availability and efficiently utilize spare parts, the repair strategy was changed from "spare parts for each tank" to "common spare parts shared by all tanks". Table 4 shows DTL results for Case-C. Because of this change, availability of DTL was increased by 2% from that in Case-B, while the total numbers of repair parts was significantly decreased (5→2 for Drive loops, 5→1 Ion pumps). A summary of Case-C is shown in Fig. 3. The availability of the Accelerator Module is now 89.2%, which is higher than the required value of 88%. Therefore, the DTL configuration and repair strategy of Case-C is recommended.

Table 4 RAM Results of Case-C.

System	Subsystem	Assembly	Number of Parts Working	Number of Parts Spare	Failure Rate (1/hr) One Part	Failure Rate (1/hr) Total	MTBF (hr)	MTTR* (hr)	MTTR factor*	Steadystate Availability	Mission Reliability
DTL			1			2.16E-03	1.26E+03	9.61E+01	7.59E-02	9.29E-01	9.26E-01
	DTL Tank		1			1.61E-03	1.75E+03	9.65E+01	5.51E-02	9.48E-01	9.62E-01
		Cavity	5		2.00E-07	1.00E-06	1.00E+06	4.38E+03	4.38E-03	9.96E-01	1.00E+00
		Drive loop	18	2	5.00E-05	9.00E-04	3.33E+03	1.44E+02	4.32E-02	9.59E-01	9.99E-01
		Ion pump	20	1	2.50E-05	5.00E-04	4.00E+03	2.40E+01	6.00E-03	9.94E-01	9.97E-01
		Support structure	5		2.00E-07	1.00E-06	1.00E+06	1.68E+02	1.68E-04	1.00E+00	1.00E+00
		Cooling system controller	5		4.17E-05	2.08E-04	4.80E+03	4.00E+00	8.33E-04	9.99E-01	9.66E-01
	Diagnostics		8	1	4.17E-05	3.33E-04	6.00E+03	2.40E+01	4.00E-03	9.96E-01	9.98E-01
	DT & Quads		1		1.00E-06	2.17E-04	4.61E+03	7.23E+01	1.57E-02	9.85E-01	9.64E-01
		DT	1		1.00E-06	1.00E-06	1.00E+06	7.20E+01	7.20E-05	1.00E+00	1.00E+00
		DT chain w/o failures torelable	97	0		9.70E-05	1.03E+04	7.20E+01	6.98E-03	9.93E-01	9.84E-01
		Quad magnet	1		1.00E-06	1.00E-06	1.00E+06	7.20E+01	7.20E-05	1.00E+00	1.00E+00
		Quad chain w/o failures torelable	120	0		1.20E-04	8.33E+03	7.20E+01	8.64E-03	9.91E-01	9.80E-01

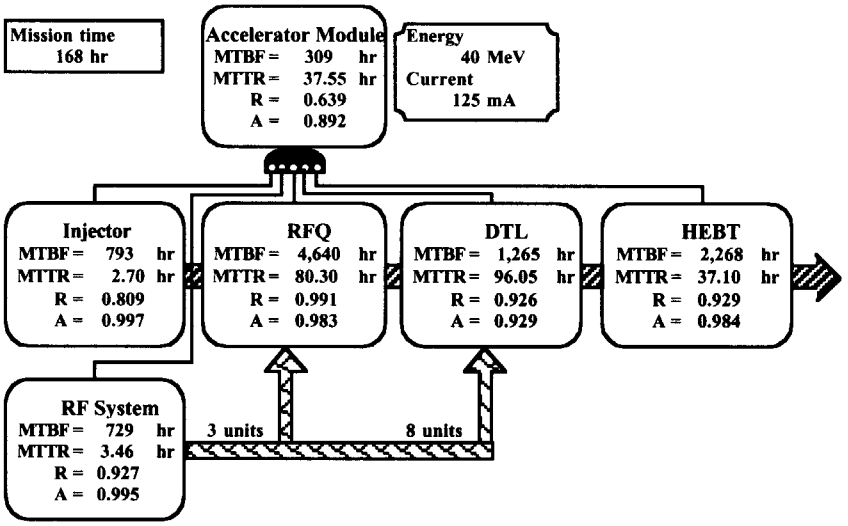


Fig. 3 Summary of RAM in Case-C.

(6) Summary

The RAM analysis of the Accelerator System was performed to evaluate the effects of changes in the IFMIF design since the CDA design was analyzed. Calculation methods were revised to give correct value of MTBF. Using this method, three cases were examined. The change in the number of DTL tanks did not produce significant changes in availability. Employing a repair strategy of common spare parts of Drive loops and Ion pumps for the DTLs, the required availability (88%) for the Accelerator will be achieved.

References

[1] Fusion Neutronics Laboratory (Ed. M. Ida et al.), IFMIF International Fusion Materials Irradiation Facility Conceptual Design Activity Reduced Cost Report, a Supplement to the CDA by the IFMIF Team, JAERI-Tech 2000-014 (2000).

[2] M. Ida, et al., Thermal-hydraulic characteristics of IFMIF liquid lithium target, to be published in Fusion Engineering and Design.

[3] IFMIF-CDA Team (Ed. H. Maekawa et al.), Minutes of the Second IFMIF-CDA Design Integration Workshop, May 20-25, 1996, Tokai, Japan, JAERI-Conf 96-012 (1996).

3.4.9 DI83A-EU : Safety Analysis and Assessment

(1) Brief Task Description

This task concerns the review of the hazard analysis for the accelerator and test cell facilities in the light of the rational design version, adopting the FMEA (Failure Modes and Effects Analysis) methodology, oriented towards detailing on a component-by-component basis all the possible failure modes and identifying their effects on the plant.

Furthermore, for some major accidents, potentially leading to the damage of the plant or/and cause hazard to the environment and the public, a probabilistic internal events analysis is performed, adopting the event tree technique, aimed at assessing the plant risk in terms of accident frequencies quantification.

Contributor

Name	Party	Institute	E-mail address
L. Burgazzi	EU	ENEA	burgazzi@bologna.enea.it

(2) Hazard Analysis Review

Safety analysis review for the test cell and accelerator facilities has been performed applying the FMEA (Failure Modes and Effects Analysis) approach in order to identify the potential failures inducing an accident in the plant or simply a stop in the operating phase, with reference to the updated plant: the outcome of the present analysis is the identification of relevant hazards and the identification of major initiating events of accident sequences. FMEA is a bottom-up technique oriented towards detailing, on a component-by-component basis, all possible failure modes, identifying their effects on the plant and relative mitigating features and ranking the accidents according to their severity and frequency.

The present safety review reveals that, in the light of plant modifications submitted in the new rational design version, test facilities operation does not challenge the plant safety and off-site consequences can be excluded.[1] The foregoing detailed safety analysis pointed out as major event loss of vacuum in the test cell due to either malfunction of the test cell vacuum pumping system or loss of leaktightness of the test cell itself: since the backwall rupture and lithium spill in the test cell is not completely negligible, the provision for vacuum condition in the test cell greatly reduces the relative hazard should such an event occur.

The study underlined also the hazard associated with the release of potentially contaminated gas to cells surrounding the test cell, that is access cell, test cell technology room and operating areas, resulting thus in a radioactivity increase. Lastly the hazards related to events concerning the VTAs (Vertical Test Assemblies) systems, involving both gas release to the test cell atmosphere and loss of test assemblies thermal control, are negligible.

The hazards related to the accelerator are confined within the IFMIF security boundaries and the main findings stress what was found in the previous CDA phase: although great care must be exercised to protect workers and site personnel, there is negligible risk to the public from operating the accelerator.[2]

The most severe hazard indicated by the analysis is the production of a radiation field in the accelerator tunnel, which calls for a restricted and controlled access to accelerator areas. There are actually two different levels of contributors to this hazard: the former concerns the continuous beam spill in normal operation, the latter relates the radiation source due to loss-of-beam accidents.

A continuous beam spill, present at some level during all hours of normal beam operation, produces an ambient radiation field which is likely to be the dominant contributor to the dose rate that personnel working in the tunnel will receive. In addition it will activate all nearby accelerator components, as well as the concrete tunnel structure itself. Thus, in order for personnel to enter the accelerator tunnel as soon as possible after beam-off for inspection and maintenance, it is important to understand the level of activation and the decay characteristics as function of spill level, energy and irradiation time.

Conversely the most severe beam-loss accident is identified as the total loss of the extracted beam: initiators considered are typically the accidental closures of beam intercepting devices (vacuum valves for example), or failure of a beam-line magnet and beam extraction system. The failures of the beam devices are conservatively considered as instantaneous, resulting in a sudden source of radiation (in reality losses distributed in time and space are more likely to occur) thus presenting the most severe restraints with respect to the access to the contaminated area.

In addition the foregoing detailed safety analysis pointed out as major events loss of vacuum in the beam line which in turn resuls in beam loss accident and the release of non-ionizing radiation, i.e. radiofrequency waves, from the radiofrequency system, challenging again the safe access of personnel to the accelerator.

Monitoring, control and protection systems act as most relevant lines of defense to face the off normal events, while personnel protection from radiation hazards relies on passive shielding and restricted and controlled access to accelerator areas.

Preliminary estimates of the probabilities of occurrence of initiating events are made, where possible, on account of the available published failure data or alternatively on the basis of subjective/engineering assessment. Conservative assumptions are made to compensate for the simplified method of analysis and to account for the uncertainties associated with some of the parameters. The analysis has provided as a result a set of Postulated Initiating Events (PIEs), together with the total frequency and the list of component failures which could induce the PIE (a set of elementary accident initiators is grouped under a PIE taking into account the similarity of accident development in terms of mitigating features and possible consequences): this assures the complete list of major initiating events of accident sequences, helpful to the further accident sequence quantification phase. The events are classified by event likelihood of occurrence, according to Table 1. The overall set of PIEs identified by the FMEA are reported in Tables 2 and 3, respectively for the test cell facilities and the accelerator. [1], [2]

Table 1 Event sequences categorization.

EVENT CATEGORY	EVENT DESCRIPTION	EVENT FREQUENCY
I	Operational Events	More than one per year
II	Likely Events	$1\sim10^{-2}$/y
III	Unlikely Events	$10^{-2}\sim10^{-4}$/y
IV	Extremely Unlikely Events	$10^{-4}\sim10^{-6}$/y
V	Hypothetical Sequences	Less than 10^{-6}/y

Table 2 Test Cell list of identified Postulated Initiating Events.

PIE code	PIE Description	Category
CLR	Release of contaminated gas in cells other than test cell (access cell, test cell technology room and operating areas)	III
LF-CS	Loss of flow in the test cell liner and heat shield Cooling System	II
LV-TC	Loss of vacuum in the Test Cell	III
N/S	Not Safety relevant initiator	II

Table 3 Accelerator list of identified Postulated Initiating Events.

PIE code	PIE Description	Category
BL	Loss of beam	II
LV-B	Loss of vacuum in the beam line	II
RF	Release of radio frequency waves from radio frequency transport tubes	III
N/S	Not Safety relavant initiator	NA

(3) Plant Safety Assessment

An activity aimed at the safety assessment of the IFMIF plant has been carried out applying the PRA (Probabilistic Risk Assessment) approach: this work has been finalized to the identification and quantification, in terms of frequencies of occurrence, of the dominant accident sequences occurring during normal operation and potentially leading to damage of the IFMIF plant and, as extreme consequence, harming the environment and the public.

The adopted methodology and calculation tool have been respectively the Fault Tree (FT) and Event Tree (ET) technique, widely utilized in the PRA studies, and RISK SPECTRUM code, a PC software package for system risk and reliability analysis. [3]

Synthetically, the methodology embraced for the analysis consists of the following major tasks:

a. Identification of initiating events or initiating event groups of accident sequences: each initiator is defined by a frequency of occurrence;
b. Systems analysis: identification of functions to be performed in responding to each initiating events to successfully prevent plant damage or to mitigate the consequences and identification of the correspondent plant systems that perform these functions (termed front-line systems): for each system the probability of failure is assessed, by fault tree model;
c. Accident sequences development by constructing event trees for each initiating event or initiating event groups, to assess the frequencies of all relevant accident sequences and eventual grouping of the accident sequences into sequence families or Plant Damage States, basing on consequences and similarity of accident evolution and plant response.

a. The initiating events considered in this study are limited to internal initiators - neither external events, such as earthquakes and floods, nor area events, such as fires or internally caused floods, are taken into account - that are assumed to occur during the normal operation of IFMIF plant. The initiating events of the accident sequences have been identified based on the outcome of the safety analysis review of Target, Test Cell and Accelerator Facilities, performed by applying the Failure Modes and Effects Analysis (FMEA) methodology. A preliminary analysis of the PIEs allows to disregard any of them for the consequent evaluation, i.e. those actually not triggering an accident sequence or being involved by other ones or simply representing themselves a plant hazardous state: this preliminary screening process highlights as relevant initiating events the ones relative to the failures involving the target system, which is designed to assure the required functions (chiefly the cooling of the target assembly), as shown in Table 4.

Table 4 List of Postulated Initiating Events of accident sequences.

PIE code	PIE Description	Category
LF	Loss of flow in the Target Li loop	II
LFCT	Loss of flow in the Cold Trap cooling loop	II
LH	Loss of heat sink	II
Li-LOCA	Lithium LOCA	II
LP	Loss of Li purification	II
LS1	Lithium spill in the Test Cell	III
LTR1	Li-Or Cooler tube rupture	III
Or-LOCA	Organic LOCA	III
W-LOCA	Water LOCA	III
Ar-LOCA	Argon LOCA	III

b. The most relevant safety systems or front-line systems having the function of stopping the accident sequence evolution and mitigating the consequences are the Emergency Beam Shutdown

System, the Beam Isolation System for the beam-target interface, the Heating Ventilation and Air Conditioning (HVAC) and Vacuum Systems for lithium fire prevention, respectively for the lithium cell and for the test cell.
At this stage of the design, some of the mitigative and preventive features are developed, mostly qualitatively: this remark applies significantly to the Emergency Beam Shut-Down and to the Beam Isolation System. Because a highly reliable Emergency Beam Shut-Down is envisaged, the probability of failure to shut-down the beam is assigned the value 1.0E-4/d (d: demand); similarly the Beam Isolation System, consisting of a set of fast acting valves placed downstream the final dispersion energy cavities in the HEBT of the accelerator, is assigned the reliability value 1.0E-3/d. It has to be underlined that the uninterruptable power supply (e.g. backup batteries) is provided for the protection system (e.g. emergency beam shut-down and target/beam isolation), improving thus their availability. The same approach concerns other important safety features, as operator recovery actions, Li Cell isolation and Test Cell integrity, appointed to withstand the accident evolution, which are evaluated through engineering judgement.
Conversely, FT models are constructed for the front-line systems, including the Exhaust Gas Detritiation System, and for the Electrical Power Distribution System, as main support system, in order to assess the respective unavailability, as listed below:

- Li Cell HVAC
- Test Cell Vacuum
- Exhaust Detritiation System for Tritiated Air
- Exhaust Detritiation System for Tritiated Argon Gas
- Electrical Power Distribution System

The evaluated failure probability values relative to the foregoing systems are reported in Table 5: for completeness, also the failure probabilities relative to the remainder of the safety systems are reported.

Table 5 Unavailability values for safety systems.

System	Failure probability
Electrical Power Distribution System	7.88E-4
HVAC for Li Cell	1.29E-3
Test Cell Vacuum	1.06E-2
EDS Argon	1.9E-2
EDS Air	2.57E-2
Emergency Beam Shutdown	1.0E-4
Beam Isolation System	1.0E-3
Human Action	1.0E-3
Li Cell Isolation	2.7E-4
Test Cell Integrity	1.0E-3

c. The accident sequence scenarios have been modeled through the event tree technique which allows to identify all the different chains of accident sequences deriving from the selection of the initiating events. Event tree development implies each sequence represents a certain combination of events, corresponding to failed or operating safety systems.
ET analysis, besides developing all the accident sequences coming from an initiator, allows the grouping of such sequences within sequence families or plant status. The grouping is based on common attributes in terms of consequences on the plant and plant response to the accident.
The methodology followed for the assessment of the accident sequences is summarized in the following steps:

- For each PIE an ET is developed to identify the possible important accident scenarios from a safety point of view (mitigative features and safety protections are investigated): this allows to delineate the accident sequences.
- Each ET branch (sequence) induces a plant status in faulted conditions. The plant status could be safety relevant or not safety relevant, on account of the consequences on the plant.

Generally, for each ET few safety relevant plant status are identified: going on with the ET development a classification of plant status (sequence family), termed also Plant Damage State(PDS), is performed. Each PDS is classified according to the accident evolution and the consequences.

At the end of the ET analysis, to each PDS a frequency of occurrence is assigned by adding the frequencies of all the single sequences as contributors. The ETs, starting from the initiators, branch down following success or failure of the mitigating features or front-line systems that match the ET headings, providing therefore a set of alternative consequences.

The outcome of the sequence is classified OK if the final status of the plant is no damage due to a sufficient number of safety systems correctly operated, while accident sequences implying a damaged plant state are classified in PDS and an identifier is given to each sequence family.

The accident sequences are categorized into two broad families: the former concerns the LOCA (Loss of Coolant Accident) events, the latter is pertaining to the LOFA (Loss of Flow Accident) events. During the analysis, as far as one of the consequences is the loss of heat removal from the target, it is worth noting that one of the safety attributes of the target is the very low decay heat, that decreases very rapidly with time so that it can be neglected, therefore not requiring a residual heat removal system. In addition, all of the coolant loops are at low pressure and at low temperature: these conditions result in a low stored energy in the coolants and ultimately in lower consequences in case of break in the primary coolant system. For instance loss of primary coolant inventory due to coolant flashing will not occur and the confinement system is not subjected to any significant pressure increase of a large pipe break.

As stated before, the results of ET analysis, in terms of end sequences probability and qualitative consequences, allow for the definition of the most important sequences within each single ET: these important sequences being classified in PDS.

The event trees are grouped into nine PDSs with common attributes with the respective frequencies. From the quantification point of view, the probability of each PDS is assigned to the sum of its contributors and the worst sequence in the group should be selected as representative sequence for the consequences estimation, generally the one with the highest frequency. This procedure is also considered to be conservative.

The results by sequences appear within each ET picture in Figs. 1-10, while the results by PDS are summarized in Table 6 by total frequencies.

Table 6 Accident sequences frequencies.

PDS Code	Description	Freq. (1/y)
PDS1	Target overheating	3.3E-12
PDS2	Li fire in the Li cell	1.29E-5
PDS3	Li fire in the Li cell without isolation	3.49E-9
PDS4	Li fire in the Li cell and Target overheating	1.29E-15
PDS5	Li fire in the Li cell without isolation and Target overheating	3.49E-19
PDS6	Radioactive impurity accumulation	2.1E-12
PDS7	Li intrusion in the beam line	1.0E-9
PDS8	Li fire in the test cell	1.06E-5
PDS9	Li fire in the test cell without test cell integrity	1.06E-8

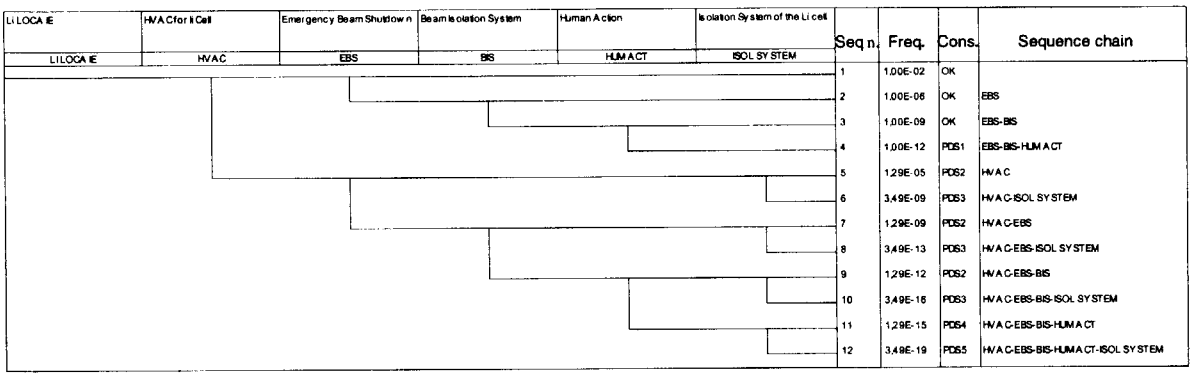


Fig. 1 Lithium LOCA Event Tree.

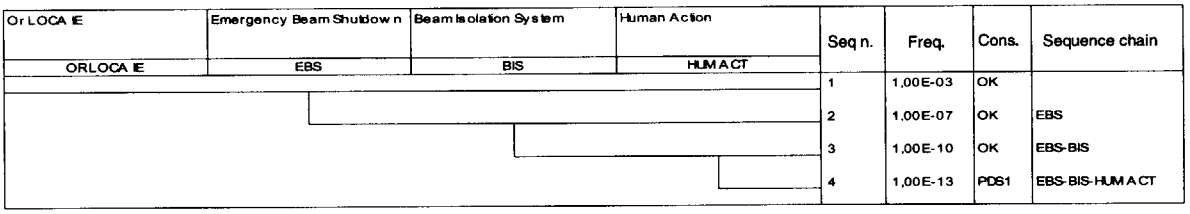


Fig. 2 Organic oil LOCA Event Tree.

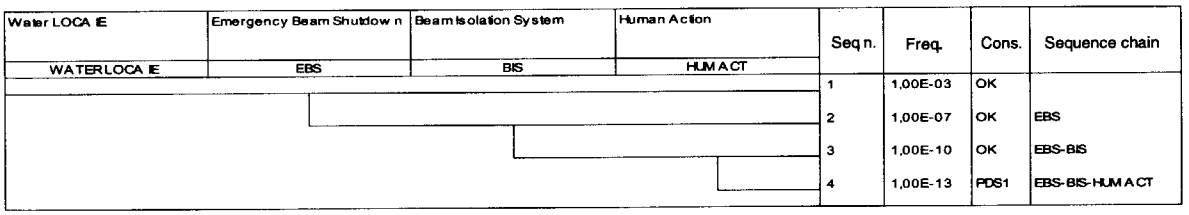


Fig. 3 Water LOCA Event Tree.

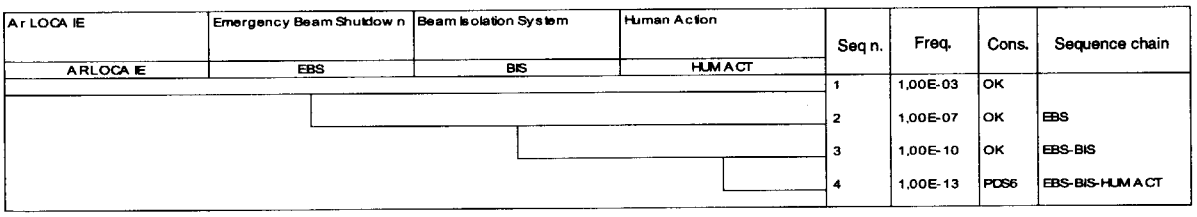


Fig. 4 Argon LOCA Event Tree.

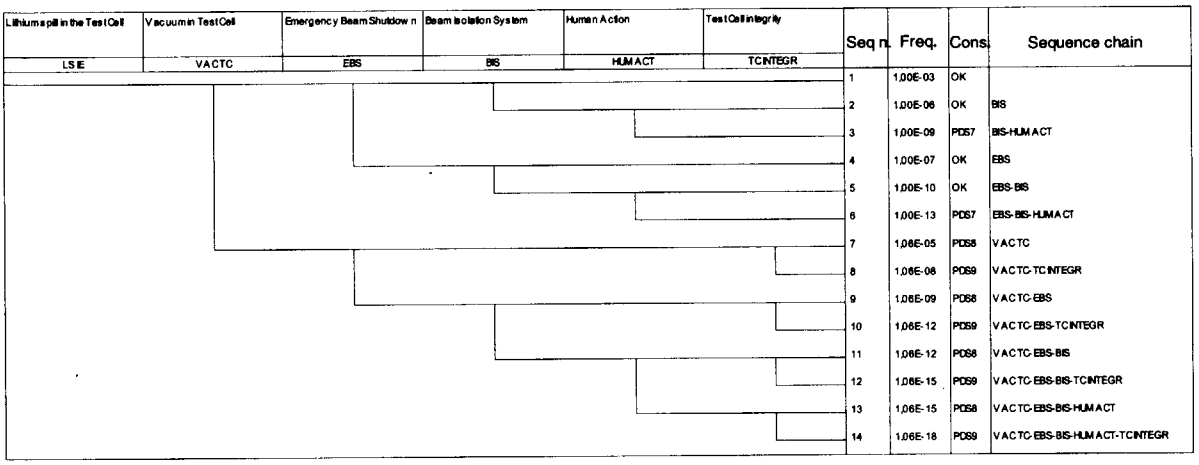


Fig. 5 Lithium spill in the Test Cell Event Tree.

Li-Or HX tube rupture IE	Emergency Beam Shutdow n	Beam Isolation System	Human Action	Seq n.	Freq.	Cons.	Sequence chain
LI-OR-HX-TR IE	EBS	BIS	HUM A CT				
				1	1,00E-03	OK	
				2	1,00E-07	OK	EBS
				3	1,00E-10	OK	EBS-BIS
				4	1,00E-13	PDS1	EBS-BIS-HUM A CT

Fig. 6 Li-organic cooler tube rupture Event Tree.

Loss of flow in the target lithium loop IE	Emergency Beam Shutdow n	Beam Isolation System	Human Action	Seq n.	Freq.	Cons.	Sequence chain
LF IE	EBS	BIS	HUM A CT				
				1	1,00E-02	OK	
				2	1,00E-06	OK	EBS
				3	1,00E-09	OK	EBS-BIS
				4	1,00E-12	PDS1	EBS-BIS-HUM A CT

Fig. 7 Loss of flow in the Li loop Event Tree.

Loss of heatsink IE	Emergency Beam Shutdow n	Beam Isolation System	Human Action	Seq n.	Freq.	Cons.	Sequence chain
LHS IE	EBS	BIS	HUM A CT				
				1	1,00E-02	OK	
				2	1,00E-06	OK	EBS
				3	1,00E-09	OK	EBS-BIS
				4	1,00E-12	PDS1	EBS-BIS-HUM A CT

Fig. 8 Loss of heat sink Event Tree.

Loss of flow in the cold trap cooling loop IE	Emergency Beam Shutdow n	Beam Isolation System	Human Action	Seq n.	Freq.	Cons.	Sequence chain
LFCTCL IE	EBS	BIS	HUM A CT				
				1	1,00E-02	OK	
				2	1,00E-06	OK	EBS
				3	1,00E-09	OK	EBS-BIS
				4	1,00E-12	PDS6	EBS-BIS-HUM A CT

Fig. 9 Loss of flow in the Cold Trap cooling loop Event Tree.

Loss of lithium purification IE	Emergency Beam Shutdow n	Beam Isolation System	Human Action	Seq n.	Freq.	Cons.	Sequence chain
LIPUR IE	EBS	BIS	HUM A CT				
				1	1,00E-02	OK	
				2	1,00E-06	OK	EBS
				3	1,00E-09	OK	EBS-BIS
				4	1,00E-12	PDS6	EBS-BIS-HUM A CT

Fig. 10 Loss of Lithium purification Event Tree.

The uncertainty analysis, provided in order to add credibility to the model and to "legitimize" the obtained frequency values, gives the results reported in Table 7. The uncertainty analysis shows a large variability in the results, mainly due to the high uncertainties in the systems reliability assessment (values used to quantify the ET model have to be considered affected by a certain degree of uncertainty): notwithstanding this, even if the highest frequency, on the range of the obtained values, is considered, such value is not so far from the expected one (i.e. mean value) to represent a safety concern for the plant and therefore one can conclude that the sequences are correctly evaluated on the probabilistic standpoint.

Table 7 Event Trees uncertainty analysis.

PDS Code	5th percentile	Median	95th percentile
PDS1	9.14E-16	6.71E-14	7.19E-12
PDS2	2.48E-8	1.07E-6	4.58E-5
PDS3	1.12E-12	9.22E-11	7.48E-9
PDS4	2.49E-20	4.85E-18	1.28E-15
PDS5	2.45E-24	6.32E-22	1.77E-19
PDS6	3.25E-16	2.65E-14	3.36E-12
PDS7	1.98E-13	1.36E-11	1.37E-9
PDS8	2.5E-8	9.77E-7	3.89E-5
PDS9	5.43E-12	3.62E-10	2.29E-8

(4) Conclusions

Hazard analysis, performed applying the FMEA (Failure Modes and Effects Analysis) approach, showed that Test Cell and Accelerator Facilities don't present significant potential hazards and the risk during IFMIF operation with respect to the public and the environment is negligible.

A probabilistic safety assessment based on event tree technique has been performed to evaluate the safety of the IFMIF plant: the analysis was oriented towards identifying and quantifying, in terms of expected frequency, the accident sequences that could occur to the plant facilities and could lead to IFMIF damage and environmental hazard, as extreme consequence.

The study has allowed for the development of all accident sequences resulting from selected initiators relative to IFMIF plant and their grouping within sequence families, denoted as plant damage states, on account of the plant response and accident evolution. The frequency assigned to each family sequence is the sum of the contributions relative to all sequences ending into that particular plant state.

The outcome of the analysis shows that IFMIF plant is quite safe and presents no significant hazard to the environment: in fact all the sequences implying potential undesired effects as release to the outside, show very low frequencies, well below the limit for credible accident (1.0E-6) and they don't need to be further analyzed.

Conversely the study has pointed out some sequences involving the Li fire in the test cell as well as in the lithium cell, however without any outside releases, to be categorized within the extremely unlikely sequences class.

Finally the analysis highlighted also another relevant safety concern relative to the failure of the EDSs, required to process the tritiated gases: this accident implies the possible release of tritium to the outside through the Nuclear HVAC, due to the ineffectiveness of properly treating the gases (e.g. compressor failure) or area contamination by tritium due to component leakage. The occurrence of the accident could be avoided by appropriate design modifications (e.g. the introduction of redundant components, as compressors, or an emergency storage tank, kept under vacuum to collect effluents in case of an outage of the EDS), in order to improve the relative reliability.

References

[1] ENEA Report CT-SBA-00011 "Test Facilities Safety Analysis Review: Failure Mode and Effect Analysis of Test Facilities", July 2001

[2] ENEA Report CT-SBA-00012 "IFMIF Accelerator Safety Analysis Review: Failure Mode and Effect Analysis of Accelerator", February 2002

[3] "Risk Spectrum® PSA Professional Version 1.20 - User's Manual", RELCON AB, December 2000

3.4.10 DI83B-JA : Safety Assessment for Two-stage IFMIF

(1) Brief Task Description

There are two main issues for IFMIF safety. One is radiation including generation of radioactive nuclides, such as tritium (^{3}H) and beryllium-7 (^{7}Be), and activated materials. The greatest concern is ^{3}H and treatment facilities for solid, liquid and gaseous radioactive wastes that include ^{3}H have been designed. Another issue is liquid lithium (Li) as it is combustible in air and reactive with water. The liquid Li in IFMIF also contains ^{3}H, ^{7}Be, and other radioactive materials. Measures to prevent Li leaks and suppress Li fires have been designed.

Safety assessment of the IFMIF facility was carried out in the CDA using Failure Modes and Effects Analysis (FMEA). The CDA analysis concluded that safe construction and operation of IFMIF without significant environmental impact was possible at reasonable cost and using proven technology. However, IFMIF safety conditions were changed with design for the reduced cost, staged construction IFMIF. Therefore the safety assessment was repeated for the first and second stages of IFMIF.

The result is that the changes to staged construction and cost reduction would not reduce IFMIF safety. The important expected failures can be easily enough detected and treated that they will not spread nor lead to severe effects.

Contributors

Name	Party	Institute	E-mail address
M. Ida	Japan	JAERI	ida@ifmif.tokai.jaeri.go.jp
H. Takeuchi	Japan	JAERI	takeuchi@fnshp.tokai.jaeri.go.jp

(2) IFMIF Features That Relate to Safety

IFMIF is an accelerator based intense neutron source that provides a large volume for irradiation of fusion materials, and the capability to examine the irradiated specimens in its Post Irradiation Examination (PIE) facility. For these purposes, the subsystems (Accelerator system, Target system, Test facilities and conventional facilities) have features as follows;

(a) Accelerator System

In the Accelerator system, continuous wave (CW) deuteron (D^+) beams with combined total current of 250 mA are accelerated to an energy of 40 MeV. The feature of high-energy large-current D^+ beams that requires safety consideration is generation of radiation, radioactive nuclides, and activated materials. A small fraction of the D^+ beams collides with the accelerator components, and generate neutrons and gamma rays, especially at the high-energy end of the beam lines. Deuterium (^{2}H) and ^{3}H generated in the Li target are absorbed on inner surfaces of the components of the beam lines. Quantities of these radioactive nuclides and activation affect working conditions during beam tuning and maintenance. The atmosphere in the accelerator hall is activated by the neutrons and must be treated through the detritiation system. While electromagnetic field may affect worker health, its influence is far less than the effect of radiation and radioactive materials.

(b) Target System

In the Target system, a large amount (about 9 m^3) of liquid Li is circulated. Water and air must be excluded from the Li loop and the Test Cell, since Li is reactive with water and Li will burn spontaneously in air. Furthermore, the liquid Li contains radioactive nuclides such as ^{3}H and ^{7}Be produced continuously by the D-Li reaction. The production rates are 7 g/y for ^{3}H and 1.5 g/y for ^{7}Be. While most of these nuclides are trapped in yttrium hot traps (for ^{3}H) and cold traps (for ^{7}Be, O, C), the release of the nuclides to the environment is a safety consideration in the event of Li leakage or Li fire.

(c) Test Facilities Including Remote Handling

Tests on irradiated specimens and the tritium release test module (TRTM) are carried out in the Test facilities. Remote handling techniques are used to keep workers from the irradiated specimens, target back-wall examination, and other work on irradiated materials. Measurement of ^{3}H release from the TRTM is a normal event operation of the Tritium Laboratory. Liquid and solid radioactive wastes are also produced in the Tritium laboratory and PIE facilities. While substances in and from the PIE facilities may also present chemical hazards and should be carefully treated, chemical treatment of them is not considered to be as difficult as accommodation of the hazards of radiation and radioactive materials.

(d) Conventional Facilities

In the Conventional facilities, argon (Ar) gas and air containing ^{3}H are confined to appropriate regions with differential pressure controls. Treatment of these radioactive gaseous wastes is continuous in normal operation, and as needed during maintenance. Treatment systems for liquid and solid radioactive wastes do not required continuous operation. Radiation shielding is achieved passively by the shielding structure of buildings. Worker access to regions with high dose rate is controlled by hardware and the working time in radiation zones is controlled administratively.

(3) Assessment method

For the reduced cost, staged construction IFMIF [1], safety was reviewed using the same methods of Failure Modes and Effects Analysis (FMEA) as used in the CDA. [2] This qualitative assessment is suitable for IFMIF as a new type of facility, for which quantitative data do not exist. In this method, failures in IFMIF were identified and classified from the viewpoints as follows;

- Ease of detection;
  - A: Easy (Immediately detected and alarmed),
  - B: Limited (Detected with delay or needs observation),
  - C: Difficult (No detection available),
- Frequency of occurrence
  - A: Operational events (> 1per year),
  - B: Likely events (1 to 0.01 per year),
  - C: Unlikely events (0.01 to 0.0001 per year),
  - D: Extremely unlikely events (< 0.0001 per year), and
- Risk potential
  - I: Normal (Operational caution required),
  - II: Danger (Limited function),
  - III: Minor hazard (Immediate halt and repair),
  - IV: Major hazard (Accident, damage of facility),
  - V: Extreme (Possible environmental effects)

Human errors were not assessed in the FMEA. Those are to be assessed using Fault Tree Analysis (FTA) methods. Any failure mode caused by a natural disaster such as flood or earthquake was not assessed, since no specific site for IFMIF has yet been identified.

This assessment provides an overview of potential IFMIF failure modes, identifies severe failures, and points out measures to prevent them as follows;

(4) Accelerator Safety

(a) Impact of Staged Construction and Cost Reduction

The change of staged construction from three to two stages does not produce a change in the result of the qualitative FMEA analysis. While reducing the number of DTL modules and changing the energies at the RFQ and the DTL brought cost reductions, these changes did not impact the safety as evaluated by the FMEA analysis. Removal of the Energy Dispersion Cavity (EDC), the buncher cavities and the related RF power sources and RF transport did not affect the safety, since there is adequate temperature margin to avoid Li boiling at the point of maximum energy deposition. (With

removal of EDC, standard deviation of D^+ energy 0.5 MeV decreases to about 0.2 MeV and the peak energy deposition is estimated to increase to about 1.5 times of that with the EDC operating. This sharp peak raises the temperature of Li, for example to about 730°C in case of a flow velocity of 10 m/s. However, the boiling point of Li is 988°C and provides enough margin[3]) Removal of the circulator and the dummy load did not affect safety, since another protection scheme for the reflected RF power is provided.

(b) Overview of Failures

There are no failure modes with difficult detection (Grade C), since there are many monitors for vacuum, RF power, beam position, and temperatures in the Accelerator system and most of these are rapid function systems. There are many failure modes, especially failures of beam control, with frequent occurrence (Grade A) in the Accelerator system (and fewer of these in the Target and Test facilities). These failures will reduce the availability of the Accelerator system, and thus of IFMIF. However, most of these do not lead to severe accidents. Furthermore, most of them can be recovered within short times and without requiring any repair operations. There is considerable experience with these events in existing accelerators.

(c) Important Failure

There is only one likely event (Grade B) leading to a major hazard (Grade IV) identified for IFMIF. This is failure of an RF window caused by thermal stress or metallic coating deposition. However, this failure grows slowly enough to be detected and the system shut down before complete vacuum loss. Therefore, this failure would not lead to any severe hazard. Furthermore, this failure can be avoided with preventive maintenance. A test on an RF window during EVEDA is planned and will provide guidelines on the maintenance needed to avoid failures.

(5) Target safety

(a) Impact of Staged Construction and Cost Reduction

Staged construction does not result in any changes for the Target system, which must be constructed in the first stage. The number of target assemblies was reduced from two in the CDA to one in the current design. The spare sets of cold traps, hot traps for N removal (using Ti or V-10%Ti getter) and hot traps for H isotopes (using Y getter) were removed from the facility. Furthermore, the Li loop layout of components and piping was revised. Consequently, the Li inventory was reduced from $21m^3$ to $9m^3$. While this reduction of components and Li inventory may reduce probability and scale of failures, they did not change the safety as determined by the qualitative FMEA analysis.

(b) Overview of Failures

There is no failure mode with difficult detection (Grade C). Detection equipment examined, developed and tested in KEP through EVEDA would produce easy or quick failure detection. For example, swelling of the target back-wall will be detected by a laser distortion monitor. There are two failure modes with frequent occurrence (Grade A); excessive Li evaporation and poor vacuum in the Target system. However, these can be easily detected by monitoring pressure and in any case, would not lead to severe hazards.

(c) Important Failures

The most important failure in the Target system is back-wall rupture. However, this failure would be quickly detected by a Li leak detector. Propagation of hazards due to a Li leak is mitigated by the confinement system vacuum of 0.1 Pa and steel liner in the Test Cell. Lithium fires in the Li Loop Area are prevented by gutters to catch spills under Li piping and by the argon atmosphere. Any Li splash into the Accelerator system is prohibited by fast-acting gate valves between the two systems.

(6) Test Facilities Safety

(a) Impact of Staged Construction and Cost Reduction

All PIE facilities will be constructed in the first stage. This does not change the safety conditions, since safety systems for the irradiation and PIE facilities are designed to work independently. Removal of the planned NaK cooling for VTA-1 from the CDA design eliminates concern for a NaK leak, which was one of most severe hazards in the Test facilities. The number of Test Cells and Test Cell Technology Rooms were both reduced from two to one. While this change may slightly reduce availability of irradiation testing, design to optimize the room arrangement, such as combining the Access Cell and the Service Cell, would compensate for any loss of availability. These changes would improve the safety.

(b) Overview of Failures

There is no failure mode with difficult detection (Grade C). The most frequent (Grade A) failures are liquid spills and ^{3}H release in the Access Cell and the Tritium laboratory. However, these failures are easily detected and the rooms can be easily cleaned. Most components serving the Test facility (except those circulating Li, He and NaK) are not in use during irradiation operation. Therefore, most failures do not lead to severe hazards.

(c) Important Failure

The only major hazard (Grade IV) identified was a Li spill in the Test Cell due to a back-wall rupture in the Target system. However, effects of this failure are mitigated by the vacuum condition and the cell structure as mentioned above.

(7) Summary

The change to staged construction and cost reduction do not reduce IFMIF safety. Reducing component numbers and quantities, simplification of equipment and optimization of arrangement are all expected to improve the IFMIF safety. The most important failures (failure of an RF window and a back-wall rupture) are easily detected, do not propagate failures in other systems, and do not lead to severe effects. Detection methods to be developed and optimizations to be performed during EVEDA are expected to further improve IFMIF safety.

References

[1] Fusion Neutronics Laboratory (Ed. M. Ida et al.), IFMIF International Fusion Materials Irradiation Facility Conceptual Design Activity Reduced Cost Report, a Supplement to the CDA by the IFMIF Team, JAERI-Tech 2000-014 (2000).

[2] IFMIF CDA Team (Ed. M. Martone), IFMIF International Fusion Materials Irradiation Facility Conceptual Design Activity Final Report, ENEA Report RT/ERG/FUS/96/11 (1996).

[3] M. Ida, et al., Thermal-hydraulic characteristics of IFMIF liquid lithium target, to be published in Fusion Engineering and Design.

3.4.11 DI85-EU : Safety Analysis and Assessment - Occupational Radiation Exposure -

(1) Brief Task Description

The IFMIF conceptual design documented in the CDA report and CDA reduced cost report were reviewed and were found to contain a significant level of radiation protection discussion and related measures. Such measures include shielding, radiation zoning and access control. Collective worker doses assessed have the potential to be relatively high.

Several key issues have been identified and discussed with the aim of finding possible solutions or suggesting the direction for issue resolution:

- selection of materials, for the potentially most-activated components;
- the isotopic separation of ^{6}Li for the target fluid;
- the corrosion rate for austenitic steel and liquid lithium;
- the placement of lithium on the outside of the heat exchanger tubes, rather than inside the tubes;
- tritium concentrations in the accelerator hall;
- radiation protection requirement for the lithium equipment rooms and argon atmosphere in these rooms;
- exhaust gas processing system.

International radiation protection practices have been discussed as well as the ALARA (as low as reasonable achievable) requirements. At an estimated facility dose of 1800 p-mSv/a, IFMIF is clearly above current operating experience.

The results of this study [1] serve to send the project a strong message – worker radiation exposure protection will be a tough challenge for the designers.

Contributors

Name	Party	Institute	E-mail address
T. Pinna	EU	ENEA	pinna@frascati.enea.it
A. Natalizio	EU	ENSAC for ENEA	tony.natalizio@sympatico.ca

(2) Introduction

This task addressed the issues associated with worker radiation exposure of the International Fusion Materials Irradiation Facility (IFMIF) and is based on the design concept documented in the CDA report [2] and CDA reduced cost report [3]. The objectives of this study were:

- to review the CDA design from a worker dose perspective,
- to identify key radiation protection issues and to suggest possible design improvements, with respect to such issues, as appropriate,
- to review international radiation protection practices, with the aim of providing suitable benchmarks for individual and collective doses,
- to discuss the application of the ALARA requirement at this stage of the design activity, and
- to develop some worker radiation protection guidelines to assist the designers in the future development of the design.

(3) Identification of Radiation Hazardous Activities

There are two basic ways in which workers can be exposed to radiation in the IFMIF facility. The first is through carefully planned activities, such as routine inspections of the facility, interactions necessitated by the test program and routine maintenance. The second is through unplanned situations, or incidents, which are expected to occur infrequently during the life of the facility. Although the latter has the potential for overexposing workers, while the situation persists, unplanned exposures do not contribute significantly to the lifetime facility dose [4]. Accordingly, in this preliminary evaluation, the focus will be on planned events.

(a) Routine Inspections

Routine inspections include activities such as leak-testing of the vacuum boundary, recalibration of sensitive instruments and safety tests.

(b) Test Program Interactions

The preparation of samples, their insertion and removal from the test cell and post-irradiation examinations and testing is the key program activity. Although the insertion and removal of test assemblies, from the test cell, will be performed with the aid of remote handling equipment, the activity will not be free of worker radiation exposure.

(c) Routine Maintenance

Routine maintenance covers all of the activities needed to maintain the IFMIF facility in proper working order. It covers planned maintenance work (preventative maintenance) and work needed to repair failed equipment.

(4) Potential Radiation Hazards

(a) Accelerator

a) Prompt Radiation

Prompt radiation refers to the deuteron beam and any high-energy particles and γ-rays emitted from potential interactions between the beam and beam tube, and between the beam and the target. This is referred to as prompt radiation because it disappears when the beam is turned off.

The primary means for mitigating the effects of prompt radiation are Shielding and Access-control during accelerator operation

b) Residual Radiation

Deuteron beam interactions with the beam tube and target can generate radiation that will not disappear when the beam is turned off. This is referred to as residual radiation and arises from neutron and deuteron activation of the accelerator components, including the target assembly. Some neutron-activation of accelerator cooling water and the air inside the accelerator hall will also occur.

c) Cooling Water Activation

A cooling water system, or systems, is required to cool the RFQ (Radio Frequency Quadrupole) accelerator, the Drift Tube Linear (DTL) accelerator, beam dumps, and possibly other devices exposed to neutron activation.

The primary water activation products in the cooling water system will be tritium and short-lived radionuclides such as ^{15}O, ^{13}N and ^{11}C which do not pose a long-term hazard as their half-lives are 20 minutes or shorter. The component cooling water (or service water) system, however, will also contain neutron sputtering products from the structural material exposed to the beam or neutron flux.

d) Cryogenic Coolant Activation

Impurities in the cryogenic gases may become activated, when they are exposed to the neutron flux. Another consideration is neutron-induced sputtering inside the cooling tubes, if they are exposed to significant neutron fluxes.

e) Air Activation inside Accelerator Hall

Neutron-activation of the air produces tritium. While it is not expected that the T production rate would exceed the Derived Emission Limit (as HTO DEL $\approx 2\times10^5$ TBq/a), there is the potential to raise an ALARA concern. Accordingly, T production rate should be calculated.

(b) Lithium Target

a) Lithium Reactions

The dominant reactions in the lithium target are expected to be the following:

$^{7}Li + d = \gamma + {}^{9}Be$ [16.7 MeV] [a]
$^{7}Li + d = n + 2\alpha$ [15.1 MeV] [b]
$^{7}Li + d = n + {}^{8}Be$ [15.0 MeV] [c]
$^{7}Li + d = \alpha + {}^{5}He$ [14.2 MeV] [d]
$^{6}Li + d = n + {}^{7}Be$ [3.38 MeV] [e]
$^{6}Li + n = {}^{4}He + {}^{3}H$ [? MeV] [f]

Of the reaction products, ^{9}Be is stable, ^{8}Be is very short-lived, ^{5}He is very short-lived, ^{7}Be is a gamma emitter with a half-life of 53.37 days, ^{4}He is stable and ^{3}H is a beta emitter with a half-life of 12.3 years. Therefore, the hazardous reaction products appear to be ^{7}Be and ^{3}H. These nuclides are produced only by ^{6}Li (reactions [e] & [f]) and, therefore, could be eliminated by eliminating ^{6}Li from the lithium target (i.e., enriching the lithium target from 92.6 to 100% ^{7}Li). Furthermore, the neutron produced in reaction [e] is a low-energy neutron and is not important to the IFMIF mission. Therefore, if reactions [e] and [f] where eliminated by using only ^{7}Li as the target material, the relevant neutron flux would not be significantly affected.

b) Back-Plate Sputtering

The materials under current consideration by the project are ferritic steel and vanadium. Of the two, vanadium is preferred because, in addition to its low-activation properties, it has good corrosion resistance when used with liquid lithium.

c) Lithium Piping System Corrosion

The corrosion rate for austenitic steel in liquid lithium at 500°C is several orders of magnitude greater than that found in PWR loops, hence, this combination of component material and coolant could be a poor selection, particularly from a worker dose perspective. Corrosion performance at lower temperatures (~300°C) could be significantly better, but it needs to be demonstrated. Vanadium, could be a much better choice, as its corrosion rate with high-temperature lithium is about an order of magnitude less than that of PWR loops, hence, it should be given serious consideration.

d) Lithium Equipment Rooms Inert Atmosphere

Maintaining the lithium equipment rooms at a pressure above atmosphere violates an important radiation protection requirement. All rooms containing radioactivity must be maintained at a pressure below those that are radiation-free, and below atmospheric pressure, to prevent the uncontrolled release of radioactivity to "clean" rooms and the environment. Accordingly, the requirement for maintaining the lithium equipment rooms above atmospheric pressure needs to be reconsidered. Furthermore, maintaining an argon atmosphere in these rooms potentially increases the maintenance time and the associated worker doses. Therefore, the requirement for an argon atmosphere should be reconsidered, taking into account the potentially higher worker doses.

(c) Test Cell

a) Test Assemblies Activation

Test assemblies (highly activated) will be handled remotely. Nevertheless, activities associated with the test cell are expected to contribute significantly to worker radiation exposure. Test assemblies are the focus of the entire facility; and although, in theory, the test assembly design is simple, in practice, servicing the test assemblies may not be so simple.

b) Test Cell Technology Room Hazards

The test cell technology room is being designed for unlimited access. Maintenance activities, on the equipment located inside, could potentially result in the release of radioactive material inside

the room. Therefore, the ventilation system exhaust needs to be filtered prior to discharge to the environment.

c) Access Cell Hazards

The access cell is being designed for limited access. Maintenance on the equipment located inside is likely to release tritium and other radioactive material into the cell atmosphere. Accordingly, the ventilation system exhaust from the access cell should be filtered and possibly detritiated prior to discharge to the environment. During maintenance activities, it is likely that a large ventilation flow will be required to maintain the airborne concentration of tritium within acceptable levels.

(d) Plant Services

a) Central Vacuum System Hazards

The central vacuum system collects the exhaust from the accelerator and beam tube vacuum pumps, the lithium target assembly vacuum pumps and the quench-tank vacuum pumps. Activated particles and tritium will be contained in the exhaust gas, so the central vacuum system has the potential to be a significant contributor to worker dose, hence, the number of components requiring maintenance should be minimized.

b) Exhaust Gas Processing System Hazards

Test cell technology room and access cell are not identified in the design report between the sources for the exhaust gas processing system, but they could have significant impact on the capacity, and design, of such a system. For example, given the large volume of the access cell, and the need to maintain low levels of airborne concentration in it, the air flow-rate required may be too large for a batch system to be practical. Therefore, the current concept for the exhaust gas processing system should be reviewed in light of the above comment, and with the objective of streamlining the system to reduce potential worker doses associated with its maintenance.

c) Heat Rejection System Hazards

The present design (with intermediate circuit to cool the accelerator) reduces the potential for radioactive releases to the environment, but adds unnecessary complexity and may add to the maintenance work to be performed in close vicinity to activated equipment.

(5) Radiation Exposure Parameters

The worker dose associated with performing a given task is proportional to:

- the time taken to perform the task,
- the radiation fields in the work location,
- the airborne radioactivity, in the work location,
- the number of workers required to perform the task.

To obtain an estimate of worker doses for the entire facility requires a taxonomy of all the tasks to be performed in a radiation environment and a characterization of that environment.

At this early stage of the IFMIF design, it is not possible to perform such a detailed assessment. Nevertheless, it is important to identify the facility components and tasks that might dominate the collective worker dose.

(6) Worker Dose Estimate for IFMIF

(a) TRIUMF Facility

Although the proposed IFMIF facility has elements, such as a liquid lithium target, that are not present in other large accelerator facilities, it is useful to consider the experience of high-energy accelerators as a possible benchmark for IFMIF worker radiation exposure. The TRIUMF facility, in Vancouver, Canada, offers an opportunity for such benchmarking.

The TRIUMF facility comprises a large ion cyclotron accelerator and two small accelerators that produce medical isotopes. The main accelerator is a sector-focusing, isochronous cyclotron that

accelerates negative hydrogen ions to a maximum energy of 520 MeV. The energy of the extracted proton beams is continuously variable from 183 to 520 MeV. Four beams may be extracted simultaneously at independently variable energies and intensities. One beam feeds multiple targets in the meson hall, a second feeds multiple targets in the proton hall, a third feeds the isotope separation accelerator (ISAC) and a fourth beam is used for radioisotope production. The proton beams are guided down the evacuated beam pipes by magnetic fields produced by a variety of dipole and quadrupole electro-magnets. For ease of maintenance the ion sources are located away from the cyclotron and outside the primary concrete shielding. The ion beam is steered and focused along the 35 m long injection line by a periodic system of electrostatic quadrupoles and deflectors. The negative hydrogen ions are injected axially into the cyclotron with an energy of 290 keV by means of 27 kV electrostatic spiral electrodes.

(b) Radiation Exposure Benchmark

The approach used in this study utilized the available operating experience from the TRIUMF accelerator facility both as bench-mark and to develop an empirical worker dose model. To utilize the TRIUMF data, it was necessary to adapt the TRIUMF worker dose categories to IFMIF. The following TRIUMF dose categories were used:

- Accelerator
- Targets
- Vacuum Pumping
- Remote Handling
- Plant Services
- Technical, Engineering & Administrative Support

Several years of data were analyzed to obtain averages for each dose category. Significant variations existed from year to year, both in average doses and number of dose exposures. These are due primarily to the experimental nature of the facility, which means that the nature of the experiments/tests can change from year to year, and that modifications are carried out from time to time. In any case, adequate averages were obtained over a suitable time period.

While this facility has some similarities (e.g. high voltage and hydrogen beams) with the proposed IFMIF facility, it also has some significant differences. In addition, there are systems in IFMIF that are not present in TRIUMF (and vice versa). Therefore, additional dose categories had to be developed specifically for IFMIF. These include the lithium loop and the air and gas purification systems.

The following are the key differences between the TRIUMF and IFMIF accelerators, from a worker dose perspective. Firstly, TRIUMF is a cyclotron accelerator whereas IFMIF is a linear accelerator. Secondly, TRIUMF has solid targets whereas IFMIF has liquid lithium targets. Thirdly, IFMIF has a higher capacity factor (6,000 vs. 3,000 h/year); and lastly, IFMIF has a much larger power (~60xTRIUMF) and consequently, greater shielding requirements.

All the differences have been taken into account in [1] and the results of the base case estimate are summarized in Table 1. In this table, IFMIF1 is a linear accelerator with the same power and operating profile as TRIUMF. The difference is that the IFMIF1 vacuum pumping dose is larger due to the impact of the liquid lithium target. As noted above, the potential difference in dose between a cyclotron and linear accelerator was ignored in the base case estimate. IFMIF2 is the same as IFMIF1 except that it operates twice as many hours per year, hence the IFMIF2 doses are twice the IFMIF1 doses. IFMIF3 has a higher power level than IFMIF2 (60x). This factor was accounted for by doubling the IFMIF2 doses. IFMIF4 has two IFMIF3 accelerators, hence, the doses are again doubled. Finally, IFMIF is the same as IFMIF4, but includes the dose associated with the lithium loops, and the impact of the lithium loops on the remote-handling dose, and the dose associated with the air/gas purification systems. The lithium loop dose was assumed equal to the IFMIF targets dose, the additional remote handling dose due to the lithium loop was assumed equal to the IFMIF remote handling dose, and the air/gas purification systems dose was assumed equal to the plant services dose.

Following this base-case estimate, we turned our attention to estimating the uncertainty associated with the total dose. We looked at each key factor in the above table and assigned a range to it, as defined below.

Vacuum Pumping (VP) Dose Uncertainty

$IFMIF1_{VP} = TRIUMF_{VP} + a * TRIUMF_{VP}$, where $0.5<a<2$

Accelerator (Ac) Type Dose Uncertainty

$IFMIF1_{Ac} = b * IFMIF1_{Ac}$, where $0.5<b<2$

Beam Power Dose Uncertainty

$IFMIF3 = c * IFMIF2$, where $1<c<3$

Lithium Loop Dose Uncertainty

$IFMIF_{Li\text{-}loop} = d * IFMIF_{Target}$, where $0.5<d<2$

Remote Handling (RH) Dose Uncertainty

$IFMIF_{RH} = IFMIF4_{RH} + e * IFMIF4_{RH}$, where $0.5<e<2$

Air/Gas system Dose Uncertainty

$IFMIF_{Air/Gas} = f * IFMIF_{PS}$, where $0.5<f<2$

The first approach, in trying to estimate the magnitude of the total dose uncertainty, was to perform a single-parameter sensitivity analysis of the key factors using only the min. and max. values of the ranges defined above. The second approach [5] utilized a Monte Carlo uncertainty analysis. Both approaches are discussed below.

Table 1 Worker Dose Estimate for IFMIF (p-mSv/a).

		Parameters Accounting for Differences in the two Facilities				
		Vacuum pumping & accelerator type	Capacity factor	Beam power & activation level	N° of accelerators (2 in IFMIF)	Systems not in TRIUMF
Dose Category	**TRIUMF**	**IFMIF1**	**IFMIF2**	**IFMIF3**	**IFMIF4**	**IFMIF**
Accelerator	52	***52*** ($IFMIF1_{Ac}$)	104	***208***	416	416
Targets	22	22	44	***88***	176	176 ($IFMIF_{Target}$)
Lithium loop						***176*** ($IFMIF_{Li\text{-}loop}$)
Vacuum Pumping	15 ($TRIUMF_{VP}$)	***30*** ($IFMIF1_{VP}$)	60	***120***	240	240
Remote Handling	24	24	48	***96***	192 ($IFMIF4_{RH}$)	192
Lithium Loop Impact on Remote Handling						***192*** ($IFMIF_{RH}$)
Plant Services	14	14	28	***56***	112	112 ($IFMIF_{PS}$)
Air/gas purification systems						***112*** ($IFMIF_{Air/Gas}$)
Technical, Engineering& Administrative Support	31	31	62	***124***	186	186
TOTALS	**158**	**173**	**346**	**692**	**1322**	**1802**

a) Single-Parameter Sensitivity Analysis

Twelve calculations of total dose were performed using single minimum and maximum values of each one of the key factors defined in the above functions, keeping the others fixed to the base-case values, as shown in Table 2.

These twelve sensitivity calculations, plus the base-case calculation, provide thirteen estimates of the IFMIF facility annual dose. The mean value of the 13 estimates is 1795 p-mSv/a and the standard deviation is 402 p-mSv/a. From this we concluded, initially, that the IFMIF annual dose would likely be in the range of 1000 to 2600 p-mSv/a (about two standard deviations on each side of the mean). It was this rather large dose range that led to the more detailed uncertainty analysis. The coefficients in Table 2 refer to the coefficients used in the Monte Carlo analysis so that the two could be compared.

Table 2 Results of single-parameter sensitivity analysis for IFMIF worker dose.

Parameters considered to take into account differences					Worker Dose (p-mSv/a)	
Description	**Coeff.**	**Base case**	**Min**	**Max**	**Min**	**Max**
Vacuum pumping	**a**	1	0.5	2.0	1742	1922
Accelerator type	**b**	1	0.5	2.0	1594	2218
Beam power & activation level	**c**	2	1.0	3.0	901	2703
Lithium loop	**d**	1	0.5	2.0	1714	1978
Lithium Loop Impact on RH	**e**	1	0.5	2.0	1706	1994
Air/gas purification systems	**f**	1	0.5	2.0	1746	1914

b) Monte Carlo Uncertainty Analysis

The Monte Carlo uncertainty analysis used the same functions defined above. In this analysis, however, the IFMIF dose was calculated repeatedly using randomly-generated values of a, b, c, d, e & f, within the individual ranges specified above. As demonstrated later, 100,000 calculations were sufficient to reach the desired accuracy. The results of the calculations are shown in Fig. 1.

The mean and standard deviation for this distribution are 1543 and 343 p-mSv/a, respectively. Calculating the 5th and 95th percentile of the actual distribution the minimum and maximum dose rate are 1025 and 2130 p-mSv/a, respectively.

The range of the estimated IFMIF dose is now considerably smaller than the one evaluated by the Single-Parameter Sensitivity Analysis. Furthermore, the various iterations performed have correctly identified the importance of the accelerator beam power on the annual worker dose, and pointed out the importance of shielding required for such a sub-system.

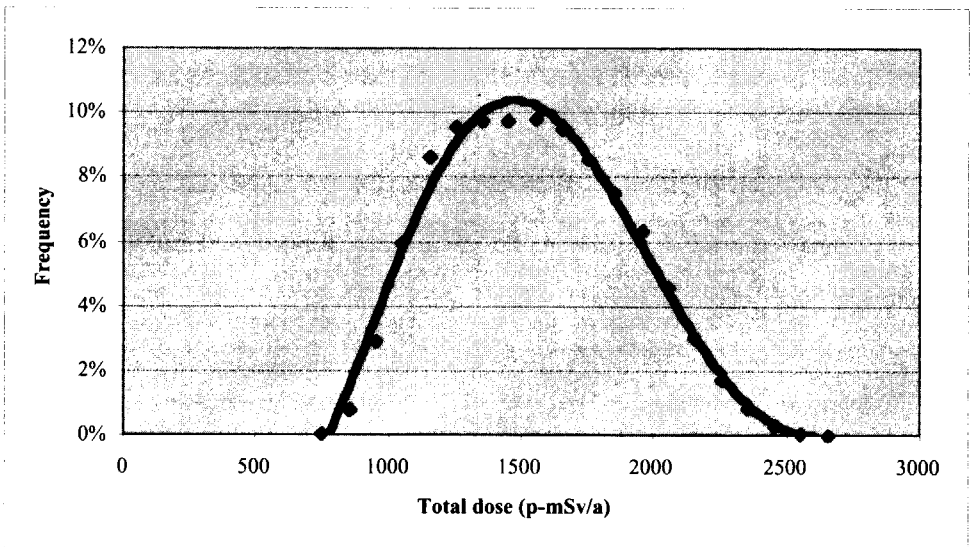


Fig. 1 Dose distribution from Monte Carlo analysis.

(7) Radiation Protection Requirements

The radiation protection requirements for workers are stipulated in the regulations of national governments. However, the new recommendations of the International Commission on Radiation Protection (ICRP) are quickly becoming the international standards. European countries, however, have adopted an even stricter limit. In Table 3 are reported such limits.

In practice, the need to comply with the ALARA (as low as reasonably achievable) requirement forces nuclear facilities and nuclear laboratories to do much better than the regulatory dose limits. In fact, in many areas of the fission industry, average worker doses are approaching the ICRP limit for non-radiation workers (1 mSv/a). In [1] the ALARA process is discussed.

Table 3 Limits for worker radiation exposure for individuals.

Type of Worker	Latest ICRP Recommendation	Latest European regulatory Limits
Radiation Worker	100 mSv per 5 years 50 mSv/a	20 mSv/a
Non-Radiation Worker	1 mSv/a	1 mSv/a

(8) Radiation Protection Practices

Preliminary estimates for IFMIF indicate that, with the current design and staffing information, average worker doses would be of the order of 12 mSv/a (1800 p-mSv/150p).
This value is significantly higher than 1 mSv/a, which is fast becoming standard industry practice. This result is sufficient to suggest that there is significant need for improving the IFMIF design with respect to worker doses.

Although the ICRP does not establish collective dose limits for a nuclear facility, collective dose targets have become standard practice, as a means of judging dose performance from operating facilities, on an annual basis.

Collective doses from nuclear facilities vary widely, depending on the type of facility (nuclear laboratory, research reactor, or power reactor) and range anywhere from 100-1200 p-mSv/a.

The TRIUMF facility, for example, has recorded doses in the range of 200-1100 p-mSv/a during the past ten years (1991-2000), with an average of about 450 p-mSv/a. At an estimated facility dose of 1800 p-mSv/a, IFMIF is clearly above current operating experience, and further emphasizes the need for design improvements.

(9) Radiation Protection Guidelines

Although, the ALARA optimization process is the key project decision-making tool, some design guidelines are necessary to steer the design in the right direction, before the optimization process is started. These guidelines are not requirements, and design decisions based on such guidelines could eventually be revised on the basis of a formal optimization assessment.

Accordingly, the number of such guidelines should be kept to a minimum. They are normally based on industry best-practices that have stood the test of time. These include:

- radiation dose rates,
- airborne activity concentrations,
- worker access and radiation contamination control (radiation zoning).

(a) Dose Rates

Experience indicates that, in fission reactor plants, about 80% of the annual collective dose occurs during maintenance activities; and the remaining 20% occurs during refueling, in-service inspections and surveillance. The TRIUMF experience is not too different. Therefore, it is important to find ways to minimize the personnel exposure during maintenance activities. While many factors, such as an effective radiation exposure policy, an effective training program and a disciplined approach to dose planning fall into the operations domain, shielding falls largely into the facility design domain. Proper and effective shielding is thus an important means of reducing maintenance doses.

There will be areas in the facility where frequent access will be necessary for normal operation, inspections and surveillance and areas where access will be restricted to qualified personnel for short periods only.

a) Frequent Access

Frequent access is assumed to mean up to 2000 hours per year (40 h/week x 50 weeks/year). The maximum dose rate in such areas should not exceed 10 μSv/h to ensure that the average 20 mSv/a regulatory limit will not be exceeded.

Recommended guideline for IFMIF: in frequent access areas, the dose rate should not exceed 10 μSv/h.

b) Restricted Access

In fission reactor plants, annual maintenance activities are typically contained within a four-week period, and during this time, maintenance is performed inside areas that are normally restricted. Therefore, assuming up to 160 hours per year in restricted access areas (40 h/week x 4 weeks) implies a maximum dose rate of 125 μSv/h.

At TRIUMF, the guideline is that no maintenance operation should require more than 0.5 mSv per person per day (dose rate of 62.5 μSv/h) or more than 3 mSv per month (dose rate of 18.8 μSv/h).

Recommended guideline for IFMIF:

- in restricted access areas, where maintenance is to be performed, the dose rate should not exceed 100 μSv/h, one day after beam shutdown, or prior to commencement of the activity. A longer cool-down period, of course, has to be balanced against a potentially lower facility availability.

Some restricted areas may require access for inspection and surveillance. These are activities, or tasks, that typically require less than one hour to perform, and could be performed on a regular basis (e.g., daily/weekly/monthly). In such areas, a dose rate of 1 mSv/h could be tolerated. This is consistent with TRIUMF guidelines.

Recommended guideline for IFMIF:

- in restricted access areas, where the task duration is less than one hour, the dose rate should not exceed 1 mSv/h.

Recommended guideline for IFMIF:

- at the design stage, all areas with radiation fields in excess of 1 mSv/h should be considered inaccessible.

(b) Radiation Zoning

It is aimed at reducing doses to their practical minimum, by controlling the spread of radioactive material. The focus of radiation zoning is the prevention of uncontrolled flow of radioactive material from a radiation zone to a non-radiation zone.

Airborne radioactivity is controlled by a ventilation system designed to keep radiation zones under a negative pressure, relative to non-radiation zones and the environment, which is at atmospheric pressure.

Typically, in nuclear facilities, there are three zones defined as follows:

- Zone 1 – radiation-free zone (has no nuclear equipment or contamination),
- Zone 3 – radiation zone (has nuclear equipment and contamination), and
- Zone 2 - is a buffer zone between 1 and 3. It normally has no radiation but has the potential to be contaminated from Zone 3.

Any movement of personnel, or equipment, from Zone 3 to Zone 2 and from Zone 2 to Zone 1 must be monitored for radioactive contamination.

Recommended guideline for IFMIF:

- the current IFMIF zoning concept, as presented in Fig. 2.7.2-12 of the Conceptual Design Activity Final Report, could be simplified from 5 zones to 3, thereby also simplifying the monitoring requirement and the ventilation system requirements.

- all ventilation exhausts from Zone 3 should be directed to a nuclear-grade ventilation system equipped with suitable filters and shielding.
- all Zone 3 rooms, where tritium is expected to be present in concentrations above one DAC, should be equipped with air, or gas, detritiation systems, as appropriate.
- all Zone 3 rooms requiring frequent access should have an air concentration less than one DAC.
- all Zone 3 rooms with restricted access should have an air concentration less than ten DACs. All Zone 3 rooms with air concentrations above ten DACs should be considered inaccessible without proper protective clothing and breathing apparatus.
- all liquid drainage from Zone 3 should be directed to an active drainage system, equipped with suitable radiation monitoring, to prevent the uncontrolled release of radioactivity to the environment.

The derived air concentration (DAC) is defined as the airborne concentration of a specific radio-nuclide that will produce a dose of 20 mSv when a worker is exposed to it for 2000 hours per year.

(10) Conclusion

The key conclusion of this study is that shielding of accelerator components requiring maintenance access could be a design challenge. Furthermore, achieving the desired plant availability could also be a challenge, as the maintenance dose rate is a function of the component shielding effectiveness, including self-shielding, (i.e., quantity and quality of the shielding material) and the time from machine shutdown (the cool-down period). In many cases, when the outer shielding (external to the component) is removed for maintenance, the only parameter left to control worker exposure is the cool-down period. Therefore, material selection and specifications, to minimize key component activation, may be the only design tool to satisfy the ALARA requirement for occupational radiation exposure.

The worker dose reduction suggestions discussed in the report are:

- Material activation properties, including decay time, should be considered in the material specification of accelerator, target and test assembly components.
- The shielding design philosophy needs to be well defined to ensure that it is consistent with the facility availability objective.
- The elimination of ^{6}Li from the lithium target (i.e., enriching the lithium target from 92.6 to 100% ^{7}Li) is suggested as a means of eliminating, or reducing, the production of ^{7}Be and ^{3}H, with the added benefit that the ^{6}Li removed from the target lithium could be used in the test assembly to enhance the tritium breeding effectiveness.
- The use of high-purity cryogens in the superconducting magnets is recommended to avoid contamination of the cryogenic cooling system. Furthermore, the sputtering phenomena inside cryogenic coolant tubes exposed to high-energy particles, needs to be assessed.
- The corrosion rate for austenitic steel and liquid lithium at 500°C is several orders of magnitude greater than that found in PWR loops. Although the rate could be lower at 300°C, other materials, such as vanadium alloy should be considered for use in lithium system piping, heat exchanger and target back-plate. Low corrosion and activation rates should be specified for these components.
- The tritium production rate, in the accelerator hall, and other rooms (i.e.: cooling water system room), should be calculated to confirm that an air detritiation system will not be required for these areas.
- Maintaining the lithium equipment rooms at a pressure above atmosphere violates an important radiation protection requirement. All rooms containing radioactivity must be maintained at a pressure below those that are radiation-free, and below atmospheric pressure, to prevent the uncontrolled release of radioactivity to "clean" rooms and the environment. Accordingly, the requirement for maintaining the lithium equipment rooms above atmospheric pressure needs to be reconsidered.

- An argon atmosphere in the lithium equipment rooms potentially increases the maintenance time and the associated worker doses. The requirement for an argon atmosphere should be reconsidered, taking into account the potentially higher worker doses.
- The exhaust gas processing system design (currently a batch system) should be reviewed to ensure that it is practical given the anticipated large air/gas flows.

The results of this, and the previous study [6], indicate that worker radiation exposure will provide a significant challenge to the project team. Accordingly, there is the need for future detailed studies, during the design process, to ensure that sufficient feedback is provided to designers, as the design progresses. This is particularly true with respect to those issues already identified in this report.

The implicit assumption in the dose model used to estimate the IFMIF collective worker dose is that, from a worker dose perspective, there is no significant difference between maintaining and operating a linear accelerator and a cyclotron accelerator. This is a major assumption and should be verified in a future study, by examining the collective worker dose experience of high-energy and high-power linear accelerators.

References

[1] A. Natalizio, T. Pinna, IFMIF worker radiation exposure: indications on requirements and, preliminary dose evaluation, ENEA Report, FUS-TN-SA-SE-R-028, October 2001.

[2] M. Martone (editor), IFMIF International Fusion Materials Irradiation Facility Conceptual Design Activity Final Report, ENEA Frascati Report, RT/ERG/FUS/96/11, November 1996.

[3] IFMIF International Fusion Materials Irradiation Facility, Conceptual Design Activity, Reduced Cost Report a supplement to the CDA By the IFMIF Team; edited by Japan Atomic Energy Research Institute; JAERI-memo 11-183, December 1999.

[4] A. Natalizio and T. Pinna; Assessment of the Impact of Postulated Accidents on Occupational Radiation Exposure for two fusion power plant designs; ENEA Report TR04/99; October 1999.

[5] T. Pinna, A. Natalizio, M. T. Porfiri, Methodology for worker dose evaluation of proposed nuclear facilities at the conceptual design stage, Probabilistic Safety Assessment and Management PSAM6, Vol. II, Elsevier Press, 2001, pp. 2049-2056.

[6] C. Rizzello, T. Pinna, S. Giamocante, Safety analysis review and preliminary ORE evaluation for IFMIF; ENEA Report TR06/2000; July 2000.

3.4.12 DI91-JA : Examination of Licensing and Regulations

(1) Brief Task Description

In IFMIF, energetic deuteron beams from the accelerators are injected into a liquid Li target. The neutrons generated are used for irradiation of candidate materials and the materials are evaluated in post irradiation examination (PIE). The safety requirements of IFMIF are set by many laws and regulations covering radiation hazards due to radioisotopes, fire, electromagnetic waves, and handling of dangerous materials.

Laws and regulations applicable to IFMIF were examined based on the assumption of a Japanese site. The application of these laws and regulations are due to radiation such as neutrons and gamma rays, radioisotopes such as tritium and beryllium-7, and the large amount of lithium. The main items to be regulated are worker dose, concentrations of radioisotopes in gaseous and liquid wastes, and seismic requirements of buildings and other structures.

Contributors

Name	Party	Institute	E-mail address
M. Ida	Japan	JAERI	ida@ifmif.tokai.jaeri.go.jp
H. Takeuchi	Japan	JAERI	takeuchi@fnshp.tokai.jaeri.go.jp

(2) General Examination of Laws and Regulations Applicable to IFMIF

(a) Elements and Equipment

Based on the examples at fission power plants and general chemical plants in Japan, laws and regulations applicable to the IFMIF facility and equipment will include the following;

- Laws and Regulations related to Radiation and Radioactive Safety
- Laws and Regulations related to Safety at General Industries
- Laws and Regulations related to High-pressure Vessels and Equipment
- Laws and Regulations related to Mechanical Equipment
- Laws and Regulations related to Piping Equipment
- Laws and Regulations related to Electrical Equipment
- Laws and Regulations related to Control / Measurement Equipment
- Laws and Regulations related to Construction
- Laws and Regulations related to Ventilation Equipment
- Laws and Regulations related to Fire Control Equipment

(b) Applicable Laws

Assuming the IFMIF site is in Japan, Japanese laws relating to atomic energy and radiation are:

- The Atomic Energy Basic Law [1]
- The Nuclear Reactor Regulation Law [2]
- The RI Law [3], and related laws
- The Law concerning Compensations for Loss due to Activities for Atomic Energy [4], and related laws

The Atomic Energy Basic Law applies to IFMIF, since radiation-generating apparatus are installed in IFMIF and radiation and radioactive materials are generated. However, the Nuclear Reactor Regulation Law does not apply to IFMIF, since there is neither the handling of nuclear materials, nuclear fuels, nor use of a reactor. The RI Law is applied to IFMIF. Therefore, before IFMIF construction, applications for licenses are executed based on the RI Law, and judgments are made by regulating authorities that IFMIF meets the standards. Following this decision, a license will be issued for IFMIF, and the facility can be operated after facility examination by the regulating authority.

The Law concerning Compensations for Loss due to Activities for Atomic Energy originally applied to compensation for loss due to activities for atomic energy, such as a reactor operation, and it

is applied to facilities regulated under the Nuclear Reactor Regulation Law. However, to respond to any loss due to accidents in IFMIF, this law will need to be taken into consideration, since IFMIF generates and holds large amounts of radioactive material.

Other non-atomic laws that apply to IFMIF and not related to atomic energy or radiation are as follows;

- The Industrial Safety and Health Law
- The Labor Standards Law
- The High Pressure Gas Safety Law
- The Fire Service Law
- The Electricity Utilities Industry Law
- The Radio Law
- The Building Standard Law
- Other laws (depending on the site condition; including proximity to the sea, rivers, industrial regions, etc.)

(c) Relationship between Element / Equipment and Applicable Laws

Two laws, the Atomic Energy Basic Law and the RI Law and related laws and regulations, apply mainly to one element; "Radiation and Radioactive Safety" out of several elements considered. The applicability of the Law concerning Compensations for Loss due to Activities for Atomic Energy and related laws is not clear at this stage.

The Industrial Safety and Health Law and related laws and regulations are widely applicable to most elements except for two; "Radiation and Radioactive Safety" and "Fire Control Equipment". The Labor Standards Law is applicable to the element; "Safety at General Industries". The High Pressure Gas Safety Law is applicable to most elements except; "Radiation and Radioactive Safety" and "Mechanical Equipment". The Fire Service Law is applicable to most elements except "Radiation and Radioactive Safety". The Electricity Utilities Industry Law is applicable mainly to three elements; "Safety at General Industries", "Electrical Equipment" and "Control / Measurement Equipment". The Radio Law is applicable only to; "Electrical Equipment". The Building Standard Law is applicable to four elements; "Safety at General Industries", " Construction", "Ventilation Equipment" and "Fire Control Equipment".

(3) Examination of the Seismic Protection Architecture of IFMIF

(a) Seismic Standards Applied to IFMIF

There are clear provisions for seismic protection architecture in the Nuclear Reactor Regulation Law and related laws / regulations, while there is no such clear provision in the RI Law and related ones. For example, requirements on seismic protection architecture are provided [5] under the system of the Nuclear Reactor Regulation Law. Also under the system of the RI Law, to ensure public safety, consideration of the seismic protection architecture will be necessary for facilities in which large amounts of radioactive material are handled. It provides that facilities using RI shall be installed in locations with a low probability of landslides or submersion [6]. This provision can be extended to the seismic protection architecture. For example, it provides that seismic protection performance shall be ensured to correspond to the quantity of tritium in facilities using or holding tritium [7].

Although the RI Law system will be applied to IFMIF, the seismic protection architecture of IFMIF buildings is estimated on a preliminary basis as follows, based on "the Guideline of Aseismatic Design" [8] for power reactor facilities.

(b) Application of Grade of Seismic Protection

Based on the Guideline of Aseismatic Design, an industry standard, "the Guideline JAEG 4601" [9] was established. Based on this guideline, the seismic protection grade applied to IFMIF is examined as follows;

Classification of seismic protection grades : In the Guideline JAEG 4601, the seismic protection grades are provided as follows

- Class As : Applied to
  - Anything having the potential to cause loss of coolant at failure
  - Anything necessary for emergency shutdown of a reactor, and, keeping it in safe shutdown
  - Storage facilities for used nuclear fuel
  - Reactor vessels
- Class A : Except for things of Class As, applied to
  - Anything having the potential to cause radiation hazard to the public at failure
  - Anything necessary for public protection from radiation hazard at a reactor accident
- Class B: Except for things of Classes As and A, applied to
  - Anything concerning highly radioactive materials
- Class C: Except for things of Classes As, A and B, applied to
  - Facilities concerning radioactive materials
  - Facilities not concerning radiation safety

Standard strength of earthquakes : In the Guideline JAEG 4601, the relationship between the seismic protection grades and the standard strength of earthquakes is provided as follows;

- Class As: The design shall be executed in consideration of;
  - Earthquake with the standard strength of S1 and S2
- Class A: The design shall be executed in consideration of;
  - Earthquake with the standard strength of S1

where S1 and S2 are defined as follows;

- S1: The maximum strength earthquakes forecasted from the engineering viewpoint, i.e.
  - Evidence of past earthquake occurrences around the site
  - Possible earthquake occurrences because of highly active faulting around the site
- S2: The maximum strength of earthquakes having possibility of occurrences from the geological viewpoints

Classification of seismic protection grades and radiation exposure : In the Guideline JAEG 4601, the relationship between the seismic protection grade and radiation exposure concerning radioactive materials is examined. The radiation exposure should not exceed the value in "The Guideline of Judgement on Location" [10], in case that a facility failure is possible at standard strength S2. In the case of S1, which occurs more frequently than S2, the radiation exposure should be less than that in S2. Functional integrity should be ensured at the S1 for a facility having the possibility of radiation exposure more than 5 mSv due to a failure of only that facility. This measure can keep the radiation exposure lower than the value in the Guideline, even on the assumption of the facility failure at S2.

In the Guideline of Judgement on Location, a guideline of distance to the site border is provided with radiation exposures as follows;

On thyroid (of child) : 1.5 Sv (per accident)
On whole body : 0.25 Sv (per accident)

In "The Guideline of Judgement on Safety Assessment" [11], which specifies the basic policy on safe design of the facility, it is required to avoid significant risk of radiation exposure to the surrounding population in an accident. The risk is low if the effective dose on the neighboring population is estimated not to exceed 5 mSv per accident. The ICRP recommended the main limit of 1 mSv as an annual maximum effective dose to the public. Auxiliary limits of 5 mSv / year over several years is also permitted, if the annual effective dose averaged over a lifetime does not exceed 1 mSv. This limit is applied to radiation exposure for normal operating conditions. However, in The Guideline of Judgement on Safety Assessment, this limit is applied also to low probability accidents. Therefore, the limit of 5 mSv in the Guideline JAEG 4601 is read as the limit of 5 mSv in the

Guideline of Judgement on Safety Assessment. The following preliminary examination of seismic protection grade for IFMIF is executed with this limit.

(c) Preliminary Safety Assessment of Potential Accidents in IFMIF

Assessment scenario : To assess the seismic protection grade of IFMIF, the radiation exposure to the public is estimated for a case of IFMIF failure due to an earthquake. To be conservative, the assessment scenario is assumed as follows. In IFMIF, most of the radioactive materials are in the liquid lithium and the hot and cold traps in the lithium loop. An earthquake causes failures of IFMIF buildings and lithium loop components, and the whole lithium inventory is released and burns in the air. Consequently, all radioactive materials contained in the liquid lithium are released into the air. However, the radioactive materials contained in the traps are kept in the traps.

Estimation : Isotopes Be-7 and H-3 are main radioactive nuclides generated and contained in the lithium loop. The estimated amounts of Be-7 and H-3 that are released into the air within the first hour of a lithium fire are:

Be-7 : 1.98×10^{15} Bq (assumed to be released within 1 hour)
H-3 : 4.41×10^{14} Bq (assumed to be released within 1 hour)

The released radioactive material diffuses and reaches the site border. Since the site location is not determined at this stage, air concentration of the radioactive materials at the site border is estimated using the following assumptions, based on "The Meteorological Guideline" [12].

Atmosphere Stability : Grade F
Wind Speed : 1 m/s
Effective Height of Release : 0 m
Distance to Site Border : 600 m
Neglecting Building Influence

The atmosphere stability of grade F is the most stable condition among all grades A – F and corresponds to a condition at night, less cloudy, and with wind speed less than 3 m/s.

Under these conditions, as shown in Tables 1 – 2 and Figs. 1 – 2, the public dose at the site border is estimated as follows;

Dose due to Be-7 : 47 mSv
Dose due to H-3 : 4 mSv
Total : 51 mSv

Table 1 Be-7 concentration in air from a severe accident.

Total Release 1.98E+15 Bq (within 1hr)
Release Rate 5.50E+11 Bq/s Release Height 0m

Distance to Site Border [km]	Be Concentration [Bq/m3]					
	Atmosphere Stability : A	B	C	D	E	F
0.2	1.55E+08	2.86E+08	5.47E+08	1.36E+09	2.47E+09	5.44E+09
0.4	3.47E+07	7.61E+07	1.55E+08	3.93E+08	7.22E+08	1.66E+09
0.6	1.06E+07	3.30E+07	7.46E+07	1.94E+08	3.61E+08	8.48E+08
0.7	6.15E+06	2.37E+07	5.65E+07	1.49E+08	2.79E+08	6.60E+08
0.8	3.64E+06	1.76E+07	4.43E+07	1.19E+08	2.24E+08	5.33E+08
0.9	2.19E+06	1.35E+07	3.58E+07	9.73E+07	1.84E+08	4.42E+08
1	1.35E+06	1.06E+07	2.96E+07	8.15E+07	1.55E+08	3.74E+08
2	1.90E+04	1.89E+06	8.50E+06	2.61E+07	5.18E+07	1.29E+08
4	2.75E+01	2.63E+05	2.45E+06	8.71E+06	1.83E+07	4.73E+07
7	1.71E-02	4.32E+04	9.01E+05	3.71E+06	8.23E+06	2.19E+07
10	4.86E-05	1.22E+04	4.77E+05	2.19E+06	5.05E+06	1.36E+07
20	2.88E-11	7.88E+02	1.39E+05	8.12E+05	2.04E+06	5.68E+06
40	2.01E-19	3.39E+01	4.11E+04	3.16E+05	8.75E+05	2.51E+06
70	1.31E-27	1.92E+00	1.54E+04	1.52E+05	4.62E+05	1.35E+06
100	1.20E-33	2.62E-01	8.26E+03	9.73E+04	3.14E+05	9.32E+05

Table 2 Tritium concentration in air from a severe accident.

Total Release 4.41E+14 Bq (within 1hr)
Release Rate 1.23E+11 Bq/s Release Height 0m

Distance to Site Border [km]	H3 Concentration [Bq/m3]					
	Atmosphere Stability : A	B	C	D	E	F
0.2	3.45E+07	6.37E+07	1.22E+08	3.02E+08	5.50E+08	1.21E+09
0.4	7.73E+06	1.70E+07	3.46E+07	8.75E+07	1.61E+08	3.69E+08
0.6	2.36E+06	7.35E+06	1.66E+07	4.32E+07	8.05E+07	1.89E+08
0.7	1.37E+06	5.27E+06	1.26E+07	3.32E+07	6.22E+07	1.47E+08
0.8	8.11E+05	3.92E+06	9.88E+06	2.64E+07	4.98E+07	1.19E+08
0.9	4.89E+05	3.01E+06	7.98E+06	2.17E+07	4.10E+07	9.85E+07
1	3.00E+05	2.36E+06	6.60E+06	1.81E+07	3.46E+07	8.34E+07
2	4.22E+03	4.21E+05	1.89E+06	5.81E+06	1.15E+07	2.88E+07
4	6.12E+00	5.86E+04	5.46E+05	1.94E+06	4.07E+06	1.05E+07
7	3.80E-03	9.61E+03	2.01E+05	8.27E+05	1.83E+06	4.87E+06
10	1.08E-05	2.71E+03	1.06E+05	4.88E+05	1.12E+06	3.04E+06
20	6.42E-12	1.75E+02	3.11E+04	1.81E+05	4.54E+05	1.27E+06
40	4.48E-20	7.55E+00	9.14E+03	7.03E+04	1.95E+05	5.59E+05
70	2.92E-28	4.28E-01	3.43E+03	3.39E+04	1.03E+05	3.01E+05
100	2.67E-34	5.82E-02	1.84E+03	2.17E+04	7.00E+04	2.08E+05

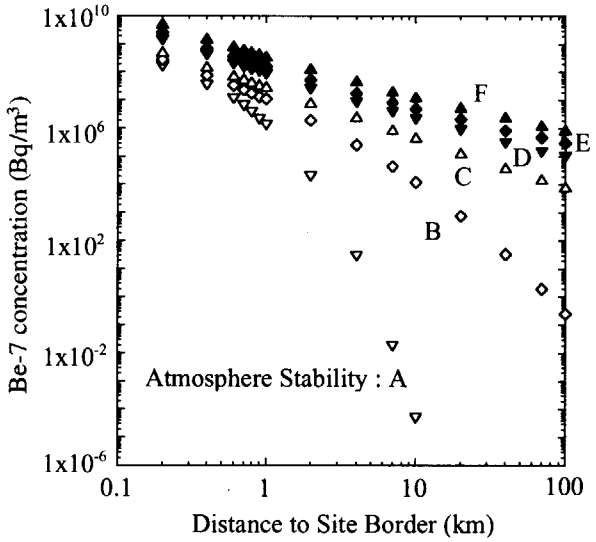


Fig. 1 Be-7 concentration in air from a severe accident.

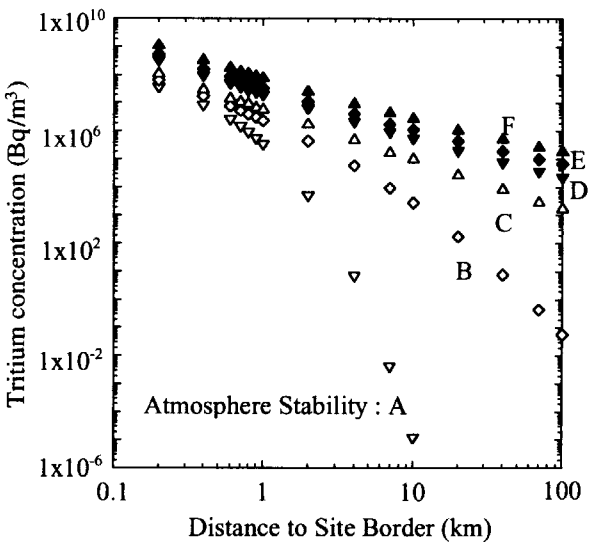


Fig. 2 Tritium concentration in air from a severe accident.

(d) Seismic Protection Grades Applied to Potential IFMIF Problems

Since the estimated dose is far larger than 5 mSv, the limit in the Guideline JAEG 4601, function integrity needs to be assured for standard strength S1 and the seismic protection grade is to be Class A. The public dose may decrease to 1/10 of the mentioned value and the seismic protection grade may decrease to Class B, through detailed analysis after the site location is selected, with conditions of distance to site border : 600 m and atmosphere stability : Grade F. However, the design and examination is to be conducted with seismic protection Grade A, in consideration of other radioactive nuclides not estimated above.

The estimated dose is about 100 mSv at a distance of 400 m, still less than the limit 0.25 Sv in the Guideline of Judgement on Location. However, the estimated dose is about 330 mSv at a distance of 200 m. Therefore, the distance to the site border needs to be more than 400 – 600 m

Remaining issues to be examined are:

- Estimate of effects of radioactive nuclides with short lifetimes other than Be-7, H-3
- Measures to reduce release of radioactive nuclides from the lithium loop

  While the release of the whole inventory is assumed in the above estimation, a possibility to be examined is a reduced release due to solidification of some of the lithium or chemical reaction with lithium to produce a stable compound, for example.
- Estimate of the release of radioactive nuclides from the hot and cold traps

(4) Examination of the tritium handling facility

In IFMIF, large amounts of tritium are contained in the lithium loop and other tritium is generated through the irradiation tests. The IFMIF system to treat this tritium is examined. Seals that will contain tritium must be considered, since molecular tritium permeates through metals. Moreover, the tritium treatment is difficult, since tritium easily reacts with other materials and easily burns. For tritium sealing, other measures than for other radioactive nuclides are needed because of the physical and chemical property of tritium. A guideline [13] has been established to ensure safety of facilities that handle large amounts of tritium, and to help in evaluations of safety.

The guideline is applied to facilities defined in the RI Law to use RI, and, handling large amounts of unsealed tritium. The facilities handling large amounts of tritium are defined as either;

- A facility for use of tritium with planned annual usage ≥ 10000 Ci (3.7×10^{14} Bq), and, with maximum planned daily usage ≥ 1000 Ci (3.7×10^{13}Bq), or any structurally connecting facility; or,
- A facility for storage of tritium with storage capacity ≥ 10000 Ci (3.7×10^{14} Bq), or any structurally connecting facility.

IFMIF is neither a facility for use nor for storage. However, its design must meet the requirements in this guideline, since more than 3.7×10^{14}Bq of tritium is generated and large amount of tritium is handled in IFMIF. Based on the guideline, requirements for IFMIF design are as follows;

(a) Confinement

Guideline-1) Adoption of multi-septum confinement

To prevent contamination of work and circumference environments, a concept of multi-septum confinement shall be adopted to the corresponding facility. For IFMIF, this is, for example;

- 1st confinement : Examination equipment, tritium storage equipment, etc.
- 2nd confinement : Grove box, Cell, Hood, etc.
- 3rd confinement : Workrooms, etc.

Guideline-2) Installation of waste facility

To prevent contamination of work and surrounding environments, a waste facility shall be installed in the corresponding facility.

Guideline-3) 1st confinement

Measures to prevent leaks and permeation of tritium shall be adopted in design and fabrication of the first confinement.

Guideline-4) Detritiation facility for 1st confinement

A detritiation facility shall be included in the exhaust system of the first confinement, if needed.

Guideline-5) 2nd confinement

Measures to prevent leaks and permeation of tritium, and ensuring adequate exhaust rates shall be adopted to the second confinement.

Guideline-6) Detritiation facility for 2nd confinement

A detritiation facility shall be included in the second confinement, if needed.

Guideline-7) 3rd confinement

Air-tightness and ventilation shall be adequate in the third confinement.

Guideline-8) Detritiation facility for 3rd confinement

A detritiation facility shall be included in the exhaust system of the third confinement, if needed.

(b) Radioactive Waste Treatment

Guideline-1) Gaseous radioactive waste

- Tritium release to the environment shall be as low as possible
- Tritium (as molecular or vapor) concentration averaged over three months at a site border shall be 1/10 or less of the corresponding value on the Table in the Notice [14].
- Tritium concentration in the exhaust gases shall be continuously measured.

Guideline-3) Liquid radioactive waste

- Tritium release to the environment shall be as low as possible
- Tritium concentration averaged over three months at a drainage at the site border shall be 1/10 or less of the corresponding value on the Table in the Notice [14].
- Liquid waste with tritium concentration exceeding the above-mentioned values shall be stored in a facility with exhaust equipment to prevent any concentration increase in the room atmosphere.

(c) Tritium Measurement

Guideline-1) Measurement methods

- Tritium measurement systems and methods shall be consistent with methods of confinement, storage and waste treatment for tritium in the corresponding facility.
- The system shall be able to detect tritium leaks and permeation from the first and second confinements.
- The system shall be able to function during abnormal and emergency conditions.

Guideline-2) Arrangement of measurement systems

- Measurement equipment shall be installed to detect leaks and permeation from recovery, storage, and experiment systems to a grove box, in cases where those systems are installed in the grove box.
- Measurement equipment shall be installed to detect leaks and permeation from the glove box to the work environment.

(d) Safety Measures

Guideline-1) Consideration of fire and explosion

Measures shall be considered to prevent occurrence of fire and explosion, and to avoid their extensions.

Guideline-2) Consideration of disasters

Measures shall be considered to avoid hazards to the facility and equipment due to disasters such as earthquake, flood, typhoon and heavy snow.

Guideline-3) Consideration of operational errors

Preventive measures and emergency procedures shall be considered to avoid operational errors and the causes of accidents, in handling large amount of tritium.

Guideline-4) Consideration of blackouts

Appropriate measures shall be considered for loss of power in the tritium facility and equipment.

Guideline-6) Consideration of common use:

Facilities and equipment important for safety monitoring and response shall not be available for common use.

Guideline-8) Consideration of accidents and abnormal events:

The facility shall be designed to provide multiple confinement for accidents and abnormal events. Appropriate measures shall be provided to support appropriate site safety activities, announcement and communication, and for radiation protection of the worker, corresponding to scale of potential accidents and abnormal events.

(5) Examination of Laws and Regulations Concerning Use of Lithium

(a) Characteristics of Liquid Lithium [15]

Lithium (Li) is an alkali metal that has desirable properties as a reactor coolant, such as low specific gravity, high specific heat, high thermal conductivity and low viscosity. However, compared to sodium (Na), Li is corrosive to structure materials, and reactive with nonmetallic impurities such as oxygen (O), nitrogen (N), carbon (C) and hydrogen (H). Furthermore, safe handling of Li is difficult, because of highly burning and difficult fire extinction.

(b) Chemical Reactions and Safety of Lithium [15]

Reaction of lithium and water: While this reaction is as active as that of Na and water, this reaction generates LiOH and H_2 gas. At room temperature, Li in a wet atmosphere quickly becomes black and at long times, becomes a white powder. This change is the formation of compounds Li_3O, LiOH, LiOH-H_2O and, ultimately, Li_2CO_3.

Reaction of lithium with oxygen and nitrogen at room temperature: While Li does not easily react with O_2 without water at temperatures lower than 373 K, it reacts and generates LiO_2 above 373 K. While Li slowly reacts with N_2 without water, it exothermally reacts with N_2 in the presence of any water, even at room temperature, and generates Li_3N. This compound is very corrosive to iron and steels.

Reaction of liquid lithium: Liquid Li easily and actively burns in air, producing dense white smoke. Once burning, Li reacts with almost all gas except rare gas and causes fire. Lithium also actively reacts with many materials such as sand, concrete and CCl_4, and causes fires. Materials with which it does not react include most metals, graphite powder, and zirconium silicate.

(c) Laws and Regulations for Lithium

Laws and regulations covering the use of lithium in Japan include the following;

The Fire Service Law [16] : The purpose of this law is to prohibit, monitor, and suppress fire, so as to protect the life and property of citizen from the hazards of fire. In this law, dangerous materials are categorized, corresponding to their properties, into six groups; Group-1 (Oxidizable solids), Group-2 (Combustible solids), Group-3 (Pyrophoric / Water-forbidden materials), Group-4 (Flammable liquids), Group-5 (Self-reactive materials) and Group-6 (Oxidizable liquids). The regulations cover storage, handling, production and transfer of dangerous materials, and equipment, working methods, and inspection. Article 2 of this law covers lithium as an alkali metal (Group-3: Pyrophoric / Water-forbidden materials). Use of Li is regulated if quantities exceed limits as follows;

Li (solid) : 50 kg (Alkali metal Grade-2)
Li (powder, 30% purity) : 10 kg (Alkali metal Grade-1)

The Industrial Safety and Health Law [17] : In this law, dangerous materials are categorized in nearly the same manner as in the Fire Service Law. They are categorized into five groups; Explosive materials (corresponding to the Group-5 in the Fire Service Law), Ignitable materials, Oxidizable materials (almost corresponding to the Group-1), Flammable materials and Combustible gases. Furthermore, the Flammable material is divided into four sub-groups with temperature: t (°C); $T < -30$, $-30 \leq T < 0$, $0 \leq T < 30$, $30 \leq T < 60$. Li is categorized as an Ignitable material under this law. [18]

(d) Problems with Lithium Handling

There are no strict requirements on lithium handling provided by the laws and regulations mentioned above. However, careful consideration is needed in safety design of IFMIF, since the liquid lithium used in IFMIF is very reactive. For example, the allowable level of air contained in argon gas must be established. Argon gas is used to isolate lithium from air. An example of a similar limit is in the JOYO fast fission reactor. The allowable level of O_2 is 4 wt% or less in the N_2 atmosphere to protect the liquid sodium coolant.

(6) Summary

Laws and regulations applicable to the IFMIF were examined based on the assumption of a Japanese site. The main applicable laws are "The Law concerning the Prevention from Radiation Hazards due to Radioisotopes and Others" and "The Fire Service Law". The former applies to IFMIF because of radiation such as neutrons and gamma rays, and radioisotope such as tritium and beryllium-7. The main items to be regulated are worker dose, concentration of radioactive isotopes in gaseous in liquid wastes, and seismic protection design of buildings and equipment. The Fire Service Law concerns are due to the large amount of lithium in IFMIF.

References

[1] The Atomic Energy Basic Law, Japanese law, first established December 19, 1955 (Law No. 186).
[2] The Law concerning the Regulations of Nuclear Material Substances, Nuclear Fuel Substances and Nuclear Reactors, Japanese law, first established June 10, 1957 (Law No. 166).
[3] The Law concerning the Prevention from Radiation Hazards due to Radioisotopes and Others, Japanese law, first established June 10, 1957 (Law No. 167).
[4] The Law concerning Compensations for Loss due to Activities for Atomic Energy, Japanese law, first established June 17, 1961 (Law No. 147).
[5] The Cabinet Order concerning Technical Standards on Design and Construction Measure of Reactors used for Examination and Study, Japanese Cabinet order, first established March 25, 1987 (Order No. 11).
[6] The Enforcement Order of the RI Law, Japanese Cabinet order, first established September 30, 1960 (Order No. 259).
[7] Report of Specialists Meeting for Safety Judgement on Facilities Handling Large Amount of Tritium, Report of Japanese Science Technology Agency, August, 1985.
[8] The Guideline of Judgement on Aseismatic Design concerning Power Reactor Facilities, Decision by the Nuclear Safety Commission of Japan, July 20, 1981.

[9] JAEG 4601, Supplement-1984 with title "Importance Grade, Allowable Stress" of "the Technical Guideline on Aseismatic Design for Nuclear Power Plant", Japan Electric Association, 1984.
[10] The Guideline of Judgement on Reactor Location and its Application, Atomic Energy Commission of Japan, May 27, 1964.
[11] The Guideline of Judgement concerning Safety Assessment of Light Water Power Reactor Facilities, Decision by the Nuclear Safety Commission of Japan, August 30, 1990.
[12] The Meteorological Guideline concerning Safety Analysis of Power Reactor Facilities, Decision by the Nuclear Safety Commission of Japan, January 28, 1982.
[13] The Report of Specialist Meeting for Safety Judgement on Large Amount Tritium Handling Facilities, Nuclear Safety Commission of Japan, August 1985.
[14] The Issue to Determine Quantities of Radioactive Isotopes, Note of Japanese Science Technology Agency, May 18, 1988 (Note No. 15).
[15] N. Nakamura et al., Status of study on lithium chemical properties and compatibilities to materials (in Japanese), Journal of the Japan Institute of Metals, 21, 3 (1982).
[16] The Fire Service Law, Japanese law, first established July 24, 1948 (Law No. 186).
[17] The Industrial Safety and Health Law, Japanese law, first established July 8, 1972 (Law No. 57).
[18] The Enforcement Order of the Industrial Safety and Health Law, Japanese Cabinet order, first established August 19, 1972 (Order No. 318).

3.4.13 DI93-JA : Analysis of the Schedule and Future Plans of the IFMIF Project

(1) Brief Task Description

The schedule and future plans from Engineering Validation and Engineering Design Activity (EVEDA) through construction, operation and decommission must be analyzed to assure that the IFMIF project matches the schedule for the development of fusion materials, to efficiently use IFMIF resources, and for efficient use of the facility once operation begins.

In KEP, the schedule leading up to IFMIF construction and Tasks in the Transition phase (19 tasks in 2003) and EVEDA (49 tasks in 2004 – 2009) were proposed. Approximate estimates of costs for the EVEDA tasks were developed. A draft of a new Annex under the current IEA Implementing Agreement was proposed and is under examination by the IFMIF Ad-hoc Working Group under the Executive Committee of the Implementing Agreement. The Working Group is also examining possible organization of the EVEDA.

Contributors

Name	Party	Institute	E-mail address
M. Ida	Japan	JAERI	ida@ifmif.tokai.jaeri.go.jp
H. Takeuchi	Japan	JAERI	takeuchi@fnshp.tokai.jaeri.go.jp

(2) Schedule

The IFMIF schedule to the point of full-power operation was discussed and tentatively determined as shown Table 1.[1]

(a) Schedule from KEP to EVEDA

EVEDA in 2004 – 2009 is planned to validate longtime operation of each subsystem (Accelerator, Target and Test Facilities) and to carry out design integration and engineering design of the mentioned subsystems and conventional facilities. While the current KEP activity is being carried out under Annex II of the IEA Implementing Agreement for a Programme of Research and Development on Radiation Damage in Fusion Materials, the next activity should be carried out under a new framework defined in Annex IV. In EVEDA, tests for engineering validation will involve transfer of equipment to the testing facilities, and assignment of personnel for the testing and design integration activities. These activities may not be within the scope of Annex II. The year 2003 is dedicated to transition from KEP to EVEDA.

(b) Schedule for Construction and Operation

The first stage of construction in 2010 – 2016 is planned to allow first stage operation with one accelerator. The second stage construction in 2017 – 2019 will occur while stage one IFMIF is operating. Construction, Operation and Decommissioning Activities (CODA) will require establishment of new agreements and new organization among the participating parties. Preparations such as IFMIF site selection and licensing are included in CODA.

(3) Work Items

Work items in the Transition phase and EVEDA were discussed at the IFMIF design integration meeting and then proposed to the IFMIF Executive Subcommittee March 11 - 14, 2002.

(a) Tasks in the Transition Phase

Tasks and contributing parties in the Transition phase in 2003 are shown in Table 2. Most tasks are preparations for EVEDA, such as specifications of reference designs, selections of methods, design and preliminary experiments for testing in EVEDA, and preparation of databases. Transition activities are to be carried out under Annex II.

Table 1 IFMIF schedule.

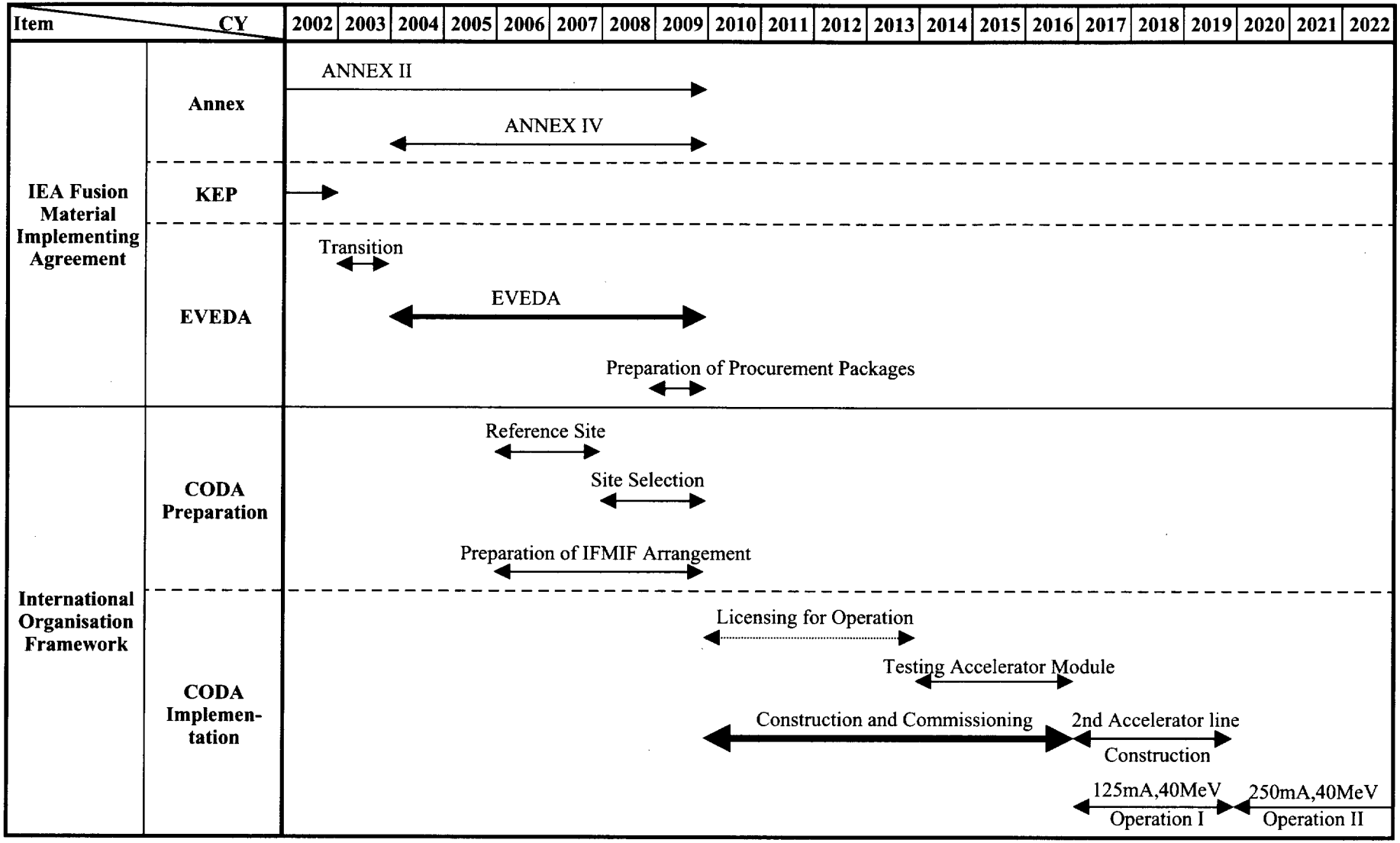


Table 2 Tasks in Transition Phase.

	Task ID	Task Title	Overview of Task Content	Justification	Contributing Party			
					EU	JA	US	RF
Accelerator	AC-1	Development of critical accelerator components	- Operations of chosen injector system to demonstrate performance and reliability - Long term test of RF Window - Develop non-interceptive diagnostics for high power CW beams	Continue KEP R&D Activity of critical accelerator components to achieve RAM goals	X	X		
	AC-2	Accelerator Physics/ Engineering Design	- Establish updated reference design for RFQ & DTL - Perform detailed design of Matching Section - Prepare specification for change of Diacrode frequency to 175 MHz - Perform detailed design of HEBT - Maintain system level integrated design effort	Incorporate KEP results into system design and develop subsystem specifications	X	X	X	
	AC-3	Analysis of possible alternatives	- Analyze H2+ source development required to achieve ~100 mA output - Perform simulation design of electrostatic LEBT specific to IFMIF requirement - Perform engineering evaluation of 4-rod RFQ	- Source desired for IFMIF commissioning to reduce activation - Recent developments from other programs with electrostatic LEBT's need evaluation - 4-rod RFQ needs continued analysis from KEP	X	X		
Target	TG-1	Flow stability in Li and water exp.	- Long term Li loop exp. - Water exp at different curvature - Diagnostics for Li/Water exp.	Obtain additional data for EVEDA to reduce uncertainty margins	X	X		
	TG-2	Li purification/ monitors/ corrosion/ erosion	- Characteristics of impurity trap systems - Material selection of monitors	Obtain additional data for EVEDA to improve reliability	X	X		X
	TG-3	Engineering Design	- Examination of interface items - EVEDA Li test loop - Remote handling system	Establish base design for EVEDA phase	X	X		
Test Facilities	TF-1	Improve reference design of High Flux Test Module	Validation of capsule fabrication C10; detailed thermo-fluid dynamics calculations	Incorporate KEP results into the reference design	X	X		
	TF-2	D-Li reaction: Evaluation of source term	Experimental and theoretical verification of the D-Li source term	Reduce significantly the current neutron yield uncertainties of 20%	X	X		
	TF-3	Provide nuclear data above 20 MeV	Completion of data file preparation and neutron transport benchmark tests between 20-50 MeV	Indispensable input for neutron transport and nuclear inventory calculations (long term activity)	X	X		
	TF-4	Detailed 3D-calculations of the nuclear response	Provide complete nuclear response based on detailed geometry of revised test modules	The nuclear respose (e.g. n-flux, dpa, gas production rates) is THE important information for designers and users (long-term activity)	X	X		
	TF-5	Miniaturized neutron/gamma monitors	Specification of reference design	Incorporate KEP results into the reference design	X			
	TF-6	Micro-tomography system	Specify reference design and perform underlying tests for confirmation	The reference asembly is based on KEP findings and additional experiments performed during 2003	X			
	TF-7	He gas prototype facility	Definition of He has prototype facility and evaluation of existing EU loops	To perform tests on 1:1 sized test module prototypes an adequate He-loop is necessary	X			
	TF-8	Updated Design of the Test Cell subsystems	Establish updated reference design outline for (i) the test cell configuration, (ii) the HFTM high performance version, (iii) the MFTM with integrated neutron moderator/reflector	Incorporate KEP results into the reference design	X	X		
	TF-9	SSTT; CT specimen development	Development of specimens and testing methodology for Fracture toughness tests	CT specimen and testing technology development is inevitable for the fusion community	X	X		
Design Integration	DI-1	Basic Concept of Operation	- Examination of specification for the whole sytem control - Consistency check among all subsystems	In order to perform system design, a basic concept is needed.	X	X		
	DI-2	Survey for regulation concept	- Worker & Public Safety Assement - Examination of guidelines and collection of data for licensing - Estimation of Test Cell shielding performance	To start the negotiation with authority, a regulation concept is needed.	X	X		
	DI-3	IFMIF data base	Set up of IFMIF web-site	To facilitate information exchange	X	X	X	
	DI-4	Reference Design	Update Ref. Design Configuration and Cost Evaluation	To Maintain integrated design and project management	X	X	X	

Table 3 Tasks in EVEDA (1/2).

		No.	Task	Contents	Cost (MICF)	Schedule 2004 2005 2006 2007 2008
Accelerator	Eng. Validation	AF-1a	H_2^+ ion source	Develop H2+ ion source for beam commissioning	1.5	
		AF-1b	RFQ	Construct RFQ (cold model, high power structure)	11.5	
		AF-1c	RF Power Amplifier System	Construct one RF Power Amplifier System including RF windows, RF Controls (Requires diacrode scaled to 175 MHz)	8.5	
		AF-1d	RFQ Operation	Operate RFQ with high power RF	2.0	
		AF-1e	DTL	Construct first drift tube and quadrupole of DTL	0.5	
		AF-1f	Diagnostics	Development of beam diagnostics, instrumentation	3.0	
	Eng. Design	AF-2a	Detailed final design	Detailed final design of accelerator components and sub-systems	2.9	
		AF-2b	HEBT Design	Detailed design of HEBT	0.5	
		AF-2c	Instrumentation & Control	Design instrumentation and computer control system	1.0	
		AF-2d	System activation and safety consideration	Design activities related to system activation and safety.	0.2	
		AF-2e	Interface Control	Design activities related to interface issues.	0.4	
Target	Eng. Validation	TG-1a	Coordination	Coordination of overall target tasks	0.1	
		TG-1b	Construction of Li test loop	Construction of EVEDA Li test loop. This include components cost of a main loop, an electromagnetic pump, a primary/secondary heat exchanger. Various diagnostics and tritium/impurity monitors&traps are not included.	8.2	
		TG-1c	Operation and Li jet dynamics tests	Operation of Li test loop and validation of the Li loop performance in long term operation.	2.6	
		TG-1d	Diagnostics	Li jet thickness monitor in Li test loop, Distortion monitor of the target assembly, In-site inspection method of erosion/corrosion , Surface temperature monitor, Li vapor monitor	2.8	
		TG-1e	Li purification system	Validation of on-line /off-line diagnostic and removal of tritium, 7Be,C,N and O	1.6	
		TG-1f	Remote handling system	Development and verification of remote handling system of the back wall and target assembly.	1.7	
	Eng. Design	TG-2a	Main and Purification Loops	Design of the target assembly, the Li main loop, the Li purification loop.	1.2	
		TG-2b	Diagnostics	Design of various diagnostics and arrangements	0.3	
		TG-2c	Remote Handling System	Design of the remote handling system for the target assembly and/or the back wall	1.0	
		TG-2d	Safety, Vacuum, Control	Safety analysis and design of vacuum system and control system	1.5	
Design Integration	Eng. Design	DI-2a	Design of buildings	Design works for buildings are performed to be enough to make procurement specifications corresponding to the construction.	0.6	
		DI-2b	Design of utilities	Design works for power and water supplies, ventilation, evacuation etc. are performed to be at the mentioned level.	0.4	
		DI-2c	Analysis of operation flow and design of central control	Operation flow is analyzed from startup to shutdown in normal/off-normal conditions, and design works for central control are performed.	0.8	
		DI-2d	Revise of radiation shielding	Adequate specification of radiation shielding is determined by shielding calculation and other methods and used for the building design.	0.7	
		DI-2e	RAM analyses for staged IFMIF	Availability of whole facility is calculated using failure probability of every component, mean time of repair, etc., and IFMIF adequacy as an irradiation facility is validated.	0.6	
		DI-2f	Safety assessments for staged IFMIF	Failure mode and its effect are analyzed, and it is validated that the facility is able to deal with the failures and the effects.	0.8	
		DI-2g	Preparations for licenses and regulations	Preparation works are performed for licenses or regulations about radiation, nuclear fuel material, electromagnetic wave, dangerous material, high-pressure gas, earthquake and fire.	0.8	
		DI-2h	Cost estimation with results of EVP and design works	Cost evaluation is performed on IFMIF construction, operation and decommission using component specification more clarified through EVP activity.	0.3	

Table 3 Tasks in EVEDA (2/2).

		No.	Task	Contents	Cost (MICF)	Schedule 2004	2005	2006	2007	2008
Test Facilities	Eng. Validation	TF-1a	Engineering design and fabrication of full scale HFTM	Engineering design and fabrication of full scale prototype with assembled rigs, capsules, specimens, instrumentation and active heating capacity	1.8					
		TF-1b	Tests on full scale HFTM	Tests of full scale prototype with assembled rigs and specimens to test (1) remote handling of assembling/disassembling procedures, (2) thermal hydraulics, instrumentation and cooling						
		TF-1c	Upgrade existing helium gas loop	Significant upgrade of existing He gas loop (compressor, instrumentation, tubing, purification system) for prototype testing of HFTM and MFTMs	0.6					
		TF-1d	Irradiation test in fission reactor	Irradiation of instrumented rigs in materials test reactor to verify system design and active heating under real loading conditions	1.2					
		TF-1e	Engineering design and system evaluation of full scale MFTM for in-situ creep fatigue tests	Engineering design and system evaluation of full scale prototype for 3 instrumented push-pull fatigue specimen, and integrated neutron moderator	0.5					
		TF-1f	Engineering design and system evaluation of full scale MFTM for in-situ tritium release tests on ceramic breeders and compatibility tests	Engineering design and system evaluation of full scale prototype with purge gas tubes and instrumentation for every individual rig, and integrated neutron moderator	0.7					
		TF-1g	Engineering design and system evaluation of full scale MFTM for in-situ experiments for insulation coatings of structural materials	Engineering design and system evaluation of full scale prototype of an instrumented mock-up, and integrated neutron moderator	0.5					
		TF-1h	Engineering design and system evaluation of VIT system	Engineering design and system evaluation of full scale prototype of an instrumented mock-up, and integrated neutron moderator	0.3					
		TF-1i	Construction, fabrication and test of less than full scale VTA prototype	Construction, fabrication and test of VTA mock-ups with integrated coolant ducts and instrumentation to test (1) remote controlled precise positioning, (2) sealing, (3) assembling and disassembling of test modules	0.8					
		TF-1j	Full evaluation of source term D-Li nuclear reactions to reduce significantly the current neutron yield uncertainties of ±20%	(1) Broad based neutron time-of-flight measurements from IFMIF relevant Li(d,nx) reactions, (2) Data processing and implementation of experimental data in existing libraries	0.3					
		TF-1k	Nuclear data above 20 MeV	(1) Completion of data file preparation, (2)Neutron transport benchmark tests	0.4					
		TF-2l	Calculation of the complete neutron response throughout the entire test cell equipped with reference test modules	MCNP, NYOY and McDeLi-code calculation for 3D distribution of all nuclear responses, including decay heat and nuclear inventory.	0.5					
		TF-1m	Prototype fabrication and test of on-line miniaturized neutron / gamma monitors	After fabrication the monitors are tested (1) in fission reactor, (2) in light ion particle accelerator.	0.4					
		TF-1n	Prototype fabrication and test of IFMIF micro-tomography system	Transmission and emission tomography systems will be tested to verify suitability for structural integrity tests on assembled rigs and HFTM	0.4					
		TF-1o	RAM studies	RAM studies	0.2					
		TF-1p	SSTT: Development of miniaturized fracture toughness specimen	User specific development; (1) Data generation from irradiated and reference samples, (2) Modeling of size effects	0.5					
	Eng. Design	TF-2a	Test cell improvement and engineering design of entire test cell, access cell, test module handling cell	(1) Design improvement of entire test cell (including steel liner, shield plugs, VTAs, VIT and test cell cover), (2) Engineering Design	2.0					
		TF-2b	Specification, engineering design of complete maintenance and remote handling systems, incl. universal robot system and auxiliary systems	Design based on (1) detailed evaluation of all remote handling scenarios, (2) manufacturer experience from reactor decommissioning	1.0					
		TF-2c	Test Cell technology room and test facility control room; specification of instrumentation and design of all devices	Layout and specification of both rooms	0.4					
		TF-2d	Engineering design of "post irradiation examination" facilities	Neutronics and manufacturers' supported design of (1) Conventional hot cell laboratory, (2) Shielded glove box laboratory, (3) Tritium laboratory	1.5					

(b) Tasks in EVEDA

Tasks, roughly estimated costs, and tentative schedules for the Transition phase, 2004 - 2009, are shown in Table 3. Except for Design Integration (DI), tasks for each subsystem include both Engineering Validation (EV) and Engineering Design (ED). These EV and ED are expected to be carried out under a new Annex IV.

During the EV for the Accelerator, an ion source, an RFQ and a set of RF power amplifier systems will be fabricated and tested. The ion source generates $H2^+$ ions for beam commissioning. While the RFQ is a cold model, it is to be tested to examine performance at high power loading. Endurance test of an RF power supply will be performed in RFQ system. Testing on the RF power amplifier system includes testing of RF windows and RF controls. As the ED for the Accelerator, detailed designs will also be developed for the Accelerator system and components.

For the Target, a lithium test loop will be fabricated and tested to examine the characteristics of longtime loop operation. Diagnostic methods for the target section will be examined to ensure target stability in longtime operation. Lithium purification systems consisting of hot and cold traps and impurity monitors will be validated. Remote handling device to exchange and weld / cut the target assembly will be developed and tested, but not in the lithium loop. Along with the EV, ED of the IFMIF Target will be carried out.

For the Test Facilities, a full scale High Flux Test Module (HFTM) is to be fabricated and tested. Engineering designs and system evaluations are planned for three types of full scale Medium Flux Test Modules (MFTMs) and a full scale Vertical Test Assembly (VTA). Improvements in neutron calculation and nuclear data are expected. ED for Test Facilities will include the Universal Robot System (URS) and Post Irradiation Examination (PIE) facilities.

The DI tasks include not only design of buildings, shielding, utilities and central control but also RAM and safety analysis, in preparation for licensing and cost estimation.

As summarized in Table 4, the roughly estimated costs for EV and ED Tasks are 53 and 19 MICF, where 1 MICF = 1 Million of the IFMIF Conversion Factor (approximately 1 Million US dollar in January 1996). The total cost for EVEDA is 72 MICF.

Table 4 Cost of EVEDA Tasks.

	Engineering Validation	Engineering Design	Total
Accelerator	27	5	32
Target	17	4	21
Test Facilities	9	5	14
Design Integration	-	5	5
Total	53	19	72

Unit : MICF

(c) Framework for EVEDA

For efficient and responsible implementation of the EVEDA work, a basic organizational framework for EVEDA has been examined. It is proposed in a draft of Annex IV, developed by the Working Group. This draft including an EVEDA organization is still under evaluation and discussion.

The proposed organization for EVEDA is shown in Fig. 1. The Participants of the planned Annex IV will establish an IFMIF Steering Committee for implementation and supervision of EVEDA. The Steering Committee will designate an IFMIF Project Leader and will establish a Joint Central Team (JCT) at a Joint Work Site for international work that includes design integration. The Project Leader will report to the Steering Committee. The staff members of the JCT will be seconded by the Participants and will assist the Project Leader at JCT on work including design integration such as building and utilities. A Leading Participant for each subsystem (Accelerator, Target, Test Facilities and Conventional Facilities) coordinates work on the respective subsystem and reports to the JCT. Contributing Participants execute ED and EV with transfer of equipment to testing facilities,

assignment of specialists to testing facilities and JCT, and exchange of information among the Participants.

(4) Summary

A schedule that starts with the Transition Phase, EVEDA, and continues through construction and operation was proposed. Tasks in the Transition Phase (19 tasks in 2003) and EVEDA (49 tasks in 2004 – 2009) were examined and proposed. Costs for the EVEDA tasks were roughly estimated. A draft of a new Annex under the current IEA Implementing Agreement, to cover EVEDA activities, was proposed and is under examination by the IFMIF Ad-hoc Working Group under the Executive Committee of the Fusion Materials Implementing Agreement.

Reference

[1] IFMIF Ad-hoc Working Group, Minutes of the IFMIF Ad-hoc Working Group on March 14, 2002, Tokyo.

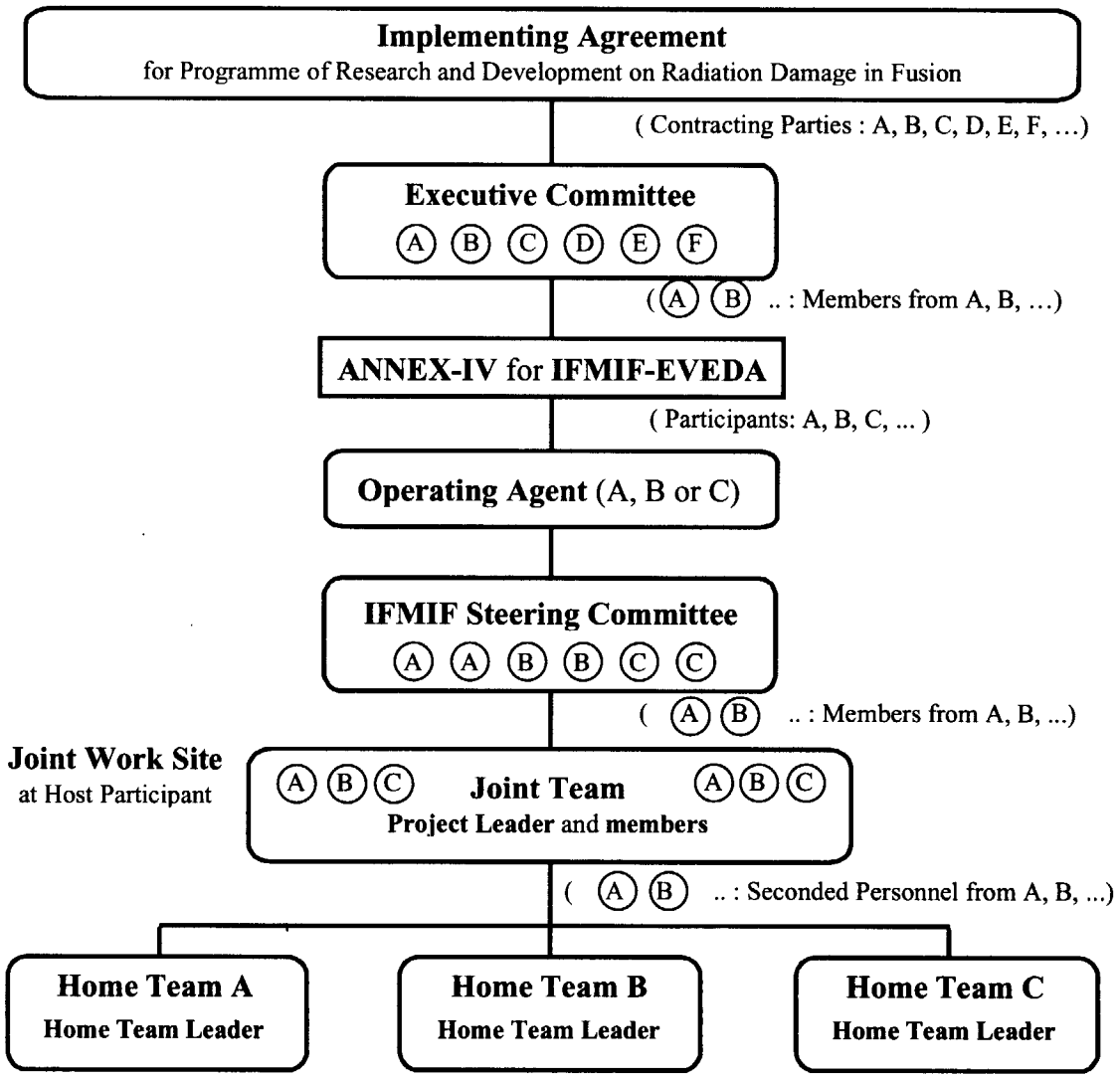


Fig. 1 Possible Organization and Personnel Assignment for EVEDA.

3.4.14 DI95-JA : Cost Estimation

(1) Brief Task Description

Through the former cost estimation for a reduced cost IFMIF completed in 1999 [1], the Total Capital Estimated Cost (TEC) for IFMIF construction was revised from 797 MICF (Million IFMIF Currency Factor) as the estimation in 1996 [2] to 488 MICF, including Allowance for Indeterminates (AFI). Cost estimation should be performed alongside progresses in design work and KEP activities, which may influences the cost estimates. Furthermore, the planned IFMIF construction schedule was changed from three stages (total duration of 15 years) to two stages (10 years). Therefore, the cost estimation was revised.

The result is there was no significant change in the estimated cost even with the change in staged construction. There were no large changes in the IFMIF design during KEP. To complete developments remaining beyond EVEDA, additional funds would be needed mainly for RFQ testing and any modification that may be needed in the construction phase.

Contributors

Name	Party	Institute	E-mail address
M. Ida	Japan	JAERI	ida@ifmif.tokai.jaeri.go.jp
H. Takeuchi	Japan	JAERI	takeuchi@fnshp.tokai.jaeri.go.jp

(2) Conditions and Methods for Cost Estimation

(a) Changes in Staged Construction

The IFMIF construction plan was changed from three stages (5 years for each stage, thus 15years for total duration) to two stages (7 years for the first stage, 3 years for the second stage) through the international meetings for IFMIF in 2002.

In the plan for three-stage construction, the first and the second accelerators were to be constructed in the first and the third Stages respectively. The second Stage was to be dedicated to construction of the PIE facility and increase in the current in the first accelerator from 50 mA to 125 mA deuteron beam. The whole Target System was to be constructed during the first Stage to reduce total construction cost of that system.

In the revised plan for two-stage construction, only the second accelerator and related facilities such as the second Accelerator Building, and additional electrical, cooling, ventilation and control equipment are to be constructed in the second Stage. The IFMIF is to be operated with deuteron current of 125 mA in the first Stage operation and 250 mA in the second. The PIE facilities are to be constructed in the first Stage for examinations on specimen irradiated in stage one operation with deuteron beam current of 125 mA.

(b) Methodology of Cost Estimation

The methodology used to estimate costs is basically the same as those of the former Cost Reports in 1996[2] and 1999 [1]. The Work Breakdown Structure (WBS) has not been changed from that in 1999. For comparison with the former values, currency conversion factors are the same as those of the former Cost Report in 1996 as follows:

1 ICF (IFMIF Currency Factor) = 1 U.S. Dollar = 105 Yen = 0.807 Euro

Material and Labor fees were estimated using cost mostly estimated by Japanese industries, and industry engineering fees used values mostly estimated by Japanese industries (in work time) and converted into international value (international average of payment/time x time = cost). These international average rates are as follows:

Manager :	195 kICF/year	(WBS 1-6)	Engineer :	161 kICF/year	(WBS 1-6)
Labor :	98 kICF/year	(WBS 2-6)	Support :	93 kICF/year	(WBS 1)

(c) KEP and EVEDA

In the KEP, technical changes were not significant enough to change the cost of components. These costs are the same as those in the former estimates. Also the AFI was not changed.

In the former cost estimates in 1999 [1], the Total Estimated Cost (TEC) was 488 MICF with the assumption that all development would be completed before the construction phase (i.e. in EVEDA). New cost estimates were performed with the same assumption. Additional development costs were separated from construction costs.

(3) Results of Construction Cost Estimates

The estimated cost for IFMIF construction was changed only due to the change in staged construction. The former estimate assuming three-stage construction is shown in Table 1. The TEC was 487.8 MICF, where TEC is an estimated summary including the cost of design, fabrication, testing, installation and all project management costs from project approval to the beginning of facility startup and commissioning. TEC of each Stage (1st-Stage, 2nd-Stage, 3rd-Stage) was 303.6, 63.3 and 120.9 MICF respectively. The current estimate assuming two-stage construction is shown in Table 2. The TEC was slightly reduced from 487.8 MICF to 484.1 MICF due to simplification of planning (from three stages to two stages) and reduction of construction duration (from 15 years to 10 years). However, these effects are shown only as costs for Project Management and Accelerator Facility as follows;

The TEC for Project Management (WBS 1) was reduced to 17.6 MICF. The detailed estimate is shown in Table 3. The assumed number of personnel was 14 persons for 7 years of the first Stage and 10 persons for 3 years of the second Stage. The required number of persons was increased from 10, 6 and 8 persons at the 1st, 2nd and 3rd Stages in the former estimation, due to increase of work in the first Stage and elimination of the third Stage. However, the total cost was slightly reduced.

Table 1. Construction cost estimated in December 1999.

WBS	Subsystem	EVP development reducing construction cost	Construction Phase				Covered by running cost in Operation Phase
			1st Stage (5 years)	2nd Stage (5 years)	3rd Stage (5 years)	Total (15 years)	
1.0	Project Management		**7.7** 50 PY	**4.6** 30 PY	**6.2** 40 PY	**18.5**	
2.0	Test Facilities	• URS technology	**62.3** Irradiation facilities	**33.1** PIE facilities	**0.0**	**95.4**	• Examination equipment
3.0	Target Facility	• Target assembly remote handling technology	**40.1** Completion at 1st Stage	**0.0**	**0.0**	**40.1**	• Spare Hot/Cold traps • Remote handling for traps
4.0	Accelerator Facility	• RFQ	**98.4** 1st-Acc. (50mA)	**25.6** RF power up (125mA)	**93.2** 2nd-Acc. (250mA)	**217.2**	
5.0	Conventional Facilities		**85.6**	**0.0**	**19.9** Expansion for 2nd-Acc.	**105.5**	
6.0	C. C. & C. I.		**9.5**	**0.0**	**1.6**	**11.1**	
	· Total		**303.6**	**63.3**	**120.9**	**487.8**	

Unit : MICF

The TEC for the Accelerator Facility (WBS 4) was slightly reduced to 214.4 MICF. The TEC for the first accelerator was slightly reduced, while that for the second was not changed. The detailed estimate is shown in Table 6. The cost for accelerator management (WBS 4.1) was changed according to duration change from "6 managers x 5years + 3.6 managers x 2.5 years" to "6 managers x 7 years" in the first Stage. The management cost was not changed for the second accelerator. Installation cost for the first accelerator (WBS 4.3.1) was changed. The first accelerator is to be commissioned to full power of 125 mA in the first Stage. Therefore, installation and checkout costs of the RF System (WBS 4.3.1.6) and cost of Acceptance Testing (WBS 4.3.1.8) were changed to the same as those of the second accelerator. For the Accelerator System Control (WBS 4.3.1.9), the cost was given as the total of those of the first and second stages in the former estimation.

Table 2. Construction cost estimated in September 2002.

WBS	Subsystem	EVEDA development reducing construction cost	Construction Phase			Covered by running cost in Operation Phase
			1st Stage (7 years)	2nd Stage (3 years)	Total (10 years)	
1.0	Project Management		**13.0** 84 PY	**4.6** 30 PY	**17.6**	
2.0	Test Facilities	• URS technology	**95.4** Completion at 1st Stage	**0.0**	**95.4**	• Examination equipment
3.0	Target Facility	• Target assembly remote handling technology	**40.1** Completion at 1st Stage	**0.0**	**40.1**	• Spare Hot/Cold traps • Remote handling for traps
4.0	Accelerator Facility		**121.2** 1st Acc. (125mA)	**93.2** 2nd Acc. (250mA)	**214.4**	
5.0	Conventional Facilities		**85.6**	**19.9** Expansion for 2nd Acc.	**105.5**	
6.0	C. C. & C. I.		**9.5**	**1.6**	**11.1**	
	Total		**364.8**	**119.3**	**484.1**	

Unit : MICF

Table 3 Cost for Project Management.

Currency Units=kilo IFMIF Currency Factor								
WBS					Element	On-site Proj Man.	TEC	Rationale and Detail
1	2	3	4	5		(a)	(m)	
1	**0**	**0**	**0**	**0**	**Project Management**	**17,579**	**17,579**	
	1	**0**	**0**	**0**	**Project Management and Administration**	**20.0%**		
		1	0	0	Administration	10.0%		International average Engineer : 161 (60%)
		2	0	0	Cost Control	3.3%		Manager : 195 (20%)
		3	0	0	Schedule	3.3%		Support : 93 (20%)
		4	0	0	Documentation	3.3%		International average labor cost : 154.2 kICF/yr
	2	**0**	**0**	**0**	**Systems Engineering**	**15.0%**		
		1	0	0	Design Integration	5.0%		
		2	0	0	Systems Analysis	3.3%		1st Stage(125mA) : 12person x 7yrs
		3	0	0	Requirements/Spec	3.3%		2nd Stage(250mA) : 10person x 3yrs
		4	0	0	RAM Analysis	3.3%		Total : 114PY (17578.8 kICF = 4% of TEC)
	3	**0**	**0**	**0**	**Environment., Safety & Health Document.**	**10.0%**		
	4	**0**	**0**	**0**	**Quality Assurance**	**10.0%**		4% of TEC is possible.
	5	**0**	**0**	**0**	**Development Oversight**	**5.0%**		(e.g. NSLS I, Tevatron I,II, PEP, SLC, MFTF-B)
	6	**0**	**0**	**0**	**Construction Management**	**40.0%**		

Table 4 Cost for Test Facilities.

Currency Units=kilo IFMIF Currency Factor						Total Estimated Capital Cost (TEC)											
						Off-IFMIF Site						On-Site At IFMIF					
						Off-Site	Industry		Instit'al		Off-site	Const. Contractor		Instit'al			On-site
WBS					Element	Facil.Manag.	Mat'l/Lab	Engin'g	Engin'g	AFI	Total	Mat'l/Lab	Engin'g	Engin'g	AFI	Total	
1	2	3	4	5		(b)	(c)	(d)	(e)	(f)	(g)	(h)	(i)	(j)	(k)	(l)	(m)
2	**0**	**0**	**0**	**0**	**Test Facilities**	**1,691**	**44,169**	**11,176**	**2,607**	**7,893**	**65,845**	**15,042**	**4,440**	**3,301**	**5,117**	**27,901**	**95,437**
1	**0**	**0**	**0**		**Test Facility Management**	**1,691**	**0**	**0**	**0**	**0**	**0**	**0**	**0**	**0**	**0**	**0**	**1,691**
	1	0	0		Project Management and Administration			644			644		322			322	
	2	0	0		Systems Engineering			161			161		81			81	
	3	0	0		Environment., Safety & Health Document.			161			161		0			0	
	4	0	0		Quality Assurance			161			161		161			161	
2	**0**	**0**	**0**		**Test Facility Subsystems**	**0**	**44,169**	**11,176**	**2,607**	**7,893**	**65,845**	**13,542**	**4,440**	**3,301**	**5,117**	**26,401**	**92,246**
	1	0	0		Vertical Test Assemblies for Test Cell I		5,398	1,281	1,334	1,474	9,487	69	0	775	169	1,013	10,500
		1	0		VTA1-NaK		0	0	0	0	0	0	0	0	0	0	0
		2	0		VTA1-He		2,690	752	111	710	4,263	0	0	277	55	332	4,595
		3	0		VTA2-He Fatigue		1,178	192	46	283	1,700	0	0	221	44	266	1,966
		4	0		VTA2-He Breeders		1,085	301	332	344	2,062	0	0	277	55	332	2,394
		5	0		VIT-System		437	36	814	129	1,417	69	0	0	14	83	1,500
		6	0		Shield Plug		8	0	30	8	46	0	0	0	0	0	46
	2	0	0		Test Cell I		3,241	129	645	753	4,768	276	32	66	37	412	5,180
		1	0		Test Cell Cover		1,080	0	195	191	1,467	0	0	0	0	0	1,467
		2	0		Test Cell Liner		799	0	178	195	1,173	63	0	0	13	75	1,248
		3	0		Heat Shield		792			198	991	158				158	1,149
		4	0		Seal Plate		291	0	30	64	385	0	0	0	0	0	385
		5	0		Camera System		116	0	174	58	348	55	0	0	11	66	415
		6	0		Neutron Source Diagnostics		84	0	0	17	101	0	0	0	0	0	101
		7	0		Test Cell Diagnostics		45	0	0	9	54	0	0	0	0	0	54
		8	0		Emergency Shutdown System		34	0	66	20	120	0	0	66	13	80	200
	3	0	0		Test Cell Technology Room I		1,744	81	0	11	1,836	960	129	57	17	1,164	3,000
		1	0		Assembly and Testing						0					0	0
		2	0		Cooling System		929				929	546				546	1,476
		3	0		Vacuum Pumping System		492				492	24				24	516
		4	0		Ar Backfill System		270				270	360				360	630
		5	0		Diagnostics and Controls		53	0	0	11	64	26	0	57	17	101	164
		6	0		Subsystem Power		0	0	0	0	1	4	0	0	1	4	5
	4	0	0		Vertical Test Assemblies for Test Cell II		0	0	0	0	0	0	0	0	0	0	0
	5	0	0		Test Cell II		0	0	0	0	0	0	0	0	0	0	0
	6	0	0		Test Cell Technology Room II		0	0	0	0	0	0	0	0	0	0	0
	7	0	0		Test Facility Control Room		371	0	91	93	555	3	0	223	45	271	827
		1	0		Assembly and Testing		0	0	0	0	0	0	0	57	11	69	69
		2	0		Data Acq - VTA 1 - NaK		0	0	0	0	0	0	0	0	0	0	0
		3	0		Data Acq - VTA-1 - He		45	0	0	9	54	0	0	33	7	40	94
		4	0		Data Acq. - Creep Fatigue		111	0	29	28	168	0	0	57	11	69	237
		5	0		Data Acq - Tritium Release		108	0	24	26	158	0	0	0	0	0	158
		6	0		Data Acq - VIT		61	0	38	20	119	0	0	29	6	35	154
		7	0		Supervisory Computer		46	0	0	9	55	0	0	46	9	55	110
		8	0		Subsystem Power		0	0	0	0	1	3	0	0	1	4	4
	8	0	0		Access Cell		7,908	737	0	1,713	10,357	5,659	322	199	1,172	7,352	17,709
		1	0		Assembly and Testing		0	0	0	0	0	0	0	92	18	110	110
		2	0		Cell Structure		2,286	0	0	457	2,743	4,731	0	10	948	5,690	8,433
		3	0		Universal Robot		3,950	309	0	852	5,110	247	0	0	49	296	5,406
		4	0		Manipulator System		0	0	0	0	0	0	0	0	0	0	0
		5	0		Maintenance Support Equipment		1,672	348	0	404	2,424	62	0	98	32	191	2,615
		6	0		Infrastructure		0	0	0	0	0	619	0	0	124	743	743
	9	0	0		Service Cell		0	0	0	0	0	0	0	0	0	0	0
	10	0	0		Test Module Handling Cell		2,618	506	0	576	3,699	2,249	161	82	567	3,059	6,758
		1	0		Assembly and Testing		0	0	0	0	0	0	0	66	13	79	79
		2	0		Cell Structure		686	0	0	137	823	1,954	0	11	393	2,358	3,181
		3	0		Manipulator Systems		669	165	0	167	1,000	0	0	0	0	0	1,000
		4	0		Bridge Crane		857	0	0	171	1,029	86	0	5	18	109	1,138
		5	0		Maintenance Suprt Equip		397	99	0	99	595	21	0	0	4	25	620
		6	0		Infrastructure		9	0	0	2	11	188	0	0	138	326	338
	11	0	0		PIE Hot Cell		7,125	362	0	14	7,502	1,427	97	65	13	1,602	9,104
		1	0		Assembly and Testing		0	0	0	0	0	0	0	65	13	79	79
		2	0		Cell Structure		3,839	0	0	0	3,839	893	0	0	0	893	4,732
		3	0		Manipulator Systems		3,214	0	0	0	3,214	7	0	0	0	7	3,221
		4	0		Bridge Crane		0	0	0	0	0	63	0	0	0	63	63
		5	0		Infrastructure		0	0	0	0	0	419	0	0	0	419	419
		6	0		Examination Equipment		0	0	0	0	0	0	0	0	0	0	0
		7	0		Transportation Equipment		71	0	0	14	86	46	0	0	0	46	132
	12	0	0		Shielded Glove Box Laboratory		7,614	604	0	657	8,875	750	302	71	164	1,287	10,163
		1	0		Assembly and Testing		0	0	0	0	0	0	0	71	14	86	86
		2	0		Struct and Suprt Systems		7,614	0	0	657	8,271	750	0	0	150	900	9,171
		3	0		Examination Equipment		0	0	0	0	0	0	0	0	0	0	0
	13	0	0		Tritium Laboratory		8,150	7,478	536	2,603	18,767	179	3,398	1,170	2,421	7,167	25,934
		1	0		Assembly and Testing		0	680	215	179	1,073	0	680	215	895	1,789	2,861
		2	0		Tritium Facilities Hot Cell		3,950	4,079	215	1,127	9,371	107	1,359	857	382	2,705	12,076
		3	0		Gloveboxes		4,200	2,719	107	1,298	8,324	71	1,359	98	1,145	2,673	10,997
	14	0	0		Maintenance Systems		0	0	0	0	0	1,970	0	591	512	3,073	3,073
	15	0	0		Waste Storage Cell		286	32	0	48	366	48	48	0	0	96	461
	16	0	0		Storage Cell		1,905	16	0	0	1,921	306	32	0	0	338	2,259
3	**0**	**0**	**0**		**System Installation and Checkout**	**0**	**0**	**0**	**0**	**0**	**0**	**1,500**	**0**	**0**	**0**	**1,500**	**1,500**
	1	0	0		Installation												
	2	0	0		Facility Verification Testing												

The TECs for other facilities were not changed. These were 95.4 MICF for Test Facilities (WBS 2), 40.1 MICF for Target Facility (WBS 3), 105.5 MICF for Conventional Facilities (WBS 5) and 11.1 MICF for Central Control and Common Instrument (WBS 6) as shown in Tables 4, 5, 7 and 8 respectively.

(4) Development Costs during the Construction Phase

The former estimated construction cost was 488 MICF as shown in Table 1, with the assumption of completion of development before the construction phase, while EVEDA activities and their cost were not clear at the time (1999). Also the newly estimated construction cost 484 MICF as shown in Table 2 is based on the same assumption. However, EVEDA cost 72 MICF mentioned in the report for the Task DI93 is not enough to complete all development, especially those of the Accelerator. Therefore, some additional cost will be needed in the construction phase for that development. As shown in Table 9, this development is to be carried out within the framework of the Construction, Operation and Decommissioning Activity (CODA). To accomplish these activities, the duration of the first stage was extended from five to seven years.

This development consists of testing (and minor modification, if needed) of components of the accelerator. In this stage, costs for the testing seem to be dominated by that for testing of a prototype RFQ. With the assumption of RFQ testing time of 6240 h (= 40h/week x 52weeks/year x 3year), required power 1.56 MW (roughly estimated 1.6×10^{-19}J/eV x 5MeV x $1/1.6\times10^{-19}$C x 0.125C/s x 2.5) and international average rate 0.103 ICF/kWh [2], the cost of electric power is 1.00 MICF. With the assumption of testing personnel consisting of two Managers (195kICF/year/person), eight Engineers (161kICF/year/person) and twelve Laborers (98kICF/year/person), the personnel cost in three years is 8.56 MICF. The minimum required cost for this test would be about 10 MICF.

Table 5 Cost for Target Facility.

Currency Units=kilo IFMIF Currency Factor						Total Estimated Capital Cost (TEC)											
						Off-Site	Off-IFMIF Site					On-Site At IFMIF					
						Off-Site	Industry		Instit'al		Off-site	Const.	Contractor	Instit'al		On-site	
WBS					Element	Facil.Manag.	Mat'l/Lab	Engin'g	Engin'g	AFI	Total	Mat'l/Lab	Engin'g	Engin'g	AFI	Total	
1	2	3	4	5		(b)	(c)	(d)	(e)	(f)	(g)	(h)	(i)	(j)	(k)	(l)	(m)
3	**0**	**0**	**0**	**0**	**Target Facility**	**5,395**	**20,933**	**2,244**	**2,516**	**2,569**	**28,263**	**3,343**	**2,510**	**251**	**305**	**6,409**	**40,068**
	1	**0**	**0**	**0**	**Subsystem Management**	**5,395**											**5,395**
		1	0	0	Project Management and Administration		0	975	98	54	1,126						1,126
		2	0	0	Systems Engineering		0	966	97	53	1,116						1,116
		3	0	0	Environment., Safety & Health Document.		0	712	644	68	1,424						1,424
		4	0	0	Quality Assurance		0	805	81	44	930						930
		5	0	0	Other Costs		0	762	0	38	800						800
	2	**0**	**0**	**0**	**Subsystems**		**20,933**	**2,244**	**2,516**	**2,569**	**28,263**	**0**	**0**	**0**	**0**	**0**	**28,263**
		1	0	0	Lithium Target System		1,243	306	805	235	2,589	0	0	0	0	0	2,589
			1	0	Assembly and Testing		0	0	0	0	0	0	0	0	0	0	0
			2	0	Components		1,243	306	805	235	2,589	0	0	0	0	0	2,589
				1	Target Assembly		719	78	644	144	1,585	0	0	0	0	0	1,585
				2	Beam-Target		524	228	161	91	1,004	0	0	0	0	0	1,004
				3	Target-Test Cell Interface		0	0	0	0	0	0	0	0	0	0	0
		2	0	0	Lithium Cooling System		9,941	664	697	1,130	12,432	0	0	0	0	0	12,432
			1	0	Assembly and Testing		0	0	0	0	0	0	0	0	0	0	0
			2	0	Components		9,941	664	697	1,130	12,432	0	0	0	0	0	12,432
				1	Main Li Loop		5,367	349	322	604	6,642	0	0	0	0	0	6,642
				2	Primary Heat Removal System		4,058	299	322	468	5,147	0	0	0	0	0	5,147
				3	Secondary Heat Removal System		516	16	53	58	643	0	0	0	0	0	643
				4	Tertiary Heat Removal System (Water Cooling)		0	0	0	0	0	0	0	0	0	0	0
		3	0	0	Lithium Purification & Monitoring System		4,822	951	966	674	7,412	0	0	0	0	0	7,412
			1	0	Assembly and Testing		0	0	0	0	0	0	0	0	0	0	0
			2	0	Components		4,822	951	966	674	7,412	0	0	0	0	0	7,412
				1	Li Purification System		3,254	715	483	445	4,897	0	0	0	0	0	4,897
				2	Impurity Monitoring System		1,567	236	483	229	2,515	0	0	0	0	0	2,515
		4	0	0	Lithium Recovery System		10	2	16	3	31	0	0	0	0	0	31
		5	0	0	Control System		4,917	322	32	527	5,799	0	0	0	0	0	5,799
		6	0	0	Ventilation System		0	0	0	0	0	0	0	0	0	0	0
		7	0	0	Maintenance Systems		0	0	0	0	0	0	0	0	0	0	0
	3	**0**	**0**	**0**	**Installation and Checkout**		**0**	**0**	**0**	**0**	**0**	**3,343**	**2,510**	**251**	**305**	**6,409**	**6,409**
		1	0	0	Installation		0	0	0	0	0	3,016	1,746	175	247	5,184	5,184
		2	0	0	Verification Testing		0	0	0	0	0	98	161	16	14	289	289
		3	0	0	Startup		0	0	0	0	0	229	603	60	45	937	937

Table 6 Cost for Accelerator Facility.

WBS	Element	Total Estimated Capital Cost (TEC)											
	Currency Units=kilo IFMIF Currency Factor		Off-IFMIF Site					On-Site At IFMIF					
		Off-Site	Industry		Instit'al		Off-site	Const. Contractor		Instit'al		On-site	
1 2 3 4 5		Facil.Manag. (b)	Mat'l/Lab (c)	Engin'g (d)	Engin'g (e)	AFI (f)	Total (g)	Mat'l/Lab (h)	Engin'g (i)	Engin'g (j)	AFI (k)	Total (l)	(m)
4 0 0 0 0	**Accelerator Facility (1st Stage)**	**9,240**	**52,845**	**19,251**	**6,330**	**15,958**	**94,383**	**11,088**	**3,018**	**100**	**3,349**	**17,555**	**121,178**
1 0 0 0	**Accelerator Facility Management**	**9,240**											
1 0 0	Project Management and Administration		0	2,800	0	280	3,080						3,080
2 0 0	Systems Engineering		0	2,800	0	280	3,080						3,080
3 0 0	Environment., Safety & Health Document.		0	1,400	0	140	1,540						1,540
4 0 0	Quality Assurance		0	1,400	0	140	1,540						1,540
2 0 0 0	**Subsystems**		**52,845**	**19,251**	**6,330**	**15,958**	**94,383**	**0**	**0**	**0**	**0**	**0**	**94,383**
1 0 0	Accelerator Equipment Preliminary Design		0	5,800	5,300	1,700	12,800	0	0	0	0	0	12,800
2 0 0	Accelerator Equipment Physics		0	2,151	0	323	2,473	0	0	0	0	0	2,473
3 0 0	Accelerator #1 (Castor)		50,025	9,970	830	13,283	74,108						74,108
1 0	Injector		1,200	600	100	380	2,280						2,280
2 0	RFQ System		3,000	500	300	570	4,370						4,370
3 0	DTL System		13,500	1,450	200	2,273	17,423						17,423
4 0	HEBT System		1,080	300	170	155	1,705						1,705
5 0	RF Drive Loop			1,910	60	296	2,266						2,266
6 0	Accelerator & HEBT Thermal Control			1,130		170	1,300						1,300
7 0	RF Power System		31,245	4,080	0	9,440	44,765						44,765
	RF Power System		0	0	0	0	0						0
1	RF Control Systems		2,726	303	0	1,060	4,089						4,089
2	RF Predriver Systems		1,364	151	0	530	2,045						2,045
3	RF Driver & Final Power Amplifier Systems		16,994	2,500	0	3,899	23,393						23,393
4	RF Transport Systems		3,410	379	0	1,326	5,115						5,115
5	Cavity Resonance Control Systems		1,364	152	0	531	2,047						2,047
6	Switchgear Systems		1,310	142	0	508	1,960						1,960
7	Cooling Systems		0	0	0	0	0						0
8	RF Station Control & Monitoring Systems		1,350	150	0	525	2,025						2,025
9	Integration Equipment and Services		2,727	303	0	1,061	4,091						4,091
4 0 0	Accelerator #2 (Pollux)		0	0	0	0	0						0
5 0 0	Beam Calibration Dumps		820	330	0	173	1,323						1,323
6 0 0	Accelerator System Control		2,000	400	200	390	2,990						2,990
7 0 0	Accelerator Support Systems		0	600	0	90	690						690
8 0 0	Maintenance Systems		0	0	0	0	0						0
3 0 0 0	**Subsystem Installation and Checkout**		**0**	**0**	**0**	**0**	**0**	**11,088**	**3,018**	**100**	**3,349**	**17,555**	**17,555**
1 0 0	Accelerator #1 (Castor)							11,088	3,018	100	3,349	17,555	17,555
1 0	Injector System							450	125	0	115	690	690
2 0	RFQ System							750	150	0	135	1,035	1,035
3 0	DTL Tank #1 System							150	400	0	83	633	633
4 0	DTL Tank #2-#5 System							400	500	0	135	1,035	1,035
5 0	HEBT System							400	300	0	70	770	770
6 0	RF Systems							5,738	383	0	2,142	8,263	8,263
7 0	Beam Dump Systems							700	160	0	129	989	989
8 0	Full Power Acceptance Test (125mA)							2,000	1,000	100	465	3,565	3,565
9 0	Accelerator System Control							500	0	0	75	575	575
2 0 0	Accelerator #2 (Pollux)							0	0	0	0	0	0
4 0 0 0 0	**Accelerator Facility (2nd Stage)**	**3,300**	**50,709**	**8,548**	**970**	**12,997**	**73,224**	**10,488**	**2,758**	**100**	**3,362**	**16,708**	**93,233**
1 0 0 0	**Accelerator Facility Management**	**3,300**											
1 0 0	Project Management and Administration		0	1,000	0	100	1,100						1,100
2 0 0	Systems Engineering		0	1,000	0	100	1,100						1,100
3 0 0	Environment., Safety & Health Document.		0	500	0	50	550						550
4 0 0	Quality Assurance		0	500	0	50	550						550
2 0 0 0	**Subsystems**		**50,709**	**8,548**	**970**	**12,997**	**73,224**	**0**	**0**	**0**	**0**	**0**	**73,224**
1 0 0	Accelerator Equipment Preliminary Design		0			0	0	0	0	0	0	0	0
2 0 0	Accelerator Equipment Physics		0	1,924	0	289	2,213	0	0	0	0	0	2,213
3 0 0	Accelerator #1 (Castor)		0	0	0	0	0						0
4 0 0	Accelerator #2 (Pollux)		48,709	5,724	770	12,244	67,447						67,447
1 0	Design Updates		0	500	0	100	600						600
2 0	Injector System		1,200	600	100	380	2,280						2,280
3 0	RFQ System		3,000	500	300	570	4,370						4,370
4 0	DTL System		13,500	0	200	2,055	15,755						15,755
5 0	HEBT System		1,080	300	170	155	1,705						1,705
6 0	RF Power Supply System		29,929	3,824		8,984	42,737						42,737
	RF Power System		0	0	0	0	0						0
1	RF Control Systems		2,550	283	0	992	3,825						3,825
2	RF Predriver Systems		1,275	142	0	496	1,913						1,913
3	RF Driver & Final Power Amplifier Systems		16,541	2,338	0	3,776	22,655						22,655
4	RF Transport Systems		3,188	354	0	1,240	4,782						4,782
5	Cavity Resonance Control Systems		1,275	142	0	496	1,913						1,913
6	Switchgear Systems		1,250	140	0	487	1,877						1,877
7	Cooling Systems		0	0	0	0	0						0
8	RF Station Control & Monitoring Systems		1,300	142	0	505	1,947						1,947
9	Integration Equipment and Services		2,550	283	0	992	3,825						3,825
5 0 0	Beam Calibration Dumps		0	0	0	0	0						0
1 0	Movable Beam Calibration Dump		0	0	0	0	0						0
2 0	Fixed Beam Dump		0	0	0	0	0						0
6 0 0	Accelerator System Control		2,000	400	200	390	2,990						2,990
7 0 0	Accelerator Support Systems		0	500	0	75	575						575
8 0 0	Maintenance Systems		0	0	0	0	0						0
3 0 3 0	**Subsystem Installation and Checkout**		**0**	**0**	**0**	**0**	**0**	**10,488**	**2,758**	**100**	**3,362**	**16,708**	**16,708**
1 0 0	Accelerator #1 (Castor)							0	0	0	0	0	0
2 0 0	Accelerator #2 (Pollux)							10,488	2,758	100	3,362	16,708	16,708
1 0	Injector System							450	125	0	115	690	690
2 0	RFQ System							750	150	0	135	1,035	1,035
3 0	DTL Tank #1 System							150	300	0	60	510	510
4 0	DTL Tank #2-#5 System							400	500	0	225	1,125	1,125
5 0	HEBT System							400	300	0	130	830	830
6 0	RF Systems							5,738	383	0	2,142	8,263	8,263
7 0	Full Power Acceptance Test (125mA)							2,000	1,000	100	465	3,565	3,565
8 0	Accelerator System Control							600	0	0	90	690	690

In case modifications are needed after the testing, additional costs for the modification would be needed. The cost for one set of Injector (2.28 MICF) and RFQ (4.37 MICF) is 6.65 MICF. With consideration of the engineering costs for design modification, the total required cost for a new Injector and RFQ would be roughly 10 MICF.

(5) Operation Cost in the CODA Phase

The operating cost can be roughly estimated in this stage with some assumptions. The operation costs mainly consist of Personnel Cost, Cost of Electrical Power, and Spare Parts Costs. The Personnel Cost was estimated with assumption that required personnel are 68 Engineers and 98 Laborers for crews of four shifts. The cost is 20.6 MICF/year (= 161 kICF x 68 + 98 kICF x 98). The Cost of Electricity was estimated with assumptions of a Japanese site. The fee depends on the facility scale (50 MVA in IFMIF case) and amount of electricity used (kWh). The cost is 34.6 MICF/year (= 8.9 MICF + 25.7 MICF) and 21.7 MICF/year (= 8.9 MICF + 0.5 x 25.7 MICF) for 250 mA and 125 mA operations, respectively. The spare parts cost was estimated as 24.0 MICF/year with assumption that the cost is 5% of the total construction cost. As a result, the operation cost was roughly estimated as 70 MICF/year and 80 MICF/year for 125 mA and 250 mA operations respectively.

Table 7 Cost for Conventional Facilities.

Currency Units=kilo IFMIF Currency Factor	Total Estimated Capital Cost (TEC)											
		Off-IFMIF Site					On-Site At IFMIF					
	Off-Site	Industry		Instit'al		Off-site	Const. Contractor		Instit'al		On-site	
WBS Element	Facil.Manag.	Mat'l/Lab	Engin'g	Engin'g	AFI	Total	Mat'l/Lab	Engin'g	Engin'g	AFI	Total	
1 2 3 4 5	(b)	(c)	(d)	(e)	(f)	(g)	(h)	(i)	(j)	(k)	(l)	(m)
5 0 0 0 0 Conventional Facilities (1st Stage)	**2,461**	**24,684**	**1,726**	**0**	**38**	**26,448**	**54,025**	**2,421**	**0**	**205**	**56,652**	**85,561**
1 0 0 0 Conventional Facility Management	**2,461**											**2,461**
1 0 0 Project Management and Administration			975					488				
2 0 0 Systems Engineering			161					32				
3 0 0 Environment., Safety & Health Document.			403					0				
4 0 0 Quality Assurance			161					242				
2 0 0 0 Buildings		**7,126**	**760**	**0**	**38**	**7,924**	**32,405**	**1,069**	**0**	**0**	**33,474**	**41,398**
1 0 0 Accelerator Complex		1,112	129	0	38	1,279	4,046	193	0	0	4,240	5,519
2 0 0 Target Complex		0	386	0	0	386	23,874	773	0	0	24,647	25,034
3 0 0 Test and Examination Complex		2,682	64	0	0	2,746	268	13	0	0	281	3,027
4 0 0 Building High Bay		3,331	129	0	0	3,460	330	26	0	0	356	3,816
5 0 0 Support Facilities		0	26	0	0	26	2,057	64	0	0	2,122	2,147
6 0 0 Stack		0	26	0	0	26	1,829	0	0	0	1,829	1,854
3 0 0 0 Plant Services		**17,558**	**966**	**0**	**0**	**18,524**	**19,567**	**1,352**	**0**	**0**	**20,919**	**39,443**
1 0 0 Heating, Ventilation and Air Conditioning		3,515	258	0	0	3,773	4,575	322	0	0	4,897	8,670
2 0 0 Power System Substation		4,558	193	0	0	4,751	2,051	129	0	0	2,180	6,930
3 0 0 Heat Rejection System		2,236	129	0	0	2,364	6,133	386	0	0	6,520	8,884
4 0 0 Utility System		229	26	0	0	254	330	26	0	0	356	610
5 0 0 Radioactive Waste Treatment Systems		5,730	258	0	0	5,987	5,699	386	0	0	6,085	12,073
6 0 0 Electric System		1,065	77			1,142	479	77	0	0	556	1,698
7 0 0 Central Vacuum System		227	26			253	299	26			325	577
4 0 0 0 Site Improvements		**0**	**0**	**0**	**0**	**0**	**2,053**	**0**	**0**	**205**	**2,259**	**2,259**
1 0 0 Roads and Parking						0					0	0
2 0 0 Grading and Landscaping						0					0	0
3 0 0 Storm Drainage						0					0	0
5 0 0 0 0 Conventional Facilities (2nd Stage)	**457**	**5,191**	**412**	**0**	**38**	**5,641**	**11,801**	**811**	**0**	**1,227**	**13,839**	**19,937**
1 0 0 0 Conventional Facility Management	**457**											**457**
1 0 0 Project Management and Administration			156					156				
2 0 0 Systems Engineering			32					16				
3 0 0 Environment., Safety & Health Document.			64					0				
4 0 0 Quality Assurance			16					16				
2 0 0 0 Buildings		**1,112**	**142**	**0**	**38**	**1,292**	**4,438**	**219**	**0**	**0**	**4,657**	**5,949**
1 0 0 Accelerator Complex		1,112	142	0	38	1,292	4,438	219	0	0	4,657	5,949
2 0 0 Target Complex		0	0	0	0	0	0	0	0	0	0	0
3 0 0 Test and Examination Complex		0	0	0	0	0	0	0	0	0	0	0
4 0 0 Building High Bay		0	0	0	0	0	0	0	0	0	0	0
5 0 0 Support Facilities		0	0	0	0	0	0	0	0	0	0	0
6 0 0 Stack		0	0	0	0	0	0	0	0	0	0	0
3 0 0 0 Plant Services		**4,078**	**270**	**0**	**0**	**4,349**	**7,363**	**592**	**0**	**1,227**	**9,182**	**13,531**
1 0 0 Heating, Ventilation and Air Conditioning		778	64	0	0	842	750	129	0	0	879	1,722
2 0 0 Power System Substation		0	0	0	0	0	0	0	0	0	0	0
3 0 0 Heat Rejection System		2,236	129			2,364	6,133	386	0	1,227	7,746	10,111
4 0 0 Utility System		0	0	0	0	0	0	0	0	0	0	0
5 0 0 Radioactive Waste Treatment Systems		0	0	0	0	0	0	0	0	0	0	0
6 0 0 Electric System		1,065	77	0	0	1,142	479	77	0	0	556	1,698
7 0 0 Central Vacuum System						0					0	0
4 0 0 0 Site Improvements		**0**	**0**	**0**	**0**	**0**	**0**	**0**	**0**	**0**	**0**	**0**

(6) Summary

The estimated construction cost for the reduced cost IFMIF was 484 MICF, which was little changed from that in the former estimate even with the change in staged construction, where only the second accelerator and its relating facilities are to be constructed in the second stage of the two-stage construction. Slight changes in the costs for Project Management and Accelerator Facility were mainly due to reduction of the construction duration. There were only small changes in IFMIF design during KEP.

Other than the construction costs, additional development costs of 10 – 20 MICF would be needed mainly for RFQ testing (and modification) during the construction phase, since EVEDA cost of 72 MICF is not enough to complete all development.

The operation cost was very roughly estimated to be 70 – 80 MICF/year depending on D^+ beam(s) current.

References

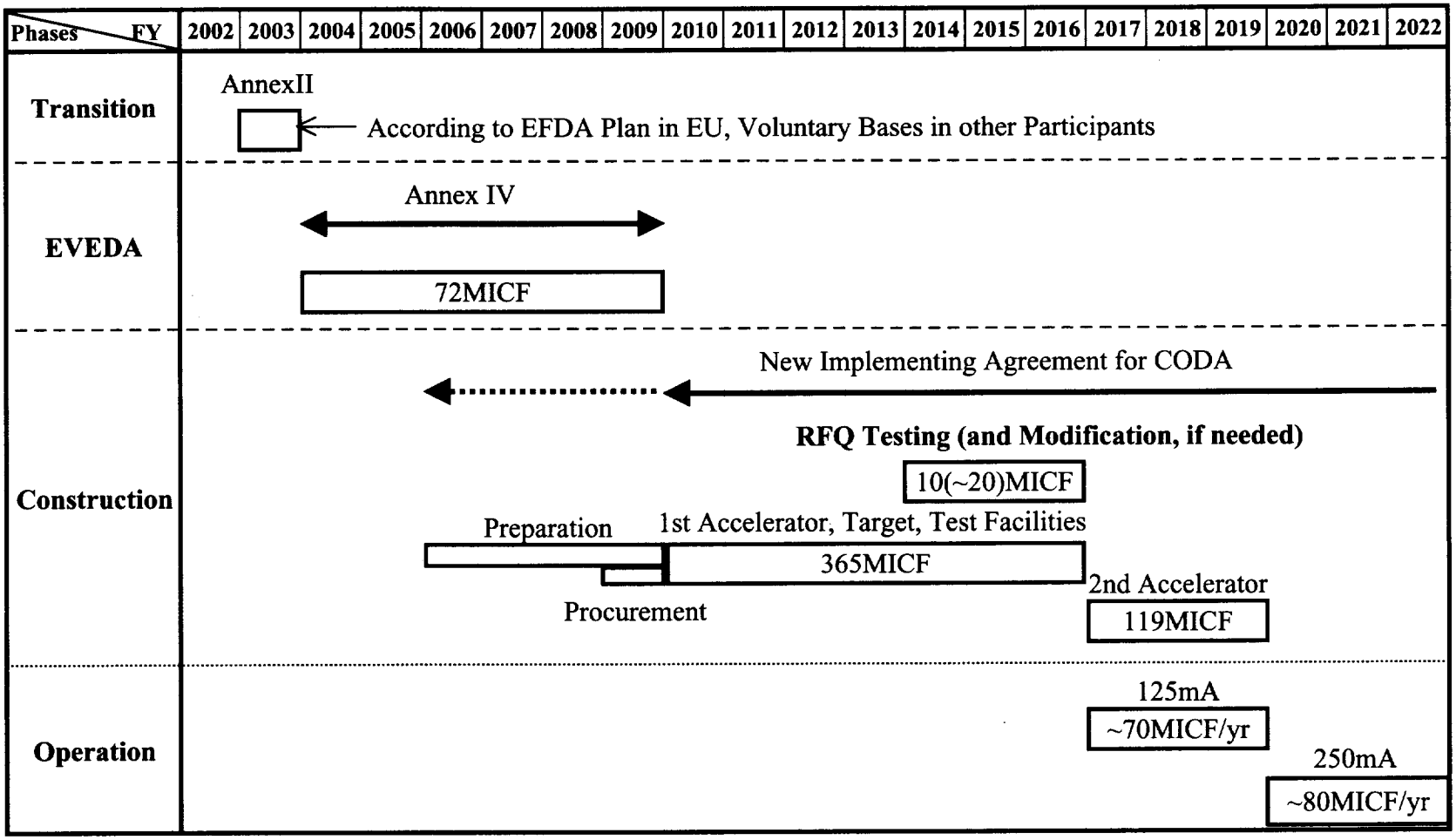
[1] Fusion Neutronics Laboratory (Ed. M. Ida et al.), IFMIF International Fusion Materials Irradiation Facility Conceptual Design Activity Reduced Cost Report a Supplement to the CDA by the IFMIF Team, JAERI-Tech 2000-014 (2000).

[2] M. J. Rennich (Ed.), IFMIF International Fusion Materials Irradiation Facility Conceptual Design Activity Cost Report, ORNL Report, ORNL/M-5502 (1996).

Table 8 Cost for central Control and Common Instrument.

Currency Units=kilo IFMIF Currency Factor						Total Estimated Capital Cost (TEC)											
						Off-Site	Off-IFMIF Site					On-Site At IFMIF					
WBS					Element	Off-Site	Industry		Instit'al		Off-site	Const. Contractor		Instit'al			On-site
						Facil.Manag.	Mat'l/Lab	Engin'g	Engin'g	AFI	Total	Mat'l/Lab	Engin'g	Engin'g	AFI	Total	
1	2	3	4	5		(b)	(c)	(d)	(e)	(f)	(g)	(h)	(i)	(j)	(k)	(l)	(m)
					(1st Stage)												
6	**0**	**0**	**0**	**0**	**Central Control and Common Instrument**	**512**	**5,815**	**660**	**0**	**287**	**6,763**	**1,354**	**802**	**0**	**97**	**2,252**	**9,527**
	1	**0**	**0**	**0**	**Facility Management**	**512**											**512**
		1	0	0	Project Management and Administration		0	78	98	9	184	0	117	195	16	328	512
	2	**0**	**0**	**0**	**Common Instrumentation Subsystems**		**4,020**	**306**	**0**	**251**	**4,577**	**1,056**	**359**	**0**	**97**	**1,511**	**6,088**
		1	0	0	Beam Instrumentation		361	0	0	36	397	0	121	0	36	157	554
		2	0	0	Radiation Monitoring		2,750	113	0	143	3,006	514	129	0	32	675	3,681
		3	0	0	Video Monitoring		311	64	0	19	395	177	40	0	11	228	623
		4	0	0	Access Control		149	32	0	9	190	171	40	0	11	221	412
		5	0	0	Announciator		90	16	0	5	112	114	24	0	7	145	257
		6	0	0	Information Display Stations		265	81	0	39	384	80	0	0	0	80	464
		7	0	0	Safety and Emergency Equipments		93	0	0	0	93	0	5	0	0	5	97
	3	**0**	**0**	**0**	**Central Control Subsystems**		**1,796**	**242**	**0**	**36**	**2,073**	**298**	**81**	**0**	**0**	**378**	**2,452**
		1	0	0	Central Control		0	0	0	0	0	0	0	0	0	0	0
		2	0	0	LAN		243	81	0	36	360	80	0	0	0	80	440
		3	0	0	Interlock Logic		0	0	0	0	0	0	0	0	0	0	0
		4	0	0	Central Display Panel		0	0	0	0	0	0	0	0	0	0	0
		5	0	0	Sequence Synchronizer		0	0	0	0	0	0	0	0	0	0	0
		6	0	0	Dummy Substation		0	0	0	0	0	0	0	0	0	0	0
		7	0	0	Operation and Configuration Control		0	0	0	0	0	0	0	0	0	0	0
	4	**0**	**0**	**0**	**System Installation and Checkout**		**0**	**113**	**0**	**0**	**113**	**0**	**362**	**0**	**0**	**362**	**475**
		1	0	0	Installation and Test		0	32	0	0	32	0	121	0	0	121	153
		2	0	0	System Verification Testing		0	81	0	0	81	0	242	0	0	242	322
					(2nd Stage)												
6	**0**	**0**	**0**	**0**	**Central Control and Common Instrument**	**381**	**668**	**129**	**0**	**80**	**876**	**203**	**64**	**0**	**27**	**294**	**1,551**
	1	**0**	**0**	**0**	**Facility Management**	**381**											**381**
		1	0	0	Project Management and Administration		0	31	98	6	135	0	39	195	12	246	381
			1	0	Administration												
			2	0	Schedule												
			3	0	Documentation												
	2	**0**	**0**	**0**	**Common Instrumentation Subsystems**		**357**	**64**	**0**	**42**	**464**	**150**	**32**	**0**	**18**	**200**	**664**
		1	0	0	Beam Instrumentation		0	0	0	0	0	0	0	0	0	0	0
		2	0	0	Radiation Monitoring		286	0	0	0	286	103	0	0	0	103	389
		3	0	0	Video Monitoring		62	0	0	0	62	35	0	0	0	35	98
		4	0	0	Access Control		0	0	0	0	0	0	0	0	0	0	0
		5	0	0	Announciator		9	0	0	0	9	11	0	0	0	11	20
		6	0	0	Information Display Stations		0	0	0	0	0	0	0	0	0	0	0
		7	0	0	Safety and Emergency Equipments		0	0	0	0	0	0	0	0	0	0	0
	3	**0**	**0**	**0**	**Central Control Subsystems**		**310**	**48**	**0**	**36**	**395**	**43**	**16**	**0**	**6**	**66**	**460**
		1	0	0	Central Control		0	0	0	0	0	0	0	0	0	0	0
		2	0	0	LAN		0	0	0	0	0	0	0	0	0	0	0
		3	0	0	Interlock Logic		0	0	0	0	0	0	0	0	0	0	0
		4	0	0	Central Display Panel		0	0	0	0	0	0	0	0	0	0	0
		5	0	0	Sequence Synchronizer		0	0	0	0	0	0	0	0	0	0	0
		6	0	0	Dummy Substation		0	0	0	0	0	0	0	0	0	0	0
		7	0	0	Operation and Configuration Control		0	0	0	0	0	0	0	0	0	0	0
	4	**0**	**0**	**0**	**System Installation and Checkout**		**0**	**16**	**0**	**2**	**18**	**10**	**16**	**0**	**3**	**28**	**46**
		1	0	0	Installation and Test		0	0	0	0	0	0	0	0	0	0	0
		2	0	0	System Verification Testing		0	0	0	0	0	0	0	0	0	0	0

Table 9 Costs for IFMIF-EVEDA and Construction.



4. Summary

In accordance with the FPCC recommendation, the Key Element Technology Phase of IFMIF (KEP) activities were carried out during 2000-2002 as an international collaboration by the European Union (EU), Japan, the Russian Federation (RF) and the United States (US) under the IEA Implementing Agreement for Fusion Materials. The objective of the KEP was to reduce the risk factors of the key technology to achieve continuous long-time operation of each subsystem. The KEP activities included the designs of subsystem and of the whole IFMIF concept that had evolved through the CDA, CDE, and the cost reduction and staging study. Important tasks were identified for the KEP phase of the IFMIF project, Task descriptions were prepared, and performing institutions identified. The Task Description report was published in 2000. Through international meetings, progresses of the Tasks were reviewed and contents of some Tasks were revised for more efficient execution. The interim results of most Tasks up to June 2001 were reviewed and published as a KEP Interim Report. Significant progress has been made since then, especially in the experimental Tasks for Accelerator, Target and Test Facilities. There was also steady progress in the Design Integration tasks. The result is that, 83 KEP Tasks were completed, and are reported in this document.

4.1 Accelerator

Twenty-six tasks related to the accelerator were completed by CEA Saclay, IAP Frankfurt, JAERI and Advanced Energy Systems (AES) Inc. The accelerator reference design was considerably improved as a result of work during the KEP phase.

The Tasks included investigations of injector options (ECR type in Saclay; volume type in IAP; filament-driven multi-cusp and mirror field ECR types in JAERI). Several one-month tests on the ECR type SILHI ion source showed 95% availability at 100 mA proton beam, demonstrating that this source is fully qualified for IFMIF. Experiments on the JAERI test stand showed that the ECR ion source is more promising than the multi-cusp type. The ECR source was chosen for the IFMIF accelerator reference design.

The beam dynamics design for the 4-vane RFQ was fully developed by two groups during the KEP phase, and is now a robust preliminary reference design. The DTL reference design was also detailed, including beam performance and cooling. Alternative technologies for the RFQ (4-rod RFQ) and other types of DTL (IH-DTL and SC-CH-DTL) were investigated to explore potential advantages to IFMIF. Component activation during operation was estimated. Analyses of HEBT were performed.

A fully operational 1000-hour test of the 200 MHz Thales Diacrode, identified as the RF source final amplifier in the reference design, showed stable operation into a resistive load at 1MW CW. This is an extremely important result, as it demonstrates that a fully qualified RF source for IFMIF is available. The investigation of power sources to be used as the IFMIF driver amplifier showed that the solid state power source is preferable in reliability.

4.2 Target

Nineteen tasks were completed at ENEA, IPPE, JAERI and the universities of Osaka and Tokyo. Some of the experimental tasks will continue into the next phase of the IFMIF project.

A water jet experiment with a flow velocity of up to 20 m/s showed that the main cause of the wave growth on the lithium target is wall roughness in the nozzle. Utilizing this result, the lithium flow experiment has been carried out with modification of the existing lithium loop. The relatively calm flow without violent waves or splashing of the fluid was obtained with the tested nozzle. As part of the evaluation of the replaceable back wall options, another water jet experiment is under preparation in order to measure the effects of the back wall curvature and the step at the nozzle joint on flow stability.

The non-flowing test for impurity control in lithium showed that chromium is more efficient as the nitrogen getter than Ti or V-Ti-alloys for high concentrations of nitrogen. On the other hand, the V-Ti alloy was an effective getter for low nitrogen concentrations. Modification of the LIFUSE III loop is in progress to obtain corrosion data with a maximum lithium flow velocity of 10 m/s.

Thermal-hydraulic analysis on the lithium target showed that there is adequate boiling margin at the lithium surface and in the lithium flow. The transient analysis of the loop showed that lithium solidification can be prevented by flow-rate control.

Safety analysis using FMEA concluded that the target safety is assured and any environmental impact is negligible.

A remote-handling concept was developed and tests are under preparation for two methods of target assembly replacement: either the whole assembly can be replaced at the lip seal by cutting and welding using a YAG laser, or partial replacement of a Bayonet type back-plate can be performed without moving the target assembly.

4.3 Test Facilities

Twenty-four tasks were completed at FZK, JAERI, CRPP-EPFL, IPP-NPI, NILPRP and the universities of Kyoto, Kyushu and Tohoku.

Calculations using the combined Li(d,xn) reaction cross sections and the newly developed Monte Carlo Code have reduced the uncertainty of the source neutron field from about ±35 to ±20%. High-resolution time-of-flight (TOF) measurements of the D-Li neutron spectra are being performed at Ed=20-40 MeV. The intermediate energy activation file IEAF-2001 was developed to deal with 679 target nuclides (Z=1-84) with approximately 51,000 excitation functions for neutrons with energy up to 50 MeV, and this has improved the reliability of activation analysis calculations. The initial activation analyses showed that the same radioisotopes are produced during exposures in IFMIF or Demonstration Fusion Reactor (DEMO) for the reduced-activation ferritic (RAF) steels.

A neutron reflector of RAF steel has been designed for the HFTM, which allows homogeneous temperature profiles, increases high-flux volume by ~20% and decreases flux gradient by ~10%. The neutron transport calculations for the MFTM showed that the shape of the neutron spectrum can almost perfectly match that for a DEMO-type blanket by using a proper neutron spectral shifter and a neutron reflector. Two 8 mm diameter fission chambers have been fabricated and irradiated in a thermal reactor, and a suitable cyclotron irradiation is scheduled. A micro-tomography system has been set up for the non-destructive verification of the structural integrity of modules in the test cell.

Detailed flow plans for all remote-handling operations of the test facilities have been developed. The design of the tritium laboratory has been improved so that the tritium processing systems meet the Japanese requirement for tritium discharge into the atmosphere of less than 5×10^{-4} Bq/cm^3.

4.4 Design Integration

Fourteen KEP tasks were completed at ENEA and JAERI.

The Main Building layout with a ground floor size of 170 m × 60 m was designed to contain the Accelerator, Target, Test Facilities and utilities. The building height is 26 m above ground and 11 m below ground, based on the results of the earlier cost reduction study. The utilities for the IFMIF were designed based on the assumption of a Japanese site. The Heating, Ventilation and Air Conditioning (HVAC) systems were classified based on the radiological risk. The estimated total electric power and the heat rejection capacity are 50 MVA and 40 MW respectively. The Radioactive Waste Treatment System was designed for liquid, gaseous and solid wastes.

Shielding calculation using the Monte Carlo computer code MCNPX with the data library LA150 showed that a 4.3 m thick front wall of the Test Cell was enough to limit the worker dose rate to less than 10 μSv/h. A bubble type counter was selected to monitor neutrons in the Test Cell. The elements of the Test Cell shielding with large cross sections for activation were identified.

The entire IFMIF system was evaluated and verified to be consistent at its operation. In Occupational Radiation Exposure (ORE) analysis, guidelines on access control and facility design were developed based on the estimated worker dose. FMEA and Event Tree analyses showed no environmental hazard.

A schedule for IFMIF construction; tasks for the next phase, Transition Phase (19 tasks); and the following phase, EVEDA (49 tasks), were proposed. The impact of a change in the planned staged construction was found to have little effect on the total construction cost.

4.5 Next Phase

The next phase of the IFMIF project, the Transition Phase starting in 2003, is needed for the smooth and effective transition from KEP to EVEDA. Experiments underway or in preparation are to be continued in the Transition Phase. The design of each subsystem will be refined based on the results from these experimental activities. A comprehensive report covering all the IFMIF activities from the CDA through the KEP will be published in 2003. This will more clearly define the IFMIF reference design and the technical achievements of the project, and will serve as the starting point for the EVEDA in 2004.

Acknowledgements

The IFMIF Executive Subcommittee is highly impressed with the dedication and enthusiasm of the IFMIF team. Also, appreciation is expressed for the continued interest and support of the Executive Committee for the IEA Implementing Agreement on Fusion Materials and the IEA-FPCC. Thanks are also extended to Dr. F. W. Wiffen and his wife, Donna Wiffen, for their contributions to the editing of the text of this KEP Report.

Appendix-A

Detailed List of Development in KEP

Classification		Item	Necessity	Development Item / Method	KEP					EVEDA
1	2				Task ID	US	EU	RF	JP	
Test Facilities	Experimental Verification of Test Methods and Modules	High Flux Test Module (HFTM)	Experimental confirmation on test apparatus (structural integrity, temp.-control, fabrication)	Construction and fabrication of prototypic rigs, capsules & test module	TF11		X			X
				Testing of thermal hydraulic and instrumentation in He-loop	TF12		X			
		Medium Flux Test Module (MFTM) T Release	Detailed design of T-release test module, test structural integrity, temp.-control and gas piping	Fabrication of real size test module Experimental verification of concept He cooling						X
		Medium Flux Test Module (MFTM) Creep Fatigue	Confirm coolant concept, test instrumentation (e.g. Extensiometers, temp.-control)	Fabrication of prototype Experimental verification						X
	Neutron distribution	Spacial neutron distribution	Reduce present uncertanties by experimental verivication	Measurement of spacial distribution of Li(d,n) reaction by varying the incoming deuteron energy	TF21				X	
		Allowance of Asymmetric Irradiation Field	If another accelerator stops or unbalance of each current generates, asymmetry field is formed. Allowance should be investigated for irradiation	From analysis of irradiation field, allowance of asymmetry is made clear in experiment of material test.	TF22				X	
		Optimisation, Qualification	Layout of suitable neutron multiplier/reflector	MCNP calculation for selection of proper geometry and material	TF23		X			X
				Design study, thermal hydraulics calculacions, verification of fabrication	TF24		X			
	Test Equipment	Vertical Test Assemblies (VTA)	Tests of exact positioning are required because space between assemblies is 1mm.	Design of test equipment, control system and sensor	TF31				X	
				Fabrication of test equipment Confirmation of running of control system and sensor						X
		Micro-tomography	Probably the only tool that allows verification of structural integrity of activated and assembled specimen capsules, rigs and modules	Design of teomographic equipment Prototype fabrication Generation of typical 3d-image recontractions	TF33		X			X
		T Laboratory and T Processing	Examination of tritium processing is needed.	Examination on Arrangement of Laboratory and processing method	TF34				X	X
		Arrangement of Test Cell System	Optimisation of arrangement of power cable, cooling water line and so on for various kind of irradiation materials is needed.	Examination of optimum arrangement	TF35				X	
		Transfer of Heavy Equipment	Equipment installing in test cell have to be set up and dismantled by remote handling.	Examination of universal robot system (URS)	TF36				X	
				Development of universal robot system (URS) Confirmation test by dummy equipment						X
		Operation in Off/Normal	Off/normal influences irradiation damage. So, the operation method should be determined in compliance with materials and irradiation	On the basis of experience on irradiation experiment, the condition of irradiation should be determined. If there is no data for operation method, the necessary data have to be taken.	TF38				X	
		Cooling Method by He	For accelerator beam-off times, temperature stability has to be verified experimentally in test module mock-ups.	Examination of response in temperature control	TF39				X	
	Revision for Cost Reduction	Optimisation of Staged Construction	Irradiation plan according to staged construction is needed.	Reviewing the plan of irradiation tests and post irradiation test	TF41				X	
		PIE Facility	PIE facility design for cost reduction is needed.	Reviewing the items of post irradiation test and the layout of PIE facility	TF42	X			X	

Classification		Item	Necessity	Development Item / Method	KEP					EVEDA
1	2				Task ID	US	EU	RF	JP	
Test Facilities	Neutronics	Source Term of d-Li Reaction	The D-Li source term is of prime importance for the neutron yield, the neutron spectrum and the nuclear responses in the test cell.	Generation of complete nuclear data files for 6,7Li up to 50 MeV by calculation	TF51		X			
				Generation of nuclear data files for 6,7Li up to 18 MeV by experiments	TF52		X			
		Nuclear Data production, evaluation and processing	Nuclear data up to 50 MeV are needed for calculation of e.g. nuclear inventory, damage parameters, nuclear heating and design of shielding.	Sensitivity analysis and data evaluation for elements like Li, C, O	TF53				X	
				Data files evaluation for Z<6 isotopes with double differential cross section	TF54		X			
				Experiments for n+Fe between 2-30 MeV followed by benchmark calculations	TF55		X			
		Shielding analyses	Determination of dose rate in different areas	Evaluation of dose rates in operative and inaccessible areas Activation calculations of test modules Definition of radiological concerns based on calculated radioactive inventory	TF56		X			
		In-situ neutron / gamma monitors	Experimental monitoring of irradiation parameters	Set-up of accelerator based target station	TF57		X			
				Construction of sub-miniature fission chamber, tests on accelerator	TF58		X			
	User specific developments	Re-evaluation of Irradiation Parameters	For the reduced cost version all irradiation paramaters needs to be recalculated taking into account staging scenarios	Calculation of 3D contourplots of relevant parameters in reference materials based on cost reduced design	TF61		X			
		Review of Concept of Materials Test	To make maximum efficiency of irradiation test with limited volume and operation time	Reviewing test items to simulate materials in fusion condition Reviewing test methods and test devices	TF62				X	
		Development of Small Specimen Test Technology	The use of SSTT allows a very effective use of limited irradiation volumens and enhances significantly materials R&D	Fracture toughness specimens>: Optimization of specimen size	TF63				X	
				Development of bend bar specimens incl. test techniques; fracture analysis	TF64		X			
				Development and irradiation of various miniaturized specimens	TF65			X		

Classification		Item	Necessity	Development Item / Method	KEP					EVEDA
1	2				Task ID	US	EU	RF	JP	
Target	Stability of Li Flow	Stability of Li Jet	Li jet may be disturbed because of high-speed, broad jet and possible erosion/corrosion of reducer nozzle inner surface.	Examination of free surface behavior in water experiment under low pressure condition	TG11				X	
				Design of Li test Loop referring the JAERI and FMIT water jet experiments and simulation results	TG12		X	X	X	
				Remodelling of existing loop and verification of its performance	TG13				X	
				Fabrication of Li test loop and verification of the performance	TG14			X		X
		Cavitation	Cavitation should be avoided for flow stability and loop integrity.	Cavitation at a joint of back wall is examined in water experiment. (Current JAERI proposal does not include replaceable back wall)	TG15		X	X		
				Cavitation at EMP is examined in a small Li loop.	TG16		X		X	
	Damage and Corrosion by Li Flow	Behavior of Erosion/Corrosion	Data base for erosion/corrosion of pipe and target assembly materials under Li flow condition.	Measurement of erosion/corrosion in an existing loop	TG21				X	
				Li flow experiments for erosion/corrosion for the Li loop materials	TG22					X
		Inspection Method	Inspection method should be established.	Design of inspection method of damage and corrosion	TG23					X
				Verification of the method of damage and corrosion in Li test loop	TG24					
	Li Purification	Diagnostic Method of Impurity in Li	On-line/off-line diagnostic and removal of impurities of T, 7Be and C,N,O	Design of both methods of impurity concentration measurement (On-line/off-line diagnostics) and impurity removal	TG31			X	X	
				Verification of the both method in Li test loop	TG32			X		X
	Diagnostics for Safety and Stability on Operation	Diagnostics of Target Temperature	To operate safely Li loop, the temperature of target is very important information.	Design of mirror arrangement to reduce neutron irradiation on camera	TG33				X	
				Experiment on existing system	TG34					X
		Measurement of Jet Thickness	Monitor of reducer nozzle deformation by erosion/corrosion of nozzle inner wall by flowing Li and irradiation by neutron beam	Examination and design of measurement methods	TG35			X	X	
				Measurement test in Li test loop	TG36			X		X
		Measurement of Assembly Size and Location	Monitor of target assembly distortion around back wall by neutron-beam irradiation	Examination and design of measurement methods	TG37				X	
				Measurement test in Li test loop	TG38					X
		Li Vapour Effect on HEBT	Quantify Li accumulation rate on HEBT inner wall	Establishment of estimation methods of Li vapour towards HEBT based on Li loop experiments	TG41			X		X
	Li Safety	Li Leak, Li Fire	Events of Li leak and Li fire should be considered.	Collection and examination of existing data of Li reaction	TG51			X	X	
				Basic tests for Li fire in air contaminated Ar gas Analysis for behaviour of 7Be and T in the Li loop	TG52			X	X	X
	Loop Integrity	Transient Behaviour of Loops	Analyses of startup/shutdown procedures including beam trip	Numerical analyses by a computer code	TG61			X	X	
	Safety Analysis	Safety Analysis for Rationalized Design	Safety analyses should be performed again, because the number of target and the concept of reserved hot/cold traps have been changed.	FMEA, Dependent Failure and Accident Sequence analyses for the changed target system	TG71		X	X		
	Remote Handling	Setup Method of Target Assembly	Development of in-situ welding/cutting methods to mount/replace target assembly using a remote handling technique	Design remote handling devices	TG81				X	
				Manufacturing of remote handling devices Establishment of key methods such as a welding between different metals by remote handling	TG82		X			X

Classification		Item	Necessity	Development Item / Method	KEP					EVEDA
1	2				Task ID	US	EU	RF	JP	
Accelerator	Injector	Ion Source	Deuteron fraction : 85% Current stability : 1% Total beam current : 155mA Energy : 100keV Life t	Estimation and verification of ECR, Multi-Cusp and Volume Type Beam orbit calculation Test of ion source (100hr in KEP, 1000hr in EVP) (Test with deuter	AC11		X		X	X
				Source analyses	AC12		X			
		Low Energy Beam Transport (LEBT)	Transmission : 90%	Suppression of beam divergence using space charge neutralisation in solenoid coil focusing	AC13		X		X	
				Suppression of fluctuation of current in pulse operation						X
				Beam analyses in RFQ matching conditions	AC14		X			
				Final layout	AC15		X			
	RF Source	Durability of RF Tube	1000hr continuous operation	Test in existing facility (1000hr)	AC21		X		X	
		Window, Circulator	Durability of windows and circulator	Development on the basis of plasma heating technology	AC22				X	
		Development Test Stand	Engineering verification of RF system	Fabrication of RF system for RFQ and DTL						X
	RFQ/DTL/HEBT	Beam Loss Estimation	Protection of discharge and beam collision in the wall of accelerator tube	Beam orbit calculation and bench mark test in existing accelerator	AC31		X		X	
		Cooling of Drift Tube	For high power accelerator	Examination of cooling method	AC32				X	
				Fabrication of model DTL, Test of cooling property						X
		Optimization of RFQ	Optimisation of electric field property in RFQ	Choise of RFQ structure	AC33		X			
				Fabrication of cold model of RFQ/DTL Measurement, optimization of electric field property	AC34		X		X	
		Optimization of DTL	Optimisation of electric field property in DTL	Choise of RFQ structure	AC35		X			
				Detailed DTL Design	AC36		X			
				Engineering evaluation of DTL at 5MeV	AC37	X				
		Matching Test of RFQ/DTL/HEBT	Optimisation of matching between each accelerator	Studies of RFQ/DTL maching	AC38		X			
				Fabrication and test of prototype						X
		Estimation of Activation	Maintenance method depends on activation of accelerator.	Estimation of activation and shielding effect from orbit calculation	AC39		X		X	
				Verification with experimental results						X
		Examination of S.C. Accelerator / Solid State AMP	Reduction of electric power and beam Loss To make the best use of independent cavity, 100kW AMP should be developed.	Examination of total system Cooperation with other accelerator development project (Neutron Spallation)						X
	Beam Diagnostics	Non-destructive Diagnostics of Beam	To accelerate large current beam without beam loss, indirect diagnostics of beam should be developed.	Development of sensor, signal processing and control	AC41		X			X

Classification		Item	Necessity	Development Item / Method	KEP					EVEDA
1	2				Task ID	US	EU	RF	JP	
Design Integration	Diagnostics for Safety on Operation	Diagnostics of Neutron Spatial Distribution	Monitor of target beam intensity	Target beam intensity measuring by neutron camera	DI11		X		X	
				Experiment on existing system						X
	Estimation of Activation	Radiation Field on the Operation	Estimation of radiation in test cell is necessary for setting design condition of maintenance equipment.	Selection of element having large cross section from investigating material constituted building and equipment	DI21		X	X	X	
				Estimation of activation	DI22			X		X
	Conventional Facilities	Design of Room Space	Room space and handling lines should be arranged exactly.	Detailed design of buildings in KEP	DI41				X	
				Final design of buildings in EVP						X
		Design of Utility	Power and water supply from the outer side should be clarified.	Detailed design of utilities in KEP	DI43				X	
				Final design of utilities in EVP						X
	Central Control & Common Instruments	Design of C.C. & C.I.	Central control should be revised for rationalized IFMIF.	Detailed design of C.C. & C.I. in KEP	DI51				X	
				Final design of C.C. & C.I. in EVP						X
	IFMIF Total System	Consistency, Operation Flow	Consistency of IFMIF total system should be checked, including analysis of operation flow from startup to shutdown.	Check of consistency and analysis of operation flow	DI61	X			X	
				Review along with progress of design						X
	Radiation Shield	Evaluation of Radiation Shield	Specifications of shielding walls should be clarified for building design.	Verification of current design by computer code and data library	DI71				X	
				Review along with progress of design and calculation method						X
	RAM, Safety Assessment	RAM for Total IFMIF	RAM should be performed for 3 stages of IFMIF	RAM for 3 stages IFMIF with detailed design	DI81				X	
				RAM for 3 stages IFMIF with final design						X
		Safety Assessment for Total IFMIF	Safety assessment should be performed for 3 stages of IFMIF.	Safety analysis and assessment for IFMIF with detailed design	DI83		X		X	
				Safety analysis and assessment for IFMIF with final design						X
				Occupational Radiation Exposure evaluation of IFMIF	DI85		X			
	License, Schedule, Cost Estimation	Licences, Regulation depending the Site	Licences and regulations about radiation, nuclear fuel material, electromagnetic wave, dangerous material, high-pressure gas, earth quake and fire should be considered. Also the local condition of nature and public should be considered.	Examination and design in obedience to regulations with an assumption on site country.	DI91				X	
				Procedures for licences						X
		Schedule and Work Items in the period of IFMIF Project	Whole schedule and work items about construction, operation and decommission should be analysed.	Analysis of schedule and work items	DI93				X	
				Review of the analysis along with progress of IFMIF project						X
		Cost Estimation	Cost estimation should be performed along with progresses of design, KEP and EVP. Operation cost and cost in life cycle should be estimated.	Cost estimation with results of KEP and detailed design	DI95				X	
				Cost estimation with results of EVP and final design						X

Appendix-B. Acronyms

AES	Advanced Energy Systems Inc.
AFI	Allowance for Indeterminates
AICS	Accelerator Instrumentation & Control System
ALARA	As Low As Reasonably Achievable
ALIP	Annular Linear Induction Pump
appm	Atomic Part per Million
AOT	Accelerator Operations & Technology
APT	Accelerator Production of Tritium
ASM	Accelerator System Model
CCDTL	Coupled Cavity Drift Tube Linac
CDA	Conceptual Design Activity
CDE	Conceptual Design Evaluation
CEBAF	Continuous Electron Beam Accelerator Facility
CODA	Construction, Operation and Decommissioning Activity
CT	Compact Tension
CW	Continuous Wave
DAC	Derived Air Concentration
DCT	Disk Compact Tension
DEMO	Demonstration Fusion Reactor
DFT	Dynamic Fracture Toughness
DI	Design Integration
dpa	Displacements per Atom
DS-Cu	Alumina Dispersion Strengthened Copper
DTL	Drift Tube Linac
ECU	European Currency Units
EDA	Engineering Design Activity
ELS	Experimental Lithium System
EMQ	Electromagnetic Quadrupoles
EPS	Electrical Power System
ESNIT	Energy Selective Neutron Irradiation Test Facility
ET	Event Tree
EVEDA	Engineering Validation and Engineering Design Activity
EVP	Engineering Validation Phase
FMEA	Failure Modes and Effects Analysis
FMIT	Fusion Materials Irradiation Test Facility
FPCC	Fusion Power Coordinating Committee
fpy	Full Power Year
FTP	File Transfer Protocol
FWHM	Full Width at Half Maximum
HAZOP	Hazard Operation
HCPB	Helium Cooled Pebble Bed
HEBT	High Energy Beam Transport
HEPA	High Efficiency Particle Absorber
HFTM	High Flux Test Module
HVAC	Heating, Ventilation, and Air Conditioning
IA-FM	Implementing Agreement for a Programme of Research and Development on Radiation Damage in Fusion Materials
IAP	Institute of Applied Physics (Institut für Angewandte Physik)
ICF	IFMIF Currency Factor
ICRP	International Commission on Radiological Protection

IEA	International Energy Agency
IHEP	Institute for High Energy Physics
INPE	Institute of Nuclear Power Engineering
IPPE	Institute of Physics and Power Engineering
ITER	International Thermonuclear Experimental Reactor
JCT	Joint Central Team
KEP	Key Element Technology Phase
LAMPF	Los Alamos Meson Physics Facility
LANSCE	Los Alamos Neutron Scattering Center
LEBT	Low Energy Beam Transport
LOCA	Loss of Coolant Accident
MFTM	Medium Flux Test Module
MTBF	Mean Time Between Failures
MTTR	Mean Time To Repair
NDT	Non-Destructive Testing
NIFS	National Institute for Fusion Science
NILPRP	National Institute for Laser, Plasma and Radiation Physics
NPI	Nuclear Physics Institute
NPSH	Net Positive Suction Head
OA	Operating Agent
ORE	Occupational Radiation Exposure
PDS	Plant Damage State
PIE	Post Irradiation Examination
PKA	Primary Knock-on Atoms
RAM	Reliability, Availability, Maintainability
RF	Radio Frequency
RFQ	Radio Frequency Quadrupole
RTNS	Rotating Target Neutron Source
sccm	Standard Cubic Centimeter
SCL	Superconducting Linac
SEM	Scanning Electron Microscope
SLAC	Stanford Linear Accelerator Center
SPRFQ	Space-Periodic RFQ
SS	Stainless Steel
SSRT	Slow Strain Rate Tensile Test
SSTT	Small Specimen Test Technology
TEC	Total Estimated Cost
TEM	Transmission Electron Microscope
TIG	Tungsten Inert Gas
TPC	Total Project Cost
TRIUMF	TRI-University Meson Facility
UPS	Uninterruptable Power Supply
URS	Universal Robot System
VIT	Vertical Irradiation Tubes
VSWR	Voltage Standing Wave Ratio
VTA	Vertical Test Assembly
WBS	Work Breakdown Structure
YAG	Yttrium Aluminum Garnet

This is a blank page.

国際単位系（SI）と換算表

表1　SI基本単位および補助単位

量	名称	記号
長さ	メートル	m
質量	キログラム	kg
時間	秒	s
電流	アンペア	A
熱力学温度	ケルビン	K
物質量	モル	mol
光度	カンデラ	cd
平面角	ラジアン	rad
立体角	ステラジアン	sr

表2　SIと併用される単位

名称	記号
分，時，日	min，h，d
度，分，秒	°，′，″
リットル	l，L
トン	t
電子ボルト	eV
原子質量単位	u

1 eV=1.60218×10^{-19}J

1 u=1.66054×10^{-27}kg

表5　SI接頭語

倍数	接頭語	記号
10^{18}	エクサ	E
10^{15}	ペタ	P
10^{12}	テラ	T
10^{9}	ギガ	G
10^{6}	メガ	M
10^{3}	キロ	k
10^{2}	ヘクト	h
10^{1}	デカ	da
10^{-1}	デシ	d
10^{-2}	センチ	c
10^{-3}	ミリ	m
10^{-6}	マイクロ	μ
10^{-9}	ナノ	n
10^{-12}	ピコ	p
10^{-15}	フェムト	f
10^{-18}	アト	a

表3　固有の名称をもつSI組立単位

量	名称	記号	他のSI単位による表現
周波数	ヘルツ	Hz	s^{-1}
力	ニュートン	N	$m\cdot kg/s^2$
圧力，応力	パスカル	Pa	N/m^2
エネルギー，仕事，熱量	ジュール	J	N·m
工率，放射束	ワット	W	J/s
電気量，電荷	クーロン	C	A·s
電位，電圧，起電力	ボルト	V	W/A
静電容量	ファラド	F	C/V
電気抵抗	オーム	Ω	V/A
コンダクタンス	ジーメンス	S	A/V
磁束	ウェーバ	Wb	V·s
磁束密度	テスラ	T	Wb/m^2
インダクタンス	ヘンリー	H	Wb/A
セルシウス温度	セルシウス度	℃	
光束	ルーメン	lm	cd·sr
照度	ルクス	lx	lm/m^2
放射能	ベクレル	Bq	s^{-1}
吸収線量	グレイ	Gy	J/kg
線量等量	シーベルト	Sv	J/kg

表4　SIと共に暫定的に維持される単位

名称	記号
オングストローム	Å
バーン	b
バール	bar
ガル	Gal
キュリー	Ci
レントゲン	R
ラド	rad
レム	rem

1 Å=0.1nm=10^{-10}m

1 b=100fm^2=10^{-28}m^2

1 bar=0.1MPa=10^5Pa

1 Gal=1cm/s^2=10^{-2}m/s^2

1 Ci=3.7×10^{10}Bq

1 R=2.58×10^{-4}C/kg

1 rad=1cGy=10^{-2}Gy

1 rem=1cSv=10^{-2}Sv

（注）

1．表1－5は「国際単位系」第5版，国際度量衡局1985年刊行による。ただし，1 eVおよび1 uの値はCODATAの1986年推奨値によった。

2．表4には海里，ノット，アール，ヘクタールも含まれているが日常の単位なのでここでは省略した。

3．barは，JISでは流体の圧力を表わす場合に限り表2のカテゴリーに分類されている。

4．EC閣僚理事会指令ではbar，barnおよび「血圧の単位」mmHgを表2のカテゴリーに入れている。

換算表

力	N(=10^5dyn)	kgf	lbf
	1	0.101972	0.224809
	9.80665	1	2.20462
	4.44822	0.453592	1

粘度　1 Pa·s(N·s/m^2)=10 P(ポアズ)(g/(cm·s))

動粘度　1 m^2/s=10^4St(ストークス)(cm^2/s)

圧力	MPa(=10bar)	kgf/cm^2	atm	mmHg(Torr)	lbf/in^2(psi)
	1	10.1972	9.86923	7.50062×10^3	145.038
	0.0980665	1	0.967841	735.559	14.2233
	0.101325	1.03323	1	760	14.6959
	1.33322×10^{-4}	1.35951×10^{-3}	1.31579×10^{-3}	1	1.93368×10^{-2}
	6.89476×10^{-3}	7.03070×10^{-2}	6.80460×10^{-2}	51.7149	1

エネルギー・仕事・熱量	J(=10^7 erg)	kgf·m	kW·h	cal(計量法)	Btu	ft·lbf	eV
	1	0.101972	2.77778×10^{-7}	0.238889	9.47813×10^{-4}	0.737562	6.24150×10^{18}
	9.80665	1	2.72407×10^{-6}	2.34270	9.29487×10^{-3}	7.23301	6.12082×10^{19}
	3.6×10^6	3.67098×10^5	1	8.59999×10^5	3412.13	2.65522×10^6	2.24694×10^{25}
	4.18605	0.426858	1.16279×10^{-6}	1	3.96759×10^{-3}	3.08747	2.61272×10^{19}
	1055.06	107.586	2.93072×10^{-4}	252.042	1	778.172	6.58515×10^{21}
	1.35582	0.138255	3.76616×10^{-7}	0.323890	1.28506×10^{-3}	1	8.46233×10^{18}
	1.60218×10^{-19}	1.63377×10^{-20}	4.45050×10^{-26}	3.82743×10^{-20}	1.51857×10^{-22}	1.18171×10^{-19}	1

1 cal= 4.18605J（計量法）

= 4.184J（熱化学）

= 4.1855J（15℃）

= 4.1868J（国際蒸気表）

仕事率　1 PS(仏馬力)

= 75 kgf·m/s

= 735.499W

放射能	Bq	Ci
	1	2.70270×10^{-11}
	3.7×10^{10}	1

吸収線量	Gy	rad
	1	100
	0.01	1

照射線量	C/kg	R
	1	3876
	2.58×10^{-4}	1

線量当量	Sv	rem
	1	100
	0.01	1

（86年12月26日現在）

IFMIF-KEP International Fusion Materials Irradiation Facility Key Element Technology Phase Report

R100
古紙配合率100%
白色度70%再生紙を使用しています